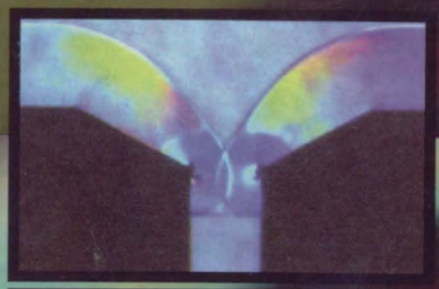

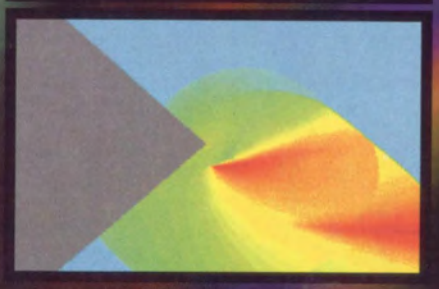

Proceedings of the
First International Conference on

Heat Transfer, Fluid Mechanics and Thermodynamics

Volume 1 ~ Part 1

HEFAT 2002

Skukuza
Kruger National Park
South Africa

8 - 10 April 2002

Editor: JP Meyer

Proceedings of the
First International Conference on

Heat Transfer, Fluid Mechanics and Thermodynamics

Volume 1 ~ Part 1

HEFAT2002

Skukuza
Kruger National Park
South Africa
8 – 10 April 2002

Editor: JP Meyer

The 1st International Conference on Heat Transfer, Fluid Mechanics and Thermodynamics was held in the Skukuza Rest Camp of the Kruger National Park from 8 to 10 April 2002. The conference was organized by HEFAT and sponsored by the South African Institute for Mechanical Engineers (SAIMechE) and the American Society for Mechanical Engineers (ASME).

Published by HEFAT, PO Box 9669, Centurion, 0046, South Africa.

ISBN: 0-86970-536-9

Acknowledgements
Figures on front cover were kindly provided by Professor BW Skews from the University of the Witwatersrand. More information can be obtained from his keynote paper in these Proceedings.

The cover page was designed by Hester Roets from the RAU.

INTERNATIONAL ADVISORY COMMITTEE

P Bansal	University of Auckland, New Zealand
A Barletta	University of Bologna, Italy
M Behnia	University of New South Wales, Australia
AE Bergles	RPI, USA
NG Choon	National University of Singapore, Singapore
G Dumitrascu	University of Iasi, Romania
SJ Eckels	Kansas State University, USA
YA Hassan	University of Texas A&M, USA
B Horbaniuc	University of Iasi, Romania
N Jambunathan	Nottingham Trent University, UK
M Kedzierski	NIST, USA
MS Kim	Seoul National University, Korea
C Machielsen	University of Delft, The Netherlands
S Moeykens	Trane, USA
K Okamoto	University of Tokyo, Japan
AT Prata	Federal University of Santa Catarina, Brazil
RK Shah	Delphi Harrison Thermal Systems, GM, USA
JR Thome	Swiss Federal Inst. of Technology, Switzerland
PS Wei	National Sun Yat-Sen University, Rep. of China

PREFACE

The purpose of most conferences and also this conference is to provide a forum for world-wide specialists in heat transfer, fluid mechanics and thermodynamics to present progress of researchers and developments, and to discuss the state of the art, the future directions and priorities in the various areas of heat transfer, fluid mechanics and thermodynamics. The additional purpose of this conference is to introduce Southern Africa to the rest of the world and to initiate research collaboration.

To start with so many papers is indeed a good beginning. More than 350 manuscripts were received and peer-reviewed and approximately 200 were accepted and are collected in these proceedings. I wish to express my sincere thanks to the reviewers whose generous efforts made it possible to select these papers. With this number of papers a meaningful forum has been created to discuss the latest developments and to come abreast with the state of the art in heat transfer, fluid mechanics and thermodynamics. As a result of the many papers received the Organizing Committee has already initiated the organization of the 2nd International Conference on Heat Transfer, Fluid Mechanics and Thermodynamics (HEFAT2003), which will hopefully be presented in June/July 2003.

Thank you to the keynote lecturers and the participants for their invaluable written and oral contributions to HEFAT2002. I also wish to extent my appreciation to the Rand Afrikaans University for hosting the conference and to the South African Institute for Mechanical Engineers (SAIMechE) and to the American Society for Mechanical Engineers (ASME) for sponsoring the conference. I also wish to extend my appreciation to the International Advisory Committee and the Organizing Committee, named and unnamed, who contributed to the success of this conference and the quality of these Proceedings.

On behalf of the Organizing Committee, I would like to welcome you all to HEFAT2002. I trust that this conference will reach the goal of bringing together scientists and engineers and inspire them to gather more knowledge in order to tackle mankind's future problems. Last but not least we would be happy if your stay in the Kruger National Park would be enjoyable, fruitful and pleasant and that you will not only see the Big Five (lion, elephant, rhino, buffalo and leopard) but also some of the best scenery in the world.

JP Meyer
Editor

CONTENTS

HEFAT2002
1st International Conference on Heat Transfer, Fluid Mechanics, and Thermodynamics
8-10 April 2002, Kruger Park, South Africa
BA1

CONSTRUCTAL DESIGN OF HEAT AND FLUID FLOW SYSTEMS

Adrian Bejan

J. A. Jones Professor of Mechanical Engineering
Duke University
Durham, NC 27708-0300, USA

ABSTRACT

This lecture is a principle-based review of a growing body of fundamental work stimulated by multiple opportunities to optimize geometric form (shape, structure, configuration, rhythm, topology, architecture, geography) in systems for heat and fluid flow. Currents flow against resistances, and by generating entropy (irreversibility) they force the system global performance to levels lower than the theoretical limit. The system design is destined to remain imperfect because of constraints (finite sizes, costs, times). Improvements can be achieved by properly balancing the resistances, i.e., by spreading the imperfections through the system. Optimal spreading means to endow the system with geometric form. The system construction springs out of the constrained maximization of global performance. This 'constructal' design principle is reviewed by highlighting applications from heat transfer engineering. Several examples illustrate the optimized internal structure of convection cooled packages of electronics. The origin of optimal geometric features lies in the global effort to use every volume element to the maximum, i.e., to pack the element not only with the most heat generating components, but also with the most flow, in such a way that every fluid packet is effectively engaged in cooling. In flows that connect a point to a volume or an area, the resulting structure is a tree with high-conductivity branches and low-conductivity interstices.

1. CONSTRUCTAL THEORY

The engineering thermodynamics literature of the last two decades reflects the important changes that have taken place in methodology in the wake of the renewed interest triggered by the energy crisis. The methods of exergy analysis, entropy generation minimization and thermoeconomics are the most established manifestations of these changes. In this paper I draw attention to an even more recent development in the method of thermodynamic optimization, namely, the construction of the system: the generation of the physical structure (topology) of the engineered system, as a result of global optimization subject to finite-resources constraints (Bejan, 2000).

The objective of the thermodynamic optimization method is to identify the ways (features, procedures) by which the system fulfills its functions while performing at the highest level possible. The objective and the constraints are key. Designs are destined to remain imperfect, because finite-size constraints such as specified heat transfer surfaces will always force currents (e.g., heat, fluid) to flow against resistances. The challenge then is to do the 'best possible' under the specified constraints. This is accomplished by spreading the imperfections through the system in optimal ways. Optimal spreading constitutes the generation of physical structure—the actual being of the engineered system.

Optimal distribution of imperfection is the principle that generates topology (construction, configuration) in flow systems. It was shown that this *constructal* principle generates morphology not only in engineered flow systems but also in naturally occurring flow systems. The thought that the constructal principle is a law of physics that accounts for the generation of flow structure everywhere is *constructal theory* (Bejan, 2000).

Important in design work is the reminder that in the beginning the physical configuration of the system is free to change. The configuration is the chief unknown, and its selection is the route to higher performance. The system is free to morph into better and better structures. The examples collected in this paper illustrate how the geometric structure of heat and fluid flow systems is derived from principle—the constructal principle of objective and constraints.

2. COOLING ELECTRONICS: OBJECTIVE AND CONSTRAINTS

Consider the main issues while designing a package of electronic components that must fit inside a given volume—the *global* constraint. The *objective* of the design is to install as uch circuitry as possible in this volume. In rough terms, this is equivalent to installing as much heat generation rate (q) as

possible, because electrical components generate heat. The highest temperatures in the package (the hot spots) must not exceed a specified value, T_{max}: this is also a global constraint, because the maximum temperature is a feature of the entire system. The exact location of the hot spots is not an issue. If the local temperature (T) rises above this allowable ceiling, the electronic functioning of the local component is threatened. In sum, the thermal design is better when q is larger. In other words, the design is better when the global thermal conductance ratio $q/(T_{max} - T_0)$ is larger, where T_0 is the initial (reference, sink) temperature of the coolant that absorbs q. Papers and reviews of the electronics cooling literature illustrate this design philosophy (Moffat and Ortega, 1988; Nakayama et al., 1988; Peterson and Ortega, 1990; Matsushima et al., 1992; Kim and Lee, 1996).

To illustrate the origin of internal structure (characteristic graininess, internal spacings) in the simplest terms, assume that the heat generation rate q is spread almost uniformly over the given volume. The electronic circuitry is mounted on equidistant vertical boards of height H, filling a space of height H, and horizontal dimensions L and W. The configuration is two-dimensional with respect to the ensuing buoyancy-driven flow, as shown in Fig. 1. The board-to-board spacing D, or the number of vertical parallel-plate channels is allowed to vary,

$$n = \frac{L}{D} \tag{1}$$

To determine the spacing D that maximizes q is a challenging task. Here I reproduce the back of an envelope method (the intersection of asymptotes) outlined first in 1984 (Bejan, 1984). The method begins with the assumptions that (a) the flow is laminar, (b) the board surfaces are sufficiently smooth to justify the use of heat transfer results for natural convection over vertical smooth walls, and (c) the maximum temperature T_{max} is closely representative of the temperature at every point on the board surface. The method consists of two steps. In the first, we identify the two possible extremes: the small-D limit and the large-D limit. In the second step, the two asymptotes are intersected to locate the D value that maximizes q.

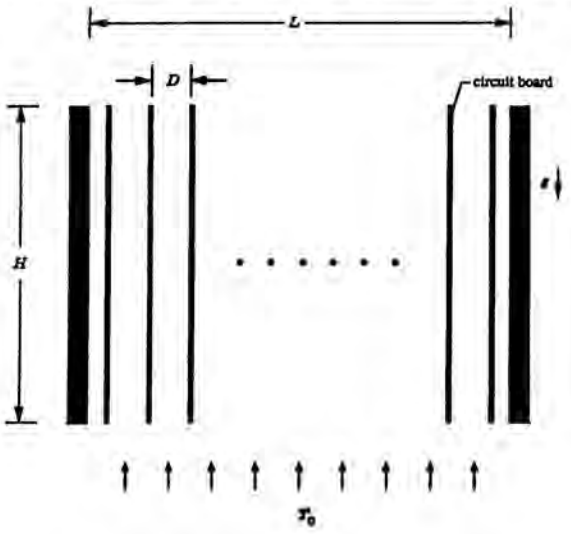

Figure 1 Two-dimensional volume that generates heat and is cooled by natural convection (Bejan, 2000).

2.1 Small Spacings. When D becomes sufficiently small, the channel formed between two boards becomes narrow enough for the flow and heat transfer to be fully developed. According to the first law we have $q_1 = \dot{m}_1 c_p (T_{max} - T_0)$ for the heat transfer rate extracted by the coolant from one of the channels of spacing D, where T_0 is the inlet temperature and T_{max} is the outlet temperature. The mass flow rate is $\dot{m}_1 = \rho(DW)U$, where the mean velocity U can be estimated by replacing $\Delta p/L$ with $\rho g\beta(T_{max} - T_\infty)$ in the Hagen-Poiseuille flow solution:

$$\rho g\beta(T_{max} - T_0) = f\frac{4}{D_h}\frac{1}{2}\rho U^2 \tag{2}$$

For laminar flow between parallel plates we have $f = 24/(UD_h/\nu)$ and $D_h = 2D$, hence

$$U = g\beta(T_{max} - T_0) \qquad D^2/(12\nu) \tag{3}$$

$$\dot{m}_1 = \rho DWU = \rho W g\beta(T_{max} - T_0)D^3/(12\nu) \tag{4}$$

The rate at which heat is removed from the entire package is $q = nq_1$, or

$$q = \rho c_p WLg\beta(T_{max} - T_0)^2 D^2/(12\nu) \tag{5}$$

In conclusion, in the $D \to 0$ limit the total heat transfer rate varies as D^2. This trend is indicated by the small-D asymptote plotted in Fig. 2.

2.2 Large Spacings. Consider next the limit in which D is large enough that it exceeds the thickness of the thermal boundary layer that forms on each vertical surface: $\delta_T \sim H\,Ra_H^{-1/4}$, where $Ra_H = g\beta H^3(T_{max} - T_0)/(\alpha\nu)$. In other words, the spacing is considered large when

$$D > H\left[\frac{g\beta H^3(T_{max} - T_0)}{\alpha\nu}\right]^{-1/4} \qquad (Pr \geq 0.5) \tag{6}$$

In this limit the boundary layers are distinct (thin compared with D), and the center region of the board-to-board spacing is occupied by fluid of temperature T_0. The number of distinct boundary layers is $2n = 2L/D$ because there are two for each D

spacing. The heat transfer rate through one boundary layer is $\bar{h}\,HW(T_{max} - T_0)$ for which $\bar{h}$ is furnished by (e.g., Bejan, 1993)

$$\frac{\bar{h}H}{k} = 0.517\,Ra_H^{1/4} \tag{7}$$

The rate of heat transfer extracted from the entire package is 2n times larger than $\bar{h}\,HW(T_{max} - T_0)$:

$$q = 2\frac{L}{D}HW(T_{max} - T_0)\frac{k}{H}0.517Ra_H^{1/4} \tag{8}$$

Equation (8) and Fig. 2 show that in the large-D limit the total heat transfer rate varies as D^{-1} as the board-to-board spacing changes (Fig. 2).

2.3 Optimal Spacings for Natural Convection. What we have determined so far are the two asymptotes of the actual (unknown) curve of q versus D. Figure 2 shows that the asymptotes intersect above what would be the peak of the actual q(D) curve. It is not necessary to determine the actual q(D) relation: the optimal spacing D_{opt} for maximum q can be estimated as the D value where Eqs. (5) and (8) intersect,

$$\frac{D_{opt}}{H} \equiv 2.3\left[\frac{g\beta(T_{max} - T_0)H^3}{\alpha\nu}\right]^{-1/4} \tag{9}$$

This D_{opt} estimate is within 20 percent of the optimal spacing deduced based on lengthier methods, such as the maximization of the q(D) relation (Bar Cohen and Rohsenow, 1984) and the

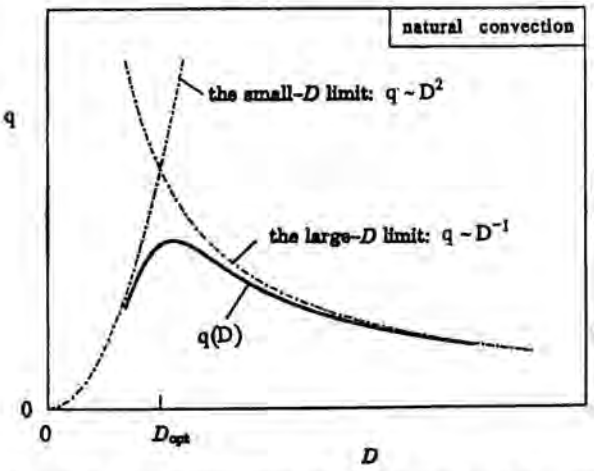

Figure 2 The intersection of asymptotes method: the maximization of the global thermal conductance of a stack of vertical plates in natural convection (Bejan, 2000).

finite-difference simulations of the complete flow and temperature fields in the package (Anand et al., 1992; Kim and Anand, 1994). An order of magnitude estimate of the maximum heat transfer rate can be obtained by substituting D_{opt} into Eq. (8),

$$q_{max} \sim 0.45k(T_{max} - T_0)\frac{LW}{H}Ra_H^{1/2} \tag{10}$$

The approximation sign is a reminder that the peak of the actual q(D) curve falls under the intersection of the two asymptotes (Fig. 2). This result also can be expressed as the maximum volumetric rate of heat generation in the H × L × W volume,

$$\frac{q_{max}}{HLW} \sim 0.45\frac{k}{H^2}(T_{max} - T_0)Ra_H^{1/2} \tag{11}$$

The assumption that the heat generation rate q is spread on equidistant vertical plates as tall as the volume was made for the sake of illustrating in the simplest terms how internal structure results from the constructal (objective and constraints) principle. Optimal internal structure is a characteristic of all systems that share the same purpose and constraints. The generality of this result is supported by many studies in which the stack of H-tall plates was replaced by arrays of internal heating elements of other shapes, for example, a package of staggered vertical plates, and a bundle of horizontal cylinders. This body of work is reviewed in Bejan (2000).

2.4 Optimal Spacings for Forced Convection. Consider now the analogous problem of installing the optimal number of heat generating boards in a space cooled by forced convection. As shown in Fig. 3, the swept length of each board is L, while the transverse dimension of the entire package is H. The width of the stack, W, is perpendicular to the plane of the figure. We retain the assumptions (a)-(c) listed under Eq. (1). The thickness of the individual board is again negligible relative to the board-to-board spacing D, and it is free to vary. The pressure difference across the package, Δp, is assumed constant and known. This is a good model for electronic systems in which several packages and other features (e.g., channels) receive their coolant *in parallel*, from the same plenum. The plenum pressure is maintained by a fan, which may be located upstream or downstream of the package.

Bejan and Sciubba (1992) showed that when the spacing D becomes sufficiently small, the overall thermal conductance of the package decreases as D^2. In the large-D limit, the overall thermal conductance decreases as $D^{-2/3}$. The intersection of the two asymptotes yields an estimate for the board-to-board spacing for maximum global thermal conductance

$$\frac{D_{opt}}{L} \equiv 2.7\left(\frac{\Delta pL^2}{\mu\alpha}\right)^{-1/4} \tag{12}$$

This spacing increases as $L^{1/2}$ and decreases as $\Delta p^{-1/4}$ with increasing L and Δp, respectively. Equation (12) underestimates by 12 percent the more exact value obtained by locating the maximum of the actual q(D) curve, and is adequate when the board surface is modeled either as uniform flux or isothermal. It has been shown that Eq. (12) holds even when the board thickness is not negligible relative to the board-to-board spacing (Mereu et al , 1993). If we use the dimensionless group Be, or Π_L (Bhattacharjee and Grosshandler, 1988; Petrescu, 1994),

$$Be = \frac{\Delta p L^2}{\mu\alpha} \tag{13}$$

so that Eq. (12) becomes $D_{opt}/L \cong 2.7Be^{-1/4}$ The way in which the design parameters influence the maximum rate of heat removal from the package can be expressed as

$$q_{max} \sim 0.6k(T_{max} - T_0)\frac{HW}{L}Be^{1/2} \tag{14}$$

$$\frac{q_{max}}{HLW} \sim 0.6\frac{k}{L^2}(T_{max} - T_0)Be^{1/2} \tag{15}$$

The similarity between the forced convection results [Eqs. (12) and (15)] and the corresponding results for natural convection cooling [Eqs. (9) and (11)] is worth noting. The role played by the Rayleigh number Ra_H in the free convection case is played in forced convection by the dimensionless group Be (or Π_L) (Petrescu, 1994).

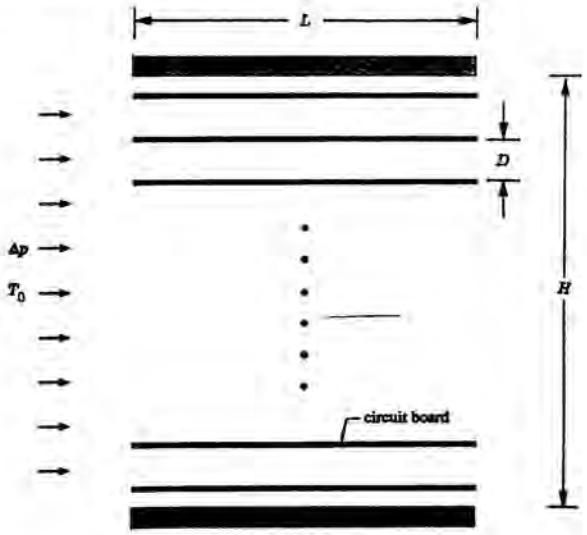

Figure 3 Two-dimensional volume that generates h eat and is cooled by forced convection (Bejan, 2000).

The optimal internal spacings belong to the volume as a whole, with its purpose and constraints, not to the individual element (e.g., L-long plate in Fig. 3) on which heat is being generated. The robustness of this conclusion becomes clear when we look at other elemental shapes for which optimal spacings have been determined. The work reviewed in Bejan (2000) shows that a volume heated by an array of staggered plates in forced convection is characterized by an internal spacing that scales with the swept length of the entire volume, L. Similarly, when the elements are cylinders in cross-flow the optimal spacing (S) is influenced the most by the overall dimension of the volume in the flow direction. The optimal spacing was determined based on the method of intersecting the asymptotes. The asymptotes were derived from the large volume of empirical data accumulated in the literature for single cylinders in cross-flow (the large-S limit) and for arrays with many rows of cylinders (the small-S limit).

3. INTERSECTING THE ASYMPTOTES

The intersection of asymptotes method (Bejan 1984, 2000) should not be confused with the method of *matched* asymptotic expansions. Matched asymptotes is an old technique of applied mathematics, in which the asymptotes are indeed fused (aligned, spliced) together through the appropriate choice of free parameters. Classical examples from fluid mechanics and heat transfer are the boundary layer solutions of Blasius (1908) and Pohlhausen (1921).

The intersection of asymptotes is quite different: it is the competition, clash, or collision of the asymptotes, not the match. It is the sharp intersection of two vastly dissimilar trends (or flow regimes, e.g., Fig. 2) that determines the spacings for optimal internal structure subject to global constraints. This competition, and how it determines optimal form is the heart of the constructal method. This method provides a much more direct route to structure optimization than the tedious and questionable (model dependent) development of the complete behavior of the system versus its varying internal structure. Not every design is important; not every point of the rounded solid-line curve sketched in Fig. 2 deserves to be determined.

The intersection of asymptotes method was applied to several important problems. First, the transition from laminar flow (viscous diffusion) to eddy motion, or rolling (organized flow) in all shear flows has been predicted on the basis of minimizing the time of transversal growth of the shear layer (Bejan, 1982, 2000). In one extreme, when the shear layer thickness is sufficiently small, viscous diffusion provides the fastest growth. In the other extreme, the rolling of the shear layer is a more effective mechanism for transporting momentum, i.e., for bringing the entire flow region to equilibrium in the shortest time possible. The intersection of these two limits yielded the *local Reynolds number criterion*

$$\frac{UD}{\nu} \sim O(10^2) \tag{16}$$

as the universal criterion that unites (predicts) all the observations on transition. In Eq. (16), U is the local

longitudinal velocity scale, and D is the local transversal length scale of the flow region. Equation (16) has been tested numerous times: for a review see Bejan (1995).

Another important phenomenon that has been predicted in most of its forms by applying the same method is Bénard convection (Nelson and Bejan, 1998). The transition from quiescent conduction to the first rolls (Fig. 4) was predicted by choosing between the two flow regimes so that the time of thermal communication across the H-thick layer is minimal. The invoked principle is the same as in the onset of turbulence, namely, the minimization of the time of approach to uniformity, and the accomplishment of minimization by selecting geometry, or flow structure.

Figure 4 is only the beginning of how the intersection of asymptotes method works in a predictive sense. Once convection is present, the choice is between a flow structure consisting of very thin vertical counterflows (cells, Fig. 5) in which adjacent streams are in intimate thermal contact, and a flow structure consisting of isolated streams (plumes, Fig. 6). Nelson and Bejan (1998) showed that if we consistently choose the configuration that maximizes thermal transport across the H-tall layer, i.e., if we intersect the two asymptotes, then all the known features of Bénard convection are predicted, especially the relationship between Nusselt number and Rayleigh number well above the onset of convection. See also the review presented in Bejan (2000).

Finally, another flow with characteristic internal structure is the flow through the cracks that develop in a solid that shrinks volumetrically during cooling ordrying. The crack size and the characteristic length scale between successive cracks have been determined based on the intersection of asymptotes method, by minimizing the overall cooling time for the entire volume (Bejan et al., 1998).

4. BALANCE BETWEEN STREAM-TRAVEL TIME AND DIFFUSION TIME

There is yet another way to see balance—optimal distribution of imperfection—as the mechanism through which the constrained system maximizes its performance. Think of the fluid that enters and bathes volumes such as those of Figs. 1 and 3, and ask how the *entire* flow region "works the hardest" toward meeting the global objective of the system. The solution is to eliminate the lazy flow regions, namely those regions where the fluid does not cool the walls. This means that we must make sure that none of the fluid leaves the system as cold as it entered. We must also eliminate the flow regions where the entire channel cross-section is choked with fluid that is practically as hot as the walls. Each ministream works the hardest when it is allowed to leave the system as soon as its fluid packets—all of them—have interacted thermally with the wall. This physical configuration is achieved when the time of longitudinal travel from inlet to exit is equal to the time of transversal diffusion across each channel.

Let us see how well this time balance works in predicting the optimal spacings reviewed in this paper, for example, the spacings between vertical plates with natural convection (Fig. 1). The longitudinal fluid travel time along each channel is

$$t_1 \sim \frac{H}{v} \tag{17}$$

where v is the vertical velocity scale for laminar boundary layer natural convection (e.g., Bejan, 1984),

$$v \sim \frac{\alpha}{H} Ra_H^{1/2} \tag{18}$$

Combined, Eqs. (17) and (18) yield the stream-flow (convection) time scale

$$t_1 \sim \frac{H^2}{\alpha} Ra_H^{-1/2} \tag{19}$$

The time of transversal thermal diffusion (t_2) can be estimated based on the viscous diffusion solution discussed in more detail in Bejan (1984, p. 213) and Bejan (1993), app. F):

$$\frac{D/2}{2(\alpha t_2)^{1/2}} \sim 1 \tag{20}$$

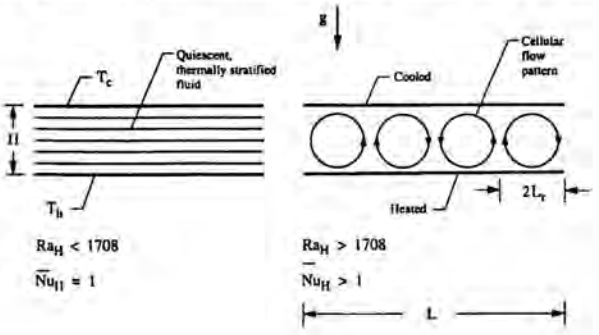

Figure 4 Horizontal fluid layer held between parallel plates and heated from below (Nelson and Bejan, 1998).

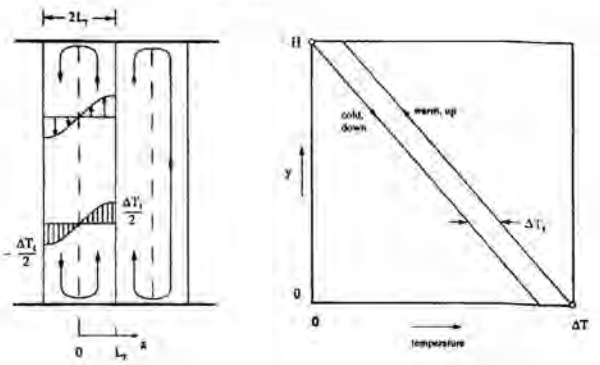

Figure 5 The geometry of the flow of Fig. 4 in the many-cells limit (Nelson and Bejan, 1998).

and note that the factor of 2 in the denominator is a peculiarity of the position (shape) of the knee in the error-function profile. Setting the t_2 scale of Eq. (20) equal to the t_1 scale of Eq. (19) we obtain

$$\frac{D}{H} \sim 4\,Ra_H^{-1/4} \tag{21}$$

This simple result is remarkable, because it reproduces the form and order of magnitude of the D_{opt} estimate obtained via the intersection of asymptotes method, Eq. (9). The same time matching argument can be used to anticipate the optimal spacing between parallel plates cooled by laminar forced convection (Fig. 3).

5. OPTIMAL FLOW PULSATIONS

More evidence that the equality of the convection and diffusion times generates optimal physical structure is provided by the discovery of optimal pulsating flow, as a means of maximizing the mass and heat transfer between two fluid reservoirs at different temperatures (Chatwin, 1975; Watson, 1983; Kurzweg and Zhao, 1984; Kurzweg, 1985). In this section we discuss only heat transfer, Fig. 7 (Rocha and Bejan, 2001). The fluid sloshes back and forth between the T_1 and T_2 reservoirs, with the time period t_p. The lateral heat transfer between the bundle of channels and the surroundings is negligible.

During the first half of the cycle, when the flow is from T_1 to T_2, the fluid coats the walls with boundary layers of temperature comparable with T_1. During the return stroke the T_2 fluid sweeps the channel, and its job is to make the closest thermal contact possible with the T_1 boundary layers created during the first stroke. The energy picked up by the T_2 fluid is then transported to the T_2 reservoir during the third stroke.

Once again, we face the problem of how to use in a best way a constrained volume. Each fluid column that fills a channel does its best when the time of residence in the channel matches the time of transversal thermal diffusion across the channel. This balance yields the optimal channel spacing, Eq. (12). This result is new. The existence of this optimal geometry has not been recognized yet in the field, where the channel geometry is assumed given, and the narrow-channel limit with Hagen-Poiseuille flow is always postulated. Recognized has been the existence of an optimal sloshing frequency ω, which maximizes the time-averaged heat transfer rate from T_1 to T_2. This result has been reported as an optimal Womersley number

$$Wo = a\left(\frac{\omega}{\nu}\right)^{1/2} \tag{22}$$

where a is the half spacing of one channel, a = D/2. Kurzweg (1985) developed optimal Wo results for parallel channels with walls as thick as the fluid channels, and wall thermal conductivity equal to the fluid thermal conductivity. He correlated the optimal results found for Pr = 0.01, 10 and 1000 by writing approximately

$$Wo \equiv \pi^{1/2}\,Pr^{-1/2} \tag{23}$$

Constructal design pinpoints not only the optimal slenderness of each channel, which is new, but also the optimal frequency found in Eq. (23). The optimal sloshing period t_p is twice the time of viscous diffusion across one channel, t_2, Eq. (20). Writing $t_p = 2t_2$ and $\omega = 2\pi/t_p$, the Womersley number definition (22) that corresponds to t_p becomes

$$Wo \sim 3.5\,Pr^{-1/2} \tag{24}$$

This result reproduces all the essential features of Eq. (23). It also provides a purely theoretical foundation for the *existence* of optimal frequencies in this class of heat and mass transfer enhancement techniques. Constructal design contributes the prediction that the proper dimensionless group for frequency is

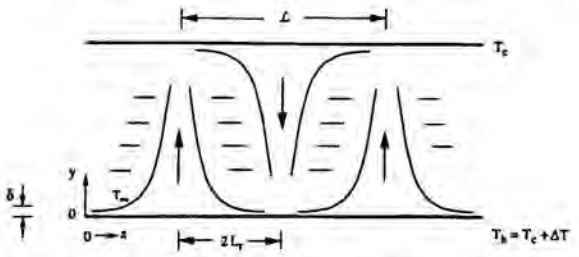

Figure 6 The geometry of the flow of Fig. 4 in the few-cells limit (Nelson and Bejan, 1998).

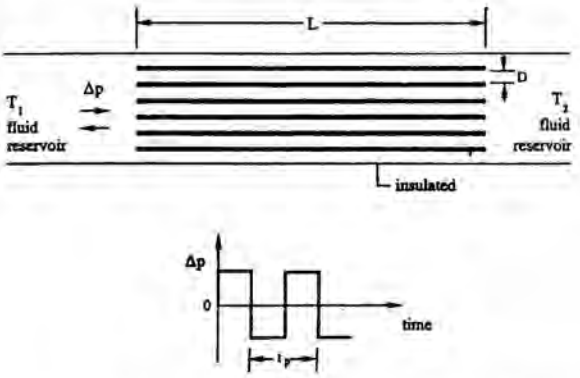

Figure 7 Insulated stack of parallel two-dimensional channels with periodic fluid flow between two end reservoirs at different temeratures (Bejan, 2000).

Wo $Pr^{1/2}$, [see Eq. (24)]. The definition of this theoretical group is $a(\omega/\alpha)^{1/2}$, which is the same as replacing ν with α in Eq. (22).

6. TREE-SHAPED FLOWS

In the constructal optimization of the volume-to-point path for heat flow it was shown that a volume subsystem of any size can have its external shape and internal details optimized such that its own volume-to-point resistance is minimal (Bejan, 1997). This principle is repeated in the optimization of increasingly larger volumes, where each new volume is an assembly of previously optimized volumes. The construction spreads, as the assemblies cover larger spaces.

As an example, consider the flow of heat from a volume to one point. The heat-flow geometry is two-dimensional. The low-conductivity material, k_0, generates heat at the uniform rate q''' per unit volume. A small (fixed) amount of high-conductivity material, k_p, is to be distributed through the k_0 material. The construction begins with the smallest volume scale (the elemental system), which is represented by the rectangular area $A_0 = H_0L_0$. The start of this sequence of volume sizes is shown in the upper-right corner of Fig. 8. the size A_0 is known and fixed by manufacturing and electrical design constraints. The system is elemental because it has only one insert of high-conductivity material. This blade has the thickness D_0, and is positioned on the long axis of the $H_0 \times L_0$ rectangle. The heat current $q'''A_0$ is guided out of A_0 through one end of the D_0 channel, which is the heat sink. The hot spots occur in the farthest corners relative to the sink.

The global volume-to-point resistance is the ratio $\Delta T_0/(q'''A_0)$, where ΔT_0 is the temperature difference between the hot spot and the heat sink. This measure is "global" because the heat current $q'''A_0$ is integrated over the system A_0, and the maximum temperature difference ΔT_0 is the excess temperature of the hot spot (or hot spots) of the elemental system: the location of the hot spots is not an issue, as long as the hot spots reside inside the system.

The composite material that fills A_0 is characterized by two numbers, the conductivity ratio $\tilde{k} = k_p/k_0$, and the volume fraction of high-conductivity material, $\phi_0 = D_0/H_0$. When $\tilde{k} >> 1$ and $\phi_0 << 1$ the global volume-to-point resistance is given by the two-term expression

$$\frac{\Delta T_0 k_0}{q'''A_0} = \frac{1}{8}\cdot\frac{H_0}{L_0} + \frac{1}{2\tilde{k}\phi_0}\cdot\frac{L_0}{H_0} \qquad (25)$$

This resistance is minimal when the ratio H_0/L_0 is equal to $2(\tilde{k}\,\phi_0)^{-1/2}$. The construction continues with the first assembly ($A_1 = H_1L_1$ in Fig. 8), which contains n_1 elemental systems, $A_1 = n_1A_0$. The heat currents produced by the elemental systems are collected by a new high-conductivity insert of thickness D_1, the left end of which is the heat sink. The hot spots are in the two right-hand corners. The global volume-to-point resistance is $\Delta T_1/(q'''A_1)$, where ΔT_1 is the excess temperature at the hot spot. The resistance can be minimized with respect to the shape parameter H_1/L_1 and the internal ratio D_1/D_0.

The same geometric optimization principle applies at larger scales. The next scale is the second construct A_2, which contains a number of first constructs (n_2, Fig. 9). The optimal external aspect ratio of the second construct is $H_2L_2 = 2$. In addition, it is possible to optimize the internal ratios of high-conductivity blade thicknesses, D_1/D_0 and D_2/D_1, where D_2 is the thickness of the central (thickest, newest) blade. In the optimized structure, the high-conductivity blades form a tree. The k_p blades are in optimal balance with the k_0 interstices: at the elemental scale, the k_p and k_0 spaces are equally important from the point of view of minimizing flow resistance.

Constructal trees look more natural if their freedom to provide easier access to their internal currents is expanded. In the elemental system of Fig. 8 (upper-right corner) it was assumed that the k_p channel stretches all the way across the volume. When this assumption is not made, we find numerically that there is an optimal spacing between the tip of the k_p channel and the adiabatic boundary of the elemental volume (Bejan, 2000). The associated reduction in global resistance is small (a few percentage points).

Another example is when the angle formed between each tributary channel and its central stem is allowed to vary. Numerical optimization of the tree structure show that there exists an optimal angle. The reduction in global flow resistance is again small.

In Fig. 9 we see the results of a fully numerical optimization of the second construct with perpendicular and constant-thickness k_p inserts (D_0, D_1, D_2), where all the other geometric parameters were allowed to vary—the aspect ratios of

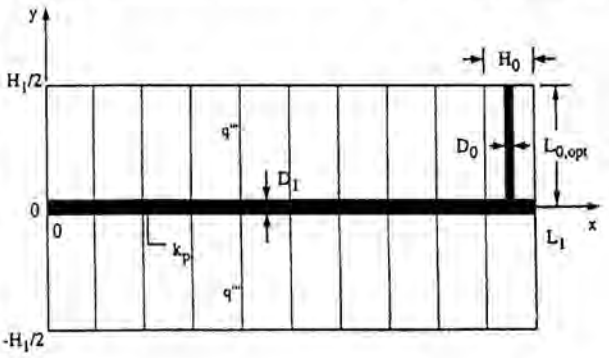

Figure 8 The first construct: a large number of elemental volumes connected to a central high-conductivity path (Bejan, 1997).

all the rectangles, large and small, the number of elemental volumes in each first construct (n_1), and the number of first constructs in each second construct (n_2). The three designs of Fig. 9 have been optimized with respect to all the parameters except n_2, and they have been drawn to scale. The figure shows the effect of fine-tuning the number n_2. This number has almost no effect on the external shape of the construct, and on the overall thermal resistance $\tilde{T} = (T_{max} - T_{min})_{min} k_0 / (q''' A_2)$. From left to right in Fig. 9, $\tilde{T}$ has the values 0.0379, 0.0354, and 0.0374.

All these minor improvements tell a very important story: the tree design is *robust* with respect to various modifications in its internal structure. This means that the global performance of the system is relatively insensitive to changes in some of the geometric details. Trees that are not identical have nearly identical performance, and nearly identical macroscopic features such as the external shape.

The same conclusions hold for many other tree-shaped flow systems, for example, fluid trees (rivers, piping networks), and convective trees (fin assemblies). These applications are reviewed in Bejan (2000). Most recently, I showed that the optimized geometry of two fluid trees arranged in counterflow is responsible for the observed proportionality (allometric law) between metabolic rate (body heat loss) and body mass raised to the power 3/4 (Bejan, 2001). In the tree counterflow, each pair of tubes in counterflow (arterial blood vs venous blood) convects one energy current in the direction of the warmer tube.

In this way, two fluid trees become one tree for heat leak by convection from the core of the animal to the ambient. Other allometric laws of physiology have been predicted in this manner (Bejan, 2000, chapter 5).

7. STRUCTURE FROM CONSTRUCTAL PRINCIPLE

We are entitled to disregard for a moment the reasoning that generated the geometries presented in this paper. We may act as natural scientists, cut open the animal—the electronics package, or the heat exchanger—and marvel at the spatial organization that we see. We marvel also at how much alike are the internal structures of contemporary systems (e.g. two competing personal computers), in the same way that a zoologist marvels at the similarity in bronchial tube sizes and numbers in two animals that have nearly the same mass. In this way we *observe* structure, and just like the natural scientist, we may go on and measure, correlate and catalogue (classify) the dimensions and patterns that we see.

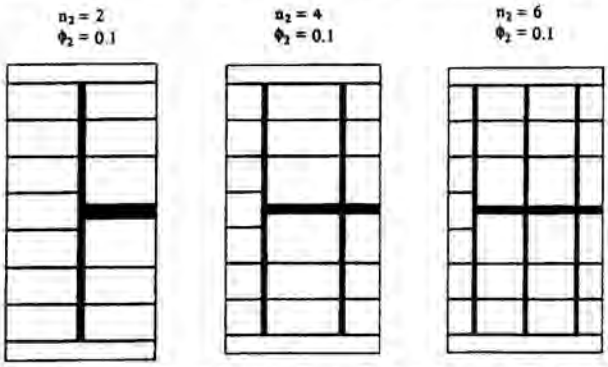

Figure 9 The second construct optimized numerically, and the effct of changing the number of first constructs, n_2 (Bejan, 2000).

In contrast with this empirical course, the results reviewed in this paper had nothing to do with observations or empiricism. We invoked consistently a single principle of purpose (conductance maximization) and constraints, and from this principle we *deduced* the optimal internal structure. We practiced theory. The discovery is that geometric form (internal structuring) emerges as the *mechanism* through which the global system achieves its objective.

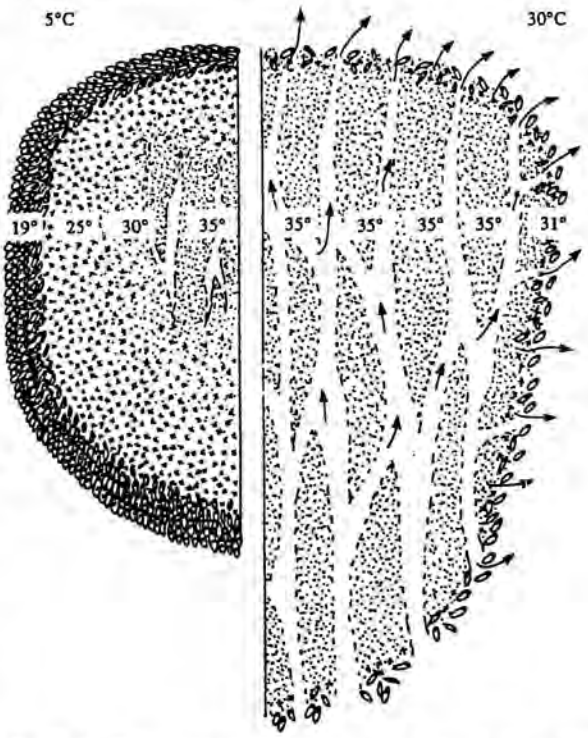

Figure 10 The regulation of temperature in a swarm of honeybees (Heinrich, 1981). The left-hand side shows the structure of the swarm cluster at a low ambient temperature. The right-hand side is for a high ambient temperature and shows the construction of almost equidistant ventilation channels with a characteristic spacing. Also indicated are the heat transfer from the swarm (arrows), areas of active metabolism (crosses), areas of resting metabolism (dots), and local approximate temperatures.

This mechanism works not only in engineering but also in nature (Bejan, 2000). Bees control the hot-spot temperatures in their swarm by opening nearly parallel vertical channels through which the ambient air cools the swarm, Fig. 10. The bees construct wider channels when the ambient air is warm and the required air flow rate is larger (Heinrich, 1981). Mud cracks are another example (Bejan et al., 1998): Cracks form at surprisingly regular intervals in volumetrically shrinking solids. The broad picture is one in which the occurrence of flow structure in engineered systems is as natural as the occurrence of flow structure in natural systems, animate and inanimate.

REFERENCES

Anand, N. K., Kim, S. H., and Fletcher, L. S., 1992, "The Effect of Plate Spacing on Free Convection between Heated Parallel Plates," J. Heat Transf., Vol. 114, pp. 515-518.

Bar Cohen, A., and Rohsenow, W. M., 1984, "Thermally Optimum Spacing of Vertical, Natural Convection Cooled, Parallel Plates," J. of Heat Transf., Vol. 106, pp. 116-123.

Bejan, A., 2001, "The Tree of Convective Heat Streams: Its Thermal Insulation Function and the Predicted 3/4-Power Relation between Body Heat Loss and Body Size," Int. J. Heat Mass Transf., Vol. 44, pp. 699-704.

Bejan, A., 2000, *Shape and Structure, from Engineering to Nature*, Cambridge University Press, Cambridge, UK.

Bejan, A., 1997, "Constructal-Theory Network of Conducting Paths for Cooling a Heat Generating Volume," Int. J. Heat Mass Transf., Vol. 40, pp. 799-816.

Bejan, A., 1993, *Heat Transfer*, Wiley, New York.

Bejan, A., 1984, *Convection Heat Transfer*, Wiley, New York, p. 157, problem 11.

Bejan, A., 1982, *Entropy Generation through Heat and Fluid Flow*, Wiley, New :York.

Bejan, A., and Sciubba, E., 1992, "The Optimal Spacing of Parallel Plates Cooled by Forced Convection," Int. J. Heat Mass Transf., Vol. 35, pp. 3259-3264.

Bejan, A., Ikegami, Y., and Ledezma, G. A., 1998, " Theory of Natural Crack Pattern Formation for Fastest Cooling," Int. J. Heat Mass Transf., Vol. 41, pp. 1945-1954.

Bhattacharjee, S., and Grosshandler, W. L., 1988, "The Formation of a Wall Jet Near a High Temperature Wall under Microgravity Environment, ASME HTD, Vol. 96, pp. 711-716.

Blasius, H., 1908, "Grenzschichten in Flüssigkeiten mit Kleiner Reibung Z.," Math. Phys.,Vol. 56, p. 1; also NACA TM 1256.

Chatwin, P. C., 1975, "On the Longitudinal Dispersion of Passive Contaminant in Oscillatory Flows in Tubes," J. Fluid Mech., Vol. 71, pp. 513-527.

Heinrich, B., 1981, "The Mechanisms and Energetics of Honeybee Swarm Temperature Regulation," J. Exp. Biology, Vol. 91, pp. 25-55.

Kim, S. H., and Anand, N. K., 1994, "Laminar Developing Flow and Heat Transfer between a Series of Parallel Plates with Surface Mounted Discrete Heat Sources," Int. J. Heat Mass Transf., Vol. 37, pp. 2231-2244.

Kim, S. J., and Lee, S W., eds., 1996, *Air Cooling Technology for Electronic Equipment*, CRC Press, Boca Raton, Florida.

Kurzweg, U. H., 1985, "Enhanced Heat Conduction in Oscillating Viscous Flows within Parallel-Plate Channels," J. Fluid Mech., Vol. 156, pp. 291-300.

Kurzweg, U. H., and Zhao, L. D., 1984, "Heat Transfer by High-Frequency Oscillations: a New Hydrodynamic Technique for Achieving Large Effective Thermal Conductivities, Phys. Fluids, Vol. 27, pp. 2624-2627.

Matsushima, H., Yanagida, T., and Kondo, Y., 1992, "Algorithm for Predicting the Thermal Resistance of Finned LSI Packages Mounted on a Circuit Board," Heat Transf. Japan. Res., Vol. 21, pp. 504-517.

Mereu, S., Sciubba, E., and Bejan, A., 1993, "The Optimal Cooling of a Stack of Heat Generating Boards with Fixed Pressure Frop, Flow Rate or Pumping Power," Int. J. Heat Mass Transf., Vol. 36, pp. 3677-3686.

Moffat, R. J., and Ortega, A., 1988, "Direct Air Cooling of Electronic Components," in *Advances in Thermal Modeling of Electronic Components and Systems*, Vol. I, A. Bar-Cohen and A. D. Kraus, eds., Hemisphere, New York, pp. 129-282.

Nakayama, W., Matsushima, H., and Goel, P., 1988, "Forced Convective Heat Transfer from Arrays of Finned Packages," in *Cooling Technology for Electronic Equipment*, W. Aung, ed., Hemisphere, New York, pp. 195-210.

Nelson, R. A., and Bejan, A., 1998, "Constructal Optimization of Internal Flow Geometry in Convection," J. Heat Transfer, Vol. 120, pp. 357-364.

Peterson, G. P., and Ortega, A., 1990, "Thermal Control of Electronic Equipment and Devices," Adv. Heat Transf., Vol. 20, pp. 181-314.

Petrescu, S., 1994, "Comments on the Optimal Spacing of Parallel Plates Cooled by Forced Convection," Int. J. Heat Mass Transf., Vol. 37, p. 1283.

Pohlhausen, E., 1921, "Der Wärmeaustausch Zwischen Festen Körpern und Flüssigkeiten Mit Kleiner Reibung und Kleiner Wärmeleitung, Z.," Angew. Math. Mech., Vol. 1, pp. 115-121.

Rocha, L. A. O., and Bejan, A., 2001, "Geometric Optimization of Periodic Flow and Heat Transfer in a Volume Cooled by Parallel Tubes,", J. Heat Transf., Vol. 123, pp. 233-239.

Watson, E. J., 1983, "Diffusion in Oscillatory Pipe Flow," J. Fluid Mech., Vol. 133, pp. 233-244.

HEFAT2002
1st International Conference on Heat Transfer, Fluid Mechanics, and Thermodynamics
8-10 April 2002, Kruger Park, South Africa
SB1

IMAGING OF COMPLEX COMPRESSIBLE FLOWS

Beric W. Skews
Flow Research Unit,
School of Mechanical, Industrial, and Aeronautical Engineering,
University of the Witwatersrand,
PO WITS, 2050,
South Africa.
E-mail: bskews@mech.wits.ac.za

ABSTRACT

The implementation of visualisation methods for the study of high-speed phenomena in gases is dealt with. Extensions to the conventional methods of shadowgraphy, schlieren and interferometry are discussed. The synergistic use of numerical methods with experimentation is highlighted, and the use of colour to add quantitative information is dealt with. The particular difficulties associated with three-dimensional flow fields and some new methods of handling them are illustrated by means of examples.

INTRODUCTION

Visualisation plays a very important role in studies of fluid behaviour. This paper examines some recent examples of a number of these techniques, and their extensions, for the study of flow fields where there are significant changes in density. The methods have the advantage of being non-intrusive. Although some of the methods have a long history, the advent of lasers and digital imaging is having significant impact on the field. Newer techniques, such as holographic interferometry, and computed tomography, together with very sophisticated computational techniques, are having important influences on the ability to access the details of a flow.

The family of techniques forming the basis of the methods dealt with here depend on the fact that there is a linear relationship between the density of a flow and its refractive index: $n-1 = K\rho$, where n is the refractive index, ρ the density, and K the Gladstone-Dale constant.

The shadowgraph technique is one of the simplest, with shadowgraphs being produced whenever a beam of light passes through a variable density field and throws a shadow of the field onto a surface. An example is the 'heat wave' arising from an object on a hot day. The conventional laboratory arrangement is given in Fig. 1. Ideally a point light source is needed, so either a pinhole or slit (the source mask) is illuminated through a suitable lens, or a laser beam is expanded to give a diverging beam, generally through a spatial filter to eliminate coherent noise. The beam is usually made parallel before passing it through the test section, by reflecting it from a parabolic mirror situated at the focal length of the source mask. For contact shadowgraphs the photographic film is placed immediately after the test section so that a full-scale shadow is created. Normally, however, a second parabolic mirror and focusing lens is used to produce a scaled image in the film plane. It can be shown that the image intensity recorded is proportional to the second derivative of density. Shadowgraphs are therefore ideal for studies of shock wave dynamics where gradients are high, but are less suitable for imaging more gradually varying phenomena such as expansion waves.

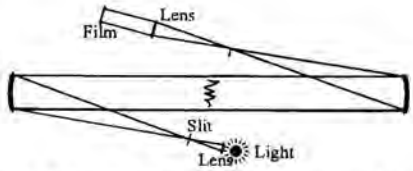

Fig. 1. Basic shadowgraph and schlieren layout

The schlieren system is very similar to that of a shadowgraph. All that is required is the addition of a knife-edge (cut-off filter) positioned at the focal point of the second parabolic mirror. An image of the source mask will exist at this point. If the knife edge cuts off about half of this image, the film plane will be uniformly grey except where light rays are deflected upwards or downwards due to the density gradients in

the test section. Thus parts of the image will become lighter or darker depending on the component of density gradient perpendicular to the knife-edge. It is apparent that schlieren systems are sensitive to the first derivative of density, but then only in one direction, that to gradient components normal to the knife-edge.

The third technique is that of holographic interferometry. Holography allows the storage of both amplitude and phase of an incident light wave. This allows for temporally separated interferometry as opposed to the more traditional methods such as Mach-Zehnder interferometry. In holographic interferometry of rapid events a double pulse laser is used to record two holograms on a single plate. The first hologram is of collimated light, such as for the shadowgraph system, that is made to pass through the test section just before the arrival of the event of interest, followed by a second pulse when the event is in the test section. The layout is indicated in Fig. 2. When the hologram is reconstructed there are two beams, which were separated in time, frozen in space at the same instant. These two beams interfere to produce fringes, which for a two-dimensional flow are lines of constant density. This technique supplies very high-resolution quantitative images.

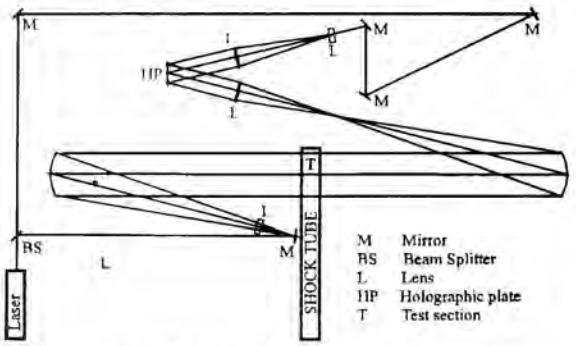

Fig. 2. Holographic interferometer set-up

This paper will illustrate these techniques, and extensions to them, applied to flows with shock waves, and particularly some wave interactions that are currently under study, such as shock/vortex interactions, and shock diffraction and reflection in two- and three-dimensions. The flows are predominantly transient, and thus many of them are essentially four-dimensional.

NUMERICAL ASSISTANCE

The combination of conventional visualisation with computational techniques is a powerful method for elucidating problems. Computational techniques by themselves require validation of some sort whereas physical experimentation frequently suffers from problems of scale, either being too large or too small. A very effective means of comparing numerical solutions with the experimental results is to manipulate the output data of the code to give images of the same type as in the experiment. Essentially this involves having a post-processor that mimics the experimental optical system, so that shadow, schlieren, or interferomtric images are the output of the code. Consider the following example.

In the study of the oblique reflection of shock waves the theoretical treatment, due to von Neumann [1], makes two main assumptions: that the flow is steady in a frame of reference fixed in the reflection point, and that the waves are plane. It is of considerable interest to establish what the effects would be if these assumptions are relaxed. If the waves are plane they will be separated by regions of uniform flow and the case of unsteady reflection off a plane wall can simply converted to the steady flow case by having a frame of reference situated in the reflection point. In fact, it is common practice in dealing with unsteady flows to shift the frame of reference to be stationary with respect to whatever point of the interaction is of interest.

For curved waves, however, the situation is less clear, and therefore it is of significant interest to establish if the von Neumann prediction of transition from regular to Mach reflection is satisfied. Some recent attempts at doing this [2] are summarised below.

The problem studied was the simultaneous diffraction of two plane waves around the rear end of a body as shown in Fig. 3a. This arrangement is chosen since the symmetry plane acts as a perfect reflection surface, being adiabatic, perfectly smooth, and completely rigid. A typical experimental interferogram, at best resolution that could be obtained in a 180 mm high shock tube, is given in Fig. 3b. It is noted that the few fringes are widely spaced and of little value in determining flow conditions in the vicinity of the reflection point. This limitation is because of the 60 mm wide test section coupled with the wavelength of the ruby laser used. Only minor improvements could be gained within the constraints of facility size. The benefits of numerical modelling immediately become apparent, since the virtual test section can be made any width, and given a powerful enough computer, significant improvements in spatial resolution can be obtained. Fig 3c shows two numerical interferograms constructed from calculations done on a Cray C90, with run times of the order of one day. The upper image shows regular, and the lower irregular, or Mach, reflection, and thus these images straddle the transition condition that is being sought. The size of each image in the context of Fig. 3a (i.e. a half-body height of 60 mm) is 188 x 63 microns, and is thus far beyond anything that could be achieved in a laboratory. Calculations with numerical element sizes down to 0.35 microns have been conducted. The half-height of the central normal shock in the case of Mach reflection is shown in Fig. 3d, for the various tests conducted. This clearly shows the scatter in experimental results and that transition predicted by the numerical code is dependent on element size in going from 92 to 2.9 micron element size. A more detailed examination shows the same to be true for smaller grids as well. The problem regarding whether curvature affects transition angle is thus yet not resolved and the example simply serves to illustrate the synergy between experimental

and numerical visualisation, providing there is confidence in the code being used.

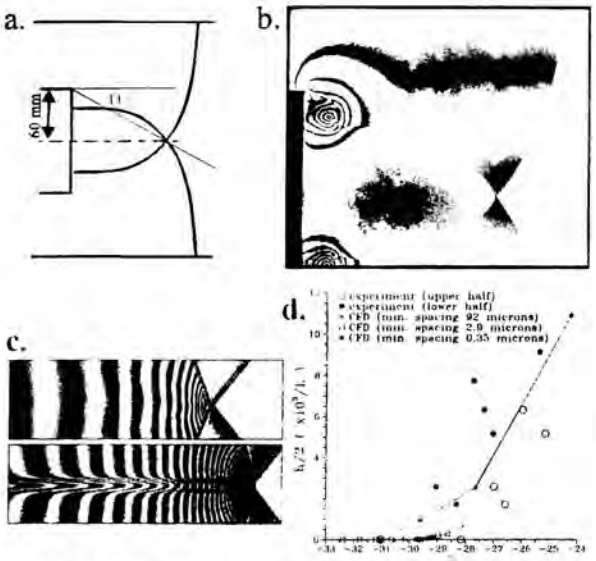

Fig. 3. The reflection of curved shock waves

The example above shows a case where the numerics are required to help clarify the experimental findings. An interesting case where the numerics are used in order to define the experimental conditions is a recent study on shock/vortex interactions [3]. Such interactions are regarded as a basic element of turbulent mixing and combustion, and are also an important feature of aerodynamic noise. The arrangement investigated was to have a shock wave on the upper surface of a wedge diffract around the wedge trailing edge and shed a spiral vortex. A second, later arriving, shock wave from the lower surface then interacts with this vortex. Studies have shown that during the interaction process very large localised pressures are developed, which are important both from the point of view of being hot-spots in combustion flows and as acoustic sources. The mechanism whereby the high pressure is generated is evident from the vertical series of shadowgraph images on the left of Fig. 4. These images are derived from numerical simulations of the process, with a postprocesser mimicking the shadowgraph optics. As the wave passes through the vortex it is pulled around on the side where the shock velocity is supplemented by the vortex velocity. The result is a convexly curved shock wave that focuses in on itself, thereby generating the pressure peak. Immediately after this implosion the wave breaks into a reflection pattern of four waves. In order to establish the path of this pressure peak, so that attempts could be made to measure it experimentally, the numerical code was run for the equivalent of 90 microseconds of shock motion, but instead of the parameters been stored at each time step, the pressure maximum at each computational node was stored for the full time. A colour plot of these maximum pressures is shown in Fig. 4. The position where the peak starts and the trajectory of the peak is clearly visible as the central red region. This data was then used as the basis for the positioning of a miniature pressure transducer in the experimental facility. The output from this transducer was then compared with that of a virtual transducer (in the numerical simulation) having the same sensing area. Very satisfactory agreement was obtained considering the very small temporal and spatial scales of the experiment.

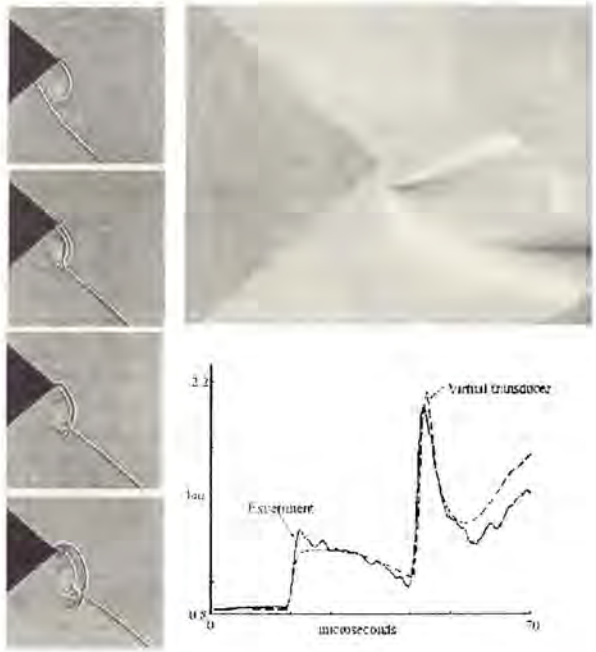

Fig. 4. Features of shock wave interaction with a vortex

THE USE OF COLOUR.

Colour is frequently used in the post-processing of CFD visualisations in order to enhance information transfer. However, it may also be used directly in experimentation in order to obtain additional quantitative information, or to extend the utility of instrumentation.

Consider the simple shadowgraph system described above. If the phenomena are very fast, as in the case of shock wave propagation into stationary air, and if high-speed cameras with microsecond inter-frame delays are not available, this usually means running a number of experiments with a single exposure per event using a short duration flash lamp and an open-shutter camera. This also requires that the phenomenon be highly reproducible. A simple alternative is to use colour to separate images in time. A means for doing this has been developed [4]

and allows three independent colour beams to appear to come from a single light source. This is different from the standard Cranz-Shardin system where a number of sources are placed in close proximity but result in a slightly different optical path through the test section for each image. Fig. 4 shows this common-axis arrangement. It uses dichroic filters, which have the property that they transmit only a selected wavelength of light and reflect the remainder. Thus little light is lost of the selected wavelength compared to conventional beam splitters. The three primary colours are extracted from three white light sources, through collimating the beams and passing them through suitable dichroic filters and then reflecting the beams. As an example, the filter at A transmits red light, whilst reflecting blue and green. The red beam then reflects off the inner surface of filter B, which transmits only green light, and reflects red and blue. Finally the red beam reflects off filter C, which transmits blue and reflects red and green. The emerging beam is then collimated onto a slit that serves as the effective light source. The light paths for the blue and green beams are similar, except that they undergo fewer reflections. Each of the light sources can be triggered independently to get whatever temporal spacing is required. This system also has a particular advantage for schlieren imaging since all three sources have a common slit, and a common knife-edge.

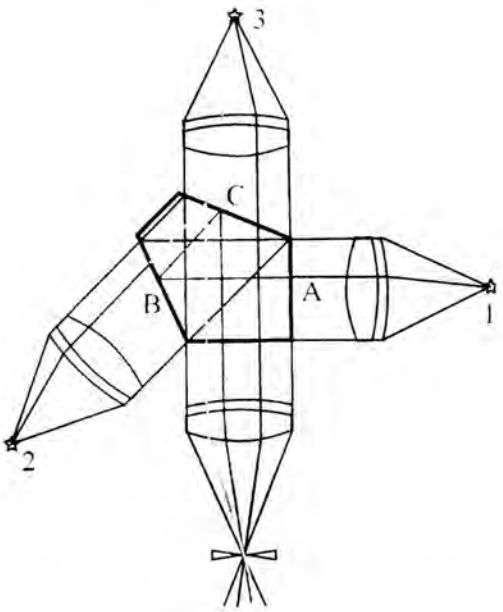

Fig.4 The optical arrangement of the three-colour source.

Fig. 5a is the raw image of a shock wave entering a contracting channel showing the three superimposed colour images. This is digitised and imported into a suitable graphics package where the colours are separated, giving the three discrete images. The green image shows the plane shock wave just before it strikes the contraction; the red image just as the wave reaches the narrow duct section; and the blue image even later. The set-up can be optimised in terms of the frequency band for each colour to minimise the cross-talk between the three channels. For good results care needs to be taken to maintain the colour balance at each step of the process, through recording, digitising, and display.

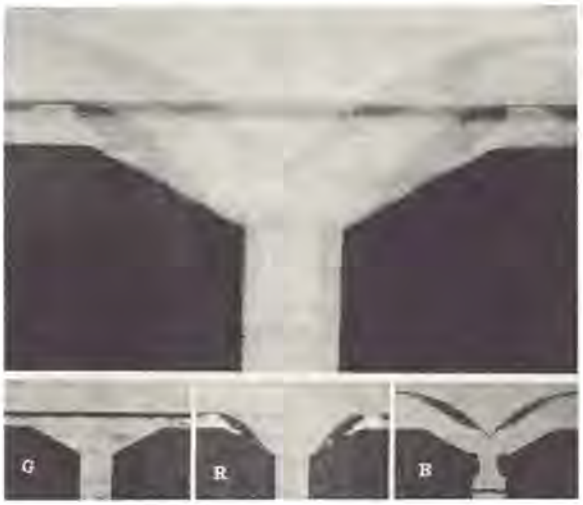

Fig. 5. Multi-flash photography using colour separation.

An interesting variation of this set-up is if the alignment of the light sources in the system are adjusted so that the three images do not coincide at the source mask, but rather are positioned at 120° to each other such as indicated in Fig. 6a, with a corresponding set of knife edges acting as the cut off filter. If all three light sources are flashed simultaneously the system then performs as three independent schlieren systems using three different colours. With a properly set up system and no disturbance in the test section the combination of the three primary colours results in a neutral grey background with equal contributions of light from the three sources. If there is a density gradient, however, there will be different contributions passing the knife-edges and the resulting colour will then give a quantitative measure of the direction of the gradient, as indicated in the image. Such colour schlieren systems are sometimes referred to as two-dimensional systems since they are not just sensitive to density gradients in one direction. The current version differs from earlier versions, such as that of Kleine and Grönig [5], which use an annular light-scattering source mask containing three colour sectors, together with a single light source. In such systems bright light sources need to be used because of the absorption as the light passes through the colour mask.

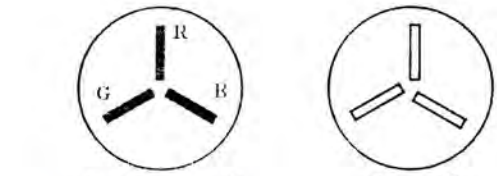

Fig. 6. Colour schlieren system with colour showing the direction of the density gradients.

An interesting application of colour coding a flow is in the use of the hydraulic analogy for supersonic flow. The differential equations for the flow of a shallow layer of water are the same as that for a two-dimensional flow of a compressible gas with a ratio of specific heats of 2. There are a number of benefits in exploring flows on such a water table, the primary one being that it is a simple matter to explore flows that are not achievable in conventional wind tunnel facilities, such as that of a supersonic body flying in a curved path. The technique described [6], uses a colour mask positioned at the focal point of a lens so that for each point on the mask a parallel beam of light of the colour of that point passes through the water surface. For a flat surface of given slope, and a camera positioned at infinity, only the colour refracted through the surface from a given position on the mask will enter the camera. An uneven surface will result in colour corresponding to different points on the mask being bent into the camera. The principle of the method is illustrated in Fig. 7. The configuration currently in use employs a 900 mm diameter Fresnel lens with a focal length of 760 mm, situated under a tiltable glass table and viewed from the top. If the colour mask consists of concentric circles with the centre on the optical axis then lines of constant colour correspond to surfaces of constant slope. Integration of these variations should thus allow the surface shape to be generated. If, however, the mask consists of a series of coloured sectors the iso-colour bands will then represent contours of constant gradient direction. The most general case where each element of a mask is of a different colour from adjacent elements then both slope and direction should be able to be extracted. Such systems would require very careful calibration. An example of flow around a wedge showing the bow wave is given in Fig. 8, together with the associated mask.

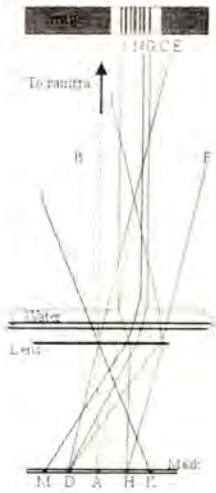

Fig. 7. Arrangement for colour coded hydraulic analogy

Fig. 8. Colour coded water table image with corresponding mask, giving colour lines of constant slope.

THREE-DIMENSIONAL FLOWS

All the above examples, although important in their own right, are simplifications, in that they are interpreted as representing nominally two-dimensional flow fields. All flows are, in fact, three-dimensional, even if they are constrained experimentally to approximate two-dimensionality. In many cases fully three-dimensional fields can also be imaged using the conventional techniques described above without any ambiguity. However, a danger exists when examining an image, is to interpret it as being two dimensional, when in fact it is not. A very interesting recent example of this occurring was in the

study of shock wave reflection transition in steady supersonic flows. The two reflection patterns described in gas dynamic textbooks are regular reflection and Mach reflection, illustrated in Fig. 9.

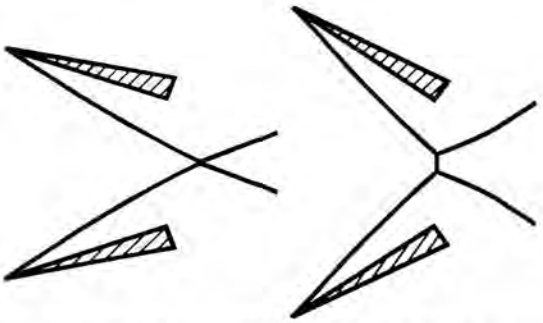

Fig. 9. Regular and Mach reflection of shock waves.

It is important to know the conditions for transition from the one type to the other because it influences the pressure distribution experienced by the reflection surface. Above a certain flow Mach number conditions arise where both these patterns are theoretically possible. Hornung et al. [7] suggested that in this dual solution domain the transition from the one type of reflection to the other would occur at the extremes of this domain. This would then result in a hysteresis occurring if the incident wave angle was increased through transition and then decreased. The puzzling thing, however, was that a number of carefully conducted experiments in supersonic wind tunnels consistently showed transition to only occur at the lower limit. Surprisingly, as numerical techniques were developed to model the flow geometry, it was found that the Hornung hysteresis did in fact occur. Recently, however, one experiment did show hysteresis [8], but not within the bounds expected. A number of studies have explored these effects.

Consider the shadowgraph image of a regular reflection between two wedges shown in Fig. 10a. The double-wedge set-up is used to again avoid the complications of reflection on a surface, and so to replicate the theoretical assumptions. The image appears to be perfectly normal and to have the expected geometry. However, if the optical axis is yawed with respect to the flow, the image of Fig. 10b is obtained, considerably different from what would be expected from a two-dimensional flow pattern. The most noticeable difference is that there is now Mach reflection where the incident waves meet, as well as an unusual protuberance immediately behind the reflection point. It is somewhat surprising that this simple modification of viewing wind tunnel flows at an angle has not previously been tried. A study of these flows through such oblique imaging [9] has given important insight, not only into the geometry of such flows, but it has also supplied one of the reasons for the discrepancy between numerical and experimental data. It is simply that, although the longitudinal flow is largely supersonic, and thus isolated from downstream influences, a transverse information path opens up under certain flow conditions allowing downstream perturbations to have access to the reflection point. An exaggerated representation of the flow is given in Fig. 10c, which illustrates the development of peripheral Mach reflections on the sides of the wedge. These peripheral reflections encroach onto the core flow as the wedge angle is increased until Mach reflection is evident on the centreline. The transition thus is dictated by the wedge aspect ratio rather than the theoretical two-dimensional considerations. Supersonic wind tunnel tests have always been conducted with finite width wedges, narrower than the test section, in order to obviate the complex interactions between the wave system and the window wall boundary layers, and thus an awareness of possible edge effects become important.

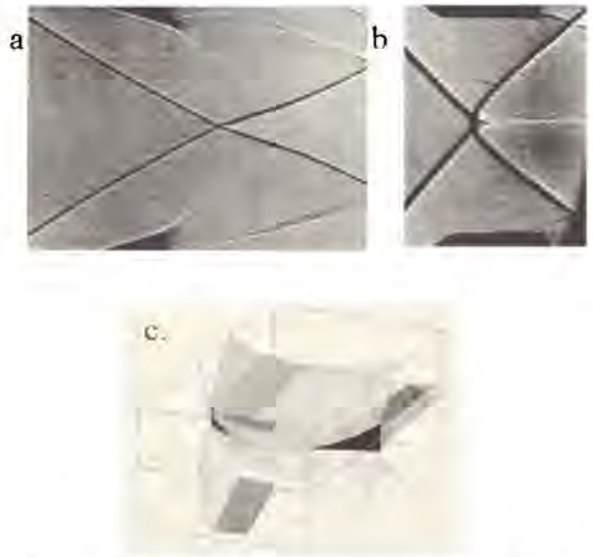

Fig. 10. Shock wave reflection between two wedges when viewed at a) 0° yaw, and b) 45° yaw. c) Interpretation of the true geometry.

In some cases oblique imaging such as that demonstrated above is insufficient to clarify the flow. A number of techniques using laser sheets to simply view a slice of the flow are now being used. These range from simple Mie scattering of light off particles seeded in the flow, with its extensions to PIV, to more sophisticated techniques such as planar laser induced fluorescence.

Consider the flow exiting from a square-exit supersonic nozzle, when the back pressure is higher than the nozzle exit pressure. The equivalent two-dimensional flow field is well understood and documented. However, little is known about the three-dimensional field, particularly how the flow exiting at the corners of the nozzle adjusts to the backpressure. If a small

quantity of water vapour is inserted into the nozzle settling chamber then particles formed from condensation within the nozzle cause the exit flow to become visible when traversed by a light sheet. The sheet is made by expanding a 1 mm laser beam through a cylindrical lens.

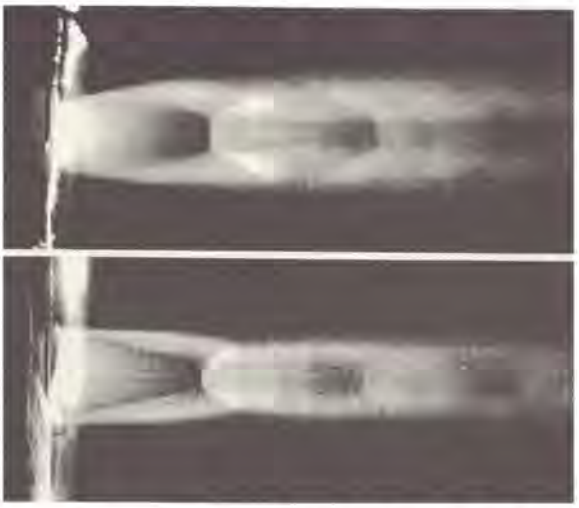

Fig. 11. Laser sheet images of the exit flow from an under-expanded supersonic nozzle. a) Normal view. b) Diagonal view.

Fig 11 shows two images obtained in this fashion, one across a diagonal of the nozzle exit, and the other parallel to a nozzle edge and also passing through the nozzle centreline. The flow is from left to right, and the light flare on the left should be ignored; it arises from reflection off the face of the nozzle block. Noticeable differences are noted in the two flow patterns. In particular, both the shape of the edge of the jet, and the development of the oblique shock waves, show a considerable asymmetry. A number of such cross sections can be taken and the full three-dimensional wave configuration established by suitable manipulation in a surface modeller on a computer [10].

It is clear from the previous discussion that interferometery is the most powerful of the conventional optical techniques for obtaining quantitative information. However, for rapidly varying flows sequential photographs of the development of a flow can only be done through multiple tests, and then only when the phenomenon is highly reproducible. One method of obtaining real time interferometry of slow events is through the use of electronic speckle pattern interferometry (ESPI). This also has the advantage of not requiring film development, the output from a CCD camera being captured and processed in real time on a computer and displayed on a monitor. Speckle interferometry has mainly been used for studies of surface deformation and movement. The technique exploits the fact that when coherent light such as a laser beam is reflected off a surface that is rough at the wavelength scale, a grainy structure known as laser speckle forms in three dimensional space. By imaging this speckle pattern and adding an on-axis reference beam, it is possible to relax the high-resolution requirements of conventional holography to the point where a CCD camera can be used. The main advantage is that images are produced instantaneously and in real time on a video screen. However, there is considerable loss in resolution and fringe visibility diminishes as fringe width approaches pixel size. CCD development is rapidly reducing this as a problem, and the one that remains for the photography of high-speed events such as shock waves is availability of digital cameras with sufficient framing rates.

Fig. 12. Single frame ESPI images of density fields.

Fig. 12 shows images of two transient flows. The first, of convection from a heated soldering could have been taken with a video camera and the temporal development of the flow examined. The second is of a shock wave emerging from the end of a small shock tube. Digital cameras of a sufficient framing rate are not yet available. Both these images were taken with a camera allowing a single frame with an exposure time of 1 μs. As digital technology develops so it may become possible to employ these techniques, in real-time, for slow-motion playback of high-speed events.

One of the most promising techniques currently being developed for the experimental study of complex three-dimensional flow fields is computed tomography (CT visualisation). A number of methods are under development but the one illustrated here uses conventional infinite fringe interferometry to capture the density data. Each light ray passing through a density field is retarded according to the

integral of the density along its path. The principle of tomography is simply that if the object is examined from enough directions the density at any one position can be reconstructed by suitable deconvolution algorithms.

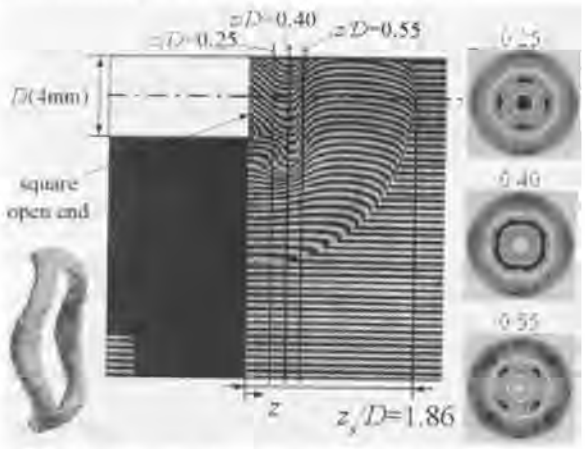

Fig. 13. Computed tomography of a shock wave exiting from a square tube. Courtesy of H Honma.

Consider the case of a plane shock wave exiting from a square section tube [12]. A typical interferogram is shown in Fig. 13. A number of such interferograms are taken from different directions and the mean density distribution along a series of planes parallel to the exit of the tube determined. Suitable algorithms are then applied which results in the density distribution on each of the planes. Results for three such planes are shown at the right of the figure. The dark area corresponds to the lowest density and thus represents the vortex. It is slowest as it emerges from the sides of the tube, and fastest at the corners. From this data a three-dimensional surface model of the vortex can be constructed, and it is shown in the bottom-left corner of the figure.

CONCLUSION

A number of visualisation methods relating to the study of compressible flow of gases have been illustrated, mainly through examples taken from the work of the Flow Research Unit at the University of the Witwatersrand. It is shown that even the complexities of unsteady, three-dimensional flows can be resolved using well-established techniques coupled with modern digital technology.

ACKNOWLEDGMENTS

A large number of the examples given in this paper have come from projects conducted by undergraduate and postgraduate students. I am grateful to them for their efforts. I am also grateful to Prof Hiroki Honma for permission to reproduce some of his CT visualisation results.

REFERENCES

[1] von Neumann J., 1943, "Oblique reflection of shocks." Explos. Res. Rep. No 12, Navy Dep.

[2] Timofeev E.V., Skews B.W., Voinovich P.A., Takayama K. 1999, "The influence of unsteadiness and three-dimensionality on regular to Mach reflection transitions: a high-resolution study." 22nd International Symposium on Shock Waves, Eds. Ball G.J., Hillier R., Roberts G.T., University of Southampton Press, 1231-1236.

[3] Barbosa F.J., Skews B.W., 2001, "Shock wave interaction with a spiral vortex". Physics of Fluids. In press.

[4] Seitz M.W., Seitz P.A., Skews B.W., 1994, "Three-color common-axis light source suitable for shock wave studies" Optical Engineering, 33, 2903-2906.

[5] Kleine H., Grönig H., 1991, "Color schlieren methods in shock wave research." Shock Waves, 1, 51-63.

[6] Skews B.W., 1998, "Colour encoded visualisation applied to the hydraulic analogy for supersonic flow." 8th International Symposium on Flow Visualization, Sorrento, Italy, 31.1-31.7

[7] Hornung H.G., Oertel H., Sandeman R.J., 1979, "Transition to Mach reflection of shock waves in steady and pseudosteady flow with and without relaxation." J. Fluid Mech. 90, 541-559.

[8] Chpoun A., Passerel D., Li H., Ben-Dor G., 1995, "Reconsideration of oblique shock wave reflections in steady flows. Part 1. Experimental investigation." J. Fluid Mech., 301, 19-35.

[9] Skews B.W., 2000, "Three-dimensional effects in wind tunnel studies of shock wave reflection." J. Fluid Mech., 407, 85-104,.

[10] Menon N., Skews B.W. 2001, "3-dimensional shock wave patterns in expanding jets." 23rd International Symposium on Shock Waves. Fort Worth, Texas, University of Texas at Arlington. In Press.

[11] Andrag R., Barbosa F.J., Skews B.W., 2000, "ESPI of a transient shock wave flow using an ultra-fast digital camera." 24th International Congress on High Speed Photography and Photonics, Sedai, Japan. In Press.

[12] Honma H., Maeno K., Ishihara M., Yoshimura T., 2000, "An interferometric CT technique for three-dimensional shock wave phenomena." 24th International Congress on High Speed Photography and Photonics, Sedai, Japan. In Press.

HEFAT2002
1ST international Conference on Heat Transfer, Fluid Dynamics and Thermodynamics
8-10 April 2002, Kruger National Park, South Africa
KS1

INSIGHT INTO MECHANICSMS AND REVIEW OF AVAILABLE MODELS FOR CRITICAL HEAT FLUX (CHF) IN POOL BOILING

Satish G. KANDLIKAR
Department of Mechanical Engineering
Rochester Institute of Technology
Rochester, NY 14623
sgkeme@rit.edu

ABSTRACT

Critical Heat Flux (*CHF*) has been a subject of interest for boiling equipment designers from design as well safety as viewpoints. Although considerable data exists in literature, a fundamental knowledge of the mechanisms responsible for the CHF phenomenon is needed to develop better predictive methods and efficient enhancement strategies. A critical assessment of the CHF models available in the literature is presented here, highlighting the needs for future research in this area.

NOMENCLATURE

D_c – cavity mouth diameter, m
g – acceleration due to gravity, m^2/s
h – heat transfer coefficient, W/m^2K
h_L – single phase heat transfer coefficient with liquid phase, W/m^2K
i_{LG} – latent heat of vaporization, J/kg
k – thermal conductivity, W/mK
K – contstant in eq. (4)
N_a – number of active cavities, number/cm^2
N_{as} – number of available cavities, number/cm^2
q – heat flux, W/m^2
q_C – critical heat flux, W/m^2
T_{sat} – saturation temperature, K
ΔT_{sat} - wall superheat, K
$\Delta T_{sat,ONB}$ - wall superheat at ONB, K
u- flow velocity, m/s
v_{LG} – specific volume difference between vapor and liquid, m^3/kg

Greek Symbols

ϕ - angle of inclination of the tube with horizontal
ψ_m - cavity mouth angle, degrees
μ_L – liquid viscosity, Ns/m^2
θ - contact angle, degrees
ρ_L, ρ_G - liquid and vapor density, kg/m^3
σ - surface tension, N/m

1. INTRODUCTION

Critical Heat Flux, or *CHF*, represents the maximum heat flux that can be dissipated by nucleate boiling. Any further increase in the wall superheat leads into transition boiling mode with deterioration in the accompanying heat transfer rate. In heat flux controlled systems, *CHF* represents the point of discontinuity where an increase in the heat flux causes a rapid temperature excursion in the wall temperature, terminating nucleate boiling and leading into film boiling mode of heat transfer.

As early as in 1888, Lang [1] recognized through his experiments with high pressure water that as the wall temperature increased beyond a certain point, it resulted in a reduction in the heat transfer rate in a nucleate boiling system. However, it was Nukiyama [2] who realized that the "maximum heat transmission rate" might occur at relatively modest temperature differences. Drew and Mueller [3] present an excellent summary of the historical development in this area. A recent survey of the critical heat flux literature is presented by Kandlikar [4].

2. THERMAL AND HYDRODYNAMIC CONDITIONS PRIOR TO *CHF*

The models proposed in the literature are generally based on the physical phenomena that are supported by experimental evidence. A brief overview of the thermal and hydrodynamic conditions existing on the heater surface prior to reaching *CHF* is presented in this section.

2.1 Nucleation and Bubble Dynamics

Bubble Characteristics over the Nucleate Boiling Range:

The bubble characteristics during nucleate boiling was investigated with a high-speed motion camera by Gaertner [5]. He identified different regions based on these characteristics as illustrated in Fig. 1. In the initial phase of nucleate boiling, discrete bubbles are formed over isolated cavities. As the heat flux increases, the bubbles depart in rapid succession forming vapor columns as shown in Fig. 1(b). Subsequently, the neighboring vapor columns merge into a large bubble. This large bubble is referred to as a vapor patch by Zuber [6], and as a hovering bubble by Haramura and Katto [7]. The thin liquid film existing under the large bubble is referred to as the macrolayer. Existence of such macrolayer has been confirmed by Kirby and Westwater [8] and Yu and Mesler [9]. Further increase in the heat flux results in a broader coverage of the heater surface with the large bubbles as shown in Fig. 1(c). Subsequently, the critical heat flux is reached, beyond which point, the degradation caused by the large vapor coverage offsets the increase in the heat transfer due to rapid bubble growth and efficient heat transfer in the macrolayer.

The focus of the present discussion is on the exact mechanism that causes the transition from the region depicted in Fig. 1(c) to the CHF condition.

Nucleation Site Density:

The key elements of pool boiling are bubble nucleation and bubble growth followed by coalescence with neighboring bubbles, and collapse or departure from the heater surface. For a given wall superheat, the range of active cavity sizes is determined by the cavity size distribution on the heater surface. At high heat fluxes, a large number of small diameter cavities are activated.

The size and shape of a cavity governs its nucleation characteristics. Griffith and Wallis [10] postulated that as a bubble grows in a cavity, it comes at the mouth of the cavity and assumes a hemispherical shape. This state also represents the point where the radius of curvature of the interface is a minimum. The cavity is assumed to be active when a bubble grows past this condition. Employing the Clasius-Clapeyron equation for the pressure difference between the vapor inside the bubble and the surrounding liquid, the wall superheat required for the bubble to grow beyond the cavity opening, (same as $\Delta T_{sat,ONB}$), was obtained as

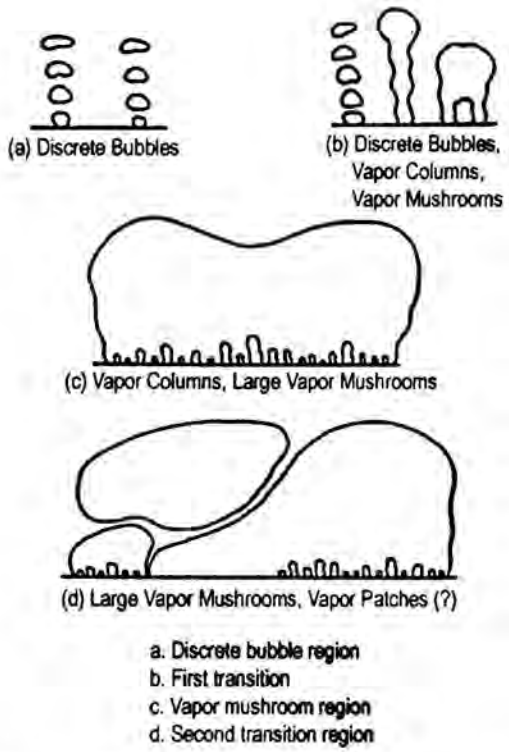

Figure 1. Bubble characteristics in different regions of nucleate boiling, Gaertner, [5].

$$\Delta T_{sat,ONB} = \frac{4\sigma T_{sat}}{\rho_V i_{LG} D_c} \quad (1)$$

where D_c is the cavity mouth diameter, m. It is seen that the wall superheat to activate a cavity varies inversely with the cavity diameter. Smaller cavities are activated at higher wall superheats.

Subsequently, Hsu [11] and Sato and Matsumura [12] considered the temperature profile in the liquid and suggested that the hemispherical bubble on a cavity will grow if the liquid temperature at the tip of the bubble was above the saturation temperature corresponding to the vapor pressure inside the bubble. Assuming that cavities of all sizes are available, the following expression for the wall superheat at the onset of nucleate boiling, ONB, was obtained.

$$\Delta T_{sat,ONB} = \frac{4\sigma T_{sat} v_{LG} h_L}{k_L i_{LG}} \left[1 + \sqrt{1 + \frac{k_L i_{LG} \Delta T_{sub}}{2\sigma T_{sat} v_{LG} h_L}} \right] \quad (2)$$

Hsu, and Sato and Matsumura also obtained an expression for the range of active cavity radii.

In deriving the above equation, the liquid temperature at the bubble tip was calculated from the single-phase convection heat transfer coefficient in the liquid phase. As boiling progresses, the actual heat transfer coefficient increases progressively. It is therefore expected that nucleation will progress toward smaller cavity sizes more rapidly with an increase in the wall superheat.

Indeed, the nucleation site density increases rapidly with an increase in the wall superheat. Nucleation is also facilitated by the availability of vapor from neighboring sites. Following a mechanistic approach, Wang and Dhir [13, 14] derived the following relationship between the nucleation site density and the wall superheat.

$$N_s(sites/cm^2) = 5.8\times10^{-5} D_c^{-5.4} \qquad (3)$$

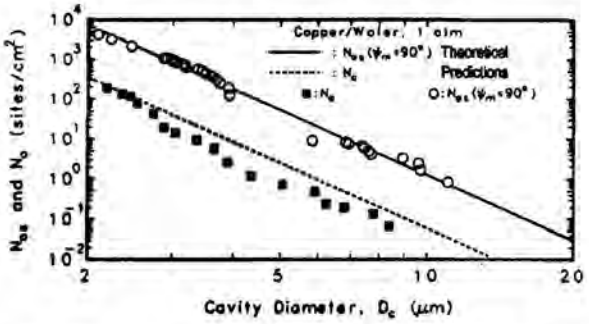

Figure 2 Active nucleation site density variation with cavity mouth diameter, D_c, for a contact angle θ =18° and cavity mouth angle ψ_m<90° , N_{ss} – number of available cavities, N_s – number of active cavities, Liaw and Dhir [26].

Since the wall superheat is inversely proportional to the cavity diameter, it follows that the nucleation site density varies as $\Delta T_{sat}^{5.4}$. Dhir [15] presented a plot showing this relationship for different values of contact angle (θ) and cavity mouth opening angle (ψ_m). Figure 2 shows such a plot for a contact angle of 18° and cavity mouth angles below 90°. It can be seen that the number of active cavities increases quite dramatically for smaller cavity diameters (on the order of a few micrometers).

Relating the active site density information to the critical heat flux condition, it becomes clear that a large number of cavities, with very small diameters, are activated at the high value of wall superheat. The conditions near the wall are therefore very crowded with nucleating bubbles.

3. CHF MODELS BASED ON HYDRODYNAMIC CONSIDERATIONS

As the heat flux is increased to the critical heat flux value, vapor generation rate increases and presents an increasing resistance to the liquid flowing toward the heating surface. The hydrodynamic models of CHF are based on the instability encountered at the liquid-vapor interface. The exact location of the interface where the instability sets in is somewhat different in different models presented in literature:

- Kutateladze [16, 17] – destruction of stability of two-phase flow near the heater surface
- Borishanskii [18] – liquid flowing coaxially in a countercurrent manner
- Zuber [19] – instability of a vapor patch over the heater surface, CHF modeling from the transition boiling side
- Chang [20] – considers a force balance on a bubble attached to a vertical surface, relative velocity between the rising bubble and the liquid reaches a critical value at CHF
- Moissis and Berenson [21] – instability in the vertical vapor columns surrounded by the counterflow of liquid flowing toward the heater surface
- Katto and Yokoya [22] and Haramura and Katto [7] – instability of vapor columns formed in the macrolayer, dryout of the macrolayer
- Sefiane et al. [23] – instability at the interface of an evaporating meniscus at the base of a bubble

Perhaps not so surprisingly, all the above formulations, with the exception of Sefiane et al.'s model (which presents a set of equations), lead to a similar expression for the critical heat flux as originally obtained by Kutateladze [17]. This shows that all the instability models, irrespective of their physical model, utilize the same functional groups in representing the instability criterion for the liquid-vapor interface. A brief description of these models is given below.

Kutateladze [16, 17] proposed that the meaning of bubble generation and departure was lost near the critical heat flux condition, which is essentially a hydrodynamic phenomenon with the destruction of the stability of the two-phase flow existing close to the heating surface. Critical condition is reached when the velocity in the vapor phase reaches a critical value. Following a dimensional analysis, he proposed the following correlation.

$$\frac{q_C''}{i_{LG}\,\rho_G^{0.5}\left[\sigma g(\rho_L-\rho_G)\right]^{1/4}} = K \qquad (4)$$

The value of K was found to be 0.16 from the experimental data.

Borishanskii [18] modeled the problem by considering the two-phase boundary in which liquid stream flowing coaxially with gas experiences instability. His work lead to the following equation for K in the Kutateladze's equation, Eq. (4)

$$K = 0.13 + 4\left\{\frac{\rho_L \sigma^{3/2}}{\mu^2 [g(\rho_L - \rho_G)]^{1/2}}\right\}^{-0.4} \qquad (5)$$

Although viscosity appears in eq. (5), its overall effect is quite small on CHF.

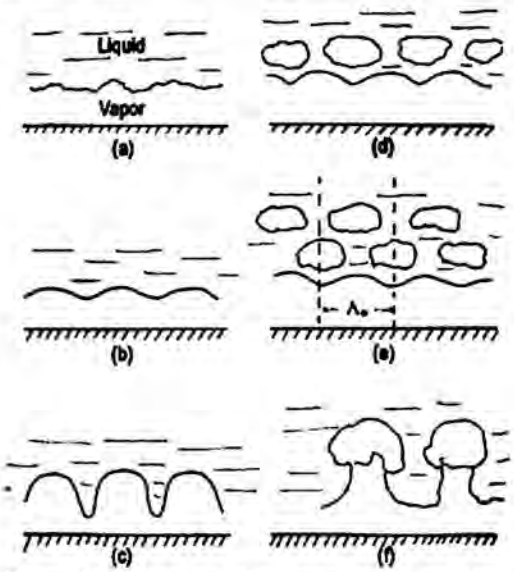

Figure 3 Instability of a liquid-vapor interface over a heated surface leading to vapor jets, Zuber [19].

Zuber [19] also postulated that vapor patches form and collapse on the heater surface as CHF is approached. According to Zuber, "In collapsing, ... [as] the vapor-liquid interface of a patch approaches the heated surface, large rates of evaporation occur and the interface is pushed violently back." Zuber considered the dynamic effects of vapor jets to be important and proposed that the Taylor and Helmholtz instabilities are responsible for the CHF condition. Figure 3 shows a heater surface covered with vapor after it has reached the critical heat flux value. The progression from (a) through (f) shows how the smooth interface experiences instability and creates vapor jets and mushrooms. In Fig. 3(c), the liquid fingers extend to the wall and are pushed back resulting in vapor jets as shown in Fig. 3(f). Using the stability criterion of a vapor sheet, Zuber obtained an equation similar to that of Kutatelazde [17], but the value of constant K ranged from 0.157 to 0.138. Simplifying the analysis further, Zuber proposed a value of K=0.131.

Chang [20] performed a force balance on a single bubble, close to its departure condition on a vertical surface. He obtained the vapor rise velocity from an expression developed for gas bubbles in a pool of liquid. The resulting departure bubble radius and relative velocity between the two phases were employed in defining the Weber number. Chang postulated that this Weber number reached a critical value at the CHF condition. This resulted in the same expression as eq. (4), with K=0.098. The CHF for vertical surfaces was taken to be 75 percent of the value predicted for a horizontal surface.

Moissis and Berenson [24] developed a model based on the interaction of the continuous vapor columns with each other. The maximum heat flux is then determined by introducing Taylor-Helmholtz instability for the counterflow of vapor flow in columns and liquid flow between them as shown in Fig. 4.

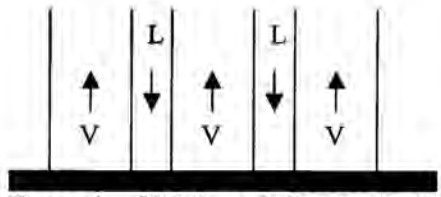

Figure 4 Moissis and Berenson's [24] model with countercurrent flow of liquid (L) between vapor columns (V) adjacent to the heated wall.

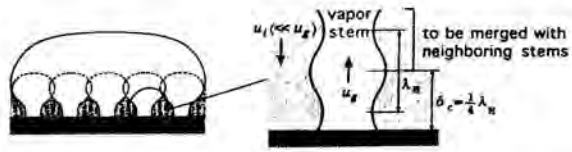

Figure 5 Macrolayer evaporation model with vapor jet instability within the macrolayer, Haramura and Katto [7].

Haramura and Katto [7] refined an earlier model proposed by Katto and Yokoya [22] and proposed that the heat transfer is related to formation and evaporation of a macrolayer under a hovering vapor bubble as shown in Fig. 5. An expression for the hovering period was obtained using the force balance between the buoyancy and inertia forces. Complete evaporation of liquid in the macrolayer within the hovering time leads to the critical heat flux condition. However, the thickness of the macrolayer is unknown in this formulation. Haramura and Katto considered the merger of the adjacent vapor stems to result in pushing the bulk liquid away from the hovering bubble. Combining with Zuber's model for the critical heat flux, Haramura and Katto obtained an expression for the thickness of the macrolayer. This approach combines the hydrodynamic and thermal aspects in a single model.

Sefiane et al. [23] considered the recoil forces in their analysis of the liquid-vapor interface instability in the contact line region. The rapid evaporation in this region generates a recoil force due to the unbalanced momentum caused by the velocity difference between the liquid and vapor phases at the interface. This recoil force was assumed to create an instability condition at the interface as shown in Fig. 6. A set of equations was developed for predicting the interface motion and the accompanying heat flux.

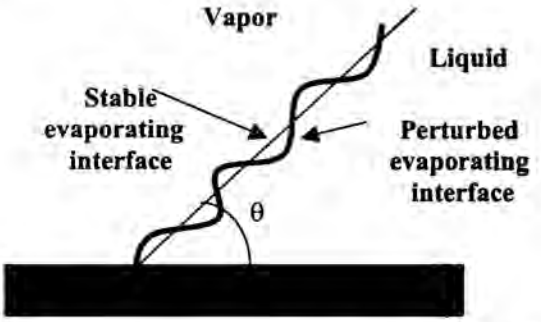

Figure 6 A liquid-vapor interface near the contact line region perturbed by the recoil forces, Sefiane et al. [23].

The models presented in this section are derived mainly on the basis of hydrodynamic considerations. One of the major drawbacks of these models is that the contact angle is not considered to be a relevant parameter. However, it is well known that the contact angle has a major influence on the CHF. Gaertner's [25] experiments clearly showed that the CHF value was dramatically reduced for a surface coated with a non-wetting plastic (very high contact angle). The bubbles coalesced and formed a vapor film underneath the liquid. Liaw and Dhir [26] observed a similar trend over a contact angle range of 0 to 108° for water boiling on a vertical plate. Although Sefine et al.'s [23] analysis considers the contact angle effect, the instability of the interface alone does not seem to be a sufficient condition for CHF condition. Drying and rewetting with considerable instability are constantly occurring during the boiling process. A review of CHF models based on thermal considerations is presented in the next section.

4. CHF MODELS BASED ON THERMAL CONSIDERATIONS

The CHF models based on hydrodynamic considerations presented in Section 3 consider the instability of the liquid-vapor interface that somehow prevents the liquid from reaching the heater surface. In Zuber's model, he considers the CHF from the transition boiling side. A vapor film covers the heated surface, and the instability of the interface causes liquid wavelets to approach the heater surface. The rapid evaporation of these wavelets causes the vapor to get violently pushed back in the form of uniformly spaced jets. Although this describes the transition boiling phenomenon, the initiation of the critical heat flux condition is not entirely clear. Haramura and Katto provide an explanation of how this condition is arrived at by proposing the macrolayer evaporation theory. They postulate that the CHF is reached when the macrolayer evaporates completely. Using the Zuber's correlation, they derived an expression for the initial macrolayer thickness. The hovering bubble in Haramura and Katto's model represents the vapor patch in the Zuber's model. Haramura and Katto's model thus provides an explanation for the formation of the macrolayer (and vapor patch in Zuber's model), but it does not provide an answer to the mechanism leading to the CHF condition.

The questions not addressed in the hydrodynamic models are the liquid supply to the wall and the expansion of the hovering vapor bubble. Further, the effect of contact angle on CHF is not included. As seen from Gaertner's [25] photographic study and Liaw and Dhir's [26] experimental investigation, CHF reduces significantly as the contact angle increases. This leads us to believe that the CHF is more intimately linked to the liquid-vapor-solid interactions at the wall, where thermal effects are important and need to be included in the modeling of CHF.

Sefiane et al. [23] present a model that addresses the contact line region and the effect of contact angle to some extent. This model includes the recoil forces that arise due to the momentum change as liquid at the interface in the contact line region evaporates into vapor. The higher vapor velocity results in an unbalanced momentum, which provides a recoil force at the interface. However, the instability of this interface initiated by the recoil forces is assumed to lead to CHF. The exact sequence of events that lead to the CHF condition following the instability condition still remains unanswered.

5. A NEW MODEL BASED ON CONTACT LINE MOVEMENT CRITERION

Critical heat flux phenomenon occurs at the heater surface. It occurs at speeds that are in the microseconds range as we see the bubble growth and collapse information generated through studies on the inkejet printers. With this is mind, although the hydrodynamic conditions occurring at the interface of the hovering bubble provide answers to the occasional contacts of liquid with the heater surface, they are not able to describe the mechanism responsible for the critical heat flux condition. The motion of the interface at the contact line holds the key to whether the vapor will push the liquid away, or the liquid front will rewet the heater and release the bubble that is covering the heater surface. A new model presented in the following sections to include the effects of contact angle and the recoil forces in determining the movement of the interface at the contact line.

5.1 Macrolayer Evaporation

The agglomeration of vapor in the vicinity of the wall restricts the flow of liquid toward the heater surface. The macrolayer under the bubble continues to evaporate. As seen from Fig. 2, the number of active sites is very large at high wall temperatures encountered near CHF. These sites are present in the thin film as well. Presence of a thin film above nucleating cavities would cause the bubbles to open up at the interface thereby increasing the bubble frequency. Heat conduction through the macrolayer is also quite efficient as the interface of the film is at saturation temperature due to evaporation of liquid. However, the limited availability of the liquid in the macrolayer leads to its eventual dryout.

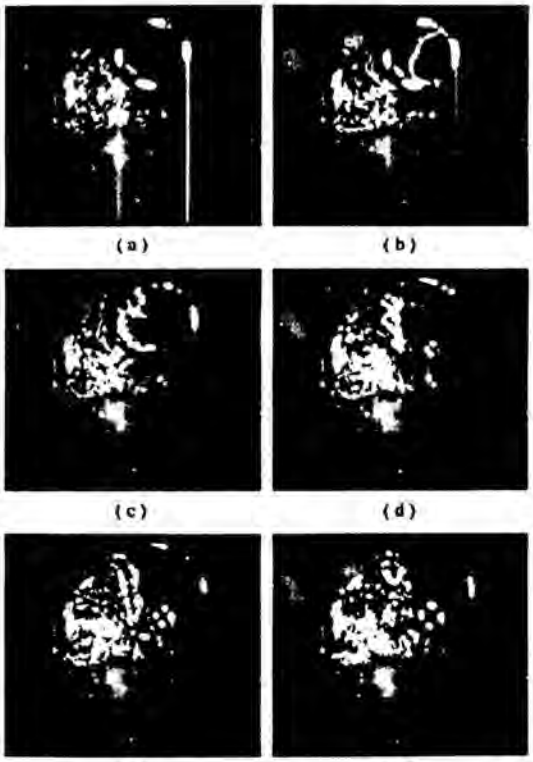

Figure 7 Development of a dryout front in the macrolayer under a bubble inside an impinging droplet, viewed from the bottom of a heated glass surface, successive frames 1 ms apart, (a) a vapor bubble identified by four bright reflections, (b) formation of a dryout front, (c) dryout front reaches the edge of the bubble, (d)-(f) liquid rewets the dry spot.

Figure 7 shows a high speed photograph of a liquid droplet boiling on a glass plate. The picture is taken with a high speed video camera looking from the underside of the glass plate. The initial glass temperature is 170°C. A bubble is formed in the liquid as identified by the four bright spots in Fig. 7(a). In the next frame, 1 ms later, a dryout front appears in the center of the bubble. The dryout front continues to expand in frame 7(c) where it almost reaches the left edge of the bubble base. In subsequent frames, the dryout front stops expanding and is seen to recede causing the rewetting of the base. This happens because the glass temperature has dropped considerably from its initial high temperature. In this case, the dryout front could not push the liquid-vapor interface further under the liquid because of the lower surface temperature.

5.2 Model Description

Kandlikar [4] presented a model that incorporates the effects of contact angle and recoil forces. Figure 8 shows a force balance on a vapor bubble growing on a horizontal heated surface. The interface is considered to be cylindrical in shape with a unit length. A force balance is performed on the left half of the cylinder. The surface tension forces act at the top of the bubble, parallel to the heated wall, $F_{s,2}$, and at the heater surface, along the interface in the contact line region, at an angle equal to the contact angle θ. $F_{s,1}$ represents the component of the surface tension force along the heater surface. The hydrostatic pressure difference between the top and the bottom of the bubble introduces a force due to gravity. The inertia forces are neglected. An additional force, F_M, due to recoil is introduced to represent the recoil force due to change in momentum as liquid evaporates into vapor with a higher velocity.

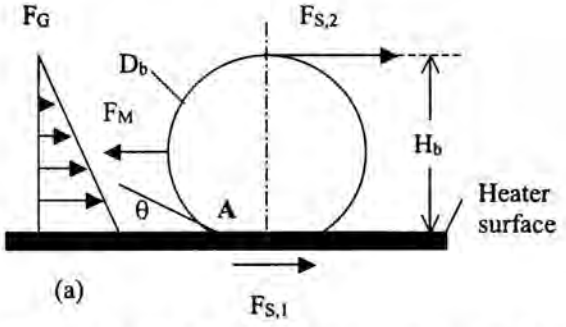

Figure 8 Force balance on a bubble experiencing a high evaporation rate in the vicinity of contact line region, Kandlikar [4].

The heat transfer from the bubble is considered to cover an area of twice the bubble diameter over the heater surface. Critical heat flux condition is reached when the recoil force overcomes the combined surface tension and hydrostatic forces along the heater surface. The final expression for the critical heat flux is given by:

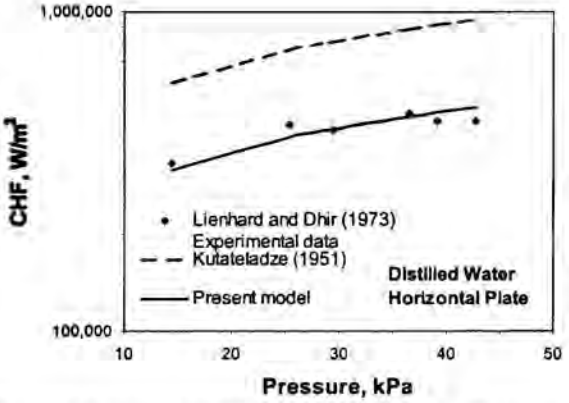

Figure 9 Variaton of CHF with pressure for distilled water boiling on a horizontal plate; comparison of present model, Kandlikar [4], (using contact angle of 45 degrees) and Kutateladze correlation with Lienhard and Dhir [27] data.

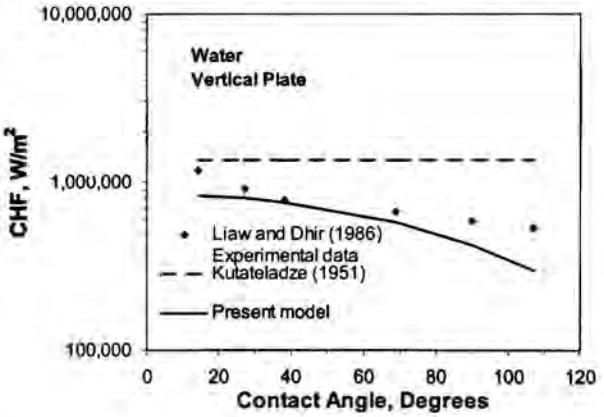

Figure 10 Effect of contact angle on CHF for water boiling on a vertical plate; comparison of present model and Kutateladze correlation with Liaw and Dhir [26] data.

$$q_C^* = i_{LG}\rho_G^{1/2}\left(\frac{1+\cos\theta}{16}\right)\left[\frac{2}{\pi}+\frac{\pi}{4}(1+\cos\theta)\cos\phi\right]^{1/2}\left[\sigma g(\rho_L-\rho_G)\right]^{1/4} \quad (6)$$

This model includes the contact angle, θ, and the orientation angle of the heater with horizontal, ϕ.

Figure 9 shows a comparison of the above model with the experimental data from Lienhard and Dhir [27]. Kutateladze [27] correlation is also shown in Fig. 9 for comparison. A contact angle value of 45° is used. It can be seen that the Kandlikar model given by eq. (6) predicts the data quite well over the entire range of pressure.

The effect of contact angle on CHF was studied by Liaw and Dhir for water on a vertical plate. Figure 10 shows a comparison of the Kandlikar model and Kutateladze model with their data. The Kutateladze correlation does not account for the contact angle variation. The Kandlikar model is able to correctly predict the CHF trend seen in the experimental data.

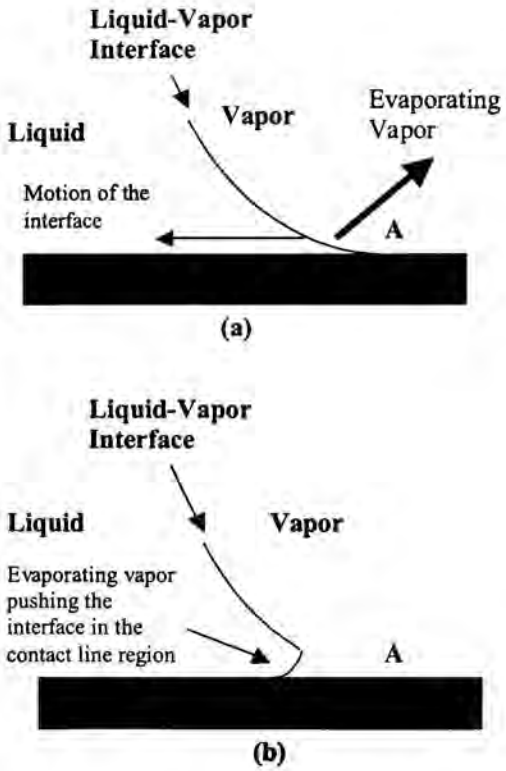

Figure 11 A schematic representation of the changes in the interface profile due to recoil forces, Kandlikar and Steinke [28].

The interface geometry in the contact line region determines the contact angle of the receding interface. The shape of the interface in this region has been investigated by Kandlikar and Steinke [28]. They obtained high-speed videos of the side views of impinging liquid droplets on a heated surface. The liquid drop spreads and recoils following the impact. The dynamic advancing and receding contact angles were measured during the spread and the recoil phases respectively. Figure 11 shows the contact angle variations with the heater surface temperature. It is seen that the dynamic receding contact angle undergoes a step change at a surface temperature around 135-

150°C and attains the same value as the dynamic advancing contact angle. The change in the dynamic receding contact angle is believed to be due to recoil forces resulting from high evaporation rates in the contact line region. A schematic representation of this behavior is illustrated in Fig. 12. The contact angle increases due to recoil forces as the interface recedes into the liquid, thereby allowing the vapor to cut under the bulk of the liquid. This phenomenon has been termed as the vapor cutback phenomenon by Kandlikar and Steinke [28].

6. CONCLUDING REMARKS

The hydrodynamic models of the CHF phenomenon are based on the instability of the interface as originally proposed by Kutateladze [17], and then refined by Zuber [19] and Moissis and Berenson.[21]. The formation of the macrolayer and the vapor patch implicit in the Zuber's model was explained by the macrolayer dryout model by Haramura and Katto [7]. The major concerns in the hydrodynamic models are: (a) the contact angle effect on CHF is not considered, (b) the actual mechanisms of CHF and transition boiling are not clearly explained.

As the heater surface temperature increases, many small diameter (a few micrometers) cavities are activated. As a result, the macrolayer under a vapor bubble evaporates rapidly and provides a high heat transfer coefficient. The dryout spot under a bubble has been observed by Kandlikar and Steinke [28] through the underside of a heated glass plate. The dryout front reached the edge of the bubble, but did not cause further expansion of the bubble as the heater surface temperature was not high enough. The vapor recoil forces and the associated receding contact angle at the edge of the bubble (in the contact line region) have been identified to play an important role in the motion of the interface near CHF. The contact angle is seen to change at temperatures near CHF condition. The theoretical model developed by Kandlikar [4] based on thermal considerations is able to correctly predict the effect of contact angle and orientation on CHF.

Future research is needed to obtain additional data on the effect of contact angle on the CHF. Another area of interest is the measurement of the dynamic contact angles for different fluids as the system approaches the CHF condition.

7. REFERENCES

1. Lang, C., 1888, *Transactions of Institute of Engineers and Shipbuilders*, Scotland, Vol. 32, pp. 279-295.
2. Nukiyama, S., 1934, "Maximum and Minimum Values of Heat Transmitted from a Metal to Boiling Water under Atmospheric Pressure," *Japanese Society of Mechanical Engineers*, Japan, Vol. 37, 367-373, S53-43.
3. Drew, T.B., and Mueller, A.C., 1937, "Boiling," *Transactions of AIChE*, Vol. 33, pp. 449-471.
4. Kandlikar, S.G., 2000, "A Theoretical Model To Predict Pool Boiling Chf Incorporating Effects Of Contact Angle And Orientation," Paper accepted for presentation in the session on *Fundamentals of Critical Heat Flux in Pool and Flow Boiling, at the ASME National Heat Transfer Conference*, Pittsburgh, August 2000. Also accepted for publication in the *Journal of Heat Transfer.*
5. Gaertner, R. F., 1965, "Photographic Study of Nucleate Pool Boiling on a Horizontal Surface," *Journal of Heat Transfer*, Vol. 87, pp. 17-29.
6. Zuber, N., 1959, "Hydrodynamic Aspects of Boiling Heat Transfer," Ph.D. thesis, Research Laboratory, Los Angeles and Ramo-Wooldridge Corporation, University of California, Los Angeles.
7. Haramura, Y., and Katto, Y., 1983, "New Hydrodynamic Model of Critical Heat Flux Applicable Widely to both Pool and Forced Convection Boiling on Submerged Bodies in Saturated Liquids, *International Journal of Heat and Mass Transfer*, Vol. 26, pp. 379-399.
8. Kirby, D.B., and Westwater, J.W., 1965, "Bubble and Vapor Behavior on a Heated Horizontal Plate During Pool Boiling Near Burnout," *Chemical Engineering Progress Symposium Series*, Vol. 61, No. 57, pp. 238-248.
9. Yu, C.L., and Mesler, R.B., 1977, "Study of Nucleate Boiling Near the Peak Heat Flux Through Measurement of Transient Surface Temperature," *International Journal of Heat and Mass Transfer*, Vol. 20, pp. 827-840.
10. Griffith, P. and Wallis, J.D., 1960, "The Role of Surface Conditions in Nucleate Boiling," *Chemical Engineering Progress Symposium*, Ser. 56, 30:49-63.
11. Hsu, Y. Y., 1962, "On the Size Range of Active Nucleation Cavities on a Heating Surface, *Journal of Heat Transfer, Trans. ASME*, Vol. 84, pp. 207-216.
12. Sato, T., and Matsumura, H., 1964, "On the Conditions of Incipient Subcooled Boiling with Forced Convection," Bulletin of JSME, Vol. 26, pp. 392-398.
13. Wang, C. H., and Dhir, V. K., 1993a, "On the Gas Entrapment and Nucleation Site Density during Pool Boiling of Saturated Water," *Journal of Heat Transfer*, Vol. 115, pp. 670-679.
14. Wang, C. H., and Dhir, V. K., 1993b, "Effect of Surface Wettability on Active Nucleation Site Density during Pool Boiling of Saturated Water," *Journal of Heat Transfer*, Vol. 115, pp. 659-669.
15. Dhir, V. K., 1999, Nucleation Site Density, Section 4.5 in Handbook of Phase Change: Boiling and Condensation, Eds. S. G. Kandlikar, M. Shoji, and V. K. Dhir, Taylor and Francis, New York.
16. Kutateladze, S.S., 1948, "On the Transition to Film Boiling under Natural Convection," Kotloturbostroenie, No. 3, pp. 10-12.
17. Kutateladze, S.S., 1951, "A Hydrodynamic Theory of Changes in a Boiling Process under Free Convection," *Izvestia Akademia Nauk, S.S.S.R., Otdelenie Tekhnicheski Nauk*, No. 4, pp. 529 (referenced in Zuber, 1959).

18. Borishanskii, V.M., 1955, "On the Problem of Generalizing Experimental Data on the Cessation of Bubble Boiling in Large Volume of Liquids," *Ts. K.I.T.*, Vol. 28, Moscow, (in Zuber, [19]).
19. Zuber, N., 1959, "Hydrodynamic Aspects of Boiling Heat Transfer," Ph.D. thesis, Research Laboratory, Los Angeles and Ramo-Wooldridge Corporation, University of California, Los Angeles.
20. Chang, Y.P., 1961, "An Analysis of the Critical Conditions and Burnout in Boiling Heat Transfer," *USAEC Rep. TID-14004*, Washington, DC.
21. Moissis, R., and Berenson, P.J., 1963, "On the Hydrodynamic Transitions in Nucleate Boiling," *Journal of Heat Transfer, Trans. ASME, Series C*, Vol. 85, August 1963, pp. 221-229.
22. Katto, Y., and Yokoya, S. 1968, "Principal Mechanism of Boiling Crisis in Pool Boiling," *International Journal of Heat and Mass Transfer*, Vol. 11, pp. 993-1002.
23. Sefiane, K., Benielli, and Steinchen, A., 1998, "A New Mechanism for Pool Boiling Crisis, Recoil Instability and Contact Angle Influence," Colloids and Surfaces, A; Physiochemical and Engineering Aspects, Vol. 142, pp. 361-373.
24. Moissis, R., and Berenson, P.J., 1963, "On the Hydrodynamic Transitions in Nucleate Boiling," *Journal of Heat Transfer, Trans. ASME, Series C*, Vol. 85, August 1963, pp. 221-229.
25. Gaertner, R.F., 1963, "Effect of Heater Surface Chemistry on the Level of Burnout Heat Flux in Pool Boiling," *Technical Information Series*, No. 63-RL-3449C, General Electric Research Laboratory, Schenectady, New York.
26. Liaw , S.P., and Dhir, V.K., 1986, "Effect of Surface Wettability on Transition Boiling Heat Transfer from a Vertical Surface," Proceedings of the Eighth International Heat Transfer Conference, San Francisco, CA, Vol. 4, pp. 2031-2036.
27. Lienhard, J.H., and Dhir, V.K., 1973, "Extended Hydrodynamic Theory of the Peak and Minimum Pool Boiling Heat Fluxes," NASA CR-2270, Contract No. NGL 18-001-035.
28. Kandlikar, S. G., and Steinke, M. E., 2001, "High Speed Photographic Investigation of Liquid-Vapor Interface and Contact Line Movement during CHF And Transition Boiling," IMECE Paper # 2-8-3-1, ASME, New York

HEFAT 2002
1st International Conference on Heat Transfer, Fluid Mechanics and Thermodynamics
8-10 April 2002, Kruger Park, South Africa
TJ1

ON RECENT ADVANCES IN MODELLING OF TWO-PHASE FLOW AND HEAT TRANSFER

Prof. John R. Thome

Laboratory of Heat and Mass Transfer (LTCM)
Faculty of Engineering Science
Swiss Federal Institute of Technology Lausanne
CH-1015 Lausanne, Switzerland
E-mail: john.thome@epfl.ch

ABSTRACT

The best approaches to modelling of two-phase heat transfer and two-phase pressure drops are based on two-phase flow pattern analysis. Many of the old-style models for evaporation, condensation and two-phase pressure drops completely ignored flow regime effects or simply treated flows as stratified (gravity-controlled) or non-stratified (shear-controlled) flows. This greatly limits their accuracy, validity and reliability, resulting in prediction errors often surpassing 100% within their supposed range of application. General methods have now begun to emerge that are based on local two-phase flow patterns and the flow structure of the two-phases. Thus, a new paradigm for modelling of two-phase flow and heat transfer is emerging in which there is no more justification for proposing new correlations that are *blind* with respect to flow regime. The status of these new developments is discussed here but most of the focus is placed on pointing out shortcomings of current and past methods. The idea is not to criticize the past and present but instead to initiate an overdue discussion on what is generally considered to be correct and instead may not be or only partly so. Thus, the focus here is a critical review of the *status quo*, not individual methods.

INTRODUCTION

Rather than writing a state-of-the-art review on what is known, the objective here is instead to raise issues about what is wrong with what we presently do. The term *wrong* here might imply that some concept, some simplification, some empirical expediency, etc. may be incorrect, incomplete or inopportune. Such a judgement is naturally subjective, and hence the present review represents primarily my own views and experience. It is offered here not to give a verdict but instead to provide testimony and thus to open the door towards a more fruitful discussion of future research in this domain. As such, it is not the objective of this review to document all the various recent prediction methods for boiling, condensation and two-phase flows but instead to raise issues about what should or should not be in them. Therefore, the focus here will be the building blocks used to construct two-phase flow pattern based models for heat transfer and two-phase pressure drops, which are: flow pattern maps and/or flow pattern transition criteria, void fraction models, two-phase flow structures, heat transfer mechanisms and pressure drop models themselves, appropriate test data and so forth. The intube processes that will be addressed are: two-phase pressure drops, evaporation and condensation.

As a first illustrative example what this means, let's take the pioneering work of Chen (1963) on intube flow boiling in vertical tubes. He proposed a new heat transfer model including nucleate boiling with flow induced boiling suppression together with liquid-phase convection augmented by a two-phase multiplier, an approach which has been influential now for nearly 40 years. This model has given us our primary physical interpretation of what is dominating heat transfer during intube evaporation as we know it today and these concepts are still those to be used tomorrow. On the other hand, numerous publications with reformulations of his method have already reached their natural limitation with respect to accuracy and reliability since they have added little to the model itself, i.e. typically only a large experimental database together with new empirical constants for adjusting a new mix of parameters. Thus, as a statistical exercise, they have reached a threshold where little further improvement can be obtained

unless one adds some significant new ideas. It is now high time that new contributions to the physical understanding of the process are made rather that continuing to propose new reformulated Chen correlations. As an example of such a positive note, the asymptotic approach of Steiner and Taborek (1992) and their introduction of an onset of nucleate boiling criterion for modelling flow boiling inside vertical tubes mark a significant step forward, although it is not a flow regime based model. The challenge at hand today is to additionally interpret the particular process by flow pattern and by two-phase flow structure, which essentially means proposing a marriage between two disciplines: *two-phase flow* (fluid flow experts primarily interested in predicting adiabatic flow transitions) and *two-phase heat transfer* (heat transfer experts primarily interested in predicting condensation and evaporation heat transfer coefficients).

Intube condensation is also a good example of where local flow regime is important. Many methods have been proposed for gravity-controlled and shear-controlled condensation inside horizontal tubes. The effect of the flow regime is important but has nevertheless largely been ignored, where simplified criteria have often been proposed to delineate stratified and non-stratified flows based on a statistical analysis of the heat transfer database rather than flow pattern observations. For example, the widely quoted and widely emulated approach of Akers, Deans and Crosser (1959) for predicting intube condensation relies only on an equivalent Reynolds number, which they defined as

$$Re_e = \frac{DG_e}{\mu_L} \qquad (1)$$

where the equivalent mass velocity G_e is:

$$G_e = G\left[(1-x)+x\left(\frac{\rho_L}{\rho_V}\right)^{1/2}\right] \qquad (2)$$

and G is the total mass velocity of liquid plus vapor through the channel. Thus, there is nothing in this criterion about the flow instability encountered when passing from an annular flow to a stratified-wavy flow. This point leads to another important issue: step changes in heat transfer coefficients across a transition boundary or criterion. For instance, the heat transfer correlation of Akers, Deans and Crosser gives the local condensation heat transfer coefficient as:

$$\frac{\alpha_c D}{\lambda_L} = C\,Re_e^n\,Pr_L^{1/3} \qquad (3)$$

where the values of the parameters C and n are as follows:

- For $Re_e > 50000$, C = 0.0265 and n = 0.8;
- For $Re_e < 50000$, C = 5.03 and n = 1/3.

Hence, at a value of $Re_e = 50000$, we have a ratio of 1.217 for the second criterion relative to the first, which represents a step change increase in heat transfer for a small decrease in vapor quality. In this case, the step change is not that large, only 22%, but it is not observed experimentally and means that the trends in the experimental data are not correctly reflected in the prediction method.

In this light, rather than reformulating new methods based on old ideas, there is significant potential for progress by creating new heat transfer models that include more physics of the actual flow structure. To do this, one must first predict (identify) the local two-phase flow pattern based on the local flow conditions, which requires a reliable two-phase flow pattern map. Secondly, some simplified but realistic geometrical formulation of the flow structure must be assumed for physically describing the flow. In order to quantify an annular flow structure assumed to be an annular ring for instance, at the minimum a void fraction model is required to predict the relative cross-sectional areas occupied by the two-phases. The heat transfer or pressure drop model can also be formulated to represent the appropriate heat transfer and frictional mechanism(s) occurring around the perimeter of the tube, which may be locally wet or dry depending on the flow regime. Thus, a stratification angle or dry angle is required to represent these two respective perimeters. The interaction between the two-phases may also be important, such as the effect of interfacial waves on friction and transition or vice-versa. This flow pattern type of approach is not new but in the past was primarily implemented with just one flow pattern in mind and has resulted in a patchwork of methods with conflicting transition criteria and step changes in predicted values from one flow pattern to another.

Furthermore, it is common in heat exchanger design codes to find that two or more different void fraction models are used for predicting the static pressure drop, the momentum pressure drop, the frictional pressure drop and the heat transfer coefficient. Thus, the idea is now to work towards a unified method that avoids these inconsistencies and which is applicable for a representative number of the flow

regimes in order to arrive at a general unified prediction method for both two-phase heat transfer and two-phase pressure drops.

FLOW PATTERN MAPS AND TRANSITION CRITERIA

Numerous flow pattern maps have been proposed over the years for predicting two-phase flow regime transitions in horizontal and vertical tubes under *adiabatic* conditions. The maps of Taitel and Dukler (1976) and Baker (1954) are widely quoted for horizontal tubes. Specifically for condensation, flow pattern maps have been proposed by Breber, Palen and Taborek (1980), by Tandon, Varma and Gupta (1982) and recently by Cavallini et al. (2002). In addition, numerous methods have been proposed to differentiate between stratified and non-stratified condensation, such as those by Sardesai, Owen and Pulling (1981), Shah (1979) and Dobson and Chato (1998). Another new map has been proposed by Kattan, Thome and Favrat (1998a) for adiabatic and evaporating flows in horizontal tubes, backed by over 1000 flow pattern observations for seven different refrigerants. For vertical tubes, the maps of Fair (1960) and Hewitt and Roberts (1969) are widely cited. Barnea (1987) has proposed a general map for adiabatic upward, downward or horizontal flow inside tubes of any of those orientations. With respect to our present topic, the long term goal is to arrive at a *unified flow pattern map* for modeling heat transfer and pressure drops during evaporation, condensation and adiabatic flows within horizontal, vertical and inclined tubes while still accounting for the evident differences in these processes.

The first problem one confronts in proposing a flow pattern based heat transfer or pressure drop model is choosing the most appropriate flow pattern map. Kattan, Thome and Favrat (1998a) for instance found that the Taitel and Dukler map was only able to correctly identify about 50% of their flow pattern observations. Similarly, criteria for horizontal flows to distinguish stratified from non-stratified flows in boiling, typically with the liquid Froude number, defined as

$$Fr_L = \frac{G^2}{\rho_L^2 g D} \qquad (4)$$

were proven experimentally to also be particularly unreliable, with the Fr_L threshold sometimes off by an order of magnitude. Hence, in the end, they proposed a new version of the Steiner (1993) flow pattern map which in turn is a modified version of the original Taitel-Dukler map. Figure 1 illustrates this map whose transition equations are evaluated to present the map in a G vs. x format that is easier to read than the prior log-log maps, showing the new updated version of this map by Thome and El Hajal (2002) applied to R-134a with its properties at 4°C for two diameters of tube.

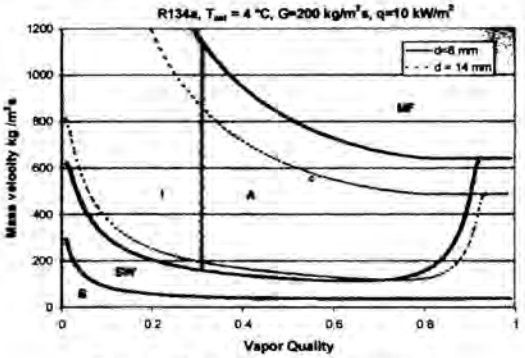

Figure 1. Two-phase flow pattern map evaluated for R-134a.

In general, the problems and challenges arising from use of flow pattern maps can be summarized as follows:

1. There are a large number of existing maps to choose from and it is difficult to know which is the best since no "blind taste tests" exist;
2. Many different flow regime names are used, subcategories may be identified as well, and also different definitions of what constitutes a particular flow regime, which makes a quantitative comparison of competing flow pattern maps essentially impossible;
3. Flow pattern identification from flow observations is subjective, even when using one set of flow regime names with clearly stated qualitative descriptions of each, and this leads to uncertainty from one observer to another, especially near transitions where reliable data are most critical;
4. Some flow pattern maps include flow transition zones between the stable regimes while others do not, making comparison between such transition equations possible only on a very qualitative basis;
5. The transition zone around transition curves predicted on maps can be quite large (±50 kg/m^{2}s for the annular to stratified-wavy transition is typical), analogous to the transition zone between laminar and turbulent single-phase flows, and often is characterized by the flow cycling between the two flow patterns until one finally dominates;

6. Flow pattern transitions may exhibit hysteresis depending on whether the flow rate is increased or decreased from one steady-state condition to the next.
7. Representative flow pattern observations for all the important transitions from one flow pattern to its bordering patterns are not usually available and hence the location of the border is well defined.
8. Existing maps are primarily for adiabatic flows and hence diabatic effects must be added to them.

Thus, quickly a long list of issues can be identified which have no simple solutions. The choice or development of the flow pattern map has a particularly important influence on the accuracy and reliability of the resulting heat transfer or pressure drop model, however. Consequently, including flow pattern observations as part of experimental studies on two-phase heat transfer and pressure drops is vital and should be included.

VOID FRACTION

Void fraction is defined as the cross-sectional area occupied by the vapor or gas phase relative to that of the flow channel, which because of the different densities and velocities of the respective phases is not equal to the vapor quality. In an annular flow, for instance, if the simplified flow structure is assumed to be an annular liquid ring of uniform thickness without interfacial waves and without liquid entrainment in the central vapor core, and assuming that $\delta << D$, the thickness of the liquid ring is:

$$\delta = \frac{D(1-\varepsilon)}{4} \tag{5}$$

where δ is the liquid film thickness, D is the internal tube diameter and ε is the cross-sectional void fraction of the vapor. Void fraction models may be classified as follows:

- Homogeneous model (assumes the two phases travel at same velocity);
- Momentum models (they minimize some parameter, such as momentum or kinetic energy);
- Drift flux models (they account for the radial velocity distribution in the two phases);
- Models for specific flow regimes;
- Empirical methods.

The homogeneous model is applicable when the vapor and liquid phases travel at nearly the same velocity, such as near the critical point or at very high mass velocities where the flow regime is either bubbly flow or mist flow. The homogeneous void fraction is given by

$$\varepsilon = \frac{1}{1+\left(\frac{1-x}{x}\right)\frac{\rho_v}{\rho_L}S} \tag{6}$$

where the velocity ratio S is

$$S = \frac{u_v}{u_L} \tag{7}$$

For equal velocities of the gas phase u_V and the liquid phase u_L, this expression reverts to the homogeneous void fraction, i.e. when S = 1. For upward and horizontal co-current flows, u_V is nearly always greater than u_L such that $S \geq 1$. In this case, the homogeneous void fraction is the upper limit on possible values of ε. For vertical down flows, u_V may be larger or smaller than u_L, such that when $S < 1$ the homogeneous void fraction is the lower limit on the value of ε. Some widely quoted models as those of Zivi (1964), Chisholm (1972) and the various drift flux models. For example, the Zivi void fraction equation is used in numerous condensation heat transfer models over the years, where the velocity ratio S is

$$S = \frac{u_G}{u_L} = \left(\frac{\rho_L}{\rho_G}\right)^{1/3} \tag{8}$$

and hence the Zivi void fraction expression is

$$\varepsilon = \frac{1}{1+\frac{1-x}{x}\left(\frac{\rho_G}{\rho_L}\right)^{2/3}} \tag{9}$$

The Rouhani and Axelsson (1970) drift flux type of void fraction model gives the following expression for ε for horizontal flows:

$$\varepsilon = \frac{x}{\rho_V}\left[(1+0.12(1-x))\left(\frac{x}{\rho_V}+\frac{1-x}{\rho_L}\right)+\frac{1.18(1-x)\left[g\sigma(\rho_L-\rho_V)\right]^{0.25}}{G\rho_L^{0.5}}\right]^{-1} \tag{10}$$

Hence, in addition to the effects of x and the ratio of ρ_G/ρ_L in the Zivi model, this drift flux model for includes the effects of mass velocity, surface tension and buoyancy.

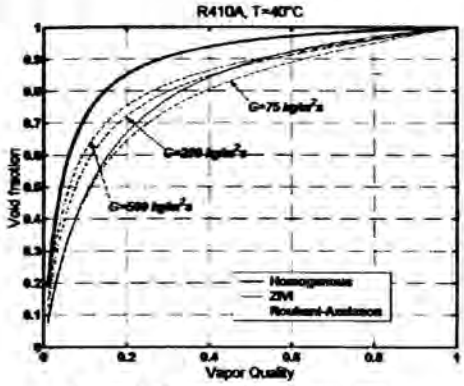

Figure 2. Comparison of void fraction equations for R-410a.

Void fractions ranges in value from $\varepsilon = 0$ at $x = 0$ to $\varepsilon = 1$ at $x = 1$. Typically, ε rises very rapidly at low vapor qualities and then progresses towards the final value of unity, although not all void fraction models correctly go to 1.0 in their limit. Figure 2 depicts a comparison among the above three methods and illustrates the important effect of G on ε. Hence, there is a big difference in ε depending on the method chosen at low vapor qualities but little absolute difference at large vapor qualities. Even so, from the above expression for δ, it is clear that a void fraction of 0.96 produces an annular film twice as thick as a value of 0.98. Hence, the void fraction model selected as the basis for a two-phase heat transfer or pressure drop model has a very big influence on the film. For instance, the Kattan, Thome and Favrat (1998b) annular film expression for the convective boiling contribution to flow boiling heat transfer is:

$$\alpha_{cb} = c\,\mathrm{Re}_L^n\,\mathrm{Pr}_L^{0.4}\,\frac{\lambda_L}{\delta} \qquad (11)$$

where the liquid film Reynolds number Re_L is based on the mean liquid velocity of the liquid is:

$$\mathrm{Re}_L = \frac{4G(1-x)\delta}{(1-\varepsilon)\mu_L} = \frac{GD(1-x)}{\mu_L} \qquad (12)$$

which reduces to the second term for annular flows. The convective boiling heat transfer coefficient in annular flow is thus very sensitive to void fraction, such that α_{cb} is proportional to $(1-x)^n/(1-\varepsilon)$, where $\varepsilon > x$ for $x \neq 0$. Hence, at fixed G and heat flux q, the slopes of experimental curves with α_{cb} vs. x are in fact determined only by the variation in x and ε. Thus, void fraction is clearly the central parameter in this and other two-phase models. The values of c and n in Eq. (11) are obtained from regression of this expression versus heat transfer data and thus are influenced by the choice of the void fraction model.

In summary, drift flux void fraction models are particularly attractive because they account for the velocity distributions in the vapor and liquid phases and hence include the effect of mass velocity on void fraction, which the other methods do not. They are also available specifically for particular flow patterns, although using different methods for different flow regimes, such as in the most recent heat transfer model of Zürcher, Favrat and Thome (2002), must be done without a step change in void fraction across a flow transition boundary. The Zivi expression is not a function of G, which is its biggest limitation to general use.

TWO-PHASE PRESSURE DROPS

The two-phase pressure drops for flows inside tubes are the sum of three contributions: the static pressure drop Δp_{static}, the momentum pressure drop Δp_{mom} and the frictional pressure drop Δp_{frict} as:

$$\Delta p_{total} = \Delta p_{static} + \Delta p_{mom} + \Delta p_{frict} \qquad (13)$$

The static pressure drop is given by

$$\Delta p_{static} = \rho_{tp}\, g\, H \sin\theta \qquad (14)$$

where the two-phase density ρ_{tp} is

$$\rho_{tp} = \rho_L(1-\varepsilon) + \rho_V\varepsilon \qquad (15)$$

For a horizontal tube, there is no change in static head, so $H = 0$ and $\Delta p_{static} = 0$ while $\sin\theta$ is equal to 1.0 for a vertical tube. The momentum pressure drop reflects the change in kinetic energy of the flow and is for the present case given by:

$$\Delta p_{mom} = G^2 \left\{ \left[\frac{(1-x)^2}{\rho_L(1-\varepsilon)} + \frac{x^2}{\rho_V \varepsilon} \right]_{out} - \left[\frac{(1-x)^2}{\rho_L(1-\varepsilon)} + \frac{x^2}{\rho_V \varepsilon} \right]_{in} \right\} \quad (16)$$

Thus, the static and momentum pressure drops are clearly dependent on the choice of void fraction model, especially at low vapor qualities where void fraction values rise rapidly.

Regarding the frictional pressure drop, these are known to be flow regime dependent and specific models for some regimes have been proposed. On the other hand, most of the methods used in practice are empirical approaches applied broadly to numerous flow patterns, such as those of Lockhart and Martinelli (1949), Friedel (1979), Grönnerud (1979), Chisholm (1973) and Müller-Steinhagen and Heck (1986). Standard and mean deviations of these approaches are still uncomfortably large. The difficult challenge is to put together one comprehensive model based on a flow pattern map for prediction of two-phase pressure drops encompassing all the flow patterns of interest. The following issues are important:

- Many existing frictional pressure drop prediction methods to not go to the correct limits at x = 0 and/or x = 1;
- Experimental data show that the frictional pressure gradient goes through a maximum at high vapor qualities and then declines towards the all vapor gradient, an important trend that only some methods capture;
- Often one void fraction method is used for calculating Δp_{static} and Δp_{mom} while another is used within the methods for Δp_{frict}, which is often an overlooked inconsistency;
- There may be an effect of the heat transfer process on Δp_{frict} not present for an adiabatic flow, such as the condensate film in the stratified-wavy regime on the top perimeter of the tube which would otherwise be dry.

INTUBE EVAPORATION

Before discussing advances being made on flow regime based flow boiling models, it is instructive to discuss the limitations posed by existing methods, many of which are widely used for thermal design of heat transfer equipment. Since there is a considerable inertia to continue using these methods, it is particularly important to challenge their real usefulness. As an example, the limitation on intube evaporation in horizontal tubes is highlighted below but some of these issues also apply to vertical tubes.

Evaporation inside horizontal tubes is a complex physical process involving nucleate boiling, convective heat transfer to the liquid and vapor phases, thin film evaporation along the top of the tube where it is wetted by intermittent large amplitude waves, dryout of liquid films, interaction of the two phases at their interface, etc. Figure 3 from Collier and Thome (1994) depicts a composite diagram of these processes.

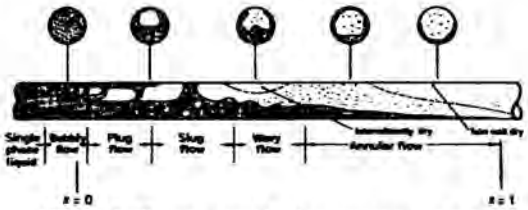

Figure 3. Flow patterns during evaporation in a horizontal tube from Collier and Thome (1994).

Numerous methods have been proposed over the years for predicting local flow boiling heat transfer coefficients for evaporation inside tubes. Since Chen (1963) proposed his model for vertical tubes, a myriad of reformulations of his method have been proposed for vertical and horizontal tubes. Furthermore, most horizontal tube methods are actually vertical tube methods fit to horizontal test data by introducing only a flow stratification criterion to delineate between stratified and non-stratified flows without any reference to the two-phase flow structure itself.

For example, Shah (1982) applied his vertical tube method to horizontal tubes by adjusting his two-phase convection multiplier C_o by adding a correction factor based on the liquid Froude number, defined so that it is $0.38\ Fr_L^{-0.3}C_o$ when $Fr_L < 0.04$, i.e. for stratified types of flow, while for non-stratified flows when $Fr_L \geq 0.04$, he applied his vertical method using the value of C_o without change. Others have since set this Froude threshold value to 0.5 and more recently 0.25 in their correlations. Classifying flow boiling data by flow regime using the Kattan, Thome and Favrat (1998a) map, Kattan, Thome and Favrat (1998b) found that these old-style methods did not predict flow boiling data in the stratified-wavy regime as accurately as they did for annular flow data; in fact, the errors were about twice as large or more.

Alternatively, Klimenko and Fyodorov (1990) proposed a modified Chen correlation for horizontal tubes with a new stratification criterion, albeit empirically fit to heat transfer data and not flow pattern observations. Subsequently, Kattan, Thome and Favrat (1995a) found that the Klimenko-Fyodorov stratification criterion only correctly identified their observations of stratified and unstratified flows about 50% of the time, similar to that they also observed for the Fr_L criterion above.

The drawbacks of these old-style methods have been described earlier by Thome (1996):

- Adapting vertical tube methods to horizontal tubes is risky because vertical tube databases include few test data at high vapor quality since dryout is reached at vapor qualities from 50-75% while high vapor qualities are an important design condition in horizontal tube applications (direct-expansion evaporators);
- They utilize a single-phase *tubular* flow correlation (Dittus-Boelter) as their starting point to predict annular liquid *film* flow heat transfer, which is not physically logical;
- These methods do not recognize the different flow patterns occurring in horizontal flow boiling, except for stratification for which they tend to poorly predict the threshold from stratified to unstratified types of flow;
- For stratified types of flows, single-phase heat transfer to the vapor phase is also present which these methods ignore;
- These methods are blind to the onset of dryout and hence do not predict the subsequent sharp decline in α_{tp} as dryout progresses around the tube from top to bottom in annular flows at high vapor qualities (partial dryout is depicted in Figure 3 at high vapor qualities);
- Some methods introduce two-phase multipliers based on interfacial parameters, such as the Martinelli parameter X_{tt}, on the convective heat transfer coefficient, which has only a tenuous relationship to the turbulent boundary sublayer at the heated wall that controls single-phase convection;
- Their predictions of local flow boiling coefficients α_{tp} versus local vapor quality x at a fixed heat flux typically often do not give a good representation of the observed experimental trends nor slope in plots of α_{tp} vs. x.

Kattan, Thome and Favrat (1998a, 1998b) recently proposed a flow regime based flow boiling model for evaporation inside horizontal tubes. They began by assuming simplified geometries representative of the two-phase flow structures for the various flow patterns and developed a new flow pattern map for identifying when a particular flow regime would occur. Their simplified flow structure geometries for describing annular, stratified-wavy and fully stratified-wavy flows are shown in Figure 4. Annular flows with partial dryout around the top of the tube were classified as stratified-wavy flows and are thus modelled accordingly. Flow structures for the intermittent, mist flow and bubbly flow regimes have yet to be proposed (their development is the topic of ongoing research). Intermittent flows, i.e. stratified flow with large amplitude waves continuously wetting the top perimeter of the tube, are currently modelled using the annular flow structure.

In Figure 4, for annular flow in the lower left diagram, the variation in the thickness of the film from top to bottom is ignored for the sake of simplicity and a uniform thickness is assumed. Utilizing a void fraction equation, the area occupied by the vapor phase is determined and hence that too of the liquid phase, such that the film thickness is calculable from the cross-sectional area of the tube. Knowing the total flow of liquid plus vapor and the local vapor quality, the mass flow rate of the liquid is easily calculated and together with its density, the mean velocity of the liquid can be determined in the film. Hence, turbulent flow heat transfer to the film can be correlated based on the mean velocity of the liquid film and film thickness. Thus, *film* flow is modelled rather than *tubular* flow as in the previous methods.

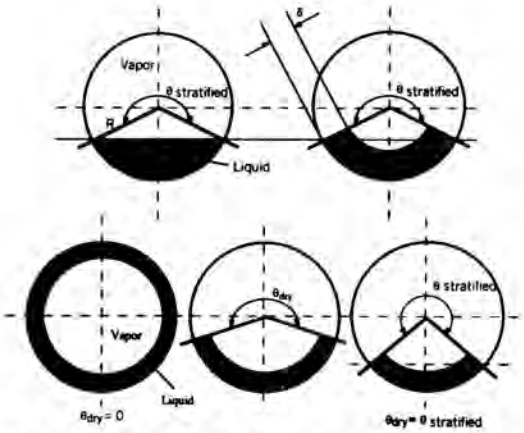

Figure 4. Flow structures for annular, stratified-wavy and fully stratified flows (left to right in bottom three diagrams) and for fully stratified flow and its film flow equivalent (top two diagrams).

The actual geometry for fully stratified flow is shown in the upper left in Figure 4 (without bubbles originating from nucleate boiling) while its equivalent geometry is assumed to be a truncated annular ring as shown in the upper and lower diagrams at the right. The stratified angle θ_{strat} is calculated from the cross-sectional area occupied by the liquid in the upper left diagram and is then used to determine the wetted angle in the diagram at the right, where for simplicity the liquid film is assumed to have a uniform thickness. The liquid film thickness can be calculated for the truncated annular ring using the same area as in the upper left diagram, which also then allows the mean liquid velocity to be determined.

For stratified-wavy flow, the liquid waves are small in amplitude and do not reach the top of the tube. Hence the top perimeter of the tube is continuously dry, similar to fully stratified flow. For simplicity, the liquid is again assumed to be distributed uniformly in an annular truncated ring as shown in the middle diagram at the bottom of Figure 4. The dry angle θ_{dry} varies between its maximum value of θ_{strat} at the threshold to fully stratified flow and its minimum value of zero at the threshold to annular flow where the wall is always all wet. Hence, these three simple geometries have a smooth geometrical transition from one flow structure to another and also allow the heat transfer models to be based on the mean liquid and mean vapor velocities. The evaporation heat transfer coefficient is applied to the wetted perimeter while a single-phase vapor heat transfer coefficient is calculated for the dry perimeter. Thus, while ignoring numerous details of the flow structure, the present geometries represent the principal features. Annular flow with partial dryout of the upper perimeter of the tube is thus modelled as stratified-wavy flow because of its similarity to this simplified flow structure. These simplified flow structure geometries were selected to make them geometrically continuous at the transition from one flow pattern to another and hence not introduce a step-change in the local heat transfer coefficient when passing from one regime to another.

The general expression of the Kattan-Thome-Favrat model for the local flow boiling coefficient α_{tp} for a tube with an internal radius R is:

$$\alpha_{tp} = \frac{R\theta_{dry}\,\alpha_v + R(2\pi - \theta_{dry})\alpha_{wet}}{2\pi R} \qquad (17)$$

The heat transfer coefficient α_{wet} on the wetted tube perimeter of $R(2\pi-\theta_{dry})$ is obtained with an asymptotic equation that combines the nucleate boiling coefficient α_{nb} and the convective boiling coefficient α_{cb} as:

$$\alpha_{wet} = \left(\alpha_{nb}^3 + \alpha_{cb}^3\right)^{1/3} \qquad (18)$$

where α_{nb} is determined with the correlation of Cooper (1984):

$$\alpha_{nb} = 55 p_r^{0.12}\left(-\log_{10} p_r\right)^{-0.55} M^{-0.5} q^{0.67} \qquad (19)$$

setting the surface roughness to 1 micron while α_{cb} is for annular liquid *film* flow:

$$\alpha_{cb} = 0.0133\left(\frac{4\,G\,(1-x)\delta}{(1-\varepsilon)\mu_L}\right)^{0.69} Pr_L^{0.4}\frac{\lambda_L}{\delta} \qquad (20)$$

The above equation includes the liquid film Reynolds number Re_L, based on the mean liquid velocity in the annular film, which is a local function of the vapor quality, annular liquid film thickness δ, and vapor void fraction ε. *Notice in particular that modelling the liquid flow as a film flow eliminates the need for the empirical two-phase multiplier found in other methods.* Also, an asymptotic method weighs the relative importance of α_{nb} and α_{cb}, so no boiling suppression factor was included. The vapor-phase heat transfer coefficient α_v is obtained with the Dittus-Boelter correlation assuming *tubular* flow over the dry perimeter of the tube ($R\theta_{dry}$) in Figure 4, so that:

$$\alpha_v = 0.023\left(\frac{GxD}{\varepsilon\mu_v}\right)^{0.8}\left(\frac{c_{p_v}\mu_v}{\lambda_v}\right)^{0.4}\frac{\lambda_v}{D} \qquad (21)$$

The Rouhani-Axelsson (1970) drift flux void fraction model, Eq. (10), is used for ε. The cross-sectional area of the tube occupied by the liquid-phase A_L is

$$A_L = A(1-\varepsilon) \qquad (22)$$

where A is the total cross-sectional area of the tube. For the fully stratified flow regime illustrated at the top left in Figure 4, the stratified angle θ_{strat} of the liquid layer in the lower part of the tube is obtained from the following implicit geometrical expression:

$$A_L = 0.5R^2\left[(2\pi - \theta_{strat}) - \sin(2\pi - \theta_{strat})\right] \qquad (23)$$

The dry angle θ_{dry} in Equation (17) is the radial angle of the tube wall that is assumed to be constantly dry for stratified types of flows and annular flows with partial dryout. For annular and intermittent flows, θ_{dry} is equal to zero and thus α_{tp} is equal to α_{wet}. As illustrated in Figure 5, the dry angle θ_{dry} varies from its lower limit of zero for annular flow at G_{high} to its maximum value equal to θ_{strat} for fully stratified flow at G_{low}, which themselves are functions of vapor quality and hence θ_{dry} is a function of G and x. A simple linear expression for the variation in θ_{dry} between G_{high} and G_{low} was assumed for simplicity:

$$\theta_{dry} = \theta_{strat}\frac{(G_{high} - G)}{(G_{high} - G_{low})} \qquad (24)$$

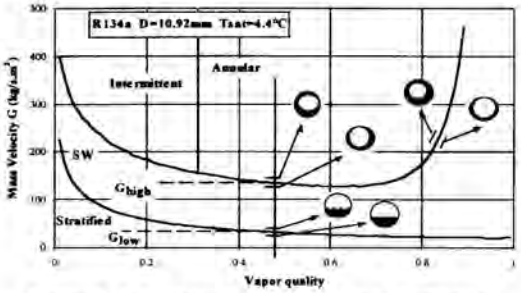

Figure 5. Two-phase flow pattern map illustrating values of G_{low} and G_{high}.

The annular liquid film thickness δ is determined by equating the cross-sectional area occupied by the liquid phase to that of a segment of an annular liquid ring as shown in Figure 4, so that:

$$\delta = \frac{A_L}{R(2\pi - \theta_{dry})} = \frac{\pi D(1-\varepsilon)}{2(2\pi - \theta_{dry})} \qquad (25)$$

For additional details, refer to the original publication.

Figure 6 illustrates a simulation of the new heat transfer model for R-134a in a 12.0 mm internal diameter tube at several different mass velocities and heat fluxes. At the lowest mass velocity (G=100), the flow is in the stratified-wavy regime over the entire range of vapor qualities shown. Hence, the local heat transfer coefficient rises slowly as the convective contribution increases with increasing vapor quality while the wetted perimeter of the tube slowly decreases. An increase in the heat flux from 5 to 10 kW/m^2 illustrates that the contribution of nucleate boiling increases with heat flux as expected, except at high vapor qualities where it tends to reduce the wetted angle. At the highest mass velocity (G=400), the flow begins in the intermittent regime at x=0.15, converts into annular flow at x=0.32, and goes on to reach its peak in heat transfer at the onset of dryout, after which the flow reverts to stratified-wavy flow and the heat transfer coefficient declines rapidly in value as θ_{dry} decreases as x increases. The increase in heat flux from 10 to 20 kW/m^2 in the intermittent and annular flow regimes results in higher heat transfer coefficients as expected, with less influence as the peak is approached since convection becomes more and more dominant. The higher heat flux causes the onset of dryout to occur at a lower vapor quality and hence the peak for 20 kW/m^2 is reached first. Because of the lower coefficients after the peak, the mean thermal performance is higher for the lower heat flux curve than for the higher one, something that would not be evident without this detailed heat transfer model. The comments regarding the intermediate mass velocity (G=200) are similar to those for G=400.

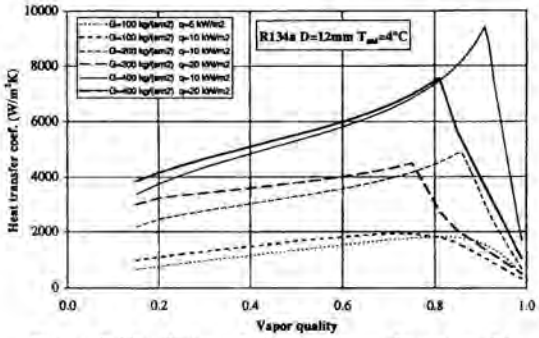

Figure 6. Simulation of Kattan-Thome-Favrat model for R-134a at 4°C.

Still, there are many unresolved issues for predicting intube flow boiling heat transfer, such as:

- Development of a mist flow heat transfer model;
- Development of a heat transfer model specifically for intermittent flow;
- Development of a bubbly flow heat transfer model;
- Extension of the heat transfer model to high reduced pressures;
- Determine if there should be boiling suppression factor acting on α_{nb} in an asymptotic method;
- The variation of the dry angle as a function of flow conditions is not well understood;
- A broader database is required for continued development of the method.

For evaporation in vertical upflow in tubes, many of the earlier comments on the old-style methods are also applicable. Flow patterns typically confronted in these applications are bubbly, slug, churn, annular and mist flows. Yet, none of the methods are based on the local flow regime. The flow boiling methods only apply to wet wall regimes, although none include a criterion for predicting the onset of dryout. Only the Steiner and Taborek (1992) method specifically limits itself to vapor qualities below 50% for this reason, while providing another method for evaporation without nucleate boiling nor dryout up to complete evaporation. Many of these methods in practice are applied to vertical downflow without correction. Kattan, Thome and Favrat (1995b) have shown that flow boiling data differ significantly in the same test section at the same test conditions for vertical upward and vertical downward flows. The author is not aware of any general flow regime based flow boiling model for vertical tubes in the open literature, although methods for predicting heat transfer in single regimes, such as bubbly flow or annular flow, exist.

INTUBE CONDENSATION

Figure 7 depicts flow patterns typically encountered for condensation inside horizontal tubes according to Palen, Breber and Taborek (1979). At high flow rates, the condensate immediately forms an annular film with some liquid entrained from interfacial waves into the high velocity vapor core. Slug flow is then encountered and eventually all the vapor is converted to liquid. Instead, at low flow rates rather than their identification of the flow as annular at the entrance region, it is probably in fact a stratified-wavy flow with Nusselt film condensation from around the top of the tube towards the stratified layer in the bottom. The flow continues as a stratified-wavy flow until stratified flow is reached at low vapor qualities. Since the Nusselt film thickness is very thin, the upper liquid film may not bridge the cross-section of the tube and some vapor may leave the opposite end without condensing.

Turning to heat transfer methods without referring to particular studies, the following shortcomings of conventional « flow patternless » methods for predicting local condensation heat transfer coefficients inside horizontal and vertical tubes can be identified:

- They are developed auspiciously for the annular flow regime but without actually modelling the flow as an annular liquid film, i.e. they typically apply a vapor fraction correction to the liquid Reynolds number in the Dittus-Boelter single-phase turbulent flow correlation, which is for tube flow and not film flow;
- Many annular flow correlations do not know where the actual boundaries of annular flow are;
- Other methods attempt to cover the complete range of flows by categorizing the flow as stratified or non-stratified, using an unreasonably simplistic approach from a two-phase flow transition point of view, such as only an equivalent Reynolds number as noted earlier in the Introduction.
- The trends in local experimental heat transfer data plotted versus vapor quality are often not respected.

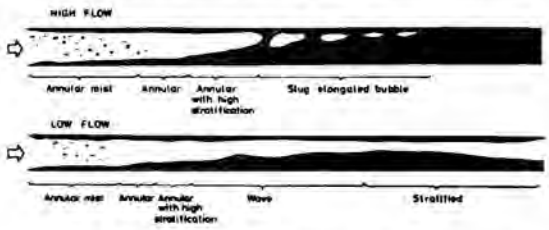

Figure 7. Flow patterns encountered for condensation inside horizontal tubes.

Recently, Dobson and Chato (1998) have proposed a flow regime based prediction method that covers two regimes: stratified-wavy flow (with film condensation from the top towards the liquid at the bottom of the tube) and annular flow. Their correlation for annular flow is

$$Nu(x) = \frac{\alpha_c D}{\lambda_L} = 0.023\,Re_{LS}^{0.8}\,Pr_L^{0.4}\left[1 + \frac{2.22}{X_{tt}^{0.89}}\right] \quad (26)$$

where the superficial liquid Reynolds number Re_{LS} is

$$Re_{LS} = \frac{G D (1-x)}{\mu_L} \quad (27)$$

and X_{tt} is the Martinelli parameter for turbulent flow in both phases. For stratified-wavy flow, first the void fraction ε is calculated using the Zivi (1964) void fraction model, Eq. (9). The angle from the top of the tube to the stratified liquid layer in the bottom θ_{strat} is then determined assuming all the liquid is stratified in the bottom (neglecting that on the walls) as

$$1 - \frac{\theta_{strat}}{\pi} \cong \frac{\arccos(2\varepsilon - 1)}{\pi} \quad (28)$$

which includes a simplification of the actual implicit geometric expression to avoid iteration. The stratified-wavy heat transfer coefficient is then obtained from the following expression with a proration between the Nusselt film condensation coefficient on the top perimeter of the tube and the forced convective heat transfer coefficient on the stratified perimeter as

$$Nu(x) = \frac{0.23\,Re_{vo}^{0.12}}{1+1.11X_{tt}^{0.58}}\left[\frac{Ga_L\,Pr_L}{Ja_L}\right]^{0.25} + (1-\theta_{strat}/\pi)Nu_{strat} \quad (29)$$

Film condensation is represented by the left term while the forced convection in the stratified liquid (based on the liquid fraction flowing alone in the tube and not as a stratified film) is correlated as

$$Nu_{strat} = 0.0195\,Re_{LS}^{0.8}\,Pr_L^{0.4}\left(1.376+\frac{c_1}{X_{tt}^{c_2}}\right)^{1/2} \quad (31)$$

They used the Soliman (1982) criterion to determine the transition from annular flow to stratified-wavy flow, whose Froude transition number Fr_{so} is

$$Fr_{so} = 0.025\,Re_{LS}^{1.59}\left(\frac{1+1.09X_{tt}^{0.039}}{X_{tt}}\right)^{1.5}\frac{1}{Ga_L^{0.5}} \quad (33)$$

for $Re_{LS} \le 1250$ while the corresponding expression for $Re_{LS} > 1250$ is

$$Fr_{so} = 1.26\,Re_{LS}^{1.04}\left(\frac{1+1.09X_{tt}^{0.039}}{X_{tt}}\right)^{1.5}\frac{1}{Ga_L^{0.5}} \quad (34)$$

Soliman concluded that the transition to wavy flow occurs for $Fr_{so} < 7$ and annular flow occurs for $Fr_{so} > 7$. Dobson and Chato noted that this criterion worked quite well based on their observations, although a symmetric annular flow was not reached until values of about 18 (they set their threshold to $Fr_{so} = 20$ to better fit their heat transfer data). The rest of their parameters can be found in their publication.

There are several drawbacks with this method. First of all, there is not a smooth transition in the heat transfer coefficient from annular flow to stratified-wavy flow but instead a significant step change in its value. Secondly, the flow regime transitions have been rather simplified, for instance ignoring fully stratified flow at low values of G. Even so, this method is a good step forward towards a complete flow regime based heat transfer model for condensation in horizontal tubes.

Several newer flow pattern based methods have also been proposed since then. Shao and Granryd (2000) proposed a stratified/non-stratified condensation prediction method that also used the Soliman transition criterion and observed that the best transition value based on heat transfer observations was between 15 and 20. Cavallini et al. (2002) proposed a new heat transfer model and flow pattern map that categorizes the flow into annular flow, transition&wavy-stratified flow and slug flow and predicted a large database very well. An even newer method by El Hajal, Thome and Cavallini (2002a, 2002b), which adapts the Kattan-Thome-Favrat flow pattern map and simplified two-phase flow structure approach from flow boiling to condensation has just been completed and submitted for publication; it accurately predicts condensation data in the annular, intermittent, stratified-wavy and stratified flow regimes for 19 different fluids and includes a new logarithmic mean void fraction method to handle void fractions from low to high reduced pressures (0.02 to 0.8) and interfacial roughness effects. It has a smooth transition in the heat transfer coefficient from each flow regime to the next.

SUMMARY

Recent developments in flow regime based models for predicting two-phase heat transfer coefficients have been reviewed and constructive comments made about the shortcomings of existing practice. In addition, useful comments are made about key aspects that should be considered with some ideas given as to what future methods should try to include. Heat transfer models based on simple geometric representations of the various flow regimes combined with the local flow regime identified utilizing a reliable and accurate flow pattern map are notably better that the older « flow patternless » methods. These new flow regime methods are also typically able to better capture the trends in the experimental data, making them more useful for optimising heat exchanger layouts. Even so, many issues still need to be addressed to improve modelling of these two-phase processes.

ACKNOWLEDGEMENT

Preparation of this review was sponsored in part by the Swiss National Science Foundation under contract no. 21/57210.99.

NOMENCLATURE

A	cross-sectional area of flow channel
A_L	cross-sectional area occupied by liquid-phase
c	empirical constant
C_o	two-phase convection multiplier
c_{pL}	specific heat of the liquid
c_{pv}	specific heat of the vapor
c_1	empirical constant
c_2	empirical constant
D	tube diameter
Fr_L	liquid Froude number
Fr_{so}	Soliman Froude transition number
G	mass velocity of liquid plus vapor
G_e	equivalent mass velocity
G_{high}	transition mass velocity into stratified-wavy flow
G_{low}	transition mass velocity into fully stratified flow
Ga_L	Galileo number of liquid
g	gravitational acceleration
H	vertical height
Ja_L	Jakob number of the liquid
M	molecular weight
Nu_{strat}	Nusselt number for stratified flow
$Nu(x)$	Nusselt number
Pr_L	liquid Prandtl number
p_r	reduced pressure
Δp_{frict}	frictional pressure drop
Δp_{mom}	momentum pressure drop
Δp_{static}	static pressure drop
Δp_{total}	total pressure drop
q	heat flux
R	radius of tube
Re_e	equivalent Reynolds number
Re_L	liquid Reynolds number
Re_{LS}	superficial liquid Reynolds number
Re_{vo}	vapor only Reynolds number
S	velocity ratio
u_L	mean velocity of liquid
u_V	mean velocity of vapor
X_{tt}	Martinelli parameter
x	vapor quality
α_c	convective condensation heat transfer coefficient
α_{cb}	convective boiling heat transfer coefficient
α_{nb}	nucleate boiling heat transfer coefficient
α_{tp}	two-phase boiling heat transfer coefficient
α_V	vapor-phase heat transfer coefficient
α_{wet}	heat transfer coefficient on wet perimeter
δ	thickness of annular liquid film
ε	vapor void fraction
λ_L	liquid thermal conductivity
λ_V	vapor thermal conductivity
μ_L	liquid dynamic viscosity
μ_V	vapor dynamic viscosity
θ	angle with respect to horizontal
θ_{dry}	dry angle of tube perimeter
θ_{strat}	stratified flow angle of tube perimeter
ρ_L	liquid density
ρ_V	vapor density
ρ_{tp}	two-phase density
σ	surface tension

REFERENCES:

- Akers, W.W., Deans, H.A. and Crosser, O.K. (1959). Condensation Heat Transfer within Horizontal Tubes, *Chem. Eng. Prog. Symp. Ser.*, Vol. 55, pp. 171-176.
- Barnea, D. (1987) A unified model for prediction of flow pattern transitions in the whole range of pipe inclination, *Int. J. Multiphase Flow*, Vol. 13, pp. 1-12.
- Baker, O. (1954). Design of pipelines for simultaneous flow of oil and gas, *Oil and Gas J.*, pp. 26.
- Breber, G., Palen, J.W. and Taborek, J. (1980). Prediction of horizontal tube-side condensation of pure components using flow regime criteria, *J. Heat Transfer*, Vol. 102, pp. 471-476.
- Cavallini, A., Censi, G., Del Gol, D., Doretti, L., Longo, G.A. and Rossetto, L. (2002). Intube condensation of halogenated refrigerants, *Int. J. HVAC&R Research*, in press.
- Chen, J.C. (1963). A correlation for boiling heat transfer to saturated fluids in convective flow, ASME Paper 63-HT-34, Boston.
- Chisholm, D. (1972). An Equation for Velocity Ratio in Two-Phase Flow, NEL Report 535.
- Chisholm, D. (1973). Pressure gradients due to friction during the flow of evaporating two-phase mixtures in smooth tubes and channels, *Int. J. Heat Mass Transfer*, Vol. 16, pp. 347-358.
- Collier, J.G. and Thome, J.R. (1994). *Convective Boiling and Condensation*, 3rd Edition, Oxford University Press, Oxford.
- Cooper, M.G. (1984). Saturated nucleate pool boiling: A simple correlation, 1st U.K. National Heat Transfer Conference, Vol. 2, pp. 785-793.
- Dobson, M.K. and Chato, J.C. (1998). Condensation in smooth tubes, *J. Heat Transfer*, Vol. 120(1), pp. 193-213.
- El Hajal, J., Thome, J.R. and Cavallini, A. (2002a). Condensation in horizontal tubes, part 1: two-phase flow pattern map, in review.
- El Hajal, J., Thome, J.R. and Cavallini, A. (2002b). Condensation in horizontal tubes, part 2: new heat transfer model based on flow regimes, in review.

- Fair, J.R. (1960). What You Need to Know to Design Thermosyphon Reboilers, *Petroleum Refiner*, Vol. 39, No. 2, pp. 105.
- Friedel, L. (1979). Improved friction pressure drop correlations for horizontal and vertical two-phase flow, European Two-Phase Flow Group Meeting, Ispra, Paper E2.
- Grönnerud, R. (1979). Investigation of liquid hold-up, flow-resistance and heat transfer in circulation type evaporators, Part IV: Two-phase flow resistance in boiling refrigerants, Annexe 1972-1, Bull. de l'Inst. du Froid.
- Hewitt, G.F. and Roberts, D.N. (1969). Studies of two-phase flow patterns by simultaneous x-ray and flash photography, AERE-M 2159, HMSO.
- Kattan, N., Thome, J.R. and Favrat, D. (1995a). Measurement and prediction of two-phase flow patterns for new refrigerants inside horizontal tubes, *ASHRAE Trans.* 101(2), SD-95-17-4.
- Kattan, N., Thome, J.R. and Favrat, D. (1995b). Boiling of R-134a and R-123 in a microfin tube, *Proc. 19th Int. Congr. of Refrigeration*, The Hague, Vol. IVa, pp. 337-344.
- Kattan, N., Thome, J. R. and Favrat, D. (1998a). Flow boiling in horizontal tubes. Part 1: Development of a diabatic two-phase flow pattern map, *J. Heat Transfer*, Vol. 120(1), pp. 140-147.
- Kattan, N., Thome, J. R. and Favrat, D. (1998b). Flow boiling in horizontal tubes. Part 3: Development of a new heat transfer model based on flow patterns, *J. Heat Transfer*, Vol. 120(1), pp. 156-165.
- Klimenko, V.V. and Fyodorov, M. (1990). Prediction of heat transfer for two-phase forced flow in channels of different orientation, *Proc. 9th Int. Heat Transfer Conf.*, Jerusalem, Vol. 5, pp. 65-70.
- Lockhart R.W. and Martinelli R.C. (1949). Proposed correlation of data for isothermal two-phase two-component flow in pipes, *Chem. Eng. Progr.*, Vol. 45, pp. 39-45.
- Müller-Steinhagen H. and Heck K. (1986). A simple frictional pressure drop corrlelation for two-phase flow in pipes, *Chem. Eng. Process*, Vol. 20, pp. 297-308.
- Palen, J.W., Breber, G. and Taborek, J. (1979). Prediction of flow regimes in horizontal tube-side condensation, *Heat Transfer Engng.*, Vol. 1(2), pp. 47-57.
- Rouhani, Z. and Axelsson, E. (1970). Calculation of volume void fraction in the subcooled and quality region, *Int. J. Heat Mass Transfer*, Vol. 13, pp. 383-393.
- Sardesai, R.G., Owen, R.G. and Pulling, D.J. (1981). Flow regimes for condensation of a vapour inside a horiontal tube, *Chem. Eng. Sci.*, Vol. 36, pp. 1173-1180.
- Shah, M.M. (1979). A General Correlation for Heat Transfer during Film Condensation inside of Pipes, *Int. J. Heat Mass Transfer*, Vol. 22, pp. 547-556.
- Shah, M. M. (1982). Chart correlation for saturated boiling heat transfer: Equations and further study, *ASHRAE Trans.*, Vol. 88(1), pp. 185-196.
- Shao, D.W. and Granryd, E.G. (2000). Flow pattern, heat transfer and pressure drop in flow condensation, Part 1: Pure and azeotropic refrigerants, *Int. J. HVAC&R Research*, Vol. 6(2), pp. 175-195.
- Soliman, H.M. (1982). On the annular-to-wavy flow pattern transition during condensation inside horizontal tubes, *The Canadian Journal of Chemical Engineering*, Vol. 60, pp. 475-481.
- Steiner, D. (1993). Heat transfer to boiling saturated liquids, *VDI-Wärmeatlas (VDI Heat Atlas)*, Editor: Verein Deutscher Ingenieure, VDI-Gessellschaft Verfahrenstechnik und Chemie-ingenieurwesen (GCV), Translator: J.W. Fullarton, Düsseldorf.
- Steiner, D. and Taborek, J. (1992). Flow boiling heat transer in vertical tubes correlated by an asymptotic model, *Heat Transfer Engng.*, Vol. 13(2), pp. 43-69.
- Taitel, Y. and Dukler, A. E. (1976). A model for predicting flow regime transitions in horizontal and near horizontal gas-liquid flow, *AIChE Journal.*, Vol. 22(2), pp. 43-55.
- Tandon, T.N., Varma, H.K. and Gupta, C.P. (1982). A new flow regime map for condensation inside horizontal tubes, *J. Heat Transfer*, Vol. 104, pp. 763-768.
- Thome, J.R. and El Hajal, J. (2002). Two-Phase flow pattern map for evaporation in horizontal tubes: latest version, *1st Int. Conf. On Heat Transfer, Fluid Mechanics and Thermodynamics*, Kruger Park, South Africa, April 8-10, Paper TJ2.
- Thome, J.R. (1996). Boiling of refrigerants: A state-of-the-art review, *Int. J. Refrig.*, Vol. 19(7), pp. 435-457.
- Zivi, S.M. (1964). Estimation of steady-state steam void-fraction by means of the principle of minimum entropy generation, *J. Heat Transfer*, Vol. 86, pp. 247-252.
- Zürcher, O., Favrat, D. and Thome, J.R. (2002). Evaporation of refrigerants in a horizontal tube: an improved flow pattern dependent heat transfer model compared to ammonia data, *Int. J. Heat Mass Transfer*, Vol. 45(2), 303-317.

HEFAT2002
1st International Conference on Heat Transfer, Fluid Mechanics, and Thermodynamics
8-10 April 2002, Kruger Park, South Africa
JA1

VAPOR-SHEAR, GEOMETRIC, AND BUNDLE-DEPTH EFFECTS ON THE INTERTUBE FALLING-FILM MODES

Y-H Wei* and A. M. Jacobi**
*Research Assistant; **Professor (Keynote Speaker)
Department of Mechanical and Industrial Engineering
University of Illinois at Urbana-Champaign
1206 West Green Street, Urbana, IL 61801
USA
E-mail: a-jacobi@uiuc.edu

ABSTRACT

An existing regime map for the falling-film modes is reviewed, and new data to extend earlier work are presented. The new results show hysteretic mode transitions are not manifest at high Weber numbers, and hysteretic effects are more pronounced at low Ga. Tube spacing can significantly impact the mode transitions, with a marked effect at a characteristic spacing. The flow regimes are generally destabilized in deep bundles, but the effect is not pronounced.

INTRODUCTION

Falling-film tube bundles operate with higher heat transfer coefficients and lower fluid inventories than do flooded bundles. Falling-film heat exchangers also have fewer problems with fouling and non-condensable gases [1][2]. Thus, falling-film heat exchangers are attractive in a wide array of thermal and chemical system applications.

Consider a liquid flowing on the outside of evenly spaced horizontal tubes in a vertical plane as shown in Fig. 1. The liquid falls from one tube to another, and as the flow rate varies, three basic flow patterns may be observed: droplets, jets, or a continuous sheet. At a very low film flow rate, the liquid departs from the bottom of the tube in the droplet mode. A gradual increase in flow rate can cause a transition from droplets to jets, and at higher flow rates a transition from jets to a liquid sheet occurs. If the liquid flow rate is then reduced, the flow changes from sheet mode to jet mode and finally returns to the droplet mode. If the transitional flow rate depends on the direction of the transition (i.e., on whether the flow rate is being increased or decreased), then the transition is said to exhibit hysteretic effects.

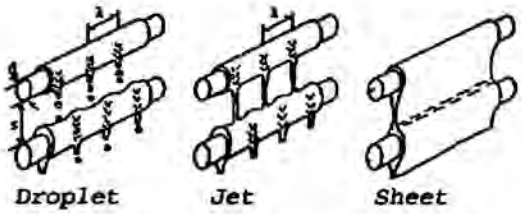

Figure 1: Ideal falling-film modes (per [3]).

The flow mode can have a significant impact on the wetting, heat transfer, and mass transfer performance of falling-film heat exchangers. Because there have only been limited methods for predicting the falling film mode, past design of falling-film bundles, especially evaporators and condensers, has depended on experience.

In 1996, Hu and Jacobi provided the first generalized flow-pattern maps for predicting falling-film mode. Although their maps had nearly 1000 flow observationsas their basis, they were limited to quiescent surroundings. The map is shown in Fig. 2, and images of the modes are shown in Fig. 3.

Literature Review

Thome recently provided a comprehensive review of the state of the art for falling-film evaporators [5]; therefore, for the current purpose a limited review of the most highly relevant papers will be given.

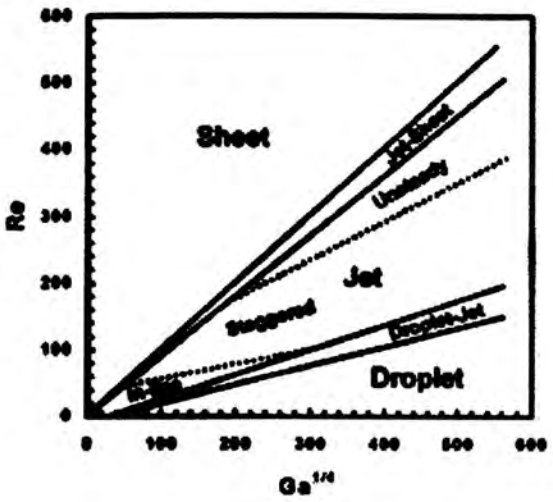

Figure 2: Flow regime map of Hu & Jacobi [4] for mode transitions in quiescent surroundings.

NOMENCLATURE

a	capillary constant, $(\sigma/\rho g)^{1/2}$, (m)
d	tube diameter (m)
d^*	dimensionless tube diameter, d/a
g	gravitational acceleration (m/s^2)
Ga	modified Galileo number, $\rho\sigma^3/\mu^4 g$
N_{tube}	tube number
Re	Reynolds number, $2\Gamma/\mu$
s	tube spacing (m)
U_g	free-stream velocity of gas (m/s)
We	Weber number, $\rho_g U_g^2 d/\sigma$

Greek Letters

Γ	total liquid mass flow rate per tube length (kg/s-m)
μ	liquid dynamic viscosity (N-s/m^2)
ρ	liquid density (kg/m^3)
σ	surface tension (N/m)

Superscript/Subscript

g	gas

properties with no subscript are for the liquid

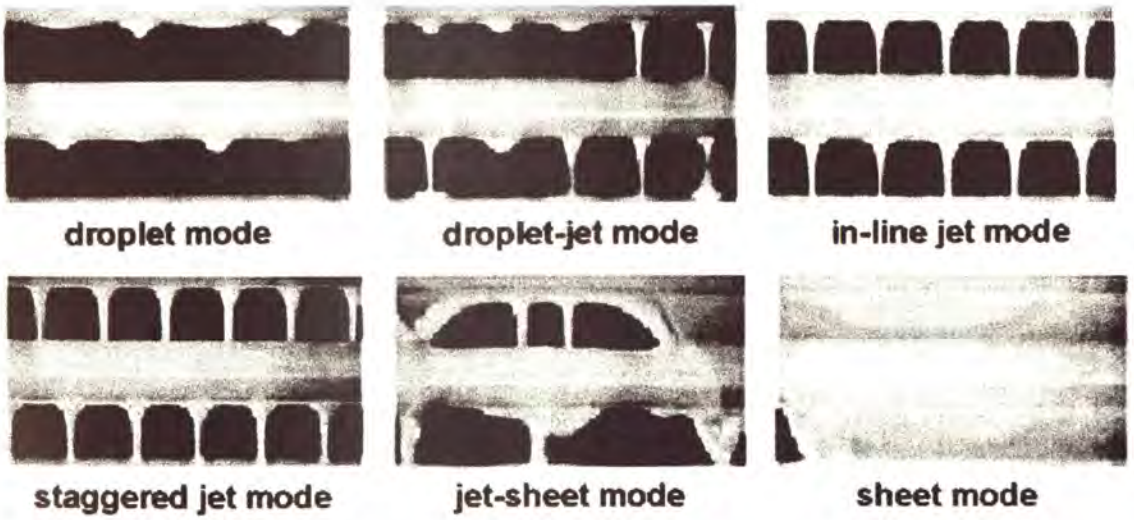

Figure 3: The falling-film modes observed by Hu & Jacobi, the white liquid is falling between horizontal tubes, with a black background.

In 1981, Lorenz and Yung [6] reported test results for a large scale, falling film evaporator having 30 tube rows. In 1982, they contrasted these large-bundle results to single-tube data of others. [7-10]. For Re>300, the average heat transfer coefficient of the bundle was equal to that of a single tube; for Re<300, the single-tube heat transfer increased with decreasing Re, but the average heat transfer coefficient of the bundle decreased. The average heat transfer coefficient of the bundle was lower than that of single tube at low Re, and this finding was attributed to film breakdown.

Dhir and Taghavi [11] described experiments using glycol, ethylene glycol, and silicone oil. The transitions were found to be independent of fluid properties and only dependent on the volume flow rate. The transitions between droplet and jet modes happened at about the same volume flow rate while increasing or decreasing the flow rate, but the flow rate at a transition from jet mode to sheet mode was reported to be about twice the flow rate at a transition from sheet mode to jet mode. Therefore, their experiment showed only significant hysteresis for the transition between the jet and sheet modes.

In a study of condensate on a vertical column of horizontal low-finned tubes using R-113, methanol, and propanol, Honda *et al.* [12] found a parameter, $K=Re/Ga^{1/4}$, to govern the transitions. Their data showed the mode transition almost uniquely depended on the value of K. For the three fluids studied, K ranged from 0.12 to 0.26 at the transition between droplet and jet modes, was 0.64 at the transition between jet and jet-sheet modes and ranged from 0.74 to 0.94 at the transition between jet-sheet and sheet modes. There was no report of transition hysteresis.

Several investigations found the Re for droplet/jet transitions to range from 150 to 200, whereas Re for the transition between jet and sheet modes varied from 315 to 600 [3][13][14]. A notable hysteresis was recorded for droplet/jet transitions, contrary to earlier work [11].

Armbruster and Mitrovic [15] showed the flow mode at moderate tube spacing mainly depends on Γ and physical properties of the liquid. In agreement with the work of Honda, they found the transitions to be characterized by $Re=AGa^{1/4}$ for water and alcohol, with differing values of A for the two fluids.

Hu and Jacobi [4] studied falling-film flows with water, ethylene glycol, hydraulic oil, water/glycol mixtures, and alcohol; they provided a generalized description of the transitions, and detailed data to explore hysteretic effects. They also provided limited data on the effects of a vertical downward flow of gas. In a simplified map neglecting hysteretic effects, they found the droplet mode prevailed at

$$Re < 0.074Ga^{0.302} \quad (1)$$

The jet mode was manifest in

$$0.096Ga^{0.301} < Re < 1.414Ga^{0.233} \quad (2)$$

and the sheet mode occurred for

$$Re > 1.448Ga^{0.236} \quad (3)$$

Summary and Objectives

In almost every falling-film heat exchanger, a flowing vapor is present; in most cases, the vapor flows upward, counter to the falling film. However, there have been no general studies of the impact of a vapor flow on falling-film modes for plain tubes. Hysteretic effects appear to depend on properties; earlier work shows different hysteretic behavior at different Ga. Further experimental data are needed to explore this behavior. Because of the nature of falling film, a small perturbation can be amplified as the film falls through the bundle. The flow modes of multiple tubes may differ from those of a single tube. Tube bundle effects on falling film have not been fully explored. In most prior work, the tube size and spacing effects on mode transitions are considered as negligible, but these effects may be important in new bundle designs where compactness is becoming an important design objective.

Thus, it is the objective of this study to develop a better understanding of the falling film modes and their transitions and hysteresis in the presence of an upward-flowing vapor, including the effects of tube spacing, tube diameter and tube bundle depth.

EXPERIMENTAL METHODS

The test facility, as shown in Fig 4, consists of a closed-circuit circulation loop of test liquid and an open-loop wind tunnel. The liquid circulation loop and the wind tunnel loop join at the test section. This facility is designed for the study of falling-film modes and transitions with or without an imposed upward flow of air from the laboratory. For studies of mode transitions in a quiescent gas, the blower can be removed, and a top and bottom cover are placed on the test section.

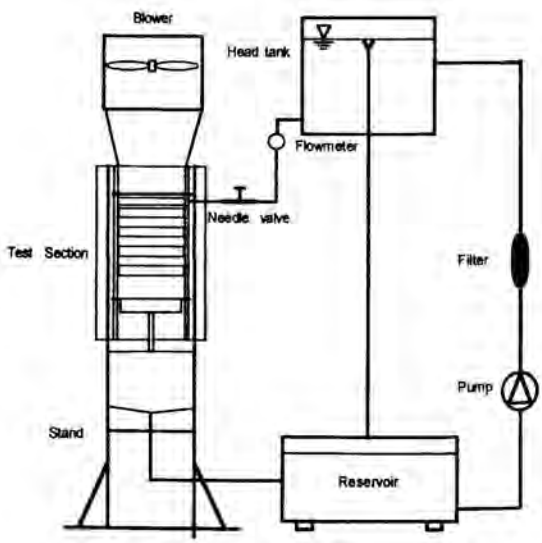

Figure 4: Schematic of the experimental facility

Liquid Loop

The liquid circulation loop consists of a reservoir, a liquid pump, a filter, an overflow head tank, a flow meter, and a needle valve. The variable speed pump delivers the test liquid in the reservoir through a filter to the overflow head tank. In the overflow head tank, the test liquid is kept at a constant level and the overflow liquid returns to the reservoir. From the head tank, the test liquid flows through the flow meter and the needle valve to the feed tube in the upper part of the test section. In the test section, the liquid issues from the feed tube on the top, flows around the first test tube, then impinges on the second test tube and then the third test tube, etc. After flowing around the fifth test tube, the test liquid falls to the catching tube. The liquid collected by the catching tube eventually returns to the reservoir.

This study adopts a method described by Mitrovic to achieve a uniform axial distribution of liquid. A series of holes, 1.0 mm in diameter, were located 1.5 mm apart (center to center) along a 395-mm length on the bottom of the feed tube. The wall thickness of feed tube is 25 mm to ensure uniform axial distribution of the fluid. The gap between the bottom of the first feed tube and the top of the first test tube is 1 mm for R-123 and 2 mm for other fluids.

Polished steel tubes with a smooth surface are used as test tubes in the falling-film studies. The outside tube diameters range from 1 mm to 80 mm.

Wind Tunnel

The purpose of the wind tunnel is to impose interfacial vapor shear on the gas/liquid interface to determine the effect of shear on falling-film mode transitions. The wind tunnel consists of a blower and test section. The test section is made from transparent PVC and has a cross section of 250 mm by 405 mm. The behavior of falling-film can be observed through the front plate of the test section. The sides of the test section support the test tubes and allow easy adjustment to the tube arrangement. The transition section between the blower and the test section is made of a flexible rubber belt to prevent transferring vibrations from the blower to the test section. The wind tunnel provides air velocities up to 15 m/s at the test section inlet—the direction of the airflow is counter to that of the falling liquid film. The approach velocity profiles are flat to within 5% at the maximum blower speed. The turbulence intensity can be less than 2% or as high as 20% under different test conditions.

Instrumentation

Liquid mass flow rates are measured using a Coriolis-effect flow meter, with accuracy of 0.1%. The fluid density and temperature can also be measured by the flow meter. The surface tension of the fluids is measured during the course of each experiment using a Du Nouy Ring Tensiometer. Air velocity in the test section is measured using a Pitot tube and electronic manometer (±0.12 Pa) and with a hot-wire anemometer. Air density is inferred from laboratory temperature, humidity and pressure. A camera is used to record images of the falling film under different conditions.

Test Procedure and Scope

Prior to a test, tubes of the desired tube diameter were placed at desired spacing in the test section. Because the falling-film flow is gravity driven, it was important for the tubes to be horizontal. Before a test, the tubes were carefully leveled by circulating liquid to obtain a jet mode and adjusting the tubes until the jets fell from fixed sites, with no drift in either direction. The test liquid circulated in the system for 2~3 hours to ensure that the tubes were fully wetted. The electronic devices were turned on and subjected to a warm up time of at least an hour. The tensiometer was set up before the test and liquid surface tension was measured during a test. If photographic equipment was employed in a test, a reference scale was photographed to provide a dimensional reference.

During the experiment, the liquid mass flow rate, surface tension, density, temperatures, laboratory temperatures, laboratory pressure, and ambient humidity were measured. The liquid flow rate was adjusted using the needle valve shown in Fig. 4. The valve was first opened sufficiently to allow the flow to take the droplet mode. Then, the valve was slowly turned in the direction of increasing liquid flow rate until the characteristics of the flow mode changed. The corresponding transition flow rate was recorded. Upon increasing the flow rate, the falling film might go through jet, and jet-sheet modes, and finally reach the sheet mode (the exact modes the falling film displays depends on the flow conditions and fluid properties). In order to study hysteretic mode transitions, the liquid flow rate was then decreased from the sheet mode until the flow returned to the droplet mode, passing through other modes during the decrease. The flow rate at each transition was again recorded. For flow experiments with vapor shear, the same procedure was adopted: the air flow rate was held constant for a battery of experiments, and the velocity profile in the test section and turbulence intensity were recorded using the hot-wire anemometer. Images of the flow were recorded.

Experimental Scope

Experiments were conducted with a range of liquids surrounded by a quiescent gas and a moving gas. The liquids included, water, glycol, a water-glycol mixture, alcohol, hydraulic oil, and R123. For a falling film surrounded by a flowing gas, the falling-film mode can depend on ten physical parameters: the liquid flow rate per unit length of tube, Γ; the dynamic viscosity of the liquid, μ; the mass density of the liquid, ρ; the gas/liquid surface tension, σ; the tube diameter, d; the inter-tube spacing, s; and gravitational acceleration, g. With an imposed gas flow, the velocity U_g, the density ρ_g and viscosity μ_g will be important. The experimental scope for the physical variables of this study is given below in Table 1.

Using dimensional analysis, seven dimensionless groups can be identified to characterize the mode transitions. The test ranges and estimated experimental uncertainties of these groups are given in Table 2.

Table 1: Experimental range of the relevant physical variable

Physical Parameter	Experimental Range
Mass flow rate per tube length, Γ	up to 3
Liquid dynamic viscotiy, μ	$5.5(10^{-4})$ to $4.4(10^{-2})$
Mass density of liquid, ρ	780 to 1490
Gas/liquid surface tension, σ	$20(10^{-2})$ to $72(10^{-2})$
Tube diameter, d	0.001 to 0.080
Tube spacing, s	0.001 to 0.080
Gas velocity, U_g	Up to 15

Table 2: Relevant dimensionless groups, the experimental range and typical uncertainty

Group	Range	Uncertainty
$Re=2\Gamma/\mu$	Up to 600	±1%
$Ga=\rho\sigma^3/g\mu^4$	$7(10^2)$ to $8(10^{10})$	±4%
s/d	1 to 10	±1%
s/a	0.7 to 68	±1%
$We=\rho_g U_g^2 d/\sigma$	Up to 180	±6%
ρ_g/ρ	$8\ (10^{-4})$ to $1.5(10^{-3})$	±1%
μ_g/μ	$4(10^{-4})$ to $2(10^{-2})$	±4%

RESULTS

The experiments show the mode transitions can be hysteretic or non-hysteretic. If the flow is relatively steady, the mode transitions are hysteretic; however, once unsteadiness of the flow reaches a certain extent, the mode transitions become non-hysteretic. Thus, both hysteretic and non-hysteretic mode classifications must be used to describe the falling-film flow patterns under different experimental conditions

Vapor Shear Effect

As shown in Fig. 5 for experiments with vapor shear, as *We* increases, the hysteretic effect at transition decreases. With an increasing *We*, hysteresis for transitions between droplet and droplet-jet modes first disappears, and then hysteresis for transitions between droplet-jet and jet modes, jet and jet-sheet modes, jet-sheet and sheet modes disappear sequentially. If *We* is increased still further, a new unsteady flow mode appears.

In quasi-steady state, there is hysteresis at the mode transitions because the initial states are different for the two directions of mode transitions. In unsteady flow, the flow can be thought as a wave structure imposed on a steady base flow; the oscillating hydraulic pressure provided by the wave structure can help to reach the required critical interfacial pressure at certain location during flow pattern transformation, thus reducing or even eliminating hysteresis.

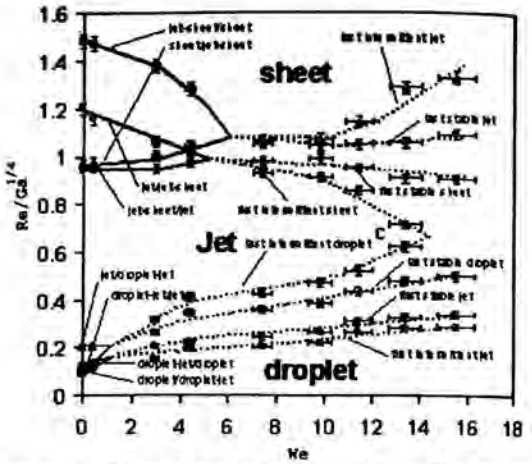

Figure 5: Vapor-shear effects on falling-film mode transitions, $Ga^{1/4}$=35.7, s/d=1, s/a=9.3.

Fluid Property Effects

Our preliminary data show that as *Ga* increases, unsteadiness increases; i.e., high-*Ga* fluids manifest unsteadiness at lower *Re* than do low-*Ga* fluids. Under quiescent conditions, for ethylene glycol there is hysteresis in all mode transitions, but for water and R123 there is almost no hysteresis in mode transitions except for at close tube spacings (s/a<4). Transitional $Re/Ga^{1/4}$ for water ($Ga^{1/4}$=530), R123 ($Ga^{1/4}$=340) and ethylene glycol ($Ga^{1/4}$=35.7) are given in Fig. 6.

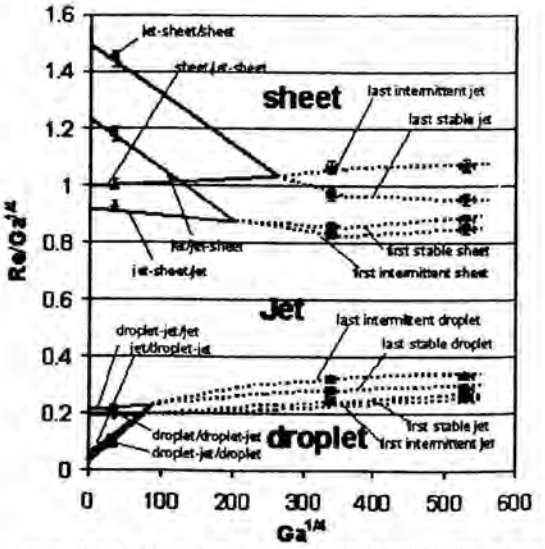

Figure 6: Fluid property effects on falling-film mode transitions, We=0, s/d=1, s/a=9.3

A fluid with a higher Ga requires a higher Re for the flow to reach the next mode up (see Figs 2 & 3). Higher Ga fluids exhibit unsteadiness at lower Re. Due to the unsteadiness in the flow, hysteresis disappears for fluids with high Ga. The data in the literature show the same trends with Ga, but no explanation has been provided prior to this hypothesis that flow unsteadiness is key. Because of limitations on our Ga range, more data are needed to further explore the Ga effect on mode transition and hysteresis.

Tube Spacing and Diameter Effects

Experiments show that the capillary tube spacing, s/a, can have a significant effect on the transition of falling-film modes. Previous research has shown $Re/Ga^{1/4}$ at any falling film transition to be almost constant for any tube spacing. However, some interesting behavior is shown in Fig. 7, a map of falling film transition under the first tube for variable dimensionless tube spacing. Under the conditions of Fig. 7, the flow transitions clearly show hysteretic behavior.

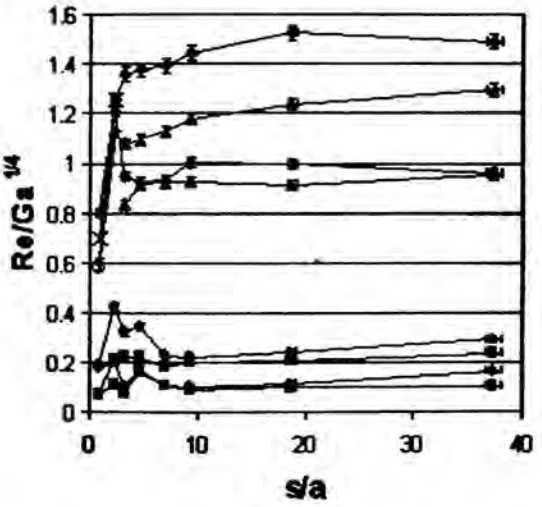

Figure 7: The effect of tube spacing on mode transitions ($Ga^{1/4}$=35.7, s/d=1); at the highest value of s/a, moving up in $Re/Ga^{1/4}$ the curves represent the following transitions: droplet-jet to droplet; jet to droplet-jet; droplet to droplet-jet; droplet-jet to jet; sheet to jet-sheet; jet-sheet to jet; jet to jet-sheet; jet-sheet to sheet.

Generally the transitional $Re/Ga^{1/4}$ increases with s/a. For small dimensionless tube spacing (s/a<2.3), when the flow rate increases to certain number, the jets become very unstable. All the transition data, except the jet-sheet to transitions, show a maximum in $Re/Ga^{1/4}$ near s/a=3. When the tube spacing is big enough (s/a>4.7 with $Ga^{1/4}$=35.7), the unstable jet mode is not manifested under this tube.

Experiments show that when d/a increases, the instability amplifying effect of each tube increases. That is the downstream flows become more unsteady at higher d/a. Using water ($Ga^{1/4}$=540) with d/a=28.5, sheet mode can be acquired only between first and second test tubes. The flow under the second test tube is so unsteady that sheet mode has not been observed. This amplifying effect of tube diameter can also be demonstrated with tube bundle depth effect.

Tube Bundle depth Effect

With the unsteadiness being amplified downstream, the falling film behavior of the second tube and those below it can be different from that of the first tube. Preliminary data are provided in Fig. 8. Due to increasing unsteadiness in the flow, the mode transitions are delayed at positions deeper in the bundle.

Suppose jets or sheets under the first tube deviate a little from the vertical plane through the central axes of tubes. This deviation can be amplified as the liquid flows around and departs from the second tube. So the flow becomes more and more unsteady downstream. When the deviation is so great that part of the liquid departing from the bottom of one tube does not fall on the outside surface of the tubes below it, "slinging" is said to occur. More data are needed to further explore the effects of tube bundle depth.

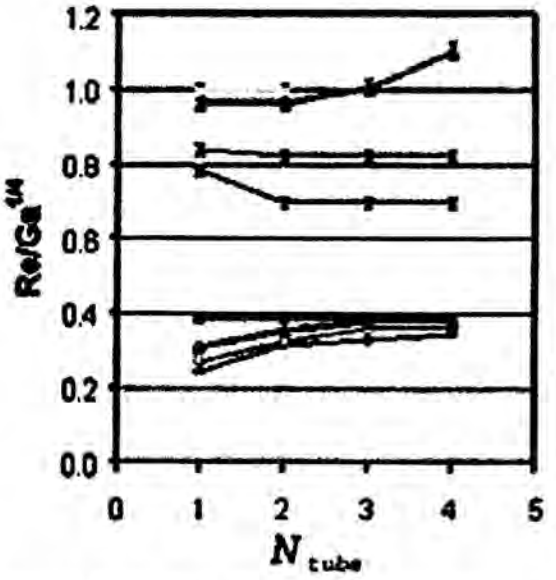

Figure 8: Bundle depth effects on the mode transitions at $Ga^{1/4}$=340, s/d=1, and s/a=17.0. N_{tube} is the position in the bundle, counting from the top. At N_{tube}=4, moving up in $Re/Ga^{1/4}$ the curves represent the following transitions: first intermittent jet; first stable jet; last stable droplet site; last intermittent droplet site; first intermittent sheet; first stable sheet; last stable jet; last intermittent jet.

CONCLUSIONS

New mode-transition data have been reported on the effects of a flowing gas, fluid properties, geometric effects, and to explore the impact of bundle depth. The following conclusions extend the current understanding of the intertube falling-film flow:

- The presence of an upward-directed gas flow destabilizes the sheet and jet modes. This destabilization reduces or removes hysteresis in the mode transitions. Hysteresis in the droplet-jet transitions disappears at low *We* (*We*>2 at $Ga^{1/4}$=35.7), and hysteresis in the jet-sheet transitions disappears at higher gas velocities (*We*>6).
- New flow classifications to include unsteady (intermittent) modes may be needed for *We*>0.
- Low-$Ga^{1/4}$ fluids exhibit more hysteretic transitional behavior than high-$Ga^{1/4}$ fluids. Marked hysteresis (more than 25% in *Re*) was observed at $Ga^{1/4}$=35.7, and almost no hysteresis was evident for $Ga^{1/4}$>300.
- Tube spacing effects can be important to mode transitions, especially at *s*/*a*<6, and there is a characteristic spacing at which the transitional *Re* reaches a local maximum.
- The flow generally becomes less stable deeper in the bundle. This effect can eliminate hysteresis and raise transitional flow rates.

REFERENCES

[1] Adams, F., Broughton, G. and Conn, A., 1936, "A Horizontal Film-Type Cooler," *Ind. Engr. Chem.*, Vol. 28, pp. 537-541.

[2] Yundt, B. and Rhinesmith, R., 1981, "Horizontal Spray-Film Evaporation," *Chemical Engineering Proceedings*, Vol. 77, pp. 69-73.

[3] Mitrovic, J., 1986, "Influence of Tube Spacing and Flow Rate on Heat Transfer From a Horizontal Tube to a Falling Liquid Film," *Proceedings of the 8th International Heat Transfer Conference*, San Francisco, Vol. 4, pp. 1949-1956.

[4] Hu, X. and Jacobi, A.M., 1996, "The Intertube Falling Film: Part 1, Flow Characteristics, Mode Transitions and Hysteresis," *Journal of Heat Transfer*, 118 pp. 616-625.

[5] Thome, J. R., 1999, "Falling Film Evaporation: State of the Art Review of Recent Work," Journal of Enhanced Heat Transfer, Vol. 6, pp. 263-277.

[6] Lorenz, J. J. and Yung, D., 1981, "OTEC-1 Heat Exchanger Test Results," *Proceedings of the Eighth Ocean Thermal Energy Conversion Conference*, Washington, D.C.

[7] Lorenz, J. J. and Yung, D., 1982, "Film Breakdown and Bundle-Depth Effects in Horizontal-Tube, Falling-Film Evaporators," *Journal of Heat Transfer*, Vol. 104, pp. 569-571.

[8] Conti, R. J., 1978, "Experimental Investigation of Horizontal-tube Ammonia Film Evaporators with Small Temperature Differentials," *Proceedings of the 5th Ocean Thermal Energy Conversion Conference*, Miami Beach, Florida, Vol. 6, pp. 161-180.

[9] Owens, W. L., 1978, "Correlation of Thin Film Evaporation Heat Transfer Coefficients for Horizontal Tubes," *Proceedings of the 5th Ocean Thermal Energy Conversion Conference*, Miami Beach, Florida, Vol. 6, pp. 71-89.

[10] Sabin, C. M. and Poppendiek, H. F., 1978, "Film Evaporation of Ammonia Film Evaporators With Small Temperature Differentials," *Proceedings of the Fifth Ocean thermal Energy Conversion Conference*, Miami Beach, Florida.

[11] Dhir, V. K. and Taghavi-Tafreshi, K., 1981, "Hydrodynamic Transition During Dripping of a Liquid from Underside of a Horizontal Tube," *ASME-Paper*, No.81-WA/HT-12.

[12] Honda, H., Uchinma, B., Nozu, S., Nakata, H. & Torigoe, E., 1991, "Film Condensation of R-113 on In-line Bundles of Horizontal Finned Tubes," *Journal of Heat Transfer*, Vol. 113, pp. 479-486.

[13] Maron-Moalem, D., Sideman, S. and Dukler, A., 1978, "Dripping Characteristics in a Horizontal Tube Film Evaporator," *Desalination*, Vol. 27, pp. 117-127.

[14] Ganic, E. N. and Roppo, M. N., 1980, "An Experimental Study of Falling Liquid Film Breakdown on a Horizontal Cylider During Heat Transfer," *Journal of Heat Transfer*, Vol. 102, pp. 342-346.

[15] Armbruster, R. and Mitrovic, J., 1994, "Patterns of falling film flow over horizontal smooth tubes," *Proceedings of 10th International Heat Transfer Conference*, Vol. 3, Brighton, UK, pp. 175-280.

HEFAT2002
1st International Conference on Heat Transfer, Fluid Mechanics, and Thermodynamics
8-10 April 2002, Kruger Park, South Africa
KJ1

LOCAL HEAT TRANSFER MEASUREMENTS DURING PHASE CHANGE PROCESSES USING MICROSCALE HEATERS

Jungho Kim
University of Maryland
Dept. of Mechanical Engineering
College Park, MD 20742

ABSTRACT

Although liquid-vapor phase change heat transfer processes have been studied for many years, there remain significant questions regarding the mechanisms by which the energy is transferred. The great majority of experimental data to date has been obtained using heater surfaces that were comparable to, or much larger than the scales at which the heat transfer occurs, enabling only average heat transfer rates and temperatures over the entire heated surface to be obtained. Little experimental data is available regarding the *local* heat transfer rates during these processes. Time and space resolved heat transfer measurements can be of great benefit in elucidating heat transfer mechanisms during phase change processes by pinpointing when and where large amounts of heat are removed. This paper describes in detail the development of two technologies to provide these measurements, and examples of their application are given.

INTRODUCTION

Local heat transfer measurement techniques can be used to provide much needed information regarding heat transfer mechanisms. The ability to determine when and where heat is transferred during a phase change process and correlating this information with visual observations can be a very powerful tool in investigating heat transfer mechanisms. Perhaps the most prevalent form of local heat transfer measurement to date for both single phase and multiphase studies has been the use of thermochromic liquid crystals (TLC) to measure temperature distributions on surfaces. TLCs have chiral (twisted) molecular structures and are optically active mixtures of organic chemicals. They show colors by selectively reflecting incident white light. Temperature-sensitive mixtures turn from colorless (black against a black background) to red at a given temperature and, as the temperature is increased, pass through the other colors of the visible spectrum in sequence (orange, yellow, green, blue, violet) before turning colorless (black) again at a higher temperature. The color changes are reversible. TLCs have been used to provide fast response wall temperature information over quite large areas for constant wall heat flux boundary conditions for boiling studies (Bayazit et al.–2001, Kenning, et al.–2000). Usually an electric current is sent through a thin stainless steel sheet, heating it. One side of the sheet is coated with black paint, then sprayed with a thin layer of unencapsulated liquid crystal. A thin polymer coating is then applied to protect the liquid crystal. The phase change heat transfer occurs on the opposite side of the stainless steel sheet. This setup provides a nearly constant heat flux boundary condition. Although most of the visualizations to date have been at low frequencies (30 Hz or below), it is possible to obtain data at frequencies as high as 500 Hz if the stainless steel sheet is thin and unencapsulated TLC is used. The advantages of using liquid crystal thermography are that it is relatively inexpensive and temperatures over large areas can be visualized. The disadvantages are that high frequency response is not possible, and the temperatures response range is somewhat limited (typically 25 °C). A similar technique is to use an infrared camera to visualize the temperature distribution on a thin, electrically heated stainless steel sheet painted black (Theofanous et al.–2000).

Some more recent work measured the local heat flux from a heated, transparent surface using laser interferometry to obtain contours of the microlayer thickness underneath growing vapor bubbles vs. time (Fath and Judd–1978 and Koffman and Plesset–1983). The rate of change of the microlayer thickness was related to the wall heat transfer through a simple energy balance. This technique allows measurements within the microlayer to be made, but measurements after bubble departure are not possible.

In this paper, two additional methods of measuring local heat transfer are discussed. The first is a passive technique utilizing a diode array that provides the temperature distribution on a surface that is heated. The second is an active technique

using microheater arrays that provides heat transfer distribution on surfaces that are held at constant temperature. The application of the second technique to two phase change processes are described.

DIODE ARRAY

Arrays of diodes can be used to measure temperature distributions on whatever surfaces they can be constructed by measuring their forward voltage drop as a function of temperature. In the following example, the diodes are made on a silicon wafer, but the same technique can be applied to diodes constructed on flexible polymer substrates (Sheats et al., 1996). The development of this exciting possibility may allow temperatures to be measured on curved surfaces that are n easily accessible, such as the inside surface of tubes.

Diode array construction. A schematic of how the diodes are connected together is shown on Figure 1 for a 3 x 3 array of diodes. If the voltage drop across diode A-2 is desired, a small current (typically 100 μA) is sent into row A while the other rows are grounded. Simultaneously, column 2 is grounded while the other columns are set to 5 V. All of the diodes in the array with the exception of A-2 are now either reverse biased (so no current flows through them), or they have no voltage drop across them. The voltage at A is then measured to obtain the forward voltage drop across diode A-2. The voltage drop across the other diodes in the array are obtained by scanning across the array.

A 32 x 32 p-n junction isolated diode array was built on a p-type wafer using VLSI techniques. A schematic of a single diode is shown on Figure 2. First, a mask was used to create a series of n-wells on the wafer. A second mask was used to implant boron to create regions of p+. A third mask was used to create regions of n+ to make a well contact by diffusing phosphorous. A fourth mask was used to open a contact via for electrical contact to the diode. Finally, a fifth mask was used to interconnect the diodes in the array. Each individual diode is 0.1 mm x 0.1 mm in size, with the entire array being 3.2 mm x 3.2 mm in size. A photograph of a single diode in the array is shown on Figure 3.

Many arrays can be made on a single wafer. Once a wafer has been processed, the wafer is diced to obtain the individual chips. These chips are epoxied to a Pin Grid Array (PGA), and connections from the chips to the PGA are made using wire-bonds. For a 32 x 32 diode array, a total of 64 wire bonds need to be made.

Scanning circuitry. A schematic of the circuitry used to scan the diodes in the array and provide signal conditioning is shown in Figure 4. The circuit receives two external signals: a start pulse and a signal from an external clock, both of which enter the counter. The start pulse tells the counter to begin counting, while the external clock is used to set the frequency at which counting occurs. The actual counting frequency is half the clock frequency. Counting frequencies of up to 2.5 MHz are possible with the current circuitry. The signal exiting the counter enters two Erasable Programmable Read Only Memories (EPROM), one for choosing the row and one for choosing the column. Every time a pulse from the clock enters the EPROMs, they output two 5-bit digital signals corresponding to row and column numbers. In the present configuration, the EPROMs are programmed to increment the column number from 1 to 32 before incrementing the row number. All of the diodes in a particular row are therefore scanned before going on to the next row. The entire array is scanned once every time the circuit receives an external start pulse.

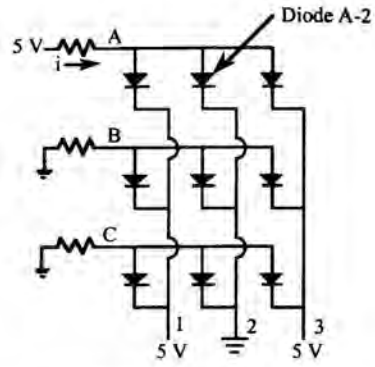

Figure 1: Example of measuring the forward voltage drop of diode A-2 in a 3x3 array.

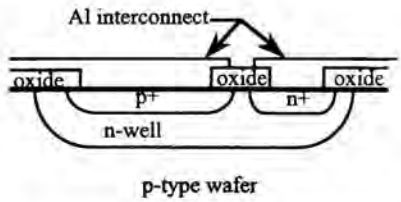

Figure 2: Schematic of diode construction.

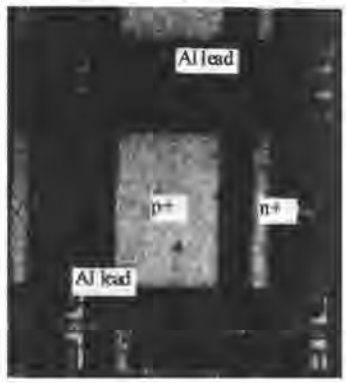

Figure 3: Photograph of a diode in the array.

The great advantage of using EPROMs is that any arbitrary subset of diodes can be scanned by simply reprogramming the EPROMs. For example, the EPROMs can be programmed to scan only those diodes underneath a nucleating bubble–since

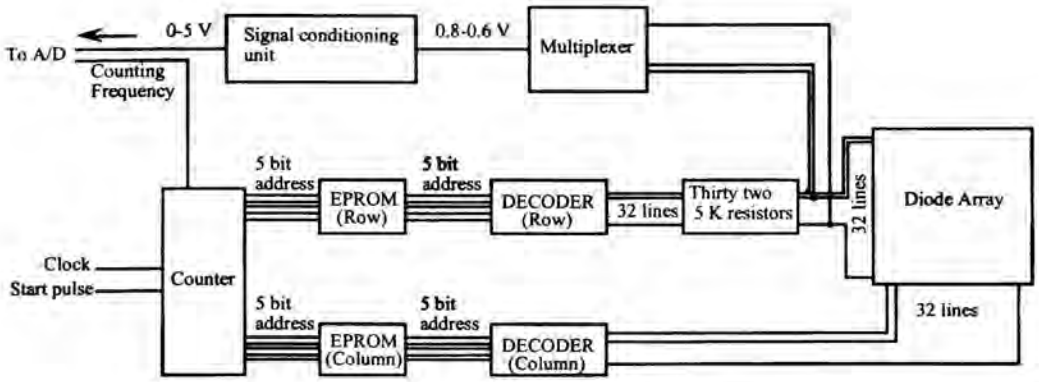

Figure 4–Block diagram of circuit.

scanning speed stays constant, each diode in this subset of diodes can be scanned at much higher frequencies than if the entire array were scanned.

The measured voltage drops across the diodes are multiplexed into one continuous signal that is typically between 0.8–0.6 V. To take advantage of the resolution of the A/D converter, this signal is sent through a signal conditioning unit that offsets, inverts, and amplifies the signal to match a 0-5 V range.

Data acquisition of the multiplexed signal is performed using an off-the-shelf data acquisition unit (Daqbook 216 from I/O Tech). This unit is capable of scanning a single channel at up to 100 kHz with 16 bits of resolution. Data acquisition is performed with the unit in the "External Trigger" mode, i.e., a data point is read every time the A/D receives a pulse from the counter.

The current used to sense the voltage drop across the diode must not influence the temperature measurement by heating the diode significantly. The energy dissipated by a typical diode with a 100 μA sensing current is 0.7 W/cm^2. While this may seem like a large heat flux, it must be remembered that the sensing current is only applied for a very short time (typically 1 μs if scanning occurs at 1 MHz for a 32 x 32 array). An upper bound on the temperature rise of the surface can be obtained by assuming that the silicon substrate acts as a semi-infinite solid subjected to a step change in wall heat flux (Incropera and Dewitt–1996):

$$T(0,t) - T_i = \frac{2q_0''(\alpha t/\pi)^{1/2}}{k}$$

For a wall heat flux of 0.7 W/cm^2 and a scanning time of 1 μs, the surface temperature rise is just 0.0005 °C, which is well within the uncertainty of the measurement. The actual temperature rise is much lower since only a small portion of the surface is heated.

Calibration. Calibration of the diode array is performed by placing it in a uniform temperature environment, and measuring the forward voltage drop of each diode as a function of temperature. For typical diodes, the forward voltage drop decreases by about 2 mV/°C around room temperature. Typical calibration curves for a few diodes in the array are shown on Figure 5. Measurement of temperatures to within 1 °C are easily achievable.

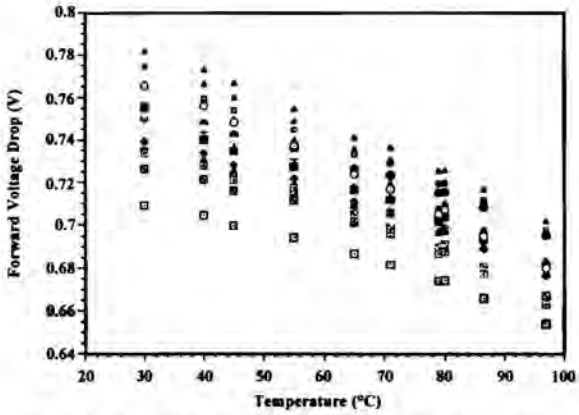

Figure 5: Typical calibration curves for diodes in the array.

Summary of advantage and disadvantages. There are two advantages of using the diode array to measure temperature distribution. First, measurements can be made at very high speeds, especially if only a portion of the array is scanned. Second, high spatial resolution is possible since diodes can be made as small as few microns in size. The primary disadvantage is the limited area that can be scanned at present.

MICROHEATER ARRAY

This technique offers the ability to measure heat transfer distributions on an isothermal surface. It can also be operated to provide the temperature distribution on the surface when the surface is heated. The local surface heat flux and temperature

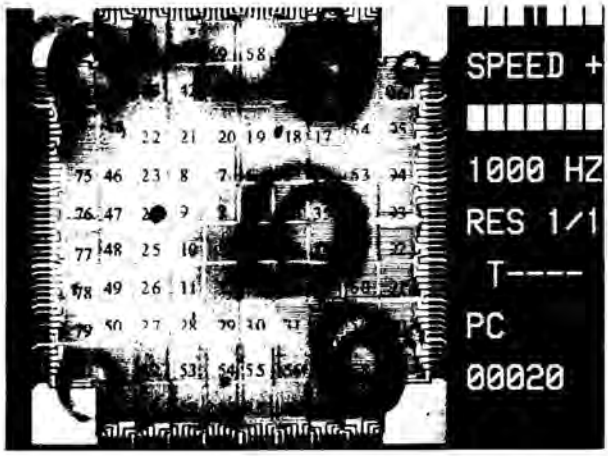

Figure 6: Photograph of saturated nucleate boiling taken through the bottom of the heater array in earth gravity. The individual heaters are labeled.

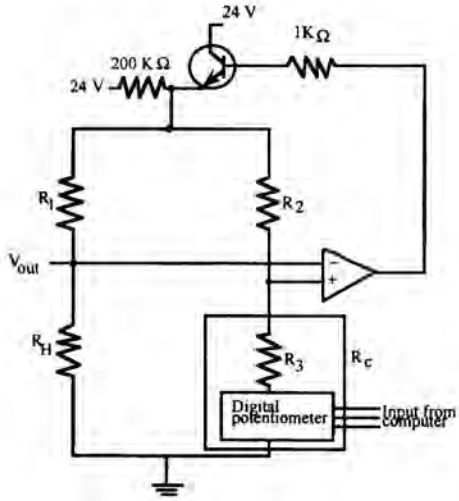

Figure 7: Schematic diagram of feedback control circuit.

measurements are provided by an array of ninety-six platinum resistance heaters deposited on a quartz wafer. A photograph of boiling on this heater array taken through the quartz substrate is shown in Figure 6. Each of the individual heaters is about 0.26 mm x 0.26 mm in size, has a nominal resistance of 1000 Ω and a nominal temperature coefficient of resistance of 0.002 $°C^{-1}$. Up to 17 heater arrays can be fabricated simultaneously on a single quartz wafer using VLSI circuit fabrication techniques. Platinum is sputtered onto the entire surface of a 500 μm thick wafer to a thickness of 0.2 μm, a layer of photoresist is deposited and patterned to define the heater geometry, then the platinum from the un-masked areas is removed using an ion mill to form a resistance heater. The platinum lines within each individual heater are 5 μm wide and spaced 5 μm apart. The spacing between each heater in the array varies from 7 μm near the center of the array to typically 40 μm between heaters on the outer edge of the array. Aluminum is then vapor-deposited to a thickness of 1 μm onto the surface, the aluminum power leads are masked off, and the remaining aluminum is removed using a wet chemical etch. A layer of SiO_2 is finally deposited over the heater array to provide the surface with a uniform surface energy. The surface was viewed under an electron microscope, and the surface roughness was found to be on the order of the thickness of the aluminum power leads to the heaters (~1 μm).

The completed quartz wafer is diced into chips, each containing a single heater array. The chips are mounted on a pin-grid-array (PGA) package using epoxy adhesive, and the pads on the PGA are connected to the power leads of the heater array chip using a conventional wire-bonding technique. The completed package is then mounted in a PGA socket that is connected to the control and data acquisition apparatus.

Electronic feedback loops. The temperature of each heater in the array is kept constant by feedback circuits similar to those used in constant temperature hot-wire anemometry as shown in Figure 7. The op-amp measures the imbalance in the bridge and outputs the necessary voltage to keep the ratio RH/R1 equal to RC/R2. The temperature of the heater is controlled by changing the wiper position of the digital potentiometer. The instantaneous voltage required to keep each heater at a constant temperature is measured (V_{out}) and used to determine the heat flux from each heater element. The large 200 KΩ resistor at the top of the bridge is used to provide a small trickle current through the heater, and results in a voltage across the heater of about 100 mV even when the op-amp is not regulating. Because all the heaters in the array are at the same temperature, heat conduction between adjacent heaters is negligible. There is conduction from each heater element to the surrounding quartz substrate (and ultimately to the walls of the chamber where it was dissipated by natural convection), but this can be measured and subtracted from the total power supplied to the heater element, enabling the heat transfer from the wall to the fluid to be determined.

The frequency response of the heaters along with the control circuit was found to be 15 kHz by measuring the time it took for the voltage across a heater to stabilize after a step change in the digital potentiometer position. Because this is much faster than the time scales typically associated with phase change heat transfer processes, the heater temperatures can be considered to be constant.

Calibration. Calibration of the heater array is performed by immersing it in a uniform temperature environment (oven or oil bath) and finding the digital potentiometer wiper position that causes the feedback loop to just begin regulating. The uncertainty in the wiper position is 1 position. Regulation of the heater temperature to within 1 °C can easily be achieved. The heat dissipated by the heater can accurately be measured. Part of this heat is transferred from the heater to the fluid, and part is conducted within the substrate. Since most applications

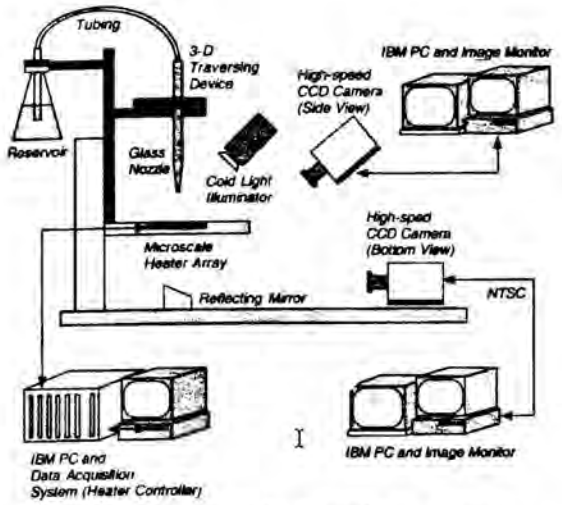

Figure 8: Schematic of droplet cooling experiment.

are interested in the former quantity, the heat conducted into the substrate needs to be quantified and subtracted from the total heat dissipation. The uncertainty in wall heat flux therefore depends on how accurately the substrate conduction can be measured, which depends on the application of the heater array. Techniques to determine substrate conduction for two applications are discussed below.

Summary of advantages/disadvantages. The advantage of the microheater array is that it provides time resolved heat transfer distribution on a surface that has effectively infinite conductivity (constant temperature). Because the temperature is controlled, it allows access to heat transfer regimes that are usually not accessible by constant wall heat flux methods. For example, the microheater array can be used to easily obtain heat transfer data in the transition boiling regime in pool boiling, or in the post CHF regime during spray cooling.

APPLICATION OF MICROHEATER ARRAY TO DROPLET COOLING

When a droplet strikes a heated surface, it flattens into a thin disk or splat whose thickness is much smaller than the diameter of the droplet, and high heat fluxes can be obtained due to the formation and evaporation of a thin liquid film on the heated surface. This process is of importance to several industrial applications such as electronic cooling and cooling of steel slabs. A fundamental study of the evaporative heat transfer from a hot surface when a droplet of FC-72 (Tsat=57 °C at 1 atm) strikes it was performed (Lee, et al.-2000). A schematic of the setup is shown on Figure 8. Data from the heater array was sampled at 3000 Hz and synchronized with high-speed digital video of the droplet striking the surface. Before the droplet impacted the heater array, the power supplied to each heater is lost only by substrate conduction (the small natural convection from the top and bottom of the substrate was neglected). Because the heaterwas held at constant temperature, the substrate conduction remained constant even after droplet impact, enabling the heat transferred from the heaters to the liquid to be determined.

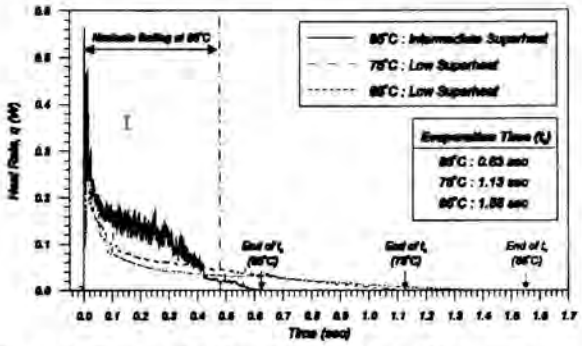

Figure 9: Time resolved heat flux for three wall temperatures.

A measure of the accuracy of the heat transfer measurements can be obtained by performing an energy balance on the drop. The total energy transferred from the wall to the drop can be obtained by integrating the measured wall heat transfer over all the heaters and the entire droplet evaporation time:

$$Q = \sum_{t=0}^{t=t_f} \sum_{i=1}^{N} q_i''(t) A_i \Delta t$$

This energy can be converted into an equivalent droplet diameter (d_{eq}) using an energy balance on the drop:

$$Q = \rho_d \pi \frac{d_{eq}^3}{6} \left[c_p (T_{sat} - T_o) + h_{fg} \right]$$

The ratio of the measured initial droplet diameter to d_{eq} was within 5% for all of the runs, indicating the heat transfer measurements were accurate.

The time variation in wall heat flux over the droplet evaporation time for three wall temperatures is shown in Figure 9. The droplet evaporation time is seen to decrease with increasing wall temperature. The trace for a wall temperature of 85 °C contains a high frequency component from drop impact to about 0.42 s. Correlation with the high-speed video indicated that this activity was due to nucleate boiling within splat. Very few bubbles were observed after 0.42 s, indicating the end of boiling.

Time resolved heat transfer distributions along with the spreading ratio shortly after impact (0<t<100 ms) for Twall=75 °C is shown in Figure 10. The data is seen to be remarkably repeatable from drop to drop. The oscillations in heat flux are seen to correspond to oscillations in the spread ratio, β.

APPLICATION OF MICROHEATER ARRAY TO BOILING HEAT TRANSFER

Boiling is a complex phenomenon where hydrodynamics, heat transfer, mass transfer, and interfacial phenomena are tightly interwoven. It is of importance to processes such as heat ex-

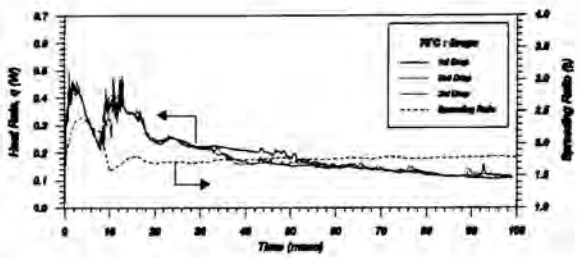

Figure 10: Time resolved heat flux shortly after droplet impact.

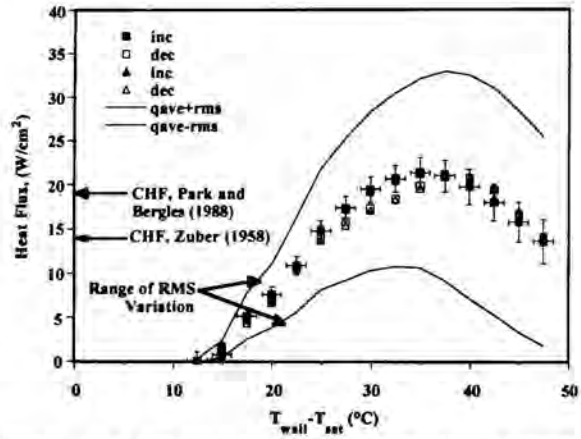

Figure 11: Boiling curve for microheater array facing upwards in earth gravity.

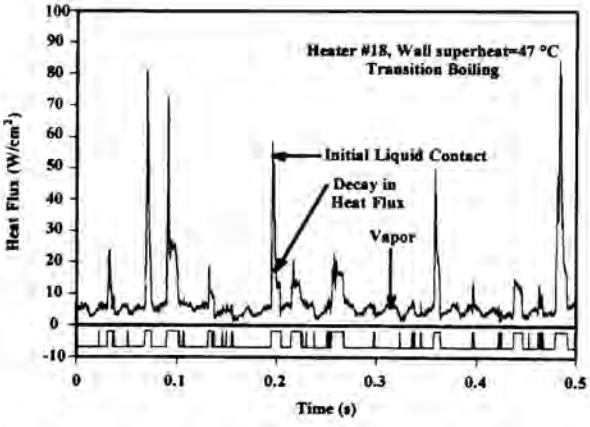

Figure 12: Heat flux trace along with the boiling function during transition boiling

change, cryogenic fuel storage and transportation, electronic cooling, and material processing due to the large amounts of heat that can be removed with relatively little increase in temperature. An understanding of boiling and critical heat flux is important to the design of heat removal equipment. Although much research in this area has been performed over the past few decades, the mechanisms by which heat is removed from surfaces by boiling are still unclear. Over the past few years, we have used the microheater array to document the pool boiling behavior in earth and microgravity environments. Examples of the heater performance in these environments is given below.

Earth gravity measurements. Saturated boiling on the heater array in the nucleate, CHF, and transition boiling regimes was documented in Rule and Kim (1999). The boiling curve for the heater array facing upward during saturated nucleate boiling for FC-72 at 1 atm is shown on Figure 11. It is seen that obtaining data at critical heat flux and during transition boiling was not a problem since the heaters were operated in constant temperature mode.

Space-resolved heat transfer measurements indicated that heaters towards the center of the array reached critical heat flux at significantly lower wall superheats (~30 °C) than the array averaged heat flux (~35 °C) due to the edge heaters blocking the flow of liquid to the inner heaters. It was also possible to distinguish regions on the heater that were covered with vapor from those where liquid contact occurred in transition boiling by using the time-resolved data from each heater to deduce a *boiling function*, a bi-modal signal that goes HIGH when boiling occurs on the surface. An example of a time-resolved signal in the transition boiling regime along with the corresponding boiling function is shown on Figure 12. The *boiling fraction* is defined as the time average of the boiling function, and represents the time fraction that boiling or enhanced convection occurs on the surface. Within transition boiling, where the surface is alternately wetted by liquid and vapor, the boiling fraction is equivalent to (1-void fraction), or the liquid fraction. The heat transfer from the edge heaters were observed to be much higher than those for the inner heaters above the temperature corresponding to CHF. The heat transfer during liquid contact in transition boiling, however, was constant for a given wall superheat for the inner heaters, and was observed to decrease with increasing wall superheat.

Microgravity measurements. Measurement of boiling in a microgravity environment was obtained using NASA's KC-135 aircraft in May, 2001. In this series of flights, the bulk liquid temperature was varied from 20 °C to 50 °C (subcooling from 36 °C to 6 °C), and measurements were made to wall superheats up to 100 °C. A summary of the test conditions is given on Table 1. Analysis of this data set is not complete, so the following results should be considered preliminary. Single frames from the high-speed video over the entire range of test conditions obtained through the bottom of the heater are shown on Figure 13. A large primary bubble is seen to form whose size is on the order of the heater array. This bubble formed from the coalescence of smaller bubbles that grew on the surface after transition into microgravity. The primary bubble increases in size with increasing bulk fluid temperature and

Flight No.	T_{bulk} (°C)	Saturation Temperature (°C) [Subcooling level (°C)]		
		Microgravity	High-g	1-g
1	39.5	59.5 [20.0]	61.2 [21.7]	61.2 [21.7]
2	49.6	56.6 [7.0]	57.9 [8.3]	58.2 [8.6]
3	30.9	56.3 [25.4]	57.6 [26.7]	57.8 [26.9]
4	23.0	55.6 [32.6]	56.9 [33.9]	56.9 [33.9]

Table 1: Summary of test conditions for each flight. The saturation temperatures for each g-level were calculated based on the measured average liquid pressure and the thermodynamic data provided by 3M.

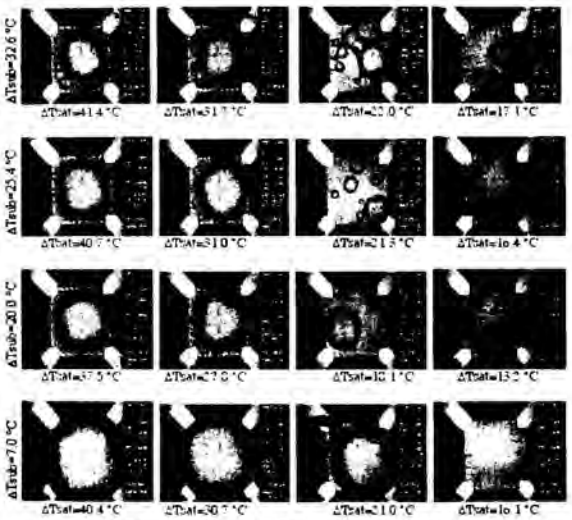

Figure 13: Bottom view images of boiling in microgravity at various subcooling and wall superheats.

wall superheat, and is fed by smaller satellite bubbles that surround it. For a given bulk temperature, the size of the satellite bubbles decreases with increasing superheat since the size to which they are able to grow is limited by the increasing size of the primary bubble. The motion of the primary bubble at low bulk temperatures was less influenced by g-jitter, since they were smaller and moved about the surface due to coalescence with the satellite bubbles. The size of the primary bubble is determined by a balance between vapor addition by evaporation of liquid at the bubble base and coalescence with satellite bubbles, and heat loss by condensation through the bubble cap.

Side-view images at selected conditions are shown on Figure 14. Strong Marangoni convection around the bubble was observed to develop, forming a "jet" of liquid into the bulk liquid. This "jet" also provided a reaction force on the

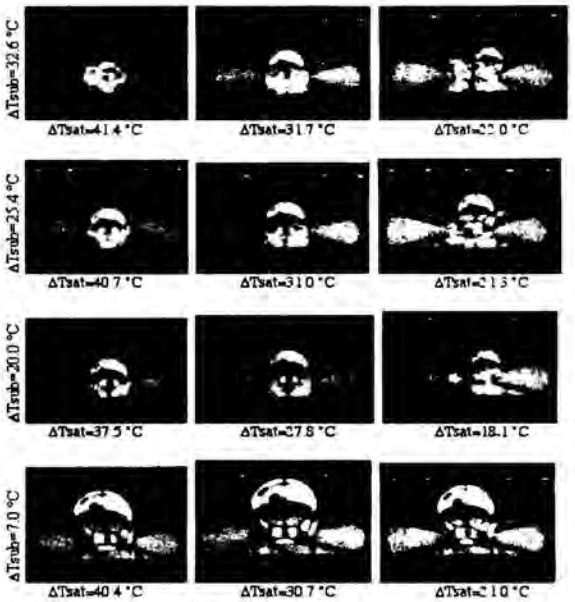

Figure 14: Side view images of boiling in microgravity at various subcooling and wall superheats.

primary bubble, keeping it on the heater.

Dryout under the primary bubble occurred for bulk temperatures 39.5 °C and below. Dryout for the edge heaters did not occur, probably due to the flow induced by the Marangoni convection. Dryout over the entire heater array occurred for T_{bulk}=49.6 °C at superheats above 30.7 °C–dryout might have occurred as low as 25.7 °C, but g-jitter caused the primary bubble to move slightly off the heater array, enabling liquid to rewet the edges of the heater. The contact line of the bubble was stable, and touched the outside of the heater array. Bubble coalescence seemed to be the mechanism by which CHF occurred under the conditions studied.

Boiling curves for microgravity, earth gravity, and high-g for various subcoolings are shown on Figure 15. The high-g boiling curve is based on the middle 20 s of the high-g data, and includes data from the pull out (~1.6 g) and pull up (~1.8 g). Separate boiling curves were generated from the data taken during the pull out and compared with those during the pull up, but little difference in the curves was observed. The effect of g-jitter must be considered for the microgravity curves. Higher wall superheat is generally associated with larger primary bubbles, which are more sensitive to g-jitter. When the primary bubble moves on the surface or departs due to g-jitter, liquid rewets the surface and results in higher wall heat transfer than would occur in a true microgravity environment. The data at high bulk temperatures and high wall superheats (especially those beyond CHF) may be artificially high as a result.

Little effect of subcooling is seen in the nucleate boiling regime for the 1 g and high-g data, which is consistent with the

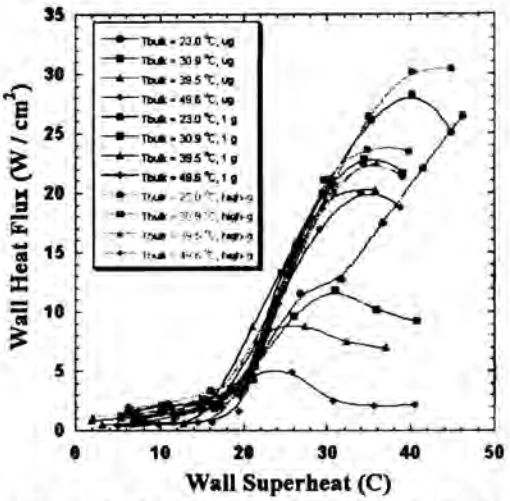

Figure 15: Boiling curve at various gravity levels and subcoolings.

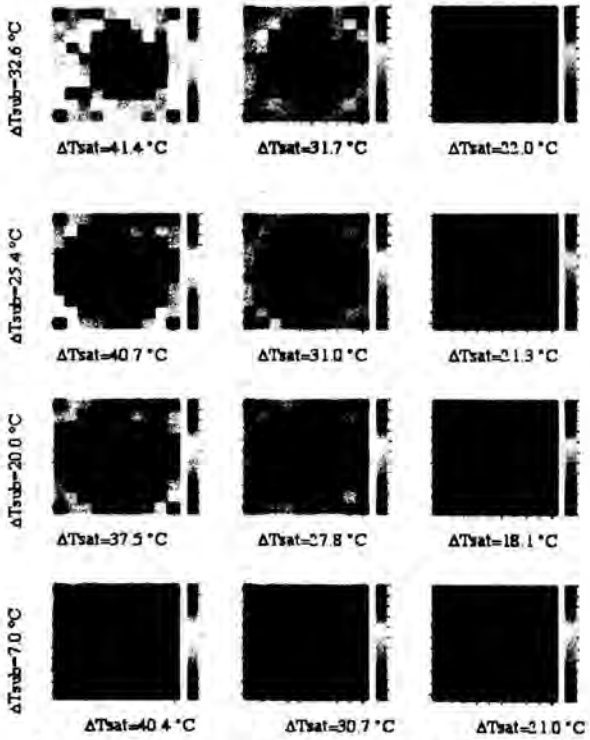

Figure 16: Time average heat transfer distribution on the surface in microgravity. Color scale varies from 0 W/cm^2 to 55 W/cm^2.

observations of previous researchers. The microgravity data tend to follow the 1 g and high-g data for ΔT_{sat}<20 °C, but drop below them for higher superheats as the primary bubble causes dryout over a successively larger fraction of the heater. CHF for the microgravity curves are significantly lower than those for the 1 g and high-g data.

The time averaged heat flux distribution from each heater in the array is shown on Figure 16. The scale has been kept the same for all images to highlight the change in heat transfer with wall superheat and subcooling. Very little heat transfer is associated with the primary bubble, even along the contact line. Much higher heat transfer rates are associated with the rapid growth and coalescence process of the satellite bubbles. A significant amount of the surface dries out before CHF. CHF occurs when the dry spot size grows faster than the increase in heat transfer outside the primary bubble. The time resolved heat flux distribution for Tbulk=20.0 °C at three superheats are shown in Figure 17. As was noted for Figure 16, much higher heat transfer is associated with the small scale boiling on the array.

In order to conditionally sample the heat flux only when boiling occurs on the surface, a *boiling function* was generated from the time-resolved heat flux data. This function is a bimodal signal that is set to HIGH when boiling occurs on the surface, and LOW otherwise. Details of how the boiling function is generated are discussed in Rule and Kim (1999). The time averaged heat flux obtained by sampling the data only when the boiling function is HIGH is referred to as the nucleate boiling heat flux, and is a measure of the heat transfer associated with the satellite bubbles.

Boiling curves generated from the nucleate boiling heat flux for microgravity, earth gravity, and high-g environments are compared on Figure 18. It is seen that the nucleate boiling heat flux collapses onto a single curve, indicating that the small scale boiling is independent of subcooling and gravity level. This suggests that if one is able to predict the extent of the dry area in microgravity, then one could to predict the microgravity boiling curve from earth or high gravity boiling heat flux data.

OTHER POTENTIAL APPLICATIONS

The microheater array is can be used for a wide range of other applications as well. Consider the case where the heaters are constructed to form a linear array, and operated in the same way described above. This linear array can then be capped off, forming a microchannel. The heat transfer coefficient distribution within this microchannel can then be measured, providing information about the flow regimes and heat transfer mechanisms. Visualization studies can also be conducted since the microheater array is semi-transparent.

The linear array can also be operated as a bubble pump. Bubbles can be nucleated at intervals along the heater array. If the bubbles are then shifted along the array by successively heating adjacent heaters, the liquid between the bubbles can be pumped through the channel. The advantages to such a pump are numerous. First, it has no moving parts to wear out. Second, because it takes a relatively high force to dislodge a bubble from a heater, high pressure differentials can be created

Figure 17: Time resolved heat transfer distributions in microgravity with Tbulk=20 °C.

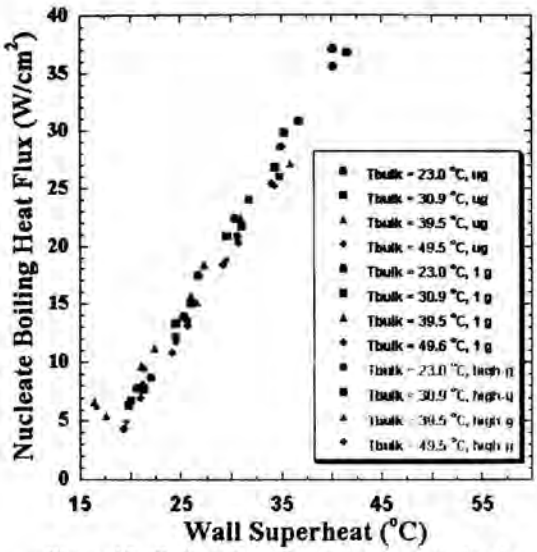

Figure 18: Boiling heat flux at three gravity levels.

across the channel. Third, because the bubble can be shifted along the channel at high velocities, high flow rates can be achieved.

The heater array can be used during combustion catalysis experiments to measure the rate of reactions. Consider the case where the platinum heaters are held at uniform temperature. With no reaction on the surface, a certain amount of power is required to keep the heater at a uniform temperature due to substrate conduction losses. Exothermic reactions on the surface of the platinum will cause the power required to keep the heater at a constant temperature to decrease, enabling the heat released by the reaction to be measured.

CONCLUSIONS

The use of a microheater array to obtain space and time resolved heat transfer distributions on a wall held at constant temperature has been described. Demonstration of the heater array has been performed for phase change processes involving boiling and droplet cooling. This technology is expected to be applicable to a wide range of additional phenomena.

ACKNOWLEDGEMENTS

This work received support from the Office of Biological and Physical Science at NASA Headquarters, the Laboratory for Physical Science, and the Air Force Research Laboratory at WPAFB. Their support is gratefully acknowledged.

REFERENCES

Bayazit, B.B., Hollingsworth, D.K., and Witte, L.C., "Heat transfer enhancement caused by sliding bubbles", Proceedings of the 2001 National Heat Transfer Conference, Anaheim, CA.

Fath, H. S., and Judd, R. L., 1978, "Influence of System Pressure on Microlayer Evaporation Heat Transfer," ASME Journal of Heat Transfer, Vol. 100, pp. 49-55.

Incropera, F.P. and Dewitt, D.P, 1996, Fundamentals of Heat and Mass Transfer, Fourth Edition, John Wiley and Sons.

Kenning, D.B.R., Bustnes, O.E., and Yan, Y. (2000) "Heat transfer to a sliding vapor bubble", Proceedings of the Engineering Foundation Conference on Boiling Phenomena and Emerging Applications, Anchorage, AK.

Koffman and Plesset (1983) "Experimental Observations of the Microlayer in Vapor Bubble Growth on a Heated Surface", Journal of Heat Transfer, Vol. 105, pp. 625-632.

Lee J., Kim, J., and Kiger, K.T., (2000) "Time and Space Resolved Heat Transfer Characteristics of Single Droplet Cooling Using Microscale Heater Arrays", International Journal of Heat and Fluid Flow, Vol. 22, pp. 188-200.

Rule, T. and Kim, J., (1999) "Heat Transfer Behavior on Small Horizontal Heaters During Pool Boiling of FC-72", Journal of Heat Transfer, Vol. 121, No. 2, pp. 386-393.

Sheats, J.R., Antoniadis, H., Hueschen, M., Leonard, W., Miller, J., Moon, R., Roitman, D., and Stocking, A., "Organic Electroluminescent Devices." *Science* 1996, 273, 884-888.

Theofanous, T.G., Tu, J.P., Dinh, T.N. , Salmassi, T., Dinh, A.T. and Gasljevic, K., "Physics of boiling at burnout." Fifth Microgravity Fluid Physics and Transport Phenomena, Cleveland, OH, August 9-11, 2000.

HEFAT2002
1st International Conference on Heat Transfer, Fluid Mechanics, and Thermodynamics
8-10 April 2002, Kruger Park, South Africa
VP1

WEAK TURBULENCE IN NATURAL CONVECTION

Peter Vadasz

Department of Mechanical Engineering
University of Durban-Westville
Private Bag X54001, Durban 4000, South Africa
e-mail: vadasz@pixie.udw.ac.za

ABSTRACT

The fundamental understanding of the transition from laminar to turbulent convection is far from being conclusive. While major efforts are under way, there is still a significant challenge in front of the scientist and engineer to uncover the complex behavior linked to this transition. In isothermal shear flows the time dependent and three dimensional form of turbulence is well established experimentally and numerically. It is caused by the non-linear terms in the isothermal Navier-Stokes equations. Weak turbulence is linked to the problem of natural convection where an additional non-linear interaction appears as a result of the coupling between the equations governing the fluid flow and the energy equation. The latter can typically cause a transition to a non-steady and non-periodic regime (referred to as weak turbulent) at much lower values of the parameter controlling the flow, when compared to the corresponding isothermal system.

INTRODUCTION

Turbulence modeling is heavily linked to co-experimental data in order to solve the systems of equations that otherwise present an ill-posed problem. The understanding of the turbulence transition mechanism accurately may in future provide tools to enhance turbulence modeling and de-link its solution from experimental data. Then the experimental data can be used only for validating such models. The present paper's contribution is towards this stated direction although it represents a small step forward in the understanding of the transition from laminar convection to weak turbulent convection. In this respect the analytical results show how the transition occurs and the hysteresis phenomenon linked to such a transition.

The objective of the present paper is therefore to present the results of transitions to chaos in a fluid layer subject to gravity and heated from below. The non-steady and non-periodic convective regime associated with a reduced set of equations is referred to as weak turbulence. This is related to "turbulence" manifesting itself in the time domain while the space domain does not exhibit irregularities in the solution. In practice, the situation is more complex, however weak-turbulence could very well describe the phenomenon occurring over a transitional range of Rayleigh numbers, while temporal-spatial turbulence (strong turbulence) is expected to manifest itself beyond this transitional range. Moreover, the weak-turbulent regime can be anticipated to persist even beyond the transitional range within the core of the convective domain, while boundary layers may incorporate the temporal-spatial effect. The results reported show that the transition from steady convection to chaos is sudden for moderate Prandtl number convection, and follows a period doubling sequence for large Prandtl number convection. Both transitions occur initially via a Hopf bifurcation producing a "solitary limit cycle", which may be associated with a homoclinic explosion. Analytical results suggesting an explanation for the appearance of this "solitary limit cycle" and explaining a well known phenomenon of hysteresis are presented as well.

NOMENCLATURE

Latin Symbols

H_* = the height of the layer.
L_* = the length of the layer.
p = reduced pressure (dimensionless).
Pr = Prandtl Number, equals ν_* / α_*
Ra = gravity related Rayleigh number, equals $\beta_* \Delta T_* g_* H_*^3 / \alpha_* \nu_*$.
Ra_a = critical Rayleigh number value for the transition from steady convection to Chaos.
R = scaled Rayleigh number, equals Ra / Ra_{cr}.
R_a = critical value of R for the transition from steady convection to Chaos.
r = absolute value of the complex amplitude.
r_o = initial condition of r.
T = dimensionless temperature, equals $(T_* - T_c) / (T_H - T_c)$
T_c = coldest wall temperature.
T_H = hottest wall temperature.
u = horizontal x component of the velocity.
v = horizontal y component of the velocity.
w = vertical component of the velocity.
x = horizontal length co-ordinate.

y = horizontal width co-ordinate.
z = vertical co-ordinate.
X = rescaled amplitude A_{11}.
Y = rescaled amplitude B_{11}.
Z = rescaled amplitude B_{20}.

Greek Symbols

α_* = thermal diffusivity.
β_* = thermal expansion coefficient.
ε = asymptotic expansion parameter.
ν_* = fluid's kinematic viscosity.
μ_* = fluid's dynamic viscosity.
ψ = stream function.
τ = long time scale.
ξ = a parameter, equals ε^2/φ .
χ = a parameter, equals φ/β.
θ = higher order frequency correction.

Subscripts

$*$ = dimensional values.
t = transitional values.

Superscripts

$\bar{}$ = complex conjugate.

GOVERNING EQUATIONS

Original System

A fluid layer subject to gravity and heated from below is considered. A Cartesian co-ordinate system is used such that the vertical axis z is collinear with gravity. The continuity, momentum and energy equations are being considered, while the Boussinesq approximation is applied for the effects of density variations. Under these conditions and for convective rolls having axes parallel to the shorter dimension (i.e. y) $v = 0$, hence the governing equations can be presented in terms of a stream function defined by $u = -\partial\psi/\partial z$ and $w = \partial\psi/\partial x$, which yields the following system of dimensionless partial differential equations

$$\left[\frac{1}{Pr}\left(\frac{\partial}{\partial \hat{t}} + \frac{\partial\psi}{\partial z}\frac{\partial}{\partial x} - \frac{\partial\psi}{\partial x}\frac{\partial}{\partial z}\right) - \nabla^2\right]\nabla^2\psi = Ra\frac{\partial T}{\partial x} \quad (1)$$

$$\frac{\partial T}{\partial \hat{t}} - \frac{\partial\psi}{\partial z}\frac{\partial T}{\partial x} + \frac{\partial\psi}{\partial x}\frac{\partial T}{\partial z} = \frac{\partial^2 T}{\partial x^2} + \frac{\partial^2 T}{\partial z^2} \quad (2)$$

where the boundary conditions for the stream function are $\psi = 0$ on all solid boundaries.

The set of partial differential equations (1) and (2) form a non-linear coupled system which together with the corresponding boundary conditions accepts a basic motionless conduction solution.

Equations (1)-(2) are presented in a dimensionless form. The values α_*/H_* , $\mu_*\alpha_*/H_*^2$, and $\Delta T_c = (T_H - T_C)$ are used to scale the velocity components (u_*, v_*, w_*) , pressure (p_*), and temperature variations ($T_* - T_C$) , respectively, where α_* is the thermal diffusivity, μ_* is fluid's viscosity, H_* is the height of the fluid layer. The height of the layer H_* was used for scaling the variables x_* , y_*, z_* and H_*^2/α_* for scaling the time t_*. Accordingly , $x = x_*/H_*$, $y = y_*/H_*$ and $z = z_*/H_*$ and $\hat{t} = t_*\alpha_*/H_*^2$. In equation (1) Ra is the gravity related Rayleigh number defined in the form $Ra = \beta_*\Delta T_* g H_*^3/\alpha_*\nu_*$.

Reduced System for Weak Turbulence

To obtain the solution to the non-linear coupled system of partial differential equations (1) and (2) we represent the stream function and temperature in the form

$$\psi = A_{11}(\hat{t})\sin(\kappa x)\sin(\pi z) \quad (3)$$

$$T = 1 - z + B_{11}(\hat{t})\cos(\kappa x)\sin(\pi z) + B_{20}(\hat{t})\sin(2\pi z) \quad (4)$$

This representation is equivalent to a Galerkin expansion of the solution in both x and z directions, truncated when $i + j = 2$, where i is the Galerkin summation index in the x direction and j is the Galerkin summation index in the z direction. Substituting (3) and (4) into the equations (1) and (2), multiplying the equations by the orthogonal eigenfunctions corresponding to (3) and (4), and integrating them over the domain, i.e. $\int_0^{\pi/\kappa} dx \int_0^1 dz\ (.)$, yields a set of three ordinary differential equations for the time evolution of the amplitudes , in the form

$$\dot{X} = Pr(Y - X) \quad (5)$$

$$\dot{Y} = RX - Y - (R-1)XZ \quad (6)$$

$$\dot{Z} = \lambda(XY - Z) \quad (7)$$

where $R = Ra/Ra_c$, $\lambda = 8/\left[(\kappa/\kappa_c)^2 + 2\right]$, $t = \left(\kappa^2 + \pi^2\right)\hat{t}$ and $\kappa_c = \pi/\sqrt{2}$. The amplitudes were rescaled with respect to their convective fixed points in the following form $\tilde{A}_{11} = \left\{(\kappa/\kappa_c)/\left[(\kappa/\kappa_c)^2 + 2\right]\right\} A_{11}$, $X = \tilde{A}_{11}/\sqrt{\lambda(R-1)}$ $\tilde{B}_{11} = \kappa_c R\, B_{11}$, $Y = \tilde{B}_{11}/\sqrt{\lambda(R-1)}$, $\tilde{B}_{02} = \pi R B_{02}$, $Z = \tilde{B}_{02}/(R-1)$. In eqs. (5) - (7) the dots $\dot{()}$ denote time derivatives $d()/dt$.

Equations (5), (6) and (7) are the Lorenz equations (Lorenz, 1963, Sparrow, 1982). The value of λ has to be consistent with the wave number at the convection threshold, which is required for the convection cells to fit into the domain and fulfil the boundary conditions. This requirement resulted in $\lambda = 8/3$, yields for porous media convection a value of $\gamma = 0.5$. With this value of γ the definitions of R and α are explicitly expressed in the form $Ra_c = 27\pi^4/4$.

WEAK NON-LINEAR SOLUTION

This method was applied by Vadasz (2000) to provide analytical insight to the transition observed computationally by Vadasz and Olek (2000). The stationary (fixed) points of the system (5), (6) and (7) are the convective solutions $X_s = Y_s = \pm 1$, $Z_s = 1$ and the motionless solution $X_s = Y_s = Z_s = 0$ (occasionally referred to as the origin). The expansion around the motionless stationary solution yields the familiar results of a pitchfork bifurcation from a motionless state to convection at $R = 1$. We expand now the dependent variables around the convection stationary points in the form

$$[X, Y, Z] = [X_s, Y_s, Z_s] + \varepsilon[X_1, Y_1, Z_1] + \varepsilon^2[X_2, Y_2, Z_2] + \varepsilon^3[X_3, Y_3, Z_3] + \ldots \quad (8)$$

We also expand R in a finite series of the form $R = R_a(1+\varepsilon^2)$ which now defines the small expansion parameter as $\varepsilon^2 = (R - R_a)/R_a$, where R_a is the value of R where the stationary convective solutions loose their stability in the linear sense (see Vadasz and Olek 2000). Therefore the present weak non-linear analysis is expected to be restricted to initial conditions sufficiently close to *any one* of the convective fixed points. Introducing a long time scale $\tau = \varepsilon^2 t$ and replacing the time derivatives in equations (5), (6) and (7) with $d/dt \to d/dt + \varepsilon^2 d/d\tau$, yields a hierarchy of ordinary differential equations at the different orders. The leading order provides the stationary solutions, while at order ε we get the familiar homogeneous linearized system that yields the following solutions

$$X_1 = a_1 e^{i\sigma_a t} + a_1^* e^{-i\sigma_a t} \quad Y_1 = b_1 e^{i\sigma_a t} + b_1^* e^{-i\sigma_a t} \quad Z_1 = c_1 e^{i\sigma_a t} + c_1^* e^{-i\sigma_a t} \quad (9)$$

where the coefficients $a_1(\tau)$, $a_1^*(\tau)$, $b_1(\tau)$, $b_1^*(\tau)$, $c_1(\tau)$ and $c_1^*(\tau)$ are allowed to vary over the long time scale τ and $\pm i\sigma_a$ are the imaginary parts of the complex eigenvalues corresponding to the linear system at marginal stability (i.e. the real part of the eigenvalues is 0). They are related to Pr and λ by the equation $\sigma_a^2 = 2\lambda Pr(Pr+1)/(Pr-\lambda-1)$, which can be established by working out the relationships between the $O(\varepsilon)$ coefficients in the solution (9). These relationships are obtained by substituting the solutions (9) into the linear equations. The relationship for R_a is also obtained in the form $R_a = Pr(Pr+\lambda+3)/(Pr-\lambda-1)$. For $\lambda = 8/3$ and $Pr = 10$ the corresponding value of R_a is $R_a \equiv 24.737$ .At higher orders a hierarchy of non-homogeneous ordinary differential equations sharing the same homogeneous operator as the leading order equations are obtained. At order $O(\varepsilon^3)$ the forcing functions belonging to the non-homogeneous part of the equations resonate the homogeneous operator unless a solvability condition is fulfilled (for details see Vadasz, 2000).

The solvability condition takes the form of a constraint on the amplitude of the solution at order $O(\varepsilon)$ and yields an amplitude equation of the form

$$\frac{da}{dt} = h_{21}[\varepsilon^2 - h_{32} a a^*]a \quad (10)$$

and a similar equation for a^*, where in equation (10) $a = \varepsilon a_1$, $a^* = \varepsilon a_1^*$ and h_{21}, h_{32} are complex coefficients which depend upon Pr, λ, σ_a and R_a. Their lengthy expressions are skipped here. The coefficient of the non-linear term in equation (10) plays a role of a particular importance as it controls the direction of the Hopf bifurcation which results from the post-transient solution to equation (10). Its impact on the solution and the corresponding analysis is presented later in this paper.

ANALYSIS AND RESULTS

Investigation of the Weak Non-Linear Results

As indicated above, the coefficient of the non-linear term in equation (10) plays a role of a particular importance as it controls the direction of the Hopf bifurcation which results from the post-transient solution to equation (10). To observe this point further we follow Vadasz (2000) and represent equation (10) for the complex amplitude, a, as a set of two equations for the absolute value of the amplitude, $r = |a|$, and its phase, θ, in the form: $a = r\exp(i\theta)$, $a^* = r\exp(-i\theta)$ with $aa^* = r^2$. Substituting this representation in equation (10) yields

$$\beta \frac{dr}{dt} = [\varepsilon^2 - \varphi r^2]r \quad (11)$$

$$\frac{d\theta}{dt} = m_{21}\varepsilon^2 - m_{31} r^2 \quad (12)$$

where the following notation was introduced to separate between the real and imaginary parts of the coefficients in equation (10) $h_{21} = h_{21}^* + i m_{21}$, $h_{31} = h_{31}^* + i m_{31}$ and $\beta = 1/h_{21}^*$, $\varphi = h_{31}^*/h_{21}^*$.

Now it can be observed that when the coefficient of the non-linear term, φ, is positive the Hopf bifurcation is forward (i.e. supercritical) while a negative value of φ yields an inverse bifurcation (i.e. subcritical). The coefficient, φ, was evaluated as a function of Pr and was observed to be negative over the whole domain of validity of the Hopf bifurcation. The relaxation time, β, was also evaluated by Vadasz (2000) and was showed to be positive for $Pr \geq 3$. Note that values of $Pr \leq 3$ are not consistent with the Hopf bifurcation and with the solutions considered here, as can be observed from the equation for R_a. For such values the solution of this system decays to the stationary points. We can therefore confirm previously suggested results (Sparrow, 1982, Wang, Singer & Bau, 1992 and Yuen & Bau, 1996) related to the Lorenz equations for other applications, that the Hopf bifurcation in this system is indeed subcritical. A further analysis of the periodic solution at slightly subcritical values of R shows that this solution is unstable for $\varepsilon^2 < 0$ (i.e. $R < R_a$). We are therefore faced with a periodic solution which exists only for $\varepsilon^2 < 0$ (i.e. $R < R_a$) but it is not stable in this domain. However it is at this point where the further investigation of the amplitude equation provides a marked insight into the details of this Hopf bifurcation at the point where the steady convective solutions loose their stability but the resulting periodic solution unfolding from the amplitude equation is unstable for $R < R_a$ and doesn't exist when $R > R_a$. The post transient amplitude solution is obtained from equation (11) in the form $r^2 = \varepsilon^2/\varphi$ which clearly yields a real value for the amplitude only when $\varepsilon^2 \leq 0$ (i.e. $R \leq R_a$) given the already established fact that $\varphi < 0$. The post-transient frequency correction, $\dot{\theta}$, can be obtained for $R \leq R_a$ by substituting the post-transient solution for r^2 into (12) in the form $\dot{\theta} = (m_{21} - m_{31}/\varphi)\varepsilon^2$.

To gain more insight into the nature of the limit cycle and the subcriticality of the Hopf bifurcation resulting from the amplitude equation we undertake further investigation of this equation. The major point being the question of where exactly the supercritical solution disappeared, what is the reason for its disappearance and what more can we learn about the unstable subcritical limit cycle. This is done by working out the transient solution of equation (11) which can be easily

obtained by a simple integration. Prior to that it is convenient to introduce the following notation, which simplifies the analysis, $\chi = \varphi/\beta$ and $\xi = \varepsilon^2/\varphi$. Clearly $\chi < 0$ over all the cases to be considered in this analysis, while $\xi > 0$ for $\varepsilon^2 < 0$ (subcritical conditions), $\xi < 0$ for $\varepsilon^2 > 0$ (supercritical conditions), and $\xi = 0$ for $\varepsilon^2 = 0$ (critical conditions). By using this notation the amplitude equation (11) takes the form

$$\frac{dr}{dt} = \chi\left[\xi - r^2\right]r \qquad (13)$$

The solution to equation (13) is obtained by direct integration in the following form $r^2 = \xi\exp(2\xi\chi t)/\left[D + \exp(2\xi\chi t)\right]$ for $\xi \neq 0$, $(\varepsilon^2 \neq 0)$ and $r^2 = 1/\left[2(\chi t - D)\right]$ for $\xi = 0$, $(\varepsilon^2 = 0)$, where D is a constant of integration to be determined from the initial conditions. By introducing the initial conditions $r = r_o$ at $t = 0$, the transient solutions take the form

$$r^2 = \frac{\xi}{\left[1 - \left(1 - \frac{\xi}{r_o^2}\right)\exp(-2\xi\chi t)\right]} \quad \text{for } \xi \neq 0\ (\varepsilon^2 \neq 0) \qquad (14)$$

$$r^2 = \frac{r_o^2}{\left[1 + 2r_o^2\chi t\right]} \quad \text{for } \xi = 0\ (\varepsilon^2 = 0) \qquad (15)$$

Clearly, both solutions (14) and (15) are valid at $t = 0$ and yield then $r^2 = r_o^2$ which can be easily recovered by substituting $t = 0$ in equations (14) and (15). Therefore the question which arises is what happens at a later time $t > 0$ which causes these solutions to disappear when $\varepsilon^2 > 0$, (i.e. when $\xi < 0$). To answer this question we separate the discussion into three cases as follows: *(i)* the supercritical case $, \varepsilon^2 > 0\ (\xi < 0)$, *(ii)* the subcritical case $, \varepsilon^2 < 0\ (\xi > 0)$ and *(iii)* the critical case $, \varepsilon^2 = 0\ (\xi = 0)$. In all three cases it should be remembered that the value of χ is always negative, while ξ is negative, zero, or positive depending on whether the conditions are supercritical, critical or subcritical , respectively.

(i) the supercritical case $, \varepsilon^2 > 0\ (\xi < 0)$,

For this case the argument of the exponent in the denominator of equation (14) and the value of ξ/r_o^2 are always negative. The denominator has at $t = 0$ a negative value and this value increases until such time that the denominator vanishes causing the solution of r^2 to become infinite. To evaluate this critical time, t_{cr}, when the solution diverges we check the condition when the denominator becomes equal to 0, providing the following result

$$t_{cr} = \frac{1}{2\chi\xi}\ln\left[1 - \frac{\xi}{r_o^2}\right] \qquad (16)$$

Obviously, since $\xi < 0$ in this case the argument of the natural logarithm is always greater than 1, therefore this critical time exists unconditionally in the supercritical regime, causing the amplitude solution to diverge, the significance of which will be discussed below.

(ii) the subcritical case $, \varepsilon^2 < 0\ (\xi > 0)$

For this case the argument of the exponent in the denominator of equation (14) and the value of ξ/r_o^2 are always positive. The denominator has at $t = 0$ a positive value and this value decreases or increases depending on the value of the ratio ξ/r_o^2. To establish the conditions for the denominator of the solution (14) to become zero and cause the solution to diverge we evaluate the critical time in a similar way as for the supercritical case, providing an identical result for t_{cr} as presented in equation (16). However, this time, under subcritical conditions $\xi > 0$, the coefficient of the natural logarithm is negative and its argument can be greater or less than 1 depending on the value of ξ/r_o^2. It is easier to notice the behavior of the solution in the subcritical case by presenting the equation for the critical time corresponding to the subcritical case in the following form, where we express explicitly the fact that $\chi < 0$

$$t_{cr} = -\frac{1}{2|\chi|\xi}\ln\left[1 - \frac{\xi}{r_o^2}\right] \qquad (17)$$

From this equation it is clear that the condition for existence of a critical time is that the argument of the natural logarithm in equation (17) be positive and less than one, i.e. $0 < \left(1 - \xi/r_o^2\right) < 1$. Otherwise, either the ln(.) function doesn't exist or the critical time becomes negative having no physical significance. The right hand side of this inequality yields: $\xi/r_o^2 > 0$, which is unconditionally satisfied under subcritical conditions ($\xi > 0$). The left-hand side provides the following condition for existence of a critical time: $\xi/r_o^2 < 1$. The interesting fact coming out from this result is that a critical time when the limit cycle solution diverges exists in the subcritical case as well, subject to the condition $\xi/r_o^2 < 1$.

(iii) the critical case $, \varepsilon^2 = 0\ (\xi = 0)$

For the critical case we use equation (15) and evaluate the condition for its denominator to vanish in order to establish the existence of a critical time in this case as well. One may expect it to exist on continuity arguments as it exists conditionally in the subcritical case and unconditionally in the supercritical case. From equation (15) it can be easily evaluated as

$$t_{cr} = -\frac{1}{2\chi r_o^2} \quad \text{for} \quad \xi = 0 \qquad (18)$$

The significance of the existence of a critical time when the limit cycle solution diverges is explained simply in terms of the breakdown of the asymptotic expansion which implicitly assumes (a) that the solution is local, around *any one (but only one)* of the fixed points, and (b) that the expansion is valid around the critical value of R, i.e. around R_o. The second assumption doesn't seem to be violated, at least not for the slightly sub-/super-critical case, however the first assumption is strongly violated by a solution which tends to infinity, starting at subcritical conditions when $\xi/r_o^2 < 1$. This condition implies $r_o^2 > \xi$, i.e. at a given subcritical value of R, as long as the initial conditions for r_o^2 are

smaller than ξ ($r_o^2 < \xi$) the solution decays, spiraling towards the corresponding fixed point around which we applied the expansion. When the initial conditions satisfy $r_o^2 = \xi$ a solitary limit cycle solution around this fixed point exists (the terminology "solitary limit cycle" is used to indicate that this limit cycle can be obtained only at $r_o^2 = \xi$). As the initial conditions move away from this fixed point and $r_o^2 > \xi$, the other fixed point may affect the solution as well, however the asymptotic expansion used doesn't allow it, and it is because of this reason that the solution diverges, indicating the breakdown of the expansion used. Therefore the divergence of the solution for $r_o^2 > \xi$ should be interpreted in this light only, i.e. the breakdown of the expansion used. While the divergence of the transient solution as $t \to t_{cr}$ indicates the breakdown of the assumed expansion, it is sensible to suggest a physical interpretation of this result as the tendency of the solution to be repelled away from the neighborhood of the present fixed point ($X_s = Y_s = Z_s = 1$) towards the other fixed point ($X_s = Y_s = -1$; $Z_s = 1$), or alternatively its tendency to orbit around both fixed points. We can imagine a process of gradually increasing the value of R towards R_o (i.e. decreasing the value of ξ towards $\xi = 0$). As we do so and we get closer to R_o a wider range of initial conditions falls into the category which satisfies the solution's divergence condition. To the question of what solution would therefore exist when this condition is fulfilled one can anticipate (with hindsight of the computational results which are presented in the next section) that the solution may move towards the other fixed point , indicating a homoclinic explosion, or wander around both fixed points suggesting a chaotic solution. Transforming the condition for this transition to occur, from $r_o^2 > \xi$, to the original physical parameters of the system by substituting the definition of ξ one can observe that there is a value of $R \le R_o$, say R_t, beyond which the transition occurs, which can be expressed in the form

$$R_t = R_o\left(1 - |\varphi| r_o^2\right) \qquad (19)$$

where the minus sign and the absolute value of φ appear in order to show explicitly that $\varphi < 0$ ($\varphi = -1.30959$ in the present case). If $R < R_t$ the solution decays, spiraling towards the corresponding fixed point, at $R = R_t$ we expect the solitary limit cycle solution, and beyond this transitional value of R, i.e. $R > R_t$, the solution moves away from this fixed point either *(a)* towards the other fixed point, or *(b)* wanders around both fixed points before it stabilizes towards one of them, or *(c)* yields a chaotic behavior by being attracted to the non-wandering set (Lorenz attractor). The present expansion can not provide an answer to select between these three possibilities. However, it is important to stress that for any initial condition r_o^2, which we choose, we can find a value of $R \le R_o$ which satisfies equation (19). At that value of R we expect to obtain a limit cycle solution and beyond it a possible chaotic solution.

To present the analytical solutions graphically the following rescaled variables relevant to equations (14)-(18) are introduced : $\tilde{r} = r/r_o$, $\tilde{t} = r_o^2|\chi|t$ and $\tilde{\xi} = \xi/r_o^2$. Substituting these rescaled variables into equations (14)-(18) transforms the solutions to the form in which they are plotted in Figures 1(a) and 1(b). Figure 1(a) shows an example of the amplitude solution (equation (14)) for three values of $\tilde{\xi}$, corresponding to sub-transitional conditions (when $\tilde{\xi} > 1$), transitional conditions (when $\tilde{\xi} = \tilde{r}^2 = 1$), and super-transitional conditions (when $\tilde{\xi} < 1$ and the solution diverges at $\tilde{t} = \tilde{t}_{cr}$). The variation of the critical time $\tilde{t}_{cr}$ with $\tilde{\xi}$ is presented in Figure 1(b) where one observes that the critical time tends to infinity as $\tilde{\xi} \to 1$. This fact suggests that it should not be difficult to obtain numerically the solitary limit cycle solution around $\tilde{\xi} \approx 1$ as the time needed for this solution to be destabilized becomes very large in this neighborhood, at least as long as the present analysis is valid, i.e. for values of r_o^2 not too far away from one of the stationary points ($r_o^2 << 1$).

Hysteresis

Experimental and numerical results of transitions to chaos in the Lorenz system (Wang, Singer & Bau, 1992, Yuen & Bau, 1996, Sparrow, 1982) suggest the existence of an hysteresis mechanism which is described as follows: when increasing the value of R gradually by approaching R_o from below the transition to chaos occurs at $R = R_o$, while repeating the same procedure, but approaching R_o from above, the transition from chaos to the stationary solution occurs at a value of $R < R_o$. Vadasz (2000) provides an explanation of the hysteresis phenomenon in connection with the transitional value of R which is presented in equation (19). When approaching R_o from below, say $R < R_t$, the initial conditions lead the solution to one of the convective fixed points, i.e. $r = 0$ (the fixed points represent the steady solutions of convective rolls moving clockwise or counterclockwise). As we gradually increase the value of R by starting the next experiment (or numerical procedure) with initial conditions taken from the post-transient previous solution obtained at the slightly lower value of R, the new initial conditions are very close to the fixed point, i.e. $r_o^2 \approx 0$ (they are not exactly at the fixed point because the post transient values of the previous solution are reached asymptotically, and at any finite time there is a slight departure between the solution and the steady state), and according to equation (19) the corresponding transitional value R_t is very close to R_o. However, when one approaches R_o from above, the initial conditions taken from the previous solution at a value of $R > R_o$ are quite large and far away from the fixed point. Therefore, in such a case it is expected to obtain a chaotic solution for subcritical values of R until the value of R_t is reached from above, which this time it could be quite far away from R_o. In graphical terms this process can be observed on Figure 1(b), where by moving towards R_o from the left with not negligible initial conditions the transition is expected when the critical time disappears, i.e. at values of $R < R_o$, while by moving towards R_o from the right and gradually decreasing the value of ξ and consequently of r_o^2 (because of the gradual process),

could keep the ratio ξ/r_o^2 greater than one, as both $\xi \to 0$ and $r_o^2 \to 0$ simultaneously. To make this explanation more transparent, the variation of the explicit critical time as a function of $(R - R_c)$ by using equation (16) and the definitions of ξ and ε^2, is presented in Figure 2(a), for different values of r_o^2. The disappearance of the critical time at $R = R_c$ is an indication that the amplitude does not diverge, and therefore a steady convective solution can be obtained. From the figure it is evident that for small values of r_o^2 (e.g. $r_o^2 = 0.001$), corresponding to the forward transition from steady convection to chaos, the asymptote of t_{cr} (i.e. the point when the critical time disappears) occurs very close to $R = R_c$, while for values of r_o^2 which are not so small, corresponding to the reverse transition from chaos to steady convection, (e.g. $r_o^2 = 0.5$) the asymptote of t_{cr} occurs at values of $R < R_c$ which are quite far away from R_c. This explains the reason for observing Hysteresis in the transition from steady convection to chaos and backwards, by using initial conditions corresponding to a previous solution at a slightly different value of R.

Comparing the computational and analytical results

The objective in the presentation of the following results is to demonstrate the appearance of the solitary limit cycle at a particular value of R prior to the first transition and to compare the computational values (obtained by using Adomian's decomposition method, Adomian, 1994) of $R = R_c$ where this transition occurs with its corresponding analytical values which where presented in eq. (19) for different initial conditions (consistent with the weak non-linear solution). While in these computations the value of R as well as the initial conditions vary from one computation to another, the values of γ and α are kept constant at $\lambda = 8/3$ and $Pr = 10$. These values of the following coefficient for the amplitude equation (11) : $\varphi = -1.30959$.

In order to compare the computational results to the analytical ones obtained via the weak non-linear theory we have to make sure that the initial conditions for the computations are consistent with the initial conditions corresponding to the weak non-linear solution. Note that the set of possible initial conditions in the weak non-linear solutions (14)and (15) because we did not include the decaying solutions in equation (9). Therefore this constraint, which is equivalent to setting $(a_{12})_{\tau=0} = 0$ and $(\theta)_{\tau=0} = 0$, is kept valid for all computational results as well.

The weak non-linear solution provides the following conditions which are necessary and sufficient to ensure the consistency of the initial conditions between the weak non-linear and the computational solutions

$$X^{(o)} = Y^{(o)} = 1 + 2r_o; \qquad (20)$$

$$Z^{(o)} = 1 + \frac{\sigma_o^2}{Pr\,(R_o - 1)}\left[X^{(o)} - 1\right] = 1 + \frac{2\sigma_o^2}{Pr\,(R_o - 1)}\,r_o \qquad (21)$$

where $X^{(o)}$, $Y^{(o)}$ and $Z^{(o)}$ are the initial conditions for X, Y and Z, respectively, and r_o is the initial condition for r, as used in the weak non-linear solution. Furthermore, using equation (20) it is noted that $r_o = \left(X^{(o)} - 1\right)/2 = \left(Y^{(o)} - 1\right)/2$. Clearly this yields negative values of r_o if $X^{(o)} < 1$ or $Y^{(o)} < 1$.

We therefore extend the definition of r and allow it to take negative values. This is equivalent to a phase shift in the limit cycle solution of the form $\tilde{\theta} = \theta + \pi$. For r_o this corresponds to a phase shift $\tilde{\theta}_o = \theta_o + \pi = \pi$, because $\theta_o = (\theta)_{\tau=0} = 0$, implicitly in the present case. It should be stressed that the solitary limit cycle was obtained computationally irrespective of whether the initial conditions were consistent with the weak non-linear solution or not; the consistency is imposed only for quantitative comparison purposes. A sequence of numerous computations was performed in order to evaluate these transitional R values. The results were presented by Vadasz (2000) and are reproduced in Figure 3, where the continuous curve represents the analytical solution expressed by equation (19), while the dots represent the computational results.

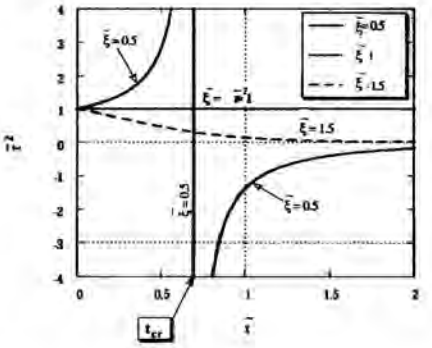

(a)

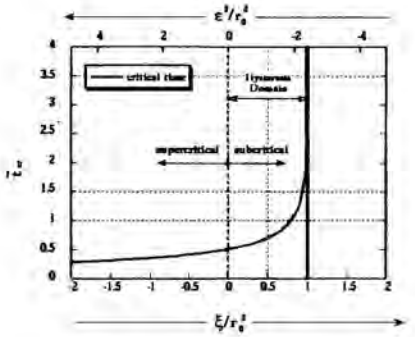

(b)

Figure 1 : (a) The amplitude solution for three values of $\tilde{\xi}$ corresponding to: *(i)* sub-transitional conditions $\tilde{\xi} = 1.5$, *(ii)* transitional conditions $\tilde{\xi} = \tilde{r}^2 = 1$, and *(iii)* super-transitional conditions $\tilde{\xi} = 0.5$. (b) The variation of the critical time $\tilde{t}_{cr}$, when the amplitude solution diverges, as a function of $\tilde{\xi}$.

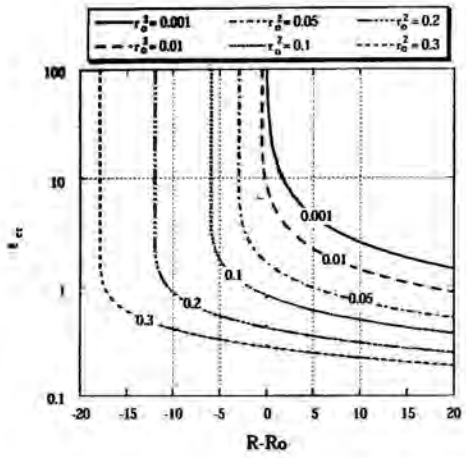

Figure 2: The critical time as a function of $(R - R_c)$ for six values of initial conditions in terms of r_o^2. The transition from steady convection to chaos (or backwards) is linked to the existence (disappearance) of this critical time, explaining the mechanism for hysteresis.

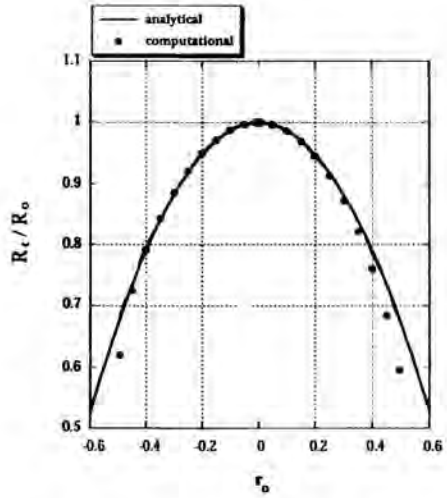

Figure 3: Transitional sub-critical values of Rayleigh number in terms of R_t/R_c as a function of the initial conditions r_o. A comparison between the weak non-linear solution (____ analytical) and the Adomian's decomposition solution (• computational).

The very good agreement between the analytical and computational solutions in the neighborhood of the convective fixed point (i.e. $|r_o| << 1$) is evident from Figure 3. As the initial conditions move away from the convective fixed point and the value of $|r_o|$ increases the computational results depart from the analytical solution, which reconfirms the validity of the weak non-linear solution in the neighborhood of a convective fixed point and its breakdown far away from this point. The departure of the computational results from the analytical ones is clearly not symmetrical with respect to $r_o = 0$. While the weak non-linear solution is symmetrical with respect to $r_o = 0$, there is no reason to expect this symmetry from the computational solution as ones moves away from the fixed point. The maximum value of $|r_o|$ for which we could obtain results and still be consistent with the weak non-linear solution around one fixed point was $r_o = \pm 0.5$. Actually at $r_o = -0.5$ the corresponding initial conditions are $X^{(o)} = Y^{(o)} = 0$ and $Z^{(o)} = 0.5$ which lie on the Z axis that is included on the stable manifold of the origin. Therefore, the computational results obtained for this set of initial conditions lead naturally to the origin producing the motionless solution. In order to evaluate the solitary limit cycle as we approach $r_o = -0.5$ we evaluated the computational solution at $r_o = -0.495$. Another interesting result from the computations is the fact that it was relatively very easy to detect the solitary limit cycle when the initial conditions were close to the convective fixed point, i.e. around $r_o = 0$. There, the critical time is very large, as established via the weak non-linear analysis, and if the value of R is sufficiently close to R_t the limit cycle appears and persists for a very long time. Naturally, in this neighborhood the accuracy in estimating the value of R_t is somewhat compromised because of the same reason. Nevertheless, if the maximum time for presenting the solution (i.e. t_{max}) is sufficiently large this accuracy problem around $r_o = 0$ can be resolved. In our case, with $t_{max} = 210$, the results provided accurate values of R_t. However, as we move away from the neighborhood of $r_o = 0$ by using initial conditions further away from the convective fixed point, it becomes more and more difficult to detect the solitary limit cycle, and more computations are needed by modifying the value of R closer and closer to R_t. While detecting the solitary limit cycle becomes more difficult as the initial conditions move away from the convective fixed point, the accuracy of the value of R_t once the limit cycle was detected becomes extremely high. For example, at $r_o = -0.2$ the limit cycle appeared at $R = R_t = 23.474475752$. The need to use 13 significant digits in order to obtain the limit cycle solution over the whole time domain just emphasizes the difficulty of detecting the limit cycle as one moves away from the convective fixed point and the associated accuracy in evaluating R_t. This is also an indication that this limit cycle becomes less and less stable as one departs from the neighborhood of the convective fixed point. As one moves even further away more significant digits are required in order to establish the value of R_t and detect the limit cycle over the whole time domain, and naturally when this process reaches the limit of over 14 digits, which corresponds to the double-precision computation, the limit cycle can not be detected for the whole time domain selected.

A further comparison between the computational and analytical results was presented by Vadasz (2000). The

comparison between the shapes of the analytical and computational limit cycles for $r_a = -0.1$ and $r_a = -0.125$ shows that they are quite close. The corresponding limit cycle solutions corresponding to values of $|r_a|$ smaller than 0.1 show that analytical and computational results overlap. On the other hand, the comparison between the analytical and computational limit cycle results corresponding to $r_a = -0.495$, i.e. quite far away from the convective fixed point shows a marked departure between the two solutions, not only in the quantitative sense as presented by the deviation of the computational value of R_c from its predicted analytical value (see Figure 3), but also qualitatively their shapes are substantially different. While the analytical periodic orbit maintains its elliptical shape similar regardless of r_a, the computational results show that as the solitary limit cycle approaches conditions consistent with the homoclinic orbit its shape is altered considerably (the shape of the homoclinic orbit is by far different than that of an ellipse).

CONCLUSIONS

The rich dynamics associated with the transition from steady convection to chaos weak turbulent fluid convection was demonstrated by using analytical as well as computational methods. The mechanism of hysteresis was also revealed and demonstrated.

ACKNOWLEDGMENTS

The author wishes to thank the National Research Foundation (South Africa) for partially supporting this study through the Competitive Industry Research Grant (CIPM-GUN2034039).

REFERENCES

Adomian, G., 1994, *Solving Frontier Problems in Physics: The Decomposition Method*, Kluwer Academic Publishers, Dordrecht.

Lorenz, E.N., 1963, "Deterministic Non-Periodic Flows", *J. Atmos.Sci.*, **Vol.20**, pp.130-141.

Sparrow, C., 1982, *The Lorenz Equations: Bifurcations, Chaos, and Strange Attractors*, Springer-Verlag, New York.

Vadasz, P., 2000, " Subcritical Transitions to Chaos and Hysteresis in a Fluid Layer Heated from Below", *Int. J. Heat Mass Transfer*, **Vol. 43**, pp.705-724.

Vadasz, P., Olek, S. 2000, "Convergence and Accuracy of Adomian's Decomposition Method for the Solution of Lorenz Equations", *Int. J. Heat Mass Transfer*, **Vol. 43**, pp.1715-1734.

Wang, Y., Singer, J., Bau, H.H., 1992, " Controlling Chaos in a Thermal Convection Loop", *J. Fluid Mechanics*, **Vol. 237**, pp.479-498.

Yuen, P., Bau, H.H., 1996, "Rendering a Subcritical Hopf Bifurcation Supercritical", *J. Fluid Mechanics*, **Vol. 317**, pp.91-109.

HEFAT2002
1st International Conference on Heat Transfer, Fluid Mechanics, and Thermodynamics
8-10 April 2002, Kruger Park, South Africa
WL1

MULTIPLICITY AND STABILITY IN TRANSPORT PHENOMENA

Liqiu Wang
Department of Mechanical Engineering
The University of Hong Kong, Pokfulam Road, Hong Kong
Email: lqwang@hku.hk

ABSTRACT

The first part of this keynote paper briefly overviews some of our recent works on bifurcation and stability. It includes universal properties of period-doubling bifurcations, new methods of detecting bifurcations and instabilities, four effective numerical schemes of capturing multiple solutions, entropy properties of limit and bifurcation points and a general numerical package for continuation, bifurcation, stability and entropy analysis in two-dimensional (2D) transport phenomena.

The second part is a numerical study on the fully-developed bifurcation structure and stability of the mixed convection in rotating curved ducts of square cross-section with the emphasis on the effect of buoyancy force. The rotation can be positive or negative. The fluid can be heated or cooled. The study reveals the rich solution and flow structures and complicated stability features. One symmetric and two symmetric/asymmetric solution branches are found with seventy-five limit points and fourteen bifurcation points. The flows on these branches can be symmetric, asymmetric, 2-cell and up to 14-cell structures. Dynamic responses of the multiple solutions to finite random disturbances are examined by the direct transient computation. It is found that possible physically realizable fully-developed flows evolve, as the variation of buoyancy force, from a stable steady multi-cell state at a large buoyancy force of cooling to the co-existence of three stable steady multi-cell states, a temporal periodic oscillation state, the co-existence of periodic oscillation and chaotic oscillation, a chaotic temporal oscillation, a subharmonic-bifurcation-driven asymmetric oscillating state, and a stable steady 2-cell state at large buoyancy force of heating.

INTRODUCTION

Transport phenomena refer to mass, momentum, energy and entropy transfer. Nonlinear transport phenomena are important and complicated; there are many solutions; nonuniqueness is the rule; sets of solutions must be described, and stable and observable subsets must be separated from the others.

A mathematical basis for the study of these hard problems is the theory of bifurcation and the theory of stability. The bifurcation theory, in its broad sense, attempts to classify and characterize properties of all solutions which an initial-value problem can support when transients have died away, initial values have been forgotten, and flows/motions are driven by boundary conditions and body forces. The stability theory, on the other hand, examines dynamic responses of steady solutions to disturbances as the time approaches infinity. In mathematics, the emphasis is traditionally placed on analytical investigations for some simplified model problems. Inspired by numerous applications and new emerging fields, the bifurcation and stability theory has to renew and reshape some of its results, through efforts of facilitating developments of numerical schemes and simulations, to have a practical significance. This is further enhanced by the availability of powerful computers and the appearance of catastrophe theory and singularity theory, and leads to continuation schemes and bifurcation algorithms.

The present keynote paper overviews some of our recent results, and shows rich features of multiplicity and stability from our numerical study of mixed convection in rotating curved ducts.

NOMENCLATURE

a = duct width/height
Dk = psedo Dean number defined in Wang &Cheng (1996b)
f = vector-valued function
$L1$ = parameter defined in Wang &Cheng (1996b)
$L2$ = parameter defined in Wang &Cheng (1996b)
Pr = Prandtl number
R_c = curvature radius
r,z = dimensionless coordinates, $r=R/a$, $z=Z/a$
R,Z,φ = coordinates
s = arc-length
u,v,w = dimensionless velocity components in directions of R,Z and φ
t_{max} = maximum dimensionless time
w_{max} = maximum streamwise velocity
y = dependent variable vector

Greek symbols

σ = duct curvature ratio, (a/R_c)
τ = dimensionless time
ψ_{max} = maximum of absolute values of secondary flow stream function

SOME RECENT WORKS

The period-doubling bifurcation leads a T-periodic solution to a 2T-periodic solution. By the period we mean the least positive period. By exposing the consequence of period-doubling bifurcations analytically, we develop the relation between these two periodic solutions for a general parameter-dependent dynamic system [1]. Such the relation is further confirmed by one example and shows that the 2T-periodic solution contains all the information of the T-periodic solution. Therefore we can infer the T-periodic solution from the 2T-periodic solution. Conversely, we may obtain the part of the 2T-periodic solution from the T-periodic solution. The work is important not only in shedding light on period-doubling bifurcations and chaos, but also in forming a benchmark of numerical accuracy checking and in providing new numerical schemes of period-doubling bifurcation detection.

For nonlinear systems of multi-degree of freedom, we develop theoretically an effective numerical method to obtain periodic solutions and their bifurcations including fold or tangential bifurcations with the constant period, period-doubling bifurcations and Hopf bifurcations. The method differs from the others mainly on its applicability to the cases of strong nonlinearity and high degree of freedom. This is also confirmed by the application of the method to several nonlinear systems.

For steady flow and heat transfer with system rotation, we develop two quasi-least-squares finite element schemes in the L^2 inner product [2]. Unlike the standard least-squares finite element scheme, these schemes lead to, for nonlinear problems, a symmetric resulting algebraic system without additional nonlinear terms. Their convergence is analyzed by a new technique, showing that they are globally convergent and can capture both nonsingular and singular solutions.

We also develop a standard and a mixed finite-element scheme for steady convective heat transfer with system rotation, temperature-dependent density and viscosity [3]. The existence and convergence are proven for the two schemes. They are shown to be globally convergent and capable of capturing both nonsingular and singular solutions. The convergence rate is optimal in H^1-norm and L^2-norm for nonsingular solutions.

Nonlinearity of Navier-Stokes equations results in flow bifurcations. This has been the subject of considerable interests, owing primarily to its fundamental importance in fluid mechanics and its applications in many practical fields. At limit and bifurcation points, there are some mathematical properties such as one or more eigenvalues of Jacobin matrix are vanished. In the theoretical and numerical analyses, these properties are used to find and clarify different singular points. Physically, stability may be lost or gained at these singular points. However, less well known are their thermodynamic features such as entropy at the limit and bifurcation points. We are applying the thermodynamic theory to analyze flow bifurcations to find thermodynamic properties of singular points that can be used to determine and clarify different bifurcations.

Our program package of numerical simulation has been developed to a general one for continuation, bifurcation, stability and entropy analysis in 2D transport phenomena. It can be used for steady or unsteady problems, and parabolic or elliptic problems, and can be readily extended to three-dimensional cases and to the other nonlinear problems. Main features of the program include: (1) a staggered mesh system, (2) a power-law, QUICK, and CONDIF formulation for the combined effect of convection and diffusion terms, (3) an equation-solving scheme consisting of an alternating direction line-by-line iterative procedure (ADI) with block correction technique, (4) a SIMPLE, SIMPLER, SIMPLEST or SIMPLEC scheme for velocity-pressure coupling, (5) Euler-Newton, arc-length, local-variable and Homotopy continuation schemes for path following, (6) several bifurcation test functions and branch switching techniques for bifurcation detection and branch switching, (7) extended system formulations for precisely determining singular points, and (8) numerical schemes for linear stability analysis and for examining dynamic responses of multiple solutions to finite random disturbances. The governing equations for dependent variables are formed in a general unified form. The dependent variables can be as many as 16. The program is programmed in a block structure. In particular, the general operations (such as calculation of coefficients and the solution of discretization equations) and problem-dependent operations (such as the specification of material parameters and the initial and boundary conditions for relevant variables) are programmed in separate blocks. The calculation of coefficients and the solution of the discretization equations are also structured in separate blocks. The calculation can be made in the Cartesian, polar, cylindrical or spherical coordinate system through introducing transformation parameters in calculating coefficients of discretization equations. Applications to the Bratu problem [4], the exothermic chemical reaction in catalyst beds [5], flows in porous media [6] and mixed convection in rotating curved ducts [7] reveal rich features of multiplicity and stability and show that the packages work well.

MIXED CONVECTION IN ROTATING CURVED DUCTS

We study the fully-developed bifurcation-driven multiplicity and dynamic responses of multiple solutions to finite random disturbances numerically by the finite-volume/Euler-Newton continuation and the direct transient computation for the mixed convection in ducts of square cross-section with the streamwise curvature, the spanwise rotation in either positive or negative direction, and the wall heating/cooling [Fig. 1 with (R, Z, φ) as the radial, spanwise and streamwise directions, respectively]. A positive rotation gives rises to a Coriolis force in the cross plane (RZ-plane) directed along positive R-direction and vice versa.

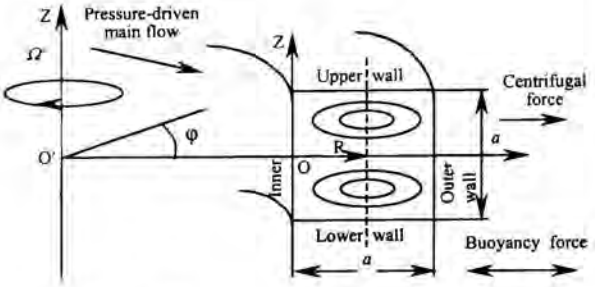

Figure 1 Physical problem and coordinate system

There are a host of areas where such flows and transport phenomena are of practical importance and where relevant issues are raised. For instance, sedimentation field-flow fractionation, one of the most powerful subtechniques of the field-flow fractionation (FFF) method of separation, uses rotating curved ducts to perform both separation and quantitation of particles and other colloidal-based substances. Aerosol centrifuges apply rotating curved ducts to the problem of separating airborne particles according to aerodynamic size. The fundamental economic gains associated with the increase of inlet fluid temperature and unit capacity lead to the use of rotating curved ducts as the cooling ducts of rotating power machinery such as gas/steam turbines and electric generators. The rotating curved ducts are also used in rotating heat exchangers, centrifugal material processing and material quality control, medical and chromatographic devices, etc. In order to calculate the pumping power needed for such devices, it is important to know the pressure drop in rotating curved ducts. Because secondary flows can enhance heat and mass transfer, knowledge of the magnitude of this effect in different ranges of operating parameters is important in designing and operating these devices. To avoid or reduce the flow-induced vibration and noise, we need to know when temporal oscillation appears. The present work can acquire a better understanding of these practical issues.

Early works on the rotating curved duct flows were constrained to two simplified limiting cases with strong or weak rotations. Ludwieg [8] developed a solution based on a momentum integral method for the isothermal flow in a square duct with a strong spanwise rotation. Miyazaki [9,10] examined the mixed convection in a curved circular/rectangular duct with spanwise rotation and wall heating by a finite difference method. Because of the convergence difficulties with the iterative method used, Miyazaki's work was constrained to the case of weak curvature, rotation and heating rate. As well, all the works employ a steady model for the fully developed laminar flow with a positive rotation of the duct. Since the solution is only for the asymptotic cases, the secondary flow revealed by these early works consists of only one pair of counter-rotating vortices in the cross-plane. The interaction of the secondary flow with the pressure-driven streamwise flow shifts the location of the maximum streamwise velocity away from the center of the duct and in the direction of the secondary velocity in the middle of the duct.

More comprehensive studies have been made in recent years by Wang & Cheng [11] and Daskopoulos & Lenhoff [12] for a circular tube, Matsson & Alfredsson [13, 14] and Guo & Finlay [15] for a high-aspect-ratio rectangular duct, and Wang & Cheng [16-19], Wang [20-22], Selmi *et al.* [23] and Selmi & Nandakumar [24] for the square and rectangular ducts with a low-aspect-ratio. All the works are for the steady fully developed flows. Wang & Cheng [11] developed an analytical solution for rotating curved flow with the effect of heating or cooling which allows to analyze the solution structure. Detailed flow structures and heat transfer characteristics were examined numerically by Wang & Cheng [17] and Wang [20-22]. The rotating curved flows were visualized using smoke injection method by Wang & Cheng [16, 18, 19]. Daskopoulos & Lenhoff [12] made the first bifurcation study numerically under the small curvature and the symmetry condition imposed along the tube horizontal central plane. Matsson & Alfredsson [13] presented the first and comprehensive linear stability analysis. Matsson & Alfredsson [14] reported an experimental study, by hot-wire measurements and smoke visualization, of the effect of rotation on both primary and secondary instabilities. Using a linear stability theory and spectral method, Guo & Finlay [15] examined the stability of streamwise oriented vortices to 2D, spanwise-periodic disturbances (Eckhaus stability). Detailed bifurcation structure and linear stability of solutions was determined numerically by Selmi *et al.* [23] and Selmi & Nandakumar [24] without imposing the symmetric boundary conditions.

It is the *relative* motion between bodies that determines the performances such as friction and heat transfer characteristics. The duct rotation introduces both centrifugal and Coriolis forces in the momentum equation describing the *relative* motion of fluids with respect to the duct. For isothermal flows of a constant property fluid, the Coriolis force tends to produce vorticity while the centrifugal force is purely hydrostatic, analogous to the Earth's gravitational field [25]. When a temperature-induced variation of fluid density occurs for non-isothermal flows, both Coriolis and centrifugal-type buoyancy forces could contribute to the generation of the vorticity [25]. These two effects of rotation either enhance or counteract each other in a nonlinear manner depending on the direction of duct rotation, the direction of wall heat flux and the flow domain. As well, the buoyancy force is proportional to the square of the rotation speed while the Coriolis force increases proportionally with the rotation speed itself [21]. Therefore, the effect of system rotation is more subtle and complicated and yields new, richer features of flow and heat transfer in general, the bifurcation and stability in particular, for non-isothermal flows. While some of such new features are revealed by our recent analytical and numerical works [11, 17, 20-22], there is no

known study on the bifurcation and stability of mixed convection in rotating curved ducts.

We note that all previous analytical/numerical studies of stability are limited to linear stability and some special disturbances. While the linear stability analysis is efficient in terms of the computation efforts required, it suffers three fundamental defects. First, it is not applicable to a finite disturbance. With a finite disturbance, a so-called stable solution based on linear stability may not be always stable. Second, it may not be so relevant for comparison with experiments. Because of the difficulty in controlling disturbances in experiments, experimental results of stability such as those by Matsson & Alfredsson [14] and Wang & Cheng [16, 18, 19] are essentially for finite random disturbances. Finally, the linear stability analysis provides no answer to the questions related to the dynamic behavior of the solutions, including how flows approach a stable solution after a disturbance, what happens to an unstable solution after a disturbance, whether all unstable solutions at a given set of parameters respond to disturbances in the same way, and whether the disturbances lead an unstable solution to the stable one at the same parameter value. Clearly, a fully transient computation is necessary to examine dynamic responses of the multiple solutions to the finite random disturbances. Such a computation is also capable of capturing the phenomena related to the transition to turbulence such as oscillation solution, periodic doubling, intermittency, and chaotic oscillation.

In previous numerical studies [12, 23, 24], branch stability is often determined by the stability of one point on the branch. This is partly due to the fact that the computation of the complete eigenvalue spectrum along the solution branches is a computationally expensive process and partly due to the assumption that the stability of solutions along a solution branch is unchanged without passing limit/bifurcation points in the literature. However, based on the bifurcation and stability theory, such a change in stability is possible [26]. Therefore, a more detailed and careful stability analysis is desirable to observe the gain and loss of flow stability along solution branches without passing limit/bifurcation points.

The present work is a relatively comprehensive study on the bifurcation structure and stability of multiple solutions for the laminar mixed convection in a rotating curved duct of square cross-section (Fig. 1). The governing differential equations in primitive variables are solved for detailed bifurcation structure by a finite-volume/Euler-Newton continuation method with the help of the bifurcation test function, the branch switching technique and the parameterization of arc-length or local variable. Transient calculation is made to examine in detail the response of every solution family to finite random disturbances. The power spectra are constructed by the Fourier transformation of temporal oscillation solutions to confirm the chaotic flow. We restrict ourself to the hydrodynamically and thermally fully-developed region and two-dimensional disturbances. So far, a detailed 3D numerical computation of flow bifurcation and stability is still too costly to conduct. A 2D model is still useful for a fundamental understanding of rotating curved duct flows. However, our assumption of fully developed flow limits our analysis to the one preserving the streamwise symmetry. There may be further bifurcation to flows that breaks this symmetry and that cannot be found in the present work.

Governing Parameters and Numerical Algorithm.

Consideration is given to a hydrodynamically and thermally fully developed laminar flow of viscous fluid in a square duct with the streamwise curvature, the spanwise rotation, and the wall heating or cooling at a constant heat flux (Fig.1). The geometry is toroidal and hence finite pitch effect is not considered. The rotation can be positive or negative at a constant angular velocity. The duct is streamwisely and peripherally uniformly heated or cooled with a uniform peripheral temperature. The properties of the fluid, with the exception of density, are taken to be constant. The usual Boussinesq approximation is used to deal with the density variation. The gravitational force is negligible compared with the centrifugal and Coriolis forces.

Consider a non-inertial toroidal coordinate system (R, Z, φ) fixed to the duct rotating with a constant angular velocity about the $O'Z$ axis, as shown in Fig. 1. We may obtain the governing differential equations, in the form of primitive variables, governing fully-developed mixed convection based on conservation laws of mass, momentum and energy. The boundary conditions are non-slip and impermeable, streamwise uniform wall heat flux and peripherally uniform wall temperature at any streamwise position. The proper scaling quantities for non-dimensionalization are chosen based on our previous experience [17]. The formulation of the problem is on full flow domain without imposing symmetric boundary conditions to perform a thorough numerical simulation. The readers are referred to Wang & Cheng [17] for the details of mathematical formulation of the problem.

The dimensionless governing equations contain five dimensionless governing parameters:one geometrical parameter σ (the curvature ratio defined by a/R_c , the ratio of duct width/height a over the radius of the curvature R_c, representing the degree of curvature), one thermophysical parameter Pr (the Prandtl number, representing the ratio of momentum diffusion rate to that of the thermal diffusion), and three dynamical parameters Dk, $L1$ and $L2$ defined by Wang & Cheng [17]. The pseudo Dean number Dk is the ratio of the square root of the product of inertial and centrifugal forces to the viscous force and characterizes the effect of inertial and centrifugal forces. $L1$ represents the ratio of the Coriolis force over the centrifugal force, characterizing the relative strength of Coriolis force over the centrifugal force. $L2$ is the ratio of the buoyancy force over the centrifugal force and represents the relative strength of the buoyancy force. A positive (negative) value of $L1$ is for the positive (negative) rotation. A positive (negative) value of $L2$ indicates the wall heating (cooling). In the present work, we set

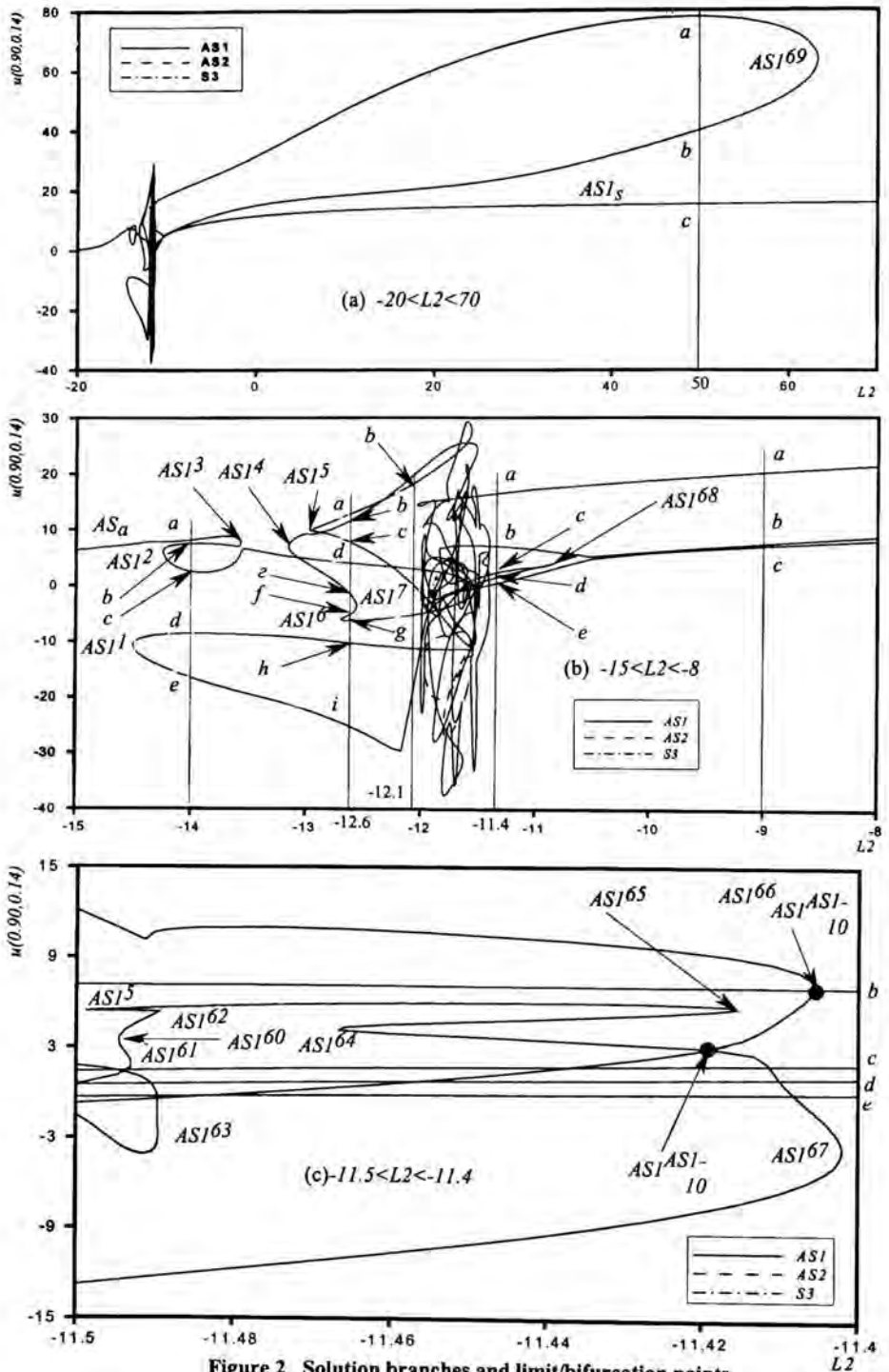

Figure 2 Solution branches and limit/bifurcation points (σ=0.02, Pr=0.7, Dk=300, and L1=28)

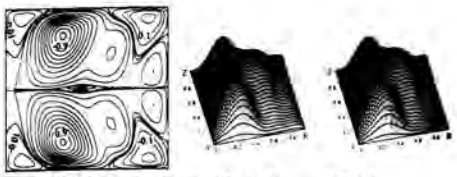

(a) $L2$=-17.0 on $AS1$ ($|\psi|_{max}$=7.14, w_{max} = 0.0606, t_{max} = 127.3)

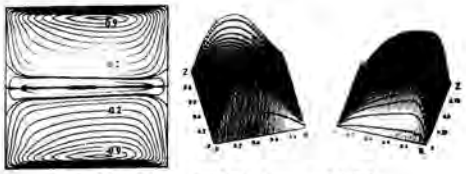

(b) $L2$=65 on $AS1$ ($|\psi|_{max}$=14.23, w_{max} = 0.0137, t_{max} = 8.9)

Figure 3 Flow and temperature fields (σ=0.02, Pr=0.7, Dk=300 and $L1$=28; left: secondary flow, middle: streamwise velocity, right: temperature)

σ=0.2 (typically used in cooling systems of rotor drums and conductors of electrical generators) and Pr=0.7 (a typical value for air) to study the effects of three dynamical parameters on the multiplicity and stability. While results regarding the effects of Dk and $L1$ are also available, we focus on the effects of $L2$ at Dk=300 and $L1$=28 in the present paper due to limited space.

The governing differential equations are discretized by the finite volume method to obtain discretization equations. The discretization equations are solved for parameter-dependence of velocity, pressure and temperature fields by the Euler-Newton continuation method with the solution branches parameterized by $L2$, the arc-length or the local variable. The starting points of our continuation algorithms are the three solutions at Dk=300, $L1$=28 and $L2$=0 from our study of the effects of Dk and $L1$. The bifurcation points are detected by the test function developed by Seydel [26]. The branch switching is made by a scheme approximating the difference between branches proposed by Seydel [26]. The dynamic responses of multiple solutions to the 2D finite random disturbances are examined by the direct transient computation. The readers are referred to [6, 7] for the numerical details and the check of grid-dependence and accuracy. The computations are carried out on the Super Computer SP2 of The University of Hong Kong.

Solution Structure. The bifurcation structure is shown in Fig.2 for $L2$ values from -20 up to 70 at σ = 0.02, Pr=0.7, Dk=300 and $L1$=28. In Fig.2, the radial velocity component u at r=0.9 and z=0.14 (where the flow is sensitively dependent on $L2$) is used as the state variable, enabling the most clear visualization of all solution branches. Three solution branches, labeled by $AS1$, $AS2$ and $S3$ respectively, are found. Here, S stands for symmetric solutions with respect to the horizontal

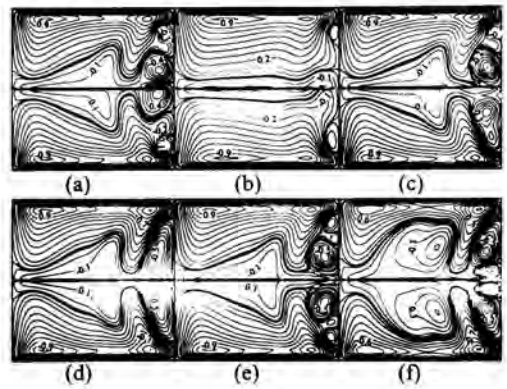

Figure 4 Typical secondary flow patterns of six solutions among thirty-nine solutions at L2=-11.7 (σ=0.02, Pr=0.7, Dk=300, and L1=28)

central plane z=0, and AS indicates that the branch has both symmetric and asymmetric solutions.

Branch $AS1$ has sixty-nine limit points labeled by $AS1^{1}$ to $AS1^{69}$, eleven bifurcation points connecting its sub-branches denoted by $AS1^{AS1\text{-}1}$ to $_{AS1}{}^{AS1\text{-}11}$, two bifurcation points connecting itself to $AS2$ labeled by $AS1^{AS2\text{-}1}$ and $AS1^{AS2\text{-}1}$, and one bifurcation point connecting itself to $S3$ denoted by $AS1^{S3}$. Branch $AS2$ has four limit points labeled by $AS2^{1}$ to $AS2^{4}$. Branch $S3$ is a symmetric solution branch and has two limit points $S3^{1}$ and $S3^{2}$. The location of fourteen bifurcation points and seventy-five limit points is available in [27]. To visualize the details of branch connectivity and some limit/bifurcation points, the locally enlarged state diagrams are also shown in Fig. 2. As Fig. 2 is only 1D projection of 12400 dimensional solution branches, all intersecting points except fourteen bifurcation points should not be interpreted as connection points of branches.

For a large $L2$ value ($L2 \le -14.5$ or $L2 \ge 63.1$), the buoyancy force dominant the mixed convection. There is unique flow and temperature field for a specified value of $L2$ in these two ranges. Figure 3 illustrates the secondary flow patterns, the streamwise velocity profiles and temperature profiles at $L2$=-17 and $L2$=65, respectively. In the figure, the stream function, streamwise velocity and temperature are normalized by their corresponding maximum absolute values ψ_{max}, w_{max} and t_{max}. A vortex with a positive (negative) value of the secondary flow stream function indicates a counter-clockwise (clockwise) circulation. The readers are referred to [17] for a detailed discussion of the flow structures shown in Fig.3 in general, their relations with physical mechanisms and driving forces and their effects on the flow resistance and heat transfer in particular.

For a $L2$ value in $-14.5 < L2 < 63.1$, however, we can have multiple solutions. Figure 4 shows typical secondary flow patterns of six solutions (thirty-nine solutions in total) at $L2$=-11.7. It is observed that the nonlinear competition of driven

forces leads to not only a rich solution structure but also complicated flow structures. Therefore, the mixed convection in rotating curved ducts is much more complicated than that available in the literature.

Stability of Multiple Solutions. Recognizing that there is no study on dynamic responses of multiple solutions to finite random disturbances in the literature, a relatively comprehensive transient computation is made to examine the dynamic behavior and stability of typical steady solutions with respect to four sets of finite random disturbances with $d=4\%$, 10%, 15% and 40% respectively. The results presented in this paper are those obtained from the disturbance with $d=10\%$ unless otherwise stated.

Seven sub-ranges are identified with each having distinct dynamic responses to the finite random disturbances. The first ranges from $L2=-20$ to $L2=-14.5$, where the finite random disturbances lead all steady solutions at any fixed $L2$ to a steady symmetric multi-cell state on $AS1_a$ with the same L2. The second covers the range $-14.5<Dk\leq-13.6$ where there is co-existence of three stable steady symmetric multi-cell states. In the third sub-range $-13.6<L2\leq12.1$, all steady solutions evolve to a temporal periodic solution. The fourth sub-range is from $L2=-12.1$ to $L2=-11.5$ where the solutions response to the finite random disturbances in the form of either periodic oscillation or chaotic oscillation. There is the co-existence of periodic and chaotic oscillations. In the fifth sub-range $-11.5<L2\leq-10.5$, all steady solutions evolve to a temporal chaotic solution. The next sub-range $-10.5<L2\leq-10.2$ serves as a transition between the chaotic oscillation and the stable steady 2-cell flow. The solutions response to the finite random disturbances in the form of subharmonic-bifurcation-driven asymmetric oscillation. In the last sub-range $L2>-10.2$, the finite random disturbances lead all steady solutions at any fixed $L2$ to a stable steady symmetric 2-cell state on $AS1_s$ with the same $L2$.

$-20\leq L2\leq-14.5$: stable steady symmetric multi-cell state Figure 5 typifies the responses of solutions on $AS1$ to the finite random disturbances. In the figure, the deviation of velocity components from their initial steady values is plotted against the nondimensional time τ at $(0.9,\ 0.14)$, $(0.94,0.1)$ and $(0.96,0.06)$ for $L2=-15$. We plot both radial (u-) and spanwise (v-) velocity components for the first point $(0.9,\ 0.14)$ while only u-velocity component is shown for the last two points. To facilitate the comparison, we use these four velocity components(either velocity itself or derivation velocity from its initial steady value) in all figures illustrating dynamic responses of the multiple solutions to finite random disturbances. It is observed that all deviation velocities vanish after a short period of time. The flows and temperature profiles return to their initial steady symmetric multi-cell one similar to that shown in Fig. 3(a).

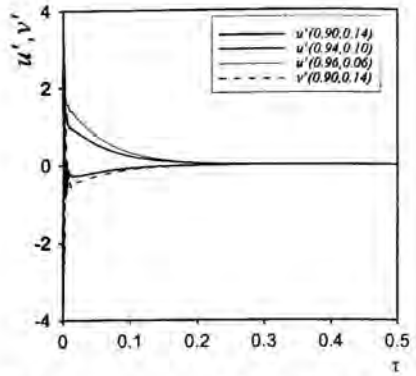

Figure 5 Dynamic responses of the solution at $L2=-15.0$ on $AS1$ to finite random disturbances: stable steady multi-cell solutions ($\sigma=0.02$, $Pr=0.7$, $Dk=300$ and $L1=28$)

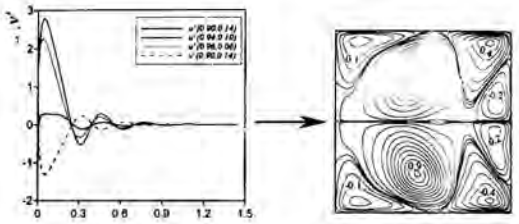

(a) a labeled in Fig. 2(b) Solution a: $u(0.90,0.14)=8.137$

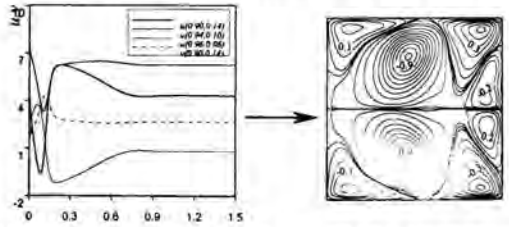

(b) d labeled in Fig. 2(b) Solution c: $u(0.90,0.14)=2.493$

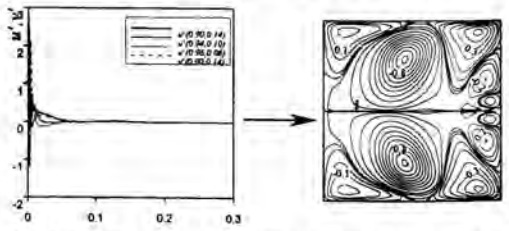

(c) e labeled in Fig. 2(b) Solution e: $u(0.90,0.14)=-16.52$

Figure 6 Dynamic responses of the solutions at $L2=-14$ to finite random disturbances: co-existence of three stable steady multi-cell states ($\sigma=0.02$, $Pr=0.7$, $Dk=300$ and $L1=28$)

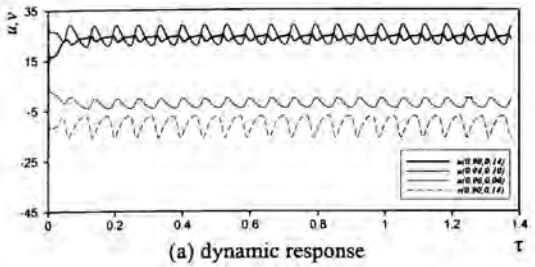

(a) dynamic response

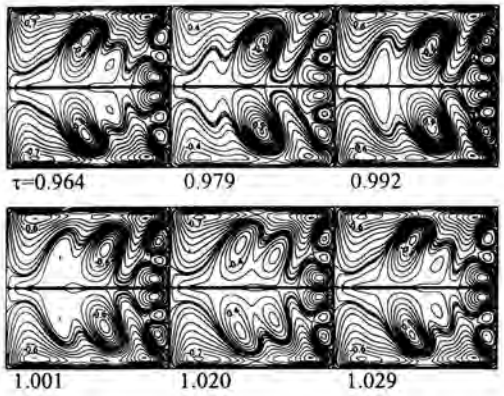

(b) typical secondary flow patterns

Figure 7 Dynamic response of solution *b* at *L2=-12.1* labeled in Fig. 2(b) to finite random disturbances: periodic oscillation and typical secondary flow patterns in one period (period=0.065; *σ=0.02, Pr=0.7, Dk=300* and *L1=28*)

-14.5<L2≤-13.6: co-existence of three stable steady symmetric multi-cell states Figure 6 illustrates the typical response of solutions *a*, *d* and *e* at *L2=-14* labeled in Fig. 2(b) to the finite random disturbances. It shows that the finite random disturbances lead eventually these solutions to the steady solutions *a*, *c* and *e*. There is co-existence of three stable steady symmetric multi-cell states *a*, *c* and e.

-13.6<L2≤-12.1: temporal periodic solution The dynamic response of solution b at *L2=-12.1* [Fig. 2(b)] is shown in Fig. 7(a). The finite random disturbances here lead the solution to a temporal periodic state with a period of *0.065*. Some typical secondary flow patters are detailed in Fig. 7(b) within one period of τ. We clearly observe the temporal oscillations between symmetric 12-cell flows and symmetric 14-cell flows. A detailed study on dynamic responses of the other solutions at *L2=-12.1* and the comparison of flow and temperature fields within one period shows that the finite random disturbances lead all the solutions at the same *L2* to the same periodic oscillation.

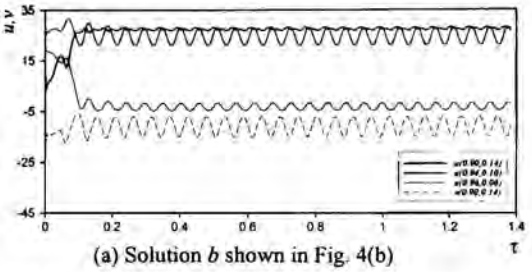

(a) Solution *b* shown in Fig. 4(b)

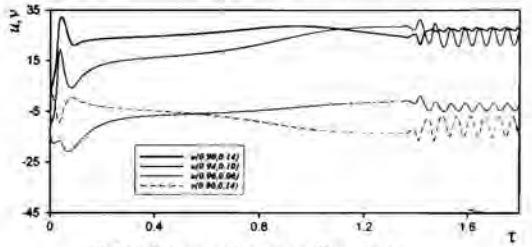

(b) Solution *c* shown in Fig. 4(c)

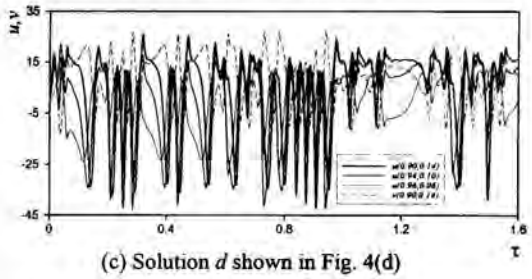

(c) Solution *d* shown in Fig. 4(d)

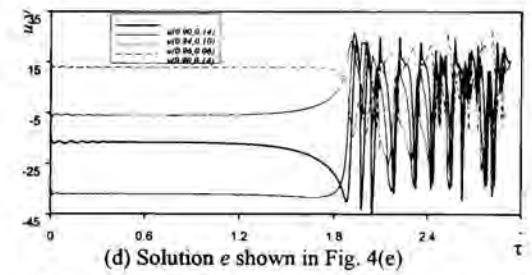

(d) Solution *e* shown in Fig. 4(e)

Figure 8 Dynamic response of four solutions at *L2*=-117 to finite random disturbance: co-existence of periodic and chaotic oscillations (σ=0.02, Pr=0.7, *Dk*=300 and *L1*=28)

A similar dynamic evolution pattern exists for all cases with different values of *L2*. This signals the similarity of flow and temperature fields within one period among the periodic states for different values of *L2* in the range *-13.6< Dk≤-12.1*. Our detailed examination of flow and temperature fields has confirmed this, and shown that the flow structures in Fig. 7(b) are typical for all *L2* in this range.

-12.1< L2≤-11.5: co-existence of periodic and chaotic oscillations The co-existence of periodic and chaotic oscillations is shown by the dynamic response of four solutions at *L2=-11.7* to the finite random disturbances in Fig. 8. While solutions *k* and *p* in Fig. 4 response to the finite random disturbances in the form of periodic oscillation, solutions *w* and *D* evolve to chaotic oscillations. The typical secondary flow patterns for the periodic oscillating solutions are similar to those in Fig. 7(b) and are characterized by symmetric patterns of twelve cells at least. Those for the chaotic oscillation are shown in Fig. 9 and are featured by symmetric and asymmetric flows of six cells at most. Furthermore, the selection of periodic or chaotic oscillation is also dependent of disturbances.

-11.5< L2≤-10.4: chaotic oscillation Figure 10 shows the dynamic response of the solution *c* at *L2=-11.4* [Fig. 2(d)] to the finite random disturbance with *d=10%*. The power spectra of four velocity temporal series in Fig. 10 are constructed by the Fourier transformation. They contain the broad-band noise, indicating the flow being chaotic [26]. Their sensitivity to the initial conditions further confirms this.

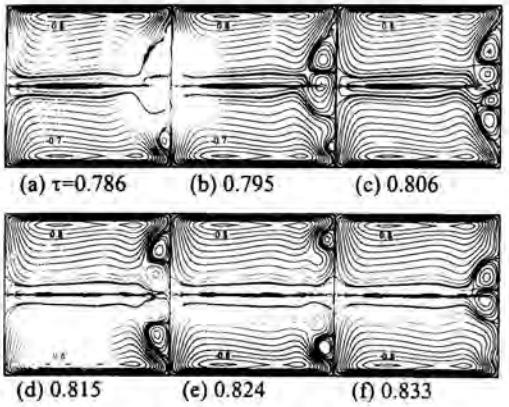

Figure 9 Typical secondary flow patterns of chaotic oscillation for the case in Fig. 8(c) (σ=0.02, Pr=0.7, Dk=300, L1=28 and L2=-11.7)

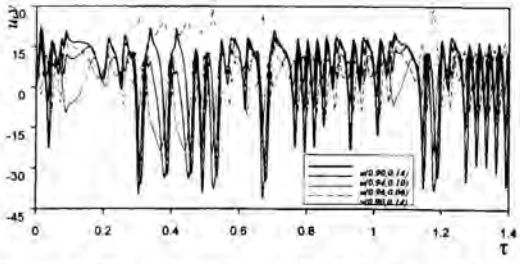

Figure 10 Dynamic response of solution *c* at *L2=-11.4* [Fig. 2(c)] to finite random disturbances: chaotic oscillation (*σ=0.02, Pr=0.7, Dk=300* and *L1=28*)

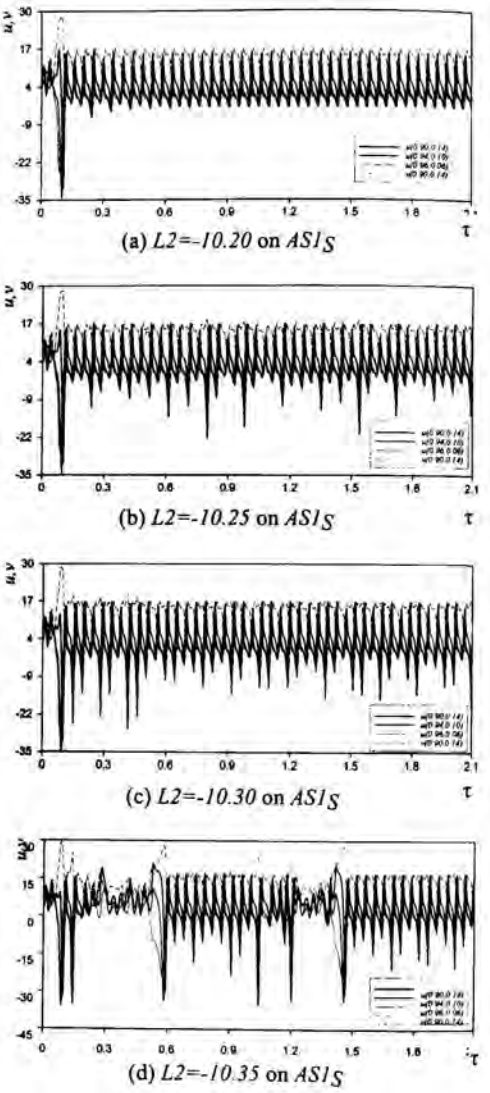

Figure 11 Dynamic response of solutions to finite random disturbances: subharmonic-bifurcation-driven oscillation (*σ=0.02, Pr=0.7, Dk=300* and *L1=28*)

-10.4<L2≤-10.2: **subharmonic-bifurcation-driven asymmetric oscillation** The transition from the stable steady flow in *L2>-10.2* to the chaotic oscillation in *-11.5< L2≤-10.4* is characterized by subharmonic-bifurcation-driven asymmetric oscillation and shown by the variation of dynamic responses of solutions as *L2* decreases from *-10.2* to *-10.35* (Fig. 11). The power spectra of the velocity temporal series in Fig. 11 are constructed by the Fourier transformation and shown in Fig.12.

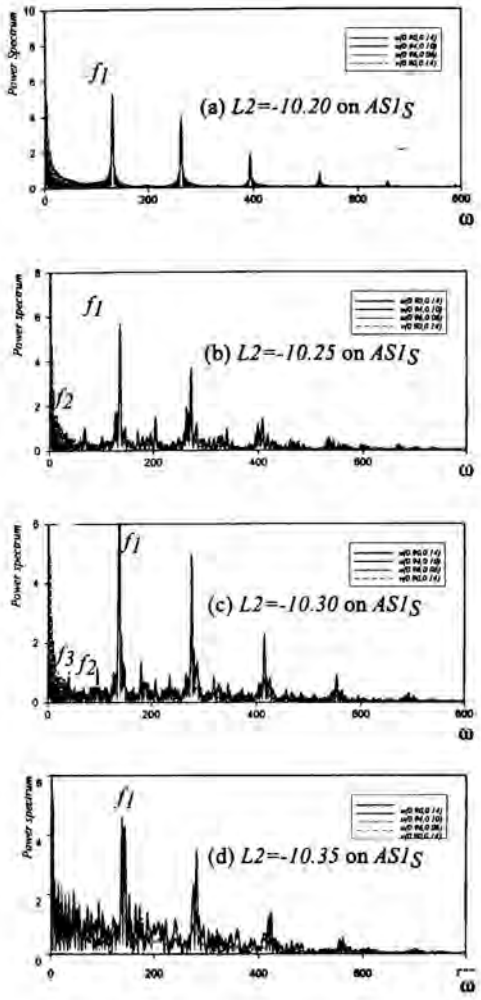

Figure 12 Power spectra of temporal series shown in Fig. 11 (σ=0.02, Pr=0.7, Dk=300 and L1=28)

At *L2=-10.2*, the oscillation is periodic and is from the Hopf bifurcation. The frequency f_1 in Fig. 12(a) is universal for all velocity components, pressure and temperature at all points in the flow domain. At *L2=-10.25*, a second frequency f_2 appears [Figs. 11(b), 12(b)]. f_2 is a half of f_1, indicating the subharmonic bifurcation. A second subharmonic bifurcation doubles the period of the temporal oscillation at *L2=-10.3*, generating another frequency f_3 that is a quarter of f_1 [Figs. 11(c) and 12(c)]. At *L2=-10.35*, the oscillation is aperiodic-like [Fig. 11(d)]; the spectrum has many closely-spaced peaks [Fig. 12(d)], forecasting the onset of chaos.

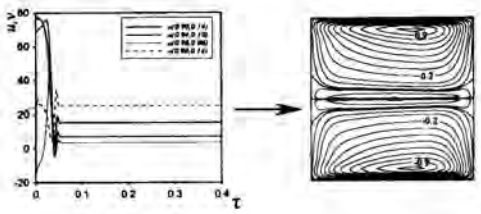

Figure 13 Evolution of solution *a* to solution *c* at *L2*=50 labeled in Fig. 2(a) (σ=0.02, Pr=0.7, Dk=300 and L1=28)

***-10.2 <L2≤70*: stable steady symmetric 2-cell state** Figure 13(a) typifies the responses of solution *a* at *L2=50* [Fig. 2(a)] to the finite random disturbances. The disturbances leads the solution *a* to the solution *c* whose secondary flow pattern is shown in Fig. 13(b). An extensive transient computation concludes that the solution on $AS1_S$ is the unique stable state in *-10.2 <L2≤70*.

CONCLUDING REMARKS

The relation between the solutions before and after period-doubling bifurcations is obtained by exposing their consequence analytically. A numerical method is developed to obtain periodic solutions and their bifurcations for nonlinear systems of multi-degree of freedom. Also developed are four effective numerical schemes of capturing multiple solutions, entropy properties of limit and bifurcation points and a general numerical package for continuation, bifurcation, stability and entropy analysis in 2D transport phenomena.

The governing differential equations from the conservation laws for the mixed convection in rotating curved ducts are discretized by the finite volume method to obtain discretization equations, a set of nonlinear algebraic equations. The discretization equations are solved for parameter-dependence of flow and temperature fields by the Euler-Newton continuation with the solution branches parameterized by *L2*, the arclength or the local variable. The bifurcation points are detected by the test function. The branch switching is made by a scheme approximating the difference between branches. One symmetric and two symmetric/asymmetric solution branches are found with fourteen bifurcation and seventy-five limit points. Both solution and flow structures are much more richer than those available in the literature.

The dynamic responses of multiple solutions to the 2D finite random disturbances are examined by the direct transient computation. The finite random disturbances are found to lead the steady solutions to a stable steady multi-cell state in *-20< Dk≤-14.5*, the co-existence of three stable steady multi-cell states in *-14.5<L2≤-13.6*, a temporal periodic oscillation in *-13.6<Dk≤-12.1*, the co-existence of periodic and chaotic oscillating states in *-12.1<L2≤-11.5*, a chaotic oscillation in -

$11.5<L2\leq10.5$, a subharmonic-bifurcation-driven asymmetric oscillation in $-10.5<L2\leq10.2$, and a stable steady 2-cell state in $-10.2<L2\leq70$.

The financial support from the Outstanding Young Researcher Award 2000-2001, the Research Grants Council of Hong Kong (RGC) and the CRCG, the University of Hong Kong is gratefully acknowledged.

REFERENCES

[1] Wang L. & Xu M. 2001, "Property of period-doubling bifurcations," Communicated to Physical Review Letters.

[2] Yang D. P & Wang L. 2001, "Quasi-least-squares finite-element schemes for steady flow and heat transfer with system rotation," SIAM Journal of Numerical Analysis (in press).

[3] Yang D. P & Wang L. 2001, "Two finite-element schemes for steady convective heat transfer with system rotation and variable thermal properties," Communicated to Computational Mechanics.

[4] Pang O. & Wang L. 2001, "Bifurcation and stability of Bratu problem," Compilation of Abstract for the First M.I.T. Conference on Computational Fluid and Solid Mechanics (ed. K. J. Bathe), p109.

[5] Qu L. & Wang L. 2001, "Multiplicity and stability of exothermic chemical reaction in catalyst beds: a numerical study," Computational Fluid and Solid Mechanics, Vol. 2, pp1353-1354.

[6] Yang T. & Wang L., 2000a, "Microscale flow bifurcation and its macroscale implications in periodic porous media," Computational Mechanics, Vol. 26, pp520-527.

[7] Wang L & Yang T. 2001, "Bifurcation and stability of forced convection in curved ducts," J. Fluid Mech. (in press).

[8] Ludwieg H., 1951, "Die ausgebildete kanalströmung in einem rotierenden system," Ing.-Arch. Bd., Vol. 19. pp296-308.

[9] Miyazaki H., 1971, "Combined free and forced convective heat transfer and fluid flow in a rotating curved circular tube," Int. J. Heat Mass Transfer, Vol. 14, pp1295-1309.

[10] Miyazaki H., 1973, "Combined free and forced convective heat transfer and fluid flow in a rotating curved rectangular tube," J. Heat Transfer, Vol. 95, pp64-71.

[11] Wang L. & Cheng K. C., 1996a, "Flow transitions and combined free and forced convective heat transfer in a rotating curved circular tube," International Journal of Heat and Mass Transfer, Vol. 39, pp3381-3400.

[12] Daskopoulos P. & Lenhoff A. M., 1990, "Flow in curved ducts: Part 2 rotating ducts." J. Fluid Mech., Vol. 217, pp575-593.

[13] Matsson O. J. E. & Alfredsson P. H., 1990, "Curvature- and rotation-induced instabilities in channel flow," J. Fluid Mech., Vol. 210, pp537-563.

[14] Matsson O. J. E. & Alfredsson P. H., 1994, "The effect of spanwise system rotation on Dean vortices," J. Fluid Mech., Vol. 274, pp243-265.

[15] Guo Y. & Finlay W. H., 1991, "Splitting, merging and wavelength selection of vortices in curved and/or rotation duct flow due to Eckhaus instability," J. Fluid Mech., Vol. 228, pp661-691.

[16] Wang L. & Cheng K. C., 1995, "Flow in curved channels with a low negative rotating speed," Physical Review E, Vol. 51, pp1155-1161.

[17] Wang L. & Cheng K. C., 1996b, "Flow transitions and combined free and forced convective heat transfer in rotating curved channels: the case of positive rotation," Physics of Fluids, Vol. 8, pp1553-1573.

[18] Wang L. & Cheng K. C., 1997, "Visualization of flows in curved channels with a moderate or high rotation speed," International Journal of Rotating Machinery, Vol. 3, pp215-231.

[19] Wang L. & Cheng K. C., 2001, "Visualization of Flows in Channels with Curvature and Rotation," Invited book chapter in: Centrifugal Processing, (ed. L. L. Regel & W. R. Wilcox), Kluwer Academic/Plenum Publishers, New York (in press).

[20] Wang L., 1997a, "Buoyancy-force-driven transitions in flow structures and their effects on heat transfer in a rotating curved channel," International Journal of Heat and Mass Transfer, Vol. 40, pp223-235.

[21] Wang L., 1997b, "Effect of spanwise rotation on centrifugal instability in rotating curved non-isothermal flows," Computational Mechanics, Vol. 19, pp420-433.

[22] Wang L., 1999, "Competition of Coriolis instability with centrifugal instability and its effects on heat transfer," International Journal of Non-linear Mechanics, Vol. 34, pp35-50.

[23] Selmi M., Nandakumar K. & Finlay W. H., 1994, "A bifurcation study of viscous flow through a rotating curved duct," J. Fluid Mech., Vol. 262, pp353-375.

[24] Selmi M. & Nandakumar K., 1999, "Bifurcation study of flow through rotating curved ducts," Physics of Fluids, Vol. 11, pp2030-2043.

[25] Wang L., 2000, "Physical Constraints of Turbulence Modeling," Invited book chapter in: New Developments and Perspectives in Turbulence (ed. J. J. Wang et al.), Science, Beijing, 189-208.

[26] Seydel, R., 1994, "Practical Bifurcation and Stability Analysis: From Equilibrium to Chaos", Springer-Verlag, New York.

[27] Yang T., 2001, "Multiplicity and Stability of Flow and Heat Transfer in Rotating Curved Ducts," PhD thesis, Department of Mechanical Engineering, the University of Hong Kong.

HEFAT2002

1st International Conference on Heat Transfer, Fluid Mechanics, and Thermodynamics

8-10 April 2002, Kruger Park, South Africa

DA1

AEROSPACE-RELATED FLUID PHYSICS, HEAT TRANSFER, AND THERMAL CONTROL RESEARCH AT THE NLR SPACE DIVISION

A.A.M. Delil
National Aerospace Laboratory NLR, Space Division
P.O. Box 153, 8300 AD Emmeloord, The Netherlands
Phone: +31 527 248229, Fax: +31 527\ 248210, E-mail: adelil@nlr.nl

ABSTRACT

Including the information published earlier [1], the aerospace-related fluid physics, heat transfer and thermal control research carried out by the NLR Space Division can be summarised by:

- Thermal conductivity investigations.
- Design and manufacture of a test rig for measuring the thermal conductance of axially loaded rotating bearings in vacuum.
- Thermal modelling of various rotating space mechanisms and the compilation of a handbook to model such mechanisms.
- Thermal performance of MLI blankets.
- Constant and variable conductance heat pipes, electro-osmotic heat pipe.
- Radiation heat transfer.
- Movable thermal joints and flexible thermal links.
- Thermal analysis and design.
- Two-phase heat transport systems: Their thermal- gravitational modelling and scaling, control methods/ algorithms. Two-phase test rigs development, components testing and calibration.
- Thermal modelling of the ESA ATLID two-phase laser head thermal control system breadboard, and the ESA capillary pumped loop engineering model.
- Development of the ESA high-efficiency low pressure drop two-phase condenser.
- Adapting liquid flow metering assemblies for use in space.
- Development of accurate ultrasonic flow meter for propellants.
- TPX I: In-orbit two-phase experiment and TPX II, a re-flight of the modified two-phase experiment (parallel thermally unbalanced condensers configuration, high pumping power sintered nickel evaporators, upgraded controllable valve).
- Loop heat pipe flight experiment.
- Flexible external insulation blanket permeability.
- Self regulating heaters.
- ESA Thermal Analyzer & Fluid Heat Transfer Solver Upgrade.
- Thermal modelling of laser heads, glove-boxes, the phased-array universal synthetic aperture radar structure, European co-operation for long-term in defence programme synthetic aperture radar antennae, avionics racks and components.
- Meteosat Second Generation propellant gauging. Experimental determination of the dielectric properties of propellants.
- Future European Space Transportation Investigations Program. Sänger aerospace plane thermal design activities.
- Critical and novel issues, AMS-2 and CIMEX-3.
- Pulsating two-phase loops and other pulsating/ oscillating heat transfer devices.
- Small dedicated satellites: Wetsat & Sloshsat-Flevo.
- Instrumentation for microgravity research.

DETAILING

The detailing is a complete overview of all relevant research activities. The presentation will highlight a selection of the most interesting and innovating issues (as it is listed in the Appendix).

Thermal conductivity

Equipment has been built to measure the thermal conductivity of anisotropic materials. Measurements, carried out in the NLR thermal vacuum chamber, confirm the model developed at NLR for the thermal conductivity of metallic honeycomb sandwich panels for space applications [2, 3]. Carbon fibre reinforced plastic sheet containing materials were investigated also [4, 5].

Under contract with Fokker Aircraft, the equipment was used to determine the thermal resistances of the hinges between the solar panels and structure of the Astronomical Netherlands Satellite [6].

Further investigations concern contact conductance (bolted joints, effects of interface filters) and the thermal resistance induced by sheet material deformation [7].

A test rig for rotating loaded bearings in vacuum

To obtain reliable results in the thermal design of space-borne mechanisms, it is important to know the thermal conductance and generated friction heat of rotating bearings in vacuum.

Under European Space Agency (ESA) contract, NLR designed and built a test rig to measure the above quantities. This test rig, still operational at the European Space Tribology Centre in Risley

(UK), accommodates three different bearing sizes (90 mm OD/55 ID, 42 OD/20 ID, 16 OD/5 ID), operated with and without lubricant. The thermal conductance of the rotating bearing is obtained by measuring the heat flux through and temperature drop across the bearing. The generated friction heat is obtained from friction torque and rotation speed measurements.

Typical test rig specifications are:

- A rotation speed adjustable from 1 to 2500 rpm.
- A pre-load ranging from 0 to 5 kg in 50 g steps.
- Inner and outer race temperatures variable between -20 and +60 °C and +20 and +70 °C respectively.

Details on the rig and measuring techniques is given in [8, 9].

Thermal modelling of rotating space mechanisms

Also for ESA a handbook has been compiled for the thermal modelling of space mechanisms [10]. The handbook presents a literature survey, step-by-step procedure, data compilations of material properties, etc. It also contains the theory basic to the thermal modelling procedure chosen. This procedure is illustrated by the results of calculations on a high speed mechanism, the reaction wheel of the Astronomical Netherlands Satellite, on a medium speed mechanism, Dornier's antenna despin mechanism, and on a low speed mechanism, Marconi's solar paddle drive.

Multilayer insulation blankets

Models describing the thermal performance of evacuated multilayer insulation blankets are usually based on the simple addition of the three mutually interacting modes of energy transfer: radiation between the shields, solid conduction via the components and their interfaces and gas conduction in the interstices, determined by residual gas pressure, outgas and the way the outgas products migrate through the blanket.

Blankets for spacecraft applications are usually made of perforated shields allowing fast depressurisation during the spacecraft launch. Perforations impair the insulation quality of a blanket, as perforations increase the effective shield emissivity (hence radiation transfer) and allow broadside pumping: Outgas products migrate via perforatios from interstice to interstice accumulating until they eventually escape at the blanket boundary.

Earlier reported models [11-13] concern either purely broadside-pumped blankets or purely edge-pumped blankets (of non-perforated shields, where the outgas products can escape only at the edges of the interstices). The pumping in most blankets for spacecraft is simultaneously edge and broadside. [13] presents the NLR model to account for this hybrid pumping.

A test apparatus was built to experimentally verify the models [13, 14]. There is good agreement between experiment and theory.

Heat pipes

Constant conductance heat pipe work consisted of a compilation of constant conductance heat pipe design data [15], performance measurements, filling procedures, the impact of filling ratio on the transport properties, and the impact of working fluid dissociation.

Considerable effort has been spent on the modelling and manufacture of an electro-osmotic heat pipe, a heat pipe with a feedback controlled pumping section, based on the phenomenon of electro-osmosis [16-18]. Unfortunately the realisation of such a heat pipe turned out to be unsuccessful since polarisation effects and dissociation of the working fluid impair a proper long-term performance, a problem for which no proper solution was found.

NLR also developed a transient thermal model for gas-loaded variable conductance heat pipes. This model can be easily implemented in existing general thermal analyzer computer programs. It is more generally valid than the Edwards/Marcus-model [19], commonly accepted in variable conductance heat pipe research, since the NLR model accounts for inertial and frictional effects of the moving vapour [20-24]. Consequently it predicts different transport and control behaviour, especially within the low vapour pressure operating range (typical for liquid metal heat pipes), start-up operation, and control. [24] presents a detailed analysis of the considerable limitations of performance and control predicted by the NLR model for a methanol variable conductance heat pipe built for experimental model validation.

An automated heat pipe test rig has been designed/ manufactured to perform the validation experiments [25].

Radiation heat transfer

Apart from thermal emissivity and solar absorptivity measurements, NLR investigated the modelling of radiation heat transfer in a magnetohydrodynamic generator channel, within the the Netherlands MHD power generation project [26].

Movable thermal joints

Within ESA's Columbus Polar Platform development, NLR studied thermal joints for deployable/ steerable radiators [27, 28]. Various options were traded. New ideas, the rotatable radial heat pipe and the movable oscillating hydrodynamic thermal joint, were proposed.

A continuously rotatable thermal joint for steerable radiators, currently under test [29, 30], is being patented.

Thermal analysis and design

Thermal modelling and design work for Columbus Resources Module [31] and Polar Platform [32, 33] was done for Fokker.

Two-phase heat transport systems

Two-phase work at NLR includes:

- A trade study on vapour quality sensors for spacecraft two-phase heat transport systems, measuring the relative vapour mass content of a flowing two-phase mixture [34, 35]. Design and manufacture of vapour quality sensors for the test bed developed the European Space Agency within the Two-Phase Heat Transport Systems-Critical Components study [36-41].
- Development of control algorithms, considered also a critical component within this study. Preliminary evaluation of control methods for the mechanically pumped two-phase heat transport systems engineering model, including development and analysis of dynamic models for its vapour pressure control loop [42-44].

– The design & manufacture of a 5 kW automated mechanically pumped two-phase freon test loop to calibrate vapour quality sensors [45].
– Thermal scaling with respect to gravity to properly predict the low-gravity performance of a two-phase heat transport system and its components using results of experiments on earth with, fluid to fluid and geometric, scale models [46-53].
– Design/manufacture/operation of an automated mechanically pumped two-phase ammonia test loop for calibration of the vapour quality sensors for a capillary pumped two-phase ammonia system, which is the Dutch/Belgian two-phase experiment (TPX I) that has flown, in the ESA In-Orbit Technology Programme, as Get Away Special G557 aboard Space Shuttle (STS60), early February 1994 [54-62].
– Two-phase heat transport component testing [63].
– TPX II: The re-flight of a modified two-phase experiment, with parallel condensers, high pumping power evaporators, improved liquid flow meters and Swalve, as Get Away Special G467 on a Space Shuttle flight end 1998 [64-66].
– Contributing to the concept, thermal/structural design, flight scenario, testing and experiment evaluation of the loop heat pipe flight experiment, a hitchhiker experiment on Space Shuttle flight (STS87), November 1997 [67-69]. This experiment was conducted by a team led by Dynatherm, consisting of the Naval Research Laboratory, NASA GSFC and the Center for Space Power, Hughes Space & Communications, the Center for Commercial Development of Space, US Air Force Wright & Phillips Laboratories, BMDO, and NLR.
- Development of ESA's high efficiency, low pressure drop condenser, with Daimler Benz Aerospace, Bradford Engineering, TAIS and Swales as subcontractors [70-72].
- The ESA study on "spatialisation" of flow metering assemblies with subcontractors SPPS Suisse/Bradford Engineering and the Société Anonyme Belge de Construction Aéronautique [73].
- Thermal modelling and design of the atmospheric LIDAR laser head thermal control breadboard, for MMS-UK [74].
- Thermal modelling and design of ESA's capillary-pumped loop engineering model [75, 76], for MMS-UK.
– Development of a two-phase thermal control system for a phased array radar module [77].

Miscellaneous

Other activities for ESA and other customers are:
– Sänger-related thermal research proposed for the two-stage to orbit space plane and the hot structure test facility, in the ramjet technology demonstration programme [78].
– Flexible external insulation blanket permeability testing [79].
– Testing of self-regulating heaters, designed to maintain their substrate temperature, by using their intrinsic material properties instead of external thermostats [80].
– ESA's flexible thermal link development for Dornier [81, 82].
– The Meteosat Second Generation Unified Propulsion System - Gauging Sensor Unit: the NLR/Bradford development of level gauges for spin-stabilised spacecraft propellant tanks, derived from the earlier developed NLR vapour quality sensor [29, 30, 83]. Work is done for ESA on the experimental determination of dielectric properties of propellants MON & MMH [84, 85] and, with Bradford, on the development of an ultrasonic flow meter for propellants. Current investigations concern the development of propellant level sensors for 3-axis stabilised spacecraft.

Thermal modelling

These modelling activities pertain to:
- The ESA Thermal Analyzer upgrading, focusing on the fluid dynamics part of the Fluid Heat Transfer Solver: The replacement of the current homogeneous flow model by physically more realistic models for two-phase flow [86].
– Detailed thermal modelling of a laser head [87].
– Thermal modelling of glove-boxes for ISS, of the structure of the phased array universal synthetic aperture radar [88], and of the heat load on ALADIN in an arbitrary ISS-related orbit [89].
– The European co-operation for long-term in defence programme [90-95]. Research and technology project 4: the Modular Avionics Harmonisation Study, thermal modelling of components/avionics racks, and the impact of high thermal load on environmental control systems and project 9: Advanced space synthetic aperture radar sensor technology, thermal design/model of synthetic aperture radar antennae.
- Future European Space Transportation Investigations Program.

Critical & novel two-phase issues, AMS and CIMEX

An inventory of critical research items has been produced, especially pertaining to problems/unresolved issues in the field of aerospace heat transfer, resulting in various publications related to extension of gravity levels [96 to 103].

AMS-2 is a 4-5 years lasting international experiment on the International Space Station ISS. It is a particle detector for high-energy cosmic rays, consisting of several sub-detectors. Its scientific goal is to detect anti-matter. NLR is involved in the overall thermal control, the thermal control of electronics, and the development of an novel carbon dioxide two-phase MPL for the Tracker experiment [104-105]. The latter loop is intended also to perform fundamental two-phase research experiments during time slots when the particle detectors will be set inactive.

CIMEX-3, NLR's Versatile Two-Phase Loop Experiment, planned to be executed (in ESA's MAP programme) in the Fluid Physics Laboratory on ISS [106], is a multi-purpose two-phase heat transport loop with a mechanically and a capillary pumped option, different types of evaporators (capillary and swirl), and the possibility to operate while using different working fluids. Detailed discussions on the rationale behind the experiment [107] illustrate that the objectives of CIMEX-3 are:
- To study micro-g two-phase flow and heat transfer issues, via transparent (swirl) evaporators and high efficiency low pressure drop condensers.
- To measure the void/mass fraction in the adiabatic line for vapour quality sensor (VQS) calibration.

- Flow pattern characterisation, creation of flow pattern maps.
- The viability demonstration of Mechanically and Capillary Pumped two-phase Loops (MPL & CPL), using different working fluids or mixtures.

Pulsating/Oscillating Heat Transfer Devices

The research [108- 112] concentrates on pulsating/ oscillating heat transfer devices, being of interest for applications in spacecraft thermal control in microgravity, in planetary partial gravity and supergravity environments, and in hypergravity acceleration levels in rotating spacecraft or manoeuvring combat aircraft [110]. Different aspects of various heat transfer devices in gravity environments ranging from micro-gravity to super-gravity are discussed. Based on an overview is of world-wide activities and the state of the art of pulsating and oscillating heat transfer device research and an assessment of commonality and difference. a baseline philosophy was defined for modelling and comparison of experimental data, in order to anticipate an easy comparison with the results of ongoing and future research activities. Several test set-ups were built, including a versatile one [113-114], allowing variation of almost all relevant parameters: Working fluid and fill charge, power, transport length, inclination with respect to the gravity vector, and the possibility to choose either the dead-end pulsating or the closed-loop oscillating configuration.

Small satellites: "Wetsat" and "Sloshsat Flevo"

A definition study was completed on Wetsat: a small spacecraft to collect data on heat and mass transport by evaporation and condensation across an annular spherical gap. Various force fields have been introduced: an electrical radial field and centrifugal fields from spacecraft spin [115].

Because of insufficient support efforts were redirected to the definition of a spacecraft to investigate dynamics of onboard liquid. After a successful precursor, the Wet Satellite Model that flew 7 minutes following a rocket launch. Its follow-up Sloshsat is currently planned for Space Shuttle launch in 2002. The Sloshsat payload, a 80 litres tank with 33 litres of water. The location of the water in the tank is determined by the Coarse Sensor Array, a uniform distribution of 137 platinum ring electrodes embedded in the tank wall [116]. The capacitance between 270 electrode pairs provides liquid height information. Prediction of the dynamics and development of the control algorithms for the spacecraft are being generated with the Sloshsat Motion Simulator. This original development at NLR is operated in the EUROSIM software environment. Further activities [117-127] finally resulted in the flight hardware, being manifested to be launched from the Shuttle.

Instrumentation for microgravity research

With the Spanish Laboratory Lamf/ETSIA NLR carried out work, within the European Space Agency High Temperature Facility Technology Study, on combustion experiment instrumentation [128], focusing on flow field mapping in opaque liquids [129, 130].

Activities within the European Space Agency Fluid Physics Instrumentation Study [131] led to the Prototype Optical Diagnostic Instrument [132], a precursor to the European Space Agency Fluid Science Laboratory Facility Development Study [133], used for thermophysical & fluid physics diagnostics [134].

Other investigations concern microscopy [135], optical diagnostics of crystal growth [136], optical detection methods for biochemical sample analysis [137], and the development of a biomass sensor [138, 139].

CONCLUDING REMARKS

In conclusion it can be said that the research done concerns all aspects of aerospace thermal control system technology, i.e.:

- All heat transfer modes: Radiation, convection, conduction.
- Development of both passive and active thermal control components, heat transport loops and other (sub-)systems, and full-scale flight systems.
- Design from component to satellite level.
- All kinds of two-phase heat transfer devices: CCHP, VCHP, LHP, CPL, MPL, VDHTD, Oscillating/Pulsating HP, etc.
- Thermal modelling and the experimental verification of the modelling results.
- Thermal/gravitational scaling of two-phase flow and heat transfer in gravity environments for microgravity spacecraft applications, for reduced gravity applications in Moon and Mars thermal control systems, and for hypergravity applications in spinning satellites, combat aircraft and supergravity planetary environment.
- Development and execution of in-orbit experiments.

It is obvious that the research activities continuously change as they have to follow the needs resulting from more and more demanding requirements for developing novel, very advanced spacecraft with extremely long lifetimes.

REFERENCES

1 Delil, A.A.M., A review of thermophysical research at the NLR Space Division, NLR-TP-97573, 3rd Seminar Heat Pipes, Heat Pumps and Refrigerators, Minsk, Belarus, 1997, Elsevier Publishers, Paris, Revue Général de Thermique, 1998, 37, 917-924.

2 Heemskerk, J.F., Delil, A.A.M., Daniels, D.H.W., Thermal conductivity of honeycomb sandwich panels for space applications, NLR MP 71016, ELDO/ESRO Scientific and Technical Review, 4 (1972), 167-178.

3 Delil, A.A.M., Heemskerk, J.F., Daniels, D.H.W., Thermal conductivity of metallic honeycomb sandwich panels, Proc. Symposium on Structural & Thermal Tests, Their Evaluation & Present Trends, Noordwijk, Netherlands, 1973, ESRO SP-95, Vol. III Thermal Tests, 47-68.

4 Assem, D. van den, Daniels, D.H.W., Determination of the thermal conductivity of carbon fibre reinforced plastic sheet material, NLR TR 77113, 1977.

5 Assem, D. van den, Daniels, D.H.W., Thermal conductance measurements of honeycomb sandwich panels with carbon fibre reinforced plastic face sheets, NLR TR 78081, 1978.
6 Delil, A.A.M., Daniels, D.H.W., Heemskerk, J.F., Thermal conductance of the hinges between solar panels and structure of the Astronomical Netherlands Satellite, NLR-TR-72077, 1972.
7 Delil, A.A.M., Heemskerk, J.F., Heat balance measurements with a thin-walled cube in a simulated space environment, NLR TR 78080, 1978.
8 Delil, A.A.M., Heemskerk, J.F., Vreeburg, J.P.B., Design report on the ESRO test rig to measure the thermal conductance and friction torque of rotating bearings in vacuum, NLR TR 74068, ESRO CR(P) 05, 1974.
9 Heemskerk, J.F., Delil, A.A.M., Vreeburg, J.P.B., A test rig to measure the thermal conductance and frictional torque of bearings in vacuum, ESA SP 111, Space Tribology Symposium, Frascati, Italy, 1975, 149-155.
10 Vreeburg, J.P.B., Delil, A.A.M., Heemskerk, J.F., Handbook for the thermal modelling of space mechanisms by the nodal network method, NLR TR 73133, ESA CR 219, 1974.
11 Delil, A.A.M. Heemskerk, J.F., A theoretical investigation of the basic thermal performance of multilayer insulation blankets, NLR TR 75063, 1975.
12 Delil, A.A.M., Heemskerk, J.F., A theoretical investigation of gas conduction effects on multilayer insulation performance, NLR TR 76018, 1976.
13 Heemskerk, J.F., Delil, A.A.M., The influence of outgas on the performance of MLI blankets with perforated shields, NLR MP 77038, paper 77-238 IAF Conf., Prague, Czechoslovakia, 1977.
14 Delil, A.A.M., Heemskerk, J.F., Multilayer insulation blankets for spacecraft applications, thermal model accounting for outgassing and different ways of gas migration, NLR MP 81051, 7th Int. Heat Transfer Conf., München, Germany, 1981, Vol. 6, 51-55.
15 Delil, A.A.M., Theory and design of conventional heat pipes for space applications, NLR TR 70001, 1977.
16 Delil, A.A.M., Some quantitative considerations on electro-osmotic flow pumping in heat pipes, NLR TR 78142, 1978.
17 Delil, A.A.M., Quantitative considerations concerning a high performance heat pipe with a short electro-osmotic pumping section, NLR TR 79113, 1979.
18 Delil, A.A.M., Fully controllable heat pipe with a short electro-osmotic pumping section, NLR MP 82049, AIAA 83-317, AIAA Aerospace Sciences Meeting, Reno, USA, 1983.
19 Marcus, B.D., Theory and design of variable conductance heat pipes, NASA CR-2018, 1972.
20 Delil, A.A.M., Limitations in variable conductance heat pipe performance and control predicted by the current steady-state model developed at NLR, NLR MP 84009, Proc. 5th Int. Heat Pipe Conference, Tsukuba, Japan, 1984, 225-231.
21 Vooren, J. van der, Delil, A.A.M., Uniaxial model for a gas-loaded variable conductance heat pipe, NLR TR 80048, 1980.
22 Vooren, J. van der, Sanderse, A., An improved flat front model for a gas-loaded variable conductance heat pipe, NLR TR 80049, 1980.
23 Delil, A.A.M., Vooren, J. van der, Uniaxial model for gas-loaded variable conductance heat pipe performance in the inertial flow regime, NLR MP 81010, Proc. 4th Int. Heat Pipe Conf., London, 1981, Advances in heat Pipe Technology, Editor: Reay, D.A. Pergamon, Oxford, UK, 1981, 359-372.
24 Delil, A.A.M., Daniels, H.A.M., Uniaxial model for gas-loaded variable conductance heat pipe performance. The effects of vapour flow friction and inertia, NLR MP 83058, Environmental and Thermal Systems for Space Vehicles, Toulouse, France, 1983, ESA SP 200, 235-241.
25 Buggenum, R.I.J. van, Daniels, D.H.W., Development, manufacture and testing of a gas-loaded variable conductance methanol heat pipe, Proc. 6th International Heat Pipe Conference, Grenoble, France, 1987, 330-337.
26 Delil, A.A.M., Radiation heat transfer in a MHD generator channel, (in Dutch) NLR TR 83068, May 1983.
27 Delil, A.A.M., Moveable thermal joints for deployable or steerable spacecraft radiator systems, NLR MP 87016, SAE 871460, 17th Intersoc. Conf. on Environmental Systems, Seattle, USA, 1987.
28 Delil, A.A.M., Considerations concerning a thermal joint for a deployable of steerable radiator for the Columbus Polar Platform, NLR TR 86055, 1986.
29 Delil, A.A.M., Pauw, A., Voeten, R.G.H.M., Put, P. van, Sensors and Components for Aerospace Thermal Control and Propellant Systems, NLR TP 97282, ESA-SP-400, 6th European Symposium on Space Environment Control Systems, Noordwijk, Netherlands, 1997, pp. 289-297; SAE 972478, 27th International Conference on Environmental Systems, Lake Tahoe, USA, 1997.
30 Delil, A.A.M., Pauw, A., Voeten, R.G.H.M., Put, P. van, Sensors and Components for Aerospace Thermal Control, Life Science and Propellant Systems, NLR TP 97504, AIP Proc. 2nd Conference on Applications of Thermophysics at Microgravity, Space Technology & Applications International Forum, Albuquerque, USA, 1998.
31 Delil, A.A.M., Heemskerk, J.F., Columbus Resource Module: Thermal Analysis of Main Body Section, Fokker Space & Systems Report COL-TN-FO-RM-TC-017, 1988.
32 Delil, A.A.M., Heemskerk, J.F., Columbus Polar Platform ORU Thermal Control: Performance Calculations & Budget Estimates, Fokker Space & Systems Report COL-TN-FO-PF-TC-021, 1987.
33 Delil, A.A.M., Heemskerk, J.F., Columbus Polar Platform ORU Thermal Control: Design and Definition, Fokker Space & Systems Report COL-TN-FO-PF-TC-024, 1988.
34 Delil, A.A.M., Quality monitoring in two-phase heat transport systems for large spacecraft, NLR MP 86012, SAE 860259, Proc. 16th Intersoc. Conf. on Environmental Systems, San Diego, USA, 1986.
35 Delil, A.A.M., Sensors for a system to control the liquid flow into an evaporative cold plate of a two-phase heat transport

system for large spacecraft, NLR TR 86001, 1986; Proc. NASDA Workshop on Prospects of Future Thermal Technology in Space, Tokyo, Japan, 1988.

36 Siepmann, R., et al., Two-Phase Heat Transport Systems - Critical Components, Final Report, ESA CR(P) 3406, Dornier RP 2061-0000 DS/67, 1992.

37 Dunbar, N., Siepmann, R., Supper, W., European two-phase heat transport technology testbed results, SAE 901271, 20th Intersociety Conference on Environmental Systems, Williamsburg, USA, 1990.

38 Delil, A.A.M., Feasibility demonstration of a sensor for high-quality two-phase flow, NLR TR 87009, 1987.

39 Delil, A.A.M., A Sensor for High-Quality Two-Phase Flow, NLR MP 88025, Proc. 16th International symposium on Space Technology and Science, Sapporo, Japan, 1988, 957-966; 1st ESA/ESTEC Workshop on Two-Phase Heat Transport Technology, Noordwijk, Netherlands, 1993, ESA-WPP-067, 157-160.

40 Delil, A.A.M., Heemskerk, J.F., Development of a sensor for high-quality two-phase flow, NLR MP 88059, Proc. 3rd European Symposium on Space Thermal Control & Life Support Systems, ESTEC, Noordwijk, Netherlands, 1988, ESA SP 288, 113-123, and 3rd International Heat Pipe Symposium, Tsukuba, Japan, 1988, and Eurotherm Seminar on Non-Equilibrium Two-Phase Flow, Rome, Italy, 1988.

41 Delil, A.A.M., Daniels, D.H.W., Experimental comparison of two-phase sensors, NLR CR 89164, 1989.

42 Zwartbol, T., Development and analysis of dynamic models, inherent stability and interaction of centrifugally pumped, parallel vapour quality control loops for TPHTS EM, NLR CR 94050, 1994.

43 Zwartbol, T., Development and analysis of dynamic models for the vapour pressure control loop for TPHTS EM, NLR CR 94051, 1994.

44 Zwartbol, T., Preliminary evaluation of control methods for TPHTS EM, NLR CR 94052, 1994.

45 Delil, A.A.M., Heemskerk, J.F., Test loops for two-phase thermal management system components, NLR TP 90155, SAE 901272, 20th Intersoc. Conf. on Environmental Systems, Williamsburg, 1990.

46 Delil, A.A.M., Two-phase heat transport systems for spacecraft - Scaling with respect to gravity, NLR TP 89127, SAE 891467, 19th Intersociety Conference on Environmental Systems, San Diego, CA, USA, 1989, SAE Transactions, Journal of Aerospace, 98, 1989, 554-564.

47 Delil, A.A.M., Thermal modelling of two-phase heat transport systems for space. Scaling predictions and results of experiments at various gravity levels, ASME/JSME Forum on Microgravity Fluid Flow, Portland, USA, 1991, ASME-FED 111, 21-27, NLR TP 91051, IUTAM Symp. Microgravity Fluid Mechanics, Bremen, Germany, 1991, 469-478; ESA-ESTEC Workshop on Two-Phase Heat Transport Technology, Noordwijk, Netherlands, 1993, ESA-WPP-067, 245-255.

48 Delil, A.A.M., Thermal gravitational modelling and scaling of two-phase heat transport systems for space: an assessment and a comparison of predictions and experimental results, NLR TP 91401, 4th European Symposium on Space Environmental Control Systems, Florence, Italy, 1991, ESA SP-324, 61-67.

49 Delil, A.A.M., Thermal gravitational modelling and scaling of two-phase heat transport systems: Similarity considerations and useful equations, predictions versus experimental results, NLR TP 91477, 1st European Symposium on Fluids in Space, Ajaccio, France, 1991, ESA SP-353, 579-599.

50 Delil, A.A.M., Gravity dependent condensation pressure drop and heat transfer in ammonia two-phase heat transport systems, NLR TP 92121, AIAA 92-4057, 1992 National Heat Transfer Conference, San Diego, CA, USA, 1992.

51 Delil, A.A.M., Gravity dependence of pressure drop and heat transfer in straight two-phase heat transport system condenser ducts, NLR TP 92167, SAE 921168, 22nd International Conference on Environmental Systems, Seattle, 1992, SAE Transactions, Journal of Aerospace, 101, 1992, 512-522.

52 Delil, A.A.M., Two-phase flow and heat transfer in various gravity environments, 4th International Heat Pipe Symposium, Tsukuba, Japan, 1994, 223-234, and Survey of Heat Transfer Research Meeting of the Assembly of International Heat Transfer Conferences, ENEA C.R.E., Casaccia, Italy, 1992.

53 Delil, A.A.M., Two-Phase Heat Transport Systems for Space Thermal Gravitational Modelling & Scaling, Similarity Considerations, Equations, Predictions, Experimental Data and Flow Pattern Mapping, CPL98 Workshop, Los Angeles, USA, 1998, and 28th International Conference on Environmental Systems, Danvers, USA, 1998.

54 Delil, A.A.M., Heemskerk, J.F., Supper, W., TPX: Two-phase experiment for Get Away Special G557, NLR TP 91206, 21st International Conference on Environmental Systems, San Francisco, USA, 1991.

55 Supper, W., Delil, A.A.M., Dubois, M., In-orbit demonstration of two-phase technology, 4th European Symposium on Space Environmental Control Systems, Florence, Italy, 1991, ESA SP-324, 607-612.

56 Delil, A.A.M., et al., In-orbit demonstration of two-phase heat transport technology: TPX/G557 development & pre-launch testing, NLR TP 93394, SAE 932301, 23rd International Conference on Environmental Systems, Colorado Springs, CO, USA, 1993, and 1st ESA/ESTEC Workshop on Two-Phase Heat Transport Technology, Noordwijk, Netherlands, 1993, ESA-WPP-067, 421-440.

57 Delil, A.A.M., In-orbit demonstration of two-phase heat transport system technology, Invited paper, Proc. 4th Int. Heat Pipe Symp., Tsukuba, Japan, 1994, 249-268, and ISTS 94-d11 at the 19th Int. symp. on Space Technology & Science, Yokohama, Japan, 1994.

58 Delil, A.A.M., et al., In-orbit demonstration of two-phase heat transport technology: TPX/G557 flight results, NLR TP 94269, SAE 9414045, 24th Int. Conf. on Environmental Systems & 5th European Symp. on Space Environmental Control Systems, Friedrichshafen, Germany, 1994, also at the ELGRA Annual Meeting, Madrid, Spain, 1994.

59 Delil, A.A.M., Two-phase experiment for the in-orbit demonstration of two-phase heat transport system technology, Invited paper Multiphase Phenomena Session of the 30th COSPAR G-1 Symposium on Microgravity Sciences: Results and analysis of recent spaceflight, Hamburg, Germany, 1995, Advances in Space Research, Vol. 16, no. 7, 113-122.
60 Delil, A.A.M., et al., TPX for in-orbit demonstration of two-phase heat transport technology - evaluation of flight & post - flight experiment results, NLR TP 95192, SAE 951510, 25th Int. Conf. on Environmental Systems, San Diego, CA, USA, 1995, also presented as invited paper at the International Seminar and Workshop on Heat Pipes, Heat Pumps and Refrigerators-Dual Use Technologies, Minsk, Belarus, 1995.
61 Delil, A.A.M., et al., In-orbit demonstration of two-phase heat transport technology in TDP1, Final Report, NLR CR 95292, 1995.
62 Delil, A.A.M., In-orbit demonstration of two-phase heat transport technology in TDP1, Executive Summary, NLR CR 95291, 1995.
63 Donk, G. van, Pauw, A., Testing of two-phase heat transport components, NLR CR 93578, Part I-V, 1993 and 1994.
64 Delil, A.A.M., Dubois, M., TPX II: Reflight of European Two-Phase eXperiment, Proc. CPL'96: International Workshop on Capillary Pumped Loops, Noordwijk, Netherlands, ESA-WPP-112, 1996.
65 Delil, A.A.M., Dubois, M., Supper, W., In-Orbit Demonstration of Two-Phase Heat Transport Technology - Status of TPX II: Reflight of the European Two-Phase Experiment, NLR TP 97283, ESA-SP-400, 6th European Symp. on Space Environment Control Systems, Noordwijk, Netherlands, 1997, SAE 972479, 27th Int. Conf. on Environmental Systems, Lake Tahoe, USA, 1997.
66 Delil, A.A.M., Dubois, M., Supper, W., ESA Two-Phase Heat Transport System Flight Experiments: TPX I & TPX II, Proc. 10th Int. Heat Pipe Conf., Stuttgart, Germany, 1997.
67 Bienert, W., et al., Loop Heat Pipe Flight eXperiment, Proc. CPL '96: Int. Workshop on Capillary Pumped Loops, Noordwijk, Netherlands, ESA-WPP-112, 1996.
68 Bienert, W., Best, F.R., DTX Loop Heat Pipe Flight Experiment, AIP Proc. Conf. on Applications of Thermophysics in Microgravity, Space Technology & Applications International Forum, Albuquerque, USA, 1998.
69 Bienert, W., et al., Loop Heat Pipe Flight eXperiment, 28th Int. Conf. on Environmental Systems, Danvers, USA, 1998.
70 Delil, A.A.M., et al., High Efficiency, Low Pressure Drop Two-Phase Condenser, NLR TP 96380, SAE 961562, 26th Int. Conf. on Environmental Systems, Monterey, USA, 1996, and CPL'96: International Workshop on Capillary Pumped Loops, Noordwijk, Netherlands, ESA-WPP-112, 1996.
71 Delil, A.A.M., et al., High efficient, low pressure drop two-phase condenser, Executive Summary, NLR CR 96001, 1996.
72 Delil, A.A.M., High efficient, low pressure drop two-phase condenser, Final Report, NLR CR 96002, 1996.
73 Delil, A.A.M., Selection of flow metering assemblies to be spatialised for aerospace heat transport, life sciences and propellant systems, 2nd European Thermal Sciences Conf., Rome, Italy, 1996.
74 Dunbar, N., ATLID Laser head thermal control breadboard, Executive Summary Report, Matra Marconi Space UK, SP537, 1995, SAE 961561, 26th Int. Conf. on Environmental Systems, Monterey, USA, 1996.
75 Dunbar, N., Supper, W., Spacecraft Capillary Pumped Loop Technology - Towards a Qualified Thermal Control Loop, Proc. 10th Int. Heat Pipe Conf., Stuttgart, Germany, 1997.
76 Es J. van, Capillary pumped loop engineering model (CLEM) thermal model final report, NLR-TR-2001-033, 2001.
77 Mastenbroek, O., Two-Phase Thermal Control System for a Phased Array Radar Module, NLR CR 97287, I & II, 1997.
78 Delil, A.A.M., Sänger-related thermal research, NLR CR 90001, 1990.
79 Mastenbroek, O., FEI blanket in-plane permeability measurement test report, NLR CR 95581, 1995.
80 Donk, G. van, Self regulating heater test and evaluation report, NLR CR 95603, 1995.
81 Hauser, A., Posselt, W., Delil, A.A.M., Kalle, S., Flexible Thermal Link, Executive Summary Report, 1997.
82 Hauser, A., Posselt, W., Delil, A.A.M., Kalle, S., Flexible Thermal Link, Final Report, 1997.
83 Hufenbach, B., et al., Comparative assessment of gauging systems and description of a liquid gauging concept for a spin-stabilised spacecraft, ESA-SP-398, 2nd European Spacecraft Propulsion Conf., Noordwijk, Netherlands, 1997, 561-570.
84 Delil, A.A.M., Characterisation of the dielectric properties of Mixed Oxides of Nitrides and Mono Methyl Hydrazine, NLR CR 97268, 1997.
85 Delil, A.A.M., Characterisation of the dielectric properties of the propellants MON & MMH, NLR TP 97503, AIP Proc. 1st Conference on Orbital Transfer Vehicles, Space Technology & Applications Int. Forum, Albuquerque, USA, 1998.
86 Heemskerk, J.F., Consultance for FHTS upgrade, NLR CR 95261, 1995.
87 Mastenbroek, O., Thermal modelling of a laser head, Final Report, NLR CR 97084, 1997.
88 Heemskerk, J.F., Thermal management and temperatures distribution, PH9420 NLR, 1994.
89 Es J. van, Knobbout, H.A., Veldman, S.M., Modelling of Transient Environmental Heat Load on the ALADIN Instrument in an Arbitrary ISS-Related Orbit, NLR-TP-2000-264, SAE-2000-01-2523, Proc. 30th Int. Conf. on Environmental Systems & 7th European Symp. on Space Environmental Control Systems, Toulouse, France, 2000.
90 Heemskerk, J.F., EUCLID report on thermal performance of components, RTP 4.1 Doc. 09.9.3.1.1-D-02-NLR, 1995.
91 Heemskerk, J.F., EUCLID report on thermal modelling issues, 09.9.3.1-D-01-NLR, 1991.
92 Heemskerk, J.F., EUCLID report on thermal design: Approach & preliminary calculation results, RTP 9.3. TR5420.1, TR6420.1, TR7420.1, 1977.
93 Es, J. van, Heemskerk, J.F., EUCLID report on thermal design: Final Report Thermal Analysis F1-band Antenna (TR

5420.3), F2-band Antenna (TR 6420.3), Dual-band Antenna (TR 7420.3), 1999.

94 Es, J. van, EUCLID report on thermal design: Executive Summary Thermal Analysis F1-band Antenna (TR 5420.4), F2-band Antenna (TR 6420.4), Dual-band Antenna (TR 7420.4), 1999.

95 Es, J. van, EUCLID RES 9.7-3218-2.1 EUCLID RTP 9.7 Report, Final report on thermal design, and Report, Final report on Thermal technology sample issue 1, 2001.

96 Delil, A.A.M., Unresolved Issues in Aerospace Heat Transfer, Panel Keynote, Intersociety Mechanical Engineering Conference and Exhibition, Anaheim, USA, 1997.

97 Delil, A.A.M., Research on Space-Related Heat and Mass Transfer Problems, Keynote paper, 11th Int. Heat Transfer Conf., Kyongju, Korea, 1998.

98 Delil, A.A.M., Unsolved Aerospace Heat and Mass Transfer Research Issues for the Development of Two-Phase Thermal Control Systems for Space, NLR-TP-99353, Int. Workshop Non-Compression Refrigeration & Cooling, Odessa, Ukraine, 1999, 21-42.

99 Delil, A.A.M., Thermal-Gravitational Modelling, Scaling and Flow Pattern Mapping Issues of Two-Phase Heat Transport Systems, Conf. on Applications of Thermophysics in Microgravity and Breakthrough Propulsion Physics, AIP Conf. Proc. 458, Space Technology & Applications Int. Forum, Albuquerque, USA, 1999, 761-771.

100 Delil, A.A.M., Some Critical Issues in Developing Two-Phase Thermal Control Systems for Space, NLR-TP-99354, Proc. 11th Int. Heat Pipe Conference, Tokyo, Japan, 1999, Vol.3, Keynote and Invited Lectures, 61-79.

101 Delil, A.A.M., Microgravity Two-Phase Flow and Heat Transfer, NLR-TP-99429, Chapter 9 of Fluid Physics in Microgravity, (Monti, R., Ed.), Overseas Publ. Associates, Reading UK, 2001.

102 Delil, A.A.M., Fundamentals of Gravity Dependent Two-Phase Flow and Heat Transfer – A Tutorial, AIP Proc. Conference on Thermophysics in Microgravity, Space Technology and Applications International Forum, Albuquerque, USA, 2001, 209-220.

103 Delil, A.A.M., Thermal-Gravitational Modelling and Scaling of Two-Phase Heat Transport Systems from Micro-Gravity to Super-Gravity Levels, AIP Conference Thermophysics in Microgravity, Space Technology and Applications International Forum, Albuquerque, USA, 2001, 221-229.

104 Delil, A.A.M., Research Issues on Two-phase Loops for Space Applications, Proc. Japan Symp. Space Flight Mechanics, Sagamihara, Japan, NLR-TP-2000-702, 2000.

105 Delil, A.A.M, Novel Two-Phase Thermal Control Activities at NLR: AMS-2 & CIMEX-3, Proc. 12th Annual Spacecraft Thermal Control Technology Workshop, El Segundo, USA, 2001.

106 Legros, J.C, Delil, A.A.M., Cerisier, P., Stephan, P., Convection and Interfacial Mass Exchange, Proc. ESA First symposium on Microgravity Research & Applications in Physical Sciences and Biotechnology, Sorrento, Italy, 2000.

107 Delil, A.A.M., CIMEX-3, a versatile two-phase loop experiment on ISS – Rationale and relation to other CIMEX experiments, NLR-TP-2000-702, 2000.

108 Delil, A.A.M., Extension of Thermal-Gravitational Modeling & Scaling of Two-Phase Heat Transport Systems to Super-Gravity Levels and Oscillating Heat Transfer Devices, Special Keynote Lecture, 6th Int. Heat Pipe Symposium, Chiang Mai, Thailand, 2000, 491-513, and ESA Proc. Two-Phase 2000 Workshop, Noordwijk, Netherlands, 2000.

109 Delil, A.A.M., Thermal-Gravitational Modelling and Scaling of Heat Transport Systems for Applications in Different Gravity Environments: Super-Gravity Levels & Oscillating Heat Transfer Devices, NLR-TP-2000-213, SAE-2000-01-2377, Proc. 30th Int. Conference on Environmental Systems & 7th European Symp. on Space Environmental Control Systems, Toulouse, France, 2000.

110 Es, J. van, Woering, A.A., High-Acceleration Performance of the Flat Swinging Heat Pipe, NLR-TP-2000-265, SAE-2000-01-2376, Proc.30th Int. Conf. on Environmental Systems & 7th European Symp. on Space Environmental Control Systems, Toulouse, France, 2000.

111 Delil, A.A.M., Issues of Various Two-Phase Heat Transfer Devices in Gravity Environments Ranging from Micro-Gravity to Supergravity, NLR-TP-2000-612, 2000.

112 Delil, A.A.M., Modelling and Scaling of Oscillating or Pulsating Heat Transfer Devices Subjected to Earth Gravity and to High Acceleration Levels, AIP Proc. Conf. on Thermophysics in Microgravity, Space Technology and Applications Int. Forum, Albuquerque, USA, 2001, 230-240.

113 Delil, A.A.M, Pulsating & Oscillating Heat Transfer Devices in Acceleration Environments from Micro-Gravity to Super-Gravity, NLR-TP-2001-001, SAE 2001-01-2240, Proc. 31st Int. Conf. on Environmental Systems, Orlando, USA, 2001.

114 Delil, A.A.M, Pulsating & Oscillating Heat Transfer Devices in Acceleration Environments Ranging from Micro-Gravity to Super-Gravity, A review of research results presented in literature, Assessment of commonalities & differences, A baseline to compare experimental data, Development of a versatile test set-up, Experiment programme definition, NLT-CR-2001-299.

115 Vreeburg, J.P.B., Still in space - The Wet Satellite, ELGRA Ann. Meeting, Zürich, Switzerland, 1987.

116 Vreeburg, J.P.B., Versteeg, M.H.J.B., Sloshsat - Preliminary design of the payload subsystem, NLR CR 95044, 1995.

117 Vreeburg, J.P.B., Dynamics and control of a spacecraft with a moving pulsating ball in a spherical cavity, IAF 96-A.603, Int. Astronautical Federation Congr., Beijing, China, 1996.

118 Vreeburg, J.P.B., Woerkom P.Th.L.M. van, Preparing for liquid motion experiments in space: Sloshsat mini-spacecraft

dynamics and control, NLR-TP-99570, 42nd Space Science and Technology Conference, Tokyo, Japan, 1998.
119 Vreeburg, J.P.B., Acceleration measurements on Sloshsat FLEVO for liquid force and location determination, NLR-TP-2000-062, 4th ESA International Conference on Spacecraft Guidance, Navigation and Control Systems, Noordwijk, Netherlands, 1999.
120 Vreeburg, J.P.B., Diagnosis of water motion in the Sloshsat FLEVO tank, NLR-TP-2000-061, IAF-99-J2.04, 50th Int. Astronautcial Congress, Amsterdam, Netherlands, 1999.
121 Vreeburg, J.P.B., Simulation of liquid dynamics onboard Sloshsat FLEVO, NLR-TP-99236, Proc. Space Technology & Applications Int. Forum, Albuquerque, USA, 1999, 836-841.
122 Vreeburg, J.P.B., Analysis of the data from a distributed set of accelerometers, for reconstruction of set geometry and its rigid body motion, NLR-TP-98343, Proc. Space Technology & Applications Int. Forum, Albuquerque, USA, 1999, 496-509.
123 Prins, J.J.M., Sloshsat FLEVO facility for liquid experimentation and verification in orbit, NLR-TP-2000-630, IAF-00-J2.05, 51th Int. Astronautical Federation Congress, Rio de Janeiro, Brazil, 2000.
124 Vreeburg, J.P.B., Woerkom P.Th.L.M. van, Momentum control of liquid-fuelled service vehicles, NLR-TP-2000-586, IAF-00-A.610, 51th Int. Astronautical Congress, Rio de Janeiro, Brazil, 2000.
125 Vreeburg, J.P.B., Identification of the geometry of accelerometers in an arrangement, NLR-TP-2000-585, IAF-00-J5.7, 51th Int. Astronautical Congress, Rio de Janeiro, Brazil, 2000.
126 Vreeburg, J.P.B., Veldman A.E.P., Transient and sloshing motions in an unsupported container, in Physics of Fluids in Microgravity, Monti, R.(ed.), Gordon and Breach Academic Publishers, 2001.
127 Vreeburg, J.P.B., Chato, D.J., Models for liquid impact onboard Sloshsat Flevo, NLR-TP-2000-584, 2000.
128 Da Riva, I., Vreeburg, J.P.B., High Temperature Facility Technology Study, WP9000, Combustion experiment instrumentation, Final Report, 1990.
129 Vreeburg, J.P.B., Krinkels, M.C.J.M., Heemskerk, J.F., Delil, A.A.M., Concept of an acoustic method for particle tracking in opaque liquids, NLR CR 89333, 1989.
130 Vreeburg, J.P.B., Method for flow field mapping in opaque liquids, NLR CR 89082, 1989.
131 Vreeburg, J.P.B., Delil, A.A.M., Huijser, R.H., Assem, D. v.d., Fluid Physics Instrumentation Study, Final Report, Vol. I to IV, ESA CR(P)2133, 1985.
132 Assem, D. v.d., Huijser, R.H., Vreeburg, J.P.B., On the development of an optical diagnostic instrument for fluid physics research in microgravity, NLR MP 86079 U, J. Phys. E: Sci. Instr., 20 (1987), 992-1000.
133 Assem. D. v.d., Huijser, R.H., Da Riva, I., Vreeburg, J.P.B., A preliminary study of a fluid science laboratory for space station (Columbus), Final Report, Vol. I to IV, NLR TR 87023, 1987.
134 Kramer, A.J., et al., Concepts for optical diagnostic instrumentation in facilities for micro-g fluid science, NLR TP 95362, 9th European Symposium on Gravity Dependent Phenomena in Physical Sciences, Berlin, Germany, 1995.
135 Kramer, A.J., Assem, D. van den, Container based automated microscope, NLR CR 94071, CR 95211-95216, 1994, 1995.
136 Assem, D. v.d., Optical diagnostics for protein crystallization in space, NLR CR 92120, 1992.
137 Assem, D. v.d., High Performance Capillary Electrophoresis in ARMADE, NLR CR 91468, 1991.
138 Assem, D. v.d., Benthem, R.J. v., Casteleijn, A.A., Development of a biomass sensor. Dual ratio versus transmission trade-off, NLR-TR-99444, 1999.
139 Assem, D. v.d., Benthem, R.J. v. Casteleijn, A.A., Self compensating real-time biomass sensor, NLR-TP-2000-433, Proc. ESA First symposium on Microgravity Research & Applications in Physical Sciences and Biotechnology, Sorrento, Italy, 2000, 1053-1059.

APPENDIX

The presentation focuses particularly on the following issues (Some relevant figures are given in the following three pages):

- Thermal conductance of loaded rotating bearings in vacuum.
- The thermal performance of multilayer insulation blankets.
- VCHP modelling and the modelling results.
- The results of the similarity (π-numbers) approach for the thermal/gravitational scaling of two-phase systems for micro-gravity, reduced-gravity, and hyper-gravity applications in aerospace.
- Constitutive equations for annular two-phase flow and heat transfer, predictions for condensation.
- ATLID and HELPD condensers, CLEM.
- In-orbit technology demonstration: TPX & LHPFX.
- Two-phase flow pattern aspects.
- Oscillating/pulsating heat transfer devices.
- The AMS-2 Tracker mechanically pumped two-phase CO_2 thermal control loop.
- CIMEX-3: Versatile two-phase loop experiments on ISS.

Test Rig to Measure the Thermal Conductance of Rotating Bearings (In Vacuum)

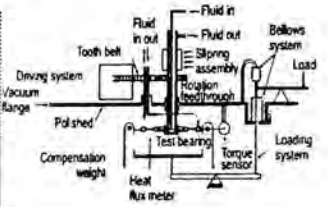

MLI Blanket Test Rig

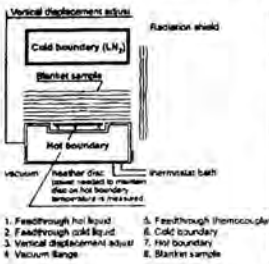

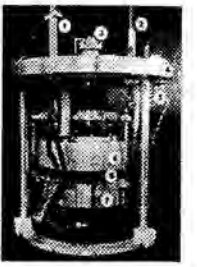

Dimension Analysis & Similarity Considerations

π-number relevance for thermal-gravitational scaling of two-phase loops

	Liquid Pump		Evaporator (Wick & Capillary)	Non-Liquid Lines (Vapour/2-Phase)	Condenser
	Adiabatic	Heating/Cooling			
π_1 = D/L – geometry	•	•	•	•	•
π_2 = Re = $(\rho u D_h)/\mu$ – inertia/viscous	•	•	•	•	•
π_3 = Fr = U^2/gD_h – inertia/gravity	•	•	•	•	•
π_4 = Eu = $\Delta p/\rho U^2$ – pressure/inertia	•	•	•	•	•
π_5 = Bo = Bond number with respect to g	•	•	•	no	•
π_6 = f – depletion = v_w/v_l			•	•	•
π_7 = density ratio = ρ_v/ρ_l			•	•	•
π_8 = viscosity ratio = μ_v/μ_l			•	•	•
π_9 = We = $(\rho u^2 D)/\sigma$ – inertia/surface tension			•	no	•
π_{10} = Pr = $(\mu C_p)/k$		•	•	•	•
π_{11} = Nu = $(hD)/k_l$ – convective/conductive		•	•	•	•
π_{12} = k_v/k_l – thermal conductivity ratio			•	•	•
π_{13} = C_{pv}/C_{pl} – specific heat ratio			•	•	•
π_{14} = $\Delta H/h_{fg}$ – enthalpy number (= h_{fg} quality)		•	•	•	•
π_{15} = $Mo_l = [g\mu_l^4(\rho_l-\rho_v)]/\rho_l^2\sigma^3$ – capillarity/buoyancy			•	•	•
π_{16} = $Ma = \sqrt{2}Bo\,Ja^2$			•	•	•
π_{17} = $(h_{fg}\rho_v\rho_l)^2$			•		•
π_{18} = $L_{ch}/\rho_l h_{fg}(\rho_l-\rho_v)$			•		•

Consequences of Similarity Approach for Applications of Thermal-Gravitational Scaling (for MPL/CPL/LHP/VPDL)

- *Geometric or fluid to fluid scaling at same g-level , and from earth-g to the reduced g-levels of Mars & Moon*
- *Hybrid scaling from earth-g to micro-g and super-g*
- *Support of (CIMEX) experiments on to determine boiling and condensation trajectories in flow pattern maps*

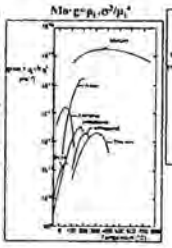

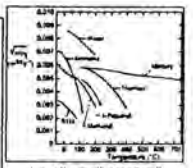

$$(\alpha/\rho_l)^{1/4} = D\cdot g^{1/4}\cdot(We/Fr)^{1/4}$$

(Up-)Flow Patterns in Heated Circular Tube and Measurement Issues for CIMEX-3

Optical observation of two-phase flow patterns in the

- *condenser*
- *swirl tube evaporator*
- *adiabatic section*

Instrumentation

- *IR cameras for observing the condenser and the evaporator*
- *CCD camera to observe the vapour line*
- *Observing the vapour line by holographic interferometry*

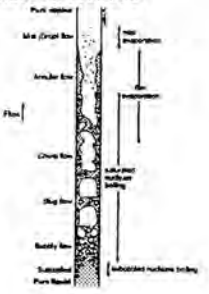

Flow Pattern Issues

Qualitative aspects of pressure gradient for various flow patterns

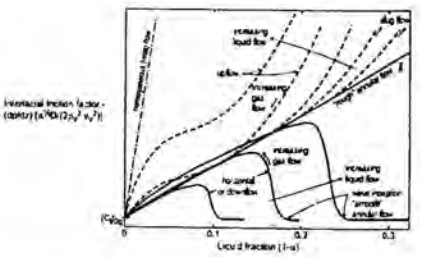

Flow Pattern Issues : Generalised Qualitative Two-Parameter Flow Regime Map for Horizontal Tube Condensation

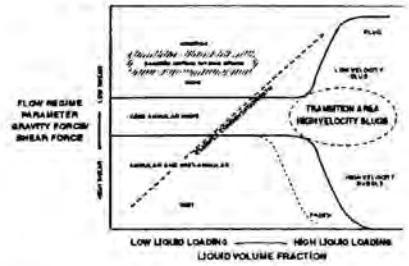

Constitutive Equations for Annular Two-Phase Flow & Heat Transfer

- *Total Pressure Gradient* $(dp/dz)_t = (dp/dz)_f + (dp/dz)_m + (dp/dz)_g$
  - *friction* $(dp/dz)_f = -(32m^2/\pi^2\rho_l D^5)(0.046)(Re_{lo})^{-0.2}[(1-X)^{1.8} + 0.4Re_{lo}^{-0.2}(1-X)^{0.8}X^{1.9} + 0.63Re_{lo}^{-0.4}X^2(1-X)^{0.8}(\rho_l/\rho_g)^{0.5}]$
  - *momentum* $(dp/dz)_m = -(32m^2/\pi^2\rho_l D^5)[(d/dz)[(1-X)^2/(1-\alpha)] + (d/dz)[X^2/\alpha(\rho_l/\rho_g)^{0.5}]]$
  - *gravity* $(dp/dz)_g = (32m^2/\pi^2\rho_l D^5)[(1-[1+(\rho_l/\rho_g)^{2/3}(1-X)/X]^{-1})\sin\theta\, D^2/8$ (horiz) $(\rho_l-\rho_{ac})/32m^2]$
- *Void - Quality Relation* $(1-\alpha)/\alpha = S(\rho_g/\rho_l)X/(1-X)$
- *Simplified Zivi-Correlation for Slip Factor* $S=(\rho_l/\rho_g)^{1/3}$
- *Condensation Heat Transfer* linear $X=1-z/L_c$ or more realistic $\dot{m}h_{lg}(dX/dz) = -\pi dD[T(z)-T_s]$
- $h = 0.018(k_l\rho_l^{1/3}D^{1/3}/\mu_l)Pr_l^{0.65}[(4\mu/dz)/\rho^{1/3} = R(4\mu_l/D)Re_l[1+(\rho_l/\rho_g)^{2/3}(1-X)/X)]$ and $0<R<1$
- *Combination Yields* $F(dX/dz, X) = 0 \rightarrow X(z)$ & Δp_t by integrating $(dp/dz)_t dz$ from 0 to L_c

Pressure Gradient Constituents Gravity-Assist & Anti-Gravity Issues

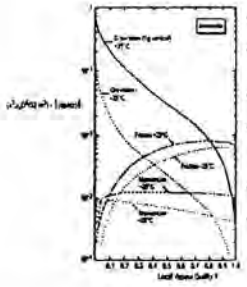

- *Impact of gravitation is smaller at lower temperature.*
- *Anti-g constituent overwhelms other gradients, below X=0.76 at 25 °C and X=0.38 at -25 °C.*
- *Annular liquid layer breaks/ falls back below these qualities.*
- *Shear-governed flow becomes (pulsating) slug, plug or churn flow, described by different equations and slip factors.*
- *Driving pressure (temperature) drops will strongly increase.*
- *(Anti-g) flow pattern maps are to be created.*

Gravity Dependent Condensation Lengths

Vapour quality along the reference duct

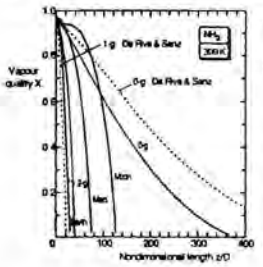

- *Condensation lengths needed considerably increase with decreasing gravity.*
- *Differences between condensation lengths at different gravity levels become less pronounced with decreasing temperature and line diameter, increasing power, and heat transfer coefficient fine-tuning or enhancement. This coefficient, which varies along the condensation trajectory through the various flow patterns, is to be derived from experiments in different gravity environments.*

ATLID Two-Phase Heat Transport System

Hybrid CPL-LHP with Two Different Parallel Direct Condensers/Radiators (MMS, NLR,BE)

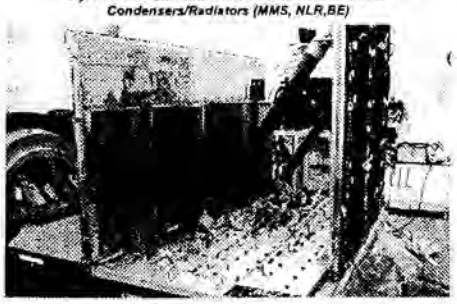

Breadboard Condenser IR Pictures to Verify Theoretical Predictions

High Efficiency Low Pressure Drop Condenser

- *Series configuration*
- *Two-phase flow in annular tube*
- *Liquid cooling in inner tube*

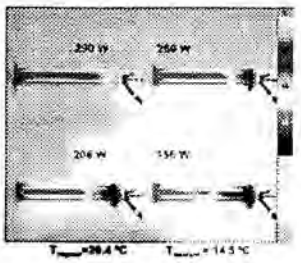

Schematics of TPX I & II

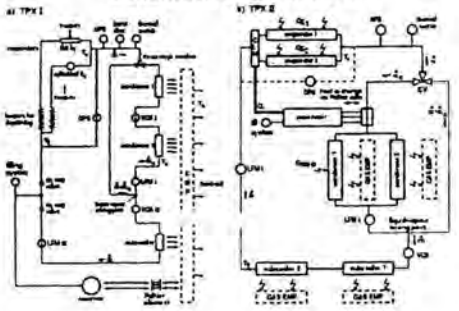

TPX I Flight Hardware

Flow Pattern Maps to be Created for Gravity Levels from Micro- to Super-G

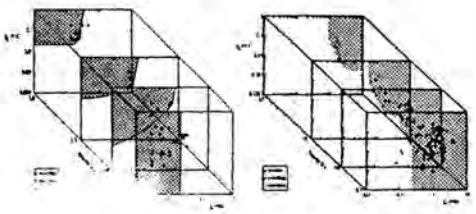

Flow *θ-dependent 3-D annular flow*

Partly Contradicting Low-G Flow Pattern Data

(Because of Different Line Dianeters, Fluids or G-Levels?)

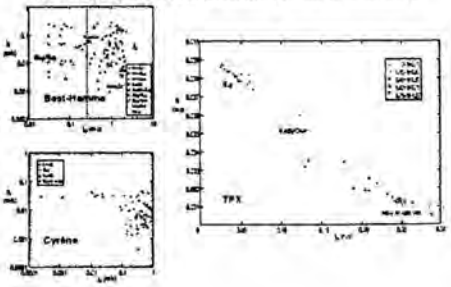

Alpha Magnetic Spectrometer on ISS

(Search for Anti-Matter, Dark & Lacking Matter)

Configuration & Tracker Two-Phase CO_2 MPL

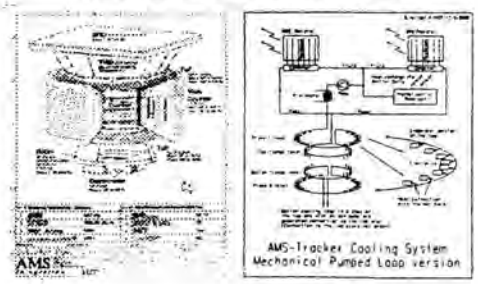

CIMEX-3

Versatile Two-Phase Loop Baseline

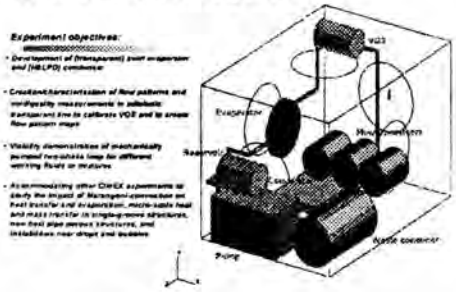

HEFAT 2002
1ST International Conference on Heat Transfer, Fluid Mechanics and Thermodynamics
8-10 April 2002, Kruger Park, South Africa
KD1

CORRELATING FLOODING DATA FOR COUNTECURRENT GAS-LIQUID FLOW IN INCLINED AND VERTICAL DUCTS

D.G. Kröger
Department of Mechanical Engineering
University of Stellenbosch
Private Bag X1, Matieland 7602
Stellenbosch
South Africa

ABSTRACT

Reference is made to various experimental investigations into adiabatic gas-liquid counterflow in inclined and vertical ducts as well as different flooding correlations that have been proposed in the past. These correlations appear to be applicable in certain cases but often fail to correlate the data of other investigators. It is shown that the proposed method of correlation, consisting of a combination of the phase Froude numbers and the Ohnesorge number succeeds in correlating the data of numerous studies.

1. INTRODUCTION

During countercurrent flow in ducts or tubes when liquid drains downwards against the walls under the action of gravity and there is upward gas flow, a transition to partial or complete upward liquid flow occurs at sufficiently high gas flow rates.

Flooding forms part of this transition. The flooding phenomenon is encountered under a variety of conditions in reflux condensers, packed columns, heat pipes and certain nuclear reactor accident scenarios and has been the subject of numerous investigations in the past. The present paper discusses the findings of experimental investigations of the effect of the fluid properties and the duct geometry and inclination on flooding. The flooding data is based on the definition originally published by Hewitt and Hall-Taylor [1]. The definition is briefly described in the next paragraph.

Consider the vertical tube shown in Fig.1. Liquid is injected into the tube at a constant rate through a porous section and is extracted smoothly at the bottom. At low gas flow rates a falling film exists [Fig. 1(a)]. As the gas flow is gradually increased, a rate is reached where the film becomes more wavy and eventually liquid is carried upwards as shown in Fig. 1(b). Liquid is now transported above the injection point and a flow pattern exists where climbing and falling film flow are occurring simultaneously as depicted in Fig.1(c) and (d). The transition from pure counterflow to simultaneous liquid up- and downflow [Fig. 1(b)] is defined as flooding while the steady-state conditions in Fig.1(c) and (d) are referred to as partial liquid delivery. With a further increase in the gas flow rate the liquid flow below the injection point changes to climbing film flow [Fig. 1(e)] and eventually all the liquid is carried upwards [Fig.1(f)].

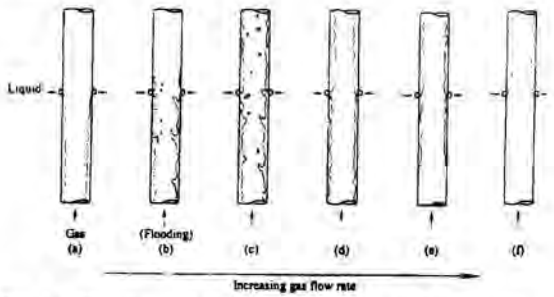

Fig. 1. Flow transitions from countercurrent flow to cocurrent upflow in vertical tubes.

Once flooding has occurred the liquid above the porous inlet does not necessarily proceed to leave the test section. In the case of low liquid flow rates it may form a hanging film above the porous inlet without a net upward flow, as described by Govan et al. [2]. At higher liquid flow rates flooding causes a direct transition from pure countercurrent flow to a state of partial liquid delivery, resulting in net upward flow of liquid (Clift et al., [3]; Suzuki and Ueda, [4]; Govan et al., [2]). Consequently a marked decrease in the liquid downflow rate is experienced. Note that depending on the gas inlet geometry, some liquid may be carried above the porous section in the form of entrained droplets prior to the condition depicted in Fig. 1(b). This is not regarded as flooding (Whalley and McQuillan, [5]; Govan et al., [2]).

The effect of the liquid properties on flooding has been addressed by a number of researchers, e.g. Feind [6], Clift et al. [3], Suzuki and Ueda [4] and Chung et al. [7] to mention a few.

More recently Zapke and Kröger [8] published flooding results where the emphasis of the investigation was on the effect of both the gas and the liquid properties.

Little has been published so far on counterflow in inclined ducts compared to the extensive information available on two-phase flow in vertical tubes. Lee and Bankoff [9, 10] investigated steam-water counterflow in an inclined channel. The flooding steam velocity was the lowest for the smaller inclination angles and increased with an increase in inclination up to approximately 30°. For 31° and 87° the flooding steam velocities were approximately equal. The same trend was found by Barnea et al. [11] who conducted air-water experiments in a 51 mm plexiglass tube. More extensive tests were conducted by Zapke and Kröger [12] to determine the effect of the duct inclination on flooding. In the following section their apparatus and experiments will be discussed in greater detail.

2. APPARATUS AND EXPERIMENTAL PROCEDURE

The configuration of inclined air-cooled reflux condensers was followed as a guideline to design an experimental apparatus. Such reflux condensers are employed as secondary condensers or dephlegmators in the power industry where the turbine exhaust steam is condensed at sub-atmospheric pressures inside finned tubes. The finned tube profile can be round, elliptical or flattened. The lower ends of the finned tubes are welded into a tube sheet to form a square-edged vapour inlet. During total reflux condensation the phase velocities are the highest at this location. Flooding is therefore most likely to occur as a result of strong phase interaction at the square-edged gas or vapour inlet. For this reason a square-edged gas inlet was employed and the liquid inlet plenum was designed to prevent the introduction of flow disturbances at the liquid feed.

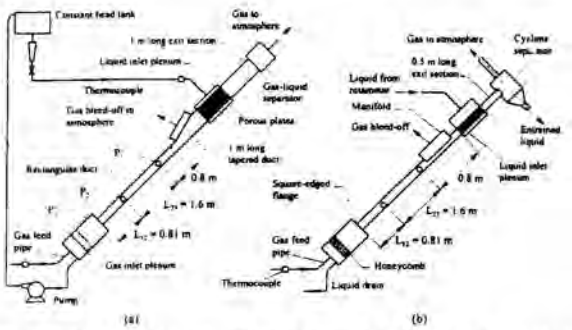

Fig. 2. (a) Schematic of the flow loop and test section configuration employed for pressure drop measurements in inclined ducts. (b) Test section configuration for flooding. No gas was bled off in the case of vertical flooding tests.

2.1 FLOW LOOP

A schematic of the flow loop is shown in Fig. 2(a). The liquid flow, supplied by a constant head tank, is monitored by calibrated rotameters. It enters the duct through a porous section, drains downwards and subsequently enters the gas inlet plenum at the square-edged flange. A pump circulates the liquid back to the constant head tank. Three standard orifice plates differing in size are employed to achieve the desired range of metered gas flow. The gas flows via an inlet plenum into the test section. The gas inlet plenum is constructed of a 0.72 m long and 0.286 m i.d. glass cylinder to enable visualisation of the draining liquid at the square-edged flange. A honeycomb section and a mesh are employed to dampen out local high velocities and to obtain a uniform velocity profile to the square-edged flange.

Water, methanol, propanol, air, helium, hydrogen and argon were used as working fluids. The exit of the test section was open to the atmosphere and hence the test pressure was just above the ambient pressure. The fluid temperature was close to the ambient temperature, i.e. ≈ 25°C. The fluid properties at the ambient conditions are given in Table 1.

Table 1.
Properties at ambient conditions ($p \approx 101.325$ N/m^2, $T \approx 295$ K) of the fluids that were used for the experimental investigation.

Fluid	Density (kg/m^3)	Viscosity x 10^6 (kg/ms)	Surface tension x 10^3 (N/m)
Air	1.196	18.230	-
Argon	1.650	22.390	-
Helium	1.653×10^{-1}	20.040	-
Hydrogen	8.325×10^{-2}	8.863	-
Water	998	958	72
Methanol	791	575	22
Isopropanol	784	2363	22

The duct profiles tested are shown in Fig. 3(a). Fig. 3(b) illustrates a typical duct assembly. Two transparent acrylic plastic sheets bolted to grooved aluminium spacers form the duct walls. Three duct heights of 50, 100 and 150 mm and two widths of 10 and 20 mm were investigated.

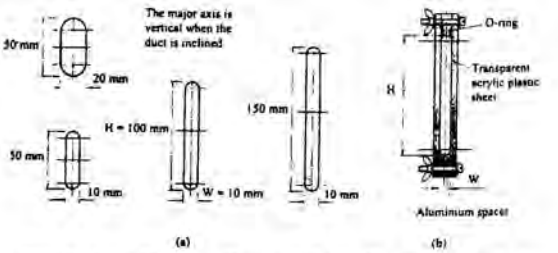

Fig. 3. (a) Duct profiles tested. (b) Cross-sectional view of the duct assembly

2.2 TEST SECTION CONFIGURTION FOR PRESSURE DROP MEASUREMENTS IN INCLINED DUCTS

The change in static pressure across the square-edged flange was measured between P_1 and P_2 as indicated in Fig.2(a), where the pressure tapping point P_1 is located inside the gas inlet plenum and P_2 is located at a distance of 0.81 m above the square-edged flange. The pressure gradient experienced by the gas flow inside the duct in the presence of the draining liquid was obtained by measuring the pressure drop over a distance of 1.6 m between P_2 and P_3. The aim of these measurements was to generate pressure gradient data for counterflow in the absence of any flow disturbances introduced in the process of feeding liquid into the test section. For this purpose a tapered duct was inserted between the constant cross-sectional area test section and the porous inlet. The tapered duct acts as diffuser to slow down the gas velocity and thus prevents the liquid flow from being disturbed as it enters through the porous plates.

The porous section inside the liquid inlet plenum was constructed similarly to the duct depicted in Fig. 3(b), except that the acrylic plastic sheets were replaced by sintered bronze plates over a length of 260 mm. The inside height of the porous section was 185 mm. In the case of the 100 and 150 mm ducts the increased flow area at the porous plates proved to be insufficient to allow for the development of a smooth stratified liquid layer in the tapered section. Holes were therefore drilled into the acrylic plastic walls along the top of the tapered duct to allow part of the gas to escape before reaching the sintered plates.

During an experimental run the liquid flow was set at a predetermined rate while pressure drop measurements were conducted for various gas flow rates. The lowest gas flow rates tested correspond to a Reynolds number of approximately 500. The gas flow was allowed to stabilise, data were recorded and the gas flow rate was increased for the routine to be repeated, until flooding occurred.

2.3 TEST SECTION CONFIGURATION FOR FLOODING EXPERIMENTS IN INCLINED AND VERTICAL DUCTS

The entire configuration illustrated in Fig. 2(a) is 7 m long and its maximum inclination is limited to $\approx 60°$ to the horizontal by the laboratory roof. To conduct flooding experiments for inclinations from near horizontal to the vertical the apparatus was shortened by removing the tapered duct and mounting the 3.21 m long constant cross-sectional area test section directly onto the liquid inlet plenum as shown in Fig. 2(b). Holes were again drilled into the duct walls along the section between pressure tapping point 3 and the liquid inlet plenum to bleed-off part of the gas before reaching the porous plates. This ensured that flooding was caused by the gas-liquid interaction at the square edged gas inlet, i.e. at the lower end of the duct.

Note that the flooding gas velocity was defined in the introduction as the gas flow rate at which liquid begins to be transported above the point of liquid injection. In the present apparatus upward transport of liquid broke down inside the zone of gas bleed-off and liquid was therefore not always propelled beyond the porous inlet. Flooding was hence defined as the conditions when liquid is propelled into the gas bleed-off zone. This may however not be regarded as a new or different definition because strictly speaking the "liquid feed" is located just below the bleed-off zone where the fill gas flow rate is still present inside the test section. Thus the transport of liquid into the bleed-off zone constitutes flooding because "liquid has been carried above the point of injection".

Exactly the same configuration was used for the flooding experiments for vertical counterflow except that no gas bleed-off was employed. In this case the test section configuration resembles the schematic depicted in Fig. 1 and the definition by Hewitt and Hall-Taylor [1] could be followed to generate flooding data.

The fluid combinations, duct geometries and inclinations tested for flooding are summarised in Table 2.

Table 2. Summary of flooding experiments.

Duct Geometry	Duct inclination to the horizontal (°)	Fluid Combination
H = 50 mm	2,10,20,40,60,70,80,90	Air-water
W = 10 mm	2,5,10,15,20,60,80,90	Air-propanol
	60,90	Air-methanol
	60	Argon-water
	60	Helium-water
	60	Helium-methanol
	60	Hydrogen-methanol
H = 100 mm	2,20,40,60,70,80,90	Air-water
W = 10 mm	2,40,60,90	Air-propanol
	60,90	Air-methanol
H = 150 mm	2,20,40,60,90	Air-water
W = 10 mm	60,90	Air-propanol
	60,90	Air-methanol
H = 50 mm	2,5,10,20,40,60,70,80,90	Air-water
W = 20 mm		

3. EXPERIMENTAL RESULTS: FLOW PATTERNS

Upon the onset of phase interaction at the square-edged gas inlet three types of flow patterns, depending on the duct inclination, were observed: (i) roll waves at inclination close to the horizontal; (ii) a distinctive vortex-type flow at intermediate angles, and (iii) churn-type flow containing elements of the vortex flow in the case of vertical ducts.

3.1 FLOW PATTERNS OBSERVED AT A DUCT INCLINATION OF 60° TO THE HORIZONTAL

At low gas flow rates there is no phase interaction and the liquid drains in the form of an undisturbed jet into the bottom plenum. Inside the test section the flow is stratified. There is no entrainment and the duct walls are dry. The pressure gradient and the entrance pressure drop are equal to the corresponding air-only values. As the gas flow rate is increased, the jet inside the plenum experiences an upward deflection as a result of the drag exerted by the gas flow. Droplets are entrained at the square-edged flange and deposited on the duct walls just above the inlet flange. The gas-liquid interface along the duct is fairly smooth but small waves travelling downwards are present. Upon a further increase in the air flow rate the jet of liquid inside the plenum is dispersed causing entrainment. Eventually an air flow rate is reached where the liquid jet is sporadically sucked into the test section.

The conditions where the draining liquid is sporadically sucked into the duct is the onset of a distinctive vortex-type flow at the square-edged flange. The vortex is formed as a result of simultaneous liquid up- and downflow when liquid draining downwards at the bottom of the duct is swept upwards by the gas flow, giving rise to the rotating action. Initially the rotational motion is confined to a small region just above the inlet flange at which time the vortex size or "diameter" is only a fraction of the duct height. As the gas flow rate is increased the vortex grows in size. Close to flooding the "diameter" approaches the duct height, as illustrated in Fig. 4. Just below the flooding gas velocity the rotating gas-liquid mixture constituting a vortex disintegrates after it has travelled ≈ 1 m up the duct. At flooding such a vortex travels all the way upwards to the gas bleed-off zone where it collapses. The flow becomes very transient in nature once vortices are present and very strong pressure pulses are generated in the process of vortex formation and disintegration.

Fig. 4 Air-water flow patterns inside the 100 mm duct inclined at 60° to the horizontal. V_G = 19 m/s, $V_L = 9.2 \times 10^{-3}$ m/s, $Re_G = \rho_G V_G D_e/\eta_G = 22300$, $Fr_{HG} = 0.41$.

3.2 FLOW PATTERNS OBSERVED IN NEAR HORIZONTAL AND VERTICAL DUCTS

At duct inclinations close to the horizontal the component of the gravity force which has to be overcome for the accumulation of liquid at the gas inlet and the subsequent upward transport thereof is relatively small. The gas velocity required to cause flooding is therefore significantly lower compared to steeper inclinations and consequently the phase interaction is less intensive. At sufficiently high gas flow rates roll waves formed at the bottom end of the test section are propelled upwards. They either disintegrate gradually or grow to bridge the duct height in which case the roll waves are propelled to the top end of the test section to cause flooding.

During counterflow in vertical ducts the flow is annular prior to the onset of strong phase interaction, instead of being stratified as in the case of inclined ducts. In the absence of gas flow the liquid drains in the form of a wavy film down the acrylic plastic walls. As the gas flow is increased the liquid starts to concentrate at the aluminium spacers, i.e. at the short sides of the duct. At fairly low air velocities, approximately 3 m/s, liquid droplets are entrained at the square-edged flange. At sufficiently high gas flow rates the droplets are carried beyond the liquid inlet sinter. The formation of a rough oscillating film at the square-edged flange follows the onset of entrainment. The liquid draining into the bottom plenum along the aluminium spacers is sporadically sucked into the test section resulting in intermittent penetration. As the gas flow rate is further increased this region of churn-type flow grows until it reaches the sinter inlet. Liquid is then transported above the sinter in the form of churning flow and flooding occurs.

These observations are very similar to those by Govan et al. [2] and Zapke and Kröger [8] for vertical tubes with square-edged gas inlets, except that vortices could be observed in the rectangular ducts from time to time.

4. EXPERIMENTAL RESULTS: FLOODING

Consider Fig 5(a) showing air-water flooding data for a duct inclination of 60° to the horizontal. The figure presents the air superficial velocity at flooding for the four rectangular ducts tested. It is evident from Fig. 5(a) that the flooding gas velocity is strongly dependent on the duct height, experiencing an increase as the duct height increases. The trend can be explained in terms of the mechanism by which flooding occurs: When the size of a liquid vortex has grown at the inlet of the duct to obstruct the flow path of the gas, it is propelled upwards and liquid travels up past the injection point to cause flooding. The weight of the liquid contained in the vortex is proportional to the duct height and the density difference between the two phases. This weight must be overcome by the drag force exerted by the gas flow which is proportional to the momentum flux $\rho_G V^2_G$. The densimetric gas Froude number based on the

duct height, is a ratio of these two forces which successfully correlates the observed height effect as illustrated in Fig 5 (b).

$$Fr_{HG} = \frac{\rho_G V_G^2}{gH(\rho_L - \rho_G)} \quad (1)$$

ρ_G and ρ_L are the gas and liquid densities respectively while V_G is the superficial gas velocity and H is the duct height.

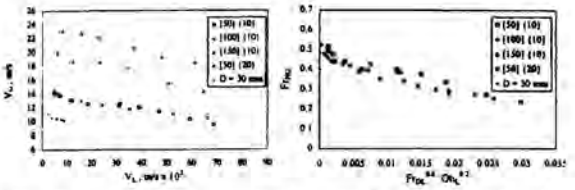

Fig. 5(a) Air-water flooding superficial velocities for rectangular ducts inclined at 60° to the horizontal. [H], mm; {W}, mm. The data for the D = 30 mm tube is taken from Zapke and Kröger [12]. (b) The data shown in Fig. 5(a) presented in a dimensionless form in terms of the densimetric Froude numbers and the Ohnesorge number.

The liquid Froude number

$$Fr_{DL} = \frac{\rho_L V_L^2}{gD_e(\rho_L - \rho_G)} \quad (2)$$

on the abscissa is based on the hydraulic diameter D_e. V_L is the superficial liquid velocity. Using different characteristic dimensions for the gas Froude number (height) and the liquid Froude number (hydraulic diameter) follows from the empirical approach to correlate the data. Attempts to correlate the data in terms of phase Froude numbers containing the same characteristic dimension or making use of a ratio of the duct height and width failed.

The Ohnesorge number [13]

$$Oh_L = \sqrt{\frac{\eta_L^2}{\rho_L D_e \sigma}} \quad (3)$$

forming part of the independent parameter on the abscissa is required to correlate the effect of the liquid properties on the flooding gas velocity. The role of the Ohnesorge number is discussed in more detail shortly. In Equation (3) σ is the surface tension and η_L is the liquid viscosity.

The duct height forming part of Fr_{HG} is critical to the correlation of the trend depicted in Fig. 5(a). Employing the hydraulic diameter in the gas Froude number fails to correlate this trend. The three ducts of 10 mm width have approximately equal hydraulic diameters and yet their flooding gas velocities differ significantly.

The Kutateladze number

$$Ku_G = \frac{\rho_G^{1/2} V_G}{\left[g\sigma(\rho_L - \rho_G)\right]^{1/4}} \quad (4)$$

frequently used in the literature to present flooding data also fails to correlate the predominant height effect. Ku_G is formed by substituting the length dimension in the Froude number with an equivalent characteristic dimension containing gravity, phase densities and surface tension. As a result the Kutateladze number does not contain a physical dimension and therefore cannot represent the physics of flooding observed in the present investigation.

Also shown in Fig. 5 (a) and (b) are flooding data by Zapke and Kröger [8] for air-water flow in a 30 mm i.d. tube with a square-edged gas inlet, inclined at 60° to the horizontal. In Fig. 5(b) the tube diameter is taken as the length dimension required in the gas Froude number. The correlation achieved is remarkable, implying that the height perceived by the vortex at flooding is the diameter. In other words the dimensionless groups given by Equations (1) and (2) successfully describe the geometry effect for both rectangular ducts and tubes when the height and diameter respectively are taken as the characteristic length dimension in the gas Froude number.

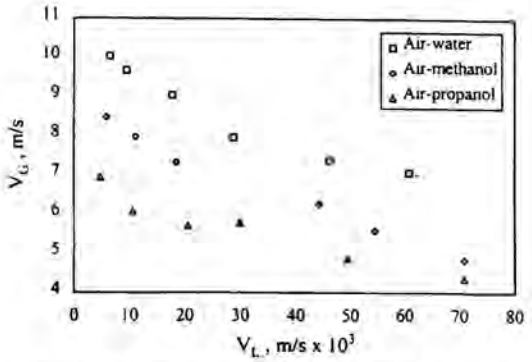

Fig. 6. Superficial velocities obtained with air-water, air-methanol and air-propanol to illustrate the effect of the liquid properties. H = 50 mm, W = 10 mm, θ = 90°.

Flooding data for air-water, air-methanol and air-propanol are shown in Fig 6. The tests were conducted with the 50 mm

duct (W = 10 mm) in the vertical position. The methanol and the propanal flood at lower gas velocities than water because of their lower densities. The fact that the propanol flooding gas velocities are lower than for methanol means that the flooding gas velocity decreases with an increase in the liquid viscosity. These two liquids have equal densities and surface tensions, while the propanol viscosity is approximately four times the viscosity of methanol. The difference in the gas flooding velocities for methanol and propanol is therefore purely a viscosity effect.

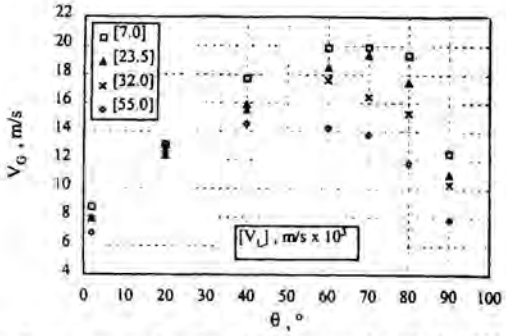

Fig. 7. Air-water flooding data measured with the 100 mm duct plotted against the duct inclination with the water flow rate as a parameter.

Air-water flooding data measured for various duct inclinations from close to the horizontal to the vertical are shown in Fig. 7. The flooding gas velocity increases with an increase in the duct inclination due to the increasing gravity component which has to be overcome in the direction of the gas flow. A maximum is reached in the range $60° < \theta < 70°$, where θ is the duct inclination to the horizontal. Above an inclination of 70° the flooding gas velocity decreases fairly sharply. The vertical ducts were found to flood at significantly lower velocities than for inclinations just off the vertical.

The effect of the duct height on the flooding gas velocity as depicted in Fig. 5(a) was observed for all the inclinations tested from close to the horizontal to 80°. In the case of counterflow in the vertical ducts, elements of churn-type flow and vortices were observed as described in Section 3.2. Here the height effect was not as pronounced as for inclined flow most probably because the vortex size did not reach the entire duct height during the churning flow. The relatively smaller vortex size partly explains the significant decrease in the flooding gas velocity experienced for a change in inclination from $\theta = 80°$ to 90°. A smaller vortex size implies the weight of the liquid contained in the vortex is less and thus a lower gas velocity is required for upward liquid transport. Furthermore the stabilising gravity component acting on the liquid film perpendicular to the duct axis vanishes as the inclination approaches the vertical. This contributes to the decrease in the flooding gas velocity.

5. FLOODING CORRELATIONS

The flooding data measured for vertical ducts is correlated by the relation

$$Fr_{HG} = \frac{0.0055}{Fr_{DL}^{0.2} Oh_L^{0.3}} \tag{5}$$

All the flooding data for vertical ducts are shown in Fig. 8 against the predicted values according to Equation (5). The majority of the data lie in a ± 15% band.

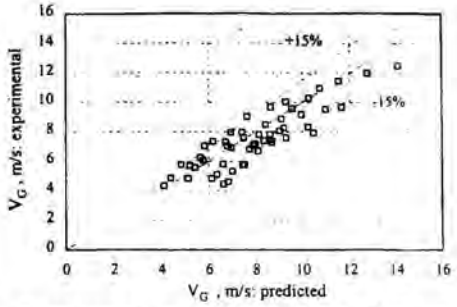

Fig. 8. Experimental versus the predicted flooding gas velocities according to Equation (5) for counterflow in vertical ducts.

The data for flooding in inclined ducts were found to correlate in terms of an exponential function

$$Fr_{HG} = K_0 \exp\left(-nFr_{DL}^{0.6} Oh_L^{0.2}\right) \tag{6}$$

where K_0 and n are functions of the duct inclination:

$$K_0 = 7.9143\times10^{-2} + 4.9705\times10^{-3}\theta + 1.5183\times10^{-4}\theta^2 - 1.9852\times10^{-6}\theta^3 \tag{7}$$

$$n = 1.8149\times10^{1} - 1.9471\theta + 6.7058\times10^{-2}\theta^2 - 5.3227\times10^{-4}\theta^3 \tag{8}$$

The flooding data measured for the inclined ducts as summarised in Table 2 are shown in Fig. 9 against the values predicted according to Equation (6). The measured values vary from as low as 5 m/s to a maximum of ≈45 m/s as a result of the wide range of dimensions, duct inclinations and fluid properties tested. The superficial velocities cover almost an

order of magnitude. According to Fig. 9 this wide range of velocities is correlated with an accuracy of ± 10%.

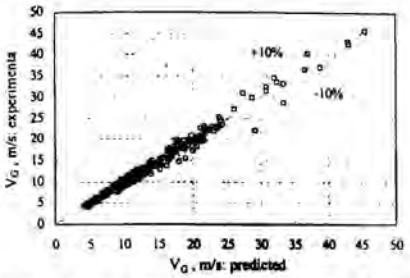

Fig. 9. Experimental versus the predicted flooding gas velocities according to Equation (6) for counterflow in inclined ducts.

6. ORIGINAL DATA/PROCESS THAT LED TO THE FROUDE-OHNESORGE NUMBER CORRELATION

During a systematic experimental program Zapke and Kröger [8, 14] investigated the effect of liquid properties on the gas flooding velocity in a vertical tube. By varying the alcohol content in an aqueous methanol solution, the viscosity, density and surface tension were varied. Five different solutions/liquids were tested, i.e. pure water, 8% methanol, 15% methanol, 28% methanol and pure methanol. Air was used as the working gas.

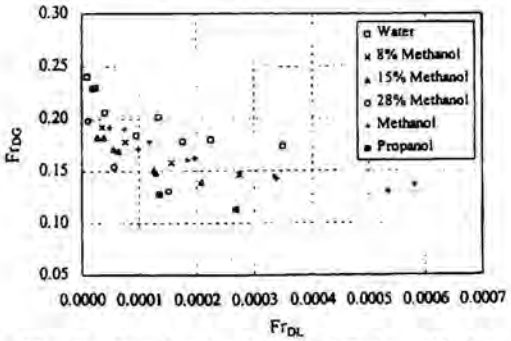

Fig. 10. Flooding data by Zapke and Kröger [8] plotted in terms of the densimetric phase Froude numbers for gas-liquid flow in a 30 mm i.d. vertical tube with a square-edged gas inlet. The percentage methanol indicates the percentage alcohol by volume of an aqueous methanol solution.

The flooding date are shown in Fig. 10. In Fig. 10 it can be seen the highest flooding gas Froude numbers were measured for pure water and pure methanol. As the percentage methanol increase, the gas Froude numbers decrease, reach a minimum and increase, for the pure methanol data to be approximately equal to the water data.

A dimensionless group that exhibits such a trend is the inverse of the Ohnesorge number defined by Equation (3). It is plotted in Fig. 11 for aqueous methanol solutions, against the percentage of methanol in the solution. Note the initial decrease, the minimum approximately midway and the subsequent increase as the percentage methanol varies from 0% to 100%, similar to the gas Froude number trend depicted in Fig. 11.

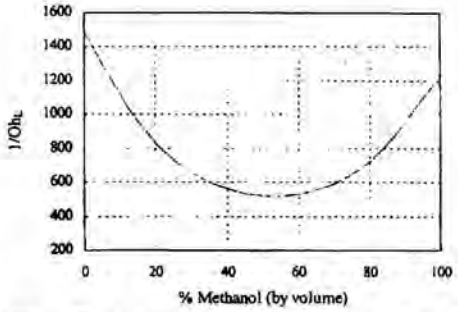

Fig. 11. The inverse of the Ohnesorge number plotted for aqueous methanol solutions. The Oh_L number is defined by Equation (3). The length dimension required is the diameter D = 30 mm.

Figs. 10 and 11 imply that the gas Froude number at flooding is some function of the liquid Froude number and the Ohnesorge number, i.e.

$$Fr_{DG} = f\left(Fr_{DL}, Oh_L\right) \qquad (9)$$

where the terms in parentheses form the independent parameter. Through a method of empirical correlation, it was found that the gas Froude number at flooding , is a function of the product $Fr_{DL}^{0.2}\, Oh_L^{0.3}$ in the case of vertical ducts and tubes. This independent parameter is introduced on the abscissa in Fig. 12 to illustrate the functional relationship proposed by Equation (9).

Note that the "minimum" exhibited in Fig. 10 does not mean that the flooding gas Froude number for a specific liquid (constant Ohnesorge number) goes to a minimum as the liquid Froude number increases. The trend under consideration is the variation of the Fr_{DG} for a constant Fr_{DL} as the Ohnesorge number is varied. In other words, Fr_{DG} for water (smallest Oh_L) is the highest, whilst Fr_{DG} for the 28% methanol solution (largest Oh_L) is lowest.

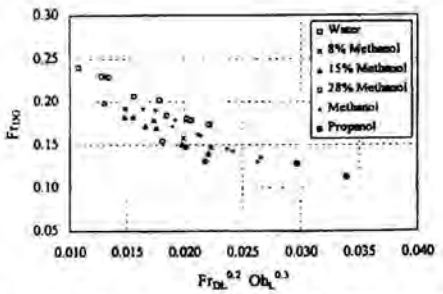

Fig. 12. The flooding data of Fig. 10 plotted against the independent parameter $Fr_{DL}^{0.2}Oh_L^{0.3}$

Also shown in Figs. 10 and 12 are two data points obtained with propanol. The two data points serve as an independent verification of the trend observed with the aqueous methanol solutions. Note the scaling effect that the Ohnesorge number has on the data of Fig. 12. The liquids with the highest Ohnesorge numbers flood at lower gas velocities. By introducing the Ohnesorge number the lowest flooding data are shifted to the right relative to the higher flooding gas Froude numbers, in order to achieve correlation.

7. DIMENSIONLESS GROUPS PREVIOUSLY USED FOR CORRELATING FLOODING DATA

Comprehensive information on empirical and theoretical flooding correlations has been published by McQuillan and Whalley [15] and Bankoff and Lee [16]. Dimensionless groups appearing in these publications other than those defined by Equations (1) and (2) are listed in Table 3.

Zapke and Kröger [8] have previously demonstrated in detail that flooding in vertical tubes is not related to the gas Reynolds number. It further implies that gas viscosity has no effect on the flooding fluid flow rates.

With reference to Table 3, the gas Reynolds number, the mass flux ratio and the viscosity ratio should therefore not be employed for the purpose of correlating flooding data.

The density ratio which has been used in the past for correlating flooding effectively forms part of the gas Froude number and is therefore eliminated as an independent parameter.

A widely known correlation for flooding is the Kutateladze correlation by Chung et el. [7]:

$$Ku_G^{1/2} + mKu_L^{1/2} = c_1 \tanh\left[c_2\left(Bo^{1/8}\right)\right] \qquad (10)$$

Ku_G and Ku_L are the gas and liquid Kutateladze numbers, i.e.

$$Ku_G = \frac{\rho_G^{1/2} V_G}{\left[g\sigma\left(\rho_L - \rho_G\right)\right]^{1/4}} \qquad (11)$$

$$Ku_L = \frac{\rho_L^{1/2} V_L}{\left[g\sigma\left(\rho_L - \rho_G\right)\right]^{1/4}} \qquad (12)$$

Bo is the Bond number and is defined as

$$Bo = \frac{D^2 g\left(\rho_L - \rho_G\right)}{\sigma} \qquad (13)$$

c_1 and c_2 are empirical constants whose values are determined by the tube end geometry, Equation (10) can be rearranged as follows:

$$\frac{Ku_G^{1/2}}{\tanh\left[c_2\left(Bo^{1/8}\right)\right]} + m\frac{Ku_L^{1/2}}{\tanh\left[c_2\left(Bo^{1/8}\right)\right]} = c_1 \qquad (14)$$

Table 3.
Dimensionless groups other than those defined by Equations (1) and (2), previously used to correlate flooding data, l represents a length dimension.

Name	Symbol	Definition
Gas Reynolds no.	Re_G	$\rho V_G l/\eta_G$
Liquid Reynolds no.	Re_L	$\rho V_L l/\eta_L$
Gas Kutateladze no.	Ku_G	$\rho_G^{1/2} V_G/\left[g\sigma\left(\rho_L-\rho_G\right)\right]^{1/4}$
Liquid Kutateladze no.	Ku_L	$\rho_L^{1/2} V_L/\left[g\sigma\left(\rho_L-\rho_G\right)\right]^{1/4}$
Bond number	Bo	$l\left[g\left(\rho_L-\rho_G\right)/\sigma\right]^{1/2}$
Inverse viscosity parameter	N	$\left[gl^3\rho_L\left(\rho_L-\rho_G\right)/\eta_L^2\right]^{1/2}$
Mass flux rate	-	$\rho_G V_G/\rho_L V_L$
Dimensionless film thickness	-	δ/l
Density ratio	-	ρ_G/ρ_L
Viscosity ratio	-	η_G/η_L
Reference viscosity Ratio	-	$\eta_{reference}/\eta_L$

The flooding data shown in Fig. 10 are plotted in terms of the dimensionless parameters defined by Equation (14) in Fig. 13. The data do not correlate. This implies that the Kutateladze-type correlation is not applicable for tube diameters close to 30 mm.

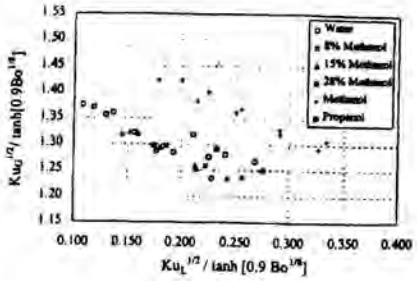

Fig. 13 The flooding data of Fig. 10 plotted in terms if the Kutateladze-type dimensionless parameters of Equation (14). The value for c_2 that is applicable for a square-edged gas inlet is 0.9.

The dimensionless liquid volume rate, which is a combination of the Kutateladze number and the Bond number, also fails to correlate the data under consideration.

The Kutateladze-type correlation originally proposed by Chung et al. [7] is based on a Kelvin-Helmholtz instability analysis by Tien et al. [17]. Subsequently Faghri et al. [18, 19] proposed exactly the same type of Kutateladze correlation. Their correlation is, however, based on an empirical model that assumes that the Wallis- and the Kutateladze-type correlations are simultaneously valid for predicting flooding. Existing flooding data indicate that this assumption may not be invalid. There is furthermore a trend to differentiate between the two types of models, where the Wallis correlation is applied for conditions when the duct dimensions affect flooding while the Kutateladze correlation is applied when the duct dimensions do not play a significant role.

Faghri et al. [18, 19] had to introduce a density correction into the Kutateladze-type correlation developed by Tien et al. [17] to correlate flooding data for liquids other than water. The reason for this may be explained by trends observed in Fig. 13 i.e. the Kutateladze-type correlation may not have been valid for the range of data used by Faghri et al. and for this reason a density correction factor was introduced to achieve better correlation.

The reference viscosity ratio has no real physical meaning and should not be considered for correlating purposes.

The dimensionless groups remaining in Table 3 are the film thickness ratio δ / l, the inverse viscosity parameter N and the liquid Reynolds number Re_L.

The film thickness ratio related to the liquid Reynolds number and the inverse viscosity parameters through the laminar film flow analysis, i.e. $\delta/l = f(N, Re_L)$. Attempts by the present authors to correlate the flooding gas Froude number as a dependent parameter in terms of the film thickness ratio failed. It implies that a combination of N and Re_L cannot serve as an independent parameter for correlating the flooding gas Froude number.

The only successful independent parameter was found to be the combination of the liquid densimetric Froude number Fr_{DL} and the Ohnesorge number Oh_L.

8. EVALUATION OF THE VALIDITY OF THE FROUDE-OHNESORGE NUMBER CORRELATION WITH REFERENCE TO PREVIOUS EXPERIMENTAL INVESTIGATIONS

8.1 DATA BY CLIFT et al. [3]

Clift et al. [3] investigated the effect of the liquid viscosity on flooding in a vertical tube of diameter D = 31.8 mm. Water and aqueous glycerol solutions were used as working fluids. The properties of the solutions tested are given in Table 4. Liquid was injected through a porous section and air entered the tube at the bottom through a bell-mouth inlet.

Table 4.
Properties of the aqeous glycerol solutions tested by Clift et al. (1966)

% Glycerol	Liquid viscosity ($kg/ms \times 10^3$)	Liquid density (kg/m^3)	Surface tension ($N/m \times 10^3$)
0% (Water)	1.32	1000	72.0
25%	2.18	1060	70.2
59%	10.4	1150	68.0
70%	23.4	1180	66.4
77%	46.0	1200	65.8
82%	82.5	1210	65.0

The flooding data by Clift et al. [3] are shown in Fig. 14 in terms of the measured phase superficial velocities. The data are replotted in Fig. 15 in terms of the Froude-Ohnesorge parameters. Excellent correlation is achieved.

8.2 DATA BY CHUNG et al. [7]

Chung et al. [7] conducted experiments with pure water, water treated with surfactants and silicon oil to establish the role of the surface tension during flooding. The properties of the liquids tested are shown in Table 5. Air was used as the working gas. The test section consisted of a plexiglas tube with an inner diameter of 31.8 mm, clamped between an upper and a lower plenum. The liquid was introduced into the vertical tube by spilling it from the upper plenum over into the tube under the action of gravity.

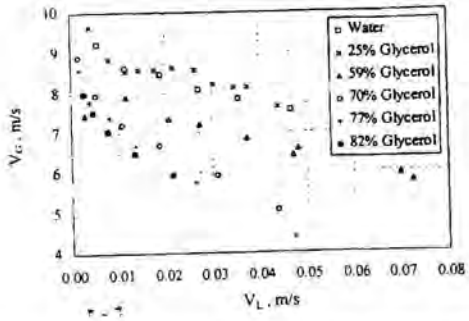

Fig. 14. Flooding data by Clift et al. [3] plotted in terms of the phase superficial velocities. The corresponding fluid properties are given in Table 4.

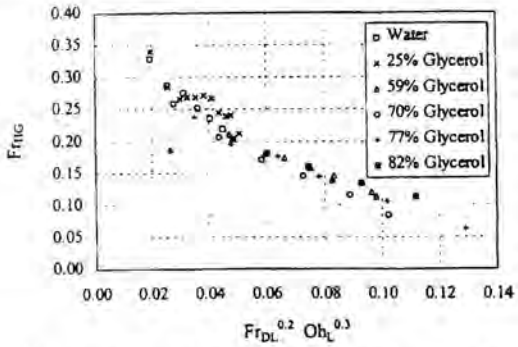

Fig. 15. The flooding data by Clift et al. [3], shown in Fig. 14 replotted in terms of the Froude-Ohnesorge numbers

Table 5.
Liquid tested by Chung et al. [7] to investigate the effect of the surface tension. The corresponding flooding superficial velocities are shown in Fig. 16.

Liquid	Liquid Viscosity (kg/ms x10^3)	Liquid density (kg/m^3)	Surface tension (N/m x 10^3)
Water 22°C	1.00	1000	72.7
Water with Surfynol SE 0.1% by weight; 20°C	1.00	1000	35.0
Water with Surfynol TG 0.1% by weight; 20°C	1.00	1000	28.0
Silicon oil; 20°C	0.82	820	17.4

In another set of experiments Chung et al. [7] made use of three different types of oils to investigate the effect of the liquid viscosity on the flooding gas velocity. The properties of the oils are given in Table 6.

Table 6.
Oils tested by Chung et al. [7] to investigate the effect of the liquid viscosity. The flooding superficial velocities are shown in Fig. 16

Type of Oil	Liquid viscosity (kg/ms x10^3)	Liquid density (kg/m^3)	Surface tension (N/m x 10^3)
Chevron white oil 3; 20°C	3.85	844.3	31.0
Chevron white oil 5; 20°C	5.25	850.8	35.0
Chevron white oil 9; 20°C	10.60	863.6	36.0

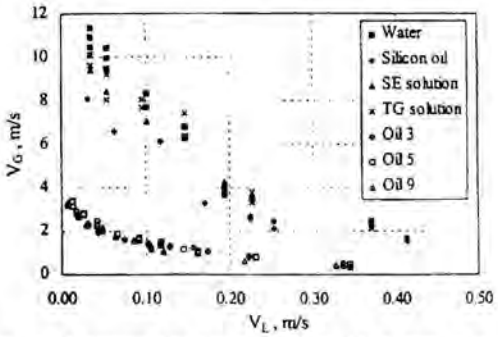

Fig. 16. Flooding data by Chung et al. [7] plotted in terms of the superficial phase velocities. The corresponding fluid properties are given in Tables 5 and 6; D = 31.8 mm.

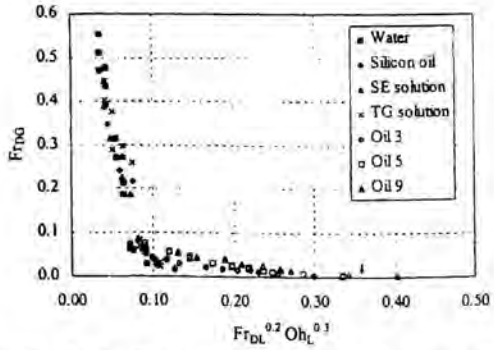

Fig. 17. The flooding data by Chung et al. [7] shown in Fig. 16 plotted in terms of the Froude-Ohnesorge numbers.

The measured flooding velocities are shown in Fig. 16. The oils flood at low air flow rates as the result of their high viscosities. The data are shown in Fig. 17 in terms of the Froude-Ohnesorge dimensionless groups. Note how well the transition from the higher flooding gas velocities (data obtained with solutions) to the lower velocities (data obtained with oils) is correlated by the proposed dimensionless groups.

9. COMMENTS AND CONLCUSIONS ON THE NEWLY PROPOSED CORRELATION METHOD

Flooding data taken from two previous investigations were expressed in terms of the phase Froude numbers and the Ohnesorge number to evaluate the general validity of the dimensionless groups. Note that each set of data was treated individually and it was not attempted to present all the data on a single graph. The reason for presenting the data separately is the strong effect that the test section geometry has on the flooding process. Flooding data generated in different test sections can be expected to differ and should therefore not be compared directly for correlating purposes.

According to a theoretical analysis by Cetinbudaklar and Jameson [20] a liquid film tends to become more unstable with an increase in the liquid viscosity. For a given liquid flow rate the film becomes thicker with an increase in viscosity. Cetinbudaklar and Jameson [20] argued that the effect of viscous damping at the wall becomes less as the film thickness increases and therefore the film becomes more unstable as the film thickness increases. Because an increase in viscosity implies an increase in the film thickness, an increase in viscosity causes the film to become unstable. It therefore appears that the Ohnesorge number is an indication of the stability if the liquid film draining down the duct wall. With an increase in the Ohnesorge number (i.e. increase in liquid viscosity) the liquid film becomes more unstable and flooding occurs at lower gas velocities. Apart from the effect of the liquid viscosity represented in the Ohensorge number, the stabilising effect of the surface tension forces is also accounted for by the Ohensorge number.

In the past the researchers often made use of the hydraulic diameter to correlate flooding data for geometries other than round. In Fig 5(a) and 5(b) it is demonstrated that the height of a rectangular duct is the required length dimension in the gas Froude number and not the hydraulic diameter. The definition for the height and width of a rectangular duct is illustrated in Fig. 18(a).

The flooding data for rectangular ducts of different height shown in Fig. 5(a), fail to correlate when employing the hydraulic diameter as the characteristic dimension in Fr_{HG}, where the hydraulic diameter is defined as

$$D_e = \frac{4 \times \text{Cross} - \text{sectional flow area}}{\text{perimeter}} \qquad (15)$$

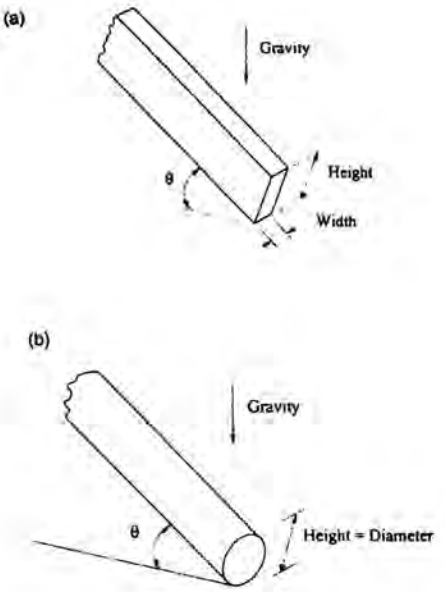

Fig. 18 (a) Definition of the height and the width of a duct. (b) Equivalent height of a tube.

In the case of tubes the diameter represents the effective height, as illustrated in Fig. 18(b). The diameter is therefore employed as the height H required in Fr_{HG}. In other word, the role of the diameter is that it represents the physical height and not that of an equivalent dimension such as defined by Equation (15).

Lee and Bankoff [9] conducted flooding tests with an inclined duct of 380 mm width. Two heights of 38 and 76 mm respectively were investigated. Similar to the present investigation, the flooding gas velocity was found to increase with an increase in the height. Lee and Bankoff [9] did however present their data in terms of a modified Wallis parameter.

$$V_G^* = \frac{\rho_G^{1/2} V_G}{\left[2Hg\sin(\theta)(\rho_L - \rho_G)\right]^{1/2}} \qquad (16)$$

In the definition of V_G^* the term 2H represents the hydraulic diameter of the channel. θ is the duct inclination. The experimental results of the present investigation have however revealed that the hydraulic diameter is not the characteristic dimension in the gas Froude number, as explained in the previous paragraph and H should have been used by Lee and Bankoff [9] for correlating purposes rather than 2H.

Lastly it should be noted that in the case of rectangular ducts the characteristic dimension or the gas and the liquid Froude number differ, i.e. the height is used for gas Froude number while the hydraulic diameter represents the length dimension in the liquid Froude number. Existing correlations like the well known Wallis [21] equation usually employ the same characteristic for both the gas and the liquid Froude number.

REFERENCES

1. Hewitt, G.F., Hall-Taylor, N.S., 1970. Annular Two-Phase Flow. Pregamon Press, Oxford.
2. Govan, A.H., Hewitt, G.R., Richter, H.J., Scott, A., 1991. Flooding and churn flow in vertical pipes. Int. J. Multiphase Flow 17, 27-44.
3. Clift, R., Pritchard, C., Nedderman, R.M., 1966. The effect of viscosity on the flooding conditions in wetted wall columns. Chemical Engineering Science 21, 87-95.
4. Suzuki,S., Ueda, T., 1977. Behaviour of liquid films and flooding in counter-current two-phase flow - part I. Flow in circular tubes. Int. J. Multiphase Flow 3, 517-532.
5. Whalley, P.B., McQuillan, K.W., 1985. Flooding in two-phase flow: the effect of tube length and artificial wave injection. PhysicoChemical Hydrodynamics 6, 3-21.
6. Feind, R., 1960. Falling liquid films with countercurrent air flow in vertical tubes. VDI Forschungsheft 481, 5-35.
7. Chung, K.S., Liu, C.P., Tien, C.I., 1980. Flooding in two-phase countercurrent flows - II: Experimental investigation. PhysicoChemical Hydrodynamics 1, 209-220.
8. Zapke, A., Kröger, D.G., 1996. The influence of fluid properties and inlet geometry on flooding in vertical and inclined tubes. Int. J. Multiphase Flow 22, 461-472.
9. Lee, S.C., Bankoff, S.G., 1983. Stability of steam-water countercurrent flow in an inclined channel. Journal of Heat Transfer 105, 713-718.
10. Lee, S.C., Bankoff, S.G., 1984. Parametric effects on the onset of flooding in flat-plate geometries. International Journal of Heat Mass Transfer 27, 1691-1700.
11. Barnea, D., Yospeh, N., Taitel, Y., 1986. Flooding in inclined pipes - effect of entrance section. The Canadian Journal of Chemical Engineering 64, 177-184.
12. Zapke, A., Kröger, D.G., 2000. Countercurrent gas-liquid flow in inclined and vertical ducts - I: Flow patterns, pressure drop characteristics and flooding. Int. J. Multiphase Flow, Vol. 26, 1439-1455.
13. Ohnesorge, W., 1936. Formation of drops by nozzles and the breakup of liquid jets. Z. Angew. Math. Mech. 16, 355-358.
14. Zapke, A., Kröger, D.G., 2000. Countercurrent gas-liquid flow in inclined and vertical ducts - II: The validity of the Froude -Ohnesorge number correlation for flooding, Int. J. Multiphase Flow, Vol. 26, 1457-1468.
15. McQuillan, K.W., Whalley, P.B., 1985. A comparision between flooding correlations and experimental flooding data for gas-liquid flow in vertical circular tubes. Int. J. Multiphase Flow 40, 1425-1441.
16. Bankoff, S.G., Lee, S.C., 1986. A critical review of the flooding literature. In: Hewitt, G.f., Delhaye, J.M., Zuber, N. (Ed.). Multiphase Science and Technology, chap. 2, Vol. 2. Hemisphere, New York, pp. 95-180.
17. Tien, C.L., Chung, K.S., Liu, C.P., 1980. Flooding in two-phase counter-current flows - I: experimental investigation. PhysicoChemical Hydrodynamics 1, 195-207.
18. Faghri, A., 1995. Heat pipe science and technology. Taylor and Francis, Washington.
19. Faghri, A., Chen, M.M., Morgan, M., 1989. Heat transfer characteristics in two-phase closed conventional and concentric annular thermosyphons. Journal of Heat Transfer 111, 661-618.
20. Cetinbudaklar, A.G., Jameson, G.J., 1969. The mechanism of flooding in vertical countercurrent two-phase flow. Chemical Engineering Science 24, 1669-1680.
21. Wallis, G.B., 1969. One-dimensional two-phase flow. McGraw-Hall, New York.

HEFAT2002
1st International Conference on Heat Transfer, Fluid Mechanics, and Thermodynamics
8-10 April 2002, Kruger Park, South Africa
CW1

THERMODYNAMIC OPTIMIZATION OF CONVECTIVE HEAT TRANSFER THROUGH CROSS-FLOW OVER SINGLE TUBE

Weihua Cai* Zhi Tao**
* M. Eng. Student; **Professor
Jet Propulsion Department Rotating Heat Transfer Division
Beijing University of Aero. & Astro.
P.O. Box 1-73, 37 Xue Yuan Rd. Haidian District
Beijing 100083 P.R.China
*E-mail: cwh@ns.ngl.buaa.edu.cn

Abstract

The first and second laws of thermodynamics, combined with the method of weighted mean value of outside fluid temperature, have been utilized to optimize the convective heat transfer through cross-flow over single tube. The spatial distribution of the field of fluid temperatures is presented. Therefore, the irreversibility losses or entropy generation rate profiles may be calculated. It is shown that the entropy generation rate may be minimized through proper selection of some parameters of the system.

Introduction

Due to wide range of design possibilities, simple manufacturing, less maintenance and low cost, the cross-flow heat exchangers are extensively used in industries, such as the petroleum, petrochemical, aeronautics and astronautics, etc. The flow arrangement is especially well suited for gas cooling and heat recuperation. Heat transfer processes are generally accompanied by thermodynamic irreversibility or entropy generation. The extensive use of heat exchangers, and in particular, the task of conserving useful energy have generated the need to produce thermodynamically efficient heat transfer processes and equipment for such processes. Entropy analysis is the useful way in using the first and second thermodynamic law to calculate and minimize the entropy generation in heat transfer processes.

The first publication regarding the concept of irreversibility in heat exchangers design appeared in 1977. In 1977 [1], A. Bejan developed the concept of number of entropy generation units Ns in designing counterflow heat exchanger for gas-to-gas applications. In 1979[2], A. Bejan continue used this concept to study the entropy generation from ducts with constant heat flux for flat plates, cylinders in cross-flow and rectangular ducts. In 1987 [3], P.K. Nag etc. investigated the convective heat transfer through a duct with constant wall temperature. It is shown that the entropy generation depends on different parameters such as the inlet temperature ratio, fluid flow heat capacity rate ratio, non-dimension heat transfer duty parameter, and flow arrangement. In 1995 [4], Y. Demirel studied the entropy generation of convective heat transfer in a packed duct with constant wall temperature and reported that the entropy generation rate may be minimized trough proper selection of operating conditions and design parameters of the system. However, these analyses of entropy generation were focused on the convetive heat transfer in ducts with either constant wall temperature or uniform heat flux. As far as the author known, there still has no publications concerning the thermodynamic optimization of convective heat transfer through cross-flow over single tube. Due to the widely application of this flow arrangement, it is very necessary to analysis the energy generation rate of this system. The main objective of the present paper is to develop a theory with explicit and accurate relation for thermal performance of cross-flow over single tube and. As a consequent, one can easily analysis the entropy generation rate of this system and minimize the irreversible loss.

Nomenclature

a	Cross sectional area of tube
A_c	Cross sectional area of outer duct $A_c = A_f \phi$
A_f	Face-winding area of the tube A_f =LD
B	Constant eq. (7)
b	Half of the tube perimeter
C^*	Heat capacity ratio $C^*=(mC_p)_1/(mC_p)_2$
C_D	Drag coefficient
C_p	Heat capacity
D	Tube diameter
F_D	Fluid drag force
J	Non-dimension duty parameter eqs. (27), (28)
K	Over all heat transfer coefficient
L	Tube length
m	Mass-flow rate
N	Ratio of tube length to diameter N =L/D

N_s Non-dimension entropy generation rate

ntu Number of heat transfer units $K\pi DL/(mC_p)$

ΔP Pressure drop inside tube eq. (21)

Q Specific heat flux

R Pumping-power ratio

$\dot{S}_{gen}$ Entropy generation rate

T Temperature of fluids

u Flow velocity of fluid flowing inside tube

v Flow velocity of fluid flowing outside tube

x Coordinate

Greek Letters

ϕ Flow passing ratio $\phi = A_c / A_f$

η Non-dimension coordinate $\eta = x/L$

μ Parameter eq. (6)

ω Weight factor eq. (5)

θ Non-dimension outside fluid temperature

τ Inlet temperature difference $\tau = T_{1i}/T_{2i}$

ξ Non-dimension inside fluid temperature

Subscripts

1 Refers to inside fluid

2 Refers to outside fluid

i Inlet

o Outlet

av Average

Short outline of method to evaluate fluid temperatures

A cross-flow over single tube arrangement is shown in Fig. 1.

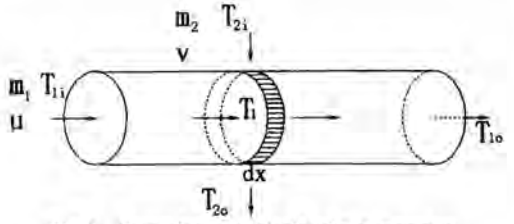

Fig. 1 Cross-flow over single tube arrangement

The symbols used here are listed in the nomenclature. The fluid outside the tube is usually air and inside, air or liquid. The overall heat transfer coefficient is assumed to be constant for the whole length of the tube, the tube side fluid is mixed only in cross section but it varies along the tube. The outer fluid is assumed unmixed. For the finned tube with cross-flow over it, these assumptions are suitable. For the plain tube, if the outer fluid is mixed insufficiently, these assumptions are still suitable.

Consider an infinitesimal small slice of the tube, the energy balance for the tube-side fluid flowing in this slice given by

$$-\frac{d\xi}{d\eta} = ntu_1(\xi - \theta) \tag{1}$$

The energy balance for the fluid outside the slice takes the following form

$$1-\theta_o = ntu_2(\theta - \xi) \tag{2}$$

where dimentionless temperature θ and ξ are expressed in dimentionless form as shown in following forms

$$\theta = \frac{T_2 - T_{1i}}{T_{2i} - T_{1i}}, \quad \xi = \frac{T_1 - T_{1i}}{T_{2i} - T_{1i}} \tag{3}$$

Symbol θ means the average temperature of fluid passing outside the tube developed by Th. Bes [5]

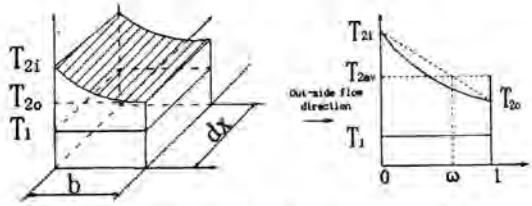

Fig. 2 Distribution of fluid temperatures in the infinitesimal small slice

In eq. (2), θ_o is the outlet dimentionless temperature of outside fluid. According to the definition in eq. (3), the inlet dimentionless temperature (θ_i) of outside fluid equals 1.

To solve this problem Bes etc. have developed a method in which the average temperature θ has been defined as the weighted average of the temperatures θ_i and θ_o. As shown in Fig.2, in the infinitesimal small slice of the tube, the fluid-inside temperature is practically constant. Therefore, this slice with appropriate volume of fluids can be treated as a small recuperator with a heat transfer surface area equal to bdx. Thus, one can easily prove that the temperature of fluid flowing around a tube along its perimeter changes exponentially in its value and that the mean difference of temperature should be calculated as the logarithmic mean of the temperature differences at the location of inlet and outlet of the tube. Therefore θ and ω may be presented as the following equations

$$\theta = \omega\theta_o + (1-\omega)\,\theta_i = \omega\theta_o + (1-\omega) \tag{4}$$

$$\omega = \frac{1}{1-e^{-ntu_2}} - \frac{1}{ntu_2} \tag{5}$$

The parameter ω is a weight factor. It is useful to introduce parameters μ and B as following forms

$$\mu = e^{-ntu_2} \tag{6}$$

$$B=\frac{1}{C^*}(1-\mu) \tag{7}$$

Where C^* is the heat capacity rate ratio as shown in nomenclature. An elimination of the temperature θ from eqs.(1), (2), (5), and (6) gives:

$$-\frac{d\xi}{d\eta}=B(\xi-1) \tag{8}$$

$$\theta_o-\mu=(1-\mu)\xi \tag{9}$$

the Eqs.(8) and (9) can be solved with boundary conditions

$$\theta_i=1, \quad \xi_i=0 \tag{10}$$

Integrating eq. (8) along the length of the tube yields the following result

$$\xi=1-e^{-B\eta} \tag{11}$$

Substituting ξ from eq. (11) into eq. (9) gives

$$\theta_o=1-(1-\mu)\,e^{-B\eta} \tag{12}$$

Eqs. (11) and (12) are the temperature distribution within this flow arrangement. With these temperatures, one can calculate the entropy generation rate of the system.

Entropy generation

This flow arrangement is mainly characterized by two types of losses, one of which is irreversibility loss due to the temperature difference and the other due to the flow drag. In this system, the entropy generation rate due to temperature differences may be expressed as

$$S_{gen,\Delta T}=(mC_p)_1 \ln\frac{T_{1o}}{T_{1i}}+\int_0^L\frac{dx}{L}(mC_p)_2\ln\frac{T_{2o}}{T_{2i}} \tag{13}$$

Combined with Eq. (3), (11) and (12) can gives

$$\frac{T_{1o}}{T_{1i}}=[1-(1-\tau)e^{-B}]/\tau \tag{14}$$

$$\frac{T_{2o}}{T_{2i}}=1-(1-\tau)(1-\mu)e^{-B\eta} \tag{15}$$

where τ is the inlet temperature ratio as shown in nomenclature. Substituting $\frac{T_{1o}}{T_{1i}}$ from eq. (14) and $\frac{T_{2o}}{T_{2i}}$ from eq. (15) into eq. (13) gives

$$S_{gen,\Delta T}=(mC_p)_1 \ln\{1-(1-\tau)e^{-B}/\tau\}+$$

$$(mC_p)_2\ln[1-(1-\tau)(1-\mu)e^{-B\eta}] \tag{16}$$

Using the expansion

$$\ln(1+x)=x-\frac{x^2}{2}+\cdots, x\in(-1,1) \tag{17}$$

when $|x|<<1$,the higher order terms can be neglected and we can obtain the following result

$\ln(1+x)\approx x$.

When $|\tau|\to 1$, the term $(1-\tau)(1-\mu)e^{-B\eta}\to 0$,

Therefore eq. (16) becomes

$$S_{gen,\Delta T}=(mC_p)_1\ln\{[1-(1-\tau)e^{-B}]/\tau\}+$$

$$(mC_p)_1(1-\tau)(e^{-B}-1) \tag{18}$$

Considering the small slice as shown in Fig. 2, the entropy generation rate due to friction may be expressed as

$$dS_{gen,\Delta p}=(mC_p)_1\frac{(-dP/dx)dx}{\rho_1 C_{p1}T_1}+\frac{F_D v dx/L}{T_{2av}} \tag{19}$$

the first term in eq. (19) represents the contribution from frictional pressure drop inside the tube, and the second term represents the contribution from flow drag outside the tube. Where

$$F_D=C_D\frac{\rho_2 v^2}{2}A_f \tag{20}$$

$$\frac{-dP}{dx}=f\frac{\rho_1 u^2}{2D}, \quad \Delta P=f\frac{\rho_1 u^2 L}{2D} \tag{21}$$

The terms C_D, f and A_f are drag coefficient, friction coefficient, and face-wind area, respectively. Substituting F_D from (20) and $\frac{-dP}{dx}$ from (21) into (19), the integrated result of eq. (19) can be written as

$$S_{gen,\Delta P}=\frac{N(mC_p)_1 fu^2}{2C_{p1}BT_{2i}}\ln\frac{\tau e^{-B}}{1-(1-\tau)e^{-B}}+$$

$$\frac{A_f C_D\rho_2 v^3}{2T_{2i}B}\ln\frac{1-\varpi(1-\tau)(1-\mu)e^{-B}}{[1-\varpi(1-\tau)(1-\mu)]e^{-B}} \tag{22}$$

According to the energy balance we can obtain

$$u=Q/[a\rho_1 C_{p1}T_{2i}(1-\tau)(1-e^{-B})] \tag{23}$$

$$v=\frac{QB}{A_c\rho_2 C_{p2}T_{2i}(1-\tau)(1-\mu)(1-e^{-B})} \tag{24}$$

Using the following definition

$$N_s=\frac{S_{gen}}{(mC_p)_1} \tag{25}$$

N_s is the entropy generation rate defined by Bejan [1]. Substituting u from eq. (23) and v from eq. (24) into (22), the final entropy generation rate can be expressed as

$$N_s=(S_{gen,\Delta T}+S_{gen,\Delta p})/(mC_p)_1$$

$$=\ln\frac{1-(1-\tau)e^{-B}}{\tau}-(1-\tau)(1-e^{-B})+$$

$$\frac{J_2^2}{2C^*B\phi[(1-e^{-B})(1-\tau)]^3}\ln\frac{1-\omega C^*B(1-\tau)e^{-B}}{[1-\omega C^*B(1-\tau)]e^{-B}}+$$

$$\frac{NJ_1^2}{2B(1-\tau)^2(1-e^{-B})^2}\ln\frac{1-(1-\tau)e^{-B}}{\tau e^{-B}} \quad (26)$$

$$\text{Where, } J_1=\frac{Qf^{1/2}}{a\rho_1(C_{p1}T_{2i})^{3/2}} \quad (27)$$

$$J_2=\frac{QC_D^{1/2}}{A_c\rho_2(C_{p2}T_{2i})^{3/2}} \quad (28)$$

J_1 and J_2 are dimentionless duty parameter presented by P.K. Nag[3],which account for the required heat transfer rate, fluid properties, inlet temperature and flow arrangement.

Calculation of optimum values

According to eq. (26), we rewrite the entropy generation rate as:

$$N_s=f(\tau,J_{1,2},N_{tu},C^*,\phi,\mathrm{N}) \quad (29).$$

It is shown that the entropy generation rate depends on parameters of $\tau, J_{1,2}, N_{tu}, C^*$, ϕ and N. So given these parameters, we can calculate the N_s.

Using air as the fluid, numerical evaluation of eq.(26) is done with parameters C^*=0.3, ϕ=4.44, D=5mm, and T_{2i}=437K. Fig.3 shows the variation of N_s with τ for different dimentionless duty parameter. It is shown that the entropy generation rate is a strong function of τ and also passing through a minimum value as τ is increased from 1. This minimum point is the optimum which the second law analysis seeks.

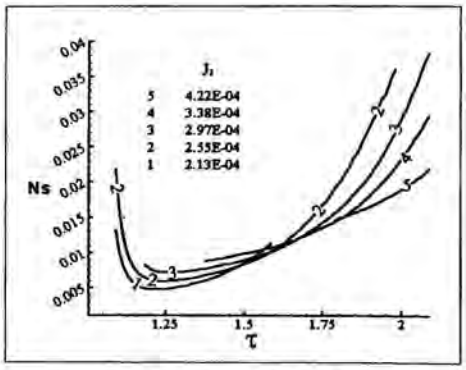

Fig. 3 Variation of N_s with τ

Fig. 4 shows the variation of different contributions of entropy generation rates with τ. In Fig. 4, $N_{s,\Delta T}$, $N_{s,\Delta P}$, $N_{s,\Delta P,1}$, and $N_{s,\Delta P,2}$ account for the entropy generation rate due to temperature difference, total flow drag of the system, frictional pressure drop of the fluid inside tube and flow drag of the fluid flowing around the tube, respectively. It is clearly shown that, when τ is increased or decreased to 1, N_s has passed through a minimum value. After that, and when τ is continued to change, N_s increases dramatically. Finally, for τ=1, $N_s \to +\infty$. The reason of above variation is that, for $\tau \to 1$, the temperature difference of T_{1i} and T_{2i} decreases. In order to achieve the particular heat transfer duty, the tube length and diameter ratio has to be increased, that is the heat transfer surface has to be increased (see Fig.5). As a consequent, the entropy generation due to flow drag of the fluid flowing around the tube ($N_{s,\Delta P,2}$), has little decrease for the parameter ϕ remaining constant. And the entropy generation due to temperature difference ($N_{s,\Delta T}$) reduces to zero. But the entropy generation rate due to frictional pressure drop of the fluid inside the tube ($N_{s,\Delta P,1}$) increases rapidly. Therefore, the total entropy generation rate of this system increases rapidly.

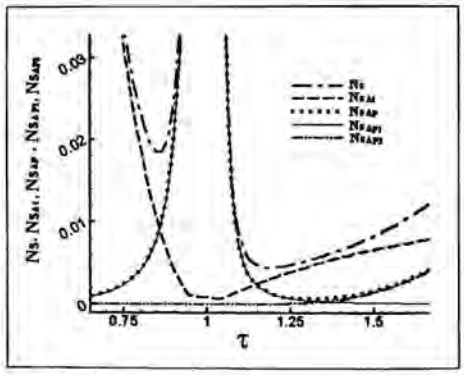

Fig.4 Variation of entropy generation with τ

Fig. 4 also shows that only at the optimum point, the entropy generation rates due to temperature difference and flow drag matched each other. Furthermore, the left part of Fig.4 for τ<1 represents the fluid inside the tube has been heated. The right part for τ>1 represents the fluid inside the tube has been cooled.

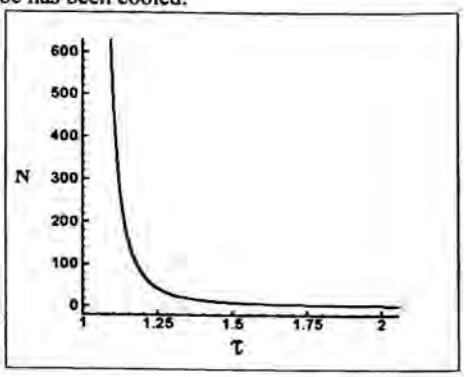

Fig.5 Variation of tube length and diameter ratio with τ

Optimum τ

When $|\tau|$ is reduced to 1, eq. (26) can be rewritten

$$N_s=(\tau-1)e^{-B}-(1-\tau)(1-e^{-B})-\frac{NJ_1^2}{2B(1-\tau)(1-e^{-B})^2}\cdot\frac{J_2^2\omega}{2C^{*2}\phi(1-e^{-B})^2(1-\tau)} \quad (30)$$

By differentiating N_s with respect to τ gives.

$$\frac{\partial N_s}{\partial\tau}=1-\frac{NJ_1^2}{2B(1-e^{-B})^2(1-\tau)^2}-\frac{J_2^2\omega}{2C^{*2}\phi(1-e^{-B})^2(1-\tau)^2} \quad (31)$$

Equating $\frac{\partial N_s}{\partial\tau}$ to zero, the optimum value of τ is obtained as

$$\tau_{opt}=1\pm\sqrt{\frac{NJ_1^2}{2B(1-e^{-B})^2}+\frac{\omega J_2^2}{2C^{*2}\phi(1-e^{-B})^2}} \quad (32)$$

Optimum R

Defining the pumping-power ratio R_1 as

$$R_1=\frac{Q}{a\Delta Pu} \quad (33)$$

Using eqs. (21), (23) and (27), eq. (33) may be written as

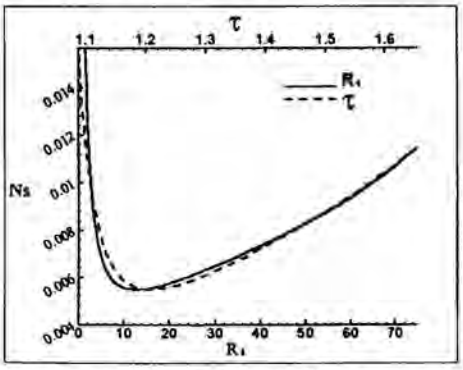

Fig. 6 Variation of N_s with R_1 and τ

$$R_1=\frac{2(1-e^{-B})^3(1-\tau)^3}{NJ_1^2} \quad (34)$$

if we define the heat flux Q always greater than zero, eq.(34) becomes

$$R_1=\frac{2(1-e^{-B})^3|1-\tau|^3}{NJ_1^2} \quad (35)$$

Since τ_{opt} corresponds to the minimum value N_s, the substituting of τ_{opt} from eq. (32) yields an optimum value of the pumping-power ratio R_{1opt}. Fig. 6 shows the variation of entropy generation rate with τ and R_1. It is shown that the value of τ for optimum value R_{1opt} not equals to the optimum value τ_{opt} but has a little deviation. The reason is that we have done some simplification when deducing the optimum value of τ. But we still can see that the value of τ for optimum value R_{1opt} is very near the optimum value τ_{opt}. Using eq. (32) the eq. (35) may be written as

$$\tau_{opt}=\frac{2\left(\frac{NJ_1^2}{2B}+\frac{\omega J_2^2}{2C^{*2}\phi}\right)^{3/2}}{NJ_1^2} \quad (36)$$

Optimum u and v

Substituting ΔP from eq. (21) and R_{1opt} from eq. (36) into eq.(33) yields:

$$u_{opt}=\left(\frac{8Q}{\pi LD\rho_1 fR_{1opt}}\right)^{1/3} \quad (37)$$

Imitating the above derivation, we define

$$R_2=\frac{Q}{F_D v_o} \quad (38)$$

As a consequent, we can obtain the following result

$$R_{2opt}=\frac{2\phi\left(\frac{NJ_1^2}{2B}+\frac{\omega J_2^2}{2C^{*2}\phi}\right)^{3/2}}{J_2^2} \quad (39)$$

Fig. 7 shows the variation of N_s with R_2. As shown in

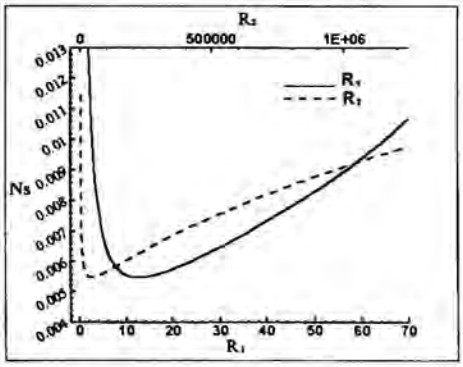

Fig. 7 Variation of N_s with R_1 and R_2

Fig. 7, the entropy generation rate is a strong function of

R_1 and R_2 and also passing through a minimum value as $R_{1,2}$ is increased from zero. Consequently, we can obtain an optimum v:

$$v_{opt} = \left(\frac{2Q}{LD\rho_2 C_D R_{opt}} \right)^{1/3} \quad (40)$$

Thus there is an optimum fluid velocity, which corresponds to the minimum loss of available power and should be used in the single tube with outer cross-flow to minimize the loss of available power.

Concluding remarks

1) Using the method of weighted mean of outside fluid inlet and outlet temperatures, we presented a study of the thermodynamic analysis of convective heat transfer through cross-flow over single tube. The analytical results presented in this paper constitute the fundamental building block for calculating and minimizing the irreversibility losses in cross-flow heat exchangers.

2) It is shown that the entropy generation rate of convective heat transfer through cross-flow over single tube, induced by temperature difference and flow drag, may be minimized through proper selection of operating parameters of the system.

3) Using the method of weighted mean of outside fluid inlet and outlet temperatures, we can also study and minimize the irreversibility losses in other cases of cross-flow arrangements. They are cross-flow with n tube rows-one pass, cross-flow with n tube rows-n passes and cross-flow with m × n tube rows-n passes. These cases will be presented in future publications.

References

1. A. Bejan, "The concept of irreversibility in heat exchanger design: counterflow heat exchangers for gas-to-gas applications", Transaction of the ASME, Vol.99, Aug.1977, pp.374-380.
2. A. Bejan, "A study of entropy generation in fundamental convective heat transfer". Transaction of the ASME, Vol. 101, Nov. 1979, pp. 718-725.
3. P.K. Nag, and P.Mukherjee, "Thermodynamic optimization of convective heat transfer through a duct with constant wall temperature", Int. J. Heat Mass Transfer. Vol.30, No. 2, pp. 401-405,1987.
4. Y.Demirel, "Thermodynamic optimization of convective heat transfer in a packed duct", Energy, Vol.20.No.10, pp. 959-967,1995.
5. Th. Bes, "Thermal performanes of codirected cross-flow heat exchangers", Heat and Mass Transfer, Vol. 31, pp.-215-222, 1996.

HEFAT 2002
1st International Conference on Heat Transfer, Fluid Mechanics, and Thermodynamics
8-10 April 2002, Kruger Park, South Africa
LS1

OPTIMAL DISTRIBUTION OF HOT WATER IN GROWING TREE-SHAPED NETWORKS

Sylvie Lorente*, Wishsanuruk Wechsatol+ and Adrian Bejan+

*Department of Civil Engineering, National Institute of Applied Sciences (INSA), 135 Avenue de Rangueil, Toulouse 31077, France,

+Department of Mechanical Engineering and Materials Science, Duke University, Box 90300, Durham, NC 27708-0300, USA

ABSTRACT

We study in this paper the distribution of hot water by insulating tree-shaped networks. The area covered by the pipes is constrained, and so is the volume of materials. The network is considered optimized when the heat losses to the ambient and the pumping power are minimized. Three configurations are first optimized: (a) the area is covered by a coiled stream on which the users are distributed uniformly, (b) each square area construct is made up of four smaller area constructs in order to build the tree-shaped network and (c) each square area is made up of two smaller area constructs (constructal network). The results show that (b) and (c) outperform the (a) design. It is also demonstrated that the third configuration provides better performance since the temperature of the hot water delivered to the farthest user is higher. Furthermore, in the constructal design, all the users of the network receive water at the same temperature.

The next step of this work consisted of adding to the network one new user at a time. This user must be connected to the network in the best place in terms of heat transfer and fluid mechanics optimization. Up to sixteen new users are linked to the network. This one-by-one growing network is then compared to the size-equivalent constructal network. It is shown that the temperature of the delivered water is higher when the constructal network is used. Yet, when the complexity of the network increases, both networks reach the same level of performance.

1. THE DISTRIBUTION OF HOT WATER

Configuration (geometry, topology) is the chief unknown and major challenge in design. The objective of this paper is to illustrate this approach to flow system design, specifically, the view that configuration itself is the unknown to be optimized. We do this by reviewing a body of recent work on the fundamental problem of distributing a supply of hot water as uniformly as possible over a given territory. This is a classical problem of civil engineering, with related subfields in piping networks, sewage and water runoff, irrigation, steam piping, etc. (Padet, 1991; Dupont, 1997; Nonclercq, 1982; Barreau and Moret-Bailly, 1977). For example, unlike in Barreau and Moret-Bailly (1977) where the flow path geometry is assumed (frozen) throughout the optimization process, in the present work the configuration is free to change, i.e., to "morph" into better patterns en route to higher levels of performance.

The distribution of hot water to users on a specified territory presents two problems to the thermal designer: the fluid mechanics problem of minimizing the pumping power, and the heat transfer problem of minimizing the loss of heat from the piping network. The two problems join hands in the minimization of the total rate of exergy destruction (Moran and Sciubba, 1994). The water flow is from one point (the source) to an area—the large number of users spread uniformly over the area.

2. STRING OF USERS

Consider an area A supplied with hot water by a stream of flow rate $\dot{m}$ and initial temperature T_i. The area is inhabited by a large number of users, $n = A/A_0$, where A_0 is the area element allocated to a single user. Let A_0 be a square with the side length L_0. Each elemental square must receive an equal share of the original stream of hot water, $\dot{m}/n$. As in all the point-area tree flows considered previously (Bejan, 2000), the fundamental question is how to connect the elements so that the ensemble (A) performs best.

We begin with the simple option of supplying a large number of elements with the same stream, which is a straight or curved line of length L (Fig. 1). The entering flow rate is $\dot{m}_i$.

The flow rate $\dot{m}(x)$ decreases linearly to $\dot{m}(0) = 0$, because each user draws the same share of $\dot{m}_i$ per unit length x. It is assumed that the number of elements is sufficiently large so that the variation of $\dot{m}(x)$ may be treated as continuous, $\dot{m}(x) = (x/L)\,\dot{m}_i$.

The temperature of the stream T(x) decreases from its original level T_i (at x = L) because of heat leakage to the ambient. It is assumed that the dominant thermal resistance between stream and ambient is posed by a cylindrical shell of thermal insulation installed on the outside of the pipe. The rate of heat loss per unit of pipe length is

$$q' = 2\pi k\,[T(x) - T_\infty] / \ln(r_o / r_i) \qquad (1)$$

where r_o, r_i, k and T_∞ are the outer and inner radii of the insulation, the thermal conductivity of the insulating material, and the ambient temperature. The temperature distribution along the water stream (or the pipe wall) is obtained by integrating the energy balance $\dot{m} c_p dT = q' dx$, from x = L where $T = T_i$

$$\frac{T(x) - T_\infty}{T_i - T_\infty} = \exp\left(-N \int_x^L \frac{dx}{x \ln(r_o / r_i)} \right) \qquad (2)$$

By analogy with the number of heat transfer units defined for heat exchangers, N is the "number of heat loss units" of the L-long pipe system, $N = 2\pi kL/(\dot{m}_i c_p)$. The temperature of the hot water delivered to the users is T(x): according to Eq. (2), this is known as soon as the distribution of thermal insulation is known, namely, the ratio r_o/r_i as a function of x. The constraint is the total amount of insulation wrapped around the pipe,

$$V\,\pi \int_x^L \left(r_o^2 - r_i^2\right) dx \qquad (3)$$

Several geometric optima characterize the best structure of the distribution of insulation. We review the main results; the details can be found in (Wechsatol et al., 2001, 2002). The geometry of the pipe and its insulation is described completely by r_o and r_i (or r_o/r_i and r_i) as functions of x. The optimal distribution of pipe size $[r_i(x)]$ can be derived from the minimization of the pumping power $\dot{W}$ required to drive $\dot{m}(x)$ through the entire system. For example, when the flow is

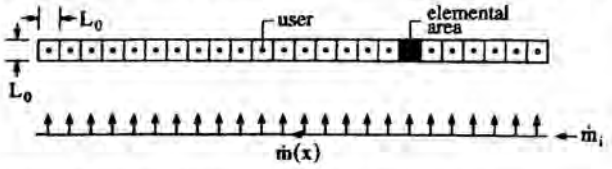

Figure 1 String of users supplied by a single hot stream.

turbulent in the fully rough regime (with nearly constant friction factor) the pipe shape for minimum pumping power and turbulent in the fully rough regime (with nearly constant fixed amount of pipe wall material is $r_i = c_1 x^{1/2}$. The factor c_1 is furnished by the wall material constraint, $c_1 = (3/2)\,L^{-3/2} \int_0^L r_i dx$.

The optimal spreading of a specified amount of insulation has been pursued in three ways, with similar results (Wechsatol et al., 2001). Here we illustrate results based on the maximization of the temperature of the hot water received by the end user (x = 0). This method leads to the conclusion that the optimal ratio of insulation radii $R = r_o/r_i$ must decrease with $\xi = x/L$ as $\xi = c_2/(R \ln R)$. Factor c_2 is pinpointed by the insulation material constraint (3) in combination with the optimized pipe radius function mentioned in the preceding paragraph

$$I_4 = \frac{V}{\pi L^2 c_1^2} = \int_0^1 \left(R^2 - 1\right) \xi d\xi \qquad (4)$$

Finally, the maximized end temperature is obtained by substituting $\xi(R)$ into Eq. (2) written for x = 0. The end temperature increases monotonically as N decreases, and as the total amount of insulation (I_4) increases. The optimal design with insulation of variable thickness is relevant for orientation, as the reference design against which more practical designs (e.g., constant insulation thickness) are evaluated.

3. USERS DISTRIBUTED UNIFORMLY ON AREA

Consider now the more practical question of how to distribute a hot-water stream to a population of users spread over an area, A. One solution is to coil the optimized string of users in such a way that the area is covered. The alternative is to introduce branches in the path of the stream, and to distribute area elements to each branch. We explored this alternative by starting with the smallest (and therefore simplest) area element, and continuing toward larger areas by assembling elements into larger constructs (Wechsatol et al., 2001). One simple rule of assembly is to use four constructs into the next, larger assembly, Fig. 2. In this case each construct covers a square area, in the sequence $A_0 = L_0^2$, $A_1 = 4L_0^2$,..., $A_i = 4^i L_0^2$.

The objective is to supply with hot water the users distributed uniformly over A_i, and to accomplish this task with minimal pumping power and a finite amount of thermal insulation. The geometry of each pipe is described by its length (a fraction of multiple of L_0), inner radius wetted by the flow (r_i, constant) and ratio of insulation radii ($R = r_o/r_i$). Note that unlike in the preceding section, the radius of each pipe segment is assumed constant. The pipe wall thickness is neglected for

the sake of simplicity.

The optimization of flow architecture consists of selecting the sequence of pipe sizes and insulation shell sizes. For pipe sizes, the global performance optimization criterion is the minimization of pumping power subject to a size constraint. For example, at the first-construct level (A_1, Fig. 2) there are two pipe sizes, one central pipe of length (3/2) L_0 and radii r_{i1} and $R_1 = (r_o/r_i)_1$, and four elemental branches of length (1/2)L_0 and radii r_{i0} and $R_0 = (r_o/r_i)_0$. The flow rate is $4\dot{m}_0$ through the root of the tree, and $\dot{m}_0$ through each branch. The flow is fully turbulent with constant friction factor. The drop in pressure (ΔP_1) from the root to the most distant user can be minimized by selecting the ratio of pipe sizes (r_{i1}/r_{i0}) subject to a water volume constraint (Wechsatol et al., 2001). If we constrain the amount of duct wall material, and if we assume that the duct thickness (t) is a constant independent of duct inner radius, then $(r_{i1}/r_{i0})_{opt} = 2^{5/6}$. An alternative is to fix the volume occupied by the ducts, and in this case $(r_{i1}/r_{i0})_{opt} = 2^{5/7}$

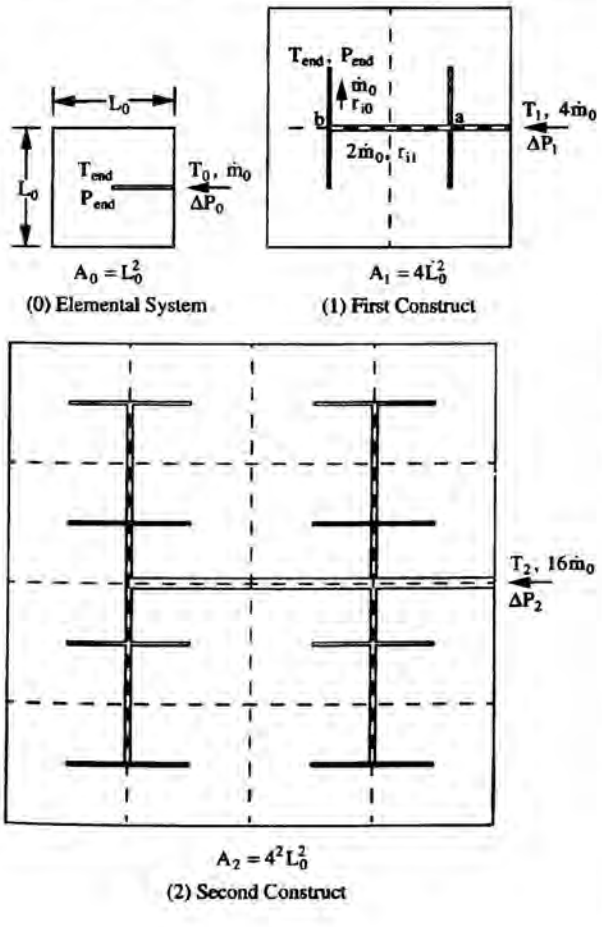

Figure 2 Sequence of square-shaped constructs.

The optimization of the insulation shells proceeds in the same steps as the pressure-drop minimization. For the element A_0 of Fig. 2, the heat-loss analysis based on Eq. (2) [with $\dot{m}_0$ = constant in place of $\dot{m}(x)$] yields

$$\frac{T_{end} - T_\infty}{T_0 - T_\infty} = \exp\left(-\frac{N_0}{\ln R_0}\right) \tag{5}$$

where the number of heat loss units is based on elemental quantities, $N_0 = \pi k L_0/\dot{m}_0 c_p$. For the A_1 construct, we find that the temperature drop from the root (T_1) to the end of the tree (T_{end}) is

$$\theta_1 = \frac{T_{end} - T_\infty}{T_1 - T_\infty} = \exp\left(-\frac{N_0}{\ln R_0} - \frac{5N_0}{4\ln R_1}\right) \tag{6}$$

The end temperature θ_1 depends on R_0, R_1 and N_0. The insulation radii ratios R_0 and R_1 are related by the insulation volume constraint

$$V_1 = \pi L_0 r_{i0}^2 \left[\frac{3}{2}\left(\frac{r_{i1}}{r_{i0}}\right)^2 \left(R_1^2 - 1\right) + \left(R_0^2 - 1\right)\right] \tag{7}$$

where (r_{i1}/r_{i0}) is known from pressure-drop minimization. Constraint (8) may be put into dimensionless form by recognizing the smallest pipe size, r_{i0}, and the dimensionless volume $\tilde{V}_1 = V_1/\left(\pi r_{i0}^2 L_0\right)$. The maximization of expression (7) with respect to R_0 and R_i, subject to constraint (8), yields the optimal step change in radii ratio, $[(R_1 \ln R_1)/(R_0 \ln R_0)]_{opt} = (5/6)^{1/2}(r_{i0}/r_{i1})_{opt}$. In view of the $(r_{i1}/r_{i0})_{opt}$ values listed

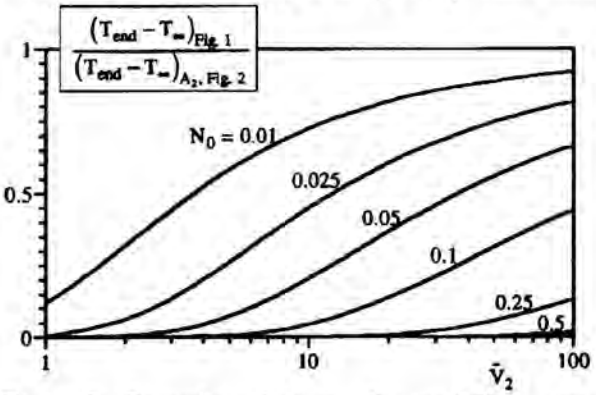

Figure 3 Comparison between the maximized water temperatures delivered to the farthest users in Fig. 1 and Fig. 2.

previously, we conclude that $R_{1,opt} < R_{0,opt}$. The maximized performance of the first construct is measured by the θ_1 values obtained by substituting into Eq. (6) the optimized geometry discussed above. The temperature of the stream delivered to the farthest user increases as the amount of insulation ($\tilde{V}_1$)increases, and as the conductivity of the material (N_0) decreases.

The optimization of the internal architecture of the second construct (A_2, Fig. 2) was performed by executing the same steps as in the optimization of the first construct. The optimized geometric features of the first construct are retained. The architectural features of the A_2 construct reinforce the overall performance of A_2 is measured by the end-user conclusions drawn at the A_1 level. In particular, the maximized overall performance of A_2 is measured by the end-user temperature

$$\theta_2 = \frac{T_{end} - T_\infty}{T_2 - T_\infty} = \theta_1 \exp\left(-\frac{5N_0/8}{\ln R_2}\right) \qquad (8)$$

where $\theta_1(N_0, \tilde{V}_1)$ is the maximized end temperature of A_1. The total insulation volume constraint for the A_2 construct is

$$\tilde{V}_2 = \frac{V_2}{\pi r_{i0}^2 L_0} = 3\left(\frac{r_{i2}}{r_{i0}}\right)^2 \left(R_2^2 - 1\right) + 4\tilde{V}_1 \qquad (9)$$

where r_{i1}/r_{i0} is a numerical factor known from the minimization of pressure drop. By maximizing θ_2 with respect to R_2 at constant N_0 and $\tilde{V}_2$ we obtain the insulation radii ratio $R_{2,opt}$ and maximized end temperature.

The relative superiority of the tree-shaped A_2 design (Fig. 2) over the string design (Fig. 1) is documented in Fig. 3. Here we show the dimensionless end temperatures produced by the two optimized schemes on the same basis—the same

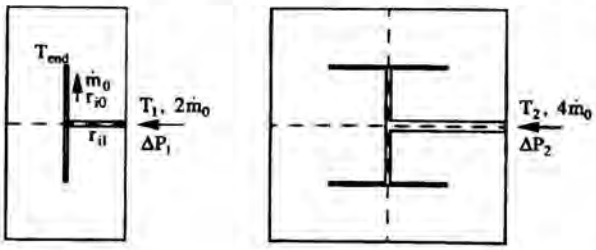

Figure 4 Sequence of constructs obtained by pairing.

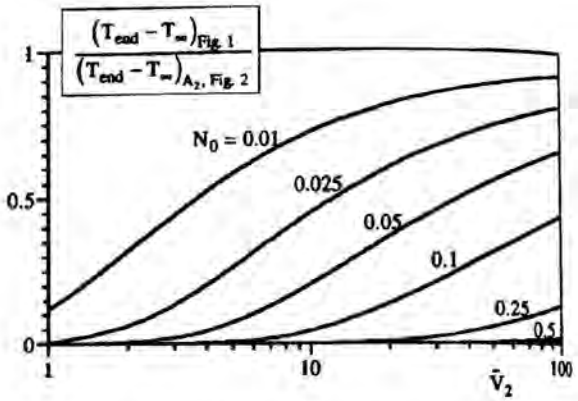

Figure 5 Comparison between the end-user temperatures of the $4L_0^2$ constructs of Figs. 2 and 4.

covered territory (A_2) and the same amount of insulation used in the entire construct (V_2). The tree-shaped design is superior, as the end-user water temperature in the scheme of Fig. 2 is consistently higher than in the coiled string arrangement of Fig. 1. The two schemes have nearly the same performance in the limit of plentiful insulation material and high water flow rate.

4. TREE NETWORK WITH REPETITIVE PAIRING

The sequence of square-shaped constructs used beginning with Fig. 2 is an assumption, not a result of optimization. To see whether a better rule of assembling small constructs into larger constructs can be found, we also considered the area doubling sequence shown in Fig. 4. Each area construct is obtained by putting together two constructs of the immediately smaller size. The area supplied with hot water increases as $A_0 = L_0^2$, $A_1 = 2L_0^2$..., $A_i = 2^i L_0^2$. The elemental area A_0 is the same as in Fig. 2. The second construct of Fig. 4 covers the same area ($4L_0^2$) as the first construct of Fig. 2.

Figure 5 summarizes the results of optimizing the performance of the A_2 construct obtained by pairing in Fig. 4. Wechsatol et al. (2001) report all the features of the optimized A_2 construct. In Fig. 5 the performance is reported relative to the performance of the $4L_0^2$ construct of Fig. 2. The comparison is for the same total amount of insulation material, which is plotted on the abscissa of the figure. The conclusion is that the tree structure generated by repeated pairing (A_2, Fig. 4) is superior to the square structure (A_1, Fig. 2). The temperature of the hot water received by the end user in Fig. 4 is consistently higher. We pursued this comparison to an even higher level of assembly—the construct of size $16L_0^2$—on the basis of the same amount of insulation material and total duct volume. Once again, the tree design based on the sequence of Fig. 4 outperforms the design based on Fig. 2. We found that the

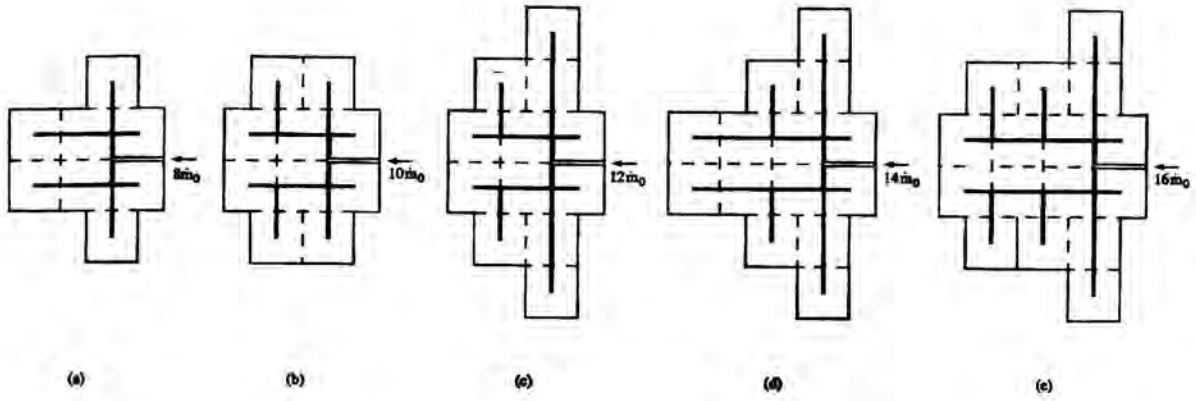

Figure 6 Growing hot-water distribution network constructed by adding one new user at a time, and placing it in the best location.

difference in the global performance of the two types of trees (Fig. 2 vs. Fig. 4) decreases as each optimized tree structure becomes more complex. The global performance becomes progressively less sensitive to the actual layout of the tubes. It is worth pointing out another useful property of the pairing sequence (Fig. 4): each user receives hot water at the same temperature. The $\dot{m}_0$ stream received by each user passesthrough the same sequence of insulated tubes. This is a very useful property, because in other tree structures such as Fig. 2, the users located closer to the root of the tree receive warmer streams than the farther users. The tree designs of Fig. 4 deliver hot water to the territory uniformly—uniformly in space and in temperature.

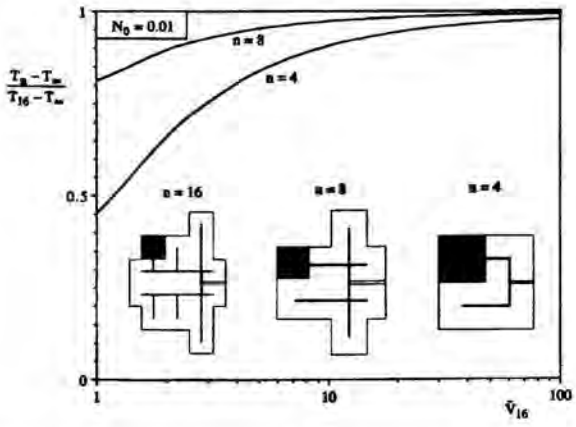

Figure 7 Comparison between the one-by-one designs of Fig. 6, showing how the performance improves as the complexity (n) increases.

5. TREE NETWORK DEVELOPED BY ADDING NEW USERS TO AN EXISTING NETWORK

Another way to construct the distribution network is to "grow it" optimally, by attaching one new user at a time (Wechsatol et al., 2002a). The growing network is optimized by placing each new user in the best spot that is available for it, i.e., in the place where the temperature of the water received by the user after attachment is the highest. Each such step can be executed only after considering all the possible positions for the new user, and by comparing the performance of each possible configuration. For example, when adding one new user to an existing network that contains six users, there are three different configurations that must be evaluated, i.e., three distinct positions that the new user may occupy in the new, larger volume.

The computational work becomes extensive as the network becomes larger and more complex. Figure 6 shows a sequence of steps in the growth of the network as the number of users increases from 8 to 16. As in the designs discussed earlier, the one-by-one constructs of Fig. 6 become better and more robust, as they grow larger and more complex. Numerical results show that although the performance of the one-by-one designs is consistently below the level achieved with the pairing construction (Fig. 4), the gap between the two shrinks as the structures become larger. Once again, optimized tree-shaped flows are robust.

Another way to see that the performance of the structure increases as its complexity increases is shown in Fig. 7. This figure brings together the one-by-one designs of Fig. 6. This time, the designs are compared on the basis of the same covered territory (A), which means that the L_0 scale of each user in Fig. 6(e) (n = 16) is the shortest. The n = 16 structure is the reference. The three designs use the same amount of thermal insulation. The k and $\dot{m}_0$ values are such that the N_0 value

based on the L_0 scale of the n = 16 case is $N_0 = 0.01$. The dimensionless volume $\tilde{V}_{16} = V_{16}/(\pi L_0 r_{i0}^2)$, where V_{16} is the total volume of the insulation (the same in all three designs), and L_0 and r_{i0} are the length and radius of the elemental pipes in the n = 16 design. Figure 7 shows that the temperature of the water received by the end-user increases as the complexity of the structure (n) increases. A characteristic of the one-by-one growth is the memory that is demented into each design. What was built prior to the attachment of the newest user is retained. This characteristic is found in other flow-shaped flows in nature, civil engineering and society.

6. CONCLUSION

The chief conclusion is that the use of geometric form (shape, structure) is an effective route to achieving high levels of global performance under constraints. The brute force approach of delivering hot water by using large amounts of insulation and flow rates (small N) is not economical. Much faster progress toward the goal of global performance maximization can be made by recognizing and treating the geometric configuration of the flow system as the main unknown of the problem (Bejan, 2000).

The constructal design method illustrated by the work reviewed in this paper can be extended to several related applications. First, networks for the distribution of chilled water require similar tradeoffs for the distribution of insulation, pipe diameters and pipe links over a territory populated by users. Second, when the territory is populated by a few large-volume users, the uniform distribution of users employed in this paper must be replaced by a few discrete nodes of consumption. Third, there are many civil engineering applications in which the nodes of consumption are fixed points on the territory, not freely moving points as in Fig. 6. Networks where some of the nodes of consumption are fixed could be approached based on the same method in future studies.

The demonstrated effectiveness of the geometric optimization method is relevant to the optimization of practically every distributed scheme for heating or cooling a specified area or volume. An example from the cooling of electronics is a disc-shaped area that generates heat uniformly: this can be cooled most effectively by covering the area with tree-shaped inserts of high conductivity material (Rocha et al., 2002b).

ACKNOWLEDGMENT. This work was supported by a grant from the National Science Foundation. Mr. W. Wechsatol also acknowledges the support received from King Mongkut's University of Technology (KMUTT), Thailand.

REFERENCES

Barreau, A., and Moret-Bailly, J., 1977, "Présentation de Deux Méthodes d'Optimisation de Réseaux de Transport d'Eau Chaude à Grande Distance," *Entropie*, Vol. 75, pp. 21-28.

Bejan, A., 2000, *Shape and Structure, from Engineering to Nature*, Cambridge University Press, Cambridge, UK.

Bejan, A., Rocha, L. A. O. and Lorente, S., 2000, "Thermodynamic Optimization of Geometry: T- and Y-Shaped Constructs of Fluid Streams," *Int. J. Therm. Sci.*, Vol. 39, pp. 949-960

Dupont, A., 1977, *Hydraulique Urbaine, Ouvrages de Transport, Elévation et Distribution*, Eyrolles, Paris.

Moran, M. J. and Sciubba, E., 1994, "Exergetic Analysis: Principles and Practice," *J. Eng. Gas Turbine Power*, Vol 116, pp. 285-290.

Nonclercq, P., 1982, *Hydraulique Urbaine Appliquée*, CEBEDOC, Liège.

Padet, J., 1991, *Fluides en Écoulement. Méthodes et Modèles*, Masson, Paris.

Wechsatol, W., Lorente, S. and Bejan, A., 2001, "Tree-Shaped Insulated Designs for the Uniform Distribution of Hot Water over an Area," *Int. J. Heat Mass Transfer*, Vol. 44, pp. 3111-3123.

Wechsatol, W., Lorente, S. and Bejan A., 2002a, "Development of Tree-Shaped Flows by Adding New Users to Existing Networks of Hot Water Pipes", *Int. J. Heat Mass Transfer*, Vol. 45, to appear.

Rocha, L.A.O., Lorente, S., Bejan, A., 2002b, "Constructal Design for Cooling a Disc-Shaped Area by Conduction", *Int. J. Heat Mass Transfer*, Vol. 45, to appear.

HEFAT 2002
1st International Conference on Heat Transfer, Fluid Mechanics, and Thermodynamics
8-10 April 2002, Kruger Park, South Africa
DA2

THERMODYNAMIC OPTIMIZATION OF A LAMINAR DIFFUSION FLAME

A. Datta[1] and A.Leipertz
Lehrstuhl für Technische Thermodynamik
Universität Erlangen-Nürnberg
D 91058, Erlangen, Germany

ABSTRACT

Thermodynamic optimization by entropy generation minimization is a tool for the optimized design of the thermal equipment. A theoretical model has been developed for a laminar diffusion flame to calculate the rate of entropy generation in such flames. Effects of the variation of the operating parameters, like fuel jet velocity and air jet temperature, on the rate of entropy generation has been investigated in order to predict a thermodynamically optimized flame situation with minimum generation of entropy. The results can be used in the optimum design of combustion chambers having diffusion flame.

INTRODUCTION

Thermodynamic optimization by entropy generation minimization can be an useful tool in the design of thermal systems and equipment. The tool is used in the heat transfer and refrigeration systems [1] and has been illustrated in several reviews and books [2 – 5] . The same technique can be used for the combustion systems as well. For the combustor of a heat engine, which produces working fluid for a subsequent work producing device (e.g. a gas turbine combustor), it is important to retain the maximum work producing capability of the working fluid at the exit of the combustor, while ensuring maximum conversion of the fuel's chemical energy into the thermal form. This can be ascertained by the minimization of the lost work in the combustor. All the irreversible processes occurring in a device generate entropy and the corresponding lost work following the Gouy-Stodola theorem ($W_{lost} = T_o E_g$). In order to keep the lost work to its minimum, it is required to minimize the entropy generation (E_g) in the device.

Many of the practical combustors operate in the diffusion combustion mode with the fuel and oxidizer fed as separate streams. A diffusion flame involves various physical and chemical processes due to fluid flow, heat transfer, mass transfer and chemical reaction within the combustor. All these processes contain internal irreversibilities, in addition to the external irreversibilities which may occur due to the exchange with the surroundings. However, for the optimization of the combustion process itself, it is required to concentrate on the internal process irreversibilities and the corresponding entropy generation only. It calls for the determination of the local velocity, temperature and concentration gradients to compute the local transport rates and the rate of chemical reaction. Computational fluid dynamic calculations solving the transport and chemical equations can provide the necessary information in this regard.

Though the flames in the practical combustion chambers fall in the turbulent regime, studies of the laminar flames are useful for many fundamental information regarding the flames. In some cases the turbulent flames are computed using the laminar flamelet models. A lot of work are available in the literature on the theoretical and experimental studies of laminar jet diffusion flames, but there is not much work leading to the calculation of the entropy production in such flames. Recently, Datta [6] made some theoretical calculations for the entropy generation in a laminar jet diffusion flame using methane as the fuel. The present work is an improvement to the earlier work of Datta [6], with a two step reaction kinetics being used, instead of the single step kinetics used earlier.

In the present work a numerical model for the calculation of a steady, axi-symmetric, laminar jet diffusion flame with co-flowing streams of fuel and air in a confined environment has been developed to evaluate the local physical transport and chemical reaction rates. These rates are then used in a general entropy transport equation to calculate the rate of entropy generation in the flame. Thermodynamic optimization seeks for the operating and design parameters which leads to the

[1] On leave from Dept. Of Power Plant Engg., Jadavpur University, Calcutta 700 091, INDIA.

minimization of the process entropy generation. With this objective, two important parameters, viz. the fuel jet velocity and the air jet temperature, are varied to study their effects on the rate of entropy generation. The information can be used as a first step for determining the conditions for the design and operation of a thermodynamically optimized combustor.

NOMENCLATURE

A	Pre-exponential factor
C_j	Concentration of species j
E	Activation energy
E_R	Rate of entropy generation
e_R	Rate of entropy generation per unit volume
M_j	Molecular weight of species j
$\overline{R}$	Universal gas constant
T	Temperature
T_n	Temperature at the dead state
ρ	Density

THEORETICAL FORMULATION

The laminar diffusion flame in a confined physical environment with central fuel stream and a co-flowing annular air stream is considered in this problem (Figure 1). The two streams mix after coming out of the tubes and produce a flammable mixture. The fuel is considered to be methane (CH_4).

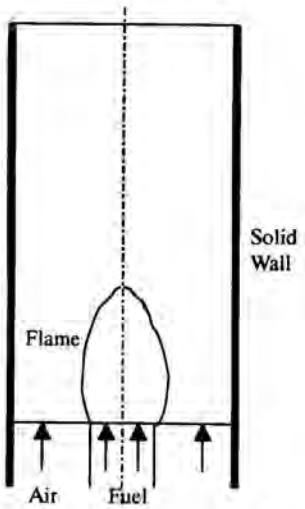

Figure 1. Physical Model of the Problem

NUMERICAL MODEL

The numerical model of diffusion flame is developed based on the following assumptions:

a) The flow is laminar, steady and axi-symmetric, produced from a jet of fuel emerging from a circular nozzle and burns in a co-flowing stream of air in a confined environment.
b) The reaction between the fuel and oxidizer proceed through a two step chemical kinetics.
c) Radiative exchange within the flame is neglected.
d) Lewis number is considered to be unity.

The conservation equations of mass, momentum, energy and species concentration are solved with their suitable boundary conditions in the confined space for the determination of the variables like pressure, velocity, temperature and concentrations of the species. The equation of state for the ideal gas mixture is used for the calculation of density. As the problem considers chemical reaction involving species like methane, oxygen, carbon-di-oxide, carbon-monoxide, water vapour and nitrogen , the species concentration equation was solved for all the species except nitrogen, which was then calculated by difference.

A two step chemical reaction kinetics was considered for the reaction of the fuel as follows:

$$CH_4 + 1.5\,O_2 \rightarrow CO + 2H_2O \qquad (1)$$

$$CO + 0.5O_2 \rightarrow CO_2 \qquad (2)$$

The reaction rate is calculated following an Arrhenius type rate equation given as,

$$\dot{\omega} = A\,\rho^{(a+b)}\,\frac{C_1^a C_2^b}{M_1^a M_2^b}\exp\left(-\frac{E}{\overline{R}T}\right) \qquad (3)$$

The subscripts 1 and 2 for C and M in equation (3) represent the 1st and 2nd reactant species in equations (1) and (2) for determining the respective reaction rates. The rate constants for the chemical reaction have been taken from the literature.

The viscosity of the medium is considered to be proportional to the temperature raised to a power of 0.7 [7], while the specific heat is evaluated considering the mixture of ideal gases with specific concentrations and temperatures. The Prandtl Number and Schmidt Number are assumed to be constant for the gases.

ENTROPY TRANSPORT EQUATION

The entropy generation rate due to the transport of heat, mass and momentum along with the chemical reaction is determined from the general entropy transport equation. The entropy generation rate per unit volume, e_R, at a point in the gas phase

can be written in the tensorial notation, following Hirschfelder et al. [8] as,

$$e_g = \frac{\Delta:\sigma}{T} + \frac{-J^q \nabla T}{T^2} + \frac{\sum\left(J_j^m \nabla \mu_j^c\right)}{T} + \frac{\sum\left(-s_j J_j^m \nabla T\right)}{T} + \frac{1}{T}\sum \lambda_j \mu_j^c \dot{\omega} \qquad (4)$$

where, σ and Δ are the stress and rate of strain tensors respectively, J^q is the heat flux per unit area and J^m_j , μ^c_j and s_j are the mole flux per unit area, chemical potential and partial molal entropy of the jth species respectively.

The first term on the right hand side of the equation (4) is due to fluid friction (momentum transfer), the second term is due to heat transfer, the third term pertains to mass transfer, the fourth term arises from the coupling between heat and mass transfer and the fifth term is due to chemical reaction.

The total entropy generation is, therefore, calculated as

$$E_g = \iiint_{\forall} e_g \, d\forall \qquad (5)$$

where, $\forall$ is the volume of the domain of interest in which all the physical and chemical processes take place.

Each term of the equation (4) is expanded in a cylindrical co-ordinate system to determine e_g, with the velocity, temperature and concentration values calculated from the numerical computation of the diffusion flame solving the respective governing equations.

METHOD OF SOLUTION

The governing equations of continuity, momentum, energy and species conservation in their conservative form are solved simultaneously by an explicit finite difference computing technique following the algorithm developed by Hirt and Cook [9]. The same technique has been adopted earlier by Datta [6] and Datta and Som [10] for the computation of diffusion flames with gaseous jets and liquid sprays respectively. The advection terms in the governing equations were discretised by a hybrid differencing scheme based on the local Peclet number associated with the cell, while the diffusion terms were discretised by the central difference scheme. A variable size adaptive grid system was considered within the axisymmetric domain of interest with the higher concentration of nodes near the periphery of the inner tube of fuel jet in order to capture the flame effectively. A numerical mesh of 75 × 38 grid nodes was used after several experiments which showed that any further refinement of the grids do not change the result appreciably. Combustion was initiated by simulating a spark by a high temperature zone near the inlet. The solution of the equations was continued till a steady state convergence was achieved. The entropy transport equation was solved with the steady state result of the laminar diffusion flame to evaluate the rate of entropy generation.

BOUNDARY CONDITIONS

Fuel and air are assumed to enter the reaction space with uniform axial velocities and uniform temperatures. The radial velocity at the inlet plane is assumed to be zero. At the outlet, the axial gradient of all the variables are set to zero. However, it is assumed that the air flows in with the ambient temperature (298 K) over the exit plane through which reverse flow occurs. Axisymmetric condition is imposed at the axis, while the outer periphery was considered to be an adiabatic and impermeable wall.

OPERATING CONDITIONS

The diameters of the fuel and air tubes issuing the jets are considered to be 12.7 mm and 50.8 mm respectively, while the length of the confined space of interest was taken as 300 mm. These dimensions conform the physical dimensions of the experimental work of Mitchell et al. [11]. In order to study the effects of the variation of fuel jet velocity and the air jet temperature on the rate of entropy generation, these parameters are varied in the different cases for which the results have been generated. The fuel jet velocity was varied from 2.668 cm/s to 6.670 cm/s, keeping the flame laminar in all the cases. The air jet temperature was varied from 300 to 600 K. The temperature of the fuel jet was maintained at 300 K and the air jet velocity was kept at 9.88 cm/s.

RESULTS AND DISCUSSION

Figures 2a and 2b show the typical temperature and velocity distributions within the confined space due to the flame for a particular operating condition. The same operating condition was employed by Mitchell et al. [11] for their experimental study of the laminar diffusion flame. The shape of the flame is depicted by the temperature profiles (Figure 2a). The gradient of temperature close to the burner is very steep and the high temperature isotherms converge towards the axis giving rise to an overventilated flame shape. This flame profile is typical for the diffusion flame with excess air supply, as maintained in this case. The high temperature central region results in a buoyancy driven flow which accelerates the gas near the axis. This is evident in Figure 2b, showing the velocity vectors. The high central velocity causes the entrainment of air from the outer periphery towards the centre, resulting into a pressure drop near the periphery. This induces flow of air from the outside ambience into the confined space through the exit plane, resulting into a big recirculating zone near the wall. Therefore, the temperature near the outer wall maintains close to the ambience over a considerable length of the chamber. The centreline temperature, on the other hand, first increases due to the energy generation as a result of the chemical reaction and

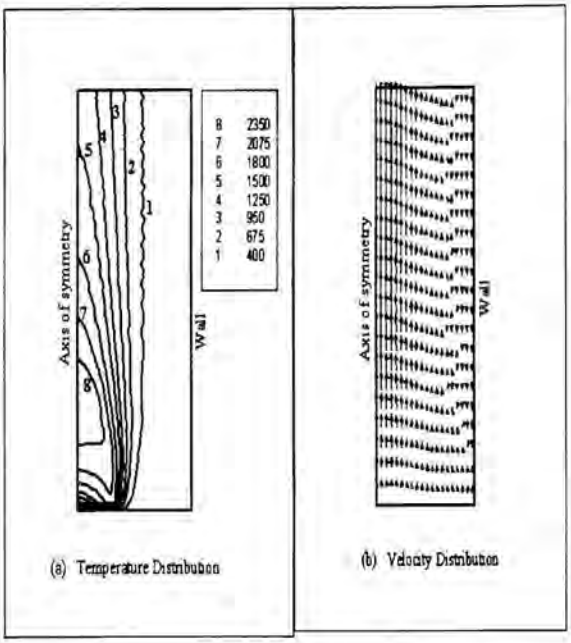

Figure 2. Temperature (K) and velocity distributions within the axisymmetric combustion space. (Fuel jet velocity = 4.478 m/s, Air jet temperature = 300 K)

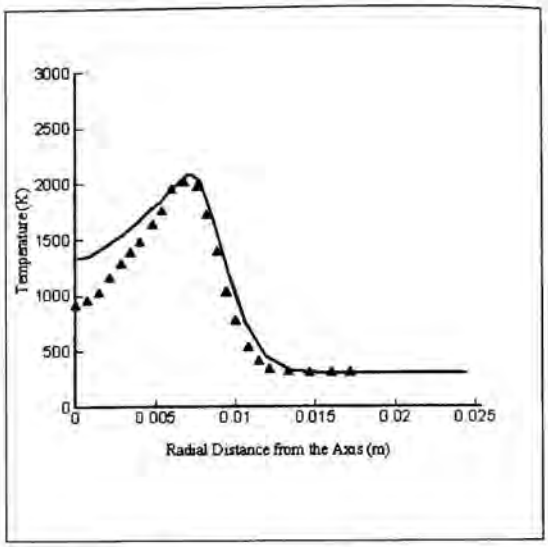

Figure 3. Comparison of the radial temperature distribution from the present calculation (——) and the experimental results of Mitchell et al. [11] (▲) at 1.2 cm above the burner exit plane

then decreases due to the transport of energy by convection and diffusion.

Figure 3 shows a comparison of the radial temperature profile obtained from the model at a certain axial position above the burner exit plane with the experimental results of Mitchell et al. [11]. Both the theoretical and experimental data show the same qualitative trend. However, there is a mismatch in the quantitative values near the central region. This mismatch can be attributed to the simplified two step kinetics used in the present model. In the actual flame there will be endothermic reactions in the fuel-rich central region, which will reduce the temperature there. The kinetics considered for the present calculation has not been able to capture these effects.

The calculation of entropy generation uses the gradient of the variables, like temperature, concentration, and velocity for its evaluation using Equation (4). The difference in temperature profile results in a quantitative variation in the prediction of the entropy generation from the exact value. However, a similar qualitative trend in the profile helps in an effective qualitative comparison of the effects of the variation of input parameters on the rate of entropy generation. Therefore, it is possible to conclude on the operating conditions that lead to the minimization of the entropy generation. The intention of the present work is to make a prediction in this direction without going for a highly complicated model with multi-step reaction kinetics and the associated complexities.

The most interesting observation from the study of entropy generation in the diffusion flame is that the contribution of the transport processes (momentum, heat and mass transfers) towards the rate of entropy generation far outweighs that of the chemical reaction. Similar observation was earlier reported in diffusion flames with single liquid droplet [12], with liquid spray [10], and with gaseous jet flames [6]. This is in contrast to the fact that in a diffusion flame the rates of transport are much slower than the rate of reaction. Analysis of the numerical results identifies heat transfer as the most important contributor towards the production of entropy out of all the transport processes. On the other hand, momentum transport is observed to have a negligible contribution. Figure 4 show the contours of the rate of entropy generation per unit volume due to chemical reaction (fig. 4a), heat transfer (fig. 4b) and the total rate (fig. 4c) for a particular operating condition. It is clear from figure 4a that the entropy generation due to the chemical reaction occurs within the thin flame volume. The flame contour can be depicted from the entropy generation plot and the shape of a typical over-ventilated diffusion flame is evident from the figure. The entropy generation due to heat transfer is high within an annular region across which a steep temperature gradient is observed.

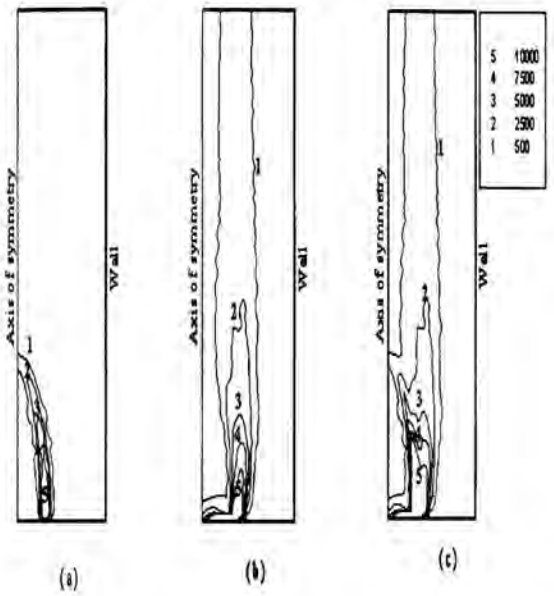

Figure 4. Contours of the rate of entropy generation per unit volume (W/m^3 K) due to chemical reaction (a), heat transfer (b) and total (c). [Fuel jet velocity = 4.478 m/s, Air jet temperature = 300 K)

The axisymmetric condition and the negligible temperature variation in the outer periphery keep the entropy generation due to heat transfer in these zones low. The highest rate of entropy generation is observed in the flame zone close to the burner exit due to the very high axial temperature gradient there. The total rate of entropy generation (fig. 4c) is apparently a combination of that due to chemical reaction (fig. 4a) and heat transfer (fig. 4b), as they are the two most important contributors towards the production of entropy.

Figure 5 shows the variation of the rate of entropy generation in a laminar jet diffusion flame with the fuel jet velocity. It shows that as the fuel jet velocity increases the rate of entropy generation also increases. The increase in the rate of entropy generation is due to the increased entropy production due to both chemical reaction and heat transfer. As the fuel jet velocity increases a longer flame is established increasing the volume of the flame zone. However, the entropy generation per unit volume does not change much. Therefore, the increased flame volume results in the higher rate of the production of the entropy due to chemical reaction when the fuel jet velocity is increased. The increased size of the flame produces high temperature gradient over a larger space which also increases the entropy generation due to heat transfer.

Figure 6 shows the variation of the rate of entropy generation in the flame with the change in air jet temperature. With the increase in air temperature the entropy production due to chemical reaction reduces marginally but that due to heat transfer appreciably falls. Therefore, the total entropy generation in the flame reduces with the increase in air jet temperature.

From the above study of the influence of two input parameters it is observed that in order to reduce the rate of generation of entropy and therefore the rate of production of lost work, it is required to reduce the fuel jet velocity and increase the air jet temperature. In other words, a laminar diffusion flame with lower fuel jet velocity and higher air jet temperature will give a thermodynamically optimized flame condition within the combustor.

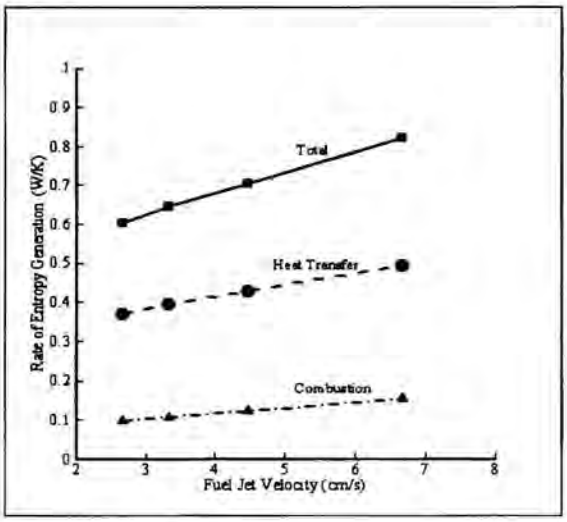

Figure 5. Variation of the rate of entropy generation with fuel jet velocity

CONCLUSION

Computational fluid dynamic calculation of a flame predicting velocity, temperature and concentration and the rate of chemical reaction can be used in computing the rate of entropy generation due to the internal irreversibilities in the flame. The information can be used in thermodynamic optimization of the flame by entropy generation minimization and in choosing the optimum operating conditions of the combustors with the flame. From the calculation of a laminar jet diffusion flame it has been observed that the entropy generation in a diffusion flame is

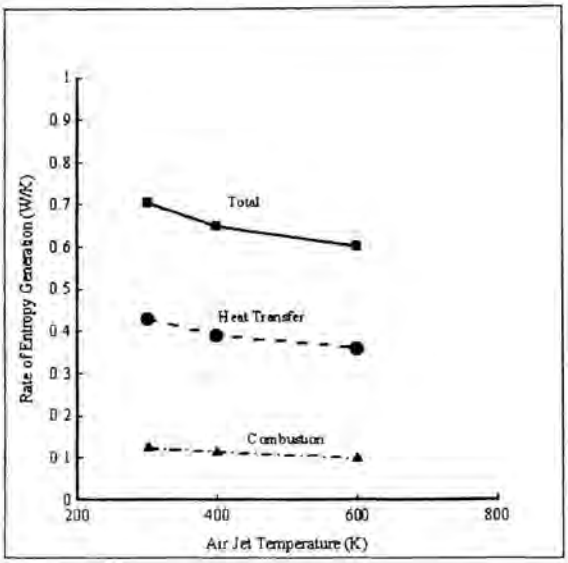

Figure 6. Variation of the rate of entropy generation with the air jet temperature

primarily due to heat transfer across the flame with the chemical reaction causing an important but secondary influence. It is further observed that in such a flame the rate of entropy generation reduces when the fuel jet velocity is low and the air jet temperature is high. Therefore, it can be concluded that from the point of thermodynamic optimization of a laminar diffusion flame it is better to maintain a lower fuel jet velocity and a higher air jet temperature.

ACKNOWLEDGEMENTS

One of the authors, A.Datta, gratefully acknowledges the support of the Alexander von Humboldt Stiftung, Germany for sponsoring him to work in Germany.

REFERENCES

[1] Bejan, A., 1998, Thermodynamic optimization in heat transfer, Proceedings of the 11th Int. Heat Transfer Conf., Vol. 1, pp. 41-50, Aug. 23-28, Korea.

[2] Bejan, A., 1996, Entropy Generation Minimization, CRC Press, Boca Raton, Fl.

[3] Bejan, A., 1988, Advanced Engineering Thermodynamics, Wiley, New York.

[4] Howell, J.R. and Buckius, R.O., 1986, Fundamentals of Engineering Thermodynamics, McGraw-Hill, New York.

[5] Kreith, F. and Bohn, M.S., 1986, Principles of Heat Transfer, Harper and Row, New York.

[6] Datta, A., 2000, Entropy Generation in a confined laminar diffusion flame, Comb. Sci. And Tech., Vol. 159, pp. 39-56.

[7] Smooke, M.D., Mitchell, R.E. and Keyes, D.E., 1989, Numerical Solutions of two-dimensional axisymmmetric laminar diffusion flames, Combustion Sci. And Tech., Vol. 67, pp. 85.

[8] Hirschfelder, J.C., Curtiss, C.F., and Bird, R.B., 1954, Molecular theory of gases and liquids, John Wiley, New York.

[9] Hirt, C.W. and Cook, J.L., 1972, Calculating three-dimensional flows around structures and over rough terrain, J. Comp. Phys.., Vol. 10, pp. 324-341.

[10] Datta, A. and Som, S.K., 2000, Thermodynamic Irreversibilities and Second Law Analysis in a Spray Combustion Process, Comb. Sci. And Tech., Vol. 142, pp. 29-54.

[11] Mitchell, R.E., Sarofim, A.F. and Clomburg, L.A., 1980, Experimental and Numerical Investigation of Confines Laminar Diffusion Flames, Comb. And Flame, Vol. 37, pp. 227-244.

[12] Hiwase, S., Datta, A., and Som, S.K., 1998, Entropy balance and exergy analysis in the process of droplet combustion, J. of Physics D: Appl. Phys., Vol. 31, pp. 1601-1610.

HEFAT2002
1st International Conference on Heat Transfer, Fluid Mechanics, and Thermodynamics
8-10 April 2002, Kruger Park, South Africa
MJ2

THERMODYNAMIC OPTIMIZATION OF METAL-FORMING PROCESSES

J. T. Maximov and V. D. Zimparov
Department of Mechanical and Manufacturing Engineering
Technical University of Gabrovo
5300 Gabrovo
Bulgaria
E-mail: Maximov@tugab.bg

ABSTRACT

An optimization method for metal-forming processes by plastic deformation based on their modeling as thermodynamic processes has been implemented. The mathematical model of the thermodynamic system has been based on fundamental equations in mechanics of deformable solid and the first and second laws of thermodynamics.

The nature of the thermodynamic optimization is in minimization of the functional of the generated entropy. This functional depends on the manufacturing parameters of the corresponding metal-forming process. The mathematical nature of the problem is minimization of a functional of functions of several variables depending of parameters.

The paper shows the outcomes from the process optimization of spherical mandrelling (SM) of steel blanks following a generalized entropy generation criterion.

INTRODUCTION

Each metal-forming process can be presented as a change in a thermodynamic system consisting of two subsystems: an impact subsystem – a tool, and a subsystem subjected to impact - a workpiece. As a result of the interaction between them, both subsystems change their stressed and strained state. Both subsystems are in fact thermomechanic materials and during their interaction mechanical and heat effects dominate over the rest. The subsystem stressed and strained state and the heat exchange processes are interrelated. Heat is generated during mechanical interaction, the subsystem temperature fields are changed respectively and the mechanical equations of the subsystem state depend on temperature. For most metal-forming processes the hypothesis about a weak relation between mechanical and heat effects is inapplicable. The published studies [1] on the stressed and strained state of metal-forming systems usually treat only certain aspects of the behavior either of the tool only or of the workpiece only and in the latter case a hypothesis about a weak relation between mechanical interaction and heat exchange has been accepted.

Because of their complexity metal-forming processes are usually studied experimentally on the "black box" principle, mainly in technological aspect. Extreme values in the defined area of variation of changeable factors of the functional dependencies defined experimentally are determined by the methods of non-linear programming [2]. Metal-forming process optimization in economic aspect by minimizing the net cost function in the end is again based upon functional dependencies obtained experimentally.

But the metal-forming process is a thermodynamic one and it would proceed "most smoothly" if the mechanical, thermal, etc. resistances overcomed were the lowest. In this aspect an optimization theory for metal-forming processes modelled as thermodynamic ones, following the entropy generation criterion considered as a quantitative indicator of the resistances overcomed has not been developed yet. Entropy generation minimization in any thermodynamic process is equivalent to its optimization.

Entropy generation minimization as a fundamental optimization approach has been developed by A. Bejan [3-7] and implemented to processes with heat and fluid flows. Feidt [8] has used this approach to optimize power systems. As far as mechanical systems with dissipative processes are concerned, the approach has been used to optimize the design of rubber damping supports [9].

Tool-workpiece systems in metal-forming processes by plastic deformation are representatives of mechanical

systems with dissipative processes and can be differentiated as a subdivision of these systems. For this group of thermodynamic systems a general-purpose optimization method for metal-forming processes by plastic deformation based on minimization of the functional of the generated entropy has been developed [10]. This method has been implemented for optimization of spherical mandrelling process (SM). The purpose of this paper is thermodynamic optimization of SM process of a round hole with a nominal diameter d=22 mm in a low-carbon steel blanks.

NOMENCLATURE

A	work (J)
E	energy per unit length (J/m)
E_k	kinetic energy (J)
F_0	area of contact point set (m^2)
f_0	conveying velocity (m/tr)
k	thermal conductivity (W/m.^{0}K)
L	length (mm)
M_e	moment of rotation (Nm)
N	consumed power (W)
n_e	rotation frequency (min^{-1})
P	force (N)
$\bar{P}$	productivity (m/s)
Q	heat (J)
q	heat flow density (W/m^2)
S_{gen}	generated entropy (J/^{0}K)
T	temperature (^{0}K)
t	time (s)
u	displacement (m)
V	volume (m^3)
v	velocity (m/s)

Greek letters

γ	mathematical operator
δ	depth of plastic deformation (m)
ε_{ij}	strain tensor
η	Lagrange variables
θ	nutation angle
ξ_{ij}	strain velocity tensor
ρ	density (kg/m^3)
σ_{ij}	stress tensor
$\Delta\tau$	time step (s)
τ	manufacturing time (s)
ω	angular velocity (s^{-1})

Subscripts

a	absolute
gen	generated
k	kinetic
Q	heat
r	relative
u	useful

Supplement

a_i	number of 3 quantities
a_{ij}	number of 9 quantities
$a_i b_i$	algebraic sum of 3 addends
$a_{ij} b_{ij}$	algebraic sum of 9 addends

NATURE OF OPTIMIZATION METHOD OF METAL-FORMING PROCESSES

Each metal-forming process can be presented as a change in a thermodynamic system consisting of two subsystems, Fig. 1: an impact subsystem – a tool 1, and a system subjected to impact - a workpiece 2. The basic parameters of the state of the thermodynamic system tool – workpiece are strain tensor, stress tensor, temperature in the two subsystems. The first one is a function of displacement vector, the second one depends on strain tensor and the mechanical characteristics of the materials of the two media and the third parameter is a function of the stress tensor and strain velocity tensor and the relative velocity of the two systems. The mathematical model [11] of the thermodynamic system tool – workpiece is built from the following functions:

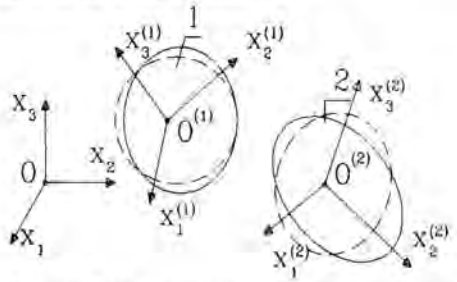

Figure 1. Coordinate systems in tool-die thermodynamic system.

$x_i = x_i\left(\eta_i^{(r)}, t\right)$, describing the movement of non-interacting subsystems in Ox_i, $r = 1, 2$;

displacement of points from the two subsystems into $Ox_i^{(r)}$: $u_i^{(r)}$;

contact point set (CPS) between subsystem (1) and subsystem (2): $F_0^{(r)}$;

strains in $Ox_i^{(r)}$: $\varepsilon_{ij}^{(r)}$;

velocities of the points in the two subsystems in $Ox_i^{(r)}$: $v_i^{(r)}$;

velocities of the strains in the two subsystems $Ox_i^{(r)}$: $\xi_{ij}^{(r)}$;

stresses in $Ox_i^{(r)}$: $\sigma_{ij}^{(r)}$;

workpiece density: $\rho^{(2)}$ (the tool density is practically constant);

heat flow density of the two subsystems in $Ox_i^{(r)}$: $q_i^{(r)}$;

temperature in the two subsystems: $T^{(r)}$

Sixty five dependencies exist among these 65 functions: law of movement - 6 equations; strain tensors - 12 dependencies; expressing the velocities by means of displacements - 6 dependencies; strain velocity tensor - 12 dependencies; equations of media movement in $Ox_i^{(r)}$ - 6 dependencies; equations of workpiece continuity $\dot{\rho}^{(2)} + \rho^{(2)} \operatorname{div} \bar{v}^{(2)} = 0$; equations of heat conductivity of media - 2 dependencies; Fourier law of heat conductivity - 6 dependencies among the heat flows and the temperature of the subsystems; mechanical equations of state - 12 dependencies; equations of CPS surfaces for both media - 2 equations:

$$
\begin{cases}
x_i = x_i\left(\eta_i^{(r)}, t\right) \\
\varepsilon_{ij}^{(r)} = \dfrac{1}{2}\left(\dfrac{\partial u_i^{(r)}}{\partial x_j^{(r)}} + \dfrac{\partial u_j^{(r)}}{\partial x_i^{(r)}} - \gamma^{(r)} \dfrac{\partial u_k^{(r)}}{\partial x_i^{(r)}} \dfrac{\partial u_k^{(r)}}{\partial x_j^{(r)}}\right) \\
\gamma^{(r)} = \begin{cases} 0, & r = 1 \\ 1, & r = 2 \end{cases}; \quad v_i^{(r)} = \dfrac{du_i^{(r)}}{dt} \\
\xi_{ij}^{(r)} = \dfrac{1}{2}\left(\dfrac{\partial v_i^{(r)}}{\partial x_j^{(r)}} + \dfrac{\partial v_j^{(r)}}{\partial x_i^{(r)}}\right) \\
\rho^{(r)} \dot{v}^{(r)} = \dfrac{\partial \sigma_{ij}^{(r)}}{\partial x_j^{(r)}} + \rho^{(r)} f^{*(r)} \\
\dot{\rho}^{(2)} + \rho^{(2)} \operatorname{div} \bar{v}^{(2)} = 0 \\
c^{(r)} \rho^{(r)} \dfrac{dT^{(r)}}{dt} - \gamma^{(r)} \lambda \sigma_{ij}^{(r)} \xi_{ij}^{(r)} - \dfrac{\partial\left(k_i^{(r)} \dfrac{\partial T^{(r)}}{\partial x_i^{(r)}}\right)}{\partial x_i^{(r)}} = 0 \\
q_i^{(r)} = -k_i^{(r)} \dfrac{\partial T^{(r)}}{\partial x_i^{(r)}}; \quad F_0^{(r)}\left(x_i^{(r)}, t\right) = 0 \\
\sigma_{ij}^{(r)} = f\left(\lambda_i^{(r)}, \varepsilon_{ij}^{(r)}, \dot{\varepsilon}_{ij}^{(r)}, T^{(r)}, \dot{T}^{(r)}, \ldots\right)
\end{cases}
\tag{1}
$$

After system integration (1) the entropy generation can be found [10]:

$$
\begin{aligned}
S_{gen} = & \sum_{r=1}^{2} \beta^{(r)} \int_{F_0^{(r)}} \int_0^{\tau} \frac{\sigma_{ij}^{(r)} v_i^{a\,(m,n)} n_j^{(r)}}{T_a^{(r)}} dt\, dF_0^{(r)} + \\
& + \sum_{r=1}^{2} \beta^{(r)} \int_{V^{(r)}} \int_0^{\tau} k_i^{(r)} \left(\frac{\operatorname{grad}_i T_a^{(r)}}{T_a^{(r)}}\right)^2 dt\, dV^{(r)} + \\
& + \int_{V^{(2)}} \int_0^{\tau} \frac{\lambda \sigma_{ij}^{(2)} \xi_{ij}^{(2)}}{T_a^{(2)}} dt\, dV^{(2)}
\end{aligned}
\tag{2}
$$

where $\beta^{(1)}$ and $\beta^{(2)}$ $\left(\beta^{(1)} + \beta^{(2)} \le 1\right)$ are coefficients, showing the distribution of the input heat into both subsystems and depend on the temperature differences of the two subsystems on CPS; λ is a coefficient showing what part of the strain energy is converted into heat ($\lambda = 0{,}85 \div 0{,}95$).

The energy used for plastic deformation can be considered as effective work A_u. The first law of the thermodynamics for thermodynamic systems tool – workpiece, can be represented as:

$$
d\bar{A}^e = dE_k + dA_Q^e + dA^m + dA^i, \tag{3}
$$

where: $d\bar{A}^e$ is elementary work of the active surface forces, action of the area, out of CPS; dE_k is the change of the system kinetic energy; dA_Q^e is the work of surface forces on CPS, which is converted into heat dQ^e; dA^m is the elementary work of body forces; $dA^i = \sum_{r=1}^{2} \int_{V^{(r)}} \sigma_{ij}^{(r)} \xi_{ij}^{(r)} dV^{(r)} dt$ is the elementary work of internal surface forces.

From Eq. (3) it can be seen that A_u is this part of the work of the workpiece internal surface forces $A^{i(2)}$ which is used for plastic deformation:

$$
A_u = \lambda A^{i(2)} = \lambda \int_{V^{(2)}} \int_0^{\tau} \sigma_{ij}^{(2)} \xi_{ij}^{(2)} dt\, dV^{(2)} \tag{4}
$$

where τ is the time for one operation cycle.

If the mechanical energy $\bar{A}^e$ input in the system tool – workpiece is used only for work to change the shape A_u, it is converted into energy of dissipation and entropy S_{gen, A_u} is generated.

The following inference can be made: The "perfect" metal-forming process is the one that satisfies the following three conditions simultaneously:

The mechanical energy input in the system tool – workpiece is completely used up only as work for shape formation A_u:

$$
\bar{A}^e = |A_u|. \tag{5}
$$

The functions $\sigma_{ij}^{(2)}$ and $\xi_{ij}^{(2)}$ satisfy the condition:

$$
A_u = \lambda \int_{V^{(2)}} \int_0^{\tau} \sigma_{ij}^{(2)} \xi_{ij}^{(2)} dt\, dV^{(2)} \to \min. \tag{6}
$$

The functional of the generated entropy S_{gen, A_u} has a minimum:

$$
S_{gen, A_u} \to \min. \tag{7}
$$

The meaning of the second condition is that a minimum amount of mechanical energy input from outside is completely dissipated, while the third condition appears to be a summarized optimization criterion of each type of metal-forming process.

Therefore the condition of minimum of generated entropy S_{gen} appears to be a summarized optimization criterion of each type of metal-forming process.

OPTIMIZATION OF SM PROCESS BY ENTROPY GENERATION MINIMIZATION (EGM)

Nature of SM process

SM is a finishing method of forming round and transverse profile holes previously drilled, by surface plastic or volumetric plastic deformation. The tool rotates around its own axis 1 at angular velocity $\bar{\omega}_r$ and at the same time it rotates around axis 2 of the hole being formed at angular velocity $\bar{\omega}_c$, Fig. 2. The absolute angular velocity of the tool with respect to the static blank is the vector sum $\bar{\omega}_a = \bar{\omega}_c + \bar{\omega}_r$, where $\theta = 2^0$, and $\angle\bar{\omega}_c\bar{\omega}_r = 180^0 - \theta$. Simultaneously, the tool translates on the axis 2 of the hole. SM is a variant of the more general method for spherical broaching and mandrelling [12, 13] during which cutting and plastic deformation are performed at the same time. For surface plastic deformation the method is successfully carried out on milling, drilling and centering machines, lathes, etc. and it considerably increases their technological potentials.

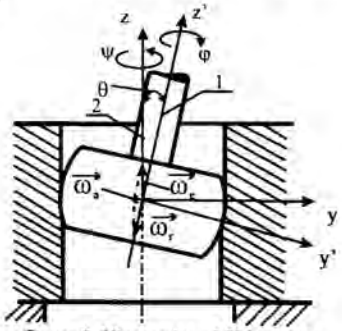

Figure 2. Kinematics of SM process

The manufacturing parameters of SM are rotation frequency of the tool spindle $n_c = 30\omega_c/\pi$, and conveying velocity of the blank (tool) f_0. Translation velocity of the blank (tool) is $f = f_{(1)}.n_c$.

The power characteristics of SM are: the moment of rotation M_c, applied to the tool spindle; the axial force F, applied to the tool (blank); consumed power N.

Feature of EGM method during the SM

The functional of the generated entropy depending on the manufacturing parameters has been approximated as a function of these parameters. The SM process optimization has been reduced to optimization of obtained function with set constraints of the manufacturing parameters (one-purpose optimization). To this purpose the functional of generated entropy is presented in a finite element formulation. Division in subfields has been made both for space and time. The values of the functional respectively of the approximating function, have been calculated numerically for various combinations of values of the manufacturing parameters. On the basis of these values an analytic type of the optimized function has been obtained.

The generated entropy functional is transformed in the following numerical form [10]:

$$S_{gen} = \sum_{k=1}^{n}\sum_{\ell=1}^{m}\frac{I_k}{\bar{T}^{(1)}_{a,k,\ell}}\Delta\tau_\ell\Delta F^{(1)}_{0,k} + \sum_{k=1}^{n}\sum_{\ell=1}^{m}\frac{\lambda\bar{\sigma}^{(2)}_{ij,k}\bar{\xi}^{(2)}_{ij,k}}{\bar{T}^{(1)}_{a,k,\ell}}\Delta\tau_\ell\Delta V^{(2)}_k + \sum_{r=1}^{2}\sum_{k=1}^{n}\sum_{\ell=1}^{m}k^{(r)}_i\left(\frac{\mathrm{grad}_i\bar{T}^{(r)}_{a,k,\ell}}{\bar{T}^{(r)}_{a,k,\ell}}\right)^2\Delta\tau_\ell\,\Delta V^{(r)}_k \qquad (8)$$

where: $I_k = \frac{1}{\Delta\tau_\ell}\int_0^{\Delta\tau_\ell}\bar{\sigma}^{(1)}_{ij,k}(t)\bar{v}^{a(1,2)}_{i,k}(t)\bar{n}^{(1)}_{j,k}dt$; $\bar{T}^{(r)}_{a,k,\ell}$, $\mathrm{grad}_i\bar{T}^{(r)}_{a,k,\ell}$, $\bar{\sigma}^{(r)}_{ij,k}$, $\bar{\xi}^{(r)}_{ij,k}$, $\bar{v}^{a(1,2)}_{i,k}$ are averaged values, respective of the absolute temperature, temperature gradients, the stress tensors and the strain velocity tensors, relative velocity of the coinciding point of the tool and workpiece on CPS in a node circumference of k-th subregion $\Delta V^{(r)}_k$, respective $\Delta F^{(1)}_{0,k}$, in the ℓ-th time step $\Delta\tau_\ell$; $k^{(r)}_i$ is heat conductivity coefficient; n is the number of subregions in the r-th subsystem; m is the number of time steps (the distribution of the input heat into bothsubsystems has been obtained automaticaly through boundary conditions in the finite element formulation).

During SM plastic deformation occurs only on CPS of the hole surface at small depth ($\delta = 0{,}1 \div 0{,}2$ mm) and CPS is a narrow band $0{,}5 \div 0{,}15$ mm wide.

Finally [10]:

$$S_{gen} = N\sum_{\ell=1}^{m}\frac{\Delta\tau_\ell}{\bar{T}^{(1)}_{a,\ell}} + \sum_{r=1}^{2}\sum_{k=1}^{n}\sum_{\ell=1}^{m}k^{(r)}_i\left(\frac{\mathrm{grad}_i\bar{T}^{(r)}_{a,k,\ell}}{\bar{T}^{(r)}_{a,k,\ell}}\right)^2\Delta\tau_\ell\,\Delta V^{(r)}_k \qquad (9)$$

where: N is the total consumed power.

Experimental research of SM process

The following experimental results have been obtained, Table 1, during SM of a round hole with diameter 22 mm and tightness $i = 0{,}15$ mm in a low-carbon steel blanks on a multi-purpose milling machine.

Optimization of SM process following a generalized entropy generation criterion

The holes formed have a length of $L = 12$mm. Table 2 shows the times $\tau = 60L/n_c f_0$, productivity $\bar{P} = n_c.f_0/60$, consumed energy E per unit of formed hole length and the calculated values of generated entropy.

The energy E is calculated by the formula:

$$E = N\tau/L, \qquad (10)$$

where: $N = \frac{\pi}{30}M_c n_c + 6x10^{-5}Pn_c f_0$ is the total consumed power.

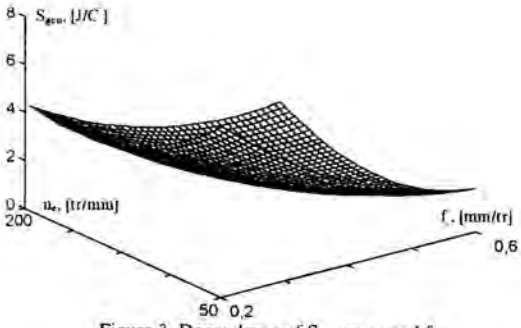

Figure 3. Dependence of S_{gen} on n_e and f_0

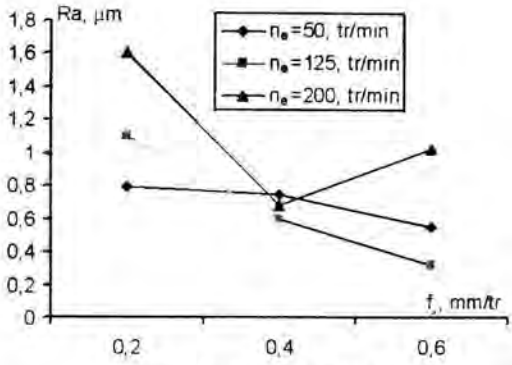

Figure 4. Dependence of Ra on f_0

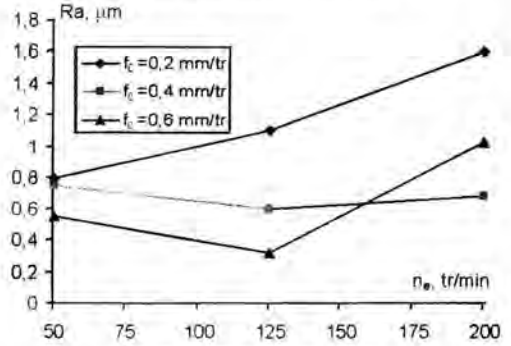

Figure 5. Dependence of Ra on n_e

The generated entropy is approximated as a function of manufacturing parameters n_e and f_0 according to the least-squares method. Complete two-dimensional polynomial of second degree has been used Fig. 3:

$$S_{gen} = 16{,}009 - 0{,}081 n_e - 35{,}137 f_0 + 0{,}046 n_e f_0 + \\ + 2{,}14.10^{-4} n_e^2 + 24{,}667 f_0^2 \quad (11)$$

The mathematical model obtained Fig. 3 is minimized at $n_e = n_e^* = 125{,}26$ tr / min , $f_0 = f_0^* = 0{,}595$ mm / tr .

Figure 4 and Fig. 5 show the surface roughness variation, Ra, in a function of manufacturing parameters n_e and f_0.

Obviously, the highest quality surface formed at minimum power consumption and maximum productivity is obtained when $n_e = n_e^* = 125$ tr/min and $f_0 = f_0^* = 0{,}6$ mm/tr . These parameters correspond to the optimum individual case of SM of a hole having nominal diameter d=22 mm in a low-carbon steel blanks.

CONCLUSION

Optimization of SM process of low-carbon steel blanks has been carried out, using EGM method to find an optimum individual case of SM.

It has been proved that the generated entropy appears to be a generalized optimization criterion: the highest quality of the formed surface for minimum power consumption is obtained for these manufacturing parameter values for which the generated entropy functional has a minimum.

The SM process optimization has reduced to a single-purpose optimization. The target function has been obtained as a result of approximation of the generated entropy functional depending on the manufacturing parameters by a function of these parameters.

The presented algorithm can be employed as an effective tool of optimization of mechanical systems with dissipative processes and in other metal-forming processes by plastic deformation.

APPENDIX

Table 1

	1	2	3	4	5	6	7	8	9
n_e, [min^{-1}]	200	200	50	50	200	50	125	125	125
f_0, [mm/tr]	0,6	0,2	0,6	0,2	0,4	0,4	0,6	0,2	0,4
P, [N]	6300	8300	7400	6600	6200	6000	5350	5700	5250
M_e, [Nm]	2,3	3,73	3,44	6,88	2,87	3,44	1,85	2,29	3,67
N, [W]	60,77	83,65	21,71	57,12	68,37	20,01	30,9	32,34	52,4

Table 2

	1	2	3	4	5	6	7	8	9
n_e, [min^{-1}]	200	200	50	50	200	50	125	125	125
f_0, [mm/tr]	0,6	0,2	0,6	0,2	0,4	0,4	0,6	0,2	0,4
τ, [s]	6	18	24	72	9	36	9,6	28,8	14,4
$\bar{P}$, [mm/s]	2	0,667	0,5	0,167	1,333	0,333	1,25	0,417	0,833
E, [J/mm]	30,38	125,48	43,42	342,72	51,28	60,03	24,72	77,62	62,9
S_{gen}, [J/^{0}K]	1,178	4,521	1,7	7,824	1,951	2,331	0,89	2,958	2,394

REFERENCES

[1] I. Reznikov, A. Heat Physics of Mechanical Working of Materials, Moscow, 1981. (in Russian)

[2] L. Collatz, W. Wetterling. Optimierungsaufgaben. Springer - Verlag, Berlin, 1966.

[3] A. Bejan. Entropy Generation through Heat and Fluid Flow. J. Wiley, New York, 1982

[4] A. Bejan. Entropy Generation Minimization. CRC Press, Boca Raton, FL, 1996.

[5] A. Bejan, G. Tsatsaronis, M. Moran. Thermal Design and Optimization. J. Wiley, New York, 1996

[6] A. Bejan. Advanced Engineering Thermodynamics. J. Wiley, New York, 1997.

[7] A. Bejan, "Entropy Generation Minimization. The new thermodynamics of finite size devices and finite time processes", J. Appl. Phys., Vol. 79, Feb. 1, 1996, pp. 1191 - 1218.

[8] Feidt M. Thermodynamiqui et optimisazion energetique des systemes et procedes. TEC et DOC. Paris, 1987.

[9] E. Mamut, "Second Low Based Optimization of Sistems whit Thermomechanical Dissipative Processes", Thermo-dynamic Optimization of Complex Energy Systems, NATO Science Series 3, High Technology - Vol. 69. Neptun, Romania, 1998. pp 297-312.

[10] Maximov, J. T., 2001, "The entropy generation in tool-die thermodynamic system as a generalized optimization criterion", Annual Journal of TU of Gabrovo, Vol. XXV. pp. 73-84.

[11] Maximov, J. T., 2000, "Generalized reference model of tool-die thermodynamic system in metal treatment processes", Annual Journal of TU of Gabrovo, Vol. XXIV, pp. 97-112.

[12] Maximov, J. T., 1990, "Kinematic and Force Analysis of Spherical Mandrelling and Broaching", PhD Thesis, TU of Gabrovo (in Bulgarian).

[13] Maximov, J. T., 1996, "On a particular application of a rigid body with a single fixed point", Annual Journal of TU of Gabrovo, Vol. XIX, pp. 28-37.

1st International Conference on Heat Transfer, Fluid Mechanics and Thermodynamics
8 - 10 April 2002. KrugerPark,South Africa
AS3

THE AC-HEATED WIRE TECHNIQUE FOR THE MEASUREMENT OF THERMAL PROPERTIES OF CONDUCTING LIQUIDS

S.R. ATALLA
Associate Professor
Department of Physics , Faculty of Science ,
Fayoum Branch,Cairo University,Fayoum ,Egypt
E-mail:satalla@menanet.net

ABSTRACT

Establishment of the temperature oscillations generated by an AC-heated thin metallic wire coated with a very thin insulating layer, and propagating in a conducting liquid, is described by a set of two differential equations, the solution of which was obtained .This solution shows that measurement of the amplitude and/ or phase of the third harmonic signal of these oscillations along with power, frequency ,and thermal properties of the wire and the insulating layer ,allows the measurement of thermal diffusivity (a), volumetric heat capacity (ρCp) and thermal conductivity(λ)of the conducting medium investigated.

Further analysis of the obtained solution shows that an essential condition to be satisfied is that thickness of the insulating layer must be small enough to allow the temperature oscillations penetrate to the conducting medium. This in turn depends upon and can be easily controlled by the frequency of the heating current.

This technique was tested measuring the mentioned thermal properties of water and mercury in the temperature range 30-90C. The obtained results are in quite good agreement with the published data. The mentioned thermal properties of aqueous solutions of NaOH (5-20%) by weight)were also investigated in same temperature range. The obtained results are reported and discussed.

INTRODUCTION

Measurement of the thermal properties of conducting liquids at high temperatures is a quite challenging experimental task . The obtained results for thermal conductivity are distorted due to convection and possible radiation at high temperatures. Mainly for this reason published experimental data for the same liquid differ considerably. Development of convection free experimental techniques is essential to get reliable data for the thermal properties of liquids. This is important for the development of the liquid state theory.

The ac-heated wire technique has been successfully used for the measurement of thermal properties: thermal diffusivity (a) ,volumetric heat capacity (ρc_p),and thermal conductivity (λ) of non-conducting liquids [1]. In [2] and [3] the ac-heated wire technique was used for the measurement of the mentioned thermal properties of some nitrate salts. All mentioned works were limited to the investigation of the thermal properties of non-conducting liquids. In [4] theory of the ac-heated wire coated with a very thin insulating layer, for the measurement of thermal properties of conducting liquids was given with approximation that the thin layer is plane. This approximation has put some strong limitations on the thickness of the insulating layer. In this work, the exact solution is given for better assessment of the obtained direct experimental results.

3.Nomenculature

r_1 - radius of the wire (m)

r_2 - outer radius of the insulating layer (m)

a -thermal diffusivity ($m^2 s^{-1}$)

C' -specific heat of the wire material($Jkg^{-1}.K^{-1}$)

Cp -specific heat of the liquid($Jkg^{-1}.K^{-1}$)

m' - mass of the wire (kg)

ω – angular frequency (rad s^{-1})

W - power per unit length (Wm^{-1})

S_1 - side area of the wire (when $r = r_1$) (m^2)

S_2 - side area of the wire (when $r = r_2$) (m^2)

I_0 -Bessel function of the zero order.

H_0-Hankel function of the zero order.

I_1 -Bessel function of the first order.

H_1-Hankel function of the first order.

Greek letters

θ - amplitude of temperature oscillations

λ -thermal conductivity of the liquid($W/m^{-1}K^{-1}$)

ρ –density (kgm^{-3})

Subscripts

1 coating layer

2 liquid

2.THEORY

The temperature oscillations generated by an ac- heated metallic wire coated with a very thin layer of insulating material, and propagating in a conducting liquid are described by the following two differential equations (Figure 1):

$$\partial^2 \theta_1/\partial r^2+(1/r)\,\partial\theta_1/\partial r-(2i\,\omega/a_1)\,\theta_1=0 \quad (1)$$

$$\partial^2 \theta_2/\partial r^2+(1/r)\partial\theta_2/\partial r-(2i\omega/a_2)\,\theta_2=0 \quad (2)$$

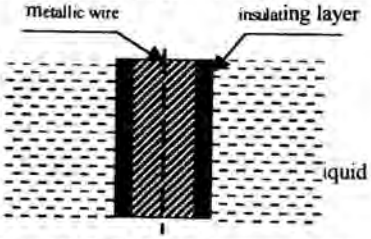

Figure 1.Coated wire immersed in the investigated liquid

We have the following boundary conditions :

$$W=2m'c'i\omega\theta_1\,|_{r=r1}-\lambda_1 S_1(\partial\theta_1/\partial r)\,|_{r=r1} \quad (3)$$

$$\theta_1 = \theta_2\,|_{r=r2} \quad (4)$$

$$\lambda_1(\partial\theta_1/\partial r)=\lambda_2(\partial\theta_2/\partial r)\,|_{r=r2} \quad (5)$$

$$\theta_2 = \theta_1\,|_{r2=r3} \quad (6)$$

Equation (3) expresses the energy balance condition at the wire-coating interface. Equations (4) and (5) express the continuity of the temperature oscillations and heat flux at the coating-liquid interface. Equation (6) expresses the fact that the temperature oscillations are damped in a thin layer surrounding the wire.

Solutions of equations (1) and (2) are written as:

$$\theta_1=A\,I_0(\sqrt{-2i\omega/a_1}\,r)+BH_0(\sqrt{-2\,i\,\omega/a_1}\,r) \quad (7)$$

$$\theta_2=C\,I_0(\sqrt{-2\,i\,\omega/a_2}\,r)+DH_0(\sqrt{-2\,i\,\omega/a_2}\,r) \quad (8)$$

Where A,B,C and D are constants to be determined from the boundary .

Let us introduce the following notations:

$$\alpha'=\sqrt{-2\,i\,\omega/a_2}\,, \quad \beta'=\sqrt{-2\,i\,\omega/a_2}$$

$$S=\beta'\lambda_2 H_1'(\beta' r_2)H_0(\alpha' r_2)-\alpha'\lambda_2 H_1(\alpha' r_2)H_0(\beta' r)$$

$$T=\alpha'\lambda_2 H_0(\beta' r_2)I_0(\alpha' r_2)-\beta'\lambda_2 I_0(\alpha' r_2)H(\beta' r)$$

$$Y=2m'c'i\omega\, I_0(\alpha' r_1)-\lambda_1 S_1\alpha' I_1(\alpha' r_1)$$

$$Z=2m'c'i\omega\, H_0(\alpha' r_1)-\lambda_1 S_1\alpha' H_1(\alpha' r_1)$$

Then we get:

$$A=WS/(SY+ZT)\,,\quad B=WS/(SY+ZT)$$

$$C=[AI_0(\alpha' r_1)+BH_0(\alpha' r_1)]/H_0(\beta' r_2)$$

For the amplitude of the temperature oscillations of the wire ,we get:

$$\theta_1=W[(T\,I_0(\alpha'.r_1)+SH_0(\alpha' r_1)/(SY+ZT)] \quad (9)$$

Let us introduce the following notations:

$$C_1=A_1+iB_1=H_0(\alpha' r_1)I_1(\alpha' r_2)+I_0(\alpha' r_1)H_1(\alpha' r_2)$$

$$C_2=A_2+iB_2=H_0(\alpha' r_2)I_0(\alpha' r_1)-I_0(\alpha' r_2)H_0(\alpha' r_1)$$

$$C_3=A_3+iB_3=H_1(\alpha' r_1)I_0(\alpha' r_2)-I_1(\alpha' r_1)H_0(\alpha' r_2)$$

Then we obtain the following formula:

$$\theta_1 = \frac{\alpha' \lambda_1 H_0(\beta' r_2) C_1 + \beta' \lambda_2 H_1(\beta' r_2) C_2}{2m'c'i\omega[\beta'\lambda_2 H_1(\beta' r_2)C_2 + \alpha'\lambda_1 H_1(\beta' r_2)C_1] - \alpha'\beta'\lambda_1\lambda_2 H_1(\beta' r_2) C_3} \quad (10)$$

Let us further introduce the following notations:

$\alpha = \sqrt{2\omega / a_1}$, $\beta = \sqrt{2\omega / a_2}$,

$\gamma = \alpha \lambda_1 / \beta \lambda_2$, $\theta_0 = W / m' c' \omega$

$\phi_1 = -her(\alpha r_1)\, ber'(\alpha r_2) + hei(\alpha r_1)\, bei'(\alpha r_2) +$
$+ ber(\alpha r_1) her'(\alpha r_2) - her(\alpha r_1).hei'(\alpha r_2).$

$\phi_2 = -her(\alpha r_1).bei'(\alpha r_2) + hei(\alpha r_1).ber'(\alpha r_2) +$
$+ ber(\alpha r_1) hei'(\alpha r_2) - her(\alpha r_1) her'(\alpha r_2).$

$\phi_3 = -her(\beta r_2)\ \phi_1 - hei(\beta r_2)\ \phi_2$

$\phi_4 = -her(\alpha r_1)\ \phi_2 + hei(\alpha r_1)\ \phi_2$

$\phi_5 = her(\alpha r_2).Ber(\alpha r_1) - hei(\beta r_2).bei(\alpha r_1)$
$-her(\alpha r_1).ber(\alpha r_2) + her(\alpha r_1).bei(\alpha r_2).$

$\phi_6 = her(\alpha r_2).ber(\alpha r_1) - hei(\beta r_1).bei(\alpha r_1)$
$- her(\alpha r_1).ber(\alpha r_2) + her(\alpha r_1).bei(\alpha r_2).$

$\phi_7 = -her'(\beta r_2).\phi_5 + hei'(\beta r_2).\phi_6$

$\phi_8 = -her'(\beta r_2).\phi_6 + hei'(\beta r_2).\phi_5$

$\phi_9 = her'(\alpha r_1) ber(\alpha r_2) - hei'(\alpha r_1)$
$.her'(\alpha r_1) + hei(\alpha r_2).hei'(\alpha r_1).$

$\phi_{10} = her'(\alpha r_1).bei(\alpha r_2) - hei'(\alpha r_1).ber(\alpha r_2) -$
$-her(\alpha r_2) hei'(\alpha r_1) + hei(\alpha r_2).her'(\alpha r_1).$

$\phi_{11} = her'(\beta r_2).\phi_9 - hei'(\beta r_2).\phi_{10}$

$\phi_{12} = -hei'(\beta r_2)\phi_9 - her'(\beta r_2).\phi_{10}$

$\phi_{13} = \phi_7 + \nu\ \phi_3$

$\phi_{14} = \phi_8 + \nu\phi_4$

$\phi_{15} = (-\phi_{12}\phi_{13} + \phi_{11}\phi_{14}) / (\phi_{13}^2 + \phi_{14}^2)$

$\phi_{16} = (-\phi_{12}\phi_{14} + \phi_{11}\phi_{14}) / (\phi_{13}^2 + \phi_{14}^2)$

$\phi_{17} = (\phi_{15} + \phi_{16}) / \sqrt{2}$

$\phi_{18} = (\phi_{16} - \phi_{15}) / \sqrt{2}$

$\eta = \rho' c' / 2\rho c,$

$\chi_{21} = \sqrt{2\omega / a_2}\, r_1$

$P = (1/\eta\chi_{21}).\phi_{17}$

$Q = (1/\eta\chi_{21}).\phi_{18}$

Finally we get :

$\theta / \theta_0 = [P^2 + (1 + Q)^2]^{-1/2}$

$\varphi = \tan^{-1}[(1+Q)/P]$

It is useful to discuss the following two special cases :

Bare wire (without any insulating layer)

If we put $\delta = (r_2 - r_1) = o$ then we get the following formula :

$$\theta_1 = \frac{W}{2m'c'i\omega - \lambda_2\sqrt{-2i\omega/a_2}[H_1(\beta' r_2)/H_0(\beta' r_2)]} \quad (11)$$

Equation (11) describes the the amplitude of temperature oscillations of a bare wire immersed in the investigated liquid [6] .

Thick layer

Another important case is when the insulating layer is thick enough that the temperature oscillations are damped within it. Then we get the following formula for the temperature oscillations of the wire :

$$\theta_1 = \frac{W}{2m'c'i\omega - \lambda_1\sqrt{2i\omega/a_1}\{H_1(\beta r_1)/H_0(\alpha r_1)} \quad (12)$$

Equations (11) and (12) allow the measurement of the thermal properties of the bulk material of the insulating layer in a separate experiment if required.

4.EXPERIMENTAL METHOD

An essential condition for the successful application of the ac- heated coated wire technique for measurement of the mentioned thermal properties of conducting liquids , is that thickness of the insulating layer must be less than the effective thickness (Λ) of the insulating layer ,where the temperature oscillations are practically damped. This condition is expressed in the form of $\delta < \Lambda$,where $\Lambda = 2\pi\sqrt{a/2\omega}$.

For frequencies 100-150Hz,and $a = 10^{-8}$-$10^{-7} m^2 s^{-1}$, we get δ = 0.05 - 0.1 mm. This means that coating the wire with layers of thickness of the order of several microns is quite satisfactory.

Another important point in this technique is the determination of the thermal properties of the coating layer itself. This is carried out *in situ* according to the technique described in [5]with the same experimental set-up described here.

Set-up

In this work, the experimental set-up described in [6]was used to carry out the test of this technique. A stainless steel wire of diameter 0.025 mm ,coated with a layer of Polyesterimide of thickness 2 microns, was immersed in the investigated liquid in a stainless steel cell (Fig.2). The inner surface of the cell was also coated with very thin insulating layer. The cell was then covered ,sealed and mounted in an electric furnace that provides the mean temperature of the investigated liquid. Then,thewire was connected as an arm in an ac-bridge fed by an ac-source at different frequencies (80-150 Hz).

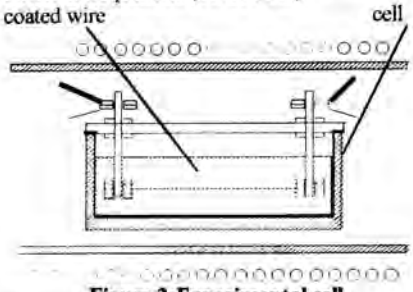

Figure 2:Experimental cell

The cell and furnace were enclosed in a water-cooled vacuum chamber (Fig.3).

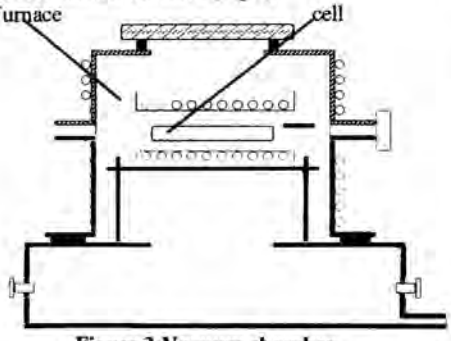

Figure 3:Vacuum chamber

Experimental Procedure and Data Reduction

The water-cooled chamber was evacuated by a vacuum pump and then filled with nitrogen gas. Then the furnace was powered and current is passed in the coated wire. When the mean temperature of the cell becomes stable, the bridge is balanced at (f),the obtained third harmonic signal corresponding to the amplitude of temperature oscillations of the wire, along with power and properties of the wire and coating at 4-5 different frequencies were measured.

Finally, the obtained data were processed by means of a specially written interactive PC computer program, based upon an iterative technique. As a result, the thermal properties (a), (ρCp) and (λ) of the liquid investigated were calculated. The mentioned thermal properties of the wire used and the coating were measured in a separate experiment as described in [5],and the role of radiation is calculated as described in [7] .To test this technique, mercury and water were investigated Then ,the thermal properties mentioned were measured for NaOH aqueous solutions at concentrations 5-20% by weight were measured.

Results

Table I gives the results of measurement of thermal diffusivity (a) volumetric heat capacity (ρCp) and thermal conductivity (λ) of mercury. As seen it increases by 10% in the temperature range 20-75 ^{0}C.After that the increase is more steep. It is recommended to do more measurements at higher temperatures. The obtained results for volumetric heat capacity are 5 % lower than those given in [8]and [9] .For thermal conductivity, the results obtained coincide very well with the results given in [8] in the investigated temperature range.

TableI:Thermal Properties of Mercury:

Property / Temperature	10^7 x a ($m^2.s^{-1}$)	10^{-6} x ρCp $J.m^{-3}.K^{-1}$	λ ($W.m^{-1}.K^{-1}$)
20	4.51	1.84	8.29
25	4.53	1.837	8.32
30	4.55	1.838	8.32
35	4.56	1.837	8.43
40	4.57	1.836	8.51
45	4.58	1.84	8.61
50	4.61	1.837	8.75
55	4.53	1.836	8.77
60	4.65	1.835	8.84
65	4.67	1.834	8.95
70	4.69	1.834	9.07
75	4.71	1.835	9.16
80	4.81	1.834	9.28
85	4.95	1.821	9.38
90	5.21	1.814	9.49

Table II gives the results of measurement of thermal diffusivity (a) of water and NaOH aqueous solutions at concentrations 5-20% by weight. The results obtained for thermal diffusivity of bi-distilled and de-ionized water, agree well up to 85^{0}C with data recommended by IUPAC given in [9].For NaOH aqueous solutions, no published data were

available. As seen ,the higher the concentration, the lower the thermal diffusivity.

TableII: Thermal diffusivity of water and NaOH aqueous solutions:

TC	10^7 x a ($m^2.s^{-1}$)				
	Concentration				
	0%	5%	10%	15%	20%
20	1.44	1.41	1.33	1.29	1.26
30	1.44	1.428	1.38	1.31	1.28
40	1.44	1.43	1.39	1.36	1.29
50	1.44	1.44	1.44	1.38	1.31
60	1.44	1.45	1.48	1.418	1.38
70	1.44	1.49	1.50	1.438	1.45
80	1.44	1.52	1.51	1.46	1.48
90	1.61	1.55	1.52	1.47	1.50

Table III gives the obtained results for volumetric heat capacity illustrated in figure(4)
for the same substances. As seen, the higher the concentration ,the higher values of volumetric heat capacity.

TableIII:Volumetric heat capacity of water and NaOH aqueous solutions

TC	10^{-6} x ρCp $J.m^{-3}.K^{-1}$				
	Concentration				
	0%	5%	10%	15%	20%
20	4.16	4.38	4.59	4.77	4.84
30	4.155	4.37	4.58	4.76	4.82
40	4.15	4.36	4.58	4.75	4.81
50	4.14	4.35	4.57	4.74	4.79
60	4.13	4.34	4.56	4.73	4.77
70	4.11	4.35	4.55	4.72	4.75
80	4.096	4.34	4.54	4.71	4.76
90	4.06	4.33	4.53	4.707	4.73

For thermal conductivity, the obtained results for the same substances are given in Table IV and in figure (7). Present data are 2% lower than data recommended by IUPAC given in [9].

Table IV:Thermal conductivity of water and NaOH aqueous solutions

TC	λ ($W m^{-1}.K^{-1}$)				
	Concentration				
	0%	5%	10%	15%	20%
20	0.599	0.618	0.598	0.610	0.614
30	0.618	0.620	0.603	0.623	0.621
40	0.628	0.632	0.622	0.631	0.634
50	0.644	0.642	0.649	0.642	0.647
60	0.652	0.669	0.664	0.654	0.654
70	0.664	0.671	0.682	0.672	0.682
80	0.667	0.685	0.698	0.688	0.697
90	0.675	0.692	0.706	0.716	0.724

Thermal conductivity decreases as concentration increases. Investigation of solutions with higher concentrations affected the insulation layer.

The analysis of the data obtained for thermal diffusivity showed that the relative standard deviation of the experimental points varied from 1.2 to 1.6 %.The combined standard uncertainty associated with the measurements was determined to be 2.8%,and the expanded uncertainty 5.6 %, for 0.95 confidence level.

For the volumetric heat capacity the relative standard deviation of the experimental points varied from 1.1 to 1.4 %.The combined standard uncertainty associated with the measurements was determined to be 2.5%,and the expanded uncertainty was 5.1%, for 0.95 confidence level.

For thermal conductivity measurements, the relative standard deviation of the experimental points varied from 1.1 to 2.2 %.The combined standard uncertainty associated with the measurements was determined to be 3.3 %,and the expanded uncertainty 6.6%, for 0.95 confidence level.

CONCLUSION

In view of the mentioned advantages, namely the suppression of convective heat transport and the possibility to calculate the contribution of radiation heat transport, the ac-heated coated wire technique is highly recommended for the measurement of thermal properties: thermal diffusivity, volumetric heat capacity and thermal

conductivity of conducting and non-conducting polar liquids.

5.REFERENCES

[1]. Atalla S.R. ,El-Sharkawy A.A, Gasser F.A.,1981,Int. J. Thermophys., Vol.2,pp 155-162.

[2]Atalla S.R.,Attia G.A,El-Naggar M.M,El-SayedT.A. El-Sharkawy A.A.,Mina N.K.,Gamal G.A.,Nagat A.T.1994, in "Proceedings of the 1st Int. Spring School and Symposium on Advances in Material Science Research", Cairo, Egypt, pp 633-642.

[3].Atalla S.R.,AttiaG.A.,El-Naggar M.M.,El-Sayed,T. El-Sharkawy. A.A,Mina N.K., Kenawy M.,1994, in "Proceedings of the 1st Int .Spring School and Symposium on Advances in Material Science Research", Cairo, Egypt, pp 623-631.

[4].S.R. Atalla, 2000 ,"A Universal Set-Up for Measurement of Thermal Properties of Solids and Liquids at High Temperatures" presented at "14 Symposium on Thermophysical Properties" NIST, Boulder, Colorado,USA,June 25-30, published in the CD Proceedings .

[5]Atalla.S.R.,"The ac-heated Wire Technique for Measurement of thermal Properties of Non-conducting Thin Solid Layers",under publication

[6]Atalla S.R.,"The ac-heated Coated Wire Technique for The Measurement of Thermal Properties of Conducting Liquids-Plane Layer Approximation",paper accepted to be presented at the"6th Asian Therrmo-Physical Properties"8-13 October 2001,India.

[7] Atalla,S.R.and Hassan,H.F.,1989, High Temp. High.Press.,Vol.21: 423.

[8]American Institute Of Physics Handbook,1994, McGraw Hill Book Co., 3dEdition.

[9]Handbook of Chemistry and Physics, 2000-2001, CRC Press 81stEdition.

HEFAT2002
1st International Conference on Heat Transfer, Fluid Mechanics, and Thermodynamics
8-10 April 2002, Kruger Park, South Africa
JB1

NON STEADY FLOW EFFECTS UPON EMULATED HUMAN LUNG FLOW PROFILES FROM A POSITIVE DISPLACEMENT FLOW GENERATOR

B. Jones
Professor of Control Engineering, Aston University, UK
M. Miller
Senior Lecturer in Respiratory Medicine University of Birmingham, UK
B.Jones@aston.ac.uk

ABSTRACT

Transient flow generators are currently used to evaluate the performance of both spirometers and PEF meters used in respiratory measurements of the human lung. As such the flow profiles are intended to emulate those provided by humans under a wide range of physiological and medical conditions. A recent Council of the European Community research programme funded the design and development of a high bandwidth flow generator in the form of a positive displacement device with precision motion control of the displacement piston. This has resulted in improvements in accuracy and repeatability of the flow profiles as compared with prior art devices.

However, experimental measurements have indicated that the generated flow profiles differ from those implied by the flow displaced by the piston of the generator. Such effects have been previously observed by respiratory clinicians and have been attributed to simple compressibility effects.

The paper presents analysis of the non steady flow process of the generator to predict delivered flow profiles. This indicates that wave effects within the system account for the observed differences between the ideal flow profiles based upon piston displaced flow and that observed at the point of delivery. The analytical technique has been used to evaluate a wide range of flow profiles with the generator coupled to spirometers having a wide range of generator output impedances. The analytical predictions are shown to be accurate and consistent with the experimentally observed flow profiles.

The motion of the pump piston is controlled by a digital motion controller and the developed mathematical model of the flow process forms the basis of a predictive control strategy. This allows the operating cycle of the generator to be compensated for wave effects and so results in a defined wave profile to be generated with a minimum of error. Since spirometric evaluations are based upon a range of different expiratory flow profiles then corrective algorithms can be stored in the controller memory and called when needed.

INTRODUCTION

The use of positive displacement pump systems to test devices used for recording lung function has shown that many hand held peak expiratory flow (PEF) meters do not record accurately [1,2] and fail to perform to current specifications [3]. The basic assumption that flow generated is directly proportional to piston displaced volume is erroneous. Methods to correct for any inaccuracy have recently been proposed [5,6] and these use a quasi-static application of Boyle's law assuming that gas compression is the cause of the errors. However, such methods are not substantiated in many

The approach adopted is to consider the system as a non steady incompressible [Low Mach Number] to predict output flow profiles for a range of inputs and pump impedance. The observed differences in the generated wave form as compared with that based upon piston displacement indicates that actual flow can be greater or less dependent upon load impedance of the spirometer or PEF meter. This suggested that the differences were due to wave reflections within the system initiated by piston motion. The model developed based upon small amplitude wave theory offered confirmation of this.

THE POSITIVE DISPLACEMENT FLOW GENERATOR

Pump systems in current use have deficiencies that limit their use for this study, necessitating a new design. The design endorsed by the American Thoracic Society [3] has several limitations, including high inertia and the low bandwidth of the drive limits fast response and high flow rates

The design chosen for the pump in this study followed the earlier vertical axis design [1] with the

drive motor located beneath the cylinder and with the outlet on top. The design utilized as many commercially available components as possible, rather than having to manufacture individual special components. The preliminary specifications for the new pump were:

- A volume displacement of eight litres with an accuracy of better than 5 mL over the full stroke of the piston.
- A maximum flow of 20 L/s being delivered within 20 ms.
- The maximum cylinder pressure to be 8 kPa with a maximum allowable leakage of 2 L/min up to this pressure.
- Possible working temperature range 15 to 35 degrees Celsius.

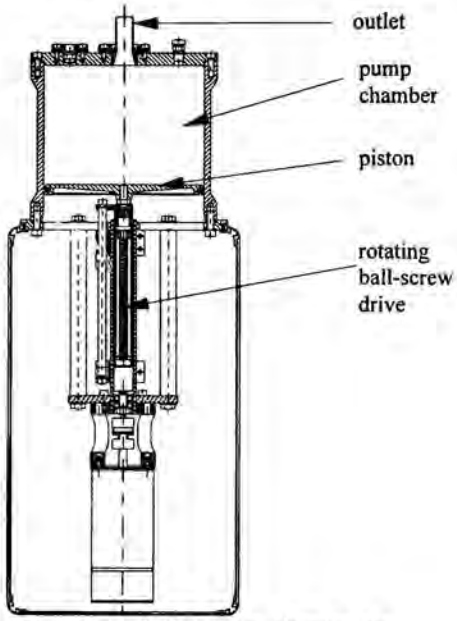

Figure 1: Technical drawing showing the pump's chamber, piston, drive, and motor.

Tests in human subjects have indicated that fewer than 0.2% of subjects exceed 15 L/s [8] and that the lower 5th percentile for 10 to 90% rise time (RT) to PEF is 30 ms [9]. On this basis the above specifications exceeds those needed to mimic human flow performance.

The pump has an aluminium chamber of 250 mm diameter and piston travel was 200 mm which optimized the geometry for the choice of motor and drive.. The piston motion was provided by a rotating ball leadscrew connected by a torsion coupling to a brushless DC servo motor used with integral amplifiers, optical shaft encoder, and servo-controller that could store 16 separate profiles in erasable programmable read only memory (EPROM) to be repetitively used independently from a computer.

A series of experiments was undertaken with two of the four artificial flow-time profiles shown in Figure 2 that spanned the 5th to the 95th percentiles for rise times and dwell times for the PEF found in humans [9]. These profiles were scaled to give a PEF of 12 L/s or 8 L/s. They were repeatedly delivered and the proportional software gain adjusted until the best agreement was achieved between the input signal to the motor and the output piston motion measured by the optical shaft encoder. Regression analysis of the results gave the required proportional gain, where RT is the rise time, and DT90 is the dwell time of flow above 90% of the peak.

These results show that very precise flows and profiles can be generated by the piston displacement dependent upon the controller sampling period of 4 ms. The resolution of flow delivered is directly dependent upon both the optical shaft encoder resolution and the sampling interval of 4 milliseconds. The encoder resolution is to within 4 pulses, which in our configuration equates to a travel of 0.00127 cm and a delivered volume of 0.623 cm^3. A difference of this volume when sampling at 4 ms equates to a possible variation in recorded flow of 0.156 L/s due to the resolution of the optical shaft encoder.

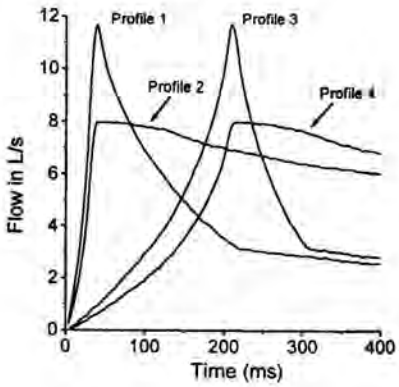

Figure 2: Four artificial flow-time profiles spanning the range of the rise time (RT) for flow to rise from 10% to 90% of the peak, and the dwell time (DT90) of flow above 90% of peak, with two profiles scaled to 12 L/s and two to 8 L/s to help distinguish them. *Profile 1*: RT 24 ms, DT90 12 ms, *Profile 2*: RT 24 ms, DT90 140 ms, *Profile 3*: RT 156 ms, DT90 12 ms, *Profile 4*: RT 156 ms, DT90 138 ms.

The Model

The positive displacement of a piston based pump, with air as the working fluid, initiates a pressure wave disturbance in the piston chamber

that is propagated through to the output tube. The system comprises a series of coupled elements. The piston in the pump is the wave generator, with the pump chamber coupled to an outlet tube where entrance losses have been minimised by the design. This tube is then coupled to the complex impedance of the various flow meters (pneumotachograph and/or mini-Wright meter) attached to the end, and finally this exhausts to the atmosphere. Analysis of the system is based on deriving non-steady flow energy equations for the various elements of this coupled system. A full explanation of this is given in the Appendix.

Under the normal working conditions for the system, with moderate pressure and temperature, the flow behaves as a perfect isentropic gas and the disturbance can be considered as a plane wave. The maximum cylinder pressure during usual test conditions is below 2 kPa and the maximum desired volumetric flow of the system is 20 L/s. A flow of 20 L/s implies a particle velocity of about 3.8 m/s through the pump's outlet, giving a Mach number of only 0.01 so the compressibility effects are negligible [7].

Under these circumstances, a much simpler incompressible model can be built. Although density does change within the thin layer next to the pressure wave-front, the change in density in the bulk of air in the chamber is very small and thus can be ignored. In other words, the air behaves like a higher density fluid such as water. The wave speed a, is constant and is given as, where K is the ratio of specific heats , and ρ is the density of air.

The continuity equation is,

$$\frac{d\rho}{dt}+\rho\frac{\partial u}{\partial x}+\frac{\rho}{A}\frac{dA}{dt}=0$$

$$a=\sqrt{\frac{K}{\rho}}$$

where A is the area, p is the pressure, u is the flow velocity, t is time, and x is a displacement in the direction of flow.

The non-steady flow equation is,

$$\frac{du}{dt}+\frac{1}{\rho}\frac{\partial p}{\partial x}+\frac{fu|u|}{2D}=0$$

where D is the pump cylinder diameter, and f is the friction force at the wall per unit mass of fluid, which is air in this instance. A solution to these equations was obtained using the method of characteristics [12], and detailed analysis is outlined in the Appendix.

In simple terms the analysis predicts the flow motion as the piston starts to accelerate and creates a pressure wave within the gas that moves at the speed of sound within the cylinder. A complex system of pressure wave reflections is set up that continuously change as the piston moves over the stroke length. The main factors that contribute to the process are,

- the pump cylinder dimensions.
- the outlet impedance conditions
- the local speed of sound - which depends on gas density and temperature.
- the shape of the flow profile to be delivered.

EXPERIMENTAL PROCEDURE

The four artificial flow-time profiles (Figure 2) used were of a similar shape to that delivered by human subjects and In addition three of the ATS flow-time profiles [3] recommended for testing PEF meters were used (No. 10, 15, and 26) which had the extremes for rise and dwell times amongst these profiles. These profiles were delivered to an optimized pneumotachograph (PT) when it was mounted directly on to the pump This was repeated with a mini-Wright meter placed between the pump and the PT, with the mini-Wright meter enclosed in a Perspex cylinder so that all the exhausted air from the meter was collected to be passed through the PT [13]. The effect of changing the start volume of gas within the pump was also checked using one of the artificial profiles.

To test if wave action was present in human lungs during a maximum forced expiratory manoeuver 15 healthy subjects and 15 patients with airflow limitation performed three PEF manoeuvers into a PT with, and without, a 32 cm extension tube added upstream to the PT, in randomized order. The subjects were naive as to how this might influence the recordings. The highest achieved PEF was recorded for each configuration.

RESULTS

Figure 3 shows the input, measured and profiles for ATS profile 26 and for the artificial profiles No. 1 and 3. It can be seen that the model also predicted the presence of wave phenomena in the build up to PEF for profile No. 3 which was not on the input signal, and also in the drop down from PEF for profiles No. 1 and 3. The wave effects were also evident on the pressure recordings from the pump cylinder. However, the model did not perfectly match the phase timing of these waves, which is almost certainly due to following error of the servo drive.

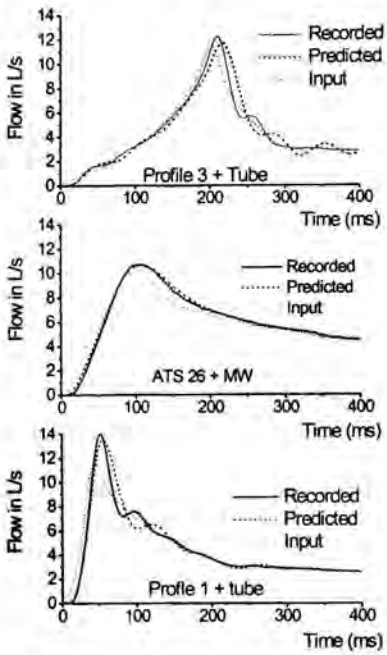

Figure 3: Plots of the input profiles, pump's output recorded with the PT, and the output predicted by the model for three input profiles, artificial profile No. 3 with the 32 cm extension tube, ATS profile No. 26 delivered through the mini-Wright meter, and artificial profile No. 1 delivered with the extension tube.

The effect of changing the pump starting volume using a profile with RT of 28 ms and DT90 of 34 ms is shown in Figure 4 and Table 5. The model and the recorded findings were in close agreement, in that when the piston started from the bottom of the pump the recorded PEF was lower than when starting nearer the top of the chamber, due to the greater chamber length in which wave effects could occur.

DISCUSSION

Data have been presented indicating that using pump systems to test PEF meters is a complex undertaking and that both the impedance characteristics of the device under test and the pump configuration have an important influence on the result. Other workers have presented data confirming discrepancies between input and output when using pump systems in this way [5,6] but these workers have assumed that the problem was due to gas compression within the pump chamber and that this dynamic compression led to a reduction in the generated flow. We contend that these discrepancies are due to wave effects within pump systems. Both the experimental results presented here and the model's analysis indicate that changes in outlet geometry and impedance can lead to either a reduction or an increase in the transient flow output relative to the input waveform.

Whilst the idea of compression due to piston motion is intuitively reasonable, air does not necessarily behave as a compressible fluid in these circumstances. Boyle's law can be applied under steady state conditions in a closed system, but when using a pump to test PEF meters the system is open at one end and conditions are never under steady state. If Boyle's law is applied using a freeze frame approach, all the dynamic aspects of the system are ignored. This compression approach may give an approximate correction for the errors involved [5,6] but fails to consider the complex dynamic transients within the pump cylinder. For instance, the compression approach could never predict the finding of a greater output flow than input flow as demonstrated in the bottom of Figure 3. With the pump under consideration and with an outlet tube of 26 mm internal diameter the local Mach speed will only reach the critical value of 0.3 when the exhaust flow from the pump is about 35 L/s. The slewing speed of the system is 34 L/s and so significant dynamic gas compression effects do not ordinarily occur. When a mini-Wright meter is attached the outlet area is different and so the local particle velocity is different. With a flow of 800 L/min the variable orifice area developed in a mini-Wright meter is such that the local Mach number is well below 0.1 and so significant dynamic gas compression effects do not occur.

The gas flow analysis identifies wave action within pump systems as being significant and reasonably accurate predictions of performance have been obtained. The data from human subjects indicated no evidence of a wave action developing within the bronchial tree. This is intuitively as expected in that the multiple branches of the system would not facilitate the propagation of compression or rarefaction pressure waves along the airways. Whilst the model derived here is a substantial aid in predicting the performance of the system it suffers the disadvantage that it relies on the use of an empirical discharge coefficient (C_d) for the device applied to the outlet of the pump. It is not possible to measure accurately the exact C_d for an instrument, and for devices offering a complex impedance to flow the C_d may change under different operating conditions. This limits the usefulness of the approach but does not negate its importance in understanding what contributes to the performance of pump systems. For instance, the model predicts that input profiles with very short dwell times lead to greater reduction in output PEF from a pump through a mini-Wright meter than do

profiles with very short rise times, as shown in Figure 5, and confirmed by our experiments.

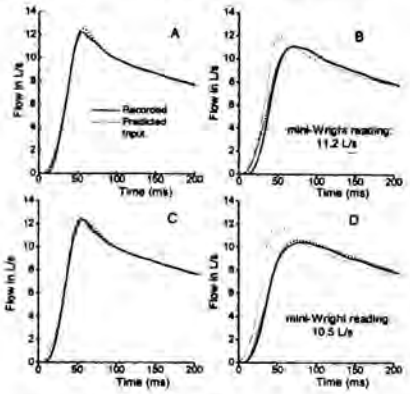

Figure 4: Plots of the input flow-time profile, the output recorded by the PT and the output predicted by the model for four different configurations of the pump:
A: recorded through the PT only with the piston starting near the top of the pump.
B: recorded with the mini-Wright meter in series with the PT and the piston starting near the top of the pump; the mini-Wright reading has been corrected for its known non-linearity.
C: recorded through the PT only with the piston starting at the bottom of the pump.
D: recorded with the mini-Wright meter in series with the PT and the piston starting at the bottom of the pump; the mini-Wright reading has been corrected for its known non-linearity.

The ATS has recommended the use of 26 arbitrarily chosen flow-time profiles for testing PEF measuring devices [3]. A different approach would be to use a more limited test regimen such that one can be confident that the devices can accurately record PEF for at least 95% of the target population. The 5th to 95th centiles for rise and dwell time for PEF have recently been published for subjects with airflow limitation [9] and these are shorter than that found in healthy subjects. These data have been used in this study to derive artificial profiles that span the ranges found. The performance characteristics of PEF meters that need to be tested are the linearity and accuracy, the frequency response, and the resistance. PEF meters should be linear across the desired range and this property can be tested using pump systems with either constant flow profiles, profiles with slow rise times, or cusp profiles [1] which are all free from wave effects in pump systems. It is easy to measure the meters' resistance at the same time. Meters must also have a sufficiently good frequency response to record PEF when the rise time and dwell times are short. The frequency response of a PT can be verified by a variety of means [16-18] which are suitable for a PT, which has a continuous analogue output, but are not suitable for PEF meters. For PEF meters with no analogue output the frequency response could be tested by using a single profile with a rise and dwell time chosen to be at the lower 5th centile for subjects with airflow limitation.

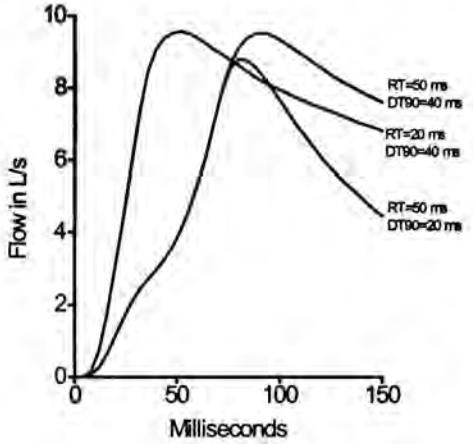

Figure 5: Output profiles predicted by the model for pump delivery through a mini-Wright meter. All profiles are for an input of 10 L/s PEF. The two output profiles predicted by the model for an input DT90 of 40 ms with RT of 20 ms and 50 ms are little different in terms of PEF. The two profiles with input RT of 50 ms but DT90 of 20 ms and 40 ms show a significant drop in the predicted PEF with the shorter dwell time.

The use of an explosive decompression device [19] to deliver this type of profile may avoid these problems and such a device has been modified to be able to do this [20]. The principle of an explosive decompression device is to pressurise a chamber of known volume to a known pressure and then release the gas suddenly. The gas can be delivered to a specified shape of profile by controlling the shape of the outlet. In this system there is no piston accelerating the gas and so wave effects are less likely. This sort of device may provide a way to calibrate hand held meters and check that their performance is adequate for recording human subjects. The only drawback with an explosive decompression device is that it needs independent calibration with a flow meter that is linear, has adequate frequency response, and has continuous

analogue output, such as a PT. However, this disadvantage is also true for the previously suggested means for correcting a pump's output [5,6] by iteratively changing the input profile until a PT recorded the desired output flow.

We conclude that discrepancies between the input and output from pump systems can be accounted for by the application of fluid mechanics and wave action. This phenomenon limits the application of a pump to deliver flow-time profiles with short rise and dwell times. The linearity of PEF meters can be successfully tested by a pump, but the frequency response aspects of their performance may be best tested using a suitable profile delivered by an explosive decompression device.

REFERENCES

[1] Miller, M. R., S. A. Dickinson, and D. J. Hitchings. 1992. The accuracy of portable peak flow meters. *Thorax* 47: 904-909.

[2] Gardner, R. M., R. O. Crapo, B. R. Jackson, and R. L. Jensen. 1992. Evaluation of accuracy and reproducibility of peak flowmeters at 1,400 m. *Chest* 101: 948-952.

[3] American Thoracic Society. Standardization of spirometry: 1995 update. 1995. *Am. J. Respir. Crit. Care Med.* 152: 1107-1136.

[4] Wright B. M. 1978. A miniature Wright peak-flow meter. *Br Med J* 2: 1627-1628.

[5] Hankinson, J. L., J. S. Reynolds, M. K. Das, and J. O. Viola. 1997. Method to produce American Thoracic Society flow-time waveforms using a mechanical pump. *Eur Respir J* 10: 690-694.

[6] Navajas, D., J. Roca, R. Farré, and M. Rotger. 1997. Gas compression artefacts when testing peak expiratory flow meters with mechanically-driven syringes. *Eur. Respir. J.* 10: 901- 904.

[7] Mironer, A. 1979. Engineering fluid mechanics. McGraw Hill.

[8] Miller, M. R., D. M. Grove, and A. C. Pincock. 1985. Time domain spirogram indices: their variability and reference values in non-smokers. *Am. Rev. Respir. Dis.* 132: 1041-1048.

[9] Miller, M. R., O. F. Pedersen, and Ph. H. Quanjer. 1998. The rise and dwell time for peak expiratory flow in patients with and without airflow limitation. *Am. J. Respir. Crit. Care Med.* 158: 23-27.

[10] Massey, B. S. 1970. Mechanics of fluids. Van Nostrand Reinhold. p185-187.

[11] Quanjer Ph. H., M. D. Lebowitz, I. Gregg, M. R. Miller, O. F. Pedersen. 1997. Peak expiratory flow: conclusions and recommendations of a Working Party of the European Respiratory Society. *Eur Respir J* 10: Suppl. 24: 2s-8s.

[12] Wylie, E. B., and V. L. Streeter. 1978. Fluid transients. McGraw Hill.

[13] Pedersen, O. F., T. R. Rasmussen, Ø. Omland, T. Sigsgaard, Ph. H. Quanjer, and M. R. Miller. 1996. Peak expiratory flow and the resistance of the mini-Wright peak flow meter. *Eur. Respir. J.* 9: 828-833.

[14] Miller, M. R., and A. C. Pincock. 1988. Predicted values: how should we use them? *Thorax* 43: 265-267.

[15] Quanjer P. H., G. J. Tammeling, J. E. Cotes, O. F. Pedersen, R. Peslin, and J-C. Yernault. 1993. Standardized Lung Function Testing. *Eur. Respir. J.* 6: Suppl 16: 5-40.

[16] Andersen H. R., and O. Bergsten. 1987. The step test method. *In:* Blood Pressure Measurements and Methods. S&W Medico Teknik A/S, Denmark. 2nd Ed. 54-65.

[17] Jackson A. C., and A. Vinegar. 1979. A technique for measuring frequency response of pressure, volume, and flow transducers. *J. Appl. Physiol.* 47: 462-467.

[18] Zock J. P. 1981. Linearity and frequency response of Fleisch type pneumotachometers. *Pflügers Arch.* 391: 345-352.

[19] Pedersen, O. F., N. Naeraa, S. Lyager, C. Hilberg, and L. Larsen. 1983. A device for evaluation of flow recording equipment. *Bull Eur Physiopathol Respir* 19: 515-520.

[20] Pedersen, O. F., T. R. Rasmussen, S. K. Kjaergaard, M. R. Miller, and Ph. H. Quanjer. 1995. Frequency response of variable orifice type peak flow meters: requirements and testing. *Eur. Respir. J.* 8: 849-855.

APPENDIX

The method adopted for the analysis of wave effects in fluids depends upon the magnitude of the changes in pressure and particle velocities. If the changes are very small then acoustic wave theory can be used and all points on the wave are considered to be propagated with the same velocity, i.e., local speed of sound. It has been shown that numerical solutions based upon acoustic wave theory have negligible error provided that the pressure changes are less than 7.5 kPa [1a, 2a]. These conditions pertain in a positive displacement piston-based device as illustrated below.

In the chamber filled with air, the pressure disturbance initiated by piston movement is propagated through the air. The propagation speed is that of sound wave speed. For small amplitude disturbance, the resultant thermodynamic properties change can be neglected. The sound speed in perfect gas can be calculated from:

$$\alpha = \sqrt{\gamma RT} \qquad (1)$$

where γ is the ratio of specific heat (1.4 for air), R is the gas constant (287.04 m^2/s^2 K for air) and T is the thermodynamic temperature. For normal room conditions the speed of a sound wave is about 340 ms/s.

$-\frac{\partial(\rho uA)}{\partial x}dx$

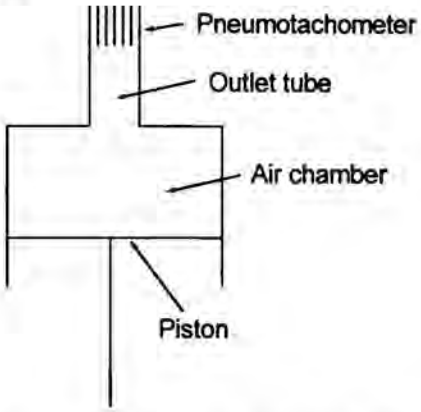

Figure A1: A schematic presentation of a piston pump system.

For systems like in Figure 1 an airflow output V(t) is the result of an input in the form of piston movement v(t), or:

$$V(t) = f(v, t, n_1, n_2, \ldots n_n) \qquad (2)$$

Where n_1, n_2 ...i_n denote the other relevant variables.

Under normal working conditions for the pump system the airflow behaves like a perfect isentropic gas flow. The disturbance induced by the piston movement can be considered as a plane wave. This basic flow equations can be derived from the flow analysis based on the element shown as in Figure A2 below.

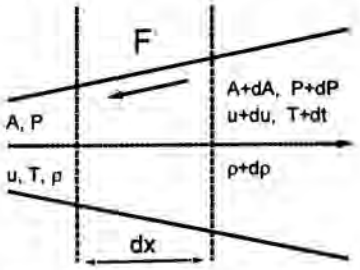

Figure A2. Representative fluid element in a duct of non-uniform cross-sectional area.

If the side area of an element whose length is dx changes from A to $A+dA$ then the volume of the element is given by $V=(A+dA/2)*dx$ and can be simplified as $A*dx$.

CONTINUITY EQUATION

The unsteady continuity equation for the fluid element in Figure A2 states: the increase in mass in the control volume equals the net rate of flow into the control volume.

The increase in mass in the control volume is:

$$\frac{\partial(\rho A dx)}{\partial t}$$

The net rate of flow into the control volume:

$$-\frac{\partial(\rho uA)}{\partial x}dx$$

So the continuity equation is:

$$\frac{\partial(\rho A dx)}{\partial t}+\frac{\partial(\rho uA)}{\partial x}dx=0$$

Expanding it and dividing it through by dx can get:

$$\rho\frac{\partial A}{\partial t}+A\frac{\partial \rho}{\partial t}+\rho u\frac{\partial A}{\partial x}+\rho A\frac{\partial u}{\partial x}+uA\frac{\partial \rho}{\partial x}=0$$

Divided by A and regrouping gives:

$$\frac{\rho}{A}(\frac{\partial A}{\partial t}+u\frac{\partial A}{\partial x})+\rho\frac{\partial u}{\partial x}+(\frac{\partial \rho}{\partial t}+u\frac{\partial \rho}{\partial x})=0$$

Introducing the total time derivative term: for any variable $N=N(t,x(t))$, the total time derivative of N is;

$$\frac{dN}{dt}=\frac{\partial N}{\partial t}+\frac{\partial N}{\partial x}\frac{dx}{dt}=\frac{\partial N}{\partial t}+u\frac{\partial N}{\partial x}$$

Therefore, the continuity equation can be written as:

$$\frac{\rho}{A}\frac{dA}{dt}+\rho\frac{\partial u}{\partial x}+\frac{d\rho}{dt}=0$$

Or:

$$\frac{d\rho}{dt}+\rho\frac{\partial u}{\partial x}+\frac{\rho}{A}\frac{dA}{dt}=0 \qquad (3)$$

MOMENTUM EQUATION

The momentum equation states: the rate of change of momentum within the control volume equals the sum of force applied to the surface of the control volume. The surface forces include pressure forces and shear forces on the control volume. The pressure forces consists of three terms: pressure

forces applied to both ends and the pressure force applied to side surface (the p is used as the distributed pressure on the side for simplicity). They are given as:

$$pA + pdA - (p + dp)(A + dA) = -Adp - dAdp$$

Or:

$$-A\frac{\partial p}{\partial x}dx$$

The shear forces, due to friction at the wall, is $\lambda\rho Adx$, where the λ is friction force for per unit mass of fluid.

$$\frac{\partial(\rho Audx)}{\partial t} + \frac{\partial(\rho Au^2)}{\partial x}dx = Adx\left(\rho\frac{\partial u}{\partial t} + \frac{\rho u}{A}\frac{\partial A}{\partial t} + u\frac{\partial \rho}{\partial t} + 2u\rho\frac{\partial u}{\partial x} + \frac{\rho u^2}{A}\frac{\partial A}{\partial x} + u^2\frac{\partial \rho}{\partial x}\right)$$

The rate of change of momentum of the control volume consists the net change of momentum in the control volume and the net efflux of momentum from the control surface. They are:

It can be written as:

$$Adx\left[\rho\left(\frac{\partial u}{\partial t} + u\frac{\partial u}{\partial x}\right) + \frac{\rho u}{A}\left(\frac{\partial A}{\partial t} + u\frac{\partial A}{\partial x}\right) + u\left(\frac{\partial \rho}{\partial t} + u\frac{\partial \rho}{\partial x}\right) + \rho u\frac{\partial u}{\partial x}\right]$$
$$= Adx\left(\rho\frac{du}{dt} + \frac{\rho u}{A}\frac{dA}{dt} + u\frac{d\rho}{dt} + \rho u\frac{\partial u}{\partial x}\right)$$

The last three terms inside the bracket is the continuity equation 3:

$$u\left(\frac{\rho}{A}\frac{dA}{dt} + \frac{d\rho}{dt} + \rho\frac{\partial u}{\partial x}\right) = 0$$

Hence the momentum equation is:

$$-A\frac{\partial p}{\partial x}dx - \lambda\rho Adx = \rho\frac{du}{dt}Adx$$

Expanding, dividing by Adx and gives:

$$\frac{\partial p}{\partial x} + \lambda\rho + \rho\frac{du}{dt} = 0$$

Or:

$$\frac{du}{dt} + \frac{1}{\rho}\frac{\partial p}{\partial x} + \frac{fu|u|}{2D} = 0 \qquad (4)$$

The friction term is rewritten using Darcy formula and f is the friction factor. The term u|u| is introduced to ensure that the wall friction always acts in the opposite direction to the direction of flow.

THE INCOMPRESSIBLE GAS MODEL

The volume flow of the system is in the order of 12 L/s, which implies a particle velocity of air much smaller than 1 m/s and a Mach number for this flow is far less than 0.1. The compressiblity of gas can be neglected and a much simpler incompressible model can be built. By using the model of, we consider the density of the air is not changed significantly during the process. In other words, the air behaves like other fluid with higher density such as water. In fact, the density is changed within the thin layer next to the pressure wavefront, but take the air in the chamber as a whole, the change in density can be neglected.

From the definition of bulk modulus of elasticity of fluid:

$$K = -\frac{dp}{dV/V} = \frac{dp}{d\rho/\rho}$$

where V is volume, and hence.

$$\frac{d\rho}{\rho.dt} = K\frac{dp}{dt} \qquad (9)$$

The wave speed **a** is constant and can be defined as:

$$a = \sqrt{(K/\rho)} \quad (10)$$

Using variable rate of flow $q = Au$, the equation 3 is obtained by as:

$$\frac{dp}{Kdt} + \frac{\partial q}{A\,\partial x} = 0$$

or:

$$\frac{dp}{dt} + \frac{\rho a^2\partial q}{A\,\partial x} = 0 \qquad (11)$$

and equation 4 is rewritten as:

$$\frac{dq}{Adt} + \frac{\partial p}{\rho\partial x} + \frac{fq|q|}{2DA^2} = 0 \qquad (12)$$

THE METHOD OF CHARACTERISTIC

The partial differential equations 11 and 12 can be further manipulated to get two normal differential equations applied to two sets of lines, the characteristic lines.

First, Equations 11 multiplied by a factor α and then added to Equations 12 gives:

$$\alpha(\frac{\partial p}{\partial t}+u\frac{\partial p}{\partial x})+\frac{\alpha\rho a^2}{A}\frac{\partial q}{\partial x}+\frac{1}{A}(\frac{\partial q}{\partial t}+u\frac{\partial q}{\partial x})+\frac{1}{\rho}\frac{\partial p}{\partial x}+\frac{fq|q|}{2DA^2}=0$$

Or:

$$\alpha(\frac{\partial p}{\partial t}+u\frac{\partial p}{\partial x}+\frac{1}{\alpha\rho}\frac{\partial p}{\partial x})+\frac{1}{A}(\frac{\partial q}{\partial t}+u\frac{\partial q}{\partial x}+\frac{1}{\alpha\rho a^2}\frac{\partial q}{\partial t})+\frac{fq|q|}{2DA^2}=0 \qquad (13)$$

If

$$u+\frac{1}{\alpha\rho}=u+\frac{1}{\alpha\rho a^2}=\frac{dx}{dt}$$

It means α=±a, and

$$\frac{dx}{dt}=u\pm a \qquad (14)$$

then the Equation 13 can be written as:

$$\pm a\frac{dp}{dt}+\frac{1}{A}\frac{dq}{dt}+\frac{fq|q|}{2DA^2}=0 \qquad (15)$$

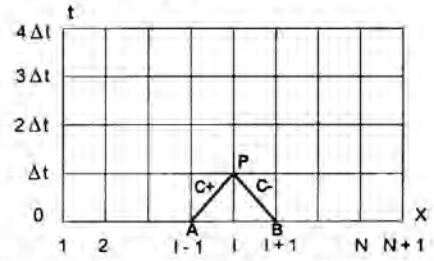

Figure A3: Space-time grid for obtaining the numerical solution.

In **t-x** plane, the grid formed by interception of the two sets of lines are not strictly regular rectangles. However, since the particle velocity u is far smaller than wave speed, the rectangular grid can be considered as regular as the space time grid shown in Figure A3 below.

Equation 14 defined two groups of lines in the t-x plane, which are named characteristics lines. In other words, the equations 11 and 12 are converted to one ordinary differential equation of independent variable as in Equations 15.

In a portion of pipes as shown in Figure A3, **x** locates a point and **t** the time at which the dependent variables **p** and **q** are to be determined. The interface variables of the pipe are state variables in both ends to the pipe. This portion of the pipe is divided into **N** sub–parts by **N+1** points. The state variables are sampled at discrete instants of time. Δt is the time interval between two sampling instants, during which the variables are assumed unchanged.

The state variable set is:

$$X=[\,p_1,p_2,\ldots..P_{n+1},q_1,q_2,\ldots..q_{n+1}\,] \qquad (16)$$

First the equation along the positive characteristic line, noted C^+ in Figure A3 is considered. By multiplying equation 15 through with $a\rho Adt$ (with the + sign only),

and integrating from **A** to **P**,

$$a\rho\int_A^P dq+A\int_A^P dp+a\rho\int_A^P\frac{fq|q|}{2DA}dt=0$$

Since $adt=dx$, the equation can be written in finite-difference form:

$$a\rho(q_p-q_A)+A(p_p-p_A)+\frac{\rho fq_A|q_A|(x_p-x_A)}{2DA}=0 \qquad (17)$$

The integration of friction term is an approximation. It is good enough when Δx and Δt are small enough. The corresponding C^- equation is integrated in a similar manner, the only difference is that $adt=-dx$, and so it becomes:

$$a\rho(q_p-q_B)+A(p_p-p_B)+\frac{\rho fq_B|q_B|(x_B-x_p)}{2DA}=0 \qquad (18)$$

Provided the state variables at points **A** and **B** are known equations can be solved simultaneously to determine variable q_p and p_p.

In applying the method to solve all the variables in the pipe, if state variable set **X**, at time $t=t_0+k\Delta t$ is known, then its value at $t=t_0+(k-1)\Delta t$ can be determined by conditions involving interface variables and the following 2N equations:

$$\begin{cases} p_I(k+1)=CP_I-bq_I(k+1) & I=1,2,\ldots..N \\ p_I(k+1)=CM_I+bq_I(k+1) & I=2,3,\ldots..N+1 \end{cases} \qquad (19)$$

where CP_I and CM_I are constants, collecting the known variables $b=a\rho/A$

Let:

$$r=\frac{\rho f\Delta x}{2DA^2}$$

Thus CP_I and CM_I are:

$$\begin{cases} CP_I=q_{I-1}(k)+bp_{I-1}(k)\,rq_{I-1}|q_{I-1}| \\ CM_I=q_{I-1}(k)-bp_{I-1}(k)\,rq_{I-1}|q_{I-1}| \end{cases} \qquad (20)$$

All the 2(N-2) internal variables can be solved by 2(N-2) equations from (19). Variables at points

I=1 and I=N+1 can be determined by two boundary conditions and two remained equations from (19).

BOUNDARY CONDITIONS.

The systems normally consist of a number of components. Three linker functions are defined for this servo pump system. The piston chamber linker links the displacement of piston x top state variable at the bottom of the chamber:

$$Pq_1 = piston.v$$

Chamber-pipe linker is a typical series coupling with simple definition as:

$$cham.pp_{n+1} = pipe.pp_1$$
$$cham.pq_{n+1} = pipe.pq_1$$

Pipe-meter linker links the pneumotachometer to the outlet pipe:

$$pipe.pq_{n+1} = AC_d\sqrt{[2(pipe.pp_{n+1} - P_0)/\rho]}$$

where C_d is the equivalent flow discharge coefficient of the meter.

The input parameters for the computer model are:

1. Length of pump chamber
2. Diameter of pump chamber
3. Length of outlet tube
4. Diameter of outlet tube
5. Discharge coefficient of the outlet tube C_d (determined by the added flow meter's impedance)
6. The flow-time input profile of piston movement.

The output parameters of the computer model are:

1. The outlet flow profile with respect to time.
2. The chamber pressure profile with respect to time.
3. The outlet tube pressure profile with respect to time.

HEFAT2002
1st International Conference on Heat Transfer, Fluid Mechanics, and Thermodynamics
8-10 April 2002, Kruger Park, South Africa
LA1

LASER-DOPPLER ANALYSIS IN THE WAKE OF A MULTIPLE FINS OSCILLATOR

A. Leder, A. Jianu

Institute of Fluidmechanics, University Rostock, Albert-Einstein-Str. 2, D-18051 Rostock, Germany
E-mail: alfred.leder@mbst.uni-rostock.de

ABSTRACT

This paper presents experimental results from a multiple fins oscillator, which has been employed to vertically oscillate the fluid in a rectangular tank filled with water. The fins perform a combined heaving and pitching oscillation while the whole oscillating machine is stationary. The distance between two adjacent fins is regarded as the oscillator characteristic length D with D = 0,05 m. While applying a time-periodic forcing, flow field measurements were carried out using a two-component laser-Doppler anemometer. The measured velocity data have been phase-synchronised with the periodic excitation by sensing the position of the oscillating fins with a Hall-probe. The wakes behind the oscillating fins show time averaged velocity profiles in the form of jets. The flow pattern comprises back-flow areas in-between the fins. Concentrated vorticity regions originating from the fins extend up to a streamwise distance of approx. 0.5D. For larger distances from the fins, the vortices become unstable and they decay into small scale vortices. At x = 2.5D the turbulent fluid motions are nearly homogeneous with a turbulence intensity of Tu ≡ 25%.

INTRODUCTION

Stirred tanks are encountered in a variety of industrial applications (blending, dispersing liquids, chemical reactors, pre-treatment stages of metal molded article coating, etc.). Flow control in tanks is currently attracting increased attention: flow destabilization (e.g., for better mixing) or flow stabilization (e.g., for eliminating unsteady loads) may be desired. The techniques may be classified into two categories: passive control (by altering the flow geometry) and active control (by applying a time-dependent forcing to the flow). Active control may be divided into open-loop (forcing is a prescribed function of time) and closed-loop schemes (forcing is a function of real-time flow response measurement) [1].

NOMENCLATURE

D	distance between two fins (length scale)
f	frequency
H	height of tank
L	length of tank
T	period of time
Tu	turbulence intensity
u^*	reference value for velocity
u	velocity-component in x-direction
w	velocity-component in z-direction
W	width of tank
x,y,z	co-ordinates
ω	rotation of the flow

Subscripts

o	averaged value at x/D = 2.5
y	in y-direction
g	total value

Mathematical symbols

$\bar{a}$	time averaged value of "a"
<a>	mean value of "a" at constant phase

In this paper, we report on two-dimensional LDA experiments in the outflow region of a multiple fins oscillator placed in a water tank. An active flow control in an open-loop scheme is investigated, which relies on directly generating instabilities by applying a harmonic forcing to the flow. The purpose of this study is to get an accurate knowledge of the basic fluid mechanics induced by a multiple fins oscillator.

Previously, thrust-producing harmonically flapping foils have been studied mainly to derive efficient propulsion-techniques. A moving flapping foil produces thrust through the flow formation downstream from the trailing edge, which, when averaged over the period of oscillation, has the form of a jet. This jet flow is unstable, acting as a narrow-band amplifier of perturbations. The harmonic motion of the foil causes unsteady shedding of

vorticity from the trailing edge [2-4]. Stationary foils have been also studied as vortex splitting devices in boundary-layer control experiments [5-7]. The linear and nonlinear inviscid theories of unsteady foil flow and thrust production have been studied in [8, 9].

The objective of the present study is to describe the time-averaged and unsteady structure of the flow field in the close vicinity of the oscillator fins for different driving frequencies. The emphasis is on the characterization of the developing flow structure and turbulence intensity, [10].

Fig. 1 illustrates the oscillating movement of a single fin, induced by a heaving motion of the oscillator-frame. The fin oscillates in a combined translational and rotational motion which is due to its own elasticity.

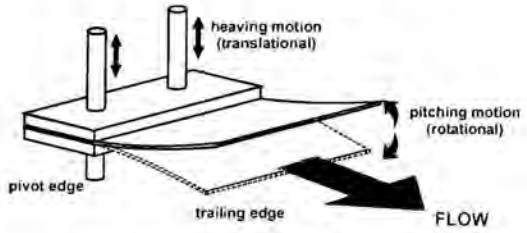

Fig.1: Oscillating motion of a single fin

EXPERIMENTAL SETUP

Flow facility

The flow facility is shown in fig. 2. The rectangular tank is 240 cm long (L) and 60 cm wide (W) and is filled with quiescent water up to a level (H) of 53 cm. At the top level there is a free surface. One of the long walls of the tank is equipped with a glass window.

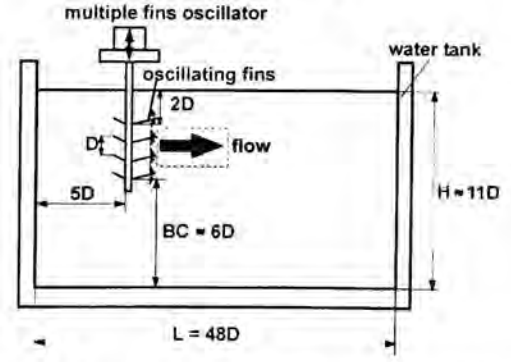

Fig.2: Sideview of rectangular water tank, (D = 0,05)

A four-fins oscillator was mounted in the vicinity of one of the short walls of the tank, with a bottom clearance BC (distance from the lowest fin to the tank bottom) equal to 28 cm and a top clearance TC (distance from the top fin to the free water surface) equal to 10 cm. The fins are 25 cm long, 5.5 cm wide and 0.08 cm thick. The distance between two adjacent fins is regarded as the oscillator characteristic length, D = 5 cm. The fins oscillate in a combined translational (heave) motion (forced by the vibrating motor) and rotational (pitch) motion due to their own elasticity. Fig. 3 illustrates the multiple fins oscillator used for these experiments.

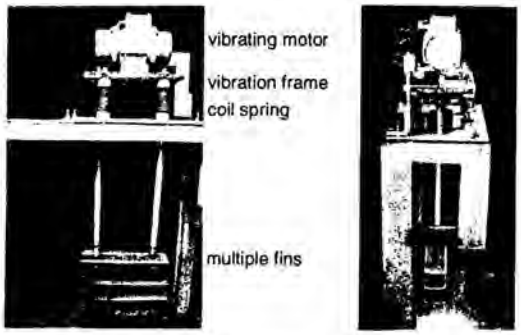

Fig.3: Front- and sideview of a four step fins oscillator

LDA set-up

The optics of the 2D LDA set-up consists of a 500 mW Ar-ion laser, a transmitter box, a 2D probe based on the colour separation method and two photo-multipliers. The 2D probe and the transmitter box are linked by glass fibers. The transmitter contains a colour separator and a frequency shifting Bragg cell. Its primary function is to extract two mono-frequency colors from the laser beam and to split each color into two beams with a 40 MHz frequency difference. Here the 514.5 nm and 488 nm color lines have been used. Two Burst Spectrum Analyzers (BSA) process the signals from the photo-multipliers. The BSA' s are interfaced to a microcomputer by GPIB interface and BSA Flow software. The measured LDA data have been phase-synchronized with the periodic actuator movement by sensing the position of the fins with a Hall-probe mounted on the frame of the oscillator. The beginning of every cycle, as detected by the Hall-probe, was time-stamped by a TTL impulse and inserted into the series of arrival time records of the validated LDA data [10].

Fig.4: Sideview of the oscillator and look at the four laser-beams of the 2D LDA-optics

Data acquisition

A measurement grid (fig. 5) was defined in the vertical plane (perpendicular to the fins) horizontally placed on the center line of the set-up. A Cartesian co-ordinate system is used with the origin (O) at the midpoint between the two lower fins. The (x, z) axes are directed streamwise (horizontal) and vertical, respectively. The component of the velocity vector in x-direction is defined as u-, in z-direction as w-component.

The probe was mounted on a 2D traverse system for accurate positioning of the measuring volume on the measurement grid. The traversing system was computer-controlled by a microcomputer linked with the BSA computer through a serial interface. BSA Flow software communicated with the traverse system through a custom-made interface software.

The grid spacing in both directions is $\Delta x = \Delta z = 0.1D$ (546 measurement points).

Geometrical variables are normalized with the oscillator characteristic length D, velocity-values with the mean streamwise velocity u^*_O, calculated by an integration of the u-component over the z-co-ordinate at x/D = 2.5. 1500 ÷ 8000 samples have been acquired per measurement position, depending on the location of the measuring volume on the grid.

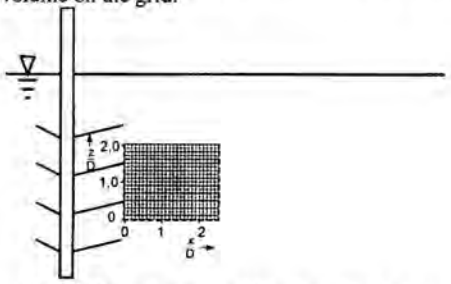

Fig.5: Measuring grid within the stirred tank

RESULTS AND DISCUSSION

As the flow pattern in the tank depends closely on the type of stirrer, detailed knowledge of the hydrodynamics close to the oscillator is important. The flow field has been measured at 37 Hz, 40 Hz and 43 Hz motor driving frequencies. The next chapter summarizes characteristic results at a forcing frequency of 40 Hz.

Flow field at 40 Hz motor driving frequency

The structure of the mean flow is shown in fig. 6. In this figure the u-signed absolute mean velocity $\left(\mathrm{sign}(u)\cdot\left[\sqrt{\overline{u}^2+\overline{w}^2}\right]/u^*_O\right)$ and uw-velocity vectors are plotted.

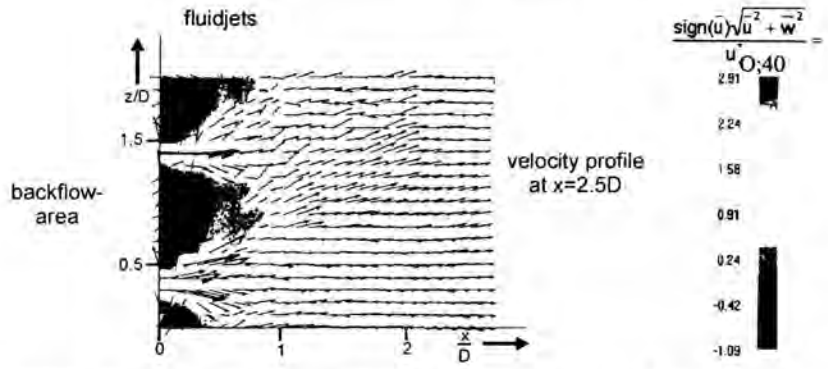

Fig. 6: Time averaged flow velocity, induced by the multiple fins oscillator; $u^*_{O;40}$ = 0,55 m/s

The flow pattern comprises three back-flow regions (above the upper fin,. below the lower fin and inbetween the fin.), extending in x direction up to a distance of approx. 0.5 D. Further downstream there exists no back-flow. The main flow is directed horizontally. At x/D = 2.5 the velocity profile shows nearly no velocity gradient in z-direction.

As already reported in literature [2], the wake behind an oscillating foil has an average velocity profile with the form of a jet. Two jets generated by the two fins can be noticed in fig. 6 and fig. 7. Consequently, the mean velocity profiles in fig. 7 for x < 1 D are characterized by two positive peaks. There exists an offset between peak positions (positions of the jet origin) and the position of the trailing edges of the fins while the vibrating machine is off. Under operation, the vibration shafts are slightly pushed backward (their working position ist slightly deviated from the vertical one) causing also a change in the fins position. With increasing x the peaks decrease in amplitude and are getting broader. For x > 1.5 D the profiles approach a constant value which slightly decreases with increasing x.

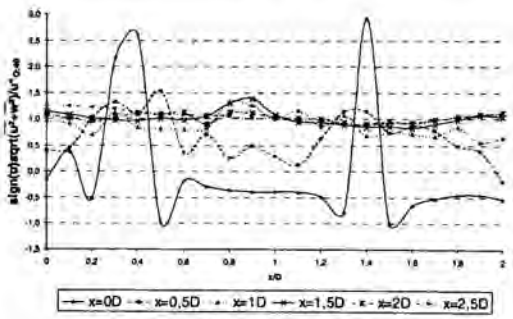

Fig.7:Development of velocity profiles; $u^*_{O;40}$ = 0,55 m/s

The fins oscillations induce an unsteady flow. The hermonic motions of the trailing edges produce periodical velocity variations within the fluid, which are resolvable with the phase locked LDA-technique [10]. To discuss the flow dynamics one period of the fins oscillations have been resolved into 10 time steps. The periodically repeated process with a duration of T = 0.025 seconds is thus represen by a frame sequence in which neighboring frames represent mean values of the represented flow quantity at constant phase with a temporal shift of Δt = 2.5 ms. Fig. 8 represents the fluid rotation ω_y around the y-axis of the co-oridnate system. The brakkets symbolize mean values at constant phase:

$$\langle \omega_y \rangle = \frac{\partial \langle u \rangle}{\partial z} - \frac{\partial \langle w \rangle}{\partial x}.$$

Fig. 8 clarifies that the fins oscillations induce within one period or 0.025 seconds one clockwise (grey, ω positive) and one counter clockwise (black, ω negative) rotating vortex structure. The vortex structures are shifted approx. 0.5 D downstream in x-direction which corresponds with a mean transport velocity of 1.0 m/s. Interactions between the counter rotating regions induce instabilities resulting into decomposition processes of the large scale vortices. Downstream of x = 1 D small scale vortices with a diameter of approx. 0.2 D could be identified. With increasing x-co-ordinate $\langle | \omega_y | \rangle$ decreases.

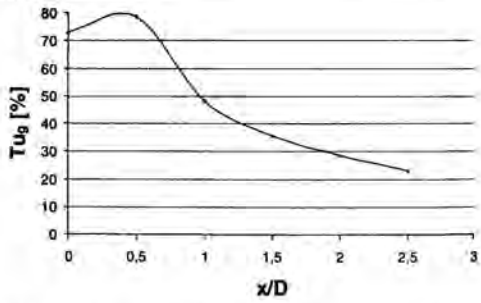

Fig.9: Variation of the turbulence intensity Tu_g along the x co-ordinate

Figure 9 displays the arithmetic mean of both measured turbulent velocity components u' and w', normalized with the reference velocity u^*_O. Tu_g represents the along the z-co-ordinate averaged turbulence intensity. Obviously Tu_g reaches a maximum value of 80% at x = 0.5 D. At this position the decay processes of the large scale vortices start. Between $0.5 \lesssim x/D \lesssim 1.0$ Tu_g decreases with a steep slope. In the region x > 1.0 D, where small scale vortices dominante the flow, the slope becomes less steep. At x/D = 2.5 the mean turbulence intensity is 24%.

Influence of motor driving frequency on the flow field characteristics

Measurements have been performed at two more oscillator frequencies, at f = 37 Hz and f = 43 Hz. Table 1 shows the dependence of the reference velocity u^*_O: u^*_O intereases with increasing frequency of the multiple fins oscillator.

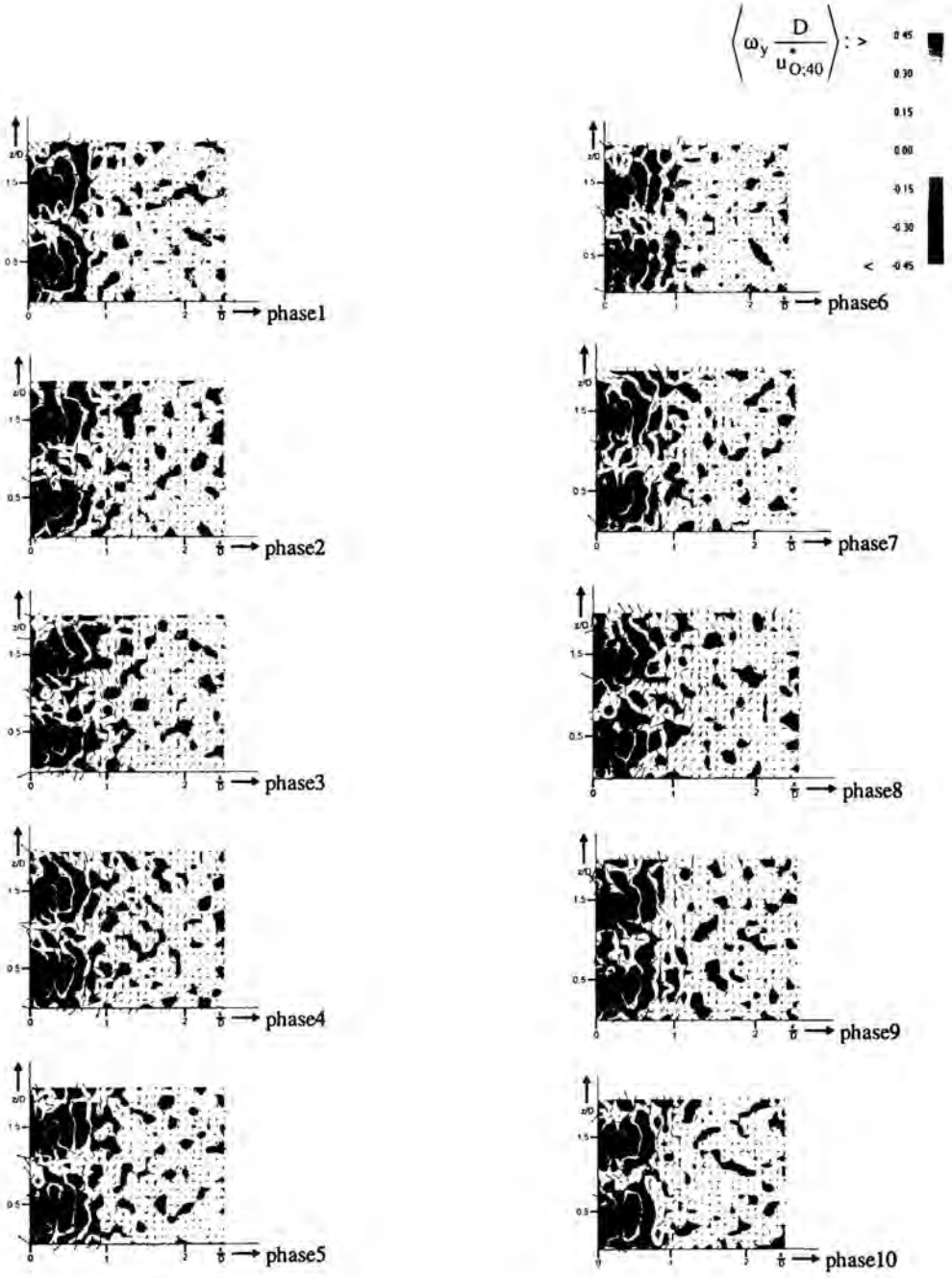

Fig.8: Phases 1-10 of fluid rotation $< \omega_y >$

Tab.1: Frequency dependence of reference velocity u_O^*

u_O^* [m/s]	37Hz	40Hz	43Hz
$u_O^* =$	0,37	0,55	0,62

The developing flow features in form of fluid jets, large scale vortices, and the decay process are very similar and show no remarkable frequency dependence. Fig. 10 illustrates the time averaged velocity profiles at two different positions (x/D = 0.0 and x/D = 2.5). Normalized with the reference velocities of Tab.1 the curves in fig. 10 are qualitatively and quantitatively nearly identical.

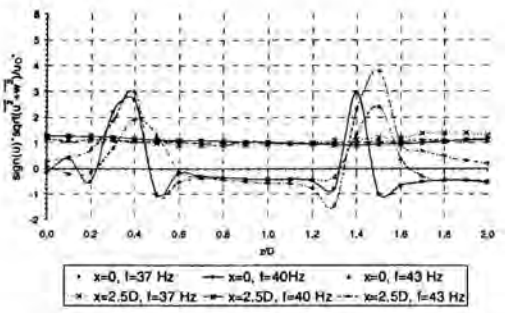

Fig.10: Induced velocity profiles at the positions x/D = 0.0 and x/D = 2.5 at the frequencies f = 37 Hz, f = 40 Hz and f = 43 Hz

Similar statements can be deduced for the behaviour of the turbulence characteristics: in normalizing the mean of the turbulent velocity components u' and w' with the frequency dependent reference velocity, a nearly identical distribution of Tu_g results. At x/D = 2.5 for all three frequencies Tu_g reaches a constant value of 25% ± 3%.

CONCLUSIONS

The objective of the present report was the description of the time-averaged and unsteady flow field close to a multiple fins oscillator (up to a streamwise distance of 2.5D) in terms of mean velocity, mean values at constant phases, and turbulence intensity. The flow pattern comprises areas of backward flow in-between the fins (extending up to a streamwise distance of 0.5D). The main flow is horizontally directed. Turbulence intensity, and spanwise vorticity have significant values in the near vicinity of the trailing edges of the fins (up to a streamwise distance of approx. 0.5D). Further downstream interaction processes between clockwise and counter clockwise rotating large scale vortices induce instabilities leading to small scale vortices. The overall features of the flow field (flow structure, turbulence intensity, vorticity) are nearly independed from the exitation frequency by scaling with u_O^*. u_O^* increases with increasing driving frequency (Tab. 1).

REFERENCES

[1] R. Gopalkrishnan, M.S. Triantafyllou, G.S. Triantafyllou and D.S. Barrett, Active vorticity control in a shear flow using a flapping foil, *J. Fluid Mech*, vol. 274, pp. 1-21, 1994.

[2] M.S. Triantafyllou, G.S. Triantafyllou and R. Gopalkrishnan, Wake mechanics for thrust generation in oscillating foils, *Physics of Fluids A*, vol. 3(12), pp. 2835-2837, 1991.

[3] K. Streitlien, G.S. Triantafyllou and M.S. Triantafyllou, Efficient foil propulsion through vortex control, *AIAA Journal*, vol. 34 (11), pp. 2315-2319, 1996.

[4] J.M. Anderson, Vortex Control for Efficient Propulsion, Ph.D.thes., Mass.Inst. of Techn., Cambridge, Mass., 1996

[5] T.C. Corke, Y.G. Guezennec and H.M. Nagib, Modification in drag of turbulent boundary layers resulting from manipulation of large-scale structures, *Proc. Viscous Drag Reduction Symp. Dallas AIAA Prog. Astro. Aero.* vol. 72, pp. 128-143, 1979.

[6] J.N. Hefner, L.M. Weinstein and D.M. Bushnell, Large-eddy break-up scheme for turbulent viscous drag reduction, *Proc. Viscous Drag Reduction Symp. Dallas AIAA Prog. Astro. Aero.* vol. 72, pp. 110-127, 1979.

[7] A.P. Dowling, The effect of large eddy break-up devices on oncoming vorticity, *J. Fluid Mech.*, vol. 160, pp. 447-463, 1985.

[8] T.Y. Wu, Hydromechanics of swimming propulsion, *J. Fluid Mech.* vol. 46, pp. 337-335, 1971.

[9] M.G. Copra, *J. Fluid Mech.* vol. 74, pp. 161, 1976.

[10] A. Leder, Abgelöste Strömungen – Physikalische Grundlagen, Vieweg, 1992.

Acknowledgement

The authors thank Japan Techno Co., Ltd., Ryushin Omasa, as well as H.J. Speck (DaimlerChrysler AG) and P. Claude (Chemetall) for supporting this study.

HEFAT2002
1st International Conference on Heat Transfer, Fluid Mechanics, and Thermodynamics
8-10 April 2002, Kruger Park, South Africa
LY1

VISUAL OBSERVATION OF WAVE-TYPE VORTEX GENERATOR IN AN ENLARGED FIN-AND-TUBE HEAT EXCHANGER

Min-Sheng Liu
Energy & Resources Laboratories
Industrial Technology Research Institute
Hsinchu, 310, Taiwan

Yur-Tsai Lin
Department of Mechanical Engineering
Yuan-Ze University
Taoyuan, Taiwan

Jerry Lo
Department of Mechanical Engineering
Yuan-Ze University
Taoyuan, Taiwan

Chi-Chuan Wang
Energy & Resources Laboratories
Industrial Technology Research Institute
Hsinchu, 310, Taiwan
E-mail:ccwang@itri.org.tw

ABSTRACT

This study presents visual observation of enlarged fin-and-tube heat exchangers with and without the presence of vortex generators. Three samples of fin-and-tube heat exchanger having inline arrangements are examined, including one plain fin and two wave-type vortex generators. For plain fin geometry at Re = 500, the horseshoe vortex generated by the tube row is not so pronounced, and a very large secondary flow circulation is seen between the first and second row. This flow re-circulation phenomenon is almost disappeared with the presence of proposed vortex generators. The presence of vortex generators significantly increase the vortrical motions of the horseshoe vortices hitting on the tubes. A much better mixing characteristics is seen by introducing the vortex generators. The frictional penalty of the proposed vortex generators are about 25~55% higher than that of the plain fin geometry. The penalty of pressure drops of the proposed vortex generators relative to plain fin geometry is relatively insensitive to change of Reynolds number.

INTRODUCTION

Vortex generators have generally been applied as a post-design method in aircraft applications to tackle a problem that was unexpected or not amenable to reliable production. For aircraft applications, exploitation of vortex generators is mainly to prevent boundary layer separation and drag reductions (such as wedge, plough, ramp, scoop, dome, wheeler, wing, and wave type, ESDU 1993 [1]). The vortex generators often take the forms of small protrusions which may be incorporated into the main surface by embossing, stamping, punching, or attaching. Figure 1 shows the commonly employed vortex generators. Swirl flow is generated as the mainstream flows across the small protrusions. Usually the vortrical motions may be classified as transverse and longitudinal vortices. The axis of a transverse vortex lies perpendicular to the flow direction while longitudinal vortices have their axes parallel to the main flow direction. The longitudinal vortex flow may swirl around the primary flow and exhibits three-dimensional characteristics. In general, longitudinal vortices are more effective than transverse vortices from the heat transfer perspective (Fiebig [2]).

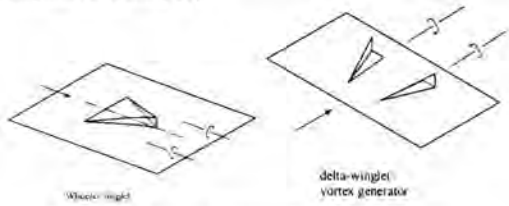

Figure 1: Various types of vortex generators.

In recent years, the exploitation of vortex generators in compact heat exchangers application had received a lot of attention. It is well known that enhanced surfaces are often employed in compact heat exchangers to effectively improve the overall heat transfer performance. Fiebig [3] points out there are three major heat transfer enhancement mechanisms of

enhanced surfaces, namely (1) developing boundary layers, (2), swirl or vortices; and (3) flow destabilization or turbulence intensification. A recent technology review article in connection to patents by Wang [4] clearly shows that the most common enhanced surfaces are the interrupted surfaces in the form such as slit, offset strip, and louver.

Though interrupted surfaces can significantly improve the heat transfer performance, the associated penalty of pressure drop is also tremendous. In contrast to the common interrupted surfaces, the vortex generator not only improves the heat transfer performance via all the three heat transfer mechanisms but also reveals comparatively small pressure drops. This is because wall friction is related to the derivative instead of streamwise velocity but spanwise and normal velocities. The vortex generators characterized the secondary flow pattern from the vortical motions is caused by the spanwise and normal velocities. Heat transfer enhancement is associated with the secondary flow but with small penalty of wall friction (Jacobi and Shah [5]). Therefore, longitudinal vortices are recognized especially suitable for heat transfer applications. The first literature reporting the heat transfer performance improvements is by Edwards and Alker [6]. They reported the local average heat transfer coefficient was about 40% higher than that of plain fin surface. For applications to the compact heat exchangers with vortex generators, Fiebig and his coworkers [7-10] had conducted very comprehensive studies in association with the influence of wing type, delta-wing type vortex generators. Very detailed information was reported about these kind of vortex generators. In this study, focus is made in on the feasibility of the new type vortex generator that is especially appropriate for the common fin-and-tube heat exchangers.

Table 1 Configuration of the test sample and the definitions of geometrical parameters of vortex generators.

	$H_{channel}$ (mm)	D (mm)	H_{VG} (mm)	α	R (mm)	D_{VG} (mm)
Plain	15	50.2	5	Base		
VG1				30°	5.0	100.2
VG3				45°	5.0	100.2

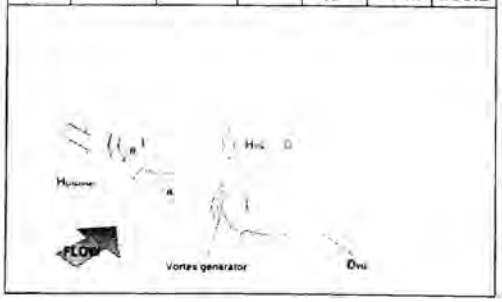

NOMENCLATURE

A_c	cross section area, (m^2)
H_{OV}	Height of vortex generator, (m)
D	tube outer diameter, (m)
D_{VG}	outer diameter of vortex generator, (m)
P	periphery of the cross section area, (m)
R	radius of curvature of the vortex generator, (m)
Re	Reynolds number based on channel height, dimensionless
ΔP_{int}	Pressure drops for interrupted surface, (Pa)
ΔP_{Plain}	Pressure drops for plain fin geometry, (Pa)
ΔP_{VG}	Pressure drops for vortex generator, (Pa)
α	angular angle of the vortex generator, degree

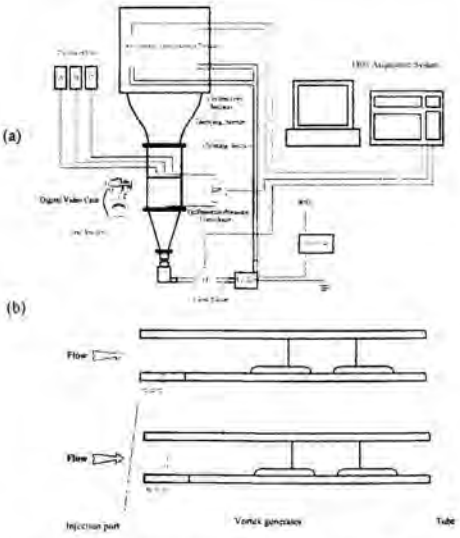

Figure 2: Schematic of (a) the test facility and (b) the arrangements of the injection port.

EXPERIMENTAL SETUP

Experiments are performed in a water tunnel as depicted in Figure 2. As shown in the figure, city water is supplied to the water tank, the water flows through in series to the contraction section, damping screen, the calm section, test section, exit contraction section, flow meter, water pump, and the connection pipe line to complete the cycle. The test section is made of transparent acrylic having a cross section of 254 mm × 15 mm. Flow visualization is performed via dye-injection technique. Two needles that are capable to inject color dye are placed at the entrance of the inlet section. For further investigating the flow phenomenon inside the heat exchanger, the injection port can be either located in the center or near the wall to keep track the trajectory behaviors (Fig. 2b). Additional dye injection port is placed at the rear of the acrylic tube to observe the flow motion of the inert region behind the tube. The color in front of the test section is red whereas the color behind the tube is blue. A total of three acrylic

test sections were made and tested. Their detailed geometrical parameters and relevant definitions of the vortex generators are shown in Table 1. The test samples include a plain fin configuration and two wave-element vortex generators. Notice that the tube layouts for the test samples are all inline arrangement. The outer tube diameter is 50.2 mm, and the channel height of the test section is 15 mm. The height of the vortex generator H_{VG} and its corresponding annular diameter D_{VG} are 5 mm and 100.2 mm, respectively. Detailed geometry of the vortex generators is seen from Figure 3. Notice that the annular vortex angle for VG3 is 45° compared to 30° of VG1.

A digital video cam is placed outside the test section to record the trajectory of the injected dye. The water flow rate was measured using a very accurate magnetic flowmeter with a calibrated accuracy of 0.002 L/s. The pressure drops across the test section were measured by a precision pressure transducer (YOKOGAWA EJ110). Resolution of this pressure differential pressure transducer is 0.3%. The water temperature inside the tank was measured by resistance temperature device (Pt100Ω) having a calibrated accuracy of 0.1°C.

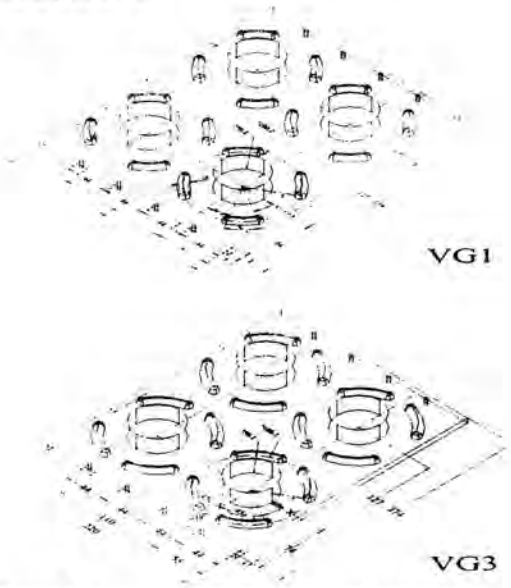

Figure 3: Detailed geometric parameters of the vortex generator.

RESULTS AND DISCUSSION

Figure 4 shows the flow visualization of plain fin geometry with Reynolds numbers of 500, 1500, and 3300. Notice that the Reynolds number is based on the hydraulic diameter of $4A_c/P$. As shown in Figs. 4b and 4c, the injected dye in front of the tube hits the round tube and twisted back a little and then swirls surrounding the round tube to the next row (see Fig. 4a). The horseshoe vortex motion is not so oblivious at this low Reynolds number. The injected dye (blue) right behind the first tube row climbs up the periphery of the tube, and then separated from the tube at an angle of approximate 110° (counting from the stagnation point of the first row). The trajectory of the blue dye than travels from the first row toward the second row. It is interesting to note that the blue dye then turns around and goes back to the first row forming a huge circulation zone. This huge re-circulation zone implies a very poor heat transfer characteristics in this region. As the Reynolds number is further increased to 1500, one can clearly see in Figs. 4e and 4f that the horseshoe vortices is clearly formed and flows following a similar trajectory like Re = 500 to the second row. The injected blue dye still forms a re-circulation cycle that is even larger than that of Re = 500. However, one can see the gap distance between the blue and the red dye is much closer than that of Re = 500. Apparently, this is due the contribution of the horseshoe vortex that bring closer the blue dye. In addition, one can see a very small amount of the blue dye was entrained to the vortex steam (red dye). A further increase of the Reynolds number to 3300, one can see the intensity of the horseshoe vortex is so strong that causes the shedding of the blue circulation zone (Figs. 4g, 4h, 4i).

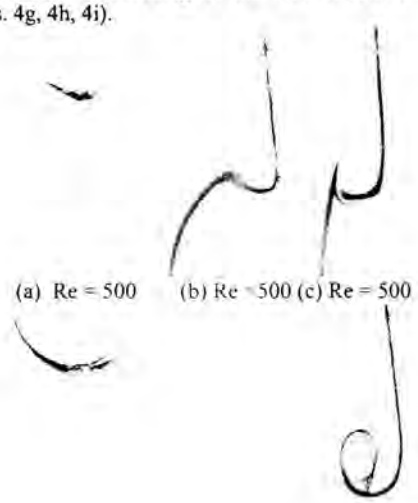

(a) Re = 500 (b) Re = 500 (c) Re = 500

(d) Re =1500 (e) Re =1500 (f) Re = 1500

(g) Re = 3300 (h) Re = 3300 (i) Re =300

Figure 4: Flow visualization of the plain fin geometry at Re = 500, 1500, and 3300.

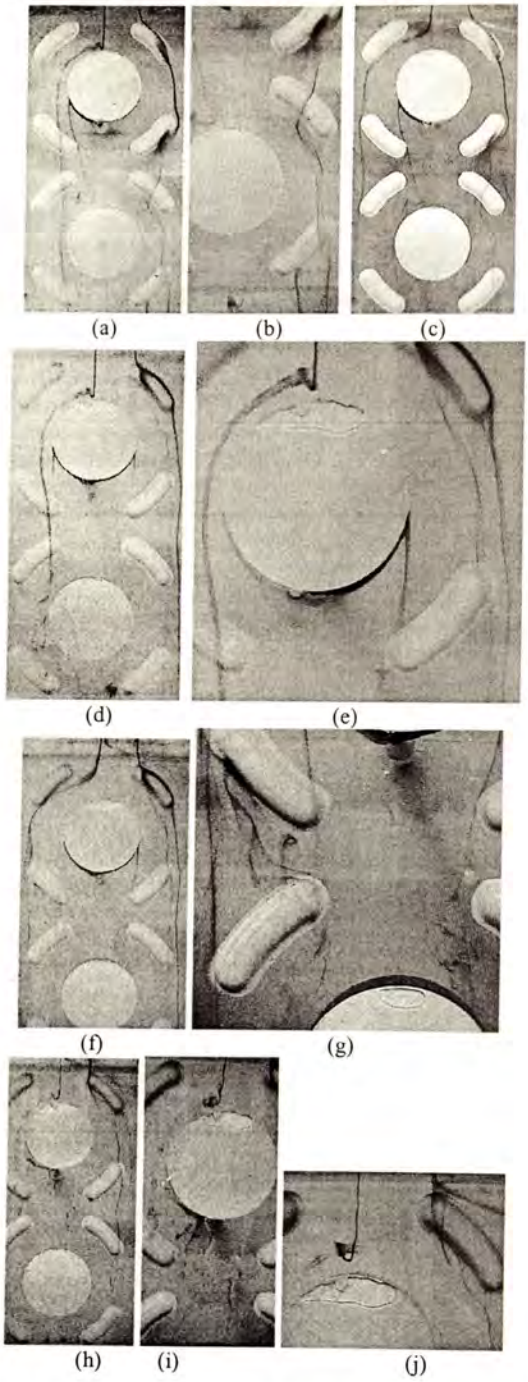

Figure 5: Flow visualization of the VG1 vortex generator (a) Re =500, center injection (b) Re = 500 (c) Re = 500, wall injection(d) Re =1500, center injection (e) Re =1500, closeup (f) Re = 1500, wall injection (g) Re =1500, closeup(h) Re = 3300, center injection (i) Re =3300 (j) Re=3300.

With the presence of vortex generator 1 (denoted as VG1), it may be expected the flow trajectory may be quite different. Figure 5 shows the visual results of Re = 500, 1500, and 3300, respectively. For the injection located at the center position, one can see the horseshoe vortex in front of the first tube is intensified by the presence of vortex generator when compared to that in plain tube at Re = 500. Interestingly, the flow circulation behind the first row is interrupted. As seen in Fig. 5a, the trajectory of the blue dye first climbs up the first row then departs at approximate 100° and travels along the tangential direction of the trailing edge of the vortex generator to the second row. The blue dye then hits the second row and bounce back. However, unlike those shown in plain fin geometry, the bounced back blue dye was directed to the horseshoe vortex from the first row and does not circulate back to the first row. The results implies the inert heat transfer characteristics behind the tube is significantly improved at this low Reynolds number with the presence of vortex generators

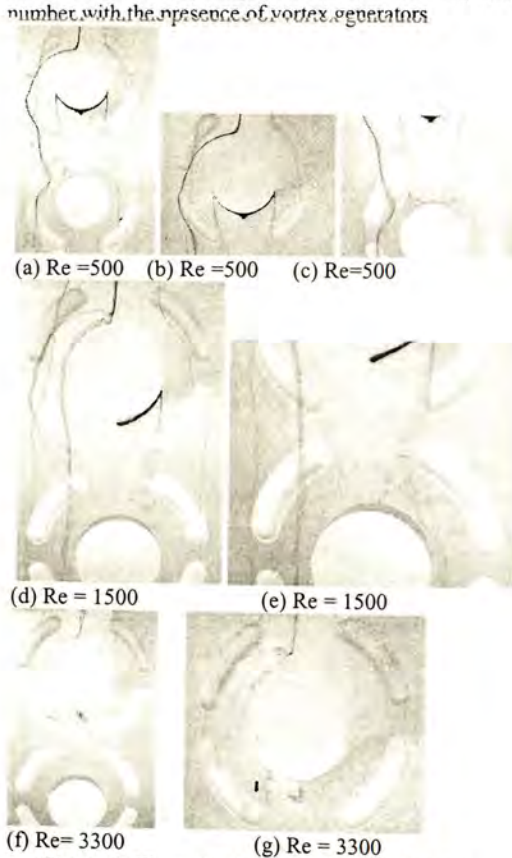

Figure 6: Flow visualization of the VG3 vortex generator at Re = 500, 1500, and 3300.

In the mean time, if the injection position is placed near the wall as shown in Fig. 5c, after passing through the first generator, the trajectory of the red dye turns around instead of hitting the tube. The red dye then flows through the concave of the first vortex generator

and flows surrounding the vortex generators towards downstream. The results may be related to the presence of vortex stream that flows across the vortex generator. As can be seen from the injected dye that is directly hitting the vortex generator, the flow shows a complicated vortrical motions. In this connection, the vortex is in fact a low pressure region, and this eventually will bring in the ambient fluid. Thus we can see that the circulation of the blue dye was interrupted by the vortex and was entrained into the vortex flow. This phenomenon can be further made clear in Figs. 5d, 5e, 5f, and 5g. With a higher Reynolds number of 1500, the trajectory of the blue dye was unable to bounce back in the second row. The vortrical motion at the trailing edge of the vortex generator (Fig. 5g) is so strong that eventually mixes up with the blue dye. For a Reynolds number of 3300, the vortex strength is strong enough to make the flow relatively unsteady. In this Reynolds number, no distinct vortex pattern can be observed (see Figs. 5h, 5i, and 5j). The blue dye behind the first row leaving the first row is completely mixed up with the horseshoe vortex from the first row.

Figure 6 shows the visual results of VG3 at Re = 500, 1500, and 3300. Note that the vortex angle for VG3 is 45° compared to VG1 of 30°. Basically, the phenomenon for VG3 is analogous to that of VG1 but accompanied with a much more intensified vortex strength. For instance, as seen from Figs. 6a and 6b, one can see the trajectory of the red dye produces a relatively pronounced vortex motion The circulation that appeared in plain fin geometry and in VG1 at Re = 500 is not seen. In addition, after hitting the vortex generator at the interception of first row and second row, one can clearly see that the blue dye exhibits a vortex sheet and flows around the second row (Fig. 6c). For VG3 at Re = 1500, the injected red dye produces strong motion that apparently induces the blue dye behind the tube and causing a turbulent motion. In addition, as can be seen from Fig. 6d, the injected red dye in the center position of inlet may be divided into two stream, one stream may be swirled into the stream at the edge of vortex generators and the other follows the horseshoe vortex that flows across the first row of the tube. For a Reynolds number of 3300, as shown in Fig. 6f, even the injected dye from the wall position reveals strong vortrical motions.

In summary, with the presence of vortex generator, the flow observation of the flow motions can be roughly described by Fig. 7. The horseshoe vortex that hits the first row will generate counter-rotating vortex, and the flow hits the first vortex generator also generates a pair of counter-rotating vortices. The pair of vortices will change their rotating direction when they flow across the second pair of vortex generator at the downstream. The corresponding pressure drops of the vortex generators and the plain fin geometry is shown in Fig. 8. As shown in the figure, the pressure drops for VG35 exceeds those of plain fin geometry by approximately 35%~55%. The pressure drops for VG3 is about 10% higher than that of VG1. The penalty of pressure drops of the proposed vortex generators relative to plain fin geometry is relatively insensitive to change of Reynolds number. This is quite different from those interrupted surfaces that often shows consecutive increase of $\Delta P_{int}/\Delta P_{plain}$ vs. Reynolds number (Wang et al. [11]). Although no heat transfer data were reported in this study, the flow patterns and the frictional performance of the vortex generators show promising prospective.

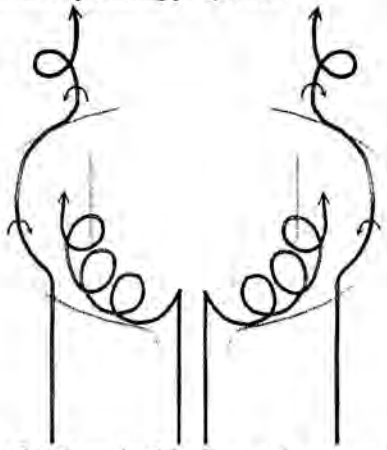

Figure 7: Schematic of the flow motions across the vortex generators.

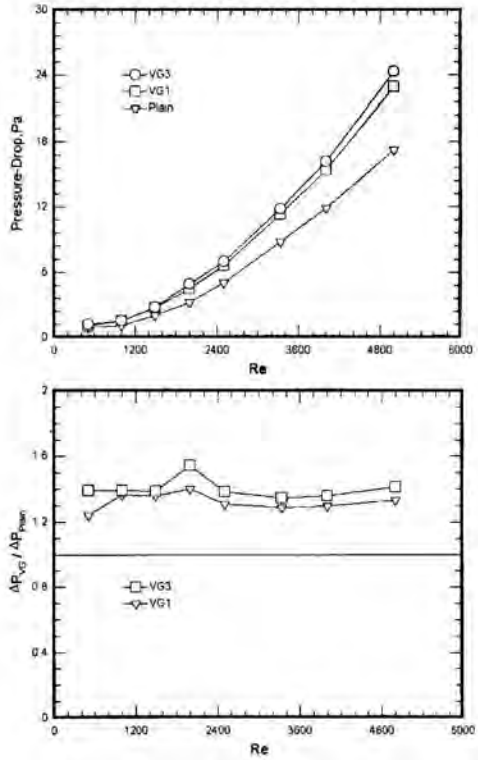

Figure 8: Frictional performance for the plain, VG1, and VG3 vortex generators.

CONCLUSIONS

This study presents flow visualization and frictional results of enlarged fin-and-tube heat exchangers having inline arrangements. Tests are performed a water tunnel by use dye-injection technique. Three samples of fin-and-tube heat exchanger are examined, including one plain fin and two wave-type vortex generators. Major conclusions of this study are summarized as follows:

(1) For plain fin geometry at Re = 500, the horseshoe vortex generated by the tube row is not so pronounced, and a very large secondary flow circulation is seen in the interval of the first and the second row.

(2) For plain fin geometry at Re = 1500, after hitting the first row of tube, the horseshoe vortex becomes more pronounced, and the flow circulation between the first and second row become larger and part of the fluid is entrained to the horseshoe vortex. As the Reynolds number is increased to 3300, the strength of the horseshoe vortices is so large that the circulation region behind the tube starts to shed vortices.

(3) With the presence of VG1 at a Reynolds number of 500, after hitting the first row, the horseshoe vortex becomes much more pronounced and the flow circulation behind the tube row is less profound. This flow circulation is completely eliminated for VG3 arrangement. In addition, the flow trajectory behind the first row for VG3 may even generate another pair of vortices when they flow across the vortex generators of the second row.

(4) For VG3 arrangement, as the flow trajectory at the wall flows over the first row, it is found that the flow was sucked into the central region due to the strong strength of the vortices.

(5) The frictional penalty of VG3 is about 10% higher than that VG1 but the flow mixing characteristics for VG3 apparently outperforms that of VG1. The pressure drops for the wave type vortex generators are about 25%~55% higher than those of the plain fin geometry. The penalty of pressure drops of the proposed vortex generators relative to plain fin geometry is relatively insensitive to change of Reynolds number.

ACKNOWLEDGMENTS

The authors would like to express gratitude for the Energy R&D foundation funding from the Energy Commission of the Ministry of Economic.

REFERENCES

[1] ESDU 93024, Engineering Science Data Unit, 1993, Vortex Generators for Control of Shock-Induced Separation Part 1: Introduction and Aerodynamics.

[2] M. Fibig, 1997, Vortices and heat transfer, ZAMM Z. angew Math. Mech., 77(1), pp. 3-18.

[3] M. Fibig, 1998, Vortices, generators and heat transfer, Trans. IChemE, Vol. 76, Part A, pp. 108-123.

[4] C.C. Wang, 2000, Technology review – a survey of the recent progress of the patents of fin-and-tube Heat Exchangers, J. of Enhanced Heat Transfer, 7, pp. 333-345.

[5] A. M. Jacobi, R.K. Shah, 1995, Heat transfer surfaces enhancement through the use of longitudinal vortices: a review of recent progress, Experimental Thermal and Fluid Science, Vol. 11, pp. 295-309.

[6] F.J. Edwards, G.J.R., Alker. 1974. The improvement of forced convection surface heat transfer using surfaces protusions in the form of (A) cubes and (B) vortex generators. Proc. 5th Int. Heat Transfer Conf., Tokyo, 2, pp. 244-248.

[7] M. Fibig, P. Kallweit, N.K. Mitra, S. Tiggelbeck, 1991, Heat transfer enhancement and drag by longitudinal vortex generators in channel flow, Experimental Thermal and Fluid Science, 4, pp. 103-114.

[8] S. Tiggelbeck, N. K. Mitra, M. Fibig, 1992, Flow structure and heat transfer in a channel with multiple longitudinal vortex generators, Experimental Thermal and Fluid Science, 5, pp. 425-436.

[9] S. Tiggelbeck, N.K. Mitra, M. Fibig, 1993, Experimental investigations of heat transfer enhancement and flow losses in a channel with double rows of longitudinal vortex generators, Int. J. Heat and Mass Transfer, 36, pp. 2327-2337.

[10] S. Tiggelbeck, N.K. Mitra, M. Fibig, 1994, Comparison of wing-type vortex generators for heat transfer enhancement in channel flows, J. of Heat Transfer, 116, pp. 880-885.

[11] C.C. Wang, C.J. Lee, C.T. Chang, 1999, Some aspects of the fin-and-tube heat exchangers: with and without Louvers, J. of Enhanced Heat Transfer, 6, pp. 357-368.

HEFAT2002
1st International Conference on Heat Transfer, Fluid Mechanics, and Thermodynamics
8-10 April 2002, Kruger Park, South Africa
MS1

MEASUREMENT OF TRANSIENT DOUBLE DIFFUSION FIELDS AND CRYSTAL GROWTH USING REAL-TIME PHASE-SHIFTING INTERFEROMETER

Shigenao MARUYAMA[1], Kentaro OHNO[1], Seigo SAKAI[1] and Kiyohiro TAKAHASHI[2]

[1]Institute of Fluid Science, Tohoku University, 2-1-1 Katahira, Aoba-ku, Sendai 980-8577, Japan
TEL&FAX: +81-22-217-5243, E-mail: maruyama@ifs.tohoku.ac.jp

[2]TOSHIBA CORPORATION, 1-1 Shibaura 1-chome, Minato-ku, Tokyo 105-8001, Japan

ABSTRACT

In the process of crystal growth in solutions, double diffusive convection due to thermal and solutal gradients occurs. A measurement system comprising a rapid heat-transfer control system and a real-time phase-shifting interferometer has been developed to investigate the transient double diffusive convection. The heat-transfer control system has a small test-cell in which the liquid temperature is controlled by non-equilibrium thermoelectric devices. In-situ observation of the transient double diffusive convection and crystal growth rates in aqueous solution are carried out by using this system. Transient double diffusive convection is observed directly and clearly. In addition to experiments, numerical simulation has been performed to compare with the present measurement results. Two-dimensional transient double diffusive convection around the seed crystal was calculated by using a numerical simulation cord. And the results show good accordance with those obtained by experimental results.

1. INTRODUCTION

Investigation of the crystal growth in solutions is closely related to effective and high quality production of medicine, food and new materials. During the process of crystal growth in solutions, double diffusive convection occurs, driven by buoyancy forces due to thermal and solutal gradients, which affects the mechanism of crystal growth. Therefore, it is important to investigate and understand the mechanism of the double diffusive convection and its effect on the crystal growth. Many previous studies have been carried out on double diffusive convection during crystal growth in solutions. Maruyama et al. [1] simulated the double diffusive convection in a cell when the direction of thermal and mass convection are the same or opposite, using thermal and solutal Rayleigh numbers as parameters. Chang et al. [2] performed an analysis to determine the influence of the ratio of thermal to solutal buoyancy on the transient double diffusive convection. They also investigated flow mechanisms and behavior of unstable vibration. Lin et al. [3] made a numerical study about the role of convection in protein crystal growth in a small cell. They found that convective transport enhances crystal growth under normal gravity field on the ground. Further more, Kranenborg et al. [4] have simulated the flows near an ice slab in a two-dimensional set up to consider buoyancy driven flows in a liquid near a cooled solid boundary. They found that the convection field was varied due to the position around the ice. Other early works on double diffusive convection in crystal growth have been summarized in reference [1]. Among the previous works, experiment of concerning crystal growth during short duration subjected to quick cooling in the aqueous solution has not been conducted.

In the present study, transient concentration distribution and solutal gradients in the process of a crystal growth subjected to quick supercooling are determined from measured double diffusion fields. In order to make an accurate measurement of the double diffusion fields, a real-time phase-shifting interferometer is adopted in which a phase dividing 3-CCD camera for the polarized beam is used. The test cell is made of the active thermal control units developed by Maruyama et al. [5] and solution around a seed crystal at the saturation temperature is rapidly cooled. A numerical simulation has been performed to compare the measured double diffusive field.

NOMENCLATURE

D Diffusion coefficient, m^2/s

f Fringe number
g Gravity acceleration, m/s^2
l Length, m
Ra_D Solutal Rayleigh number
T Temperature, °C
t Time from the beginning of experiments, s
w Concentration, wt%

Greek Symbols

β_D Volume coefficient of expansion by solute exchange
η Viscosity, Pa·s
ν Kinetic viscosity, m^2/s
ρ Density, kg/m^3
σ Supersaturation ratio

Subscripts

0 Initial
s Saturation

2. EXPERIMENTAL APPARATUS

2.1 Interferometer

The system of the experimental apparatus is shown in Fig. 1. A real-time phase-shifting interferometer was used in order to observe and measure the thermal and solutal fields of the solution. The basic arrangement of the interferometer is a Mach-Zehnder interferometer. By using a polarizing beam splitter, semiconductor laser beam (wavelength = 680nm) is separated into two beams, one for the reference and the other for the measurement. After passing through the test-cell and a compensator, the beams are combined by another beam splitter. A quarter-wave plate is placed at angle $\pi/4$ of two polarized beams. The two linearly polarized beams become right- or left circularly polarized each other. The circularly polarized beams are delivered into a specially made phase dividing 3-CCD camera. The camera has a 3-CCD prism and three polarizers and CCD sensors. The phase-shifting data are processed by a signal processor as has been described by Onuma et al. [6].and Nakadate et al. [7]. The signal data are recorded in a video recorder in gray scale. The detailed principle and system of the interferometer was described in reference [8].

2.2 Test Cell

Figure 2 shows a schematic of the test-cell used in the present experiment. It is specially designed for the transient measurement of the thermal and solutal diffusion fields. Saturated solution and a seed crystal are contained in the cell. Active thermal control units [5] installed on the upper and lower sides of the walls to control the temperature accurately in the test-cell. The active thermal control unit includes aluminum base plates, Peltier elements and heat sinks. The four Peltier elements are independently operated by a personal computer to accurate control the temperature of the solution and crystal. The temperature in the cell can be controlled rapidly.

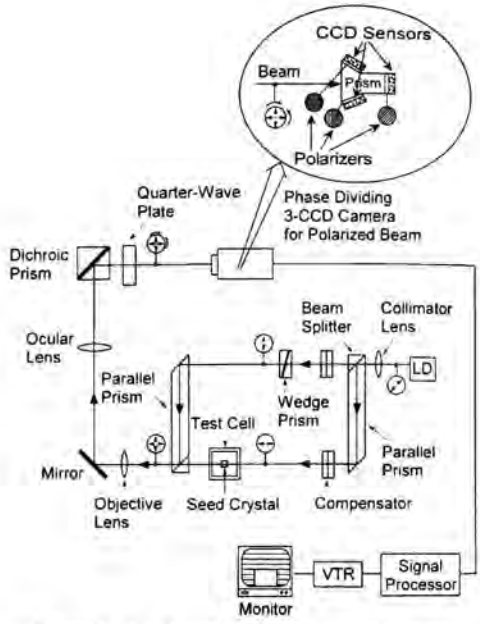

Figure 1: A schematic of experimental apparatus.

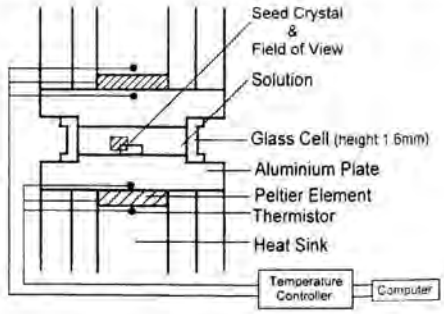

Figure 2: A schematic of the test-cell.

2.3 Temperature Profiles and Samples

The size of the glass-cell, made from quartz glass for optical measurement, is 12mm square and approximately 1.6mm in height. The seed crystal is attached on the lower base plate. The $NaClO_3$ crystal and its aqueous solution are used in the present experiments. The seed crystal has a solid rectangular shape. Before initiating a double diffusive convection experiment, temperature field in the cell is kept precisely uniform at the saturation value. As the experiment starts, the temperature control system is operated according to a programmed sequence. Temperature profiles on the lower base plate are shown in Fig. 3. The profiles on the upper base plate are the same. In the present experiments, three types of sequences cooling rate are applied.

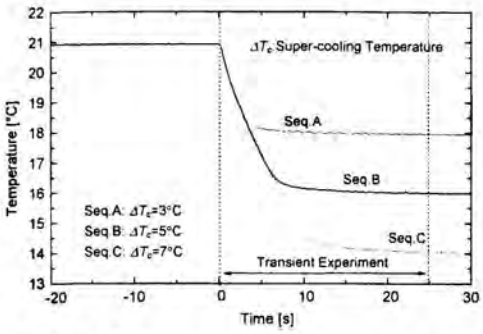

Figure 3: Various temperature sequences on the lower base plate.

3. RESULTS AND DISCUSSIONS

3.1 Relation between Fringe Shift and Temperature or Concentration

Figure 4 shows the field of view and measurement points of the temperature and surface concentration. The interferogram obtained by the present experiment is a superimposition of temperature and concentration differences. Extraction of the temperature and concentration information from interferogram is carried out as follows. Thermal diffusivity is two orders of magnitude larger than the mass diffusion coefficient in the solution. Therefore, temperature changes immediately in the solution and can be considered uniform on the same horizontal line. So, we measured the temperature change of solution at the measurement point (B) in the bulk, and assumed that the temperature at the crystal surface (A) is equal to that of the bulk. On the other hand, change of concentration is local at the crystal surface because the mass diffusion coefficient is small and it's change remains near crystal. So we measured the fringe difference between bulk (B) and crystal surface (A), and estimated the concentration in the vicinity of the crystal surface.

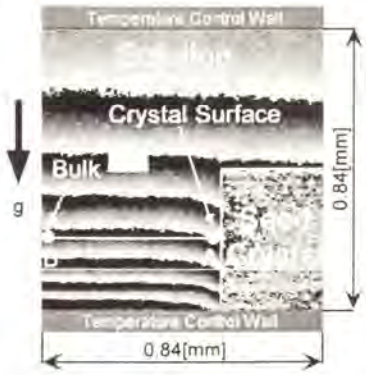

Figure 4: The measurement points for temperature and concentration.

Preliminary experiments were carried out, in order to determine the temperature and concentration fields, the relation between fringe shift on the interferogram and temperature or concentration.

The relationships between the obtained fringe numbers, f_T, and the temperature difference are determined for each saturation temperature is described in reference [9]. As an example, when the saturation temperature is 20°C, the relation is determined as follows.

$$\Delta T = \left(T - T_{\infty}\right) = 0.264 \times f_T / l_m \qquad (1)$$

Further, a specially designed test cell is set up to measure the relationship between the fringe shift and the concentration [10]. The obtained fringe number in an interferogram, f_w, is related to the concentration difference by:

$$\Delta w = \left(w - w_{\infty}\right) = 0.0732 \times f_w / l_c \,. \qquad (2)$$

Where l_m and l_c are optical path length of solution (=12mm) at crystal depth. It is noted that the relation given in Eq. (2) is for the case of 10mm optical path in the test cell. This needs to be corrected to match the length of the seed crystal.

3.2 Observation of Plumes

Interferograms around the seed crystal are presented in Fig. 5. The size of seed crystal used in these experiments is 1.56mm in width, 1.40mm in depth, and 0.68mm in height. The saturation temperature is 24°C.

When the uniform temperature distribution in the test-cell is maintained at the saturation temperature (i.e. t=0s), natural convection does not occur in the small test-cell. As the cell was cooled rapidly, in the case of ΔT_c=5°C, plumes driven by the

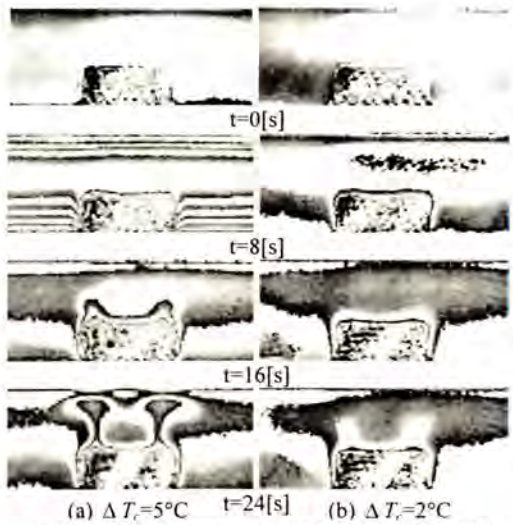

Figure 5: Interferograms around the seed crystal.

buoyancy force occurred stronger than the case of ΔT_c=2°C at the upper surface of the seed crystal.

To examine the condition of a plume's appearance, the solutal Rayleigh number, Ra_D, needs to be evaluated. The solutal Rayleigh number is defined as:

$$Ra_D = g\beta_D \frac{(w - w_r)l^3}{D\nu}, \quad (3)$$

where w is the local concentration at the measurement point, w_r is the bulk solution concentration, l is the height of the seed crystal and ν is the kinematic viscosity of the solution. The temperature dependence of ν was estimated in [11]. The volume coefficient of expansion β_D is determined from the relation between the concentration and density of $NaClO_3$ solution obtained from a preliminary experiment. The diffusive coefficient of $NaClO_3$ was measured by the authors [12].

In the case of ΔT_c=5°C, when the height of the seed crystal is 0.68mm, Ra_D is 3.10×10^4 at the time of t=24s obtained from these quantities. Similarly, in the case of ΔT_c=2°C, Ra_D is 1.53×10^4. We also made some experiments using a seed crystal with smaller height, and found that the solutal Rayleigh number has a close relation with the development of plumes. This indicates that convection along the vertical crystal surface has large effect on the formation of plume.

3.3 Supersaturation of Bulk Solution and Crystal Surface

The following results are the case of the saturation temperature T_s = 21°C and using rapid cooling sequence (Seq. A, B, and C in Fig. 3). The size of the seed crystal used in these experiments is 1.62mm in width, 1.30mm in depth, and 0.40mm in height.

Time variations of supersaturation ratio, σ_s, for three different cases of ΔT_c are shown in Fig. 6. The supersaturation ratio is defined as:

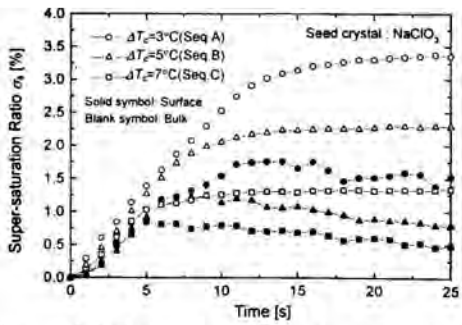

Figure 6: Variation of supersaturation ratio (σ_s) with time.

$$\sigma_s = (w - w_{sat})/w_{sat},$$

where w is the transient concentration at the measuring point and w_{sat} is the saturation concentration at the transient cooling temperature. The higher supercooling temperature ΔT_c results in a larger difference in supersaturation between the bulk and the surface. Supersaturation in the vicinity of the surface also increases immediately after the start of experiment, then it begins to decrease with time gradually. This phenomenon is clearly noticeable, particularly in the case of ΔT_c=5°C and 3°C. In the vicinity of the crystal surface, the concentration decreases as the crystal grows. Therefore, as time goes by, the decrease of supersaturation ratio becomes more noticeable than the increase by the cooling of the solution.

4 NUMERICAL SIMULATION

In the present study, numerical simulation has performed two-dimensional model is shown in Fig.7, which is similar to the experimental setup. The governing equations are the two-dimensional, time-dependent forms of the continuity, momentum, energy, and solute mass equations. These can be written as:

$$\nabla \cdot \vec{V} = 0 \quad (5)$$

$$\frac{\partial \vec{V}}{\partial t} + \vec{V} \cdot \nabla \vec{V} = -\frac{1}{\rho}\nabla p + \nu \nabla^2 \vec{V} + \vec{g} \quad (6)$$

$$\frac{\partial T}{\partial t} + \vec{V} \cdot \nabla T = \alpha \nabla^2 T \quad (7)$$

$$\frac{\partial w}{\partial t} + \vec{V} \cdot \nabla w = D \nabla^2 w \quad (8)$$

where, $\vec{v}$ is velocity vector, p is pressure and α is thermal diffusivity. The data for numerical simulation are shown in Table. 1. At the present time, the property of sodium chlorate has not been determined completely. Consequently, the unknown property is approximated to use the property of sodium chloride. The size of seed crystal used in this

Table 1: The data for numerical simulation.

$NaClO_3$ saturated aqueous solution	
thermal diffusivity λ	0.576[W/(m·K)]
constant pressure specific heat C_p	3367[J/(kg·K)]
mass diffusivity D	6.22×10^{-10}[m²/s]
coefficient of solutal expansion β_D	1.06[-]
coefficient of thermal expansion β_T	3.66×10^{-4}[1/K]
viscosity η	3.20×10^{-3}[kg/(m·s)]
$NaClO_3$ seed crystal	
thermal diffusivity λ	6.49[W/(m·K)]
specific heat C	854[J/(kg·K)]
density ρ	2.49×10^3[kg/m³]

simulation is 1.6mm in width, and 0.7mm in height.

The pressure implict with splitting of operators (PISO) method, which is common to incompressible flow simulation is employed to couple velocity with pressure.

4.1 Initial and Boundary Condition

Initial conditions are determined from the experimental data, and initial temperature and concentration is set to 20.94 °C and 49.11 %, respectively. At the cell wall we defined the non-slip condition. And as boundary condition, we use the experiment data. Temperature profiles on the lower and upper base plate, and concentration profiles on the crystal surface have used the experimental data obtained from interferogram, which is measured 0.1 second interval.

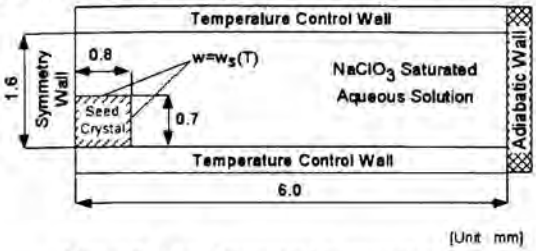

Figure 7: Two-dimensional numerical model.

4.2 Transient Distributions around the Seed Crystal

The results of numerical simulation and experiment about transient exchange around the seed crystal are shown in Fig. 8. Here, (a) and (b) are numerical simulation results and (c) is experimental result. Although the generation time of plumes have little interval between experimental and simulated results, but the results obtained from numerical simulation about the generation point, concentration boundary layer and figure of plume are good accordance with experimental results. As the time passed, the plumes rise and curve to bulk solution. Because mass of low concentration solution which rising as the plume diffuse toward bulk high concentration solution.

4.3 Concentration Distribution nearby the Crystal

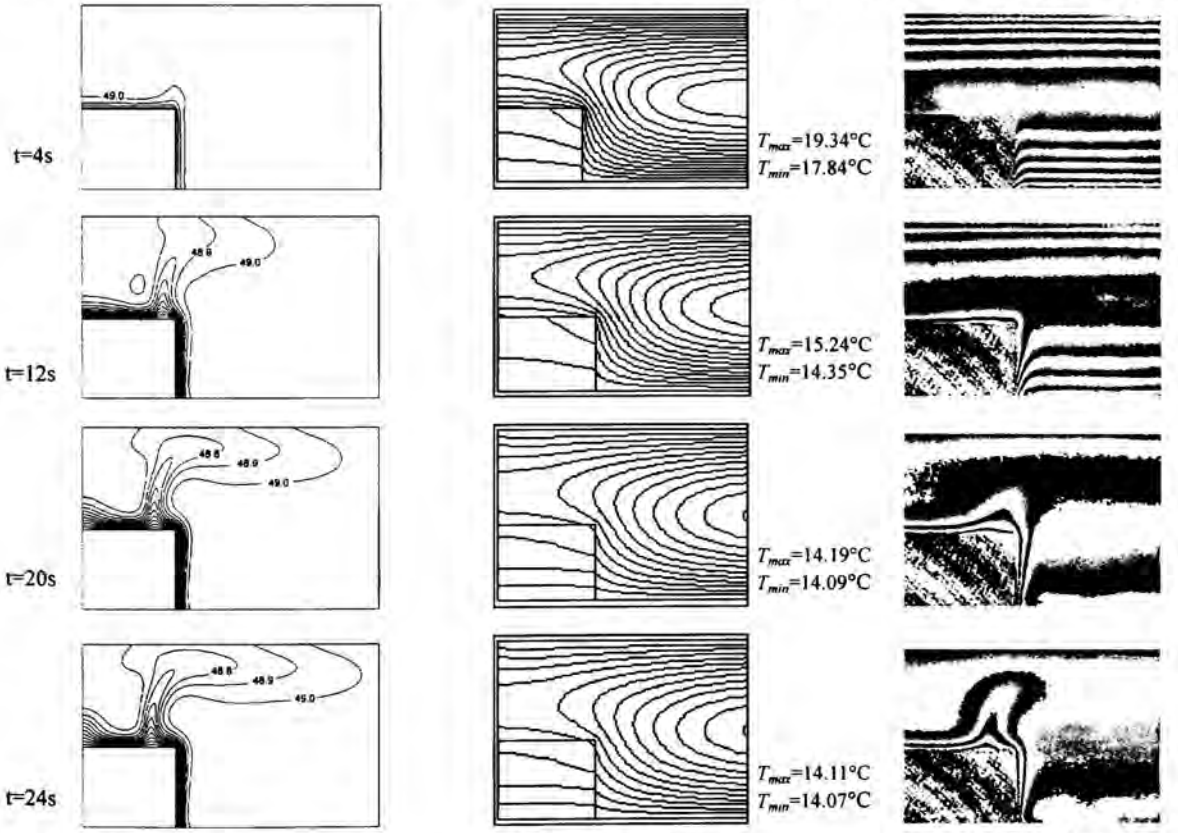

(a) Concentration contours. (b) Temperature contours. (c) Snap shots.

Figure 8: Transient exchanges around the seed crystal.(Seq.B)

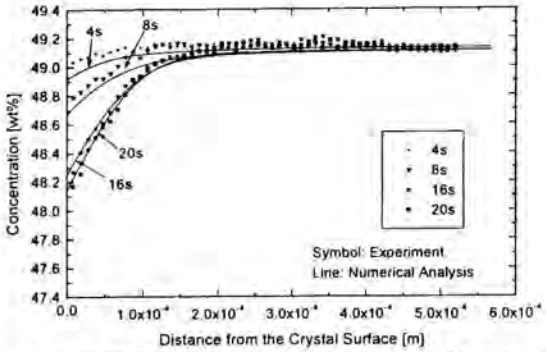

Figure 9: Concentration distribution nearby the crystal side.(Seq.B)

Surface

Figure 9 shows concentration distribution about horizontal line, which height is middle of the crystal side.

In the vicinity of the crystal surface, concentration gradient obtained by the experiment shows good accordance with those by numerical simulation is shown in Fig 9. The transient change of concentration and temperature on the crystal surface was measured and transient supersaturation ratio and the crystal growth rate obtained from the gradient of the concentration was compared with the results obtained by Bennema [13]. The present data show somehow one order of magnitude larger than that of Bennema [13]. We are conducting further investigation on the growth mechanism including the chemical potential of dehydration process. These investigation is a future objective of our research.

5. CONCLUSIONS

Transient double diffusive convection in solutions are observed and measured by employing a novel temperature control system and a real-time phase-shifting interferometer. The transient behavior of plumes can be observed in the short experimental time (about 25 seconds). The existence of plumes became clear when the supercooling temperature, ΔT_c was about 5°C.

Numerical simulation about the quick transient double diffusive fields has performed. The results from numerical simulation show that the figures of the plume and concentration boundary layer are good accordance with the experimental results. From the experiment and simulation, we can obtain the crystal growth rate accuracy to use concentration gradient from numerical simulation result.

REFERENCES

[1] S. Maruyama, Y. Miyagawa, K. Tsukamoto and T. Aihara, Transient simulation of double diffusive convection of crystal growth in microgravity, *Proc. 6th International Symp. on Transport Phenomena in Thermal Engineering*, Begel House Publishing, Vol.2, pp.1072-1077, (1993).

[2] J. Chang and T.F. Lin, Unsteady thermosolutal opposing convection of liquid-water mixture in a square cavity - flow structure and fluctuation analysis, *Int. J. Heat Mass Transfer*, Vol.36, No.5, pp.1333-1345, (1993).

[3] H. Lin, F. Rosenberger, J.I.D. Alexander and A. Nadarajah, Convective-diffusive transport in protein crystal growth, *Journal of Crystal growth*, Vol.151, pp.153-162, (1995).

[4] E. Jurjen Kranenborg and Henk A. Dijkstra, Double diffusive layer formation near a cooled liquid-solid boundary, *Int. J. Heat Mass Transfer*, Vol.41, No.13, pp.1873-1884, (1998).

[5] S. Maruyama, E. Nino and G. Ruoco, Analysis of a thermoelectrical device for active heat transfer control, *17th UIT National Heat Transfer Conference*, pp.485-492, (1999).

[6] K. Onuma, K. Tsukamoto and S. Nakadate, Application of real-time phase-shift interferometer to the measurement of concentration field, *Journal of Crystal growth*, Vol.129, pp.706-718, (1993).

[7] S. Nakadate and M. Issiki, Real-time fringe pattern proceedings and its applications, *Proc. Photo Instrum. Eng.*, Vol.2544, pp.74-86, (1995).

[8] S. Maruyama, T. Shibata, K. Tsukamoto, Measurement of diffusion fields of solutions using real-time phase-shift interferometer and rapid heat-transfer control system, *Experimental Thermal and Fluid Science*, Vol.19, pp.34-48, (1999)

[9] S. Maruyama, K. Takahashi and A. Komiya, Measurement of transient double diffusive convection and crystal growth using real-time phase-shifting interferometer, *Proc. Symposium on Energy Engineering in the 21st century*, Vol.2, pp.873-880, (2000).

[10] S. Maruyama, A. Komiya, J. Yabana and M. Higano, Measurement of mass diffusion coefficient of solutions using real-time phase-shift interferometer, *Proc. 18th Japan Symposium on Thermophysical Properties*, pp.117-120, (1997).

[11] S. Maruyama, T. Shibata, K. Tsukamoto, and K. Shimizu, Measurement of solutal and thermal diffusion in systems subjected to rapid cooling under microgravity during parabolic flight, *Heat Transfer-Japanese Research* Vol.27 (2), pp.114-129, (1998).

[12] S. Maruyama, A. Komiya, Z. Guo and T.Shimoyama, Accurate Measurement of mass diffusion field and diffusion coefficient using real-time phase-shift interferometer, *Proceedings of PSFVIP-2*, PF074, (1999).

[13] P.Bennema, Interpretation of the relation between the rate of crystal growth from solution and the relative supersaturation at low supersaturation, *Journal of Crystal Growth*, Vol.1, pp. 287-292, (1967).

HEFAT2002
1st International Conference Heat Transfer, Fluid Mechanics, and Thermodynamics
8-10 April 2002, Kruger Park, South Africa
DW1

Transition boiling phenomena including dry patches interactions

L.H Chai* and D.S Wen**

*Mechanical Engineering Department, The University of Tokyo, Tokyo 113-8656, Japan
E-mail: lhchai@photon.t.u-tokyo.ac.jp
** Department of Engineering Science, Oxford University, Parks Road, OX1 3PJ, UK
E-mail: dongsheng.wen@eng.ox.ac.uk

Abstract — Analysis of the Rayleigh-Taylor stability of local dry patch film in transition boiling incorporating the effect of heat and mass transfer was performed. The results show that heat and mass transfer at the interface will enhance the stability, increase the value of most dangerous wavelength. The occurrence of local dry patch in transition boiling system may create big temperature gradient in the vapor film and can significantly affect transition-boiling features. Dual characters of transition between nucleate boiling and film boiling: hydrodynamic and non-hydrodynamic performance could then be explained in a unified fashion. The present investigation that incorporates dry patch interaction performance is in better agreement with experimental facts.

INTRODUCTION

Transition boiling bridges the nucleate boiling and film boiling, which is encountered in a number of applications, including metallurgical quenching processes, and immersion cooling of high temperature components. Although having been studied for decades, transition boiling still holds its place as the least understood of the several boiling mechanisms [1]. Such an occurrence is attributed to the complexity of mechanisms controlling the transition boiling heat transfer, and the difficulty of performing experiments. Since the pioneering work of Berenson [2], researchers noted that the transition boiling process incorporated liquid-solid-vapor triple phases interactions. The heat transfer mechanism is hence regarded as a combined process including transient heat conduction, nucleation boiling, and film boiling heat transfer modes [3]. In transition boiling, the dry patches would form at the high-density level and at the great size, as shown in *figure1*. The wetting ratio dramatically falls as wall superheat increases. Till stable film boiling has established on the heated surface, the wetting ratio approaches zero.

Contradictions exist in literature works regarding the dynamics of dry patches or wet patches at transition boiling. Witte and Lienhard [4] and Ramilison and Lienhard [5] reported the occurrence of sudden "jumps" between nucleate boiling and film boiling regimes. Large dry patches once emerge, would flush and cover the entire heated surface. However, Bui and Dhir [6] tried, but failed to destabilize the transition-boiling mode by wiping the surface with a brush. Unger and Eichhorn [7] had neither observed any jumps in their transition boiling experiments. These authors claimed that, although certainly possible, jumps in transition boiling curve were not inevitable. Restated, the occurrence of jumps in transition boiling curve is conditional. There exists no comprehensive framework to interpret these experimental findings to date.

Actually, available literatures on transition boiling mostly encounter a time/surface-average procedure in which a stationary boiling process is assumed. During transition boiling the wall temperature is extremely non-uniform for the stochastic formation/rewet of dry patches. Dry patch dynamic feature could be largely masked by the averaging [8]. The thermal and hydrodynamic stability of dry patch may play a central role in the development of transition boiling mode.

However, in available hydrodynamic analyses, the effects of heat and mass transfer have been neglected for a long time due to the small temperature gradient. But we note that, there often exists great superheat and strong evaporation at the interface for the dry patch film in transition boiling. The strong evaporation will create a large momentum at the interface and may greatly influence the development of interfacial wave. Thus, the classical Rayleigh-Taylor method will cease to be satisfied for the stability analysis of dry patch film in transition boiling.

In an attempt to reveal the dynamic characteristics of dry patch and correspondingly analyze transition boiling phenomena, the present work focuses on the stability analysis of dry patch, taking into the effects of heat and mass transfer on the Rayleigh–Taylor wave. The features of transition boiling are then correspondingly discussed.

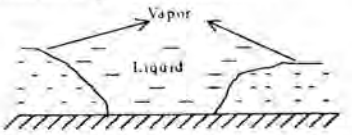

Figure1 Physical view of transition boiling

NOMENCLATURE

a thermal diffusivity ($m^2 \cdot s^{-1}$)
c constant
g gravitation acceleration ($m \cdot s^{-2}$)
G temperature gradient ($K \cdot m^{-1}$)
h liquid layer thickness (m)
h_{fg} latent heat ($J \cdot kg^{-1}$)
k wave number
P pressure (Pa)
r radius (m)
t time (s)
T temperature (^0C)
u, v velocity ($m \cdot s^{-1}$)
x, y coordinate (m)

Greek symbols

ΔT liquid superheat (^0C)
β wave growth rate
σ surface tension ($N \cdot m^{-1}$)
ρ density ($kg \cdot m^{-3}$)
l wave length (m)
λ thermal conductivity ($W \cdot m^{-1} \cdot K^{-1}$)
φ stream function

Subscripts

c critical
d dangerous
i $i=1, 2$, interface
v vapor
w wall surface
0 reference state
1 component 1
2 component 2

ANALYTICAL MODEL

The physical model of Rayleigh-Taylor stability analysis is illustrated as Fig1. It includes fluid 1 and fluid 2 with finite depth h_1 and h_2 separately; heat flux is supplied from the solid bottom.

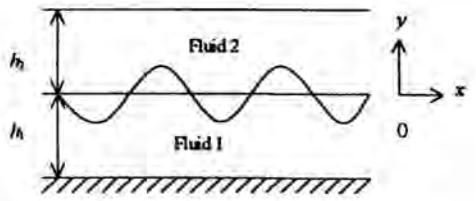

Figure 2 Analysis model

Assuming the two fluids are both imcompressible and inviscocity, we can get the control equations of the system as: (i=1, 2)

$$\frac{\partial u_i}{\partial x}+\frac{\partial v_i}{\partial y}=0 \tag{1}$$

$$\frac{\partial u_i}{\partial t}+u_i\frac{\partial u_i}{\partial x}+v_i\frac{\partial u_i}{\partial y}=-\frac{1}{\rho}\frac{\partial P}{\partial x} \tag{2}$$

$$\frac{\partial v_i}{\partial t}+u_i\frac{\partial v_i}{\partial x}+v_i\frac{\partial v_i}{\partial y}=-g-\frac{1}{\rho}\frac{\partial P}{\partial y} \tag{3}$$

$$\frac{\partial T_i}{\partial t}+u_i\frac{\partial T_i}{\partial x}+v_i\frac{\partial T_i}{\partial y}=a\left(\frac{\partial^2 T_i}{\partial x^2}+\frac{\partial^2 T_i}{\partial y^2}\right) \tag{4}$$

Introducing streamfunction, φ, that is: $u_i=\frac{\partial \varphi_i}{\partial x}, v_i=\frac{\partial \varphi_i}{\partial y}$

Eq.(1) can be rewrote as:

$$\frac{\partial^2 \varphi_i}{\partial x^2}+\frac{\partial^2 \varphi_i}{\partial y^2}=0 \tag{5}$$

and Eq.(3) becomes:

$$\frac{P_i}{\rho_i}+\frac{1}{2}(\nabla \varphi_i)^2+gy+\frac{\partial \varphi_i}{\partial t}=c \tag{6}$$

The boundary equations at the interface are the balance of mass, momentum and energy, which can be expressed as[3]:

$$\rho_1\left(v_1-\frac{dy}{dt}\right)=\rho_2\left(v_2-\frac{dy}{dt}\right) \tag{7}$$

$$P_1-P_2=\sigma\left(\frac{1}{r_1}+\frac{1}{r_2}\right)+=\rho_2\left(v_2-\frac{dy}{dt}\right)v_2-\rho_1\left(v_1-\frac{dy}{dt}\right)v_1 \tag{8}$$

$$\rho_1 h_{fg}\left(v_1-\frac{dy}{dt}\right)=-\lambda_1\frac{dT_1}{dy}-\lambda_2\frac{dT_2}{dy} \tag{9}$$

$$T_1=T_2 \tag{10}$$

$$P_1=P_v(T_2)=\left(\frac{dP}{dT}\right)_{T=T_0}T_2 \tag{11}$$

From Eq.(5) and the note that when y=0, $\varphi_1=\varphi_2$=0, the boundary conditions at $y=h_1$ and $y=h_2$ can be wrote as:

$$\begin{cases}\varphi_1=\overline{\varphi}_1\cosh k(y+h_1)e^{i(kx-\beta t)}\\ \varphi_2=\overline{\varphi}_2\cosh k(y-h_2)e^{i(kx-\beta t)}\end{cases} \tag{12}$$

Due to φ_0=0, Eq.(12) is the perturbation equation.
Assuming the perturbation equation of temperature T is:

$$T_i'=\overline{T}_i(y)e^{i(kx-\beta t)} \tag{13}$$

Combining Eq.(13) and Eq.(4), we get:

$$\begin{cases}\frac{d^2\overline{T}_1}{dy^2}-\left(k^2-\frac{i\beta}{a_1}\right)\overline{T}_1=\frac{G_1 k\overline{\varphi}_1}{a_1}\sinh k(y+h_1)\\ \frac{d^2\overline{T}_2}{dy^2}-\left(k^2-\frac{i\beta}{a_2}\right)\overline{T}_2=\frac{G_2 k\overline{\varphi}_2}{a_2}\sinh k(y-h_2)\end{cases} \tag{14}$$

where G_1 and G_2 are the temperature gradients between two fluids, defined as $G_1=(T_w-T_i)/h_1$, $G_2=(T_i-T_v)/h_2$ separately. From Eq.(14), we get the perturbation equations for temperature:

$$\begin{cases} \bar{T}_1 = A_1 \sinh(y+h_1)\sqrt{k^2 - \dfrac{i\beta}{a_1}} - i\dfrac{G_1 k\bar{\varphi}_1}{\beta}\sinh k(y+h_1) \\ \bar{T}_2 = A_2 \sinh(y-h_2)\sqrt{k^2 - \dfrac{i\beta}{a_2}} - i\dfrac{G_2 k\bar{\varphi}_2}{\beta}\sinh k(y-h_2) \end{cases} \quad (15)$$

Taking the perturbation form of press as $P_i' = \bar{P}_i(y)e^{i(kx-\beta t)}$, $y_i' = \bar{y}e^{i(kx-\beta t)}$ and combining the Eq.(6) by neglecting minor terms, we get the pressure perturbation equations:

$$\begin{cases} \bar{P}_1 = i\varphi_1\rho_1\beta\cosh kh_1 - \rho_1 g\bar{y} \\ \bar{P}_2 = i\varphi_2\rho_2\beta\cosh kh_2 - \rho_2 g\bar{y} \end{cases} \quad (16)$$

Putting the Eq.(12~16) into Eq.(7~11) and with the same perturbation forms: $f_i' = \bar{f}_i(y)e^{i(kx-\beta t)}$, the mass,momentum and energy equations can be rewrite as: (the tension terms have been neglected for convience and will reintruduce later)

$$\begin{cases} \rho_1(\bar{\varphi}_1 k\sinh kh_1 + i\beta\bar{y}) = \rho_2(-\bar{\varphi}_2\sinh kh_2 + i\beta\bar{y}) \\ \rho_1(i\beta\bar{\varphi}_1\cosh kh_1 - g\bar{y}) = \rho_2(i\beta\bar{\varphi}_2\cosh kh_2 - g\bar{y}) \\ \rho_1 h_{fg}(\bar{\varphi}_1 k\sinh kh_1 + i\beta\bar{y}) = -\lambda_2[A_2\sqrt{k^2-(i\beta/a_2)}\cosh\sqrt{k^2-(i\beta/a_2)}h_2 - \dfrac{iG_2k^2}{\beta}\bar{\varphi}_2\cosh kh_2] \\ +\lambda_2[A_2\sqrt{k^2-(i\beta/a_2)}\cosh\sqrt{k^2-(i\beta/a_2)}h_2 - \dfrac{iG_2k^2}{\beta}\bar{\varphi}_2\cosh kh_2] \\ A_1\sinh\sqrt{k^2-(i\beta/a_1)}h_1 - \dfrac{iG_1k}{\beta}\bar{\varphi}_1\sinh kh_1 + G_1\bar{y} = -A_2\sinh\sqrt{k^2-(i\beta/a_2)}h_2 \\ +\dfrac{iG_2k}{\beta}\bar{\varphi}_2\sinh kh_2 + G_2\bar{y} \\ i\beta\rho_2\bar{\varphi}_2\cosh kh_2 - \rho_2 g\bar{y} = \left(\dfrac{dP_s}{dT}\right)_{T=T_s}[-A_2\sinh\sqrt{k^2-(i\beta/a_2)}h_2 + \dfrac{iG_2k}{\beta}\bar{\varphi}_2\sinh kh_2 + G_2\bar{y}] \end{cases} \quad (17)$$

Solve the Equations of (17) and noting that , $\lambda_1 G_1 = \lambda_2 G_2$, we get the final dispersion relation for the interfacial wave with heat and mass transfer effect:

$$\left[h_{fg} + \frac{iG_1\lambda_1}{\beta}\left(\frac{\sqrt{k^2-(i\beta/a_1)}\coth\sqrt{k^2-(i\beta/a_1)}h_1}{\rho_1} + \frac{\sqrt{k^2-(i\beta/a_2)}\coth\sqrt{k^2-(i\beta/a_2)}h_2}{\rho_2}\right)\right]F_1$$

$$= -iF_2\left[\frac{G_1\lambda_1 k(\rho_2-\rho_1)}{\rho_1\rho_2\beta} + \frac{\beta}{\left(\frac{dP_s}{dT}\right)_{T=T_s}k}\left(\lambda_1\sqrt{k^2-\frac{i\beta}{a_1}}\coth\sqrt{k^2-\frac{i\beta}{a_1}}h_1 + \lambda_2\sqrt{k^2-\frac{i\beta}{a_2}}\coth\sqrt{k^2-\frac{i\beta}{a_2}}h_2\right)\right] \quad (18)$$

where

$$F_1 = \beta^2(\rho_1\cosh kh_1\sinh kh_2 + \rho_2\cosh kh_2\sinh kh_1) - gk(\rho_1-\rho_2)\sinh kh_1\sinh kh_2 \quad (19)$$

$$F_2 = \beta^2(\rho_2-\rho_1)\cosh kh_1\cosh kh_2 - gk(\rho_1\sinh kh_1\cosh kh_2 + \rho_2\sinh kh_2\cosh kh_1) \quad (20)$$

Eq.(18) is the final results of Taylor stability analysis that combine the effects of temperature gradients and finite fluid depth. Due to its complexity, it is hard to analysis the effects of heat and mass transfer on the dispersion relation. We will simplify the above results to find a theoretical solution and apply it to the critical heat transfer analysis.

For the cases currently considered, we adopted assumptions $kh_1 << 1, h_2 \to \infty$ and neglected $(\frac{dP^s}{dT})_{T=T_s}$. Equation (18) can then be simplified as

$$\beta^2 + \frac{iG_1\lambda_1}{h_{fg}(\rho_1+\rho_2 kh_1)h_1}\beta - \frac{gk^2(\rho_2-\rho_1)}{(\rho_1+\rho_2 kh_1)}\left[1 + \frac{G_1\lambda_1}{h_{fg}}\left(\frac{1}{2k\rho_2 a_2} + \frac{h_1}{3\rho_1 a_1}\right)\right]h_1 = 0 \quad (21)$$

The solution for equation (21) is

$$\beta = -\frac{G_1\lambda_1}{2h_{fg}(\rho_1+\rho_2 kh_1)h_1} \pm \sqrt{\frac{gk^2(\rho_2-\rho_1)}{(\rho_1+\rho_2 kh_1)}\left[1 + \frac{G_1\lambda_1}{h_{fg}}\left(\frac{1}{2k\rho_2 a_2} + \frac{1}{3\rho_1 a_1}\right)\right]h_1 - \frac{G_1^2\lambda_1^2}{4h_{fg}^2(\rho_1+\rho_2 kh_1)^2 h_1^2}} \quad (22)$$

We set the real part of equation (22) as

$$F(G_1,k) = \left(g - \frac{\sigma k^2}{\rho_2-\rho_1}\right)\frac{k^2(\rho_2-\rho_1)}{(\rho_1+\rho_2 kh_1)}\left[1 + \frac{G_1\lambda_1}{h_{fg}}\left(\frac{1}{2k\rho_2 a_2} + \frac{1}{3\rho_1 a_1}\right)\right]h_1 - \frac{G_1^2\lambda_1^2}{4h_{fg}^2(\rho_1+\rho_2 kh_1)^2 h_1^2} \quad (23)$$

When the real part of equation (22) is greater than zero, interface instability occurs, that is, the instability condition is:

$$F(G_1,k) \geq 0 \quad (24)$$

Equation (23) is what we will analyze later. Here the gravity g has been replaced by $g - \dfrac{\sigma k^2}{\rho_2-\rho_1}$ in order to combine the effect of surface tension. The term G_1/h_{fg} reflects the effects of heat and mass transfer on the stability and h_1 reflects the effects of finite fluid depth on the stability. From equation (23), it is obvious that, with the increase of temperature gradient, its influence on the stability increases too. Its effect is to decrease the perturbation growth rate and make instability more difficult to occur. In physical conception, this is also reasonable: when the temperature gradient is greater, stronger evaporation at the interface will be induced, which will then create a larger momentum at the interface. This kind of momentum will damp the interfacial wave, push the liquid-vapor interface away from the heater and the final result is to make the instability more difficult to take place.

When there is no temperature gradient and fluid depth is infinite, that is, $G_1/h_{fg} << 1$ and $h_1 \to \infty$, equation (24) can be simplified as

$$\left(g - \frac{\sigma k^2}{\rho_2-\rho_1}\right)\frac{k(\rho_2-\rho_1)}{\rho_2} \geq 0 \quad (25)$$

The critical Taylor wave-number and wavelength are

$$k_c = \sqrt{\frac{(\rho_2-\rho_1)g}{\sigma}} \quad (26)$$

$$l_c = 2\pi\sqrt{\frac{\sigma}{(\rho_2 - \rho_1)g}} \tag{27}$$

Which are the classical Rayleigh-Taylor expressions. When the wavelength satisfies equation (26), the wave growth rate will be greater than zero and the interface instability will occur. Differentiating equation (24), we can get the classical most dangerous wavelength

$$l_d = \sqrt{3}l_c = 2\sqrt{3}\pi\sqrt{\frac{\sigma}{(\rho_2 - \rho_1)g}} \tag{28}$$

Differentiating equation (23) and letting it equals zero, simultaneously neglecting the minor terms, we get the expression of most dangerous wavelength as:

$$3\sigma k^2 + \frac{\sigma\lambda_1}{h_{fg}\rho_2 a_2}G_1 k - g(\rho_2 - \rho_1) = 0 \tag{29}$$

The solution of equation (29) is (the minus solution was neglected)

$$k = \frac{1}{6\sigma}\sqrt{\left(\frac{\sigma\lambda_1 G_1}{h_{fg}\rho_2 a_2}\right)^2 + 12\sigma g(\rho_2 - \rho_1)} - \frac{\lambda_1 G_1}{6h_{fg}\rho_2 a_2} \tag{30}$$

The expression of most dangerous wavelength can be acquired using the relation of $l = 2\pi / k$. The results for water were pictured in *figure 3* and *figure 4*.

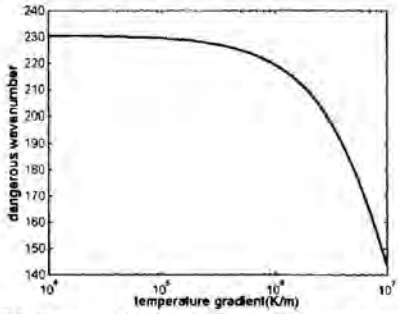

Figure 3 Influence of temperature gradient on wavenumber

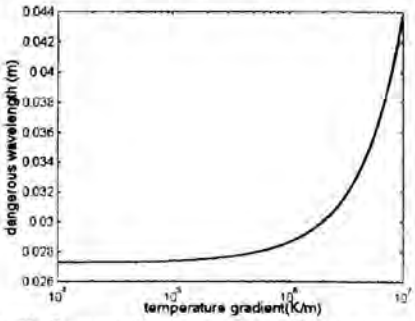

Figure 4 Influence of temperature gradient on wavelength

The results show that when the temperature gradient is less than 10^5, the heat and mass transfer effects can be neglected and the minimum wave number and most dangerous wavelength are nearly the same as the conventional results. But with the increase of temperature gradient, the effects of heat and mass transfer are becoming important. The most dangerous wavelength increases with the increase of temperature gradient.

RESULTS AND DISCUSSIONS

Temperature characteristics in transition boiling

The liquid methanol pool transition boiling experiments under atmosphere on metal plate wall with different material and thickness was conducted to investigate the wall temperature characteristics and dry patches behaviors [10].

Boiling experiments on aluminum wall of 6mm thickness and 11mm thickness, and 0.13C-12.95Cr-0.14Ni stainless steel of 11mm thickness were conducted to study the temperature difference at adjacent positions [10]. The temperatures at two adjacent points were obtained by data acquisition system, represented by x-axis and y-axis, respectively. The results for different plates are shown in *figures 5~7*. *Figure 5* shows the situation for aluminum of 11 mm thickness, *figure 6* shows the situation for aluminum of 6 mm thickness and *figure 7* shows the situation for stainless steel of 6 mm thickness. The deviation from diagonal reflects the non-uniformities in wall temperature. As shown in these figures, in transition boiling, the wall temperatures are extremely non-uniform. The wall properties and thickness greatly affect the temperature difference. The thinner the plate and the smaller the thermal conductivity, the larger the temperature difference will be. Relatively, the effect of thermal conductivity is more significant.

Effect of heat and mass transfer on stability of dry patch film will be doubtlessly evident in the transition boiling heat transfer. Corresponding dynamic performance induced by non-uniformity in wall temperature will greatly influence transition-boiling phenomena. Although only methanol was experimental investigated, one can expect that the non-uniformity in water boiling would be stronger. The following sections will focus on the analysis of heat and mass transfer effects on the dry patch stability; dry patches dynamic features resulted from thermal effects.

Hydrodynamic aspects, non-hydrodynamic aspects of transition boiling and dry patch interaction

In transition boiling, as stated in the introduction, there exist thin vapor films near the solid surface, which is enclosed by the above liquid. The assumption of equation (23) can be satisfied, so the results of *figure 3* and *figure 4* can be used in the following analyses.

The classical hydrodynamic theory on the transition between nucleate boiling to film boiling was based on traditional Rayleigh-Taylor instability, which is solely

concerned with the fluid's hydrodynamic characteristic. It is a global instability process and holds the assumptions of uniform wall temperature. Of course, if the temperature gradient in the vapor film is in the same order of 10^5 K/m, as shown in *figure 3* and *figure 4*, the effect of heat and mass transfer is small and can be neglected.

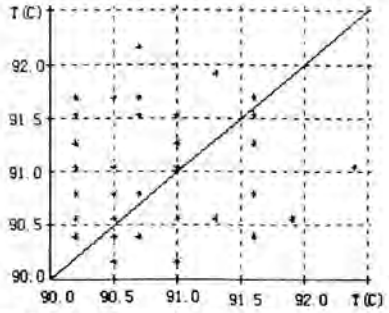

Figure 5 Temperature at two adjacent points (11mm thickness aluminum)

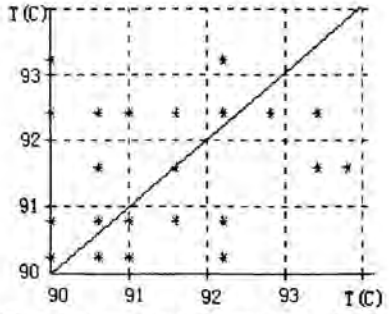

Figure 6 Temperature at two adjacent points (6mm thickness aluminum)

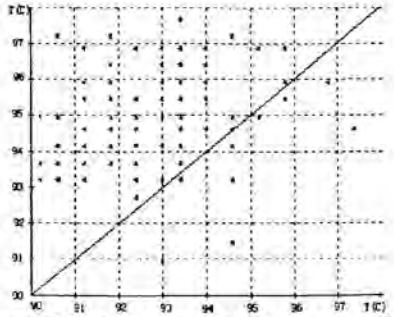

Figure 7 Temperature at two adjacent points (11mm thickness steel)

However, in the case of dry patch, heat and mass transfer influence becomes important due to its thinner depth and larger superheat [11]. Besides, in the transition boiling, the ratio of liquid and vapor will decrease. The effects of heat and mass transfer on interface stability must be considered. Reference [5] pointed that the wall temperature that can produce a dry patch may reach the Leidenfrost temperature, about 180°C for water. With the growth of dry patch, the center wall temperature in the dry patch will still rise. Indeed, dry patch is a very thin vapor film formed on the wall. Due to it large temperature difference and very thin vapor film depth, the temperature gradient G_1 is very large. From the *figure 3* and *figure 4*, when the temperature gradient is larger than 10^6, the effects of heat and mass transfer become salient and must be included in the modeling. For water boiling, $G_1 = 2\times10^6 K/m$, which is a common case in one large dry patch, the most dangerous wavelength is about 0.0302 *mm* and is 11% higher than the classical results. Indeed, in the practical conditions, the temperature gradient may often be greater than this value.

The effect of heat and mass transfer at interface is to cause the instability more difficult to occur, which means that the dry patch will become more stable when heat and mass influence is considered. The bigger the dry patch, the higher the temperature gradient will be, and more stable it will be too. As a result, for transition boiling process in which there simultaneously exist many dry patches with different sizes, the small dry patch will often be rewetted by the washing liquid and the more stable big dry patch will often coalesce and spread through the wall, then control and dominate other small dry patches, and finally cause the film boiling to locally occur in advance. In fact, it is a kind of cooperative phenomenon and self-organized behavior generated by interactions among dry patches. Restated, the vivid picture may be like this: in transition boiling, dry patches will randomly appear on the heating surface. As wall temperature increases, the number and size of the dry patches increase. Simultaneously, the liquid will constantly wash across the surface and rewet the dry patches. As the time- and area-average wall temperature increases to such a larger value that some dry patches with higher temperature and larger size will no longer be re-wetted by liquid, the dry patch will enlarge, coalesce, spread along the wall and dominate the whole boiling process, then finally induce the local occurrence of stable film boiling.

By adding the effects of heat and mass transfer on the Rayleigh –Taylor stability on the basis of classical hydrodynamic theory, we reach the idea that the transition between nucleate boiling and film boiling has the duality character, which was controlled by the solid surface temperature, that is, boiling system will exhibit hydrodynamic performance when wall temperature levels of dry patches are not very high, while when wall temperature levels of dry patches are very high, it tends to exhibit non-hydrodynamic performance (self-organized performance). Therefore, these two seemly different opinions can be explained in a unifying fashion. For transition boiling, the wall temperature levels of

dry patches usually depend on the uniformity in wall temperature, which is related to the many factors such as surface wettability, wall conductivity and thickness. With reduced wall thickness, thermal conductivity and surface wet ability the uniformity in wall temperature will increase, which results in more salient self-organizing phenomena. This corresponds to experimental findings that non-hydrodynamic effect will more obvious with reduced wall thickness and thermal conductivity [12]

Relationship with experimental observations

Regardless of the incompleteness of the conceptual approach discussed herein, we could still note the predominant role of the level and uniformity of surface temperature distributions on the interactions between dry patches. The uniformity in temperature is related to the conductivity and thickness of the wall. With reduced wall thickness and thermal conductivity the wall temperature distribution would become less uniform, which yields more apparent self-organizing behavior [13]. This corresponds to the experimental findings that burnout or rewetting would more readily occur on the heaters of reduced wall thickness and/or thermal conductivity [14].

Once self-organizing behavior prevails the process, it is more likely to be realized for the gradual transition between nucleate boiling to film boiling. The "jump" dynamics for the occurrence of transition would be depressed. On the other hand, once hydrodynamic behavior prevails the process, the transition between nucleate boiling and film boiling would tend to behave like a sudden "jump" rather than a gradual propagation dynamics.

In addition, heating modes also affect the "jump" dynamics [14]. A heat-flux controlled boiling test was commonly accomplished by allowing the overall surface temperature of the heater to rise gradually to induce film boiling (the heating stage), and then to gradually reduce the temperature to recede back to nucleate boiling mode. Therefore, self-organized condition can be easily satisfied and gradual transition would be realized. On the other hand, for temperature-controlled tests, sudden "jump" is usually expected.

It is logically but not conclusively held that the contradictions on the occurrence of "jump" as stated in the introduction can be smoothed in the present theoretical framework.

CONCLUSIONS

Analysis of Rayleigh-Taylor stability incorporating the effect of heat and mass transfer was performed and the dispersion relation for the interfacial wave was acquired. The results show that the effect of heat and mass transfer at the interface of dry patch will increase the value of most dangerous wavelength and enhance the interfacial stability. The occurrence of dry patch will create big temperature gradient in the vapor film and cause transition between nucleate boiling and film boiling to locally occur in advance, which is a kind of self-organized non-hydrodynamic process. The transition between nucleate boiling and film boiling has dual characters: hydrodynamic and non-hydrodynamic performance. It exhibits the hydrodynamic characters when the wall temperature distribution is relatively uniform, while it will show non-hydrodynamic characters for relatively non-uniform wall temperature. The present analyses can well explain the available experimental observations.

ACKNOWLEDGMENT

The project is currently supported by Japan Society for the Promotion of Science.

REFERENCE

[1] Dhir V. K., Boiling heat transfer, Annu. Rev. Fluid Mech., 30 (1998) 365-401.

[2] Berenson P.J., Experiments on pool boiling heat transfer, Int. J. Heat Mass Transfer, 5 (1962) 985-989.

[3] Pan C., Huang J.Y., Lin T.L., The mechanism of heat transfer in transition boiling, Int. J. Heat Mass Transfer. 32 (1989) 1337-1349.

[4] Witte L.C., Lienhard J.H., On the existence of two transition boiling curves, Int. J. Heat Mass Transfer, 25(1982) 771-779.

[5] Ramilison J.M., Lienhard J.H., Transition boiling heat transfer and film transition regime, ASME J. Heat Transfer, 109 (1987) 740-757.

[6] Bui T.D., Dhir V.K., Transition boiling heat transfer on a vertical surface, ASME J. Heat Transfer, 107 (1985) 756-763.

[7] Dhuga D. S., Winterton R. H. S., Measurement of surface contact in transition boiling, Int. J. Heat Mass Transfer, 28 (1985) 1869-1880.

[8] Shoji M., Boiling chaos and modeling, in: Lee D. S., (ed.), Proceeding of International Heat Transfer Conference-11st (Vol.1 Invited Keynotes), Taylor and Francis, London, 1998, pp.3-21.

[9] Hsieh D. Y., Heat and mass transfer on Rayleigh-Taylor instability, J. Basic Engineering, 1 (1973) 156-163.

[10] Chai L. H., Binary mixtures boiling under microgravity and nonlinear features of boiling, Ph. D. thesis, Tsinghua University, China, 1999.

[11] Gaertner R. F., Photographic study of nucleate pool boiling on a horizontal surface, ASME J. Heat Transfer, 87 (1965) 17-29.

[12] Tachibana F., Akiyama, M., Kawamura, H., Non-hydrodynamic aspects of pool boiling burnout, J. Nucl. Tech., 4 (1967) 121-126.

[13] Lee D. J., Stochastic simulation of non-hydrodynamic burnout on a two-dimensional matrix, Int. Comm. Heat Mass Transfer, 25 (1998) 831-841.

[14] Rajab, I., Winterton, R.H.S., The two transition boiling curves and solid-liquid contact on a horizontal surface, Int. J. Heat and Fluid Flow, 11(1990) 149-153.

Hefa2002
1st International Conference on Heat Transfer, Fluid Mechanics, and Thermodynamics
8-10 April 2002, Kruger Park, South Africa
LJ2

HEAT TRANSFER OF GAS MIXTURE WITH VAPOR CONDENSATION IN A VERTICAL TUBE

Jia Li
Beijing Institute of Civil Engineering and Architecture, Beijing 100044, China

Peng Xiao Feng
Department of Thermal Engineering, Tsinghua University, Beijing 100084, China

ABSTRACT

The convection and condensation heat transfer of vapor-gas mixtures in a vertical tube were studied theoretically and experimentally. This paper discusses the effects of the condensation of a small amount of water vapor(8%-20%)on heat transfer in a vertical tube. Comparisons of the theoretical solutions obtained through modified film model with some experimental results are in good agreement. The research shows that the condensation heat transfer of small amount of water vapor and single-phase convection heat transfer in the vapor-gas mixtures have same order of magnitude. And these two styles of heat transfer could not be neglected.

INTRODUCTION

The condensation of vapor inside a vertical tube is one of the important problems in the chemical and power industry and has been extensively studied [1-3]. The pioneering work of Nusselt had been modified recently in many aspects [4]. All these works were concerned with condensation of pure saturated vapor. However, in practical operations small amount of non-condensable gas may exist in working vapors. It was well recognized that existence of non-condensable gas in vapors could greatly reduce condensation heat transfer and deteriorate the performance of devices. Many investigations were conducted on this topic [5].

But there is some amount of water vapor in some mixtures, whose dew-point temperature is at the range of normal temperature and which would condense under the suitable cooling temperature, for example wet flue gas. Condensing boilers were designed on the basis of this characteristic. For these mixtures in which mass fraction of water vapor is about 8%-20%, it is very important to predict effectively the proportion of the sensible and latent heat contribution to total heat transfer in engineering application. Condensation of vapor-gas mixtures dfifer s from condensation of pure saturated vapor. Because water vapor mass fraction is very small, the effect of condensation of vapor on bulk flow is small and the role of non-condensable gas is dominant. Thus it may be thought that mass flux of bulk flow is kept constant. The above- mentioned characteristics should be considered in analysis of heat transfer of mixtures containing vapor.

In this paper, heat transfer of vapor-gas mixtures containing small amount of water vapor was analyzed by means of modified film model and condensing theory of Nusselt. Convection and condensation heat transfer of wet flue gas in a vertical tube were studied experimentally. The theoretical solutions agree well with experimental data.

NOMENCLATURE

c: specific heat capacity J/(kg.K)
d: diameter m
k: thermal conductivity w/(m.k)
u: velocity m/s
g: gravitational acceleration m/s^2
p: pressure pa
f: friction coefficient
m: mass flux to wall $kg/(m^2.s)$
M: condensing mass flux kg/s
y: coordinate in direction of gas flow m
h: heat transfer coefficient $w/(m^2.k)$
t: temperature ℃
δ: thickness of condensate film m
η: dynamic viscosity Pa. s
τ: shear stress N/m^2
ρ: density kg/m^3

Subscripts

i: interfacial
l: liquid

PHYSICAL AND MATHMWTICAL MODEL

Fig.1 illustrate a physical model schematically. Mixtures entered vertical tube at the rate of u_b and were cooled by water flowing counter-currently in the cooling jacket. When the temperature of cold water is lower than the dew-point temperature of mixtures in the vertical tube, vapor of mixtures could condense and form a layer of liquid film, whose thickness was δ. There are some assumptions as follow:

(1) The filmwise condensation kept annular. Mixtures Flow at the center region of tube. The surface of liquid film has no wave.

(2) Non-condensable gas played a dominant role in the mixtures. Condensate is small and the condensation film would be very thin. The effect of con on the bulk flow on the bulk flow may be negligible.

(2) Condensate flow passed down through inner tube by gravity and interfacial sheer stress. The velocity of wall surface is zero.

(3) The single-phase heat transfer of mixtures couldn't be neglected.

(4) The wall temperature of was kept constant.

(5) The wall temperature of was kept constant.

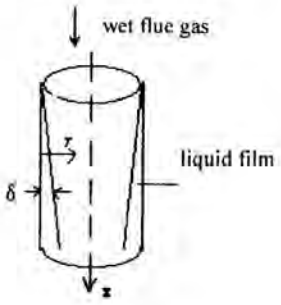

Fig.1 Physical model

Equation of motion of condensate film

According to Nusselt's assumptions, the equation of motion in the condensate layer is given by

$$\eta_l \frac{\partial^2 u_l}{\partial y^2} = \frac{dp}{dx} - \rho_l g \qquad (1)$$

Assuming the no slip condition at the tube wall surface and a velocity gradient at the gas-liquid interface, integrating Eq.(1), yields

$$u_l = \frac{1}{\eta_l}\left(\frac{dp}{dx} - \rho_l g\right)\left(\frac{1}{2}y^2 - \delta y\right) + \frac{\tau_i}{\mu_l} y \qquad (2)$$

The interface shear stress in the flow directions related to th e axial pressure gradient by

$$-\frac{dp}{dx} = \frac{4\tau_i}{d} + \frac{d(\rho_k u_k^2)}{dx} \qquad (3)$$

The interfacial shear stress is calculated based on the velocity of bulk flow

$$\tau_i = \frac{1}{2}\rho u^2 f \qquad (4)$$

Where f is the gas phase friction factor at the liquid-gas interface.

Owing to the dominant role of non-condensable gas, a small amount of vapor in mixtures at the liquid-gas interface could condense. So it may be thought that the flux of bulk gas kept basically constant. Item 2 on the right-hand of Eq.(3) may be neglected, thus Eq.(2) may be given by

$$u_l = \frac{1}{\eta_l}\left(-\frac{4\tau_i}{d} - \rho_l g\right)\left(\frac{1}{2}y^2 - \delta y\right) + \frac{\tau_i}{\mu_l} y \qquad (5)$$

The liquid flow rate is obtained by integrating the liquid velocity field over the liquid cross-sectional area. The condensing liquid flow rate would be obtained as

$$M = \rho_l \pi d \int u_l dy \qquad (6)$$

Equation of energy of mixtures

Regarding of single-phase convection heat transfer of bulk flow and condensation film, the energy balance should be that the decrease of the axial thermal enthalpy of bulk flow is equal to the single-phase heat transfer of bulk flow and condensation film. Thus

$$\frac{d}{4}\frac{dt_b}{dx} c_p \rho u - m c_{p,} (t_b - t_i) = -h^*_g (t_b - t_i) \qquad (7)$$

Where the temperature of bulk flow t_b is similar to the average temperature of bulk flow, considering the effect of the induced velocity.

For the condensation of pure saturated vapor, there is no sensible heat transfer. So it is unnecessary for Eq.(7). If pure vapor is in the superheated situation, the sensible heat was modified by latent heat of condensation and the process of whole heat transfer may be described through Nusselt's theory. But for the mixtures containing condensable gas, its sensible heat couldn't be neglected. When the amount of condensable gas of mixtures is small, for example wet flue gas, there is small amount condensate at the interface and its effect on bulk flow is negligible. Usually item 2 on the left-hand of Eq.(7) may be neglected. Thus Eq.(7) was become simple obviously and Eq.(8) can be obtained

$$\frac{dt_b}{dx} c_p \rho u = -\frac{4}{d} h^*_g (t_b - t_i) \qquad (8)$$

But for the condensation of vapor containing small amount of non-condensable gas, this item could be neglected. The energy equation at the interface was written as

$$\frac{k}{\delta_i}(t_i - t_\infty) = h_g^*(t_b - t_i) + mL \qquad (9)$$

Where film thickness δ_i, interface temperature t_i and mass flux m were unknowns.

EXPERIMENTAL REAEARCH

Experimental system of the heat transfer between wet flue gas and water consists of seven parts as shown in Fig. 2. In order to obtaining different mass fraction of water vapor, the methods are prevail through the variations of the excess air coefficients and the mixture of water vapor from steam humidifier and flue gas. The system of cooling water was connected with pump 4 and water tank 3, forming a closed circulation. Refrigerator 5 kept temperatures of cooling water in water tank constant.

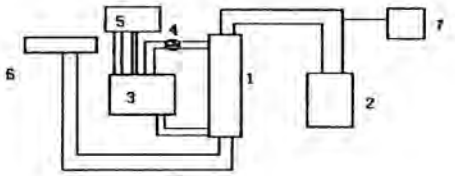

Fig. 2 Diagrammatic sketch of the test system

1 test section 2 boiler 3 water tank 4 pump
5 refrigerator 6 fan 7 steam humidifier

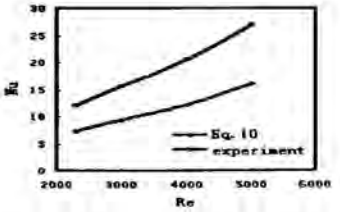

Fig.3 Comparison of experimental results and predicted value

Single-phase convection heat transfer

In this experiment, the Reynolds number of wet flue gas was in the transition region. So the gas convection heat transfer coefficient in a vertical tube was given by Von Volker Gnielinski[6].

$$Nu = 0.0214(\mathrm{Re}^{0.8} - 100)\,\mathrm{Pr}^{0.4}[1 + (\frac{d}{L})^{2/3}](\frac{T_f}{T_\infty})^{0.45} \qquad (10)$$

The correlation of convection heat transfer obtained by experimental data could be expressed in the following form as

$$Nu = 0.0358(\mathrm{Re}^{0.8} - 100)\,\mathrm{Pr}^{0.4}[1 + (\frac{d}{L})^{2/3}](\frac{T_f}{T_\infty})^{0.45} \qquad (11)$$

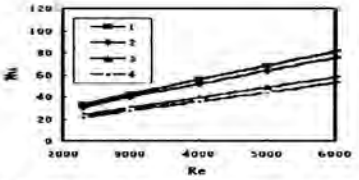

Fig.4 Experimental results at different wall temperatures (1:37.4℃, 2:38.4℃, 3:43.8℃, 4:49.2℃)

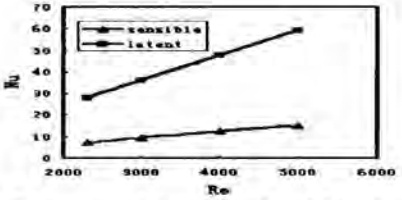

Fig.5 The comparison between sensible and latent heat transfer (t_∞=37.4℃)

Comparison of these two equations, it can be found that the coefficient of Eq.(11) is higher than that of the Eq.(10). There are two reasons. First, actual dew-point temperature of wet flue gas is higher than that of the vapor-air mixture with the same vapor concentration because of the existence of acid gas in the wet flue gas. Second, when the wall temperature is higher than the dew-point temperature of the vapor-air mixture, the wet flue gas with same vapor concentration would condense and intensify heat transfer. This would result in some increase in Nu in Eq.(11). This experimental phenomenon and fact show that the condensation of wet flue gas should further be investigated. Fig.3 illustrates the comparison between experimental results and the predictions of Eq.(10). Although there were some discrepancies, these were not substantial deviations according to the results calculation by Eq.(10).

Convection and condensation heat transfer of wet flue gas

Fig.4 illustrates the Nu-Re relation at different wall temperature. Obviously, the wall temperature is an important parameter that alters the condensation contribution to the total heat transfer in a vertical tube.

The proportion of the sensible and latent heat contribution to the total heat transfer is related to the wall temperature obviously. The correlations of convection heat transfer in form of Eq.(10) under four different wall temperature were given separately.

t_∞=37.4℃时，

$$Nu = 0.0947(\mathrm{Re}^{0.8} - 100)\,\mathrm{Pr}^{0.4}[(1+(\frac{d}{L})^{2/3}](\frac{T_f}{T_w})^{0.45} \quad (12)$$

t_w=38.4℃时，

$$Nu = 0.0884(\mathrm{Re}^{0.8} - 100)\,\mathrm{Pr}^{0.4}[(1+(\frac{d}{L})^{2/3}](\frac{T_f}{T_w})^{0.45} \quad (13)$$

t_w=43.8℃时，

$$Nu = 0.067(\mathrm{Re}^{0.8} - 100)\,\mathrm{Pr}^{0.4}[(1+(\frac{d}{L})^{2/3}](\frac{T_f}{T_w})^{0.45} \quad (14)$$

t_w=49.2℃时，

$$Nu = 0.0612(\mathrm{Re}^{0.8} - 100)\,\mathrm{Pr}^{0.4}[(1+(\frac{d}{L})^{2/3}](\frac{T_f}{T_w})^{0.45} \quad (15)$$

It can be concluded from Eq.(12) to Eq.(15) that the coefficient of equations depend on wall temperatures under the same concentration of water vapor. In fact condensation heat transfer was converted into convection heat transfer. The experimental results shoe that in range of present tests the order of magnitude of condensation and convection is same and any of these two styles couldn't be neglected.

The role of condensation must be considered carefully, whose effect on total heat transfer depends on the wall temperature. This is the characteristic of heat transfer of mixtures containing small amount of water vapor. The regressive curve of experimental results was given in Fig.5.

Not only the wall temperature but also vapor mass fraction of mixture affects condensation heat transfer. Moreover the latter could alter the mechanism of heat transfer. When the mass fraction of vapor is lower, for example 2%-3%, it can be thought that condensation heat transfer intensified convection heat transfer. Fuji. et al had discussed in great detail. When the mass fraction of vapor is higher, condensation heat transfer would intensify step by step. And when the mass fraction of vapor had gone up certainty degree, condensation heat transfer dominates the transport process and the single-phase convection heat transfer could be neglected. Fig.6 gives the comparison of Nu-Cg at the same Re. The experimental results show that the concentration of vapor in wet flue gas has the effect on heat transfer. Fig.7 illustrates the comparison between latent and sensible heat transfer component in total heat transfer. The variation of Nu in Fig.7 illustrates that the proportion of condensation heat transfer in total heat transfer increased rapidly and the role of convection heat transfer becomes smaller and smaller as vapor mass fraction increases. It can be concluded that the order of magnitude of condensation heat transfer was larger one or more than that of convection heat transfer. So convection heat transfer could be neglected. There is a conservative estimate that the critical mass fraction of vapor is defined 30% when convection heat transfer could be neglected. Of course the wall temperature must be lower than the dew-point temperature of wet flue gas, otherwise there is no condensation heat transfer. This is just the complex of heat transfer of mixtures, that is, the wall temperature and mass fraction of vapor influence condensation heat transfer simultaneously.

CONCLUSIONS

1. When mass fraction of vapor in wet flue gas is about 8%-13%, its heat transfer differs from single-phase convection heat transfer of humid air and condensation heat transfer of vapor containing small amount of non-condensable gas.
2. Condensation and convection heat transfer of wet flue gas was a complex process. It is the result of condensation and convection together. The influencing factors of condensation heat transfer of wet flue gas are vapor concentration of bulk gas and wall temperature. When wet flue gas was in a superheated situation, the influence of superheat temperature of wet flue gas on condensation is small.
3. The contribution of latent and sensible heat to the total heat transfer with the same vapor mass fraction is different. When vapor mass fraction excesses 30%, convection heat transfer could be neglected on condition that the wall temperature must be lower than the dew-point temperature of wet flue gas.

ACKNOWLEDGMENTS

This work was supported by science and technology emphasis item of Ministry of Education. (Contact No.00129) and National Science Fund Committee of Beijing (No. 3012006).

REFERENCES

1. Nusselt W. Die oberflachenkondensation des wasserdampfies, *Z Ver. Dt. Ing.* 60, 541-546 (1916).

2. Jacob M. Heat transferin evaporation and condensation-II. *Mech. Engng* 58, 729-740 (1936).

3. Carpenter F. and Colburn A.P. The effect of vapor velocity on condensation inside tubes, *Proceeding of a General Discussion of Heat Transfer, IME/ASME* (1951).

4. Dobran F. and Thorsen R.S. Forced flow laminar filmwise condensation of a pure saturated vapor in a vertical tube, Int. J. Heat Mass Transfer 23, pp161-177(1980)

5. Cossmann R. Odenthal H. P. and Renz U. Heat and mass transfer during partial condensation in a turbulent pipe flow, *Proc. 7th Int. Heat Transfer Conf.*, 5, 53-58 (1982).

6. Gnielinski V. New equations for heat and mass transfer in turbulent pipe and channel flow, Int. Chem. Eng. 16, pp161-173(1976)

HEFAT 2002
1st International Conference on Heat Transfer, Fluid Mechanics, and Thermodynamics
8-10 April 2002, Kruger Park, South Africa
ZC1

PRESSURE DROP AND HEAT TRANSFER MEASUREMENT ON AMMONIA FORCED CONVECTION BOILING IN VERTICAL TUBES

C. Zamfirescu*, C.H.M. Machielsen**, M. Nenu***
*Assoc.Professor – corresponding author; **Assoc.Professor; ***Assistant Professor
* and *** Department of Thermodynamics and Heat Transfer, Technical University of Civil Engineering, 66, Pache Protopopescu Blvd., Bucharest 2, ZIP 73232, Romania; email: calinzam@yahoo.com
** Delft University of Technology Mekelweg, 2628 CD, Delft, The Netherlands; email: c.h.m.machielsen@wbmt.tudelft.nl

ABSTRACT

The majority of the general heat transfer correlations in forced convection boiling were established based on experimental data banks for other fluids than ammonia. This is explained by the fact that the number of experimental researches for ammonia forced convection boiling published in the open literature, is extremely small in comparison with the case of other fluids. For example, in VDI Wärme Atlas, [1] it is provided a comprehensive bibliographic reference on forced convection boiling experimental researches, which includes 34 publications for water, 39 for halocarbons, 6 for hydrocarbons, and 15 for cryogenic fluids; only two experimental researches are mentioned for ammonia [2], [3].

In this paper it is presented an experimental study with ammonia in vertical upward pipe flow, carried out in a thermosyphon recirculation loop, at low pressures, heat flux and mass velocity from 4 to 136 kg/sm^2.

Experiments have been run in order to develop a data bank referring to the heat transfer of ammonia inside an electrically heated tube. The local heat transfer coefficient for boiling ammonia was measured in 10 different locations along the tube, the pressure drop was measured and the flowing regime was visualized in 3 locations, using segments of glass tube. Some correlations for heat transfer and pressure drop were evaluated against experimental data and a parametric study was made. A comparison between theoretical and experimental results indicated the Steiner-Taborek [4] and Gungor-Winterton [5] correlation makes the best predictions for ammonia's evaporation local heat transfer coefficient.

Concerning the pressure drop the correlation of Pierre [6], gave the best predictions.

Key words: ammonia, experimental work, convective boiling, upward pipe flow, correlations.

INTRODUCTION

Despite that ammonia has been used for more than a century as a refrigerant, forced convection boiling of ammonia in vertical tubes was practically not experimentally studied. However, the forced convection boiling of ammonia in vertical tubes is important in applications like, freezing the soil in mines works and in civil engineering, ice generators, or other special applications where the horizontal space is limited. Experimental data on forced convection boiling of ammonia in vertical tube may be important also as a first approximation for the local heat transfer in heat exchangers working as evaporators (which for the case of ammonia are usually placed with the channels in a vertical position providing an upward two-phase flow).

Cleis [7] conducted one of the first researches carried out for ammonia in a short vertical tube. He determined the local heat transfer coefficients in five locations along a vertical tube, but analyzed only the averaged heat transfer coefficient.

Malek and Colin [8] studied the saturated state forced convection boiling in long pipes (L=10m) and established a correlation for the global heat transfer coefficient.

Barthau [2] conducted a comprehensive experimental research for forced convection boiling of ammonia in a vertical pipe (0,030 m i.d.) at extremely high pressures, mass and heat fluxes (34-108bar, 500-1000 kg/sm2, 53-1322 kW/m2). Steiner and Taborek [4] included these data when developing their general correlation for forced convection boiling heat transfer coefficient.

Another known correlation developed based on ammonia boiling experimental data are the Shah's correlation [9], but in this case experimental data used was for horizontal two-phase flow of ammonia, and consequently the extension of Shah correlation to the prediction of heat transfer coefficients at forced convection boiling in vertical tube must by checked.

Ohadi showed in a recent critical review, [10] that no formal data base is currently available on ammonia heat transfer. This is the reason why the big majority of the known correlations for heat transfer in forced convection boiling was not experimentally validated for the case of ammonia flow boiling in tubes (ex: Gungor-Winterton [5], Kandlikar [11]).

The authors of the present paper carried-out an experimental research on heat transfer and pressure drop in forced convection boiling of ammonia in a vertical tube, in the range of subcooled boiling and first stages of saturation boiling.

NOMENCLATURE

D = diameter [m]
i = enthalpy [J/kg]
h = heat transfer coefficient [W/m^{2}K]
k = thermal conductivity [W/mK]
$\dot{m}$ = mass velocity [kg/m^{2}s]
$\dot{M}$ = mass flow [kg/s]
$\dot{q}$ = heat flux [W/m^2]
R = radius [m]
T = temperature [K]
x = quality [-]
X = Lockhart-Martinelli parameter [-]
z = vertical coordinate [m]

Greek symbols

σ = surface tension [N/m]
Φ = two-phase flow multiplier

Subscripts and Superscripts

acc = accelerative
w = wall
o = outside
i = inside
TOT = total
l = liquid phase
g = vapor phase
b = bulk flow
meas = measured
ONB = Onset of Nucleate Boiling point
LO = liquid only.
th = thermodynamic
cr = critical (for bubble radius)
TP = two-phase

EXPERIMENTAL RESEARCH

Figure 1 illustrates the experimental set-up. The forced convection boiling is produced inside the vertical pipe by electrical heating means, which is using a direct current electrical coil. The ammonia flow rate – gravitationally generated (thermosiphon effect) – was measured using an ultrasonic flowmeter.

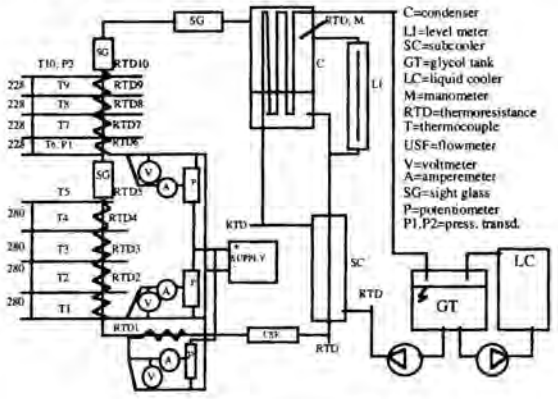

Fig.1 The experimental set-up

The test section consisted of two vertical tubes (0.032m i.d.) equipped with temperature and pressure transducers.

The local heat transfer coefficient was calculated in 10 locations along the tube based on wall temperature (RTD Pt100) and bulk flow temperature (type J thermocouples) measurements. The boiling pressure (and the corresponding saturation temperature) was measured by means of electronic pressure transducers. The boiling heat flux was determined by electrical measurements.

The flow regime was observed in three cylindrical glass tube segments. In our experiment only bubble flow and slug two-phase flow regimes were obtained.

The experimental set-up containing an amount of 47.5 kg NH_3 of 99,6% purity was thermally insulated.

The electrical signals from all the transducers used were measured by a 12 binary digits Keithley-Metrabyte data acquisition system.

The range of variation for the parameters controlling the experiments was: T_{lg}=-5...+10°C; x_g=0.01...51%, $\dot{m}$ =4...136 kg/sm^2; $\dot{q}$ =540...6500W/m^2.

The sequence of acquired data was numerically filtered following the procedure described by Taler [12]. The data sequences corresponding to the steady-state regime were then selected on the basis of the following criteria: accepted temperature variation ±0,5°C, accepted pressure variation ±0,01 bar, and ammonia flow variation below 5% by value. The steady-state periods were stated valid provided that their duration exceeded 20 minutes.

For every of the ten measure stations an equal portion of the tube length, Δz was attributed. The main steps in data processing are subsequently presented:

- The temperature of the inside wall:

$$T_{wi} = T_{wo} - \dot{q} D_i \ln\left(D_o/D_i\right)/2k_w \tag{1}$$

- The two-phase flow enthalpy for the current segment:

$$i_{TOT(z)} = i_{(z-\Delta z)} + \frac{\pi D_i \dot{q}_{(z)} \Delta z}{M} \tag{2}$$

- The thermodynamic quality on the current segment:

$$x_{th(z)} = \frac{i_{TOT(z)} - i_{l(T_{lg})}}{i_{g(T_{lg})} - i_{l(T_{lg})}} \tag{3}$$

- Check for the onset of nucleate boiling point (ONB) using the relation recommended by Steiner and Taborek, [4]. For the critical bubble radius, Steiner and Taborek indicated the for tubes in carbon steel frequently used in practice (our case), a good approximation for the critical bubble radius in equation (4) may be $R_{cr} = 1\ \mu m$.

$$\dot{q}_{ONB} = \frac{2\sigma T_{lg} h_{LO}}{R_{cr} \rho_g \left(i_g - i_l\right)} \tag{4}$$

- Computation of the vapor quality using of Levi's [11] correlation:

$$x_g = x_{th} - x_{thONB} \exp\left(x_{th}/x_{thONB} - 1\right) \tag{5}$$

- Estimation of the void fraction with the Zuber-Findlay correlation [14], in which the phase distribution parameter is given by the relation of Ishii [15]:

$$\varepsilon = x \Big/ \left\{ Co\left[x + (1-x)\frac{\rho_l}{\rho_g} \right] + 1.53 \left[\frac{\sigma g \left(\rho_l - \rho_g\right)}{\rho_l^2} \right]^{1/4} \right\} \tag{6}$$

$$Co = 1.2 - 0.2\,\rho_g/\rho_l \tag{7}$$

- Computation of frictional pressure drop gradient based on the total pressure drop (measured) and other two computed components (gravitational and accelerative):

$$\left(\frac{\Delta p}{\Delta z}\right)_f = \left(\frac{\Delta p}{\Delta z}\right)_{measured} - \left(\frac{\Delta p}{\Delta z}\right)_g - \left(\frac{\Delta p}{\Delta z}\right)_{acc} \quad (6)$$

- Computation of the two-phase flow multiplier, based on above estimated frictional pressure drop and the liquid only pressure drop:

$$\Phi_{LO}^2 = \left(\frac{\Delta p}{\Delta z}\right)_{TP} \Big/ \left(\frac{\Delta p}{\Delta z}\right)_{LO} \quad (10)$$

- Computation of the local heat transfer coefficient:

$$h(z) = \dot{q}_{(z)} \Big/ \left[T_{wi(z)} - T_{b(z)}\right] \quad (7)$$

All ten thermocouples have been calibrated using a high precision RTD Pt100. The experimental uncertainties fell within an acceptable range: for thermocouples and RTD 0,1°C; for pressure 0,6% by value, for ammonia flow 3% by value, for the electrical current 0,05A, for the voltage 0,05V, for the electrical power 2% by value, for the heat transfer coefficient 10% by value.

RESULTS AND DISCUSSIONS

The main purpose of this experimental research consisted in developing a data bank for pressure drop and heat transfer coefficient further to be used to checking the applicability of some available general correlations.

A detailed description of this data bank, which consists of 136 determinations for the local heat transfer coefficient in forced convection boiling, is given by Zamfirescu, [16].

Concerning the two-phase flow multiplier for pressure drop prediction, two correlations, namely Chisholm [6] and Pierre [6] were evaluated against the present experimental results. We may note that the Chisholm's correlation is in fact an analytical formulation of the well known Lockhart-Martinelli correlation for two-phase flow multiplier of pressure drop [18]. Figure *2* reveals that, for our experimental conditions the Pierre correlation predicted better.

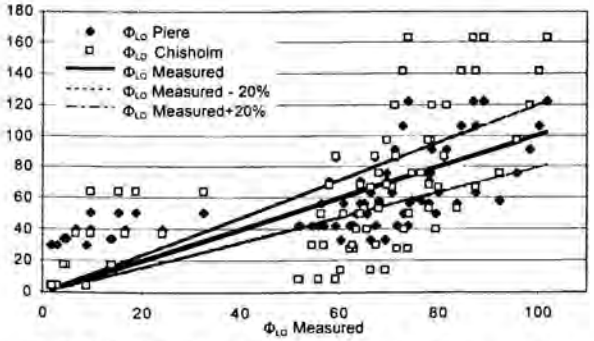

Fig.2. Evaluation of the correlations for two-phase flow pressure drop multiplier, Φ_{LO}

One important quantity which influences the two-phase flow multiplier is the Lockhart-Martinelli parameter. In *fig.*3 a parametric study of this influence is drawn for a fixed mass velocity of 45 kg/sm^2. The trend observed corresponds to the known variation for other refrigerants (like water).

An evaluation of three known forced convection boiling general correlations for the heat transfer coefficient is illustrated in *fig.4*.

The predicted values were compared to the experimentally determined ones.

For a ±20% bandwidth the Shah correlation predicted 52% of the data, the Steiner-Taborek correlation 73%, the Gungor-Winterton correlation 85%

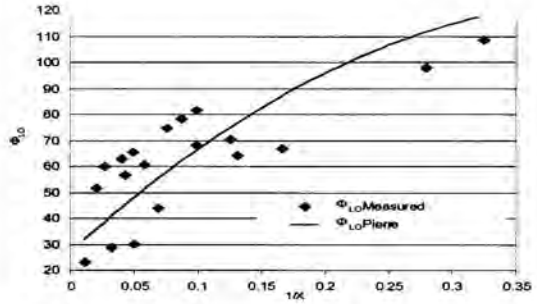

Fig.3. The influence of Lockhart-Martinelli (X) on the two-phase flow multiplier: Φ_{LO} for G = 45 kg/m^{2}s

It should be noted that Steiner and Taborek, [1] provided an evaluation of their correlation and of the Gungor-Winterton's one against the experimental data of Barthau, [7]. For the same bandwidth of ±20% the Steiner-Taborek correlation predicted for 79% of data. However, the Gungor-Winterton's one made all predictions within a 30% error.

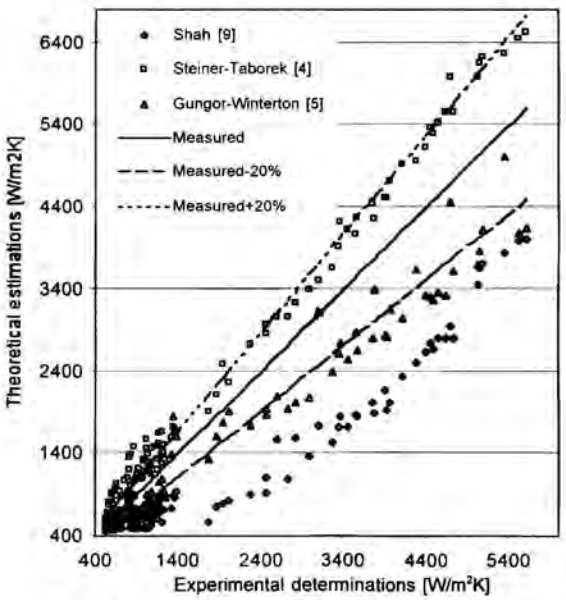

Fig.4 The evaluation of the correlations for heat transfer coefficient at forced convection boiling against experimental data

A possible explanation for this result, which is different from the present paper's result, may lay in the completely different operating conditions of Barthau's experiment that is not relevant for the refrigeration and air conditioning field.

The influence of the thermodynamic quality on the heat transfer coefficient is shown in *fig.5*. It may be seen that for more advanced

stages of the boiling process, the Steiner-Taborek's correlation made the best prediction, with respect to the experimental determinations.

The influence of the heat flux on heat transfer coefficient for different mass velocities is presented in *fig.6*.

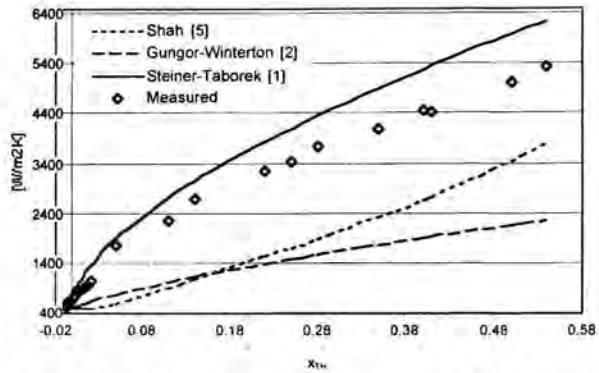

Fig.5. The influence of thermodynamic quality at 0°C on the boiling heat transfer coefficient for 5200 W/m^2, 50 kg/sm^2

For small heat fluxes, the forced convection mechanism is the dominant one. This is explained by the big influence of the mass velocity. At big heat fluxes, the mass velocity has a small influence on heat transfer, while the nucleation is more important.

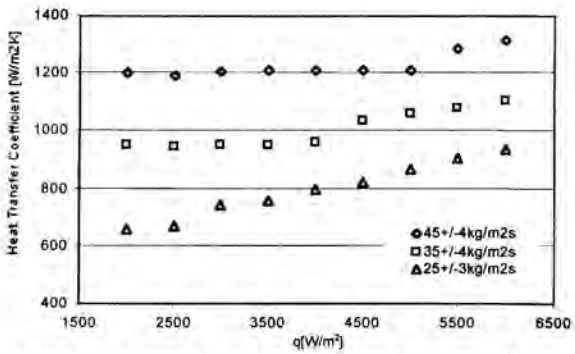

Fig.6. The influence of the heat flux on the heat transfer coefficient for x_{th}= 2.5%

CONCLUSIONS

For the range of operating parameters of this experimental work, the Pierre correlation for pressure drop made better prediction than Chisholm correlation. The Steiner-Taborek and Gungor-Winterton heat transfer correlations made estimations within a bandwidth of 20% against experimental data: the first at the superior boundary and the second at the inferior one.

The Steiner-Taborek's model gave the best results for advanced boiling stages.

As can be deduced from *fig.6*, the influence of thermodynamic quality, heat transfer and mass velocity on heat transfer is qualitatively the same for ammonia boiling and other refrigerants (i.e. freons, hydrocarbons, water).

Due to the fact that the experimental set-up was a gravitationally recirculation loop, the results of this research are especially suitable for small ammonia flooded evaporators (up to 6500W/m2 heat flux) with gravitational fluid circulation.

AKNOWLEDGMENTS

This work was financed by the Romanian Council of Research in High Education, Grant CNCSIS 95/1999. The first author whish to express also his gratitude for prof. Florea Chiriac from Technical University of Civil Engineering, Romania for his important support.

REFERENCES

[1]. VDI Wärme Atlas, 1997, Strömungssieden gesättigter Flüssigkeiten, Sect. Hba, Springer Verlag

[2]. Barthau, G., 1976, Experimental Investigation of Ammonia Flow Boiling at High Pressures, 5th All-Union Heat and Mass transfer Conf., Minsk, vol. III-1, p.200-225;

[3]. Gronerund, R., 1974, Two-phase heat resistance in boiling refrigerants – Calculation and influence on evaporator design. Intst. Fos Kjoleteknik, Trodheim. Citted by D. Steiner in VDI Wärme Atlas, 1997, Strömungssieden gesättigter Flüssigkeiten, Sect. Hba, Springer Verlag

[4]. Steiner D., Taborek, J., 1992, Flow boiling heat transfer in vertical tubes correlated as asympthotic model, Heat Tansfer Engineering, vol. 13, no.2: p.43-69;

[5]. Gungor, K., Winterton, R., 1986, A general correlation for flow boiling in tubes and annuli, Int.J. Heat and Mass Transfer, vol.29, no.3: p. 351-358;

[6]. Pierre, B., 1965, Flow resistance with refrigerants. Part I & Part 2, ASHRAE J. p. 58-65 & 73-77;

[7]. Cleis, W., 1949, Die Wärmeübergangszahl von verdampfenden Ammoniak in Senkrechten Rohr. Kälteteschik, 2, 32-54;

[8]. Malek, A., Colin, R., 1983, Ebullition de l'ammoniac en tyaux long: Transfert de chaleur et pertes de charge en tubes vertical et horizontal, Centre Techniques de Industries Mechaniques, France, CETIM, 14-011, p.1-65;

[9]. Shah, M., 1982, Chart corrélation for saturated boiling heat transfer: Equations and further study, ASHRAE Trans., vol. 88, p. 185-196;

[10]. Ohadi, M., Radermacher, Li, S., R., Dessiatoun, S., 1996, Critical review of available corrélations for two-phase flow of ammonia, Int. J. refrigeration, vol.19,no.4: p.272-284;

[11]. Kandlikar, S., 1990, A general correlation for saturated two-phase flow boiling heat transfer inside horizontal and vertical tubes, Journal of Heat Transfer, vol. 112, pp.219-228;

[12]. Taler, J., 1996, Theory of transient experimental techniques for surface heat transfer, Int. J. Heat Mass Transfer, vol. 39, no.17: p.3733-3748;

[13]. Levi, S., 1967, Forced convection sub-cooled boiling: prediction of vapour volumetric fraction, Int. J. Heat Mass Transfer 10, 951-965;

[14]. Zuber, N., Findlay, J., 1965, Average volumetric concentration in two-phase flow systems, Journal of Heat Transfer, p.453-468;

[15]. Ishii M., 1977, One-dimensional drift flux model and constitutive equations for relative motion between phases in various two-phase flow regimes, ANL-77-47;

[16] Zamfirescu, C., 1999, Contribution to the study of heat transfer at forced convection boiling of ammonia in pipes. Ph.D. Dissertation at Technical University of Civil Engineering, Bucharest, Romania

[17]. Chisholm, D., 1973, Pressure gradients due to friction during the flow of evaporating two-phase mixtures in smoth tubes and channels, Int.J.Heat Mass transfer, vol.16, p.347-358;

[18]. Lockhart, R., Martinelli, R., 1949, Proposed corellation of data for isothermal two-phase two-component flow in pipes. Chem.Eng.Progr., vol.55, no.1, p.39

HEFAT2002
1st International Conference on Heat Transfer, Fluid Mechanics, and Thermodynamics
8-10 April 2002, Kruger Park, South Africa
KT1

CONDENSATION OF MIXTURES IN SHELL-AND-TUBE CONDENSERS - THE INFLUENCE OF IMPORTANT FACTORS ON CALCULATION RESULTS

T. Karlsson* and L. Vamling**
*PhD student; **Professor
Department of Heat and Power Technology,
Chalmers University of Technology,
SE-412 96 Göteborg, Sweden
Phone: +46-31-7728535, Fax: +46-31-821928
E-mail: Tord.Karlsson@hpt.chalmers.se
E-mail: Lennart.Vamling@hpt.chalmers.se

ABSTRACT

Calculations are carried out for condensation of zeotropic refrigerant mixtures in a horizontal shell-and-tube condenser, in order to investigate possible causes for overpredictions of heat transfer found when comparing with experimental data. A rigorous calculation method is compared to an earlier used simplified method, and to experimental measurements, but the rigorous method turns out to predict even better heat transfer. Mass transfer in the gas phase is calculated to reduce heat transfer up to 10%, but this effect cannot alone explain the overprediction of heat transfer. However, investigations show that the degree of mixing in the condensate layer is of great importance, and can be one important reason for the overprediction. Geometry data turned out to have only minor effects on calculation results.

INTRODUCTION

Today's requirement of high energy-efficiency has led to a decrease in temperature driving force in many types of heat transfer equipment, for example in evaporators and condensers in heat pumps. Since the temperature driving force is decreasing, other factors influencing heat transfer may become more apparent. One example is that today more and more heat pumps use zeotropic (also called non-azeotropic) mixtures of refrigerants as working fluid, which introduces effects such as mass transport resistance in both the gas phase and the liquid phase, as well as a change in composition during evaporation and condensation. The latter leads to changes in boiling point and dew point temperatures during condensation and evaporation, called glide, which influences the available temperature driving-force.

Calculation models of evaporation and condensation can be very complicated, and especially for mixtures, results can differ appreciably from experimental results. Gabrielii and Vamling [1] pointed out that standard calculation methods can overestimate heat transfer coefficient for condensation of zeotropic refrigerant mixtures with at least 40%. The purpose of this work is to investigate possible causes to this overestimation. A number of simplifications and approximations are made in calculation models, and the influence of some of them is investigated here. This could typically be the use of empirical correlations to find heat transfer coefficients, simplifications of the geometry, and when using mixtures, predictions of mixing in both the gas phase and the liquid phase.

In this work heat transfer calculations are carried out for a shell-and-tube condenser used in a marine liquid chiller. The condenser has a total of 263 low-finned horizontal copper tubes with an outside-inside area ratio of 3.5, and a total external plain area of approximately 50 m^2. It has a cross-flow arrangement (Tema X) with two tube-side passes. Condensation of the refrigerant takes place on the shell-side, and cooling water flows inside the tubes. This particular condenser is designed to be used with R22 and to deliver around 800 kW, but it has also been run with R407C, a zeotropic refrigerant mixture consisting of 38 mol% R32, 44 mol% R134a and 18 mol% R125. The experimental facility, together with test results, is presented by Gabrielii and Vamling [1]. A schematic picture of a shell-and-tube condenser can be seen in Fig. 1.

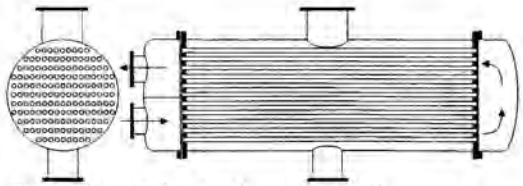

Figure 1. A shell-and-tube condenser. Vapour enters at the top on the shell-side and condensate leaves at the bottom. Cooling water flows inside the tubes.

In [1] a standard, simplified calculation method was used. Here we calculate local gas-liquid equilibrium on each tube row, taking gas phase mass transfer into account by solving Maxwell-Stefan's equations using estimated diffusivities.

THEORY

Two different methods for calculating condensing flux and heat transfer are compared. The simpler method, used by [1], is proposed by Silver [2] and further developed by Bell and Ghaly [3]. The equation for the overall heat transfer coefficient can for this method be written:

$$\frac{1}{U} = \frac{A_o}{A_i \alpha_c} + \frac{\delta A_o}{\lambda_w A_w} + \frac{1}{\alpha_l} + \frac{z}{\alpha'_g} \qquad (1)$$

where U is the overall heat transfer coefficient, A_o is outside tube area, A_i is inside tube area, α_c is the heat transfer coefficient on the coolant side (inside the tubes), δ is the thickness of the tube wall, λ_w is the heat conductivity in the tube wall and α_l is the condensation heat transfer coefficient. For a pure fluid the last term, z/α'_g is not included, but for a mixture it has to be added. The effect of this term on U depends on the temperature glide for the zeotropic mixture due to the change in composition when condensing. α'_g is the gas-phase heat transfer coefficient, here corrected for the effect of mass transfer according to Ackermann [4] and simplified by McNaught [5]:

$$\alpha'_g = \alpha_g \frac{\Phi}{\exp\Phi - 1} \qquad (2)$$

where

$$\Phi = \frac{M\left(-\frac{dx}{dA_o}\right)c_{p,g}}{\alpha_g} \qquad (3)$$

M is condensing mass flow rate, x is quality and $c_{p,g}$ is the specific heat for the bulk mixture. α_g is calculated with the Delaware method [6], a correlation for one-phase heat transfer on horizontal, finned tubes. The term z in eq. (2) is defined as

$$z = x\, c_{p,g} \frac{dT_g}{dh} \qquad (4)$$

where dT_g/dh is the slope of a predetermined temperature-enthalpy relationship obtained from the condensation curve. In the calculations carried out here, the condensation process is assumed to pass through a number of equilibrium states and the condensate film is assumed to be perfectly mixed, which is called integral condensation [6]. Dittus-Boelter's equation [7] is used to calculate α_c, the heat transfer coefficient inside the tubes to the cooling water. Finally, to calculate the heat transfer coefficient for the condensate film, α_l, the correlation of Beatty and Katz [8] is used, modified by Smith [9]. The correlation adjusts the heat transfer coefficient for condensation on a single plain tube calculated according to Nusselt [10], to account for the geometry of a finned tube bundle.

NOMENCLATURE

A	area (m^2)
c_p	specific heat (J/kgK)
F	flow rate (kg/s)
h	enthalpy (J/kg)
h_{fg}	specific enthalpy of vaporization (J/kg)
M	mass flow rate (kg/sm^2)
$\dot{n}$	molar flux towards interface (mol/sm^2)
Q	Duty (kW)
$\dot{q}_L$	sensible heat of condensate (J/kgK)
T	temperature (K)
U	overall heat transfer coefficient (W/m^2K)
x	quality

Greek Letters

α	heat transfer coefficient (W/m^2K)
δ	tube thickness (m)
ε	correction factor
Φ	parameter defined in eq. (3)
λ	conductivity (W/mK)
θ	mixing parameter for the condensate layer

Subscripts

b	bulk
c	cooling water
g	gas
i	inside
i	interface
l	condensate
o	outside
R	refrigerant
w	cooling water

When all information described above is known, the overall heat transfer coefficient, U, can be calculated. Together with temperatures in the gas bulk and the coolant water the transferred heat can be calculated. A detailed description of the calculation program used is presented by Gabrielii and Vamling [1].

The rigorous calculations carried out here are based on a further development of a calculation program developed by Sajjan [11]. The calculations use the method of Krishna and Standart [12] to solve Maxwell-Stefan's transport equations for a mixture of refrigerants. Instead of calculating an approximate overall heat transfer coefficient, an interface temperature on the surface of the condensate film has to be found. This temperature depends on the composition, as does the condensing flux. Together with calculations of local interface equilibrium an energy balance is solved:

$$\dot{n}_{tot} \cdot h_{fg} + \dot{q}_L + \alpha'_g \cdot (T_b - T_i) = \alpha_L \cdot (T_i - T_c) \qquad (5)$$

$\dot{n}_{tot}$ is the condensing flux, h_{fg} is the specific enthalpy of vaporization and $\dot{q}_L$ is the sensible heat from condensate falling from tubes above. The left-hand side is heat transferred from the gas bulk to the phase interface (the condensate surface), and the right-hand side is heat transferred from the interface to the cooling

water inside the tube. α_L in (5) is the total heat transfer coefficient from the condensate surface to the cooling water, and can be written

$$\frac{1}{\alpha_L} = \frac{A_o}{A_i \alpha_c} + \frac{\delta A_o}{\lambda_{wall} A_{wall}} + \frac{1}{\alpha_i} \qquad (6)$$

All individual heat transfer coefficients, α_c, α_i and α_g, are calculated in the same way as described for the simplified method. When local interface equilibrium is established and the energy equation (5) is in equilibrium the heat transfer from the condensing refrigerant to the cooling water can be found by calculating either side of equation (5). A more detailed description of the calculation program can be found in [11].

CALCULATION PROCEDURE

To calculate heat and mass transfer, numerical integration is used. The condenser consists of a number of tube rows, and each tube row is divided into a number of slices. One slice of all tubes in one tube row is one computational cell, as seen in Fig. 2. The equations for heat and mass transfer are solved in each computational cell, where averaged conditions are used.

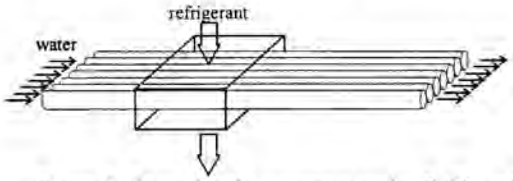

Figure 2: *Example of a computational cell. The cell covers all tubes in one tube row.*

The flow field of the refrigerant on the shell-side is not calculated. Instead, for simplicity, the condensate flow is assumed to be strictly vertical from one computational cell on a tube row to the computational cell on the tube row below, and evenly distributed over all tubes in the tube row, within the computational cell. Refrigerant gas can either be treated in the same way as the condensate, or it can be redistributed after every tube row to make the velocity into the next tube row constant along the tubes. This is simply accomplished by shifting gas between calculation cells next to each other in order to maintain composition differences along the tubes. The calculations follow the flow of the refrigerant and the cooling water, from inlet to outlet, and calculated conditions out from one computational cell become input to the next computational cell. Input parameters given to the calculations are:

- geometry of the condenser and the tubes
- which refrigerant
- refrigerant flow
- refrigerant pressure and temperature before condenser
- either number of tubes/tube rows used for subcooling or refrigerant temperature after condenser
- water flow
- water pressure and temperature before condenser

This information makes the calculations over-determined, so in order to make calculations match input data a correction factor, ε, is introduced on the overall heat transfer coefficient in each calculation cell, $U_{corr} = \varepsilon \cdot U_{calc}$. This correction factor tells us if calculations overpredicts or underpredicts heat transfer compared to experimental data, or if one calculation better predicts heat transfer than the other. A value of ε less than one implies too high calculated heat transfer since it must be decreased to match input data. The opposite is valid for ε-values greater than one.

Comparison between the methods: In order to compare the two calculation methods to see if the simplified method is a reason for overpredicting heat tranfer, while including as few other effects as possible, a number of fictitious cases are used, with the same duty as experimental runs presented in [1]. For the simplified method, the correction factor is fixed at the value one, and the pressure is adjusted to make refrigerant enter the condenser as saturated vapour and leave as saturated liquid instead of being superheated and subcooled as normally is the case in an operating condenser. The duty, water flow rate, and water temperatures in and out are the same as in experimental test runs, and they are shown in Table 1. Water inlet temperature is constant at 22 °C and the flow is 26 kg/s.

Table 1.*Data used in comparison. Pressures are adjusted to make outlet saturated.*

Case	Fluid	Q (kW)	F_R (kg/s)	P (MPa)
A	R22	716	3.4	1.23
B	R22	537	2.5	1.15
C	R22	359	1.6	1.09
D	R22	258	1.2	1.05
E	R407C	757	3.7	1.41
F	R407C	590	2.8	1.33
G	R407C	346	1.5	1.22
H	R407C	246	1.0	1.19

To investigate how the rigorous method behaves compared to the simplified, the rigorous calculations use the pressures calculatad above, and the correction factor is adjusted to make outlet saturated. A simplified, rectangular, aligned tube bundle geometry is used in the comparison, and integral condensation is assumed, which means perfect mixing in the condensate layer between condensate forming on the tube and condensate falling from the tubes above [6].

Influence of geometry data: Geometry data can be given with more or less detail, and it is interesting to know how the geometry influences the results. The tube design (diameter, number of fins, fin height etc.) must be given for some heat transfer correlations, but not necessarily the tube bundle design. A simplified, aligned, rectangular tube bundle geometry was used in [1], hence it is interesting to investigate how the correction factors change when instead of using a

rectangular, aligned tube bundle, a more accurate, circular tube bundle geometry of the condenser described in the introduction is used. The influence of staggered versus aligned tube layout in the calculations is also investigated. For an aligned layout, all condensate is transferred from one tube row to the one below. For staggered layout however, the condensate is transferred two tube rows without interfering with heat or mass transfer on the tube row between. This means an approximately halved condensate flow on each tube. Calculations are carried out with the rigorous method for the cases described above, and the correction factor is again adjusted to make outlet saturated.

Effect of subcooling heat transfer coefficient: Normally condensers are designed and operated to subcool the refrigerant a few degrees. The subcooling heat transfer has thus to be calculated as well as the condensation heat transfer. When comparing to experimental data without liquid level measurements, this level must be calculated. The liquid surface can reach one or a couple of tube rows up at the bottom of the condenser, meaning the tubes subcool the liquid instead of condense the vapour. This is sometimes considered not to influence the final result of the calculation much, therefore being roughly approximated. Another reason for making an approximation is that correlations for low-velocity liquid heat transfer on area-enhanced tubes are rare.

In absence of a correlation for heat transfer on area-enhanced tubes at the low velocities present in a condenser, where the flow is almost laminar, an approximation is made. The basis is a correlation for a bundle of smooth tubes valid for low Reynold-numbers, presented by Gnielinski et. al [6]. Further it was found that the ratio of heat transfer coefficient for turbulent conditions between bundles of smooth and enhanced tubes is approximately constant at 2.85 for different flow velocities, using correlations also presented in [6]. Therefore the heat transfer coefficient is calculated at local conditions for a smooth tube with a correlation valid for laminar flow, and then divided by 2.85. This approximation is likely to underestimate the heat transfer coefficient, thus making it interesting to investigate how sensitive the calculation results are to subcooling heat transfer.

Correction factors are adjusted for three cases of subcooling heat transfer, using the rigorous method to match calculations to experimental data. In the first case heat transfer coefficients approximated as explained above are used. The second case tests 50% better heat transfer in the subcooling region, while the third case tests 2.85 times better heat transfer than the approximation. The third case simply tests subcooling heat transfer as if all enhanced tube area is used as efficient as on a smooth tube.

Influence of mass transfer resistance: When condensing a mixture, lighter components in the gas phase are swept to the interface by the condensing flux, leading to a higher concentration of light components at the interface. This results in a lower interface temperature and therefore a decreased temperature driving force, leading to decreased heat transfer. To investigate the effect of mass transfer resistance in the gas phase, and to see if this can explain overprediction of heat transfer, values of the diffusion coefficients for the rigorous method are varied. An infinite diffusion coefficient would mean that no mass transfer resistance is present, thus maximizing interface temperature and heat transfer. The diffusion coefficients, calculated according to Fuller [13], were multiplied by factors between 1/8 to 32 for two different cases, one with high duty and one with low duty, and the correction factors were adjusted to make calculations match experiments.

As well as mass transfer resistance in the gas phase, there can be a mass transfer resistance in the liquid phase, however most calculations assume this to be negligible. Two extremes exist, integral condensation and differential condensation as explained in [6]. Integral condensation is when the mixing between existing condensate and new condensate forming on a tube is supposed to be perfect, that is no mass transfer resistance, while differential condensation is the opposite. For differential condensation condensate forming on a tube is assumed to stay on the surface, forming a film. This is unfavourable because it leads to a higher interface temperature in the same way as in the gas phase. Whether integral or differential condensation takes place in a condenser is difficult to know, because the mixing depends on several factors, such as liquid diffusion, the liquid flow from one tube to another, as well as drips and splashes. It is also very difficult to measure. It is possible that the true condensation regime is somewhere between the extremes. It is therefore interesting to investigate whether a mixing parameter, allowing the condensation to be between integral and differential, can compensate for the often overpredicted heat transfer for zeotropic mixtures.

The correction factor is here fixed at the value calculated for R22 at each duty, and a mixing parameter, θ, is adjusted to make calculations match experimental data. A value of one means integral condensation and a value of zero means differential condensation.

RESULTS AND DISCUSSION

Comparison between the methods: Correction factors for the rigorous method for fictious cases, assuming the simplified method as perfect, are shown in Fig. 3. It can be seen that the methods differ less than 6% for R22. The difference does not depend on the methods themselves, but rather on other dissimilarities between the calculation programs. One such dissimilarity is the calculation of α_i, where the simplified method uses Kern's method for inundation [6], while the rigorous method uses local calculations.

The difference for R407C is greater, with a maximum at low duty, where a correction factor of less than 0.7 implies more than 30% higher prediction of heat transfer. This means that using the simplified method is not the reason for overpredicting heat transfer for condensation of zeotropic mixtures.

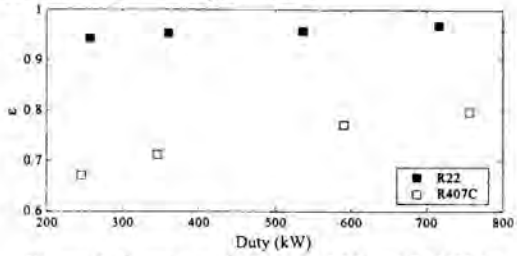

Figure 3. Correction factors for R22 and R407C for the rigorous method assuming the simplified method as perfect.

Influence of geometry data: The data for a rectangular, aligned tube bundle in Fig. 4 is the same as the data in Fig.3. The relative change in heat transfer due to different geometries is less than 7%. As expected, a circular tube bundle is equal or less efficient than a rectangular tube bundle, and staggered tube layout is more efficient than aligned layout.

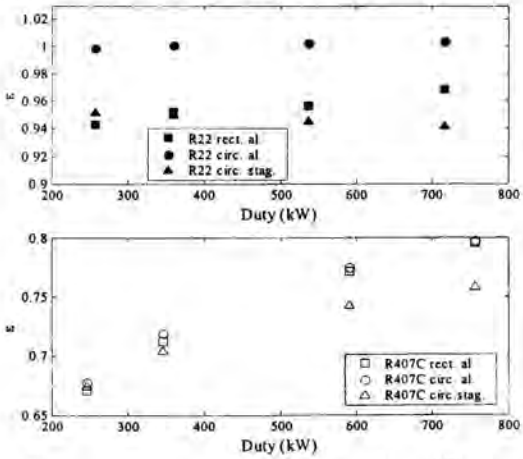

Figure 4: Correction factors for different geometries of the tube bundle, rectangular aligned, circular aligned and circular staggered.

Effect of subcooling heat transfer coefficient: Calculated correction factors in Fig. 5 matches calculations to experimental data. The influence of subcooling heat transfer on calculation results is significant for R22; an increase in subcooling heat transfer up to ideal usage of all enhanced area (a factor 2.85), decreases the correction factor up to 15%, meaning an increase in total calculated heat transfer of 15%. The reason for this is the larger area available for condensation when not as many tubes are needed for subcooling.

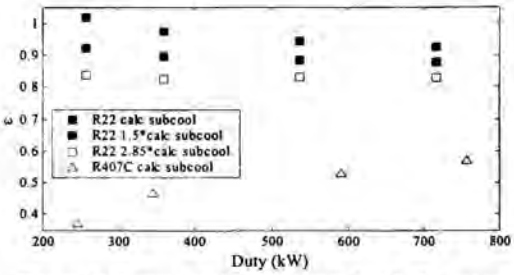

Figure 5: Correction factors to match calculations to experimental data for three different subcooling heat transfer coefficients for R22. Correction factors for R407C show an overprediction of heat transfer.

Influence of mass transfer resistance: A calculated subcooling heat transfer coefficient as described makes calculations predict heat transfer for R22 within 8% compared to experimental data, with a tendency to overpredict, as seen in Fig. 5. Correction factors for R407C between 0.35 and 0.55 tell us that calculated heat transfer is too high and must be suppressed in order to match experimental data. In the calculations a mass transfer resistance in the gas phase is calculated, but it uses estimated gas diffusivities, which are not necessarily correct. The relative change in heat transfer for different diffusion coefficients is presented in Fig. 6. The value 1 on the x-axis corresponds to the estimated diffusion coefficients, where also the relative correction factor is 1. High x-values means high diffusion coefficients, and minor mass transfer resistance. Both curves level out at high x-values, meaning that mass transfer resistance is not present any more. At low duty, the curve levels out at a relative correction factor of 0.9, meaning an increase in heat transfer of 10%. In other words, the mass transfer resistance with the estimated diffusion coefficient reduces calculated heat transfer by 10%. Fig. 6 also shows that an error in estimating the diffusion coefficient of a factor 10 leads to calculation errors of heat transfer of -10% to +25% at a low duty. The effect is smaller for higher duties. An overestimation of the coefficient leads to an overestimation of heat transfer, but this effect cannot by itself explain the overestimation of heat transfer compared to experimental data.

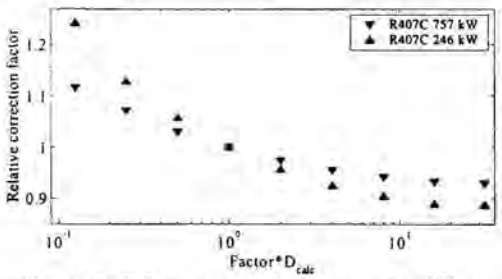

Figure 6: Relative correction factors for different values of diffusion coefficients in the gas-phase.

A mixing parameter, θ, described in the "calculation procedure" section, is used to describe the mass transfer resistance/mixing in the liquid phase. In Fig. 7 the value of this parameter that results in a correction factor close to 1 is given. This means that if the condensation is *not* integral, this could be one explanation to the overestimation of heat transfer. Lower mixing parameters for higher duties indicate worse mixing than at low duties. Since the film is thicker at high duties, this implies that diffusion could be a governing mixing process.

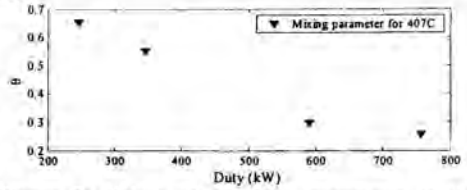

***Figure 7:** Values of a mixing parameter in the condensate film that matches calculations to experiments while using a correction factor equal/close to 1.*

General discussion: The investigation above shows a possible explanation to the overprediction of heat transfer in earlier work [1]. Since it is difficult to know anything about the mixing in the condensate layer, there is no definite answer to the question. The rigorous method seemed to perform worse than the simplified method compared to experiments with the assumption of integral condensation. However, if the real process is closer to differential, it means that the rigorous method is better to predict heat transfer. To better understand this matter, a detailed study of the condensate film has to be carried out.

CONCLUSIONS

Calculations carried out for zeotropic refrigerant mixtures in a shell-and-tube condenser led to the following conclusions:

- A simplified method used in earlier calculations was not the reason for overpredicting heat transfer.
- Calculations are not very sensitive to geometry data.
- Mass transfer resistance reduces heat transfer about 10%, but the result is sensitive to the estimation of diffusivities.
- Absence of perfect mixing in the condensate layer is shown to be a possible reason for overprediction of heat transfer.

REFERENCES

[1] Gabrielii, C., Vamling, L., 1997, "Replacement of R22 in shell-and-tube condensers: experiments and simulations", *International Journal of Refrigeration*, Vol. 20, pp. 165-178.

[2] Silver, L., 1947, "Gas cooling with aqueous condensation", *Trans. Inst. Chem. Eng.*, Vol. 25, pp. 30-42.

[3] Bell, K., Ghaly, M. A., 1972, "An approximate generalized design method for multicomponent/ partial condensers", *AIChE Symp. Ser.*, Vol. 69, pp. 72-79.

[4] Ackermann, G., 1934, "Forschungsheft", No. 382, pp. 1-16.

[5] McNaught, J. M., 1979, "Mass-transfer correction terms in design methods for multi-component/partial condensers", *Proceedings of the 18th Natl. Heat Conf. San Diego*, pp. 111-118.

[6] Heat Exchanger Design Handbook, VDI-Verlag, *Hemisphere Publishing*, ch. 2.5, 2.6, 3.3.

[7] Dittus, F.W. and Boelter, L.M.K., 1930, *Univ. of Calif. Pubs. Engr.*, 2:443

[8] Beatty, K.O., Katz, D.L., 1948, "Condensation of Vapours on Outside of Finned Tubes", *Chem. Eng. Prog.*, Vol. 44, pp 55-70.

[9] Smith, R. A., 1986, Vaporizers: Selection Design & Operation, *Longman Scientific & Technical*.

[10] Nusselt, W., 1916, "Surface condensation of water vapours", *Z. Ver. Dtsch. Ing.*, Vol 60, pp. 569-575.

[11] Sajjan, D., 1999, "Condensation of Zeotropic Refrigerant Mixtures in Shell-and-Tube Condensers", Licentiate thesis, Department of Heat and Power Technology, Chalmers University of Technology, Sweden.

[12] Krishna, R., Standart, G.L., 1976, "A Multicomponent Film Model Incorporating a General Matrix Method of Solution to the Maxwell-Stefan Equations", *AIChE Journal*, Vol. 2, No. 2, pp. 383-389.

[13] Fuller, E.N., Schettler, P.D., Giddings, J.C., 1966, "A new method for prediction of binary gas-phase diffusion coefficients", *Industrial and Engineering Chemistry*, Vol 58, No. 5, pp. 19-27.

HEFAT2002
1st International Conference on Heat Transfer, Fluid Mechanics, and Thermodynamics
8-10 April 2002, Kruger Park, South Africa
HS1

PRESSURE OSCILLATIONS IN HORIZONTAL SUBMERGED STEAM JET CONDENSATION

Soon Joon Hong*, Byung Ki Lim**, Seok Cho***, Se Young Chun***,
Yong Soo Kim****, and Goon Cherl Park****

* Future and Challenge Tech. Co., Bldg. 130-202, Seoul National University, San 56-1, Shillim-Dong, Kwanak-Gu,Seoul, 151-742, Korea
E-mail : sjhong70@snu.ac.kr

** Department of Mechanical Engineering, Hanyang University
17, Haengdang-Dong, Seongdong-Gu, Seoul, 133-791, Korea

*** Korea Atomic Energy Research Institute
150, Dukjin-Dong, Yusong-Gu, Taejon, 305-353, Korea

**** Department of Nuclear Engineering, Seoul National University,
San 56-1, Shillim-Dong, Kwanak-Gu,Seoul, 151-742, Korea

ABSTRACT

The pressure oscillations of submerged steam jet condensation were investigated. When the steam mass flux was under 300 kg/m^{2}s, the frequency increased as the steam mass flux increased. However, over the steam mass flux 300 kg/m^{2}s, the frequency decreased as the steam mass flux increased. The frequency always decreased as the pool temperature increased. For the high steam mass flux region, analytical model was developed. The proposed model excellently predicted the experiment.

INTRODUCTION

Steam jet condensation in a subcooled water pool can occur in a number of industrial operations. In particular, Advanced Power Reactor 1400MW (APR1400), an advanced type of Pressurized Water Reactor (PWR) in Korea, adopts an In-containment Refueling Water Storage Tank (IRWST) and spargers in it, which increases the quenching efficiency of steam and alleviates probable pressure surge induced by the sudden discharge of the high pressure steam. For the design and operation it is essential to understand the phenomena of submerged steam jet condensation. Especially, the pressure oscillation during steam jet condensation may directly damage the structures or resonate with the structures. Eventually, the structure may be directly damaged or the fatigue can cumulate in them.

Steam jet condensation has been investigated as a function of steam mass flux, pool subcooling (pool temperature) and nozzle diameter in following four areas; jet shape and length, heat transfer coefficient, condensation regime map, and pressure oscillation. For the wide range of steam mass flux and pool temperature, the jet penetration length, heat transfer coefficient, and condensation regime map have been studied. Recently, Cho et al.' map [1] covers up to steam mass flux 450 kg/m^{2}s and pool temperature 95℃ as shown in Fig. 1. Pressure oscillation was intensively studied by Damasio et al. [2]. They suggested an experimental frequency correlation using Strouhal number for frequency (St), steam Reynolds number (Re), pool Jacob number (Ja), and Weber number (We) up to maximum steam mass flux 250 kg/m^{2}s. The frequency is proportional to steam mass flux and pool subcooling, but inversely proportional to nozzle diameter. Nariai et al. [3] analytically studied on the pressure oscillation, and well predicted experimental data. However, they were all limited to steam mass flux up to 300 kg/m^{2}s. Thus, studies for the higher steam mass flux, which is expected in the sparger of APR1400 [4], are required.

Therefore, the objective of this study is to investigate the dominant frequency of pressure oscillation in submerged horizontal steam jet condensation. The range of steam mass flux was 200~900 kg/m^{2}s, and that of pool temperature was 35~95℃. In particular, the high steam mass flux region (>300 kg/m^{2}s) was intensively investigated.

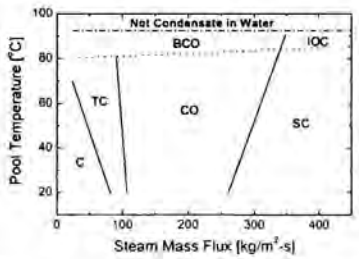

Figure 1: Condensation Regime Map by Cho et al. [1]

NOMENCLATURE

b	effective width of jet or liquid dominant region (m)
c_{pl}	specific heat of water (J/kgK)
d	diameter of jet or vapor dominant region (m)
d_0	hole diameter (m)
f	frequency (Hz)
G_0	steam mass flux at the exit of hole (kg/m^{2}s)
h_{fg}	latent heat of water (J/kg)
k	expansion coefficient of jet or liquid dominant region
n	coefficient of polytropic process
P_v	pressure of vapor cone or vapor dominant region (Pa)
P_∞	pressure of liquid dominant region (Pa)
R	radius of bubble (m)
T_s	steam temperature (K)
T_∞	ambient or liquid temperature (K)
t	time (s)
u	velocity (m/s)
V	volume (m^3)
W_l	net work done against the liquid dominant region (J)
X	steam jet penetration length (m)
X_ε	equilibrium length of steam jet penetration (m)
x	distance in the direction of jet axis (m)
ε	perturbation
γ	ratio of specific heat
ρ_l	density of water or liquid dominant region (kg/m^3)

TEST FACILITY AND MEASUREMENTS - GIRLS

GIRLS (General Investigation Rig for Liquid/Steam Jet Direct Contact Condensation) was constructed as shown in Fig. 2. Demineralized and degassed water was used. Cylinder pool was used in this study, whose diameter is 1.8m, height 1.5m, water level 1.3m. Sparger was a pipe of 1 inch and schedule 40. Near the end of the sparger, the steam was horizontally discharged into subcooled water through a single hole of diameter 10mm. The submergence of the steam jet is 1.1m. In the cylinder pool, a cooling system was installed for the sake of easy control of pool temperature, and acoustic sponge covered the inner wall in order to prevent the resonance of pressure oscillation with the wall.

In order to measure pressure oscillation when steam jet condenses in subcooled water, pressure transducers of piezoelectric type were used. For the minute measurement, noise level tests were conducted, and the maximum noise level was turned out to be about 1.6Pa [4]. Pool temperature was represented by the average of 6 measurements. The standard deviation of pool temperature was maintained within 0.5℃, and that of steam flowrate was within 2.0 kg/hr during the measurement time.

Pool water level was 1.3 m, and the hole of sparger was submerged with the depth of 1.1m. Pool temperature was varied with 5℃ step from 35~95℃. Steam mass flux was varied from 200~900 kg/m^{2}s. These series of experiment were designated as A-series.

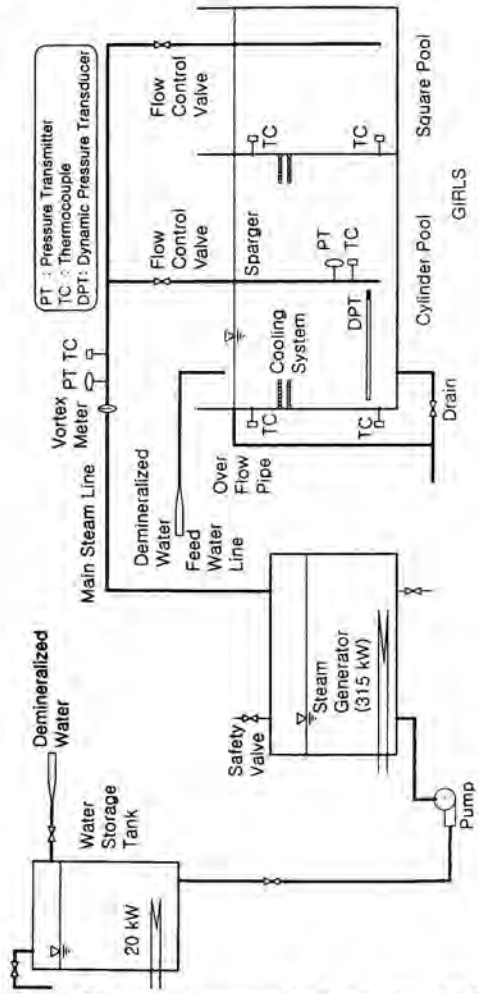

Figure 2: Schematic Diagram of the Test Facility, GIRLS

DATA ANALYSIS METHOD - GAPF

The pressure oscillations of steam jet condensation are known to be extremely complex and to have strong randomness. Thus, it is very difficult to find the dominant frequency. Fourier transform (or Fast Fourier Transform (FFT)) is known to be a powerful tool to find the frequency by transforming the time

domain to frequency domain. Based on this FFT, averaging method was adopted as shown in Fig. 3. And these processes were coded with C++ computer language, and named as GAPF (GIRLS Analysis Program based on FFT). The GAPF has the effect of several tests by just one test, and the randomness greatly decreases. The GAPF makes the curves smooth and makes it easy to find the dominant frequency. More detailed description, benchmarking, and performance are attributed to Hong [4].

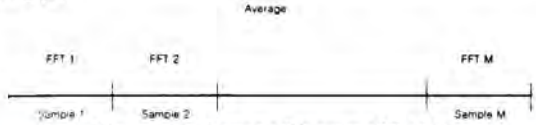

Figure 3: Schematic Diagram of GAPF

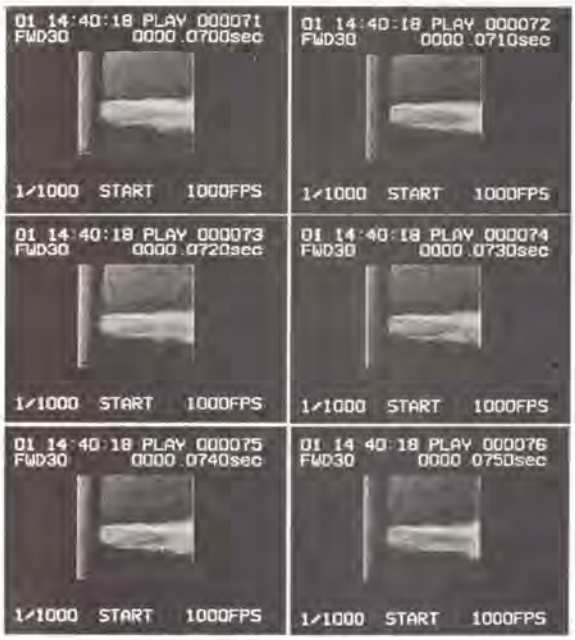

Figure 4: Six Sequent Photographs of High Speed Camera at Pool Temperature 47℃ and Steam Mass Flux 625kg/m^{2}s (Frequency=282Hz, Period = 0.0035s)

RESULTS AND DISCUSSIONS

Fig. 4 is the sequent photographs taken by high speed camera of 1000frame/s for pool temperature 47℃ and steam mass flux 625 kg/m2s as a representative case. The steam jet consists of vapor cone, two phase mixture, and main region as investigated by Kim, H. Y. [5]. Initially injected vapor cone encounters the cold pool water, and near the end of the cone the local water temperature increases. The increase of pool temperature decreases the condensing power of water. Thus, in order to condense all the steam provided, the cone is inevitably prolonged and obtains larger heat transfer area. The prolonged cone again meets new fresh cold water, and the condensing power is more than the provided steam. Then, vapor cone becomes short. However, the warm water is soon cumulated near the end of the cone. These processes are cycled, and these are the initiation of instability. As a result, the length of steam jet is varied, and such a variation of the length induces the pressure oscillation according to the equation of state.

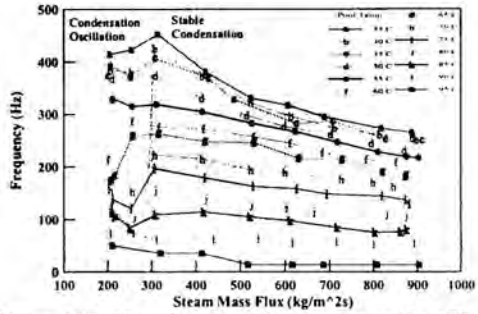

Figure 5: Test Results - Frequency vs. Steam Mass Flux

Fig. 5 is the test result. The frequencies at the steam mass flux 200 kg/m^{2}s are very similar with those of Damasio et al. [2]. This figure suggests the frequency data for regime transition according to steam mass flux. The frequencies tend to increase as the steam mass flux increases, when the steam mass flux is lower than about 300 kg/m^{2}s. However, over the steam mass flux 300 kg/m^{2}s, the frequencies tend to decrease as the steam mass flux increases. Such a different trend is related with condensation regime map proposed by Cho et al. (Fig. 1) [1]. They classified the regimes at about 300 kg/m^{2}s, which is the critical steam mass flux at 1~2 atm.

There are clear differences between condensation oscillation (denoted 'CO' in Fig. 1) and stable condensation (denoted 'SC'). The most outstanding difference is the motion of the interface near circumference of the jet. In CO, there are violent oscillations of circumference, however, in SC only the oscillation of the jet end is noticeable. For CO, the circumference oscillates violently within the finite boundary. Thus, the oscillation frequency increases as the steam mass flux increases, since the higher steam mass flux makes the circumference to reach the maximum expansion more rapidly. Nariai et el. [3] successfully modeled the frequency of condensation oscillation by spherical bubble model and hemispherical bubble model. These two models simulate the motion of entire jet, not the end part.

In SC, the oscillation of the end of steam jet is an important mechanism of steam jet oscillation. Thus, the longer the jet length, the more time the oscillation requires. Noting that the jet length is prolonged as the steam mass flux increases, it is reasonable that the frequency gets lower. With the same manners, as the pool temperature increases, the jet length is prolonged and resultantly the frequency gets lower.

ANALYTIC MODEL

The governing equation is based on the balance of kinetic energy that the steam jet gives and the ambient water receives when the steam jet grows. On this basic idea, the theory of submerged turbulent jet was adopted [6,7]. We suggest Fig. 6 as a simplified structure of submerged steam jet to set up the one dimensional balance equation.

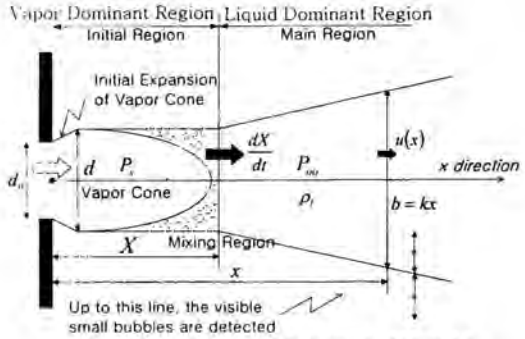

Figure 6: Modeling of Submerged Steam Jet

The mass conservation at the point X and x gives

$$\rho_l\left[\frac{dX}{dt}\right]\left[\frac{\pi}{4}d^2\right]=\rho_l\left[u(x)\right]\left[\frac{\pi}{4}(kx)^2\right] \tag{1}$$

where k is the effective expansion coefficient of liquid dominant region, and $u(x)$ is area-averaged velocity at x. Thus, the liquid velocity at x is

$$u(x)=\left(\frac{d}{kx}\right)^2\frac{dX}{dt} \tag{2}$$

Throughout the liquid dominant region $X<x<\infty$, the liquid gains the following kinetic energy from the motion of the vapor dominant region;

$$KE=\int_X^\infty\frac{1}{2}\rho_l u^2(x)dV=\frac{\pi}{8}\rho_l\frac{d^4}{k^2}\left(\frac{dX}{dt}\right)^2\frac{1}{X} \tag{3}$$

The net work W_l done against the liquid dominant region as the vapor dominant region grows from $x=0$ to X is given by

$$W_l=\int_0^X P_s\frac{\pi}{4}d^2dx-P_\infty\frac{\pi}{4}d^2X \tag{4}$$

In this equation P_s is the pressure of vapor dominant region (or vapor cone). The second term subtracts work done against the liquid dominant region to accommodate the volume change of the vapor dominant region. Equating the Eq. (3) and Eq. (4), arranging, and differentiating with respect to X

$$X\frac{d^2X}{dt^2}-\frac{1}{2}\left(\frac{dX}{dt}\right)^2-\frac{1}{\rho_l}\left(\frac{k}{d}\right)^2(P_s-P_\infty)X^2=0 \tag{5}$$

The Eq. (5) was named as 'one-dimensional submerged steam jet equation', or simply 'jet equation', for further development in this study.

In order to solve the jet equation, perturbation solution method was used. For the Eq. (5), following initial conditions were considered.

$$t=0,\quad X=X_E(1+\varepsilon),\quad \frac{dX}{dt}=0 \tag{6}$$

The equilibrium jet length is disturbed by the amount εX_E in Eq. (6). A series expansion of $X(t)$ is assumed in the form

$$X(t)=X_0(t)+\varepsilon X_1(t)+\cdots \tag{7}$$

If only terms up to the order of ε are kept, the problem will be linearized. For the pressure of vapor dominant region, it was assumed that the vapor dominant region undergoes the polytropic process, and given by

$$\begin{aligned}P_s&=P_\infty\left(\frac{V_E}{V}\right)^n=P_\infty\left(\frac{X_E}{X}\right)^n\\&=P_\infty\left[\frac{X_E}{X_0(1+\varepsilon X_1/X_0+\cdots)}\right]^n\\&=P_\infty\left(\frac{X_E}{X_0}\right)^n\left(1-\varepsilon n\frac{X_1}{X_0}+\cdots\right)\end{aligned} \tag{8}$$

, where n is a coefficient of polytropic process. The other terms in jet equation also can be expanded in the similar manners. From this process, the governing Eq. (5) and initial conditions are linearized, and the 1st order sets are as followings with the 0th order solution $X_0(t)=X_E$;

DE: $$\frac{d^2X_1}{dt^2}+n\frac{P_\infty}{\rho_l}\left(\frac{k}{d}\right)^2\frac{X_1}{X_E^2}=0 \tag{9}$$

ICs: $$X_1(0)=X_E,\quad \dot{X}_1(0)=0 \tag{10}$$

From the solution of Eq. (9), the frequency is given by

$$f=\frac{1}{2\pi}\frac{1}{X_E}\frac{k}{d}\sqrt{\frac{nP_\infty}{\rho_l}} \tag{11}$$

PREDICTION OF EXPERIMENTS

In order to predict the frequencies using Eq. (11), the expansion coefficient of liquid dominant region, k, was decided as 0.07 from the photos of Fig. 4 and Kim, H. Y. [5]. $k=0.07$ is corresponding to near the half width of expansion of liquid dominant region in Fig. 6. The jet diameter d is 12.4 mm for 10 mm hole from Kim, H. Y. [5]. Adiabatic process was assumed, and $n=\gamma=1.32$. The ambient pressure or water pressure P_∞ was assumed to be atmospheric pressure, 101325 Pa, and the density of water was obtained from steam table.

For the equilibrium jet length, X_E, experimental correlations of Kim, H. Y. [5] was selected, and given by

$$\frac{X}{d_0} = 0.51 B^{-0.70} \left(G_0 / G_m\right)^{0.47} \quad (12)$$

$$B = c_p \left(T_s - T_\infty\right) / h_{fg} \quad (13)$$

$$G_m = 275 kg/m^2 s \quad (14)$$

For the range of steam mass flux over 300 kg/m^{2}s and pool temperature 35~75℃, most of the predictions were within error band 15% as shown in Fig. 7. In Fig. 7, the average deviation and root mean square (RMS) were calculated as follows;

$$Average\ Deviation = \frac{1}{N} \sum_i^N \left(f_{pred} - f_{exp}\right)_i \quad (15)$$

$$RMS = \sqrt{\frac{1}{N} \sum_i^N \left(f_{pred} - f_{exp}\right)_i^2} \quad (16)$$

From these calculations, it was found that the Eq. (11) slightly under-predicted the experimental data.

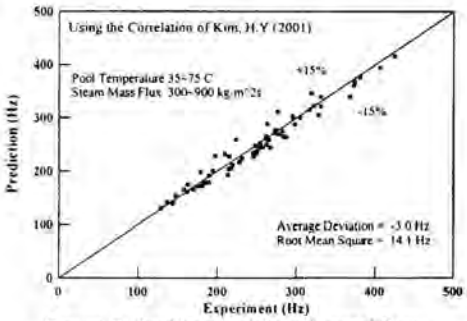

Figure 7: Prediction of Experimental Data

CONCLUSION

The pressure oscillations of submerged steam jet condensation for high steam mass flux were investigated. Experiment showed a different trend of dominant frequency with the reference of steam mass flux 300 kg/m^{2}s. When the steam mass flux was under 300 kg/m^{2}s, the frequency increased as the steam mass flux increased. However, when the steam mass flux was over 300 kg/m^{2}s, the frequency decreased as the steam mass flux increased. The frequency decreased as the pool temperature increased regardless of steam mass flux. For the high steam mass flux region, analytical model was developed based on the balance of kinetic energy that the steam jet gives and the water receives, adopting the theory of submerged turbulent jet. The proposed model excellently predicted the experiments with the error band 15%.

REFERENCES

[1] Cho, S., Song, C. H., Park, C. K., Yang, S. K., and Chung, M. K., 1998, "Experimental Study on Dynamic Pressure Pulse in Direct Contact Condensation of Steam Discharging into Subcooled Water", First Korea-Japan Symposium on Nuclear Thermal Hydraulics and Safety, NTHAS98, Pusan, Korea

[2] Damasio, C., Del Tin, G., Fiegna, G. and Malandrone, M., 1985, "Experimental Study on the Unstable Direct Contact Condensation Regimes", Proc. of the 3rd Int. Topical Meeting on Reactor Thermal Hydraulics, pp. 6.C-1 ~ 6.C-8

[3] Nariai, H. and Aya, I., 1986, "Fluid and Pressure Oscillations occurring at Direct Contact Condensation of Steam Flow with Cold Water", Nuclear Engineering and Design, Vol. 95, pp. 435-45

[4] Hong, S. J., 2001, "Dynamic Characteristics of Steam Jet Condensation in Sparger", PhD. Dissertation, Seoul National University (SNU)

[5] Kim, H. Y., 2001, "A Study on the Characteristics of Direct Contact Condensation of a Steam Jet Discharging into a Quenching Tank through a Single Horizontal Pipe", PhD. Dissertation, Korea Advanced Institute of Science and Technology (KAIST)

[6] Schlichting, H., 1979, "Boundary-Layer Theory", 7th Ed., McGraw-Hill

[7] Blevins, R. D., 1984, "Applied Fluid Dynamics Handbook", Van Nostrand Company

HEFAT 2002
1st International Conference on Heat Transfer, Fluid Mechanics, and Thermodynamics
8-10 April 2002, Kruger Park, South Africa
TJ2

TWO-PHASE FLOW PATTERN MAP FOR EVAPORATION IN HORIZONTAL TUBES: LATEST VERSION

Prof. John R. Thome and Dr. Jean El Hajal

Laboratory of Heat and Mass Transfer
Department of Mechanical Engineering
Swiss Federal Institute of Technology Lausanne
CH-1015 Lausanne, Switzerland
E-mail: john.thome@epfl.ch

ABSTRACT

A two-phase flow pattern map was originally proposed by Kattan, Thome and Favrat (1998a) as part of a new flow pattern based flow boiling model for predicting local heat transfer coefficients during evaporation in horizontal tubes in the fully stratified flow regime, the stratified-wavy regime, the intermittent flow regime, the annular flow regime and for annular flow with partial dryout in Kattan, Thome and Favrat (1998b). Since then, an improved version of this flow pattern map has been proposed by Zürcher, Thome and Favrat (1999) by empirically correcting two of the transition boundaries based on extensive new flow pattern observations for ammonia, but which still requires an iterative solution of numerous equations. Zürcher, Favrat and Thome (2001) have since proposed an even more detailed method for predicting flow pattern transitions by taking into account the intertwined effects of void fraction on flow transition and flow pattern on void fraction, resulting in a very effective map but very complex to implement. In the newest version of this map, whose goal was to simplify the method to avoid iterative calculations as much as possible while retaining its accuracy, the Rouhani-Axelsson (1970) void fraction equation is used in the transition equations rather than the original method of Taitel and Dukler (1976) in this map. This provides a simpler method for calculating the transitions and gives equivalent results. Simulated flow maps for R-134a, R-22 and R-410a are then shown and also the effect of tube diameter on the transition boundaries. Future directions in flow map developments are discussed, such as application of this map to *intube condensation*.

INTRODUCTION

Numerous flow pattern maps have been proposed over the years for predicting two-phase flow regime transitions in horizontal tubes under adiabatic conditions. The map of Taitel and Dukler (1976) is often quoted as well as that of Baker (1954). Some others are those of Hashizume (1983) and Steiner (1993). For evaporation, instead, little is available for predicting flow patterns other than assuming that adiabatic maps apply to diabatic conditions.

Figure 1 from Collier and Thome (1994) depicts the typical flow regimes observed during evaporation inside a horizontal tube, including cross-sectional views of the flow structure. The flow patterns observed are bubbly flow, plug flow, slug flow, stratified-wavy flow, annular flow and annular flow with partial dryout. Presently, flow patterns are classified as follows: *fully-stratified* flow (**S**), *stratified-wavy* flow (**SW**), *intermittent* flow (**I**), *annular* flow (**A**), *mist* flow (**MF**) and *bubbly* flow (**B**). Intermittent flow covers both plug and slug flow (it is essentially a stratified-wavy flow pattern with large amplitude waves that wash the top of the tube). For a detailed definition of the flow patterns used here, refer to those in Collier and Thome (1994).

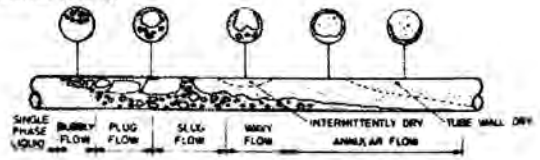

Figure 1. Two-phase flow patterns during evaporation inside a horizontal tube.

As an initial step in this direction, Kattan, Thome and Favrat (1998a) proposed a modification of the Steiner map, which in turn is a modified Taitel-Dukler map, and have introduced a method for predicting the onset of dryout at the top of the tube in evaporating annular flow among other improvements. Since then, Zürcher, Thome and Favrat (1999) have proposed an updated version based on new flow pattern observations for ammonia taken at mass velocities down to about 10 kg/m^{2}s. Zürcher, Favrat and Thome (2001) then proposed a much more complete method for predicting flow pattern transitions by taking into account the interrelationship between void fraction and flow pattern transition, resulting in a very effective map but very complex to implement. The objective here is to describe the newest version of our flow pattern map with its simplified calculation scheme.

UPDATED FLOW PATTERN MAP

The flow regime transition boundaries of the original Kattan-Thome-Favrat flow pattern map are depicted in Figure 2. Bubbly flow is not shown as it occurs at very high mass velocities.

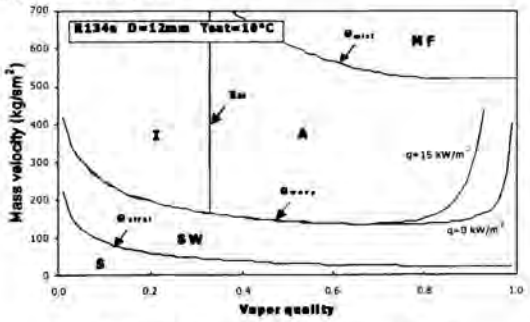

Figure 2. Kattan-Thome-Favrat flow pattern map illustrating flow regime transition boundaries.

Figure 3 defines the geometrical dimensions of a stratified flow, where P_L is the wetted perimeter of the tube, P_V is the dry perimeter in contact with only vapor, h is the height of the completely stratified liquid layer, P_i is the length of the phase interface, and A_L and A_V are the corresponding cross-sectional areas. These six dimensions are normalized using the tube internal diameter d_i to obtain six dimensionless variables:

$$h_{Ld} = \frac{h}{d_i}, P_{Ld} = \frac{P_L}{d_i}, P_{Vd} = \frac{P_V}{d_i}, P_{id} = \frac{P_i}{d_i}$$
$$A_{Ld} = \frac{A_L}{d_i^2}, A_{Vd} = \frac{A_V}{d_i^2} \quad (1)$$

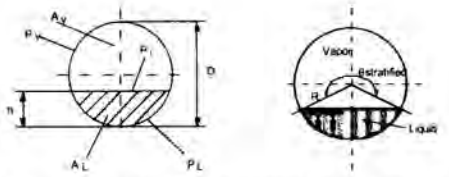

Figure 3. Geometrical parameters for two-phase flow in a circular tube

In this formulation, there are six equations that must be solved iteratively to find the value of h. Furthermore, this calculation is *defacto* a void fraction model (of Taitel-Dukler) since the cross-sectional area of the flow occupied by the vapor is determined, while the flow boiling model of Kattan, Thome and Favrat (1998b) uses instead the Rouhani-Axelsson drift flux model for the void fraction, which advantageously gives the void fraction as a function of total mass flux G_{total} which the above method does not. Hence, it makes sense to use the same void fraction model in both the flow pattern map and the flow boiling heat transfer model, for which the Rouhani-Axelsson model is a better choice as a general method, given as:

$$\varepsilon = \frac{x}{\rho_V}\left[\left(1+0.12(1-x)\left(\frac{x}{\rho_V}+\frac{1-x}{\rho_L}\right)\right) + \frac{1.18(1-x)\left[g\sigma(\rho_L-\rho_V)\right]^{0.25}}{G_{total}\rho_L^{0.5}}\right]^{-1} \quad (2)$$

Then, from the cross-sectional area of the tube A, the values of A_L, A_V, A_{Ld} and A_{Vd} are directly determinable without iteration:

$$A_L = A(1-\varepsilon) \quad (3) \qquad A_V = A\varepsilon \quad (4)$$
$$A_{Ld} = \frac{A_L}{d_i^2} \quad (5) \qquad A_{Vd} = \frac{A_V}{d_i^2} \quad (6)$$

The stratified angle of the dry perimeter of the tube θ_{strat} in Figure 3 remains the only parameter which must be solved

for in an iterative manner from the following geometrically defined equation:

$$A_{Ld} = \frac{1}{8}\left[(2\pi - \theta_{strat}) - \sin(2\pi - \theta_{strat})\right] \quad (7)$$

The dimensionless liquid height can then be determined from the geometric expression:

$$h_{Ld} = 0.5\left(1 - \cos\left(\frac{2\pi - \theta_{strat}}{2}\right)\right) \quad (8)$$

P_{Ld} and P_{Vd} are no longer used in the solution. The geometric expression for P_{id} in terms of θ_{strat} is:

$$P_{id} = \sin\left(\frac{2\pi - \theta_{strat}}{2}\right) \quad (9)$$

Now the transition curve between stratified-wavy flow and intermittent and annular flow is determined using the updated expression of Zürcher, Thome and Favrat (1999) for G_{wavy}, where G_{wavy} is in kg/m^{2}s:

$$G_{wavy} = \left\{\frac{16\,A_{Vd}^3\,g\,d_i\,\rho_L\,\rho_V}{x^2\pi^2\left(1-(2h_{Ld}-1)^2\right)^{0.5}} * \left[\frac{\pi^2}{25\,h_{Ld}^2}(1-x) - F_1(q)\left(\frac{We}{Fr}\right)_L^{-F_2(q)} + 1\right]\right\}^{0.5} + 50 - 75e^{-\left(\frac{\left(x^2-0.97\right)^2}{x(1-x)}\right)} \quad (10)$$

Similarly, the transition curve from stratified-wavy flow to fully stratified flow is determined using the other updated expression of Zürcher, Thome and Favrat (1999) for G_{strat} where G_{strat} is in kg/m^{2}s:

$$G_{strat} = \left\{\frac{(226.3)^2 A_{Ld}\,A_{Vd}^2\rho_V(\rho_L-\rho_V)\mu_L g}{x^2(1-x)\pi^3}\right\}^{\frac{1}{3}} + 20x \quad (11)$$

The other transition curves are determined as in the original method. Thus, the transition between intermittent flow and annular flow (the vertical line on Figure 2) is given by x_{IA}, which is determined by setting the Martinelli parameter X_{tt} equal to 0.34, as:

$$x_{IA} = \left\{\left[0.2914\left(\frac{\rho_V}{\rho_L}\right)^{-1/1.75}\left(\frac{\mu_L}{\mu_V}\right)^{-1/7}\right] + 1\right\}^{-1} \quad (12)$$

This transition has a low bound where it intersects the transition curve of G_{wavy} as shown in Figure 2 and also has an upper bound where it intersects the transition curve of G_{mist} (which is not quite visible in Figure 2). The transition curve from annular and intermittent flow to mist flow gives G_{mist} as:

$$G_{mist} = \left\{\frac{7680A_{Vd}^2 g d_i \rho_L \rho_V \left(\frac{Fr}{We}\right)_L}{x^2\pi^2\xi}\right\}^{0.5} \quad (13)$$

This expression is first evaluated at all values of x to find the minimum value of G_{mist}, which is set to G_{min} at x_{min}, and then $G_{mist} = G_{min}$ for all values of x from $1 \geq x > x_{min}$. Finally, the last transition is that to bubbly flow G_{bubbly}, which is:

$$G_{bubbly} = \left\{\frac{256\,A_{Vd}\,A_{Ld}^2 d_i^{1.25}\rho_L(\rho_L-\rho_V)g}{0.3164\,(1-x)^{1.75}\pi^2\,p_{id}\mu_L^{0.25}}\right\}^{1/1.75} \quad (14)$$

In the above equations, the ratio of the liquid Weber number to the liquid Froude number is given by

$$\left(\frac{We}{Fr}\right)_L = \frac{g d_i^2 \rho_L}{\sigma} \quad (15)$$

while the friction factor is given by the expression

$$\xi = \left[1.138 + 2\log\left(\frac{\pi}{1.5A_{Ld}}\right)\right]^{-2} \quad (16)$$

The non-dimensional empirical exponents $F_1(q)$ and $F_2(q)$ were added to the G_{wavy} boundary equation to include the effect of heat flux on the onset of dryout of the annular

film, i.e. the transition of annular flow into annular flow with partial dryout, the latter which is classified as stratified-wavy flow by the map. These parameters are determined as:

$$F_1(q) = 646.0\left(\frac{q}{q_{crit}}\right)^2 + 64.8\left(\frac{q}{q_{crit}}\right) \quad (17a)$$

$$F_2(q) = 18.8\left(\frac{q}{q_{crit}}\right) + 1.023 \quad (17b)$$

where the Kutateladze (1948) correlation for the critical heat flux q_{crit} was used to normalize the local heat flux:

$$q_{crit} = 0.131\,\rho_V^{1/2} h_{LV} [g(\rho_L - \rho_V)\sigma]^{\frac{1}{4}} \quad (18)$$

IMPLEMENTATION OF NEW VERSION

The initial values required to evaluate the map are: vapor quality (x), total mass velocity of the liquid and vapor (G_{total}), tube internal diameter (d_i), heat flux (q), liquid density (ρ_L), vapor density (ρ_V), liquid dynamic viscosity (μ_L), vapor dynamic viscosity (μ_V), surface tension (σ), and latent heat of vaporization (h_{LV}). The local flow pattern is determined by the following procedure:

1. Choose the values of d_i, G_{total} and q and also those of the physical properties;
2. Choose the value of x for $0 < x < 1$;
3. Evaluate Equation (2);
4. Evaluate Equations (3), (4), (5), and (6);
5. Equation (7) is solved iteratively to find θ_{strat};
6. Equations (8), and (9) are evaluated;
7. Equations (15), (16), (17a), (17b) and (18) are then evaluated;
8. Equations (10), (11), (12), (13), and (14) are evaluated;
9. Compare values obtained with Equations (10), (11), (12), (13), and (14) to the given values of x and G_{total} to identify the particular flow pattern.

For the flow pattern transitions during the thermal design of an evaporator, one should use the design value of G_{total} to evaluate the transition equations. To construct a flow pattern map, either small steps in G_{total} can be used to find the transition points for the curve or a fixed value G_{total} in the general range of interest can be assumed. The effect of the value of G_{total} is evident but is not very significant for the principle transition curves of practical design interest, i.e. G_{strat}, G_{wavy} and G_{mist}, has no effect on x_{IA} but a large effect on G_{bubbly} (see next section). Hence, G_{total} is fixed and x is varied to find the transition points for the transition curves in that case.

COMPARISONS AND SIMULATIONS

Flow pattern map simulations have been run for refrigerant R-134a for its properties at a saturation temperature of 4°C and a heat flux of 10,000 W/m^2, typical of air-conditioning applications. Figure 4 shows the Kattan-Thome-Favrat (1998a) map with the improvements of Zürcher-Thome-Favrat (1999), indicated as "old", compared to the new map evaluated at a fixed value of $G_{total} = 200$ kg/m^{2}s and plotted on a large mass velocity scale to show all the transition curves but for which the stratified and wavy flow transitions are barely evident on the lower axis. The transition to bubbly flow occurs at mass velocities on the order of 2000 kg/m^{2}s, which are not of much practical interest for direct-expansion evaporators. Figure 5 shows the same transition curves on a smaller mass velocity scale (without the bubbly flow curve). For the transition between stratified-wavy flow to intermittent flow, the movement of the curve is shifted to the right, which predicts the more recent flow pattern data of Zürcher, Favrat and Thome (2001) for ammonia better than before (not shown here for space limitations). The effect on this same curve at high vapor qualities is insignificant considering that these boundaries are transition regions, similar to the single-phase transition from laminar to turbulent flow. The effect on the mist flow transition curve is relatively insignificant at the high vapor qualities that are of interest to the thermal design of direct-expansion evaporators (also see comments in next section).

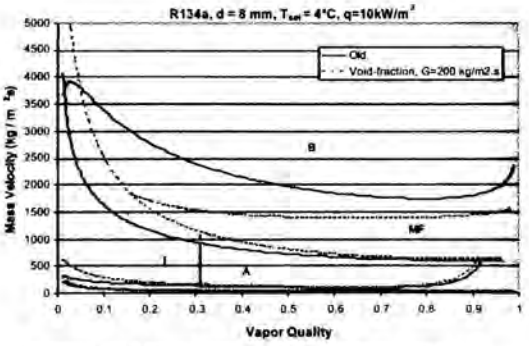

Figure 4. Old versus new flow pattern transitions (all transitions).

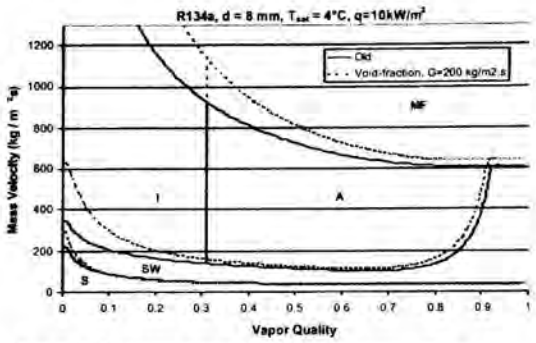

Figure 5. Old versus new flow pattern transitions (w/o bubbly flow).

Figure 6 shows the effect of choosing different fixed values of G_{total} (50, 200 and 1000 kg/m²s) for evaluating the transition equations for R-134a in an 8 mm tube. The effect is negligible, except for the mist flow transition. Hence, to visualize the flow pattern map near design conditions, it can be plotted up for a fixed value of G_{total} near the design conditions. The movement of the curves is attributable to the change in void fraction with mass velocity in Eq. (2). Hence, while the void fraction effects on the curves are expected to be correct, no experimental validation is possible without measuring void fractions as part of our two-phase flow pattern observation tests, which is a topic of future research.

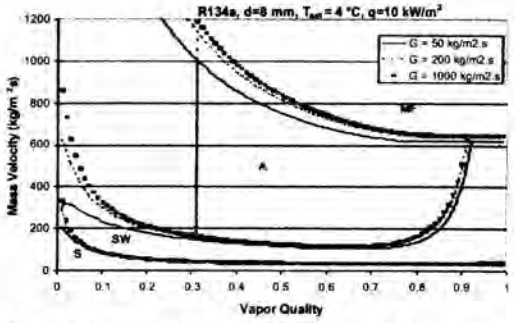

Figure 6. New map showing effect of G_{total} on transitions.

Figure 7 depicts the effect of tube diameter, 8 mm vs. 14 mm that are typical of direct-expansion evaporators, on the transitions for R-134a. Some shifts in the curves can be observed with an enlargement of the annular flow regime boundaries being most significant.

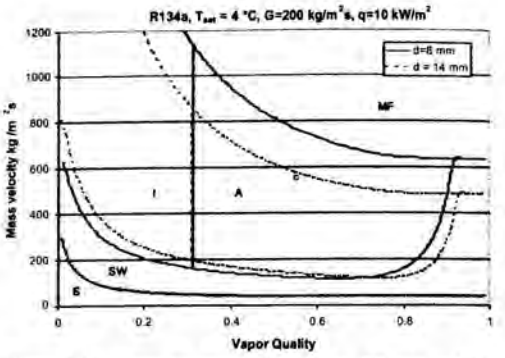

Figure 7. New map comparing transitions of 8 mm and 14 mm tubes.

Figure 8 depicts a comparison of the transition curves for the three refrigerants R-134a, R22 and R410a, two of which are replacements for R22. R22 and R410a have nearly the same transition curves, expect for that from intermittent to annular flow, which is not significant for flow boiling heat transfer as the Kattan, Thome and Favrat (1998b) heat transfer model in fact successfully predicts intermittent heat transfer data assuming the annular flow heat transfer model.

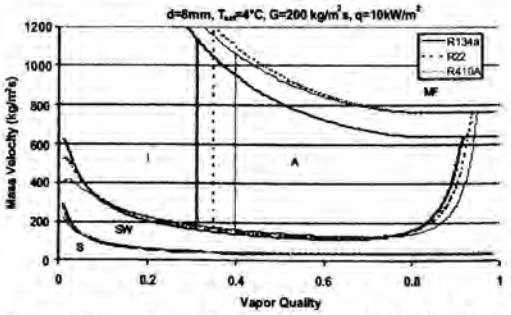

Figure 8. New map comparing transitions of R-134a, R-22 and R-410a.

Hence, the newest version of the two-phase flow pattern map has been presented here which now uses the same void fraction model as in the corresponding flow boiling heat transfer model. In addition, the transition equations are now properly a function of void fraction and mass velocity. Finally, the newest version is easier to implement and has an accuracy similar to that of the more theoretically advanced version presented recently in Zürcher, Favrat and Thome (2001).

FUTURE DIRECTIONS

Our future directions in flow map developments and applications are as follows:

Mist flow transition: The transition equation between the mist flow and annular flow regimes is still that from the Steiner/Taitel-Dukler maps. Flow pattern observations will be taken in the near future to develop a representative database for this transition and thus further verify the accuracy of this transition equation.

Tube diameters: Our present database, while extensive, only covers tubes with internal diameters from 12 to 14 mm. While it is reasonable to expect it to be valid for a wider range because of its fundamental basis originating from the Taitel-Dukler transition theories and Steiner's own database, we are presently obtaining new flow pattern data with the objective to cover tube diameters from 3 to 22 mm, which would be typical of nearly all tube diameters used in heat exchangers (with the exception of fired heaters where tube diameters up to 150 mm are used).

Heat transfer for intube condensation: With several physically justifiable modifications, the adiabatic version of the new flow pattern map is thought to be applicable to condensation within horizontal tubes. A new condensation version of the flow pattern map has in fact already been developed together with a new condensation heat transfer model based on the local two-phase flow structure, similar to our flow boiling model, and will all be described in a future publication.

Two-phase pressure drops: Two-phase pressure drops are known to be a function of flow pattern. Hence, another of our objectives is to develop a flow pattern based frictional pressure drop model that respects the two-phase flow structure of the various flow regimes.

Void fraction measurements: Void fractions should be measured as they play a significant role in flow pattern transition equations. We have recently begun to simultaneously measure void fractions with our flow pattern observations.

SUMMARY

The newest and easiest to implement version of the Thome and coworkers two-phase flow pattern map is described for evaporation in horizontal tubes. The new map predicts flow pattern data for seven different refrigerants covering a wide range of mass velocities (10 to 500 kg/m²s), vapor qualities (0.01 to 0.99) and saturation pressures (about 0.1 to 0.9 MPa). The new map is valid for both adiabatic and diabatic (evaporating) flows.

NOMENCLATURE

A	cross sectional area	m^2
d_i	tube diameter	m
g	acceleration of gravity	m/s^2
G_{bubbly}	bubbly flow transition mass velocity	kg/m^2s
G_{min}	minimum transition mass velocity	kg/m^2s
G_{mist}	mist flow transition mass velocity	kg/m^2s
G_{strat}	stratified flow transition mass velocity	kg/m^2s
G_{total}	total mass velocity of liquid and vapor	kg/m^2s
G_{wavy}	wavy flow transition mass velocity	kg/m^2s
h	liquid height	m
h_{LV}	latent heat of vaporization	J/kg
P_i	liquid-vapor interface	m
P_L	wetted perimeter	m
P_V	dry perimeter	m
q	heat flux	W/m^2
x	vapor quality	-
x_{IA}	intermittent to annular flow transition quality	-
X_{tt}	Martinelli parameter	-

Greek

μ	dynamic viscosity	Ns/m^2
ξ	friction factor	-
ρ	density	kg/m^3
σ	surface tension	N/m

Dimensionless numbers

$F_1(q)$	Non-dimensional exponent	-
$F_2(q)$	Non-dimensional exponent	-
Fr	Froude number	-
We	Weber number	-

Subscripts

crit	critical
d	dimensionless
L	liquid
V	vapor

REFERENCES

- Baker, O. (1954). Design of Pipe Lines for Simultaneous Flow of Oil and Gas, *Oil and Gas J.*, July, pp. 26.
- Collier, J. G. and Thome, J. R. (1994). *Convective Boiling and Condensation*, 3rd Edition, Oxford University Press, Oxford.

- Hashizume, K. (1983). Flow Pattern and Void Fraction of Refrigerant Two-Phase Flow in a Horizontal Pipe, *Bulletin of JSME*, Vol. 26, No. 219, pp. 1597-1602.

- Kattan, N., Thome, J. R. and Favrat, D. (1998a). Flow Boiling in Horizontal Tubes: Part 1- Development of a Diabatic Two-Phase Flow Pattern Map, *J. Heat Transfer*, Vol. 120, No. 1, pp. 140-147.

- Kattan, N., Thome, J. R. and Favrat, D. (1998b). Flow Boiling in Horizontal Tubes: Part 3- Development of a New Heat Transfer Model Based on Flow Pattern, *J. Heat Transfer*, Vol. 120, No. 1, pp. 156-165.

Rouhani, Z. and Axelsson, E. (1970). Calculation of Void Volume Fraction in the Subcooled and Quality Boiling Regions, *Int. J. Heat Mass Transfer*, Vol. 13, pp. 383-393.

- Steiner, D. (1993). Heat Transfer to Boiling Saturated Liquids, *VDI-Wärmeatlas (VDI Heat Atlas)*, Editor: Verein Deutscher Ingenieure, VDI-Gessellschaft Verfahrenstechnik und Chemieingenieurwesen (GCV), Translator: J.W. Fullarton, Düsseldorf.

- Taitel, Y. and Dukler, A. E. (1976). A Model for Predicting Flow Regime Transitions in Horizontal and Near Horizontal Gas-Liquid Flow, *AIChE Journal*, Vol. 22, No. 2, pp. 43-55.

- Zürcher, O., Thome, J.R. and Favrat, D. (1999). Evaporation of Ammonia in a Smooth Horizontal Tube: Heat Transfer Measurements and Predictions, *J. Heat Transfer*, Vol. 121, pp. 89-101.

- Zürcher, O., Favrat, D. and Thome, J.R. (2001). Development of a Diabatic Two-Phase Flow Pattern Map for Horizontal Flow Boiling, *Int. J. Heat Mass Transfer* ,in press

Proceedings of HEFAT2002
1st International Conference on Heat Transfer, Fluid Mechanics, and Thermodynamics
April 8-10, 2002, Kruger Park, South Africa
DF1

TWO-PHASE FLOW WITH PHASE CHANGE IN POROUS MEDIA : A LOCAL NON-EQUILIBRIUM MODEL

F. Duval*, C. Béchaud*, F. Fichot* and M. Quintard**

* IPSN C.E. Cadarache 13108 St Paul Lez Durance. France. Email: duval@sand.cad.cea.fr
** IMFT. al. Soula. 31400 Toulouse. France. Email: quintard@imft.fr

ABSTRACT

A three-temperature macroscopic model is derived using the method of volume averaging to describe two-phase flow with phase change in a porous medium. Macroscopic equations are obtained considering local thermal non-equilibrium between the three phases and a closed form of the phase evaporation rate is proposed depending on the effective properties and macroscopic temperatures. The volume averaging theory provides local closure problems which allow to determine effective properties such as macroscopic heat transfer coefficients and thermal dispersion coefficients. The closure problems are solved for simple unit cells and analytical solutions are presented. A numerical validation is performed which compare solutions of the three-equation model with exact solutions obtained from direct pore-scale simulations. In the case of more complex unit cells, it is first necessary to solve the two-phase flow problem at the pore level. The two-phase flow equations are solved by a diffuse interface model and direct numerical simulations are presented. Afterwards, two-dimensional heat transfer properties are obtained. Finally, a two-dimensional macroscopic simulation of a two-phase flow with phase change in a heated porous bed is presented. Results show the capacity of the macroscopic model to take into account large macroscopic temperature differences, such as those expected in nuclear safety simulations.

NOMENCLATURE

$A_{\beta\sigma}$	area of the $\beta-\sigma$ interface (m^2).
$\mathbf{b}_{\beta\sigma}$	vector mapping variable (m).
$C_{p\beta}$	β-phase heat capacity ($J.kg^{-1}.K^{-1}$).
d_p	particle diameter (m).
$h_{\beta\sigma}^{\text{eff}}$	effective heat transfer coefficient ($W.m^{-3}.K^{-1}$).
k_β	thermal conductivity of the β-phase ($W.m^{-1}.K^{-1}$).
$\mathbf{K}_\beta^*$	effective thermal dispersion tensor for the β-phase ($W.m^{-1}.K^{-1}$).
Δh	heat of vaporization per unit mass ($J.kg^{-1}$).
$\mathbf{l}_i$	unit lattice vectors.
$\dot{m}_e$	mass rate of evaporation ($kg.m^{-3}.s^{-1}$).
$\mathbf{n}_{\beta\sigma}$	unit normal vector directed from the β-phase towards the σ-phase.
S	liquid saturation.
$s_{\beta\sigma}^{\gamma}$	scalar mapping variable.
T_β	β-phase temperature (K).
T^{sat}	saturation temperature (K).
$\langle T_\beta \rangle$	superficial average temperature of the β-phase (K)
$\langle T_\beta \rangle^\beta$	intrinsic average temperature of the β-phase (K)
$\tilde{T}_\beta$	spatial deviation temperature in the β-phase (K)
$\mathcal{V}$	averaging volume (m^3)
$\mathbf{v}_\beta$	β-phase velocity ($m.s^{-1}$).
$\langle \mathbf{v}_\beta \rangle^\beta$	intrinsic phase averaged velocity ($m.s^{-1}$).
$\mathbf{w}$	speed of displacement of the liquid-vapor interface ($m.s^{-1}$).

Greek letters

ε	porosity.
ε_β	volume fraction of the β-phase.
ρ_β	density in the β-phase ($kg.m^{-3}$).
ϖ	volumetric power ($W.m^{-3}$).

Subscripts

g, ℓ, s	gas, liquid, solid phase.
i	interface.

INTRODUCTION

Two-phase flow with phase change in porous media appears in a large number of engineering applications including drying process, heat-exchangers design and nuclear safety. The assumption of local thermal equilibrium, that leads to a one-temperature macroscopic model, is acceptable for many physical situations involving partially saturated porous media with phase-

change like, for instance, most drying processes [5, 21]. The one-temperature model does not require numerous macroscopic heat transfer properties, which greatly reduces the complexity of the heat transfer analysis. However, when the physical properties are highly contrasted and when the particle or pore diameters are not small enough, the constraints associated with the local thermal equilibrium are no longer valid [17]. Moreover, when there is an important heat generation in the solid phase the system may become rapidly far from local thermal equilibrium [9]. For instance, the assumption of local thermal equilibrium is called into questions in the case of debris bed cooling [6]. For situations in which local thermal equilibrium fails to be valid, two and three-equation models have been proposed [2, 4, 11, 20]. These models were obtained heuristically. Since the heat transfer coefficients that appear in these models are very difficult to determine experimentally, they are generally determined by using correlations based on generalizations of results obtained in the case of single-phase flows through porous media or two-phase flows in pipes. From a theoretical point of view, a three-equation model has been proposed based on the volume averaging theory [14]. However, this model does not take into account the phase change process. The purpose of this paper is to develop a three-temperature macroscopic model based on the volume averaging theory for describing heat transfer in porous heat generating media subject to a two-phase flow with phase change. In this new model, the evaporation rate depends on the macroscopic temperatures and the phase change or saturation temperature at the liquid-vapor interface. Both macroscopic heat transfer coefficients and evaporation rate can be determined analytically for some simplified geometries or numerically for more complex configurations, from local boundary value problems.

AVERAGED EQUATIONS

The problem under consideration is illustrated in Fig. 1, where the solid phase is assumed to be fixed. It is assumed further that the properties of the fluids do not change strongly with temperature. At this point, we assume that the velocity of the two phases are known fields which have to be determined for a given position of the interface.

The governing differential equations that describe the heat transfer process for the three phases subjected to a homogeneous volumetric power ϖ are given by :

$$(\rho C_p)_g \frac{\partial T_g}{\partial t} + (\rho C_p)_g \nabla . (\mathbf{v}_g T_g) = \nabla . (k_g \nabla T_g) \tag{1}$$

$$(\rho C_p)_l \frac{\partial T_l}{\partial t} + (\rho C_p)_l \nabla . (\mathbf{v}_l T_l) = \nabla . (k_l \nabla T_l) \tag{2}$$

$$(\rho C_p)_s \frac{\partial T_s}{\partial t} = \nabla . (k_s \nabla T_s) + \varpi \tag{3}$$

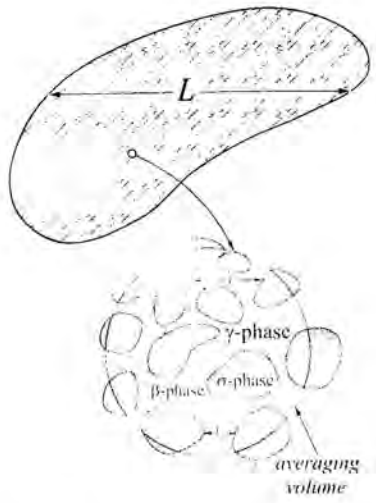

Figure 1. Homogeneous three-phase system.

The boundary conditions at the gas-solid, liquid-gas and liquid-solid interfaces are :

$$\text{B.C.1} \qquad T_g = T_s \qquad \mathbf{n}_{gs} . k_g \nabla T_g = \mathbf{n}_{gs} . k_s \nabla T_s \tag{4}$$

$$\text{B.C.2a} \qquad T_l = T^{sat} \qquad T_g = T^{sat} \tag{5}$$

$$\text{B.C.2b} \quad \mathbf{n}_{lg} . \Delta h \rho_l (\mathbf{v}_l - \mathbf{w}) = \mathbf{n}_{lg} . (k_g \nabla T_g - k_l \nabla T_l) \tag{6}$$

$$\text{B.C.3} \qquad T_l = T_s \qquad \mathbf{n}_{ls} . k_l \nabla T_l = \mathbf{n}_{ls} . k_s \nabla T_s \tag{7}$$

We recall below the volume-averaged continuity equations [21]

$$\frac{\partial \varepsilon_g \rho_g}{\partial t} + \nabla . (\varepsilon_g \rho_g \langle \mathbf{v}_g \rangle^g) = \dot{m}_g \tag{8}$$

$$\frac{\partial \varepsilon_l}{\partial t} + \nabla . \left(\varepsilon_l \langle \mathbf{v}_l \rangle^l \right) = -\frac{\dot{m}_g}{\rho_l} \tag{9}$$

In these equations, the mass rate of evaporation $\dot{m}_g$ is given by :

$$\dot{m}_g = -\frac{1}{\mathcal{V}} \int_{A_{gl}} \rho_g \mathbf{n}_{gl} . (\mathbf{v}_g - \mathbf{w}) \, dA \tag{10}$$

The different average temperatures are defined according to :

$$\langle T_\beta \rangle = \frac{1}{\mathcal{V}} \int_{\mathcal{V}_\beta} T_\beta d\mathcal{V} = \frac{\mathcal{V}_\beta}{\mathcal{V}} \frac{1}{\mathcal{V}_\beta} \int_{\mathcal{V}_\beta} T_\beta d\mathcal{V} = \varepsilon_\beta \langle T_\beta \rangle^\beta \tag{11}$$

The pore-scale temperature deviation in the β-phase is defined according to Gray's decomposition [7]:

$$T_\beta = \langle T_\beta \rangle^\beta + \tilde{T}_\beta \tag{12}$$

From the pore-scale equations 1-3, volume averaging leads to the following macroscopic equation for the liquid phase:

$$\begin{aligned}
&\varepsilon_l (\rho C_p)_l \left(\frac{\partial \langle T_l \rangle^l}{\partial t} + \langle \mathbf{v}_l \rangle^l . \nabla \langle T_l \rangle^l \right) + (\rho C_p)_l \nabla . \langle \tilde{\mathbf{v}}_l \tilde{T}_l \rangle \\
&\quad \dot{m}_g C_{pl} \left(\langle T_l \rangle^l - T^{sat} \right) = -\nabla \varepsilon_l . k_l \nabla \langle T_l \rangle^l \\
&+\nabla \left[\varepsilon_l k_l \nabla \langle T_l \rangle^l + \frac{k_l}{\mathcal{V}} \int_{A_{lg}} \mathbf{n}_{lg} \tilde{T}_l \, dA + \frac{k_l}{\mathcal{V}} \int_{A_{ls}} \mathbf{n}_{ls} \tilde{T}_l \, dA \right] \\
&\quad + \frac{k_l}{\mathcal{V}} \int_{A_{lg}} \mathbf{n}_{lg} . \nabla \tilde{T}_l \, dA + \frac{k_l}{\mathcal{V}} \int_{A_{ls}} \mathbf{n}_{ls} . \nabla \tilde{T}_l \, dA
\end{aligned} \tag{13}$$

Equations similar to 13 are available for both the gas and solid phases but are not listed here. In order to obtain a closed form for equation 13, one needs to develop a boundary value problem for $\tilde{T}_l$. This problem is derived from equations 2 and 13 and by introducing the spatial decomposition 12 in the boundary conditions 5 and 7. Equation 6 is an auxiliary condition [19] that allows us to determine the mass rate of evaporation at the macroscopic level on the basis of the closure problems derived later.

Several macroscopic non-equilibrium source terms involving averaged temperatures can be found in the boundary value problem for the deviations. A closed form of the averaged equation 13 can be obtained if the deviations are represented in terms of these macroscopic source terms [15]. A convenient form for the mapping between averaged temperatures and liquid deviation temperatures is expressed as follows

$$\begin{aligned}
\tilde{T}_l = &\mathbf{b}_{lg} . \nabla \langle T_g \rangle^g + \mathbf{b}_{ll} . \nabla \langle T_l \rangle^l + \mathbf{b}_{ls} . \nabla \langle T_s \rangle^s \\
&- s^l_{ll} (\langle T_l \rangle^l - T^{sat}) - s^l_{gl} (\langle T_g \rangle^g - T^{sat}) \\
&- s^l_{sl} (\langle T_s \rangle^s - T^{sat})
\end{aligned} \tag{14}$$

Here $\mathbf{b}_{l\beta}$ and $s^l_{\beta l}$ are referred to as closure variables for which we need to develop local closure problems. It is assumed that the flow, at the closure level, is quasi-static [10, 14]. We refer to [14, 17, 15] for a complete description on how to derive these problems. The closure problem for the scalar s^β_{ll} mapping variables is given by

$$\rho_g C_{pg} \mathbf{v}_g . \nabla s^g_{ll} = k_g \nabla^2 s^g_{ll} - \varepsilon_g^{-1} \left(h^{gl}_{ll} + h^{gs}_{ll} \right) \tag{15}$$

$$\rho_l C_{pl} \mathbf{v}_l . \nabla s^l_{ll} = k_l \nabla^2 s^l_{ll} - \varepsilon_l^{-1} \left(h^{lg}_{ll} + h^{ls}_{ll} \right) \tag{16}$$

$$0 = k_s \nabla^2 s^s_{ll} + \varepsilon_s^{-1} \left(h^{sg}_{ll} + h^{sl}_{ll} \right) \tag{17}$$

$$\text{B.C.1} \quad s^g_{ll} = s^s_{ll} \quad , \quad \mathbf{n}_{gs} . k_g \nabla s^g_{ll} = \mathbf{n}_{gs} . k_s \nabla s^s_{ll} \tag{18}$$

$$\text{B.C.2a} \quad s^l_{ll} = 1 \quad , \quad s^s_{ll} = 0 \tag{19}$$

$$\text{B.C.3} \quad s^l_{ll} = s^s_{ll} + 1 \quad , \quad \mathbf{n}_{ls} . k_s \nabla s^s_{ll} = \mathbf{n}_{ls} . k_l \nabla s^l_{ll} \tag{20}$$

$$s^\beta_{ll}(\mathbf{x} + \mathbf{l}_i) = s^\beta_{ll}(\mathbf{x}) \, , \, i = 1, 2, 3 \, , \, \beta = g, \ell, s \tag{21}$$

$$\langle s^\beta_{ll} \rangle = 0 \, , \, \beta = g, \ell, s \tag{22}$$

In this problem, Eq. 21 corresponds to periodicity boundary conditions for $\tilde{T}_\beta$ [17], and we have adopted the following notation

$$h^{\beta\sigma}_{ll} = \frac{k_\beta}{\mathcal{V}} \int_{A_{\beta\sigma}} \mathbf{n}_{\beta\sigma} . \nabla s^\beta_{ll} \, dA \tag{23}$$

Equations similar to Eq. 14 are available for the other phases [3]. Using representation 14 and some approximations [17, 18, 15, 14], the averaged equation 13 for the liquid phase becomes

$$\begin{aligned}
&\varepsilon_l (\rho C_p)_l \left(\frac{\partial \langle T_l \rangle^l}{\partial t} + \langle \mathbf{v}_l \rangle^l . \nabla \langle T_l \rangle^l \right) = \nabla . \left(\mathbf{K}^*_l . \nabla \langle T_l \rangle^l \right) \\
&\quad - \left(h^{lg}_{ll} + h^{ls}_{ll} - \dot{m}_g C_{pl} \right) \left(\langle T_l \rangle^l - T^{sat} \right) \\
&- \left(h^{lg}_{gl} + h^{ls}_{gl} \right) \left(\langle T_g \rangle^g - T^{sat} \right) - \left(h^{lg}_{sl} + h^{ls}_{sl} \right) \left(\langle T_s \rangle^s - T^{sat} \right)
\end{aligned} \tag{24}$$

In this equation, $\mathbf{K}^*_l$ and $h^{\gamma\sigma}_{\beta l}$ are the effective thermal dispersion tensor and effective heat exchange coefficient respectively. These macroscopic properties are defined explicitly in terms of the mapping variables and can be calculated from local closure problems. Similar developments can be made for the other phases, results are given in [3].

The mass rate of evaporation that appears in the macroscopic equation 24 is derived from the surface averaging of the auxiliary condition 6, it takes the form:

$$\dot{m}_g \, \Delta h = \sum_{\beta = \ell, g, s} \left(h^{gl}_{\beta l} + h^{lg}_{\beta l} \right) \left(\langle T_\beta \rangle^\beta - T^{sat} \right) \tag{25}$$

RESULTS FOR ONE-DIMENSIONAL UNIT CELLS

Analytical solutions for the local closure problems may be obtained in some simplified geometrical configurations such as stratified media [14, 17, 15]. Unit cells associated with the stratified systems consider Solid-Liquid-Gas (SLG) and Solid-Gas-Liquid (SGL) configurations.

The thickness of the strata ℓ_l, ℓ_g and ℓ_s are defined according to the characteristic length of the unit cell H by $\ell_\beta = H\varepsilon_\beta$.

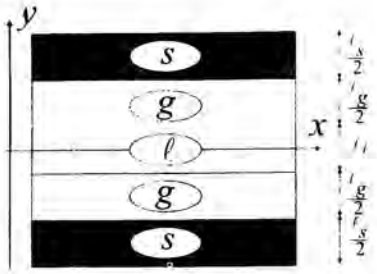

Figure 2. Stratified unit cell : Solid-Gas-Liquid (SGL) case.

$H = \ell_\ell + \ell_g + \ell_s$. In the case of the stratified SGL unit cell, macroscopic heat exchange coefficients are obtained as :

$$H^2 h_{\ell\ell}^{ex} = \frac{12k_\ell}{\varepsilon_\ell}, \quad H^2 h_{g\ell}^{ex} = \frac{24k_g(2\varepsilon_s k_s + 3\varepsilon_g k_s)}{\varepsilon_g(4\varepsilon_s k_g + 3\varepsilon_g k_s)}$$
$$H^2 h_{\ell g}^{ex} = \frac{72k_g k_s}{(4\varepsilon_s k_g + 3\varepsilon_g k_s)}, \quad H^2 h_{gg}^{ex} = \frac{48k_s k_g}{(4\varepsilon_s k_g + 3\varepsilon_g k_s)} \qquad (26)$$
$$H^2 h_{sg}^{ex} = \frac{24k_s k_g}{(4\varepsilon_s k_g + 3\varepsilon_g k_s)}$$

The transport coefficients which are not listed are equal to zero. For complex and realistic unit-cells, one needs to solve numerically the boundary value problems for $\mathbf{b}_{\ell\beta}$ and $s^{\ell}_{\beta r}$. Numerical procedures to solve these problems can be found in [17, 15]. In this case, a direct numerical simulation, based on a diffuse interface model [1, 8], is performed at the pore-scale to provide the required velocity fields and the interface position.

NUMERICAL EXPERIMENTS

In this section, following [16] in the case of two-phase systems, we present a comparison between averaged temperatures computed from direct solution of the pore-scale equations 1-2-3 and theoretical predictions of the three-equation model. This has been done for the symmetric unit-cell shown in Fig. 2.

At the pore level, the one-dimensional heat-diffusion moving boundary problem is calculated numerically using an enthalpy method on the half-cell $0 \leq y \leq H/2$. At the macroscopic level, the three-temperature model and equation 9 provide average temperatures and liquid saturation evolutions. The considered system is repeated infinitely in all directions so there is no gradient of the macroscopic temperatures.

Two tests are performed to evaluate the validity of the model. The first test case starts with a saturated porous medium $S = 1$, $H = 0.01$ m, $\varepsilon_s = 0.6$ and local thermal equilibrium : $\langle T_\beta \rangle^\beta = T^{sat}$, the volumetric power in the solid phase is given by $\varpi = 10^7\,\mathrm{W.m^{-3}}$. The second test case starts with an unsatured porous medium $S = 0.9$ without volumetric power but with an initial temperature difference between the s-phase, g-phase and ℓ-phase : $\langle T_s \rangle^s = \langle T_\ell \rangle^\ell + 60\,\mathrm{K}$, $\langle T_g \rangle^g = \langle T_\ell \rangle^\ell + 30\,\mathrm{K}$ and $\langle T_\ell \rangle^\ell = T^{sat}$. The values of the thermo-physical properties are : $(\rho C_p)_\ell = 4\,10^6\,\mathrm{J.m^{-3}.K^{-1}}$, $(\rho C_p)_g = 2\,10^3\,\mathrm{J.m^{-3}.K^{-1}}$, $(\rho C_p)_s = 3.5\,10^6\,\mathrm{J.m^{-3}.K^{-1}}$, $k_\ell = 0.68\,\mathrm{W.m^{-1}.K^{-1}}$, $k_g = 0.25\,\mathrm{W.m^{-1}.K^{-1}}$, $k_s = 17\,\mathrm{W.m^{-1}.K^{-1}}$, $T^{sat} = 373\,\mathrm{K}$, $\Delta h = 2\,10^6\,\mathrm{J.kg^{-1}}$.

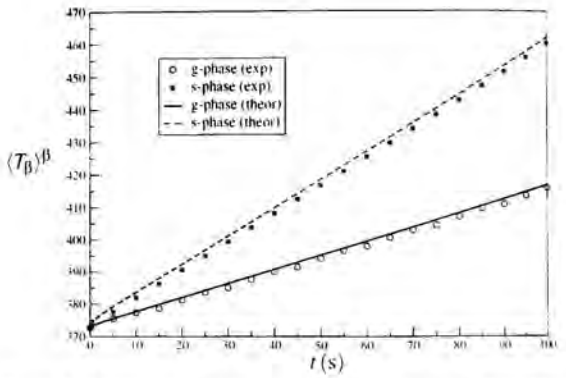

Figure 3. Macroscopic temperatures : comparison between theoretical results and numerical experiments. Test 1 (with volumetric power).

Figs. 3 and 4 show the macroscopic temperatures $\langle T_g \rangle^g$ and $\langle T_s \rangle^s$ as functions of time for both the theoretical solution and the pore-scale numerical experiment. The macroscopic temperature of the liquid phase remains constant during the phase change process, $\langle T_\ell \rangle^\ell = T^{sat}$, and is not plotted here. The theoretical results are in very good agreement with the numerical experiments despite the fact that both tests are strongly unsteady. Fig. 5 represents the evolutions of the liquid saturation $S = \varepsilon_\ell / \varepsilon$ and shows also a very good agreement. It must be noticed that the "experimental" liquid saturation is obtained indirectly from the temperature field, because of the use of an enthalpy method. This numerical method does not provide the exact position of the phase change boundary (no explicit front tracking). This explains the slight difference when averaged liquid and gaseous temperatures are close to each other as shown in Fig. 5 for the second test.

TWO-DIMENSIONAL MACROSCOPIC SIMULATION

The three-equation model presented in this paper has been implemented in the three-dimensional module of the CATHARE2 code [12]. CATHARE2 is a two-fluid six-equations

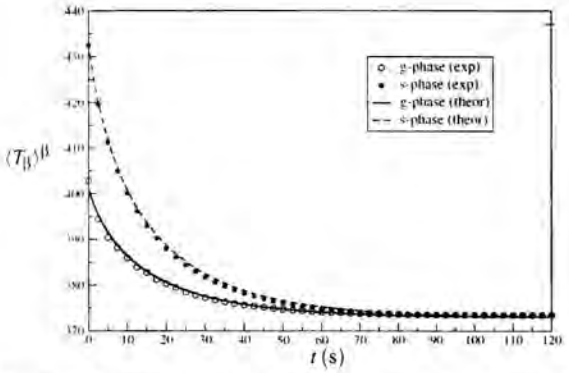

Figure 4. Macroscopic temperatures : comparison between theoretical results and numerical experiments. Test 2 (without volumetric power).

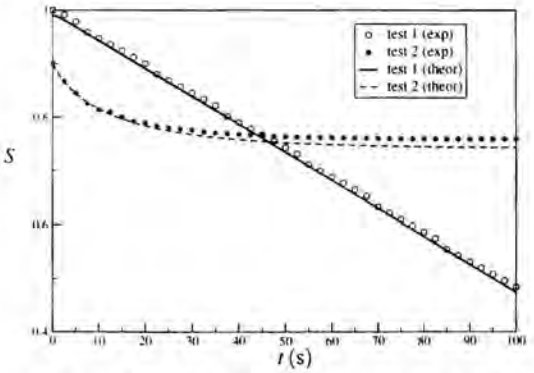

Figure 5. Liquid saturation : comparison between theoretical results and numerical experiments.

thermal-hydraulic code. We refer to [3] for the implementation and the procedure to deal with the non-equilibrium terms and the effective properties. At the macroscopic level, the averaged momentum equations are described by the classical generalized Darcy's law [3, 9].

The considered problem is a porous medium formed by spherical particles ($\varepsilon = 0.5$, $d_p = 10^{-3}$ m), uniformly heated with $\varpi = 2.10^6\,\mathrm{W.m^{-3}}$. The porous bed occupies the lower left corner of a cavity of width : 0.2 m, and height : 1 m, as shown in Fig. 6. The heated bed is flooded by liquid injection at the empty bottom side with $\langle \mathbf{v}_l \rangle^l = 0.05\,\mathrm{m.s^{-1}}$.

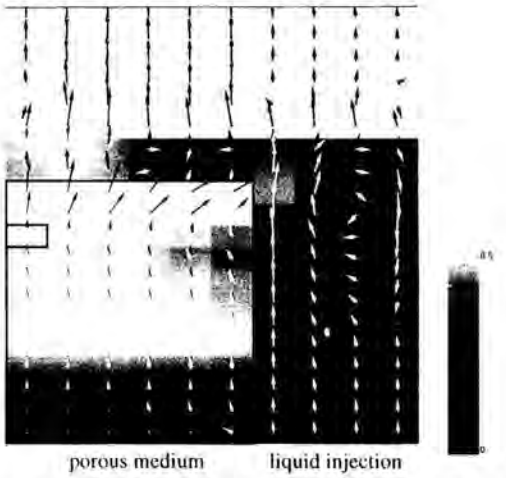

Figure 6. Void fraction $\alpha = 1 - S$ and velocity fields (black arrows : g-phase, white arrows : ℓ-phase). Black frame : porous medium. Reference pressure : $2.1\,10^6$ Pa.

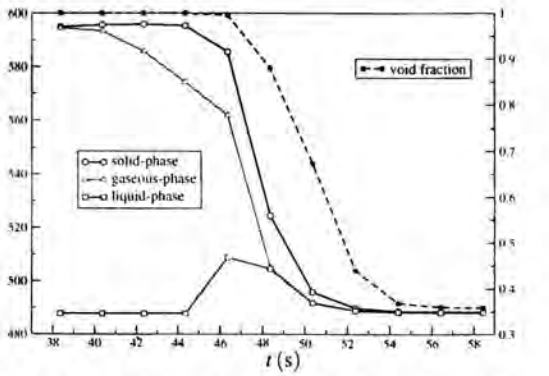

Figure 7. Macroscopic temperatures and void fraction evolutions for the grid block located at the left border as marked in Fig. 6. Left y-axis : $\langle T_\beta \rangle^\beta$, right y-axis : α.

The flow velocities and the void fraction distribution plotted in Fig. 6 show the importance of the two-dimensional convection on porous media coolability as mentioned in [3, 6, 13]. In Fig. 7, the evolutions of the macroscopic temperatures and void fraction at a particular location of the computational domain illustrate the importance of the non-equilibrium model in such reflooding pro-

cesses. Large temperature differences appear when the coolant flow is evaporated in an overheated porous bed.

CONCLUSION

A three-equation model to describe two-phase flow with phase change in a porous medium has been proposed using the framework of the volume averaging theory. Thermal non-equilibrium is considered. Macroscopic equations involve effective properties and relevant non-equilibrium terms. Differences between the macroscopic temperatures and the saturation temperature appear explicitly in the macroscopic equations and in the closed form of the mass rate of evaporation. In addition, several local problems have been derived that provide a mathematical determination of the effective properties. These effective properties have been calculated in the case of simple one-dimensional unit-cells. For these cases, the comparison between theoretical predictions of the three-equation model and pore-scale numerical experiments showed a good agreement, and this confirms the interest of the three-equation model. Finally, a two-dimensional macroscopic simulation illustrates the ability of the model to deal with non-equilibrium situations and strong unsteady processes.

REFERENCES

[1] D.M. Anderson, G.B. McFadden, and A.A. Wheeler. Diffuse-interface methods in fluid mechanics. *Annual Review of Fluid Mechanic*, 30:139–165, 1998.

[2] S. Angelini, W.W. Yuen, and T.G. Theofanous. Premixing-related behaviour of steam explosions. In *CSNI Specialists Meeting on Fuel-Coolant Interactions*, pages 99–129, Santa Barbara, California, USA, January 1993. OECD Nuclear Energy Agency. NUREG/CP-0127.

[3] C. Béchaud, F. Duval, F. Fichot, M. Quintard, and M. Parent. Debris bed coolability using a 3-D two phase model in a porous medium. In *ICONE 9*, Nice, 8-12 April 2000.

[4] G. Berthoud and M. Valette. Development of a multidimensional model for the premixing phase of a fuel-coolant interaction. *Nuclear Engineering and Design*, 149:409–418, 1994.

[5] J.V. Daurelle, F. Topin, and R. Occelli. Modeling of coupled heat and mass transfers with phase change in a porous medium : Application to superheated steam drying. *Numerical Heat Transfer*, A(33):39–63, 1988.

[6] E. Decossin. Numerical investigations on particulate debris bed coolability : Critical analysis of the Silfide experimental project. In *Ninth International Topical Meeting on Nuclear Reactor Thermal Hydraulics (NURETH-9)*, October 1999. San Francisco, California.

[7] W.G. Gray. A derivation of the equations for multi-phase transport. *Chemical Engineering Science*, 30:229–233, 1975.

[8] D. Jacqmin. Contact-line dynamics of a diffuse fluid interface. *Journal of Fluid Mechanics*, 402:57–88, 2000.

[9] M. Kaviany. *Principles of Heat Transfer in Porous Media*. Mechanical Engineering Series. Springer, second edition, 1995.

[10] D. Lasseux, M. Quintard, and S. Whitaker. Determination of permeability tensors for two-phase flow in homogeneous porous media : Theory. *Transport in Porous Media*, 24:107–137, 1996.

[11] V.V. Likhanskii, A.I. Loboiko, and O.V. Khoruzhii. Critical heat fluxes when boiling occurs in a non-uniform heat-releasing porous medium. *Atomic Energy*, 84(4):230–236, 1998.

[12] F. Majhoub, I. Dor, and C. Morel. The three-dimensional module of the Cathare code. Technical Report 99-032, SMTH/LMDS/EM, May 1999.

[13] P. Mayr, M. Burger, M. Buck, W. Schmidt, and G. Lohnert. Investigations on the coolability of debris in the lower head with WABE-2D and MESOCO-2D. *OECD/CSNI Workshop on In-Vessel Core Debris Retention and Coolability*, March 1998.

[14] F. Petit, F. Fichot, and M. Quintard. Ecoulement diphasique en milieux poreux : Modèle à non-equilibre local. *Int. J. Therm. Sci.*, 38:239–249, 1999.

[15] M. Quintard, M. Kaviany, and S. Whitaker. Two-medium treatment of heat transfer in porous media : Numerical results for effective properties. *Advances in Water Resources*, 20:77–94, 1997.

[16] M. Quintard, B. Ladevie, and S. Whitaker. Effect of homogeneous and heterogeneous source terms on the macroscopic description of heat transfer in porous media. In *Symposium on Energy Engineering in the 21st Century*, volume 2, pages 482–489, Hong Kong, January 2000.

[17] M. Quintard and S. Whitaker. One and two-equation models for transient diffusion processes in two-phase systems. *Advances in Heat Transfer*, 23:369–464, 1993.

[18] M. Quintard and S. Whitaker. Local thermal equilibrium for transient heat conduction : Theory and comparison with numerical experiments. *International Journal of Heat and Mass Transfer*, 38(15):2779–2796, 1995.

[19] M. Quintard and S. Whitaker. Dissolution of an immobile phase during flow in porous media. *I&EC Research*, 38(3):833–844, 1999.

[20] M. Sozen and K. Vafai. Analysis of the non-thermal equilibrium condensing flow of a gas through a packed bed. *International Journal of Heat and Mass Transfer*, 33(6):1247–1261, 1990.

[21] S. Whitaker. Coupled transport in multiphase systems : A theory of drying. *Advances in Heat Transfer*, 31:1–102, 1998. Academic Press,New-York.

HEFAT2002:
1st International Conference on Heat Transfer, Fluid Mechanics, and Thermodynamics
8-10 April 2002, Kruger Park, South Africa
LV1

REFRIGERANT OUTGASSING FROM COMPRESSOR LUBRICANT OIL FLOWING THROUGH PIPES

V. T. Lacerda, A. T. Prata
Department of Mechanical Engineering
Federal University of Santa Catarina
88040-900 Florianópolis, SC - BRAZIL

F. Fagotti
Brazilian Compressor Industry - EMBRACO
89219-901 Joinville, SC - BRAZIL

ABSTRACT

The interaction between the refrigeration oil and the refrigerant working fluid is relevant to several phenomena occurring inside refrigerating systems. Regarding the refrigeration cycle, good miscibility of oil and refrigerant assure easy return of circulating oil to the compressor through the reduction of the oil viscosity. Inside the compressor the lubricant is mainly used for leakage sealing, cooling of hot elements and lubrication of sliding parts. In the compressor bearing systems the presence of refrigerant dissolved in the oil greatly influences the performance and reliability of the compressor due to the outgassing experienced by sudden changes in temperature and pressure resulting in a two-phase mixture with density and viscosity strongly affecting the lubricant characteristics. A general understanding of the oil-refrigerant mixture flow is crucial in developing lubrication models to be used in analysis and simulation of fluid mechanics problems inside the compressor. In the present investigation the refrigeration oil flow with refrigerant outgassing is explored experimentally. A mixture of oil saturated with refrigerant is forced to flow in two straight horizontal tubes of constant diameter. One tube is used for flow visualization and the other is instrumented for pressure and temperature measurements. At the tubes inlet liquid state prevails and as flow proceeds the pressure drop reduces the gas solubility in the oil and outgassing occurs. Initially small bubbles are observed and eventually the bubble population reaches a stage where foaming flow is observed. Pressure and temperature distributions are measured along the flow and from that mixture quality and void fraction were estimated. The flow visualization allowed identification of the two-phase flow regimes experienced by the mixture and the applicability of some flow regime maps was verified.

INTRODUCTION

The present investigation deals with a two component liquid mixture flowing through a small diameter pipe. One component has a very low vapor pressure and remains in the liquid state throughout the pipe length. The other component has a vapor pressure that is attained along the pipe length resulting in evaporation and outgassing from the liquid mixture. Outgassing due to solubility reduction is a common phenomenon that occurs in engineering and nature. In this work the motivation to explore outgassing comes from its application to the refrigeration industry, particularly to compressor design.

With the replacement of chlorofluorcarbons (CFCs) and hydrochlorofluorcarbons (HCFCs) refrigerants due to environmental problems (Groll [1]), the solubility and miscibility between refrigerants and lubricant oils became of crucial importance and debate. This is so because of importance that refrigerant absorption and release from the oil has on both the compressor design and on the global performance of the refrigerating system (Lacerda et al. [2]).

The refrigerant solubility in the lubricating oil increases with pressure and decreases with temperature as shown in Fig. 1 for a mixture of 1, 1, 1, 2-tetrafluorethane (R-134a) and ester oil EMKARATE RL10H. In flow regions with adverse pressure gradient such the ones typical of constant diameter pipe flow, refrigerant is released from the liquid mixture and

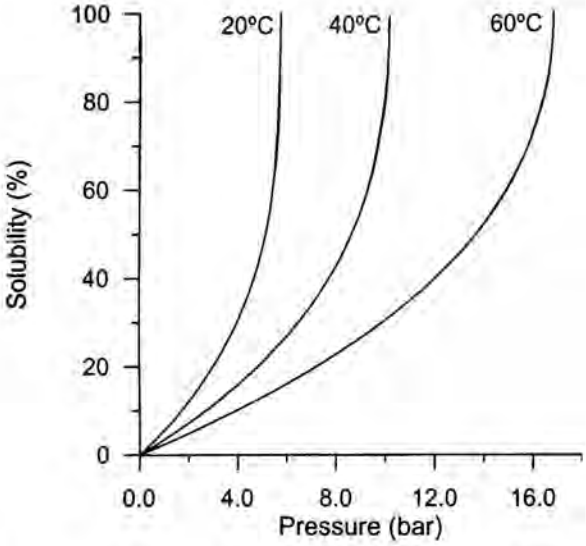

Fig. 1 Solubility of R-134a in ester oil EMKARATE RL10H (from data of ICI Group of Companies).

bubbles may occur. Eventually, bubble formation can become so intense that a foaming flow can be observed. Examples where this can occur in refrigerating systems, particularly inside the compressor, include the bearings and the piston-cylinder clearance in reciprocating configurations.

This contribution focuses on the experimental investigation of oil-refrigerant mixture flow with refrigerant outgassing occurring due to solubility decrease. An experimental setup was designed and built to promote the mixture flow through two straight horizontal constant diameter tubes. One tube is made of glass and is used for flow visualization, and the other is a metallic tube that is instrumented for pressure and temperature measurements. In what follows the experimental setup is described and results are explored focusing on the understanding of general aspects of the mixture flow. The main motivation of the present work is to improve the understanding of this complex flow to construct physical and mathematical models for exploring the fluid mechanics within the compressor parts.

EXPERIMENTAL SETUP

The experimental test facility was designed to produce a steady flow of oil and refrigerant mixture where the pressure drop would suffice to reduce the refrigerant solubility in the oil yielding several configurations of the resulting two-phase flow. A general view of the experimental apparatus is shown in Fig. 2.

As seen from the Fig. 2 there are four tanks, two for high pressure and two for low pressure. The high-pressure vessel, HPV, seen on the right hand side of the figure, is responsible for

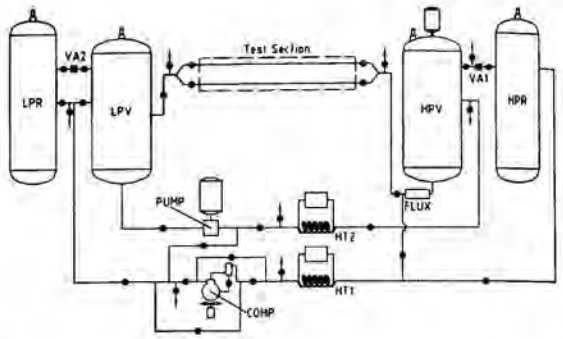

Fig. 2 Schematic view of experimental apparatus.

producing the oil-refrigerant liquid mixture in equilibrium and for forcing the mixture through the test section. During operation liquid mixture is removed from the bottom of the HPV and carried to the test section as indicated in the figure. On the other extreme of the test section the oil-refrigerant mixture, now existing in two phases, is stored in the low-pressure vessel, LPV. The experimental run does not occur on a continuous basis because the return of the oil-refrigerant mixture to the HPV would disturb the equilibrium condition at this vessel. Both HPV and LPV contain electrical resistances in their interior so that temperature as well as gas release from the oil-refrigerant mixture can be controlled.

During a typical experimental run the pressure difference between the HPV and the LPV was kept constant. Because oil and refrigerant are continuously removed from the HPV and taken to the LPV, two secondary reservoirs were employed to maintain the pressure at constant values, the high-pressure reservoir, HPR, and the low-pressure reservoir, LPR, both seen in Fig. 2.

Pressure transducers and temperature sensors were installed at the HPV and LPV to monitor the thermodynamic state of both gas and liquid phases. At the HPV a level transducer was installed allowing the indication of the mass flow rate during the experimental run. The mass flow rate was also measured from a coriolis type flowmeter placed between the HPV and the test section. This meter also measured density and temperature and was used to validate the results from the level transducer.

Two straight horizontal tubes placed parallel and having approximately 5.30 m are the main parts of the test section. One tube was made of tempered borosilicate glass with internal diameter of 3.03 mm, and is employed for flow visualization. The other tube was manufactured by the Bundy® process and have twelve pressure taps alternated with twelve cupper-constantan thermocouples (0.127 mm diameter). Both the pressure taps and the thermocouples were properly installed in the tube-wall in such a way that they were non-intrusive to the two-phase flow. The internal diameter of the bundy tube is 2.86 mm.

Table 1 Typical properties for refrigerant, oil, and saturated mixture at 3 bar.

		ρ (kg/m^3)			μ (cP)			
T (°C)	w	ref	oil	mixture	ref	oil	mixture	
5	0.590	1379.8	899.2	1150.5	0.2359	39.69	0.81	2.29
10	0.424	1363.1	896.2	1063.9	0.2238	33.16	2.53	4.38
20	0.262	1328.8	890.1	985.3	0.2014	22.87	4.55	6.66

A more detailed description of the experimental apparatus and the experimental procedures can be found in Lacerda et al. [2] and the complete description is presented at Lacerda [3].

RESULTS AND DISCUSSIONS

More than one hundred runs were performed with pressure saturation varying from 2.0 to 4.5 bar and temperature around 20 °C. For all runs use was made of refrigerant R-12 and mineral oil SUNISO 1GS, regardless of the discontinuous use of such refrigerant from the industry. This is so because the present research focuses on the mechanism of refrigerant outgassing and the occurrence of two-phase flow, which are independent of the particular oil and refrigerant employed. The mixture R-12 and mineral oil has the advantage that its properties are better known, and that problems like high hygroscopicity and material compatibility are absent, contrary to the R-134/polyol-ester mixture, for example. Typical values for density and viscosity for R-12, mineral oil, and saturated mixture are presented in Table 1. The two values for the mixture viscosity refer to measurements performed by the oil supplier (first column) and calculations (second column). For calculating the mixture viscosity shown in the table use was made of the oil and refrigerant viscosity in conjunction with the following equation (Baustian et al. [4]),

$$\mu = [y\mu_{ref}^{1/3} + (1-y)\mu_{oil}^{1/3}]^3 \quad (1)$$

where y is the refrigerant molar fraction. Because of the departure between measurements and calculations, whenever needed use was made of the measured viscosity.

Typical pressure and temperature distributions are shown in Figs. 3 and 4, respectively. For this case the pressure at the inlet and outlet of the tube is 4.099 and 1.880 bar, respectively, and the inlet and outlet temperature is 19.20 and 1.63 °C, respectively. The refrigerant mass fraction at the tube entrance is 0.467 (mass of refrigerant/mass of mixture), and the mass flow rate throughout the tube is 33.56 kg/h, which correspond to Re = 2,220 at the tube entrance. The time duration for this run was 21 minutes. The two small horizontal lines at each experimental data indicate the maximum and minimum values measured at each particular location.

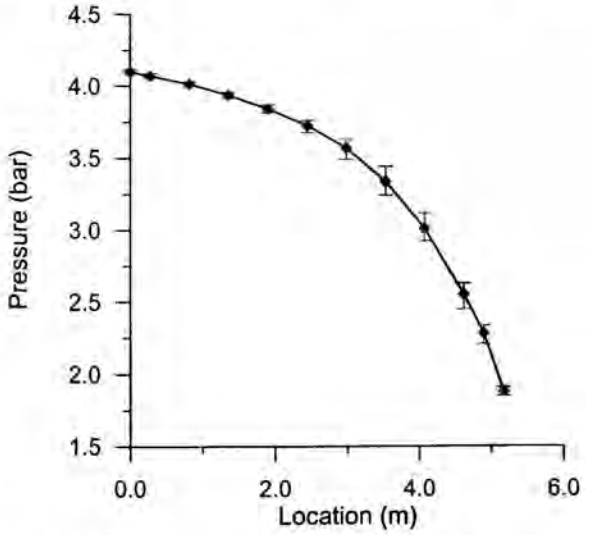

Fig. 3 Pressure distribution along the tube for an oil-refrigerant mixture flow.

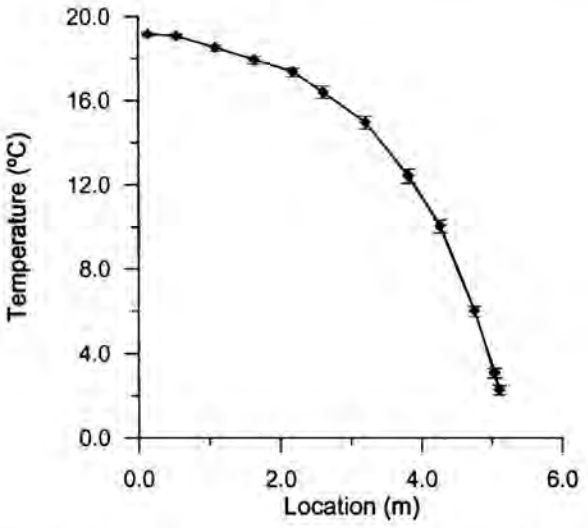

Fig. 4 Temperature distribution along the tube for an oil-refrigerant mixture flow.

As can be observed from Fig. 3, the pressure distribution presents a linear part for the first three data points indicating that a single phase flow prevails for those points and pressure drop is due to friction only. The presence of small amount of refrigerant in the gas phase for those three points is not sufficient to alter the flow from the single-phase pattern. From the third data point onwards the pressure gradient does not remain constant and starts to increase. This is so because the outgassing from the liquid mixture considerably decreases the density at each cross section, which in turn accelerates the flow to maintain the constant mass flow rate. The pressure drop considerable increases to comply with friction and fluid acceleration.

As pressure decreases and gas is released from the liquid mixture, the temperature decreases to keep up with the latent heat requirements for evaporation, as shown in Fig. 4. The test section is not insulated, but the heat provided from the ambient by natural convection is negligible when compared to the heat taken from the gas and liquid mixture flow for evaporating the refrigerant. At the tube exit the temperature was in general less than the water triple point temperature and frost formation is always observed outside the tube because of ambient vapor solidification.

Flow visualization will now be explored for pressure values of 3.731 and 1.020 bar at the high and low-pressure vessels, respectively. The liquid mixture temperature at the high-pressure vessels was kept at 25.4 °C and the Reynolds number at the tube entrance is Re = 811.

Figure 5 shows seven photographs taken at three axial locations along the tube: 70.0, 266.8 and 504.5 cm. It should be noted that for all photographs the flow is from right to left. The first two photographs shown in Fig. 5a are for location 70.0 cm downstream the tube. Either isolated bubbles of large diameters or small clusters of smaller diameter bubbles are observed. The bubbles are concentrated at the upper part of the tube because of gravity. Interesting to observe in the first figure is that the bubbles are not spherical and on the back and upper part an elongation is seen. This may indicate that there could be a relative velocity between bubbles and liquid mixture.

Figure 5b shows three photographs for location 266.8 cm, which correspond more or less to the intermediate location of the glass tube. At this location a large population of small diameter bubbles is seen indicating that the diameter has been reduced and in general no coalescence occurred. The number of bubbles increases along the flow, which is related to the appearance of new nucleation sites. The influence of gravity is reduced as the bubble distribution is rather uniform across the pipe section. The three photographs for the same axial location show that a truly steady flow is not observed, according to the differences in the bubble patterns occurring for the same axial location.

The two last photographs shown in Fig. 5c are for location 504.5 cm. Bubbles are no longer identified in those two figures. The continuous and homogeneous structure observed mainly in the last figure is indicative of foaming flow.

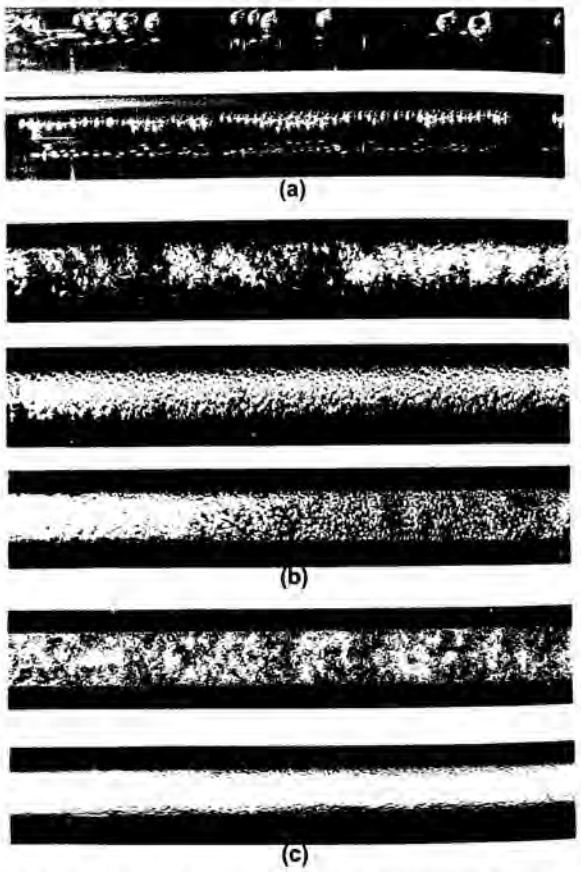

Fig. 5 Flow visualization for oil-refrigerant mixture flow at different tube locations; (a) 70.0 cm, (b) 266.8 cm, (c) 504.5 cm.

Contrary to what is observed in refrigerant flow with small amounts of oil, where several flow patterns as stratified, annular and slug are encountered, the oil-refrigerant mixture flow investigated here presents only two patterns, that is, bubble and foaming flow.

The ability to predict flow patterns is essential in modeling the oil-refrigerant mixture. Different types of flow regimes maps have been developed in the literature, as can be seen in Spedding and Spence [5], and in Rouhani and Sohal [6]. It is not rare that these regime maps fail to predict observed flow patterns, particularly when the geometrical parameters and physical properties of the phases are varied, as shown by Spedding and Spence [5].

Between the existing maps, the one proposed by Taitel and Dukler [7] is interesting because it has perhaps the most carefully conceived theoretical basis (Carey, [8]). This map was favorably compared with a great number of experimental flow regimes (Taitel and Dukler [7], Barnea et al. [9]),

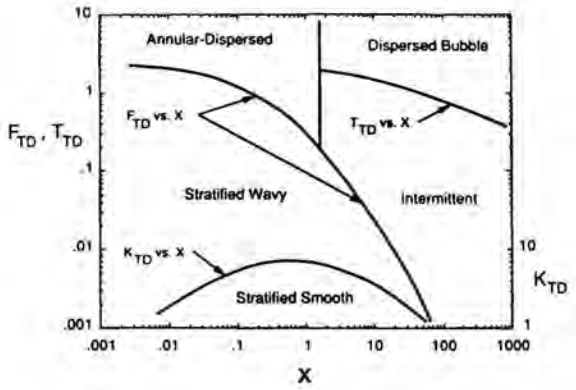

Fig. 6 Original Taitel-Dukler flow regime map for horizontal tubes (from Carey [8]).

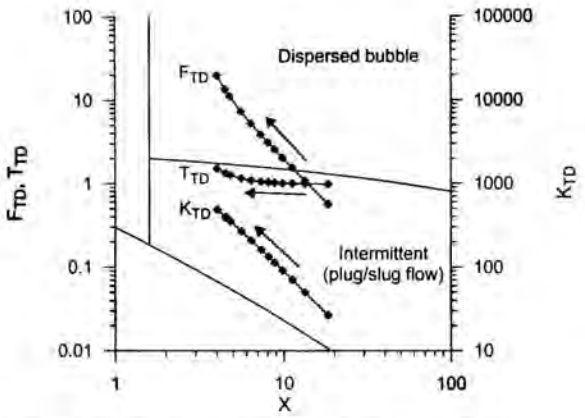

Fig. 7 Path followed by an oil-refrigerant mixture flow on the Taitel-Dukler map.

including experiments that had phase change along the flow so that several different local flow patterns occurred between the tube inlet and outlet (Breber et al. [10]). The Taitel-Dukler flow regime map for horizontal tubes is shown in Fig. 6. The horizontal coordinate is the Martinelli parameter X and the vertical dimensionless parameter varies depending on the specific transition being considered. These parameters, F_{TD}, T_{TD} and K_{TD}, can be found in numerous textbooks, such as Collier and Thome [11] or Carey [8].

Figure 7 presents the result of the typical run explored in Figs. 3 and 4 plotted on the Taitel-Dukler map. The arrows indicate flow the direction, from the inlet to the outlet of the tube. As seen in the figure, the curves are concentrated on the upper right corner of the map shown in the Fig. 6. The parameters F_{TD} and K_{TD} plotted in Fig. 7 are distant from the transition lines for which they have significance, and the parameter that determines the flow pattern is the T_{TD}.

As seen in Fig. 5, the flow pattern varies from large bubbles or clusters of smaller bubbles (which are intermittent) to a large population of small bubbles, and eventually foaming flow is observed. The parameter T_{TD} shown in the Fig. 7 lies on the intermittent area along the flow and does not cross the transition line to bubbly flow, indicating that the Taitel-Dukler map does not agree satisfactory with the present experiments. In this regard it should be noted that the Taitel-Dukler map does not take into account the surface tension influence and, in certain cases, it is unable to predict all the patterns transitions, notably with tubes of small diameters (Barnea et al. [9], Breber et al. [10], Rouhani and Sohal [6], Spedding and Spence [5]). It must be observed that the tubes of the present test section have internal diameter smaller than those often reported in the literature.

In preparing Fig. 7, F_{TD} and K_{TD} were plotted to provide further insight about the flow regime encountered here. It is interesting to see that despite of being apparent meaningless between the transition from intermittent to bubbly flow, F_{TD} somehow represent what was observed in the present experiments. Also worth noting is the linear behavior of the K_{TD} parameter in Fig. 7.Breber et al. [10] proposed a flow map regime based on the analytical work of Taitel and Dukler [7]. The coordinates for this map are X and j_g*, the "dimensionless gas velocity", which is identical to the parameter F_{TD} derived by Taitel and Dukler [7]. Its boundaries are simple horizontal and vertical lines, which encompass a broad transition and result in a particularly easy to use map for modeling purposes. This map was verified by Breber et al. [10] and by Ewing et al. [12] using experimental data for condensation of pure compounds and for mixture of air and water, respectively, and good consistence was observed.

Figure 8 presents result from the present investigation plotted on the Breber map. As seen in the figure, a good

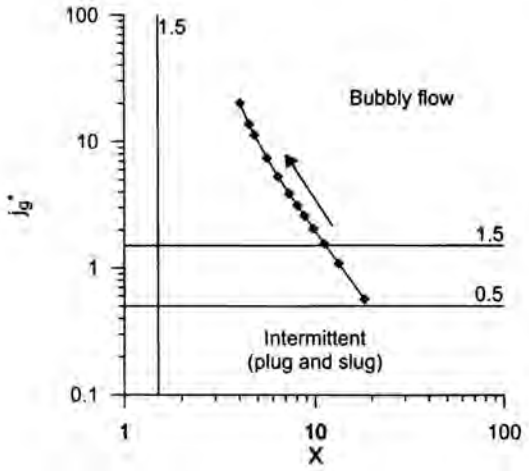

Fig. 8 Path followed by an oil-refrigerant mixture flow on the Breber map.

agreement is observed, since the flow begins with an intermittent to bubbly transition area and finish in the bubbly flow area, as confirmed by Fig. 5.

CONCLUSIONS

An experimental setup was designed and built to investigate refrigerant outgassing from lubricant oil that is forced to flow in straight horizontal small diameter tube. The main motivation to the work is to improve the understanding of this type of mixture flow for developing physical models to be used in analysis and simulation of lubricating process occurring inside the compressor.

Pressure drop along the flow causes refrigerant release from the liquid mixture due to decrease in refrigerant solubility in the oil. The energy required to keep up with the refrigerant evaporation is provided by the liquid mixture, which, in turn, has, its temperature decreased. Outgassing eventually reaches a stage where foaming flow is observed.

For most of the two-phase flow region the oil-refrigerant mixture presents only a bubble pattern where, as void fraction increases, the bubble population increases and the bubble diameter decreases.

A typical result was plotted on the Taitel-Dukler map and on the map proposed by Breber et al. [10]. The Taitel-Dukler map fails to predict the flow patterns observed here. However, the Breber map yielded a good agreement with the patterns identified and with its transitions, indicating that the Breber map can be used as a first approximation in predicting the flow patterns in an oil-refrigerant mixture flow.

REFERENCES

[1] Groll, E. A. Update on CFC substitutes in the USA with respect to vapor compression technology. Proceedings of the International Compressor Engineering Conference at Purdue, West Lafayette. Vol. 1, pp. 95-101, 1996.

[2] Lacerda, V. T., Prata, A. T. & Fagotti, F. Experimental characterization of oil-refrigerant two-phase flow. Proceedings of the ASME – Advanced Energy System Division – 2000. Vol. 40, pp. 101-109, 2000.

[3] Lacerda, V. T. Caracterização experimental do escoamento bifásico de uma mistura óleo e refrigerante em dutos de pequeno diâmetro. Master of engineering thesis. Federal University of Santa Catarina. Florianópolis, Brazil, 2000.

[4] Baustian, J. J., Pate, M. B. & Bergles, A. E. Properties of oil-refrigerant mixtures with application to oil concentration measurements: part I. ASRHAE Transactions. Vol. 92, Part 1a, pp. 55-73, 1986.

[5] Spedding, P. L. & Spence, D. R. Flow regimes in two-phase gas-liquid flow. International Journal of Multiphase Flow. Vol. 19, No. 2, pp. 245-280, 1993.

[6] Rouhani, S. Z. & Sohal, M. S. Two-phase flow patterns: a review of research results. Progress in Nuclear Energy. Vol. 11, No. 3, pp. 219-259,1983.

[7] Taitel, Y. & Dukler, A. E. A model for predicting flow regime transitions in horizontal and near horizontal gas-liquid flow. AIChE J. Vol. 22, pp. 47-55, 1976.

[8] Carey, V. P. Liquid-vapor phase-change phenomena: an introduction to the thermophysics of vaporization and condensation process in heat transfer equipment. Hemisphere Publishing Corporation. United States of America, 1992.

[9] Barnea, D., Luninski, Y. & Taitel, Y. Flow pattern in horizontal and vertical two phase flow in small diameter pipes. Canadian Journal of Chemical Engineering. Vol. 61, October, pp. 617-620, 1983.

[10] Breber, G., Palen, J. W. & Taborek, J. Prediction of horizontal tubeside condensation of pure components using flow regime criteria. Journal of Heat Transfer. Vol. 102, pp. 471-476, 1980.

[11] Collier, J. G. & Thome, J. R. Convective boiling and condensation. 3rd Edition. Oxford University Press. Oxford, 1994.

[12] Ewing, M. E., Weinandy, J. J. & Christensen, R. N. Observations of two phase flow patterns in a horizontal circular channel. Heat Transfer Engineering. Vol. 20, No. 1, pp. 9-14, 1999.

HEFAT2002
1st International Conference on Heat Transfer, Fluid Mechanics and Thermodynamics
8-10 April 2002, Kruger National Park, South Africa
LW1

An Experimental Study on the Flow Characteristicsof Oil-Water Two-Phase Mixture in Horizontal Straight Pipes

Wenhong Liu,Liejin Guo,Tiejun Wu and Ximin Zhang

State Key Laboratory of Multiphase Flow in Power Engineering,
Xi'an Jiaotong University, Xi'an, 710049,P.R.China
Tel/Fax: ++86 29 2668769; Email: *lwh@mfnl.xjtu.edu.cn* or *lj-guo@xjtu.edu.cn*

ABSTRACT

In this paper the flow patterns and their transitions of oil-water two-phase flow in horizontal pipes were both experimentally and theoretically studied. The experiments were conducted in two kinds of horizontal straight tubes, which are made of Plexiglas pipe and stainless steel pipe with 40mm ID respectively. No.46 mechanical oil and tap water were used as working fluids ($\mu_O/\mu_W = 164.9$, $\rho_O/\rho_W = 0.89$ and $\sigma_{OW} = 31.47mN/m$ at 15℃). The ranges of flow parameters in experiment were as follows: $u_{SO} = 0.04\sim1.2$ m/s and $u_{SW} = 0.04\sim2.2$ m/s. The flow patterns were identified by observation through the transparent windows made of Plexiglas tubes and by transient fluctuation signals of differential pressure drop, the different kinds of flow patterns are defined as and distinguished from each other according to the distribution relationship between oil and water phase in the pipe. In addition to the experimental results, semi-theoretical transition criteria for the flow patterns were proposed. Comparisons of the proposed transitional criteria with available data in liquid-liquid systems show reasonable agreement.

NOMENCLATURE

ID Inner diameter of the pipe (m)
u Fluid velocity (m/s)
R Input ratio of oil to water in volume
Ku *Kutadelaze* number
We *Weber* Number
Fr *Froude* number
Re Reynolds number
d Oil bubble's diameter (m)
g Gravitational constant ($kg \cdot m/s^2$)
t Temperature (℃)

Greek Letters

ρ Density of the liquids (kg/m^3)
ε Input phase fraction
σ Interfacial tension (N/m)
μ Liquid viscosity ($Pa \cdot s$)

Subscripts

O Oil phase
W Water phase
SO Superficial velocity of oil
SW Superficial velocity of water
m Mixture velocity of the liquids
cr Critical point of oil droplets
OW Oil-water interface

INTRODUCTION

In pipelines for oil production, mixtures of oil and water are transported over long distances. Compared to gas-liquid and liquid-solid two-phase flow, there are few studies concerning the oil-water two immisicible liquid flows [4]. Understanding of the distinction features of oil-water flows is not only extremely important for the design of pipelines and production logging instruments, but also crucial in predicting the amount of free water in contact with the pipe wall that could cause corrosion problems. Knowledge of the distinctive features of oil-water mixtures systems, together with those for gas-liquid systems, can be used as a basis to understand the more complex case of gas-oil-water mixtures in the future.

Liquid-liquid flow in pipes can adopt different flow configurations, depending on the distribution of the liquid-liquid interface. The flow patterns play an essential role in oil-water flows. Russel et al. (1959) found three flow patterns in horizontal pipeline: bubble, stratified and mixed flow. Ariachakran et al. (1989) developed experimental oil-water flow pattern maps, and found that the flow pattern in oil-water mixture depended primarily on mixture velocity, input water fraction and oil viscosity when oil is continuos phase. Nadler and Mewes (1995) conducted an investigation of the flow pattern

of oil/water two-phase flow in a horizontal straight pipe with 59mm ID. The flow patterns were distinguished in detail and a flow pattern map was presented. In their study no intermediate flow was observed at all. Li Guangjun and Guo Liejin et al (2000) reported an experimental research on the oil-water liquid-liquid two-phase flow patterns and their transitions in both horizontal and vertical helically coiled tubes, The effect of the dimensions and different locations of the helically coiled tubes on flow pattern transition and phase inversion point were also examined.

Although lots of work on oil/water liquid-liquid two-phase flow has been conducted in the past 50 years. Some uncertainties still exist. As pointed out by Hewitt (1997), the transition from gas-liquid flow to liquid-liquid two-phase flow study is still a difficult journey. A lot of work has to be done before we could get a clear, deep and generalized understanding in this area.

For the purpose of providing some more data and deep understanding of liquid-liquid two-phase flow, some new experiments were conducted in two kinds of horizontal straight tubes, which are made of Plexiglas pipe and stainless steel pipe with 40mm ID respectively. Based on experimental observation and analysis on phenomena, the flow patterns of oil-water two-phase mixture flows in horizontal pipes were classified into seven flow patterns, and the factors that affect the transition mechanisms of different flow regimes were discussed. In addition to the experimental results, semi-theoretical transition criteria for the flow patterns were proposed. Comparisons of the proposed transitional criteria with available data in liquid-liquid systems show reasonable agreement.

EXPERIMENTAL APPARATUS AND PROCEDURE

Experimental Apparatus

A new advanced test facility for Air-oil-water three-phase flow was designed, constructed and operated in our Laboratory (see Fig.1). It is capable of coping with up to three phase flows in pipelines at a pressure up to 8 bars. Air was supplied by an air compressor. Oil and water were pumped by two centrifugal pumps respectively and mixed each other in a liquid-liquid mixer and then enter into the test section before through a three phases fluid mixer. In present experiment, only oil and water were employed. After passing through the test section, the mixtures were led into a separation tank, where oil and water were separated by gravity. Finally the oil and water were pumped back to a storage tank for further circulation.

The test sections include two parallel straight pipes which shown schematically in Fig.2, one of them is made of an internal diameter 40mm Plexiglas pipe, and the other is made of stainless steel pipe with the same inner diameter

The flow rates of oil and water were measured by using orifice plates with different ranges, which were carefully calibrated prior to the experiment. The temperatures of the working fluids in the test section were measured at the inlet of the test section by using thermocouples with an accuracy of 0.2 ℃. The pressure of the working fluids in the test section was measured at the inlet of the test section. Two DP1151 differential pressure transducers were used to measure the pressure drop over the whole test section. The arrangements and locations of the pressure transducer were shown in Fig. 2. The flow pattern was distinguished by visual observation and complemented with the analysis of the pressure drop signals. All the signals representing the flow rates, temperature, pressure and differential pressure were transmitted to a PHILIPS computer by a cable and recorded by using IMP acquisition system. The experimental data were saved in a hard disk or floppy disks for further processing.

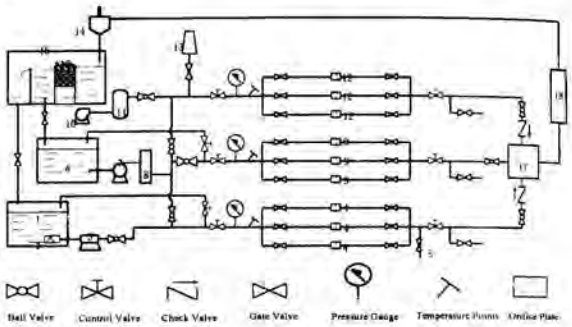

1.Oil Tank;2.Oil Filter;3.Oil Pump;4.Oil-Loop Orifice Plates;5.Oil Sample;6.Water Tank;7.Water Pump;8.Water Stabilizer;9.Water-Loop Orifice Plates;10.Air Compressor;11.Air Stabilizer;12.Gas-Loop Orifice Plates;13.Noise Reducer;14.Gas-Liquid Separator;15.Oil-Water Separator;16.Wavy-Plate Unit;17.Three-phase Mixer;18.Test Section

Fig.1 Experimental WOA flow facility

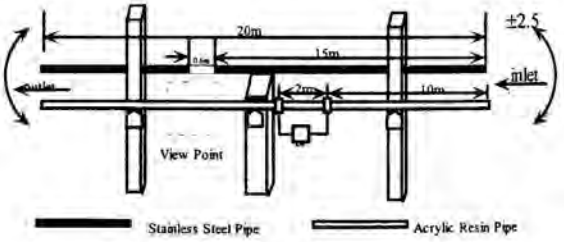

Fig.2 Schematic diagram of test sections

Experimental Procedure

In the present experiments, the oil-water liquid-liquid two-phase flow characteristics were researched. During these oil-water two-phase flow experiments the water flow rate was kept constant and the oil flow rate was increased stepwise. At each oil and water flow rate combination, the flow pattern was carefully observed and recorded and at the same time the other parameters, were also sampled and recorded. In order to minimize the random errors, all the values were averaged using 1000 separate samples. The above procedure was repeated until the final oil flow rate value of interest or the maximum oil flow rate was reached. Then a new water flow rate was chosen and the above procedure was repeated. For these oil-water experiments, the oil superficial velocity ranges from *0.04 to 1.2m/s* and the water superficial velocity from *0.04 to 2.2m/s*. The volume fraction (water-cut) of water in the oil/water mixture changes

from 0.05 to 0.976. The system pressure is in the range of 1 to 2 bar (gauge) and the temperature of the working fluids was kept in the range of 5~20 ℃. No. 46 Mechanical Oil was used. Before the experiment, the oil properties, such as viscosity, density and surface tension with water were measured, and are shown in Table 1.

Table 1 Properties of oil used in present study

Properties	Formula	Unit
Density	$\rho_o = 893 + 0.614t$	kg/m^3
Viscosity	$\mu_o = 623.9e^{-0.054t} \times 10^{-3}$	$Pa \cdot s$
Interfacial tension with water	$\sigma_{ow} = (36.97 - 0.38t) \times 10^{-3}$	N/m

RESULTS AND DISCUSSION

Classification of flow patterns

As above mentioned, some previous investigations on oil-water two-phase flow were carried out and different flow patterns were distinguished, however, the differences still exit. In present investigation, seven flow patterns were distinguished and observed according to our observation and analysis, the detailed classifications of following flow patterns were given which are schematically shown in Fig.3.

Stratified flow pattern (ST), occurs at the lower mixture velocity conditions, here the two fluids flow in separate layers on the top and the bottom of the pipe according to their densities and their interface was disturbed (see Fig.3. (a)).

As the mixture velocity increased drops appeared at the interface region and the flow pattern became Stratified Wavy with Drops (SWD)(see Fig.3. (b)). This flow pattern exited over a higher range of conditions in the stainless steel pipe (u_{SO}=0.055~0.1002m/s and u_{SW}=0.055~0.101m/s) than in the Plexiglas (u_{SO}=0.054~0.091m/s and u_{SW}=0.054~0.091m/s).

Three Layer flow pattern (3L), here there are distinct continious layers of oil and water at the top and bottom of the pipe respectively but in the interface there existed a layer of drops, while drops of each phase could appear within the other phase (see Fig.3(c)). When R equals 1:1, 1:2, 2:1 and 3:1, whereas for moderate superficial velocity, the 3L flow pattern were obtained both in Plexiglas and stainless steel pipes. For example: when $R=1:1$, the velocity range is u_{SO} = 0.1~0.121m/s and u_{SW} = 0.1~0.121m/s in Plexiglas pipe, while in stainless steel pipe, the velocity range is u_{SO} = 0.125~0.357 m/s and u_{SW} = 0.122~0.348 m/s.

Oil-Droplets Stratified flow (ODST), which is similar to the mixed flow pattern defined by Arirachakaran et al (1989), occurs at higher water fraction conditions. Within this flow pattern, the oil phase characterized by different size droplet, exists in the continuous water. Owing to the effect of the buoyancy force, all the oil droplets agglomerate at the upper part of the tube, while the water phase flows at the lower part (see Fig.3. (d)). The flow pattern were obtained in the two pipes when R less than 5:1. In the plexiglas pipe, oil superficial velocity ranges from 0.3 to 0.509m/s and water superficial velocity ranges from 0.06 to 0.1m/s while in the stainless steel pipe oil superficial velocity ranges from 0.403 to 0.5m/s and water superficial velocity ranges from 0.081 to 0.102.

Fully Dispersed or Mixed Flow pattern (M), here one phase is dispersed more or less uniformly into the other and occupy a whole pipe cross section (see Fig.3 (e)), which is similar to the dispersed flow defined by Arirachakaran et al (1989) in horizontal flows and to the oil bubble flow observed by Govior et al (1961) in vertical oil/water flow. According to experimental observation, all the oil phase characterized by the oil droplets and distributed homogeneously in the continuous water phase. This flow pattern occurs under higher mixture velocity. For all the oil to water ratio, the flow pattern were obtained in the experiment.

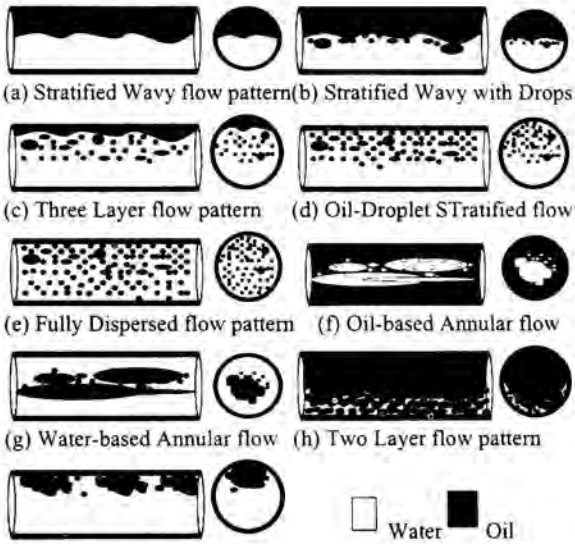

(a) Stratified Wavy flow pattern (b) Stratified Wavy with Drops
(c) Three Layer flow pattern (d) Oil-Droplet STratified flow
(e) Fully Dispersed flow pattern (f) Oil-based Annular flow
(g) Water-based Annular flow (h) Two Layer flow pattern
(i) Slug flow pattern

Fig.3 Classifications of oil/water flow patterns

Slug Flow, occurs under the condition of higher water flow rate and lower oil flow rate, where large continuous oil pockets similar to Taylor bubbles can be observed, the oil-water interface is not stable enough and the pocket could break up very quickly into small droplets (see Fig.3. (i)). When R<1:3, the slug flow was appeared in the two pipes, and the corresponding superficial velocities were u_{SO}= 0.06~0.072 m/s and u_{SW} = 0.18~0.214 m/s.

Two Layer Flow Pattern (2L), occurs at higher oil to water ratio at lower mixture velocity, where the continuos oil layer at the top of the pipes and a layer of droplets at the bottom of the pipes can be observed, the interface of two layers is diminish. (See Fig.3. (h)). In the Plexiglas pipe, when the R equals 5:1, the flow pattern is appeared firstly. The corresponding superficial velocity is u_{SO} = 0.206 m/s and u_{SW}= 0.04 m/s. When the R is large than 5:1, the 2L flow pattern is easily obtained. The flow pattern in the steel pipe had same

trends, and the first spatial distribution appeared when u_{SO} = 0.265 m/s and u_{SW} = 0.053 m/s.

Oil based Annular Flow (OA), occurs under the condition of higher oil flow rate and lower water flow rate, where the oil phase flows along the tube wall are a continuous phase, while water flows in the core of the tube are water droplets and water filaments. When the R large than 9:1, the oil based annular flow is obtained in the Plexiglas pipe as such variables : u_{SO} = 0.469~0.982 m/s and u_{SW} = 0.048~0.068 m/s and a little difference in the stainless steel pipe, u_{SO} =0.469~1.006m/s, u_{SW} =0.053~0.187m/s.

It is worthwhile to note that the oil-water flow pattern of water-based annular flow was not observed in the present experiment, which is mainly due to the low viscosity oil employed in our experiment. It was concluded that the oil with such viscosity is not high enough to keep stable oil core existing in the core of the water annular (Arirachakaran et al, 1989)

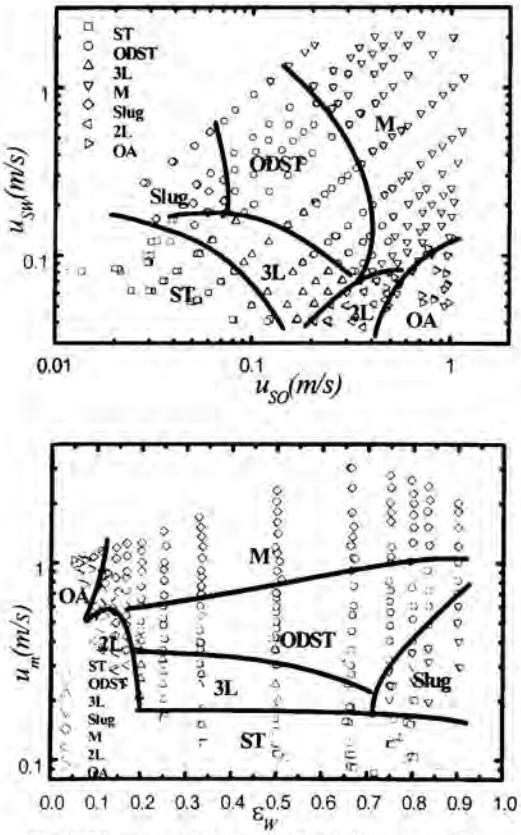

Fig.4. Flow patterns in the Plexiglas test section

Flow Pattern Maps

Seven flow patterns were observed and the spatial distributions of the oil-water interface for the experimental flow patterns are shown in Fig.3. The corresponding experimental flow pattern map with superficial velocity coordinates are presented in Fig.4 and Fig.5. As complement, flow pattern map based on mixture velocity $u_m = u_{SW} + u_{SO}$ and the water fraction $\varepsilon_W = u_{SW}/u_m$ are also shown. Fig.4 shows the flow pattern maps of the Plexiglas pipe. Fig.5 shows the flow pattern map of the stainless steel pipes.

In fig.4 the flow patterns observed in the Plexiglas pipe are shown in a diagram of the superficial velocities of the oil and the water phase. In the figure the solid lines represent a constant oil-water ratio, which is $R = 0$ in the case of water flowing along in the pipe and $R = \infty$ in the case of oil flowing alone.

In the range of low superficial oil and water velocities the stratified flow regimes (ST) is observed. In the case of oil-water ratios less than $R = 1/3$ the oil is flowing under the top of the pipe dispersed in droplets within the water phase. Increasing the velocities of both phases results in increasing turbulence in the flow and the formation of dispersions.

The experiment indicates that flow region and their transitions have similar trends in plexiglas pipes and stainless steel pipes, but the quantities are shifted.

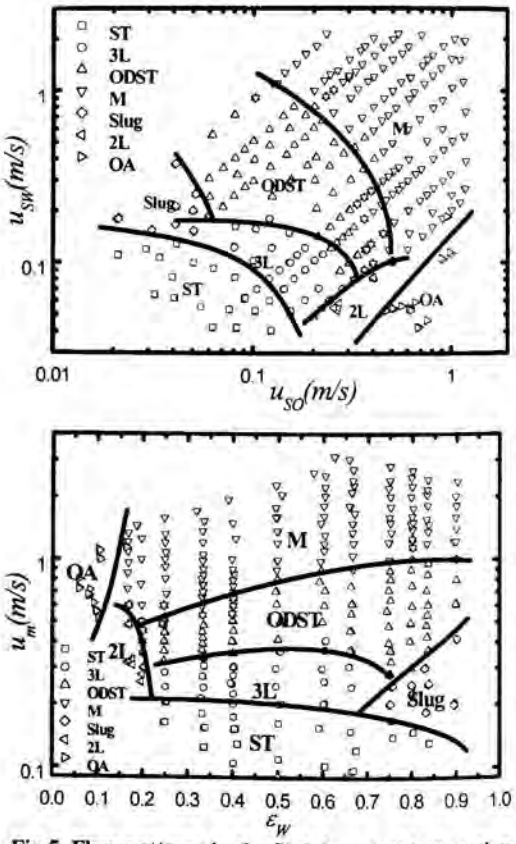

Fig.5. Flow patterns in the Stainless steel test section

Modeling Flow Pattern Transitions

The flow structure of oil-water mixtures in pipes is quite different from that of gas-liquid mixtures. The different flow

structure is mainly caused by the large liquid-liquid momentum transfer capacity and small buoyancy effects. Also, the lower free energy at the interface allows the formation of shorter interfacial waves and smaller dispersed phased phase droplet size. Therefore, oil-water systems are expected to behave different than gas-liquid systems.

Unfortunately, little work has been done in describing the flow regimes that occur in oil-water two-phase flow. This study addresses the determination of the oil-water flow pattern that exists when the fluid physical properties (density, viscosity and interfacial tension), the operational variables (phase flow rates) and geometrical variables are given.

ST/Non-ST (3L,ODST and Slug) Boundary

For low oil and water superficial velocities, the flow is gravitational dominated and the phases are segregated. A further increase in the flow rates causes the appearance of droplets close to the interface. When R is less than 1:3 (the water fraction is 75%) and the oil superficial velocity large than 0.06m/s, the water superficial velocity large than 0.18m/s, The slug flow pattern appears; When R <1:5, any stratified flow disappear in this experiment.instead of slug flow. The reason of the slug flow pattern forming is that the oil wettabillity to the pipe wall and large water flow velocity. When R was large than 1:3, the breakup of the interface will not occur due to small energy dissipation in the pipe wall region. Thus the 3L-flow pattern is formed. As flow rates increased, the droplet layer is increased, until the ODST is formed. Take into account the interaction among oil inertia force, the water gravity and the interfacial tension between oil and water, together with *Froude* number and *Weber* number. Based on the two numbers above, we can obtain *Kutadelaze* number:

$$Ku = (WeFr_O^2)^{0.25} = u_{SW}\rho_O^{0.5}/[g(\rho_W - \rho_O)\sigma_{OW}]^{0.25} \quad (1)$$

Regression the experimental data, the following equation is obtained:

$$Ku = 9.2(\mathrm{Re}_W/\mathrm{Re}_O)^{-0.42} \quad (2)$$

$$u_{SO}\rho_O^{0.5}/(\Delta\rho g\sigma)^{0.25} = 9.2(\rho_W\mu_O u_{SW}/\rho_O\mu_W u_{SO})^{-0.42} \quad (3)$$

Standard Error of the estimate is 0.18, Coefficient of Multiple Determination is 0.94. The result is shown in Fig.6 and Fig.7.

3L/ODST Boundary

In oil-water two-phase flow at sufficiently low input rates ratio, the oil phase may form a swarm of drops (or bubbles) dispersed in water phase. Due to the float up process and the consequent coalescence, the dispersed phase drops may maintain their shape and dispersed pattern provided they are small enough, so that surface tension overcome those due to buoyancy.

Based on Taitel and Dulker's analysis of gas-liquid two-phase flow in horizontal pipes for the transition from slug flow to dispersed flow, the transition from 3L to ODST are mainly induced by buoyancy force and water turbulence intensity for oil/water two-phase flow in horizontal stratified pipes. When the water turbulence intensity is large than the buoyancy force, mutual penetration of vortices takes place in each of the phases. This interfacial turbulence leads to the dispersion of the liquids. The ODST is formed according to the effects above, the following criteria for the this transition is obtained:

$$We_W = 0.103(\rho_O/\rho_W)^{-1.01}(\mu_W/\mu_O)^{-1.01}(u_{SO}u_{SW})^{-1.01} \quad (4)$$

where

$We_W = \rho_W u_{SW}^2 d/\sigma_{OW}$

Standard Error of the Eq.(4) is 0.011;Coefficient of Multiple Determination is 0.98. The result is also shown in Fig.6 and Fig.7.

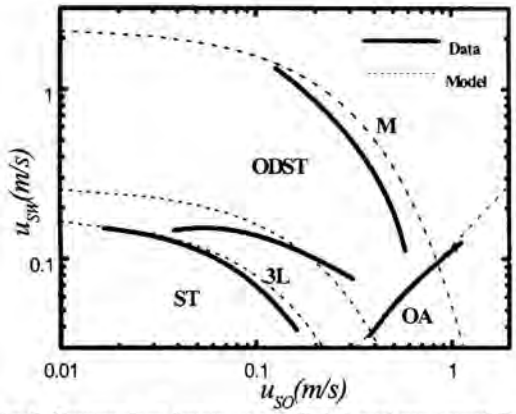

Fig.6. Comparison between predicted and measured flow pattern transitions in Plexiglas pipe

Mixed Flow pattern Boundary

As discussed above, increasing u_{SW} while maintaining low u_{SO}, the turbulent breakage forces tends to destroy large bubbles. According to Hinze's (1955) model, originally developed for liquid-liquid dispersion, the maximum dispersed phase diameter is related to turbulent dissipation scaled , by:

$$d_m = C_1(\varepsilon_O)l_d^{-0.4}(\sigma_{OW}\rho_W)^{0.6} \quad (5a)$$

$$l_d = 2fu^3/d \quad (5b)$$

$$d_{cr} = \{6\sigma/[(\rho_W - \rho_O)g]\}^{0.5} \quad (5c)$$

And

$$u = u_{SO} + u_{SW} \quad (6a)$$

$$f = 0.046(\rho d u_m/\mu_W)^{-0.2} \quad (6b)$$

$$\varepsilon_O = u_{SO}/(u_{SO} + u_{SW}) \quad (6c)$$

Where the constant $C_1(\varepsilon_O)$ may be generally related to in situ hold up and is to be determined by experiments. Utilizing in yields

$$d_m/d_{cr} = C_2(\varepsilon)We_m^{0.1}Fr_m^{-0.5}\mathrm{Re}_m^{0.08} \quad (7)$$

where

$$We_m = \sigma_{OW}/(\rho_O u_m^2 d) \quad (7a)$$

$$Fr_m = \rho_O u_m^2/(\Delta\rho g d) \quad (7b)$$

$$\mathrm{Re}_m = \rho_O u_m d/\mu_W \quad (7c)$$

Obviously, as the maximum drop size is smaller than the critical size, the small drops maintaining their identity and a fully dispersed pattern may prevail. Thus, a fully dispersed

pattern is expected for $d_m / d_{cr} < 1$.

In Eq.(7), let $d_m/d_{cr}=1$, one may obtain C_2 according to the experimental data, utilizing Eq.(5), the following is deduced

$$C_2 = We_m^{-0.1} Fr_m^{0.5} Re_m^{-0.08} \quad (8)$$

Using transition data in the experiment, we can obtain C_2, thus the relationship of ε_o and C_2 is:

$$C_2 = 2.72\varepsilon_o^{-0.42} \quad (9)$$

Standard Error of Eq(9) is 0.22; Coefficient of Multiple Determination is 0.89.

From the above discussion, the semi-theoretical transiti on criteria is obtained:

$$2.72u_{so}^{-0.42} = \rho_w^{0.52}\sigma^{-0.1}\mu_w^{0.08}d^{-0.48}u_m^{0.7} / \sqrt{(\rho_w - \rho_o)g} \quad (10)$$

Given the properties of the fluids and u_{SO}, we can calculate u_m, further calculate the superficial water velocity u_{SW}. The result is shown in fig.6. and fig.7.

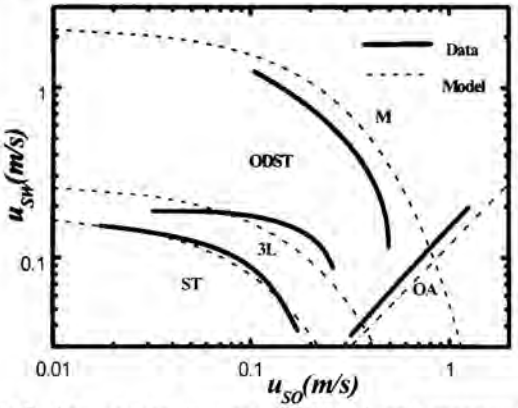

Fig.7. Comparison between predicted and measured flow pattern transitions in Stainless steel pipe

Oil-based Annular Boundary

Transition criteria for gas-liquid two-phase flow can give some notes to oil-water liquid-liquid two-phase flow. As in gas-liquid flow, gas interia force and liquid gravity force are key factors: other reference is also noted that the surface tension may result in more for oil/water two-phase flow. Thus we can use *Froude* number and *Weber* number to describe the transition for annular flow in oil-water two-phase flow, then the *Kutadelaze* number is obtained

$$Ku = (WeFr_O^2)^{0.25} = u_{SO}\rho_O^{0.5} / [g(\rho_w - \rho_O)\sigma_{OW}]^{0.25} \quad (11)$$

Here, the *Froude* number and *Kutadelaze* number were used in the transition criteria for oil based annular flow

$$(Fr_{ll}\, Ku)^2 = 9.8 \quad (12)$$

Standard Error of eq (12) is 0.023; Coefficient of Multiple determination is 0.95. The result is shown in Fig.6 and Fig.7.

CONCLUSIONS

The following main conclusions can be drawn from our investigation:

(1) The flow patterns observed in experiments are similar to those defined by previous investigators, though there exists substantial differences in the conditions under which they occur. Seven flow patterns are defined and observed in both pipes. Oil-based annular flow appears at about water fraction below 10% in our experiments;

(2) In the horizontal pipes, the slug flow of oil-water flow is different from that in gas-liquid flow, large continuous oil pockets similar to Taylor bubbles can be observed, the oil-water interface is not stable enough and the pocket could break up very quickly into small droplets;

(3) Comprehensive mechanistic models developed for gas-liquid flow cannot be readily extended to oil-water systems. Semi-theoretical transition criteria for the flow patterns were proposed. Comparisons of the proposed transitional criteria with available data in liquid-liquid systems show reasonable agreement.

ACKNOWLEDGMENTS

This work is currently supported by the NNSFC (National Nature Science Foundation of China) through contracts No.59995460-2 and No.59725616.

REFERENCES

[1] Russell,T,W.F and Charles,M.E,The effect of the less viscious liquid in the laminar flow of two immiscible liquids,Can. J.Chem.Engng 37,1959,pp18-24

[2] S.Arirachakaran, K.D.Oglesby, M.S.Malinowsky, An Analysis of Oil/Water Flow Phenomena in Horizontal Pipes, SPE18836, 1989

[3] M.Nadler and D Mewes, Flow Induced Emulsifcation in The Flow of Two Immiscible Liquids in Horizontal Pipes, Int.J.Multiphase Flow, Vol.23, No, 1,pp.55-68, 1997

[4] Li Guangjun, Guo Liejin, Gao Hui, et al, Flow Patterns of Oil-Water Liquid-liquid Two-phase Flow in Helically Coiled Tubes, Journal of Chemical Industry and Engineering (China). Vol.51 No.2, 2000

[5] Guo Liejin,Li Guangjun and Chen Xuejun,Flow Patterns and their transition Characteristics of Oil-Gas-Water Three-phase Flow in Horizontal Helically Coiled Tubes, Journal Of Xi'an Jiaotong University, Vol.31,No.4,pp54-60.

[6] Chen Xuejun; Guo Liejin, Flow patterns and pressure drop in oil–air–water three-phase flow through helically coiled tubes, International Journal of Multiphase Flow,Volume,25, Issue: 6-7, September,pp1053-1072 1999

[7] Hewitt, G.F., From gas-liquid to liquid-liquid two-phase Flow, a Difficult Journey. In: Int. Symp. on Liquid-Liquid Two-Phase Flow and Transport Phenomena, Antalya, Turkey, November 3-7,1997.

[8] N.Brauner and D.Moalem Maron, Flow Pattern Transitions in Two-phase Liquid-Liquid Flow in Horizontal Tubes, Int.J.Multiphase Flow, Vol.18. No.1, pp.123-140, 1992

[9] J.L.Trallero, Intevep S.A and J.P.Brill, A Study Of Oil-Water Flow Patterns in Horizontal Pipes, SPE 36609, 1996

[10] P.Angeli, G.F.Hewitt, Flow Structure in Horizontal Oil-Water Flow, Int.J.Multiphase Flow, 26(2000), 1117-1140

HEFAT 2002
1'st International Conference on Heat Transfer, Fluid Mechanics and Thermodynamics
8-10 April 2002, Kruger Park, South Africa
NO1

NUMERICAL SIMULATIONS ON THE TRANSITION BETWEEN STRATIFIED AND SLUG FLOW

Ole Jørgen Nydal and Trygve Wangensteen
Norwegian University of Science and Technology, Trondheim, Norway

ABSTRACT

Transient flow simulations are made with two types of criteria for the stratified to slug flow regime transition. One considers the stability of stratified flow and the other the stability of slug flow. The stratified criterion is often applied for gas-liquid flows at atmospheric conditions, while the slug criterion appears to be more appropriate for high pressure systems.
Numerical experiments have been made to study the difference between the two flow regime transition criteria on transient gas-liquid flows. Some problems related to discontinuities across flow regime transitions in a two fluid model are presented. Numerical experiments with slug initiation in a dynamic slug tracking model are demonstrated, showing a region in the flow map with metastable slug flow

INTRODUCTION

Offshore hydrocarbon production always involves multiphase flow of the oil and gas in wells and pipelines. A number of both transient and steady state flow models are currently in use for analysis and design of such multiphase transportation systems. Transient flow models are particularly important computational tools, as the occurrence of liquid slugging in pipelines often represents a production limiting factor. Flow models are used in the design phase of a pipeline system, to avoid the severe slugging phenomena, and during operation of pipelines, to limit or control the slugging.

Here we are concerned with the onset of slugging from stratified flow. Observations in laboratories, and in field lines, indicate that discontinuities may occur across the transition from stratified flow to slug flow. When the flow regime changes from stratified flow to slug flow, the initial slugs may turn out to be very large before the slug characteristics approach more normal values.

Experimental investigations have shown that the stratified flow is meta-stable in a band of flow rates where slug flow will prevail provided slugs are initiated ([1],[2]), . This range of flow rates with meta-stable flow can be quite large for low pressures systems, but vanishes for high pressure systems. The pressure levels, for which the meta-stable stratified flow region vanishes, is a question to be answered by further experimental investigations. Here, the flow regime transition problem has been investigated numerically and the following is a report on some aspects of transient two phase flow modeling with flow regime changes.

FLOW MODELS

Two classes of transient flow models are considered, denoted here as "standard flow models" and "slug tracking models".

Standard flow models

In a standard transient flow model the transient conservation equations are formulated and solved numerically. In this class of models normal slug flow is regarded as an averaged flow, where information on individual slugs are lost and only average pressure drop and liquid fractions (holdup) are computed in time and along the pipeline. The averaged slug flow scheme may be applied in both two fluid models (separate momentum equation for liquid and gas) and in drift flux formulations (mixture momentum equation and slip relation). Long liquid slugs are captured in the numerical solution, provided they cover many grid cells.

The class of standard transient flow models require friction closure relations, and/or slip relations for stratified flow and for slug flow, as well as criteria for flow regime transitions.

Slug tracking models

Numerical schemes have been, and are currently being developed, for tracking of individual slugs and bubbles. Commercially available flow simulators include sophisticated front tracking schemes for non-diffusive numerical resolution of gas-liquid fronts [3],[4],[5]. This slug tracking feature have proved to be very valuable, as it provides a more correct representation of the slug flow phenomenon and as it generates useful flow information for the design engineer (e.g. slug statistics).

Slug tracking models require similar type of basic closure relations as the standard flow models. However, instead of flow regime transition criteria, slug initiation models have to be supplied, including time, position and initial conditions (length, liquid and border velocity) for the slugs.

Flow regime transition criteria

Two main approaches are often discussed in the literature on flow regime transition criteria: stability analysis of stratified flow and stability analysis of slug flow ([7]). In deriving the stratified criteria, a linear stability analysis is performed on the two fluid model. The well known simplified analysis of Taitel and Dukler (see the review [8]) on solitary perturbation of the liquid layer gives the following transition criterion, for horizontal flows:

$$U_g > C_2 \left[\frac{(\rho_l - \rho_g) g A_g}{\rho_g (dA_l / dh_l)} \right]^{1/2} \qquad C_2 = 1 - \frac{h_l}{D} \qquad (2.1)$$

The second approach in deriving transition criteria is to consider the stability of a slug [9],[10],[2]. Given the introduction of a slug in stratified flow, the slug will survive if the tail velocity is equal to, or smaller than the front velocity. The front velocity is derived from volumetric flow balances across the front and the tail velocity is set equal to the expected bubble velocity in developed slug flow. For the case of no gas entrainment into the slug, the criterion becomes:

$$U_b < U_g \qquad (2.2)$$

U_g is the gas velocity in stratified flow and U_b is the bubble velocity represented by:

$$U_b = C_o U_m + U_o \qquad (2.3)$$

U_m is the superficial mixture velocity and U_o is a bubble drift velocity in stagnant fluid [11].

Including the gas entrainment into the slugs leads to the more general criterion ([9],). This criterion may also be written in terms of holdup.

$$U_b < U_g \frac{\alpha - \alpha_s \frac{U_{gs}}{U_g}}{\alpha - \alpha_s} \qquad (2.4)$$

Both the slug stability and the stratified stability criteria are derived from transition considerations alone. A third approach in establishing transition criteria is to simply accept the transition as the point of intersection of flow models for each regime. The flow conditions where the pressure drop and holdup are equal for each regime will then be taken as the point of transition.

The slug stability criteria corresponds with the point of continuity in holdup between the stratified and slug flow regimes [9]. This assumes that the limiting form of slug flow, with zero slug fraction, exists at the point of transition. In reality the flow at the point of transition may become system dependent. Often it is seen that one slug is created as another leaves the pipe and strong wavy flow may be observed.

NUMERICAL TESTS

Numerical tests have been made on the transient simulation of gas-liquid flow with flow regime transition from stratified to slug flow. The flow in a straight, horizontal pipe has been computed with a two fluid model, and with a slug tracking model. The models will be briefly described and the results compared for simulations along a constant Usg line applying the transition criteria of stratified stability and slug stability.

Flow regime transitions

Figure 1 shows flow maps generated with a Matlab implementation of the Taitel & Dukler criterion, equation (2.1) and with the slug stability criterion equation (2.4). The maps are generated with an arbitrary friction factor in stratified flow, and are only meant as a qualitative illustration of the effect of the pressure (gas density) on the transition lines. At low pressure, the slug stability line is below the stratified stability line, and opposite at high pressure.

A standard "unit cell model" is solved for averaged slug flow [8] assuming steady stratified flow in the bubble and gas entrainment into the slugs according to a slug void fraction correlation.

For high pressure, the line of slug stability is above the stratified stability line. Slug flow, as described by a unit cell model, will not be possible below the slug stability line. Below the line the slug fraction will become negative. For high pressure systems the stratified criteria will therefore not be possible to use in a transient flow model based on the unit cell model for slug flow.

The sample computations are made at a low pressure, in order to illustrate the behavior of standard flow models and slug tracking models when the metastable region is traversed. In computations applying the stratified stability as flow regime transition criterion, the liquid holdup has to fall from a high stratified flow value to a lower averaged slug flow value and the excess liquid has to be blown out of the pipe in a transient. A standard model will give the averaged liquid flow out of the pipe whereas a slug tracking model will show the individual characteristics of the large slugs carrying the excess liquid.

Standard flow model

A two fluid model is formulated and solved for a pipe segment of final length. The single volume model is simplified by neglecting the acceleration term, and both phases are assumed incompressible.

The mass conservations equations for incompressible flow are:

$$\frac{\partial}{\partial t}(\alpha) + \frac{\partial}{\partial x}(\alpha \cdot U_g) = 0 \qquad (3.1)$$

$$\frac{\partial}{\partial t}(H) + \frac{\partial}{\partial x}(H \cdot U_l) = 0 \qquad (3.2)$$

Adding the two equations of continuity leads to:

$$\alpha U_g + H U_l = \left[U_{sg} + U_{sl} \right]_{inlet} = U_m \qquad (3.3)$$

and a relation for the void fraction

$$\alpha = \frac{U_m - U_l}{U_g - U_l} \qquad (3.4)$$

The momentum equations (neglecting the spatial acceleration) are:

$$\frac{\partial}{\partial t}(\alpha U_g) = -\frac{\alpha}{\rho_g}\frac{\partial p}{\partial x} - \frac{F_g}{\rho_g} - \frac{F_i}{\rho_g} - \frac{G_g}{\rho_g} \quad (3.5)$$

$$\frac{\partial}{\partial t}(H U_l) = -\frac{H}{\rho_l}\frac{\partial p}{\partial x} - \frac{F_l}{\rho_l} + \frac{F_i}{\rho_l} - \frac{G_l}{\rho_l} \quad (3.6)$$

F represents the wall and interface friction terms and G the gravity term. P is the pressure.

Inserting the mass equations into the momentum equations gives:

$$\rho_g \alpha \frac{\partial}{\partial t}(U_g) - \rho_g U_g \frac{\partial}{\partial x}(\alpha U_g) = -\alpha \frac{\partial p}{\partial x} - F_g - F_i - G_g \quad (3.7)$$

$$\rho_l H \frac{\partial}{\partial t}(U_l) - \rho_l U_l \frac{\partial}{\partial x}(H U_l) = -H \frac{\partial p}{\partial x} - F_l + F_i - G_l \quad (3.8)$$

Combining the two momentum equations (3.5) and (3.6) gives:

$$\frac{\partial}{\partial t}\left[U_{sg} + U_{sl}\right]_{inlet} =$$

$$-\left(\frac{\alpha}{\rho_g} + \frac{H}{\rho_l}\right)\frac{\partial p}{\partial x} - \frac{F_g}{\rho_g} - \frac{F_l}{\rho_l} - F_i\left(\frac{1}{\rho_g} - \frac{1}{\rho_l}\right) - \frac{G_g}{\rho_g} - \frac{G_l}{\rho_l} \quad (3.9)$$

These equations are solved for both stratified flow and for averaged slug flow. For stratified flows the standard forms of the single phase friction factors are applied (Colebrook type), using Reynolds numbers based on the hydraulic diameters of liquid (assuming free surface flows) and gas (assuming closed duct flows) [8]. The interface friction term is likewise written on the simple, and commonly used, form applying an effective friction factor λ_i .

$$F_i = \frac{1}{2}\rho_g \lambda_i \left(U_g - U_l\right)^2 \frac{S_i}{4A} \quad (3.10)$$

Determination of the interface friction term is one of the large challenges in 1D stratified flow modeling. The interface friction factor in these computations is simply set equal to the gas friction factor, multiplied by a constant.

The friction terms in the two fluid model must also be specified for averaged slug flow, and a "unit cell model" is applied for this purpose. The total frictional pressure drop in the two fluid model must equal the pressure drop of the averaged slug flow and the interface friction must provide a slip computation which corresponds with the slip values of the averaged slug flow. One way of integrating an averaged slug flow model into a transient two fluid model is described in [12].

The frictional pressure drop in the unit cell model is set equal to the sum of the friction terms in the gas and liquid momentum equation:

$$-\left(\frac{\partial p}{\partial x}\right)_{slug\ fric} = F_g + F_l \quad (3.11)$$

A relative velocity is computed from the unit cell model. The friction factor corresponding to this slip ratio is then derived from the holdup equation, which is an equation obtained from the two momentum equations by elimination of the pressure drop:

$$F_i = \alpha F_l - (1-\alpha)F_g + \alpha G_l - (1-\alpha)G_g \quad (3.12)$$

In the present sample computations, the pressure at the outlet is set constant and tests are made with a constant gas flow rate and with varying liquid flow rate at the inlet. The equations are discretized on the control volume and integrated explicitly in time. The computational sequence for each time step is the following:

The pressure equation (3.9) gives the pressure from the changes in the inlet flow rates The momentum equations (3.7) and (3.8) give the velocities, applying friction terms for the flow regime determined from the flow regime transition criteria. The combined mass equations give the holdup, equation (3.4)

SLUG TRACKING MODEL

Sample computations have been made with a slug tracking model similar to the one described in [6]. The model formulation is based on slugs and bubbles as moving computational objects. Slugs are incompressible whereas bubbles are compressible. Mass and momentum conservation equations for slug sand bubbles are formulated for moving an open control volumes. The liquid in the slugs is determined from a dynamic force balance across the slug, including wall friction, gravity and pressure forces from the neighboring bubbles. The pressure in the bubbles are determined from the compressibility of a constant gas mass, which is set at the time of initiation of the bubble. The gas-liquid fronts behave either as a front, which propagates according to the flow balances, or as a bubble nose, applying a relation of the type given in equation (2.3) ([11]).

The slugs and bubbles are organized in linked lists. Slugs and bubbles may be generated and disappear during the computations, according to the behavior determined from the mass and momentum balances and the bubble propagation relation.

The sample computations have been made without gas entrainment into the slugs.

In standard flow models, flow regime criteria are needed in order to determine the friction laws for the appropriate flow regime. In slug tracking models, slug shave to be initiated and the following describes the procedures which have been tested.

Flow regime tests (slug stability or stratified stability) are made in the bubble at the pipe inlet. If the criteria predict slug initiation, a liquid slug is inserted in the middle of the bubble. The initial slug length is set equal to 10 number of diameters and the initial liquid velocity in the slug is set to the mixture volumetric flux (superficial velocity). The liquid for the slug is taken from the upstream part of the bubble, which has been split by the new slug.

The introduction of a slug is difficult to do smoothly in a fully transient model. Insertion of a slug normally perturbes the system of slugs and bubbles and some time is required for dampening of the perturbations. During the oscillations induced by the introduction of a new slug, the flow regime test could fire prematurely. A waiting time is therefore applied before the

transition tests become active again, after a slug has been initiated.

An estimate of the slug unit period can be derived from the volumetric flow balances of steady slug flow (unit cell model) and this can be applied as the waiting time before the flow regime tests are resumed. The total liquid flow balance and the balance between the slug and the bubble, are:

$$U_{sl}=S_f U_{ls} H_s+(1-S_f)U_{lb}H_b \tag{4.1}$$

$$H_b(U_{lb}-U_b)=H_s(U_{ls}-U_b) \tag{4.2}$$

The slug fraction S_f becomes:

$$S_f=\frac{T_s}{T}=\frac{L_s}{L}=1-\frac{U_{sl}-U_{ls}H_s}{U_b(H_b-H_s)} \tag{4.3}$$

S_f is the time, or length fraction of the slug part of the unit cell. Subscripts indicate ls for liquid in slug, lb for liquid in bubble, b for bubble and s for slug.

The holdup in the bubble region of the unit cell (H_b) enters into the relation for the slug fraction. Applying the holdup fraction at the time of flow regime test did not work satisfactorily, and frequently resulted in slug fractions above or below unity. The full unit cell slug flow model could be solved, in order to obtain H_b. A simplified estimate, which has been tested here, is to apply a value for H_b from the liquid volumetric flow balance across the slug, equation (4.2), by assuming zero velocity in the liquid layer under the bubble. For inclined flows, a terminal velocity from the gravity-friction balance could likewise be attempted. Assuming no initial void fraction in the slugs, gives $U_{ls}=U_m$, and the estimate for the slug fraction becomes simply (as also seen directly from (4.1) :

$$S_f=\frac{U_{sl}}{U_m} \tag{4.4}$$

The estimate of the slug period is then:

$$T=\frac{T_s}{S_f}=\frac{L_s}{S_f U_b}=\frac{U_m L_s}{U_{sl}U_b} \tag{4.5}$$

where U_b is determined from (2.3) using the local superficial velocities in the transient. L_s is the initial slug length which has to be specified as one of the initial conditions for a new slug.

The initiation procedure, with a waiting time equal to the slug period estimate before the flow regime testing is activated again after a slug initiation, turned out to work satisfactorily in the present computations. The estimate in equation (4.5) provided the required shorter slug period with increasing liquid flow rate.

RESULTS

Two fluid model

Figure 2 shows the results of sample computations with the two fluid model applied for a horizontal pipe segment and with gas density equal to 17 kg/m^3. For this case the difference between the stratified and the slug criteria is quite small, but even these small differences cause problematic performance of the numerical model. These problems will be magnified as the pressure is reduced and the differences between the stratified and the slug criteria increases.

The liquid flow rate is increased continuously from a value in the stratified region to a value in the slug flow region. Three transition models are applied. The first is the slug stability. The second is the stratified stability and the third is a mixed criterion where the stratified criterion is applied when in stratified flow and the slug stability criterion is applied when in slug flow.

For the slug stability criterion the holdup and the pressure drop changes smoothly from stratified to slug flow. The transition corresponds with the point of continuity in holdup, and no numerical problems appear.

The stratified criterion gives numerical oscillations in which the flow regime changes between stratified and slug flow. This induces pressure oscillations, and holdup oscillations (the holdup oscillations are too small to be visible in the holdup plots). The numerical oscillations are due to problems with the basic transition criterion, and will appear for all time step values, but with different magnitudes. Clearly, such behavior is problematic in a transient flow simulator.

The discontinuous friction models across the stratified-slug transition gives flow regime flipping in the transient computations. As the solution enters slug flow, the friction terms increase and causes the solution to go back to stratified flow. An additional complicating factor is due to the fact that the criterion itself is dependent on the holdup. If the actual holdup is used in the stratified transition criterion, this will lead to two transition lines depending on whether the transition is approached from slug flow or from stratified flow.

One remedy to the flow regime flipping problem is to apply the combined criterion, which is shown as the intermediate lines in the holdup plots. The holdup increases along the stratified flow solution until the stratified criteria fires and slug flow is selected. As long as the solution is in the slug flow regime, the slug stability criterion is then active and not the stratified criterion. When entering into slug flow the pipe has more liquid than the steady slug flow solution would give, and the excessive liquid is blown out in a transient and the solution approaches the slug flow holdup values.

Solving for the stratified flow holdup, and using this value in the stratified stability criterion, is also a possible scheme.

Slug tracking model

The results from the sample computations with the slug tracking model are shown in Figures 4 and 5. The case considered is a 20 m long pipe with air and water at ambient pressure. A constant gas mass flow rate is specified at the inlet (equivalent to 2 m/s superficial velocity) and the liquid flow rate is, after stabilization on 0.025 m/s superficial velocity, ramped continuously up to 1 m/s during 200 seconds.

The transient behavior of the system depends on the rate of change of the liquid flow rate. Tests are made with slug initiation according to the slug stability criterion and to the stratified criterion. The slug criterion fires earlier than the

stratified criterion and slugs are generated with an increasing frequency according to the period estimate ((4.5)). A closer inspection of the results shows that the slugs stabilize at a final slug length varying between 12 and 14 number of diameters at the low and high liquid flow rates, respectively. The small evolution from the initial slug length of 10 diameters, indicates that the period estimate is reasonably good.

Figure 4 shows the total liquid content in the pipe as it varies in time with the increasing liquid flow rate. After slugs are initiated with the slug stability criterion the liquid content oscillates as a result of liquid leaving the pipe as individual slugs. The liquid content in the pipe appears to approach with the stratified holdup line, although the details at the point of transition are not clear.

With the stratified criterion, the delayed onset of slugging induces a transient behavior of the whole system. After initiation, the slug grows continuously as it propagates towards the end of the pipe. This removes a large amount of liquid from the system and a new slug is not initiated before the pipe has been filled up again. Sometimes, an intermediate new slug is initiated at the time when a slug leaves the pipe.

CONCLUSION

Numerical simulations have been made with a two fluid model and with a slug tracking model. The case is a horizontal pipe with constant gas flow rate and a varying liquid flow rate, giving transition from stratified to slug flow. Simulations are made with two types of transition criteria: stability of stratified flow and stability of slug.

The slug criterion corresponds with flow regime transition at the point of continuity in liquid fraction, and the simulations are numerically stable.

The stratified criterion gives discontinuities across the transition. This leads to numerical instabilities for the two fluid model. For slug tracking simulations, the stratified criterion leads to the development of very long slugs.

NOMENCLATURE

A	Area of cross section (m^2)
C_o	Bubble velocity parameter (-)
D	Diameter (m)
F,G	Friction and gravity terms
g	gravity (m/s^2)
H	Liquid holdup (-)
h_l	Liquid height (m)
L_s	Slug length (m)
P	Pressure (Pa)
S	Wetted perimeter (m)
S_f	Slug fraction (-)
T	Slug period (s)
U	Velocity (m/s)
U_o	Bubble drift velocity (m/s)
α	Void fraction (-)
λ	Friction factor (-)
ρ	Density (kg/m^3)

Subscript

g	gas	s	slug
b	bubble	i	interface
m	mixture	l	liquid

REFERENCES

[1] Experimental data on inlet and outlet effects on the transition from stratified to slug flow in horizontal tubes K. Bendiksen and D. Malnes. 1987 Int. J. Multiphase Flow Vol. 13, No. 1, pp. 131-135, 1987

[2] Necessary conditions for the existence of stable slugs Z. Ruder, P.J. Hanratty and T. J. Hanratty Int. J. Multiphase Flow, Vol. 15, No. 2 pp. 209-226, 1989

[3] The Dynamic Two-Fluid Model OLGA: Theory and Apllication
Bendiksen, K.H., Malnes, D., Moe, R. & Nuland, S. 1991 . SPE Prod. Engng May, 171-180.

[4] Numerical simulation of slugging in pipelines Straume, T., Nordsveen, M. & Bendiksen, K. FED-vol 144, Multiphase Flow in Wells and Pipelines ASME 1992.

[5] PeTra: A novel computer code for simulation of slug flow M. Larsen, E. Hustvedt, and P. Hedne, T. Straume SPE 38841 1997

[6] Dynamic Slug Tracking Simulations for Gas-Liquid Flow in Pipelines Nydal O. J. and Banerjee, S. Chem. Eng. Comm., 1996, Vols. 141-142, pp. 13-39

[7] Separated flow modelling and interfacial transport phenomena T. J. Hanratty Applied Scientific Research 48: 353-390, 1991

[8] Two phase slug flow Taitel, Y. & Barnea, D 1990 (Edited by Harnett, J.P. & Irvine, T.F.Jr) Vol 20 pp 83-132 Academic Press, NY

[9] Onset of Slugging in Horizontal Gas-Liquid Pipe Flow, Bendiksen, K., & Espedal, M. Int. J. Multiphase Flow 18 (2), 237-247 (1992).

[10] Advances in slug flow characterization for horizontal and slightly inclined pipes S.L. Scott and GE. Kouba SPE 20628 1990

[11] An experimental investigation of the motion of long bubbles in inclined tubes Bendiksen, K 1984. Int.J.Multiphase Flow, 10,. 4, 467-483

[12] On the Modelling of Slug Flow Bendiksen, K.H, Malnes, D. & Nydal, O.J.: Chem. Eng. Comm.,1996,Vols. 141-142, pp. 71-102

FIGURES

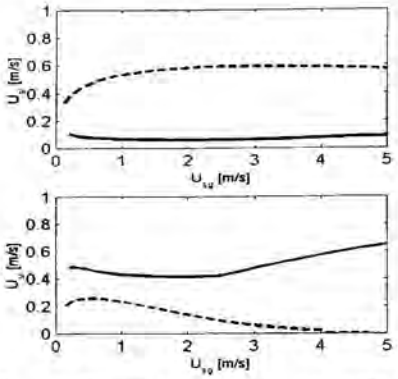

Figure 1 Flow regimes according to stratified stability criterion (dashed line) and to slug stability criterion (solid line). Upper curve ρ_g = 1 kg/m^3 , lower curve ρ_g = 50 kg/m^3

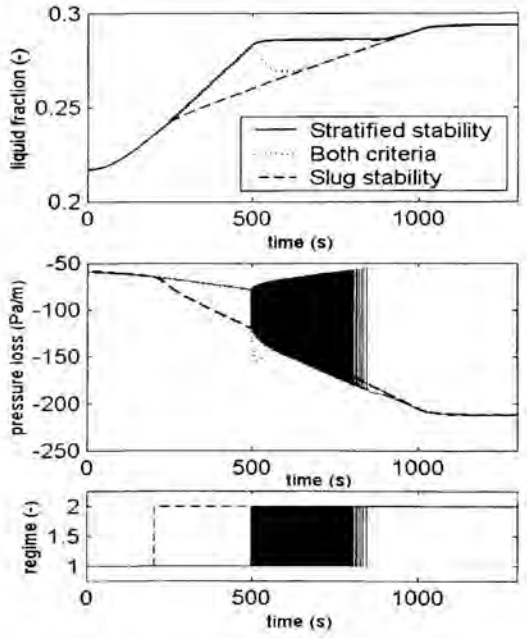

Figure 2 Computations with simplified two fluid model in single control volume. Constant Usg = 2 m/s. U_{sl} increases with time. ρ_g = 17 kg/m^3

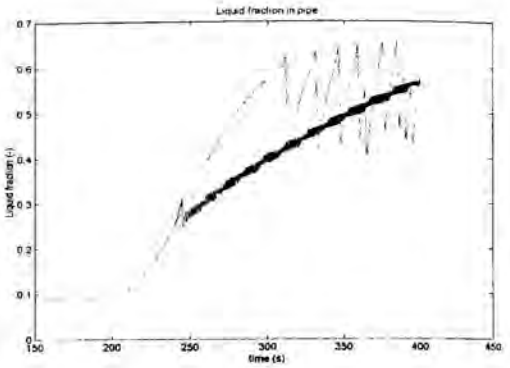

Figure 3 Computations with slug tracking model showing the total liquid fraction in a horizontal pipe. Usg = 2 m/s. . ρ_g = 1 kg/m^3 U_{sl} increases with time from 0.025 at T=200s to 1 m/s at T=400s.
Lower curve: Slug stability flow regime criterion
Upper curve: Stratified stability criterion

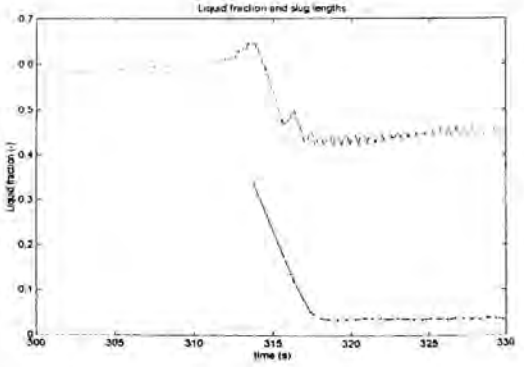

Figure 4 Computations with slug tracking model. Stratified stability criterion until transition and slug criteria thereafter. Constant Usg = 2 m/s. . ρ_g= 1 kg/m^3
U_{sl} increases with time from 0.025 at T=200s to 1 m/s at T=400s.
Lower curve: Maximum length of individual slugs (fraction of pipe length)
Upper curve: Liquid fraction in the pipe

HEFAT2002
1st International Conference Heat Transfer, Fluid Mechanics, and Thermodynamics
8-10 April 2002, Kruger Park, South Africa
HV1

SIMULATION OF BOILING ENVIRONMENTS USING GEOMETRICAL AUTOMATA

V. Herrero*, G. Guido-Lavalle and A. Clausse*****
* Instituto de Estudios para la Excelencia Competitiva, Garay 125, Buenos Aires, Argentina.
** Universidad Argentina de la Empresa, Lima 717, 1073 Buenos Aires, Argentina.
*** CNEA-CONICET-IEEC, Universidad Nacional del Centro, 7000 Tandil, Argentina.
E-mail: vherrero@austral.edu.ar

ABSTRACT

The model of spherical automata is implemented and applied to the simulation of boiling environments. Computational experiments show that the system is able to capture essential features of two-phase flows, providing flexibility to be applied to a wide range of practical problems. Two computational experiments are simulated and compared against experimental data: non-equilibrium boiling flow in vertical heated channels, and the influence of the subcooling degree on the bubble plume over a horizontal heater immersed in stagnant liquid. A set of effective parameters representing turbulence agitation, critical breakup size, probability of coalescence and detachment radius, are determined by fitting the experimental void fraction profiles.

INTRODUCTION

Wherever two immiscible fluids are forced to flow together, one of them tend to concentrate in bubbles, the other fluid acting as a continuous carrying environment. Usually bubbly environments are described by means of partial differential equations in terms of the average fields representing the physical variables in some detail [1]. Among the numerous models, the most classical are the homogeneous flow, the drift-flux, and the two-fluid model. In general, the flow is characterized by means of macroscopic global magnitudes, representing the relative amount of each fluid component, the number of bubbles per unit volume, the interfacial area density, the average bubble size, etc.

A different perspective in two-phase flow modeling is the bubble population balance [2], which calculates the flow variables by tracking the bubble stock, through book-keeping coalescences, breakups, evaporations and condensations. Here a computer version of population balance is presented, where bubbly worlds are created using geometric automata [3] resembling real boiling environments.

NOMENCLATURE

α = *Void Fraction*
N = *Bubble Number Density*
A = *Interfacial Area Density*
Z = *Distance from the Heater*
$X(t)$ = *Indicator Function*
I = *Interfacial Impact Rate*
Rd = *Detachment Radius*
Ag = *Agitation Velocity Component*
Cr = *Break Up Frequency*
Rc = *Break Up Critical Radius*
Cd = *Condensation Parameter*

THE MODEL

The automata are mathematical entities defined by states that change following iterative rules. Ultimately, the rules represent the interaction of each automaton with its neighborhood. For example, cellular automata are operations associated with elements of a spatial lattice, resembling atoms in crystals.

In order to simulate a bubbly environment, the grid of cellular automata is dismissed in favor of a trajectory generator. The bubbles are represented by spheres, which change their radii and move inside a spatial domain. The set of bubbles' operations are the following:

a) *Buoyancy*: The position of the center is displaced upward a distance d_b (Fig. 1a)
b) *Turbulence*: The center is displaced a distance in a random direction θ (Fig. 1b).
c) *Confinement*: Any bubble moving out of the tube environment through a lateral wall is reintroduced attached to the border (Fig. 1c).
d) *Coalescence*: When two or more bubbles collide, they coalesce giving birth to a new bubble conserving the total volume (Fig. 1d).
e) *Breakup*: Bubbles larger than a critical size, are allowed to break up into two bubbles conserving the total volume (Fig. 1e).

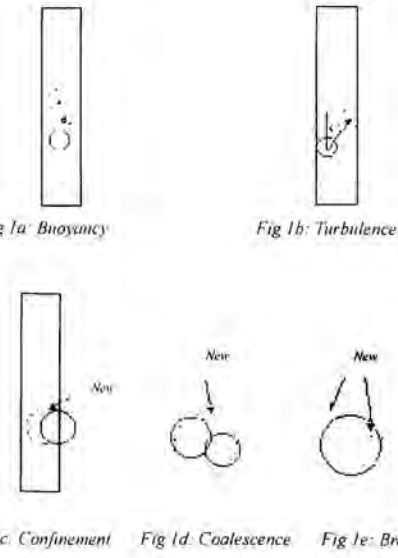

Fig 1a: Buoyancy *Fig 1b: Turbulence*

Fig 1c: Confinement *Fig 1d: Coalescence* *Fig 1e: Break up*

Figure 1. Automata rules.

The computational experiment runs till a void fraction, or other variable, profile under dynamic equilibrium is reached. The dynamic equilibrium state is assumed when, in average and in each point, the coalescence and break up mechanisms are balanced.

Case study a: non-equilibrium boiling flow in vertical heated channels

A case of boiling flow was studied to compare with available experimental data. The problem consists of a 2 m vertical tube containing a long axial electrical heater, and filled with stagnant water (Fig. 2)[4].

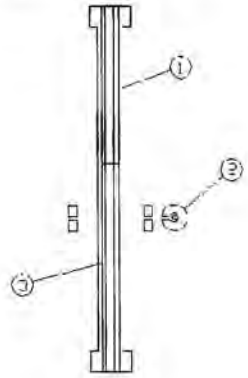

Figure 2. Diagram of the experimental boiling environment. 1, glass tube; 2, γ ray-meter; 3, heater.

Water starts to boil in small bubbles near the heater wall, and then rise guided by buoyancy forces[5], leaving the tube through the top. In order to model this particular environment, an additional operation was prescribed:

f) *Slugging*: if the radius of a bubble exceeds the tube lateral dimension, the gas sphere changes to a cylinder slugging the tube. These elongated bubbles cannot break up.
g) *Detachment*: Bubbles are constantly pumped into the tube by appearing and detaching from the heater walls. The input rate is proportional to the heat power.
h) *Evaporation*: Each rising bubble growths with a rate proportional to its interfacial area.

Changing the heat power input, the bubble size distribution along the channel also changes to accommodate the bubble balance. Several global magnitudes can be calculated in order to monitor the dependence of the steady-state variables with the power input [8]:

- *Void fraction (α)*: Average fraction volume occupied by bubbles.
- *Bubble number density (N)*: Average number of bubbles per unit volume.
- *Interfacial area density (A)*: Average area of the bubbles per unit volume.

Figures 3 shows the void fraction profile along the tube for different power inputs. It can be seen that the simulation compares fairly well with the experiments.

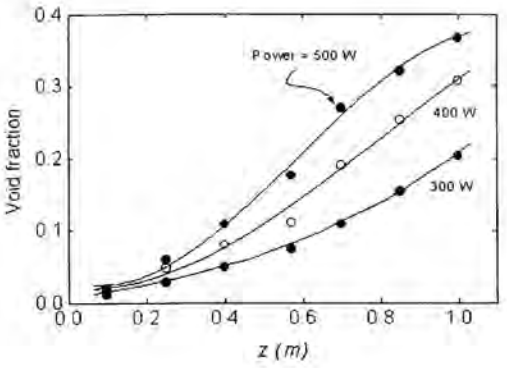

Figure 3. Void fraction profile.

Figs. 4 and 5 show the corresponding bubble number and the interfacial area density profiles.

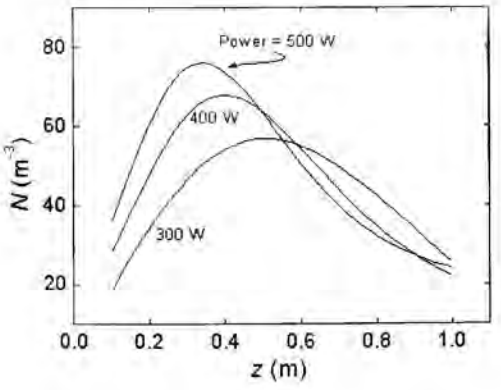

Figure 4. Bubble number density profile.

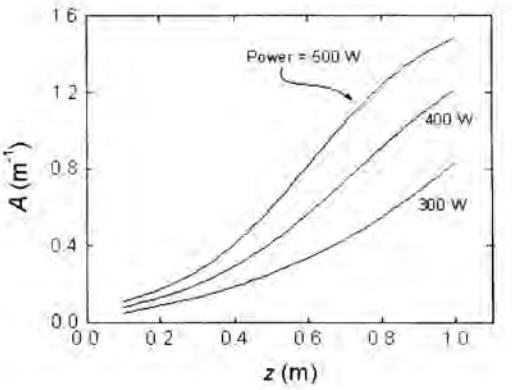

Figure 5. Interfacial area density profile.

Figure 6 shows the evolution of the histogram of bubble radii (called bubble population function) along the tube. It is interesting to observe the effect of coalescence and bubble growth in higher positions. At the end of the tube (z = 1 m) there is a bimodal distribution of bubbles, coexisting small bubbles with large slugs. This phenomenon is observed in experiments when the void fraction is larger that 0.25, and is called the bubbly-slug flow pattern transition.

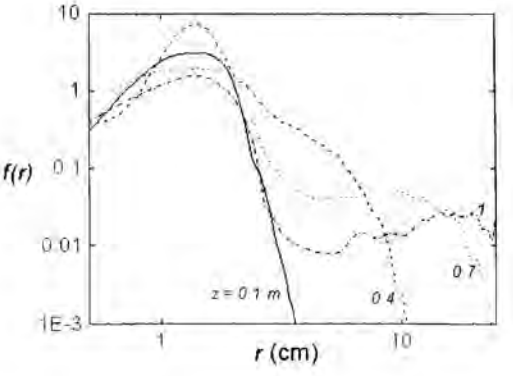

Figure 6. Bubble population function along the column (500 W).

Case study b: subcooling degree on the bubble plume over a horizontal heater immersed in stagnant liquid

The experiment [6] was a bubble plume rising from an horizontal heater immersed in R-11 refrigerant. The experimental data used were the void fraction and the interfacial impact rate, both calculated by means of the phase indicator function.

The automata simulation in this experiment has two main objectives: to study for the first time the subcooling boiling conditions and to simulate a case where the tridimensional description is imperative in order to obtain realistic results

Figure 7 shows the experimental device: researchers placed the heater inside a stainless steel cylindrical vessel, filled with the refrigerant liquid at atmospheric pressure. The experimental measurements were performed with different heat fluxes ranging from nucleate boiling to values close to critical heat flux. The simulation data were compared to available data for three different subcooling degrees: 0^0 C, 3^0 C and 6^0 C.

The heater was a thin platinum foil horizontally placed in the vessel. The measurements were performed by an optical phase detection probe [7], placed in different positions along the vertical line beginning in the middle of the heater. The resultant signal (phase indicator function) is 1 when the probe is immersed in gas and 0 when the probe is immersed in liquid. The same logic was utilized to simulate the indicator function with virtual probes in the tridimensional space of the automata.

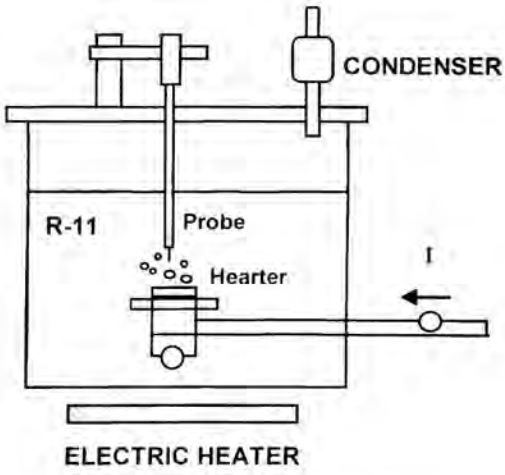

Figure 7: experimental apparatus

The measured and simulated void fraction and interfacial impact rate are defined as:

$$\alpha = \frac{1}{T}\int_0^T X(t)dt \,. \qquad (1)$$

$$I = \frac{Number\ of\ interfaces\ impacting\ the\ probe}{T} \qquad (2)$$

where T is the time interval of measurement at each position and $X(t)$ is the indicator function.

The visual observations during the experiments, showed a bubbly plume, with a detachment radii of approximately 1 mm, rising from the activated nucleation sites on the heater. Figure 8 shows the axial profiles for α and I measured for different subcoolling degrees. It can be seen that, in general, both magnitudes decrease as the distance from the heater increase, due to condensation and bubble dispersion.

Automata Plume

The tridimensional automata sphere system inherits the three basic tasks (to move, to break up and to coalesce) from the automata class. In order to model the experimental border conditions, the following rules were implemented:

1. Bubbles born at the activated nucleation sites with a detachment frequency proportional to the heater power.
2. The nucleation sites create bubbles in an random way with a given radii, used as a numerical control parameter.
3. Bubbles have a velocity with a vertical component given by the terminal rise velocity and a agitation component with a module that is a fraction of the vertical component with a random direction.
4. The R-11 fluid properties were utilized together with the bubble radius in order to obtain the terminal rise velocity with the Wallis correlation [5]

Zero-subcooling simulation

The zero-subcooling case was first studied. Since no condensation occurs once the bubble detaches the heater, the dispersion mechanism is isolated.

A virtual probe reproduced the experimental conditions: when the distance between the center of any bubble and the probe position is less than the bubble radius, the probe a logic value of 1 is registered; otherwise, the logic value assigned, each time step, to the virtual probe is 0.

Figure 8 shows the simulated and experimental void fraction and interfacial impact rate profiles. The parameters values used to adjust the data are shown in table 1.

Detachment radius	Rd = 0.5 mm
Agitation velocity component	Ag = 55 %
Break up frequency	Cr = 2
Break up critical radius	Rc = 1 mm

Table 1: Value of main parameters

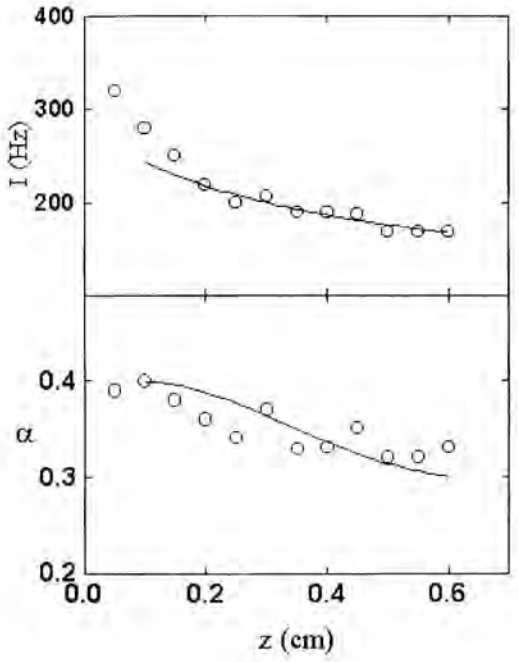

Figure 8: Void fraction and interfacial impact rate at zero subcooling: experimental (circle) and automata (curve) values.

Bubbly plume in subcooled liquid

As subcooling increases, the void fraction and impact rate profiles fall rapidly with the distance from the heater, mainly due to condensation. The condensation process was simulated by the Condensation task, that works at each iteration step, multiplying the automata volume by a condensation parameter smaller than 1. Experimental and simulation results are shown in figure 9 for a subcooling of 6^0C.

Subcooling Level	Condensation Parameter
0^0 C	1
3^0 C	0.997
6^0 C	0.995

Table 2: Condensation parameter values for the different subcooling levels (time step: 50 μseg)

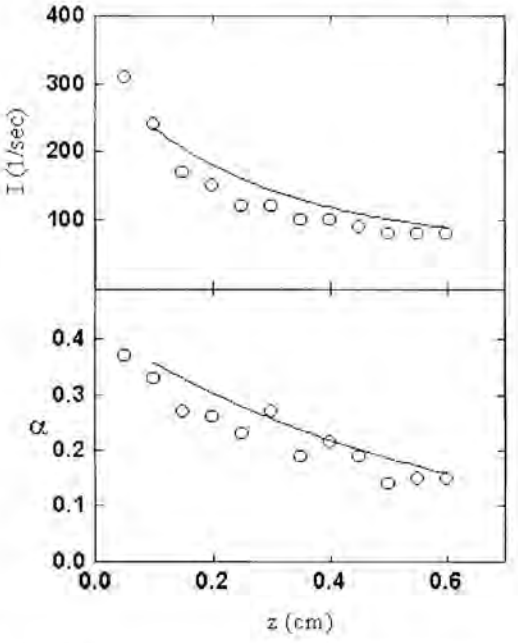

Figure 9: Void fraction and interfacial impact rate at 6^0 C subcooling: experimental (circle), automata (curve).

Sensitivity analysis to control parameters

The response of the void fraction and interfacial impact rate profile to control parameter changes was studied. The parameters analyzed were:

- Breakup probability
- Turbulent agitation
- Detachment volume

It was found that the detachment radius has the most significant effect on the system behavior. This is not a surprise since this parameter establishes the border conditions, and affects the bubble velocity. The larger the bubble volume, the less the void fraction and the larger the interfacial impact rate. The second parameter concerning its effect on the system was the agitation velocity.

Figure 10. shows the automata plume sensitivity to the detachment radius.

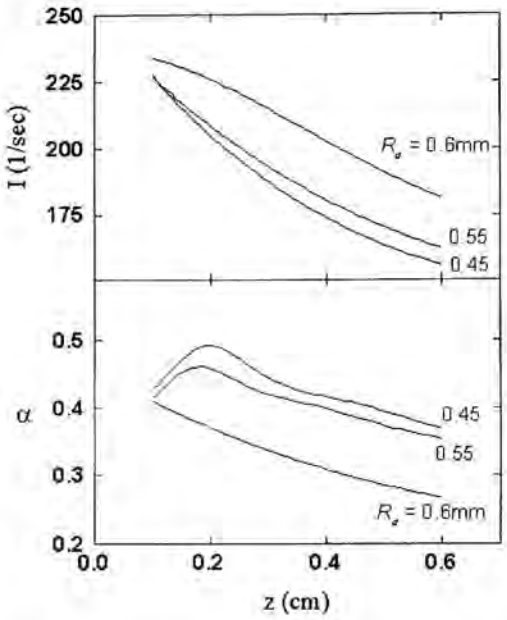

Figure 10: Automata plume sensitivity to detachment radius

CONCLUSIONS

A model of automata was developed to simulate a boiling environment. Computational experiments showed that the system is able to capture the essential physics underlying bubbly flows, and compares fairly well with the experiments.

The tool should be seen from a perspective showing the potential of automata models to simulate complex realities. It is hoped that the ideas and results presented herein stimulate other researchers to further investigate other collective processes using the proposed methodology.

The application of the automata to simulate a bubbly plume in pool boiling has also been demonstrated. The application of tridimensional simulation allowed us to add a realistic perspective to the free movement of bubbles in a stagnant medium.

The sensitivity study allowed us to identify which parameters are the most significant. It was found that the agitation velocity and the detachment radius are the most important in the simulated cases.

The potential of the automata lies in their capacity to recover the individual bubbly behavior lost in most of the models that use averaged variables from a very simple tool. In addition geometrical automata should be combined with fluid-dynamics or heat transfer, otherwise the result of it would be some garish pictures without any physical meaning.

Finally, this application showed the real value of the automata in the study of two phase flow; specifically in studying the effects of local conditions on global experimental measurements.

ACKNOWLEDGMENTS

The work of this paper is a summary of part of the work done by the first author under the supervision of the two second authors for a Ph.D. Degree in Nuclear Engineer at Instituto Balseiro.

REFERENCES

1. Zuber, N. and Findlay, J., Average Volumetric Concentration in Two-Phase Systems, *J. Heat Transfer*, vol. 87, pp. 453-468, 1965.
2. Clausse, A., Bubble population models of gas-liquid flows, *Trends in Heat, Mass & Momentum Transfer*, vol. 3, p.49, 1997.
3. Rudy Rucker's Cellular Automata Laboratory. Rudy Rucker and autodesk, Inc. 1989.
4. V. Herrero et. al. *Non-equilibrium effects in void fraction distribution,* Nuclear Engineering and Design 154 (1995) 183-192.
5. F. N. Peebles and H. J. Garber. *Chemical Engineering Progress,* 1953, 49, 88-97.
6. Carrica, P. M., Leonardi, S. A. and Clausse, A., Experimental Study of the Two-Phase Flow Dynamics in Nucleate and Film Pool Boiling, *Int. J. Multiphase Flow*, vol. 21, p. 405, 1995.
7. Iida, Y. & Kobayashi, K., An Experimental Investigation on the Mechanism of Pool Boiling Phenomena by a Probe Method, *4th Int. Heat Transfer Conference*, 5, B1.3, 1969.
8. Guido Lavalle, G., Carrica, P. M., Clausse, A. and Qazi, M. K., A Number Density Constitutive Equation, *Nucl. Eng. Des.*, vol. 152, p. 213, 1994.

HEFAT2002
1st international Conference on Heat Transfer, Fluid Mechanics, and Thermodynamics
8-10 April 2002,Kruger Park,South Africa
VV2

A SEMI-THEORETICAL ANALYSIS OF BOILING HEAT TRANSFER

C. B.Vijaya Vittala
Mechanical Engineering Department, NERIST, Arunachal Pradesh-791 109, India
S.Bhaumik, S.C.Gupta* and V.K.Agarwal
Chemical Engineering Department,University of Roorkee, Roorkee-247 667, India
*E-mail : satisfch@rurkiu.ernet.in

ABSTRACT

A semi-theoretical model has been developed to predict heat flux during boiling of liquids at atmospheric and sub-atmospheric pressures.It considers the simultaneous operation of transient heat conduction from heated surface to saturated liquids, evaporation of microlayer existing beneath the bubble and natural convection from areas unaffected by bubble activity and also an empirically determined equation for the diameter of vapor bubble in growth period. This model has been compared against experimental data of other investigators and the predicted values of heat flux have been found to match well within an error of ±20%.

INTRODUCTION

Nucleate boiling is a complex phenomenon due to large number of interacting variables involved. There have been several empirical and semi-theoretical models to describe the mechanism involved in this process. But, none of them is truly capable of its wide spread adoption for predicting heat flux. Recently, some of the investigators [6,18,20] have established that several heat transfer mechanisms operate simultaneously in boiling process instead of a single one and the contribution of each depends upon the operating variables, surface characteristics and boiling liquids. In addition, the concept of dry spot has also gained prominence in the growth of bubbles. These factors stimulate a need for an investigation of ebullition cycle for predicting heat flux during nucleate boiling of liquids at atmospheric and sub-atmospheric pressures.

NOMENCLATURE

A	heat transfer surface area (m^2)
A_{inf}	bubble influence diameter (m^2)
C_p	specific heat (J/ kg K)
D	diameter (m)
D_b	bubble departure diameter (m)
D_d	dry spot area diameter (m)
d	diameter of heating tube (m)
g	gravitational acceleration (m/s^2)
Gr	Grashof number $\left(gd^3\beta\Delta T/\nu^2\right)$
h	heat transfer coefficient (W/m^2 K)
Ja	Jakob number $\left(\rho_l C_p \Delta T_w / \rho_g \lambda\right)$
k	thermal conductivity (W/mK)
N	number of nucleation sites
n	nucleation site density (sites/m^2)
P	pressure (kPa)
Pr	Prandtl number $\left(C_p \mu/k\right)$
Q	heat rate (W)
q	heat flux (W/m^2)
T	temperature (°C or K)
ΔT	superheat (°C or K)
t	time (s)

Greek letters

α	thermal diffusivity (m^2/s)
δ	microlayer thickness (m)
λ	latent heat of vaporization (J/kg)
ρ	density (kg/m^3)
σ	surface tension (N/m)
γ	interfacial energy (N/m)

Subscripts

b	bubble
c	cavity
g	growth
i	inner
l	liquid
NC	natural convection
s	solid
sat	saturated condition
v	vapor(gas)
W	waiting
w	wall

ANALYSIS

Nucleate boiling is a cyclic process. Heat transfer from heated surface to saturated liquids adjacent to surface occurs by transient conduction and consequently, a thin layer of superheated liquid develops. This, in turn, leads to originate vapor bubble at the nucleation sites of the surface. At this stage the vapor bubble, in its embryo, contains a very thin layer of liquid in the base. Subsequently, heat is released by the evaporation of upper portion of the liquid microlayer and thereby, expansion of the bubble takes place. This is continued till the bubbles attains a maximum size and then it detaches leaving an evacuated space which is immediately filled by the liquid rushing from bulk. This completes the ebullition cycle.The time period for the development of superheated liquid layer and the origin of vapour bubble is usually referred as waiting period whereas the remaining period of the ebullition cycle devoted to bubble growth is growth period.

In this paper, heat transfer rate for a single bubble has been determined separately for each of the above periods and the cumulative heat transfer rate per bubble for the cycle has been obtained. Mathematically, it can be expressed as

$$Q_{Total} = (Q_W + Q_g) \times N$$

Following assumptions are made in this analysis :

- The vapor bubble is spherical in shape.
- A dry spot exists in the liquid microlayer beneath the vapor bubble.
- Entire amount of heat is transferred to the liquid.
- Liquid is at saturation temperature corresponding to pressure existing in it.
- Low heat flux condition prevails.

Waiting period

Heat transfer during this period occurs by transient heat conduction from heating surface to the adjacent liquid that has entered into the space evacuated by the departure of vapor bubble. Considering liquid layer surrounding the heating surface to be a slab of semi-infinite length and of finite thickness, instantaneous heat flux conducted to the liquid layer is geven by [10].

$$q = \frac{k_l \Delta T_w}{\sqrt{\pi \alpha_l t}} \qquad (1)$$

Average heat flux conducted during waiting period, t_w is

$$\bar{q} = \frac{\int_0^{t_w} \frac{k_l \Delta T_w}{\sqrt{\pi \alpha_l t}}}{\int_0^{t_w} dt} = \frac{2 k_l \Delta T_w}{\sqrt{\pi \alpha_l t_w}} \qquad (2)$$

The heat flux given by Eq.(2) passes through the area of bubble influence. As shown by Hsu and Graham [6] and Han and Griffith [4], the area of bubble influence has a diameter equal to two times of the diameter of bubble at the time of its departure, i.e $D_{inf} = 2 D_b$, so area of influence becomes πD_b^2. Following is the empirical expression recommended by Cole & Shulman [2] for departure diameter of vapor bubble for boiling of distilled water and organic liquids at atmospheric and sub-atmospheric pressures.

$$D_b = \left(\frac{133.3}{P}\right)\left[\frac{\sigma}{g(\rho_l - \rho_v)}\right]^{\frac{1}{2}} \qquad (3)$$

Hence,total heat flow rate during waiting period is as follows:

$$\bar{Q}_W = \frac{2 k_l \Delta T_w}{\sqrt{\pi \alpha_l t_w}} \times \pi \left(\frac{133.3}{P}\right)^2 \left[\frac{\sigma}{g(\rho_l - \rho_v)}\right] \qquad (4)$$

Growth period

The vapor bubble grows on a very thin liquid film which is formed between the bubble and the heated surface. The liquid microlayer contains a dry spot of vapor. The bubble takes up heat by the evaporation of thin liquid film during growth period. It dissipates heat by conduction to the surrounding liquid at its upper half.

Instantaneous heat flux through the vapor liquid interface is as given by Sernar & Hooper [14]:

$$q_b = \frac{k_l \Delta T_{sat}}{\sqrt{\pi \alpha_l t}} \qquad (5)$$

They also obtained the following equation for the instantaneous heat flux through the base by assuming one dimensional heat conduction from a semi infinite solid :

$$q_s = \frac{k_s \Delta T_w}{\sqrt{\pi \alpha_s t}} \qquad (6)$$

Eqs. (5 & 6) yield :

$$q_b = \frac{\gamma k_l \Delta T_{sat}}{\sqrt{\pi \alpha_l t}} \qquad (7)$$

where

$$\gamma = \sqrt{\frac{k_s \rho_s C_{ps}}{k_l \rho_l C_{pl}}}$$

Contact area between the bubble and the heating surface, A_c is:

$$A_c = \frac{\pi D^2}{4}\left[1 - \left(\frac{D_d}{D}\right)^2\right]$$

or

$$A_c = \psi \frac{\pi D^2}{4} \qquad (8)$$

where $\psi = \left[1 - \left(\frac{D_d}{D}\right)^2\right]$

According to Unal [16] the ratio $\frac{D_d}{D}$ for a given pressure remains constant and the value of ψ for pressures less than 17,700 kN/m^2 is approximately equal to unity.
An energy balance on the evaporating microlayer provides :

$$\frac{\gamma k_l \Delta T_{sat}}{\sqrt{\pi \alpha_l t}} \times \frac{\pi D^2}{4} \psi = -\frac{d\left(MC_{pl}\Delta T_w\right)}{dt} \qquad (9)$$

where M is the instantaneous mass of evaporating microlayer. It is as follows :

$$M = A_c \delta \rho_l = \psi \frac{\pi D^2}{4} \delta \rho_l \qquad (10)$$

where δ is the thickness of evaporating microlayer.
Substituing the value of M from Eq.(10) in Eq. (9), the following equation is obtained :

$$\frac{\gamma k_l \Delta T_{sat}}{\sqrt{\pi \alpha_l t}} \times \frac{\pi D^2}{4} \psi = -\frac{d\left(\psi \frac{\pi D^2}{4} \delta \rho_l C_{pl} \Delta T_w\right)}{dt} \quad \text{or}$$

$$\frac{d\delta}{dt} + \frac{2\delta}{D}\frac{dD}{dt} = -\frac{\gamma\sqrt{\alpha_l}}{\sqrt{\pi t}} \qquad (11)$$

Using the experimental data of Siegel & Keshok [15] for the growth of vapour bubbles in saturated boiling of distilled water at atmospheric pressure, the following equation has been developed by using regression analysis :

$$D = 1.664 \frac{Ja}{Pr^{0.5}} \sqrt{\alpha_l t} \qquad (12)$$

Eq.(12) has been tested against the experimental data of earlier investigators for the boiling of distilled water and organic liquids at atmospheric and subatmospheric pressures.
omparison between experimentally measured values of oubble diameter for distilled water and predictions due to Siegel and Keshok [15] , Saini et. al. [12] , Plesset and Zwick [11], Swadiski [cf. 9] at atmospheric pressure and Cole and Shulman [1] at 12.93 kN/m^2 pressure is is shown in Fig.1. It is seen from the plot that the prediction due to the above equation are in good agreement with the experimental values within a maximum error of ±20 %. Experimental values of bubble diameter obtained by Cole and Shulman [1] for boiling of carbon tetrachloride at 18.21 kN/m^2 pressure,n-pentane at 101.3 kN/m^2 pressure, toluene at 6.33 kN/m^2 pressure, acetone at 29.30 kN/m^2 pressure and by Akiyama

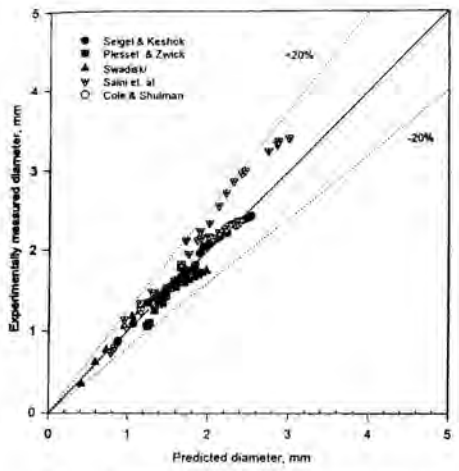

Fig. 1. Comparison of bubble diameter predicted by Eq. (12) with the experimental values for boiling of distilled water

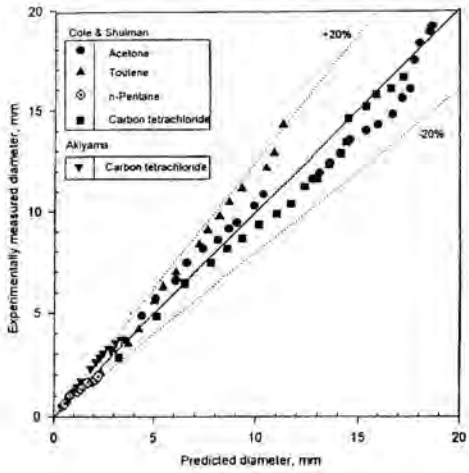

Fig. 2. Comparison of bubble diameter predicted by Eq. (12) with the experimental values for boiling of organic liquids

[cf.13] for boiling of carbon tetrachloride at 40.11 kN/m^2 pressure have been plotted against the predictions due to Eq.(12) in Fig.2. The plot indicates a good agreement between the two within a maximum error of ±20 %. Therefore, Eq.(12) can be safely employed to predict instantaneous bubble diameter during growth period.

Use of Eq. (12) in Equation (11) leads to :

$$\frac{d\delta}{dt}+\frac{\delta}{t}=-\frac{\gamma\sqrt{\alpha_l}}{\sqrt{\pi t}} \tag{13}$$

Equation (13) is solved with the boundary condition of $\delta = 0$ at $t = t_g$ and the following expression is obtained :

$$\delta=\frac{2}{3}\frac{\gamma\sqrt{\alpha_l}}{\sqrt{\pi}}\sqrt{t}\left[\left(\frac{t_g}{t}\right)^{\frac{3}{2}}-1\right] \tag{14}$$

Equation (14) is used for the determination of thickness of microlayer as a function of time from the knowledge of growth period, t_g and physico-thermal properties of the liquid and heating surface involved in the process of boiling.

Heat transfer rate per bubble during the growth period is given by :

$$Q_b = A_c\delta\rho_l\lambda \tag{15}$$

Substituting the values of A_c from Eq. (8) and δ from Eq. (14) into Eq. (15), following expression is obtained :

$$Q_b=\frac{\sqrt{\pi(1.664)^2\gamma\psi}}{6}\frac{Ja^2}{Pr}\alpha_l^{\frac{3}{2}}\rho_l\lambda t^{\frac{3}{2}}\left[\left(\frac{t_g}{t}\right)^{\frac{3}{2}}-1\right] \tag{16}$$

Average heat flow rate associated per bubble during growth period is as follows :

$$\overline{Q}_g=\frac{\int_0^{t_g}Q_b\,dt}{\int_0^{t_g}dt}=\frac{0.492\gamma\psi Ja^2}{Pr}\alpha_l^{\frac{1}{2}}\rho_l\lambda t_g^{\frac{1}{2}} \tag{17}$$

Heat flow rate during ebullition cycle

Since growth period and waiting period occur in series in a cycle, average heat transfer rate per cycle is :

$$\overline{Q}_{b,cycle}=\left(\overline{Q}_W\times t_w+\overline{Q}_g\times t_g\right)\times\frac{1}{\left(t_w+t_g\right)} \tag{18}$$

Applying the condition $t_w=3t_g$ as given by [17] and substituting Eqs.(4 & 17) into Eq. (18), following expression is obtained :

$$\overline{Q}_{b,cycle}=\left\{\begin{aligned}&\frac{1.535k_l\Delta T_w}{\sqrt{\alpha_l t_g}}\times\left(\frac{133.3}{P}\right)^2\left(\frac{\sigma}{g(\rho_l-\rho_v)}\right)\\&+\frac{0.123\gamma\psi Ja^2}{Pr}\alpha_l^{\frac{1}{2}}\rho_l\lambda t_g^{\frac{1}{2}}\end{aligned}\right\} \tag{19}$$

Equation (19) provides heat transfer rate per bubble originating from a single nucleation site. Hence, for the entire heating surface containing N number of nucleation sites, total heat transfer rate associated with bubbles is :

$$\overline{Q}_{Total,b}=\overline{Q}_{b,cycle}\times N$$

or

$$\overline{q}_{Total,b}=\left\{\begin{aligned}&\frac{1.535k_l\Delta T_w}{\sqrt{\alpha_l t_g}}\times\left(\frac{133.3}{P}\right)^2\left(\frac{\sigma}{g(\rho_l-\rho_v)}\right)\\&+\frac{0.123\gamma\psi Ja^2}{Pr}\alpha_l^{\frac{1}{2}}\rho_l\lambda t_g^{\frac{1}{2}}\end{aligned}\right\}\times\frac{N}{A} \tag{20}$$

Growth period, t_g is obtained by substituting bubble departure diameter, D from Eq. (3) into Eq. (12):

$$t_g=\frac{Pr}{Ja^2\alpha_l(1.664)^2}\left(\frac{133.3}{P}\right)^2\left(\frac{\sigma}{g(\rho_l-\rho_v)}\right) \tag{21}$$

Hence, Eq. (21) assumes the following form :

$$\overline{q}_{Total,b}=\left\{\begin{aligned}&\frac{2.554k_l\Delta T_w Ja}{Pr^{0.5}}\times\left(\frac{133.3}{P}\right)\left(\frac{\sigma}{g(\rho_l-\rho_v)}\right)^{0.5}\\&+\frac{0.0267\gamma\psi\,Pr^{0.5}}{Ja}\alpha_l\lambda\left(\frac{133.3}{P}\right)^3\left(\frac{\sigma}{g(\rho_l-\rho_v)}\right)^{\frac{3}{2}}\end{aligned}\right\}\times\frac{N}{A} \tag{22}$$

Heat flux associated with natural convection

Heat from the area outside the zone of bubble influence is transferred by natural convection. Therefore, heat flux in this region is as follows:

$$q_{NC}=h\left(1-A_{inf}\frac{N}{A}\right)\Delta T_w \tag{23}$$

The value of heat transfer coefficient, h in natural convection is obtained by the following correlation [5]:

$$\frac{hd}{k_l}=C\left(Gr\times Pr\right)^n \tag{24}$$

where the values of constant, C and exponent, n depend upon the product of Grashof number and Prandl number. These values are listed in [5].

Total heat flux for boiling

Total heat flux associated during boiling is given by :

$$q_{Total,Boiling} = q_{Total,B} + q_{NC}$$

or

$$\bar{q}_{Total,Boiling} = \left\{ \frac{2.554 k_l \Delta T_w Ja}{Pr^{0.5}} \times \left(\frac{133.3}{P} \right) \left(\frac{\sigma}{g(\rho_l - \rho_v)} \right)^{0.5} + \frac{0.0267 \gamma \psi Pr^{0.3}}{Ja} \alpha_l \lambda \left(\frac{133.3}{P} \right)^{1} \left(\frac{\sigma}{g(\rho_l - \rho_v)} \right)^{\frac{1}{2}} \right\} \times \frac{N}{A} + h\left(1 - A_{Inf} \frac{N}{A}\right) \Delta T_w \qquad (25)$$

The value of ψ is unity as mentioned above.

Equation (25) can be used for the calculation of heat flux transferred from heating surface to boiling liquid at a given pressure and wall superheat from the knowledge of physico-thermal properties of liquid and heating surface and the experimental data of nucleation site density. Experimentally determined values of nucleation site density for boiling of distilled water due to Gaertner[3] ,Kurihara and Mayor [8] and Wang & Dhir [19], of acetone due to Kurihara & Mayor [8] and of carbon tetrachloride due to Kirby & Westwater [7] and Kurihara & Mayor [8] are employed in Eq.(25) to determine heat flux.The predictions have been compared with the experimentally obtained values in Fig.3. The plot indicates a good match between the two within an error of ±20%. Thus, Eq.(25) can be used to predict heat flux for the boiling of liquids.

It also brings out that several heat transfer mechanisms namely; transient conduction from heating surface to the saturated liquid surrounding it, evaporation of the microlayer existing beneath the bubble and natural convection from portion unaffected by bubble activity operate simultaneously in the boiling of liquids at atmospheric and sub-atmospheric pressures. The analysis is applicable at low values of the heat flux so that isolated vapor bubbles develop on the heating surface leaving a portion unaffected by the activity of vapor-bubbles for natural convection.

CONCLUSION

1. An empirical equation for bubble diameter during growth period of ebullition cycle of boiling has been developed. The computed diameter of bubble has been found to agree well with the experimental data of earlier investigators for the boiling of distilled water and organic liquids at atmospheric and subatmospheric pressures.
2. An analytical expression has been obtained to predict heat flux during boiling of liquids from the knowledge of pressure, wall superheat, boiling liquids and heating surface properties and experimentally determined nucleation site density. The predictions from the model have been found to be in good agreement with the experimental data of earlier investigators.
3. It has been established that transient heat conduction from the heated surface to boiling liquids, evaporation of microlayer containing dry spot and the natural convection from the area outside the bubble influence area operate simultaneously in the process of boiling of liquids.

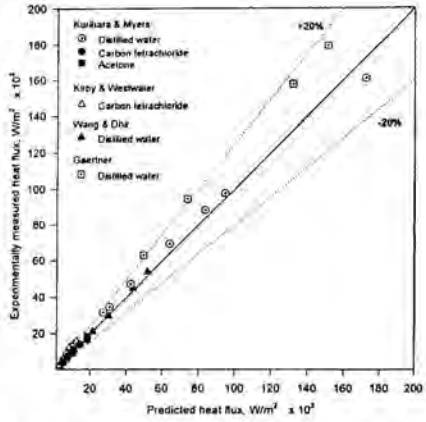

Fig.3.Comparison of heat flux predicted by Eq.(25) with the experimentally- measured heat flux

REFERENCS

1. Cole, R. and Shulman, H.L.,1966, " Bubble growth rates at high Jakob numbers", Int. J. Heat Mass Transfer, Vol. 9, pp 1377-1390, 1966
2. Cole, R.and Shulman, H.L.,1966, "bubble departure diameters at subatmospheric pressures", Chem. Engg. Prog. Symp. Ser. , Vol. 62,no.64 pp 6-16.
3. Gaertner, R.F.,1965, "Photographic study of Nucleate pool boiling on a horizontal surface", Trans. ASME ,J.Heat transfer, pp 18-29.
4. Han, C.Y. and Griffith, P., 1965, " The mechanism of heat transfer in nucleate pool boiling",part II,Int. J. Heat Mass Transfer, Vol. 8, pp 905-914.
5. Holman,J.P.,1997, "Heat transfer",8th ed.,McGraw-Hill,Inc.,Newyork
6. Hsu, Y.Y. and Graham R.W., 1976, "Transport Processes in Boiling , Two-Phase Systems",

Hemisphere publishing corporation and Mc Graw-Hill.
7. Kirby, D.B. and Westwater, J.W., 1964, "Bubble and vapour behaviour on a heated horizontal plate during pool boiling near burnout.", Heat transfer, Chem. Symp., Seri., Vol. 61., No. 57., p 236-238.
8. Kurihara, H.M. and Myers, J.C., 1971, " The effect of superheat and roughness on boiling liquids", AIChE J., Vol. 17, pp 1050-1056.
9. Lee R.C. and Nydahl J.E.,1989,"Numerical Calculation of bubble growth in nucleate boiling from Inception through departure., Trans. ASME. J., Heat Transfer. Vol. 41.
10. Mikic, B.B. and Rohsenow, W.M., 1969, "A new correlation of pool boiling data including the effect of heating surface characteristics", Tran. ASME, J. Heat Transfer, pp 245-250.
11. Plesset, M.S. and Zwick, S.A.,1952, " A nonsteady heat diffusion problem with spherical symmetry",J Appl. Physics,vol. 23, no. 1,pp 95-98.
12. Saini, J.S., Gupta, C.P., and Lal, S.,1975, " Evaluation of micro layer contribution to bubble growth in nucleate pool boiling using new bubble growth model", Int. J. Heat Mass Transfer, Vol. 18, pp-469-472.
13. Saini, J.S.,1975, "Study of bubble growth and departure in nucleate pool" ,Ph.D. Thesis,Deptt. Of Mech. & Ind. Engg.,University of Roorkee,Roorkee,India
14. Semar,V. and Hooper,F.C.,1969, "The initial vapor buble growth on a heated wall during nucleate boiling",Int. J. Heat Mass Transfer, Vol. 12, pp 1627-1639.
15. Siegel,R and Keshok,E.G.,1964,"Effects of reduced gravity on nucleate boiling bubble dynamics in saturated water", AIChE J,vol. 10,no. 4, pp 509-517.
16. Unal,H.C.,1976, "Maximum bubble diameter, maximum bubble growth time and bubble growth rate during the subcooled nucleate flow boiling of water up to 17.7 MN/m^2 ", ,Int. J. Heat Mass Transfer,vol. 19,pp 643-649.
17. van Stalen, S.J.D.,1966,"The mechanism of nucleate boiling in pure liquids and in binary mixtures, part I & II, Int. J. Heat Mass Transfer, Vol. 9, pp 995-1020 & 1021-1046.
18. van Stalen, S. and Cole,R.,1979,"Boiling Phenomena",HemesphererPublishingCorporation, Washington.
19. Wang, C.H. and Dhir, V.K.,1993, "Effect of surface wettability on active nucleate site density during pool boiling of water on a vertical surface", Trans. ASME, J. Heat Transfer, Vol. 115, pp-659-669.
20. Webb,R.L.,1994. " Principles of Enhanced Heat Transfer", Wiley, Newyork.

HEFAT2002
1st International Conference on Heat Transfer, Fluid Mechanics, and Thermodynamics
8-10 April 2002, Kruger Park, South Africa
WH1

BUBBLE GENERATION ON A HEATED FINE WIRE

H. Wang, X.F. Peng and B.X. Wang
Department of Thermal Engineering, Tsinghua University, Beijing 100084, China
Email: pxf-dte@mail.tsinghua.edu.cn **Fax: (8610)62770209**

ABSTRACT

Relationship between bubbles and temperature profile of a heated wire was analyzed in present research. Physical models were proposed to analyze the dynamic processes and understand the mechanism of interaction among a few bubbles. It was observed that the bubble formation or growing at a nucleate site could cause a significant or sharp temperature decrease and greatly impress the bubble generation during bubble formation and growing in the adjacent region, even breaking off bubble growing and/or generation in this influenced region. Comparing with a heating plane, a fine wire has weaker heat capacity and weaker capability of heat conduction, this is an important reason for higher superheat of boiling on a fine wire. Numerical simulation of bubble interaction was carried out and some interesting phenomena were explored.

NOMENCLATURE

a	thermal diffusivity (m/s)
c	specific heat (J/kg K)
q_b	average heat transfer rate of bubble (W)
Q_{v0}	heat absorbed by embryo bubble (J)
q_v	inner heat source rate of wire (W)
R_d	bubble departure radius (m)
Tg	super heat (K)
S	distance between two sites (m)
w	cross section area of wire (m^2)
x	coordinate along the wire (m)

Greek Letters

α	convection heat transfer coefficient
θ	temperature (K)
ρ	density (kg/m^3)
τ	time (s)
τ_b	bubble growth time (s)

Subscripts

b	bubble
d	bubble departure
1	nucleate site1
2	nucleate site2

INTRODUCTION

So far, there are no comprehensive theoretical models available to describe the dynamical processes because of the great complexity that characterizes boiling phenomenon. After his review of traditional boiling theories and available investigations, Dhir [1] appealed to people to understand boiling renewedly. Sadasivan [2-4] indicated that what conventional theories ignored is just the nonlinear characteristics of boiling process.

The investigations on nonlinear characteristics of boiling process were conducted by several investigators and show us more essential mechanism of nucleate boiling. However, there are still many problems remained to be understood. Much work just illustrated the nonlinear interaction qualitatively and the mathematic description of dynamical process of interaction among nucleation sites is highly lacking.

Henley and Hummel [5] first mentioned the interaction among nucleation sites in 1967. Then, Eddington and Kenning [6] suggested that the interaction of the bubble emission phenomena occurs at an adjacent site. In their experiment, a method of determining the bubble population data by studying bubble nucleation from supersaturated gas solutions was developed. The nucleation results showed that there were many more cavities satisfying the site activation requisite condition than those actually activated during boiling on the surface. The failure of apparently stable sites to nucleate was attributed to thermal interference from an already active site.

Obviously, there is an urgent demand for understanding the nonlinear phenomena and bubble/site interaction in boiling. In present work, the relationship between bubbles and temperature distribution of a heated wire was analyzed theoretically.

THEORETICAL MODEL AND ANALYSIS

The whole process of a bubble growth was separated into three periods: embryo period, growing period and waiting period. During embryo period, bubble was considered as an instant heat source absorbing heat from heating wire; While during growing period, bubble was considered as a continuous

heat source; In waiting process, the influence of bubble was considered as an instant heat source, and the attention was paid to know how the influence of bubble penetrates along the heating wire with time passing. Heating wire was assumed to be one-dimensional with infinite length. Boiling occurred in saturated liquid.

Influence of single bubble on wire temperature

While in the embryo period, an embryo bubble is considered as a point heat source that absorbs heat instantly. The temperature field is described as:

$$\theta = \frac{-Q_{r0}}{2w\rho c\sqrt{\pi a\tau}}\exp[\frac{-x^2}{4a\tau}] \qquad (1)$$

in which Q_{r0} is the heat that supplies to the embryo bubble. Equation (1) shows the influence of the formation of an embryo bubble to the temperature field on the heating wire. Usually, embryo bubble is very small and value of Q_{r0} is tiny consequently.

When a bubble generates, it first forms an embryo bubble at active nucleate site, then it absorbs heat and departs. This generation process could be prompt if it is in saturated liquid. The bubble causes a temperature sinking at its site. We want to clarify how the temperature sinking at nucleate site penetrates along the heating wire. To simplify the calculation, a bubble is considered as a segment of heat source that absorbs heat instantly. The temperature change with time passing and location variation is derived as:

$$\theta(x,\tau) = -4\frac{(q_b - q_v)\cdot\tau_b}{2\cdot w\cdot\rho\cdot c}[erf(\frac{x+R_d}{\sqrt{4a\tau}}) - erf(\frac{x-R_d}{\sqrt{4a\tau}})] + \frac{-Q_{r0}}{2w\rho c\sqrt{\pi a\tau}}\exp[\frac{-x^2}{4a\tau}] + \frac{1}{2\pi\cdot\alpha}\{q_v - [q_v - Tg\cdot 2\pi\cdot\alpha]\exp(-2\pi\cdot\alpha\cdot\tau/w\cdot\rho\cdot c)\} \qquad (2)$$

The first term of right side of Equation (2) represents the influence from bubble. The second term represents the influence from embryo bubble. In fact the second term can be ignored because embryo bubble just absorb much less heat from wire than that of normal bubbles.

To illustrate the actual temperature, water-copper wire combination was considered as an example. Working fluid, water, was assumed to be saturated at atmospheric pressure, and radius of copper wire was r=0.05mm, water-copper contact angle 30 degree. Referring to classical boiling theory and experimental measurement, the critical temperature for site activation was taken as 110°C. With these specified conditions the dynamical temperature behavior was numerically simulated. Figure 1 presents the superheat change at point x=0 on the wire and at the time of 0.014 second. The wire temperature significantly decreases from the point of x=0 to x=2.1mm. More close to the origin point (x=0) it is, more rapidly temperature decreases. And by time pass, temperature close to the bubble site would recover promptly. The influence of a single bubble to heated wire is local and short-lived.

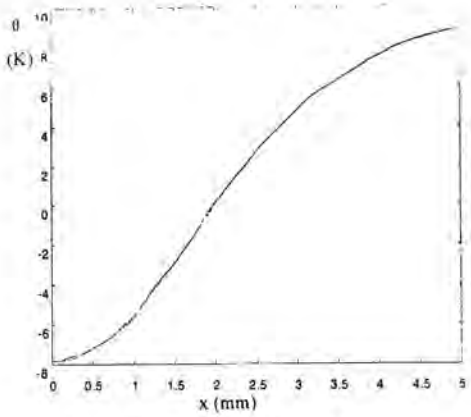

Fig.1 temperature change at 0.014s for a single bubble

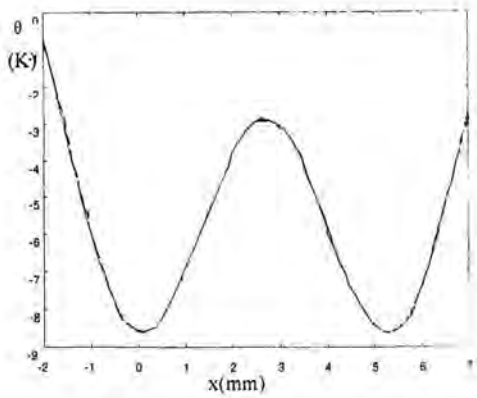

Fig.2 temperature change at 0.014s for two bubbles

Interaction between two or more bubbles

By superposition of temperature, temperature dynamical aspect caused by two bubbles formation and growing can be obtained. With the same conditions for the single bubble situation as in Fig.1, the numerically simulated result is illustrated in Fig.2. The highest decrease of temperature is 8.6K, 0.7K higher compared with the single bubble generation in Fig.1, and the influence range of bubble growth is wider. Considering the interaction between two bubbles, the

temperature is given as

$$\theta_{12} = \frac{-Q_{b1}}{4 \cdot w \cdot \rho \cdot c \cdot R_d}\left[erf\left(\frac{S + R_{d1}}{\sqrt{4a\tau}}\right) - erf\left(\frac{S - R_{d1}}{\sqrt{4a\tau}}\right)\right]$$

$$+\frac{-Q_{r01}}{2w\rho c\sqrt{\pi a\tau}} e^{-\frac{S^2}{4a\tau}} \qquad (3)$$

Distance between two bubbles, S, is an important factor for the interaction between two bubbles. For same water-copper combination and conditions as previous simulations, temperature influence from bubble 1 to bubble2 is shown in Fig.3 and Fig.4 corresponding to $S=3R_d$ and $S=9R_d$ respectively.

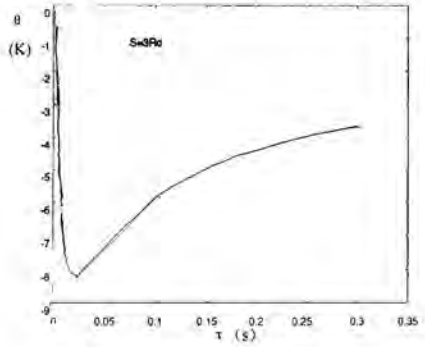

Fig.3 Temperature influence for $S=3R_d$

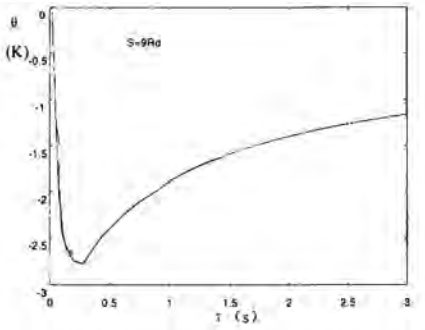

Fig.4 Temperature influence for $S=9R_d$

From Fig.3 the temperature decrease of site 2 caused by bubble 1 could even be –8K for $S=3R_d$, while the decrease only –2.7K for $S=9R_d$. It is obvious that longer distance between two sites results in weaker interaction between them. On the other hand, the time in which the temperature influence spreads from site 1 to site 2 will be longer. $S=3R_d$, the temperature of site 2 decreases to the lowest value at 0.025s, while for $S=9R_d$, the temperature of site 2 decreases to the lowest value at 0.24s. If it takes a relative longer time for influence to spread from site to site, the interaction could be very weak.

Influence of bubble growth on superheat

For a bubble growing at the site, it works as a heat source that absorbs heat continuously. The dynamical temperature was derived as:

$$\theta = \frac{q}{wc\rho}\left\{\sqrt{\frac{\tau}{\pi a}} \cdot \exp\left(\frac{-x^2}{4a\tau}\right) - \frac{x}{2a} \cdot erfc\left(\frac{x}{2 \cdot \sqrt{a\tau}}\right)\right\} +$$

$$\frac{1}{2\pi r \cdot \alpha}\{q_v - [q_v - Tg \cdot 2\pi r \cdot \alpha]\exp(-2\pi r \cdot \alpha \cdot \tau / w \cdot \rho \cdot c)\} \qquad (4)$$

Clearly, the growing of a bubble might be interrupted by the temperature sharp decreasing caused by heat absorption of bubble growing at adjacent sites. The radius of the wire imposes great influence on the temperature change at bubble sites. Comparing Fig.5 with Fig.6 for r=0.05mm and r=0.015mm respectively, it is easy to see that the lowest value of θ changes from –10.2K to –20K as wire diameter recedes. For the investigated cases, the difference is almost twice.

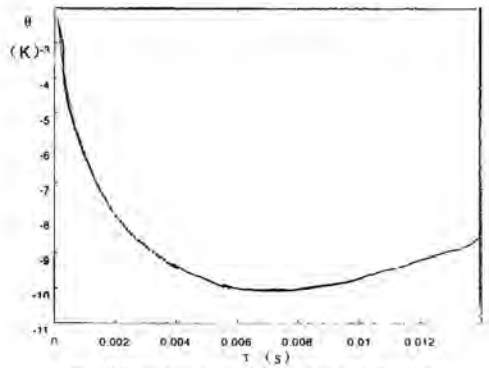

Fig.5 Temperature change for r=0.05mm

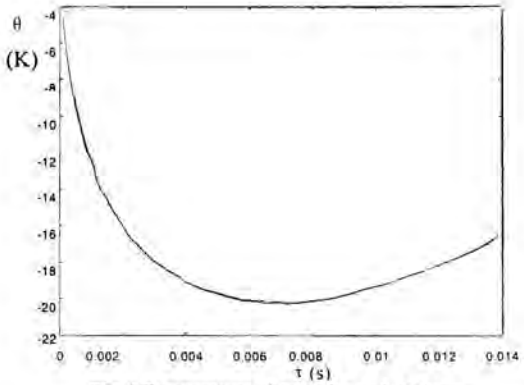

Fig.6 Temperature change for r=0.015mm

BUBBLE GENERATING SIMULATION

Two sites with same nucleation temperature

Based on the work above, a program was made to simulate the thermal interaction between two sites. Simulation condition is as same as in Fig.1. In the case simulated there were two adjacent bubble sites, site 1 and site 2. The parameters of two sites were assumed to be identical and the distance between them was S. Because of being heated continuously, both sites would reach activation critical temperature, T_i, and site 1 produces a bubble first, which would correspondently cause some disturbance on adjacent sites.

Result of simulation for bubble number of each site is shown in Table 1. The departure diameter of the bubble was calculated through empirical formulation as D_d=2.6mm[1]. Process time is the time lasted for boiling process that was simulated in computer. Case 1 to case 3 is for 10 seconds, and case 4 and case 5 for 100 seconds.

Table 1 Simulation results of bubble number

Case	Dist-ance	Time step (second)	Process time (second)	Number at site 1	Number at site 2
1	$1D_d$	0.001	10	29	13
2	$2D_d$	0.001	10	23	19
3	$7D_d$	0.001	10	21	21
4	$1D_d$	0.001	100	221	203
5	$3D_d$	0.001	100	213	212

Comparing the results of case 1 to case 3, some conclusions reached are as follows.

[1]. Though the critical temperature for bubble producing, Ti, was same to both sites, two sites produced different number of bubbles. Case 1, for example, site 1 produced 29 bubbles, while site 2 only produced 13 bubbles.

[2]. Interaction between two sites would be weaker as the distance of two sites increased. From case 3 in which distance was 7 times bubble departure diameter, it is obvious that the interaction was very weak, and both sites produced 21 bubbles, same to each other.

Compared case 4 with case 5, resemble result could be obtained. When distance is 1 times departure diameter, site 1 and site 2 produces 221 and 203 bubbles, respectively. However, when distance increases to 3 times departure, site 1 and site 2 produces 213 and 212 bubbles respectively, almost the same number. This means very weak interaction between two sites. Generally, there is not any distinct and direct interaction between two sites if the separating distance between two sites exceeds three times departure diameter [7-9].

Time sequence of bubble producing of site 1 for case 1 is plotted in Fig.7, in which each "*" symbol represents site 1 producing bubble once. X-axis is time. It is obvious that time distribution of bubble producing of site1 was not uniform, sometimes tight and sometimes sparse, which indicated the influence from site 2.

Time sequence of bubble producing of site 1 for case 2 is plotted in Fig.8. Time distribution of bubble producing of site 1 was also not uniform. It is obvious when $S = 2D_d$ there is still strong interaction between two sites.

Time sequence of bubble producing of site 1 for case 3 is plotted in Fig.9. Time distribution of bubble producing of site 1 was almost uniform, which indicates the influence from site 2 was weak.

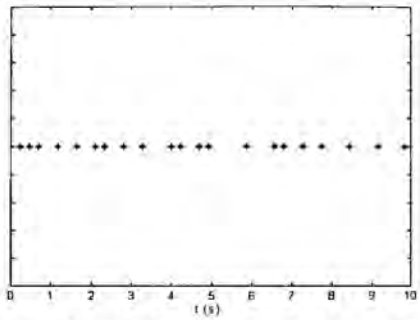

Fig.7 Bubble producing sequence at site 1 (case 1 $S=D_d$)

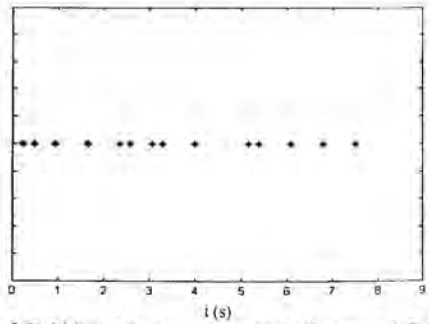

Fig.8 Bubble producing sequence at site1(case 2 $S=2D_d$)

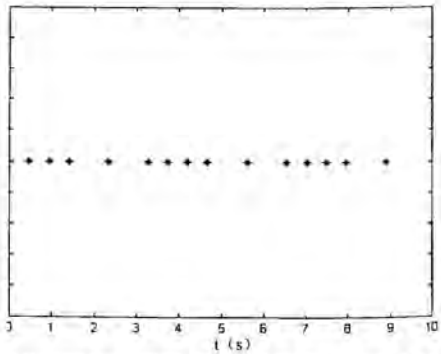

Fig.9 Bubble producing sequence at site 1 (case 3 $S=7D_d$)

Two sites with different critical temperature

In actual boiling process, different sites have different construction, which leads to different critical temperature to produce bubbles. Some sites need high super heat and some sites just need lower super heat. Here critical temperature of site 1 was assumed to be higher than site 2, i.e., bubble producing of site 1 would be difficult than site 2. The simulation results are shown in Table 2.

Table 2 Results of bubble production

	Distance	Ti_1-Ti_2 (K) (Ti_1>Ti_2)	Time step (second)	Process time (second)	Number at site 1	Number at site 2
1	$1D_d$	0.1	0.001	10	18	24
2	$1D_d$	0.2	0.001	10	7	35
3	$1D_d$	0.5	0.001	10	0	42
4	$3D_d$	0.1	0.001	10	21	21
5	$3D_d$	0.2	0.001	10	19	23
6	$3D_d$	0.5	0.001	10	14	28

From Table 2 and the comparison with Table 1, we can make analysis as follows:

[1]. Because bubble producing at site 1 is more difficult than at site 2, site 1 was in inferior position relative to site 2. For case 3 in Table 2, the critical temperature of site 1 was higher than site 2 by 0.5K, and site 1 produced zero bubble during simulated time, i.e., site 1 was depressed by site 2 completely.

[2]. With increasing of the distance between two sites, the interaction intensity decreases swiftly. Compared case 3 with case 6, when distance increased to $3D_d$, site 1 could produce 14 bubbles. Obviously, the distance plays very important role in interacting of nucleate sites.

CONCLUSION

The mathematical descriptions of a heating wire temperature were established to understand the thermal influence of bubbles and or nucleate sites on the wire. The temperature characteristics of the wire with bubble producing were analyzed and local temperature would sharply be decreased due to bubble nucleation and growing. The temperature decrease caused by bubble growing may explain why boiling on the wire needs higher super heat than boiling on the wall surface with identical thermal fluid and boundary conditions.

The analysis of multi-bubble growth indicates that interaction between bubbles is highly affected by radius of wire and distance between two bubble sites. A numerical investigation was conducted to simulate the bubble producing and growing on the wire. These dynamical behaviors demonstrate the thermal influence between bubbles.

ACKNOWLEDGEMENT

This research is currently supported by the National Natural Science Foundation of China (Contracts No. 59625612 and 59976016).

REFERENCES

[1]. Dhir V. K., 1990, nucleate and Transition Boiling Heat Transfer Under Pool and External Flow Conditions," Proceeding of International Heat Transfer Conference-9st, London: Taylor and Francis, pp.129-155

[2]. Sadasivan P Unal C and Nelson R A., 1994, nonlinear Aspects of High Heat Flux Nucleate Boiling Heat Transfer: Formulation," LAUR-94-2222, also ASME HTD-Vol.298: pp.91-102

[3]. Sadasivan P Unal C and Nelson R A. , 1994, nonlinear Aspects of High Heat Flux Nucleate Boiling Heat Transfer," Results. LAUR-94-106-Revised, also ASME HTD-Vol.298: pp103-114

[4]. Sadasivan P Unal C and Nelson R A., 1995, nonlinear Aspects of High Heat Flux Nucleate Boiling Heat Transfer, " J. Heat Transfer, Vol.117: pp981-989

[5]. Henley, J. J., and Hummel, R. L., 1967, " Third Factor in Boiling Nucleation," Industrial and Engineering Chemistry, Fundamentals, Vol. 6, No. 4, pp. 603-606

[6]. Eddington, R.I., and Kenning, D.B.R., 1978, the Prediction of Flow Boiling Bubble Populations From Gas Bubbles Nucleation Experiments, " Proceedings of the 6th International Heat Transfer Conference, Toronto. Vol.1. pp.275-279

[7]. Kenning D.B.R., Victor H. and Del Valle M., 1981, Fully-Developed Nucleate Boiling: Overlap Of Areas Of Influence And Interference Between Bubble Sites, " International Journal of Heat and Mass Transfer. Vol. 24(6) pp.1025-1032

[8]. Chekanov V.V., 1977, Interaction of Centers in Nucleate Boiling," Translated from Teplofizika Vysokikh Temperatur, Vol.102(3) pp.121-128

[9]. Sultan M. and Judd R. L., 1983, Interaction of the Nucleation Phenomena at Adjacent Sites in Nucleate Boiling, Journal of Heat Transfer, " Vol.105, pp.3-10

Proceedings of HEFAT2002
1st International Conference on Heat Transfer, Fluid Mechanics, and Thermodynamics
8-10 April 2002, Kruger Park, South Africa
BR1

Condensation of R134a inside smooth tubes with and without polyol ester based lubricant

R. Bassi and P. K. Bansal
Department of Mechanical Engineering,
The University of Auckland,
Private 92019, Auckland, New Zealand
(Email: p.bansal@auckland.ac.nz)

ABSTRACT

This paper presents a comparative study of the condensation heat transfer coefficients in a smooth tube when operating with pure refrigerant R134a and its mixture with lubricant Castrol "Icematic SW". The lubricant is a synthetic polyol ester based oil commonly used in lubricating the compressors. Two concentrations of R134a-oil mixtures of 2% and 5 % oil (by mass) were analysed. The runs were carried out for a range of saturation temperatures of R134a between 35 and 45 °C. The mass flow rates of the refrigerant and the mixtures were carefully maintained at 1g/s, with a vapour quality varying between 0.02-0.98. The effects of vapour quality, flow rate, saturation temperature and temperature difference between saturation and tube wall on the heat transfer coefficient are investigated by analysing the experimental data. Finally experimental results are compared with predictions from earlier models [1-4].

Key words: Two phase, in tube condensation, R-134a, refrigerant-oil mixture, condensation, heat transfer.

INTRODUCTION

A typical problem in a vapour compression refrigeration system is the mixing of small amounts of compressor lubricant in the refrigerant during the compression stage of the cycle. This mixture then becomes the working fluid and is responsible for the heat transfer in the cycle. It is believed that the mixing of the oil influences the performance of the condenser and thus affects the performance of the entire system. This paper therefore investigates the condensation of the oil-refrigerant mixture in a horizontal smooth tube.

The influence of oil on the condensation of a refrigerant has been investigated since 1962 [5] involving refrigerants CFC12 and HCFC22. These studies had reported a drop in the heat transfer coefficients as a result of the mixing of oil in the refrigerant. Tichy [6] reported 10% and 23% reduction in CFC 12 heat transfer coefficients at 2% and 5% 300 SUS napthenic base oil concentrations respectively. Schlager [7] reported that the condensation of HCFC22 and 150 SUS napthenic oil mixture resulted in a 13% decrease in the heat transfer with 5% lubricant (by mass) in the mixture. Eckels and Pate [8] investigated the effects of the mixing of oil in CFC12 and HFC134a. They found a drop of around 10% in the heat transfer for CFC12 and 5% 150 SUS napthenic oil mixture but no significant effect of 165 SUS PAG oil on the heat transfer coefficient of HFC134a. Due to the fact that various researchers used different definitions for the saturation temperature, there could be some variation in the comparative analysis of the results. However, recently Shao [3, 9, 10] studied the effect of the mixture of R134a and ester based oil on the heat transfer inside the condenser. A drop of about 10 and 20% in the two-phase condensation heat transfer coefficient of R134a was found, when oil concentration was increased 2% and 5% (by mass) respectively. However, the oil used and the experimental details in the present study are different to those used by Shao.

The aim of this paper is to investigate the effects of the mixing of Castrol "Icematic SW", a synthetic polyol ester based oil, in R134a on its performance in condensers. This mixture is commonly used in the domestic refrigeration systems in New Zealand. The effects of this mixture on the refrigeration cycle were unknown in the international market, specifically for systems operating in the atmospheric conditions in New Zealand.

NOMENCLATURE

Symbol	Units	Quantity
A	m^2	Area
C	W/K	Heat capacity
c_p	J/kg.K	Specific Heat
d	m	Diameter
E	-	Effectiveness
Fr	-	Froude number
F_1, F_2	-	Dimensionless
g	m/s^2	Gravity
G	$Kg/s.m^2$	Mass flux
Ga	-	Galileo number
h	J/kg	Enthalpy
k	W/m.K	Thermal conductivity
$\dot{m}$	Kg/s	Mass flow rate
p	kPa (kN/m^2)	Pressure
Re_v	$= \frac{G_v d_i}{\mu_l}\left(\frac{\rho_l}{\rho_v}\right)^{0.5}$	Vapour Reynolds number in two-phase.
$\dot{Q}$	W	Heat rate
ΔT	K	Temperature Difference
T	K	Temperature
U	$W/m^2.K$	Overall heat transfer coefficient
V	m/s	Velocity
x	-	Vapour quality
X_{tt}	-	Lockhart-Martinelli parameter

Greek Symbols	Quantity
ν	: Kinematic Viscosity
α	: Heat transfer coefficient
ρ	: Density
Φ	: Condensate angle
β	: Mass transfer coefficient
μ	: Dynamic Viscosity

Subscripts

c	: Critical
eq	: Equivalent
fg	: Liquid-vapour
h	: Hydraulic
i	: Internal/Inner
l	: Liquid at saturation pressure
lo	: Liquid and outer
o	: Outer
v	: Vapour at saturation pressure

TEST FACILITY

A test facility was designed specifically to investigate the heat transfer during condensation of pure refrigerant and refrigerant-oil mixtures inside smooth horizontal tubes. It allowed in-tube heat transfer, temperature and pressure drop data to be collected over a wide range of operating conditions. The facility had a maximum working pressure of around 1 MPa, while the mass flux of the refrigerant varied up to 650 $kg/m^2.s$.

Experimental rig

The experimental rig is shown in Figure 1. The purpose of this rig was to supply a working fluid to the inlet of the test section with varying thermodynamic states. The experimental rig had five loops, namely the preheating, superheating, temperature stabilisation, condensation, and the cooling water loop. Each of these loops was designed primarily to achieve a specific thermodynamic state of the refrigerant.

In a vapour compression refrigeration cycle, a compressor circulates the refrigerant through the system, however, in order to determine the effect of a known concentration of lubricant in R134a, a compressor could not be used to pressurise the refrigerant. This was necessary to avoid the contamination of the refrigerant with an unknown concentration of oil. Therefore, a new system had to be designed for the experiments to enable the refrigerant flow through the system by generating a pressure differential between two refrigerant bottles, located at the extreme ends of the apparatus (ref. Figure 1).

The pressure inside the starter bottle was increased to around 930 kPa by heating the refrigerant inside the starter bottle to the corresponding saturation temperature of 35-37 °C using heater 1 (at location 3) and a PID controller. The pressure of the starter bottle was measured using the pressure transducer located at 4. The pressure inside the receiver bottle was kept around 430kPa at room temperature, (15-20 °C, New Zealand atmospheric conditions). The flow rate of the refrigerant was controlled at 1 g/s using a needle valve and Micro motion flow meter at locations 18 and 19. Temperatures were measured at locations 5 and 21 using PT100 (a temperature sensor) and pressures were taken using pressure transducers at locations 4 and 22.

The effect of oil was investigated by letting the refrigerant flow through the two-phase region using heat exchanger 1. This heat exchanger used a water bath where water was heated to 48 °C with the aid of heater 2 and controlled using a PID controller at location 8. The refrigerant (or refrigerant-oil mixture) flowed through a copper coil of 3.125 mm ID and 3.5 mm OD, submerged

in the hot water. The refrigerant leaving this heat exchanger was measured to be at 38 °C. Sight glasses were placed at locations 6 and 10 to indicate the state of the refrigerant (single or two phase). Temperature of the refrigerant was measured using thermocouples attached at the inlet and exit (locations 7 and 9 respectively) of the heat exchanger.

A temperature stabilisation chamber was placed after location 10 to attain a specific temperature of the refrigerant entering the condenser. The chamber was a 300 mm long hollow cylinder with 26 mm ID and 32 mm OD made out of brass. It was wrapped evenly with motor heating tape to heat the refrigerant inside the chamber. Hence the temperature of the refrigerant entering the condenser was consistently maintained around 39 °C providing about 3 degrees of overall superheat. Refrigerant temperature, measured at location 11 using PT100, was used to control the chamber temperature at 42 °C with the aid of a PID controller at location 12. A pressure transducer placed at location 13 monitored the pressure of the refrigerant entering the condenser.

The condenser was designed to be a counter-cross flow heat exchanger. The length of the condenser coils, made out of smooth copper tubes with 3.125 mm ID and 3.5 mm OD, was 3.6 m. This was then folded into 17 passes across the shell. The temperature of the refrigerant was measured using thermocouples along the condenser at locations 14 (condenser inlet), 15 (middle of the condenser) and 16 (condenser exit).

The condenser was water-cooled, where the water flow rate was controlled at 5 g/s using a manual control valve and monitored with the vortex flow meter at location 25. The cooling water was supplied at a constant temperature of 23°C using heater 3 and a PID controller. Water temperature was measured with thermocouples at locations 26 and 27.

EXPERIMENTAL INVESTIGATIONS

Data Reduction

The following section describes the analysis to determine the internal heat transfer coefficients of R134a and R134a-oil mixtures from the data. It was assumed that stratified film condensation [12] takes place inside the tube.

Calculating the internal heat transfer coefficient

Based on the temperatures and pressures, the net heat flow across the condenser can be defined as-

$$\dot{Q} = UA_0 \Delta T \tag{1}$$

$$\text{where } \frac{1}{UA_0} = \frac{1}{\alpha_i A_i} + \frac{\ln\left(d_0/d_i\right)}{2\pi kL} + \frac{1}{\alpha_0 A_0} \tag{2}$$

$$\frac{\alpha_i \cdot d_i}{k} = Nu_i \tag{3}$$

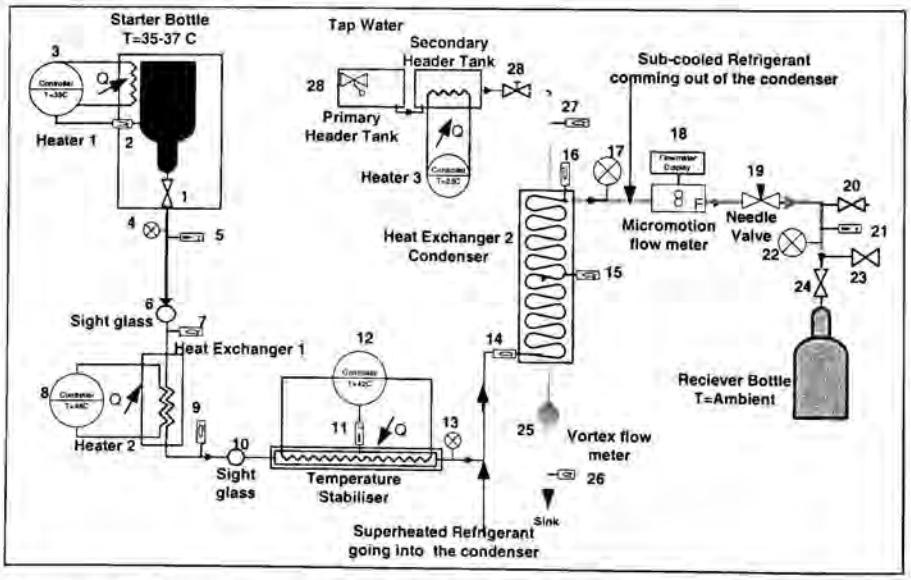

Figure 1: Experimental rig for measuring in-tube condensation heat transfer for R134a/oil mixture.

The Reynolds number was higher than 24000. The Nusselt number could be evaluated [12] as

$$Nu = 0.084 \cdot (Pr_l)^{\frac{1}{3}} \cdot (Re_v)^{0.67} \cdot \left[\frac{h_{lg}}{Cp_l \cdot (T_{saturation} - T_{surface})} \right]^{\left(\frac{1}{6}\right)} \quad (4)$$

Re_v>24000

$$\alpha = \Omega \left[\frac{k_l^3 \rho_l [\rho_l - \rho_v] g \, h_v}{\mu_l D (T_{saturation} - T_{wall})} \right]^{\frac{1}{4}} \quad (5)$$

where the parameter Ω [12] is defined by-

$$\Omega = \frac{\Phi \cdot \beta}{\pi} \quad (6)$$

EXPERIMENTAL DATA

It can be seen from Figures 2a and 2b that the system was in steady state for most of the time during the experiments. In order to compare individual runs, it was necessary to ensure that the results from each run were repeatable. This was done by maintaining exactly the same settings (temperatures and flow rates) for each run. The variation in the system response could be observed from Figures 2a and 2b. These plots reveal that between each run of any of the concentrations, there is little variation (±0.5°C), ensuring that the experimental results were repeatable and hence comparable.

The uncertainties introduced in the data are given in Table 1 in the Appendix. However, these errors would be nullified due to the comparative analysis of the heat transfer coefficient.

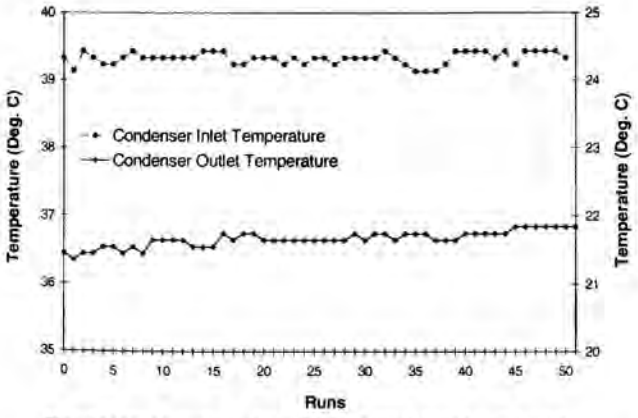

Figure 2a: Variation of refrigerant inlet (right axis) and exit (left axis) temperatures in the condenser

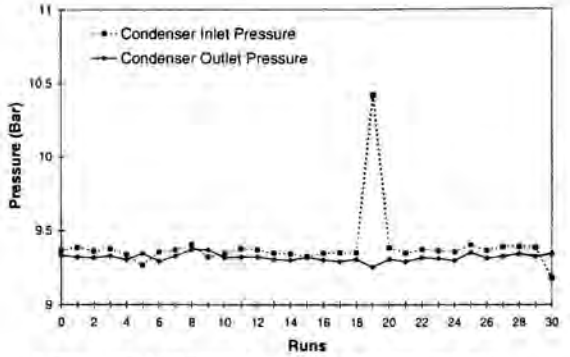

Figure 2b: Variation of Condenser inlet and exit pressures

Variation of in-tube heat transfer coefficient with R134a-oil mixture

The heat transfer coefficients on the refrigerant side for the three concentrations of the refrigerant-oil mixture are shown in Figure 3. These concentrations were pure R134a, R134a + easter oil (2% by mass) and R134a + easter oil (5% by mass). It can be seen from Figure 3 that the internal condensation heat transfer coefficient reduces by 5% and 10% respectively as the oil concentration in the refrigerant was increased by 2% and 5% (by mass).

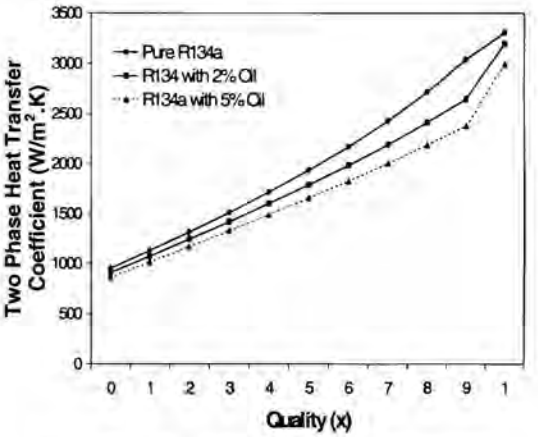

Figure 3: Variation of condensation heat transfer coefficient for a mixture of R314a and ester oil.

Shao [3] recently studied the effect of oil (SW32) in R134a on heat transfer during condensation. SW32 oil was, however, different from the one used in the current investigation. Both the current and Shao's studies

revealed that there is a drop in the internal heat transfer coefficient due to oil contamination. However, the percentage drop evaluated in this study is lower than Shao's. This can be attributed to the fact that heat transfer coefficient of the mixture was evaluated using the refrigerant properties and not the mixture properties, and that the oil used in the two experiments were different.

Comparison of experimental heat transfer coefficient for pure R134a with earlier models [1-4]

The experimental heat transfer coefficient (following Equations 1-6) was compared with earlier models [1-4]. The details of these models are given in the Appendix. It may be noted that the Shah [1] correlations were not developed specifically for R134a but were used as generic correlations for condensation of refrigerants in two-phase. The model of Cavallini and Zecchin [2] was developed primarily for condensation of R134a in two phase flowing inside annular sections. Therefore, this model would be more useful in comparing the experimental heat transfer coefficients from the present study. This model uses mass flux through the system and is based on the Nusselt number approach. The models of Travis [11] and Dobson [4] were also used specifically for the flow of R134a inside condensing tubes in two-phase. They used Lockhart-Martinelli parameter to account for the variation in the quality of the refrigerant where the properties are defined at the boundaries of the saturation curve. The Traviss model under predicted the heat transfer coefficients by more than 30% and hence this model was not included in Figure 4.

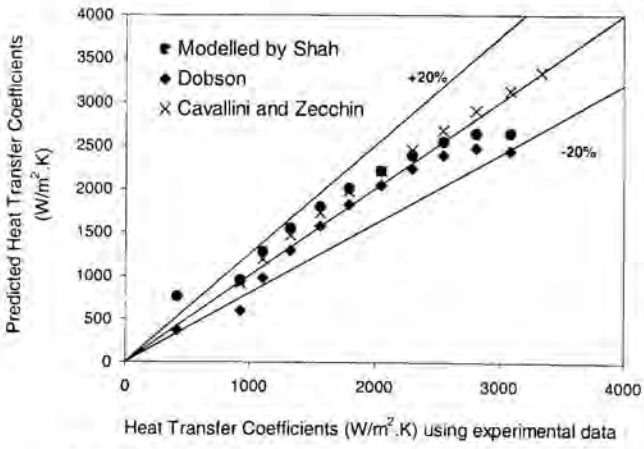

Figure 4: Comparison of heat transfer coefficients (from this study) of pure R134a with model predictions [1, 2, 4].

Figure 4 shows the comparison of the experimental in-tube condensation heat transfer coefficients from the present study for pure R134a with predictions from earlier models. However, it may be noted that the condenser type and the flow pattern in this study were different from those used in previous studies. The predictions from Cavallini and Zecchin [2] were the best (over predicting only by about 8%), followed by Dobson [4] and Shah [1]. Models of Shah and Dobson disagreed by up to 20% with the experimental values

CONCLUSIONS

Contamination of R134a with synthetic polyol ester-based oil resulted in a decrease in the in-tube condensation heat transfer coefficient of the working fluid. The coefficient decreased respectively by 5% and 10% when R134a was mixed with 2% and 5% oil (by mass). Comparisons of the experimental data revealed that the model by Cavallini and Zecchin was the best in predicting the in-tube condensation heat transfer coefficient for pre R134a to within 8%.

ACKNOWLEDGMENTS

One of the authors (R Bassi) is thankful to Mr. A Gupta for his assistance during the experiments of the project. The authors are also thankful to Fisher & Paykel NZ Ltd. for sponsoring the project.

REFERENCES

[1] Shah, M.M. "A general correlation for heat transfer during film condensation in tubes", International Journal of Heat and Mass Transfer (1979), 185-196.

[2] Cavallini, A. Zecchin, R. "A dimensionless correlation for heat transfer in forced convection condensation", 6th International Heat Transfer Congress, (1974), vol.3, 309-313.

[3] Shao, D.W., Granryd, E., "Heat transfer and pressure drop of HFC134a-oil mixture in a horizontal condensing tube", International Journal of Refrigeration, Volume 18, No. 8, 524-533, (1995a).

[4] Dobson, MK, Chato, J.C. "Condensation in smooth horizontal tubes", Journal of Heat Transfer, Transactions of ASME 1998;120:193-213.

[5] Chato, J.C. "Laminar condensation inside horizontal and inclined tubes", ASHRAE J.,Vol. 4, 52-60, (1962).

[6] Tichy, J.A., Macken, N.A., Duval, W.M.B. "An experimental investigation of heat transfer in forced convection condensation of oil-refrigerant mixtures", ASHRAE transaction, 1985, 297-309.

[7] Schlager, L.M., Pate, M.B., Bergles, A.E. "Evaporation and condensation of refrigerant-oil mixtures in a smooth tube and micro-fin tube", ASHRAE Transactions, 1988, 194-166.

[8] S.J. Eckels, M.B. Pate, " An experimental comparison of evaporation and condensation heat transfer coefficients for HFC-134a and CFC-12", International Journal of Refrigeration, Volume14, March 1991, 70-77.
[9] Shao, W., Granryd, E., "Flow condensation of pure and oil contaminated refrigerant HFC134a in a horizontal tube", Proceedings of International Refrigeration Conference., Purdue, USA, 317-322, July, (1994a).
[10] Shao, W., "The effect of oil on R134a enthalpy", Applied Thermodynamics and Refrigeration, KTH, Stockholm, Trita-REFR No 93/13, (1992b).
[11] Traviss, D.P., Rohsenow, W.M., Baron, A.B. Forced convection inside tubes: A heat transfer equation for condenser design. ASHRAE Transactions. (1972), vol. 79, 157-165.
[12] Hewitt, G.F., Hemisphere Hand book of Heat Exchanger Design, Hemisphere Publishing Corporation, New York, 1990, 2.6.1-2.6.5.

APPENDIX

Table 1: Uncertainties in the experimental set-up.

Component(s)	Specification	Uncertainty
Refrigerant Bottles	2 x 9 kg	-
Heater 1	1 x Air heater	± 0.1 °C
Heater 2	1 x Water heater	± 0.1 °C
Heater 3	1 x Water Heater	± 0.1 °C
Thermocouples	T type made out of Copper Constantan.	± 0.5 °C
PT100	3 x Platinum resistance core. Standard BS1904	± 0.1 °C
Pressure Transducers	4xOEM pressure transducer M6420-50	± 0.1 %
PID controller	Standard	-
Heating Tape	Motor Heating Tape. 99W/1.701m.	-
Micro-motion Flow Meter	D6 Micro Motion	± 0.2% of the flow
Needle valve	3.25 mm L series metering valves	
Vortex Flow meter	Black leather grained polypropylene	± 1.25 % of the flow

Details of earlier models for comparison with this study are given below.

Author	Correlation
Shah [1]	$Nu = Nu_l \cdot (1-x)^{0.8}\left(1+\frac{3.8}{Z^{0.95}}\right)$, $Z=\left(\frac{1}{x}-1\right)^{0.8}\cdot\left(\frac{p}{p_c}\right)^{0.4}$, $Nu_l = 0.023 Pr_l^{0.4}\cdot Re_{lo}^{0.8}$
Cavallini - Zecchin [2]	$Re_l=\frac{G(1-x)d_i}{\mu_l}$, $Re_v=\frac{G(x)d_i}{\mu_v}$, $G=\frac{\dot{m}_{ref}}{A_{in}}$, $Re_{eq}=Re_v\cdot\left(\frac{\mu_v}{\mu_l}\right)\cdot\left(\frac{\rho_l}{\rho_v}\right)^{0.5}+Re_l$, $Nu=\frac{h_l d_i}{k_l}=0.05\cdot Re_{eq}^{0.8}\cdot Pr_l^{0.33}$
Traviss [11]	$X_{tt}=\left(\frac{\rho_v}{\rho_l}\right)^{0.5}\cdot\left(\frac{\mu_l}{\mu_v}\right)^{0.1}\cdot\left(\frac{1-x}{x}\right)^{0.9}$, $Nu=\frac{\alpha_l d_i}{k_l}=Pr_l\cdot Re_l^{0.9}\cdot\frac{F_1(X_{tt})}{F_2(Re_l,Pr_l)}$, $Re_l=\frac{G(1-x)d_i}{\mu_l}$, $F_1=0.15\left[\frac{1}{X_{tt}}+\frac{2.83}{X_{tt}^{0.476}}\right]$, $F_2=5Pr_l+5\ln(1+5Pr_l)+2.5\ln(0.00313Re_l^{0.812})$ For $Re_l>1125$
Dobson [4]	For $Re_l \geq 1250$: $Fr=1.26\cdot Re_l^{1.04}\cdot\left(\frac{1+1.09\cdot X_{tt}^{0.039}}{X_{tt}}\right)^{1.5}\cdot\frac{1}{Ga^{0.5}}$, $Ga=g\cdot\rho_l\cdot(\rho_l-\rho_v)\cdot\frac{d_i^3}{\mu_l^2}$, $Nu=0.023\cdot Re_l^{0.8}\cdot Pr_l^{0.3}\cdot\frac{2.61}{X_{tt}^{0.805}}$ For $Fr>18$

HEFAT2002
1st International Conference on Heat Transfer, Fluid Dynamics and Thermodynamics
8-10 April 2002, Kruger National Park, South Africa
TP1

COMPUTATION OF UNSTEADY COMPLEX GEOMETRY FLOWS USING NOVEL NON-LINEAR TURBULENCE MODELS

Paul G. Tucker
Fluid Dynamics Research
Centre, The University of
Warwick, Coventry, CV4 7AL,
UK

ABSTRACT

Novel, nonlinear turbulence models are applied to an unsteady complex geometry flow. These models are found to improve predicted turbulence intensities. However, relative to linear models, convergence is difficult to achieve and clipping of some non-linear Reynolds stress components is required along with velocity field smoothing. The latter is naturally achieved through multilevel convergence restriction operators. As a result of convergence difficulties, non-linear model computational costs are so high that they detract from any modest accuracy gains.

INTRODUCTION

There have been numerous studies involving URANS predictions for vortex shedding behind cylinders. These (see for example [1-4]) clearly demonstrate the deficiencies of linear eddy viscosity models when predicting unsteady flows. Notably, the dissipative standard k-ε model erroneously gives rise to steady flow. Tucker and Pan [5] make URANS computations for flow in the complex congested Fig. 1 system (an idealized electronics system). Two fans drive the flow. A wide range of linear turbulence models is tried. These give significantly different values of turbulence kinetic energy (k) and hence viscosity. This, as would be expected, gives quite different unsteadiness amplitudes. Based on the above linear URANS turbulence model poor performances attention is being turned to non-linear models. For example, Tatsumi *et al.* [6] make nonlinear URANS predictions for flow over a backward facing step. Kimura and Hosoda [7], revisit the computation of flow around square cylinders using an essentially non-linear model [8]. Barakos and Drikakis [9] consider the non-linear model prediction of aerofoil shock induced oscillations. The above non-linear model work is quite inconclusive. Although Large Eddy Simulation (LES) and Reynolds stress models show greater potential than linear model URANS predictions [10,11] they are computationally expensive. Therefore, potentially less expensive non-linear models are here further explored using the demanding Fig. 1 geometry.

NUMERICAL METHOD

Following [2,4] governing equations are presented in a phase-averaged form. For conservation of momentum

$$\frac{\partial\langle U_i\rangle}{\partial t}+\frac{\partial\langle U_i\rangle\langle U_j\rangle}{\partial x_j}=-\frac{1}{\rho}\frac{\partial\langle P\rangle}{\partial x_i}+\frac{\mu}{\rho}\frac{\partial}{\partial x_j}\left(\frac{\partial\langle U_i\rangle}{\partial x_j}+\frac{\partial\langle U_j\rangle}{\partial x_i}\right)+\frac{\partial\left\langle-\overline{u_i'u_j'}\right\rangle}{\partial x_j} \quad (1)$$

where $\langle U\rangle$ is an averaged fluid velocity component, u' is the turbulence fluctuating component, ρ the fluid density, μ viscosity, $\langle P\rangle$ averaged static pressure, t time and x the spatial co-ordinate.

'Boussinesq' approximations

The role of the turbulence model is to approximate the $\left\langle-\rho\overline{u_i'u_j'}\right\rangle$, Reynolds stress terms in Equation (1). Unless otherwise stated, to approximate these a [12] quadratic 'Boussinesq' approximation is used in the following form

$$\left\langle-\overline{u_i'u_j'}\right\rangle=-n_0\frac{2}{3}\langle k\rangle\delta_{ij}+2\frac{\mu_t}{\rho}S_{ij}+n_1\left[\begin{array}{l}4C_DC_\mu\dfrac{\mu_t}{\rho}\dfrac{\langle k\rangle}{\langle\varepsilon\rangle}\left(S_{ik}S_{kj}-\dfrac{1}{3}S_{mn}S_{mn}\delta_{ij}\right)+\\ 4C_FC_\mu\dfrac{\mu_t}{\rho}\dfrac{\langle k\rangle}{\langle\varepsilon\rangle}\left(\overset{\circ}{S}_{ij}-\dfrac{1}{3}\overset{\circ}{S}_{mm}\delta_{ij}\right)\end{array}\right] \quad (2)$$

The term S_{ij} is the mean strain rate. The $\overset{\circ}{S}_{ij}$ term, is called the Oldroyd derivative, which can be expressed as

$$\overset{\circ}{S}_{ij}=\frac{\partial S_{ij}}{\partial t}+\langle U_k\rangle\frac{\partial S_{ij}}{\partial x_k}-\frac{\partial\langle U_i\rangle}{\partial x_k}S_{kj}-\frac{\partial\langle U_j\rangle}{\partial x_k}S_{ik} \quad (3)$$

In the above μ_t is the turbulent viscosity and n_0 and $n_1 = 0$ or 1 depending on the model used. For example, $n_1 = 0$ gives a standard linear Boussinesq approximation.

Turbulence energy and dissipation equations

When $\langle k \rangle$ is required, the following differential transport equation is used

$$\frac{\partial \langle \Phi \rangle}{\partial t} + \frac{\partial \langle U_j \rangle \langle \Phi \rangle}{\partial x_j} = \frac{1}{\rho}\frac{\partial}{\partial x_j}\left(\Gamma_\phi \frac{\partial \langle \Phi \rangle}{\partial x_j} \right) - T_1 \langle \overline{u_i' u_j'} \rangle \frac{\partial \langle U_i \rangle}{\partial x_j} - T_2 \quad (4)$$

where $\langle \Phi \rangle = \langle k \rangle$, $\Gamma_k = \mu + \mu_t / \sigma_k$ (where σ_k is the diffusion Prandtl number for k), $T_1 = 1$ and $T_2 = \langle \varepsilon \rangle$ (the rate of dissipation of turbulence kinetic energy). By setting $\langle \Phi \rangle = \langle \varepsilon \rangle$, $\Gamma_\varepsilon = \mu + \mu_t / \sigma_\varepsilon$ (where σ_ε is the diffusion Prandtl number for ε), $T_1 = C_{\varepsilon 1} \langle \varepsilon \rangle / \langle k \rangle$, and $T_2 = C_{\varepsilon 2} \langle \varepsilon \rangle^2 / \langle k \rangle$, an equation for the dissipation of k is gained. For some, more approximate, modelling approaches, the rate of dissipation is related to normal wall distances (see later). The various models used will now be outlined. Essentially, the differences between linear and non-linear models is in essence, minor being reflected through the terms included in the Boussinesq approximation above. Unless otherwise stated $n_{l1} = n_{l2} = 1$ in Equation (2) giving nonlinear models. The different models will now be described. Each model will be given a different label and the subscripts l and h is used to differentiate between low and high Reynolds number models, respectively.

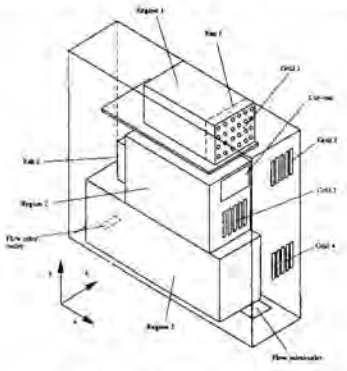

Figure 1: Schematic of idealized system considered

Mixing length model

For reference purposes a standard mixing length (ml_l) model is used. For this

$$\mu_t = \rho \langle l_\mu \rangle^2 \left[2 \frac{\partial \langle U_i \rangle}{\partial x_j} S_{ij} \right]^{1/2} \quad (5)$$

where $\langle l_\mu \rangle$ is a mixing length. In the near wall region the Van Driest damping function is used. In Equation (2) $n_{l1} = n_{l2} = 0$.

nl-k-l models

The non-linear k-l (nl-k-l) models are implemented in the framework of [13]. Equation (4) is solved for $\langle \Phi \rangle = \langle k \rangle$, and $\langle \varepsilon \rangle$ defined using

$$\langle \varepsilon \rangle = \frac{\langle k \rangle^{3/2}}{\langle l_\varepsilon \rangle} \quad (6)$$

where $\langle l_\varepsilon \rangle = C_{\varepsilon l} y \left(1 - n_2 e^{-A_\varepsilon \langle y^+ \rangle / c_\mu^{3/4}} \right)$ and $\langle y^+ \rangle = y \rho \langle k \rangle^{1/2} C_\mu^{1/4} / \mu$. The turbulent viscosity can be expressed as

$$\mu_t = \rho C_\mu \langle l_\mu \rangle \langle k \rangle^{1/2} \quad (7)$$

where $\langle l_\mu \rangle = C_{\mu l} y (1 - n_2 e^{-A_\mu \langle y^+ \rangle / c_\mu^{3/4}})$. When $n_2 = 1$, the length scales $\langle l_\varepsilon \rangle$ and $\langle l_\mu \rangle$ have the near wall damping functions of Wolfshtein giving a low Reynolds number non-linear model designated here the nl-k-l_l. Predictions are also made with $n_2 = 0$ and computationally economical logarithmic wall functions [14].

nl-k-ε model

For this, Equation (4) is solved with $\langle \Phi \rangle = \langle k \rangle$ and $\langle \varepsilon \rangle$ and the turbulent viscosity found using

$$\mu_t = \rho C_\mu \frac{\langle k \rangle^2}{\langle \varepsilon \rangle} \quad (8)$$

For all results presented, the standard model with logarithmic wall functions is used (nl-k-ε_h).

Zonal models

With these, for $\langle y^+ \rangle \geq 60$ the nl-k-ε method is used and for $\langle y^+ \rangle < 60$ the k-l_l or nl-k-l_h models are applied. To connect the differing models at the $\langle y^+ \rangle = 60$ interface the following patching condition is required (rearranged for $\langle \varepsilon \rangle$).

$$\langle k \rangle^{3/2} = \langle l_\mu \rangle \langle \varepsilon \rangle \quad (9)$$

Two non-linear approaches are tried. These are designated the nl-k-ε_h/k-l_l and nl-k-ε_h/ nl-k-l_l. The latter is fully non-linear. The former uses a linear near wall model (i.e. for $\langle y^+ \rangle < 60$ n_l

$= 0$. For all the models discussed above, their linear counterparts can be fully recovered by setting $n_0=n_1=0$ in Equation (2). These will be compared with later and are identified by omission of the *nl* prefix.

Features specific to non-linear models

Non-linear contributions from Equation (2) are differentiated and then directly incorporated into the momentum equations. Following Speziale [12], velocities in the non-linear part of the 'Boussinesq' approximation are smoothed. Here, an 18-point distance weighted averaging is used. The averaging is performed using multigrid restriction operators (see [15]).

Speziale's 'Boussinesq' approximation does not have a high degree of realizeability. This is clearly shown by Mompean *et al.* [16] where, for channel flows, near walls the streamwise normal stress component $\overline{u_1'u_1'}$ takes on excessively high values approaching $40u_\tau^2$. Also the $\overline{u_2'u_2'}$ and $\overline{u_3'u_3'}$ components can take on negative values (ensuring the sum of the three components is equal to k) which can be of greater magnitude than the correct positive values. Fortunately, for low Reynolds number predictions, this strange behaviour (which evidently is mostly due to the Oldroyd derivatives) does not occur – Speziale's original model readily transfers into a low Reynolds number form [17]. However, from tests carried out as part of this work, the aforementioned lack of realizability can give rise to numerical instabilities. These are found especially severe when modelling relatively low Reynolds number flows with wall functions – as first of wall grid nodes move closer towards walls Reynolds stress realizability decreases. Just such flows (for which it is difficult to ensure wall function expressions are employed sufficiently far from walls) are found in electronic systems which is a strong focus of the present work. Therefore,

for the complex geometry clipping of nonlinear 'Boussinesq' contributions is required. In the discretization process contributions to the turbulence equations are split into two parts. All the non-linear contributions are treated as source terms. For all predictions an initially linear solution is produced and then the non-linear source term is included in the computation. Two clipping approaches are tried. Either the magnitude of the nonlinear contribution to the total Reynolds stress component is limited so that it is no greater than the value arising from the linear part of the 'Boussinesq' approximation. Alternatively, gradient contributions are limited in a similar way. The latter approach avoids large gradient discontinuities in non-linear contributions and so this approach is to be preferred. The use of clipping to enforce turbulence model realizability is not new (see, for example [18,19]). The standard constants given in [5] are used in the models.

Turbulence Intensities

The flow to be studied is unsteady. Consequently, the measured instantaneous velocity u is the sum of U (the time-averaged velocity) and fluctuations due to turbulence u' and also unsteadiness u'' (i.e. $u=U+u'+u''$ or $u=\langle U\rangle+u'$). Measurements of turbulence intensity to be compared with have not been corrected for the effect of flow unsteadiness. These intensities can be expressed as

$$T_i' = \frac{\sqrt{\overline{(u'+u'')^2}}}{U} \qquad (10)$$

Comparisons is also made with predictions of T_i (where the periodic fluctuation is filtered out i.e. $u''=0$ in Equation (10)) and T_i'

General program features

The governing flow equations are discretized using a 2nd order CONDIF/SIMPLE based finite volume technique. Generally a fully implicit time scheme is used. Normal wall distances required in some turbulence models are calculated using a differential equation based technique [15].

Numerical details

Full details of boundary conditions are given in [5].Sensibly grid independent predictions are made using a base grid with at least 101 x 89 x 45 control volumes in the x, y and z directions, respectively. These are constructed so that at first off-wall grid nodes y^+_{ave} is around 2 and 15 for the low and high Reynolds number turbulence model predictions, respectively. To check for grid independence a 209 x 193 x 100 grid prediction is made. For sensibly time step independent predictions, time steps of $\Delta t = 0.001$ s are used.

Where complex geometry predictions and measurements are spatially compared, percentage errors are given. The following experimental data point summations are made for velocities

$$Error_U = \frac{\sum_{exp} |\phi_{exp} - \phi_{num}|}{U_0 \sum_{exp} 1}, \quad Error_{T_i} = \frac{\sum_{exp} |\phi_{exp} - \phi_{num}|}{\sum_{exp} |\phi_{exp}|} \qquad (11)$$

and turbulent intensities T_i where, U_0 is the approximate average return flow velocity for the system, obtained by integrating over velocity profiles (U_0 = 1.5 m/s) and ϕ_{exp} corresponds to an experimental data point and ϕ_{num} a numerical value.

DISCUSSION OF RESULTS

To validate the implementation of newly added non-linear 'Boussinesq' terms, standard test cases are used. These comprise backwards facing step and channel flows. Excellent agreement is found with benchmark data.

Comparisons are made with LDA measurements having an estimated accuracy ± 5% along the lines/profiles shown in Fig. 2. The exact locations of profiles 1-6 are: X=0.53, Y=0.73; X=0.37, Y=0.73; X=0.41, Z=0.06; X=0.41, Z=0.10; X=0.37, Z=0.57 and X=0.41, Z=0.96, respectively (X, Y and Z are dimensionless coordinates such that $X = Y = Z = 1$ correspond to the maximum extent of the system). Comparisons are also made with thermistor based mean flow temporal velocity variation measurements for six central points on profiles 1-6.

Temporal Velocity Variations

The thermistor-based measurements show the average velocity unsteadiness amplitude is about 0.25 m/s. Fig. 3, is a plot of averaged, predicted amplitude against turbulent viscosity for the different turbulence models. Open symbols represent linear turbulence model predictions, closed non-linear and the full and dotted lines respective best fits to these. The horizontal dashed line gives the measured amplitude. As can be seen, linear model amplitudes vary significantly, decreasing with increasing μ_t. This has some consistency with the observations of [20]. For the non-linear models, some momentum equation,

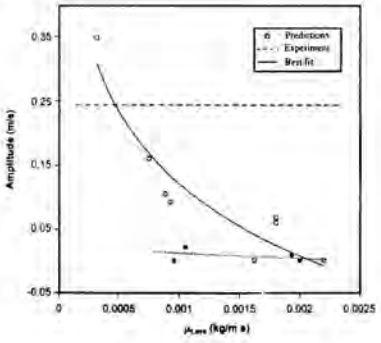

Figure 3: Variation of unsteadiness amplitude with turbulent viscosity

Reynolds stress components are not incorporated through diffusion terms and the trend of decreasing amplitude with increasing turbulent viscosity is no longer observed.

Flow Structure

Fig. 4, shows mid-axis x-y plane, k-l_l model, instantaneous streamline and axial velocity ($\partial U/\partial t$) contour plots at different times. Plots suggest the major predicted unsteadiness

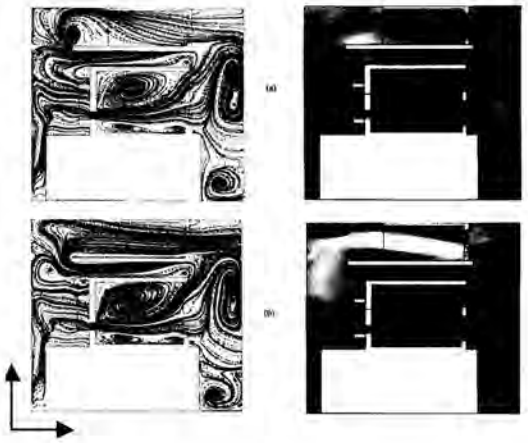

Figure 4: Plots of mid x-y plane streamlines and horizontal velocity component unsteadiness.

source is separation arising from Fan 1 rapidly turning the flow through 180°. This, (see Frame (a)) causes massive x-y plane separation. Eventually (see Frame (b)) the vortex arising from separation collapses. The collapse and regeneration of this vortex repeats exactly in time. For non-linear solutions the flow is either fixed in a separated or attached mode, the attached being the preferred.

Velocity and Intensity Magnitude Comparisons

Fig. 5, plots measured against predicted velocities for profiles 1-6. If agreement is perfect the measurements, represented by symbols, should fall on the 45° reference line. Frame (a) gives ml_l and k-ε_h results, (b) k-l_h and nl-k-l_h, (c) k-l_l and nl-k-l_l and (d) k-ε/k-l_l, nl-k-ε/k-l_l and nl-k-ε/nl- k-l_l results. Mixing length predictions are included for interest. Most measured points tend to be positioned under the line, i.e. velocities returned by the different models are low. The percentage error (velocity and intensity) for each profile and model based on (12) is summarised in Table 1. The table shows the k-ε_h model has a similar accuracy to the mixing length. This is in part due to the sensitivity of results to wall functions (see [5]).

Table 1 Summary of percentage error

Model	$Error_U$	$Error_{Ti}$
ml_l	21	_
k-l_h	18	-53 (-56)
nl-k-l_h	17	-52 (-52)
k-l_l	19	-47 (-50)
nl-k-l_l	19	-45 (-46)
k-ε_h	20	_
k-ε/k-l_l	15	-34 (-34)
nl-k-ε/ k-l_l	17	-33 (-33)
nl-$k\varepsilon$/nl- k-l_l	16	-33 (-33)

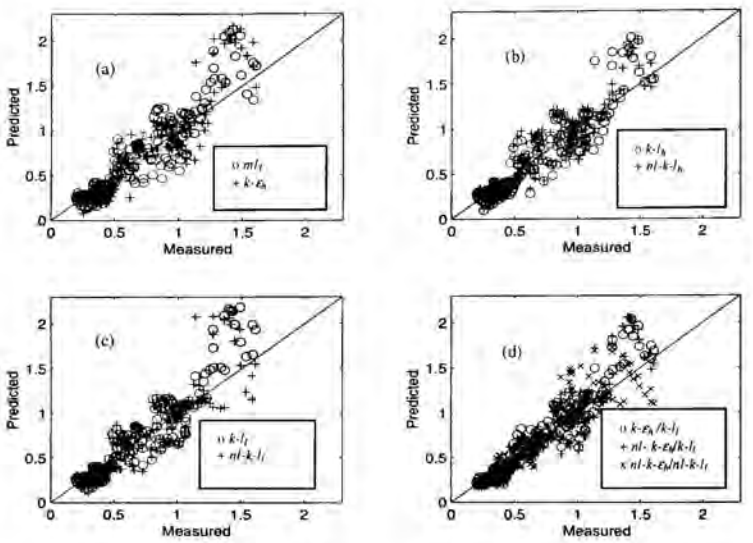

Figure 5: Plots measured against predicted velocities for profiles 1-6.

Therefore, k-ε_i results and those for its non-linear counterpart will not be further considered. The key observation from Table 1 is that for the present complex flow, inclusion of non-linear terms has overall not helped velocity predictions.

Fig. 6, shows the equivalent plot to Fig. 5 (ignoring the ml and k-ε_i models) for T_i'. The intensities, like velocities, are under-predicted (the k-ε_i model badly over-predict intensities). The intensity under-prediction can in part be attributed to the velocity under-prediction. Percentage total intensity (T_i') errors for all models are summarized in the lower row of Table 1. The minus signs reflect the under-prediction. The far right hand terms, in parenthesis, represent average T_i' (i.e. true turbulence intensities containing just the stochastic turbulent component) values. The non-linear models all appear to give T_i' improvements. A key point to note is that, for this complex case, typically, relative to linear models, the non-linear models required at least 3 times more computing time. Bearing this in mind, any accuracy improvements seem rather small.

CONCLUSIONS

For relatively simple geometries and steady flows non-linear models have seen significant testing showing some success. However, they have seen less use in highly complex geometries and unsteady flows such as the present. For such systems the additional terms introduced by non-linear eddy viscosity models do not, relative to computational cost, appear that beneficial. Also, for the present cases, the extra terms, relative to linear models, tend to damp unsteadiness. Although further testing is required, results suggest the simpler, more constrained models, at present, are a sensible choice for many complex geometry applications. Constrained models, although not having, for complex flows, the potential for high accuracy are also less likely to go too far wrong. For geometries with many channel forming plane walls (such as found in electronic systems), on the grounds of computational economy, the mixing length model does not appear an unreasonable choice. However, the diminished and non-smooth turbulence viscosity fields of such models can again mean that convergence is problematic.

ACKNOWLEDGMENTS

The support of EPSRC grant GR/N05581 is gratefully acknowledged.

REFERENCES

[1.] Franke R. and Rodi W. 1993 Calculation of vortex shedding past a square cylinder with various turbulence models. 8th Int. Symp. of Turbulent Shear Flows, Munich, pp. 189-204

[2] Johansson S. H., Davidson L. and Olsson E. 1993 Numerical simulation of vortex shedding past triangular cylinders at high Reynolds number using a k-ε turbulence model, Int. J. Numer. Meth. Fluids, Vol. 16, pp. 859-878

[3] Durbin P. A. 1995 Separated flow computations with the k-ε-v^2 model, AIAA J., Vol. 33, No. 4, pp. 659-664

[4] Bosch G. and Rodi W. 1998 Simulation of vortex shedding past a square cylinder with different turbulence models, Int. J. for Numer. Meth. Fluids, Vol. 28, pp. 601-616

[5] Tucker P. G. and Pan Z. 2001 URANS Computations for a complex internal isothermal flow, Comput. Meth in Appl. Mech. and Eng, Vol. 190, pp. 2893-2907

[6] Tatsumi K., Iwai H., Neo E. C., Inaoka K. and Suzuki K. 1999 Prediction of time-mean characteristics and periodical fluctuation of velocity and thermal fields of a backward-facing step, Proc. 1st Int. Symp. on Turbulence and Shear Flow, Santa Barbara, pp. 139-144

[7] Kimure I. and Hosoda T. 1999 3-D unsteady flow structures around rectangular column in open channels by means of non-linear k-ε model, Proc. 1st Int. Symp. on Turbulence and Shear Flow, Santa Barbara, pp. 1001-1006 (1999)

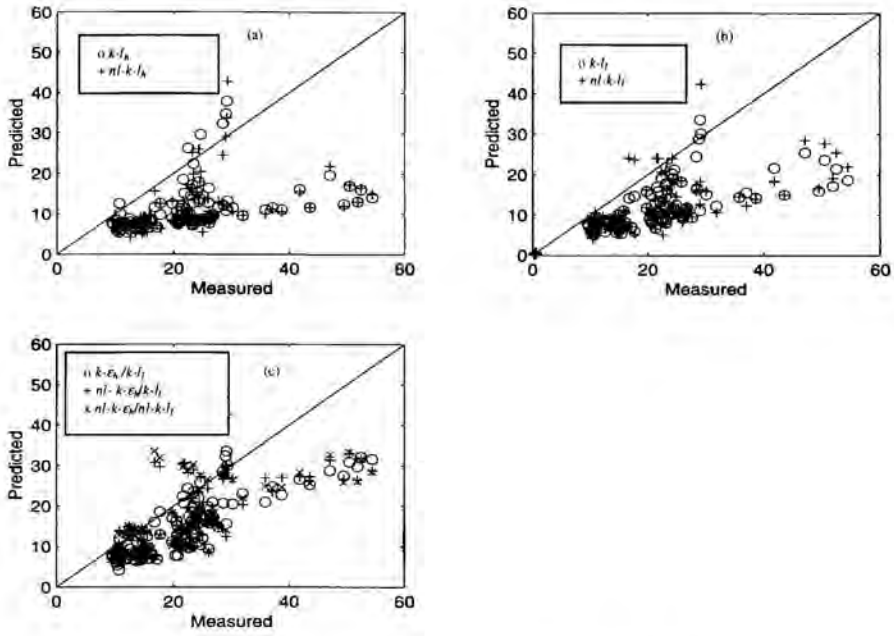

Figure 6: Plots measured against predicted intensities for profiles 1-6.

[8] Gatski T. B., and Speziale C. G. 1993 On explicit algebraic stress models for complex turbulent flows, J. of Fluid Mechanics, Vol. 254, pp. 59-78

[9] Barakos G. and Drikakis D. 1999 Numerical simulation of transonic buffet flows using various turbulence closures, Proc. 1st Int. Symp. on Turbulence and Shear Flow , Santa Barbara, pp. 995-1000

[10] Nishimura M., Tokuhiro A., Kimura N. and Kamide H. 1999 Computational study on quasi-planar jets mixing with low Reynolds number turbulent stress and flux equation models, NURETH-9 San Francisco, California, October 3-8, CDROM

[11] Pascal H., Jakirlic S. and Hanjalic K. 2000 DNS and RANS-Modelling of in-cylinder turbulence subjected to axial compression, Proc. of the 3rd Int. Symp. on Turbulence Heat and Mass Transfer, Nagoya, Japan – Turbulence, Heat and Mass Transfer 3, pp. 479-486

[12] Speziale C. G. 1987 On non-linear k-l and k-ε models of turbulence, J. of Fluid Mech., Vol. 178, pp. 459-475

[13] Wolfshtein M. 1969 The velocity and temperature distribution in one-dimensional flow with turbulence augmentation and pressure gradient, Int. J. Heat Mass Transfer, Vol. 12, pp. 301-318

[14] Launder B. E. and Spalding D. B. 1974 The numerical computation of turbulent flows, Comput. Meth. Appl. Mech. Eng., Vol. 3, pp. 269-289

[15]. Tucker P. G. 2001 Computation of unsteady internal flows, Kluwer Academic Publishers

[16] Mompean G. Gavrilakis S. Machiels L. and Deville M. O. 1996 On predicting the turbulence-induced secondary flows using nonlinear k-ε models, Phys. Fluids, Vol. 8, No. 7, pp. 1856-1868.

[17] Rokni M. 1999 Personal Communication.

[18] Suga K., Nagaoka M., Horinouchi N. , Abe K. and Kondo Y. 2000 Application of a three equation cubic eddy viscosity model to 3-D turbulent flows by the unstructured grid method, Proc. 3rd Int. Symp. on Turbulence, Heat and Mass Transfer, pp. 373-380

[19] Andre J. C., De Moor G., Lacarrere P. , Therry G. and du Vachat R. 1977 The clipping approximation for inhomogenous turbulence, Proc. Symp. on Turbulent Shear Flows University Park, Pennsylvania, Vol. 1, pp. 4.39-4.46

[20] Brackenridge J. B 1960 Transverse oscillations of a liquid jet, J. of the Acoustical Society of America, Vol. 32, No. 10, pp. 1237-1242

HEFAT2002
1st International Conference on Heat Transfer, Fluid Mechanics, and Thermodynamics
8-10 April 2002, Kruger Park, South Africa
VJ1

EFFECT OF WALL INCLINATION AND REYNOLDS NUMBER ON THE MEAN FLOW AND TURBULENCE CHARACTERISTICS IN A TWO-DIMENSIONAL WALL JET PART A: EXPERIMENTAL STUDY

J. M. Villafruela*, R. Villanueva†, F. Castro‡ and M. T. Parra*
*Associate Professor, † Doctorate student, ‡ Professor
Department of Energetic Engineering and Fluid Mechanics,
School of Engineering - University of Valladolid
Paseo del Cauce s/n - E47011 - Valladolid (Spain)
E-mail: manolo@eis.uva.es

ABSTRACT

An experimental study of the flow field in a two-dimensional wall-jet has been conducted. All measurements were carried out using hot-wire anemometry. The experimental facility has a nozzle aspect ratio of 100. Mean velocities and Reynolds stresses were determined with nozzle Reynolds numbers in the range 10^3 to $3 \cdot 10^3$, and four different inclination angles between the wall and the nozzle of the wall to the nozzle ($\beta = 0°$, 10°, 20° and 30°).

Results indicate that all wall-jets are self-preserving in the developed region. Normal to the wall two regions can be identified: one similar to a plane free jet and the other similar to a boundary layer. Downstream the interaction between these two regions creates a mixed or third region. For $\beta > 10°$, there appears a recirculating flow region that increases with β. Downstream the wall-jet becomes self-preserving for all angles. The spreading rate and maximum velocity decay rate are dependent on both the Reynolds number and the wall inclination angle. Has been observed that the logarithmic region increases with the distance from the nozzle and with the Reynolds number.

INTRODUCTION

Launder and Rodi [1] define a wall jet as "a shear flow directed along a wall where, by virtue of the initially supplied momentum, at any station, the streamwise velocity over some region within the shear flow exceeds that in the external stream". The resulting flow can be represented as the simplest system containing both a wall boundary layer in the inner region and a free shear layer in the outer region. The strong interaction between these two layers creates intense mixing at the interface, which can be thought of as a mixed or third region [1]. For example, this interaction results in a low spreading rate (less than for the corresponding free jet) and the displacement of the location of zero shear stress away from the point of maximum mean velocity. The near wall region is characterized by a short universal mean velocity profile and a high turbulence level caused by the influence of the outer region.

This type of flow has many interesting industrial applications. The flow over the external cowl of a fan-jet engine, the flow over an extended slotted flap of an airfoil and the flow generated by the windshield defroster in a vehicle are all examples of wall jets. Wall jets are used in gas turbine blades and combustion chamber walls exposed to either hot or corrosive gases. Wall jets also appear in the deflectors used in air- conditioned conduction.

In some practical applications the jet is injected parallel to the wall. This is refereed to as the parallel wall jet. In most practical applications the jet is injected with an angle to a solid wall; this configuration is referred to as an inclined wall jet.

Due to the interesting physics and the engineering applications of wall jets many investigations have been conducted over the years. Launder and Rodi [1] have reviewed most of the published data of parallel wall jets until 1981. Kobayashi and Fujisawa [2], Wygnanski et al. [3] Abrahamsson et al. [4], Zhou et al. [5] and Venas et al. [6] reported more recently experimental investigations. All of these investigations employed hot wire anemometry techniques. Karlsson *et al.* [7] and Schneider and Goldstein [8] have presented measurements

using laser Doppler anemometry. These investigations indicate a higher turbulence level in the outer region of the wall jet than was found using hot-wire data. Forthmann [9] reported the first experimental study of an inclined wall jet. Recently, the effect of the inclination angle β on the development of the initial velocity field of an inclined wall jet was investigated by Lai and Lu [10,11] using both thermal and laser Doppler anemometry (LDA).

The objective of the present work was to obtain the velocity field in parallel and inclined wall jets using hot-wire anemometry. The initial and developed regions were studied. The experiments were carried out on airflow without any external stream. The nozzle exit Reynolds number ranged between 10^4 and 3×10^4. Four different wall angles were used (0°, 10°, 20° and 30°).

NOMENCLATURE

A_U, A_y, B_y, B_U potential law coefficients
b inlet height (m)
B logarithmic law coefficient
c_f skin friction coefficient $[2\tau_w/\rho U_m^2]$
J_0 kinematic momentum flux at the inlet $[U_0^2 b]$ (m^3/s^2)
k turbulent kinetic energy (m^2/s^2)
p pressure (Pa)
Q forward flow rate per unit length (m^2/s)
Q_0 forward flow rate at the inlet per unit length $[U_0 b]$ (m^2/s)
Re Reynolds number $[U_0 b/\nu]$
Re_m Reynolds number $[U_m y_m/\nu]$
U streamwise velocity (m/s)
U_m maximum velocity in a profile x = constant (m/s)
U_0 inlet velocity (m/s)
U^+ velocity in wall coordinates $[U/U_\tau]$
U_τ friction velocity $[(\tau_w/\rho)^{1/2}]$ (m/s)
uv turbulent shear stress (m^2/s^2)
x streamwise coordinate (m)
x_R reattachment distance (m)
X_0 virtual origin, x position where $U_m=U_0$ (m)
y coordinate normal to the wall (m)
y_m y position of the maximum velocity in a profile (m)
$y_{1/2}$ half-width, y position of a profile where $U=U_m/2$ (m)
y^+ wall normal coordinate $[yU_\tau/\nu]$
β inclination angle of the velocity at the exit
ε turbulent energy dissipation rate (m^2/s^3)
ε_w turbulent energy dissipation rate at wall (m^2/s^3)
κ von Karman constant
τ_w wall shear stress $[\rho\nu(\partial U/\partial y)_w]$ (N/m^2)
ν kinematic laminar viscosity (m^2/s)

EXPERIMENTAL SETUP

An overall view of the experimental setup is shown in Fig. 1. This facility consists of a centrifugal blower, a settling chamber, a two-dimensional nozzle, and a flat horizontal plate (with a length of 2.0 m and a width of 1.0 m). In order to obtain two-dimensional flow, and to shield the wall-jet from any external disturbances, two vertical walls surround the wall-jet. A vertical back wall above the slot is used to create a well-defined boundary condition at the nozzle exit The entire wall jet facility is located in a large laboratory hall to minimise any possible secondary flows.

The nozzle is a slot with a height of b = 10.0±0.05 mm and aspect ratio of 100:1 to form the two-dimensional wall jet. Turbulence and secondary motions caused by the fan are minimized at the settling chamber with three fine screens, a honeycomb section, and a 10 to 1 contraction to get a uniform "top-hat" mean velocity profile.

Outside the thin wall boundary layers, the mean velocity is flat within 0.25% and the streamwise free stream turbulence is of the order 0.3%. The spanwise mean velocity variation of the slot was found be less than 0.5%.

All measurements were conducted using a constant temperature anemometer system, Dantec StreamLine® with three CTA 90C10 modules with a miniature single-wire probe for the boundary layer 55P15 and miniature cross-wire probe 55P63. Hot-wire probes were calibrated using a Dantec calibration system 90H10. Anemometer voltages were transformed into velocities using a polynomial curve fit. Directional calibration was employed for cross-wire probes.

Stepper motors in the three coordinates were used to drive the traversing mechanism. The velocity near the solid surface was measured at Δy intervals of 0.0125mm.

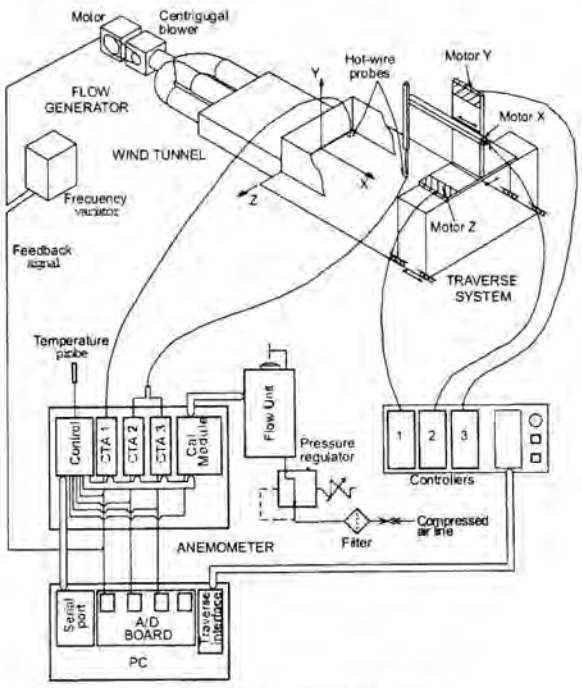

Figure 1: Overview of setup.

RESULTS AND DISCUSSION

Parallel wall jet

While the jet develops downstream, its velocity is reduced and it is expanded normal to the wall. Analysing the behaviour of maximum velocity (U_m) and half-width ($y_{1/2}$) was used to investigate the decrease in velocity and normal expansion to the wall respectively.

Mean velocities

There is agreement between the mean velocity profiles measured in this work and those obtained with thermal anemometry by Wygnanski *et al.* [3] and Abrahamsson *et al.* [4]. Profiles measured agree with those of Karlsson *et al.* [7] which were obtained using LDA except in the outer region (Fig. 2). The differences between the measuring techniques are due mainly to the high local turbulence levels, being so high that local flow reversals occur. This effects can not be captured by conventional hot-wire anemometry, which in this situation are known to produce high values for the mean velocity and low estimates for the variance.

Wygnanski *et al.* [3] observed differences in mean velocity profiles in the outer region with the Reynolds number. These differences have not been observed in this work, nor in the work of Abrahamsson *et al.* [4]. As Abrahamsson *et al.* [4] pointed out these deviations are probably due to the influence of experimental conditions, *i.e.* secondary flows and room draught.

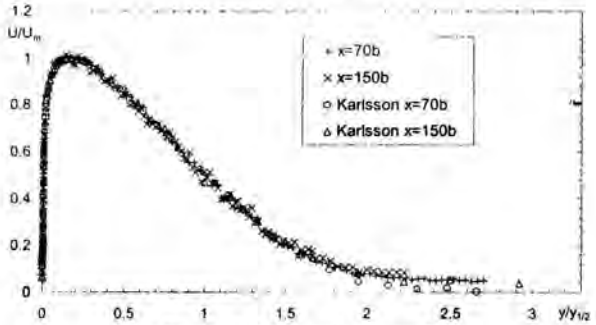

Figure 2: Mean velocity profiles

Maximum mean velocity

Dimensional considerations [12] say that the maximum velocity in each transverse section varies linearly with $x^{-1/2}$. In Fig. 3, the streamwise development of maximum velocity $(U_0/U_m)^2$ is compared with experiments from other authors [3,4,7,13] for analogous Reynolds numbers.

For increasing Reynolds number a decrease in the slope is observed, as well as displacement of the virtual origin (X_0). Narasimha [14] claimed that the inlet momentum flux (J_0) and the kinematic viscosity (ν) were more suitable for the scaling. The streamwise velocity distribution of the three Reynolds numbers collapse into one single curve using the scaling:

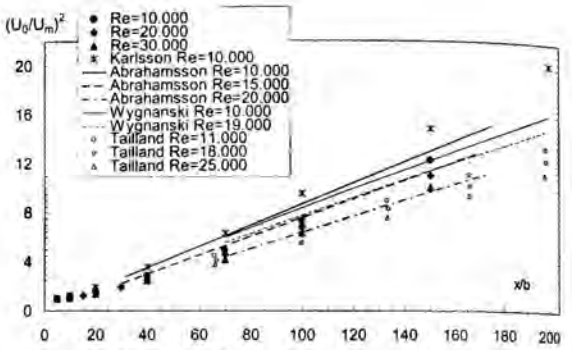

Figure 3: Decay of maximum velocity.

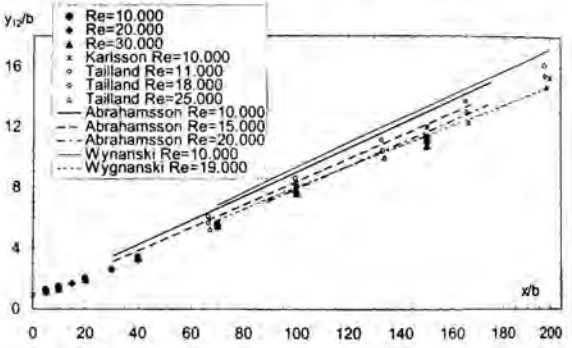

Figure 4: Streamwise development of half-width.

$$\left[U_m \frac{\nu}{J_0}\right] = A_U \left[(x - X_0)\frac{J_0}{\nu^2}\right]^{B_U} \qquad (1)$$

The coefficients obtained are slightly different from those of Wygnanski *et al.* [3] and Abrahamsson *et al.* [4] (Table I). The exponent agrees with those of other authors but no the constant. This is probably due to the fact that the determination of the constant is very sensitive to the election of the exponent. The little differences with Wygnanski *et al.* [4] data can be due to different boundary conditions in the facilities [4].

Table 1: Power law coefficients for U_m.

	Wygnanski [3]	Abrahamsson [4]	Present
A_U	1.473	0.538	0.7704
B_U	-0.472	-0.415	-0.4374

Half-width

The half-width ($y_{1/2}$) is used usually to measure the spread rate of the wall jet. Dimensional considerations [12] said that $y_{1/2}$ varies linearly with distance from inlet x. Launder & Rodi [1] confirm this trend and obtain a range for the slope of $dy_{1/2}/dx = 0.073 \pm 0.002$. The slopes of the half-width obtained in this work have been 0.0717, 0.0706 and 0.0679 for the Reynolds numbers of 10^3, $2 \cdot 10^3$ and $3 \cdot 10^3$ respectively (Fig. 4).

Using the scaling of Narasimha (Fig. 7) is obtained a power law for the streamwise development of the half-width:

$$\left[\frac{y_{1/2}}{\nu^2}\frac{J_0}{}\right] = A_y\left[(x - X_0)\frac{J_0}{\nu^2}\right]^{B_y} \quad (2)$$

The exponent agrees with those of other authors, however the constant A_y does not. This is probably due to the same reason as for A_U. (Table 2)

Table 2: Power law coefficients for $y_{1/2}$.

	Wygnanski [3]	Abrahamsson [4]	Present
A_y	1.440	0.564	9.246
B_y	0.881	0.925	0.804

Wall shear stress

It is difficult to measure the wall shear stress in the wall jet due to the small thickness of the inner region. The values of the skin friction (c_f) obtained by calibrated surface impact tubes (e.g. the Preston tube measurements by Bradshaw & Gee [15] and Abrahamsson *et al.* [3]) are comparable to the factors determined by the direct force measurement (e.g. Alcaraz [16]) and with those obtained from velocity gradient measured with LDA by Karlsson *et al.* [7]. The results are adjusted at the expression proposed by Bradshaw & Gee [15]:

$$c_f = 0.0315 Re_m^{-0.182} \quad (3)$$

However, attempts were made to obtain the c_f by measuring the velocity gradient in the viscous sublayer using hot-wires (Tailland & Mathiew [13], Wygnanski *et al.* [4], and in this work provide values of the order of 20% or 30% below the predicted values of Bradshaw & Gee [15] (Fig. 5). When the hot wire is close to the wall the temperature and velocity are modified around the wire due to the presence of the wall.

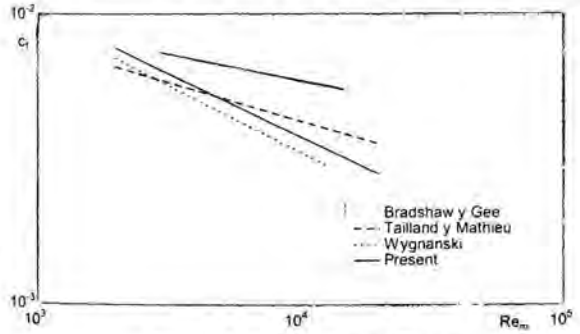

Figure 5: Skin friction coefficient.

Near wall region

In figure, the velocity profiles are scaled in wall coordinates with friction velocity (U_τ) and the kinematic viscosity (ν). Friction velocity is obtained from wall shear stress, which itself is obtained through the velocity gradient in the viscous region. Different authors show the existence of a logarithmic region ($20 < y^+ < 80$) in the wall jet as in the case of boundary layers expressed by:

$$U^+ = (1/\kappa) Ln(y^+) + B \quad (4)$$

where the coefficients take the value κ=0.41 and B=5.0. In the most ancient bibliography [1] and quite recently [3] is questioned the existence and extension of the logarithmic region.

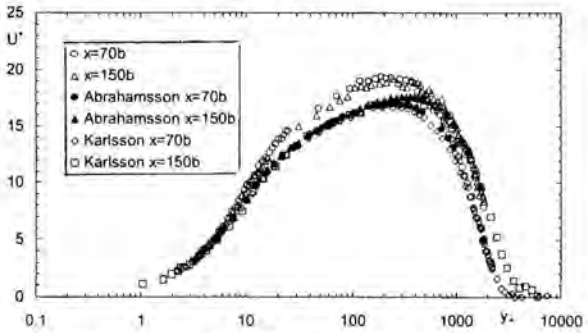

Figure 6: Velocity profiles in the inner region Re = 10^3.

In Fig. 6 the velocity profiles measured with data of other authors in two longitudinal positions is compared. A zone is observed where the velocity profile satisfies equation (4) with the constants κ=0.41 and B varying between 5 and 10. A growth of the logarithmic region both with x-coordinate and Reynolds number was observed. For values of $y^+ < 30$, a linear dependency between U^+ and y^+ is obtained. The difference in the velocity profiles of Karlsson *et al.* [7] and Abrahamsson *et al.* [4] could be due to the errors in the estimation of the skin friction.

Turbulence fields

Karlsson *et al.* [7] and Abrahamsson *et al.* [4] have accomplished measurements of turbulent magnitude employing the LDA and HW respectively. Their measurements agree until $0.6y_{1/2}$ where hot-wire provides inferior turbulence levels. This difference can be attributed to the different measuring techniques. For all non-zero stresses (u^2/U_m^2, v^2/U_m^2, w^2/U_m^2 and uv/U_m^2), there exists a similar behaviour for different longitudinal positions and Reynolds numbers.

For the streamwise turbulence intensity u^2/U_m^2, the existence of two maxima has been proven, one of them in the inner region and the other in the outer region. Normal velocity fluctuations v^2/U_m^2 shows is appreciated a maximum in 0.8 $y_{1/2}$ with a level of 2.5%. The shear stress measurements accomplished with hot-wire agree mutually, but they are different from the measurements accomplished through LDA (Fig. 7). A minimum in the interior region ($y^+ \approx 100$) and a maximum in $0.8y_{1/2}$ are observed. With inner region scales is appreciated the lack of similarity from $y^+ \approx 100$. Furthermore the

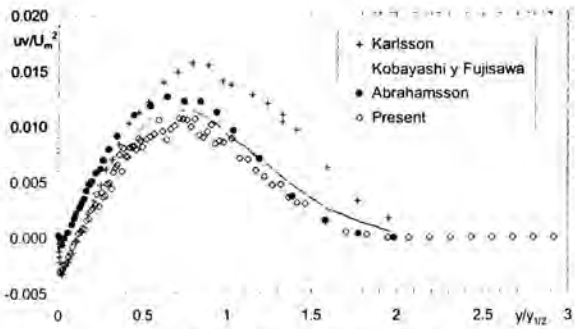

Figure 7: Shear stress in x/b=70.

position of shear stress sign change does not coincide with the maximum mean velocity position

Inclined wall jet

Measurements at the central section for x/b = 5, 10, 15, 20, 30, 40, 70, 100 and 150; for Re=10^3, $2{\cdot}10^3$and $3{\cdot}10^3$ and β = 10°, 20° and 30° were accomplished. In each point, 8000 samples were taken during 8 seconds.

Mean velocities

The principal difference in respect of the parallel wall jet appears in the initial zone due to the fact that in the inclined jet has a normal velocity to the wall. According to Lai & Lu [10,11] there appears a recirculation zone which extension increases with the inclination angle (β). The influence zone of the jet is extended a greater length normal to the wall, dragging more fluid from the surroundings.

For increasing Reynolds numbers (Fig. 8) the velocity profiles move away from the wall and the inflection point that appears close to the wall is moved away from it. This seems to indicate a larger recirculation zone for high Reynolds numbers in the longitudinal and normal directions. The reattachment distance (x_R) grows with Reynolds number in the range 10^3 <Re< $3{\cdot}10^3$ for β = 30°. It was not observed by [10,11] in the range 6.670<Re<13.340.

Close to the nozzle the jet is bent toward the wall until it is attached. This is known as the Coanda effect. For increasing inclination angles it is appreciated that the maximum velocity point is moved away with respect to the wall (this displacement is attenuated downstream). In spite of the fact that thermal anemometry measures suffer errors by the back flow, in the position x=5b the change of the slope that appears in the speed profile close to the wall would indicate the presence of recirculation (Fig. 9). This slope change disappears downstream where the flow is totally attached.

Downstream, for x≥70b the mean velocities are similar, independent of Reynolds number and inclination angle, which is the same behaviour for a parallel jet.

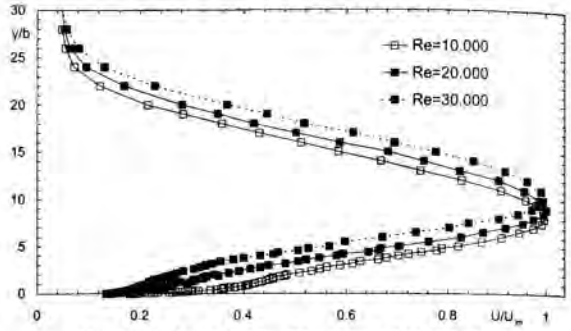

Figure 8: Velocity profiles for β=30° in x=5b.

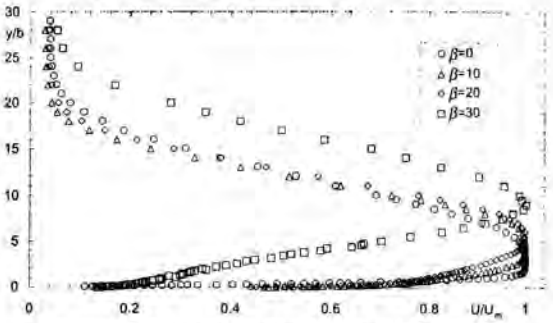

Figure 9: Velocity profiles for Re=$2{\cdot}10^3$ in x=5b.

Half-width and maximum velocity

The same as in parallel jets the position of the half-width is independent of the Reynolds number. For a fixed Reynolds number is appreciated an increase in half-width with the angle, even though the differences between β=10° and β=20° are minimal.

The evolution of $(U_0/U_m)^2$ for fixed β is analogous to parallel jet. It is a linear evolution with x/b and a decrease of $(U_0/U_m)^2$ for increasing Reynolds number. For foxed Reynolds number this parameter shows a trend to increase its slope with the inclination angle.

CONCLUSIONS

An experimental facility for the study of plane wall jets (parallel and inclined) up to Reynolds numbers of $3{\cdot}10^3$ has been designed and built. For the characterization of the wall jets, thermal anemometry has been used. Measurements of the velocity field for a 2D parallel and inclined wall jets for Reynolds numbers of 10^3, $2{\cdot}10^3$ and $3{\cdot}10^3$, inclination angles of 10°, 20° and 30°, from x=10b to x=150b have been taken.

Downstream of the nozzle, there exists similarity in the velocity profiles when scaled with the local maximum velocity and the half-width for parallel and inclined wall jets.

The inverse of maximum velocity squared varies linearly with the longitudinal distance, reducing the slope for increasing Reynolds numbers. The half-width presents a linear evolution

with a small decrease of the slope for increasing Reynolds numbers. The dependencies with the Reynolds number presented in the maximum velocity and half-width disappear when they are scaled with the kinematic momentum flux at the inlet.

The wall shear stress obtained from the velocity profile measured with thermal anemometry is affected by errors.

The measurements showed the existence of a logarithmic region. The length of this region increases with downstream position and with increasing Reynolds number. However, until 1994 were thought that this region was disappeared downstream.

For the streamwise turbulence intensity, the existence of two maxima has been proven, one in the inner region close to the wall and other in the outer region. The normal velocity fluctuations have only one maximum in the outer region. For the shear stress, it is observed that the measurements accomplished with thermal anemometry present a good conformity themselves but they disagree with the measurements accomplished with LDA. For the shear stress, there is a minimum in the inner region and a maximum in the outer region. Furthermore the location of the sign change does not coincide with the maximum mean velocity point.

For all the angles studied, inclined wall jets suffer a bend toward the wall until it attaches. For inclination angles greater than 10°, there appears a recirculating region in the vicinity of the nozzle. The extension of this region increases with the angle and the Reynolds number.

In the longitudinal evolution of the inclined wall jets can be distinguished two zones. There is an initial development zone close to the nozzle where the characteristics of the jet depend strongly on the inclination angle. The other zone is downstream where velocity profiles are independent of Reynolds number and inclination angle when the data are scaled with the maximum velocity and the half-width.

There is a linear behavior of the half-width with the downstream distance, however it has not been found to be dependent on the Reynolds number, but does depend on the angle, increasing the half-width with the inclination.

The longitudinal evolution of the maximum velocity with the Reynolds number is analogous to that of parallel plane wall jets for all the angles. The inverse of the squared maximum velocity increases its slope with the inclination angle.

ACKNOWLEDGMENTS

This work was supported by the Spanish Ministery of Education, grant 1FD97-1454.

REFERENCES

[1] Launder, B. E. and Rodi, W., 1981, "The turbulent wall jet", Prog. Aerospace Sci., 19, 81-128.

[2] Kobayashi, R. and Fujisawa, N., 1982, "Turbulence characteristics of plane wall jets", Institute of High Speed Mechanics, Tohoku University, 352, Japan.

[3] Wygnanski, I. and Katz, Y. and Horev, E., 1994, "On the applicability of various scaling laws to the turbulent wall jet", J. Fluid Mech., 234, 669-690.

[4] Abrahamsson, H. and Johansson, B. and Lofdahl, L., 1992, "A turbulent plane two-dimensional wall-jet in a quiescent surrounding", Eur. J. Mech., B/Fluids., 13 (5), 533-556.

[5] Zhou, M. D., Heine, C. and Wygnanski, I., 1996, "The effects of excitation on the coherent and random motion in a plane wall jet", J. Fluid Mech., 310, 1-37.

[6] Venas, B., Abrahamsson, H., Krogstad P. A., and Lofdahl, L., 1999, "Pulsed hot-wire measurements in two and there dimensional wall jets," Experiments in Fluids, 27 (3), 210-218.

[7] Karlsson, R. I. and Eriksson, J. and Persson, J., 1992, "LDA measurements in a plane wall jet in a large enclosure", 6th International symposium on applications of laser techniques to fluid mechanics. Lisbon, Portugal., 13, (5), 533-556.

[8] Schneider, M. E. and Goldstein, R. J., 1994, "Laser Doppler measurement of turbulence parameters in a two dimensional plane wall jet," Phys. Fluids, 6 (9), 3116-3129.

[9] Forthmann, E., 1936, "Turbulent jet expansion", English Traslation N.A.C.A. TM-789. (Original paper in German, 1934, Ing. Archiv, 5)

[10] Lai, J. C. S. and Lu, D., 1996, "Effect of wall inclination on the mean flow and turbulence characteristics in a two-dimensional wall jet", Int. J. Heat and Fluid Flow, 17, (4), 377-385,August.

[11] Lai, J. C. S. and Lu, D., 2000, "An inclined wall jet: Mean flow characteristics and effects of acoustic excitation", Experiments in fluids, 29, (1), 45-55.

[12] Rajaratnam, N., 1976, "Turbulent jets", Elsevier, 5, Developments in water science, Amsterdam.

[13] Tailland, A. and Mathieu, J., 1967, "Jet pariétal", Journal de Mecanique, 6, 103-131.

[14] Narasimha, R. and Narayan, K. and Parthasarathy S.P., 1973, "The Turbulent Wall Jet", Prog. Aerospace Sci., 81-128.

[15] Bradshaw, P. and Gee, M. T., 1960, "Turbulents wall jets with and without an external stream", Aero. Res. Council, R&M, 3252.

[16] Alcaraz, E. and Charnay, G and Mathieu, J., 1977, "Measurements in a wall-jet over a convex surface", Phys. of Fluids, 20, 203-210.

HEFAT2002
1st International Conference on Heat Transfer, Fluid Mechanics, and Thermodynamics
8-10 April 2002, Kruger Park, South Africa
VJ2

EFFECT OF WALL INCLINATION AND REYNOLDS NUMBER ON THE MEAN FLOW AND TURBULENCE CHARACTERISTICS IN A TWO-DIMENSIONAL WALL JET PART B: NUMERICAL STUDY

J. M. Villafruela *, R. Villanueva †, F. Castro ‡ and M. T. Parra *
*Associate Professor; † Doctorate Student; ‡ Professor
Department of Energetic Engineering and Fluid Mechanics,
School of Engineering - University of Valladolid
Paseo del Cauce s/n - E47011 - Valladolid (Spain)
E-mail: manolo@eis.uva.es

ABSTRACT

Three two-equation turbulence models with near-wall corrections are assessed by applying them to calculate two-dimensional parallel and inclined wall jets. These turbulence models assume gradient transport and isotropic normal stresses. The equilibrium turbulence assumption is relaxed with near wall corrections. The predictions of the simulations with a nozzle exit Reynolds number in the range 10^4-$3 \cdot 10^4$ and four different inclination angles ($\beta = 0°$, 10°, 20° and 30°) of the wall to the nozzle are compared with experimental data.

Simulations indicate that all wall jets are self-preserving in the developed region. For $\beta > 10°$, simulations predict a recirculating flow region that increases with the inclination angle similar to the experimental results. Downstream the wall jet reattaches and becomes self-preserving for all angles. The effect of Reynolds number and angle influence on the flow is the same as that in experimental measurements. Scaling numerical results with momentum and viscosity, it was found that the streamwise development of the half-width and maximum mean velocity was independent of the slot Reynolds number.

INTRODUCTION

There are two regions in a cross section of a two-dimensional wall jet: an inner region from the wall to the point of maximum mean velocity, and an outer region that extends to the edge of the jet [1]. The outer region of the wall jet is similar to a plane free jet, while the inner layer has been understood as a boundary layer with zero pressure gradient. The interaction among these two regions creates an intermediate region with its own characteristics. For that reason, this simple flow proved difficult to model [2]. The wall jet represents a challenge to current turbulence models that claim to be performing well for other types of simple and complex flows.

The most common method used to predict to predict turbulent flows are the turbulent Eddy Viscosity Models (EVM). In these models, the Reynolds stresses are related to the mean velocity gradients through the turbulent viscosity concept introduced by Boussinesq in 1877.

Launder and Rodi [1] presented a summary of the RANS models utilised in the prediction of wall jets. They found that neither the mixing-length models nor those of two equations predict correctly the behavior of the wall jet. The standard k-ε model predicts a growth rate greater than 30% from the experimental results.

Launder and Rodi [1] pointed out that the effects of the outer region on the inner layer increase as the flow develops, thus preventing the normal growth of the log-law region. Therefore, the use of wall-functions to calculate wall jets would be not appropriate and the near-wall region needs to be remodelled. This implies that the assumptions of local equilibrium turbulence and Reynolds stress isotropy might have to be relaxed in wall jet modeling.

The development of turbulence models improved with DNS data available for wall-bounded turbulent flows. Gerodimos and So [2] simulated the parallel wall jet with four low Reynolds number two-equation turbulence models that had already shown their efficiency in other simple flows. Good correspondence with the experimental results was obtained, especially with the model of Sarkar and So [8]. For the same flow Vasic [4] compared, two models of two equations with two high Reynolds number RSTMs, showing that RSTMs provided better results. However, two-equation models analyzed by Vasic [3] were quite obsolete. Even though there are numerous

experimental and numerical studies of the parallel wall jet, there are not so many numerical studies on the inclined wall jet evolving on a flat surface.

The two-equation models suppose that a clear scales separation exists, therefore they can not take into account the Reynolds stress anisotropy or the lack of local equilibrium turbulence effects. To consider these effects without appealing to a RSTM, anisotropic versions for the Reynolds stress tensor based on non-linear models can be used [4, 5]. However, these expressions are reduced in the case of parallel wall jet to the customary linear relationship. The equilibrium turbulence assumption can be relaxed introducing alterations close to the wall in the equations because of the low Reynolds numbers that exists. This provides the near-wall two-equation models. In this work three of them were used: the LS model of Launder and Sharma [6], the YS model of Yang and Shih [7], and the SSA model of Sarkar and So [8].

NOMENCLATURE

A_U, A_y, B_y, B_U potential law coefficients
b inlet height (m)
B logarithmic law coefficient
f_1, f_2 damping functions
J_0 kinematic momentum flux at the inlet $[U_0^2 b]$ (m^3/s^2)
k turbulent kinetic energy (m^2/s^2)
P mean kinematic pressure p/ρ (m^2/s^2)
P_k k production $[-\overline{u_i u_j}(\partial U_i/\partial x_j)]$ (m^2/s^3)
Re Reynolds number $[U_0 b/\nu]$
T_t turbulent temporary scale (s)
U streamwise mean velocity (m/s)
U_m maximum velocity in a profile x = constant (m/s)
U_0 inlet velocity (m/s)
U^+ velocity in wall coordinates $[U/U_\tau]$
U_τ friction velocity $[(\tau_w/\rho)^{1/2}]$ (m/s)
$\overline{uv}$ turbulent shear stress (m^2/s^2)
x streamwise coordinate (m)
x_R reattachment distance (m)
X_0 virtual origin (m)
y coordinate normal to the wall (m)
y_m y position of the maximum velocity in a profile (m)
$y_{1/2}$ half-width, y position of a profile where $U=U_m/2$ (m)
y^+ wall normal coordinate $[yU_\tau/\nu]$
β inclination angle of the velocity at the inlet (°)
ν_t eddy viscosity (m^2/s)
χ, ζ near-wall correcting functions (m^2/s^3, m^2/s^4)
ε turbulent energy dissipation rate (m^2/s^3)
$\hat{\varepsilon}$ reduced turbulent energy dissipation (m^2/s^3)
κ von Karman constant
τ_w wall shear stress $[\rho\nu(\partial U/\partial y)_w]$ (N/m^2)
ν kinematic laminar viscosity (m^2/s)
$\sigma_k, \sigma_\varepsilon, C_\mu, C_{\varepsilon 1}, C_{\varepsilon 2}$ turbulence model constants

TURBULENCE MODELS

The complete transport equations for incompressible wall jets expressed in a cartesian coordinates are shown below:

$$\frac{\partial U_i}{\partial x_i} = 0 \tag{1}$$

$$\frac{DU_i}{Dt} = -\frac{\partial P}{\partial x_i} + \nu \frac{\partial^2 U_i}{\partial x_j^2} - \frac{\partial u_i u_j}{\partial x_j} \tag{2}$$

$$\frac{Dk}{Dt} = \frac{\partial}{\partial x_j}\left[\left(\nu + \frac{\nu_t}{\sigma_k}\right)\frac{\partial k}{\partial x_j}\right] + P_k - \varepsilon + \chi \tag{3}$$

$$\frac{D\varepsilon}{Dt} = \frac{\partial}{\partial x_j}\left[\left(\nu + \frac{\nu_t}{\sigma_\varepsilon}\right)\frac{\partial \varepsilon}{\partial x_j}\right] + C_{\varepsilon 1} f_1 \frac{1}{T_t} P_k - C_{\varepsilon 2} f_2 \frac{\hat{\varepsilon}}{T_t} + \xi \tag{4}$$

The near-wall correcting functions (ξ, χ), damping functions (f_1, f_2, f_μ), parameters (T_t, $\hat{\varepsilon}$), constants (σ_k, σ_ε, $C_{\varepsilon 1}$, $C_{\varepsilon 2}$, C_μ) and wall boundary conditions for the three near wall turbulence models were found in Gerodimos and So [2]

METHODS OF SOLUTION

To carry out the numerical simulation the FIRE v7.2a code was employed. It has been necessary to implement in this code the near-wall turbulence models modifying the standard k-ε turbulence model.

For the parallel wall jet, it was attempted to follow the grid recommendations made by Gerodimos and So [2]. The optimum grid (248x55 cells) provided the independence of results with respect to the grid, for all the turbulence models. It is necessary to locate several cells in the viscous region to calculate the velocity gradient with sufficient accuracy.

The numerical study of the inclined wall jet (Fig. 1) has been accomplished in two computational domains. The initial region ($x<15b$) has been solved with a grid of 264x100. For the developed region ($10b<x<210b$) a grid was employed which corresponded to with that of parallel wall jet. The results of the initial region in x=10b are introduced as boundary conditions in the developed region.

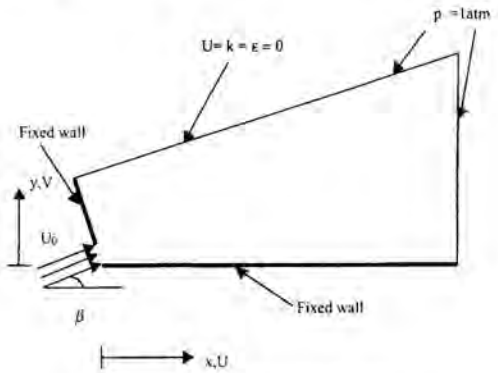

Figure 1: Boundary conditions.

In both XY-faces of the domain is imposed symmetry condition (*i.e.* null normal gradient of any variable). An entry velocity value (15, 30 or 45 m/s which correspond to Re = 10^4, $2{\cdot}10^4$ and $3{\cdot}10^4$ respectively) and the appropriate inclination angle is imposed at the inlet nozzle. The turbulent kinetic energy at the inlet has a value of 1% of inlet velocity and the turbulent length scale has a value of 0.001m (10% of b). Wall boundary conditions are imposed in the whole plane y=0 and over the nozzle. Atmospheric static pressure conditions have been imposed in the upper and right boundaries. Additionally, values of the streamwise component of velocity, turbulent kinetic energy (k) and its dissipation rate (ε) have been annulled in the upper boundary, following the recommendations of Gerodimos and So [2].

To accelerate convergence, the initial simulation was done with a coarse grid. These results have been used as an initial state for a new simulation using a refined grid. The grid has been refined repeatedly until independent results were obtained with respect to the grid.

A finite volume formulation was used and also the CTVD (Central Total Variation Diminishing Scheme). Method SIMPLE (Semi-Implicit Method for Pressure-Linked Equations) is used to link the momentum and continuity equations is an iterative "estimate and correct" procedure.

To prove that the flow has reached the steady state, maximum velocity, half-width and volume flow in different streamwise positions were monitored. It is important to choose magnitudes that characterise the behaviour of the flow.

RESULTS AND DISCUSSION

Simulation results are presented and discussed by comparing with experimental data (Abrahamsson [9], Karlsson [10] and Villafruela [11]).

Parallel wall jet

Mean velocities

There is a good agreement between the mean velocity profiles provided by all near-wall two-equation turbulence models and the experimental results. However, the k-ε model gives the worst prediction of the parallel wall jet, as was expected.

All the models predict a linear growth of half-width in the developed flow zone (Fig. 2). The SSA model predicts a slope of 0.072 that is better agreement with the experimental date range. All the models are able to predict the linear behavior of the inverse of squared maximum velocity $(U_0/U_m)^2$ (Fig. 3). The experimental data shows a greater slope than provided by all near-wall turbulence models. The half-width growth rate and the mean velocity profiles predicted by the standard k-ε model show deviations from experimental results. The predictions of the standard k-ε model are farther from the experimental results than others. The experimental rate between the maximum velocity point and the half-width $y_m/y_{1/2}$ takes the value 0.15. The SSA model with a value of 0.12 is the turbulence model that more accurately predicts this feature.

Turbulence fields

The model predicts turbulence kinetic energy and shear stress profiles closest to the experimental data. For these magnitudes the four models predict similarity in the region x>70b, according to Abrahamsson [9] (Fig 4).

Near wall region

The velocity profiles are scaled in wall coordinates with friction velocity (U_τ) and kinematic viscosity (ν).

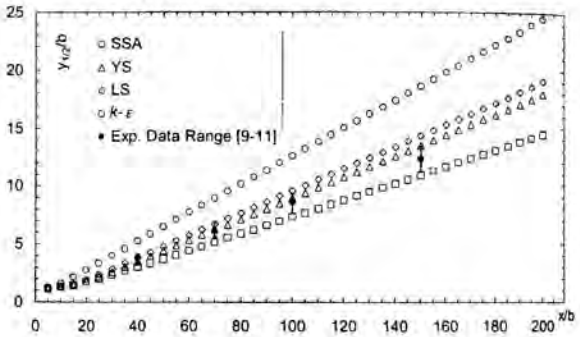

Figure 2: Streamwise development of half-width.

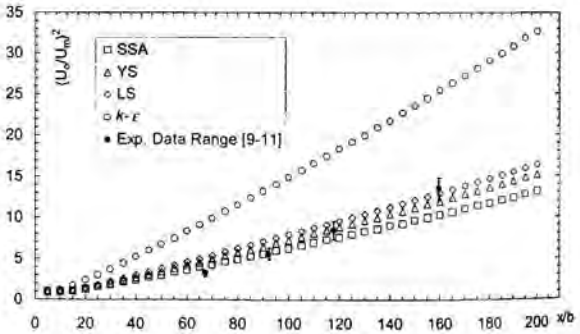

Figure 3: Decay of maximum velocity.

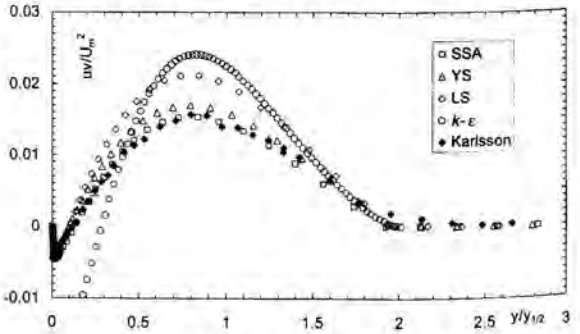

Figure 4: Shear stress profiles x=70b.

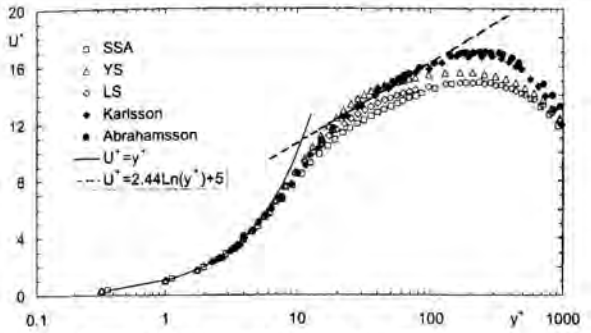

Figure 5: Velocity profiles in the inner region.

Various authors [1, 9] show the existence of a logarithmic region ($20< y^+<80$) in the parallel wall jet, as in the case of boundary layers, expressed by:

$$U^+ = (1/\kappa)Ln(y^+) + B \qquad (6)$$

where the coefficients take the value κ =0.41 and B=5.0. The turbulence models predict the logarithmic region with smaller extension that in experiments (Fig. 5). All turbulence models yield the correct value of Von Karman constant (κ), however yield different values for B coefficient (Table 1).

Table 1: Extension of logarithmic region and coefficient values.

MODEL	Logarithmic region	κ	B
SSA	$20 < y^+ < 50$	0.41	3.8
YS	$20 < y^+ < 40$	0.41	5.5
LS	$20 < y^+ < 50$	0.41	4.3

Turbulent kinetic energy and turbulent shear stress profiles in wall coordinates are reproduced accurately by the three turbulence models near the wall.

Reynolds number effects

With analysis of previous results it can be established that the SSA model predicts a behavior of the parallel wall jet closer to experimental results. This turbulence model was used to accomplish a parametric study about the influence of exit Reynolds number in the parallel wall jet evolution in the range $10^4 < Re < 3\cdot10^4$.

The mean velocity profiles are similar for the three Reynolds numbers studied. A viscous region and the logarithmic region were observed. The logarithmic region increases with the distance to the nozzle and the exit Reynolds number in agreement with Abrahamsson [9] and Karlsson [10] experimental results.

In previous experiments [9] it has been observed that the half-width is reduced and maximum velocity increases as the

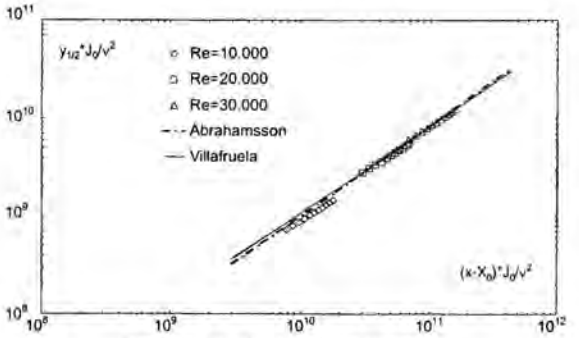

Figure 6: Half-width for different *Re*.

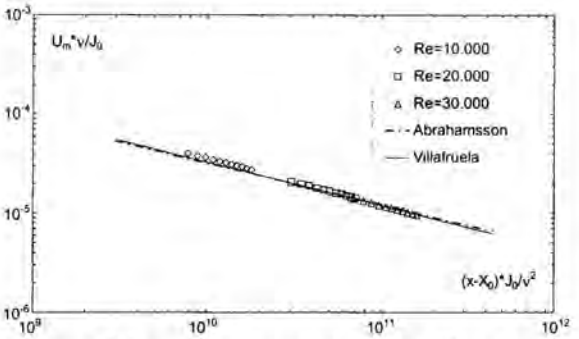

Figure 7: Decay of maximum velocity for different *Re*.

Reynolds number increases. The same effects have been obtained with numerical simulation.

The dependency of half-width and maximum velocity whit Reynolds number disappears using the scaling proposed by Narasimha [12] (momentum flux and the kinematic viscosity). With this scale, simulation results and experimental data in the developed region of the jet agree with a potential law (Fig. 6 and 7):

$$\left[y_{1/2}\frac{J_0}{\nu^2}\right] = A_y\left[(x-X_0)\frac{J_0}{\nu^2}\right]^{B_y} \qquad (7)$$

$$\left[U_m\frac{\nu}{J_0}\right] = A_U\left[(x-X_0)\frac{J_0}{\nu^2}\right]^{B_U} \qquad (8)$$

where X_0 is the virtual origin that corresponds with the x position where maximum velocity (U_m) and exit velocity (U_0) coincide.

Inclined wall jet

The SSA model is used for simulations with inclination angles of 10°, 20° and 30° and Reynolds numbers of 10^4, $2\cdot10^4$ and $3\cdot10^4$.

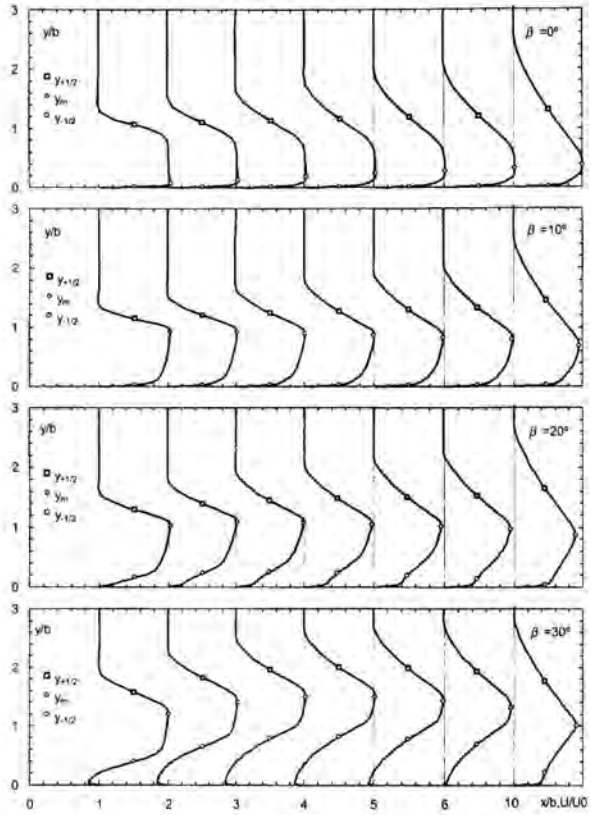

Figure 8: Velocity profiles in the initial region for different β.

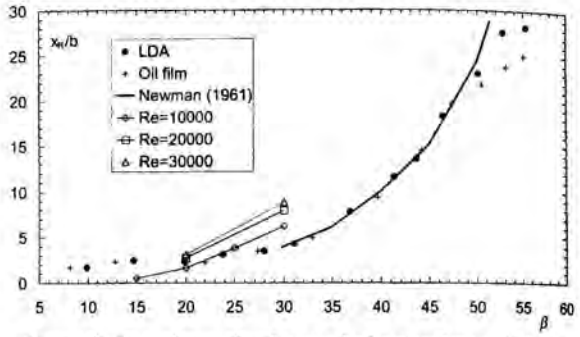

Figure 9: Experimental and numerical reattachment distance.

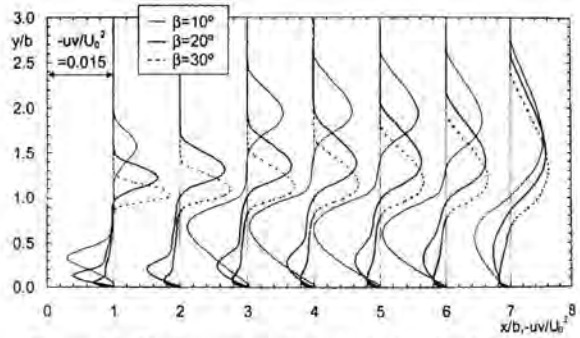

Figure 10: Shear stress profiles in initial region for $Re=10^4$.

Initial region

Fig. 8 shows the influence of the inclination angle on velocity field for the initial region. The velocity profile loses its flat shape and is bent toward the wall until it reattaches. This is known as the Coanda effect.

By increasing β it was found that the opening of the jet increase. The reattachment distance (x_R) increase with β angle. Lai and Lu [13] noted that the position of the reattachment point is independent of the exit Reynolds number within the range $6.670<Re<13.340$. Within the range used in this work ($10^3 <Re<3\cdot10^3$) the reattachment distance (x_R) grows for increasing Reynolds number (Fig. 9).

The maximum velocity and half-width position (y_m, $y_{1/2}$) develop in a different way in the initial region for different β angles (Fig 8).

In Fig. 10 it is appreciated the existence of two shear stress extremes. A minimum close to the wall, typical of momentum transfer between the internal shear layer and the recirculating region, and a maximum in the outer region corresponding to the interaction between the edge of the jet and quiescent surroundings. Both shear layers grow downstream until arriving to overlap.

Developed region

Locations $x>70b$ show similar velocity profiles in the inclined wall jet when they are scaled with $y_{1/2}$ and U_m, and when they are represented in wall coordinates. Simulations for inclined wall jets show an increase in the extension of logarithmic region with Re.

Numerical simulation predicts a linear variation of $(U_0/U_m)^2$ with x/b in the developed region, as well as the trend to increase its slope with Re except for $\beta=30°$. There are differences in the value of the slope and especially in the value of the virtual origin X_0 for different Re. The half-width growth with x/b and the slope is the same as the experimental data. Variation of this parameter with β is not appreciated in numerical results.

Numerical simulation predicts an independent behavior of y_m with respect to β in developed region.

CONCLUSIONS

The FIRE code was used to simulate the two-dimensional wall jet flow. Three near-wall two-equation turbulence models were implemented. The parallel wall jet has been simulated for

$Re=10^4$ with the k-ε standard model and three near-wall two-equation models: LS, YS and SSA. Results have been contrasted with several experiments. The three near-wall turbulence models predict the parallel wall jet with more precision than k-ε standard model, especially the growth rate of the jet.

The turbulence model whose results are in better agreement with measurements is the SSA. Predictions of this turbulence model about velocity field agree very well with measurements. This model has been used to simulate parallel and inclined wall-jet at different Reynolds numbers and angles, showing good agreement with experimental data.

In the initial region, the numerical model predicts a recirculating flow region for inclination angles greater than 10° and reproduces the effects of inclination angle and Reynolds number in this region found in experiments.

In the developed region, the numerical model predicts a linear variation of the inverse squared of U_m as well as the trend to increase its slope with Reynolds number, except for 30°. Discrepancies with the experimental data emerge on the value of that slope and especially on the displacement of the virtual origin.

For the half-width in the parallel wall jet, the numerical results predict a linear growth with the same slope found in measurements. However numerical results for inclined wall jets do not present much variation of this parameter with inclination angle, in disagreement with experimental data. The possible causes are the small capacity of the models based on the Boussinesq hypothesis to predict flows affected by strong curvature.

ACKNOWLEDGMENTS

The Spanish Ministry of Education supporteo this work, grant 1FD97-1454.

AVL has supplied the source code of several subroutines that permitted to implement the near-wall turbulence models.

REFERENCES

[1] Launder, B. E. and Rodi, W., 1983, "The Turbulent Wall Jet Measurements and Modelling," Annual Review of Fluid Mechanics, 15, 429-459.

[2] Gerodimos, G. and So, R. M. C., 1997, "Near-wall Modeling of Turbulent Wall Jets, " Journal of Fluids Engineering, 119, 304-313.

[3] Vasic, S., 1997, "Comparative Validation on Turbulence Models in Prediction of the Plane Wall Jet, " Seventh annual conference of the computational fluid dynamics, Society of Canada, Halifax 1997.

[4] Speziale, C. G., 1987, "On Nonlinear K-l and K-ε Models of Turbulence, " Journal of Fluid Mechanics, 178, 459-475.

[5] Gatski, T. B. and Speziale, C. G., 1993, "On Explicit Algebraic Stress Models for Complex Turbulent Flows," Journal of Fluid Mechanics, 254, 59-78.

[6] Launder, B. E. and Sharma, B. I.,1974, "Application of the Energy Dissipation Model of Turbulence to the Calculation of Flow Near a Spinning Disc," Letters in Heat and Mass Transfer, 1, 131-138.

[7] Yang, Z. and Shih, T. H., 1993, "New Time Scale Based k-ε Model for Near-wall Turbulence, " AIAA Journal 1993, 31, 1191-1198.

[8] Sarkar, A. and So, R.M.C., 1997, "A critical evaluation of near-wall two-equation models against direct numerical simulation data", Int. J. Heat and Fluid Flow 1997, 18, 197-208.

[9] Abrahamsson, H., Johansson, B. and Lofdahl, L., 1994, "A Turbulent Plane Two-dimensional Wall Jet in a Quiescent Surrounding," Eur. J. Mech., B/Fluids, 13, 5, 533-556.

[10] Karlsson, R. I. and Eriksson, J. and Persson, J., 1992, "LDA measurements in a plane wall jet in a large enclosure," 6th International symposium on applications of laser techniques to fluid mechanics. Lisbon, Portugal 1992.

[11] Villafruela, J. M., 2001, "Estudio numérico y experimental de chorros de pared planos paralelos e inclinados", PhD thesis, University of Valladolid.

[12] Narasimha, R, Narayan, K. and Parthasarathy, S.P., 1973, "The Turbulent Wall Jet", Prog. Aerospace Sci., 81-128.

[13] Lai, J. C .S. and Lu, D., 2000, "An inclined wall jet: Mean flow characteristics and effects of acoustic excitation, " Experiments in fluids, 29, (1), 45-55.

HEFAT2002
1st International Conference on Heat Transfer, Fluid Mechanics, and Thermodynamics
8-10 April 2002, Kruger Park, South Africa
AF1

LOW TURBULENCE NATURAL CONVECTION IN AN AIR-FILLED SQUARE CAVITY WITH AND WITHOUT PARTITONS

F. Ampofo and T. G. Karayiannis
School of Engineering Systems and Design
South Bank University
103 Borough Road
London SE1 0AA, UK
E-mail:tassos.karayiannis@sbu.ac.uk

ABSTRACT

An experimental study of low-level turbulence natural convection in an air filled vertical square cavity with and without partitions was conducted. The cavity was 0.75 m high × 0.75 m wide × 1.5 m deep giving 2-D flow. The hot and cold walls of the cavity were isothermal at 50 °C and 10 °C respectively giving a Ra number of 1.58×10^9. The velocity and temperature distribution was systematically measured at different locations in the cavity and an experimentally obtained contour plot of the thermal field of the air flow in the cavity is reported for low turbulence natural convection in such cavities for the first time. The local and average Nusselt numbers are also presented. The experiments were conducted with very high accuracy and as such the results can form experimental benchmark data and will be useful for validation of Computational Fluid Dynamics (CFD) codes.

INTRODUCTION

Natural convection in standard and partitioned enclosures is of importance in many engineering applications. These include energy transfer in rooms and buildings, nuclear reactor cooling, solar collectors and electronic equipment cooling. Natural convection in a rectangular cavity (empty or partitioned) is also a very good vehicle for both experimental and theoretical studies. In experimental terms, the geometry of the rectangular cavity is simple and its boundary conditions are relatively easy to assess so that researchers can focus on the measurements of important quantities such as velocity and temperature profiles. In numerical terms, the flow phenomena in the cavity are complicated and plentiful that intrigue both physicists and engineers. However, in spite of the developments in the measurement technology and instruments, as well as in numerical methods and computers, fully describing the fluid flow and heat transfer in such geometry still remains a challenge. In experimental studies, the flow is very sensitive to the experimental conditions. Further, boundary conditions on the horizontal cavity surfaces, defined in numerical work as adiabatic or perfectly conducting, are not easily realised in experiments, e.g. in a water filled cavity, the thermal boundary conditions on these surfaces lie somewhere in between the above two limiting cases (Nansteel and Grief, 1984). Different fluids, e.g. air and water may exhibit significantly different temperature and fluid flow patterns in cavities of similar dimensions (Olson et al., 1990). Although, convection in enclosures has been extensively studied both experimentally and numerically, only a limited number of investigators have studied partitions on the cavity walls. In addition, CFD predictions for both standard and partitioned cavities do not always compare successfully with the experimental findings. Up to now, none of the CFD codes developed can correctly predict the whole velocity and temperature fields. The discrepancy between the experimental and numerical results is obvious.

An experimental study of heat transfer and fluid flow in standard and multi-partitioned air filled square cavity was conducted. The main objective of the study was to provide highly accurate turbulent convection data which can be used for the validation of CFD codes used in the design of electronic equipment and in the building industries. It is believed that a CFD code, which can predict the fluid flow and heat transfer in these standard and congested cavities, can be used with confidence in electronic equipment cooling studies and design optimisation.

NOMENCLATURE

AR_x:	aspect ratio	$AR_x = H/L$	
AR_z:	aspect ratio	$AR_z = D/L$	
D:	depth of the cavity		m
g:	gravitational acceleration		m/s^2
H:	height of the cavity		m
k:	thermal conductivity		W/m K
l:	length of partition		m
L:	width of the cavity		m
Nu:	local Nusselt number	$Nu = hL/k$	
Ra:	Rayleigh number	$Ra = [g\beta(T_h - T_c]\ L^3)/\alpha\nu$	
T:	temperature		°C, K
x, y, z:	Cartesian co-ordinate		
X,Y,Z:	dimensionless co-ordinates		

Greek letters

α:	thermal diffusivity	m^2/s
β:	thermal expansion coeff.	1/K
μ:	dynamic viscosity	kg/m.s
ν:	kinematic viscosity	m^2/s

Subscripts

c:	cold wall
h:	hot wall
w:	wall

EXPERIMENTAL FACILITY AND PROCEDURE

A fully automatically controlled natural convection test rig, see figure 1, has been carefully designed and constructed. The system can be divided into five parts, namely the temperature control system, the cavity, facilities for measuring the air temperature and velocity separately and a facility to measure them simultaneously. The temperature control system maintained a constant temperature water flow to chambers attached to the hot and cold plates, see figure 2. It comprised of a PC, a Schlumberger 3531F data acquisition system, a multi-loop PID (proportional-integral-differential) temperature-process controller and low noise K-type thermocouples. The computer controlled the data logging system to record the thermocouple readings and to send the signal to the PID controller. The PID controller sent pulses to the burst firing trigger modules to alter the heating power. The burst firing trigger modules switched the power on and off at zero voltage. The cold and hot water, which were controlled at predetermined temperatures, were pumped through the water chambers at a rate of 40 L/min. The test cavity, shown in figure 2, was 0.75 m high × 0.75 m wide × 1.5 m deep. The depth of the cavity resulted in a 2-D flow in the mid-plane of the cavity. The hot and cold walls of the cavity were made of 6 mm mild steel plate and maintained isothermal at 50 ± 0.15 °C and 10 ± 0.15 °C respectively giving a Ra number of 1.58×10^9. The top and bottom walls were made from 1.5 mm mild steel sheet and provided highly conducting boundaries. The temperatures on these isothermal and horizontal walls were measured using K-type thermocouples. The partitions were 150 mm long, 1.5 m wide and made of 3 mm thick pure aluminium (1050A H22). A total of five (removable) partitions were installed on the hot wall of the cavity at 125 mm apart. Two guard cavities surrounded the passive vertical walls to reduce the heat exchange with the ambient. The room temperature was controlled at 30 ± 0.2 °C chosen to be equal to the average of hot and cold walls temperatures. An E type thermocouple of diameter 25.4 μm was carried by a computer controlled two-dimensional displacement device (accurate to 0.1 mm) and was used to measure the temperature in the cavity. The temperature in the multi-partitioned cavity was read by a 16 bit data logging card (WB-ASC16 A/D card) at 50 Hz sample rate. For every location, 4096 readings were taken. The temperature was accurate to within 0.1 K. A back scatter, 2D Laser Doppler Anemometer (LDA) with a Burst Spectrum Analyser (BSA) and a 40 MHz frequency shift Bragg cell was used in the velocity measurements in the multi-partitioned cavity. The laser source was a 300 mW argon laser. The measured velocity range was from –0.5082 to +0.5082 m/s with a resolution of 6.20E-5 m/s and at a bandwidth of 0.125 MHz. The laser beams entered the cavity through the guard cavity at an angle of 3.5° to the isothermal wall. A front lens with a focal length of 1200 mm was used. The probe volume dimensions were 0.31 mm (diameter) × 9.8 mm (length). Incense smoke was used as seeding which lasted for more than 24 hours. For every measuring point, either 20000 readings were taken or the measurement lasted for 8 minutes. The uncertainty in the velocity measurement was ±0.07 %. The temperature and velocity in the cavity without partitions were measured simultaneously. The facility used is shown in figure 1 but without the WB-ASC16 A/D card. Instead a new A/D converter board mounted in the same PC running the BSA flow software to control the LDA was used. The A/D board was set to start sampling the analog inputs (in this case temperature signal) at the same time as the LDA processors. Synchronisation of the A/D data with the LDA data was performed via a cable connecting the BSA SyncBus to the connector box. For every measuring point, 10000 velocity and temperature readings were acquired simultaneously. All the above measurements were taken at the mid-plane of the cavity on a very fine non-uniform mesh. During all the measurements, the experimental conditions were kept as steady as possible. Experimental repeatability was verified. The maximum deviation between readings obtained during experiments performed at different times was 0.5 K for the temperature and 2 mm/s for the velocity. For each parameter measured both the mean and fluctuation quantities were recorded. The mean velocity and temperature distributions are presented in this paper. As a first stage, velocity and temperature results for the standard cavity were compared, with excellent agreement, to the earlier work of Tian and Karayiannis (2000) done in the same cavity. Further details are available in Ampofo, 2001.

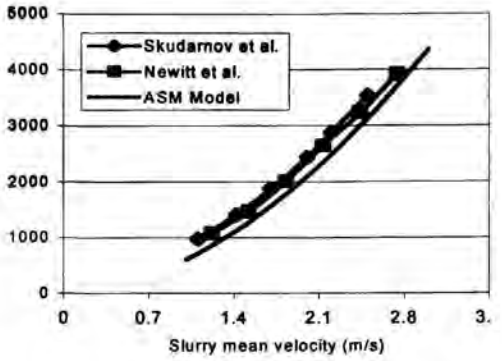

(a) Silica sand-water slurry, ρ_s=2381 kg/m, α_s=20%

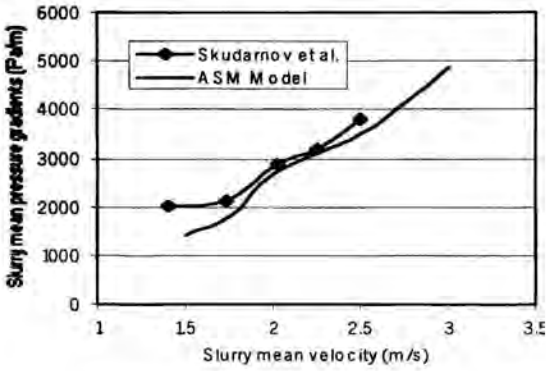

(b) Zircon sand-water slurry, ρ_s=4223 kg/m, α_s=10%

Fig. 2 Comparisons of the numerical solutions from algebraic slip mixture model with experimental data from Skudarnov and Newitt et al. in fully developed turbulent flow (d=0.0221m, d_p=97-110 microns).

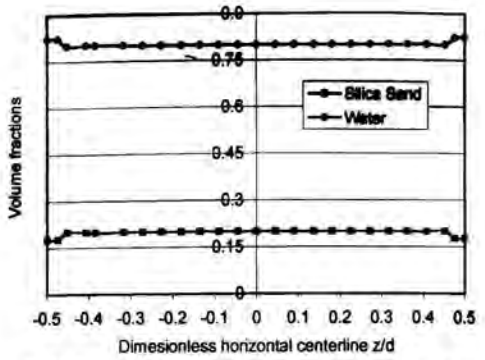

(a) Volume fraction distribution along the horizontal centerline

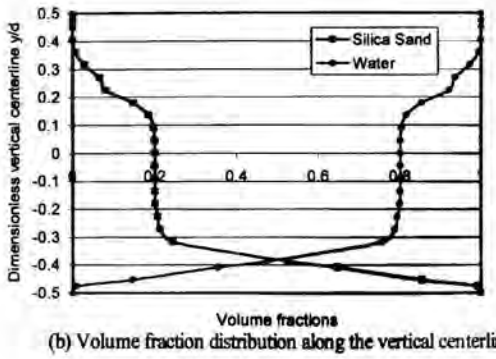

(b) Volume fraction distribution along the vertical centerline

Fig. 3 Volume fraction distributions of silica sand and water along horizontal and vertical centerlines (ρ_s=2381 kg/m^3, α_s=20%, d=0.0221m, d_p=110 microns, V=2 m/s).

4.2 Volume Fraction and Slurry Density

The volume fraction and slurry density are important parameters in slurry flow analysis. In practical experiments, it is impossible to measure the volume fraction and slurry density at any point of the pipe cross-sectional area, but it is easy to obtain them in numerical investigation.

Figure 3 shows the volume fraction distribution of silica sand-water slurry flow when V=2 m/s, α_s=20%, ρ_s=2381 kg/m^3, ρ_w=998 kg/m^3, d=0.0221m, and d_p=110 microns. As shown in Fig. 3(a), the volume fractions of silica sand and water are almost kept as constants along most of the horizontal centerline. The volume fraction of water along the horizontal centerline would have a slight increase near the wall, while the volume fraction of silica sand along the horizontal centerline has a slight decrease. It is believed that this small change in the volume fraction along the horizontal centerline is mainly caused by the sharp velocity change in the turbulent boundary condition.

The volume fractions of silica sand and water would have a sharp change along the vertical centerline, as shown in Fig. 3(b). On the top of the pipeline, the volume fraction of water approaches unit, and the volume fraction of silica sand is close to zero. This means that most of the fluid on the top of the pipeline is water. In the central part of the pipeline, the volume fractions of silica sand and water are almost kept as constants. In the lower part of the pipeline, the volume fraction of silica sand is rapidly increased to unit, and the volume fraction of water approaches zero. This indicates that most of the slurry flow in the lower part of the pipeline would be silica sand when the slurry flow is in heterogeneous and sliding bed flow (or moving bed flow).

different heights. The boundary layers start at the bottom of the hot wall and at the top of the cold wall with a small peak velocity and large thickness. The boundary layer becomes thinner along the flow direction and the peak velocity increases. The boundary layer reached minimum thickness at about Y=0.45 at the hot wall and Y=0.55 at the cold wall. The velocity peak reaches its maximum value (0.230 m/s) at this location. After this point, the layer gets thicker in the direction of flow with the peak velocity decreasing. In the partitioned cavity, the vertical velocity profile increased steeply from the isothermal walls to a peak (with the highest peak near the cold wall) and then decreased rapidly to slightly negative values. This means that there was a flow reversal. In-between successive partitions, the vertical velocity then increased reaching another peak around the tip of the partitions. Away from the partitions (X=0.4 and X=0.8) the fluid was stationary. The fluid flow was mainly limited in the near wall area along the cold wall. The flow boundary layer along the isothermal walls can be seen clearly from the vertical velocity profiles at different heights. The boundary layers start at the bottom of the hot wall and at the top of the cold wall. The boundary layer becomes thinner along the flow direction and the peak velocity increases. Along the cold wall, the boundary layer reached minimum thickness at about Y=0.51 and the velocity peak reaches it maximum value (0.261 m/s) at this location. After this point, the layer gets thicker in the direction of flow with the peak velocity decreasing.

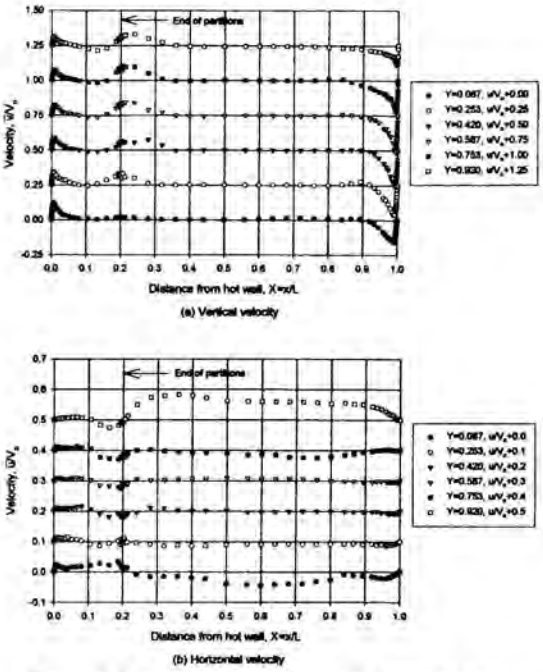

Figure 4. Mean velocity profiles at different heights in the partitioned cavity.

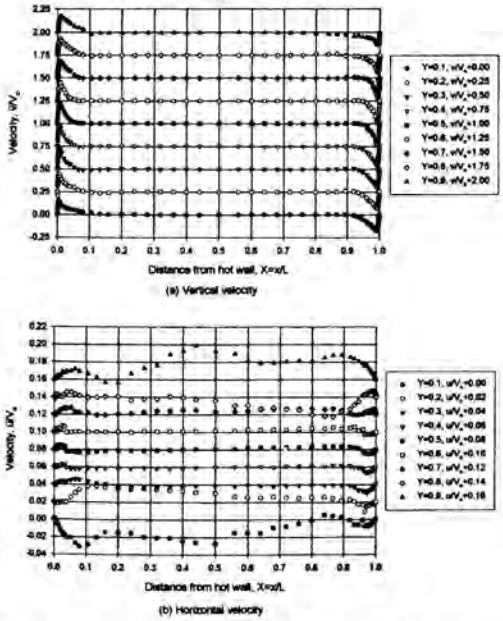

Figure 3. Mean velocity profiles at different heights in the standard cavity.

As mentioned above, the horizontal walls were highly conducting and the real temperature distribution on them in the standard cavity is shown in figure 5 and compared with the ideal perfectly conducting walls which give a linear temperature distribution (LTP). This measured temperature distribution is recommended for numerical modeling.

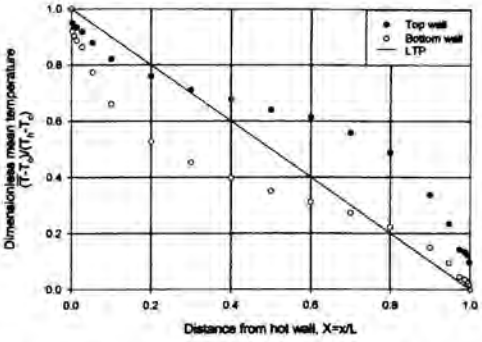

Figure 5. Temperature distribution along the horizontal walls in the standard cavity.

The temperature distribution at different heights in both the empty and partitioned cavities are shown in figures 6 and 7 respectively. The measurements for the partitioned cavity were taken centrally between successive partitions. In both cases, the temperature changed steeply near the isothermal walls in the horizontal direction. In the case of the empty cavity, after the initial sharp decrease (from the hot wall) and increase (from the cold wall), the temperature remained fairly constant (from X~0.1 to X~0.9) indicating that the fluid in this region of the cavity was nearly stationary. For the partitioned cavity, after an initial sharp decrease, the temperature remained fairly constant form X~0.01 to X~0.15 near the hot wall. A small increase was observed after the second partition. The temperature started to decrease before the end of the partitions (X~0.15). Away from the partitions (X~0.3 to X~0.9), the temperature remained constant, indicating that the fluid in this region of the partitioned cavity was stationary. In both cases, the fluid was stratified in the core of the cavities. A contour plot across half of the partitioned cavity and between two successive partitions located at heights 375 mm and 500 mm from the bottom wall is shown in figure 8. From this figure, it can be seen that the boundary layer thickness on the hot wall increased with the fluid flow as expected. Similar temperature profiles were found between every two successive partitions.

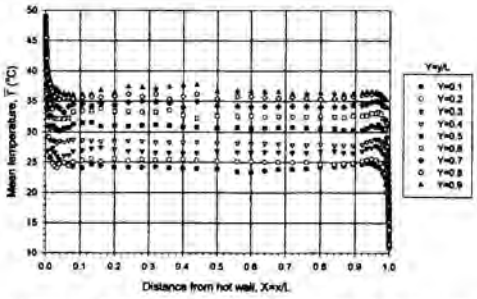

Figure 6. Mean temperature distribution as different heights in the standard cavity.

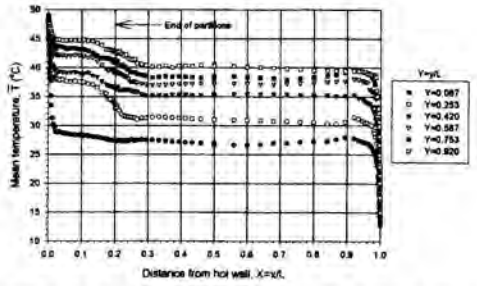

Figure 7. Mean temperature distribution as different heights in the partitioned cavity.

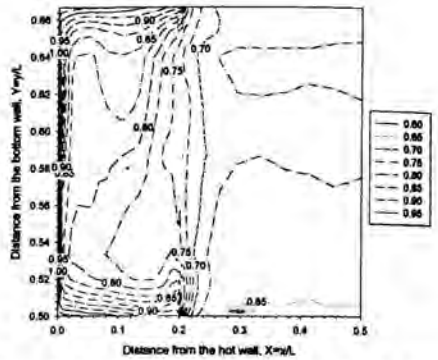

Figure 8. Contour plot of temperature distribution, $(\bar{T}-T_c)/(T_h-T_c)$, between two successive partitions.

Contour plots of the thermal field across the empty and the partitioned cavities are shown in figures 9 and 10 respectively. These are based on all the experimental data. The data were inserted into a 41×41mesh in the case of the empty cavity and 52×98 mesh in the case of the partitioned cavity. From these figures, the dimensionless temperature at the core of the whole cavity was 0.5175 (30.7 °C) in the empty cavity and 0.65 (36 °C) in the partitioned cavity. The temperature at the core of the partitioned cavity is about 20 % higher than the mean temperature (and the ambient). The effect of this in terms of the heat lost through the passive vertical walls, i.e. through the guard cavities was minimal.

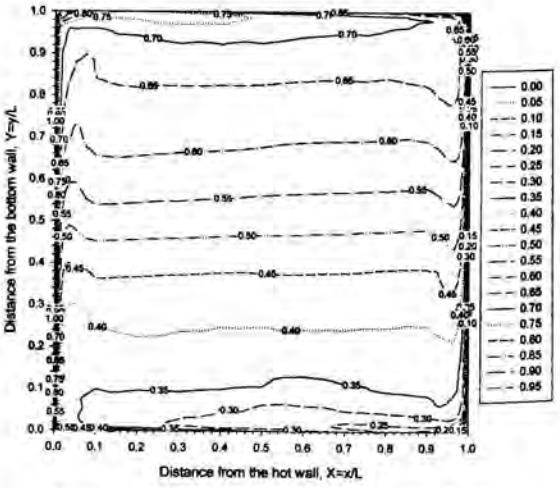

Figure 9. Contour plot of temperature distribution, $(\bar{T}-T_c)/(T_h-T_c)$, in the standard cavity.

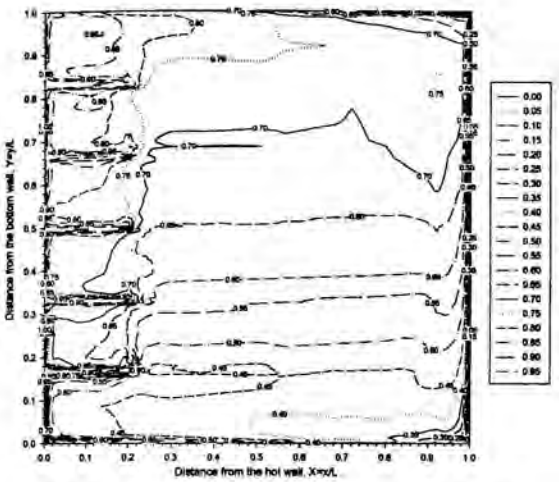

Figure 10. Contour plot of temperature distribution, $(T-T_c)/(T_h-T_c)$, in the partitioned cavity.

The Nusselt number along the walls can be determined using the measured temperature in the thermal conductive boundary layer where the heat flux is constant. The local Nusselt number is defined as:

$$Nu = -\frac{L}{T_h - T_c}\left.\frac{\partial T}{\partial x}\right|_w \qquad (1)$$

The local Nusselt number on the hot wall for both partitioned and empty cavities is shown in figure 11. The local Nu number on the hot wall reaches a maximum at the bottom of the wall because of thinner thermal boundary there. The measured maximum Nu value is about 110 for the partitioned cavity and 135 for the empty cavity. The thickness of the boundary layer on the hot wall is increasing along the flow direction so that the local Nu number decreases rapidly. The Nu distribution in-between partitions was similar in shape to that obtained in an empty cavity with a maximum value near the upper surface of a partition and a reduction to a minimum near the bottom of the next partition. At mid-height, the local Nu number is about 25 for the partitioned cavity and 58 for the empty cavity. The corresponding minimum Nu value on the hot wall is about 10 and 17. The average Nu number was 34 for the partitioned cavity and 62.9 for the empty cavity. The partitioned cavity offered a lower heat transfer rate along the hot wall as compared to the empty cavity with the same dimensions and under the same experimental conditions. This was probably due to the length of the partitions (X=0.2). However, the heat transfer from the hot wall (including partitions) increased from 98 W to 199 W for the standard and partitioned cavities respectively.

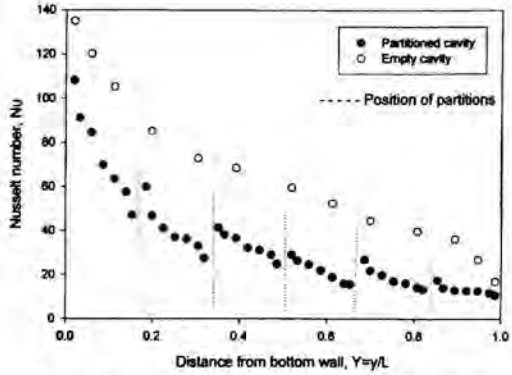

Figure 11. Local Nusselt number along the hot wall.

CONCLUSIONS

A detailed temperature and velocity distribution in a cavity with and without partitions at the hot wall was presented. The temperature field indicated boundary layer structure on the hot wall in-between partitions and also along the cold wall. Beyond the partitions the temperature was fairly uniform along the x-direction with stratification in the y-direction. The local and average Nu number was obtained and indicated that partitions of this length tend to reduce the heat transfer rates along the hot wall compared with similar cavities without partitions. The velocity field also indicated that the flow is limited in a narrow strip along the walls and also around the tip of the partitions. The fluid in the core of the cavity was stationary and stratified in both cases. The results described in this paper were obtained with high precision and can be useful as a benchmark data for the validation of CFD codes. Such numerical simulation should include realistic boundary conditions at the top and bottom horizontal walls as given in this study.

REFERENCES

Nansteel, M. W. and Griet, R., Natural Convection in Enclosures with Two- and Three-Dimensional Partitions, Int. J. Heat and Mass Transfer, Vol. 27, No. 4, pp. 561-571, 1984.

Olson, D. A., Glicksman, L. R. and Ferm, H. M., Steady-State Natural Convection in Empty and Partitioned Enclosures at High Ra Numbers. ASME J. HT, Vol. 112, pp. 640-647, 1990

Tian, Y. S. and Karayiannis, T. G., Low Turbulence Natural Convection in an Air Filled Square Cavity, Part I: Thermal and Fluid Flow Fields, Int, J. Heat and Mass Transfer, Vol. 43, pp. 849-866, 2000.

Ampofo, F., Ph.D. Thesis, Turbulent Natural Convection in an Air Filled Standard and Partitioned Square Cavity, South Bank University, 2001.

HEFAT2002
1 st International Conference on Heat Transfer, Fluid Mechanics, and Thermodynamics
8-10 April 2002, Kruger Park, South Africa
DG3

EXPERIMENTAL STUDY OF THE EFFECT OF HYDRODYNAMIC UNSTEADINESS ON A TURBULENT TUBE GAS FLOW STRUCTURE AND HEAT TRANSFER

G. A. Dreitser*, V. B. Bukharkin** and V. M. Kraev***
*Doctor, Professor, Head of the Department, **Scientist; ***Doctor, Scientist,
Department of Aviation-space Thermal Technik;
Moscow Aviation Institute,
Volokolamskoe shosse 4, 125993,
Moscow, Russia,
E-mail: heat204@mai.ru

ABSTRACT

The measurements methods are devised and experimental data on the profiles of the longitudinal and radial velocity components are obtained to study the turbulent structure of an unsteady isothermal and nonisothermal gas flow in a tube. The two-hot wire X-shaped mobile probe of constant temperature was used. The profiles of the longitudinal and radial velocity components, their pulsations, the temperature pulsations, correlations and heat transfer at gas flow acceleration and deceleration conditions are presented. These parameters are shown to differ noticeably from their quasi-steady values in the unsteady processes.

INTRODUCTION

Unsteady thermal and hydrodynamic processes play an important role in nature and technology. Experimental and theoretical studies conducted by Dreitser with coworkers [1-4, 7] of unsteady thermal and hydrodynamic processes in gas and liquid flows in channels have shown that for a turbulent flow the difference between the unsteady heat transfer coefficient and the quasisteady value is significant (their ratio changed within 0.4...3.5) and the effect of turbulence structure on unsteady heat transfer is essential for both gases and liquids. Fundamental studies of unsteady turbulent structure in channels are required for understanding of the nature of these processes and for obtaining the experimental results for creation of unsteady turbulent flow model. This work is a continuation of investigation, which was reported in on International Symposiums [8-10]..

NOMENCLATURE

d	diameter (m)
g	gravity acceleration (m/s^2)
G	flow rate (kg/s)
$\partial G/\partial \tau$	flow rate acceleration (kg/s^2)
K	parameter of hydrodynamic unsteadiness
K^*_g	parameter of hydrodynamic unsteadiness
l	length (m)
Nu	heat transfer coefficient
Pr	Prandtl number
Pr_t	turbulent Prandtl number
Re	Reynolds number
r	tube radius (m)
R	radius of channel (m)
T_f	mean flow temperature (K)
T_w	wall temperature (K)
$\sqrt{\overline{T'^2}}$	temperature pulsations (K)
U	flow velocity (m/s)
U_0	average flow rate velocity (m/s)
$\overline{U_r}$	radial component of mean velocity (m/s)
$\overline{U_x}$	longitudinal component of mean velocity (m/s)
$\overline{U_{x0}}$	steady value of longitudinal component of mean velocity (m/s)
$\sqrt{\overline{U_r'^2}}$	pulsations of radial component of velocity (m/s)
$\sqrt{\overline{U_{r0}'^2}}$	steady value of radial component of velocity (m/s)
$\sqrt{\overline{U_x'^2}}$	pulsations of longitudinal component of velocity (m/s)
$\sqrt{\overline{U_{x0}'^2}}$	steady value of longitudinal pulsations of velocity (m/s)
$\overline{U_x'U_r'}$	correlations of longitudinal and radial pulsations of velocity (m^2/s^2)
$\overline{U_x'U_{r0}'}$	steady value of correlations of longitudinal and radial pulsations of velocity (m^2/s^2)

$\overline{U_r'T'}$ correlations of radial pulsations of velocity and temperature pulsations (m/s K)

$\overline{U_r'T_0'}$ steady value of correlations of radial pulsations of velocity and temperature pulsations (m/s K)

x longitudinal coordinate (m)

y radial coordinate, distance from a wall of channel (m)

Greek Letters

ξ hydraulic resistance coefficient

ε_v turbulent viscosity (m^2/s)

ν kinematic viscosity (m^2/s)

τ time (s)

τ_0 complete time of unsteady process (s)

Subscripts

f flow

t turbulent parameter

w wall

0 steady parameter

EXPERIMENTAL METHOD

At the Moscow Aviation Institute the experimental setup was designed to study the turbulent structure of gas flow under the hydrodynamic and thermal unsteady conditions. A problem is to determine the influence of increase and decrease of the gas mass flow rate in time on turbulent structure in isothermal (T_w/T_f=1) and nonisothermal (T_w/T_f=1.1) conditions, namely, the fields of the longitudinal and radial components of mean velocity ($\overline{U_x}$, $\overline{U_r}$), the pulsations of longitudinal and radial components ($\sqrt{\overline{U_x^2}}$, $\sqrt{\overline{U_r^2}}$), the temperature pulsations ($\sqrt{\overline{T'^2}}$), their correlations ($\overline{U_x'U_r'}$, $\overline{U_r'T'}$) and consequently – on turbulent viscosity (ε_v), heat transfer coefficient Nu and hydraulic resistance coefficient ξ. The description of the experimental setup, the measuring system, the probes and the experimental procedure is presented in [8-11]. The measurements were carried out in channel of circular cross section. A working gas is compressed air. The experimental setup is a vertically located pipe with internal diameter d=0.0428 m and length of l=3 m. The structural turbulent characteristics of gas flow were measured with hot-wire systems TSL To investigate the turbulent flow structure the X-shaped two-wire (model 1243) probes for measuring the axial and radial components of the instantaneous flow temperature are used. The probe is a tungsten 8 μm dia and 1.5-2 mm long wire fastened on special legs and placed in the flow. The two-wire X-shaped probe represent a combination of two wires crossing at 90^0, each of which is located in the flow at 45^0 to the main flow direction and to the plane of a cross-section. To avoid the hydrodynamic influence of the legs and the holder the probe wires are placed upstream.

The experiments were carried out at various values of mass flow rate changing $\partial G/\partial\tau$. Necessary $\partial G/\partial\tau$ was provided with variable mass flow rate, and time of unsteady process. As the criterion of hydrodynamic unsteadiness is used the dimensionless parameter

$$K_g^* = \frac{\partial G}{\partial \tau} \frac{1}{G} \sqrt{\frac{d}{g}}. \qquad (1)$$

The experiments were carried out for values of mass flow rate G=0.005...0.02 kg/s and processes times τ=2.3, 3.4, 4.5 s. A ranges of changing of regime parameters were: for Reynolds number Re=3000...25000; parameter of hydrodynamic unsteadiness $|K_g^*|$=0...1.11, $\partial G/\partial\tau$=0...0.01 kg/s^2. The methodic of experiment was presented by *Dreitser et al.* [6].

RESULTS

Isotherrmal conditions (T_w/T_f=1)

In given section results of measurements, performed under isothermal conditions - T_w=T_f=293.15 K are presented. The profile of average axial velocity at acceleration went to more full, and at delay - less (Fig. 1). The same results were presented by *Markov* [5].

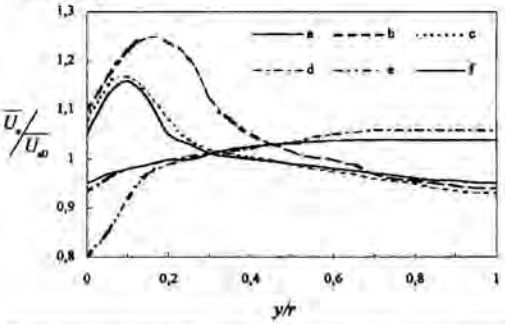

a – Kg^*=0.92, τ'/τ_0=0.3; b – Kg^*=1.11, τ'/τ_0=0.5; c – Kg^*=0.4, τ'/τ_0=0.7; d – Kg^*=-0.4, τ'/τ_0=0.3; e – Kg^*=-1.11, τ'/τ_0=0.5; f – Kg^*=-0.92, τ'/τ_0=0.7.

Figure 1: Profiles of axial velocity (Re=3100...9400; T_w/T_f=1).

In the core of a flow the axial speed differs from its steady values on 7-8% at maximum values of $|K_g^*|$. A zone y/r=0.05...0.25 is allocated, in which essential differences from stationary level are observed: at acceleration - increase of velocity at 30%; at delay - reduction by 20% at maximum $|K_g^*|$. It is possible to note, that the increase of axial velocity pulsations in zone y/r=0.05...0.25 on 30...40% is observed at maximum $|K_g^*|$ and at acceleration of a flow, and at deceleration - decrease of these pulsations on 10...25% (Fig.2).

At acceleration of a flow in zone y/r=0.05...0.25 radial pulsations (Fig. 3) are higher than stationary values on 25...40%. At deceleration reduction of radial pulsations in zone y/r=0.05...0.3 is observed on 15% at maximum values $|K_g^*|$.

The similar results is obtained at analysis of the diagram of the correlation of axial and radial velocity pulsations (Fig. 4). In

zone y/r=0.05...0.25 the correlation exceed appropriate stationary values approximately in 3 times at maximum $|K_g^*|$.

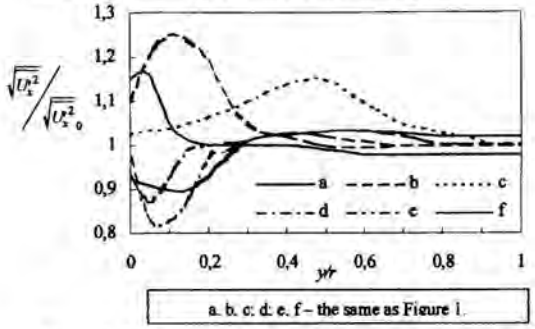

Figure 2: Profiles of axial velocity pulsations (Re=3100...9400; T_w/T_f=1).

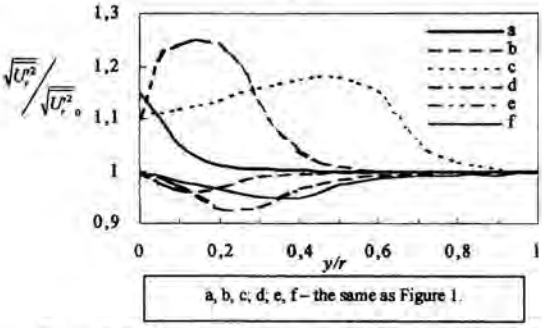

Figure 3: Profiles of radial velocity pulsations (Re=3100...9400; T_w/T_f=1).

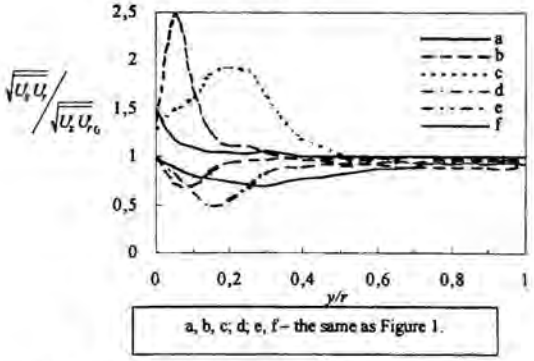

Figure 4: Profiles of correlations of axial and radial velocity pulsations (Re=3100...9400; T_w/T_f=1).

The correlation of radial velocity pulsations and temperature pulsations is presented on Fig. 5. The increase of correlation of radial velocity pulsations and temperature pulsations in zone y/r=0.05...0.3 approximately in 2.5 times at acceleration was found.

According to analysis of Fig. 2, 3, 4 and 5, it is possible to make a conclusion about displacement of a zone of turbulence generation, corresponded with a maximum of a correlation profile, from the wall region to the core of a flow in time.

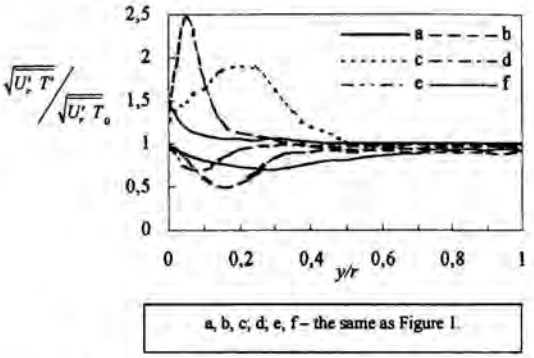

Figure 5: Profiles of correlations of radial velocity and temperature pulsations correlations (Re=3100...9400; T_w/T_f=1).

It is necessarily to input the parameter of hydrodynamic unsteadiness also and a factor of time of process at the analysis of unsteady processes. Thus the maximum values of the correlations are observed at maximum $|K_g^*|$. and decreasing in 2 times at deceleration.

Nonisotherrmal conditions (T_w/T_f=1.1)

The described below results were obtained wall temperature T_w=373.15K. The temperature of air at the entrance of the pipe was T_f=293.15K.

At acceleration the profile of axial velocity (Fig. 6), as well as in isothermal case, was more full, the maximum change of velocity reaches 40% at $|K_g^*|$=max, whereas in isothermal case - 30%. In all regimes at nonisotermal conditions the expansion of the zone of structure changes and its shift to the core of a flow was found.

At deceleration of a flow the influence of unsteadiness is qualitatively the same as for isothermal case, i.e. profile of velocity went less full, but changes are more noticeable, than for the isothermal mode.

In Fig. 7 data of the pulsations of axial velocity are presented.

The pulsations of radial velocity at acceleration (Fig. 8) in zone y/r=0.05...0.3 increase up to 27%, and in the core remain about at the level of quasisteady values.

At deceleration of flow it is observed the decrease of pulsation velocity on 5...7% in wall region, for y/r=0.05...0.3 (as for the isothermal case). It is clear, that in nonisothermal

conditions the characteristics of a flow return to steady level noticeable longer (Fig. 6-8).

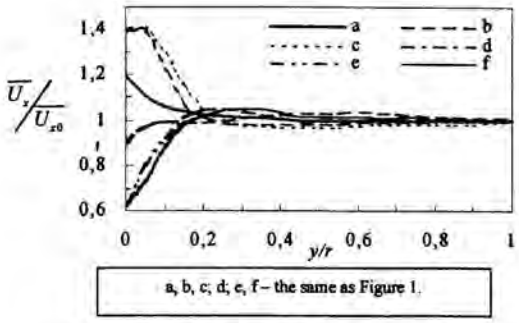

Figure 6: Profiles of axial velocity (Re=3100...9400; T_w/T_f=1.1).

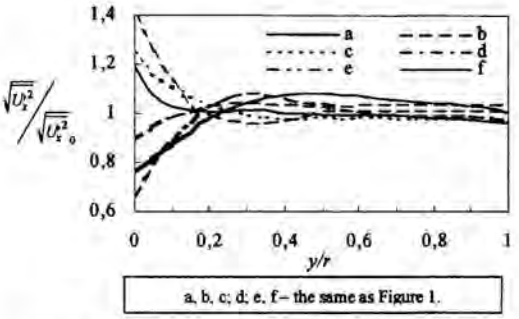

Figure 7: Profiles of axial velocity pulsations (Re=3100...9400;

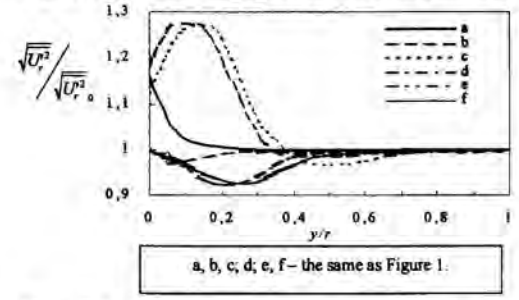

Figure 8: Profiles of radial velocity pulsations (Re=3100...9400; T_w/T_f=1.1).

Behavior of velocity pulsations, correlations between the pulsations of radial velocity and the pulsations of temperature (Fig. 9,10) remains the same, as at isothermal conditions, but stabilization of flow in nonisothermal case takes more time.

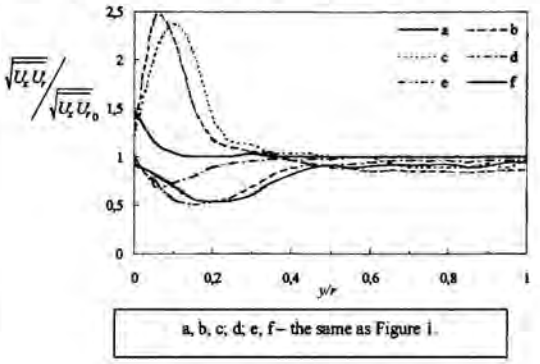

Figure 9: Profiles of axial and radial velocity pulsations correlations (Re=3100...9400; T_w/T_f=1.1).

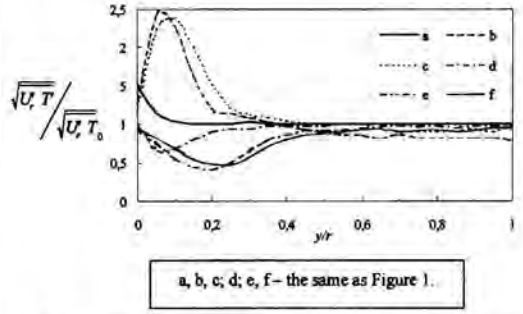

Figure 10: Profiles of radial velocity and temperature pulsations correlations (Re=3100...9400; T_w/T_f=1.1).

Turbulent viscosity and heat transfer coefficient

Turbulent viscosity and heat transfer coefficients in hydrodynamic unsteadiness conditions (previous sections) were calculated.

The turbulent viscosity coefficient was calculated by equation:

$$\frac{\varepsilon_v}{\nu} = -\frac{\overline{U_z' U_r'}}{\frac{\partial U_z}{\partial r}} \qquad (2)$$

On Fig. 11 and Fig. 12 a turbulent viscosity coefficient is presented at isothermal and nonisothermal conditions respectively. This figures show that turbulent viscosity coefficient exceed a respective steady values in the zone y/r=0.05...0.3 in 2...2.5 times at acceleration. At deceleration was found decrease of this parameter.

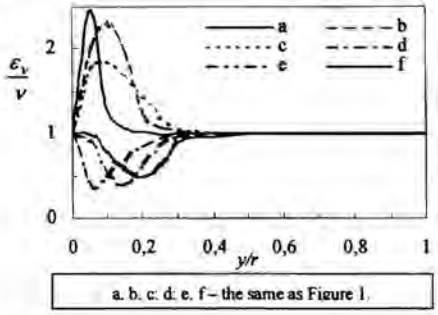

a, b, c, d, e, f – the same as Figure 1.

Figure 11: Profiles of turbulent viscosity coefficient (Re=3100...9400; T_w/T_f=1).

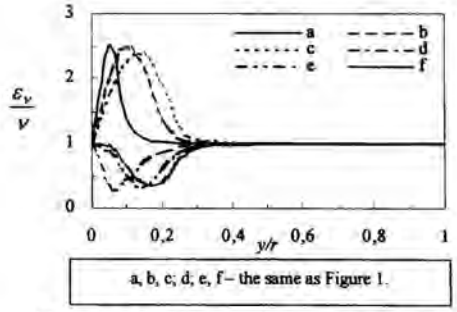

a, b, c, d, e, f – the same as Figure 1.

Figure 12: Profiles of turbulent viscosity coefficient (Re=3100...9400; T_w/T_f=1.1).

The difference of results at nonisothermal conditions (T_w/T_f=1.1) from isothermal (T_w/T_f=1) consists in slower stabilization of flow.

The heat transfer coefficient in the all range of regimes parameters was calculated by Lions integral:

$$\frac{1}{Nu} = 2\int_0^1 \frac{\left(\int_0^R \frac{\overline{U}_x}{U_0} R\,dR\right)^2}{\left(1+\frac{Pr}{Pr_t}\frac{\varepsilon_v}{\nu}\right)} dR \qquad (3)$$

Authors obtained other parameter of hydrodynamic unsteadiness.

$$K_g^* = \frac{dG}{d\tau}\frac{1}{G}\sqrt{\frac{d}{g}} \qquad (4)$$

The parameter K^*_g can be calculated from K_g

$$K_g = K_g^* \left(\frac{\sqrt[3]{d^2}\sqrt{g}}{\nu}\right) \qquad (5)$$

The result of experimental investigations of unsteady heat transfer coefficient may be generalized using the parameter K^*_g

Authors [1, 11] obtained equations at acceleration and deceleration. At Re_b = 15000...60000, K_g = 0...30 (gas flow rate increases):

$$K = \frac{Nu}{Nu_0} = 1 + 0.04\left[\left(4.1 - 1.9\frac{T_w}{T_f}\right) + \frac{39.6 - 24.4\frac{T_w}{T_f}}{\left(Re_b \cdot 10^{-4}\right)^2}\right] \cdot \qquad (6)$$

$$\cdot \left|K_g\right|^{2.4 - 1.4 Re_f \cdot 10^5}$$

At Re_b = 15000...60000, K_g = -30...0 (gas flow rate decreases):

$$K = \frac{Nu}{Nu_0} = 1 + \left[\left(0.66 + 0.275\frac{T_w}{T_f}\right)\left(0.915 + 0.08 Re_f \cdot 10^{-5}\right) \cdot \left|K_g\right|^{0.25 Re_f \cdot 10^{-5} - 0.16} - \left(\frac{0.045\frac{T_w}{T_f}}{\left|K_g\right|} - 1\right)\right] \qquad (7)$$

The calculated data were compared with experimental data of heat transfer coefficient, which had been obtained in [1, 2, 11]. The change of heat transfer coefficient an unsteady process is presented in Figs. 13 and 14.

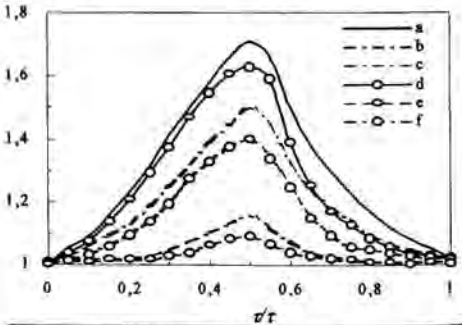

a-c - the calculated data; d-f -the results of experimental investigations of unsteady heat transfer.

Figure 13: Heat transfer coefficient at gas flow acceleration (Re=9300...28000; T_w/T_f=1.1).

As seen from this figure, the difference between our results and experimental data on unsteady heat transfer is 5...7%. It means that our experiments and calculations were carried out right. Experimental and calculated data were compared at maximum values of K^*_g in a flow acceleration (Fig. 13), for a, d - 1.11; b, e - 0.67; c, f - 0.023. In a flow deceleration data were compared at minimum values of K^*_g (fig. 14), for a, d - -1.11; b, e - -0.67; c, f - -0.023.

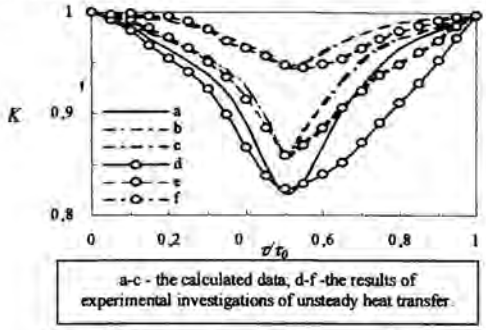

Figure 14: Heat transfer coefficient at gas flow acceleration (Re=9300...28000; T_w/T_f=1.1).

CONCLUSION

It is established, that in unsteady gas flow in tubes there is the reorganization of a structure of axial velocity. At acceleration process the profile of axial velocity goes more full, at deceleration process - less. The essential influence of an unsteadiness on intensity of pulsations is observed, at that the maximum difference of unsteady parameters from their stationary values is observed at maximum value of hydrodynamic unsteady parameter $|K_g^*|$.

Obtained results allow to determinate an intermediate zone y/r=0.05..0.4 in flow. Just in this zone there is the main reorganization of a flow in non-stationary conditions and just main differences from stationary flow are observed here. Authors found out, that a maximum of pulsations moves during an unsteady process from the wall region of the channel to the core of a flow.

The resulted data testify to amplification of the unsteadiness influence at nonisothermal conditions. As a whole the qualitative picture remains similar with isothermal case, but quantitative values of hydrodynamic parameters of flow are higher.

Authors found out, that the structure of flow goes to steady form at non-isothermal conditions slower, as at isothermal case.

The flow acceleration increases unsteady heat transfer coefficient and flow deceleration decreases this coefficient.

ASKNOWLEDGEMENTS

The support of the Russian Research Foundation under its Project №00-15-95554 (The Program of Support of Leading Scientific Schools of Russia) is gratefully acknowledged.

REFERENCES

[1] Kalinin, E.K. & Dreitser, G.A., 1970, Unsteady Convective Heat Transfer and Hydrodynamics in Channels, *Advances in Heat Transfer*: vol.6, pp. 367-562.

[2] Dreitser, G.A., Markovsky, P.M., Maloletov, I.L., Isaev, S.G., Chetirin, V.F., 1991, Effect of Hydrodynamic Unsteadiness on a Turbulent Tube Gas Flow Structure and Heat Transfer. *Experimental Heat Transfer, Fluid Mechanics and Thermodynamics. Elsevier:* pp. 891.

[3] Dzyubenko, B.U., Dreitser, G.A., Ashmantas, L.A., 1990, Unsteady Heat Transfer and Mass Transfer in Helical Tube Brandles. New York. *Hemisphere Publishing.*

[4] Kalinin, E.K., Dreitser, G.A., Kostyuk, V.V., Berlin, I.I., 1983, Calculation Method of Conjugated Heat Transfer Problems. Moscow. *Mashinostroenie.*

[5] Markov, S.B., 1973, Experimental Investigation of Velosity Structure and Hydravlic Resistance in Unsteady Headed Turbulent Flows. *Isv. AN USSR (Rus), Mech. Zidkosti i Gasa.* N2, 65.

[6] Dreitser, G.A., Neverov, A.S., Miakochin, A.S., Chetirin, V.F., Balashov, V.V., Markovsky, P.M., Maloletov, I.L., 1998, Methodical problems of studying unsteady convective heat transfer and turbulent flows structure in channels and closed volumes and development of the appropriate experimental setups and measuring systems, *Proceeding of the 1st World Conference on Experimental Heat Transfer, Fluid Mech. and Thermodynamics. Dubrovnik, 1988, Elsever, NewYork-Amsterdam-L.* pp. 816-823.

[7] Kalinin, E.K. & Dreitser, G.A., 1994, Unsteady Convective Heat Transfer in Channels. *Advances in Heat Transfer*: vol.25, pp. 1-150.

[8] Dreitser, G.A., Neverov, A.S., Bukharkin, V.B. & Kraev, V.M., 1994, Experimental Study of the Structure of Turbulent Unsteady Gas Flows in Tubes. *Proc. 1st International Symposium on Turbulence, Heat and Mass Transfer,* vol. 2, pp. 17.4.1-17.4.6.

[9] Dreitser, G.A., Bukharkin, V.B., Kraev, V.M. & Talanov, V.A., 1996, Experimental Study of the Effect of Hydrodynamic Unsteadiness on a Turbulent Gas Flow Structure and Heat Transfer. *Proc. 6th Internation Symposium on Flow Modelling and Turbulent Measurements*, pp. 159-166 .

[10] Dreitser, G.A., Bukharkin, V.B., Kraev, V.M. & Neverov, A.S., 1998, Experimental Study of the Effect of Hydrodynamic Unsteadiness on a Turbulent Gas Flow Structure and Heat Transfer. *Proc. 11th International Heat Transfer Conference.*

[11] Dreitser, G.A. 1998, Unsteady Convective Heat Transfer in turbulent gas and fluid flow in Channels. *Teploenergetika, №12, pp 29 - 38.*

HEFAT2002
1st International Conference on Heat Transfer, Fluid Mechanics, and Thermodynamics
8-10 April 200, Kruger Park, South Africa
FA1

LARGE EDDY SIMULATION OF TURBULENT FLOW IN A ROTATING PIPE

A. A. Feiz*, M. Ould-Rouis** and G. Lauriat***
*PhD Student; **Lecturer; ***Professor
LETEM, Université de Marne-la-Vallée,
77454 Marne-la-Vallée Cedex 2,
France,
E-mail: feiz@univ-mlv.fr

ABSTRACT

In this paper, we report a large eddy simulation (LES) of fully developed turbulent pipe flow, in the non-rotating and rotating cases. We describe features of flow at a fixed Reynolds number (Re=4900) and for various rotation numbers (N). The 3-D incompressible time dependent flow is computed in cylindrical coordinate. The simulation is performed by a finite difference scheme, second order accurate in space and in time. Two subgrid scale (SGS) models are used (a dynamic model and the usual Smagorinsky model). The characteristics of the flow field reproduced are described and compared to available data of literature.

INTRODUCTION

The turbulent circular pipe flow has attracted the interest of several investigators. The simplest case of non-rotating pipe has been extensively studied experimentally [1, 2] and numerically. Most of pipe flow numerical simulations have studied stability and transition [3, 4]. Some direct numerical simulations (DNS) have been performed. Using mixed finite difference and spectral methods, Nikitin [5] was able to obtain satisfactory agreement with experimental data, inside the Reynolds number range of 2250-5900. Unger et al. [6] obtained excellent agreement with experiments, using a second order accurate finite difference. They confirmed that pipe flow at low Reynolds number deviates from universal logarithmic law. Zhang et al. [7] reported simulation of low to moderate Reynolds number turbulent pipe flow obtained with a 3-D spectral code. Their initial results agree satisfactorily with both experiments and previous numerical simulations. Eggels et al. [8] have carried out DNS and experiments in order to investigate the differences between fully developed turbulent flow in an axisymmetric pipe and a plane channel geometry. Most of the statistics on fluctuating velocities appear to be less affected by the axisymmetric pipe geometry.

When a flow is introduced to an axially rotating pipe, fluids are given a tangential component of the velocity by the moving wall and the flow in the pipe exhibits a complicated three dimensional nature. The high levels of turbulence and large shearing rates associated with swirling flows enhance the mixing process and provide a more homogeneous flow fluids. The role of the swirl flow is of great importance for the overall performance of the gas turbine. Recently, the numerical simulation of turbulent rotating pipe flow has received some interest. Eggels et al. [9] used a DNS of the turbulent rotating pipe flow for moderate values of the rotation number. They confirmed numerically the drag reduction observed in experiments. Orlandi and Fatica [10] have also performed DNS of the turbulent rotating pipe flow. Their investigation was devoted to the study of the range of N not considered by Eggels et al. [9], that is the investigation of the flow field at high values of N ($N \leq 2$) but not so high as to include re-laminarization, and to the analysis of the modifications of the near-wall vortical structures, for a more satisfactory explanation of the drag reduction. They showed that a degree of drag reduction is achieved in the numerical simulations just as in the experiments and that the changes in turbulence statistics are due to the tilting of the near-wall streamwise vortical structures in the direction of rotation. The more recent study by Orlandi and Ebstein [11] is an extension of the previous one. N has been increased up to 10. These authors have evaluated the budgets for the Reynolds stresses at high rotation rates. These budgets are useful to those interested in developing new one-closure turbulence models for rotating flows.

Investigations devoted to LES of turbulence pipe flow are very limited in the literature. The first LES work on fully developed turbulent pipe flow is given by Unger and Friedrich [12]. LES have been applied to flows in complex geometries to a very limited extent. The major reasons for this are due to the need for describing the non-trivial geometry accurately whilst limiting the number of computational grid points. LES predictions on turbulent pipe flow with rotation are extremely rare. There are only three works which deal with the turbulent rotating pipe flow. Eggels and Nieuwstadt [13] used a Smagorinsky model and showed that their numerical results

compared reasonably well with the experimental data. However these experimental data was not measured in the fully developed flow zone. Recently, Yang and McGuirk [14] using LES, examined the effects of swirl driven by the rotating wall of the pipe. Their numerical results compare reasonably well with the experimental data of Imao and Itoh [15]. However, the performance of the dynamic subgrid scale model was only slightly better than that of the Smagorinsky model in their study. They pointed out that the reason may be attributed to the use of a fine mesh and the turbulent flow being fully developed. They have confirmed numerically by LES the experimental observations that turbulence decreases with an increase in pipe rotation due to the stabilizing effect of the centrifugal force.

In this study, we present initial results for Large Eddy Simulation of a rotating pipe flow at a moderate Reynolds number (Re=4900). The numerical results are compared to simulations obtained for the same Reynolds number, namely the DNS by Orlandi and Fatica [10] which compare reasonably well with experimental available data. The main objective of this work is to study fully turbulent rotating pipe flow by LES and to assess the performance of two different subgrid scale models (a dynamic model and the Smagorinsky model) in swirling flow case, in particular to examine whether the effects of swirl driven by the rotating wall of the pipe are captured directly by LES.

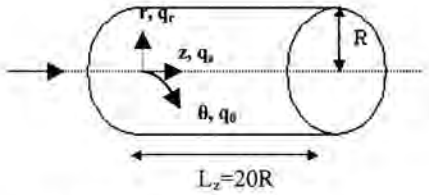

Figure 1. Schematic of turbulent flow in an axially rotating circular pipe.

NOMENCLATURE

D	pipe diameter
L_z	length of the computational domain
N	rotation number
r	coordinate in radial direction
R	pipe radius
S_{ij}	rate of strain tensor
u_τ	shear stress velocity
$U_b=U_p/2$	bulk velocity
U_p	centreline steamwise velocity of the laminar Poiseille flow
v'_r, v'_θ, v'_z	fluctuating velocity components
$\overline{v'_r v'_z}$	one of the six Reynolds stress components
y	distance from the wall
$y^+=(1-r)\,u_\tau/\nu$	distance from the wall in viscous wall units
z	coordinate in axial direction

Greek letters

$\Delta=(r\,\Delta r\,\Delta\theta\,\Delta z)^{1/3}$	characteristic gridspacing
Δ_r	gridspacing in radial direction
Δ_θ	gridspacing in circumferential direction
Δ_z	gridspacing in axial direction
ν	kinematic viscosity
θ	coordinate in circumferential direction

BASIC EQUATIONS AND NUMERICAL PROCEDURE

The turbulent pipe flow, Figure 1 is considered. The governing equations of the incompressible newtonian fluid flow (3D Navier-Stokes equations) are rewritten in terms of the new variables $q_r=r.v_r$, $q_\theta=v_\theta$ and $q_z=v_z$ to avoid the singularity at the axis r=0. In a cylindrical polar coordinate system, the equations are given in dimensionless form using U_p, the centreline streamwise velocity of the laminar Poiseuille flow and the pipe radius R as velocity and length scales respectively [16].

$$\frac{\partial \overline{q_r}}{\partial r}+\frac{\partial \overline{q_\theta}}{\partial \theta}+r\frac{\partial \overline{q_z}}{\partial z}=0$$

$$\frac{\partial \overline{q_\theta}}{\partial t}+\frac{1}{r^2}\frac{\partial \overline{r q_\theta}\,\overline{q_r}}{\partial r}+\frac{\partial \overline{q_\theta}\,\overline{q_\theta}}{\partial \theta}+\frac{\partial \overline{q_\theta}\,\overline{q_z}}{\partial z}+N\overline{q_r}=-\frac{1}{r}\frac{\partial \overline{P}}{\partial \theta}+\frac{1}{Re}\left[\frac{1}{r^2}\frac{\partial r^2\hat{\tau}_{r\theta}}{\partial r}+\frac{1}{r}\frac{\partial \hat{\tau}_{\theta\theta}}{\partial \theta}+\frac{\partial \hat{\tau}_{z\theta}}{\partial z}\right],$$

$$\frac{\partial \overline{q_r}}{\partial t}+\frac{\partial}{\partial r}\left(\frac{\overline{q_r}\,\overline{q_r}}{r}\right)+\frac{\partial}{\partial \theta}\left(\frac{\overline{q_\theta}\,\overline{q_r}}{r}\right)+\frac{\partial \overline{q_r}\,\overline{q_z}}{\partial z}-\overline{q_\theta}\,\overline{q_\theta}=Nr\overline{q_\theta}-r\frac{\partial \overline{P}}{\partial r}+\frac{1}{Re}\left[\frac{\partial r\hat{\tau}_{rr}}{\partial r}+\frac{\partial \hat{\tau}_{r\theta}}{\partial \theta}+r\frac{\partial \hat{\tau}_{rz}}{\partial z}-\hat{\tau}_{\theta\theta}\right],$$

$$\frac{\partial \overline{q_z}}{\partial t}+\frac{1}{r}\frac{\partial \overline{q_r}\,\overline{q_z}}{\partial r}+\frac{1}{r}\frac{\partial \overline{q_\theta}\,\overline{q_z}}{\partial \theta}+\frac{\partial \overline{q_z}\,\overline{q_z}}{\partial z}=-\frac{\partial \overline{P}}{\partial z}+\frac{1}{Re}\left[\frac{1}{r}\frac{\partial r\hat{\tau}_{rz}}{\partial r}+\frac{1}{r}\frac{\partial \hat{\tau}_{z\theta}}{\partial \theta}+\frac{\partial \hat{\tau}_{zz}}{\partial z}\right].$$

The dimensionless numbers are defined as $Re=U_pR/\nu$ (Reynolds number) and $N=2\Omega R/U_p$ (the rotation number which is related to Rossby number, N=1/Ro). A mean pressure gradient in the q_z equation maintains a constant bulk velocity U_b.

The total stresses $\hat{\tau}_{ij}=\overline{\tau_{ij}}+\tau'_{ij}$ are $\hat{\tau}_{ij}=(1+\nu_T Re)\overline{S_{ij}}$ where the strain tensor expressed by the variables q_i is

$$\begin{pmatrix} S_{\theta\theta} & S_{r\theta} & S_{z\theta} \\ S_{r\theta} & S_{rr} & S_{rz} \\ S_{z\theta} & S_{rz} & S_{zz} \end{pmatrix} =$$

$$\begin{pmatrix} \left[\frac{1}{r}\frac{\partial q_\theta}{\partial \theta} + \frac{q_r}{r^2}\right] & \frac{1}{2}\left[r\frac{\partial (q_\theta / r)}{\partial r} + \frac{1}{r^2}\frac{\partial q_r}{\partial \theta}\right] & \frac{1}{2}\left[\frac{1}{r}\frac{\partial q_z}{\partial \theta} + \frac{\partial q_\theta}{\partial z}\right] \\ S_{r\theta} & \frac{\partial (q_r / r)}{\partial r} & \frac{1}{2}\left[\frac{1}{r}\frac{\partial q_r}{\partial z} + \frac{\partial q_z}{\partial r}\right] \\ S_{z\theta} & S_{rz} & \frac{\partial q_z}{\partial z} \end{pmatrix}$$

The eddy viscosity ν_T has different expressions depending on the subgrid model used :

Smagorinsky Model :

In this model, the subgrid scale eddy viscosity is related to the deformation of the resolved velocity field as :

$$\nu_T = (C_s \Delta)^2 |S| = (C_s \Delta)^2 \left[\overline{2 S_{ij} S_{ij}}\right]^{1/2}$$

In the present study, the Smagorinsky coefficient C_S is set equal to 0.15. For a discussion on the value and the interpretation of this constant, we refer to Mason and Callen [23]. This subgrid model largely used in LES of isotropic turbulence produced good results. When it was applied to inhomogeneous and in particular to wall bounded flows the constant was modified.

Dynamic Eddy Viscosity Model :

The dynamic model provides a methodology for determining an appropriate local value of the Smagorinsky coefficient. The model was proposed by Germano et al. [17], with important modifications and extensions provided by Lilly [18].

In this model, the constant C_d is not given *a priori*, but is computed during the simulation from the flow variables. The turbulent viscosity is expressed using an eddy viscosity assumption as :

$$\nu_T = C_d (\Delta^2) \left[\overline{2 S_{ij} S_{ij}}\right]^{1/2}$$

but C_d is dynamically determined as follows.

Two different filter width are introduced ; the test filter $\tilde{\Delta}$ is larger than the computational filter Δ and it is applied to the momentum equations. Germano et al. [17] derived an exact relationship between the subgrid scale stress tensors at the two different filter widths (Germano identity). Substitution of a Smagorinsky form $|S| = \sqrt{2 S_{ij} S_{ij}}$ for the subgrid scale stress into Germano identity, along with some additional assumptions (Lilly, [18]), leads to the expression for the constants

$$C_d = -\frac{1}{2\Delta^2} \frac{\left\langle L_{ij} M_{ij} \right\rangle}{\left\langle M_{ij} M_{ij} \right\rangle} \qquad (1)$$

where the second order tensors L_{ij} and M_{ij} are given as follows :

$$L_{ij} = \tilde{\bar{q}}_i \tilde{\bar{q}}_j - \tilde{\bar{q}}_i \tilde{\bar{q}}_j = -2 C_d \Delta^2 M_{ij}$$

$$M_{ij} = \frac{\tilde{\Delta}^2}{\Delta^2} \tilde{\left|\bar{S}\right|} \tilde{\bar{S}}_{ij} - \tilde{\left|\bar{S}\right|} \tilde{\bar{S}}_{ij}$$

The constant could be positive or negative. The positive values are linked to energy flowing from large to small scales and the negative to energy going from small to large scales (backward energy transfer). The angled brackets in equation (1) denotes averages in the homogeneous direction.

Numerical procedures :

The governing equations are discretized on a staggered mesh in cylindrical coordinates. The simulation is performed by a difference scheme, second order accurate in space and in time, based on a fractional step method. The advancement in time uses a third order Runge Kutta explicit scheme for the non-linear term while the viscous term employs a Crank Nicholson implicit scheme. A uniform computational grid and a periodic boundary conditions are applied to the circumferential and axial directions. In the radial direction, non-uniform meshes specified by a hyperbolic tangent function are employed. On the pipe wall, the usual no-slip boundary condition is applied.

Orlandi and Fatica [10] indicate that the convergence to the statistical steady state is reached when the length is increased to L_z=15R and L_z=20R. In the present study, we performed simulations on a pipe of length L_z=20R using grids 65×39×65. The final statistics are accumulated by spatial averaging in the homogeneous streamwise and circumferential directions and by time-averaging. The runs using the Smagorinsky subgrid scale model and a dynamic subgrid scale model, have been carried out for the non-rotating pipe wall and for the rotating pipe wall at two different rotation rates N=1 and N=2, at Reynolds number of 4900.

RESULTS AND DISCUSSION

In Figure 2, we plot the axial mean velocity profile versus the wall distance y for various rotation numbers (N=0, 1, 2). When the pipe is rotating the streamwise velocity increases near the centre and decreases near the wall. The computational mean velocity profile gradually approaches Poiseuille profile, due to stabilizing effect of the centrifugal force.

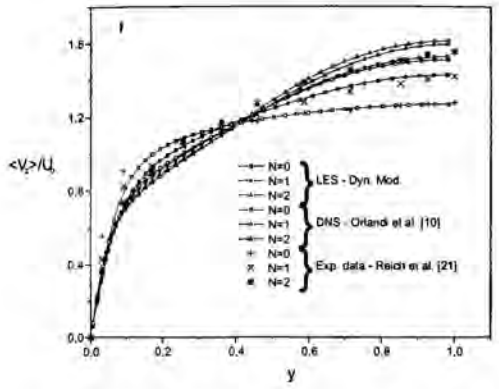

Figure 2. Axial mean velocity normalized by the bulk velocity U_b as function of the wall distance.

This laminarization phenomena is the deformation of the axial velocity profile into a shape similar to the laminar one and the decrease of the friction factor caused by the pipe rotation. This observation has been reported by other investigators (Nishibori K. et al. [19] ; Hirai S. et al. [20]). Rotation has a very marked influence on the suppression of the turbulent motion and on the drag reduction (see experiments by Nishibori et al. [19] ; Reich and Beer [21] ; Imao and Itoh [15]). Orlandi and Fatica [10], using DNS, added a further contribution by relating the drag reduction to the modifications of the near-wall vortical structures.

Figure 3 shows the streamwise velocity profile normalized by the wall shear velocity versus the distance from the wall in wall units y^+. The viscous sublayer is well resolved in the numerical simulations, yielding the linear velocity distribution $V_z^+=y^+$ for $y^+<5$. The agreement is not so good with the log law at larger distances from the wall ($y^+>30$), for both the present LES results and DNS by Eggels et al. [9]. Similar observations have been reported for the DNS by Orlandi and Fatica [10]. This agrees with most experimental and numerical results (Zhang et al. [7] ; Ebstein and Orlandi [11]) which

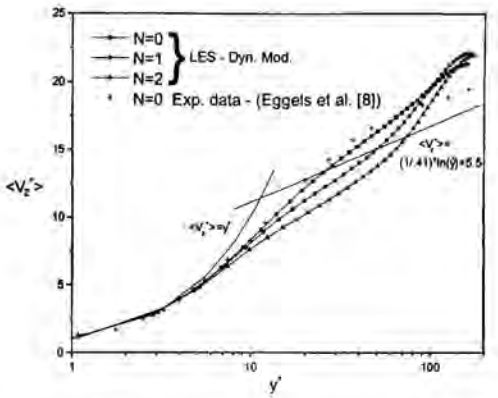

Figure 3. Axial mean velocity normalized on u_τ as function of the distance (in wall units) from the wall.

show that the log-law is not observed in the pipe flow for $Re \leq 9600$ ($Re=D\,U_b/\nu$) in contrast to plane channel flow. One could give a best fit of the logarithmic velocity distribution to the LES pipe flow data. However, theoretically, the log-law is only justified at large Reynolds numbers (Tennekes and Lumley [22]).

The results presented in Figures 2 and 3 are obtained using the dynamic subgrid scale model. Indeed the results obtained using a Smagorinsky model and the results obtained using a dynamical model are almost identical and therefore have not been shown. However, there are some differences between the predicted statistics of turbulence obtained using the Smagorinsky and dynamic models as can be seen in Figures 4-6.

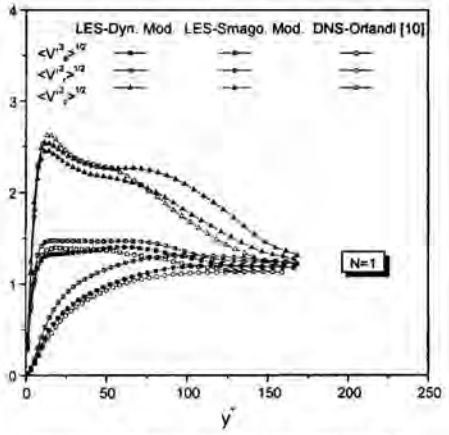

Figure 4. Root-mean-square (rms) profiles of azimuthal, radial and axial velocity components.

Figure 4 illustrates the rms velocity profiles for N=1. It can be observed that the rotation of the wall has large effects on the rms, these effects being more pronounced for the streamwise rms velocity. Similar observations have been reported by

Eggels et al. [8] and by Orlandi and Fatica [10]. In addition, the fluctuating velocity components with both subgrid scale models are quite close to those of the DNS [10]. However, the numerical results obtained using the dynamic subgrid scale model are slightly better. The streamwise rms velocity is presented for various rotation numbers N in Figure 5. Near the wall, the peak is reduced when N increases. For N=2 and N=1, the distributions tend to get the same values. Orlandi and Fatica [10] indicate that this tendency is, in a certain sense, an isotropization of turbulence when the rotation rate increases. Note that the distributions of $\left\langle v'^{2}_{r} \right\rangle^{1/2}$ (or $\left\langle v'^{2}_{\theta} \right\rangle^{1/2}$) also tend to get the same values when the pipe rotates.

The simulated rms with both subgrid scale models are close to those of DNS but the results calculated using the dynamic subgrid scale model indicate a slightly better agreement. It is worth mentioning however, that there is a discrepancy in the simulation using the Smagorinsky model for N=0. In fact, the peak in the axial rms profile is obtained but at somewhat larger distance from the wall (at $y^+ \approx 23$); furthermore, the peak is too broad in this simulation. This deviation can be attributed to the application of the Smagorinsky model. Nevertheless, the simulated rms are in reasonable agreement with the computed ones by Orlandi and Fatica [10].

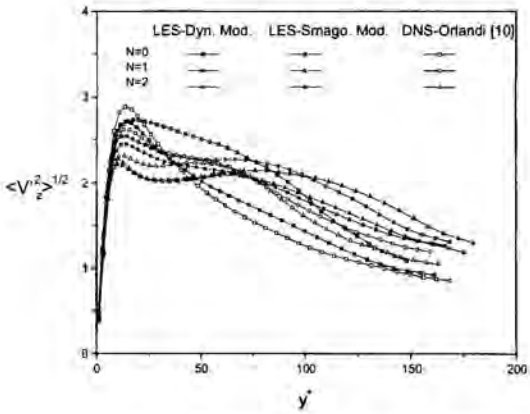

Figure 5. Root-mean-square (rms) profiles of axial velocity.

The Reynolds shear stresses distributions are shown in Figure 6, for N=2. The only non negligible stress in the non-rotating pipe is $\left\langle v'_{r} v'_{z} \right\rangle^{+}$. When the pipe rotates, this stress is reduced and the other two stresses $\left\langle v'_{r} v'_{\theta} \right\rangle^{+}$ and $\left\langle v'_{\theta} v'_{z} \right\rangle^{+}$ increase. From Figure 6, it becomes clear that the three Reynolds stresses are comparable. Near the rotating wall, the high values of $\left\langle v'_{\theta} v'_{z} \right\rangle^{+}$ are related to the tilting of the near wall vortical structures (Orlandi and Fatica [10]). In the core region of the flow, the behaviour of $\left\langle v'_{\theta} v'_{z} \right\rangle^{+}$ is close to linear. The Reynolds stresses computed using a Smagorinsky model are larger than the ones computed using a dynamic model. The Reynolds stresses predicted using a dynamic model are slightly better : they are much closer to the DNS by Orlandi and Fatica [10]. However, one can note that the Reynolds stresses simulated using a dynamic model differ slightly from the ones obtained by Orlandi and Fatica [10], especially for $\left\langle v'_{r} v'_{z} \right\rangle^{+}$ for N=0. This discrepancy is probably due to a lack of convergence. Indeed Orlandi and Fatica [10] indicate that a great number of samples are requested to get fully converged profiles.

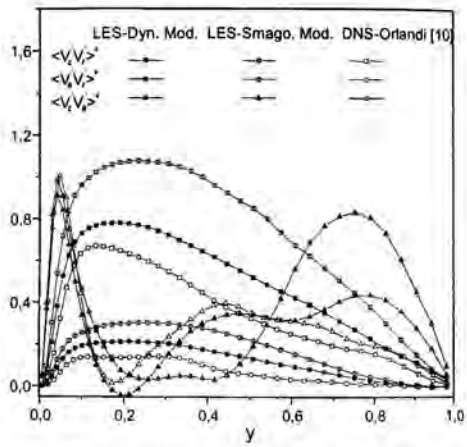

Figure 6. Reynolds shear stress in wall units for N=2.

CONCLUSION

In this study, we have applied the LES technique through the rotating and non-rotating turbulent pipe flow. The simulations were carried out in the same range of rotation numbers and the same Reynolds number considered in the DNS by Orlandi and Fatica [10]. These authors have compared their numerical results with the experimental results by Reich and Beer [21], and DNS by Eggels et al. [8]. The results of the present simulations compare, in general, reasonably well with the DNS by Orlandi and Fatica [10], despite some discrepancies. It is observed that the intensity of turbulence in the rotating pipe decreases gradually with an increase in pipe rotation due to stabilizing effect of the centrifugal force. The dynamic model gives better performance for predicting the fully developed turbulent pipe flow with and without rotation and is more promising than the Smagorinsky model, due to the absence of an external constant.

We can conclude that all phenomena in the rotating and non-rotating turbulent pipe flow can be captured directly by LES. LES is thus a suitable technique to simulate this kind of turbulent flows. This study is our first contribution towards a check of the applicability of the Smagorinsky and the dynamic models to swirling flows. Further refinement of this study and gaining some more experience in the performance of LES technique, may improve the efficiency. One of our objectives is to check the influence of the Reynolds number on the

characteristics of the swirl flow as well as the influence of different subgrid scale models. This will help us in the future, to study the fully developed flow in a straight rotating heated pipe and find the dependence of some properties of the flow, such as the axial and azimuthal stresses and the Nusselt number on the rotation number, Reynolds and Rayleigh numbers. Our final purpose is to use LES to predict the thermo-convective transfers.

ACKNOWLEDGEMENTS

The authors would like to thank Professor Orlandi who furnished different codes (DNS, SGS routines). Furthermore, we would like to thank the referees for their useful comments.

REFERENCES

[1] Laufer, J., 1954, "The structure of turbulence in fully developed pipe flow," NACA Report 1174.

[2] Lawn, C. J., 1971, "The determination of the rate of the dissipation in turbulent pipe flow," J. Fluid Mech., **48**, pp. 477-505.

[3] Itoh, N., 1977, "Non-linear stability of parallel flows with subcritical Reynolds number. part 2. stability of pipe Poiseuille flow to finite axisymmetric disturbances," J. Fluid Mech., **82**, pp. 469-479.

[4] Patera, A. T. and Orszag, S. A., 1981, "Finite-amplitude stability of axisymmetric pipe flow," J. Fluid Mech., **112**, pp. 467-474.

[5] Nikitin, N. V., 1993, "Direct three-dimensional numerical simulation of turbulence and transition in a pipe–Poiseuille flow," In Bulletin of APS, Vol. 38, No. 12, p. 2311.

[6] Unger, F., Eggels, J. G. M., Friedrich, R. and Nieuwstadt, F. T. M., 1993, "On second and higher order statistics in fully-developed turbulent pipe-flow," In Proc. 9th Symp. on Turbulent Shear Flows, Aug.16-18, Kyoto, Japan, pages 2/1/1-2/1/6.

[7] Zhang, Y., Gandhi, A., Tomboulides, A. G. and Orszag, S. A., 1994, "Simulation of pipe flow. Applications of Direct and Large Eddy Simulations to transition and turbulence," AGARD Conf. Proc., 551, pp. 17.1-17.9.

[8] Eggels, J. G. M., Unger, F., Weiss, F., M. H., Westerweel, J., Adrian, R. J., Friedrich, R. and Nieuwstadt, F. T. M., 1994, "Fully developed turbulent pipe flow : a comparison between direct numerical simulation and experiment," J. Fluid Mech., **268**, pp. 175-209.

[9] Eggels, J. G. M., Boersma, B. J. and Nieuwstadt, F. T. M., 1994, "Direct and large eddy simulations of turbulent flow in axially rotating pipe," Preprint.

[10] Orlandi, P. and Fatica, M., 1997, "Direct simulations of turbulent flow in a pipe rotating about its axis," J. Fluid Mech., **143**, pp. 43-72.

[11] Orlandi, P. and Ebstein, D., 2000, "Turbulent budgets in rotating pipes by DNS," International Journal of Heat and Fluid Flow, **21**, pp. 499-505.

[12] Unger, F. and Friedrich, R., 1991, "Large eddy simulation of fully-developed turbulent pipe flow," In Proc. 8th Symp. on Turbulent Shear Flows, Sept. 9-11, Munich, Germany, pp. 19-3-1 – 19-3-6.

[13] Eggels, J. G. M. and Nieuwstadt, F. T. M., 1993, "Large-eddy simulations of turbulent flow in an axially rotating pipe," In Proc. 9th Symp. on Turbulent Shear Flows, Aug.16-18, Kyoto, Japan, pp. 310-313.

[14] Yang, Z. and McGuirk, J.J., 1999, "LES of Rotating Turbulent Pipe Flow with Two Subgrid Scale Models, Proc. of Turbulence and Shear Flow Phenomena - 1, Banerjee, S. and Eaton, J. (eds.) , USA, pp. 863-868.

[15] Imao, S. and Itoh, M., 1996, "Turbulent characteristics of the flow in an axially rotating pipe," Int. J. Heat and Fluid Flow, **17**, pp. 444-451.

[16] Fatica, M., Orlandi, P. and Verzicco, R., 1994, "Direct and Large Eddy Simulations of Round Jets," Voke et al. (eds.), Kluwer Academic Publishers, pp. 49-60.

[17] Germano, M., Piomelli, U. and Cabot, W. H., 1991, "A dynamic subgrid-scale eddy viscosity model," Phys. Fluids A, **3**, pp. 1760-1765.

[18] Lilly, D. K., 1992, "A proposed modification of the Germano subgrid-scale closure method," Phys. Fluids A, **4**, pp. 633-635.

[19] Nishibori, K., Kikuyama, K. and Murakami, M., 1987, "Laminarization of turbulent flow in the inlet region of an axially rotating pipe," JSME Intl J., **30**, pp. 255-262.

[20] Hirai, S., Takagi, T. And Matsumoto, M., 1988, "Prediction of the laminarization phenomena in an axially rotating pipe flow," Trans. ASME J. Fluids Engng., **110**, pp. 424-430.

[21] Reich, G. and Beer, H., 1989, "Fluid flow and heat transfer in axially rotating pipe 1. Effect of rotation on turbulent pipe flow," Intl J. Heat Mass Transfer, **32**, pp. 551-561.

[22] Tennekes, H. and Lumley, J. L., 1972, "A First Course in Turbulence," MIT Press.

[23] Mason, P. J. and Callen, N. S., 1986, "On the magnitude of the subgrid scale eddy coefficient in large-eddy simulations of turbulent channel flow," J. Fluid Mech., **162**, pp. 439-462.

HEFAT2002
1st International Conference on Heat Transfer,
Fluid Mechanics, and Thermodynamics
8-10 April 2002, Kruger Park, South Africa
LJ1

NUMERICAL INVESTIGATIONS OF SLURRY PIPELINE TRANSPORTATION IN FULLY DEVELOPED TURBULENT FLOW

J. Ling, P.V. Skudarnov, C.X. Lin, and M.A. Ebadian
Hemispheric Center for Environmental Technology
Florida International University
10555 West Flagler Street
Miami, FL 33174 USA

ABSTRACT

In this paper, a simplified 3-D two-phase flow algebraic slip mixture model is introduced to obtain the numerical solution in sand-water slurry flow. In order for the study to obtain the precise numerical solution in fully developed turbulent flow, the RNG $K-\varepsilon$ turbulent model was used with the algebraic slip mixture model. An unstructured (block-structured) non-uniform grid was chosen to discretize the entire computation domain, and a control volume finite difference method (CVFDM) was used to solve the governing equations. The mean pressure gradients from the numerical solutions were compared with the authors' experimental data and that in the open literature. The solutions were found to be in good agreement when the slurry mean velocities were higher than the corresponding critical deposition velocity. Moreover, the numerical investigations have illustrated some important slurry flow characteristics, such as volume fraction distributions, slurry density, slurry mean velocity distributions, and slurry mean skin friction coefficient distributions in fully developed turbulent flow, that have never been displayed experimentally.

NOMENCLATURE

$\vec{a}$	secondary phase particle's acceleration, m/s^2
d_p	solid particle diameter, m
E	empirical constant
f_m	mean friction coefficient
I	turbulent intensity level
K	turbulent kinetic energy, m^2/s^2
k_v	von Karman's constant
k_p	turbulent kinetic energy at point p, m^2/s^2
L	pipeline length, m
Pr_t	turbulent Prandtl number for energy
S	modulus of the mean rate-of-strain tensor
V	slurry mean velocity, m/s
$\vec{u}_m$	mass-averaged velocity, m/s
$\vec{u}_{Dk}$	drift velocity, m/s
$\vec{u}_p$	mean velocity of the fluid at point p, m/s
$\vec{v}_{qp}$	slip velocity, m/s
y_p	distance from point p to the wall, m
ΔB	roughness function
$\Delta p/\Delta L$	mean pressure gradient of the slurry flow, P$_w$/m

Greek Symbols

α_k	volume fraction of solids
β	coefficient of thermal expansion
ρ_m	mixture density, kg/m^3
ρ_s	solid particle density, kg/m^3
ρ_w	water density, kg/m^3
ε	dissipation rate of turbulent kinetic energy, m^2/s^3
μ_m	viscosity of the mixture, kg/m.s
τ_{pq}	particulate relaxation time, s

Subscripts

i, j, k	general spatial indices
m	mixture
s, w, z	silica sand, water, and zircon sand

1. INTRODUCTION

Slurry pipeline transportation is a popular mode of transportation in various industries. It has several advantages, such as its friendliness to the environment and relatively low operation and maintenance costs. In general, slurry transportation is divided into three major flow patterns: 1) pseudohomogeneous flow (or homogeneous flow) and

heterogeneous flow, 2) heterogeneous and sliding bed flow (or moving bed flow), and 3) saltation and stationary bed flow (Doron and Barnea 1996). Pseudohomogeneous flow is a slurry flow pattern in which the slurry flow is at a very high velocity and all solid particles are distributed nearly uniformly across the pipe cross-section. With a decrease in slurry flow rate, the heterogeneous flow pattern occurs when there is a concentration gradient in a direction perpendicular to the pipe axis, with more particles transported at the lower part of the pipe cross-section, as is the case in most practical applications. As the slurry flow rate is reduced further, the solid particles accumulate at the bottom of the pipe and form a moving bed layer, while the upper part of the pipe cross-section is still occupied by a heterogeneous mixture. When the slurry flow rate is too low to suspend all solid particles, a stationary bed layer at the bottom of the pipe cross-section is observed. This is the saltation and stationary bed flow (Vocaldo and Charles 1972; Parzonka et al. 1981). The slurry velocity associated with the formation of a stationary bed layer is called the critical deposition velocity. A bed layer in the slurry flow is unstable and dangerous during the operation of pipeline transportation. It probably enhances pipe wear and causes plugging or blockage of the pipeline. As a result, it should be avoided in design and operation of the pipeline transportation system.

Slurry flow is very complex. In a survey of the open literature on slurry transport investigations, it was found that most laboratory investigations were made to determine the pressure gradients and critical deposition velocities of slurry flows. Doron et al. (1987) and Doron and Barnea (1993) proposed two-layer and three-layer models of the slurry flow, and Wilson and Pugh (1988) put forward a dispersive-force modeling in heterogeneous slurry flow, but these models were derived based on single-species slurry flow and can not determine the slurry density and particle distributions or the slip velocity between the liquid and solid particles. Nassehi and Khan (1992) provided a numerical method for the determination of slip characteristics between the layers of a two-layer slurry flow, but no comparisons of experimental results and numerical solutions were reported. In this paper, a simplified two-phase flow algebraic slip mixture model (Manninen et al. 1996) is introduced to obtain the numerical solution in sand-water slurry flow. A control volume finite difference method (CVFDM) is used to solve the governing equations, and an unstructured (block-structured) non-uniform grid is chosen to discretize the entire computation domain.

2. CALCULATION MODELS

2.1 Governing Equations

The algebraic slip mixture (ASM) model can model two-phase flow (fluid or particulate) by solving the momentum equation and continuity equation for the mixture, the volume fraction equation for the secondary phase, and an algebraic expression for the relative velocity. The continuity equation for the mixture is

$$\frac{\partial}{\partial t}(\rho_m)+\frac{\partial}{\partial x_i}(\rho_m u_{mi})=0 \qquad (1)$$

The momentum equation for the mixture can be expressed as

$$\frac{\partial}{\partial t}\rho_m u_{mj}+\frac{\partial}{\partial x_i}\rho_m u_{mi}u_{mj}=-\frac{\partial p}{\partial x_j}+\frac{\partial}{\partial x_i}\mu_m\left(\frac{\partial u_{mj}}{\partial x_i}+\frac{\partial u_{mi}}{\partial x_j}\right)+\rho_m g_j+F_j$$

$$+\frac{\partial}{\partial x_i}\sum_{k=1}^{n}\alpha_k\rho_k u_{Dk,i}u_{Dk,j} \qquad (2)$$

where n is the number of phases, F is the body force, α_k is the volume fraction of solids, ρ_m is the mixture density, and μ_m is the viscosity of the mixture, which are expressed as

$$\rho_m=\sum_{k=1}^{n}\alpha_k\rho_k \quad \text{and} \quad \mu_m=\sum_{k=1}^{n}\alpha_k\mu_k \qquad (3)$$

$\vec{u}_m$ and $\vec{u}_{Dk}$ are mass-averaged velocity and drift velocities, which are expressed as

$$\vec{u}_m=\frac{\sum_{k=1}^{n}\alpha_k\rho_k\vec{u}_k}{\rho_m} \quad \text{and} \quad \vec{u}_{Dk}=\vec{u}_k-\vec{u}_m \qquad (4)$$

The slip velocity is defined as the velocity of the secondary phase (p) relative to the primary phase (q) velocity:

$$\vec{v}_{qp}=\vec{u}_p-\vec{u}_q \qquad (5)$$

The drift velocity and slip velocity are connected by the following expression:

$$\vec{u}_{Dp}=\vec{v}_{qp}-\sum_{i=1}^{n}\frac{\alpha_i\rho_i}{\rho_m}\vec{v}_{qi} \qquad (6)$$

The basic assumption in the algebraic slip mixture model is that, to prescribe an algebraic relation for the relative velocity, a local equilibrium between the phases should be reached over short spatial-length scales. The form of the slip velocity is

$$\vec{v}_{qp}=\tau_{qp}\vec{a}=\frac{\rho_p d_p^2}{18\mu_q}\vec{a} \qquad (7)$$

where $\vec{a}$ is the secondary phase particle's acceleration, τ_{pq} is the particulate relaxation time, and d_p is the particle diameter.

The volume fraction equation for the secondary phase is

$$\frac{\partial}{\partial t}(\alpha_p\rho_p)+\frac{\partial}{\partial x_i}(\alpha_p\rho_p u_{mi})=-\frac{\partial}{\partial x_i}(\alpha_p\rho_p u_{Dp,i}) \qquad (8)$$

This algebraic slip mixture model can be applied in laminar and turbulent two-phase flows. In practice, since the slurry transportation is in fully developed turbulent flow, the RNG $K-\varepsilon$ turbulent model is used with the algebraic slip mixture model. The turbulent kinetic energy in the RNG $K-\varepsilon$ turbulent model is

$$\frac{\partial}{\partial t}(\rho_m k)+\frac{\partial}{\partial x_i}(\rho_m u_{mi}k)=\frac{\partial}{\partial x_i}[(a_k\mu_m\frac{\partial k}{\partial x_i})]+\mu_t S^2+\beta g_i\frac{\mu_t}{\mathrm{Pr}_t}\frac{\partial T}{\partial x_i}-\rho_m\varepsilon \qquad (9)$$

Dissipation rate of the turbulent kinetic energy is

$$\frac{\partial}{\partial t}(\rho_m\varepsilon)+\frac{\partial}{\partial x_i}(\rho_m u_{mi}\varepsilon)=\frac{\partial}{\partial x_i}[(a_\varepsilon\mu_m\frac{\partial\varepsilon}{\partial x_i})]+C_{1\varepsilon}\frac{\varepsilon}{k}\mu_t S^2-C_{2\varepsilon}\rho_m\frac{\varepsilon^2}{k}-R \qquad (10)$$

where the coefficients a_k and a_ε are the inverse effect Prandtl numbers for k and ε, respectively. In the high-Reynolds-

number limit, $a_k = a_\varepsilon \cong 1.393$. $C_{1\varepsilon}$ and $C_{2\varepsilon}$ are equal to 1.42 and 1.68. β and Pr_t are the coefficients of thermal expansion and turbulent Prandtl number for energy. S is the modulus of the mean rate-of-strain tensor, S_{ij}, which is defined as

$$S = \sqrt{2S_{ij}S_{ij}} \quad \text{and} \quad S_{ij} = \frac{1}{2}\left(\frac{\partial u_i}{\partial x_j} + \frac{\partial u_j}{\partial x_i}\right) \tag{11}$$

R in Eq. (10) was expressed as

$$R = \frac{C_\mu \rho_m \eta^3 (1 - \eta/\eta_0)}{1 + \zeta \eta^3} \cdot \frac{\varepsilon^2}{k} \tag{12}$$

where $\eta = S \cdot k/\varepsilon$, $\eta_0 \approx 4.38$, $\zeta = 0.012$, and $C_\mu = 0.085$.

2.2 Boundary Conditions

Non-slip boundary condition is imposed on the walls, and heat transfer is not considered in the entire computation domain. Besides, in the near-wall zone, the standard wall function proposed by Lauder and Spalding (1974) was chosen for this paper due to its wide application in industrial flows. When the mesh is such that $y^* \le 11.225$ at the wall-adjacent cells, the viscous force is dominant in the sublayer. The laminar stress-strain relationship can be applied

$$u^* = y^* \tag{13}$$

$$y^* = \frac{\rho_m C_\mu^{\frac{1}{4}} k_p^{\frac{1}{2}} y_p}{\mu_m} \tag{14}$$

The logarithmic law for the mean velocity is known to be valid for $y^* > 11.225$ (Fluent Inc. 1996). It can be expressed as

$$u^* = \frac{1}{k}\ln(Ey^*) \tag{15}$$

where k is von Karman's constant, C_μ is turbulence model constant, and k_p and y_p are the turbulent kinetic energy at point p and distance from point p to the wall, respectively.

To simplify the simulations, the mean velocity inlet boundary condition and pressure outlet boundary condition are imposed on the inlet and outlet of slurry pipeline:

$$u_{x,inlet} = \text{const},\ u_{y,inlet} = u_{z,inlet} = 0, \text{ and } p_{outlet} = \text{const} \tag{16}$$

The turbulence intensity level, I, is set to 4% for the intermediate velocities in slurry flows.

3. NUMERICAL COMPUTATION

3.1 Physical Problems and Grid System

The geometry and physical problems studied are as follow:

Horizontal straight pipeline length, L=1.4 m; inner diameter of the pipe, d=0.0221 m; range of the volume fraction of solids, α_s, is 10% to 20%; range of mean velocity of the slurry flow is 1 m/s to 3 m/s; the densities of silica sand and zircon sand are 2380 kg/m^3 and 4223 kg/m^3; mean particle diameter, d_p, is 0.00011 m.

The length of the computation domain, $x/d \ge 50$, was based on the suggestions from Wasp (1979) and Brown (1991) to ensure that fully developed flow results could be obtained in the pipeline computation domain. A multi-block unstructured non-uniform grid system with hexahedral elements was used to discretize the computation domain, as shown in Fig. 1. This unstructured grid system has five blocks to form the entire computation pipeline. The distribution of the grid on the circumference of computation pipeline is uniform, and each hexahedral element in the grid system contains 27 nodes. The grid independent study was made to select the optimum grid distribution in this investigation, as shown in Table 1. From Table 1, V was the mean velocity of the slurry flow, and $\Delta p/\Delta L$ and f_m were the mean pressure gradient of the slurry flow and mean friction coefficient in fully developed turbulent flow, respectively. f_m could be obtained from

$$f_m = \frac{1}{2\pi}\int_0^{2\pi} f_\theta d\theta \tag{17}$$

where $f_\theta = \dfrac{\tau_w}{\frac{1}{2}\rho_m V_m^2}$

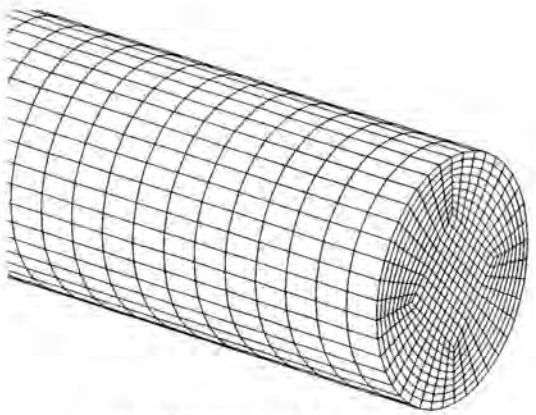

Fig. 1 Unstructured grid of the slurry pipeline.

Table 1
Grid independent test (V =2 m/s, $57 \le x/d \le 61$, α_s =0.189, d_p=0.00011 m, silica sand-water slurry flow).

Cross-sectional×axial	224×300	340×300	460×300	500×300	460×400	460×500
Total Cells	67,200	108,000	138,000	150,000	184,000	230,000
$\Delta p/\Delta L$ (Pa/m)	2,220	2,205	2,184	2,177	2,094	2,154
f_m	2.53	2.463	2.325	2.325	2.335	2.335

The grid distribution, 460×400, shown in Table 1 could ensure a satisfactory solution for the slurry flow presented in this paper.

3.2 Numerical Method

In the numerical investigation of the slurry transportation, all governing equations, wall boundary conditions, and inlet and outlet boundary conditions were solved in a Cartesian coordinate system by the CFD solver, FLUENT 5, which used a control volume finite difference method (CVFDM). Heat transfer was neglected, and the slurry flows were steady-state in this investigation. At the same time, the slurry flows were in pseudohomogeneous flow (or homogeneous flow), and heterogeneous flow and sliding bed flow (or moving bed flow). The second-order upwind scheme was selected as the discretization scheme in the governing equations. The SIMPLEC algorithm from Dormaal and Raithby (1984) was used to resolve the coupling between the velocity and the pressure. To avoid the divergence, the under-relaxation technique was applied in all dependent variables. In the investigation, the under-relation factor for the pressure, p, was 0.2 and 0.3; that for the velocity components was 0.5-0.7; and those for the turbulence kinetic energy and turbulence dissipation rate were 0.6-0.8. The segregated solver was adopted to solve the governing equations sequentially. In the segregated solution method, each discrete governing equation was linearized implicitly with respect to that equation's dependent variable. A point implicit (Gauss-Seidel) linear equation solver was used in conjunction with an algebraic multi-grid (AMG) method to solve the resultant scalar system of equations for the dependent variable in each cell. The numerical computation was considered converged when the residual summed over all the computational nodes at n^{th} iteration, R_ϕ^n, satisfied the following criterion:

$$\frac{R_\phi^n}{R_\phi^m} \le 10^{-4} \qquad (18)$$

where R_ϕ^m is the maximum residual value of ϕ variable after m iterations.

All the numerical computations in this paper were based on the grid distribution, 460×400, and carried out in an SGI Original 2000 at HCET.

4. RESULTS AND DISCUSSIONS

4.1 Comparisons of Numerical and Experimental Data

The slurry mean pressure gradient is an important parameter in slurry transportation and pipeline design. To verify and check the numerical results from the algebraic slip mixture model, a lab-scale flow loop has been constructed at HCET, and extensive experiments for the silica sand-water and zircon sand-water slurry flows have been made (Skudarnov et al. 2001). These experimental data from HCET and other experimental data from Newitt et al. (1955) are compared with the numerical results, as shown in Fig. 2.

Figure 2(a) shows the comparison of the numerical results with the experimental data from Skudarnov et al. at HCET and Newitt et al. in silica sand-water slurry flow with the same pipeline geometry, volume fraction, particle size, and particle density. Figure 2(b) illustrates the comparison of the numerical results with the experimental data from Skudarnov et al. in zircon sand-water slurry flow. Based on the experimental investigations made by Skudarnov et al., the critical deposition velocity shown in Figs. 2(a) and (b) are 0.97 m/s and 1.58 m/s, respectively.

It is clear that in Fig. 2(a) all slurry mean velocities for numerical results and experimental data are higher than the critical deposition velocity, and the numerical results are still in good agreement with the experimental data although the numerical results from the algebraic slip mixture model result in a little under-prediction. From Fig. 2(b), the numerical results are still in good agreement with the experimental data, and a little under-prediction from the numerical results exists when the mean velocities of the zircon sand-water slurry flow in the numerical and experimental investigations are higher than the critical deposition velocity. A big discrepancy between the numerical results and experimental data takes place when the mean velocities of slurry flow in the numerical and experimental investigations are lower than the critical deposition velocity, and the discrepancy would be further increased with a decrease in the slurry mean velocity.

Because the available pipeline flow area would be reduced and friction loss would be increased, the pressure gradient in the slurry flow would be increased if the slurry velocity is lower than the corresponding critical deposition velocity and a stationary bed of solids is formed in experiments. However, the algebraic slip mixture model cannot change its available flow area if the slurry flow velocity is lower than the corresponding critical deposition velocity. As a result, it is evident that the algebraic slip mixture model can provide a little under-predicted pressure gradient only as the slurry mean velocity is higher than the critical deposition velocity, and the algebraic slip mixture model would result in a larger deviation if the slurry mean velocity is lower than the critical deposition velocity.

The density distribution of the silica sand–water slurry flow along the vertical centerline is shown in Fig. 4. Figure 4(a) shows the density distribution in the cross-sectional area of the pipeline in V=2 m/s. Figure 4(b) illustrates the density distribution along the vertical centerline in V=2 and 3 m/s. Like the volume fraction of water, on the top of the pipeline, the slurry density is close to the density of water, 998.2 kg/m^3.

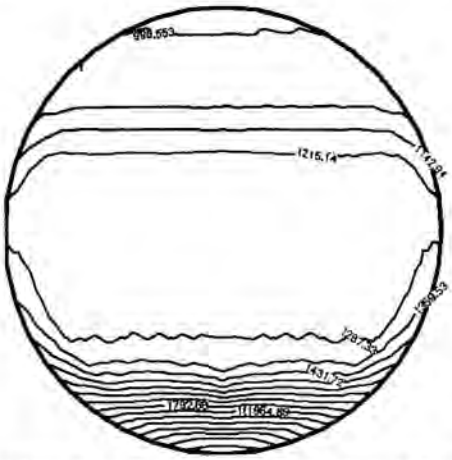

(a) Density distribution at the cross-sectional area, V=2 m/s

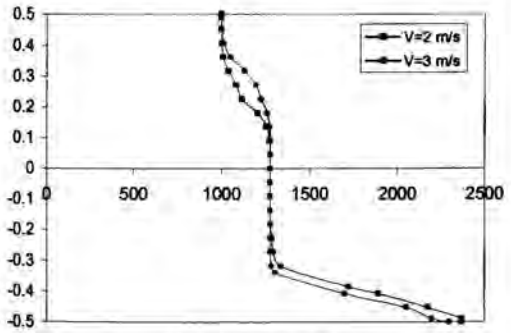

(b) Density distribution along the vertical centerline

Fig. 4 Mean density distribution of the silica sand-water slurry flow (ρ_s=2381 kg/m^3, ρ_w=998.2 kg/m^3, α_s=20%, d=0.0221m, d_p=110 microns).

In the lower part of the pipeline, the slurry density is approaching the density of silica sand, 2381 kg/m^3. In the central part of the pipeline, the slurry density is kept a constant, which is roughly equal to its mean density. It should be pointed out that the slurry flow region in the central part with the constant density would be increased as the slurry mean velocity is increased, as shown in Fig. 4(b).

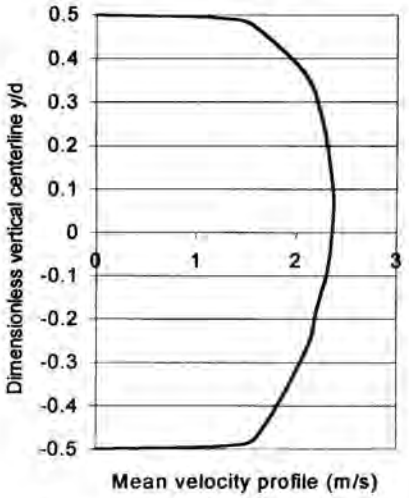

(a) Velocity profile along the vertical centerline

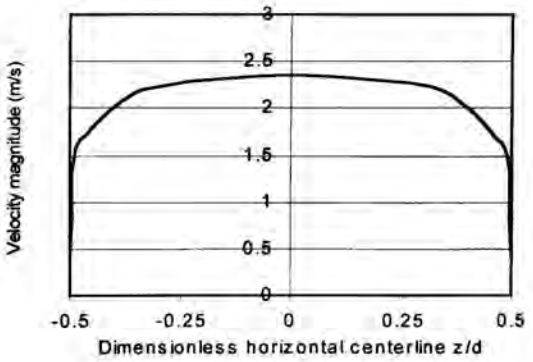

(b) Velocity profile along the horizontal centerline

Fig. 5 Mean velocity profiles of the silica sand-water slurry along the vertical and horizontal centerlines in fully developed turbulent flow (ρ_s=2381 kg/m^3, α_s=20%, d=0.0221m, d_p=110 microns, V=2 m/s).

4.3 Slurry Mean Velocity Distributions and Skin Friction Factors

The velocity distribution of the slurry flow in the pipeline is affected by the volume fraction, density distribution, mean velocity, and viscosity of the slurry flow. As a result, the velocity profile of the slurry flow along the vertical centerline is totally different from those of laminar and turbulent flows. In general, the velocity profiles in the laminar and turbulent flows are symmetric, and liquid densities and viscosities are kept as constants in the vertical direction. However, in the

slurry flow, since the density of solid particles is usually bigger than that of liquid, the density, viscosity, and volume fraction of the slurry flow in the lower part of the cross-sectional area of the pipeline should be larger than those in the upper part. Figure 5(a) shows the mean velocity profile along the vertical centerline in the silica sand-water slurry flow when V=2 m/s, α_s=20%, ρ_s=2381 kg/m^3, ρ_w=998 kg/m^3, d=0.0221m, and d_p=110 microns. As shown in Fig. 5(a), the slurry mean velocity near the wall drops down sharply due to the strong viscous shear stress in the turbulent boundary layer. In the outer flow, the mean velocity profile along the vertical centerline in the slurry flow is asymmetric due to the density and viscosity distributions in the slurry flow. The slurry mean velocity in the upper part of the vertical centerline is larger than that in the lower part, and the slurry maximum velocity appears at the upper part of the pipeline not at the centerline since the density and viscosity distributions of the slurry flow in the upper part are smaller than that in the lower part. Figure 5(b) shows the slurry velocity profile along the horizontal centerline. The slurry velocity profile is symmetric since the density and viscosity of the slurry flow along the horizontal centerline are symmetric.

The slurry mean skin friction factors from the pipeline inlet to the exit are shown in Fig. 6. All slurry mean skin friction factors would drop sharply from the pipeline inlet, then be raised gradually. At $x/d \approx 50$, the slurry mean skin friction factors approach stable values. Figure 6 indicates that the slurry mean skin friction factor would be kept constant in the fully developed turbulent flow. At the same time, Fig. 6 shows that the slurry mean skin friction factor increases with the slurry mean velocity and solid particle density in increase. This means that a higher slurry mean velocity and bigger solid particle density would result in a bigger flow loss and slurry mean pressure gradient in slurry pipeline transportation.

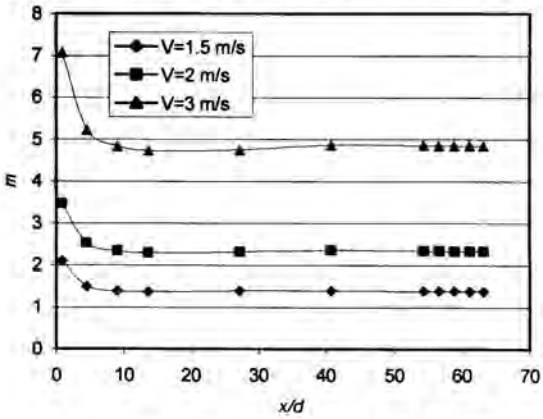

(a) Silica sand-water slurry, ρ_s=2381 kg/m, α_s=20%

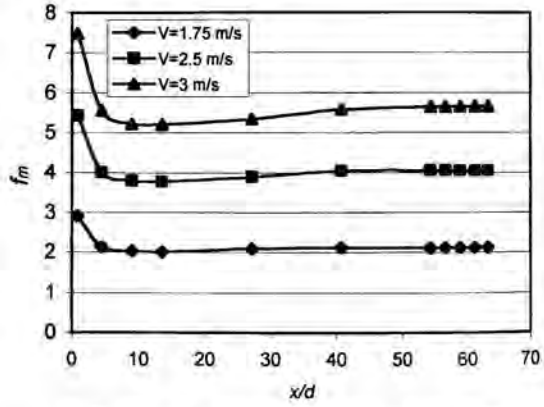

(b) Zircon sand-water slurry, ρ_s=4223 kg/m, α_s=10%

Fig. 6 Slurry mean skin friction coefficient distributions from the entrance to fully developed region (d=0.0221m, d_p=110 microns).

5. CONCLUSIONS

The numerical investigation in slurry flow is valuable and interesting research. It can provide much information that cannot be obtained in experiments. Based on the ranges and conditions of the numerical investigation, the following conclusions can be made:

1. The algebraic slip mixture model can provide a good prediction for slurry flow in fully developed turbulent flow, as the slurry mean velocity is higher than the corresponding critical deposition velocity. The numerical results for the pressure gradients are in good agreement with the experimental data.
2. The volume fraction and density distribution of silica sand-water slurry flow along the horizontal centerline is symmetric, while the volume fractions and density of slurry flow would have a sharp change along the vertical centerline. In heterogeneous and sliding bed flow (or moving bed flow), most of the water would flow on the top of the pipeline, while most of the silica sand would be transported in the lower part of the pipeline. In the central part of the pipeline, the slurry volume fraction and density are kept constants.
3. Mean velocity profile along the horizontal centerline in the slurry flow is symmetric, but that in the vertical centerline is asymmetric. The slurry mean velocity in the upper part of the vertical centerline is larger than that in the lower part since the slurry density and volume fraction distribution in the upper part is smaller than that in the lower part. Slurry mean skin friction factor would be kept as a constant in the fully developed turbulent flow, and it increases as the slurry mean velocity and solid particle density increase.

ACKNOWLEDGMENTS

The authors gratefully acknowledge the financial support of the National Science Foundation (NSF) under Award No. CMS-0085645.

REFERENCES

Dormaal, J., and Raithby, G.D., 1984, "Enhancement of the SIMPLE Method for Predicting Incompressible Flow Problems," *J. Numerical Heat Transfer*, Vol. 7, pp.147-158.

Doron, P., and Barnea, D., 1996, "Flow Pattern Maps for Solid-Liquid Flow in Pipes," *Int. J. Multiphase Flow*, Vol. 22, pp. 273-283.

Doron, P., and Barnea, D., 1993, "A Three-Layer Model for Solid-Liquid Flow in Horizontal Pipes," *Int. J. Multiphase Flow*, Vol. 19, pp. 1029-1043.

Doron, P., Granica, D., and Barnea, D., 1987, "Slurry Flow in Horizontal Pipes-Experimental and Modeling," *Int. J. Multiphase Flow*, Vol. 13, No. 4, pp. 535-547.

Fluent Inc., 1996, *FLUENT 5: User's Guide*, Vols. 1-4.

Launder, B.E., and Spalding, D.B., 1974, "The Numerical Computation of Turbulent Flows," *Computer Methods in Applied Mechanics and Engineering*, Vol. 3, pp. 269-289.

Manninen, M., Taivassalo, V., and Kallio, S., 1996, "On the Mixture Model for Multiphase Flow," *VIT Publications*, Technical Research Center of Finland.

Nassehi, V., and Khan, A. R., 1992, "A Numerical Method for the Determination of Slip Characteristics Between the Layers of a Two-Layer Slurry Flow," *Int. J. for Numerical Method in Fluids*, Vol. 14, pp. 167-173.

Newitt, D.M., Richardson, J.F., Abbot, M., and Turtle, R.B., 1955, "Hydraulic Conveying of Solids in Horizontal Pipes," *Trans. Inst. Chem. Engrs.*, Vol. 33, No. 2, pp. 93-113.

Parzonka, W., Kenchington, J. M., and Charles, M. E., 1981, "Hydrotransport of Solids in Horizontal Pipes: Effects of Solids Concentration and Particle Size on the Deposit Velocity," *Can. J. Chem. Engng*, Vol. 59, pp. 291-296.

Skudarnov, P.V., Kang, H.J., Lin, C.X., Ebadian, M.A., Gibbons, P.W., Erian, F.F., and Rinker, M., 2001, "Experimental Investigation of Single- and Double-Species Slurry Transportation in a Horizontal Pipeline," *Proc. ANS 9th International Topical Meeting on Robotics and Remote Systems*.

Vocaldo, J. J., and Charles, M. E., 1972, "Prediction of pressure gradient for the horizontal turbulent flow of slurries," *Proc. 2nd Int. Conf. on the Hydraulic Transport of Solids in Pipes, Coventry, England, Paper No. C1*, pp. 1-12.

HEFAT2002
1st International Conference on Heat Transfer, Fluid Mechanics, and Thermodynamics
8 - 10 April 2002, Kruger Park, South Africa
VS1

MIXING EFFICIENCY OF TURBULENCE IN ENVIRONMENTAL FLOWS

S K Venayagamoorthy[1], D D Stretch[1], J W Rottman[2, 3], and K K Nomura[2]

[1]School of Civil Engineering, University of Natal, Durban 4041, South Africa
[2]Department of Mechanical & Aerospace Engineering, University of California, San Diego, CA 92093-0411, USA
[3]Science Applications International Corporation, San Diego, CA 92121, USA
venayagamoorthys@nu.ac.za, stretchd@nu.ac.za, jrottman@mae.ucsd.edu, knomura@mae.ucsd.edu

ABSTRACT

Mixing efficiency is important for the parameterization of mixing processes that occur in environmental flows. In this study, direct numerical simulations (DNS) of transient turbulent mixing events in a stably stratified fluid have been used to investigate mixing efficiency as a function of the initial turbulence Richardson number $Ri = N^2L^2/u^2$, where N is the buoyancy frequency, L is the turbulence length scale, and u the turbulence velocity scale. Comparison of the DNS results with grid turbulence experiments has been carried out. There is broad qualitative agreement between the experimental and DNS results. However the experiments suggest a maximum mixing efficiency of about 6% while DNS gives values about five times higher. Reasons for this discrepancy are discussed: we conclude that the most likely explanation is inaccuracy in determining the initial turbulence energy input for the experiments. The flow structures that evolve in these flows are also reported. We find that as the stratification increases the turbulence develops from randomly shaped isotropic patches to randomly distributed pancake-shaped structures.

1. INTRODUCTION

The mixing efficiency of stably stratified flows is defined as the proportion of the turbulent kinetic energy that goes into increasing the potential energy of the fluid by irreversible mixing. An understanding of how the mixing efficiency is affected by stratification is important for the parameterization of mixing in environmental flows, e.g. in modelling pollution dispersion in the atmosphere and in climate or weather modelling. The mixing efficiency of grid turbulence in a uniformly stratified fluid has been measured in the laboratory by Britter (1985), Rottman & Britter (1986), and Rehmann & Koseff (2000). The experiments involved towing a bi-planar grid through water that was uniformly stratified using salinity or temperature variations. The mixing efficiency in these experiments was measured as a function of the grid Richardson number $Ri_G = (NM/U)^2$, where N is the buoyancy frequency of the fluid, M is the grid mesh length, and U is the grid towing speed. The mixing efficiency was measured as the ratio of the change in potential energy of the fluid to the amount of work done towing the grid through the tank. The Reynolds numbers Re for these experiments, based on the tow speed and the grid mesh length, range from 1,000 to 10,000. The Schmidt number Sc is 700 for the salt-stratified experiments and the Prandtl number Pr is 7 for the heat-stratified experiments.

The results of the experiments are fairly consistent:

(a) There appears to be no strong dependence on the molecular diffusivity (although there are some uncertainties about this conclusion)
(b) For $Ri < 0.1$, the mixing efficiency increases approximately linearly with Ri
(c) For $0.1 < Ri < 1$, the mixing efficiency increases approximately like $Ri^{1/2}$
(d) For larger Ri, the mixing efficiency appears to approach a constant value of about 6%.

Since none of the laboratory experiments can achieve values of Ri much greater than about 10, there remains some uncertainty about the strongly stable limit. Various other types of experiments have suggested that mixing efficiency may decrease for large Ri (e.g. Linden, 1979).

In the research described here, direct numerical simulations (DNS) of transient turbulent mixing events are carried out in order to study the detailed physics of mixing. The results are used to determine the mixing efficiency as a function of the initial turbulence Richardson number for comparison with the grid-turbulence experiments.

2. DIRECT NUMERICAL SIMULATIONS

Our numerical experiments involved direct numerical simulation (DNS) of a homogeneous, transient (i.e. decaying) turbulent flow field in the presence of a uniform background density gradient. The DNS scheme we used, described in detail by Riley et al (1981), computes fully resolved solutions of the 3-D Navier

Stokes equations with the Boussinesq approximation. The solutions were computed in a 2π–periodic box of 32^3, 64^3 or 128^3 grid points. The strength of the stable stratification is characterized by an initial Richardson number, $Ri = (NL/u)^2$, where N is the (constant) Brunt Vaisala frequency, L is the initial turbulence length scale, and u the initial turbulence velocity scale. The range of values covered in our simulations was $0 < Ri < 1000$. The initial Reynolds numbers $Re = uL/\nu$ varied in the range $100 < Re < 400$. Prandtl (or Schmidt) numbers used for the simulations were in the range $0.1 < Pr < 2.0$ but with most of the results generated using $Pr = 0.5$. These values of Pr are substantially smaller than those for the laboratory experiments because we are not able to resolve the scalar field at larger Pr.

2.1 Initialization of the Flow

The numerical simulations were initialized in the usual way with a solenoidal, Gaussian, isotropic velocity field with an energy spectrum given by (see e.g. Townsend 1976):

$$E(k) = Cu^2 L^5 k^4 \exp[-\tfrac{1}{2}k^2 L^2] \qquad (1)$$

where C is a constant scaling factor. The initial density fluctuations (and hence the initial turbulent potential energy) were set to zero. Experimental measurements indicate that the potential energy close to the grid (say at $x/M = 10$) is typically a very small fraction (< 1%) of the kinetic energy (Keller & Van Atta, 2000). The above initialisation scheme is thus a reasonable model for the initial state of stratified grid-generated turbulence.

2.2 Energetics and mixing efficiency

Our interest is in the energetics and mixing characteristics integrated over the full duration of these transient turbulent flows. In particular, we wanted to answer the following question: "Integrated over the duration of the turbulence decay, how much of the initial kinetic energy goes into increasing the potential energy of the fluid as compared to the fraction that is dissipated directly into heat"? The time-integrated contributions of buoyancy flux, kinetic energy and potential energy dissipation rates were therefore computed for each of the simulations in order to determine the ultimate fate of the initial energy supplied to the flow. The energetics of homogenous stably stratified turbulent flows are described by equations (2) and (3).

$$\frac{d}{dt}(KE) = -b - \varepsilon_{KE} \qquad (2)$$

$$\frac{d}{dt}(PE) = +b - \varepsilon_{PE} \qquad (3)$$

where the buoyancy flux $b = (-g/\rho_0)\,\overline{\rho w}$, the kinetic energy $KE = \tfrac{1}{2}(\overline{u^2} + \overline{v^2} + \overline{w^2})$, the potential energy $PE = \tfrac{1}{2}g/\rho_0(-\partial\overline{\rho}/\partial z)^{-1}\,\overline{\rho^2}$, and ε_{KE}, ε_{PE} are the kinetic energy and potential energy dissipation rates respectively. The mixing efficiency is defined by

$$\eta = \int_0^t b\,dt \Big/ \big(KE(0) - KE(t)\big) \qquad (4)$$

where time $t = 10L/u$

3. RESULTS

The results of the numerical experiments are summarized in figure 1, which shows the variation of the mixing efficiency as a function of the Richardson number Ri. The mixing efficiency at low Richardson numbers Ri is small, e.g. 0.3 percent for $Ri = 0.004$. This can be attributed to the turbulence vigorously mixing fluid of

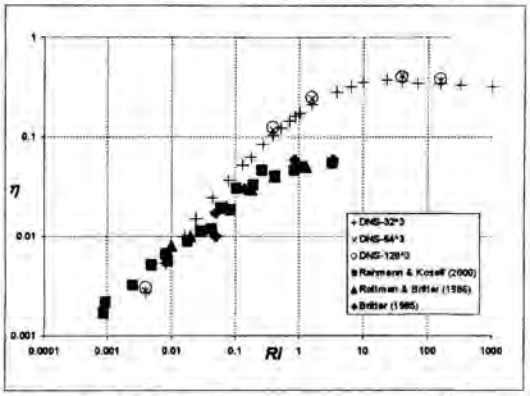

Figure 1: Mixing efficiency results from DNS and experiments.

nearly constant density so that only small changes in potential energy are produced and most of the kinetic energy is dissipated directly into heat. The peak mixing efficiency is about 37% and occurs at $Ri = 23$. Under more strongly stratified conditions (higher Ri), the mixing efficiency seems to approach a constant value of approximately 30%. The small decrease in mixing efficiency as the strength of stratification increases seems to be associated with oscillations in buoyancy flux (see figure 2). These oscillations are due to buoyancy restoring forces that drive fluid elements back towards their equilibrium levels in the density gradient with an associated negative buoyancy flux. These negative values contribute to reducing the time integrated buoyancy flux and hence the mixing efficiency.

Figure 1 also shows experimental results of mixing efficiencies by Britter (1985), Rottman & Britter (1986) and Rehmann & Koseff (2000) superimposed with the DNS results of this investigation. We assume that $Ri_G = Ri$ however we note that the definitions used for Ri are different for the DNS and laboratory experiments. It can thus be argued that the two data sets could be shifted along the x-axis to allow for this.

The general trend in the mixing efficiency with increasing stratification is qualitatively similar for the experiments and the DNS. There are however significant quantitative differences: in particular the maximum mixing efficiency measured in the grid experiments was only 6%, compared to values of 30% or more for the DNS results.

Neither the DNS nor experimental results show significant changes in mixing efficiency with varying

Reynolds and Prandtl numbers for $Ri < 10$, although the parameter ranges investigated in each case were small.

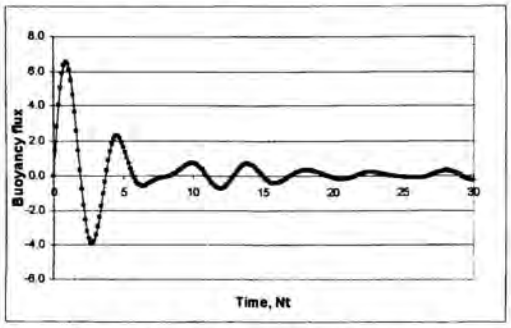

Figure 2: A plot of the vertical buoyancy flux as a function of time (non-dimensionalised by the buoyancy frequency) for Ri =158

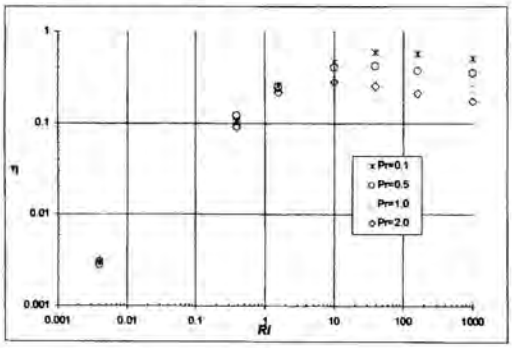

Figure 3: Mixing efficiency results from DNS at Re = 200 (64^3 resolution) and for varying Prandtl numbers

The DNS results did however give decreases in the mixing efficiency with increasing Prandtl numbers in the strongly stratified regime $Ri > 10$ (see figure 3). It is not clear whether these molecular effects are associated with the low Reynolds numbers of the simulations. Since the experiments were for the regime $Ri < 10$, we tentatively conclude that molecular effects cannot explain the discrepancy between the DNS and experimental results.

An alternative explanation for the low mixing efficiencies obtained in the experiments concerns the experimental determination of the energy input into the turbulence. The ratio of the work done in towing the grids to the turbulent kinetic energy may be expressed as $W/E = C_D. U^2/q_0^2$ where C_D is the drag coefficient of the grid, $1/2\ q_0^2$ is the turbulent kinetic energy, and U is the towing speed. In the experiments it was assumed that this ratio is unity i.e. that all the work done in towing the grid goes into the turbulence. Drag coefficients were reported as $C_D \sim 1$. Direct turbulence measurements were not made in these experiments but other grid turbulence measurements typically yield $q_0/U \sim 0.1$ near the grid (say at $x/M = 10$). These estimates suggest that only a small proportion of the towing work emerges in the form of turbulent kinetic energy downstream of the grid. If this is the case, it explains the apparently low values of mixing efficiencies reported for the experiments. We speculate that small amplitude "sloshing" modes are initiated by the grid tows and that their energy accounts for the "missing" energy in the experiments.

4. FLOW VISUALIZATIONS

Three-dimensional visualizations of the turbulence structure have been carried out for a range of stratification strengths and at various times in the evolution of the flows. A sample of the results are shown in figure 4 where iso-surfaces of enstrophy (magnitude of the square of the vorticity) at $ut/L = 3.2$ and for various Richardson numbers are shown. The iso-surface magnitude is three times the mean square value in each case. The enstrophy "structures" for small stratification (low Ri) are randomly shaped isotropic patches. However in the strongly stratified cases, randomly distributed pancake-shaped structures oriented almost in the horizontal plane can be seen. The enstrophy in these patches is dominated by horizontal vorticity. Kimura and Herring (1996) have also previously noted the presence of pancake-shaped vortex patches in their decaying turbulence simulations. It is not yet clear whether the observed pancake-shaped features are associated with the formation of layers, or whether they are linked to the potential vorticity modes noted in previous work (see e.g. Riley & Lelong, 2000).

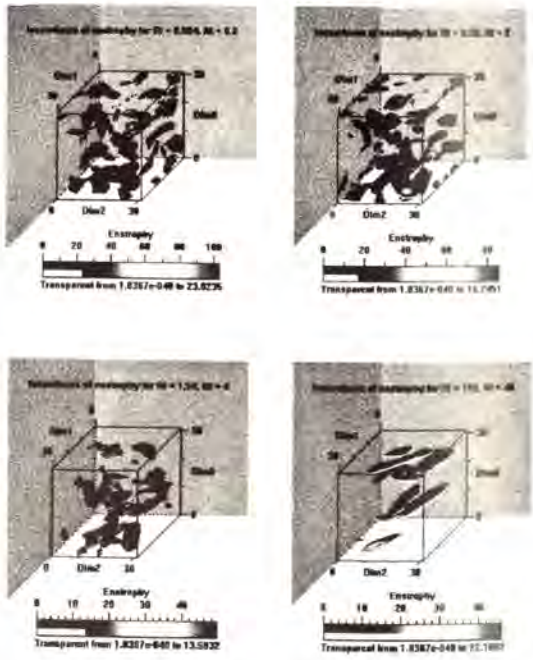

Figure 4: Iso-surfaces of enstrophy for Ri = 0.004, 0.39, 1.58, 158 at t = 3.2. The iso-surface magnitude is three times the mean-square value in all the plots

The changes in the turbulence structure as the stratification increases are consistent with a strong suppression of the vertical displacements of fluid

elements. However as can be seen in figure 1, the mixing efficiency is largest for these strongly stratified cases. This implies the reduced vertical dispersion is compensated for by increased density differences as the stratification increases so that the potential energy changes are higher compared to the weakly stratified flows. For $Ri \geq 10$, these effects balance each other giving approximately constant mixing efficiency.

5. CONCLUSIONS

In this investigation, stably stratified decaying turbulence has been studied using direct numerical simulations (DNS). The focus was mainly on evaluating the mixing efficiency for varying strengths of stratification and on using flow visualisation in order to gain understanding of the structural features of this class of turbulent flows.

The conclusion that can be drawn about mixing efficiency is that it increases with increasing stratification and then approaches a constant value of about 30% at Richardson numbers greater than 10. The energetics is characterized by the exchange between kinetic and potential energies and associated oscillations in the buoyancy fluxes.

Grid turbulence experiments have suggested much lower values of the mixing efficiency. It appears from this investigation that the discrepancy cannot be attributed to molecular effects, but that it may be related to inaccurate accounting of the initial energy budget in the laboratory experiments

Visualizations of the turbulence structure indicate significant changes as the stratification increases although detailed interpretation of these changes requires further analysis. It appears that the turbulence structure for strong stratification resembles randomly scattered pancakes that are flattened in the horizontal plane as suggested by Kimura and Herring (1996).

ACKNOWLEDGEMENTS

DDS would like to acknowledge the contribution of Prof. J. Riley (University of Washington) who provided the DNS code used in this work.

REFERENCES

Britter, R.E. (1985), Diffusion and decay in stably stratified turbulent flows. In *Turbulence and Diffusion in stable environments* (ed. J.C.R. Hunt). Claredon.

Kimura, Y. & Herring, J.R. (1996), Diffusion in stably stratified turbulence, *J.Fluid Mech.*, **328**, 253-269

Keller, K.H. & Van Atta, C.W. (2000), On the evolution of turbulent kinetic and potential energies in homogeneous stratified shear turbulence. *Submitted.*

Linden, P.F. (1979) Mixing in stratified fluids. *Geophys. Astrophys. Fluid Dyn., 13, 2-23*

Rehmann, C.R. & Koseff, J.R. (2000), Mean potential energy change in weakly and strongly stratified grid turbulence. Submitted to *J.Fluid Mech.*.

Riley, J.J., Metcalfe, R.W. & Weissman, M.A. (1981), Direct numerical simulations of homogenous turbulence in density stratified fluids. *In Non-linear properties of internal waves.* Proc. AIP Conference, La Jolla Institute, 1981 (ed. B.J. West)

Riley, J.J. & Lelong, M-P (2000), Fluid motions in the presence of strong stable stratification. *Ann. Rev. Fluid Mech., 32, 613-657.*

Rottman, J.W. & Britter, R.E. (1986), The mixing efficiency and decay of grid-generated turbulence in stably stratified fluids, Proc. 9th Australasian Fluid Mech. Conf., Auckland, New Zealand, 8-12 Dec 1986.

Townsend, A.A. (1976), The structure of turbulent shear flow. Cambridge University Press.

HEFAT2002
1st International Conference on Heat Transfer, Fluid Mechanics, and Thermodynamics
8-10 April 2002, Kruger Park, South Africa
BC1

SIMULATION OF FLOW ACROSS CIRCULAR CYLINDERS WITH DISCRETE VORTEX METHOD

Chen Bin* Guo Liejin** Yang Xiaogang***
*Ph.D Student; **Professor, ***Visiting Scholar (Now working in University of Paisley, UK)
State Key Laboratory of Multiphase Flow in Power Engineering,
Xi'an Jiaotong University,
Xi'an 710049
P. R. China,
E-mail: chenbin71@263.net

ABSTRACT

A discrete vortex method based on potential flow and boundary-layer integration is developed to characterize viscous flow across single circular cylinder and two cylinders. The potential flow are determined by surface vorticity method and the separation points are chosen according to relatively simple separation criterion. With this method, the phenomena of vortices shedding and their interaction can be visualized clearly. Meanwhile the vorticity distribution, drag and lift coefficients of each cylinder, instantaneously changed flow and vorticity field are achieved. Moreover, through the statistical analysis, the turbulence characteristics are figured out such as turbulence intensities and shear stress.

INTRODUCTION

The separated flow across circular cylinders has attracted more and more attentions because of its practical and fundamental importance. First it is a problem applied abundantly in industry, such as flow across cylinders in heat exchanger, flow around oilrig in the sea, airflow around buildings, etc. Second, the flow across circular cylinder is regarded as a classical problem with results well documented and still under further investigation. This kind of three-dimensional unsteady turbulent shear flow involves with a series of theoretical and practical problems[1], for instance, unsteady separation of flow, evaluation of shear layers, vortex shedding, pairing and merging, transition from laminar flow to turbulence and so forth.

Numerical simulation is an efficient tool to investigate this kind of unsteady flow. But the nonlinear govern equation and varying boundary condition deeply hind the successful simulation. Until now finite difference method, large-eddy simulation, direct simulation had been used to solve this problem. In the application of these methods two shortcomings are found. One is that researchers have to confront with the additional work of grid generation to fit the complicated geometry domain and the multitudinous grid number also considerably influences the computation efficiency. The another one is that if turbulence model is used, the remarkable loss of turbulence fluctuation information is not avoided, so the achievement of instantaneously accurate turbulence characteristics becomes very difficult.

Discrete vortex method (DVM) is a promising method to simulate the flow across cylinders[2][3]. With this method a number of point vortices are positioned into the potential flow field to characterize the continuously distributed vorticity. Then the whole flow field can be obtained through the calculation of the complicated evaluation of vortex shedding, development and roll up. No turbulence model is adopted so the loss of fluctuation information is avoided[4].

NOMENCLATURE

C_D	Drag coefficient
C_L	Lift coefficient
C_p	Surface pressure coefficient
$K(s_n,s_m)$	Coupling coefficient
$L(s_n,s_m)$	Coupling coefficient
P	Fluid pressure
R_e	Renold number
Δs	Element length
Δt	Time step
u,v	Velocity components in x,y plane
W_∞	Uniform stream velocity
z	Complex number, vortex position
α	Attack angle
$\gamma(s)$	Vorticity strength
Γ	Vortex strength
ρ	Fluid density
ν	Fluid viscosity
ξ, ζ	Gaussian random number

THEORY

In present paper DVM is used to simulate the flow across cylinders in different situations. The vorticity transport equation for a fluid of uniform density ρ and viscosity ν subjected only to irrational body forces is given by

$$\frac{D\omega}{Dt} = \frac{\partial\omega}{\partial t} + u\cdot\nabla\omega = \omega\cdot\nabla u + \nu\nabla^2\omega \qquad (1)$$

For two-dimensional flow, equation (1) reduces to

$$\frac{D\omega}{Dt} = \nu\nabla^2\omega \qquad (2)$$

According to Chorin[5], the vorticity equation (2) is divided into convection and diffusive part and the two equations are solved sequentially.

$$\frac{\partial\omega}{\partial t} + u\cdot\nabla\omega = 0 \qquad (3a) \quad \text{and} \quad \frac{\partial\omega}{\partial t} = \nu\nabla^2\omega \qquad (3b)$$

Equation (3a) characterizes two-dimensional, incompressible and invisid flow. If the flow field concerned does not exist an internal boundary and the free-stream conditions at infinity is known, equation(3a) can be solved to give the Biot-Savart Law.

$$u(r) = -\frac{1}{4\pi}\iiint\frac{(r-r')\times\omega(r')}{|r-r'|^3}dv(r') + U_\infty(t) \qquad (4)$$

On the basis of invisid solution, the viscous diffusion (equation 3b) can be simply simulate by the random walk method. The details of this method will be shown later.

Nascent vortices and Separation condition

If U_s is the velocity just outside the boundary layer at separation point, we can calculate the rate at which vorticity is shed into the wake from $\frac{\partial \Gamma}{\partial t} = \frac{1}{2}U_s^2$. The vortex has to be placed at the point such that the no-slip and the no-back-flow condition are satisfied. The circulation and position of nascent vortex can be determined in two ways: placing the new vortex of circulation $\frac{1}{2}U_s^2\Delta t$ on the tangent to separation at a distance of $\frac{1}{2}U_s\Delta t$ from the separation position, or set circulation $0.4U_s^2\Delta t$ and distance $\frac{1}{4}U_s\Delta t$ [6]. The former is selected in this paper. Determination of mobile separation point can be performed by boundary layer integration or even turbulence modeling[7].

Representation of the flow field

Analysis of flow using vortex method requires exact or approximate methods to satisfy the condition that the resulting flow is parallel to the cylinder surface, or that the normal velocity relative to the cylinder is zero at least a number of collocation points. It is well known that potential flow across single circular cylinder can be simulated by superposition of uniform flow and doublets. For the flow across circular cylinders Martensen's surface vorticity method is powerful[8][9].

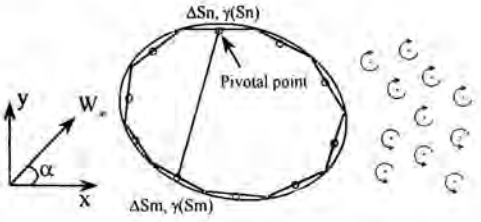

Fig.1 Discretization of cylinder surface

In the surface vorticity method, the surface of the concerned cylinder is simplified to N discrete elements of length ΔS and of strength $\gamma(S_n)\Delta S_n$ concentrated at pivotal points(selected at the mid points of the elements) as shown in Fig.1. Each $\gamma(S_n)$ satisfied non-singular Freholm integral equation[6], which can be reduced to a set of linear equations as follows:

$$\sum_{n=1}^{M}\gamma(s_n)K(s_n,s_m)\Delta s_n = -W_\infty\left(\frac{dx_m}{ds}\cos\alpha_\infty + \frac{dy_m}{ds}\sin\alpha_\infty\right) \quad (5)$$

where α_∞ is the inclination of W_∞ to the x axis and s is distance measured around the body profile. $K(s_n,s_m)$ is a coupling coefficient. If there are N vortices Γ_i shedding from the cylinder into the outer flow field, equation (1) can be extended simply as follow:

$$\sum_{n=1}^{M}\gamma(s_n)K(s_n,s_m)\Delta s_n = -W_\infty\left(\frac{dx_m}{ds}\cos\alpha_\infty + \frac{dy_m}{ds}\sin\alpha_\infty\right) - \frac{1}{2\pi}\sum_{i=1}^{N}\Gamma_i L(i,m) \quad (6)$$

the expressions of above coupling coefficients can be seen in [8][9].

When $\gamma(S_n)$ is calculated from equation (6), the velocity at any point outside the cylinder can be obtained through Biot-Savart law by summing up the velocity components due to the induction of the surface vortices, shedding vortices and the main stream velocity.

$$u_m = W_\infty\cos\alpha + \sum_{n=1}^{M}\gamma(s_n)K(s_n,s_m)\Delta s_n + \sum_{\substack{i=1\\ i\neq m}}^{N}\Gamma_i L(i,m) \quad (7a)$$

$$v_m = W_\infty\sin\alpha + \sum_{n=1}^{M}\gamma(s_n)K(s_n,s_m)\Delta s_n + \sum_{\substack{i=1\\ i\neq m}}^{N}\Gamma_i L(i,m) \quad (7b)$$

Then applying forward difference, the new position of all shedding vortices can be advanced by:

$$x_{new} = x_{old} + u_m\Delta t \quad (8a)$$

$$y_{new} = y_{old} + v_m\Delta t \quad (8b)$$

However a central difference approach can be used to average two forward difference steps to achieve a much better estimate of vortex convection shown in Fig.2.

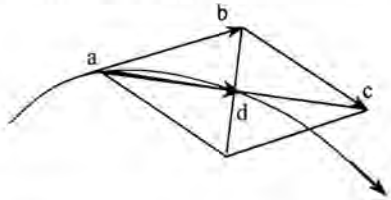

Fig.2 central difference estimate of vortex convection[10]

$$x_{md} = x_{ma} + 0.5(u_{ma} + u_{mb})\Delta t \quad (9a)$$

$$y_{md} = y_{ma} + 0.5(v_{ma} + v_{mb})\Delta t \quad (9b)$$

In order to simulate the viscous diffusion, random walk method is introduced here and the vortex motion can be described by[5]

$$x_{md} = x_{ma} + 0.5(u_{ma} + u_{mb})\Delta t + \xi \quad (10a)$$

$$y_{md} = y_{ma} + 0.5(v_{ma} + v_{mb})\Delta t + \zeta \quad (10b)$$

ξ and ζ are two independent sets of Gaussian random numbers, each having a zero mean and a standard deviation $\sigma = \sqrt{2\Delta t/\mathrm{Re}}$.

Pressure coefficient

The Bernoulli's equation applied to the potential flow appears

$$P_\infty + \frac{1}{2}\rho W_\infty^2 = P + \frac{1}{2}\rho V_s^2 \quad (11)$$

Pressure coefficient: $C_p = \frac{P - P_\infty}{\frac{1}{2}\rho W_\infty^2} = 1 - \left(\frac{V_s}{W_\infty}\right)^2$

The non-dimensional drag and lift coefficients are defined such that[6]

$$C_D = -\frac{1}{2}\int_0^{2\pi} C_p\cos\theta d\theta \quad (12a)$$

$$C_L = -\frac{1}{2}\int_0^{2\pi} C_p\sin\theta d\theta \quad (12b)$$

Note that θ is the angle of inclination to the real axis and the integral is in an counterclockwise sense.

Amalgamation of vortices

Two or more vortices could be amalgamated into a central line vortex in numerous ways and for a number of reasons: to limit the unrealistically large velocities induced in each other, to minimize their propensity to orbit about each other, to reduce the computer time. Amalgamation is an approximation and there is no correct or guaranteed way to perform it. It has been customary to amalgamate two or more vortices into a single vortex strength Γ, placed at their center of vorticity, given by[3]

$$z = \sum \Gamma_j z_j / \sum \Gamma_j \qquad (13)$$

RESULTES

In this paper the DVM is used to simulate flow across one single cylinder and two cylinders. The non-dimensional main stream velocity is 1, the non-dimensional radius of cylinder is 0.5 and the Re number is 1×10^4. For convenient, take the attacl angle 0 degree. Through the analysis of decision and computer time, each cylinder is divided into 64 elements. Time step is 0.05 and 1000 steps are advanced. With the advance of time step, the amount of vortices in the flow field will increase very quickly. In order to reduce the prohibitively large computational times, a amalgamation domain with limited width is set at the downstream of the cylinder (Red lines shown in Fig.3a) where the vortices will amalgamate together according to the method mentioned above on the basis of the fact that induction between vortices will be so small as to be neglected when the distance is large enough.

Results for single cylinder

The result of flow field is shown in Fig.3. Fig.3a illustrates the flow pattern of wake behind cylinder. In the figure the green and magenta cloud represent the vortices shedding from upper and lower side of the cylinder, respectively. And the length of each short line characterize the strength of its vorticity. It is shown that after 1000 time steps the Von Karman vortices are established regularly. The upper and lower side vortex cloud are not convected independently. The vortices shedding from upper side rotate clockwise while those from lower side rotate counterclockwise. Mutual Entrainment occurred between these two clouds. Meanwhile the amalgamation domain is set 20R away from the cylinder surface and the width is 3R. When vortex cloud entered the domain, they are amalgamated to one vortex according to equation (13). It is concluded that DVM is first an advantageous technique to accomplish flow visualization.

Because of point vortex means local vorticity, the vorticity contour of the whole flow field can be plotted easily. It is seen that the vorticity is mainly concentrated in the near wake region. The closer the region is to the cylinder surface, the denser the vorticity is, and vice visa.

Since the vorticity of the pivot points on the cylinder surface and the shedding vorticity are known, the instantaneously changed velocity field can be calculated by summing up the velocity components due to the main stream velocity and induction of the surface and shedding vortices. Fig.3c shows a instant of flow field. From the result it is found that the maximum velocity is 1.9976 and minimum velocity is 0.012, which agrees well with exact solution.

The time dependent drag and lift coefficients are shown in Fig.4, of which green and red curves represent drag and lift coefficients, respectively. The mean value of C_D is 1.16 and the peak value of C_L is 0.84, which is similar with results of [11].

Fig.3a flow across single circular cylinder

Fig. 3b vorticity contour

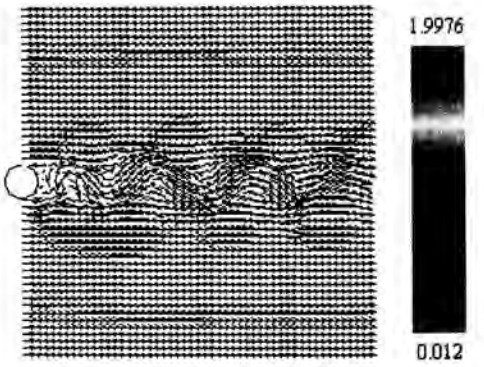

Fig. 3c velocity vector

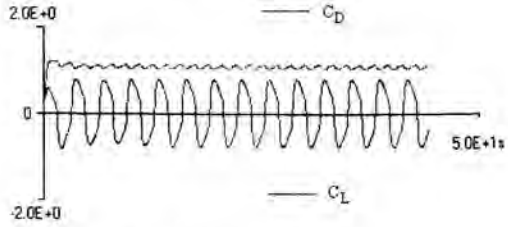

Fig.4 drag and lift coefficients

In order to study the effect of viscous diffusion with DVM, profiles of shear stress, longitudinal and cross-stream turbulence intensities are presented at different downstream cross-section of the wake , shown in Fig.5(abc). On each figure six cross-sections are used to display the profile of corresponding value (X is the main stream direction and Y is cross-section direction). Fig. 5a is the distribution of longitudinal turbulence intensities. Two peaks appear at Y=1.5R looking like 'M'. At different cross-section, the shape of distribution is similar and the peak value decreases with increasing X, which means farther away from the cylinder.

Fig.5b is the distribution of cross-stream turbulence intensities, which behaves symmetry and only one peak appears. As longitudinal turbulence intensity, the cross-stream turbulence also decreases with increasing X. Both the fact imply that the turbulence intensity will dissipate along flow direction. Fig. 5c is the distribution of shear stress u'v'. The peak value varied sharply at different cross-section. It is about $0.05U^2$ near the cylinder and $0.01U^2$ far away from the cylinder. So it seems that the distribution becomes more and more flat along the flow direction. The statistic results are found that they are in reasonable agreement with experimental measurements (Lourenco and Shih[12] show that the peak values of r.m.s. u' and v' components are about 0.25 and 0.4). The slightly difference may be associated with the modeling limitations of a two-dimensional simulation or with numerical simplifications relating to representation of those point vortices out of computational domain by vortex amalgamation.

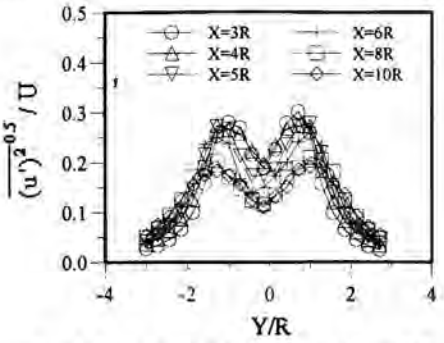

Fig. 5a longitudinal turbulence intensities at different downstream cross-section of the wake

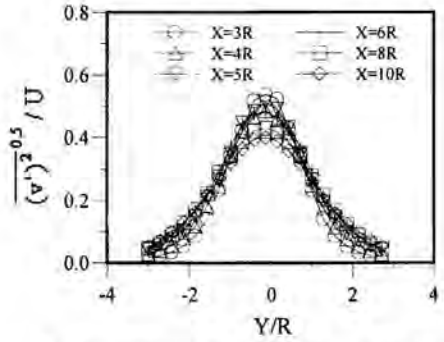

Fig. 5b cross-stream turbulence intensities at different downstream cross-section of the wake

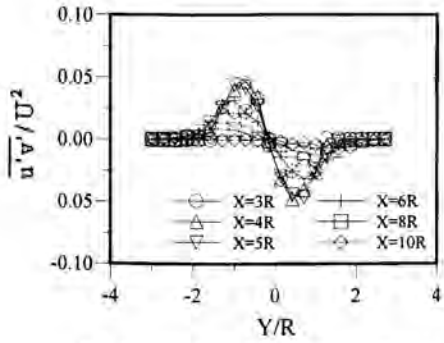

Fig. 5c shear stress distribution at different downstream cross-section of the wake

Results for two cylinders

One of the advantages of surface vorticity method and DVM is that they can be easily extended to situation of multi-cylinders. This is very important when we investigate the interaction between cylinders happened abundantly in industry. In this paper two cylinders are placed into the flow field with pitch-to-diameter ratio 2.0.

Fig. 6a flow field behind two cylinders

Fig. 6b vorticity contour

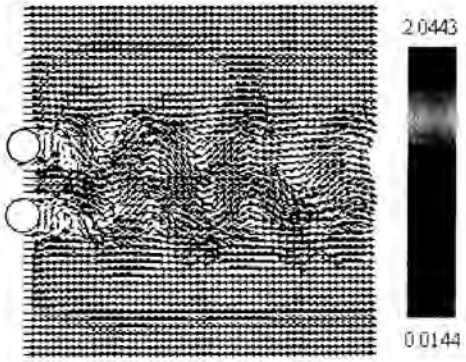

Fig. 6c velocity vector

Fig.8a illustrates the flow pattern of wake behind two cylinders. It is shown that behind the two cylinders there are only independent Von Karman vortices in a short distance away from

the cylinder. In the far flow field these two Von Karman vortices intertwist each other and can't be distinguished clearly. All the vortices tend to converge together according to their symbol, i.e., color in the figure. This tendency can also be found in Fig. 8b, which is the vorticity contour. The vorticity mainly concentrated at the region near the cylinder just like those behind single cylinder. Mutual interaction occurred not only between different vortices shedding from the same cylinder, but also between different cylinders. Furthermore, the drag and lift coefficients are considerably different with those of single cylinder. From Fig. 9 it is found that drag coefficients become 1.37 and the lift coefficients become 1.05. It implies that there is disturbance between these two cylinders, which results in the change of drag and lift coefficients.

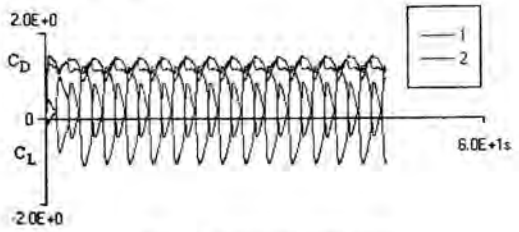

Fig.7 drag and lift coefficients

Just like single cylinder, the profiles of shear stress, longitudinal and cross-stream turbulence intensities are also presented at different downstream cross-section of the wake . shown in Fig.8(abc). For longitudinal turbulence intensities shown in Fig. 8a, two 'M' overlap each other. The maximum peak value is a little larger than that of single cylinder and for the same 'M', the peak value of inner side is higher than that of outer side, which indicates there are strong interaction and momentum transfer between two wakes and mainstream. But this interaction will decrease with increasing X. At last when X=10R, the distribution becomes symmetry. Fig.8b is the distribution of cross-stream turbulence intensities, which behaves symmetry and two peaks appear. As longitudinal turbulence intensity, the cross-stream turbulence also decreases with increasing X. The difference between single cylinder and two cylinders is that there is superposition area behind two cylinders. Moreover the maximum value also increases from 0.4 to 0.65 because of the interaction. The same result appears in the distribution of shear stress u'v' shown in Fig. 8c. The shape of the distribution is not changed so much except for the overlap area and the peak value increases from $0.05U^2$ to $0.08U^2$.

CONCLUSION

The DVM and surface vorticity method provides a powerful technique in the simulation of flow across circular cylinders. In this paper surface vorticity method are used to obtain the potential flow across cylinders and the DVM is used to simulate the separate flow. First of all, the flow pattern of single cylinder and two cylinders show that DVM is a quite well method to conduct flow visualization. It is very convenient to understand the process of vortex shedding, paring, amalgamating, the establishment of Von Karman vortices and their interaction (case of two cylinders). Secondly the velocity and vorticity field, drag and lift coefficients, turbulence intensities and shear stress

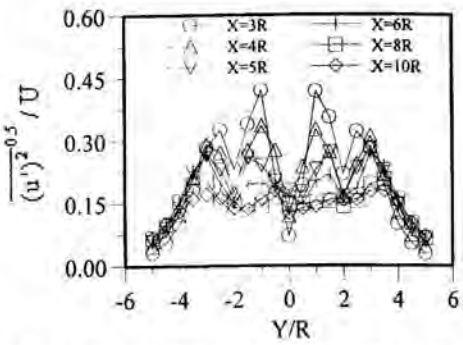

Fig. 8a longitudinal turbulence intensities at different downstream cross-section of the wake

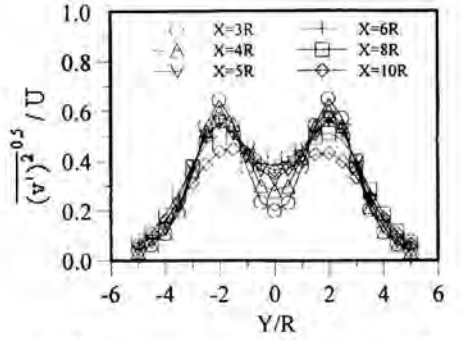

Fig. 8b cross-stream turbulence intensities at different downstream cross-section of the wake

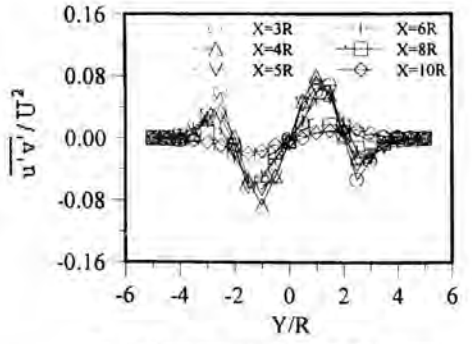

Fig. 8c shear stress distribution at different downstream cross-section of the wake

are numerical simulated respectively for single cylinder and two cylinders. The fact that results of single cylinder are in reasonable agreement with experimental measurements imply that this method is also applicable to two cylinders. It is shown that there are considerable difference between results of single cylinder and two cylinders. The reason is that there are strong interaction between two wakes and main stream, which leads to the increment of drag and lift coefficient, turbulence intensity

and shear stress.

ACKOWLEDGEMENTS

The author wishes to thank the jointly financial support of National Basic Research Priorities Program of China (approved No. G1999022308) and National science fund for distinguished young scholar project 59725616.

REFERENCES

[1] Xia X. Q, 1991, "Engineering Separation Flow Dynamics", Press r Beijng University of Aeronautics and Astronautics ,Beijing

[2] Chen Bin, el al, 1999, "An Review on the Numerical Methods of the Two-Phase Flow Across a Tube Bundle", J. of Basic Science and Engineering in Chinese, Vol. 7 No.1, pp.60-66

[3] T. Sarpkaya, 1988, "Computational Methods with Vortices-The 1988 Freeman Scholar Lecture", J. Fluids Eng., Vol.111, pp.5-52

[4] Yang X. G., 1995, "Two-Phase Flow Dynamical Simulations and Modelling", Ph. D thesis, University of Birmingham.

[5] Chorin A. J., 1973, "Numerical Study of Slightly Viscous Flow", J, Fluid Mech., Vol. **57**, pp. 785-796

[6] P. K. Stansby, 1980, "A Numerical Study of Vortex Shedding From One and Two Circular Cylinders", Aeronautical Quarterly, Vol. **32**, Pt.1, pp. 48-68

[7] T. Sarpkaya, R. L. Schoaff, 1979, "Inviscid Model of Two-Dimensional Vortex Shedding by a Circular Cylinder", AIAA J., Vol. 17, No.11, pp. 1193-1200

[8] K. Lam, 1987, "Potential Flow Calculation by Surface Vorticity Method and Computer Graphics", Computer &Graphics, Vol.**11**, No.1, pp.35-47

[9] R; I. Lewis, 1981, "Surface Vorticity Modelling of Separated Flows from Two-Dimensional Bluff Bodies of Arbitrary Shape", J. Mechanical Engineering, Vol. **23**, No. 1, pp.1-12

[10] R. I. Lewis, 1991, "Vortex Element Methods for Fluid Dynamic Analysis of Engineering Systems", Cambridge University Press, New York.

[11] Bearman, P. W., Wadcock, A. J., 1973, "The Interaction between a Pair of Circular Cylinder Normal to a Stream", J. Fluid Mech., Vol. 61.

[12] Lourenco, L. M., Shih, C., 1993, "Characteristics of the Plane Turbulent neat wake of a circular, a Particle Image Velocimetry Study", private communication (data taken from Beaudan and Moin, 1994)

HEFAT 2002
1st International Conference on Heat Transfer, Fluid Mechanics and Thermodynamics
8-10 April 2002, Kruger Park, South Africa
BC2

EMPLOYING COMPUTATIONAL FLUID DYNAMICS IN THE MODELLING OF ENERGY STORAGE IN AIR CONDITIONING SYSTEMS: THE MODELLING OF LATENT HEAT STORAGE

C. Bothma* and L. Pretorius**
*M.Eng. Student; **Professor
Department of Mechanical Engineering,
Rand Afrikaans University,
P.O.Box 524, Auckland Park, 2006,
South Africa.
Email: lp@ing1.rau.ac.za

ABSTRACT

Latent heat storage occurs when heat is stored in a medium coupled with phase change [1], [6], [7]. As energy is exchanged, the medium undergoes change of phase, i.e. from solid to liquid, liquid to gas or vice versa. The phase change requires an amount of energy, called latent heat of fusion.

This paper is concerned with the modelling of phase change (latent) heat storage using CFD (Computational Fluid Dynamics) techniques. Using a locally developed CFD software application Flo++ [8], a user routine is developed to define both temperature in terms of enthalpy as well as enthalpy in terms of temperature throughout the melting process.

A variety of industries may benefit from the implementation of CFD in the modelling of latent heat storage, including the design and optimisation of air conditioning systems (for commercial as well as residential air conditioning), cold transport and cold storage as well as electronics cooling technology.

NOMENCLATURE

C_P	Constant pressure specific heat (kJ/kgK)
$C_{p,f}$	Specific heat of the liquid phase (kJ/kgK)
$C_{p,s}$	Specific heat of the solid phase (kJ/kgK)
E	Energy (kJ)
f(x1)	Quadratic function defining C_p over range x1
g(x2)	Quadratic function defining C_p over range x2
h	Enthalpy (kJ/kg)
Δh	Enthalpy difference (kJ/kg)
h(x3)	Quadratic function defining C_p over range x3
h1	Enthalpy at the beginning of the melting range (kJ/kg)
h2	Enthalpy at the end of the melting range (kJ/kg)
h_{sf}	Heat of fusion (kJ/kg)
i(x4)	Quadratic function defining C_p over range x4
j(x0)	Quadratic function defining C_p over range x0
k(x5)	Quadratic function defining C_p over range x5
m	Mass (kg)
Δt	Time step (s)
T	Temperature (K)
T1	Temperature at the beginning of the melting range (K)
T2	Temperature at the end of the melting range (K)
T_{sf}	Phase change temperature (K)
ΔT	Temperature difference (K)

INTRODUCTION AND BACKGROUND

Phase change materials (PCM's) can store or release relatively large amounts of energy at near isothermal conditions [1], [5], [6].

The energy stored and released under these conditions, called latent heat, h_{sf}, is defined as the amount of heat absorbed or released in order for a material to undergo phase change. For example, the amount of heat required to completely change 1kg of ice from the solid phase to the liquid phase would be 2834.8 kJ at 0°C [2].

Thus the energy E required to completely change the phase of a mass m of a PCM is defined as [1], [6]

$$E = mh_{sf} \quad (1)$$

at the melting temperature of the material.

Considering the complete transformation process from a temperature below the melting temperature, T_1 up to a temperature above the melting temperature, T_2, the change in specific enthalpy, Δh, would be [6]

$$\Delta h = C_{p,s}(T_{sf}-T1) + h_{sf} + C_{p,f}(T_2-T_{sf}) \quad (2)$$

Where

$C_{p,s}$; $C_{p,f}$ = Specific heat of the solid and liquid phases respectively

T_{sf} = The theoretically constant temperature around which the phase change takes place.

The behaviour of PCM's may be implemented in air conditioning systems and can lead to substantial energy

cost savings. By cooling the PCM at night or at off-peak times, the stored "cold energy" can be used for air cooling in the day or in peak times when electrical energy is more expensive. The opposite is also possible, where a PCM can be heated in the day and the stored energy released at night for heating purposes

The purpose and target of this study is to investigate the implementation of computational fluid dynamics (CFD) in the simulation of the energy storage in a PCM and the consequent release of energy into a fluid stream.

This will allow an engineer or analyst to experiment with different PCM's to fulfil a certain cooling or heating requirement without actually going to the expenses of physical experimentation. This will substantially shorten the design cycle for air conditioning systems involving energy storage and as a consequence, engineers will be able to develop heat storage technology faster, more accurate and at a lower cost.

IMPLEMENTING PHASE CHANGE CONDITIONS FOR A PCM IN SPECIFIC CFD SOFTWARE.

The locally developed CFD software, Flo++, was employed in this study [8].
Flo++ offers the flexibility of user coding in a unique user file that is created for every model geometry. The engineer may edit this file to incorporate the necessary user functions for a specific task which is then linked to the solver module.

A user routine to modify or define the specific heat in a material can be incorporated in the CFD software. This user routine allows for three different scenarios.

- The specific heat value may be defined in terms of temperature.
- The enthalpy of the material may be specified in terms of temperature.
- Both the specific heat and the enthalpy may be defined in terms of each other.

In the last two cases, where the enthalpy and temperatures are defined, the specific heat is calculated by

$$C_p = \Delta h/\Delta T \qquad (3)$$

For the purpose of this study, the scenario defining the specific heat as well as the scenario defining both the temperature and enthalpy was considered.

As a solid medium is heated from a temperature below its melting temperature, the specific enthalpy rises at a rate (in terms of the temperature) equal to the specific heat value over the temperature difference and therefore the specific heat is assumed constant and is easily defined in the user code.

When the material reaches its melting temperature, or the temperature at the beginning of its melting range, the physical properties of the material changes and therefore the specific heat value can be considered to change to simulate the specific enthalpy change.

After the melting process is complete, the specific heat value becomes that of the liquid phase and is assumed to be constant once more.

In the melting region, the following is assumed:

Since [2]

$$dh = C_p dT \qquad (4)$$

$$\int_{T1}^{T2} C_p \, dT = \int_{h1}^{h2} dh \qquad (5)$$

thus

$$h_{sf} = \int_{T1}^{T2} C_p \, dT \qquad (6)$$

where $h_{sf} = h2 - h1$, and Cp is a function of T between T1 and T2, the temperature extremes of the melting range. For simulation purposes, the constant melting temperature is considered to consist of a narrow range of temperatures around the melting temperature. This ensures continuity in the function.

Since the h_{sf} value is known, the function Cp(T) may be defined as any function between T = T1 and T = T2 where the integral, or the area under the curve is equal to h_{sf}.

The graph shown in figure 1 was derived for the specific heat for ice and water by assuming that the function of Cp between T1 and T2 consists of four consecutive quadratic functions. Water was initially chosen because of the extensive nature of available data [2].

The graph consists of six functions,
j(x0) and k(x5) are the constant specific heats of the ice phase and water phase respectively.

f(x1), g(x2), h(x3) and i(x4) are the four quadratic functions making up the overall function. The ranges x0,..,x5 are the defining ranges of x-values for each function and are defined as follows:

x0	(240,272)
x1	(272,272.5)
x2	(272.5,273)
x3	(273,273.5)
x4	(273.5,274)
x5	(274,290)

The functions and defining ranges were chosen in such a fashion that equation (6) holds true with the melting range defined between 272 K and 274 K.

These functions were programmed into the user file, defining Cp in terms of T.

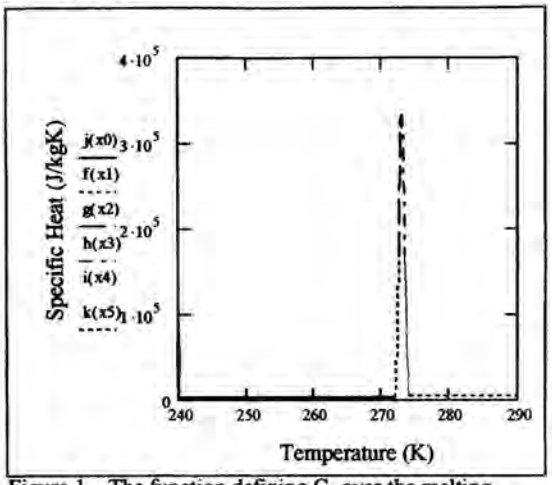

Figure 1 The function defining C_p over the melting range

As was expected [4], the solver software encountered some problems in the solution of the temperature and enthalpy values. The reason being [4] that over a very small temperature increment, the value of the specific heat changes substantially and if the chosen solution time step is not extremely low, say in the order of $\Delta t = 0.0001$s the entire peak may be missed.

This results in substantial simulation times, leading to unnecessary expenses.

In the middle of the melting range, the sign of the gradient of the function also changes over a very small interval, causing further calculation problems.

Consequently this method was abandoned and it was decided to create a user function that explicitly defines temperature in terms of enthalpy and enthalpy in terms of temperature.

From information found on tables for the properties of ice, water and steam [2], the graphs in figures 2 and 3 were derived:

In order to investigate the possibility of simulating latent heat storage by using the functions shown in figures 2 and 3, these were programmed into the user code for a one-dimensional as well as a two-dimensional model geometry and the transient results are shown in the following paragraphs.

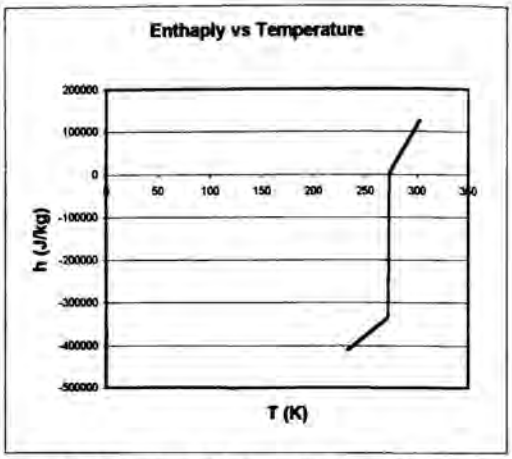

Figure 2 The values of enthalpy in terms of temperature for the Ice/Water CFD Model.

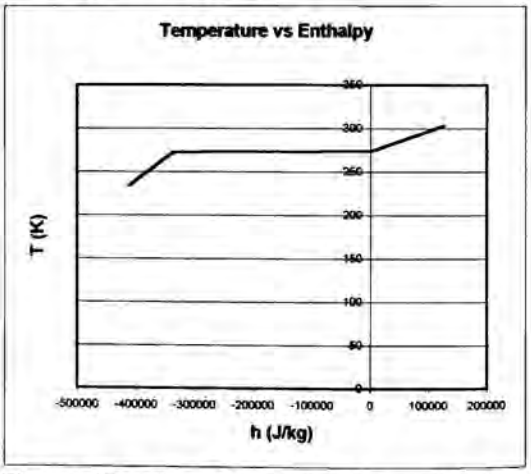

Figure 3 The values of temperature in terms of enthalpy for the Ice/Water CFD Model.

ONE-DIMENSIONAL ICE/WATER CFD MODEL AND RESULTS

A simple one-dimensional block of ice, i.e. one row of cells, was created and a constant temperature boundary condition was applied at one end.

The properties of the one-dimensional model was defined as follows:

Number of cells:	50
Total length of model:	0.1 m
Initial temperature:	271 K
Defined east boundary temperature:	303 K
Other boundaries:	Adiabatic
Time step:	0.01s (fixed)

Figure 4 shows the results for the model at 1s, 10s, 60s and 600s where the movement and change of the melting front is clearly indicated by the lighter shade which defines the range of temperatures from 272K to 274K.

TWO-DIMENSIONAL ICE/WATER CFD MODEL AND RESULTS

The model that was used in the above simulation, which defines the properties of water and ice at various temperatures, may now be used in other CFD model geometries where the material used to store heat is to be analysed.

An example of such a case is shown in figure 5 where a two-dimensional island of phase change material is placed in a flow channel allowing conjugate heat transfer between the PCM (Water/Ice) and the passing air.

The properties of the two-dimensional model was defined as follows:

No. of cells	600
Total length of model	0.15 m
Length of ice/water island	0.05 m
Initial temperature of ice/water:	271 K
Initial air temperature:	320 K
Inlet air temperature:	320 K
Inlet air velocity:	0.1 m/s
Air density: [1]	1 kg/m^3
Air viscosity: [1]	1.9E-7 N.s/m^2
Flow condition:	Laminar
Other boundaries	Adiabatic
Time step	0.01s (fixed)

Figure 5 depicts the simulated velocity vectors in the flow channel containing the island of material.
Figure 6 shows only the Ice/Water section of the model and with the melting front at 10s, 100s, 400s and 600s respectively in the PCM. Again the movement of the melting front is depicted by the lighter shade defining the temperature range from 272K to 274K.

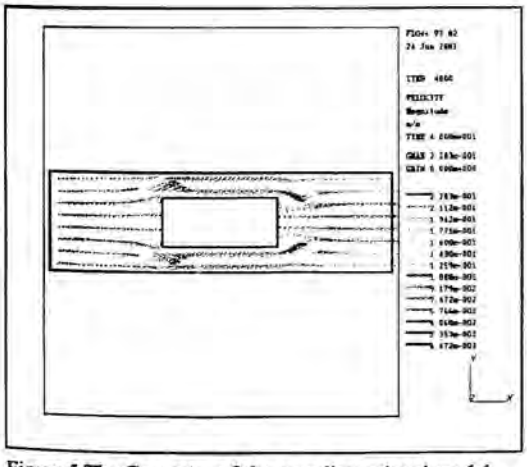

Figure 5 The Geometry of the two-dimensional model.

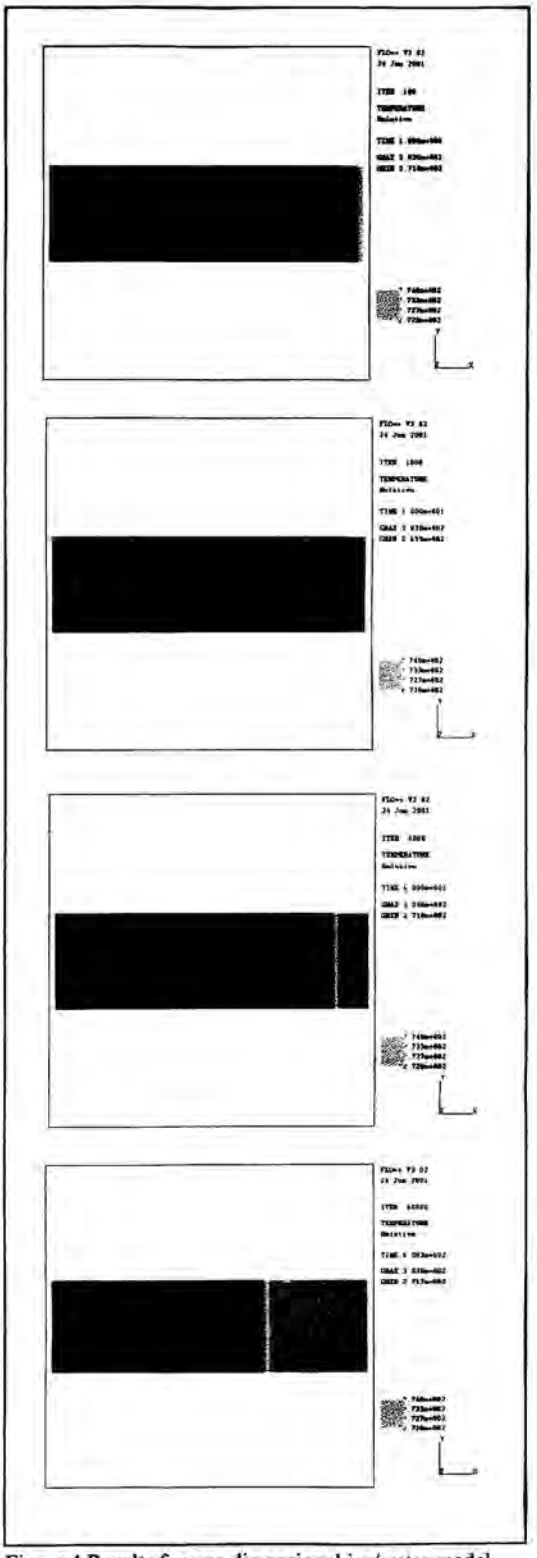

Figure 4 Results for one-dimensional ice/water model

DISCUSSION OF RESULTS AND CONCLUSION

Although experimental correlation for the mathematical model will at this stage be useful, it can be seen from the results that this method of simulating the melting process of a Phase Change Material is achievable and easily modifiable.

It may be applied in the investigation of latent heat storage for various geometries and flow conditions, making modelling and simulation of such systems achievable without the necessity of large experimental set-ups and measuring equipment.

Modifications to a system can easily be analysed and the optimal design of such systems can be obtained with less effort and lower cost.

FUTURE WORK

The mathematical definitions of the temperature vs. enthalpy and enthalpy vs. temperature may be adjusted to suit a specific material, in the case of this study, the properties of SASOL M3M Paraffin Wax will be used in geometries similar to the above for further analysis.

The material definition may also be used in another CFD model geometry to investigate a range of different conditions, such as shown in the previous section.

It would thus also be possible to add heat transfer augmentation devices to the geometry to investigate the effect of enhanced heat transfer on the melting process of a PCM.

The disadvantage of the current model is that it assumes that heat transfer occurs only by conduction through the liquid phase of the PCM.

For geometries where convection driven heat transfer within the PCM plays a dominant roll [3], this method is not accurate.

In the future, it would be useful to develop a method where not only the temperature and enthalpy is defined but where other physical properties of the material are also defined in terms of temperature. This philosophy would necessitate the re-definition of cell groups and material definition driven by the heat transfer calculation for each time step.

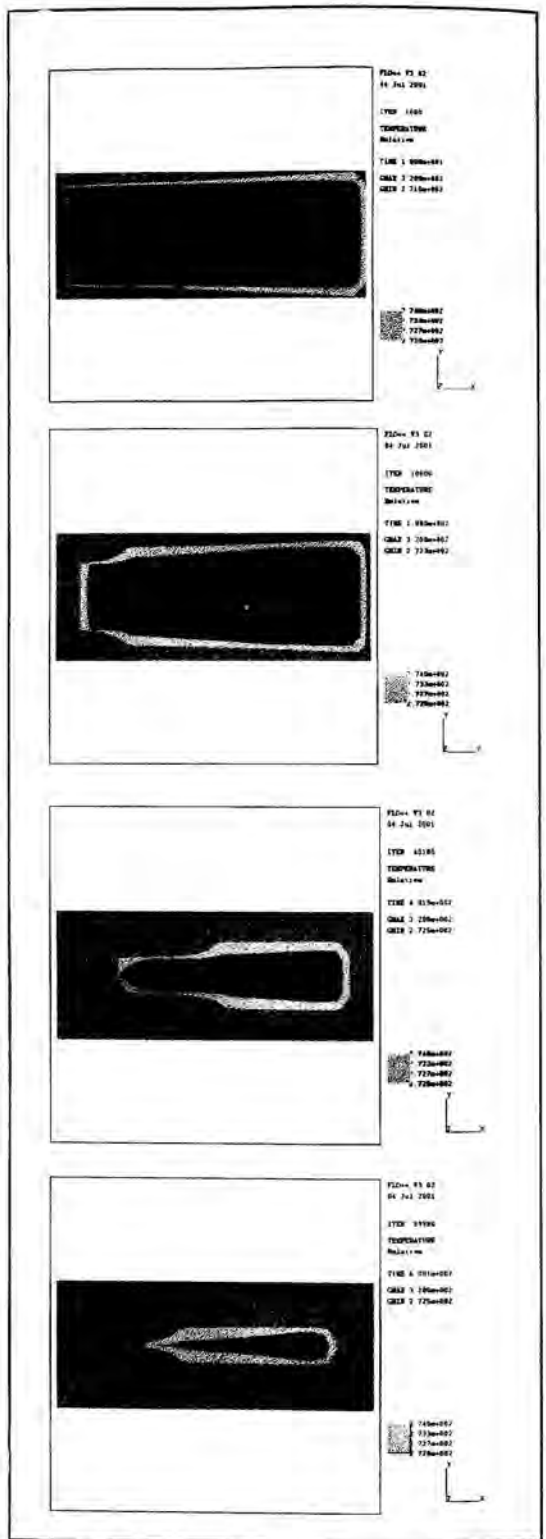

Figure 6 The Ice/Water Island, showing the results of the two-dimensional conjugate heat transfer model.

REFERENCES

[1] F.P. Incropera and D.P. de Witt, 1996, Introduction to Heat Transfer", John Wiley and Sons.

[2] Sonntag / Van Wylen, 1991, "Introduction to Thermodynamics" Third Edition, John Wiley and Sons.

[3] A Hernandez –Guerrero, S M Aceves, E Cabrera-Ruiz, J C Baltazar-Cervantes, 1999, "The Modèling of the charge and discharge processes in energy storage cells", Energy Conversion and Management 40 (1999) 1753-1763.

[4] O.C. Zienkiewicz, 1980, "The Finite Element Method"

[5] T. Kiatsiriroat, J.Tiansuan, T. Suparos, K. Na Thalang, 1999, "Performance Analysis of a direct-contact thermal energy storage-solidification", Renewable Energy 20 (2000) 195 – 206.

[6] G. Beckmann, P.V. Gilli, 1984, "Thermal Energy Storage", Springer-Verlag.

[7] J.Jensen, 1980, "Energy Storage", Newnes-Butterworths.

[8] Flo++ CFD Package User's Manual.

HEFAT2002
1st International Conference on Heat Transfer, Fluid Mechanics, and Thermodynamics
8-10 April 2002, Kruger Park, South Africa
CT1

NUMERICAL MODELING OF FLUID FLOW AND HEAT TRANSFER PROCESSES BY GENERIC FUNDAMENTAL COMPONENTS

T.T. Chow
Principal Lecturer
Division of Building Science & Technology,
City University of Hong Kong,
Tat Chee Avenue, Kowloon,
Hong Kong SAR, China.
Email: bsttchow@cityu.edu.hk

ABSTRACT

Computer simulation has been widely applyied in building thermal performance appraisal studies. Nevertheless, many building simulation software tools currently in use still possess internal structures and modelling approaches which restrict their future extension in response to growing user aspirations. An interoperability problem exists amongst the large variety of available modelling and simulation environment, and it gets more pressing every year with the trend towards increased complexity and heterogeneous systems to be simulated. In order to develop the next generation software, many research efforts have been spending on making them fully building and plant integrated, possessing detailed mathematical representations, and highly flexible in applications. A generalised modelling approach using elementary entities called primitive parts (PPs) is one possible solution for this goal. In this paper, practical examples are used to illustrate how thermal components can be modelled by means of the PPs. In particular, the capability of the PP approach to model two-phase fluid flow is demonstrated.

INTRODUCTION

The thermal environment of a building is a result of the interaction of various heat and mass transfer processes such as conduction, solar transmission, long wave radiation exchange, convection, air movement, and fluid flows in the environmental control plant, etc. This makes the mathematical representations of the underlying processes highly non-linear, inter-related, and depending on time-varying parameters [1]. Nevertheless, heat transfer fundamentals are essentially the same applying to the building envelope or the plant equipment. In thermal simulation, what requires to satisfying the diversifying simulation objectives is a simulation environment that attempts to process the representing thermal system dynamically and to the desirable level of detail [2]. The target is to represent all relevant phenomena, and to process these phenomena together so that the inter-relationships are preserved. This can be achieved by establishing sets of conservation equations for different spatial regions, and then arranging for solving these equations over time.

In a numerical sense, one way to couple building and plant in the thermal model is by combining the energy and flow balance equations, often in the matrix form, for both the building side and the plant side [3,4]. The equation set can be solved either directly or by iteration. A thermal component is made discrete by subdividing it physically into a number of interconnecting finite volumes. These volumes are then assumed to possess uniform properties that can vary over time, and represent homogeneous and mixed material regions. This is often known as the finite-volume state-space conservation approach.

The coupling between heat and fluid flow is achieved by iteratively solving the building/HVAC thermal model and a fluid flow network [5,6]. The flow network is composed of nodes, components, and connections joining nodes by components. A mass balance is performed at each time step to solve the flow through each connection. These flows are then used to establish the mass flow dependent coefficients of the next time step, with iteration invoked for the case of strongly coupled flow.

NOMENCLATURE

A	area, m^2
A	matrix coefficient, future time step
B	matrix coefficient, present time step and excitation
C	specific heat capacity of solid, J/kg.K

Cp specific heat of fluid at constant pressure, J/kg.K
h convective heat transfer coefficient, W/m^2.K
H_{fg} latent heat of evaporation, J/kg
Ni primitive part connectivity index
M mass, kg
m mass flow rate, kg/s
Q heat flux, W
t time, s
x dryness fraction

Greek Letters

α weighting factor in numerical solution scheme
θ temperature, °C

Superscript

$*$ present time row

Subscripts

a air (dry)
i inside
l latent
r 2-phase fluid
s solid
sat saturated
v vapor
w liquid
wt fluid entirely at liquid state

PRIMITIVE PART MODELING

An efficient way to construct a thermal component model is the re-use of existing (sub-) component models. The process is first to subdivide a physical component under consideration into pieces, then to select and integrate the basic (sub-) component models to produce the desired compound model. One most generalized way of applying this concept is through the use of a library of generic objects called "primitive parts". Each primitive part (PP) is a small finite-volume conservation-equation set that describes one particular aspect of heat and/or mass exchange process. 27 PPs, as listed in Table 1, are identified as the 'building blocks'. The generic nature of the PPs makes the technique applicable to most thermal systems. The advantages lie in the fully integrated building and plant simulation, controlled complexity of the source code, the inter-operability of simulation platforms [7], etc. The technique provides a unified mathematical structure, and has the potential to support extensibility through inheritance, and, offers a way to update models as the state-of-the-art evolves. The software is then no longer required to incorporate new (and perhaps endless) thermal components in the routine library. The use of individual PP and the advantages have been discussed in previous literature [8]. Shown below are examples of applying PP technique in assembling plant component models from heat transfer tubing; the components involve moist air and two-phase fluid flows.

Table 1: List of Primitive Parts.

1	**Thermal conduction**
1.1	solid to solid
1.2	with ambient solid
2	**Surface convection**
2.1	with moist air
2.2	with 2-phase fluid
2.3	with 1-phase fluid
2.4	with ambient
3	**Surface radiation**
3.1	with local surface
3.2	with ambient surface
4	**Flow upon surface**
4.1	for moist air; 3 nodes
4.2	for 2-phase fluid; 3 nodes
4.3	for 1-phase fluid; 3 nodes
4.4	for moist air; 2 nodes
4.4	for 1-phase fluid; 2 nodes
5	**Flow divider & inducer**
5.1	Flow diverger (for all fluid)
5.2	Flow multiplier (for all fluid)
5.3	Flow inducer (for all fluid)
6	**Flow converger**
6.1	for moist air
6.2	for 2-phase fluid
6.3	for 1-phase fluid
6.4	for leak-in moist air from outside
7	**Flow upon water spray**
7.1	for moist air
8	**Fluid injection**
8.1	water/steam to moist air
9	**Fluid accumulator**
9.1	for moist air
9.2	for liquid
10	**Heat injection**
10.1	to solid
10.2	to vapor-generating fluid
10.3	to moist air

HEAT TRANSFER TUBING

A 4-row counterflow chilled-water air-cooling coil can be taken as identical layers of heat transfer tubing connected to the chilled-water inlet and outlet headers. Figure 1 shows a 16-node model of the coil composed of 4 heat-transfer tubes. Each tube is a 4-node component model using the finite volume heat balance technique. Details of the modeling technique have been discussed in Chow [9]. The explicit model of the cooling coil

allows an accurate and microscopic representation of the thermal performance, including the transport delay phenomenon, heat and mass transfer at individual tubes, etc.

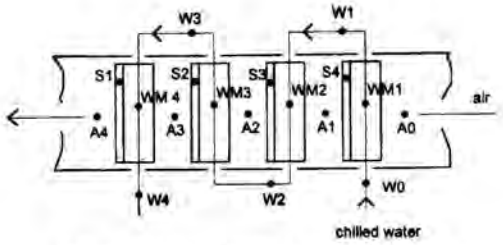

Figure 1: Chilled Water Cooling Coil Model.

With the PP approach, each heat transfer tube can be modeled by using two PPs namely;

4.3 Flow upon surface for 1-phase fluid; 3 nodes

4.4 Flow upon surface for moist air; 2 nodes

The PP model gives almost the identical mathematical structure and simulation results as the conventional finite-volume state-space heat-balance model [10]. The development concept is further elaborated in the two-phase boiling tube model described in the section below.

BOILING TUBE

When a two-phase fluid, like wet steam, flows inside a tube, different physical processes occur depending on the thermal states of the fluid at the ends of the tube. The mass balance within a short time interval (so incompressible flow can be assumed) gives

$$m_r = m_{w0} + m_{v0} = m_{w1} + m_{v1} \tag{1}$$

where the subscripts *w* and *v* are for liquid and vapor, and *0* and *1* are for inlet and outlet respectively (Figure 2). Two cases of inlet steam conditions are considered as follows.

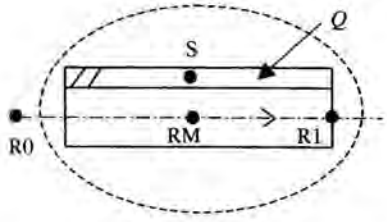

Figure 2: 3-node Wet Steam Tube Model.

wet vapor at inlet

This refers to the case of $m_{w0} > 0$, $m_{v0} > 0$, and $\theta_{r0} = \theta_{sat}$ at the tube inlet. By taking $\theta_{rm} = \theta_{sat}$ the cooling rate ($-Q$) at the tube surface is given by

$$Q = h_i A_i(\theta_s - \theta_{rm}) = h_i A_i(\theta_s - \theta_{sat}) \tag{2}$$

Q is then positive in value. The latent heat content of the steam at the inlet is

$$Q_l = m_{v0} H_{fg} \tag{3}$$

If $Q_l > Q$, then the exit fluid is still at wet steam condition, then $\theta_{r1} = \theta_{sat}$ and this gives

$$m_{w1} = m_{w0} - (Q / H_{fg}) \tag{4a}$$

$$m_{v1} = m_{v0} + (Q / H_{fg}) \tag{4b}$$

If $Q_l \le Q$, then $m_{w1} = m_r$, $m_{v1} = 0$, and

$$\theta_{r1} = \theta_{sat} - \frac{Q_c - Q_l}{m_r Cp_w} \tag{5}$$

superheated steam at inlet

This refers to the case of $m_{w0}=0$, $m_{v0}=m_r$ *and* $\theta_{r0}>\theta_{sat}$ at the tube inlet. The superheat content of the steam at the inlet is

$$Q_{sp} = m_{v0} Cp_{v0}(\theta_{r0} - \theta_{sat}) \tag{6}$$

If $Q_{sp} > Q$, then the exit steam is still at superheated condition, so $m_{w1}=0$, $m_{v1}=m_{v0}$ and this gives

$$\theta_{r1} = \theta_{r0} - \frac{Q}{m_{v0} Cp_v} \tag{7a}$$

$$\theta_{rm} = \frac{\theta_{r0} + \theta_{r1}}{2} \tag{7b}$$

If $Q > Q_p$ but $Q < (Q_{sp}+Q_l)$, then the exit fluid is at wet steam condition, so

$$m_{w1} = m_{w0} + \frac{Q - Q_{sp}}{H_{fg}} \tag{8a}$$

$$m_{v1} = m_{v0} - \frac{Q - Q_{sp}}{H_{fg}} \tag{8b}$$

If $Q > (Q_{sp}+Q_l)$, then the exit fluid is at liquid water condition, then $m_{v1}=0$, $m_{w1}=m_r$ and

$$\theta_{r1} = \theta_{sat} - \frac{Q - Q_{sp} - Q_l}{m_r C p_w} \qquad (9)$$

The above check-then-calculate procedure avoids unnecessary iterations before arriving at the correct solution and enhances computational stability. Iteration however is unavoidable if the steam in tube remains at superheated state throughout. In all these cases the component matrix template is as in equation (10).

$$\begin{bmatrix} A1 & A2 & 0 & 0 \\ A4 & A5 & A6 & A11 \\ 0 & A8 & A9 & 0 \end{bmatrix} * \begin{bmatrix} \theta_x \\ \theta_{rm} \\ \theta_{r1} \\ \theta_{r0} \end{bmatrix} = \begin{bmatrix} B1 \\ B2 \\ B3 \end{bmatrix} \qquad (10)$$

where the A coefficients are the future time step coefficients and the B coefficients are the present time step and excitation coefficients.

The following example demonstrates the use of the boiling tube model in an investigation of the thermal effect on the steam-side of the tube as a result of a change in heat flux distribution along the tube. A hypothetical situation has been used for the computation. A 20mm diameter and 10m long boiling tube-section was considered. The working pressure was taken as 5 bars. For simulation purpose the entire tube was decomposed into 10 numbers of sub-sections, each of length either 0.5 m or 1.5 m. This is indicated in Figure 3. Shorter sub-sections are used at the two ends in order to give more accurate predictions for those regions where changes in fluid temperature are likely to occur (i.e. in the regions likely occupied by liquid water or superheated steam). To represent each sub-section, a 3-node wet steam tube model has been developed using the following two primitive parts (see Figure 2):

4.2	Flow upon surface for 2-phase fluid
10.1	Heat injection to solid

The energy matrix coefficients of these two PPs are given in Appendix. By these, the matrix coefficients in equation (10 were computed at each simulation time step through th addition of PP coefficients, for instance,

$A1 = A(42,1) + A(101,1)$
$A2 = A(42,2)$
$A4 = A(42,4)$
$A5 = A(42,5)$
$A6 = A(42,6)$
$A8 = A(42,8)$
$A9 = A(42,9)$
$A11 = A(42,11)$
$B1 = B(42,1) + B(101,1)$
$B2 = B(42,2)$
$B3 = B(42,3)$

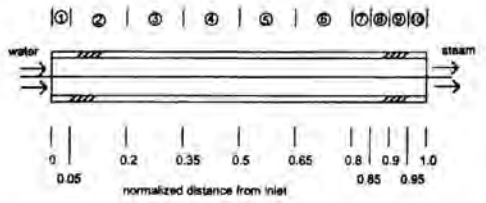

Figure 3: Boiling Tube Divided into 10 Sections.

In this demonstration, the heat energy from the fuel was considered as directly "injected" to the metallic tubing. The inside surface convective heat transfer coefficient depends on whether the fluid is at liquid state or at vapor state at a particular time step. Figure 4 shows the simulation results of the steady state fluid conditions along the boiling tube under a uniform heat flux of 3 kW/m. The tube wall temperature and dryness fraction distribution are also given. It can be seen that the fluid in tube is mainly at the wet vapor state. Accordingly, the tube temperature is uniform along the length until the superheated region is reached. The dynamic responses of the steam temperature at the outlet and the tube wall temperature of the last sub-section (0.5 m long) to a sudden disturbance (temporal loss of uniformity) of heat flux are shown in Figure 5. A drop in outlet steam temperature can be observed at the beginning of the change. This is because the tube temperature of the last section requires time to rise up to the steady state value when the fluid inside has changed from wet vapor state to superheated state.

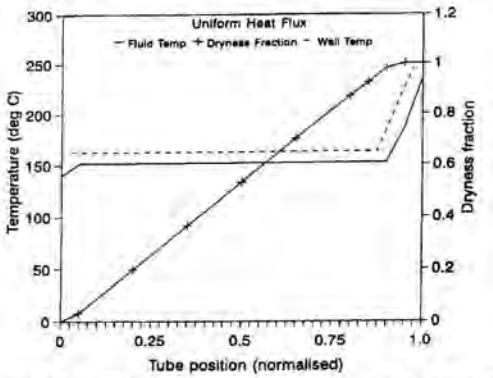

Figure 4: Axial Temperature Distribution under Uniform Heat Flux.

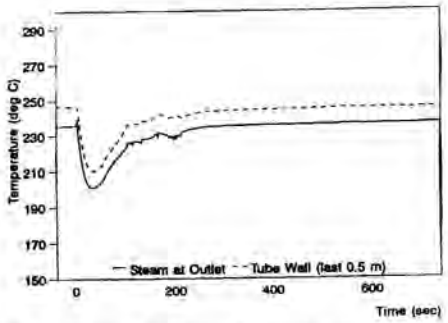

Figure 5: Dynamic Response of Temperature at the Last Tube Section with Short Heat Flux Disturbance.

SUMMARY

The optimal thermal design of building or plant often requires an overall performance analysis, with each component functioning as an integral part of the whole. Flexibility must be offered in the next generation simulation software to allow for more freedom of the users to select or re-construct component models to suit individual simulation task. The primitive part approach enables both building and plant component models, at various levels of mathematical representations, being constructed using the same set of elementary sub-component models. The ultimate goal is to support the automatic formulation of mathematical models of components, based on explicit descriptions of components as distinct from an approach in which pre-constructed models are links to define a system.

The applications of the PPs in heat transfer tubing forming cooling coil and boiler tubing have been demonstrated in this paper. The theoretical treatment in 2-phase fluid flow was also illustrated.

ACKNOWLEDGMENTS

The author expresses his thanks to the City University of Hong Kong for providing research fund in supporting the ongoing development of the work.

REFERENCES

[1] Aasem, E., et al., 1994, "Current Building Systems Modelling Potential of ESP-r," Proceedings of 4th System Simulation in Buildings, Liege, Belgium, pp. 427-445.

[2] Shah, D.J., 2001, "Generalized Engineering Modeling and Simulation (GEMS)", Proceedings of 7th International IBPSA Conference, Rio de Janeiro, Brazil, pp.723-730.

[3] Clarke, J.A., 1989, "Building Energy Simulation: the State-of-the-Art," Solar and Wind Technology, Vol.6, No.4, pp. 345-355.

[4] Boyer, H., et al., 1996, "Thermal Building Simulation and Computer Generation of Nodal Models," Building and Environment, Vol.31, No.3, pp.207-214.

[5] Clarke, J.A., 1999, "Prospects for Truly Integrated Building Performance Simulation," Proceedings of 6th International IBPSA Conference (BS'99), Kyoto, Japan, pp.1147-1154.

[6] Okuyama, H., Kimura, K.I. and Kawashima, R., 2001, "Building Thermal Network Model Based on State-space System Theory", Proceedings of 7th International IBPSA Conference, Rio de Janeiro, Brazil, pp.1051-1058.

[7] Elmqvist, H. and Mattsson, S.E., 1997, "Modelica – the Next Generation Modeling Language – an International Design Effort," Proceedings of 1st World Congress on System Simulation, WCSS'97, Singapore.

[8] Chow, T.T., Clarke, J.A. and Dunn, A., 1997, "Primitive Parts: an Approach to Air-conditioning Component Modelling," Energy and Buildings, Vol. 26, pp. 165-173.

[9] Chow, T.T., 1997, "Chilled Water Cooling Coil Models from Empirical to Fundamental," Numerical Heat Transfer, Part A, Vol. 32, pp.63-83.

[10] Chow, T.T. and Clarke, J.A., 1998, "Theoretical Basis of Primitive Part Modelling," ASHRAE Transactions, Vol. 104, Part 2, pp. 299-312.

APPENDIX

Part No. 4.2 Flow upon surface (for 2-phase fluid)

3 Nos. of Nodes:

S - solid surface
RM - fluid in contact
R1 - leaving fluid

1 No. of Connection:

R0 - incoming fluid

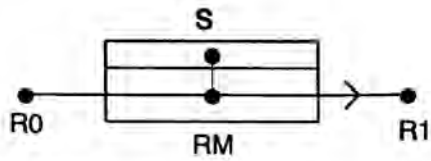

Energy flow matrix:

$$\begin{bmatrix} A(42,1) & A(42,2) & 0 & 0 \\ A(42,4) & A(42,5) & A(42,6) & A(42,11) \\ 0 & A(42,8) & A(42,9) & 0 \end{bmatrix} * \begin{bmatrix} \theta_s \\ \theta_{rm} \\ \theta_{r1} \\ \theta_{r0} \end{bmatrix} = \begin{bmatrix} B(42,1) \\ B(42,2) \\ B(42,3) \end{bmatrix}$$

where,

i) when $\theta_{rm} = \theta_{sat}$

self-coupled and cross-coupled coefficients:

$A(42,1) = -\alpha C_{rs} - (M_S C_S / Ni_S \cdot \delta t)$

$A(42,2) = 0$

$A(42,4) = 0$

$A(42,5) = 1$

$A(42,6) = 0$

$A(42,8) = 0$

$A(42,9) = 1$

$A(42,11) = 0$

present-time and excitation coefficients:

$B(42,1) = [(1-\alpha)\, C_{rs}^{*} - M_S^{*} C_S^{*} / (Ni_S \cdot \delta t)]\, \theta_S^{*}$
$- (1-\alpha) C_{rs}^{*}\, \theta_{rm}^{*} - \alpha C_{rs}^{*}\, \theta_{sat}$

$B(42,2) = \theta_{sat}$

$B(42,3) = \theta_{t1}$

where θ_{t1} is at the value of the previous iteration or of the previous time step.

ii) If $\theta_{rm} \neq \theta_{sat}$ for a particular time step, then

self-coupled and cross-coupled coefficients:

$A(42,1) = -\alpha C_{rs} - M_S C_S / (Ni_S \cdot \delta t)$

$A(42,2) = \alpha C_{rs}$

$A(42,4) = \alpha C_{rs}$

$A(42,5) = -\alpha C_{rs} - M_W C p_{wm} / (Ni_{rm} \cdot \delta t)$

$A(42,6) = -\alpha C_{r1}$

$A(42,8) = -1$

$A(42,9) = 1$

$A(42,11) = -\alpha C_{r0}$

present-time and excitation coefficients:

$B(42,1) = [(1-\alpha)\, C_{rs}^{*} - M_S^{*} C_S^{*} / (Ni_S \cdot \delta t)]\, \theta_S^{*}$
$- (1-\alpha) C_{rs}^{*}\, \theta_{rm}^{*} - \alpha C_{rs}^{*}\, \theta_{sat}$

$B(42,2) = -(1-\alpha) C_{rs}^{*}\, \theta_S^{*}$
$+ [(1-\alpha)\, C_{rs}^{*} - M_W^{*} C p_{wm}^{*} / (Ni_{rm} \cdot \delta t)]\, \theta_{rm}^{*}$
$+ (1-\alpha) C_{r1}^{*}\, \theta_{r1}^{*} - (1-\alpha) C_{r0}^{*}\, \theta_{r0}^{*}$

$B(42,3) = 0$

where,

$C_{rs} = h_{rs} A_{rs}$

$M_W = M_{wt} (1 - x_{r1})$

Notes:

1. No accumulation of fluid mass in the component is generally assumed (i.e. incompressible flow and therefore $m_{r0} = m_{rm} = m_{r1}$).
2. Q_S represents the heat transfer rate from solid surface to fluid at 2-phase flow,
   $Q_S = h_{rs} A_{rs} (\theta_S - \theta_{sat})$
   If $Q_S > 0$, fluid is heated, or the vice versa.
3. Under 2-phase flow fluid temperatures θ_{rm} and θ_{r1} are determined at the same time when the 1st & 2nd mass balances are solved; the following 3 individual cases are considered separately:
   Case A: $m_{w0} \neq 0$ & $m_{v0} \neq 0$
   (2-phase flow at inlet)
   Case B: $m_{w0} > 0$ & $m_{v0} = 0$
   (sub-cooled liquid at inlet)
   Case C: $m_{w0} = 0$ & $m_{v0} > 0$
   (superheated vapor at inlet)

Part No. 10.1 Heat injection (to solid)

1 No. of Node:
S – solid

1 No. of Excitation:
Q - heat input

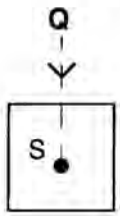

Energy flow matrix:

$[A(101,1)] * [\theta_s] = [B(101,1)]$

where,

$A(101,1) = -M_S C_S / (Ni_S \cdot \delta t)$

$B(101,1) = -[M_S^{*} C_S^{*} / (Ni_S \cdot \delta t)]\, \theta_S^{*} - [\alpha Q + (1-\alpha) Q^{*}]$

HEFAT2002
1st International conference on Heat Transfer, Fluid Mechanics, and Thermodynamics
8 – 10 April 2002, Kruger Park, South Africa
FR1

THE THERMAL BOUNDARY LAYER TRANSFER FOR NONISOTHERMAL SURFACES USING THE MODIFIED MERK SERIES OF CHAO AND FAGBENLE

by
R. Olayiwola Fagbenle,* PhD
Mechanical Engineering Dept. University of Ibadan, Ibadan, Nigeria.
e-mail: LayiFagbenle@hotmail.com

Abstract

The Chao and Fagbenle modification of the Merk series has been employed for the analysis of laminar boundary layer transfer for nonisothermal surfaces. In addition to the Prandtl number and the pressure gradient, a third parameter (the temperature parameter) was introduced in the analysis. Solutions of the resulting universal functions for the thermal boundary layer have been obtained for Prandtl number 0.72, 1, and 10 and for a range of the pressure gradient parameter λ and the temperature parameter γ. Very good agreement was obtained for the heat transfer in wedge-type flows with existing results. Efforts continue to find applications in nonsimilar flows for comparative purposes.

INTRODUCTION:

A detailed survey of the several procedures for predicting the transport behavior of boundary layer flows right from the earliest series of Blasius [1] to the local similarity wedge method of Gortler [2] Meksyn [3] and Merk [4] has been provided by Chao and Fagbenle [5]. A corrected form of Merk series was put forth by Chao and Fagbenle[5] and the resulting universal functions tabulated for forced convection of Newtonian fluids over isothermal surfaces. The Merk series besides generally giving better agreement with only one term than the other methods and with experiment, additionally makes possible rapid calculations of the transfer quantities with the aid of a limited number of universal functions. This essential feature has since been gainfully employed by later researchers in both natural and mixed convection flows [6-9].

In the present work, the Merk series are applied to the thermal laminar boundary layer forced convection flow over nonisothermal surfaces, $T_w(x)$, resulting in a 3-parameter set of universal functions, akin to the three-parameter "Merk-Chao-Fagbenle" series developed by Cameron et al [8] and Meissner et al [9] for the mixed convection flows. The resulting universal functions indeed reduce to those arising in the constant wall temperature problem for constant temperature parameter.

NOMENCLATURE

b	constant in power function wall temperature variation $(T_w(x)-T_\infty)=bx^n$
c	constant in power function main stream velocity variation $\frac{U}{2\nu} = c\,x^m$
f	dimensionless velocity function defined in equation (6)
L	reference length
m	exponent in power function mainstream velocity variation
n	exponent in power function wall temperature variation
Nu	Nusselt number
Pr	Prandtl number
r(x)	distance from a surface element of body of revolution to its axis of symmetry
T	temperature
U	velocity at the edge of the boundary layer
u	local velocity component parallel to the surface of the body
v	local velocity component perpendicular to the surface of the body

* Formerly Director of Energy Affairs and later Energy Advisor, Ministry of Minerals, Energy and Water Affairs, P|Bag 00378 Gaborone, Botswana, Southern Africa.

x spatial coordinate parallel to the surface of the body

y spatial coordinate perpendicular to the surface of the body

α thermal diffusivity

γ temperature parameter, defined in (15)

η dimensionless coordinates, defined in (5)

θ dimensionless temperature, defined in (10)

λ pressure gradient parameter, defined in (9)

ν kinematic viscosity

ς dimensionless coordinate, defined in (5)

ψ stream function, defined in (7)

Subscripts

$i(\geq 0)$ refers to the hierarchy of universal function

w refers to the wall or surface condition

∞ refers to the undisturbed free stream.

GOVERNING EQUATIONS:

The laminar boundary layer equations for steady, incompressible, uniform property fluid and non-dissipatives flow are,

for the flow boundary layer:

$$(ru)_x + (rv)_y = 0 \qquad (1a)$$

$$uu_x + vu_y = UU_x + \nu u_{yy} \qquad (1b)$$

with associated boundary conditions

$$u(x,0)=v(x,0)=0$$

$$u(x,y)\rightarrow U(x) \text{ as } y \rightarrow \infty \qquad (2a,b,c)$$

and for the thermal boundary layer:

$$uT_x + vT_y = \alpha T_{yy} \qquad (3)$$

with boundary conditions

$$T(x,0)=T_w(x)$$

$$T(x,y) \rightarrow T_\infty \text{ as } y\rightarrow \infty \qquad (4a,b)$$

where T_∞ is assumed constant.

Following Chao and Fagbenle [5] we introduce the dimensionless coordinates (ς, η) and the dependent variable $f(\varsigma, \eta)$:

$$\varsigma = \int_0^x \frac{U(x)}{U_\infty}\frac{r^2}{L^2}\frac{dx}{L}$$

$$\eta = \left(\frac{\mathrm{Re}}{2\varsigma}\right)^{\frac{1}{2}}\frac{U(x)}{U_\infty}\frac{r}{L}\frac{y}{L} \qquad (5a,b)$$

and

$$\psi(x,y) = U_\infty L\left(\frac{2\varsigma}{\mathrm{Re}}\right)^{\frac{1}{2}} f(\varsigma,\eta) \qquad (6)$$

where $\Psi(x,y)$ is the stream function defined by

$$u = \frac{L}{r}\frac{\partial \psi}{\partial y}, \quad v = -\left(\frac{L}{r}\frac{\partial \psi}{\partial x}\right) \qquad (7a,b)$$

The velocity components thus become

$$\frac{u}{U} = \frac{\partial f}{\partial \eta}$$

$$\frac{v}{U} = -\left(\frac{r}{L}\right)\frac{1}{(2\varsigma\,\mathrm{Re})^{\frac{1}{2}}}\left[f + 2\varsigma\frac{\partial f}{\partial \varsigma} + \left(\lambda + \frac{2\varsigma}{r}\frac{dr}{d\varsigma} - 1\right)\eta\frac{\partial f}{\partial \eta}\right] \qquad (8a,b)$$

where the pressure gradient "wedge" parameter λ is defined as

$$\lambda = \frac{2\varsigma}{U}\frac{dU}{d\varsigma} \qquad (9)$$

The momentum equation is accordingly transformed as given in [5] into

$$f''' + ff'' + \lambda[1-(f')^2] = 2\varsigma\frac{\partial(f'f)}{\partial(\varsigma,\eta)} \qquad (10)$$

with boundary conditions

$$f(\varsigma,0) = f'(\varsigma,0) = 0$$

$$f'(\varsigma,\eta) \rightarrow 1 \text{ as } \eta \rightarrow \infty \qquad (11a,b,c)$$

where the primes denote differentiation with respect to η and $\frac{\partial(f'f)}{\partial(\varsigma,\eta)}$ is the Jacobian.

We now define the dimensionless temperature

$$\theta(\varsigma,\eta) = \frac{T(x,y)-T_\infty}{T_w(x)-T_\infty} \qquad (12)$$

whereas in [5], T_w was taken as a uniform temperature. Hence , the thermal energy equation transforms to

$$\theta'' + \mathrm{Pr}\, f\theta' - \mathrm{Pr}\, f'\theta = 2\varsigma\,\mathrm{Pr}\frac{\partial(\theta,f)}{\partial(\varsigma,\eta)} \qquad (13)$$

with boundary conditions

$$\theta(\varsigma,0) = 1,\ \theta(\varsigma,\eta) \rightarrow 0 \text{ as } \eta \rightarrow \infty \qquad (14a,b)$$

and where

$$\gamma = \frac{2\zeta}{T_w(x)-T_\infty}\frac{d(T_w(x)-T_\infty)}{d\zeta} \qquad (15)$$

is the temperature parameter for the nonisothermal surface problem. Equation (13) thus has the additional term $-Pr\gamma f'\theta$ which the constant surface temperature problem lacks. Of course with $T_w(x)$=constant, $\gamma = 0$ and equation (13) reduces exactly to the same equation given in [5].

We now focus attention on the transformed thermal energy equation since the transformed momentum equation is unchanged, and we seek the series solution

$$f(\zeta,\eta) = f_0(\lambda,\eta) + 2\zeta\frac{d\lambda}{d\zeta}f_1(\lambda,\eta) + 4\zeta^2\frac{d^2\lambda}{d\zeta^2}f_2(\lambda,\eta) + (2\zeta\frac{d\lambda}{d\zeta})^2 f_3(\lambda,\eta) + \ldots$$

$$\theta(\zeta,\eta) = \theta_0(\lambda,\eta) + 2\zeta\frac{d\lambda}{d\zeta}\theta_1(\lambda,\eta) \qquad (16a,b)$$
$$+ 4\zeta^2\frac{d^2\lambda}{d\zeta^2}\theta_2(\lambda,\eta) + (2\zeta\frac{d\lambda}{d\zeta})^2\theta_3(\lambda,\eta)$$

The following hierachy of differential equations results on substituting (16a,b) into (13) and (14):

$$\theta_0'' + Pr[f_0\theta_0' - \gamma f_0'\theta_0] = 0 \qquad (17)$$

$$\theta_1'' + Pr[f_0\theta_1' - (\gamma+2)f_0'\theta_1] = \qquad (18)$$
$$Pr[\gamma f_1'\theta_0 - 3f_1\theta_0' + \frac{\partial(f_0,\theta_0)}{\partial(\lambda,\eta)}]$$

$$\theta_2'' + Pr[f_0\theta_2' - (\gamma+4)f_0'\theta_2] = \qquad (19)$$
$$Pr[\gamma f_2'\theta_0 - 5f_2\theta_0' + f_0'\theta_1 - f_1\theta_0']$$

$$\theta_3'' + Pr[f_0\theta_3' - (\gamma+4)f_0'\theta_3] = Pr[\gamma(f_1'\theta_2 + f_2'\theta_1) \qquad (20)$$
$$- 3f_1\theta_2' - 5f_2\theta_1' + 2f_1'\frac{\partial(f_0,\theta_1)}{\partial(\lambda,\eta)} + \frac{\partial(f_1,\theta_0)}{\partial(\lambda,\eta)}$$

with boundary conditions

$$\theta_0(\lambda,0)=1$$
$$\theta_i(\lambda,0)=0 \quad (i>0)$$
$$\theta_i(\lambda,\eta)\to 0 \text{ as } \eta\to\infty \quad (i>0) \qquad (21a,b,c)$$

Numerical solutions and estimate of their accuracy:

Numerical solutions for the equations for f_i(i=0,1,1,2, and 3) have been extensively tabulated by Chao and Fagbenle in the appendix of [5] and need not be repeated in this work. The numerical solutions and estimates of their accuracy were also extensively discussed in [5] and confirmed by later researchers such as Cameron et al [8] who commented that their own results for the case of forced convection when compared to the results of Chao and Fagbenle showed that , " for the first order equations, the results match for the first four significant figures", and that " higher order functions occasionally differ by as much as 10%, but over most of the range for λ the difference is 1% or less". They further correctly observed that "for a series (i.e. the Merk series) which converges rapidly, the higher order terms are much smaller the first order term and have little effect on the overall solution".

Previous work on variable surface temperature problems have been generally on wedge type flows with power law surface variation, viz. $(T_w(x)-T_\infty)=bx^n$ and free stream velocity $\frac{U}{U_\infty}=cx^m$. In such flows, the wedge parameter λ is related to the temperature parameter γ by $\gamma=n(2-\lambda)$. Furthermore the first temperature universal function $\theta_0$is also the complete solution on account of the fact that λ=constant in such flows. It is well known that for wedge flows and power law wall temperature variation both the velocity and temperature fields are similar and the complete solution to the problem is given by the heat transfer function.

$$Nu\,Re^{-\frac{1}{2}} = -\frac{r}{L}(\frac{U}{U_\infty})(2\zeta)^{-\frac{1}{2}}\theta_0'(\lambda;0;Pr;\gamma) \qquad (22)$$

and the temperature profile by

$$\theta(\varsigma,\eta) = \theta_0(\lambda;\eta;Pr;\gamma) \qquad (23)$$

The wall derivatives of the universal functions $\theta'_0(\lambda,0)$ have been generated for :

$-0.15\le\lambda\le 1.0$ in steps of $\Delta\lambda=0.05$,

$0 \le n \le 5$ in steps of $\Delta n=0.25$ and for Pr=0.72, 1 and 10 and representative tabulations appear in

tables 1 and 2 for λ=-0.15 and 0 and for λ=0.5 and 1.0 respectively

While noting that generally, previous work on variable surface temperature problems have been on wedge flow with power law wall temperature, such problems unfortunately do not bring out the essential features of Merk's method which aim at nonsimilar problems. Efforts are under way at finding such nonsimilar problems in the literatures to which the present results can be applied for comparative purposes. It should be remarked however that a number of examples of wedge flows with power law wall variations were considered and the present heat transfer results compare very favourably with results in the literature.

The flows considered were the Blasius flow (λ=0;Pr=0.72) and the stagnation flow (λ=1;Pr=1 and Pr=10). Comparison made with results of Chapman and Rubesi [10], Levy [11], Lighthill [12], Fettis [13], Schuh [14] and Imai [15] were within 4% in the worst case but generally within 1%.

CONCLUDING REMARK

The series method of Merk which was corrected and extended by Chao and Fagbenle [5] has been applied to the boundary layer flows over surfaces of non-uniform temperature. Equations governing the first four temperature universal functions θ_i(i=0,1,2, and 3) have been obtained, these being functions of three parameters, namely, Pr, λ and γ. Tabulations of the wall derivatives of the first temperature universal functions $\theta_o$have been provided for Pr=0.72, 1 and 10 and $0 \leq n \leq 5$ for the wedge flow with power law wall temperature variation. Efforts are under way to find nonsimilar flows to which the present results would be applied to bring out the essential features of Merk's method.

Table 1: Wall Derivatives of Universal Temperature Functions

$\theta_o'(\lambda,0)$; γ=n(2-λ); λ=-0.15 and 0.0

λ=-0.15				
N	γ	Pr		
		0.72	1.0	10.0
0	0	0.36776189	0.40933631	0.85084867
0.25	0.54	0.44695913	0.49672152	1.03153651
0.5	1.08	0.50578582	0.56169846	1.16680102
1	2.15	0.59352972	0.65877273	1.37029291
2	4.30	0.71490901	0.79335099	1.65460348
3	6.45	0.80343343	0.89166528	1.86342385
4	8.60	0.87494402	0.97115657	2.03273972
5	10.75	0.93578981	1.03883186	2.17714050

λ=0.0			
γ	Pr		
	0.72	1.0	10.0
0	0.41809128	0.46959999	1.02974731
0.5	0.50971913	0.57140650	1.24608125
1	0.57964597	0.64908194	1.41122067
2	0.68587589	0.76713237	1.66271396
4	0.83507471	0.93308866	2.01739679
6	0.94481675	1.05526158	2.27916266
8	1.03381900	1.15439494	2.49165042
10	1.10972693	1.23897037	2.67345431

Table 2: Wall Derivatives of Universal Temperature Functions

$\theta_o'(\lambda,0)$; γ=n(2-λ); λ=0.5 and 1.0

λ=0.5				
n	γ	Pr		
		0.72	1.0	10.0
0	0	0.47561389	0.53897894	1.23889199
0.25	0.38	0.56238971	0.63595860	1.44866679
0.5	0.75	0.63276353	0.71449034	1.61767989
1	1.50	0.74447889	0.83903703	1.88496831
2	3.00	0.90725422	1.02040976	2.27375939
3	4.50	1.02932155	1.15641797	2.56540382
4	6.00	1.12911974	1.26762642	2.80400659
5	7.50	1.21460210	1.36289360	3.00850561

λ=1.0			
γ	Pr		
	0.72	1.0	10.0
0	0.50143407	0.57046525	1.33879679
0.25	0.56652015	0.64343361	1.49821100
0.5	0.62264815	0.70625971	1.63463553
1	0.71662550	0.81130133	1.86157695
2	0.86095459	0.97239415	2.20809071
3	0.97270988	1.09703108	2.47566455
4	1.06542611	1.20040456	2.69749177
5	1.14549395	1.28966573	2.88903274

ACKNOWLEDGEMENT

The magnanimous effort of Mr T.A.O. Salau, a fellow faculty member, in quickly typing the manuscript on the computer, is greatly appreciated.

REFERENCES

1. H. Blasius, Grenzschichten in Flüssigkeitn mit kleiner Reinbung , Z. Math, Phys. 56, 1-37 (1908). English translation in NACA TM 1256.
2. H. Görtler, A new series for the calculation of staedy laminar boundary layer flows, J. Math. Mech. 6, 1-66 (1957)
3. D. Meksyn, New Methods in Laminar Boundary Layer Theory, Chapters 6, 7 and 9. Pergamon Press, Oxford (1961)
4. H.J. Merk, Rapid calculations for boundary layer transfer using wedge solutions and asymptotic expansions, J. Fluid Mech. 5, 460-480 (1959)
5. B.T. Chao and R.O. Fagbenle, On Merk's method of calculating boundary layer transfer, Int. J. Heat Mass Transfer 17, 223-240 (1974)
6. H.W. Kim, D.R. Jeng and K.J. De Witt, Momentum and Heat transfer in power law fluid flow over two dimensional or axisymmetric bodies of arbitrary contour. Int. J. Heat Mass Transfer 26, 245-259 (1983)
7. T.A. Chang, D.R. Jeng and K.J. De Witt, Natural convection to power law fluids from two dimensional or axisymmetric bodies of arbitrary contour. Int. J. Heat Mass Transfer 31, 615-624 (1988)
8. M.R. Cameron, D.R. Jeng and K.J. De Witt, Mixed convection and natural convection from two-dimensional or axisymmetric bodies of arbitrary contour. Int. J. Heat Mass Transfer 34, 582-587 (1991).
9. D.L. Meissner, D.R. Jeng and K.J. De Witt, Mixed convection to power-law fluids from two-dimensional or axisymmetric bodies. Int. J. Heat Mass Transfer 37, 1475-1485 (1994)
10. D.R. Chapman and W.M. Rupesin, Temperature and velocity profiles in the compressible laminar boundary layer with arbitrary distribution of surface temperature, J. Aero. Sci. 16, 547-565 (1949).
11. S. Levy, Heat transfer to constant property laminar boundary layer flows with power-function free stream velocity and wall-temperature variation. J, Aero. Sci. 19, 341-348 (1952)
12. M.J. Lighthill, Contributions to the theory of heat transfer through a laminar boundary layer. Proc. Roy. Soc. London A202, 359-377 (1950)
13. H.E. Fettis, On a differential equation occurring in the theory of heat flow in boundary layers with Hartre's velocity profile. J. Aero. Sci. 21, 132-133 (1954)
14. H. Schuh, On asymptotic solutions for the heat transfer at varying wall temperatures in a laminar boundary layer with Hartree's velocity profiles. J. Aero. Sci. 20, 146-147 (1953)
15. I. Imai, On the heat transfer to constant property laminar boundary layers with power-function free-stream velocity and wall-temperature distributions. Quart. J. Appl. Math. 16, 33-45 (1958)

HEFAT2002
1st International Conference on Heat Transfer, Fluid Mechanics and Thermodynamics
8-10 April 2002, Kruger National Park, South Africa
MT1

NUMERICAL PREDICTION OF DEVELOPING LAMINAR MIXED CONVECTION IN AN INCLINED TUBE FOR DIFFERENT REYNOLDS NUMBERS

T. Maré, P. Noirault and J. Miriel
GRGC, INSA de Rennes
35043 Rennes Cedex, France
thierry.mare@iutsm.univ-rennes1.fr

N. Galanis
THERMAUS, Université de Sherbrooke
Sherbrooke, QC, Canada J1K 2R1
nicolas.galanis@gme.usherb.ca

ABSTRACT

The three dimensional, elliptical, steady state, laminar conservation equations for developing mixed convection in an isothermal tube have been solved numerically. The flow field in an inclined tube is highly asymmetrical unlike that for a vertical tube. In the entry region of inclined tubes, the velocity below the centerline decelerates rapidly and reaches a minimum value which decreases, as the Reynolds number becomes smaller. For Re=25 and $Gr=10^6$ an asymmetrical flow reversal zone is observed which is unlike those in vertical and horizontal tubes. Far downstream the flow is isothermal and the velocity profile tends towards the Poiseuille distribution.

INTRODUCTION

Mixed convection in tubes has been studied both experimentally [1] and numerically [2] because of its widespread occurrence in engineering installations (heat exchangers, nuclear reactors, solar collectors, etc.). Experimental investigations usually provide only partial results such as axial velocity profiles, temperature distributions, average heat transfer coefficients and overall pressure losses. However, in order to design such installations and to predict their off-design performance, it is desirable to obtain a more complete description of the velocity, pressure and temperature distributions under all operating conditions. To achieve this goal it is necessary to solve the partial differential equations expressing the conservation of mass, energy and momentum. These equations are non-linear, elliptic in all three directions and coupled, because of the buoyancy force generated by the temperature gradients. For steady state, laminar, fully developed conditions, Hallman [3] has obtained an analytical solution. For developing, unsteady and turbulent flows the solution can only be determined numerically.

Most studies of mixed convection in tubes have focussed on vertical and horizontal flows. Jackson et al [4] presented a comprehensive review of early experimental and theoretical studies for the vertical case. More recently, Wang et al [5] studied numerically the steady state developing laminar flow of a Boussinesq fluid in an isothermal pipe. They identified the regime of reverse flow for horizontal and vertical tubes. Similar results were presented by Zghal et al [6] for a vertical pipe with uniform heat flux at the fluid-solid interface. Su and Chung [7] performed a linear stability analysis and found that mixed convection flow in a vertical pipe with constant heat flux can become unstable at low Reynolds and Rayleigh numbers irrespective of the Prandtl number. The effects of the tube's inclination on the flow structure as well as on the axial evolution of the average wall-shear stress and of the average Nusselt number were investigated by Orfi et al [8]. Further results [9] showed the existence of multiple solutions for different combinations of Pr, Re, Gr and tube inclinations. They were, however, obtained using an axially parabolic model and did not therefore predict flow reversal which has been observed experimentally [10].

The purpose of the present study is to extend the previous numerical results by solving the elliptical equations for laminar, developing, and steady state mixed convection in an inclined isothermal tube. In this paper we present the model, the solution method and results for flows with aiding buoyancy.

NOMENCLATURE

D	internal tube diameter
g	acceleration of gravity
L	tube length
P	pressure

R, ϕ, Z	radial, circumferential, axial coordinates
T_O	uniform temperature at Z = 0
T_W	wall temperature
V_O	mean axial velocity
V_R, V_ϕ, V_z	velocity components
X, Y, Z	cartesian coordinates
α	tube inclination
β	thermal expansion coefficient
a	thermal diffusivity
$\theta = \frac{T - T_0}{T_W - T_0}$	non-dimensional temperature
μ	dynamic viscosity
ρ	density
$u = Vz/V_0$, $Ue = V_0$	non-dimensional velocity
r=R/D, y=Y/D	non-dimensional coordinates

FORMULATION AND NUMERICAL PROCEDURE

The problem under consideration and the coordinate system are shown in Figure 1. The plane defined by x=0 is vertical. A Newtonian fluid enters an isothermal tube with a parabolic velocity profile and a uniform temperature. The flow is directed upwards and the wall temperature is higher than the fluid entry temperature. The fluid is considered incompressible with constant physical properties, except for the density in the buoyancy terms where the Boussinesq approximation is applied. Steady state conditions are assumed to prevail while the dissipation and pressure work are neglected.

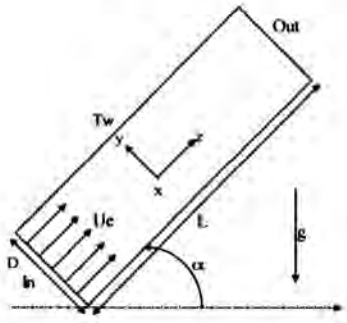

Figure 1. Schematic representation of system.

Under these assumptions the governing equations in cylindrical coordinates are as follows:

$$\frac{1}{R}\frac{\partial}{\partial R}\left(RV_R\right) + \frac{1}{R}\frac{\partial V_\phi}{\partial \phi} + \frac{\partial V_Z}{\partial Z} = 0 \qquad (1)$$

$$\rho\left(V_R\frac{\partial V_R}{\partial R} + \frac{V_\phi}{R}\frac{\partial V_R}{\partial \phi} - \frac{V_\phi^2}{R} + V_Z\frac{\partial V_R}{\partial Z}\right) =$$

$$= \mu\left(\nabla^2 V_R - \frac{V_R}{R^2} - \frac{2}{R^2}\frac{\partial V_\phi}{\partial \phi}\right) - \frac{\partial P}{\partial R} - \rho g \cos\alpha \cos\phi \qquad (2)$$

$$\rho\left(V_R\frac{\partial V_\phi}{\partial R} + \frac{V_\phi}{R}\frac{\partial V_\phi}{\partial \phi} - \frac{V_\phi V_R}{R} + V_Z\frac{\partial V_\phi}{\partial Z}\right) =$$

$$= \mu\left(\nabla^2 V_\phi - \frac{V_\phi}{R^2} - \frac{2}{R^2}\frac{\partial V_R}{\partial \phi}\right) - \frac{1}{R}\frac{\partial P}{\partial \phi} + \rho g \cos\alpha \sin\phi \qquad (3)$$

$$\rho\left(V_R\frac{\partial V_Z}{\partial R} + \frac{V_\phi}{R}\frac{\partial V_Z}{\partial \phi} + V_Z\frac{\partial V_Z}{\partial Z}\right) =$$

$$= \mu\nabla^2 V_Z - \frac{\partial P}{\partial Z} - \rho g \sin\alpha \qquad (4)$$

$$V_R\frac{\partial T}{\partial R} + \frac{V_\phi}{R}\frac{\partial T}{\partial \phi} + V_Z\frac{\partial T}{\partial Z} = a\nabla^2 T \qquad (5)$$

where $\rho = \rho_0[1 - \beta(T - T_0)]$ (6)

The boundary conditions are:
for Z = 0 and $0 \le R \le D/2$:
$V_R = V_\phi = 0$, $T = T_O$ and $V_Z = 2\,V_O[1 - 4\,(R/D)^2]$
for $0 < Z < L$ and R = D/2 :
$V_R = V_\phi = V_z = 0$ and $T = T_W$
for Z = L and $0 \le R \le D/2$ all derivatives with respect to Z are equal to zero.

The set of partial differential equations was discretized with the control volume technique FLUENT. A first order upwind method was used to interpolate the variables while the PISO algorithm was introduced for the velocity – pressure coupling. This algorithm PISO perform two additionanl corrections: neighbor correction end skewness correction. The pressure was calculated with a body-force weighed scheme and a segregated solution method was used to solve the discrete equations sequentially. The discretization grid is uniform in the circumferential direction and non-uniform in the other two directions: it is finer near the tube entrance and near the wall where the velocity and temperature gradients are large. Different grid distributions have been tested to ensure that the calculated results are grid independent. The adopted grid is uniform in the circumferential direction and non-uniform in the other two directions with greater density near the tube entrance and the wall where velocity and temperature gradients are large. It consists of 24, 32 and 100 nodes in the circumferential, radial and axial directions respectively.

RESULTS AND DISCUSSION

The results are presented in non-dimensional form. Reference quantities used are the tube diameter D, the mean axial velocity V_o and the difference $(T_W - T_O)$. With this formulation, the solution of the partial differential equations depends on the tube inclination and the following three non-dimensional groups:

$Pr = \mu/a\rho, \quad Re = \rho V_o D/\mu, \quad Gr = g\beta\rho^2 D^3(T_w - T_o)/\mu^2$ (7)

Alternatively, the Reynolds, Richardson and Péclet numbers can be used to characterize the flow conditions. All the results presented here were calculated with Pr = 0.7.

Validation

In order to validate the model and the numerical procedure, the calculated velocity and temperature profiles for Re = 380 and Gr = 10^6 were compared with corresponding measured values [11] for a vertical tube. Figure 2 shows that the agreement is quite good except for the temperature very close to the tube entry. However, according to the authors of the experimental study, these measured temperature values are not reliable due to important end effects. Therefore, we consider that the model and numerical scheme provide a good description of the hydrodynamic and thermal fields. Thus, they can be used to pursue the objectives of our study.

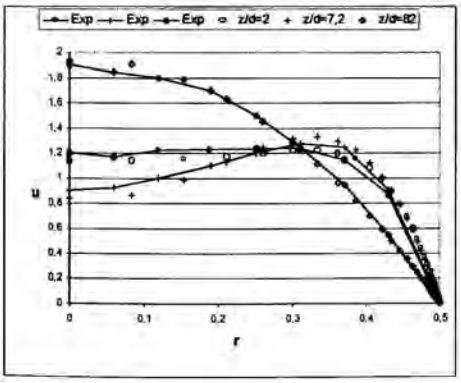

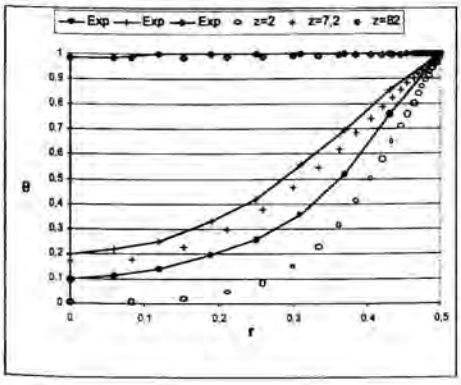

Figure 2. Comparison of measured and calculated velocity & temperature profiles (α=90°, Pr=0.7, Re=380, Gr=10^6) Exp = Zeldin and Schmidt, z=Z/D

Effects of inclination

Figures 3 and 4 respectively compare the velocity and temperature distributions in the plane X = 0 for vertical and inclined (α= 45°) tubes with the previously specified flow conditions (Re = 380, Gr = 10^6).

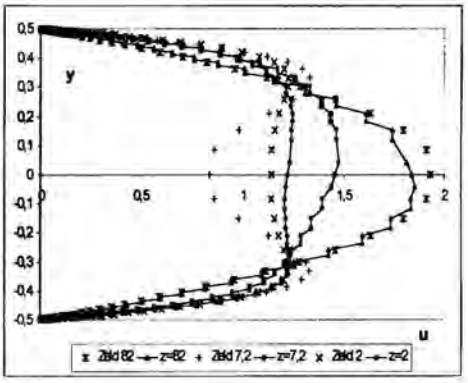

Figure 3. Comparison of calculated velocities for α=90° and α=45° (Pr=0.7, Re=380, Gr=10^6, X=0) Zeld = Zeldin and Schmidt, z=Z/D

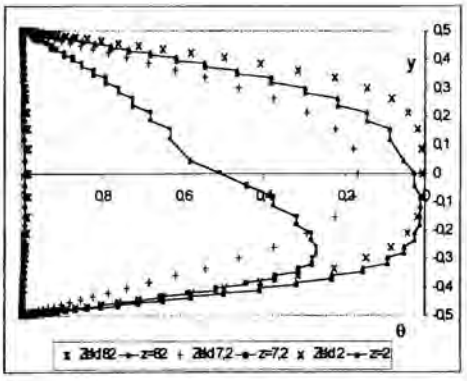

Figure 4. Comparison of calculated temperatures for α=90° and α=45° (Pr=0.7, Re=380, Gr=10^6, X=0) Zeld = Zeldin and Schmidt, z=Z/D

In the case of the vertical tube, the velocity and temperature fields are axisymetric. The temperature is lowest

at the centerline and increases monotonically with distance from the tube axis. The buoyancy induced acceleration corresponding to this temperature distribution gives rise to a velocity profile, which exhibits a maximum away from the centerline. Thus at Z/D = 2 (i.e. close to the tube entrance) the velocity at the centerline is approximately 1.1 and its maximum value occurring at Y/D = ±0.35 is approximately 1.2. This distortion is even more pronounced at Z/D = 7.2 where the centerline velocity is approximately 0.8 and its maximum value is 1.3. Very far downstream, at Z/D = 82, the temperature tends to become uniform (θ= 1) and the buoyancy effects disappear. Therefore, the velocity profile tends to the parabolic Poiseuille distribution as $Z \rightarrow \infty$.

In the case of the inclined tube, symmetry with respect to the centerline does not exist. At any given cross section the warm fluid rises towards the top half of the tube. Thus the minimum temperature occurs in the bottom half as shown in Figure 4. Heat transfer in the XY plane is augmented beyond the conductive transport by the corresponding buoyancy induced motion. Thus, at any given cross section, the minimum temperature in the inclined tube is higher than the corresponding value in the vertical tube. This difference is present at Z/D = 2 but is more evident at Z/D = 7.2. The corresponding axial velocity profiles are also influenced by the combined effect of the axial and cross-sectional components of the buoyancy force. They are also quite different from those in the vertical tube, especially at Z/D = 7.2. At that particular cross section, the maximum velocity occurs slightly above the centerline and is approximately equal to 1.5. The difference between the slopes of this distribution at the top and bottom of the tube should be noted: it indicates that the wall shear stress varies considerably along the circumference. Far downstream, at Z/D = 82, the temperature again tends to become uniform (θ= 1) but the velocity profile is not as close to the parabolic Poiseuille distribution as for the vertical tube.

Effects of the Reynolds number

Figures 5 and 6 respectively show the velocity and temperature axial evolution for three different radial positions in the plane X = 0 of an inclined tube (α= 45°).

In the zone immediately following the tube entrance (Z/D < 5) the radial temperature gradient is very important and a considerable fraction of the fluid is still at T_o (θ= 0). In this zone, the velocity undergoes significant variations as Z increases and the influence of the Reynolds number is indeed considerable. It must be noted that, in this zone, the velocity profile is not symmetrical with respect to the centerline as shown earlier (fig. 3). The most significant characteristic of the velocity variation in this zone is its important decrease which occurs shortly after the tube entrance. This phenomenon is

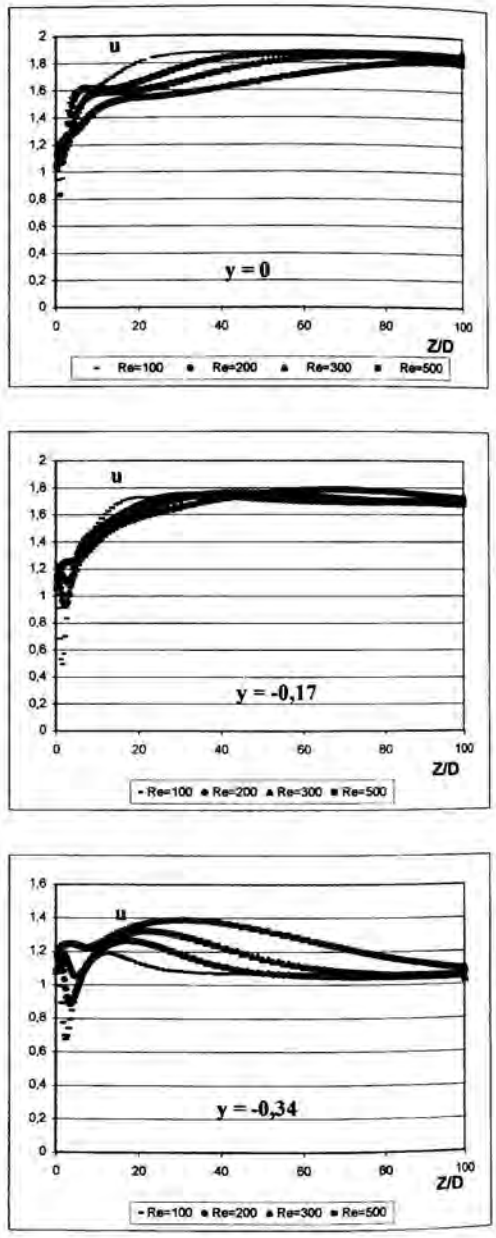

Figure 5. Effect of Re on the velocity evolution at selected radial positions (α=45°, Pr=0.7, Gr=10^6, X=0)

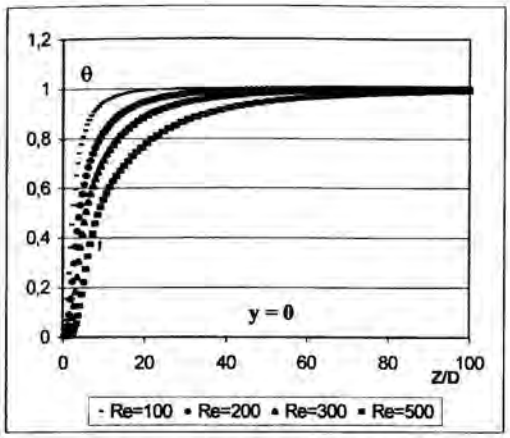

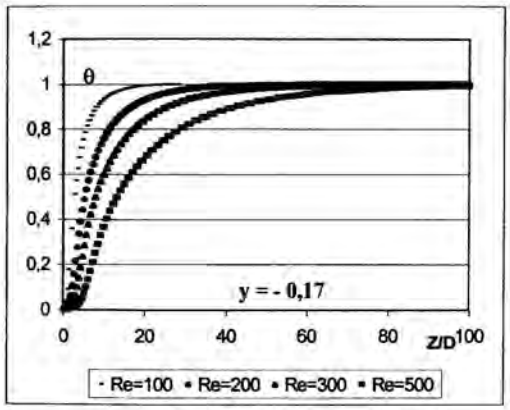

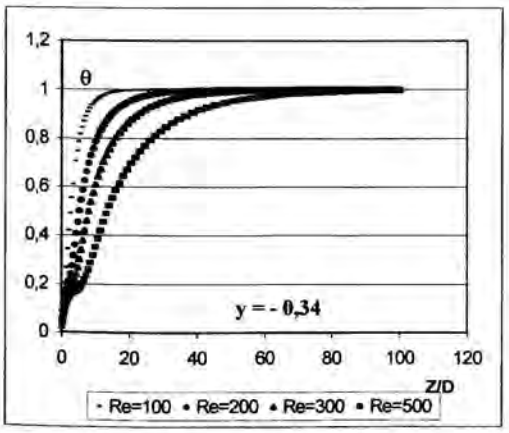

Figure 6. Effect of Re on the temperature evolution at selected radial positions (α=45°, Pr=0.7, Gr=10^6, X=0)

most pronounced at Y/D = -0.17. The minimum value of V/V_o decreases when the Reynolds number decreases. This evolution of the velocity is due to the fact that the hot fluid is moving to the top of the tube under the influence of the Y component of the buoyancy force. Furthermore, the hot fluid in the top half of the tube accelerates in the X direction under the influence of the corresponding component of the buoyancy force. Therefore, to preserve continuity, the axial velocity in the bottom half of the tube decreases. Since Gr = constant, these effects of buoyancy become progressively more important as the Reynolds number decreases (or, equivalently, as the Richardson number increases). Thus, it is understandable that the minimum velocity decreases as Re decreases.

Based on these observations and tendencies, we can expect that the minimum velocity may become negative if the Reynolds number is sufficiently small. Figure 7 illustrates such a situation with flow reversal for Re = 25. This flow field is dominated by natural convection. We notice that, in this case, the zone of negative velocities extends on both sides of the centerline but it's extent, as well as the velocity profile, are not symmetrical with respect to the tube axis. This velocity profile along the vertical diameter of the tube is therefore characterized by the existence of two asymmetrical points with V = 0. This position of the flow reversal zone is very different from those observed in vertical [5,6] and horizontal [5] tubes. Thus, for vertical tubes, the flow reversal zone is symmetrical about the tube axis. On the other hand, for horizontal tubes the flow reversal zone is attached to the upper part of the wall. For this last geometry there is therefore only one point on the vertical diameter (other than at Y = ± D/2) where V = 0.

Finally, as noted earlier, at the tube outlet (Z/D = 100) the temperature distribution is essentially uniform. The corresponding velocity profile is symmetrical and independent of the Reynolds number. This is consistent with the analytical solution for fully developed laminar isothermal flow. However, the numerical values are slightly smaller than the ones predicted by the parabolic Poiseuille distribution. We attribute this result to the fact that the tube is not sufficiently long to achieve developed hydrodynamic conditions.

Figure 7. Velocity vectors showing flow reversal (α=45°, Pr=0.7, Re=25, Gr=10^6, X=0)

CONCLUSION

Developing mixed convection in an isothermal inclined tube has been analyzed numerically. The hydrodynamic and thermal fields are quite different from those in a vertical tube. In particular, the position of flow reversal (which has been observed for Re=25, Gr=10^6) is very different from those in horizontal and vertical tubes.

REFERENCES

[1] Barozzi G.S., Zanchini E. and Marotti M., 1985, "Experimental Investigation of Combined Forced and Free Convection in Horizontal and Inclined Tubes", Meccanica, 20 no. 1, pp. 18-27.

[2] Choudhury D. and Patankar S.V., 1988, "Combined Forced and Free Laminar Convection in the Entrance Region of an Inclined Isothermal Tube", ASME J. Heat Transfer, 110, pp. 901-908.

[3] Hallman T.M., 1956, "Combined Forced and Free Laminar Heat Transfer in Vertical Tubes with Uniform Internal Heat Generation", ASME J. Heat Transfer, pp. 1831-1841.

[4] Jackson J.D., Cotton M.A. and Axcell B.P., 1989, "Studies of Mixed Convection in Vertical Tubes", Int. J. Heat & Fluid Flow, 10, no. 1, pp. 2-15.

[5] Wang M., Tsuji T. and Nagano Y., 1994, "Mixed Convection with Flow Reversal in the Thermal Entrance Region of Horizontal and Vertical Pipes", Int. J. Heat Mass Transfer, 37 no.15, pp. 2305-2319.

[6] Zghal M., Galanis N. and Nguyen C.T., 2001, "Developing Mixed Convection with Aiding buoyancy in Vertical Tubes: a Numerical Investigation of Different Flow Regimes", Int. J. Therm. Sci. (in press).

[7] Su Y-C. and Chung J. N., 2000,"Linear Stability Analysis of Mixed Convection Flow in a Vertical Pipe", J. Fluid Mech., 422,pp. 141-166.

[8] Orfi J., Galanis N. and Nguyen C. T., 1998, "Laminar Mixed Convection in the Entrance Region of Inclined Pipes with High Uniform Heat Fluxes", ASHRAE Transactions, 104 pt. 2, pp. 417-428.

[9] Orfi J., Galanis N. and Nguyen C.T., 1999, "Bifurcation in Steady Laminar Mixed Convection Flow in Uniformly Heated Inclined Tubes", Int. J. Num. Meth. Heat & Fluid Flow, 9 no. 5, pp. 660-676.

[10] Lavine A.S., Kim M.Y. and Shores C.N., 1989, "Flow Reversal in Opposing Mixed Convection Flow in Inclined Pipes", ASME J. Heat Transfer, 111, pp. 114-120.

[11] Zeldin B. and Schmidt F.W., 1972, "Developing Flow with Combined Forced Free Convection in an Isothermal Vertical Tube", ASME J. Heat Transfer, 94, pp.211-223.

HEFAT2002
1st International Conference in Heat Transfer, Fluid Mechanics and Thermodynamics
8-10 April 2002, Kruger Park, South Africa
HB1

A NUMERICAL STUDY OF ENERGY SEPARATION IN A JET FLOW

B. Han* and R.J. Goldstein**
*Post-Doc Research Associate; **Professor
Department of Mechanical Engineering
University of Minnesota
111 Church Street SE
Minneapolis, MN55455
U.S.A.
E-mail: rjg@me.umn.edu

ABSTRACT

"Energy separation" is the re-distribution of the total energy in a flowing fluid without external work or heat, so that some portion of the fluid has higher and other portion has lower total energy (temperature) than the remaining fluid. In the present study, the mechanism of energy separation is investigated numerically in a viscous circular free jet. A numerical code is developed to solve mass, momentum and total energy conservation equations using an equal-order linear finite element and fractional four-step method.

The computational results show that the roll-up and transport of vortices induce a pressure fluctuation in the flow field. Fluid, which flows through the disturbed pressure field, exchanges pressure work with the surroundings and separates into higher and lower total temperature regions. The results also indicate that vortex-pairing process significantly intensifies the pressure fluctuation in the flow field. The corresponding total temperature difference between hot and cold regions is also intensified. This implies that the vortex pairing process is a very important process in intensifying energy separation.

INTRODUCTION

"Energy separation" is the re-distribution of the total energy in a flowing fluid without external work or heat, so that some portion of the fluid has higher and other portion has lower total energy (temperature) than the remaining fluid. Since this interesting phenomenon was observed in a vortex tube (or Ranque-Hilsch tube) in the 1930's, many researchers have reported that energy separation could be observed in various flow situations including free jets [1-3], impinging jets [4] and flows across a circular cylinder. [5, 6] However, the detailed mechanism of energy separation is not yet fully understood.

A theoretical model for energy separation was provided recently by Eckert [7]. He suggested two physical mechanisms of energy separation. One is the imbalance between the energy transport by viscous shear work and by heat conduction. The other is due to pressure fluctuation within a flow field caused by moving vortices. Unlike the energy separation due to shear/conduction imbalance, that from pressure fluctuation has time-dependent characteristics. He also pointed out that energy separation in a viscous flow is caused by both mechanisms. Kurosaka et al. [5] proposed a more detailed model of total temperature variation around a transporting vortex in a vortex street.

Though most previous studies were based on time-averaged temperature measurements, research on the instantaneous mechanism of energy separation is essential to understand the phenomena due to the pressure fluctuation. Recently a few studies were performed to investigate the instantaneous mechanism experimentally and numerically. Fox et al. [1] performed a numerical analysis of energy separation in an inviscid and non-heat conducting jet and investigated the mechanism of energy separation. They showed that energy separation in a jet flow is caused by the pressure fluctuation induced by the large scale coherent structure of ring vortices. Han and Goldstein [8] carried out a numerical analysis for a plane shear layer by solving the two-dimensional Navier-Stokes equations. However, their analysis assumed a non-heat conducting fluid.

In the present study, the mechanism of energy separation is numerically investigated in a viscous, and heat-conducting jet flow. Not only the energy separation by the pressure fluctuation, but also that by the shear/conduction imbalance is studied. The effect of Re_D on the coherent vortical structure and the energy separation is also investigated. The results reveal the mechanism of instantaneous energy separation and will improve the understanding of energy separation.

NOMENCLATURE

c_p	Specific heat of a fluid at constant pressure
D	Diameter of nozzle
k	Thermal conductivity of a fluid

p	Static pressure
Pr	Prandtl number of a fluid, $=\frac{\mu c_p}{k}$
r	Radial coordinate
Re_D	Reynolds number based on a nozzle diameter, $=\frac{\rho U_e D}{\mu}$
S	Energy separation factor, $=\frac{T_t - T_{t,o}}{U_e^2/2c_p}$
S'	R.M.S. value of energy separation factor fluctuation
S_m	Time-averaged energy separation factor
T_s	Static temperature
T_t	Total temperature
$T_{t,o}$	Total temperature of the jet at the nozzle exit
t	Time
u	Velocity component in x direction
$\underline{u}$	Velocity vector
U_e	Velocity at the nozzle exit
v	Velocity component in r direction
v_d	Disturbance profile at the inlet plane
x	Axial coordinate from the nozzle exit

Greek Letters

δ_o	Initial shear layer thickness
χ	Scalar variables for the boundary condition at the outlet
ω	Vorticity
ω_j	Frequency of disturbance
ϕ_j	Phase angle of disturbance
ρ	Density of a fluid
μ	Dynamic viscosity of a fluid
τ_{ij}	Viscous shear stress tensor

MATHEMATICAL AND NUMERICAL FORMULATION

The computational domain and coordinate system are illustrated in Fig. 1. A jet with a very thin initial shear layer exits a circular nozzle with velocity U_e into a stationary fluid of the same composition. The governing equations are mass conservation and unsteady Navier-Stokes equations, and total energy conservation equation. With the assumptions of incompressible, constant properties and axisymmetry, the nondimensional governing equations can be written as follows:

$$\nabla \cdot \underline{u} = 0 \tag{1}$$

$$\rho \frac{D\underline{u}}{Dt} = -\nabla p + \mu \nabla^2 \underline{u} \tag{2}$$

$$\rho c_p \frac{DT_t}{Dt} = \frac{\partial p}{\partial t} + k\nabla^2 T_s + \nabla \cdot \left(\underline{u} : \tau_{ij}\right) \tag{3}$$

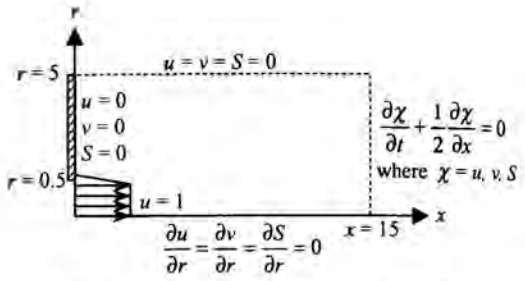

Fig. 1 Schematic diagram of the calculation domain

Eqs. (1) and (2) can be nondimensionalized using U_e as characteristic velocity and the nozzle diameter D as characteristic length. The pressure, p, is normalized by ρU_e^2. Nondimensional variables are denoted by superscript "*".

$$\nabla^* \cdot \underline{u}^* = 0 \tag{4}$$

$$\frac{D\underline{u}^*}{Dt^*} = -\nabla^* p^* + \frac{1}{\mathrm{Re}_D}\nabla^{*2}\underline{u}^* \tag{5}$$

For the total energy conservation equation, the energy separation factor, S, is introduced as a nondimensional temperature.

$$\mathrm{S} = \frac{T_t - T_{t,o}}{U_e^2/2c_p} \tag{6}$$

$$\frac{D\mathrm{S}}{Dt^*} = \frac{1}{2}\frac{\partial p^*}{\partial t^*} + \frac{1}{\mathrm{Re}_D \mathrm{Pr}}\nabla^{*2}\left(\mathrm{S} - \underline{u}^* \cdot \underline{u}^*\right) + \frac{2}{\mathrm{Re}_D}\nabla^* \cdot \left(\underline{u}^* : \tau_{ij}^*\right) \tag{7}$$

For convenience, the superscript "*" will be dropped. Using the axisymmetry and boundary layer assumptions, Eq. (7) is reduced as follows:

$$\frac{DS}{Dt} = \frac{1}{2}\frac{\partial p}{\partial t} + \frac{1}{\mathrm{Re}_D \mathrm{Pr}}\nabla^2 S + \frac{2}{\mathrm{Re}_D}\left[1 - \frac{1}{\mathrm{Pr}}\right]\frac{1}{r}\frac{\partial}{\partial r}\left(ru\frac{\partial u}{\partial r}\right) \tag{8}$$

Eqs. (4) and (5) are discretized and solved by the equal-order finite element and fractional four-step method [9]. The total temperature field is calculated after the velocity field is obtained. The detailed procedures of simplification and discretization are described in [3].

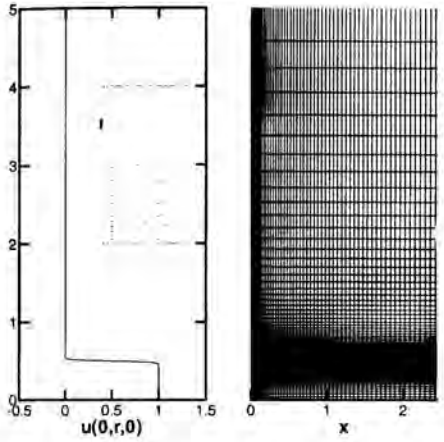

Fig. 2 Velocity profile and grid near the inlet

The boundary conditions are illustrated in Figure 1. At the inlet plane, a velocity profile with a thin initial shear layer is employed for the streamwise velocity and shown in Fig. 2.

$$u(0,r,t)=0.5\left[1-\tanh\left(\frac{D}{\delta_o}(2r-1)\right)\right] \qquad (9)$$

The ratio of initial shear layer thickness to the diameter of the jet, δ_o/D, is assumed to be 1/30, close to the value in experimental studies including Seol [10].

Within the initial shear layer, small disturbances are introduced in the radial velocity component. Through stability analysis of inviscid flow with the same velocity profile as Eq. (9), the most unstable frequency and two-sub-harmonic frequencies are selected as the frequencies of the disturbance.

$$v(0,r,t)=\varepsilon\sum_{j=1}^{3}v_{d,j}(r,t)e^{-i(\omega_j t+\phi)} \qquad (10)$$

At the inlet, all the velocity components and energy separation factor are assumed to be zero, except at the nozzle opening and the top of the domain. Along the symmetry axis ($r=0$), symmetric boundary conditions ($\frac{\partial}{\partial r}=0$) are adopted for all variables. At the outlet plane, a convective boundary condition is employed for all variables to handle vortex passing across the plane as follows [11]:

$$\frac{\partial\chi}{\partial t}+\frac{1}{2}\frac{\partial\chi}{\partial x}=0 \quad \text{where } \chi=u,\ v,\ S \qquad (11)$$

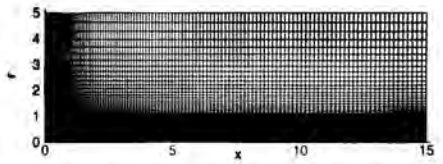

Fig. 3 Computational grid (120 × 76)

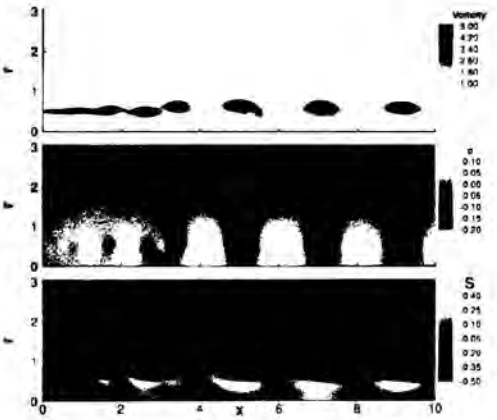

(a) When $t = 45$

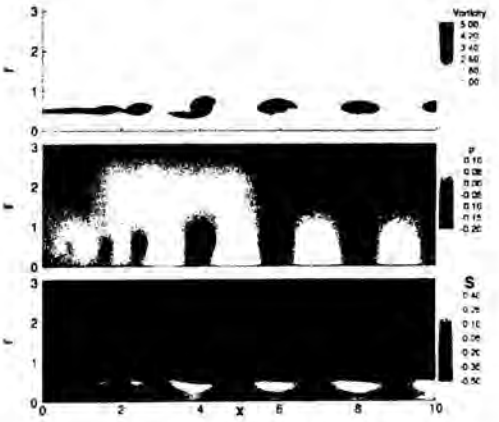

(b) When $t = 46.5$

Fig. 4 Instantaneous vorticity, pressure and energy separation factor distribution for $\mathrm{Re}_D = 1.0\times10^4$

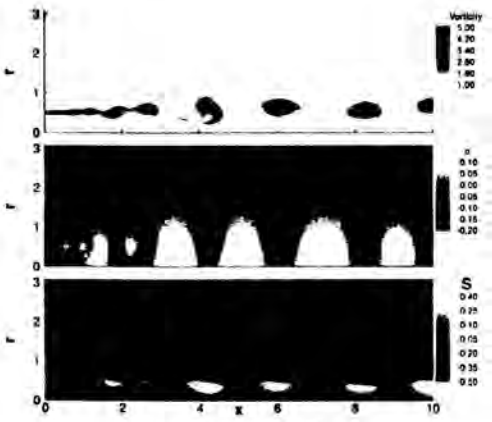

(a) $Re_D = 2.0\times10^3$

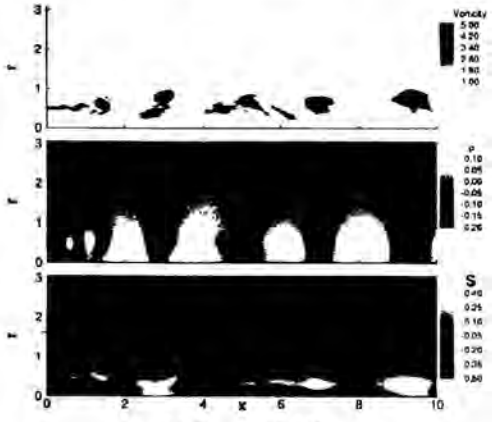

(b) $Re_D = 1.0\times10^4$

Fig. 5 Instantaneous vorticity, pressure and energy separation factor distribution with different Reynolds number when $t = 45$

A grid of 120 in x-axis and 76 in r-axis is used (Fig. 3). For better results, more grid points are located along the axis of $r = 0.5$. Calculations are performed with three different Reynolds number- 1.0×10^3, 2.0×10^3 and 1.0×10^4. Pr is assumed to be 0.7. The velocity, pressure and total temperature data are saved after all initial conditions are washed away.

RESULTS AND DISCUSSION

Vorticity is a convenient variable to describe the motion of a vortex in a flow field. The vorticity (ω) is defined as:

$$\omega = \frac{\partial v}{\partial x} - \frac{\partial u}{\partial r} \tag{12}$$

Throughout this section, the vorticity is used to describe the motion of the coherent vortical structure.

Instantaneous vorticity, pressure and total temperature distributions of the axisymmetric jet with $Re_D = 1.0\times10^3$ at two different time steps are shown in Fig. 4. This clearly illustrates the connection between the pressure fluctuation due to the coherent structure of vortices and the energy separation. In the vorticity distribution, the development of the coherent vortex structure is clearly observed. Pressures near the center of vortices are lower than the surroundings, and there is a local minimum. Between the minimum points, local maximum pressure points exist. Since the vortex is moving with a certain velocity, the distortion in pressure field is also moving. Due to the motion, fluid at the front-half of vortex experiences negative $\frac{\partial p}{\partial t}$ (i.e. does pressure work on the surrounding fluid), and fluid at the rear-half has a positive $\frac{\partial p}{\partial t}$ (i.e. pressure work done on it by the surrounding fluid is added). Therefore, fluid loses energy passing through the front-half of the vortex, and gains energy through the rear-half.

Around $x = 4$, pairing of two vortices occurs at t=46.5. As observed in a plane shear layer [8], the pressure distortion and the temperature difference between hot and cold regions are significantly intensified after the pairing. The locations of instantaneous hot and cold regions are almost symmetric with respect to the center of vortices, which is different from the results of the plane shear layer in [8]. This difference is believed to originate from the difference in pathlines of each flow situations. After $x = 5$, the strength of vortices, pressure fluctuation and energy separation start to decrease.

The results for different Reynolds numbers are shown in Fig. 5. As the Reynolds number increases, the coherent vortical structure develops more rapidly and the strength of the structure increases. As already observed in the plane shear layer, random motion and small scale vortices can be also observed.

Time-averaged total temperature profiles at several streamwise locations are presented at Fig. 6. Very near the nozzle, no significant energy separation is noticeable. As the flow goes downstream, the total temperature difference increases very rapidly. One more interesting thing is that the magnitude of energy separation factor in the cold region of the jet is much larger than that of the hot region. That can be explained with overall energy balance over a control volume surrounding the computational domains. When a fluid enters the control volume with the same total energy for each flow situations, the same amount of total energy should leave the control volume. In other words, the energy flux leaving the control volume should be the same, which is represented by the product of velocity and total enthalpy. Therefore, the magnitude of energy separation factor in the cold region of the

jet is larger than that in the hot region, since the velocity around the cold region is much smaller than that around the hot region. Detailed calculation of the total energy balance is shown in [3].

Fig. 7 shows the total temperature fluctuation. For higher Reynolds number cases, two peaks are observed at $x = 1.0$ one for hot region and the other for cold region. When $Re_D = 1.0\times10^3$, only a single peak can be noticeable. As the flow goes downstream ($x = 2.0$), two peaks can be observed for all calculation cases. The same trend was observed in a plane shear layer [8].

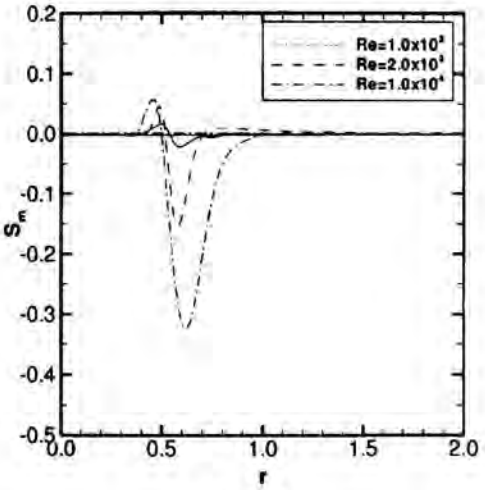

(a) $x = 1.0$

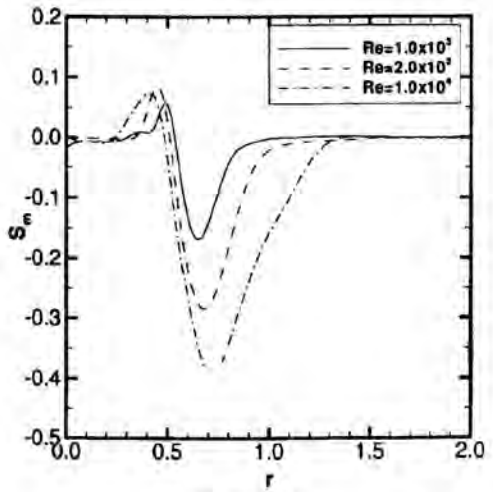

(b) $x = 2.0$

Fig. 6 Time averaged energy separation factor profile

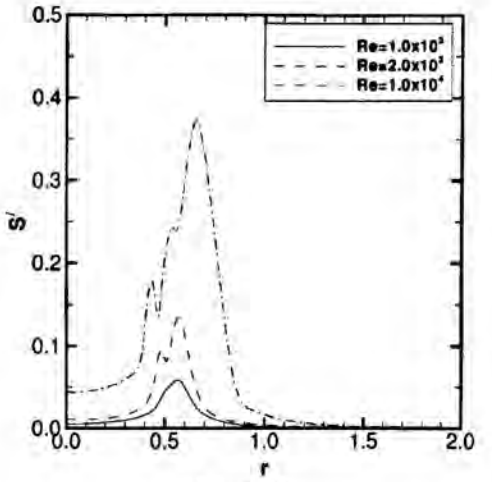

(a) $x = 1.0$

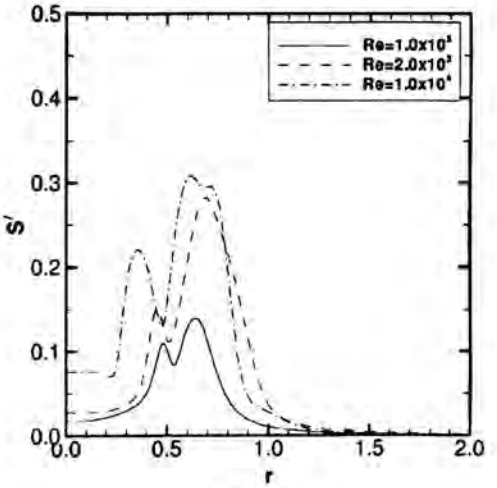

(b) $x = 2.0$

Fig. 7 Energy separation factor fluctuation profile

CONCLUSION

A numerical study clearly shows the mechanism of instantaneous energy separation in a circular jet. A computational code using an equal-order finite element and four-step fractional step method is developed to solve the two-dimensional unsteady flow and total temperature fields in cylindrical coordinates. Three different Reynolds numbers-

1.0×10^3, 2.0×10^3 and 1.0×10^4 are considered. The following conclusions can be obtained from the results.

1. Transport of the large coherent structure of vortices induces pressure fluctuation in flow fields. A fluid which flows through the disturbed pressure field exchanges pressure work with the surrounding fluid, and separates into higher and lower total energy regions.
2. Energy separation due to the pressure fluctuation is generally a much stronger process than that due to the imbalance between shear work and heat conduction when the Prandtl number of a fluid is close to unity.
3. Vortex pairing significantly increases the pressure fluctuation in the flow field. The corresponding total temperature difference between hot and cold regions is also increased.
4. The locations of instantaneous hot and cold regions in the circular jet are almost symmetric with respect to the center of vortices, which is different from the results for the plane shear layer. This difference is believed to originate from the difference in pathlines of the two flow situations.

ACKNOWLEDGMENTS

This work was supported by the Engineering Research Program of the Office of Basic Energy Sciences at the U. S. Department of Energy. The present study was carried out with IBM SP supercomputer at the University of Minnesota Supercomputing Institute.

REFERENCES

[1] Fox, M. D., Kurosaka, M., Hedges, L., and Hirano, K., 1993, "The Influence of Vortical Structure on Thermal Fields of Jets," *Journal of Fluid Mechanics*, **255**, pp. 447-472.

[2] Seol, W. S., and Goldstein, R. J., 1997, "Energy Separation in a Jet Flow," *Journal of Fluid Engineering*, **119**, pp. 74-82.

[3] Han, B., 2001, "Instantaneous Energy Separation in a Jet Flow," Ph. D. Thesis, University of Minnesota, Minneapolis.

[4] Goldstein, R. J., Behbahani, A. I., and Heppelman, K. K., 1986, "Streamwise Distribution of the Recovery Factor and the Local Heat Transfer Coefficient to an Impinging Circular Air Jet," *International Journal of Heat and Mass Transfer*, **29**, pp. 1227-1235.

[5] Kurosaka, M., Gertz, J. B., Graham, J. E., Goodman, J. R., Sundaram, P., Riner, W. C., Kuroda, H., and Hankey, W. L., 1987, "Energy Separation in a Vortex Street," *Journal of Fluid Mechanics*, **178**, pp. 1-29.

[6] He, B., 1997, "Energy Separation for High Speed Flow across a Circular Cylinder," M. S. Thesis, University of Minnesota, Minneapolis.

[7] Eckert, E. R. G., 1987, "Cross Transport of Energy in Fluid Streams," *Wärme-und Stoffübertranung*, **21**, pp. 73-81.

[8] Han, B., and Goldstein, R. J., 1999, "Instantaneous Energy Separation in Shear Layer," *Proceedings of the Seventeenth Symposium on Energy Engineering Science*, Argonne National Laboratory, Argonne, Illinois, pp. 63-73.

[9] Choi, H. G., Choi, H., and Yoo, J. Y., 1997, "A Fractional Four-Step Finite Element Formulation of the Unsteady Incompressible Navier-Stokes Equations Using Supg and Linear Equal-Order Element Methods," *Computer Methods in Applied Mechanics and Engineering*, **143**, pp. 333-348.

[10] Seol, W. S., 1993, "Energy Separation in a Jet Flow," Ph. D. Thesis, University of Minnesota, Minneapolis.

[11] Gresho, P. M., 1991, "Some Current CFD Issues Relevant to the Incompressible Navier-Stokes Equations," *Comput. Methods Appl. Mech. Engr.*, **87**, pp. 201-252.

HEFAT2002
1st International Conference on Heat Transfer, Fluid Mechanics, and Thermodynamics
8-10 April 2002, Kruger Park, South Africa
HL1

APLICATION OF QUASI-STEADY-STATE THERMODYNAMIC MODEL OF LARGE LOW-TEMPERATURE RADIANT HEATING SYSTEM WITH TAKAHASHI CONTROL METHOD

J. Gass
Institute of Energy Technology, The Swiss Federal Institute of Technology, 8092 Zurich, Switzerland

K. Hemzal
Faculty of Mechanical Engineering CTU Prague, Technicka 4, 166 07 Prague, Czech Rep.

L. Hach
Yamaguchi University, Faculty of Engineering, Tokiwadai 2-16-1, Ube 755-8611, Japan
E-mail: hach@po.cc.yamaguchi-u.ac.jp

ABSTRACT

The work presents investigations on the main thermodynamic characteristics of space of an administrative building with built-in large surface low-temperature radiant heating system (L-TRHS) in order to provide a mathematical model for on-line control purposes. Method of investigation is based on the law of conservation of thermal energy and implements the sub-structuring method allowing coupling of model's linear reductions by non-linear heat transfer laws. The L-THRS model's time characteristics were put into Takahashi control algorithm, and through simulation of real thermal states confirmed 3rd-order model reliability. In this paper, careful selection of system boundaries and temperature measurement evaluation for better estimation of enormous thermal capacity of the construction and thermal inertia, respectively, both decisive for time characteristics of the space as main parameters in control loop, are emphasized.

INTRODUCTION

The energy for heating houses and administrative buildings requires a significant part of the total energy used during winter heating season and depends strongly on heaters' performance themselves. One of them, the *low-temperature radiant heating system* (further L-THRS) spread over past decades into various industrial installations and many administrative buildings as well, nowadays [1], [8]. Even though its installations were widespread, there still wasn't available any complete unsteady-state theory over temperature distribution and consequently heat flux throughout the plates [1], [2] (supplied initially by steam). Yet, they impose a difficult task when it comes to their controlling. In order to maintain the desired thermal comfort within the heated space, the ratio of L-THRS thermal inertia and thermal inertia of the space where L-THRS are embedded, appears to be decisive for any attempt to regulate their heat output. To accomplish it, reduce the energy consumption and get a required comfortable temperature there, means mostly to carry out an energy audit with extent depending on financial sources. A part of such investigation was conducted on an administration building with the low-mass structure of envelope and considerably large thermal capacitance in other its parts. The built-in L-TRHS is supplied by water at the temperature range 30-55°C.

At chosen reference space were examined its thermal characteristics, suitable for its mathematical model, including overall thermal responses of the space. The L-TRHS's thermal and thermodynamic parameters were evaluated, fit into model and through series of simulation tests were adjusted model parameters and predict the order of the system (4-order).

At the second step the model was used for controlling the heat flux into the reference room at a control system with Takahashi algorithm [3], [4] in order to maintain the desired indoor temperature. The widely used practice of adjusting input water temperature inversely to outdoor air temperature (basic open-loop approach) was altered through global and surface radiant heating panel temperatures which are bound through Kalous equations [2].

NOMENCLATURE

A	surface area (m^2)
A,B,C,D	state-space model matrixes
c	specific heat ($J.K^{-1}.kg^{-1}$)
d	diameter (m)
F	shape factor (-)
F	transfer function
h	heat transfer coefficient ($W.m^{-2}.K^{-1}$)
k	thermal conductivity ($W.m^{-1}.K^{-1}$)
K	controller parameter (-)
	(K_P – proportional, K_I – integral)

p	Laplace variable
q	heat flux per unit surface area ($W.m^{-2}$)
Q	heat flux (W)
r_0	controller gain
R	thermal resistance ($W^{-1}.m^2.K$)
s	(wall) thickness (m)
T	thermodynamic temperature (° K)
t_p	(slab) mean surface temperature (° C)
t_{inw}	input water temperature (° C)
w	water equivalent of (reference room) content per unit wall area ($J.m^{-2}.K^{-1}$),
x,y	distance (m)
u, x, y	state-space variables (vectors)

Greek letters

α	absorptivity (-)
ε	emissivity (-)
θ	temperature (non-dimensional)
ν	ventilation rate (-)
ρ	density ($kg.m^{-3}$)
σ	Stefan-Boltzmann constant
τ	time (s), transmissivity (-)
τ_i	controller's integral time constant (s)
τ_s	system time constant (s)
τ_u/τ_n	ratio of time constants (-) (τ_u - time lag (s), τ_n - transition time (s))
$\Delta\tau$	sampling time (s)

Subscripts

a,b	air, layer
c	ceiling
cv	convective
cd	conductive
f	floor
g	globe
h	heater
i	internal
inf	infiltration
hms	hemispheric envelope
max	maximal
min	minimal
o	outdoor
r	radiant
rs	system
tz	transport time delay (s)
tot	total
vc	controlled ventilation
w	wall
wf	window

1. OBJECT IDENTIFICATION

1.1 System Boundaries–Reference Space

The investigated heating system supplies a six story reinforced concrete building including mostly offices and seminar rooms using heating water at operating temperature input/output to each register 55/45°C (design condition) by 2 separate main pipelines, each to the opposite building front and back faced wall. Apart from the individual room temperature – it was necessary to accept some control draft on the existing 2-ways supply lines, accounting for about 6 room per floor per pipe, altogether about 50 rooms per pipe. Under these conditions a draft about *reference space* was prepared, which is subjected to 'thermal' averaging all rooms supplied by 1 pipe. Due to the enormous heat storage capability of the ceiling compared to the other construction parts, the space with the longest response delay to the controller's action was preferable. That is, the controller has to get the information about the most critical part of the heating register.

System boundaries of reference room coincide with wall surfaces where thermal values and/or material properties are known or calculated. Summarized heat fluxes, Fig. 1, crossing boundary layers give net heat losses (gains), subject to L-TRHS's covering.

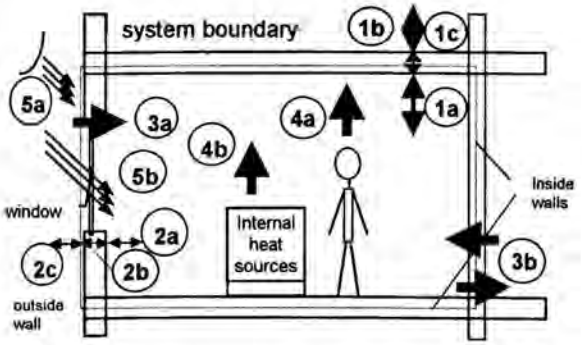

Heat fluxes on inside walls:
1a - convection +radiation
1b - conduction
1c - convection +radiation
3a – heat flux by infiltration
4a –internal heat source – occupants (convection + radiation)
4b - intern heat source- el. device, lightening, etc. (convection + radiation)

Heat fluxes on outside walls:
2a - convection +radiation
2b - conduction
2c - convection +radiation
3b - heat flux by infiltration
5a -heat flux by sun radiation (non transparent outside wall)
5b - heat flux by sun radiation (window)

Figure 1: Heat sources and heat fluxes through reference space.

1.2 Model Set Up

Based on selected fluxes in Fig. 1, all heat fluxes involved could be described on system boundaries (Fig. 1, dashed line) by employing Fourier's law onto isothermal surface parts on:

- outside and inside walls (1a,b),
- fenestration part (1c),
- heater panel (1d).

$$-k_{wo,j}\left[\frac{\partial T_{wo}}{\partial x}\right]_{x=0} = h_{wo,j}(\tau)\left[T_{wo,j}(\tau)-T_a(\tau)\right]+h_{wo,r}(\tau)\sum_k F_{wo,k}\left[T_{wo,j}(\tau)-T_{w,k}(\tau)\right]+$$
$$+w\frac{A_{wo}}{A_{tot}}\frac{\partial T_a(\tau)}{\partial \tau}-\left\{\frac{1}{A_{tot}}\left[A_{wo}\alpha_{wo}q_s(\tau)+(1-cv)Q_i(\tau)\right]\right\} \quad (1a)$$

$$-k_{w,j}\left[\frac{\partial T_{w,j}}{\partial x}\right]_{x=0} = h_{w,j}(\tau)\left[T_{w,j}(\tau)-T_a(\tau)\right]+h_{w,r}(\tau)\sum_k F_{w,w_k}\left[T_{w,j}(\tau)-T_{w,k}(\tau)\right]+$$
$$+w\frac{A_{w,j}}{A_{tot}}\frac{\partial T_a(\tau)}{\partial \tau}-\left\{\frac{1}{A_{tot}}\left[A_{w,j}q_s(\tau)+(1-cv)Q_i(\tau)\right]\right\} \quad (1b)$$

$$-k_{wf,j}\left[\frac{\partial T_{wf}}{\partial x}\right]_{x=0} = h_{wf,j}(\tau)\left[T_{wf,j}(\tau)-T_a(\tau)\right]+h_{wf,r}(\tau)\sum_k F_{wf,w_k}\left[T_{wf,j}(\tau)-T_{w,k}(\tau)\right]+$$
$$+w\frac{A_{wf}}{A_{tot}}\frac{\partial T_a(\tau)}{\partial \tau}-\left\{\frac{1}{A_{tot}}\left[A_{wf}\tau_{wf}q_s(\tau)+(1-cv)Q_i(\tau)\right]\right\} \quad (1c)$$

$$-k_{h,j}\left[\frac{\partial T_{h,j}}{\partial x}\right]_{x=0} = h_{h,j}(\tau)\left[T_{h,j}(\tau)-T_a(\tau)\right]+h_{h,r}(\tau)\sum_k F_{h,w_k}\left[T_{h,j}(\tau)-T_{w,k}(\tau)\right]+$$
$$+w\frac{A_h}{A_{tot}}\frac{\partial T_a(\tau)}{\partial \tau}-\left\{\frac{1}{A_{tot}}\left[A_hQ_s(\tau)+(1-cv)Q_i(\tau)\right]\right\} \quad (1d)$$

Outside wall and window are exposed to the external environment with both direct and indirect radiation along with the heat exchange by convection.

$$-k_{wo,e}\left[\frac{\partial T_{wo}}{\partial x}\right]_{x=s_{wo}} = \alpha q_s(\tau)+h_{wo,e}(\tau)\left[T_e(\tau)-T_{wo,e}(s_{wo},\tau)\right]+$$
$$+h_{wo,e,r}(\tau)\sum_k\left[T_{e,r}(\tau)-T_{wo,e}(s_{wo},\tau)\right] \quad (1e)$$

$$-k_{wf,e}\left[\frac{\partial T_{wf}}{\partial x}\right]_{x=s_{wf}} = \tau_{wf}q_s(\tau)+h_{wf,e}(\tau)\left[T_e(\tau)-T_{wf,e}(s_{wf},\tau)\right]+$$
$$+h_{wf,e,r}(\tau)\sum_k\left[T_{e,r}(\tau)-T_{wf,e}(s_{wf},\tau)\right] \quad (1f)$$

In similar manner the passage space on opposite side to the outside wall would be considered (heat exchanges with others adjacent rooms were negligible since are heated on the same temperature regime):

$$-k_{w,j}\left[\frac{\partial T_{w,j}}{\partial x}\right]_{x=s_{w,j}} = h_{w,j}(\tau)\left[T(s_{w,j},\tau)-T_{a,adj}(\tau)\right]+h_{w,r}(\tau)\sum_k F_{w,w_k}\left[T_{w,j}(\tau)-T_{w,k}(\tau)\right]+$$
$$+w_{adj}\frac{\partial T_{a,adj}(\tau)}{\partial \tau}-\left\{\frac{1}{A_{tot}}\left[A_{w,j}\alpha_s q_s(\tau)+(1-cv)Q_i(\tau)\right]\right\} \quad (1g)$$

Heat exchange between the room of a volume V and external environment by infiltration and controlled ventilation is proportional to the ventilation rate [5]:

$$Q_v(\tau)=Q_w(\tau)+Q_{inf}(\tau)=\rho_a Vc_a\left[T_{a,e}(\tau)-T_{a,i}(\tau)\right]\frac{v}{3600}\ (W) \quad (2)$$

The L-TRHS itself creates temperature environment more favorable for occupants as for temperature stratification, comparing to any other classic heating method. The temperature field becomes more flat even at edges and the concept of *the hemisphere surface envelope* is useful as an imaginary surface over the investigated plane-walls. Assumption of uniformity in temperature and radiosity remains the same as for the virtual walls. In addition such assumption applies to irradiation, so for inst. the outside wall's net radiation heat flux on room faced surface:

$$q_{wo}(\tau)=\sum_{j=1}^{5}\frac{\sigma A_{wo}\left[T_{wo}(\tau)^4-T_j(\tau)^4\right]}{\frac{1-\varepsilon_{wo}}{\varepsilon_{wo}A_{wo}}+\frac{1}{A_{wo}F_{wo-j}}+\frac{1-\varepsilon_j}{\varepsilon_jA_j}} \quad (3)$$

where $\varepsilon = 0.9$ for all ε_j, $j = 1, 2...7$, and $\varepsilon = \rho$. The imaginary hemisphere envelope spanning around circle plate with the same square area as actual wall, i.e. F_{wo}=1.0, and $F_{wo\text{-}hms}A_{wo} = F_{hms\text{-}wo}A_{hms}$ with $\varepsilon_{wo} = \varepsilon_{hms}$:

$$q_{wo}(\tau)=\frac{\sigma A_{wo}\left[T_{wo}(\tau)^4-T_{hms}(\tau)^4\right]}{\frac{3-\varepsilon}{2\varepsilon}} \quad (4)$$

Thus values of the radiant heat-transfer coefficient h_r involved at Eq. (1a)-(1g):

$$h_r(\tau)=\frac{2\sigma\varepsilon\left[T_i(\tau)^2+T_{hms}(\tau)^2\right]\left[T_i(\tau)+T_{hms}(\tau)\right]}{3-\varepsilon} \quad (5)$$

Such expression accounts for all fluxes exchanging radiant heat of walls' surfaces which 'see' each other (each surface radiates to an imaginary surface, having characteristics resulting in almost the same radiation heat exchange as for multi surface case) [7]. The equation system (1a)-(1g) with complementary conditions of thermal steady - or nearly quasi-steady-state, i.e. $\left[\frac{dT_j}{d\tau}\right]_{eq.} \cong 0$, $j = 0, 1, 2...9$; (6 x walls, window, indoor air and supply water temperature) would be capable of depicting almost all of thermal states in its vicinity.

The above drafted *mathematical model of reference room* (hereafter MOS) governs all significant thermal loads, which may occur in the reference space. For completing the model we applied Kirchhoff's current laws, used in dc circuit theory, allowing us to rearrange equations without requiring any other mathematical apparatus. Moreover, they allowed us to reduce the 5-order model to that of 4-order. Then the schema of the heating register (radiant panel) and equations related to the reference room were set into the 4-order system with initial conditions T_{hw0}, T_{b0}, T_{d0}, T_{i0} and T_{w0} and put into matrix form, Eq. (6).

$$\dot{x}(\tau) = A(\tau)x(\tau) + B(\tau)u(\tau)$$
$$y(\tau) = C(\tau)x(\tau) + D(\tau)u(\tau) \qquad (6)$$

$$\mathbf{A}=\begin{bmatrix} f_2 & 0 & f_3 & 0 \\ 0 & k_2 & k_3 & 0 \\ g_1 & g_2 & g_3 & g_4 \\ e_2 & e_3 & h_1 & h_2 \end{bmatrix} \qquad \mathbf{B}=\begin{bmatrix} f_1 & 0 & 0 & 0 & 0 & 0 \\ k_1 & 0 & 0 & 0 & 0 & 0 \\ 0 & 0 & g_5 & g_6 & g_7 & 0 \\ e_1 - 1 & h_3 & 0 & 0 & e_5 \end{bmatrix}$$

$$\mathbf{C}=[0\ 0\ 1\ 0]^T \qquad \mathbf{D}=[0] \qquad (7)$$

Material properties and other qualities are described by linearized functions e, f, g and k and fixed to average values within respective thermal band. This state-space form of equation system (1a)-(1g) with matrices **A**, **B**, **C** and **D** fully describes the examined space as linear stable system. Its parameters were estimated for thermal equilibrium of the examined room, i.e. $\frac{dT_j(\tau)}{d\tau} = 0,\ j = 1,2,\ldots m.$; ($m$ – number of input variables), for which was also calculated the heat supply amount (according to the Swiss standard SIA 384/2) necessary to provide the desired thermal state (indoor air 20°C) there.

2. TEMPERATURE DISTRIBUTION OF L-TRHS' SLAB ACCORDING TO KALOUS*-KOLLMAR

2.1 Analytical Solution

Thermal states of heating radiant panel were modeled under defined initial thermal conditions. The method of finite differences (FDM) was employed for part of block of ceiling panel in order to map the temperature field inside the panel. Geometrical disposition of embedded water pipes at the cross-section of the panel is shown in Fig. 2.

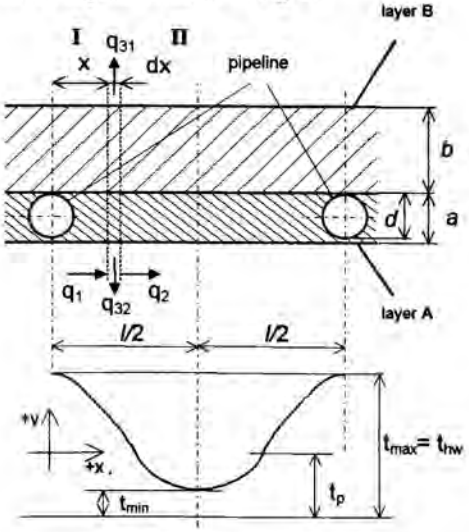

Figure 2: Radiant slab cross-section with temperature distribution between 2 embedded pipes.

Temperature distribution between two neighboring pipes could be find through solution of the energy conservation principle equating the energy entering and leaving a thin plate element dx, Fig. 2, with cross-section area *I*, resp.*II*.

Output variable – *the mean surface temperature* T_d ove. L-TRHS's register was the main output of the MOS. From boundary conditions at distance x = 0mm (Fig.2) and at the center between the two closest tubes $x=l/2$ the heat flux due to symmetry does not go through, and problem solved under both conditions yields to *an average (effective) temperature between the two closest tubes* [2]:

$$t_p = \frac{t_{hw}}{\cosh\left(m\frac{l}{2}\right)} + \frac{1}{3}\left[t_{hw} - \frac{t_{hw}}{\cosh\left(m\frac{l}{2}\right)}\right] \qquad (8)$$

There were further analytical studies [1] with expressions of mean surface temperature similar to Eq. (8), however, if the pipes are closer to the plate's surface [8] (space ratio $d/a > 0.9$, Fig. 2), Kalous equations provide satisfied values. The temperature distribution onto the bottom (ceiling) surface is likely to follow a part of parabolic curve between the points inside the tube (the highest temperature) and the two nearest pipes' centerline.

2.2 Comparing the Temperature Distribution Over The Heating Plate

For following initial and boundary conditions was calculated temperature distribution inside of radiant slab according to Kalous and finite difference method (FDM). As FDM-computational scheme was implied an orthogonal 2-dimensional net with varying grid size in both directions x and y, decreasing towards central axis and emitting plate surface, respectively (Fig. 3, left). Isothermal patterns across half cross-section after 5 hours from input water temperature change (quasi-steady thermal state) shows Fig. 3 right (half pipe in left bottom edge). The solutions' comparison of temperature distribution on surface area, for the half of length of segment at Fig. 3, is drawn in Fig. 4. There could be seen a small difference in calculation of t_p, less then 4%.

Initial and boundary conditions of radiant slab

$x = \langle 0; l/2\rangle$, l = 200 mm, $y = \langle 0;267\rangle$ mm.
$y_a = \langle 0;50\rangle$ mm, $y_b = (50;267\rangle$ mm
$\tau < 0$ s $\quad T_{hw} = 293$ K $\quad dT_{hw}/d\tau = 0$
$\forall x = \langle 0; l/2\rangle$: $\quad T_i = 293$ K
$\forall x\, x\, y \subseteq (0;100) \times (0;267)$ mm : $T = 293$ K $\wedge\ dT/d\tau = 0$
$\tau \geq 0$ s $\quad T_{hw} = 323$ °C
$\theta(0,y)=1$, $\theta(100,y)=1$, $\theta(x,0)=0$, $\theta(x,267)=0$,
where $\quad \theta=(T - T_i)/(T_{hw} - T_i)$.

* Doc.Ing.Dr.Karel Kalous (1896-1942) – outstanding Czech scientist persecuted by nazi regime during World War II.

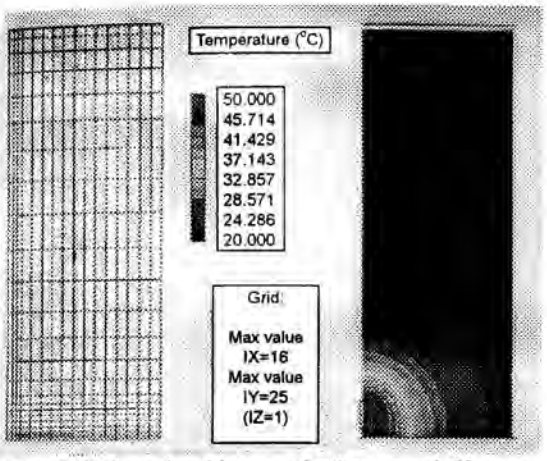

Figure 3: 2-dimensional heat conduction across half cross-section of radiant slab. Grid network (left), temperature field with isothermal lines (right) and temperature scale (center).

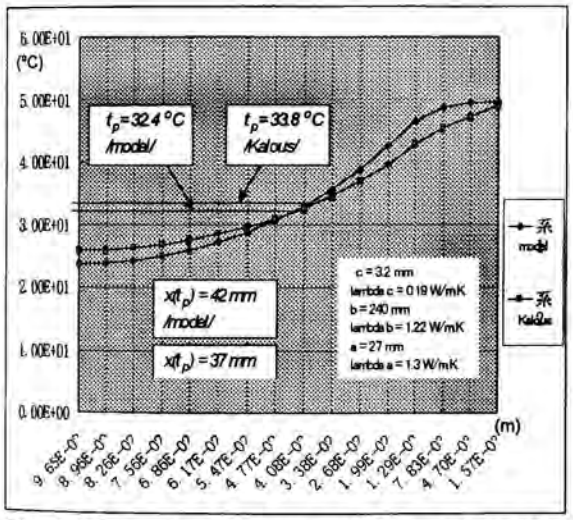

Figure 4: Comparison of temperature fields on radiant slab's surface area on one half distance between two nearest pipelines, according to Kalous and FDM.

3. MOS TRANSFER FUNCTION. CONTROLLER PARAMETERS SETTING

For evaluation, the MOS was put into the closed control loop object-controller and used Laplace transformation in continuous p-domain:

$$\frac{L\{y\}}{L\{u\}} = \frac{F_S(p)}{1 + F_S(p).F_R(p)} \qquad (9)$$

utilizing the generalized notation of the closed-loop feedback control system with object – reference room (transient function $\mathbf{F_S}(p)$) and PI controller (tr.f. $\mathbf{F_r}(p)$). With an unit step input is further obtained wished transient output, here for unit step disturbance – $u_1(\tau)$:

$$y(p) = \frac{F_s(p)}{1 + F_s(p)P(1 + \frac{I}{p})} \cdot \frac{1}{p} \qquad (10)$$

In such form, all necessary tests of the proposed MOS were conducted to verify its reliability and accuracy, respectively. The comparison of the model's outputs with measured data was satisfied on most critical tests, including MOS's transient responses on harmonic input signals and random inputs, Fig. 5. Thus prepared, the reference model was put into the closed loop with controller in order to generate a model error as the main criterion for adjusting the actual controller's parameters, i.e. *controller gain* and *integral constant*.

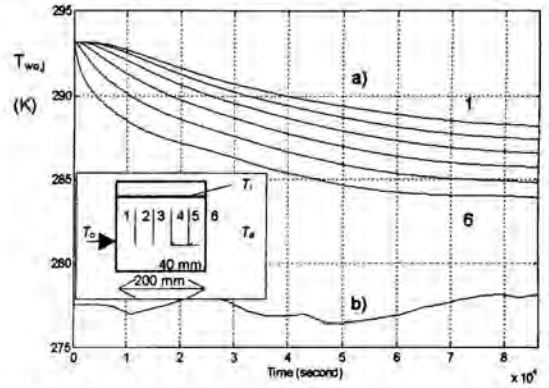

Figure 5:. The temperature transient responses (a) across 200 mm thick plain concrete outside wall suddenly exposed to outdoor ambient air temperature (b) from initial uniform wall temperature T_i=293K at time τ = 0 s.

For a non-continuous (digital) controller with proportional and sum components, i.e. discrete analogy of normal PI controller (PS type), was employed *Takahashi algorithm* [3], [4]. Its requirements are not critical as long as the sampling period is short enough, i.e. much less then the L-THRS's time constants themselves. If derivation part of full PSD control function would be eliminated, then for remained two parameters, controller gain and integral time yields:

$$K_p = \frac{0,9}{R\left(\tau_u + \frac{\Delta\tau}{2}\right)} - \frac{1}{2}K_I \qquad (11\,a)$$

$$K_I = \frac{0,27\,.\Delta\tau}{R\left(\tau_u + \frac{\Delta\tau}{2}\right)^2} \qquad (11\,b)$$

where $R = K/\tau_n$, $K_p = r_0$, $K_I = r_0.\Delta\tau/\tau_I$ and $\Delta\tau << \tau_s$. The controller gain and its integral constant, resp. parameter K_I

were tuned for the experiment into the values in Table 1, which also show values recommended by Ziegler-Nichols method and the difference in % between both methods.

Table 1: Controller parameters (Takahashi method and method Ziegler-Nichols).

Parameter	Sym-bol	Dimen-sion	TAKA-HASHI	ZIEGLER-NICHOLS	Diffe-rence
Proportion. Constant (gain)	R_0	-	25,6	30,6	19%
Integral time constant	τ_I	s (h)	25 430 (7,1)	25 550 (7,1)	0,4%
Integral constant	K_I	-	0,91	1,08	18,5 %
Sampling period	$\Delta\tau$	S	900	900	-

As experimental device was used a flexible control system AS 1000 (Staefa Control System, Co.) equipped with non-continuos (digital) PS controller. The controller evaluates the model error of output vector y and sends control signal to acting 3-ways valve managing mixing water on the input into the heating system.

4. CONCLUSION

By means of identification was completed mathematical model of the single-zone space with the L-TRHS in order to examine its thermodynamics – time responses upon various internal and external heat loads. Applied Kalous equations and simplified concept of the hemisphere surface envelope enabled replacing shape factor calculus, lowered the MOS order and replaced its major non-linearity. The system was classified as stable 3rd-order process, slightly non-linear, with enormous thermal inertia – with ratio $\tau_u/\tau_n \cong 0{,}26$ and causes which affect it:

1. The combination of higher fenestration – more then 50 %, middle-light type of outside walls without sufficient insulation supplements to produce some thermal resistance and a predominantly radiative way of heating as well, creates conditions of considerable unbalance between the heat supply and its actual need. These differences, caused mostly by outside climatological changes and the speed of those changes, could be well balance in this radiant type of heating system due to self-controlling effect.
2. That kind of response could not be confused with heat delivery through embedded heating body itself as it often does even nowadays. The non-readiness almost of all L-TRHS depends on possessing huge thermal capacity (in our case ceiling's body accounts 75% of all surrounding construction parts) inevitably determined through largeness rather then the thermal resistance itself.

On the control part:

3. L-TRHS with *bigger ratio* of time constants ($\tau_u/\tau_n > 0{,}2$) requires set up the heating curve carefully, if used in control praxis (still a main practice). According to expectations, L-TRHS's thermal inertia lenghtens the time of one's control transition band and thus causes heat losses when overheating is taking place.
4. Because of the L-TRHS's moving from one working thermal state to the next one pointed by controller, time lag between controller's action and heat rate reaching L-TRHS's emitting surface prevents any attempt to meet demands on large heat rate changes in shorter time. Therefore by no control means available nowadays is it possible to react to thermal needs faster than allowed by the heating panel body itself. From the standpoint of control strategy there are no differences among control algorithms when applied under such conditions.

ACKNOWLEDGMENTS

The presented work is part of a project carried out at CTU Prague, Dep. of Environmental Technology, Laboratory of Energy Systems of SIT Zurich and supported by CTU grant No 10028254. Authors would like to thank the representatives of Staefa Co. System Prague for their technical assistance and provided experimental devices.

REFERENCES

[1] Kollmar, A., "Die Wärmeabgabe der Rohrdecken - heizung",*Gesundheits-Ingenieur* (80), 1959, pp.1-32.

[2] Kalous, K. and Pulkrábek, J., *"Ústřední vytápení. část prvá"*, Vedecko-technické nakladatelstvi, Praha, 1950, (in Czech.).

[3] Takahashi, Y., *"The theory of dynamical systems controlled by computers" (translation)*, 1974, The Technical Sciences, Publishing Company, Tokyo,.

[4] 高橋安人, 1985.3出版年, "ディジタル制御", 件名 NDLSH:制御理論, 出版者 東京 : 岩波書店, (in Japanese).

[5] ASHRAE Handbook of Fundamentals, 1989a, Chapter 23, 25, 28, Atlanta,.

[6] Dear, de R., "Ping-Pong Globe Thermometers for Mean Radiant Temperatures", *H&V Engineer*, Volume 60, No 681.

[7] Ménézo, Ch.P., Castanet, S.N. and Roux, J.J., "Simulation of Heat Transfer in Buildings Using Reduced Models Coupled With Non Linearities" 1998, Heat Transfer 1998, *Proceedings of 11th IHTC*, Vol.4, pp.343-348, Kyongju, Korea, August 23-28.

[8] DIN 4725, 1992, Teil 2,3,4, Warmwasser-Fußboden-heizungen. Wärmetechnische Prüfung, Heizleistung und Auslegung, Aufbau und Konstruktion, VDI-Verlag GmbH, Duesseldorf, Mai.

[9] Firm catalogues Staefa Control System, Co., 2001.

HEFAT2002
1st International Conference on Heat Transfer, Fluid Mechanics, and Thermodynamics
8-10 April 2002, Kruger Park, South Africa
KM2

IMAGE RECONSTRUCTION OF TWO-PHASE FLOW SYSTEM WITH ELECTRICAL RESISTANCE TOMOGRAPHY TECHNIQUE

Min Chan Kim*, Sin Kim**, Kyung Youn Kim***, Heon Ju Lee**, Yoon Joon Lee**
*Department of Chemical Engineering
**Nuclear Engineering and Energy Engineering
***Department of Electronic Engineering
Cheju National University
Cheju, 690-756, Korea
E-mail: sinkim@cheju.ac.kr

ABSTRACT

The present study intends to confirm the possibility of Electrical Resistance Tomography (ERT) technique for the visualization of two-phase fields. A numerical model was developed to solve the electrical field induced by the applied currents in the forward problem stage and to find the search steps minimizing the difference between the measured and the calculated boundary voltages in the inverse problem stage. The partial differential equation governing the electrical field is discretized in context of the finite element. Also, in this study, a 32-electrode ERT measurement system was made. Combining the numerical model and the ERT system, experimental works were carried out to reconstruct the images of two-phase flow fields simulated with static phantoms. The quality of the reconstructed images based on the phantom experiments indicates that the developed ERT system is able to generate designed current signals and to measure the resulting voltages within the error range that can be coped with by the proposed ERT numerical model. Also, the experimental results show the potential usefulness of ERT technique in imaging two-phase flow fields.

INTRODUCTION

The two-phase flow can occur in various processes such as heat exchanger, steam power generation, oil or natural gas pumping system, and nuclear reactor under the normal accidental conditions. The heterogeneous phase distribution affects the thermal hydraulic phenomena significantly and the determination of the phase distribution is important for developing analytical methods to predict the phenomena. There has been much effort to develop the techniques to measure two-phase flow fields. The techniques are classified into two groups, intrusive and non-intrusive techniques according to whether flow fields are disturbed or not by measuring equipments. As non-intrusive ones, X-ray imaging, computerized tomography (CT), gamma densitometry, magnetic resonance imaging (MRI) and ultrasonic imaging have been suggested and devised.

Recently, the Electrical Resistance Tomography (ERT) technique originated from medical imaging is employed to visualize two-phase flow phenomena, because it has good time resolution and is a non-intrusive technique [1,2]. Also, it does not require expensive hardware setups. The ERT technique is composed of a measurement system and an image reconstruction algorithm. The former injects different predetermined electrical current patterns to the object system and collects voltages through the electrodes placed along the system boundary. Based on the relationship between the injected current pattern and the measured boundary potential, the latter solves the forward and inverse problems iteratively to reconstruct the phase distribution.

This paper introduces a new reconstruction algorithm for electrical resistance imaging technique and evaluates the high-resolution capability of the technique to visualization of phase distribution in two-phase systems. The ERT reconstruction problem is a nonlinear ill-posed inverse problem. Therefore, various regularization methods have been proposed to weaken the ill-posedness and to obtain stable solution. The most often-used regularization methods in ERT for medical applications are the variations of Tikhonov regularization like Levenberg-Marquardt method and the subspace regularization [3]. The latter is efficient when prior information is available as in the case of medical imaging. In medical practices, the approximate locations and sizes of the imaging objects like internal organs and bones are usually known. However, the subspace regularization does not seem to be adequate to the visualization of the two-phase field, where the phase distribution is very irregular. Another major difference between medical imaging and two-phase flow visualization lies in the resistivity contrast. In general, the ERT reconstruction for medical purposes usually experiences resistivity contrast up to several tens, but in the two-phase flow system the resistivity contrast of liquid and vapor phases is much higher, practically infinite. The present study considers several Tikhonov-type regularization methods to compare their performances in the ERT inverse problems with high contrasts. Also, this study designs a 32-electrode ERT

system that is comprised of electrical circuits to generate and measure electrical signals and the electrodes. Combining the numerical model and the ERT apparatus developed in this study, experimental works are carried out to reconstruct the images of the two-phase flow fields simulated with static phantoms.

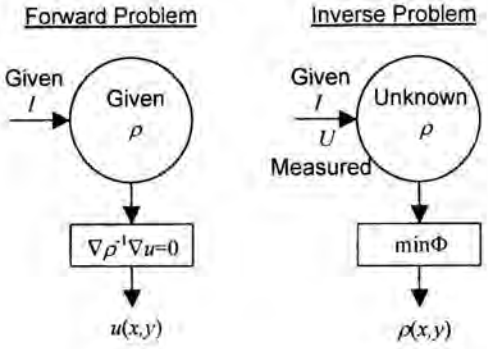

Figure 1: Basic Concept of ERT.

ELECTRICAL RESISTANCE TOMOGRAPHY

The conceptual feature of the ERT system is given in Fig. 1. Mathematically, the ERT is composed of the 'forward problem' to obtain the voltage distribution with the given resistivity distribution and the known boundary conditions and the 'inverse problem' to reconstruct the resistivity distribution using the measured boundary voltages. The details of the forward and inverse problems are discussed as below.

Forward Problem

If the resistivity distribution $\rho(x,y)$ and boundary current I_l through the l-th electrode e_l are known, the electrical potential distribution $u(x,y)$ within the problem domain Ω with boundary $\partial\Omega$ can be obtained by solving the following Laplace equation

$$\nabla\cdot\left(\frac{1}{\rho}\nabla u\right)=0, \qquad (x,y)\in\Omega \tag{1}$$

and the Neuman type boundary conditions

$$\int_{e_l}\frac{1}{\rho}\frac{\partial u}{\partial \nu}dS = I_l \quad (x,y)\in e_l, \quad l=1,2,\ldots,L \tag{2}$$

$$\frac{1}{\rho}\frac{\partial u}{\partial \nu}=0 \qquad (x,y)\in\partial\Omega\setminus\cup_{l=1}^{L}e_l \tag{3}$$

$$u+z_l\frac{1}{\rho}\frac{\partial u}{\partial \nu}=U_l \quad (x,y)\in e_l, \quad l=1,2,\ldots,L. \tag{4}$$

where ν is the outward directed normal vector and U_l denotes the voltage on the l-th electrode. Equation (4) considers the effect of the contact impedance between the electrode and the flow domain and z_l denotes effective contact impedance at l-th electrode. The contact impedance is due to the imperfect contact between the electrodes and the object. In addition, the following two condtions for the injected current and measured voltages are needed to ensure the uniquness of the solution.

$$\sum_{l=1}^{L}I_l=0 \quad \text{and} \quad \sum_{l=1}^{L}U_l=0. \tag{5}$$

Since the above equation can not be solved analytically for the arbitrary resistivity distribution, numerical method like the finite element method (FEM) should is used. This study adoptes FEM and meshes are shown in Fig. 2. The resistivity within the element is assumed to be constant, then the above differential equation is approximated in terms of a system of algebraic equations. The details of the finite element formulation and the solution procedure for the ERT problems can be found in Woo [4] or in Vauhkonen [5].

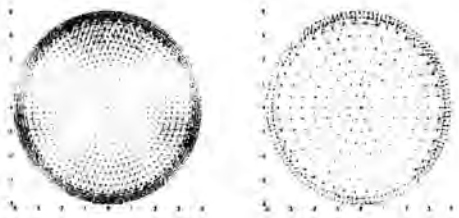

Figure 2: FEM Meshes for Forward (Left) and Inverse (Right) Problems.

Inverse Problem

The inverse problem of ERT maps the boundary voltages from real or artificial experiments to resistivity image. The objective function may be chosen to minimize the error in the least square sense,

$$\Phi(\rho)=\frac{1}{2}[V-U(\rho)]^T[V-U(\rho)] \tag{6}$$

where V is the vector of measured voltage and $U(\rho)$ is the calculated boundary voltage vector that must be matched V

To find ρ which minimizes the above object function, its derivarivative is set to zero as:

$$\Phi'(\rho)=-[U']^T[V-U]=0 \tag{7}$$

where $[U']_{ij}=\frac{\partial U_i}{\partial \rho_j}$ is the Jacobian matrix. The solution of the above Eq. (7) uses the Newton-Raphson linearization about a resistivity vector ρ^k at k-th iteration as

$$\Phi'(\rho^{k+1})=\Phi'(\rho^k)+\Phi''(\rho^k)(\rho^{k+1}-\rho^k)=0 \tag{8}$$

The term Φ'' is called the Hessian matrix, expressed as

$$\Phi''=[U']^T U'-[U'']^T\{I\otimes[V-U]\} \tag{9}$$

where $\otimes$ is the Kronecker matrix product. Since U'' is difficult to calculate and relatively small, the second term in

the above equation is usually omitted [6]. Therefore the Hessian matrix is modified as

$$\Phi'' = [U']^T U' = J^T J = H \,. \tag{10}$$

Thus, the iterative equation for the updating the resistivity vector based on the above regularized object function is expressed as

$$\rho^{k+1} = \rho^k + H^{-1}\left\{J^T\left(V - U\left(\rho^k\right)\right)\right\} \tag{11}$$

where J and H are the Jacobian and the Hessian matrix respectively.

Regularization

The Hessian matrix is known to be ill-conditioned. The ill-posedness is caused by the lack of the information. This is the result of limitations of the boundary measurement, which is very sensitive to resistivity change in the periphery and insensitive to resistivity change at the center. The ill-conditioning degrades the performance of image reconstruction algorithm. Many inverse problems, including ERT, have to be modified to overcome this problem. The idea of the method of regularization is to replace the ill-posed problem by a nearby well-posed problem. In the Tikhonov regularization, this can be done by considering a minimization of augmented least squares functional:

$$\Phi(\rho) = \frac{1}{2}[V - U(\rho)]^T [V - U(\rho)] + \frac{\alpha}{2}\left[R\left(\rho - \rho^*\right)\right]^T \left[R\left(\rho - \rho^*\right)\right] \tag{12}$$

where R is the regularization matrix, α is the regularization parameter and ρ^* is the reference resistivity vector. According to the choice of R and ρ^*, one can have various regularizations like the first order difference (FOD) [6], the Levenberg-Marquardt (LM) regularization [7,8], the implicitly scaled Levenberg-Marquardt (isLM) regularization [9] and so on. It is known that if the resistivity distribution can be assumed to be continuous FOD is a good choice and LM and isLM are suitable for the inverse problems whose iterative solutions are bounded but fluctuating [6]. These three regularization methods were tested numerically [10]. The results indicated that isLM and FOD could reconstruct electrical resistance images very well even for measurement data contaminated by 2% errors and show good performance for high resistivity contrast system up to 1:1000. Hence, this study employs isLM, where $R^T R$ is modeled as a diagonal matrix whose diagonal components are those of $J^T J$, and $\rho^* = \rho^k$.

Other Numerical Issues

There are many data collecting methods such as neighboring method, cross method, opposite method, multi-reference method and adaptive method. The characteristics of these methods are summarized in Webster's work [6]. Among these, the adaptive method, where desired current distribution can be obtained by injecting current through all the electrodes simultaneously, is known to be the best method for arbitrary resistivity distribution. Hence, this study injects trigonometric current patterns into 32 electrodes simultaneously.

The proper initial guess is important, sometimes crucial, for the convergence of the inverse problem. If prior information on the object to be imaged is available one could attain a good convergence characteristic. Since, unlike medical ERT problems, the phase distribution in a two-phase flow is quite arbitrary, little information is known *a priori*. Hence, this study attempts to estimate a constant resistivity value representing the two-phase flow field considered based on a linear relation between the boundary voltage and the internal resistivity, instead of seeking a proper initial distribution.

The contact impedance that is caused by the imperfect contact between an electrode and an object is inevitable in reality. A problem with the contact impedance is that a relation between currents at electrodes and voltages across the object is not given for arbitrary real situations. Hence, before applying the ERT procedure to the real imaging problem, one needs to estimate the contact impedance, which will be considered in the reconstruction algorithm. Invoking the contact impedance, the boundary voltage should be a function of the contact impedance as well as the interior resistivity distribution. Assume that the contact impedance remains unchanged during each experiment; one can fix the dependency of the resistivity distribution by considering a homogeneous medium with a single phase. Namely, before each phantom experiment, in order to determine the contact impedance, one measures boundary voltages without inserting objects simulating bubbles. The contact impedance estimated in homogeneous situation is used for the image reconstruction of the distribution of the dispersed phase.

SIMULATION RESULTS AND DISCUSSIONS

The resolution of the ERT system depends on the various variables, such as resistivity contrast and distribution, injected current pattern, regularization method, and measurement error. Therefore, for the verification of the present ERT model and its appropriateness to the two-phase flow system, a series of simulations is conducted. In numerical simulation, the mesh structures in the forward and inverse problems should be different from each other to avoid the cancellation of errors in the forward model (known as an *inverse crime*). Also, as shown in Fig. 1, a coarse mesh is used for the inverse problem to reduce computational load.

As a convergence criterion for the inverse problem, the root-mean-squared global error defined as

$$\varepsilon = \sqrt{\frac{(U - V)^T (U - V)}{V^T V}} \tag{13}$$

is used. If ε is less than predetermined small value, the convergence is assumed and the reconstruction algorithm is stopped. In this study, 10^{-3} is adopted as a stopping criterion. Experience shows that the quality of reconstructed image does not improve after several iteration steps, so maximum iteration number is set to 10.

The examples are shown in Fig. 3 and the reconstructed images in Fig. 4. In numerical simulations, this study ignores

the contact impedance and sets the resistivity values of continuous phase (e.g. liquid) and dispersed phase (e.g. vapor) to 10Ωm and 10,000Ωm, respectively. Namely, the resistivity contrast of the two phases is set to be 1000. To simulate measurement error this study adds some uniformly distributed random noise. The noise levels are set to 2% of the corresponding measured voltages.

At first, a flow domain with a single bubble located in the center is reconstructed in Fig. 3. It should be noted that even though this example looks very simple it is not easy to reconstruct because the voltages measured on the boundary electrodes are insensitive to the resistivity change of the object located deep inside. Under the assumption of no measurement error, the present image reconstruction algorithm predicts the location and the size of the simulated bubble quite reasonably within 4 iterations. According to the numerical experiments by Kim et al. [10], as the resistivity contrast increases the required number of iterations also increases. For example, when the contrast is two the converged results are obtained with just 2 iterations, while for the contrast 10 the problem requires 3 or 4 iterations for the convergence. When the contrast is greater than 100, 4 or 5 iterations are needed to obtain the converged results. As for the regularization parameter, in the present study, after repeating the same problem with various regularization parameters ranging from 1×10^{-6} to 1.0, the regularization parameter is chosen to show the best reconstruction image. The quality of the reconstruction becomes worse as the regularization parameter increases. In this, $\alpha=10^{-5}$ is used.

Also, Fig. 3 depicts the effect of the measurement error on the reconstructed image. The more noise is added to the measured voltage, of course, the worse image is predicted due to the deterioration of the relationship between the injected currents and the measured voltages. Hence, as the level of measurement noise increases, the inverse procedure requires higher regularization parameter, which should be 0.01~1.0 as per regularization method to stabilize the solution. The reconstructed images shown in Fig. 3 are not converged within 10 iterations and more iteration does not improve the images. Nevertheless, the numerical results reproduce the true image quite reasonably.

For the investigation of the effect of target size and location on the image reconstruction, there is an attempt to reconstruct the simulated two-phase fields with two and three artificial bubbles, respectively. In view of the second example with two bubbles, one of which is bigger than the other while both are located at nearly same distance from the wall, the bigger one is predicted more clearly. On the other hand, Fig. 3 implies that for two targets with nearly same size the one closer to the wall can be reconstructed more clearly.

IMAGE RECONSTRUCTION BASED ON PHANTOM EXPERIMENTS

Because of ill-posed characteristics of ERT inverse problem, the practical test is important to evaluate the performance of ERT system. We perform several phantom experiments and reconstruct images based on the experimental data to evaluate the performance of this reconstruction algorithm and hardware setups.

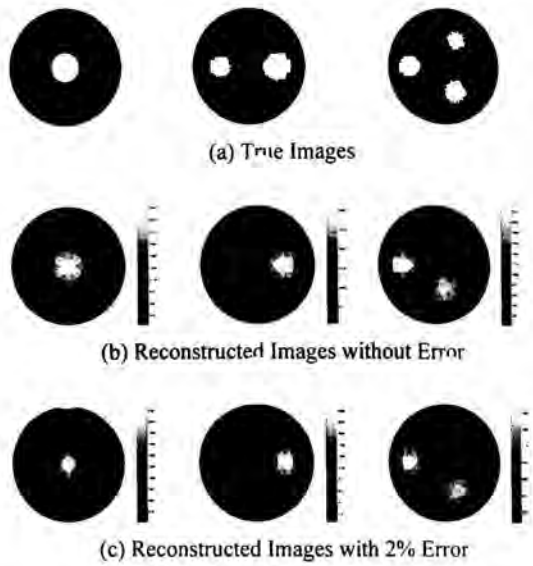

(a) True Images

(b) Reconstructed Images without Error

(c) Reconstructed Images with 2% Error

Figure 3: Image Reconstruction with Synthetic Data.

Experiments

A cylindrical phantom with diameter 8cm and height 33cm is used. Thirty-two stainless steel electrodes are mounted on the inner surface of phantom and covers approximately 76% of the circumference. The phantom was filled up with 0.15% saline solution having resistivity of 330Ωcm. Two kinds of cylindrical plastic targets with diameter of 1cm and 2cm each, whose resistance is practically infinite, are placed in the phantom to simulate vapor phase.

The current generated by current generation circuit in the form of trigonometric function is injected into the 32 electrodes simultaneously, and the resulting voltages are measured. Total number of current patterns used in the experiments is 31. The frequency of the current is 50 kHz. It is estimated that the errors involved in the generation of injected currents and in the measurement of boundary voltages for homogeneous medium are maintained less than 1%.

Reconstructed Images

Figure 4 describes the effect of the target location and size on the reconstructed images. As the target is smaller and farther from the wall, namely the electrodes, the predicted images become worse. All of the results are subject to the experimental error and then the regularization parameter is set to 0.1. As in the numerical experiments with considering measurement errors, the results are not obtained within the maximum number of iterations, 10. It should be noted that the absolute magnitude of the resistivity of the saline water is

hardly predicted, especially when the target is small. Also, the predicted resistivities of the targets or the resistivity contrasts between two phases are not identical to each other. As the target is smaller and farther to the wall, the estimated contrast decreases below 10, which is worse than in numerical experiments. Nevertheless, from the reconstructed images one can identify the location of the bubble clearly and also estimate the size to a certain extent. Another experiment is conducted with two simulated bubbles and the reconstructed images are also shown in Fig. 4.

Phantom experiments carried out to evaluate the performance of the ERT algorithm and to validate the ERT measurement system developed in the present study show a similar trend to the numerical experiments discussed above in point of the effect of the target size and location on the reconstructed image. The quality of the reconstructed images based on the phantom experiments also says that the developed ERT system is able to generate the designed current signal and to measure the resulting voltages within the error range that can be coped with by the present ERT algorithm.

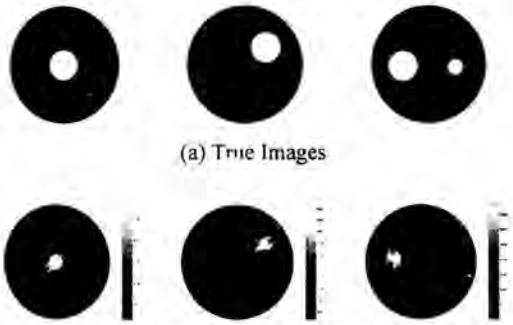

(a) True Images

(b) Reconstructed Images

Figure 4: Image Reconstruction with Experimental Data.

CONCLUSIONS

The present work intends to apply the ERT (electrical resistance tomography) technique to the visualization of two-phase flow system. To mitigate the ill-posedness of the ERT inverse problem to obtain stable solution, implicitly scaled Levenberg-Marquardt regularization is employed. For the verification of the ERT algorithm and the experimental setup, numerical and phantom experiments are conducted.

The reconstructed images with synthetic and experimental data show that implicitly scaled Levenberg-Marquardt algorithm gives fairly good images. If the error is introduced, higher regularization parameter is required. The ability to distinguish targets that are bigger and closer to the wall is better.

Although the absolute magnitude of the predicted resistivity is not good enough, the reproduced contrast is sufficient to distinguish the dispersed phase (i.e. bubble) from the continuous phase (i.e. liquid). In view of the presented results, the ERT system may have a good possibility as an alternative for the two-phase flow visualization and it is expected that the ERT is useful to extract valuable information from the two-phase flow field.

ACKNOWLEDGEMENT

This work was supported by the Nuclear Academic Research Program of the Ministry of Science and Technology (MOST).

REFRENCES

[1] Jones, O.C., Lin, J.T., Ovacik, L., and Shu, H. 1993, "Resistance Imaging Relative to Gas-Liquid Systems," Nuclear Engineering and Design, Vol. 141, pp. 159-176.

[2] Cho, K.H., Kim, S. and Lee, Y.J., 2001, "Resistance Imaging of Two-Phase Flow Field with Mesh Grouping Algorithm," Nuclear Engineering and Design, Vol. 204, pp. 57-67.

[3] Vauhkonen, M., Vadasz, D., Karjalainen, P.A., Somersalo, E. and Kaipio, J.P., 1998, "Tikhonov Regularization and Prior Information in Electrical Resistance Tomography," IEEE Transactions on Medical Imaging, Vol. 17, pp. 285-293.

[4] Woo, E.J., 1990, Finite Element Method and Reconstruction Algorithm in Electrical Resistance Tomography, Ph.D. Dissertation, University of Wisconsin at Madison, Wisconsin. USA.

[5] Vauhkonen, M., 1997, Electrical Resistance Tomography and Prior Information, Ph.D. Dissertation, Kuopio University, Finland.

[6] Webster, J.G. (ed.), 1990, Electrical Impedance Tomography, Adams Hilger, Bristol, U.K.

[7] Hua, P., Webster, J.G. and Tompkins, W.J., 1988, "A Regularised Electrical Resistance Tomography Reconstruction Algorithm," Clinical Physics and Physiological Measurement, Vol. 9, Suppliment A, pp. 137-141.

[8] Yorkey, T.J., Webster, J.G. and Tompkins, W.J., 1987, "Comparing Reconstruction Algorithms for Electrical Resistance Tomography," IEEE Transactions on Biomedical Engineering, Vol. 34, pp. 843-852.

[9] Chenny, M., Isaacson, D., Nowell, J.C., Simske, S. and Globe, J., 1991, "NOSER; An Algorithm for Solving the Inverse Conductivity Problem," International Journal of Imaging Systems and Technology, Vol. 2, pp. 66-75.

[10] Kim, M.C., Kim, S., Kim, K.Y. and Lee, Y.J., 2001, "Regularization Methods in Electrical Impedance Tomography Technique for the Two-Phase Flow Visualization," International Communications in Heat and Mass Transfer, Vol. 28, pp. 773-782.

HEFAT2002
1st International Conference on Heat Transfer, Fluid Mechanics, and Thermodynamics
8-10 April 2002, Kruger Park, South Africa
KV1

SWIRLING WALL JETS PAST AXISYMMETRIC BODIES FOR NON-NEWTONIAN POWER-LAW FLUIDS

Václav Kolar
Institute of Hydrodynamics, Academy of Sciences,
Pod Patankou 5, 166 12 Prague 6, Czech Republic
Tel: +420.2.33109095
Fax: +420.2.33324361
E-mail: kolar@ih.cas.cz

ABSTRACT

The similarity solution of laminar wall jets with swirl on bodies of revolution for non-Newtonian power-law fluids is presented. The functional dependence of length, velocity and pressure similarity scales on shape and swirl parameters and flow behaviour index is determined. The already published results related to the similarity solution obtained are discussed.

INTRODUCTION

Various types of wall jets are often used in industrial applications and engineering practice, especially for external solid surface conditioning associated with heat and mass transfer. The knowledge of relevant flow characteristics and governing flow parameters is necessary for studying these transport phenomena. It is worth mentioning that heat transfer from external surfaces of axisymmetric bodies of arbitrary contour has been widely investigated in boundary-layer flows (e.g. Lin and Chao 1974, Kim *et al.* 1983, Chang *et al.* 1988).

The contribution presents the similarity solution of swirling wall jets on bodies of revolution for non-Newtonian power-law fluids. The physical and geometrical meaning of all parameters appearing in the course of similarity procedure is treated in detail. The governing role of parameters characterizing the surface geometry and the rate of rotation is explicitly shown.

The flow-structure complexity of wall jets arises from the presence of a wall, the inner wall-jet region being significantly affected by the body surface. Based on the original idea of Glauert (1956) applied to plane and radial wall jets the integral energy equations dealing with the so-called 'flux of exterior momentum flux' have been recently introduced for the case of swirling wall jets on bodies of revolution, see Kolář *et al.* (1990). The latter study (dealing with turbulent flow regime) presents a detailed similarity analysis of the global scales (namely length, velocity and pressure scales) as functional dependences on the so-called swirl parameter (expressing the rate of rotation) and the shape parameter (characterizing the geometry of the body of revolution). Filip *et al.* (1991, hereinafter referred to as FKH) have shown how to cope with the *non-swirling* wall-jet flow past axisymmetric bodies for power-law fluids. A special case of the *non-swirling* radial wall jet for power-law fluids was solved by Mitwally (1978).

As shown below, the above mentioned results can be further extended for the case of *swirling* wall jets for power-law fluids. It should be noted, that in many shear-flow problems numerical solutions and sophisticated flow modelling should be preceded, or completed, by the similarity analysis revealing analytically the role of relevant flow parameters and their clear physical and geometrical meaning. Moreover, in the present case, the similarity analysis provides a significant simplification of the given problem formulation for further (analytical or numerical) calculations.

NOMENCLATURE

$A(x), B(x), E(x), T_1(x), T_3(x), P_1(x)$ ... similarity coefficients
$A(\zeta), B(\zeta)$ ... similarity coefficients
C, C_1, C_2, D ... constants
e ... swirl parameter
$f(\eta), f(\overline{\eta}), h(\eta), T_2(\eta), T_4(\eta), T(\eta), P_2(\eta)$ ... similarity functions
$F \equiv F(n)$ ... quantity defined by (45)
K, n ... power-law model parameters
p ... pressure
q ... velocity resultant in ζ-direction (Fig. 2)
r ... local radius of the body of revolution
u, v, w ... velocity components in coordinate syst. (x, y, ϕ)
x, y ... coordinates in axial plane (Fig. 1)
x_0, ζ_0 ... quantities representing a virtual origin of the jet
W, Z ... integral invariants defined by (44) and (54) resp.
$\delta(x), \delta(\zeta)$ ... jet width
ζ ... curvilinear surface coordinate (following the resulting 'helical' fluid motion past the body surface, Fig. 2)
$\eta, \overline{\eta}$ ... similarity variables defined by (13) and (37) resp.
ξ ... quantity defined by (27)
ϕ ... polar coordinate
ρ ... fluid density
τ ... shear-stress resultant in ζ-direction (Fig. 2)

$\tau_{xy}, \tau_{\phi y}$ ... stress tensor components

ψ ... stream function, $u = r^{-1}\partial\psi / \partial y,\ v = -r^{-1}\partial\psi / \partial x$

ψ ... stream function, $q = \xi^{-1}\partial\psi / \partial y,\ v = -\xi^{-1}\partial\psi / \partial\zeta$

Δp ... transverse pressure difference, $\Delta p \equiv p - p_\infty$

PROBLEM FORMULATION

Taking into account the axisymmetric shape of the body of revolution, we use the curvilinear coordinate system (x, y, ϕ) with the curvilinear surface coordinate x defined in axial plane according to Fig. 1 where r is a local body radius, $r \equiv r(x)$.

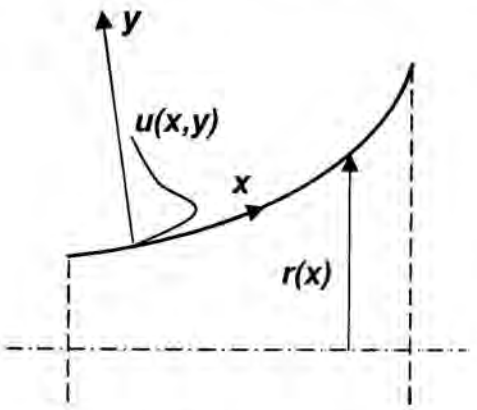

Figure 1: Geometry of the coordinate system (axial plane).

The *swirling wall* jets past axisymmetric bodies for power-law fluids are described by the set of (three) equations of motion ($\partial / \partial\phi \equiv 0$ with respect to axisymmetry)

$$u\frac{\partial u}{\partial x} + v\frac{\partial u}{\partial y} - w^2 \cdot \frac{r'(x)}{r(x)} = \frac{1}{\rho}\cdot\frac{\partial \tau_{xy}}{\partial y}, \tag{1}$$

$$w^2 \cdot \frac{\left(1 - r'^2(x)\right)^{1/2}}{r(x)} = \frac{1}{\rho}\cdot\frac{\partial(\Delta p)}{\partial y}, \tag{2}$$

$$u\frac{\partial w}{\partial x} + v\frac{\partial w}{\partial y} + uw\cdot\frac{r'(x)}{r(x)} = \frac{1}{\rho}\cdot\frac{\partial \tau_{\phi y}}{\partial y} \tag{3}$$

where (within the frame of boundary-layer approximations)

$$\tau_{xy} = K\left(\sqrt{\left(\frac{\partial u}{\partial y}\right)^2 + \left(\frac{\partial w}{\partial y}\right)^2}\right)^{n-1}\cdot\frac{\partial u}{\partial y}, \tag{4a}$$

$$\tau_{\phi y} = K\left(\sqrt{\left(\frac{\partial u}{\partial y}\right)^2 + \left(\frac{\partial w}{\partial y}\right)^2}\right)^{n-1}\cdot\frac{\partial w}{\partial y}, \tag{4b}$$

by the continuity equation

$$\frac{\partial}{\partial x}\left(r(x)u\right) + \frac{\partial}{\partial y}\left(r(x)v\right) = 0, \tag{5}$$

and by the *corresponding* boundary conditions

$$u(x,0) = 0,\ v(x,0) = 0,\ w(x,0) = 0, \tag{6a, b, c}$$

$$\lim_{y\to+\infty} u(x,y) = 0,\ \lim_{y\to+\infty} w(x,y) = 0, \tag{7a, b}$$

$$\lim_{y\to+\infty} \tau_{xy}(x,y) = 0,\ \lim_{y\to+\infty} \tau_{\phi y}(x,y) = 0, \tag{8a, b}$$

$$\lim_{y\to+\infty} p(x,y) = p_\infty. \tag{9}$$

The jet flow is governed by the explicitly shape-dependent centrifugal and Coriolis forces, see (1)-(3). The equations of motion are derived under the following assumptions:

- usual boundary-layer approximations;
- $r''(x)$ does not attain extreme values;
- $\delta(x) << r(x)$; hence, the curvature terms in the equations of motion are neglected as well as the longitudinal pressure change following the assumptions of Boltze for boundary-layer flow on bodies of revolution (Schlichting 1968). The assumption that $\delta(x)$ is comparatively small to the shape parameter $r(x)$ has been widely (though implicitly) used for boundary-layer similarity solutions for power-law fluids, e.g. Lin and Chao (1974), Kim *et al.* (1983), Chang *et al.* (1988). This assumption is also a basis for modified Mangler's transformation applicable to (*non-swirling*) boundary-layer flows past axisymmetric bodies for power-law fluids, see Acrivos *et al.* (1965).

In addition, only divergent body shapes are considered, i.e. $r'(x) > 0$.

The similarity procedure below employs the Glauert-type integral energy equations dealing with the so-called 'flux of exterior momentum flux' (derived using (1), (3) and (5)-(8))

$$\frac{\partial}{\partial x}\int_0^\infty \rho\, r(x)\, u\left(\int_y^\infty \rho\, r(x)\, u^2\, \mathrm{d}y\right)\mathrm{d}y =$$

$$= \int_0^\infty \rho\, r(x)\, u\left(\int_y^\infty \rho\, r'(x)\, w^2\, \mathrm{d}y\right)\mathrm{d}y - \int_0^\infty \rho\, r^2(x)\, u\,\tau_{xy}\, \mathrm{d}y, \tag{10}$$

$$\frac{\partial}{\partial x}\int_0^\infty \rho\, r(x)\, u\left(\int_y^\infty \rho\, r^2(x)\, uw\, \mathrm{d}y\right)\mathrm{d}y = -\int_0^\infty \rho\, r^3(x)\, u\,\tau_{\phi y}\, \mathrm{d}y. \tag{11}$$

SIMILARITY ANALYSIS

It is assumed that the flow field is similar, so let us introduce generalized similarity transformations in the form

$$\psi(x,y) = A(x)\cdot f(\eta), \tag{12}$$

$$\eta(x,y) = B(x)\cdot y \quad (\equiv y/\delta(x)), \tag{13}$$

$$w(x,y) = E(x)\cdot h(\eta), \tag{14}$$

$$\tau_{xy}(x,y) = \rho\cdot T_1(x)\cdot T_2(\eta), \tag{15}$$

$$\tau_{\phi y}(x,y) = \rho\cdot T_3(x)\cdot T_4(\eta), \tag{16}$$

$$\Delta p(x,y) \equiv p(x,y) - p_\infty = \rho\cdot P_1(x)\cdot P_2(\eta). \tag{17}$$

Substituting the above similarity transformations into equations (1)-(3) we obtain

$$T_2' + \frac{AA'B}{r^2T_1}\cdot f f'' + \frac{1}{T_1}\left[\frac{r'A^2B}{r^3} - \frac{AA'B}{r^2} - \frac{A^2B'}{r^2}\right]\cdot f'^2 + \frac{r'E^2}{rBT_1}\cdot h^2 = 0, \tag{18}$$

$$P_2' - \frac{\left(1-r'^2\right)^{1/2}E^2}{rP_1B}\cdot h^2 = 0, \tag{19}$$

$$T_4' + \frac{A'E}{rT_3}\cdot f h' + \frac{1}{T_3}\left[-\frac{AE'}{r} - \frac{r'AE}{r^2}\right]\cdot f' h = 0 \tag{20}$$

where the primes indicate differentiation with respect to the arguments. Eq. (19), i.e. the transformed Eq. (2), serves only for the determination of the transverse pressure distribution *after* the determination of the velocity field.

A detailed similarity procedure, quite analogous to that in Kolář *et al.* (1990), leads to the partial similarity results summarized as follows

(i) for the similarity functions:

$$f'(\eta) \equiv h(\eta) \quad \textit{for all } \eta \in [0,+\infty) \tag{21}$$

$$T_2(\eta) \equiv T_4(\eta) \quad (\equiv T(\eta)) \quad \textit{for all } \eta \in [0,+\infty) \tag{22}$$

$$T' + C_1\cdot f f'' + C_2\cdot f'^2 = 0 \tag{23}$$

(ii) for the similarity coefficients:

$A(x), B(x), E(x), \ldots$
determined as $A(x; C_1, C_2), B(x; C_1, C_2), E(x; C_1, C_2), \ldots$

(iii) for the spatial flow geometry:

$$\frac{w(x,y)}{u(x,y)} = \frac{\tau_{\phi y}(x,y)}{\tau_{xy}(x,y)} = \frac{e}{\left(r^2(x) - e^2\right)^{1/2}} \tag{24}$$

where e is the swirl parameter (to be discussed later).

It should be noted that the similarity structure of the stress tensor components $\tau_{xy}, \tau_{\phi y}$ is, at first, *a priori* assumed (transformations (15) and (16)). Secondly, as can be easily verified, the obtained partial similarity results, namely (21) in item (i), are consistent with the original power-law model given by (4a, b) within the frame of the generalized similarity transformations adopted, namely (12)-(14).

TRANSFORMATION OF THE ORIGINAL PROBLEM FORMULATION

The spatial flow geometry given by (24) can be considered as a crucial starting point for introducing the velocity and shear-stress resultants, q and τ respectively, see Fig. 2 (last page)

$$q = \left(u^2 + w^2\right)^{1/2} = ru/\xi = rw/e, \tag{25}$$

$$\tau = \left(\tau_{xy}^2 + \tau_{\phi y}^2\right)^{1/2} = r\tau_{xy}/\xi = r\tau_{\phi y}/e, \tag{26}$$

where

$$\xi \equiv \xi(x) = \left(r^2(x) - e^2\right)^{1/2}, \tag{27}$$

and for introducing a differential element $\mathrm{d}\zeta$ in the resulting flow direction past the axisymmetric body surface (ζ may be considered as the curvilinear surface coordinate following the resulting 'helical' fluid motion past the body surface)

$$\mathrm{d}\zeta = \mathrm{d}\xi / r'. \tag{28}$$

By combining (27) and (28) we have

$$\frac{\mathrm{d}\xi}{\mathrm{d}r} = \frac{\mathrm{d}\zeta}{\mathrm{d}x} = \frac{r}{\xi}. \tag{29}$$

Substituting relations (25)-(29) in Eqs. (1), (3), (4a, b), (5), (6a, b, c), (7a, b) and (8a, b) we obtain a simplified formulation of the original problem in the form

$$q\frac{\partial q}{\partial \zeta} + v\frac{\partial q}{\partial y} = \frac{1}{\rho}\cdot\frac{\partial \tau}{\partial y}, \tag{30}$$

$$\frac{\partial}{\partial \zeta}(\xi q) + \frac{\partial}{\partial y}(\xi v) = 0 \tag{31}$$

where

$$\tau = K\left|\frac{\partial q}{\partial y}\right|^{n-1}\cdot\frac{\partial q}{\partial y}, \tag{32}$$

with the boundary conditions

$$q(\zeta,0)=0\,,\quad v(\zeta,0)=0\,, \tag{33a, b}$$

$$\lim_{y\to+\infty} q(\zeta,y)=0\,, \tag{34}$$

$$\lim_{y\to+\infty} \tau(\zeta,y)=0\,. \tag{35}$$

The set of equations and conditions (30)-(35), obtained in terms of the flow-direction, velocity and shear-stress resultants, represents nothing but 'non-swirling' problem formulation of the wall-jet flows past axisymmetric bodies for power-law fluids already solved in FKH.

It appears that in the course of the above procedure we lost the valuable information dealing with the transverse pressure distribution. However, just *after* 'recovering' the desired similarity solution for the original velocity components u, w using (25) the pressure distribution can be determined from Eq. (2), or from the adequate similarity Eq. (19).

SIMILARITY SOLUTION

The solution is sought in the similarity form

$$\bar{\psi}(\zeta,y)=\bar{A}(\zeta)\cdot f(\bar{\eta})\,, \tag{36}$$

$$\eta(\zeta,y)=B(\zeta)\cdot y \quad (\equiv y/\delta(\zeta)) \tag{37}$$

where the stream function $\bar{\psi}$ fulfils

$$q=\xi^{-1}\partial\bar{\psi}/\partial y,\quad v=-\xi^{-1}\partial\bar{\psi}/\partial\zeta\,. \tag{38a, b}$$

The transformations (25)-(29) are exclusively x-dependent, consequently the universal transverse similarity structure of the velocity field remains unchanged, so $\bar{f}\equiv f$. Numerical results for the similarity function f are obtained for the corresponding similarity equation and boundary conditions, namely

$$n\cdot|f''|^{n-1}\cdot f'''+f\,f''+C\cdot f'^{2}=0\,, \tag{39}$$

$$f(0)=0,\quad f'(0)=0,\quad f(\infty)=0 \tag{40a, b, c}$$

in FKH where numerical calculations are based on the application of modified fourth order Runge-Kutta method. The constant C depends on the flow behaviour index n, $C\equiv C(n)$ (for a given n there is a unique value of C) and the above mentioned solution is presented in the range $0.6\le n\le 1.9$.

The length and velocity similarity scales of interest, i.e. jet width $\delta(\zeta)$ and maximum velocity in ζ-direction q_{max}, $q_{max}=\xi^{-1}\bar{A}\cdot B$, are determined as (cf. FKH)

$$\delta(\zeta(x))=\frac{1}{D}\cdot\left(\frac{K}{\rho F}\cdot D^{2n-1}\right)^{(1+C)F}\cdot\xi^{-1}\cdot\left(\int_{\zeta_0}^{\zeta}\xi^{n+1}\,\mathrm{d}\zeta\right)^{(1+C)F}, \tag{41}$$

$$q_{max}(\zeta(x))=D\cdot\left(\frac{K}{\rho F}\cdot D^{2n-1}\right)^{-CF}\cdot\left(\int_{\zeta_0}^{\zeta}\xi^{n+1}\,\mathrm{d}\zeta\right)^{-CF} \tag{42}$$

where

$$D=\left(\frac{\rho}{W}\int_0^{\infty}(f')^{\frac{C+1}{C}}\,\mathrm{d}\bar{\eta}\right)^{-C}, \tag{43}$$

$$W=\int_0^{\infty}\rho\,\xi\,q^{\frac{C+1}{C}}\,\mathrm{d}y \quad (\equiv const \text{ for a given value of } n), \tag{44}$$

$$F\,(\equiv F(n))=\left(n+1+(2n-1)C\right)^{-1}. \tag{45}$$

To obtain quantities $\delta(x)\equiv\delta(\zeta(x))$ and $q_{max}(x)\equiv q_{max}(\zeta(x))$ from (41) and (42) we have to return to the transformation relations (27) and (28). For the integral appearing in (41) and (42) it follows directly

$$\int_{\zeta_0}^{\zeta}\xi^{n+1}\,\mathrm{d}\zeta=\int_{x_0}^{x}r(x)\left(r^2(x)-e^2\right)^{n}\,\mathrm{d}x\,. \tag{46}$$

The final results regarding velocity field in terms of the original coordinates and velocity components can be summarized as

$$u=q\left(r^2-e^2\right)^{n}/r,\quad w=q\,e/r \tag{47a, b}$$

where

$$q=D\cdot\left(\frac{K}{\rho F}\cdot D^{2n-1}\right)^{-CF}\cdot\left(\int_{x_0}^{x}r(x)\left(r^2(x)-e^2\right)^{n}\,\mathrm{d}x\right)^{-CF}\cdot f(\eta), \tag{48}$$

$$\eta\equiv y/\delta(x), \tag{49}$$

$$\delta(x)=\frac{1}{D}\cdot\left(\frac{K}{\rho F}\cdot D^{2n-1}\right)^{(1+C)F}\cdot\left(r^2(x)-e^2\right)^{-1}\cdot\left(\int_{x_0}^{x}r(x)\left(r^2(x)-e^2\right)^{n}\,\mathrm{d}x\right)^{(1+C)F} \tag{50}$$

The parameters C, D, F appearing in (48) and (50) have been already introduced. Note that in (43) we put simply $\eta\equiv\eta$ with respect to the only characteristic transverse length scale $\delta(x)\equiv\delta(\zeta(x))$. However, the integral invariant W, the swirl parameter e and the virtual origin of the jet x_0 need an explanation, see next section. Numerical calculations of the similarity function $f(\eta)$ are described in detail by FKH

considering the range of the flow behaviour index n, $0.6 \le n \le 1.9$. For the special case of a Newtonian fluid, $n = 1$, the similarity equation (39) significantly simplifies. The solution of (39), (40a, b, c) for $n = 1$ was found by Glauert (1956).

Finally, the substitution of the peripheral velocity component w in Eq. (2), or in the adequate similarity Eq. (19), from (47b) and (48) yields the pressure scale $P_1(x)$ and the pressure similarity function $P_2(\eta)$

$$P_1(x) = D\left(\frac{K}{\rho F}\cdot D^{2n-1}\right)^{(1-C)F}\cdot\left(\frac{1-r'^2}{r^2-e^2}\right)^{1/2} \cdot\frac{e^2}{r^3}\cdot\left(\int_{x_0}^{x} r(x)\left(r^2(x)-e^2\right)^{n/2}\,\mathrm{d}x\right)^{(1-C)F}, \qquad (51)$$

$$P_2(\eta) = -\int_{\eta}^{\infty} f'^2(\eta)\,\mathrm{d}\eta\,. \qquad (52)$$

DISCUSSION

The integral quantity W represents a specific wall-jet flow invariant which can be obtained within the frame of similarity analysis only (cf. FKH). This quantity which may be understood as a 'generalized flux of momentum flux', serves as a certain substitution for the Glauert-type integral invariant dealing with the 'flux of exterior momentum flux'

$$\int_0^{\infty}\rho\,\xi(x)\,q\left(\int_y^{\infty}\rho\,\xi(x)\,q^2\,\mathrm{d}y\right)\mathrm{d}y = const \qquad (53)$$

which is valid exclusively for the wall-jet flow of a Newtonian fluid, $n = 1$.

The obtained solution (43)-(50) holds for an arbitrary swirl parameter e and in a limit case $e \to 0$ naturally reduces to the solution obtained in FKH. Again, within the frame of similarity analysis, the swirl parameter e can be expressed as

$$e = Z / W \qquad (54)$$

where Z represents another integral invariant of the form

$$Z = \int_0^{\infty}\rho\,\xi\,rw\,q^{\frac{1}{C}}\,\mathrm{d}y \quad (\equiv const \text{ for a given value of } n). \qquad (55)$$

In practice, the parameters Z, W and x_0 naturally subject to an individual experimental arrangement. Z and W may be approximated by outflow parameters at the nozzle exit using a suitable iterative approach (note that both Z and W contain the quantity ξ defined by (27)). The location of a virtual origin of the jet x_0 approaches the position of high-speed nozzle exit for a nozzle width $\to 0$ and an outflow velocity $\to \infty$.

Obviously, for the integral invariant W in a limit case $e \to 0$ we obtain

$$\lim_{e\to 0} W \equiv \lim_{e\to 0}\left(\int_0^{\infty}\rho\,\xi\,q^{\frac{C+1}{C}}\,\mathrm{d}y\right) = \int_0^{\infty}\rho\,r\,u^{\frac{C+1}{C}}\,\mathrm{d}y\,, \qquad (56)$$

i.e. just the integral quantity introduced in FKH for the case of *non-swirling* wall jets on bodies of revolution for power-law fluids.

CONCLUSIONS

The similarity solution of laminar wall jets with swirl past axisymmetric bodies for non-Newtonian power-law fluids has been presented. The analytical expression for the length, velocity and pressure similarity scales has been explicitly determined. The parameters (shape and swirl parameters, power-law model parameters, integration constants and integral conditions) appearing in the similarity solution obtained possess a specific physical and geometrical meaning which should be considered carefully.

The similarity procedure adopted is based on two main steps:

(i) using generalized similarity transformations to obtain partial results, especially those for the spatial flow geometry;

(ii) to employ these partial similarity results for the transformation of the original 'swirling' problem formulation into the formally 'non-swirling' problem formulation.

The step (ii) provides a significant simplification for further (analytical or numerical) calculations of relevant flow characteristics as shown in the present work. Consequently, it provides a significant simplification of the problem formulation for further calculations of associated heat and mass transfer (to/from the axisymmetric body surface) as well.

ACKNOWLEDGMENTS

The support of GA Acad. Sci. of the Czech Rep. through grant A2060803 and of Acad. Sci. of the Czech Rep. through K2076106 is gratefully acknowledged.

REFERENCES

Acrivos, A., Shah, M. J., Petersen, E. E. (1965): *On the solution of the two-dimensional boundary-layer flow equations for a non-Newtonian power law fluid.* Chem. Eng. Sci. **20**, 101-105.

Chang, T.-Ch. A., Jeng, D. R., De Witt, K. J. (1988): *Natural convection to power-law fluids from two-dimensional or axisymmetric bodies of arbitrary contour*, Int. J. Heat Mass Transfer **31**, 615-624.

Filip, P., Kolář, V., Hájek, R. (1991): *Similarity prediction of wall jets past axisymmetric bodies for power-law fluids.* Acta Mech. **88**, 167-173.

Glauert, M. B. (1956): *The wall jet.* J. Fluid Mech. **1**, 625-643.

Kim, H. W., Jeng, D. R., De Witt, K. J. (1983): *Momentum and heat transfer in power-law fluid flow over two-dimensional or axisymmetrical bodies.* Int. J. Heat Mass Transfer **26**, 249-259.

Kolář, V., Filip, P., Curev, A.G. (1990): *On the swirling wall jets on bodies of revolution.* Int. J. Eng. Sci. **28**, 115-121.

Lin, F. N., Chao, B. T. (1974): *Laminar free convection over two-dimensional and axisymmetric bodies of arbitrary contour.* Trans. ASME, J. Heat Transfer **96**, 435-442.

Mitwally, E. M. (1978): *Solutions of laminar jet flow problems for non-Newtonian power-law fluids.* Trans. ASME, J. Fluids Engng. **100**, 363-366.

Schlichting, H. (1968): *Boundary Layer Theory.* McGraw-Hill, New York.

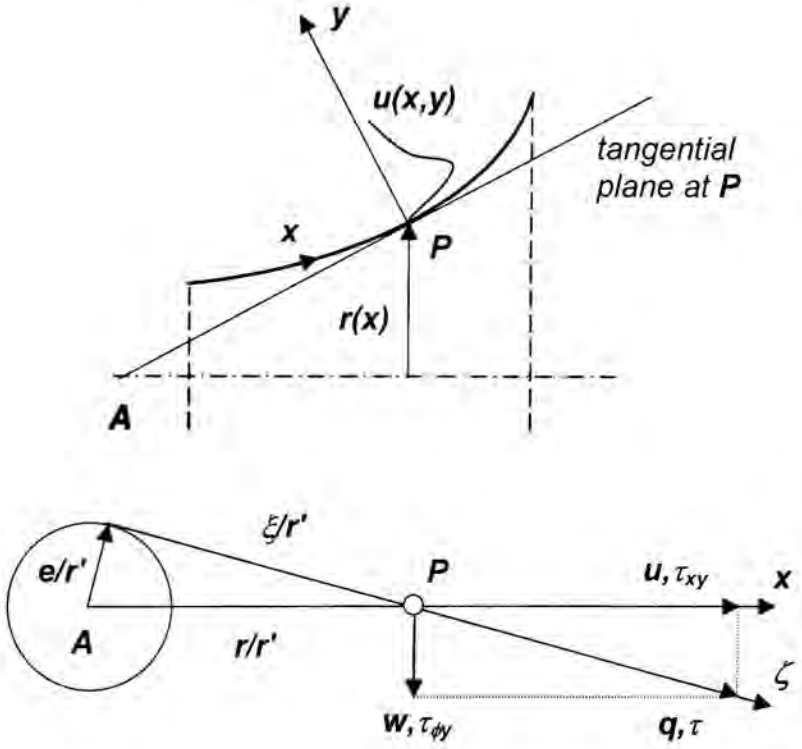

Figure 2: Flow resultants projected onto the tangential plane at the point *P*.

HEFAT2002
1st International Conference on Heat Transfer, Fluid Mechanics, and thermodynamics
8-10 April 2002, Kruger Park, South Africa
LS2

Modeling of Darcy-Forchheimer Drag Tensor for Fluid Flow through a Non-Orthotropic Porous Medium

S. L. Lee and C. H. Kao
Department of Power Mechanical engineering
National Tsing Hua University
Hsinchu 30043, Taiwan

ABSTRACT

An incompressible fluid flow across a bank of square columns is modeled as a non-Darcy flow through a non-orthotropic porous medium. The continuity equation and the momentum equations in pore scale are solved numerically. The Darcy-Forchheimer drag tensor is then determined from the superficial velocity under a prescribed pressure gradient in the global scale. The superficial velocity is found unnecessarily parallel to the pressure gradient. The angle between them would increase when the pressure gradient increases. It could be as large as 20° when the pressure gradient is large. This implies that significant errors might arise if the bank of the square columns is treated as an orthotropically anisotropic porous medium. Such a non-orthotropic flow is not investigated in the past.

INTRODUCTION

In general, the bulk resistance to an incompressible fluid flow through a porous medium is expressible as [1]

$$-\frac{\partial \bar{p}}{\partial x} Re_c \left(\frac{\ell}{L}\right)^2 = r_{xx}\bar{u} + r_{xy}\bar{v} + r_{xz}\bar{w} \qquad (1)$$

$$-\frac{\partial \bar{p}}{\partial y} Re_c \left(\frac{\ell}{L}\right)^2 = r_{yx}\bar{u} + r_{yy}\bar{v} + r_{yz}\bar{w} \qquad (2)$$

$$-\frac{\partial \bar{p}}{\partial z} Re_c \left(\frac{\ell}{L}\right)^2 = r_{zx}\bar{u} + r_{zy}\bar{v} + r_{zz}\bar{w} \qquad (3)$$

where the local volume-averaging pressure $\bar{p}$, the characteristic Reynolds number Re_c, and the superficial velocity $(\bar{u}, \bar{v}, \bar{w})$ have been normalized with the characteristic velocity U_c and the characteristic length in global scale L. The Darcy-Forchheimer drag tensor (a symmetric matrix)

$$\begin{bmatrix} r_{xx} & r_{xy} & r_{xz} \\ r_{yx} & r_{yy} & r_{yz} \\ r_{zx} & r_{zy} & r_{zz} \end{bmatrix} \qquad (4)$$

is non-dimensionalized with the characteristic length in pore scale ℓ. Equations (1)-(3) reveal that the gradient of the local volume-averaging pressure is proportional to the superficial velocity with the coefficient tensor (4). If the local volume-averaging pressure gradient is always parallel to the superficial velocity such that the drag tensor reduces to

$$\begin{bmatrix} r_{xx} & r_{xy} & r_{xz} \\ r_{yx} & r_{yy} & r_{yz} \\ r_{zx} & r_{zy} & r_{zz} \end{bmatrix} = \begin{bmatrix} r & 0 & 0 \\ 0 & r & 0 \\ 0 & 0 & r \end{bmatrix} \qquad (5)$$

then the porous medium is called an isotropic porous medium. Otherwise, it is an anisotropic porous medium. Among anisotropic porous media, an orthotropic porous medium possesses a drag tensor that becomes a diagonal matrix whenever the coordinate axes are parallel with the principal axes of the porous medium, i.e.

$$\begin{bmatrix} r_{11} & r_{12} & r_{13} \\ r_{21} & r_{22} & r_{23} \\ r_{31} & r_{32} & r_{33} \end{bmatrix} = \begin{bmatrix} r_{11} & 0 & 0 \\ 0 & r_{22} & 0 \\ 0 & 0 & r_3 \end{bmatrix} \qquad (6)$$

where the subscripts 11, 22, and 33 denote the principal axes. The porous medium is non-orthotropic if the drag tensor never reduces to a diagonal matrix.

The drag tensor depends on the pore structure of the porous medium. It should be properly modeled before the local volume-averaging Navier-Stokes equation is solved. There are a few drag models available for isotropic porous media (5). Ergun's [2], Ward's [3] and Beavers and Sparrow's [4] correlations

from experimental data are some of the examples. However, drag modeling for anisotropic porous media is still lacking. Recently, Lee and coworker [5, 6] formulated a bank of circular cylinders as an orthotropic porous medium. The velocity and the pressure across a bank of circular cylinders in pore scale were solved numerically. A Darcy-Forchheimer drag tensor was then derived from the pore scale solution. They remarked that the Darcy-Forchheimer drag could be anisotropic even when the matrix of the porous medium is geometrically isotropic [6].

In the present study, a bank of square columns is treated as a non-orthotropic porous medium. Fluid flow across the square columns is solved when a local volume-averaging pressure gradient at various magnitudes and directions is imposed. The Darcy-Forchheimer drag tensor is then determined from the pore scale solution. Such a non-orthotropic flow is not investigated in the past.

THEORETICAL ANALYSIS

Flow in Global Scale

The superficial velocity of a fluid flow through a two-dimensional non-orthotropic porous medium is governed by the system of partial differential equations [1, 6]

$$\frac{\partial \overline{U}}{\partial X}+\frac{\partial \overline{V}}{\partial Y}=0 \tag{7}$$

$$\frac{1}{\varepsilon^2}\left(\rho\overline{U}\frac{\partial \overline{U}}{\partial X}+\rho\overline{V}\frac{\partial \overline{U}}{\partial Y}\right)=-\frac{\partial \overline{P}}{\partial X}-\left(R_{xx}\overline{U}+R_{xy}\overline{V}\right)+\frac{\mu}{\varepsilon}\left(\frac{\partial^2\overline{U}}{\partial X^2}+\frac{\partial^2\overline{U}}{\partial Y^2}\right) \tag{8}$$

$$\frac{1}{\varepsilon^2}\left(\rho\overline{U}\frac{\partial \overline{V}}{\partial X}+\rho\overline{V}\frac{\partial \overline{V}}{\partial Y}\right)=-\frac{\partial \overline{P}}{\partial Y}-\left(R_{yx}\overline{U}+R_{yy}\overline{V}\right)+\frac{\mu}{\varepsilon}\left(\frac{\partial^2\overline{V}}{\partial X^2}+\frac{\partial^2\overline{V}}{\partial Y^2}\right) \tag{9}$$

where (X,Y) is the global coordinates, $(\overline{U},\overline{V})$ is the corresponding superficial velocity, and $\overline{P}(X,Y)$ is the local volume-averaging pressure over the liquid phase. The matrix $\mathbf{R}_{ij}$ is known as Darcy-Forchheimer drag tensor. The notation ε stands for the porosity of the porous medium. All of the physical properties such as the density ρ and the viscosity μ of the fluid are assumed constant. After introducing the dimensionless transformation

$$x=X/L,\quad y=Y/L,\quad \overline{u}=\overline{U}/U_c,\quad \overline{v}=\overline{V}/U_c$$
$$\overline{p}=(\overline{P}-P_{ref})/(\rho U_c^2),\quad \overline{p}^*=Re_c\,\overline{p},$$
$$Re_c=\rho U_c L/\mu \tag{10}$$

Eqs. (7)-(9) become

$$\frac{\partial \overline{u}}{\partial x}+\frac{\partial \overline{v}}{\partial y}=0 \tag{11}$$

$$\frac{Re_c}{\varepsilon}\left(\overline{u}\frac{\partial \overline{u}}{\partial x}+\overline{v}\frac{\partial \overline{u}}{\partial y}\right)=-\varepsilon\frac{\partial \overline{p}^*}{\partial x}-\varepsilon\left(\frac{L}{\ell}\right)^2\left(r_{xx}\overline{u}+r_{xy}\overline{v}\right)+\frac{\partial^2\overline{u}}{\partial x^2}+\frac{\partial^2\overline{u}}{\partial y^2} \tag{12}$$

$$\frac{Re_c}{\varepsilon}\left(\overline{u}\frac{\partial \overline{v}}{\partial x}+\overline{v}\frac{\partial \overline{v}}{\partial y}\right)=-\varepsilon\frac{\partial \overline{p}^*}{\partial y}-\varepsilon\left(\frac{L}{\ell}\right)^2\left(r_{yx}\overline{u}+r_{yy}\overline{v}\right)+\frac{\partial^2\overline{v}}{\partial x^2}+\frac{\partial^2\overline{v}}{\partial y^2} \tag{13}$$

where the dimensionless Darcy-Forchheimer drag tensor is defined by

$$\mathbf{r}_{ij}=\begin{bmatrix} r_{xx} & r_{xy}\\ r_{yx} & r_{yy}\end{bmatrix}=\frac{\ell^2\mathbf{R}_{ij}}{\mu} \tag{14}$$

Note that ℓ is the characteristic length of the porosity matrix. The characteristic length of the global scale L and the characteristic velocity U_c are to be determined according to the characteristics of each individual problem under study.

In a region far from the wall or in the "fully developed" region, the superficial velocity $(\overline{u},\overline{v})$ could be independent of the coordinates. Under such a situation, Eq. (11) is trivial, and Eqs. (12) and (13) reduce, respectively, to

$$r_{xx}\overline{u}+r_{xy}\overline{v}=-\frac{\partial \overline{p}^*}{\partial x}\left(\frac{\ell}{L}\right)^2 \tag{15}$$

$$r_{yx}\overline{u}+r_{yy}\overline{v}=-\frac{\partial \overline{p}^*}{\partial y}\left(\frac{\ell}{L}\right)^2 \tag{16}$$

or

$$\begin{Bmatrix}(-\partial\overline{p}^*/\partial x)(\ell/L)^2\\ (-\partial\overline{p}^*/\partial y)(\ell/L)^2\end{Bmatrix}=\begin{bmatrix} r_{xx} & r_{xy}\\ r_{yx} & r_{yy}\end{bmatrix}\begin{Bmatrix}\overline{u}\\ \overline{v}\end{Bmatrix} \tag{17}$$

in matrix form. Similarly, one has

$$\begin{Bmatrix}(-\partial\overline{p}^*/\partial x^*)(\ell/L)^2\\ (-\partial\overline{p}^*/\partial y^*)(\ell/L)^2\end{Bmatrix}=\begin{bmatrix} r_{x^*x^*} & r_{x^*y^*}\\ r_{y^*x^*} & r_{y^*y^*}\end{bmatrix}\begin{Bmatrix}\overline{u^*}\\ \overline{v^*}\end{Bmatrix} \tag{18}$$

if the governing equations (11)-(13) are formulated in another Cartesian coordinate system (x^*, y^*).

Suppose the coordinate system (x^*, y^*) is defined by rotating the global coordinates (x,y) counterclockwise with an angle ϕ as shown in Fig. 1, then the components of the velocity and pressure gradient between the two coordinate systems follow the relationships

$$\begin{Bmatrix}\overline{u}\\ \overline{v}\end{Bmatrix}=\begin{bmatrix}\cos\phi & -\sin\phi\\ \sin\phi & \cos\phi\end{bmatrix}\begin{Bmatrix}\overline{u^*}\\ \overline{v^*}\end{Bmatrix} \tag{19a}$$

$$\begin{Bmatrix} -\partial\bar{p}^*/\partial x \\ -\partial\bar{p}^*/\partial y \end{Bmatrix} = \begin{bmatrix} \cos\phi & -\sin\phi \\ \sin\phi & \cos\phi \end{bmatrix} \begin{Bmatrix} -\partial\bar{p}^*/\partial x'' \\ -\partial\bar{p}^*/\partial y'' \end{Bmatrix} \tag{19b}$$

Substitution of Eqs. (19a) and (19b) into Eq. (18), one arrives at

$$\begin{Bmatrix} (-\partial\bar{p}^*/\partial x)(\ell/L)^2 \\ (-\partial\bar{p}^*/\partial y)(\ell/L)^2 \end{Bmatrix} = \begin{bmatrix} \cos\phi & -\sin\phi \\ \sin\phi & \cos\phi \end{bmatrix} \begin{bmatrix} r_{x''x''} & r_{x''y''} \\ r_{y''x''} & r_{y''y''} \end{bmatrix} \begin{bmatrix} \cos\phi & \sin\phi \\ -\sin\phi & \cos\phi \end{bmatrix} \begin{Bmatrix} \bar{u} \\ \bar{v} \end{Bmatrix} \tag{20}$$

This implies

$$\begin{bmatrix} r_{xx} & r_{xy} \\ r_{yx} & r_{yy} \end{bmatrix} = \begin{bmatrix} \cos\phi & -\sin\phi \\ \sin\phi & \cos\phi \end{bmatrix} \begin{bmatrix} r_{x''x''} & r_{x''y''} \\ r_{y''x''} & r_{y''y''} \end{bmatrix} \begin{bmatrix} \cos\phi & \sin\phi \\ -\sin\phi & \cos\phi \end{bmatrix} \tag{21}$$

as compared with Eq. (17). It is interesting to note that if the coordinate x'' is parallel to the negative pressure gradient (see Fig. 1), then the drag tensor will reduce to a diagonal matrix

$$\begin{bmatrix} r_{x''x''} & r_{x''y''} \\ r_{y''x''} & r_{y''y''} \end{bmatrix} = \begin{bmatrix} r_{x''x''} & 0 \\ 0 & r_{y''y''} \end{bmatrix} \tag{22}$$

for orthotropic porous media [1]. In this connection, $r_{x''x''}$ and $r_{y''y''}$ are the principal values of the drag tensor with respect to the principal axes x'' and y''. Therefore, it would greatly simplify the formulation even for non-orthotropic porous media, if one models the drag tensor $r_{x''x''}$, $r_{x''y''}$, $r_{y''x''}$, and $r_{y''y''}$ for the closure of the problem (11)-(13) through the use of Eq. (21).

Flow in Pore Scale

Consider an incompressible laminar fluid flow across a bank of square columns. Each of the columns has the square cross section of $s \times s$. The columns are arranged in parallel with a center-to-center distance ℓ as shown in Fig. 1. The dimensionless coordinate system (x', y') parallel to the arrangement of the square columns is defined based on the length scale ℓ. The pore scale ℓ is assumed very small as compared to the characteristic length L of the flow in global scale ($\ell << L$) such that the bank of square columns can be treated as a porous medium. Let a "constant" negative pressure gradient $-\Delta P/\ell$ in the global scale is imposed on the flow at the directional angle ϕ_p with respect to the x' axis. This gives rise to a periodic flow in the pore scale with a constant pressure drop $\Delta P \cos\phi_p$ after each period $\ell \cos\phi_p$ in the "fully developed" region. Thus, only the flow inside a unit cell $0 \le x' \le 1$ and $0 \le y' \le 1$ (see the dashed lines in Fig. 1) is needed to solve [5, 6].

After making the assumptions, the dimensionless governing equations are expressible as

$$\frac{\partial u'}{\partial x'} + \frac{\partial v'}{\partial y'} = 0 \tag{23}$$

$$Re_p\, u' \frac{\partial u'}{\partial x'} + Re_p\, v' \frac{\partial u'}{\partial y'} = -\frac{\partial p^*}{\partial x'} + \frac{\partial^2 u'}{\partial x'^2} + \frac{\partial^2 u'}{\partial y'^2} \tag{24}$$

$$Re_p\, u' \frac{\partial v'}{\partial x'} + Re_p\, v' \frac{\partial v'}{\partial y'} = -\frac{\partial p^*}{\partial y'} + \frac{\partial^2 v'}{\partial x'^2} + \frac{\partial^2 v'}{\partial y'^2} \tag{25}$$

where (u', v') is the dimensionless velocity based on U_p, and the dimensionless quantities

$$Re_p = \frac{\rho U_p \ell}{\mu}, \quad U_p = \sqrt{\Delta P/\rho},$$
$$p = (P - P_{ref})/\Delta P, \quad p^* = Re_p\, p \tag{26}$$

have been employed. The associated boundary conditions are of the periodic type

$$u'(x', y') = u'(x' - 1, y'),\ v'(x', y') = v'(x' - 1, y'),$$
$$p^*(x', y') = p^*(x' - 1, y') - Re_p \cos\phi_p \tag{27}$$

at $x' = 1 \pm \Delta x'$, and

$$u'(x', y') = u'(x', y' - 1), \quad v'(x', y') = v'(x', y' - 1),$$
$$p^*(x', y') = p^*(x', y' - 1) - Re_p \sin\phi_p \tag{28}$$

at $y' = 1 \pm \Delta y'$, where $0 < \Delta x' << 1$ and $0 < \Delta y' << 1$. Note that the no-slip condition should be imposed on the surfaces of the square columns. Thus, there is no need to solve the governing equations inside the solid. For convenience, the pressure level is set as $p^* = 0$ at the point $(x', y') = (1, 0.5)$.

The governing equations (23)-(25) and the associated boundary conditions (27) and (28) constitute a system of partial differential equations. They can be efficiently solved on a non-staggered grid system with the weighting function scheme [7, 8] along with the NAPPLE algorithm [9] and the SIS solver [10]. In the present study, the primary variables (u', v', p^*) are obtained for each set of prescribed values of (Re_p, ϕ_p, s/ℓ). The numerical procedure is iterated until the solution (u', v', p^*) converges within a prescribed tolerance *Tol*, i.e.

$$\frac{Max\left|u'_k - (u'_k)^0\right|}{V_{max}} < Tol \tag{29a}$$

$$\frac{Max\left|v_k' - (v_k')^0\right|}{V_{max}} < Tol \qquad (29b)$$

$$\frac{Max\left|(p^*)_k - (p^*)_k^0\right|}{(p^*)_{max} - (p^*)_{min}} < Tol \qquad (29c)$$

where the subscript k denotes the k-th grid point, and the superscript 0 stands for the result of the previous iteration. The notation V represents the magnitude of the dimensionless velocity

$$V = \sqrt{(u')^2 + (v')^2} \qquad (30)$$

Once the velocity is known, the dimensionless volumetric flow rate $(q_{x'}, q_{y'})$ in (x', y') coordinates can be evaluated from

$$q_{x'}(x') = \frac{Q_{x'}}{U_p\,\ell} = \int_0^1 u(x', y')\,dy' \qquad (31a)$$

$$q_{y'}(y') = \frac{Q_{y'}}{U_p\,\ell} = \int_0^1 v(x', y')\,dx' \qquad (31b)$$

It is noted that both $q_{x'}(x')$ and $q_{y'}(y')$ can be proven to be constant from the theorem of Reynolds transport. This implies that the superficial velocity $(\overline{U'}, \overline{V'})$ in the global scale can be written as

$$\overline{U'} = U_p\,q_{x'}, \quad \overline{V'} = U_p\,q_{y'} \qquad (32)$$

and thus the direction of the superficial velocity is

$$\phi_v = \tan^{-1}\left(\frac{q_{y'}}{q_{x'}}\right) \qquad (33)$$

It should be noted here that for non-orthotropic porous media the superficial velocity is not necessarily parallel to the negative pressure gradient (i.e. $\phi_v \neq \phi_p$). When resolved into components in the coordinates (x^*, y^*) with x^* being parallel to the negative pressure gradient, the dimensionless volumetric flow rate becomes

$$\begin{Bmatrix} q_{x^*} \\ q_{y^*} \end{Bmatrix} = \begin{bmatrix} \cos\phi_p & \sin\phi_p \\ -\sin\phi_p & \cos\phi_p \end{bmatrix} \begin{Bmatrix} q_{x'} \\ q_{y'} \end{Bmatrix} \qquad (34)$$

and the superficial velocity is

$$\overline{U^*} = U_p\,q_{x^*}, \quad \overline{V^*} = U_p\,q_{y^*} \qquad (35)$$

in the global scale. For a flow through an orthotropic porous medium, the component q_{y^*} should be zero. Otherwise, the porous medium is non-orthotropic.

Modeling of Drag Tensor

As mentioned earlier, through the use of Eq. (21) one has only to model the drag tensor $r_{x^*x^*}$, $r_{x^*y^*}$, $r_{y^*x^*}$, and $r_{y^*y^*}$ for the closure of the problem (11)-(13). In the global scale, the pressure gradient is expressible as

$$-\frac{\partial \overline{P}}{\partial X^*} = \frac{\Delta P}{\ell}, \quad -\frac{\partial \overline{P}}{\partial Y^*} = 0 \qquad (36)$$

or

$$-\frac{\partial \overline{p}^*}{\partial x^*} = \left(\frac{U_p}{U_c}\right)^2\left(\frac{L}{\ell}\right) Re_c = \left(\frac{U_p}{U_c}\right)\left(\frac{L}{\ell}\right)^2 Re_p,$$

$$-\frac{\partial \overline{p}^*}{\partial y^*} = 0 \qquad (37)$$

if a negative pressure gradient $-\Delta P/\ell$ parallel to the x^* axis is imposed on the flow. Similarly, the dimensionless superficial velocity $(\overline{u^*}, \overline{v^*})$ can be evaluated from

$$\overline{u^*} = \frac{\overline{U^*}}{U_c} = \left(\frac{U_p}{U_c}\right) q_{x^*}, \quad \overline{v^*} = \frac{\overline{V^*}}{U_c} = \left(\frac{U_p}{U_c}\right) q_{y^*} \qquad (38)$$

as observable from Eq. (35) Substitution of Eqs. (37) and (38) into (18) yields

$$r_{x^*x^*}\,q_{x^*} + r_{x^*y^*}\,q_{y^*} = Re_p \qquad (39)$$

$$r_{y^*x^*}\,q_{x^*} + r_{y^*y^*}\,q_{y^*} = 0 \qquad (40)$$

In the present study, the flow rate (q_{x^*}, q_{y^*}) under a given pressure Reynolds number Re_p is obtained. Therefore, there are four unknowns (i.e. the drag tensor $r_{x^*x^*}$, $r_{x^*y^*}$, $r_{y^*x^*}$, and $r_{y^*y^*}$) in the two equations (39) and (40). If the drag tensor is assumed symmetric ($r_{x^*y^*} = r_{y^*x^*}$), then one more condition is needed for the uniqueness of the drag tensor. For convenience, let Eqs. (39) and (40) be rewritten as

$$r_{x^*x^*} = (Re_p - r_{x^*y^*}\,q_{y^*})/q_{x^*} \qquad (41)$$

$$r_{y^*y^*} = -r_{y^*x^*}\,q_{x^*}/q_{y^*} \qquad (42)$$

This means that there is a numerical difficulty in determining $r_{y^*y^*}$ when $q_{y^*} = 0$. To circumvent this problem, one assigns

$$r_{y^*x^*} = r_{x^*y^*} = -c\,q_{y^*} \qquad (43)$$

such that

$$r_{x^*x^*} = (Re_p + c\,q_{y^*}^2)/q_{x^*} \qquad (44)$$

$$r_{y^*y^*} = c\,q_{x^*} \qquad (45)$$

where c is an arbitrary nonzero positive constant. For simplicity, the constant c is assigned as $c = 100$ in the present study. In summary, the "principal" drag tensor ($r_{x^*x^*}$, $r_{x^*y^*}$, $r_{y^*x^*}$, and $r_{y^*y^*}$) can be determined from Eqs. (43)—(45). The drag tensor (r_{xx}, r_{xy}, r_{yx}, and r_{yy}) in the global coordinates (x, y) is then evaluated from Eq. (21). It is quite interesting to note that for orthotropic porous medium (or when q_{y^*} is zero), Eq. (43) becomes

$$r_{x^*y^*} = r_{y^*x^*} = 0 \qquad (46)$$

RESULTS AND DISCUSION

Numerical results of dimensionless flow rate (q_{x^*}, q_{y^*}) in pore scale are obtained for a "porosity" with $s/\ell = 0.6$. The pressure Reynolds numbers considered here are Re_p = 50, 100, 150, 200, 250, and 300. Under each pressure Reynolds number, the pressure angle ϕ_p of about every 3° in the range $0 \le \phi_p \le 45°$ is studied. For $45° < \phi_p \le 360°$, results of the dimensionless flow rate (q_{x^*}, q_{y^*}) can be determined by

$$q_{x^*}(\phi_p) = q_{x^*}(90° - \phi_p), \quad q_{y^*}(\phi_p) = -q_{y^*}(90° - \phi_p) \quad \text{for } 45° \le \phi_p < 90° \tag{47a}$$

$$q_{x^*}(\phi_p) = q_{x^*}(180° - \phi_p), q_{y^*}(\phi_p) = -q_{y^*}(180° - \phi_p) \quad \text{for } 90° \le \phi_p < 180° \tag{47b}$$

$$q_{x^*}(\phi_p) = q_{x^*}(360° - \phi_p), q_{y^*}(\phi_p) = -q_{y^*}(360° - \phi_p) \quad \text{for } 180° \le \phi_p < 360° \tag{47c}$$

due to geometric symmetry. To be within the laminar flow regime, the pressure Reynolds number Re_p considered here is less than 300. Nevertheless, it is practical in most applications in view of the definition of Re_p in Eq. (26) while the pore scale ℓ is very small.

Figures 2—4 illustrate the dimensionless streamlines and isobars at $Re_p = 300$ for $\phi_p = 0°$, 30° and 45°, respectively. The increment of the isobars is 0.1, while that of the streamlines is one tens of the total flow rate

$$q = \sqrt{q_{x'}^2 + q_{y'}^2} \tag{48}$$

The dimensionless stream function is defined by either

$$\psi(x', y') = \psi(x', 0) + \int_0^{y'} u(x', y')\, dy' \tag{49a}$$

$$\psi(x', 0) = \begin{cases} 0 & \text{if } 0 \le x' \le s/2 \\ -\int_{s/2}^{x'} v(x', 0)\, dx' & \text{if } s/2 \le x' \le (1 - s/2) \\ \psi(1 - s/2, 0) & \text{if } (1 - s/2) \le x' \le 1 \end{cases} \tag{49b}$$

or

$$\psi(x', y') = \psi(0, y') - \int_0^{x'} v(x', y')\, dx' \tag{50a}$$

$$\psi(0, y') = \begin{cases} 0 & \text{if } 0 \le y' \le s/2 \\ \int_{s/2}^{y'} u(0, y')\, dy' & \text{if } s/2 \le y' \le (1 - s/2) \\ \psi(0, 1 - s/2) & \text{if } (1 - s/2) \le y' \le 1 \end{cases} \tag{50b}$$

Figure 2 reveals a symmetric flow field about the x' axis. This implies that the superficial velocity $(\bar{u}, \bar{v})$ is parallel to the averaged pressure gradient, i.e. $\phi_v = \phi_p$. Similar situation occurs in Fig. 4 when $\phi_p = 45°$ due to the alignment of the averaged pressure gradient and the porosity structure. However, it is not the case when $\phi_p = 30°$ as observable from Fig. 3. This will be discussed later.

In the present computations, three uniform grid systems with 81×81, 121×121, and 161×161 grid points are employed. The tolerance used for the convergence criterion (29a)—(29c) is $Tol = 10^{-6}$. Figure 5 illustrates the results of $q_{x'}(x')$ for the case of $Re_p = 100$ and $\phi_p = 0°$ based on each of the three grid systems. The grid mesh with 161×161 grid points is seen to provide a flow rate with a variation less than 0.2 percent. Thus, all of the results presented in this paper including Fig. 2—4 are based on the finest grids (161×161). The resulting flow rates (q_{x^*}, q_{y^*}) at various Re_p and ϕ_p values are depicted in Table 1. There is no reliable experimental data to validate their accuracy. Fortunately, the purpose of the present study is to propose a simple numerical procedure for examining the importance of the non-orthotropy of a porous medium and for modeling of the drag tensor.

The deflection angle $(\phi_v - \phi_p)$ between the superficial velocity and the negative pressure gradient is shown in Fig. 6 as a function of ϕ_p with the Reynolds number Re_p being a parameter. From Fig. 6, one sees that the deflection angle is zero at the two particular angles $\phi_p = 0°$ and $\phi_p = 45°$ due to geometric symmetry. By contrast, when $0° < \phi_p < 45°$ flowing in the x-direction would be easier than flowing in the y-direction for the fluid. The deflection angle thus is negative as shown in Fig. 6 (except for the case $Re_p = 50$ with $31° < \phi_p < 45°$). It could be as large as –21° at $\phi_p = 27°$ when $Re_p = 300$. Under such a situation, the porous medium cannot be assumed orthotropic.

Finally, the resulting drag tensor ($r_{x^*x^*}$, $r_{x^*y^*} = r_{y^*x^*}$, and $r_{y^*y^*}$) as a function of ϕ_p and Re_p are presented in Fig. 7, 8, and 9, respectively. When the system of differential equations (11)—(13) is applied on an incompressible flow through a porous medium with a structure as shown in Fig. 1, the drag tensor r_{xx}, r_{xy}, r_{yx} and r_{yy} can be estimated from

Figs. 7—9 and Eqs. (21). Their values would vary with the coordinates (x,y) if the local Reynolds number Re_p and pressure angle ϕ_p (and thus ϕ) are space-dependent.

CONCLUSION

Modeling of Darcy-Forchheimer drag tensor for a fluid flow through a porous medium with periodic structure is performed in the present paper. As an illustration, a bank of square columns is treated as a porous medium, while an incompressible laminar flow goes through it. In the present work, fluid flow in the pore scale is obtained numerically. The Darcy-Forchheimer drag tensor is then determined from the resulting superficial velocity under a prescribed pressure gradient in the global scale. The bank of the square columns is found not to be an orthotropic porous medium, because the superficial velocity is not necessarily parallel to the pressure gradient. The angle between them could be as large as 20° when the pressure gradient is large. The simple method proposed in the present paper can be employed to determine the Darcy-Forchheimer drag tensor for porous media of periodic structure.

ACKNOWLEDGMANT

The authors wish to express their appreciation to the National Science Council of Taiwan for the financial support of this work through the contract NSC 89-2212-E007-032.

REFERENCE

[1] Kaviany M., 1995, "Principle of Heat Transfer in Porous Media," 2nd ed., Spring-Verlag, New York, pp. 17-20.

[2] Ergun, S., 1952, "Fluid Flow through Packed Columns," *Chemical Engineering Progress*, **48**, pp. 89-94.

[3] Ward, J. C., 1964, "Turbulent Flow in Porous Media," *ASCE J. of Hydraulic Division*, **90**, pp. 1-12.

[4] Beavers, G. S., and Sparrow E. M., 1969, "Non-Darcy Flow through Fibrous Porous Media," *ASME J. of Applied Mechanics*, **36**, pp. 711-714.

[5] Lee, S. L., and Yang, J. H., 1997, "Modeling of Darcy-Forchheimer Drag for Fluid Flow across a Bank of Circular Cylinders," *Int. J. Heat Mass Transfer*, **40**, pp. 3149-3155.

[6] Yang, J. H., and Lee, S. L., 1999, "Effect of Anisotropy on Transport Phenomena in Anisotropic Porous Media," *Int. J. Heat Mass Transfer*, **42**, pp. 2673-2681.

[7] Lee, S. L., 1989, "Weighting Function Scheme and Its Application on Multidimensional Conservation Equations," *Int. J. Heat Mass Transfer*, **32**, pp. 2065-2073.

[8] Lee, S. L., and Sheu, S. R., 2000, "A New Numerical Formulation for Incompressible Viscous Free Surface Flow without Smearing the Free Surface," *Int. J. of Heat Mass Transfer*, **44**, pp. 1837-1848.

[9] Lee, S. L., and Tzong, R. Y., 1992, "Artificial Pressure for Pressure-Linked Equation," *Int. J. Heat Mass Transfer*, **35**, pp. 2705-2716.

[10] Lee, S. L., 1989, "A Strongly-Implicit Solver for Two-Dimensional Elliptic Differential Equations," *Numer. Heat Transfer*, **16B**, pp.161-178.

Table 1 Results of $(q_{x'}, q_{y'})$ at various Re_p and ϕ_p.

ϕ_p \ Re_p	50	100	150	200	250	300
0°	0.3146 0.0000	0.6032 0.0000	0.8778 0.0000	1.1380 0.0000	1.3852 0.0000	1.6247 0.0000
3°	0.3142 -0.0020	0.6001 -0.0191	0.8736 -0.0373	1.1350 -0.0526	1.3766 -0.0657	1.6062 -0.0778
6°	0.3130 -0.0037	0.5901 -0.0366	0.8573 -0.0726	1.1136 -0.1028	1.3506 -0.1286	1.5757 -0.1525
9°	0.3109 -0.0051	0.5732 -0.0506	0.8290 -0.1035	1.0766 -0.1479	1.3065 -0.1858	1.5251 -0.2210
12°	0.3084 -0.0061	0.5492 -0.0589	0.7871 -0.1267	1.0215 -0.1844	1.2427 -0.2341	1.4531 -0.2800
15°	0.3053 -0.0065	0.5180 -0.0588	0.7279 -0.1375	0.9442 -0.2072	1.1571 -0.2695	1.3625 -0.3272
18°	0.3023 -0.0065	0.4839 -0.0498	0.6522 -0.1307	0.8436 -0.2111	1.0441 -0.2860	1.2394 -0.3546
20°	0.3002 -0.0063	0.4621 -0.0399	0.5974 -0.1161	0.7652 -0.2012	0.9456 -0.2800	1.1431 -0.3604
24°	0.2962 -0.0054	0.4301 -0.0200	0.5131 -0.0816	0.6217 -0.1632	0.7694 -0.2548	0.9291 -0.3406
27°	0.2937 -0.0045	0.4161 -0.0092	0.4761 -0.0611	0.5467 -0.1319	0.6411 -0.2108	0.7557 -0.2892
30°	0.2914 -0.0036	0.4077 -0.0023	0.4527 -0.0445	0.4981 -0.1049	0.5525 -0.1630	0.6188 -0.2277
33°	0.2898 -0.0027	0.4030 0.0014	0.4375 -0.0308	0.4651 -0.0801	0.4865 -0.1188	0.5272 -0.1686
36°	0.2885 -0.0019	0.4002 0.0029	0.4274 -0.0192	0.4404 -0.0527	0.4449 -0.0755	0.4667 -0.1127
40°	0.2873 -0.0010	0.3985 0.0024	0.4192 -0.0084	0.4172 -0.0189	0.4097 -0.0219	0.4004 -0.0200
42°	0.2870 -0.0006	0.3980 0.0016	0.4168 -0.0047	0.4108 -0.0094	0.3995 -0.0093	0.3883 -0.0076
45°	0.2868 0.0000	0.3978 0.0000	0.4155 0.0000	0.4072 0.0000	0.3944 0.0000	0.3826 0.0000

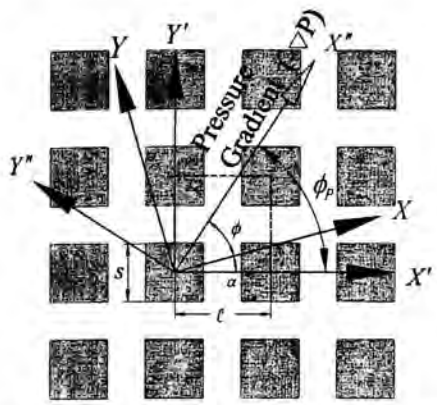

Fig. 1 The flow configuration and coordinate systems

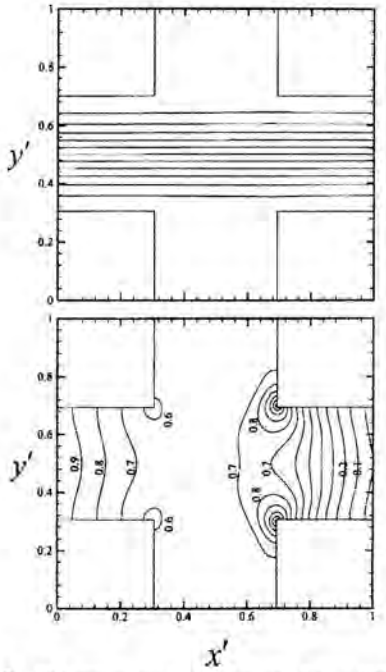

Fig. 2 The streamlines and isobars at $Re_p = 300$ and $\phi_p = 0°$

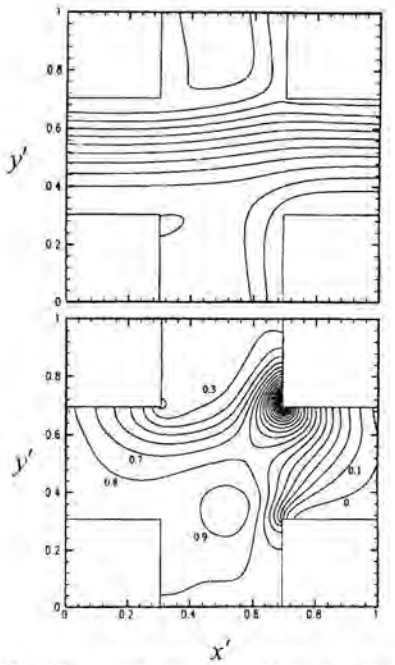

Fig. 3 The streamlines and isobars at $Re_p = 300$ and $\phi = 30°$

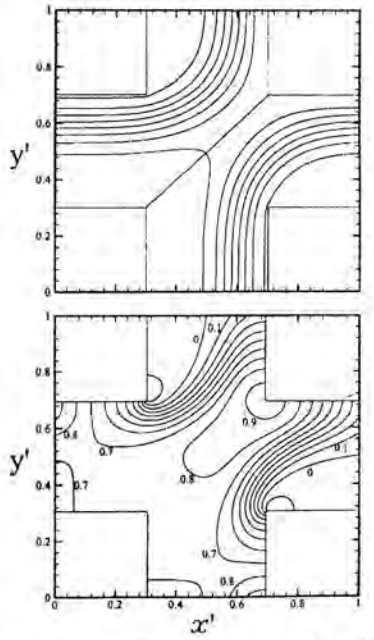

Fig. 4 The streamlines and isobars at $Re_p = 300$ and $\phi_p = 45°$

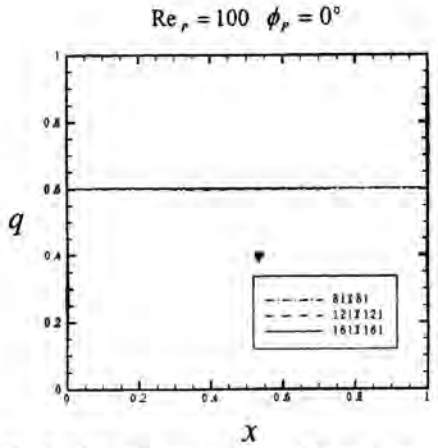

Fig. 5 Grid influence on the $q_{x'}(x')$ results at $Re_p = 100$ and $\phi_p = 0°$

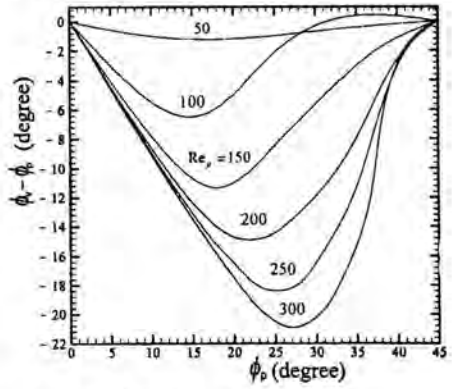

Fig. 6 The deflection angle between the superficial velocity and the negative pressure gradient

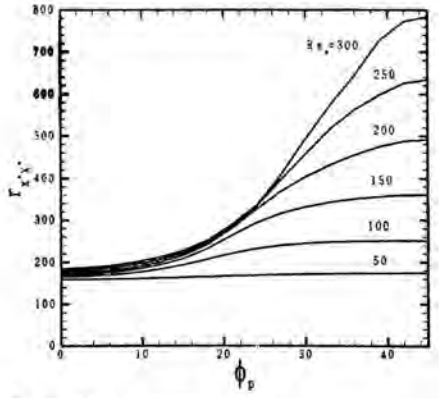

Fig. 7 The drag component $r_{x^*x^*}$

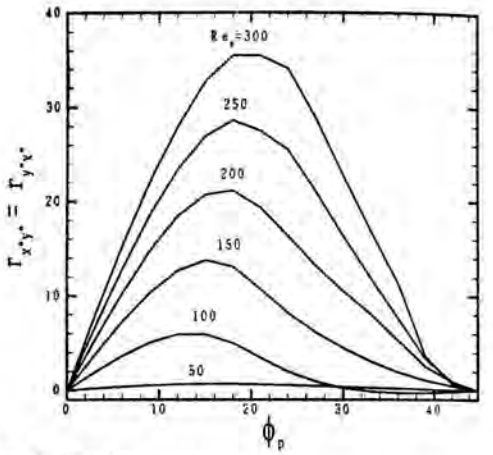

Fig. 8 The drag component $r_{x^*y^*}$

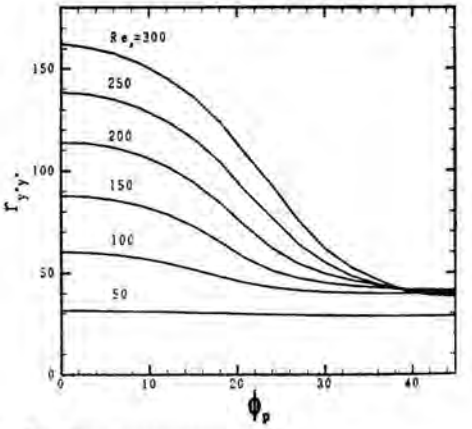

Fig. 9 The drag component $r_{y^*y^*}$

HEFAT2002
1st International Conference on Heat Transfer, Fluid Mechanics, and Thermodynamics
8-10 April 2002, Kruger Park, South Africa
LS3

2D LOCALIZATION OF A HEAT SOURCE USING ARTIFICIAL NEURAL NETWORKS

Sylvain LALOT[1] and Stéphane LECOEUCHE[1,2]
1) E.I.P.C., Campus de la Malassise, BP 39
62967 Longuenesse Cedex, France
slalot@eipc.fr (corresponding author)
2) Laboratoire I3D, USTL, Bâtiment P2,
59655 Villeneuve d'Ascq, France
slecoeuche@eipc.fr

ABSTRACT

The feasibility of the 2D localization of a constant heat source using artificial neural networks (ANNs) is studied. First, the structure is described and examples of a temperature field and of a temperature profile are given. Then the ANNs abilities are presented. The learning database and the 3 test data sets are introduced along with quality criteria. Then 13 networks are studied (7 Back Propagation Networks - BPNs, and 6 Radial Basis Function Networks - RBFNs). It is shown that BPNs have better generalization abilities for the studied problem. Then the influence of the number of neurons in the hidden layer is studied, leading to the optimal value. The analysis of the quality criteria shows that the maximum distance between an identified heat source and its actual location is smaller than 0.35% of the minimum length of the domain.

Keywords: Localization, Inverse thermal problem, Neural networks, Heat source.

NOMENCLATURE

H	height of the domain	**[m]**
h	heat transfer coefficient	[W/m².K]
I	input vector	
L	length of the domain	**[m]**
Q_v	power of the heat source	**[W]**
q	heat flux	**[W]**
T	temperature	[K or °C]
W	connection weight vector	
x	first coordinate	**[m]**
y	second coordinate	**[m]**

Greek symbols

λ	thermal conductivity	[W/m.K]

Subscripts

a	ambient
h	heat source

INTRODUCTION

The aim of the present study is to show the feasibility of the localization of a constant heat source in a 2D structure, using the temperature profile on one outer edge of the domain. The structure that has been chosen is a rectangle having 3 insulated sides and one side in contact with air through a convection coefficient (figure 1). As the latter would be the only visible edge in a real application, it serves as a basis of the study. It can be seen in figure 1, that the chosen values for all parameters are not physical values. But for a feasibility demonstration, this is sufficient. It has to be noted that the heat source being not very powerful, the values of the temperature on the convecting edge will be quite low.

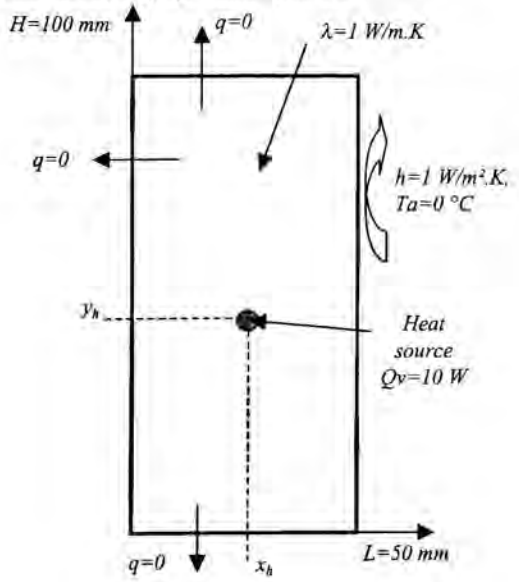

Fig. 1: Schematic of the structure

The heat source may be located at any point within the structure. The temperature profile on the considered edge depends on this position (Figure 2). The temperature field is obtained using a finite difference scheme (Incropera and de Witt, 1996).

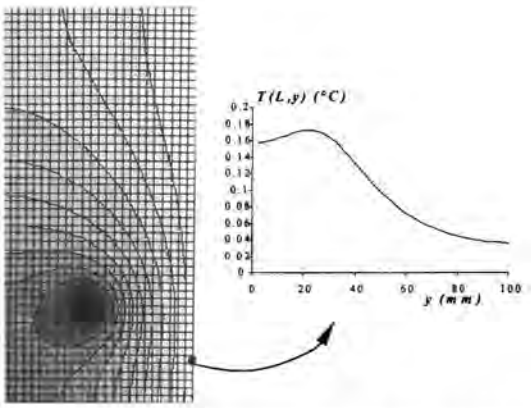

Fig. 2: Example of a temperature field and of the corresponding temperature profile

As a given temperature profile corresponds to a unique location of the heat source, carefully studying the temperature profile should lead to the possibility of finding the location of the heat source. Many methods could be used to solve this inverse problem (Tarantola, 1987) (Kirsch, 1996) (Olson and Throne, 2000) (Shin and Lee, 2000) (Eurotherm, 2001). Most of the methods use regularization techniques or Eigensystem techniques. But none of them present the advantages of the neural networks in solving the inverse conduction problem (ICP). Artificial neural networks (ANNs) have proved to be efficient in many identification problems: identification of the population of water droplets in a dry steam flow (Lurette, 1998); identification of parameters of large scale plants (Pham and Oh, 1999); identification of the parameters of circulation heaters and solar collectors (Lalot and Lecoeuche, 2000), (Lalot, 2000); identification of heat exchangers (Diaz et al., 2001). To enlarge the available tools for ICP solving, and as a first step towards real-world problem solving, it has been chosen here to test some ANNs on a 2D problem.

PRINCIPLES OF THE LOCALIZATION

Mc Culloch and Pitts have introduced the first artificial neuron in 1943. Since then, many neural networks have been proposed (Marren et al., 1990): the Perceptrons, the Hamming networks, the Radial Basis Function Networks (RBFNs), the Probabilist Neural Networks, the Self-Organizing Maps (SOMs), the Learning Vector Quantization, the Back Propagation Networks (BPNs) ... They differ one another by the type of neurons, their architecture, their learning rule. All these characteristics determine their main application field: classification, optimization, identification...

For example, the Perceptrons use hyperplanes to form and separate convex regions; they are used for classification; the SOMs use unsupervised training and are not suitable for inverse problem solving; the RBFNs use overlapping circular hyperballs to represent the data and are used in system modeling, classification and prediction; BPNs use a specific propagation of the error to modify the connection weights during the learning phase. They are also used for modeling and prediction. See (kosko, 1992) for more details.

Finally, the architectures that are tested in this study are the RBFNs and the BPNs that are feedforward networks (Figure 3).

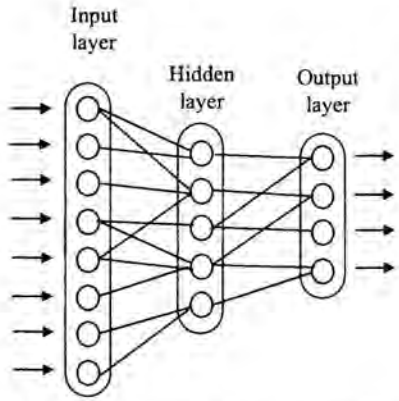

Fig. 3: Schematic of a feedforward network

In any case, once the architecture is chosen, the difficulties are to find the number of hidden layers (several layers might be used), the number of neurons in each layer, the type of neural activity (or transfer) function, and the type of output function (figure 4). As there is no analytical approach, only experiments lead to an efficient solution.

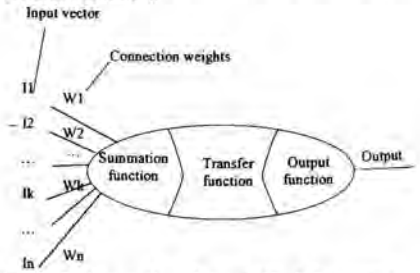

Fig. 4: Schematic of an artificial neuron

This is done in two major steps: a learning phase and a validation phase. In this study a supervised training is necessary: during the learning phase the ANN knows the outputs it should find for the input vectors that are contained in the learning database. The input vectors components are samples located on the temperature profile. During this study, no significant difference has been found between 25 or 50 samples per profile. As the computational time is not very much increased, it has been chosen to use 50 samples on each temperature profile, for 35 heat source learning locations (Figure 5)

During the validation phase, the network does not know the outputs. To be able to measure the quality of the learning, it has been chosen to test the architecture on known couples (temperature profiles/heat source coordinates). In this study, it has been chosen to build the test data sets as follows (figure 5):

- 1st set: the coordinate of the heat source y_h is already present in the learning database
- 2nd set: the coordinate of the heat source x_h is already present in the learning database
- 3rd set: none of the coordinates is already present in the learning database

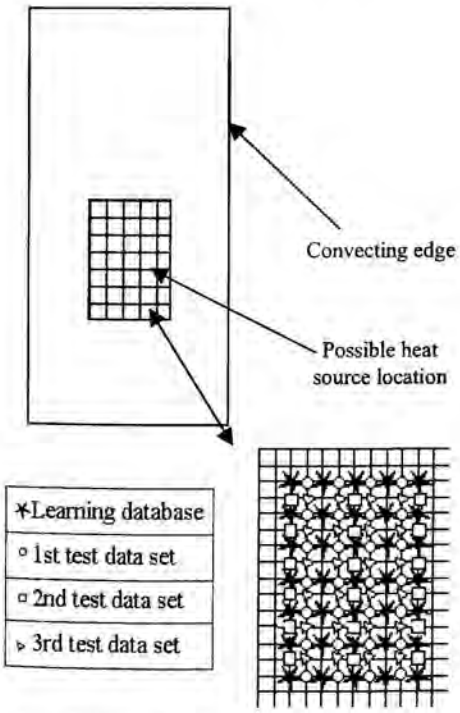

Fig. 5: Definition of the learning and test databases

Figure 6 shows the temperature profiles for the different databases.

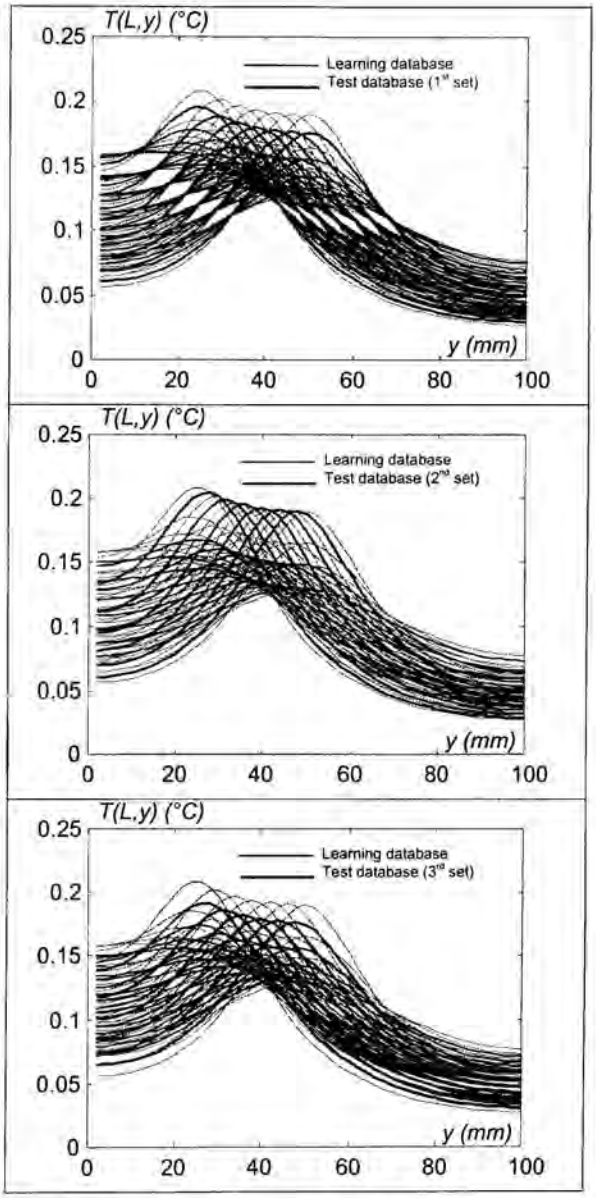

Fig. 6: Temperature profiles on the convecting edge

In this study, the quality of the learning phase is measured using 3 criteria. All are based on the Euclidean distance between the identified heat source location and the actual heat

source location. The first criterion, the most global one, is the mean value of the Euclidean distances for all the 70 test locations. The second criterion is the correlation matrixes for the two heat source coordinates. The third criterion is the histogram of the distances.

RESULTS

During this study, the following networks have been tested:

Architecture	Back Propagation						RBF		
# of neurons on the hidden layer	1	5	10	20	30	50	20	30	50
Linear output function			X				X	X	X
Hyperbolic tangent output function	X	X	X	X	X	X	X	X	X

All the networks have only one hidden layer, and the Extended Delta-Bar-Delta learning rule is used in any case. Satisfactory results being obtained, no further improvement has been looked for.

Global learning abilities

Figure 7 shows the comparison of typical evolutions of the learning error and of the test error (1st criterion) for a RBFN and a BPN.

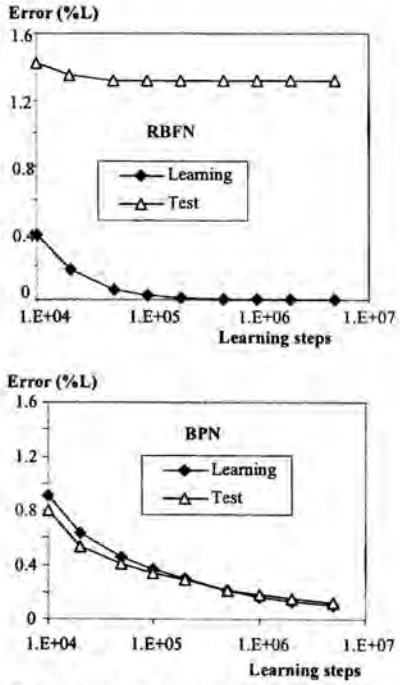

Fig. 7: Typical evolutions of the learning and test errors

It can be seen in Figure 7, and this is a general conclusion, that RBFNs learn more quickly than BPNs. In our case, the difference between the number of learning steps that are necessary to achieve a good training is about one order of magnitude. This is due to the fact that the BPNs use the back propagation of the error to adjust the values of the connection weights. This should be done avoiding local minima that does not exist in the RBFNs procedure. For more details see (NeuralWare, 1993) or (Looney, 1997).

It can be seen, and this is also a general conclusion, that although RBFNs are able to perfectly learn, their generalization abilities are not as good as those of the BPNs. In our study, the test error is always close to the learning error for BPNs when the test error for RBFNs is never less than 1% (even with 50 neurons on the hidden layer). This is due to the fact that the very first phase of the training of the RBFNs is a clustering phase: the neurons of the hidden layer learn to be the center of clusters of the input vectors. Then the modification of these centers is quite difficult and the generalization abilities are reduced, compared to those of the BPNs.

It is also important to note that the test error of the BPNs does not increase. This shows that no over learning occurs for these networks.

Influence of the output function

The output function may serve to smooth the output of the transfer function. A linear output function reproduces the output of the transfer function on the output of the neuron. An hyperbolic tangent output function does the same thing as long as the approximation $th(x)=x$ is valid. For other values coming from the transfer function a large modification is damped by the asymptotic shape of the function.

When significant difference exists, the advantage goes to the hyperbolic tangent output function for the RBFNs.

The improvement is much more obvious for the BPNs. The error is about 5 times smaller for the hyperbolic tangent output function. This explains why a linear output function has been considered for only one case.

Influence of the number of neurons on the hidden layer

As already mentioned, there is no analytical rule to determine the adequate number of neurons on the hidden layer of neural networks and experiments must cover a large range of values. Figure 8 shows the evolution of the test error (1st criterion) for the BPNs having a hyperbolic tangent output function.

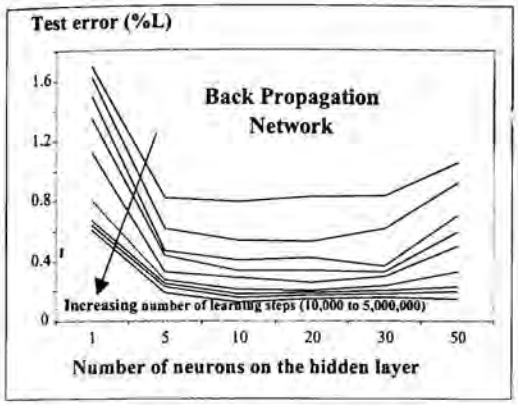

Fig. 8: Evolution of the test error versus the number of neurons on the hidden layer

It can be clearly seen that few neurons (less than 5 neurons) on the hidden layer leads to very bad results. It can also be observed that increasing the number of neurons does not lead to better results, even for very large numbers of learning steps. This can be explained by the fact that, in that case, not enough information is contained in the learning database; the number of neurons on the hidden layer is too large as compared to the number of samples on the temperature profile.

The lowest value of the test error is always obtained for 10 neurons on the hidden layer. So, it can be concluded that this is a good choice for the present study.

A similar analysis leads to find 30 neurons on the hidden layer for the RBFNs.

All these results show that a simpler architecture and more accurate results are obtained using BPNs. This is why the following results are presented only for the BPNs.

Visualization of the other quality criteria

As a matter of fact, the first criterion is a global criterion. So, it is informative to visualize the two other criteria for the selected BPN (10 neurons on the hidden layer) to see if the results are valid over the whole identification domain.

This is done in two ways. Firstly, the correlation matrixes are plotted; no point should be out of the diagonal. Secondly, the histograms of the distances are plotted. This gives a more accurate view on the quality of the identification.

Figure 9 shows the correlation matrixes for the third test data set.

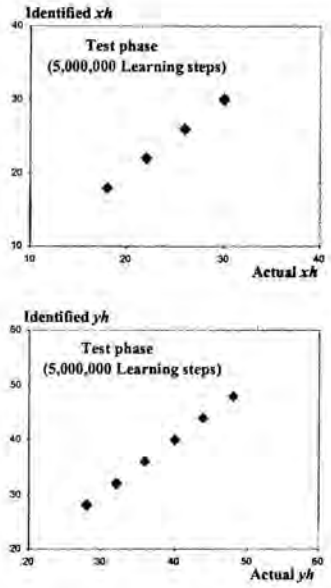

Fig. 9: Correlation matrixes for the third test database

This shows that the quality of the identification is constant over the whole domain.

This can be confirmed by the study of the histograms of the distances. Figure 11 shows the histograms for the learning database (for two different values of the number of learning steps).

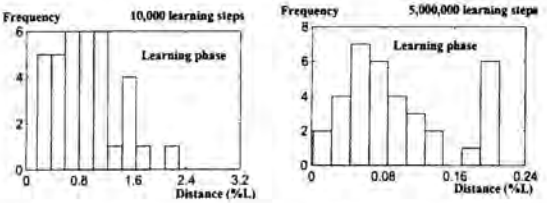

Fig. 11: Histograms of the distances during the learning phase

It can be seen that the distances are divided by a factor of about 10 between 10,000 learning steps and 5,000,000 learning steps.

Figure 12 shows that this improvement for the third test database is not as high as for the learning database, the

distances being divided by a factor of about 5 between 10,000 learning steps and 5,000,000 learning steps.

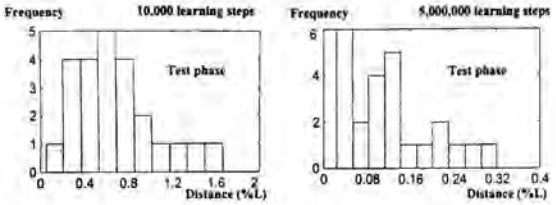

Fig. 12: Histograms of the distances for the third test data set

The analysis of the histograms for the two other test databases shows that the maximum distance between an identified heat source and the corresponding actual location is smaller than 0.35% of the smallest dimension of the domain (L). This can be considered as an accurate result, knowing that the distance between any two points contained in the databases is larger than 4% of L.

CONCLUSION

It has been shown that artificial neural networks can be successfully used to localize a heat source within a 2D domain. It has been found that Back Propagation Networks lead to better results than Radial Basis Function Networks.

It has been shown that the histograms of the distances are a more powerful tool than the correlation matrixes for the evaluation of the quality of the learning.

Future studies will address the 3D localization of a heat source, and then the localization of time varying or space varying heat sources.

REFERENCES

Diaz, G., Sen, M., Yang, K. T., and McClain, R. L., 2001, "Dynamic prediction and control of heat exchangers using artificial neural networks", International Journal of Heat and Mass Transfer, Vol. 44, N° 9, May 2001, pp. 1671-1679

Eurotherm, 2001, Proceedings of the Seminar n° 68, "Inverse problems and Experimental Design in Thermal and Mechanical Engineering", Poitiers, 5-7 March

Incropera, F. P., and de Witt, D. P., 1996, Fundamentals of heat and mass transfer, (4th edition), John Wiley and Sons, New-York

Kirsch, A., 1996, "An introduction to the mathematical theory of inverse problems", Springer-Verlag, New-York

Kosko, B., 1992, Neural Networks and Fuzzy Systems, Prentice-Hall, Englewood Cliffs, NJ

Lalot, S., 2000, "Identification of the time parameters of solar collectors using artificial neural networks", proceedings of 3rd ISES-Europe Solar Congress, Copenhagen, Denmark, June 19-22

Lalot, S., and Lecoeuche, S., 2000, "Identification of the time parameters of electrical heaters using artificial neural networks", proceedings of the 2000 ASME National Heat Transfer Conference, paper NHTC2000-12153

Looney, C. G., 1997, "Pattern Recognition using Neural Networks – Theory and Algorithms for Engineers and Scientists" Oxford University Press, New-York

Lurette, C., 1998, "Etude de faisabilité d'évaluation de distribution de taille de gouttelettes au niveau d'une turbine à vapeur par des méthodes neuronales", Industrial placement report, EDF (Direction des Etudes et de la Recherche à Chatou) - EIPC

Marren, A., Harston C., Pap, R., 1990, "Handbook of neural computing applications", Academic Press Inc., San Diego CA

NeuralWare, 1993, "Neural Computing – A technology Handbook for Professional II/PLUS and NeuralWorks Explorer, NeuralWrae Inc., Pittsburgh, PA

Olson, L. G., and Throne, R. D., 2000, "The steady inverse heat conduction problem: a comparison of methods for inverse parameter selection", proceedings of the 2000 ASME National Heat Transfer Conference, paper NHTC2000-12022

Pham, D. T., and Oh, S. J., 1999, "Identification of plant inverse dynamics using neural networks", Artificial Intelligence in Engineering, Vol. 13, N° 3, pp 309-320

Shin, M., and Lee, J.-W., 2000, "Prediction of the Inner Wall Shape of an Eroded Furnace by the Nonlinear Inverse Heat Conduction Technique", Fluid and Thermal Engineering, Special issue on innovative thermal and fluid technology on energy and environment, Series B, Vol. 43, N°4, pp 544-549

Tarantola, A., 1987, "Inverse problem theory - Methods for data fitting and model parameter estimation", Elsevier, Amsterdam

HEFAT2002
1st International Conference on Heat Transfer, Fluid Mechanics and Thermodynamics
8 – 10 April 2002, Kruger Park, South Africa

MC2

MODELING OF LIQUID FLOW IN FLAT HEAT PIPES

Muraleedharan, C., Jayaraj, S., Jilani, G.
Department of Mechanical Engineering,
Calicut Regional Engineering College,
Calicut, Kerala, India. Pin. 673 601.
murali@crec.ker.nic.in

ABSTRACT

Heat pipe is a simple heat transporting device of very high 'effective thermal conductance'. Other than conventional circular heat pipes, flat rectangular heat pipes can be employed for carrying large heat fluxes. In the heat pipe, the working fluid flows from the evaporator to the condenser through the vapour core as vapour, while the condensed liquid substance flows back to the evaporator from the condenser along the wick structure. The present work is an attempt to analyse the liquid flow in the flat heat pipe through the wick structure at steady operating conditions. The two-dimensional continuity and momentum equations are solved employing stream function-vorticity approach. Alternating Direction Implicit (ADI) finite difference scheme is used for discretising the equations. Stream lines, velocity distribution, velocity profiles and pressure variation are obtained for various Reynolds number values and different porosity values.

INTRODUCTION

Though the heat pipe is a simple device, the fluid flow phenomenon that takes place inside it is highly complex. The liquid working substance contained in the porous wick evaporates by taking heat from the heat source at the evaporator zone. This vapour reaches the condenser region flowing through the vapour core. At the condenser region, the vapour condenses by rejecting heat to the sink.

The flow through the wick structure of a heat pipe is considered as the flow of liquid through a porous medium. Rao and Wang (1991) reported the natural convection in vertical porous cylinder with uniform heat generation and side wall cooling. They used partial Galerkin method and finite difference method in their analysis. Stream lines and vertical velocity profiles were obtained.

Zhu and Vafai (1998) carried out numerical study for the steady in- compressible vapour and liquid flow in an asymmetrical flat plate heat pipe. The three dimensional model developed was extended to account for the vapour flow reversals, the liquid flow in the vertical wicks, the coupling of the liquid flow with the top and bottom wicks, the non-Darcian effects of the liquid flow through the porous wick and also the gravitational effects. The velocity profiles and pressure distribution, both in vapour and liquid regimes were found to be in good agreement with the experimental results.

Unnikrishnan and Sobhan (1997) obtained the transient distribution of field variables in the vapour and wick regions of a flat heat pipe. Their two dimensional analysis employing a finite difference procedure based on SIMPLER algorithm revealed that the wick porosity does not have a significant effect on the velocity and pressure distributions in the vapour core region. The transient model of a flat heat pipe developed by Sobhan *et al.* (2000) involves the solution of two-dimensional continuity, momentum and energy equations coupled with equation of state in the vapour core, transport equations for the porous wick medium and two dimensional heat equation for the container wall. Using finite difference method the variation of temperature, pressure and velocity fields were obtained.

The present work is an attempt to obtain the steady state distribution of velocity and pressure in the liquid wick region of the flat heat pipe using finite difference method. The results are obtained with water as working substance using stream function-vorticity approach. Numerical results are presented for different Reynolds number and porosity values.

NOMENCLATURE

Ar	aspect ratio
C_E	Ergun's constant
Da	Darcy's number
h_w	thickness of wick structure
l	dimensional length
L	nondimensional length
P	nondimensional pressure
q	heat flux
Re	Reynolds number
t	dimensional time
u	dimensional vertical velocity
u_o	vertical velocity at the interface
U	nondimensional vertical velocity
v	Dimensional axial velocity
V	nondimensional axial velocity
X	nondimensional transverse distance
Y	nondimensional axial distance

Greek Letters

ε porosity
μ viscosity
ρ density
τ nondimensional time
Ω vorticity
ψ stream function

Subscripts

a adiabatic
c condenser
e evaporator
l liquid
m mean
∞ reference

MATHEMATICAL FORMULATION

The sectional view of the flat heat pipe is shown in Fig. 1. Since the simulation of the real physical model is quite complex, appropriate assumptions made in order to obtain equivalent mathematical model without affecting the results are:

(i) Flow is laminar and two-dimensional.
(ii) Effect of compressibility is neglected.
(iii) The liquid wick matrix is isotropic and homogeneous.
(iv) Body forces are neglected.
(v) Thermophysical properties of the fluid and the porous matrix are constant.

Dimensionless Parameters

Nondimensionalising the system of equations and the corresponding boundary conditions helps in resolving the sharp velocity gradients present in the flow field.

The dimensionless variables used are:

$$X=\frac{x}{h_w},\ Y=\frac{y}{h_w},\ U=\frac{u}{u_o},\ V=\frac{v}{u_o},\ P=\frac{(p-p_\infty)}{\rho_l u_o^2},$$

$$Re=\frac{\rho_l u_o h_w}{\mu_l},\ \tau=\frac{u_o t}{h_w},\ C_E=1.75\frac{\varepsilon^{\frac{3}{2}}}{\sqrt{150}},\ Ar=\frac{h_w}{l_e+l_a+l_c} \quad (1)$$

Vorticity Transport Equations

In the analysis of two dimensional incompressible flows, the stream function-vorticity formulation is the most popular approach. For two-dimensional laminar incompressible flow in porous wick, the governing equations for stream function and vorticity in pseudo-transient form are:

Stream Function

$$\frac{\partial\psi}{\partial\tau}=\Omega+\frac{\partial^2\psi}{\partial X^2}+\frac{\partial^2\psi}{\partial Y^2} \quad (2)$$

Vorticity Transport Equation

$$\frac{\partial\Omega}{\partial\tau}+U\frac{\partial\Omega}{\partial X}+V\frac{\partial\Omega}{\partial Y}=\frac{1}{Re}\left[\frac{\partial^2\Omega}{\partial X^2}+\frac{\partial^2\Omega}{\partial Y^2}\right]-\frac{\varepsilon\Omega}{Re\,Da}-\frac{\varepsilon C_E}{\sqrt{Da}}\left[V\frac{\partial|U|}{\partial X}-V\frac{\partial|U|}{\partial Y}+|U|\Omega\right] \quad (3)$$

where the dimensionless stream function, ψ and vorticity, Ω are defined as,

$$U=\frac{\partial\psi}{\partial Y},\ V=-\frac{\partial\psi}{\partial X},\ \ \Omega=\frac{\partial V}{\partial X}-\frac{\partial U}{\partial Y} \quad (4)$$

The imposed temporal and boundary conditions are:

Interface (X=0): $0\le Y\le L_e$, $\psi=-Y$ $\Omega=-\frac{\partial^2\psi}{\partial X^2}$

$L_e<Y\le(L_e+L_a)$, $\psi=-L_e$ $\Omega=-\frac{\partial^2\psi}{\partial X^2}$

$(L_e+L_a)\le Y\le 1/Ar$, $\psi=(Y-1/Ar)$ $\Omega=-\frac{\partial^2\psi}{\partial X^2}$

Bottom wall (X=1): $0\le Y\le 1/Ar$, $\psi=0$ $\Omega=-\frac{\partial^2\psi}{\partial X^2}$

Left wall (Y=0): $0<X<1$, $\psi=0$ $\Omega=-\frac{\partial^2\psi}{\partial Y^2}$

Right wall (Y=1/Ar): $0<X<1$, $\psi=0$ $\Omega=-\frac{\partial^2\psi}{\partial Y^2}$ (5)

Numerical Solution Strategy

The governing equations are discretised by using Alternating Direction Implicit (ADI) finite difference scheme. The famous Thomas algorithm is employed as the matrix solver for the solution of resulting linear algebraic finite difference equations.

RESULTS AND DISCUSSION

The solution of the governing equations pertinent to the present study has been obtained using the developed computer code. Results are obtained for different Re values and porosity values. Stream lines, velocity distribution, velocity profiles and pressure variation are plotted.

Stream lines

Stream lines in the liquid wick region as shown in Fig.2 corresponds to Ar = 0.0036 and Re = 0.1 and 10. At all Re values the stream lines obtained are smooth and well defined. At the condenser section and evaporator section all stream lines are found to be perpendicular to the interface, indicating no flow along the interface. At low Re values the stream lines are well distributed in the whole domain. While at higher Re values the stream lines are found to be nearer to the interface showing concentration of mass flow closer to the interface.

Axial Velocity Distribution

Fig. 3(a) shows the axial velocity distribution in the wick region for various Re values (Re = 0.1, 1, 10 and 20) with Ar = 0.0036 and ε = 0.5. Flow of liquid in the porous wick structure is from the condenser zone to the evaporator region. At the condenser section, the axial velocity increases due to addition of liquid mass to the wick by condensation of vapour at the vapour - wick interface. This increase in axial velocity occurs up to the end of the condenser zone. The variation of the velocity is not found to be strictly linear as the vertical component is not included in predicting the distribution. At the adiabatic section, the axial velocity distribution is parallel to the interface and bottom wall showing no addition or removal of liquid in the region. In the evaporator region, due to uniform evaporation of liquid, mass depletion occurs in the wick. Hence the axial velocity decreases gradually along the direction and reaches zero when Y = 0.

Fig. 3(b) shows the axial velocity distribution for different wick structure at Re = 10. The porosity values considered to obtain these data are 0.75, 0.70 and 0.65. This is plotted at X = 0.5 (middle of the liquid wick). Though the nondimensional axial velocity distribution is somewhat similar, the actual velocity will be different. As the porosity increases, the axial velocity decreases due to the effective increase in area of flow.

Axial Velocity Profile

Visualising the axial velocity profiles of the liquid flow through the porous wick can lead to interesting conclusions. Normally the velocity in porous wick is assumed to be uniform at every cross section corresponding to one-dimensional flow. An attempt is made here to plot the two-dimensional axial velocity profiles at various cross sections along the longitudinal direction of the heat pipe (Figs.4 and 5). But the axial velocity profiles shown in these figures convey the deviations of the velocity profile highly different from the one-dimensional flow assumption. It is observed that the velocity nearer to the interface is maximum. Velocity profiles are not strictly parabolic and satisfying the no slip boundary conditions at the solid wall and liquid - vapour interface. The magnitude of the velocity increases as the fluid moves away from the extreme ends of the heat pipe (See Figs.4 and 5). Fig. 6 shows similar comparison for different ε values (ε =0.65, 0.70 and 0.75) at constant Reynolds number (Re=10) and aspect ratio (Ar = 0.0023).

Pressure Variation

When the working medium flows in the heat pipe it experiences two types of pressure drops: the pressure drop in the vapour core and the pressure drop in the liquid phase. Out of these the latter is larger in magnitude. Fig. 7(a) shows the pressure drop in the liquid-wick region for different Re values with respect to the pressure at the evaporator end (Y = 0) . As Re value increases, velocity of flow increases, and pressure drop also increases. Moreover, as the porosity of the wick structure decreases, the velocity increases, and correspondingly increase will result in the pressure drop. Fig. 7(b) shows the pressure drop in the liquid phase for Re = 10 at different porosity values (ε = 0.75, 0.70 and 0.65). It is observed that the pressure drop increases with decrease in porosity of the wick structure which is caused by the increase in the velocity of liquid flow.

CONCLUSIONS

The liquid flow analysis in flat heat pipe leads to the following conclusions.

- The liquid velocity distribution has similarity with Poiseuille flow.
- The velocity maxima have been observed closer to the wick – vapour interface.
- Pressure drop increases with Reynolds number.
- Pressure drop in the wick increases with decrease in porosity.
- No pressure build up has been observed in liquid- wick region.

REFERENCES

1. Nield, D.A and Bejan, A, "Convection in Porous Media", Springer-Verlag, New York, 1992.
2. Rao, Y.F and Wang, B.X, "NaturalConvection in Vertical Porous Enclosures with Internal Heat Generation", Int. J. of Heat and Mass Transfer, Vol.34, No.1, pp. 247-252, 1991.
3. Sobhan, C.B, Garimella, S.V andUnnikrishnan, V.V, "A Computational Model for the Transient Analysis of Flat Heat Pipes", 7th ITHERM 2000, Las Vegas, Nevada, Vol.2, pp. 106-113, 2000.
4. Unnikrishnan, V.V and Sobhan, C.B, "Finite Difference Analysis of the Transient Performance of a Flat Heat Pipe", 10th Int. Conf. on Numerical Methods in Thermal Problems, Swansea, UK, pp. 391-400, 1997.
5. Zhu, N and Vafai, K, "Vapour and Liquid Flow in an Asymmetrical Flat Plate Heat Pipe: A Three Dimensional Analytical and Numerical Investigation", Int. J. of Heat and Mass Transfer, Vol.41, No.1, pp. 159-174, 1998.

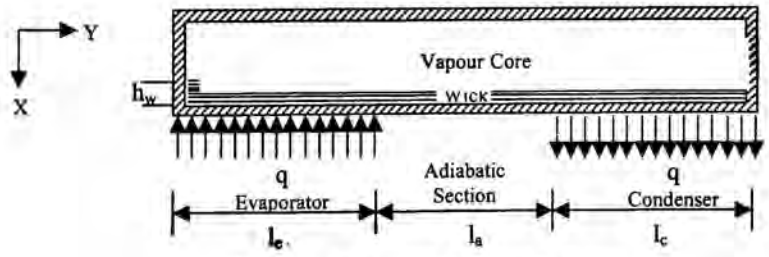

Fig. 1 Longitudinal Section of Heat Pipe

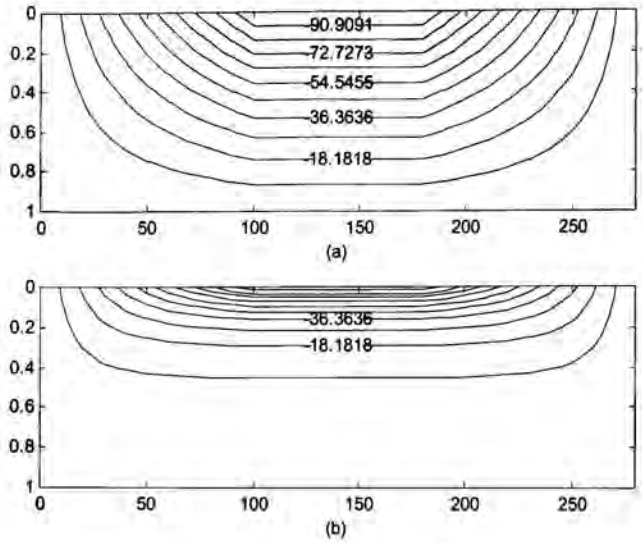

Fig. 2 Stream Lines at Ar=0.0036, ε=0.50
(a) Re=0.10, (b) Re=10

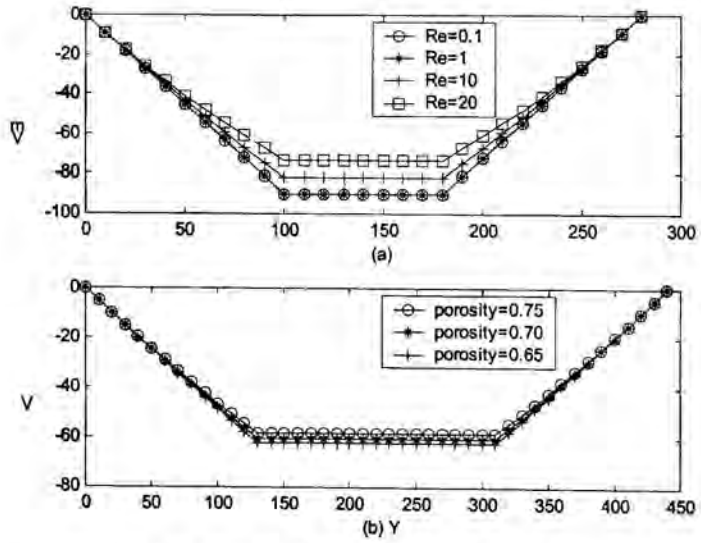

Fig. 3 Axial Velocity Distribution in the Liquid Wick Region
(a) at Various Re Values and Ar=0.0036, ε=0.50
(b) at Different Porosity Values and Re=10, Ar=0.0023, X=0.50

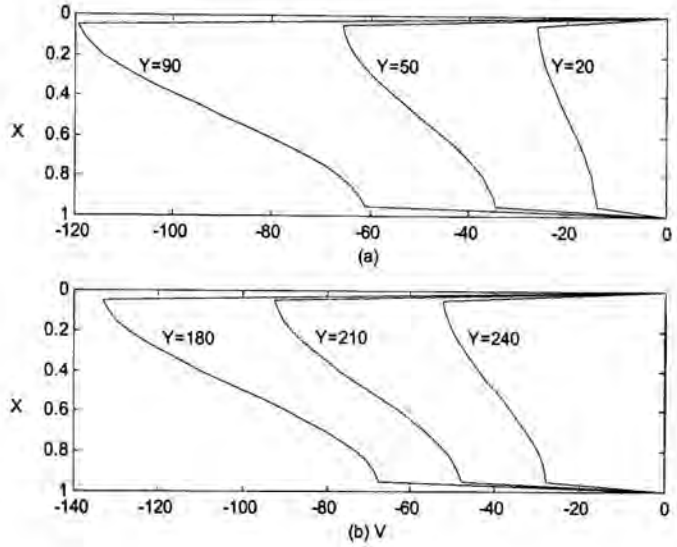

Fig. 4 Axial Velocity Profiles at Re=0.10, Ar=0.0036, ε=0.50

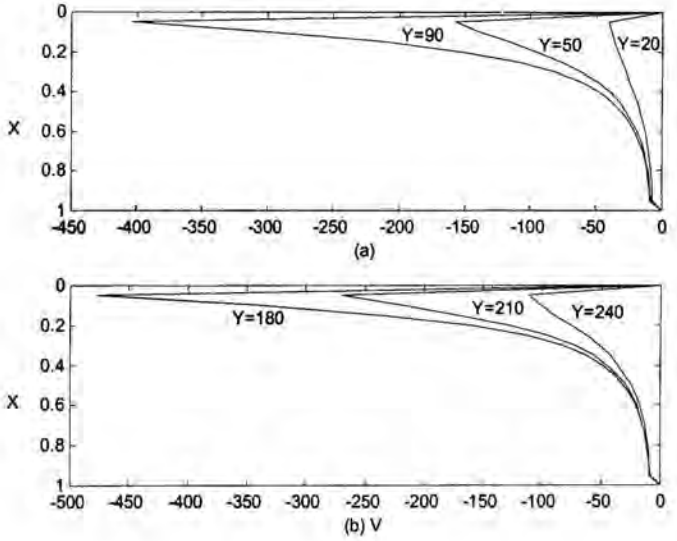

Fig. 5 Axial Velocity Profiles at Re=10, Ar=0.0036, ε=0.50

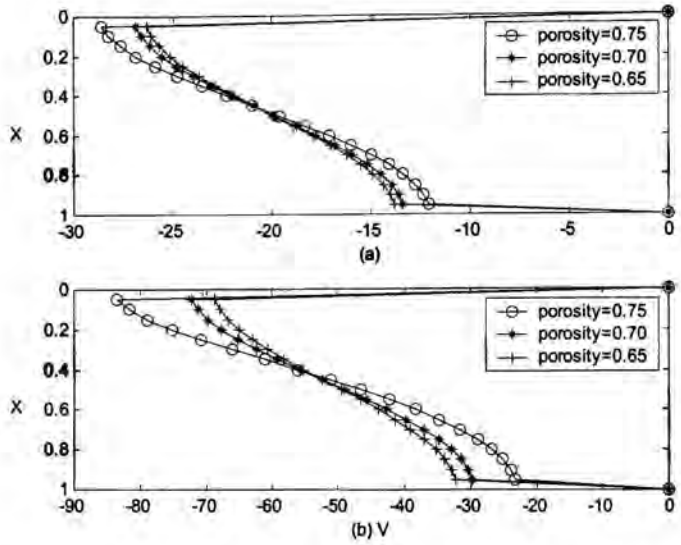

Fig. 6 Comparison of Axial Velocity Profiles for Different Porosity Values at Re=10: (a) Y=40, (b) Y=340

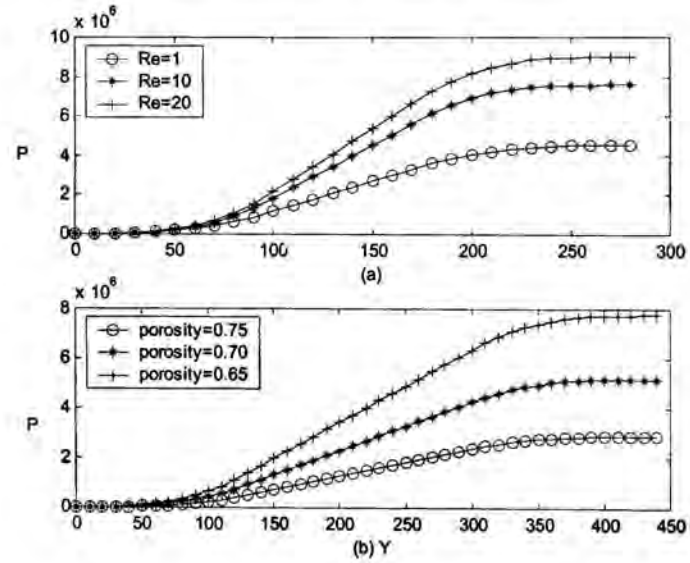

Fig. 7 Mean Pressure Variation Along the Liquid Wick Region
(a) at ε = 0.50 and for Various Re Values, (b) at Re=10 and for Different Porosity Values

HEFAT2002
1st International Conference on Heat Transfer, Fluid Mechanics, and Thermodynamics
8-10 April 2002, Kruger Park, South Africa
MC4

THERMAL CONVECTION IN A FLUID SATURATED SPARSELY PACKED POROUS LAYER OVERLAYING A SOLID LAYER

Calvin Mackie* and Zhaoqin Meng**
*Assistant Professor, **Ph.D. Candidate
Department of Mechanical Engineering
Tulane University
New Orleans, LA 70118
Email: Calvin.Mackie@Tulane.edu

Carsie A. Hall, III
Assistant Professor
Department of Mechanical Engineering
University of New Orleans
New Orleans, LA 70148

ABSTRACT

This analytical study considers the incipient convection of a fluid saturated sparsely packed porous medium overlaying a solid layer. A linear stability analysis is performed to determine the effects of the permeability and solid layer on the conditions for incipient convection under limiting thermal boundary conditions of constant temperature and constant heat flux. The flow in the porous medium is modeled using the Brinkman-extended Darcy model. The analysis shows that the stability of the system is affected significantly by the presence of the porous medium, thickness of the solid layer, and the thermal boundary conditions. Additionally, the primary effect of increasing the thermal conductivity and solid thickness fraction for a system with a constant heat flux boundary is to increase the stability of the system, while increasing the permeability acts to decrease the stability. Moreover, the present results bridge the thermal convection gap between dense porous medium and fluid layers overlaying a solid layer.

NOMENCLATURE

c	Specific heat
f	Temperature perturbation variable
$\vec{g}$	Gravitational acceleration vector
D	D=d/dz
Da	Darcy number
F	Solid temperature perturbation variable
K	Permeability
L	Length of the system
Pr	Prandtl number
q	constant heat flux at lower boundary
Ra	Rayleigh number based on q or ΔT
Ra_c	Critical Rayleigh number for system
T	Temperature
v	Velocity vector for fluid, v = v(u, v, w)
ΔT_L	Temperature difference across the porous layer

Greek Symbols

α	Ratio of the fluid, α_L, to solid diffusivity α_S.
β	Coefficient of volumetric thermal expansion
∇_H^2	$\partial^2/\partial x^2 + \partial^2/\partial y^2$
ε	Solid thickness fraction
κ	Thermal conductivity
λ	Solid to fluid thermal conductivity ratio, κ_s/κ_L
μ	Dynamic viscosity
ν	Kinematic viscosity
ρ	Ratio of the density of the fluid, ρ_L, to the solid, ρ_S
Φ	Pattern planform

Subscripts

b	Basic state
c	Critical conditions
L	Fluid
m	melting temperature variable
s	Solid

INTRODUCTION

Since the initial studies by Horton and Rogers [1] and Lapwood [2], the phenomena surrounding convection in porous media has received increased interest. The problem of thermoconvective instability in a horizontal porous layer driven by buoyancy effects has been studied extensively in the literature in recent years as documented in numerous review articles [3]. The present study focuses on the effects of the permeability of a porous medium overlaying a solid layer on

the criterion for incipient convection in the interstitial fluid; Based on a linear stability analysis, the investigation attempts to bridge the gap between the clear fluid and the Darcy porous limit.

A porous layer overlaying a solid layer is important in seafloor hydrothermal systems as the evolution of the permeability as a result of thermostresses plays a significant role on the developing flow field [4,5]. The initial work in porous media related to the subject of an impermeable boundary was performed by Donaldson [6] and extended by McKibbin [7]. Considering an isothermal solid boundary and Darcy medium, it was found that the critical Rayleigh number is decreased by the presence of the solid impermeable boundary [7]. Applying a constant heat flux boundary for a classical dense porous medium, Wang [8] determined that the critical Rayleigh number for the porous layer increased with the thickness of the solid layer, counter to the constant temperature scenario [7]. Although different boundary conditions were applied, these studies considered only the Darcy model of the porous medium. It has been shown that the permeability of the porous medium may affect the criterion for the onset of incipient convection [9,10]. Additional permeability studies with multilayered media indicate that large permeability differences are needed to affect the incipient convection [11,12].

The present analysis study includes the Brinkman-extended porous flow model that allows for the investigation of sparsely packed media as well as a dense (low permeability) porous media by parametrically changing the permeability from that corresponding to a Darcy model of the flow to a vanishing one. Furthermore, this study focuses on the effect of solid boundary and constant temperature and heat flux boundary conditions on the criterion for incipient convection. A greater understanding of the influence of such variables on the convective stability of a complex system is ascertained.

PROBLEM STATEMENT

A quiescent horizontal layer of a pure fluid in a gravitational field heated from below does not always remain so in the presence of an adverse density gradient beyond a threshold value which is capable of giving rise to fluid motion. This observation may be applied to a fluid saturated porous layer with variable permeability overlaying a solid boundary. The analytical model utilized in this parametric study is formulated under the assumption that fluid motion within the porous medium is described via a Newtonian, Boussinesq model of the Navier Stokes equations, written for a fluid saturated porous medium. The fluid velocity through the medium is deemed sufficiently small, conforming to the Darcy regime, or, at most, to the Brinkman-modified Darcy regime. The upper plate is maintained at a constant temperature, T_0. The heat transfer at the lower surface is constant heat flux, q, or a constant temperature T_1 as shown in Fig. 1. For the fluid, the temperature field may be obtained from a simultaneous solution of the thermal energy and continuity equations, together with

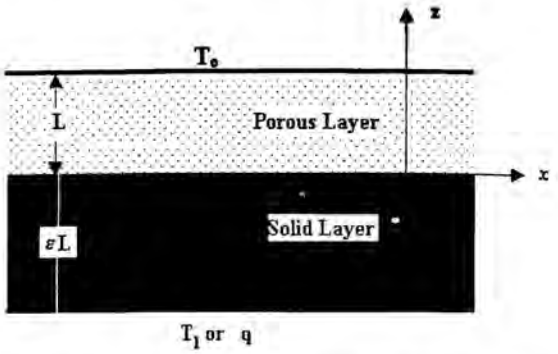

Fig. 1 Porous layer overlaying a solid layer with a constant heat flux boundary (**CHF**) or Constant temperature boundary (**CTB**).

the Boussinesq model of the Darcy-extended momentum equation. These are expressed, respectively, as

$$\rho_L c_L \sigma_H \left[\frac{\partial}{\partial t} + \vec{v}\cdot\nabla\right] T_L = \kappa_L \nabla^2 T_L, \tag{1}$$

where σ_H is the heat capacity ratio.

$$\nabla\cdot\vec{v} = 0 \tag{2}$$

and

$$c_a \rho_L \frac{\partial \vec{v}}{\partial t} = -\nabla P - \left(\frac{\mu_L}{K}\right)\vec{v} + \mu_{eff}\nabla^2\vec{v} + \rho_L \beta\left(T_L - T_{ref}\right)\vec{g}\cdot\vec{k}, \tag{3}$$

where c_a is a constant that depends on the geometry of the porous medium [3]. The Brinkman-extended model satisfies not only the impermeability and no-slip conditions but reduces to a form of the Navier-Stokes model as the medium permeability approaches infinity ($K\rightarrow\infty$) and to the conventional Darcy model as the medium permeability approaches zero ($K\rightarrow 0$). Since there exists no bulk motion in the solid, the temperature field within the solid layer is described by the thermal energy equation, namely

$$\frac{\partial T_s}{\partial t} = \alpha_s \nabla^2 T_s. \tag{4}$$

The boundary condition on the top surface is

$z = L,\ T_L = T_1.$

On the interface separating the saturated fluid and the solid boundary,

$$T_S(0) = T_L(0),\quad \kappa_S \frac{dT_S}{dz}\Big|_0 = \kappa_L \frac{dT_L}{dz}\Big|_0 \text{ and } w(0) = 0 \tag{6}$$

At the base of the solid layer, the boundary could either be maintained at constant temperature,

$$T_S(-\varepsilon L) = T_1 \tag{7}$$

or at constant heat flux, q, such that

$$q = -\kappa_S \frac{dT_S}{dz}\Big|_{-\varepsilon L}. \tag{8}$$

Basic State and Stability Analysis

Initially, the stationary system is in a static equilibrium state with no fluid motion, hydrostatic pressure distribution and a purely conductive temperature profile. The scales for the pertinent variables v, x (and y, z), t and p are chosen, respectively, as α_L/L, L, $(\sigma_H L^2)/\alpha_L$, and $(\rho_L \nu_L \alpha_L)/L^2$. The temperature difference across the system is used to scale the temperature when there is constant temperature boundary at z=0; when there exists a constant heat flux at the lower boundary, the applicable scale for the temperature is qL/κ_L. The basic state under consideration is a stagnant layer of fluid with a hydrostatic pressure distribution, and purely conductive temperature distributions in the fluid and solid when present. Next, a linear perturbation model of the system is developed by considering a slight change in temperature due to a slight heating of the lower surface. Introduction of the standard perturbations (denoted by primes) into the governing equations, followed by linearization in the disturbance quantities and normalization with the applicable scales, yields the perturbation model for the fluid as,

$$\left[\frac{\partial T_L'}{\partial t} - w'\right] = \nabla^2 T_L', \quad \vec{\nabla}\cdot\vec{v}' = 0, \tag{9}$$

and

$$\overline{Pr}\frac{\partial \vec{v}'}{\partial t} + \nabla p' + \left(\frac{1}{Da}\right)\vec{v}' - \tilde{\mu}\nabla^2\vec{v}' + Ra\, T_L'\cdot\vec{k} = 0, \tag{10}$$

where $\overline{Pr} = (c_a/\sigma_H)Pr^{-1}$ and w' is the vertical component of the perturbation velocity $\vec{v}$. For the solid,

$$\frac{\partial T_s'}{\partial t} = \frac{\alpha_s}{\alpha_L}\nabla^2 T_s'; \tag{11}$$

Solution of the preceding set of equations results in a sufficient condition to ascertain the stability boundary of the sparsely packed fluid saturated porous layer. After eliminating the pressure from the fluid momentum equation by taking the curl twice and retaining only the z-component of the resulting equation, yields

$$\overline{Pr}\frac{\partial}{\partial t}\nabla^2 w + \frac{1}{Da}\nabla^2 w + \tilde{\mu}\nabla^2(\nabla^2 w) + Ra\nabla_H^2 T_L = 0, \tag{12}$$

where the primes have been dropped.

The boundary conditions transform on the top surface and interface accordingly; however, at the base of the solid layer, the boundary condition is,

$$T_s(-\varepsilon) = 0 \qquad \text{or} \qquad \frac{dT_s}{dz}|_{-\varepsilon} = 0. \tag{13}$$

The variables become separable under the normal modes assumption, yielding solutions of the form $\{T_S, T_L, w\} = \{F(z), f(z), \hat{w}(z)\}e^{\sigma t}\Phi(x,y)$, where $\sigma = \sigma_r + i\sigma_i$ is the time constant which contains σ_r, the growth rate, and σ_i, the frequency of the disturbance; $\Phi(x,y)$ is the planform function which determines the cellular structure of the fluid motion, and satisfies the two dimensional membrane equation, $\Phi_{xx}+\Phi_{yy} = -k^2\Phi$.

Substitution of normal modes into the linear perturbation model [Eq. (11)] results in the normal-mode disturbance equations for the solid layer that can be solved with the applicable transformed boundary conditions [Eqs. (13 -14)] to yield,

$$F(z) = \frac{Df(0)}{\lambda k}\frac{Sinh[k(z+\varepsilon)]}{Cosh[k\,\varepsilon]} \tag{14}$$

for a constant temperature boundary, and

$$F(z) = \frac{Df(0)}{\lambda k}\frac{Cosh[k(z+\varepsilon)]}{Sinh[k\,\varepsilon]} \tag{15}$$

for a constant heat flux boundary. The disturbance of the fluid temperature at the interface, the thermal conductivity ratio and the solid thickness fraction play significant roles in the temperature disturbance for the solid region as shown in [Eqs. (14 - 15)]. Substitution of the normal modes into the expression generated by combining Eqs 9 and 12, forms a sixth order single-variable perturbation equation in terms of the normal mode fluid perturbation temperature, f,

$$(D^2-k^2)^3 f + \frac{1}{Da}(D^2-k^2)^2 f - Ra\,k^2 f = 0. \tag{16}$$

where it has been assumed that the principle of exchange of stability is valid and marginal stability curve is characterized by a growth rate of zero, i.e., $\sigma = 0$. The boundary conditions transform accordingly as

$$\left.\begin{array}{llll} (D^2-k^2)f(0)=0 & & D(D^2-k^2)f(0)=0 & \\ f(1)=0 & (D^2-k^2)f(1)=0 & & D(D^2-k^2)f(1)=0 \end{array}\right\} \tag{17}$$

with one additional condition that is determined by the thermal boundary of the lower surface. Solutions for the temperature distribution in the solid layer [Eqs. (14 - 15)] are substituted into the heat and mass flux matching conditions at the interface to yield,

$$f(0) - \frac{Tanh[k\,\varepsilon]}{\lambda k}Df(0) = 0 \tag{18 a}$$

for a lower constant temperature boundary and

$$f(0) - \frac{Coth[k\,\varepsilon]}{\lambda k}Df(0) = 0 \tag{18 b}$$

for a lower constant heat flux boundary. As λ approaches finite values the influence of the solid and the associated thermal conductivity becomes more pronounced; it is this region that we seek to clarify the influence of such parameters on the thermal convective stability of system. The sixth-order system constitutes an eigenvalue problem from which the onset of instability can be derived. The essential task is to find the lowest occurring Rayleigh number, namely Ra_c, and wave number, namely k_c, for prescribed values of ε and Da, which lead to a solution of f(z) that satisfies the governing system. The critical parameters are determined parametrically using a shooting method in conjunction with a minimization program via a Runge-Kutta integration method. For details of the numerical scheme, the reader is referred to Sparrow [13].

RESULTS AND DISCUSSION

The linear stability analysis for the system has two experimentally verifiable results: the critical temperature difference for the onset of convection and the corresponding critical wavelength. For a range of boundary conditions varying from constant temperature to constant heat flux, the incipient conditions for convection in a sparsely packed porous

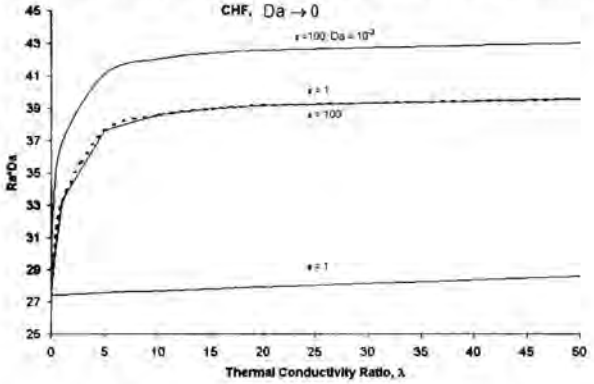

Fig. 2 Critical Rayleigh-Darcy number, Ra*Da, versus as a function of ε for Da →0 (CHF).

medium overlaying a solid layer are parametrically determined for different thermal conductivity ratios, permeabilities, and lower boundary solid thickness fractions.

Constant Heat Flux Boundary

Figures 2-4 note the critical conditions for a system with a constant heat flux, and display the primary effect of increasing the thermal conductivity and solid thickness ratio is to increase the stability of the system regardless of the permeability. The degree to which the stability is impacted changes with permeability as compared to the classical cases. Considering the classical Lapwood convection scenario consisting of a dense medium (Da → 0), Fig. 2 illustrates the effect of the solid thickness is to stabilize the system. Any additional solid thickness tends to act as insulation, thus, creating a challenging environment for growth and manifestations of disturbances; a solid thickness fraction greater than unity, in conjunction with a thermal conductivity increase greater than ten, shows no appreciable change in the Rayleigh-Darcy number for a constant permeability medium, i.e. Darcy number. Increasing the thermal conductivity ratio or increasing the thermal diffusivity of the solid as compared to the fluid rapidly increases the stability of the system initially and eventually reaches a plateau as the conductivity ratio continues to increase. Additionally, Fig. 2 shows that when no solid is present (ε = 0, thus λ = 0), the Ra*Da of the classical porous medium case with a constant heat flux boundary [Ra*Da = 27.10 (Nield, 1968)] is recovered. Figure 3 further displays that making the system less dense (increasing the Darcy number) relative to the classical medium (Da → 0) tends to destabilize disturbances, along with increasing the solid thickness and solid thermal conductivity.

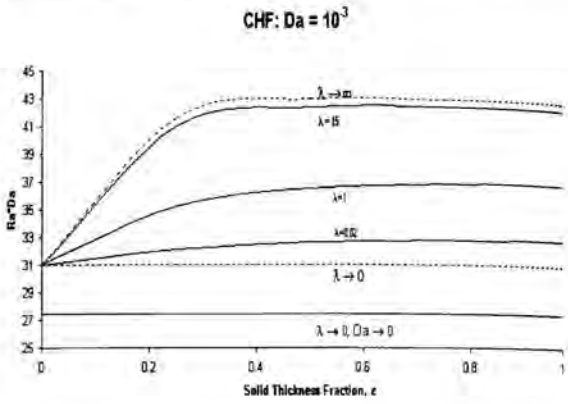

Fig. 3 Critical Rayleigh-Darcy number, Ra*Da, versus as a function λ of for Da =10^{-3} (CHF).

Figure 3 displays the relative increase in stability ascertained with a corresponding increase in thermal conductivity ratio. For a constant heat flux impermeable boundary, increasing the thickness and thermal conductivity of the solid causes appreciable increase in the Rayleigh-Darcy number. As the system becomes less dense, considering all the possible combination of system variables still produces a system that is less stable as the clear fluid limit is approached. Intuitively, as the system becomes less dense disturbances are allowed additional area to grow and develop; consequently, the

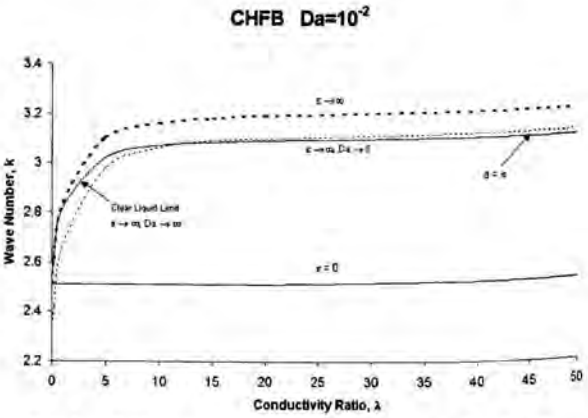

Fig. 4 Critical wave number, k, versus λ as a function ε, Da =10^{-2} (CHF).

magnitude of the Rayleigh numbers (Ra) actually increase for increased permeability. Figures 2-3 appear counter-intuitive but the reader is reminded that the graphs are based on Ra*Da rather than Ra alone

The wave numbers are also affected by the aforementioned parameters. Figure 4 shows that if there is no solid present ($\varepsilon = 0$), the wave number is a constant and corresponds to the established value for constant heat flux boundaries [8, 14]; however, the wave number increases with increasing solid thickness, which represents an increase in the number of cells due to the increasing insulating effect of the boundaries. Disturbances created at the boundary persist, as opposed to being damped out by the conductivity of the boundary. Furthermore, for a sparsely dense medium with $Da=10^{-2}$, the corresponding wave numbers associated with increasing solid thickness and thermal conductivity are greater than that corresponding to the classical dense porous medium ($k = \pi$) and clear fluid ($k = 3.08$) limits.

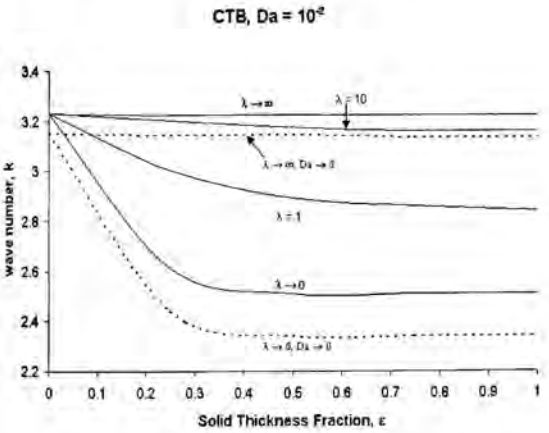

Fig. 5 Critical Rayleigh-Darcy number, Ra*Da versus ε as a function λ of for $Da = 10^{-2}$ (CTB).

Constant Temperature Boundary

Figures 5-7 display the critical conditions for a prescribed constant temperature boundary; counter to the constant heat flux results, the primary effect of increasing the thermal conductivity and solid thickness fraction is to decrease the stability of the system regardless of the permeability. Figure 5 demonstrates the effects of increasing the thermal conductivity of the solid. As the thermal conductivity increases, the results of the classical case ($Ra*Da = 4\pi^2 = 39.48$) are approached. As the thermal conductivity is decreased, the results are similar to those of the constant heat flux case, as expected. Furthermore, for a constant permeability, increasing the thermal conductivity of the solid tends to stabilize disturbances while increasing the solid thickness destabilizes the system when there is a departure from an infinite thermal conductivity ratio.

Figure 5 shows that increasing the amount of solid acts to decrease the stability of the system by lowering the relative Rayleigh-Darcy number. These results for the classical porous case ($Da \to 0$) reflect those in the literature [7]. The effect of the permeability with a constant temperature boundary, like the constant heat flux boundary, decreases the stability of the system. Figure 5 also shows that the effect of the permeability of the system is not negligible when determining the stability of the system as the amount of solid is increased relative to the length of the model. For a constant thermal conductivity, Fig. 6 shows the relative magnitude of the Rayleigh Darcy number for different permeabilities; additionally, it is shown that decreasing the permeability stabilizes the system by producing smaller Rayleigh-Darcy numbers, i.e. larger Rayleigh numbers. Relative to the classical Lapwood scenario, increasing the permeability and thermal conductivity, and decreasing the solid thickness, produces a less stable system. Physically, the

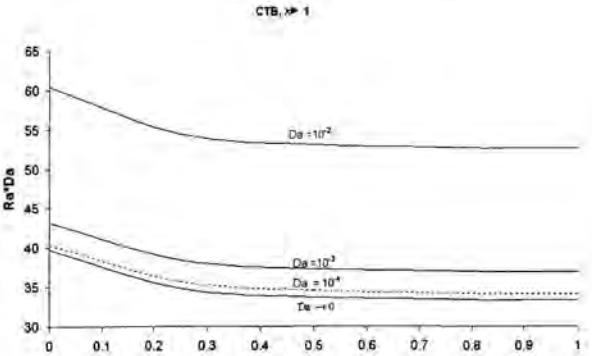

Fig. 6 Critical Rayleigh-Darcy number, Ra*Da versus ε for different values of Da for $\lambda = 1$ (CTB).

increase in thickness of the solid makes it more difficult for disturbances to diffuse at the boundary; therefore, disturbances will tend to attenuate with increasing solid thickness or the decease in thermal conductivity at a boundary.

Figure 7 displays the shift in the size of the wave numbers due to the change in permeability, solid thickness and thermal conductivity ratio. It is expected that the wave numbers would be larger for larger permeability. However, it is shown that decreasing the thermal conductivity and increasing solid thickness tend to constrain the growth of cellular development with the onset of convection.

CONCLUSIONS

The Brinkman-extended Darcy model employed in this work allows for the comparison between the critical phenomena in a sparsely packed fluid vis-à-vis that in a dense porous layer. Results for the critical conditions for a prescribed constant temperature boundary was counter to that for the constant heat flux results; the primary effect of increasing the thermal conductivity and solid thickness fraction for constant temperature boundary is to decrease the stability of the system

regardless of the permeability, whereas the opposite occurred with a constant heat flux boundary. As the permeability of the system increased, the stability of the system became less pronounced as disturbances were less affected by the constraining presence of the porous medium. Lastly, the results indicated that the permeability of system must be taken into account when stability issues are in question.

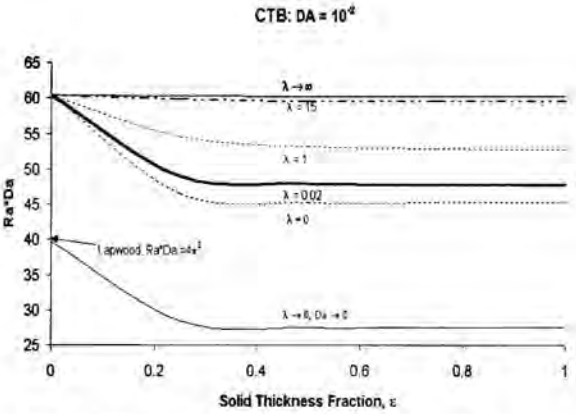

Fig. 7 Critical wave number, k, versus ε as a functio λ and Da $=10^{-2}$ (CTB).

ACKNOWLEDGEMENTS

The authors acknowledge the support for this work provided by the Louisiana Board of Regents under the grant no. LEQSF-RA-A-33. A portion of this research was funded by the NSF-Louis Stokes Louisiana Alliance for Minority Participation program for summer visiting faculty.

REFERENCES

[1] Horton, C.W. and Rogers, F.T., Jr., 1945. Convection currents in a porous medium. J. Applied Physics, 16, 367-370.

[2] Lapwood, E. R., 1948. Convection of a fluid in a porous medium. Proc. Camb. Phil. Soc., 44, 508-521.

[3] Bejan, A. and Nield, D., 1992. *Convection in Porous Media*, Springer-Verlag, New York, 8-9.

[4] Rosenberg, N. D., F. J. Spera and R. M. Haymon, 1993. The relationship between flow and permeability field in seafloor hydrothermal systems, Earth and Planetary Science Letters 116, 135-153.

[5] Lowell, R. P., Rona, P.A. and Von Herzen, R. P., 1995, Seafloor hydrothermal systems, J. Geophys. Res., 100, 327-352.

[6] Donaldson, I. G., 1962. Temperature Gradients in the Upper Layers of the Earth's Crust due to Convective Water Flows, J. Geophys. Res. 67, 3449-3459.

[7] McKibbin, R. 1983. Convection in an aquifer above a layer of heated impermeable rock. New Zeal. J. Science, 26, 49-64.

[8] Wang, C. Y., 1999. Onset of convection in a fluid saturated porous layer overlaying a solid layer which is heated by constant heat flux, ASME J. Heat Transfer, 121, 1094-1097.

[9] Walker, K.L. and Homsy, G. 1964. A note on convective instabilities in Boussinesq fluids and porous media. ASME J. Heat Transfer, 99, 6-12.

[10] Mackie, C., 2000. Thermal convection in a sparsely packed porous layer saturated with suspended particles, Int. Comm. Heat Mass Transfer, 27, No.3, 315-324.

[11] McKibbin, R. O'Sullivan, M. J., 1980. Onset of convection in a layered porous medium heated from below. J. Fluid Mechanics, 96, 375-393.

[12] McKibbin, R. O'Sullivan, M. J., 1981 Heat transfer in a layered porous medium heated from below. J. Fluid Mechanics, 111, 141-173.

[13] Sparrow, E., Munro, W., and Jonsson, V., 1964. Stability of the flow between rotating cylinders: the wide gap problem, J. Fluid Mechanics, 20, 35-46.

[14] Nield, D. A., 1968. Onset of thermohaline convection in a porous medium. Water Resources Res. 11, 553-560.

HEFAT2002
1st International Conference on Heat Transfer, Fluid Mechanics, and Thermodynamics
8-10 April 2002, Kruger Park, South Africa
MD1

THE EFFECTS OF WIND SPEED, DIRECTION AND DURATION ON CROSSCURRENTS AT THE PORT OF DURBAN ENTRANCE

David W. Mardon and Derek D. Stretch

School of Civil Engineering, University of Natal, Durban, 4041, South Africa
mardond@nu.ac.za, stretchd@nu.ac.za

ABSTRACT

Our research aims to identify the key space/time characteristics of the currents near the Port of Durban entrance channel to enable a predictive model to be developed for application to port operations. We report an analysis of current measurements focussing on the effects that wind speed, wind direction and wind duration have on near-shore currents. We find that the near-shore currents can be divided into two basic depth regimes: the surface currents (the top 2 to 3 metres) whose driving mechanism is mainly the local wind conditions, and subsurface currents (below 4 metres) that are independent of local wind conditions and are related to larger scale ocean circulation and weather patterns. Predictive models for the currents clearly need to distinguish between these two depth zones and account for the different driving mechanisms in each case.

1. INTRODUCTION

The Port of Durban is located on the eastern seaboard of South Africa. The entry of ships into the Port is affected by severe cross-track drift under certain weather conditions. Near shore ocean conditions such as those that exist along the entrance channel to the port can involve high wind and wave conditions as well as complex crosscurrents which all contribute to the cross-track drift of ships entering the port. The dominant factor causing the cross-track drift is the cross-currents. Along the entrance channel there are complex spatial and temporal variations in the cross-currents. Our research aims to identify the key space/time characteristics of the currents and the associated forcing mechanisms in order to develop a predictive model to improve the safety of port operations.

Durban is the busiest container port in Africa. For the city to maintain its competitiveness, significant expansion may be required during the next few years, including a widening of the entrance channel to allow larger "post-Panamax" vessels to enter the port safely.

Adverse wind and waves conditions coupled with complex crosscurrents near the port entrance have in the past forced the intermittent closure of the port with substantial economic implications [5]. The safety and efficiency of the port operations relies heavily on the skill and experience of the pilots who guide the ships into the port. Real-time information on the nature of crosscurrents and how they affect the ships could assist pilots in developing their skills and reduce the risk associated with guiding ships into the port under adverse conditions. To be able to provide this information there is a need to fully understand the mechanisms that give rise to the currents in the near shore region at the entrance to the port.

Figure 1: Map of the Port of Durban and entrance channel

The entrance channel to the Port of Durban has an orientation of 215.5° as can been seen in figure 1. This is within the range of values of the dominant wind directions, which are from the NNE or SW direction. Wind forces therefore have only small direct effect on ship movements in the entrance channel. It is the crosscurrents that have the most influence on the safe entry of vessels into the port. Previous studies, [1] & [2], concerning the entry of vessels into the harbour have concluded that North-westerly currents have a greater influence on ships than South-easterly currents [2]. For South-easterly currents the pilots appear to be able to safely manoeuvre ships into the port for current speeds up to 0.8 m/s. The limiting speed for North-westerly currents is lower at about 0.5 m/s. Note that the convention is to specify currents by the direction *towards* which they are flowing, unlike winds that are specified by the directions *from* which they blow.

A method for estimating the direct effect of wind, waves and crosscurrents on vessels as they enter the port has been developed [3]. The process uses digital imaging to capture images of vessels entering the port. Using this technique the tracks of the vessels can be determined, as well as the cross-track drift velocity at intervals along the ship tracks. Conclusions from the research include that shorter-term wind averages have the strongest influence on the cross-track drift of shallow draft vessels. Deeper draft vessels are essentially unaffected by local wind patterns [3].

The aim of the research reported here is to gain a better understanding of the structure and dynamics of the surface and sub-surface currents, particularly their forcing mechanisms. For example a question we wished to address was " to what depth are near-shore currents driven by local wind patterns and at what depths are they unaffected by local wind patterns but are driven by larger scale ocean circulation or weather patterns".

2. ANALYTICAL METHODS

2.1 Data used for analysis

Two sets of data were analysed for this research:

(a) Local weather data was obtained for a 29-month period starting from February 1998 until July 2000, from a weather station near the harbour entrance. The data included average wind speed and direction at 20-minute intervals and measured at a height of 102m above sea level.

(b) Current data from an acoustic doppler current profiler (ADCP) located near the entrance channel was analysed for a one-month period during February and March 1998. The data included current speeds and directions at 1-metre depth intervals up to 17 metres, at 10-minute intervals.

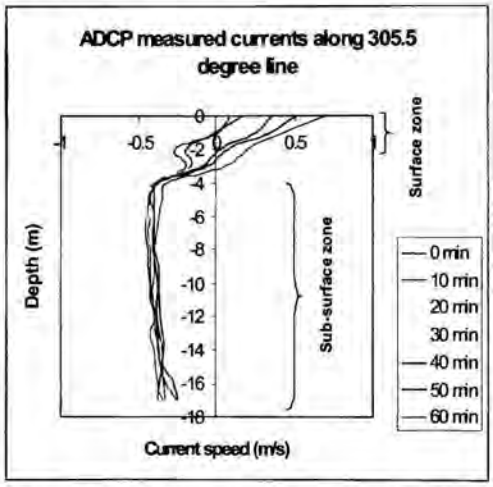

Figure 2: Typical current profiles measured at 10min intervals over a 1-hour period

2.2 Speed, direction & duration analysis.

Joint probability analysis of speed, direction and duration of the wind and currents was carried out to determine the general characteristics of the winds and currents. The results will be presented in the form of wind and current roses. Based on preliminary analysis of profiles such as those in figure 2, a surface current was defined as the average currents from the 0m level down to the -2m level. A sub-surface current was defined as the average current from -4m down to the -17m level. We shall refer to the region between these depth ranges as the interaction zone between the surface and sub-surface currents.

Statistical speed-duration analysis of the wind data was also carried out to determine the average duration that the wind of a specified speed blew from a certain direction. Currents were similarly analysed in order to determine any common trends that would imply interdependence. We anticipated that given an appropriate lag time, if the wind maintained a relatively constant direction and magnitude for a long duration, a wind driven current would be induced at larger depths.

Both wind and currents were analysed using what we shall refer to as a "vector particle progression" (VPP) method. The VPP shows the path that a particle would follow if it were advected by the wind or current vectors, measured at a point as a function of time. VPP is thus an integration of the wind or current vectors. The method allows the accumulated effects of the wind and currents to be visualized and analysed.

2.3 Wind-current correlation analysis

Correlation analysis was used to quantify the statistical inter-dependence between wind and currents.

Winds and currents were each analysed using the auto-correlation coefficient defined in the usual way as:

$$\rho_{(X(t),X(t+\Delta t))} = Cov(X, X(t+\Delta t)) / \sigma_x^{\,2}$$

The auto-correlation coefficient (ACC) measures the relationship between the same data offset by a lag or lead-time, Δt. The lag time required for the coefficient to drop to zero can be used as a characteristic time scale for the variable. The time scales for the wind and currents could thus be compared.

The wind and currents (from various depths) were also analysed using cross correlation coefficients (CCC) defined as:

$$\rho_{X,Y} = Cov\,(X, Y(t+\Delta t)) / \sigma_X \cdot \sigma_Y$$

where

$$Cov\,(X, Y(t+\Delta t)) = \left(\overline{X \bullet Y(t+\Delta t)} - \overline{X} \bullet \overline{Y(t+\Delta t)}\right)$$

and σ_x and σ_y are the standard deviation of X and Y respectively.

Varying the lag times (Δt) between the currents and the wind, the lag with the highest correlation coefficient value could be found. This lag characterises the time scales for the wind to have a significant on the current at specific depths.

Note that the CCC can also be used for vector arguments, with the products interpreted as scalar products. We refer to this as the vector cross correlation coefficient (VCCC).

3. RESULTS

3.1 Speed, direction and duration

3.1.1 Wind and Current roses

The wind rose for the period during ADCP testing is shown in figure 3 and reveals some key features. Winds blew predominantly from the NNE and SW direction (the prevailing wind directions at this location) during the period analysed. This is roughly parallel to the port entrance channel axis (215.5°). There were no cases of wind speeds greater than 20 m/s during the test period.

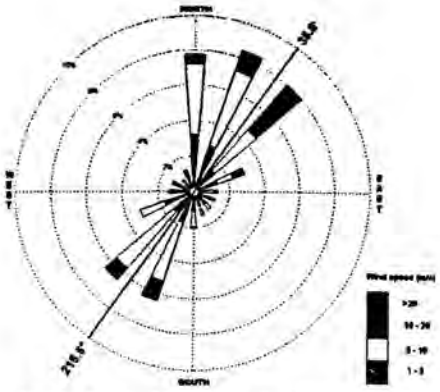

Figure 3: Wind rose for period of the ADCP measurements

The current rose for the surface current, shown in figure 4, reveals similarities to the wind rose in figure 3. The surface current flowed predominantly in a south-westerly direction. When the surface current left the SW sector it normally flowed in an east-north-easterly direction. The similarity between the wind and surface-current roses suggests that the wind is the main forcing mechanism for these currents.

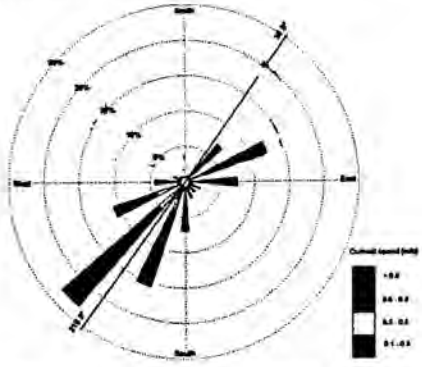

Figure 4: Current rose for the surface current

The current rose for the sub-surface current is shown in figure 5, and has a completely different pattern from that of the surface currents.

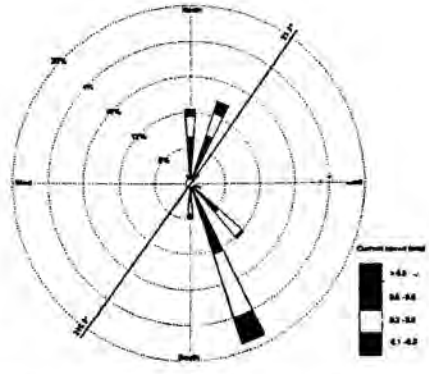

Figure 5: Current rose for the subsurface current

The subsurface current flowed predominantly in a SSE direction. This is important because this is almost perpendicular to the entrance channel and could play a significant role in cross-track drift velocities for ships entering the port. Comparing the wind rose (figure 3) and the sub-surface current-rose (figure 5), suggests that local wind conditions were not a significant factor in the forcing for the sub-surface currents.

3.1.2 Duration analysis

Average durations for the wind from various directions are shown in table 1.

Speed (m/s)	NNE (hrs)	ENE (hrs)	ESE (hrs)	SSE (hrs)	SSW (hrs)	WSW (hrs)	WNW (hrs)	NNW (hrs)
< 5	3.34	1.63	1.15	1.16	1.69	1.02	0.89	0.81
5 - 10	1.88	1.10	1.00	2.00	1.27	1.10		0.38
10 - 20	1.83	2.17		0.33	0.64	0.50		
> 20								

Table 1: Wind direction and durations (45° sectors)

The longest average duration found for the wind during the test period was 3.3 hours in the NNE sector (45° sector size) but this was for wind speeds lower than 5m/s and would possibly not contribute significantly to surface current generation. An average duration of 2.2 hours was found for wind speeds 10 - 20m/s in the ENE direction. The average durations were shorter than expected. The results indicate that either the wind speed and/or direction changes on average (for all sectors) every 1.3 hours. This could make current prediction difficult.

peed /s)	NNE (hrs)	ENE (hrs)	ESE (hrs)	SSE (hrs)	SSW (hrs)	WSW (hrs)	WNW (hrs)	NNW (hrs)
.3	0.33	0.58	0.50	0.49	0.48	0.41	0.57	0.42
.3 - 0.6	0.46	0.82	0.62	0.58	0.73	0.72	0.58	0.42
.6 - 0.7	0.38	0.48	0.43	0.40	0.51	0.44	0.36	
.7	0.49	1.93	0.54	0.53	0.66	0.61	0.48	0.67

Table 2: Current direction and duration for surface current (45° sectors)

For the surface current the longest average duration was 1.9 hours for current speeds greater than 0.7 m/s in a ENE direction (45° sector size). The maximum duration of 1.9 hours for the surface current is consistent with the duration of 2.2 hours found for the wind. This indicates that wind driven currents have short reaction times to changes in wind conditions. Predictions for wind driven currents should therefore use short-term wind averages.

peed /s)	NNE (hrs)	ENE (hrs)	ESE (hrs)	SSE (hrs)	SSW (hrs)	WSW (hrs)	WNW (hrs)	NNW (hrs)
.3	1.03	0.71	0.80	1.32	0.70	0.62	0.49	0.94
.3 - 0.6	1.72	0.49	0.96	3.10	0.61	0.33	0.33	0.33
6 - 0.7	1.05	0.83		2.25	0.33			
.7	1.56			5.78	0.33			

Table 3: Current direction duration for sub-surface current (45° sectors)

Average durations for the sub-surface currents were longer than for the surface currents. For the SSE direction, which was the dominant direction, the durations were longest, with a max of 5.8 hours for current speeds greater than 0.7m/s. The persistence of these currents suggest that they

are independent of local wind patterns. Longer durations also suggest some stability in the sub-surface current, which should make prediction of these currents simpler.

3.1.3 Vector particle progression

The vector particle progression for the wind is shown in figure 6, and for currents (at various depths) in figure 7.

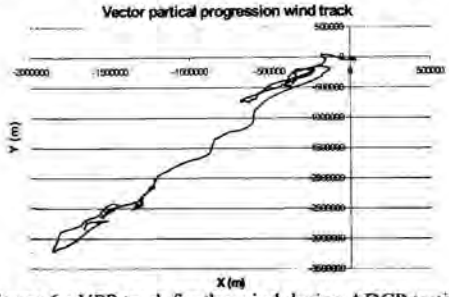

Figure 6 : VPP track for the wind during ADCP testing

The relatively straight and narrow banded track in figure 6 illustrates the predominance of the prevailing wind directions during the test period.

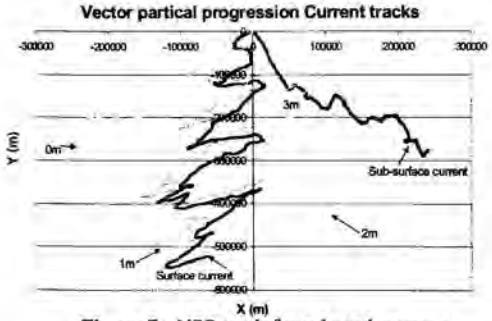

Figure 7 : VPP track for selected currents

The result in figure 7 provides a good illustration of the how the currents change with depth. There is a marked change in the dominant direction between the surface and sub-surface currents.

Comparing the VPP plots for the wind and currents, there is a noticeable similarity in the direction of the vector particle progression paths of the wind and the surface current at 0m depth. The wind VPP has an average bearing of roughly 210° while the current vector has a bearing of roughly 212.5°. This is again consistent with a strong link between the local wind and the surface current.

There is a visible difference in the general direction of the surface and sub-surface direction. The currents swing around from roughly 212° at 0m to a bearing of roughly 141° for the sub-surface current. The shortness of the VPP path for the 3m depth suggests that it is in the interfacial region between the surface and sub-surface currents

There seems to be a quasi-periodicity in the VPP tracks of surface currents, with regular changes in direction. The time scale of these changes is approximately 6 days. This coincides well with the return period of low-pressure cells that move up the coast on average every 6 days [4]

3.2 Wind-Current correlation

3.2.1 Auto-correlation

The auto-correlations of the wind data resolved into components perpendicular and parallel to the port entrance channel are shown in figures 8 and 9.

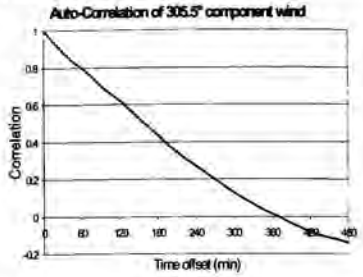

Figure 8: Auto-correlation of the wind component in the 305.5° direction.

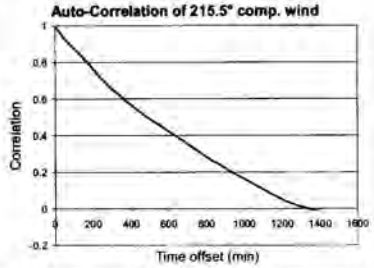

Figure 9: Auto-correlation of the wind component in the 215.5° direction.

The time where the wind ACC dropped to zero was approximately 6 hours for the component in the 305.5° direction and approximately 22½ hours in the 215.5° direction. We note that the 215.5° direction is a prevailing wind direction, hence the long time scale.

Auto-correlations of the surface current yielded time scales of about 7 hours in the 305.5° direction and approximately 23 hours in the 215.5° direction. For the sub-surface current the correlation time scales were about 28 hours in the 305.5° direction and 29 hours in the 215.5° direction.

There is therefore similarity in the correlation time scales of the wind and surface currents that confirms the conclusion that the local wind is the main forcing for the surface currents. The sub-surface current has much longer time scales that are similar for both directional components, which indicates that the current is relatively stable and persistent in its prevailing directions.

3.2.2 Cross-correlation

One-hour averages of the wind and current data, resolved into components perpendicular and parallel to the channel axis were analysed using cross-correlation analysis. To avoid the de-correlating effects of low-speed winds, only wind speeds exceeding specified threshold values were used. The maximum cross-correlation results for different current depths and lag times are shown in table 4.

When the average surface current and the wind were analysed reasonable cross-correlation coefficients were

found. A threshold wind speed of 3 m/s and a lag time of 2 hours gave a maximum correlation of 0.53. This confirms the dependence of the surface current on local wind conditions. The cross-correlation coefficients found for sub-surface currents were very low, confirming that they are essentially independent of local wind conditions.

Current depth (m)	Cross-correlation Coefficient	Wind speed threshold	Lag time (hrs)
Surface	0.53	3.0 m/s	2 hours
0m	0.36	2.5 m/s	2 hours
1m	0.53	3.0 m/s	2 hours
2m	0.45	3.5 m/s	2 hours
3m	0.32	3.5 m/s	3 hours
4m	0.25	3.5 m/s	3 hours
Sub-surface	0.17	3.5 m/s	4 hours

Table 4: Maximum wind-current cross-correlations and corresponding lag times and threshold speeds.

The fact that higher coefficients were found for higher wind threshold speeds indicates that higher wind speeds have a stronger influence in forcing the surface currents. The lag time of 2 hours indicates that surface current predictions may best be done using short-term wind averages.

Results from a vector cross-correlation analysis, using 20-minute averages for the wind and currents, are shown in Table 5.

Current depth (m)	Vector correlation Coefficient	Wind speed threshold	Lag time (min)
Surface	0.77	8 m/s	40 min
0m	0.69	8 m/s	0 min
1m	0.73	8 m/s	40 min
2m	0.69	8 m/s	40 min
3m	0.68	9 m/s	240 min
4m	0.46	9 m/s	80 min
Sub-surface	0.27	----	----

Table 5: Maximum wind-current vector cross-correlations and corresponding lag times and threshold speeds.

The maximum cross-correlation coefficient was again obtained for the surface currents. Correlations for the 0m level are slightly lower because the current measurements at the surface are affected by the waves. The increase in threshold speed for maximum correlations in the case of deeper currents, indicates that the higher the wind speed the deeper the currents that it can influence. The short lag times (about 40 minutes) reinforces our previous conclusion that current predictions should be made using short-term wind averages.

The tendency for lag times to increase with depth is consistent with the expected behaviour of wind driven currents.

4. DISCUSSIONS AND CONCLUSION

In this paper the effects of wind on near-shore ocean currents have been analysed. Analysis of current profiles has revealed the characteristic vertical structure of the currents near the port entrance and their temporal behaviour.

A surface current zone is present within the top 2 to 3 metres depth. The surface current is strongly dependent on local wind conditions. The six-day quasi-periodicity of the surface currents coincides well with the return period of low-pressure cells that move up the coast on average every 6 days [4]. Further analysis of a longer period of current data is needed to verify this.

The sub-surface current zone extends from depths of approximately 4m below the surface. Sub-surface currents appear to be relatively stable and are not strongly affected by local wind and wave conditions. We speculate that these currents are forced by larger-scale phenomenon.

This paper presents only the preliminary results of this research. In particular, the results are drawn from only one month of data. Longer term measurements are planned which will further clarify the relationship between the wind and surface currents as well as provide further understanding of the sub-surface currents and their forcing. This will form the basis for predictive modelling of currents outside the Port of Durban.

ACKNOWLEDGMENTS

We are grateful to the CSIR and to PORTNET for facilitating access to the data used in this research. In particular we would like to thank Dr. Marten Grundlingh, Mr Dave Phelp, Mr Hans Moes (CSIR) and Mr Dorian Bilse (Portnet) for their assistance.

REFERENCES

[1] CSIR (1999a), Port of Durban: Entrance Channel Crosscurrents. Part ADCP Transects. CSIR Report ENV-C 99018A. Stellenbosch.

[2] CSIR (1999b), Port of Durban: Ship Manoeuvring Simulations To Determine The Optimum Width Of The Port Entrance Channel For Fully Laden Post-Panamax Container Vessels. CSIR Report ENV-S-C 98127. Stellenbosch.

[3] Patel, S. & Stretch, D.D. (2001), Effects of Winds, Waves and Currents on Durban's Port Operations. Proc of *ICPMRDT* - Int Conference on Port & Maritime R&D and Technology, Singapore, 29-31 Oct, 2001.

[4] Preston – White, R.A. & Tyson, P.D. (1973), Note on pressure oscillations over South Africa. Monthly Weather Review, Volume 101, #8, pp 650 – 653

[5] Stretch, D.D. (1999), Adverse weather and wave characteristics at the Port of Durban: May 1998. Submitted to Water SA.

HEFAT2002
1st International Conference on Heat Transfer, Fluid Dynamics and Thermodynamics
8-10 April 2002, Kruger National Park, South Africa
MG1

MODELING OF UNSTEADY TRANSFER PROCESSES IN TWO-PHASE FLOW "DROPLETS-GAS"

G. Miliauskas* and V. Sabanas**
*Professor; **Ph.D. student
Department of Thermal and Nuclear Energy,
Kaunas University of Technology,
Donelaicio 20, LT-3006 Kaunas,
Lithuania,
E-mail: gimil@mf.ktu.lt

ABSTRACT

The state of radiating two – phase flow "droplets – gas" has been modeled numerically. The method of complex research of unsteady heat and mass transfer allows examining the interaction of complex transfer processes in semitransparent droplets and in their vicinity. The transformations of two-phase flow's state are calculated according to the energy consumption for heating and evaporating of liquid droplets. The selectivity o radiation absorption in semitransparent droplets is evaluated. Due to intense interaction of processes, the redistribution of the maximum place of droplet temperature field and the change of the direction of total heat flux's conductivity component vector take place. It is shown that dynamics of state change of two-phase system depends on the way the droplets are heated and is highly sensitive to the ratio of flow rates of dispersed liquid and gas.

INTRODUCTION

Despite of the fact that liquid fuel burning, drying of materials in dispersed form, the decrement of flame front, changing of the state of high temperature gas by spraying liquid and other widely used thermal technologies are quite distinctive, they all are related due to the fact that their efficiency depends on the intensity of interphase transfer in two-phase "droplets – gas" system. The rate of state change of such system depends on combined heat and mass transfer in condensed discrete media. In order to modernize the above-mentioned technologies, it is necessary to be able to control processes taking place in these technologies. For that it is necessary to know them thoroughly, also to understand the peculiarities of the interaction of combined transfer processes. Their researches are quite complicated due to the fact that the transfer processes in the thermal technologies are distinctly unsteady; their interaction occurs under the intensive influence of selective radiation and phase transformations; boundary conditions of heat and mass transfer are changing all the time.

It is quite expensive and complicated to research transfer processes in high-temperature two-phase flows experimentally, therefore numeric methods are widely used. Modern computers allow modeling dispersed flow state transformations according to the individual changes of condensed particle states and the change of state of carrying media, caused by previous ones. For that it is necessary to calculate total heat flux density in characteristic particles of condensed media and the intensity of their interphase transformations. The results of such research have to be generalized for entire gathering of particles. In the above-mentioned thermal technologies liquid droplets represent the condensed particles. Despite "droplet" researches have been carried out for more than one hundred years, there is no complete method, which could evaluate the interaction of combined transfer processes in evaporating droplets. For the simplification of research, the premises are made that let to avoid the necessity of evaluation of all three heat transfer ways in droplets. These premises abridge the boundaries of research method, but let to evaluate the peculiarities of transfer processes in the situations when the above mentioned premises are valid. When the influence of radiation is canceled, it is possible to evaluate the influence of liquid circulation on the heat exchange in droplets [1-3]. In case of non-circulation of liquid inside evaporating droplet, the interaction of transfer process can be

calculated according to radiation-conduction model in the cases of steady [4] and unsteady [5, 6] heat and mass transfer. The selectivity of radiation absorption in semitransparent droplets and spectral-optical effects in the surface of interphase contact have significant influence on the interaction of transfer processes in semitransparent droplets. Spectral radiation models, describing radiation heat transfer in semitransparent droplets [6-11] and in their media [12] thoroughly allow to model combined energy transfer in two-phase flows.

The aim of this work – to examine the dependence of the change of two-phase flow state on the ratio of flow rates of dispersed liquid and gas, and the way semitransparent liquid droplets are heated.

RESEARCH TECHNIQUE

Dispersed system is made, as liquid is dispersed into gas, flowing in adiabatic channel. It is foreseen that the initial state of two-phase flow is fully determined; spherically symmetrical droplets are evenly distributed in the channel's cross-section. The droplets do not scatter, coalesce, no chemical reactions occur, the effects of viscous dissipation are indistinct, absolutely black source can produce radiation, its temperature equals to that of gas. As liquid droplets are heated intensively, they evaporate, therefore mass flows of condensed discrete media and carrying media of the flow change. Mixture of gases cools and changes its composition. Transformations the state of carrying media are calculated according to energy consumption for heating and evaporating of liquid droplets. The rate of change of gas enthalpy depends on the intensity of droplet heating and in case of monodispersed flow is described by:

$$\frac{d\left(\rho_g h_g\right)}{dt} = -4\pi N R^2 q_\Sigma^+(t). \qquad (1)$$

Total heat flux density on the external side of semitransparent droplet surface in case of combined heating depends on the intensity of radiation absorption and on convective heat flux density from gas to the droplet: $q_\Sigma^+(t) = q_r^+(t) + q_c^+(t)$. In case of convective droplet heating: $q_\Sigma^+ \equiv q_c^+$. Part of energy, supplied to the droplet, is used for its heating, another part is used for evaporating. The intensity of phase transformations depends on the distribution of the energy supplied to the droplet between the components q_h and q_f:

$$m(t) = \frac{q_f(t)}{L} = \frac{q_\Sigma^+(t) - q_h(t)}{L} = \frac{q_\Sigma^+(t) - q_\Sigma^-(t)}{L}. \qquad (2)$$

The intensity of energy, used for heating of droplet mass, is shown by total heat flux density in the internal side of droplet surface: $q_\Sigma^-(t) = q_r^-(t) + q_l^-(t) = q_r^-(t) + \lambda_L \partial T(r,t)/\partial t\big|_{r=R^-}$.

In the case of radiative - conductive energy transfer temperature field in heating and evaporating droplet is described by the equation:

NOMENCLATURE

A	channel cross-section area (m^2)
a	thermal diffusivity (m^2/s)
B	transfer number
C	drag coefficient
c	mass specific heat, J/(kg K)
D	mass diffusivity (m^2/s)
G	flow rate (kg/s)
g	dimensionless flow rate [G_L/G_g]
h	enthalpy per unit mass (J/kg)
L	latent heat of evaporation (J/kg)
m	mass flux density (kg/s m^2)
n	number of the term in infinite sum
N	concentration of droplets (m^{-3})
P	pressure (Pa)
Pr	Prandtl number
q	heat flux density (W/m^2)
R	radius of a droplet (m)
Re	Reynolds number
R_μ	universal gas constant
r	coordinate of a droplet (m)
T	temperature (K)
t	time (s)
w	velocity (m/s)

Greek Letters

η	dimensionless coordinate [r/R]
λ	thermal conductivity (W/m K)
μ	molecular mass (kg/mol)
ρ	density (kg/m^3)

Subscripts

c	convective
f	evaporation
g	gas
h	heating
i	time index in a digital scheme
j	index of a droplet cross-section
k	index of a channel cross-section
L	liquid
l	conductive
m	mass average
R	surface of a droplet
r	radiation
v	vapor
Σ	total
0	initial state
∞	far from a droplet

Superscripts

$'$	variable
$+$	external side of a surface
$-$	internal side of a surface

$$T(r,t)=T_R(t)+\frac{2}{r}\sum_{n=1}^{\infty}sin(n\pi\eta)\int_0^t f_n(t')\times$$
$$\times exp\left[-a\left(\frac{n\pi}{R}\right)^2(t-t')\right]dt', \quad (3)$$

$$f_n(t')=(-1)^n\frac{R}{n\pi}\frac{T_R(t')}{dt'}+\frac{1}{R\rho c}\int_0^R q_r(r',t')$$
$$\times[sin(n\pi\eta)-(n\pi\eta)cos(n\pi\eta)]dr'. \quad (4)$$

Unsteady temperature field in semitransparent evaporating droplet can be calculated according to the Eq. (3) only when the time-functions, which define the changes of droplet radius $R(t)=f_R(t)$ and droplet surface temperature $T_R(t)=f_{T_R}(t)$ are known. Dynamics of evaporation and moving of a spherically symmetrical droplet are defined by equations:

$$\frac{dR(t)}{dt}=-\frac{m(t)}{\rho_L}, \quad (5)$$

$$\frac{dw_L(t)}{dt}=\frac{9}{R}\frac{\rho_g\left(1+0.2\,Re^{0.63}\right)(1+B)^{-0.2}}{\rho_L\,Re}\frac{|w_g-w_L|}{(w_g-w_L)^{-1}}. \quad (6)$$

Transfer processes in a droplet and in its surroundings are closely related. Since they are unsteady, the intensity of energy fluxes on droplet surface changes. Therefore the temperature of droplet surface changes as well. Instant values and rate of change of the temperature depend on the interaction of the transfer processes. At every time instant the temperature of droplet surface must be such that it assures the equality of energy fluxes, taken to the droplet and taken away from it. That allows constructing the functional for calculation of the temperature of evaporating droplet surface:

$$\frac{2+0.57\,Re^{1/2}\,Pr^{1/3}}{(1+B)^{0.7}}\frac{\lambda_{gv}(T_g-T_R)}{2R}+$$
$$+\lambda_L\frac{2\pi}{R^2}\sum_{n=1}^{\infty}\left[n(-1)^n\int_0^t f_n(t')\times\right.$$
$$\left.\times exp\left[-a\left(\frac{n\pi}{R}\right)^2(t-t')\right]dt'+(q_r^+-q_r^-)\right]-$$
$$-\frac{LD_v}{T_R}\frac{\mu_v}{RR_\mu}\left[p_{v,R}-p_{v,\infty}+\frac{\mu_v}{\mu_g}\times\right.$$
$$\left.\times\left(p\ln\frac{p-p_{v,\infty}}{p-p_{v,R}}-p_{v,R}+p_{v,\infty}\right)\right]=0. \quad (7)$$

The last member of Eq. (7) corresponds to the part of external heating energy $q_f(t)=m(t)L$, used for phase transformations.

The next-to-last member of Eq. (7) corresponds to the part of radiation on the droplet surface that enters the droplet. If spectral absorption coefficients of semitransparent material along entire radiation spectrum are finite, then radiation is not absorbed by droplet surface: $q_r^+=q_r^-$. In Eq. 6 and 7 the exponent functions of transfer number

$$B(t)=\frac{c_{vg}(t)\left[T_g(t)-T_R(t)\right]}{L(t)}\frac{q_f(t)}{q_c^+(t)} \quad (8)$$

evaluate correspondingly the influence of Stefan hydrodynamic flow on the drag coefficient of evaporating droplet and the intensity of external convective heating.

If a single droplet is evaporating in gas flow ($g_0\approx0$), then amount of energy, used for its heating and evaporating is infinitesimal, if compared to enthalpy of gas flow, therefore the state of gas practically does not change during evaporation. Thus, the function $f_{T_R}(t)$ that defines the dynamics of temperature change of the droplet surface can be calculated during entire lifetime $0\div t_f$ of the droplet. For that the predicted control time t is changed by the sum of finite time intervals l-1: $t=\sum_{i=1}^{l-1}\Delta t_i$; here t_1=0, t_l=t. Dimensionless droplet coordinate is divided into J-1 interval $\Delta\eta_j=\eta_{j+1}-\eta_j$; here η_1=0, η_J=1. Under statement that $T_g(t)\equiv const$, for every time instant t_i such temperatures $T_{R,i}$ are determined, which satisfy balance equation (Eq. (7)) with accuracy: $\left(1-q_\Sigma^+\right)/\left(q_\Sigma^-+q_{fi}\right)100\%\le0.01\%$. Then unsteady temperature field is calculated using Eq. (3), and after that other characteristics that define the intensity of unsteady heat and mass transfer in droplets are calculated. If the batch of droplets is evaporating (g_0>0), then gas temperature changes, therefore it is necessary to solve additionally Eq. (1) that defines the change of gas state. A finite number K of control cross-sections A_k is predicted in this channel. For that the channel is divided into K-1 control volumes, which are limited by adiabatic channel walls and by selected A_k cross-sections (A_1 - initial cross-section of the channel; A_K - channel cross-section, in which droplets evaporate completely). Gas temperature $T_{g,k+1}$ is selected in the cross-section of outlet of the control volume. In the first iteration the following premises are made: $w_{g,k+1}=w_{g,k}$, $w_{L,k+1}=w_{L,k}$ and $R_{k+1}=R_k$. Time Δt_k, in which droplets cross the control volume of the channel is calculated. The iterations, which were discussed in single droplet case, are executed under the statement that $t\equiv t_k+\Delta t_k$. R_{k+1}, $w_{L,k+1}$ and $G_{L,k+1}$ are specified. $w_{g,k+1}$ ir $G_{g,k+1}$ are calculated using the equations of impulse and flow rate continuity [13]. $T_{g,k+1}$ is made more exact by solving Eq. (1) numerically. Its accuracy of 0,01K is reached. The step of time

coordinate Δt_i assures that $\Delta T_{Lm,i} < 1$ K. Then the parameters of unsteady transfer are calculated very precisely [14].

Local radiative flux density inside a droplet is calculated according to the temperature field that has been specified in earlier iteration [6]. The following factors are evaluated: radiation of external source; reflection of incident light beam on droplet surface; influence of Bruster's angle and spectral - optical characteristics on radiation absorption in semitransparent droplet. The integration according to the angle of light beam descent is carried out using 5 point Gauss scheme, the integration according to radiation spectrum - using rectangular method. The range of wave numbers $10^3 \div 1{,}25\ 10^6 m^{-1}$ is divided gradually into 150 intervals.

RESULTS OF CALCULATIONS

The dependence of the state change of two-phase dispersed flow on the quantity of dispersed water and the way the droplets are heated was researched numerically. Two-phase flow was constructed by spraying water droplets, diameter $0.2 \cdot 10^{-3}$ m at 280 K temperature into the flow of dry air, having 1500 K temperature and moving with velocity of 10 m/s. The conductive heating of droplet was modeled under the statement that slip velocity of water droplets in gas equals zero. It is foreseen that in case of combined droplet heating the source of radiation is absolutely black body, its temperature corresponds to that of gas flow. When a single droplet is evaporating in gas flow, then it is assumed that g_0=0.

The change of gas state is sensitive to the ratio g_0 of sprayed liquid flow rate and the initial flow rate of gas (Fig. 1). As g_0 is increased, gas is cooled more, hence droplets evaporate completely later. Such relation qualitatively remains in all heating cases. Meanwhile, the temperature mode of evaporating droplets significantly depends on g_0 and way of heating. That is illustrated in Figure 2. When quantity of dispersed water is small, droplets first are heated intensively, later evaporate intensively and gradually begin to cool or remain isothermal (if they are heated conductively and $T_g(t) \equiv const$).

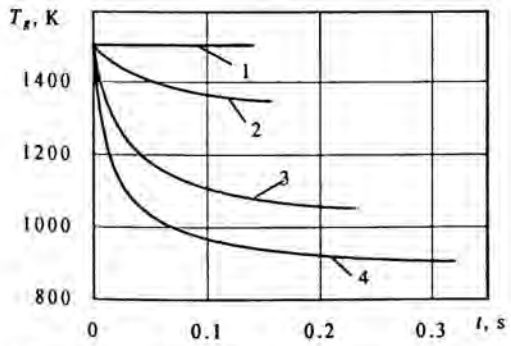

Figure 1: Dependence of gas cooling dynamics on quantity of dispersed liquid in the case of radiative-convective heating of droplets. (g_0: *1* – 0; 2 – 0.1; *3* – 0.5; *4* – 1).

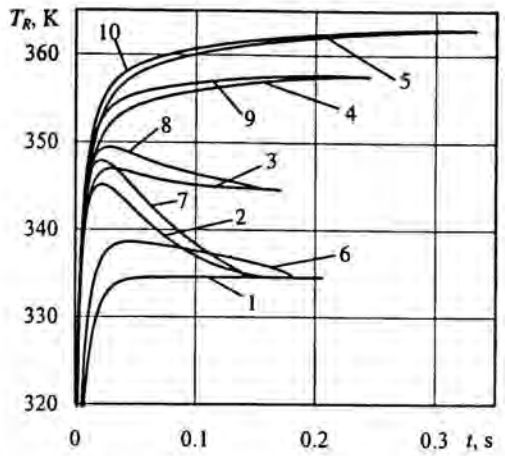

Figure 2: Dependence of temperature change of evaporating droplet surface on the way of droplet heating: *1* – conductive; *2-5* – convective; *6* – radiative-conductive; *7-10* – radiative-convective. (g_0: *1,2,6,7* – 0; *3,8* – 0.1; *4,9* – 0.5; *5,10* – 1. w_{L0}, m/s: *1,2,6,7* – 10; *3-5, 8-10* – 20).

As water spraying is increased, droplets are cooled less and less. From a certain g_0 droplets are only heating during entire evaporating process. The following fact is interesting: at higher g_0 droplets are heated up to higher temperature, though their surroundings cools to lower temperature. That is conditioned by significantly increased water vapor concentration in the carrying media of two-phase flow. Although the dynamics of droplet evaporation highly depends on the way of droplet heating, before vanishing all droplets reach temperature, which is characteristic for every g_0. A single droplet in conductive heating would heat up to this temperature, if this droplet were evaporated in gas flow, which is formed after complete evaporation of droplets. The way of droplet heating decides the change of their non-isothermality (Fig.3).

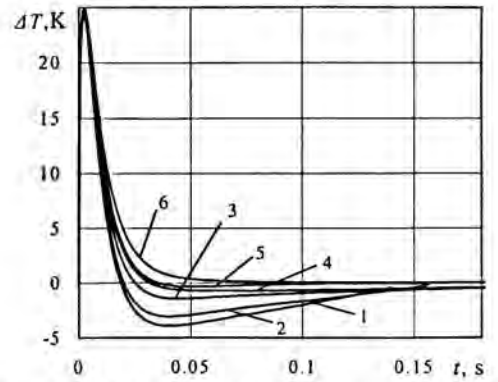

Figure 3: Change of non-isothermality $\Delta T = T_R(t) - T_m(t)$ in evaporating droplets in the cases of radiative-convective (*1-4*) and convective (*5,6*) heating.(g_0: *1,5*– 0; *2*– 0.1; *3*– 0.5; *4,6*– 1).

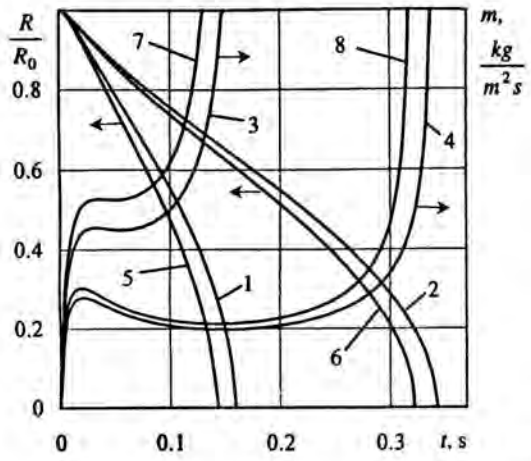

Figure 4: Change of droplet evaporation dynamics (R/R_0) and intensity (m) in the cases of convective (*1-4*) and radiative-convective heating. (g_0: *1,3,5,7* – 0; *2,4,6,8* – 1).

During heating the intensity of droplet evaporation changes significantly, as illustrated in Fig. 4. At the beginning the intensity quickly increases, as ratio q_R/q_f decreases. As droplets are heating and gas is cooled, temperatures T_g and T_R approach, furthermore, slip velocity of droplets in gas decreases (Fig. 5). Therefore evaporation intensity begins to decrease, as the intensity of droplet heating diminishes. But at the final stage of the droplet phase change their evaporation intensity begins to grow again and becomes infinite at the moment of droplet extinction. This is conditioned by the growing total heat flux density (Fig. 6), which heats the droplets. This intense growing is decided by the increasing of convective heating energy flux density, as the droplet decreases. Energy of surrounding radiation perceptible acts on the process of droplet heating and evaporation and has a decisive influence on the interaction of transfer processes in a droplet and its surroundings.

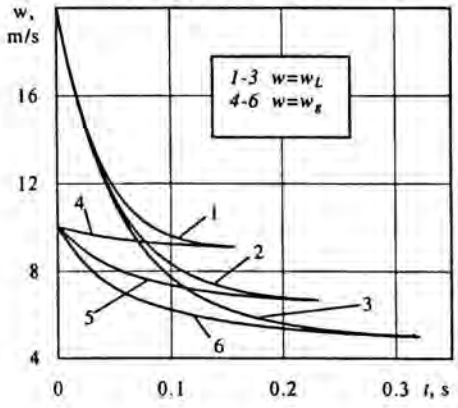

Figure 5: Dynamics of two-phase flow during radiative-convective heating of droplets. (g_0: *1,4*–0.1; *2,5*–0,5; *3,6*–1).

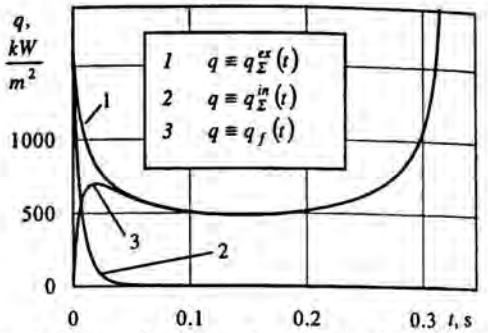

Figure 6: Energy fluxes on the surface of an evaporating droplet (g_0=1;w_{L0}=20 m/s).

At the beginning entire absorbed in the droplet energy is heating it. Radiation energy can be involved in evaporation process only when part of this energy is taken out to the droplet surface by conduction and by convection (as liquid circulates). This happens when temperature field inside the droplet is deformed and temperature vector changes its direction under influence of radiation energy. This situation is illustrated in Fig. 7.

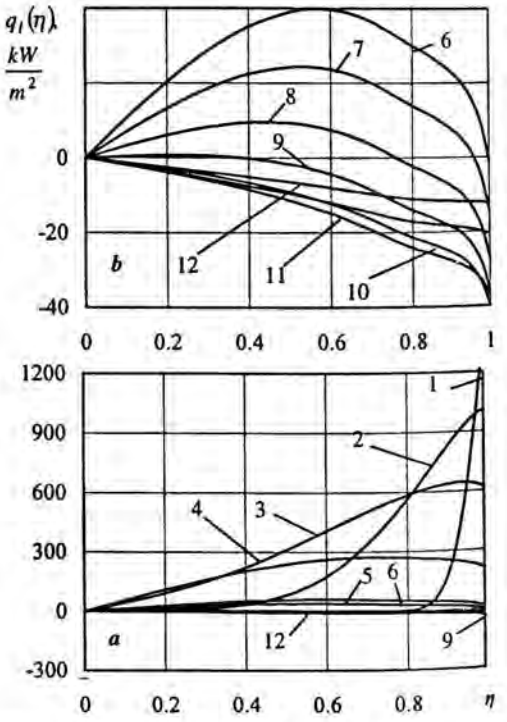

Figure 7: Change of the conductivity component of the total energy flux in a droplet: *a* – general view; b – initial and final periods of an evaporating droplet heating. (*t*, s: *1*–0.00005; *2*–0,0019; *3*–0.0048; *4*–0.012; *5*–0,023; *6*–0.026; *7*–0.029; *8*–0,033; *9*–0.04; *10*–0.054; *11*–0,085; *12*–0.3. g_0=1;w_{L0}=20 m/s).

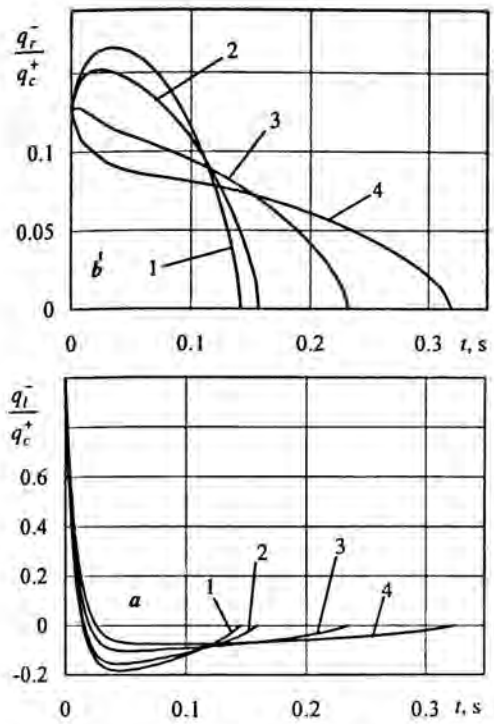

Figure 8: Change of the ratio of heat fluxes on the droplet surface (g_0: *1* – 0; *2* – 0.1; *3* – 0.5; *4* – 1. w_{L0}=20 m/s).

The ratios of the radiative component (Fig. 8a) of total heat flux density that warms the droplet and the conductive component (Fig. 8b) of total heat flux density inside the droplet with the convective heat flux density [6]. Zero values in the Fig. 7 show the place of change of local conductive heat flux; in Fig 8b - time instant, when its vector changes direction in the internal side of droplet surface.

CONCLUSION

The change of state of two-phase "droplet-gas" flow can be classified according to the peculiarities of the interaction of combined transfer processes, picking out initial, transient and final periods. The conduction component of total heat on droplet surface flux density plays very important role in the interaction of transfer processes. During the initial period this component corresponds to the part of the external convective heat flux density that heats the droplet. During the final and final periods the conduction component it shows to the part of radiative energy flux density, absorbed in the droplet; it is used for droplet evaporation. The main factors, which decide the regularities of transfer process interaction are the ratio of the initial gas flow and sprayed liquid flow, the dispersity of liquid spraying and the way of droplet heating. Only the thorough understanding and evaluation of the above-mentioned factors can lead to effective control of processes in two-phase systems.

REFERENCES

[1] Prakash, S., Sirignano, W.A., 1978, "Liquid fuel droplet heating with internal circulation," Int. J. Heat Mass Transfer, Vol. 21, pp. 885-895.

[2] Law, C.K., 1982, "Recent advances in droplet vaporization snd combustion," Prog. Energy Combust. Sci., Vol. 8, pp. 171-201.

[3] Chiang, C.H., Raju, M.S., Sirignano, W.A., 1992, "Numerical analysis of convecting, vaporizing fuel droplet with variable properties," Int. J. Heat Mass Transfer, Vol. 35, pp. 1307-1324.

[4] Miliauskas, G.J, Tamonis, M.M, Svencianas, P.P., 1985, Radiative and combined heat transfer in a spherical volume of a selectively emitting and absorbing medium (Interaction between radiation and conduction)," Heat Transfer-Soviet Research, Vol. 17, No. 4, pp. 131-139.

[5] Miliauskas, G., 1997, "Non-steady heat and mass transfer in radiating dispersed flows 2. Combined energy transfer in semitransparent particles," Energetics, No. 4, pp. 16-23.

[6] Miliauskas, G., 2001, "Regularities of unsteady radiative-conductive heat transfer in evaporating semitransparent liquid droplets," Int. J. Heat Mass Transfer, Vol. 44, pp. 785-798.

[7] Harpole, G.M., 1980, Radiative absorption by evaporating droplets," Int. J. Heat Mass Transfer, Vol. 23, pp. 17-26.

[8] Miliauskas, G.J., Tamonis, M.M., Svencianas, P.P., 1983, Radiation and combined heat transfer in spherical volume of selectively-radiating and absorbing medium (1. Determination of radiation heat flow)," Lietuvos TSR MA darbai serija B, Vol. 6(139), pp. 53-61.

[9] Lage, P.L., Rangel, R.H., 1992, "On the role of internal radiation absorption in single droplet vaporization," 30th Aerospace Sciences Meeting, 6-9 January, Reno, AIAA-92-0106, pp. 1-19.

[10] Miliauskas, G., 1996, "Optical constants dependence on temperature influence on heat transfer in water droplets," Mechanics, No. 1., pp. 32-37.

[11] Dombrovsky, L.A., 2000, "Thermal radiation from nonisothermal spherical particles of a semitransparent material," Int. J. Heat Mass Transfer, Vol. 43, pp. 1661-1672.

[12] Saiton, T., Yamazaki, K., Viskanta R., 1991, "Effect of thermal radiation on transient combustion of a fuel droplet with the finite rate of chemical reaction," Trans, Jap. Soc. Mech, Eng. B. Vol. 57., pp. 283-288.

[13] Miliauskas, G., Montvilas, R., 2000, "Non-steady combined heat and mass transfer in a gas-semitransparent liquid droplets system," 3rd European Thermal Sciences Conference, 10-13 September, Heidelberg, Germany, Vol. 2, pp. 1011-1016.

[14] Miliauskas, G., 1997, "Optimization of computation non-steady combined heat transfer in spherical volume," Mechanics, No. 1., pp. 5-13.

HEFAT2002
1st International Conference on Heat Transfer, Fluid Mechanics, and Thermodynamics
8-10 April 2002, Kruger Park, South Africa
M11

MODELING AND NUMERICAL ANALYSIS OF MIXING IN AN ACTIVELY CONTROLLED MICROMIXER

Marion Volpert,
Department of Mechanical and Environmental Engineering
University of California, Santa Barbara, CA 93106

Carl Meinhart ,
Department of Mechanical and Environmental Engineering
University of California, Santa Barbara, CA 93106

Igor Mezic,
Department of Mechanical and Environmental Engineering
University of California, Santa Barbara, CA 93106

Mohammed Dahleh
Department of Mechanical and Environmental Engineering
University of California, Santa Barbara, CA 93106

ABSTRACT

An active mixing strategy has been developed to enhance mixing of two fluid streams in a microchannel. The working principle of the mixer is to reorient the lamination of the flow from streamwise to cross-stream. Numerical solutions of the flow through the mixer are calculated by simulating the full Navier-Stokes equation, the Stokes' equation, and an analytical model based upon the superposition of elementary velocity profiles. The analytical model agrees qualitatively with Navier-Stokes and Stokes' solutions. A mixing variance coefficient is developed to quantitatively evaluate mixing efficiency for various flow configurations. The results indicate enhanced mixing for two flow configurations.

INTRODUCTION

The use of integrated microelectromechanical systems (MEMS) is expanding rapidly due to improvements in microfabrication technology. MEMS have applications in a variety of industries, including the automotive, aerospace, computer, and biomedical industries. Micro total analysis systems (μTAS) are being developed for drug discovery, drug delivery and chemical sensing (Chiem et al., 1997). Technical barriers of these systems include device packaging and interfacing, chemical surface absorption, and control of fluid motion on the microscale. The performance of these devices can be limited by the rate in which mixing occurs at the microscale.

Mixing of two fluids can be enhanced when the interface between the fluids is increased through stretching and folding, so that diffusion between the fluids only has to occur over a relatively small distance. At the macroscale, mixing can be enhanced by three-dimensional turbulent eddies that contain a continuous spectrum of length scales, which stretch and fold the fluid interface. A turbulent flow regime is characterized by a relatively high Reynolds number, which is defined as $\mathrm{Re} = U_b D_h / \nu$, where U_b is the characteristic velocity, D_h is the hydraulic diameter, and ν is the kinematic viscosity. A water flow through a 200 μm wide channel with a kinematic viscosity, $\nu = 10^{-6}$ m^2/s, and a characteristic velocity of 1cm/s, has a Reynolds number of 0.8 which precludes the existence of turbulence. For Reynolds numbers approaching zero, the flow is characterized as Stokes' flow, where inertial forces are insignificant and viscous forces are balanced by pressure forces.

In microdevices, fluids are often mixed through pure molecular diffusion. However, depending upon the rate at which diffusion occurs, the diffusion time scale, t_D, may be too large. The diffusion mixing time scale is defined as $t_D = L^2/D$, where L is the relevant mixing length (i.e. the characteristic width of the flow channel), and D is the molecular diffusivity. In practical BioMEMS applications, one is often interested in transporting and mixing biological molecules. The diffusion coefficient of hemoglobin in water, is $D = 70$ μm^2/s, and therefore it would take up to 570 s for this molecule to diffuse over a length of $L = 200$ μm.

Microscale mixers can be divided into two broad classifications, passive and active mixers. Passive mixers have been developed by Branebjerg et al. (1994, 1996). One of these mixers consisted of a zigzag-shaped channel. For sufficiently high flow rates, secondary flows were generated by the sharp microchannel corners, which enhance mixing. A second mixer design was based on lamination theory, where successive layers of fluid were separated and then recombined, creating several relatively thin layers of fluid. Miyake et al. (1993) designed a mixer using an array of 400 micro nozzles. Each nozzle produced a plume of fluid, which increased the interface area between the two fluids.

Liu et al (2000) developed a passive three-dimensional serpentine microchannel to enhance mixing by chaotic

advection. Their 3-dimensional mixer shows promise for passive mixing at Reynolds numbers ranging from 6 to 70. More recently, a three-dimensional serpentine mixer has been investigated by Yi & Bau (2000).

Most of the active mixing strategies are based upon the principle of chaotic advection. If the distance between two nearby particles separate exponentially as they advect through the flow, the particles are considered to have chaotic trajectories (Aref, 1984, Ottino, 1989). Chaotic advection can also be used to control the rate and quality of mixing (D'Alessandro et al. (1999)). Evans et al. (1997) developed a planar microfrabricated mixer, which uses a source/sink system to induce chaotic advection. Here, unmixed fluid is pumped into a mixing chamber, and then two source/sink systems are alternately pulsed and mix the fluid.

Despite previous efforts, the problem of mixing at the microscale remains. Many of the mixing strategies are effective, but only at specific flow regimes. Therefore, we present an actively controlled micromixer that can be adapted to achieve effective mixing over a wide variety of flow conditions. The working principle of the mixer is to perturb the motion of two fluid streams flowing through a main channel by oscillating flow emanating from three pairs of secondary channels at specified frequencies and phase shifts (see Figure 1). The choices of frequencies and phase shifts for optimal mixing are not obvious, and are the subject of current and future investigations. A related mixer design that incorporates three staggered secondary channels has been proposed recently by Lee et al. (2000).

NOMENCLATURE

f_i	frequency of the i^{th} secondary channel velocity, V
h	half width of the mixing channel
L	length of mixing channel
U	velocity in the x-direction (horizontal)
U_b	bulk velocity in the x-direction
V	velocity in the y-direction (vertical)
	V_m maximum velocity of the secondary channels in the y-direction
φ	phase shift of the secondary channel velocity, V
Φ	mixing variance coefficient
τ	dimensional time scale
ΔT	interval time for the calculation of Φ

2. MIXER DESIGN

The micromixer is shown in Figure 1. Flow in the main channel is manipulated by controlling time-dependent oscillating flow from three pairs of secondary channels. The secondary channels impart time-dependent cross-stream momentum on the main channel flow, which alters the fluid motion. A micrograph of the experimental chip is shown in Figure 1a, and a description of the fluid motion in the mixer is shown in Figure 1b.

a)

b)

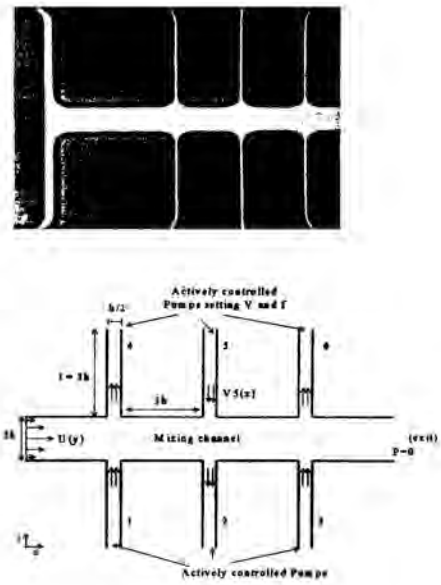

1(a) micrograph of the mixing chip, (b) schematic showing one possible flow configuration. (The device was fabricated by Robert Bayt from MIT.)

The effectiveness of the mixer is evaluated using several different flow configurations by varying the frequencies and the secondary channels. The frequencies are made non-dimensional by multiplying the actual frequency by the time scale $\tau = h/U_b$, where h is the half width of the main channel, and U_b is the bulk velocity of the flow.

The mixing channel is $2h$ high and $13.5h$ long, where h is an adjustable length scale ranging from 50 μm to 150 μm, depending on the application of the mixer. The six secondary channels are perpendicular to the main channel, and are $h/2$ wide, $5h$ long and separated from each other by a distance of $3h$. A parabolic profile is specified at the entrance of the main channel, which is eventually perturbed by the secondary channels. The pressure at the entrances of the secondary channels, far from the main channel, is specified to be sinusoidal in time, with each pair having different frequencies.

The micromixer used in the current experiments has a length scale h = 100 μm, so that the channels are 200 μm wide. The channel depths were chosen to be 100 microns. For both the experiments and the computations, we restrict our observation to a plane of fixed depth. The flow in the channels was 3-D, but for simplicity the simulations were limited to two

dimensions. By limiting the computations to two dimensions, we ignore the effect of out of plane dispersion, and assume the velocity profile is similar to that of a 2-D velocity profile. Two-dimensional simulations capture the bulk of the flow physics, but with significantly reduced computational expense. The time-dependent velocity profile in the secondary channels can be determined by solving the Navier-Stokes equations using a Fourier series expansion. For a unidirectional flow $v_y = v(x,t)$, subject to a time periodic pressure gradient the dimensional equations become

$$\frac{\partial v}{\partial t} - \nu \frac{\partial^2 v}{\partial x^2} = -\frac{1}{\rho}\frac{\partial P}{\partial y}, \tag{1}$$

$$\frac{\partial P}{\partial y} = -\rho a \sin(\omega t + \phi), \tag{2}$$

$$v(0, y) = 0,$$

$$v(2d, y) = 0. \tag{3}$$

Where in this case $2d$ is the width of the secondary channel. This is the so-called oscillating slot flow (Panton, 1984), in nondimensional variables ($\tau = \omega t$, $\eta = x/d$, $V = 3\nu v/ad^2$), the solution is

$$V(\eta,\tau) = \sum_{n=2,4,6,\ldots}^{\infty} [-(a_n \sin\phi + b_n \cos\phi) e^{-\frac{n^2\pi^2}{4\beta}\tau} + a_n \sin(\tau+\phi) + b_n \cos(\tau+\phi)] \sin(\frac{n\pi\eta}{2}), \tag{4}$$

where

$$\beta = \frac{\omega d^2}{\nu}, \tag{5}$$

$$a_n = \frac{48 n\pi}{16\beta^2 + n^4\pi^4}, \tag{6}$$

$$b_n = -\frac{192\beta}{n\pi(16\beta^2 + n^4\pi^4)}. \tag{7}$$

The frequency parameter, β, represents the ratio of the time for the viscous effect to diffuse across the channel to the period of pressure oscillation. When β is small, the imposed change is slow compared to viscous response, and the solution can be approximated with the pseudosteady solution

$$V(x',\tau) = V_{\max} x'(2 - x') \sin(\frac{\pi\tau}{2} + \phi). \tag{8}$$

The coordinate x', is the centered at each secondary channel. This flow solution is used as boundary conditions for the secondary channels, and in the analytical model presented in section 4.

4. NUMERICAL ANALYSIS

Three computational methods were used to compute the flow field. We obtained the velocity fields and the particle trajectories from Navier-Stokes simulations, Stokes' simulations, and by piecewise integrating solutions of Stokes' equation. The simulations were conducted according to the geometry shown in Figure 1b. The full Navier-Stokes simulations were conducted using *CFD2000*, which is commercially available from *Adaptive Research, Inc.* The software uses finite volume analysis to simulate a wide range of fluid flows, including heat and mass transfer problems. The mixing performance of the device was simulated using the two-phase flow feature of the CFD software to inject flow-tracing particles into the flow and calculate the particle trajectories. Time-dependent boundary conditions in the secondary channels were applied through a FORTRAN routine, which was interfaced to *CFD 2000*.

The boundary conditions were defined by a parabolic velocity profile at the entrance of the main channel, so that

$$U(y) = 1 - y^2. \tag{9}$$

The velocity profile V_i at the entrance of the i^{th} pair of secondary channels was

$$V_i = V_m \left(1 - (2x'/h)^2\right) \sin(2\pi f_i t + \phi_i). \tag{10}$$

Where, the oscillating frequency is f_i, and the phase is φ_i. The frequency may be made non-dimensional by multiplying by the time scale $\tau = h/U_m$. The maximum velocity in the secondary channels, V_m, is specified as $V_m = 4\pi f h$. This dictates that flow-tracing particles at the center of each secondary channel will travel a distance of approximately $2h$ before reversing during each oscillation; thereby slicing the flow in the main channel. Two different colors of particles were injected at the entrance of the main channel. Dark-colored particles were injected in the bottom half of the channel, while light-colored particles were injected in the top half of the channel. One particle was injected in each finite-volume element at the main channel entrance every 10 time steps.

In addition to CFD simulations, an idealized analytical solution of the flow field, denoted PS, was developed and then numerically integrated using *Matlab* software. The model consists of superposing the above defined velocities in the main channel and the secondary channels. The idealized analytical model allows one to quickly scan a large range of parameter space to determine the optimal flow configurations for mixing. In the idealized model, the mixing chamber was partitioned into three distinctive flow regions: the main channel, the secondary channels, and the intersection of the two regions. The main channel consists of steady horizontal velocity with a parabolic profile, corresponding to Eq. (9). The secondary channels consist of vertical velocity that is parabolic in space and sinusoidal in time, corresponding to Eq. (10). Since the Reynolds number of interest is relatively low, we assume that the linear Stokes' equation is nearly valid and that its solutions can be superposed. Therefore, at

the intersection of the two regions, the velocity fields are superposed. The Lagrangian evolution of flow-tracing particles is then obtained by integrating the velocity field in time, using *Matlab*.

5. ANALYSIS OF MIXING PERFORMANCE

Figure 2 shows the particle pathlines calculated using CFD, with non-dimensional secondary channel frequencies of $f_1 = f_2 = f_3 = 1/2$ for all three pairs of secondary channels. Figure 3 shows the particle paths for secondary channel frequencies $f_1 = 1/2\sqrt{5}$, $f_2 = 1/2\sqrt{2}$, and $f_3 = 1/2$, for the 1st, 2nd, and 3rd pair of channels, respectively. The results show that there is an approximately uniform distribution of pathlines at the channel exit.

2. Numerical simulation of particle trajectories in the micromixer with the same frequency specified at each secondary channel. The black and white lines are particle pathlines of two different fluids. The frequency of the three secondary channels is 1/2 with Φ equal to 0, π, and 0, respectively.

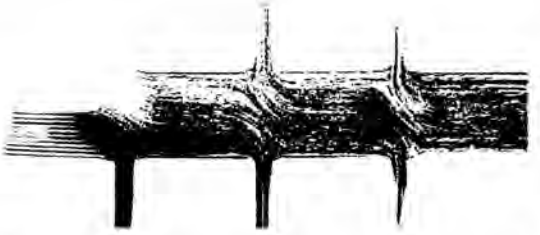

3. Numerical simulation of particle trajectories in the micromixer. The black and white lines are particle pathlines of two different fluids. The frequencies of the three secondary channels were 1/2sqrt(5), 1/2sqrt(2), 1/2 and with phase shifts 0, π, 0, respectively.

These frequencies were chosen by considering the amount of fluid displaced per period. The idea is to have at least the volume between two secondary channels, facing each other, entirely displaced during half a period, which leads in our case to a period of 2. With this requirement we decided to use different frequencies, close to the value determined, and also to use irrational frequencies so that no periodic phenomenon would develop.

A mixing variance coefficient is introduced to measure quantitatively the quality of mixing for various flow configurations, based upon the trajectories of flow-tracing particles. In the present approach, labels of 0 and 1 are specified for each particle introduced in the upper and lower half of the main channel, respectively. The channel exit is divided into S number of regions. The density of each region, ρ_i, is estimated by averaging the labels over the particles contained in that region during a specific time interval, ΔT, starting when the first particles reach the exit. The mixing coefficient is then estimated by averaging over the S regions,

$$\Phi = \frac{\sum_{S} (\rho_i - 0.5)^2}{S}. \qquad (13)$$

When there is no mixing $\Phi = 0.25$, and when there is perfect mixing $\Phi = 0$, corresponding to $\rho = 0.5$ in every region. The regions must be chosen large enough so that a sufficient number of particles are included in the average. The number of regions, S, defines the spatial scale in which mixing is observed. When S = 1, with an equal density of particles labeled 0 and 1 in the system (similar to the two undisturbed streams of dyes) Φ=0, indicating perfect mixing at that scale. Indeed the system contains the same amount of two different fluids. It is clear then that for satisfying result the value of S should be so that the length of each region is smaller or close to the diffusive length of the fluids considered.

The time evolution of the mixing variance coefficient is shown in Figure 4 for the flow field calculated using Navier-Stokes simulations and the analytical model.

The mixing coefficients are calculated for three different numbers of regions, S = 1, 3, and 10, for a starting time of t = 14. The abscissa of the Figure 4 represents the number of time interval p, so that the time considered is t = 14 +p0.25. The quality of mixing decreases significantly as the number of averaging regions, S, is increased, that is the value of Φ increases. This evolution of the mixing variance coefficient is clearly similar for results from the Navier-Stokes simulations and the analytical model. For S = 1, the entire channel is averaged, and that is where the lowest values of Φ are observed. In this case the value of Φ is not exactly zero although the number of particles from the upper and lower channels is initially the same. This can be explained as follows: at a specified point in time there are an uneven number of dark and white particles at the channel exit. The evolution observed for Φ indicates that either the mixing is not uniform throughout the channel, or there is an insufficient number of particles included in the average to estimate accurately the coefficient. The accuracy and resolution of the mixing coefficient can be improved by injecting more particles into the flow, thereby reducing noise. However, larger numbers of particles significantly increases the computational cost.

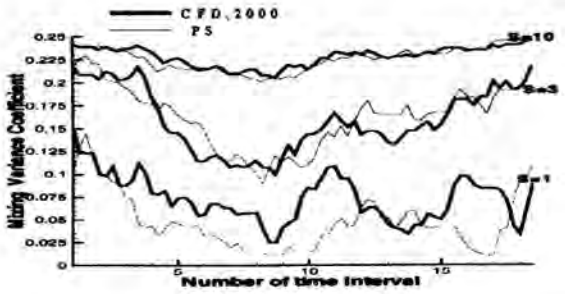

4. Comparison of the mixing coefficient for flow configuration B, calculated from the Navier-Stokes simulation (thick line), and calculated from the PS (thin line), for a number of regions at the exit of S = 1, 3, and 10. The coefficient follows the same trend between the N-S simulation and the analytical model.

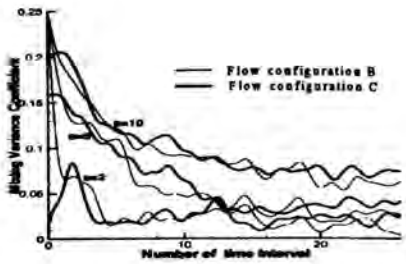

5.Mixing coefficients for two flow configurations calculated using the analytical model. Flow configuration C has secondary channel frequencies of $1/2\sqrt{5}$, $1/2\sqrt{2}$, 1/2 (thin lines), while flow configuration D has frequencies of 1/4, 1/3, 1/2 (thick lines). The velocity phase shift in each pair of secondary channels is 0, π, 0.

Since the analytical model agrees qualitatively with the N-S simulations in Figure 4, the analytical model can be used to quickly estimate the mixing performance over a wide range of flow configurations, with relatively low computational cost. Once, a small set of flow configurations have been identified, the Navier-Stokes simulations can be used to calculate more accurately the mixing performance.

The mixing coefficient shown in Figure 4 has significant noise and makes precise analysis of the mixing performance difficult. In order to reduce this noise, we increased the number of particles by a factor of 100, and reduced the sampling interval time to $\Delta T = 0.1$.

Figure 5 shows the mixing coefficient for two flow configurations (labeled C and D) using the analytical model. Flow configuration C has frequencies of $1/2\sqrt{5}$, $1/2\sqrt{2}$, $1/2$, while flow configuration D has frequencies of 1/4, 1/3, 1/2. The phase shift between the velocities of each set of secondary channels is 0, π, 0 (see Table 1). The results shown in Figure 5 indicate that flow configuration C and D exhibit good mixing, and are nearly equal in quality. The high quality of mixing of flow configuration C and D are a result of the efficient high-frequency lamination in the second and the third channel.

SUMMARY AND CONCLUSIONS

An active mixing strategy has been developed to enhance mixing of two fluids through a microchannel, based upon the principle of reorienting the direction of lamination. The mixing process occurs by reorienting the lamination from streamwise to cross-stream. Once the lamination is reoriented to the cross-stream direction, the lamination is further mixed by dispersion due to the parabolic velocity profile and molecular diffusion.

The Reynolds number used in the numerical investigation was Re = 5, based on the main channel width and centerline velocity in the main channel. Particle trajectories from numerical solutions of the Navier-Stokes equations agreed quantitatively with solutions of Stokes' equation. This indicated that the convective acceleration term in the Navier-Stokes equation does not significantly affect mixing for Re less than or equal to 5.

An analytical model based upon piecewise solutions of Stokes' equation was developed. Lagrangian particle trajectories are then estimated by integrating the velocity field over time. The results agreed qualitatively with the numerical simulations of the Navier-Stokes equations and Stokes' equations. The agreement is sufficient to justify using the analytical solution for estimating mixing effectiveness of various flow configurations. Since, the analytical simulation is computationally inexpensive, it can be used to evaluate mixing effectiveness over many different flow configurations.

In order to evaluate quantitatively mixing effectiveness, we have defined a mixing variance coefficient, φ. While the mixing variance coefficient provides a convenient metric for estimating mixing effectiveness, it is dependent on the number of flow-tracing particles used in the estimate. The size of the averaging cells determines the length scale in which the mixing effectiveness is evaluated.

The analytical model was used to calculate the mixing coefficient for two flow configurations. Flow configuration C, which has frequencies of $1/2\sqrt{5}$, $1/2\sqrt{2}$, $1/2$, while flow configuration D has secondary channel frequencies of 1/4, 1/3, 1/2. The phase shifts between the velocities of each set of secondary channels are 0, π, 0. The results indicate that both flow configurations show good mixing, with flow configuration C being slightly better than flow configuration D.

Acknowledgments

This work is supported by the National Science Foundation under the grant CTS-9874839 (C. M.), the grants DMS-980355 and AFOSR98-1-0146 (I. M.), and the grants NSF 9632820 and AFOSR 49620-97-1-0168 (M. D.). The authors would like to thank Robert Bayt from MIT for fabricating the micro-mixing devices.

REFERENCES

H. Aref, 'Stirring by Chaotic Advection' *Journal of Fluid Mechanics*, **Vol 143**, pp. 1-29, June 1984J.

Branebjerg, B. Fabius, and P. Gravesen, 'Application of Miniature Analyzers from Microfluidic Components to μTAS,' *Proceedings of Micro Total Analysis System Conference*, Twente, Netherlands, pp. 141-151, November 1994.

J. Branebjerg, P. Gravesen, J. P. Krog, and C. R. Nielsen, 'Fast mixing by lamination,' *Proceedings of the 9th Annual Workshop on Micro Electro Mechanical systems*, San Diego, CA, pp. 441-446, February 1996.

N. Chiem, C. Colyer, D. J. Harrison, 'Microfluidic Systems for Clinical Diagnostics', *International Conference on Solid State Sensors and Actuators*, Chicago, IL, vol 1, pp.183-186, june 1997.

D. D'Alessandro, M. Dahleh, I. Mezic, "Control of Mixing in Fluid Flow: a Maximum Entropy Approach", *IEEE Transactions on Automatic Control*, Vol. 44 , pp 1852-1863, October 1999.

W. M. Dean, 'Analysis of Transport Phenomena', *Oxford University Press*, New York, NY, 1998.

J. Evans, D. Liepmann, and A. P. Pisano, 'Planar laminar mixer,' *10th Annual Workshop of Micro Electro Mechanical System*, Nagoya, Japan, pp.96-101, January 1997.
P. Gravesen, J. Branejberg, and O. S. Jensen, 'Microfluidics-a review', J. Micromech. Microeng. , vol 3 (no. 4), p 168-182, Dec. 1993

Y. K. Lee, P. Tabeling, C. Shih, & C.-M. Ho, 'Characterization of a MEMS-fabricated mixing device', *Proceedings of MEMS-Vol. 2, Micro-Electro-Mechanical Systems, ASME*, Orlando FL, Nov. 2000.

R. H. Liu, K. V. Sharp, M. G. Olsen, M. A. Stremler, J. G. Santiago, R. J. Adrian, H. Aref, and D. J. Beebe, 'A Passive Micromixer: Three-Dimensional Serpentine Microchannel', *J. of MEMS*, Vol. 9, No. 2, 2000.

R. Miyake, T. S. J. Lammerink, M. Elwenspoek, and J. H. J. Fluitman, ' Micro Mixer with fast diffusion,' *Proceedings of the IEEE Micro Electro Mechanical Workshop*, Fort Lauderale, FL, pp. 248-253, February 1993.

J. M. Ottino, 'The Kinematics of Mixing: Stretching, Chaos, and Transport', Cambridge, New York: *Cambridge University press*, 1989, xiv, 364p.

M. Yi & H. H. Bau, 'The kinematics of bend-induced stirring in micro-conduits', *Proceedings of MEMS-Vol. 2, Micro-Electro-Mechanical Systems, ASME*, Orlando FL, Nov. 2000.

HEFAT2002
1st International Conference on Heat Transfer, Fluid Mechanics, and Thermodynamics
8-10 April, 2002, Kruger National Park, , South Africa
MN1

BEATING PHENOMENA IN AN ACOUSTIC RESONATOR

Normah Mohd-Ghazali
Department of Thermofluids
Faculty of Mechanical Engineering
Universiti Teknologi Malaysia
81310 UTM, Skudai
Johor, MALAYSIA
Email: nghazali@cisunix.unh.edu

John P. McHugh, and David W. Watt
Department of Mechanical Engineering
University of New Hampshire
Durham, New Hampshire, 03824
U.S.A.

ABSTRACT

Acoustic waves in a chamber are treated numerically. The governing equations are the two-dimensional viscous nonlinear Navier-Stokes system for a compressible fluid. Spatial derivatives are evaluated with finite differences. The temporal integration is semi-implicit. Heat exchanging plates are sometimes included, and are modeled with a row of grid points with zero velocity. The results without plates show the beating phenomena is present, and is modulated by the manner in which the flow is initiated. Results with plates show the same effect.

NOMENCLATURE

L length of resonator
L/H aspect ratio
M Mach number
p Pressure
Pe Peclet number
Pr Prantdl number
R gas constant
Re Reynolds number
t time
T fluctuating temperature
u,v fluctuating velocities
x,y horizontal, vertical position
Δt time-step
γ ratio of specific heats
ω Forcing frequency

INTRODUCTION

Acoustic waves in a closed rectangular chamber is treated numerically. The waves are generated by a membrane boundary condition on one wall. A simple model of heat exchanging plates are sometimes included. The simulations are motivated by thermoacoustic refrigeration, a phenomena which uses sound waves in a chamber to achieve a cooling effect. Recent interest has been directed towards the study of thermoacoustic refrigeration due to the overall simplicity of thermoacoustic devices. The thermoacoustic effect may have been used over a century ago by European glass blowers. Known as the Sondhauss effect, it was discussed qualitatively in 1877 by William Strutt (Strutt, 1945). An early modern thermoacoustic refrigerator was a testbed cryocooler built by Hofler in 1986 (Hofler, 1986). It was a gas-filled resonator containing a stack of plates and driven by a loudspeaker. Active study into thermoacoustic applications appears to have started with the Montreal Protocol (1987), an international agreement to reduce and later stop the worldwide production of harmful refrigerants. The absence of any refrigerants, moving parts, and lubricants makes thermoacoustic refrigeration an appealing replacement for current refrigeration systems (Swift, 1988). Unfortunately, previous thermoacoustic systems have low thermal efficiency, lower than their vapor-compression counterparts.

The numerical results given below treat the entire resonator, and allow the acoustic wave to evolve in time, adjusting to the no-slip boundary conditions, the presence of heat exchanging plates, and other features. Previous numerical work on thermoacoustics has mainly concentrated on the plate region where the cooling effects are observed (Worlikar, 1996), (Gopinath, 1998), Cao et. al (Cao, 1996). The current results show a beating phenomena, as well as other effects. The beating phenomena is a subhar-

monic oscillation, often discussed as a temporal modulation of the amplitude of the forced oscillation. Beating, or subharmonic oscillations, have been previously found experimentally by several authors (Atchley, 1990; Keolian, 1981) in experiments with acoustic resonators. Atchley and Kuo (Atchley, 1990) found a subharmonic motion, which they termed 'self-oscillation' at relatively large average pressure in the resonator. Self-oscillation did not appear at smaller average pressure. Keolian, et al, (Keolian, 1981) also note a subharmonic resonance in an acoustic Faraday experiment.

The results below show that a subharmonic mode appears early in the dynamics. The subharmonic mode is not strongly effected by the Reynolds number, until the Reynolds number is very low, where the subharmonic mode does not appear. However the subharmonic mode is greatly effected by the manner in which the flow is initiated.

FORMULATION

The governing equations are the Navier-Stokes, continuity, and energy equations in two dimensions, assuming a compressible Newtonian fluid with constant thermophysical properties. The equation of state is the perfect gas law. The pressure, temperature, and density are separated into mean and fluctuating parts, and all linear terms are carefully seperated from the nonlinear terms. The equations are then rescaled using the length of the chamber for a length scale, and the forcing frequency for a time scale. Density is eliminated from the system, and pressure is eliminated from the momentum equations, resulting in

$$\frac{\partial p}{\partial t} = \frac{\partial T}{\partial t} - (\nabla \cdot \mathbf{u}) - Q_p, \tag{1}$$

$$\begin{aligned}\frac{\partial^2 u}{\partial t^2} &= \frac{1}{M^2\gamma}\left(\frac{\partial^2 u}{\partial x^2} + \frac{\partial^2 v}{\partial x \partial y} - \frac{\partial^2 T}{\partial x \partial t}\right) \\ &+ \frac{1}{Re}\frac{\partial}{\partial t}(\nabla^2 u) + \frac{1}{3Re}\frac{\partial}{\partial t}\left(\frac{\partial^2 u}{\partial x^2} + \frac{\partial^2 v}{\partial x \partial y}\right) \\ &+ \frac{1}{M^2\gamma}\frac{\partial}{\partial x}(Q_p) - \frac{\partial}{\partial t}(Q_x),\end{aligned} \tag{2}$$

$$\begin{aligned}\frac{\partial^2 v}{\partial t^2} &= \frac{1}{M^2\gamma}\left(\frac{\partial^2 u}{\partial x \partial y} + \frac{\partial^2 v}{\partial y^2} - \frac{\partial^2 T}{\partial y \partial t}\right) \\ &+ \frac{1}{Re}\frac{\partial}{\partial t}(\nabla^2 v) + \frac{1}{3Re}\frac{\partial}{\partial t}\left(\frac{\partial^2 u}{\partial x \partial y} + \frac{\partial^2 v}{\partial y^2}\right) \\ &+ \frac{1}{M^2\gamma}\frac{\partial}{\partial y}(Q_p) - \frac{\partial}{\partial t}(Q_y),\end{aligned} \tag{3}$$

$$\frac{\partial T}{\partial t} = \frac{\gamma}{Pe}\nabla^2 T + (1-\gamma)(\nabla \cdot \mathbf{u}) + (1-\gamma)Q_p - \gamma Q_T, \tag{4}$$

where the nonlinear terms are combined in Q_x, Q_y, Q_p, and Q_T, and are given by

$$Q_x = u\frac{\partial u}{\partial x} + v\frac{\partial u}{\partial y}, \tag{5}$$

$$Q_y = u\frac{\partial v}{\partial x} + v\frac{\partial v}{\partial y}, \tag{6}$$

$$Q_T = u\frac{\partial T}{\partial x} + v\frac{\partial T}{\partial y} + \frac{\gamma - 1}{\gamma}\left[u\frac{\partial p}{\partial x} + v\frac{\partial p}{\partial y}\right], \tag{7}$$

$$\begin{aligned}Q_p = T&\left[\frac{\partial p}{\partial t} + u\frac{\partial p}{\partial x} + v\frac{\partial p}{\partial y}\right] + \left[u\frac{\partial p}{\partial x} + v\frac{\partial p}{\partial y}\right] \\ &- p\left[\frac{\partial T}{\partial t} + u\frac{\partial T}{\partial x} + v\frac{\partial T}{\partial y}\right] - \left[u\frac{\partial T}{\partial x} + v\frac{\partial T}{\partial y}\right].\end{aligned} \tag{8}$$

The Reynolds number, Mach number, and Peclet number are defined by

$$Re = \frac{\omega L^2}{\nu}, \tag{9}$$

$$M = \frac{\omega L}{\sqrt{\gamma R T_m}}, \tag{10}$$

$$Pe = \frac{\omega L^2}{\alpha}, \tag{11}$$

where T_m is the mean temperature, L is the length of the chamber, ω is the forcing frequency, ν is the kinematic viscosity, R is the gas constant, and α is the expansivity. Another parameter is the aspect ratio,

$$\frac{L}{H}, \tag{12}$$

where H is the height of the chamber.

Spatial derivatives are approximated with finite differences, accurate to second order. Interior grid points use standard central differences, while boundary points use one-sided second order difference schemes. The temporal integration is achieved with a semi-implicit method, where linear terms are treated implicitly, and nonlinear terms explicitly. The linear terms in (1) and (4) are treated with the Crank- Nicholson method in the usual manner. The nonlinear terms in (1) and (4) are treated with the Adams-Bashforth method.

The linear terms in the equations with second order temporal derivatives must be carefully treated to avoid severe damping of acoustic waves. For example,

$$\frac{\partial^2 u}{\partial t^2} = f(u) \tag{13}$$

is approximated with

$$\frac{u^{n+1} - 2u^n + u^{n-1}}{\Delta t^2} \cong \frac{f^{n+1} + f^{n-1}}{2}, \tag{14}$$

which can be shown to be second order accurate. Nonlinear terms are treated similarly.

Waves are forced by imposing the normal component of velocity along one side. The imposed velocity has the form

$$u(0,y) = h(y)\sin t, \tag{15}$$

where h(y) is a shape function. The shape function that corresponds to a membrane, $h = \sin y$, is considered here.

RESULTS AND DISCUSSION

Verification of computational formulation is accomplished by propagating linear acoustic waves computationally and comparing the results to the exact analytical solution. Both the linear inviscid, and viscous cases have been used for this purpose. The verification results are provided by Ghazali (Ghazali, 2001), and demonstrate that the above method is able to numerical model the acoustic waves in question.

Results without plates

Consider the flow without any heat exchanging plates. Table 1 summarized the parameters used in this study, chosen based on a typical operating condition for a thermoacoustic refrigeration system.

The desired result of the forcing, with or without plates, is a standing acoustic wave. However, the velocity field is significantly more complex than the expected standing wave. One of the key features is beating.

Table 1. PARAMETER VALUES.

M	0.7854
Pr	0.67
Re	800000
Pe	600000
L/H	4.00

The 'beating' phenomena occurs when the amplitude of an oscillation has its own oscillation. The beating effect in the present simulations can be seen by studying the total kinetic energy, $\overline{KE}$, shown in figure 1 for the present example. The simulation in figure 1 is performed for approximately 10 acoustic cycles of the forcing. Note that since kinetic energy is always positive,

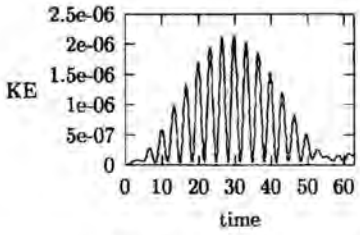

Figure 1. Total kinetic energy without plates

a cycle corresponds to two peaks of kinetic energy. The amplitude is clearly seen to have an oscillation at a frequency much lower than the forcing frequency. Subsequent cases, performed for more cycles, demonstrate that the beating effect continues, repeating the pattern shown in figure 1 very closely, indicating an oscillation phenomena rather than a transient effect.

The simplest explanation of beating is that of an oscillation with two incommensurate frequencies which are close in value. Using sinusoidal functions, the beating behavior can be modeled simply with the product of two cosine functions:

$$\cos\omega_f t \cos\omega_n t, \tag{16}$$

where ω_f and ω_n are the high and low frequencies measured in the results. Equation (16) can be arranged into the sum of two independent oscillations at two other frequencies with the fol-

lowing identity:

$$A\cos\omega_1 t + A\cos\omega_2 t = 2A\cos\left[\frac{\omega_1+\omega_2}{2}\right]t\cos\left[\frac{\omega_1-\omega_2}{2}\right]t, \tag{17}$$

where ω_1 and ω_2 are the frequencies of the individual oscillations. The frequency pairs are then related by

$$\omega_n = \frac{\omega_1-\omega_2}{2}, \tag{18}$$

$$\omega_f = \frac{\omega_1+\omega_2}{2}. \tag{19}$$

Two frequencies can be extracted from figure 1; a high frequency, ω_f, and a low frequency, ω_n. The frequency relations, (18) and (19), may then be used to determine ω_1 and ω_2.

Simulations are performed to determine the values of ω_f and ω_n for a variety of parameter values. The simulations were performed using the parameters in table 1 for an interval of Reynolds numbers. The value of ω_f and ω_n is determined directly from the average kinetic energy for each case, and the trigometric relation is used to determine ω_1 and ω_2 from these values.

Table 2 shows the results. Note that ω_f is consistently near 0.95, which is approximately the forcing frequency of unity. The value of ω_n, which will be called the envelope frequency, is seen to vary only slightly with Reynolds number, until the Reynolds number reaches a very low value, and the beating is no longer present. This trend with Reynolds number appears to be the result of excessive damping on the envelope oscillation.

Re number	w_n	w_f
40	nil	0.9520
100	0.2327	0.9520
1000	0.1348	0.9520
800000	0.1051	0.9520
10000000	0.1051	0.9520

Table 2. Beat frequencies at various Reynolds number

One explanation for the beating is that the envelope oscillation is the result of the transient behavior at the beginning of the simulation. The initial wave propagates across the chamber, reflects off of the end of the chamber, and then the incident wave and the reflected wave interact to form the standing wave. This transition from a motionless fluid to a standing wave must result in the low frequency behavior. Perhaps the forcing could be initiated such that there is no beating, both in the simulations studied here, and in a practical device. The link between the forcing and the beating is studied here by ramping up the forcing amplitude, a scheme which has been used at length in many types of numerical simulations. The amplitude is increased linearly, until a chosen time, beyond which it remains constant. The simulation continues for a total of ten cycles of the forcing, and then ω_f and ω_n are determined from the average kinetic energy. The resulting values of ω_f and ω_n are shown in table 3.

Period of linear increase(cycle)	w_n	w_f
1	0.095	0.95
2	0.087	0.95
3	0.080	0.95
4	0.074	0.95
5	0.069	0.95
6	0.065	0.96
7	0.061	0.96
8	0.057	0.96
9	0.051	0.96
10	0.051	0.96

Table 3. Beat frequencies

Note in table 3 that ω_f is only slightly affected by the ramping effect. However, ω_n is greatly affected. The value of ω_n is reduced by an order of magnitude between the case without any ramping and the case with ramping over one forcing period. The value continues to decrease as length of the ramping time increases. The results demonstrate that the beating phenomena is at least strongly influenced by the initialization procedures, and that perhaps there is a manner of starting the simulations to avoid the beating.

Results with plates

Now include heat exchanging plates in the chamber. The plates are modeled by imposing zero velocity on a row of discrete points in the interior of the chamber. The temperature is allowed to evolve in the same manner as before. Each row of points is considered to be a very thin plate, and five rows, or five plates,

are included in the present simulations. The plates are arranged parallel to the direction of wave motion.

Figure 2 shows the total kinetic energy versus time with the plates included. Note that the beating phenomena is still present. The existance of plates does have an effect on the beating, but the beating is not suppressed until many plates are included, causing severe viscous damping between plates, and corresponding blockage.

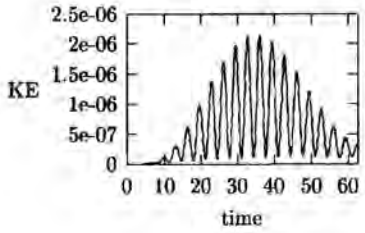

Figure 2. Total kinetic energy with plates

REFERENCES

Atchley, A.A., Hofler, T.J., Muzzerall, M.L., and Kite, M.D., "Acoustically Generated Temperature Gradients in Short Plates" *J. Acoust. Soc. Am.*, **Vol. 88(1)**, pp 251-263, 1990.

Atchley, A.A., Kuo, F. M., "Stability curves for a thermoacoustic prime mover" *J. Acoust. Soc. Am.*, **Vol. 95(3)**, pp 1401-1404, 1994.

Cao, N., Olson, J. R., Swift, G. W., and Chen, S., "Energy flux density in a thermoacoustic couple," *J. Acoust. Soc. Am.*, **99**, 1996.

Ghazali, N.M., "Numerical Simulation of Acoustic Waves in a Rectangular Chamber" *Ph.D. dissertation, in press* , Mechanical Engineering Department, University of New Hampshire, 2001.

Gopinath, A., Tait, N. L., and Garrett, S. L., "Thermoacoustic streaming in a resonant channel: The time-averaged temperature distribution," *J. Acoust. Soc. Am.*, **103**, 1998.

Hofler, T. J., "Thermoacoustic refrigerator design and performance," Ph.D. dissertation, University of California at San Diego, 1986.

Keolian, R., Turkevich, L. A., Putterman, S. J., Rudnick, I., and Rudnick, J. A., "Subharmonic sequences in the Faraday experiment: Departures from period doubling," Physical Review Letters, **47(16)**, pp. 1133-1136, 1981.

Montreal protocol on substances that deplete the ozone layer, www.ciesin.org/TG/PI/POLICY/montpro.html.

Strutt, J.W. (Lord Rayleigh), *The Theory of Sound*,ii, Academic Press, 1945.

Swift, G.W., "Thermoacoustic Engines" *J. Acoust. Soc. Am.*, **Vol. 84(4)**, pp 1145-1180, 1988.

Wheatley, J., Hofler, T., Swift, G.W., and Migliori, A., "An Intrinsically Irreversible thermoacoustic Heat Engine" *J. Acoust. Soc. Am.*, **Vol. 74(1)**, pp 153-170, 1983.

Worlikar, A. S. and Knio, O. M., "Numerical simulation of a thermoacoustic refridgerator," *Journal of Computational Physics*, **127**, 1996.

HEFAT 2002
1st International Conference on Heat Transfer, Fluid Mechanics and Thermodynamics
8-10 April 2002, Kruger Park, South Africa
OA1

HEAT AND MASS TRANSFER CORRELATIONS FOR THE DESIGN OF SMALL INDIRECT CONTACT COOLING TOWERS

Armando Oliveira and Jorge Facão
Faculty of Engineering, University of Porto
Dept. Mechanical Engineering and Industrial Management
Rua Dr. Roberto Frias, 4200-465 Porto, Portugal
E-mail: acoliv@fe.up.pt

ABSTRACT

Cooling towers are increasingly used in buildings as a component of environmental cooling systems. When compared with industrial towers, cooling towers with lower capacities and smaller dimensions can be used for this application, with inlet water temperatures ranging from 22 to 25ºC. Correlations for heat and mass transfer coefficients were obtained experimentally for a small-size indirect cooling tower, with a nominal cooling capacity of 10 kW. The new correlations are compared with existing ones and results of their application to a simplified cooling tower model are shown.

INTRODUCTION

Cooling towers are increasingly used in buildings as a component of environmental cooling systems. With chilled ceilings, because moderately high water temperatures can be used (18-20ºC supply temperature), it is possible to cool water in an indirect contact cooling tower during most of the cooling period. The cooling tower could be combined with a supplementary refrigeration plant, or used alone if a short period of overheating is allowed or energy storage or night-cooling techniques are used.

Indirect contact cooling towers have been traditionally used to remove excess heat from various industrial processes with hot water temperatures between 32 and 46ºC and typical cooling capacities above 40 kW. For chilled ceilings, cooling towers with lower capacities and smaller tower dimensions can be used with inlet water temperatures ranging from 22 to 25ºC.

Existing simplified models allow the prediction of cooling tower performance but using as input heat and mass transfer correlations which were experimentally obtained for large-size (industrial) cooling towers. Those correlations do not apply to small-size cooling towers, as requested for most building applications.

The most important coefficients used in models are the mass transfer coefficient between spray water interface and air and the heat transfer coefficient between tubes and spray water.

All correlation based models assume tube surface is completely wet, through a uniform distribution of spray water over the tube bundle. Therefore, mass and heat transfer occurs between an water film and air flow. For simultaneous heat and mass transfer, heat flux can be calculated through enthalpy potential, [1]:

$$q = \alpha_m \left(h_i - h_{air}\right) \tag{1}$$

where α_m is the mass transfer coefficient.

An enthalpy balance, for an elementary transfer surface dA, can be expressed as

$$m_{air}\, dh_{air} = \alpha_m \left(h_i - h_{air}\right) dA \tag{2}$$

which is known as the Merkel equation, [2], and which integration for the whole tower gives

$$\frac{\alpha_m A}{m_{air}} = \int_{in}^{out} \frac{dh_{air}}{\left(h_i - h_{air}\right)} \tag{3}$$

The local energy balance, for an elementary tube surface dA, can be written as

$$K\left(T_w - T_l\right) dA = \\ = \alpha_m \left(h_i - h_{air}\right) dA - m_{spray} c_{p,spray} dT_{spray} \tag{4}$$

neglecting spray rate variation and with K being the heat transfer coefficient between water inside tube and film/air interface. It can be calculated by adding all thermal resistances:

$$\frac{1}{K} = \frac{1}{\alpha_w}\frac{d_{ext}}{d_{int}} + \frac{d_{ext}}{2k_{tube}} \ln\frac{d_{ext}}{d_{int}} + \frac{1}{\alpha_{spray}} \tag{5}$$

using external tube surface as reference (d_{ext}).

When calculating tower performance, inlet conditions (water and air) are known and outlet conditions are the output. An iterative procedure is usually applied: water outlet temperature is guessed, which allows to calculate outlet air properties and the enthalpy integral in equation (3); since the integral value will not be equal to the first member of equation (3) - available number of transfer units, NTU – a new outlet temperature is used until equality is obtained.

Several models can be found in the literature, differing in simplifications assumed. The model to be considered, developed by Mizushina, [3], neglects spray temperature variation in equation (4) and considers interface conditions (h_i, T_i) constant throughout the cooling tower. Integration of equation (3) then gives

$$\frac{\alpha_m A}{m_{air}} = \ln \frac{h_i - h_{air,in}}{h_i - h_{air,out}} \qquad (6)$$

The integration of equation (4) and substitution into (6) leads to

$$\frac{T_{w,in} - T_i}{T_{w,out} - T_i} = \frac{h_i - h_{air,in}}{h_i - h_{air,out}} \exp\left(\frac{K}{\alpha_m c_{pw}} \frac{m_{air}}{m_w}\right) \qquad (7)$$

which together with the function $h_i = h_i(T_i)$ forms a non-linear set of equations for calculating (T_i, h_i).

NOMENCLATURE

A	area (m^2)
c_p	specific heat (J/kg/K)
d	tube diameter (m)
G	mass velocity, at minimum tower section ($kg/m^2/s$)
h	specific enthalpy (J/kg)
K	heat transfer coefficient between water inside tubes and spray/air interface ($W/m^2/K$)
k	thermal conductivity (W/m/K)
m	mass flow rate (kg/s)
q	heat flux (W/m^2)
Re	Reynolds number
Sh	Sherwood number
T	temperature (°C, K)
x	water vapour content in air or absolute humidity (kg water / kg dry air)

Greek letters

α_m	mass transfer coefficient for water vapour, between spray water film and air ($kg/m^2/s$)
α_{spray}	heat transfer coefficient between tube external surface and spray water film ($W/m^2/K$)
α_w	heat transfer coefficient for water inside the tubes ($W/m^2/K$)
ε	thermal efficiency
Γ	spray mass rate per length of tube (kg/s/m)

Subscripts

air	air flow
ext	external
i	interface (spray water film /air)
in	at tower inlet
int	internal
LM	logarithmic mean difference
out	at tower outlet
sat	at saturation
spray	spray water
tube	tubes
w	water inside tubes
wb	wet bulb

EXPERIMENTAL SETUP

A new indirect contact cooling tower was designed in order to be used with chilled ceilings. Design conditions were a cooling capacity of 10 kW, for an inlet water temperature of 21°C, a water flow rate of 0.8 kg/s and an air wet bulb temperature of 16°C. The tower has a section of 0.6 m x 1.2 m and a height of 1.55 m. The tube bundle has 228 staggered tubes of 10 mm outside diameter, with a pitch of 25 mm and with a total transfer area of 8.6 m^2. This corresponds to a much smaller size than usual towers. The ratio between heat transfer surface and heat exchanger volume is 25 m^2/m^3.

The tower was manufactured by Sulzer Escher Wyss (Lindau, Germany). It is much smaller than cooling tower models usually built by this manufacturer. A forced draft configuration was chosen with a crossflow fan located at air entrance. This arrangement has a lower noise level, and also leads to a lower pressure drop. It was also chosen to facilitate air flow measurements. Fig.1 shows schematically the cooling tower and main variables involved.

A test facility was assembled at Porto to test this cooling tower. The thermal load was modeled with an electrical heater located in a water tank. Tower inlet water temperature was controlled by varying heating power. Fan speed was also controlled by means of a frequency controller, which allowed changing air flow rate. Spray water flow rate could be changed manually (valve with 7 fixed positions). Cooling water flow rate could also be changed, by varying pump speed and using regulating valves.

Tower water inlet and outlet temperatures were measured with PT100 probes. Air flow rate was measured with one vane anemometer at tower outlet section. In order to measure cooling water temperature evolution, several thermocouples were connected to the tubes. The data acquisition system used a data logger - HP 34970A – and HP VEE as software.

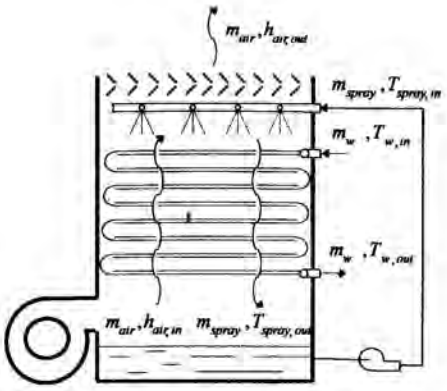

Figure 1: Indirect contact cooling tower and main variables.

MASS TRANSFER COEFFICIENT

The mass transfer coefficient can be obtained after experimental measurements and using a mass balance:

$$m_{air}\left(x_{air,out}-x_{air,in}\right)=\alpha_m\ A\ \Delta x_{LM} \tag{8}$$

where Δx_{LM} is the logarithmic mean humidity difference, defined as

$$\Delta x_{LM}=\frac{x_{air,out}-x_{air,in}}{\ln\dfrac{x_{sat,i}-x_{air,in}}{x_{sat,i}-x_{air,out}}} \tag{9}$$

Since it is difficult to know exactly the air humidity at tower outlet, due to changes along the section, an alternative method was used, using temperature (enthalpy) difference:

$$m_{air}\left(h_{air,out}-h_{air,in}\right)=\alpha_m\ A\ \Delta h_{LM} \tag{10}$$

with

$$\Delta h_{LM}=\frac{h_{air,out}-h_{air,in}}{\ln\dfrac{h_{sat,Ti}-h_{air,in}}{h_{sat,Ti}-h_{air,out}}} \tag{11}$$

Average spray temperature was used as interface temperature and outlet enthalpy was calculated after an enthalpy balance:

$$h_{air,out}=h_{air,in}+\frac{m_w c_{p_w}\left(T_{w,in}-T_{w,out}\right)}{m_{air}} \tag{12}$$

Among others, Mizushina, [3], Parker, [4], and Niitsu, [5], correlated α_m with air Reynolds number. Mizushina presented a more complete relationship involving also spray Reynolds number. Fig.2 shows experimental results obtained with the small tower as a function of air flow rate ratio (flow rate divided by maximum flow rate). A correlation for the mass transfer coefficient as a function of air mass flow ratio is:

$$\alpha_m=0.17\left(m/m_{max}\right)_{air}^{0.81} \tag{13}$$

or

$$\alpha_m=0.064\,G_{air}^{0.81} \tag{14}$$

obtained for $0.4<m_w<0.8$ kg/s, $10<T_{wb}<20$°C and $15<T_{w,in}<28$°C, with a correlation coefficient of 0.82.

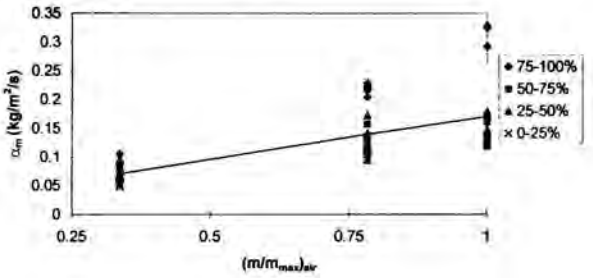

Figure 2: Mass transfer coefficient as a function of air flow rate (maximum = 1.7 kg/s). Different air humidities are identified.

In order to compare this with existing correlations, [3,4,5], obtained for different geometries, a dimensionless representation was made – see Fig.3. The correlation for the small tower lies below existing ones (with the exception of Parker's one), which were obtained for larger (industrial) towers.

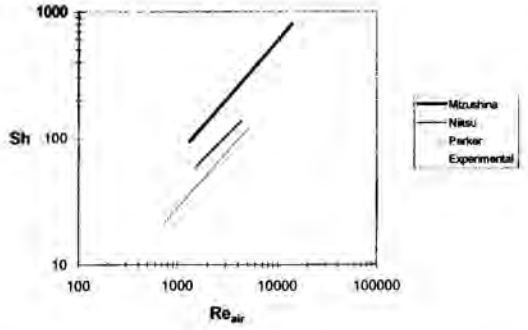

Figure 3: Comparison of mass transfer coefficient correlations.

The scatter of points in Fig.2 seems to be due mainly to air humidity: higher humidities lead to higher coefficients.

In order to express the effect of air humidity, a different correlation was attempted. The humidity was represented through the ratio dry/wet bulb air temperature (at tower inlet) – T_{air} / T_{wb} (in K). Fig.4 shows the relationship for 3 air flow rates. Note that correlation coefficients are much larger (>0.9) and that the effect of humidity is higher for higher flow rates. However, this type of correlation will increase the complexity of the numerical procedure for tower performance calculation. The effect of the error associated with the mass transfer coefficient on tower performance will be discussed in a later section.

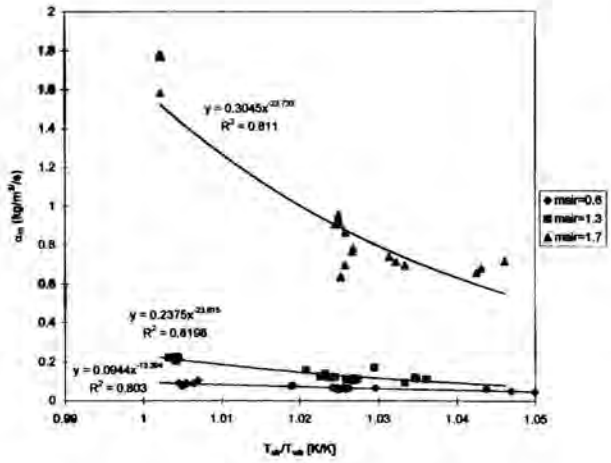

Figure 4: Mass transfer coefficient as a function of T_{air}/T_{wb} and air flow rate.

SPRAY HEAT TRANSFER COEFFICIENT

The heat transfer coefficient between tubes and spray water was calculated from experimental data and after calculating K. To calculate K the following global (balance) equation was used:

$$m_w c_{p_w}\left(T_{w,in} - T_{w,out}\right) = KA\Delta T_{LM} \qquad (15)$$

with

$$\Delta T_{LM} = \frac{T_{w,out} - T_{w,in}}{\ln\left(\dfrac{T_{w,out} - T_{spray}}{T_{w,in} - T_{spray}}\right)} \qquad (16)$$

α_{spray} was then obtained using a modified form of equation (5):

$$\alpha_{spray} = \left[\frac{1}{K} - \frac{d_{ext}}{\alpha_w d_{\text{int}}} - \frac{d_{ext}}{2k_{tube}}\ln\left(\frac{d_{ext}}{d_{\text{int}}}\right)\right]^{-1} \qquad (17)$$

Fig.5 shows experimental results for α_{spray} as a function of spray flow ratio (flow rate divided by maximum). A correlation for the heat transfer coefficient is:

$$\alpha_{spray} = 700\left(m / m_{max}\right)_{spray}^{0.358} \qquad (18)$$

or

$$\alpha_{spray} = 602\left(\Gamma / d_{ext}\right)^{0.358} \qquad (19)$$

obtained for $0.4<m_w<0.8$ kg/s, $10<T_{wb}<20$°C and $15<T_{w,in}<28$°C, with a correlation coefficient of 0.74.

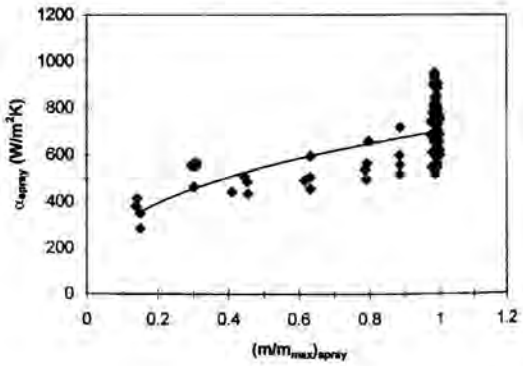

Figure 5: Heat transfer coefficient as a function of spray flow rate (maximum = 1.4 kg/s).

The scatter of points in Fig.5 is similar to the one obtained by other authors, [3,4,5]. Besides normal experimental deviations, it is also due to the range of air flow rates used. Air flow rate affects the flow of spray water around the tubes: an increase in air flow rate decreases the heat transfer coefficient. The effect of the error associated with the heat transfer coefficient on tower performance will be discussed in the following section.

Fig.6 compares equation (19) with other existing correlations. For the small cooling tower studied, spray heat transfer coefficient is also lower.

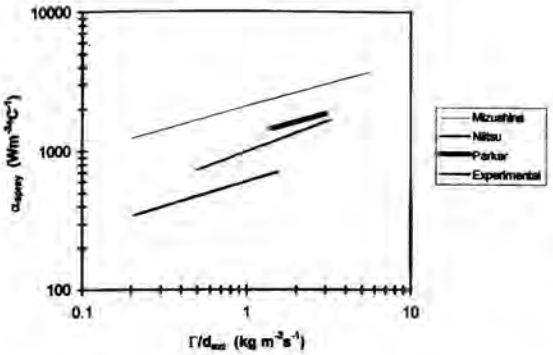

Figure 6: Comparison of heat transfer coefficient correlations.

SENSIBILITY ANALYSIS WITH SIMPLIFIED MODELS

The previous correlations can be applied to existing indirect contact cooling tower models. Mizushina's model, [3], will be considered here, expressed through equations (6) and (7). Cooling tower performance can be expressed by its thermal efficiency, defined as

$$\varepsilon = \frac{T_{w,in} - T_{w,out}}{T_{w,in} - T_{wb}} \qquad (20)$$

By applying the simplified model to the tested cooling tower, the results in Fig.7 were obtained. The influence of air and water flow rate on tower thermal efficiency can be analysed. Efficiency increases with the increase in air flow rate and decreases with the increase in water flow rate.

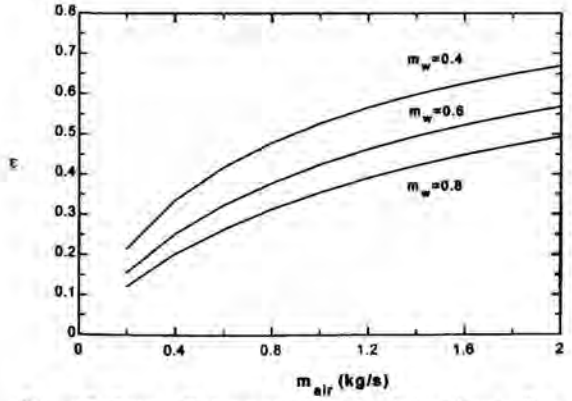

Figure 7: Tower efficiency as a function of air and water flow rate (m_{spray}=1.4 kg/s, T_{wb}=16°C).

For more details on the application of this and other models the interested reader is referred to [6].

The model can also be used to assess the influence of the error when determining mass and heat transfer coefficients on tower efficiency. Fig.8 shows the rate of change of efficiency with mass coefficient ($\partial\varepsilon/\partial\alpha_m$) for different values of air flow rate. Using $\partial\varepsilon/\partial\alpha_m$, the error on efficiency due to the error on mass coefficient can be assessed. For the maximum experimental air rate (1.7 kg/s) correlation (13) gives α_m=0.17 kg/m^2/s; if the maximum deviation in Fig.2 is assumed α_m will be equal to 0.32. The difference in thermal efficiency for the two values of α_m will be equal to 0.07 (ε=0.46 compared to 0.53). This is not too large for an extreme situation. Therefore, correlation (14) can be used with a sufficient degree of accuracy for all situations.

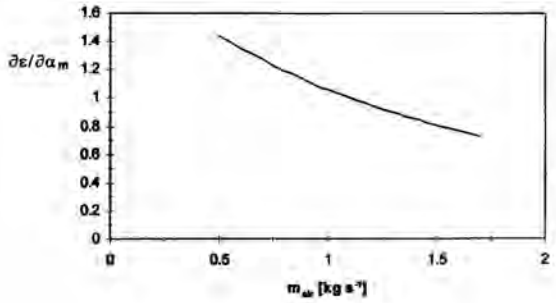

Figure 8: Rate of change of efficiency with mass transfer coefficient for different values of air flow rate (maximum spray and water rates).

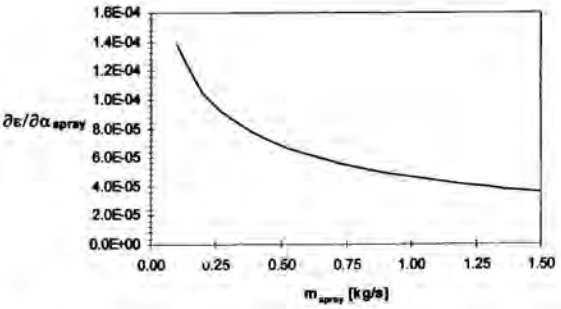

Figure 9: Rate of change of efficiency with heat transfer coefficient for different values of spray flow rate (maximum air and water rates).

Fig.9 shows the rate of change of efficiency with heat transfer coefficient ($\partial\varepsilon/\partial\alpha_{spray}$) for different values of spray flow

rate. The influence of the heat transfer coefficient on thermal efficiency is much lower than the influence of mass transfer coefficient. For the maximum experimental spray rate (1.4 kg/s) correlation (18) gives α_{spray}=697 W/m^2/K; if the maximum deviation in Fig.5 is assumed α_{spray} will be equal to 950. The difference in thermal efficiency for the two values of α_{spray} will be equal to 0.007 (ε=0.456 compared to 0.463). This is a negligible difference for this extreme situation. Therefore, correlation (19) can be used with a good degree of accuracy for all situations.

CONCLUSIONS

A small-size indirect contact cooling tower was tested and mass and heat transfer coefficients were experimentally determined. Mass transfer coefficient was correlated with air flow rate. The effect of air humidity was also discussed. Heat transfer coefficient was correlated with spray water flow rate. It was found that the present correlations lead to mass and heat transfer coefficients that are lower than the ones for large (industrial) indirect contact cooling towers.

The correlations were applied to an existing simplified model and tower performance results were obtained. The model also showed that the correlations found have a good degree of accuracy when applied to all possible operating conditions.

ACKNOWLEDGMENTS

The authors wish to thank the Commission of the European Union (DGXII) for partially funding the work done, under Joule IV research programme: ECOCOOL project.

REFERENCES

[1] Ashrae (1998). Handbook of Fundamentals. American Society Heating Refriger. Air Condit. Eng. (USA).

[2] Merkel, F. (1925). Verdunstungskuehlung. VDI Forschungsarbeiten n.275. Berlin.

[3] Mizushina, R.I.T, Miyashita, H. (1968). Characteristics And Methods Of Thermal Design Of Evaporative Coolers. Int. Chemical Engineering 8 (3).

[4] Parker, R.O., Treybal, R.E. (1961). The Heat And Mass Transfer Characteristics Of Evaporative Coolers. Chemical Engineering Progress Symposium 57 (32).

[5] Niitsu, Y., Naito, K., Anzai, T. (1969). Studies On Characteristics And Design Procedure Of Evaporative Coolers. Journal of SHASE 43 (7).

[6] Facão, J., Oliveira, A.C. (2000). Thermal Behaviour of Closed Wet Cooling Towers For Use With Chilled Ceilings, Applied Thermal Engineering 20 (13), Pergamon Press.

HEFAT2002
1st International Conference on Heat Transfer, Fluid Mechanics, and Thermodynamics
8-10 April 2002, Kruger Park, South Africa
SA3

NUMERICAL ANALYSIS OF GEYSERING

Akira Sou and Tsuyoshi Nakajima

Department of Mechanical Engineering,
Kobe University,
1-1 Rokkodai, Nada, Kobe 657-8501
Japan
E-mail: sou@mech.kobe-u.ac.jp

ABSTRACT

Numerical analysis of a geyser was performed to investigate the detailed flow mechanisms. The model was based on transient one-dimensional non-equilibrium two-fluid flow. A model of a fountain-type geyser was used, consisting of a single column with a large pool over the vent.

The calculated distributions and time histories of the void fraction and water temperature illustrated the detailed mechanisms of cyclic geyser behavior. This consisted of a pre-heating phase, an eruption phase, and a refill phase. Since the size of geyser was larger than the one of previous experiments, the refill period was relatively short. Small-scale preplays, such as bubbling, splashing, and surging before a violent eruption, were observed when a low heat flux was supplied. A simple model to predict when the next eruption will occur was proposed.

INTRODUCTION

Geysering is a typical unstable gas-liquid two-phase flow phenomenon in a vertical channel. The term "geyser" comes from the Geysir in Iceland, which used to erupt 70 m into the air [1]. A geyser consists of a long vertical water column. Heated rocks or magma are close enough to the surface of the earth to provide a heat source for the water. The flow consists of a water source that refills the column, followed by a temporary ejection caused by self-evaporation due to a decrease in the hydrostatic head. The interval between eruptions is variable, and it is difficult to predict when the next eruption will occur in most geysers, due to the complicated geometry, the high temperatures and pressures, and the behavior of underground water. The most famous geyser in the world is Old Faithful in Yellowstone National Park [2], which erupts 44 tons of water and steam up to 57 m in height over 1.5 to 5 minutes about every 65 minutes. Geysering may also occur in industry, such as in a geothermal power plant or during an incident in a nuclear reactor. It is, therefore, important to understand the detailed mechanisms of geysering.

Griffith[3] conducted experimental research without a mass input at the bottom of the vertical column. Geysering with low mass input was investigated experimentally and theoretically [4]. Some more detailed investigations were conducted recently [5,6]. Since the depth and diameter of real geysers or geothermal power plants are much larger than those of experimental facilities [3-6], and hydrostatic head is the dominant force in geysering, in this study, a large-scale geyser was investigated numerically. A transient one-dimensional non-equilibrium two-fluid model was used for the numerical model.

NOMENCLATURE

A	area	(m^2)
c	specific heat	(J/kg K)
D	diameter	(m)
e	internal energy	(J/kg)
F	force per unit volume	(N/m^3)
g	gravity acceleration	(m/s^2)
K	ratio on heated period	(-)
L	length	(m)
p	pressure	(Pa)
Q	heat input	(W)
t	time, period, duration	(sec)
T	temperature	(°C, K)
u	velocity	(m/sec)
V	volume	(m^3)
Z	height from the bottom of column	(m)

Greek Letters

α	volume fraction of each phase	(-)
ρ	density	(kg/m^3)
Γ	mass transfer rate per unit volume	(kg/m^3s)

Subscripts

0	atmosphere	B	onset of boiling
c	condensation	C	column of geyser
e	evaporation	E	eruption
F	refill	G	gas
H	heated length	i	interface
L	liquid	P	pool over the vent
S	saturation	w	wall

COMPUTATIONAL MODEL OF A GEYSER

There are two types of geyser, as shown in Fig. 1: (a) a fountain-type geyser and (b) a cone-type geyser. In the former, the eruptions occur through a pool of water over the vent in a series of separate bursts. The Grand Geyser in Yellowstone Park is a famous example of this. The latter usually consists of a cone formed at the exit, with a small or no surface pool over the vent. Old Faithful is a cone-type geyser. In most cone-type geysers, the water level drops about 10m after an eruption. Since the water supply comes from underground water that flows into the column, the interval between eruptions is strongly dependent on the characteristics of the underground water system. In fountain-type geysers, the downward flow of the water in the pool after the eruption is the major refilling source. This is the type of geyser investigated here.

The computational model used for the fountain-type geyser is shown in Fig. 2. Since most of the world's geysers are at high altitudes, the atmospheric pressure P_0 was set at 77600Pa. The initial temperature of the water in the very large pool T_P was 90°C. The total depth of the geyser ΔZ_P was 50m; this was modeled using 25 cells in the vertical direction. The diameter of the column D_C and the volume of pool V_P are shown in Fig. 2 and Table 1. The volume of water in the pool was 417 times greater than that in the column. Four heat input values were used: Q = 0.1MW, 1MW, 8MW, and 20MW. Along the heated length of the column L_H, the heat flux was assumed uniform if water existed in the cell.

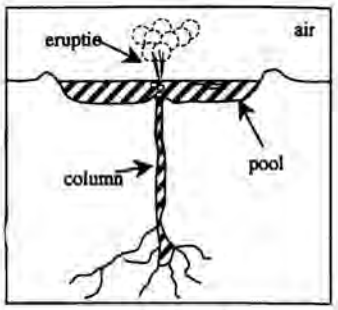

(a) Fountain-Type Geyser

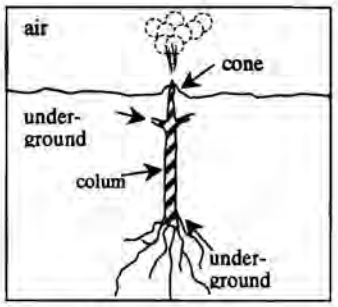

(b) Cone-Type Geyser

Figure 1: Fountain-Type Geyser and Cone-Type Geyser

Table 1: Analysis Conditions

total geyser depth; ΔZ_P (m)	50	inner diameter of column; D_C (m)	0.5
volume of column; V_C (m^3)	9.4	volume of pool; V_P (m^3)	3920
heat input; Q (MW)	0.1, 1, 8, 20	heated length; L_H (m)	44
atmospheric pressure; P_0 (Pa)	77600	initial temperature of pool; T_P (°C)	90

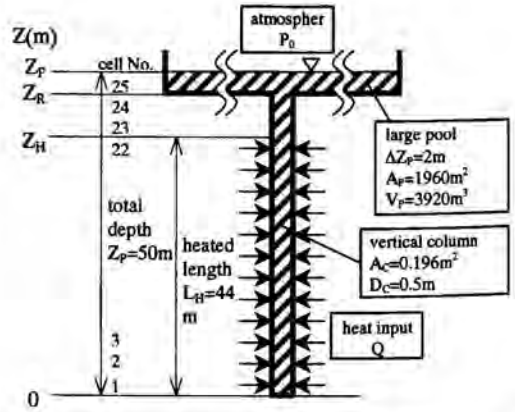

Figure 2: Computational Model of Fountain-Type Geyser

NUMERICAL METHOD

A transient one-dimensional non-equilibrium two-fluid model was used. The following mass, momentum, and energy conservation equations for gas-liquid two-phase flow were solved as the governing equations.

The mass conservation equations are given by

$$\frac{\partial\left(\alpha_L\rho_L\right)}{\partial t}+\nabla\cdot\left(\alpha_L\rho_L\mathbf{u}_L\right)=-\Gamma_e+\Gamma_c \qquad (1)$$

$$\alpha_L+\alpha_G=1 \qquad (2)$$

where α denotes the volumetric fraction (-), ρ the density (kg/m^3), t the time (sec), $\mathbf{u}$ the velocity vector (m/sec), Γ the interfacial mass transfer rate (kg/m^3sec), subscript L the liquid phase, G the vapor phase, e the evaporation, c the condensation, respectively.

The momentum conservation equations are given by

$$\frac{\partial\left(\alpha_L\rho_L\mathbf{u}_L\right)}{\partial t}+\nabla\cdot\left(\alpha_L\rho_L\mathbf{u}_L\mathbf{u}_L\right)= -\alpha_L\nabla p-\alpha_L\rho_L\mathbf{g}-\mathbf{F}_{wL}-\mathbf{F}_{iL}-\mathbf{u}_L\Gamma_e+\mathbf{u}_G\Gamma_c \quad (3)$$

$$\frac{\partial\left(\alpha_G\rho_G\mathbf{u}_G\right)}{\partial t}+\nabla\cdot\left(\alpha_G\rho_G\mathbf{u}_G\mathbf{u}_G\right)= -\alpha_G\nabla p-\alpha_G\rho_G\mathbf{g}-\mathbf{F}_{wG}-\mathbf{F}_{iG}+\mathbf{u}_L\Gamma_e-\mathbf{u}_G\Gamma_c \quad (4)$$

where p denotes the pressure (Pa), **g** the gravity acceleration (m/sec^2), **F** the momentum transfer per unit mass (N/m^3), subscript w the wall, i the gas-liquid interface, respectively.

The energy conservation equations are given by

$$\frac{\partial\left(\alpha_L\rho_L e_L\right)}{\partial t}+\nabla\cdot\left(\alpha_L\rho_L e_L\mathbf{u}_L\right)= -p\left[\frac{\partial\alpha_L}{\partial t}+\nabla\cdot\left(\alpha_L\mathbf{u}_L\right)\right]+Q_{wL}+Q_{iL} \quad (5)$$

$$\frac{\partial\left(\alpha_G\rho_G e_G\right)}{\partial t}+\nabla\cdot\left(\alpha_G\rho_G e_G\mathbf{u}_G\right)= -p\left[\frac{\partial\alpha_G}{\partial t}+\nabla\cdot\left(\alpha_G\mathbf{u}_G\right)\right]+Q_{wG}+Q_{iG} \quad (6)$$

where e denotes the internal energy (W/m^3), Q the energy transfer per unit mass (W/m^3), subscript wL the wall to liquid, iL the interface transfer from liquid to interface, wG the wall to vapor, iG the interface transfer from vapor to interface, respectively.

Closure of the equation set requires constitutive relations for the mass, momentum and energy transfers between the two phases. Constitutive equations, such as the interface mass, momentum, and energy transfer models used in the present analysis were briefly shown in Table 2. No subcooled boiling model was introduced in the present model.

Table 2: Constitutive Equations Used in the Analysis

Constitutive equation	Reference
Interface mass & energy transfer	COBRA/TRAC[7]
Interface drag	NASCA[8], Wallis[9]
Wall heat transfer	NASCA[8]

CALCULATED RESULTS FOR AN ORDINARY GEYSER

Calculated results when Q = 8MW are shown in Figs. 3-8. Figures 3-5 show the time histories of the water temperature (TL), void fraction (AG), pressure (P), water velocity (VL), and steam velocity (VG). The numbers indicated in the legends correspond to the vertical cells. In fountain-type geysers, the top end of the heated zone starts to boil, which decreases the pressure head. An eruption of the water-steam two-phase jet then occurs, until a large amount of the water in the column has been ejected. Finally subcooled water in the pool refill the column. This cyclic geysering behavior was clearly predicted in the analysis. The periods of the pre-heating phase t_H, eruption phase t_E, and refill phase t_F are indicated in Fig. 3. Since the geyser is larger than those considered in previous experiments [3-6], the refill period t_F is relatively short. The average period was 115 s.

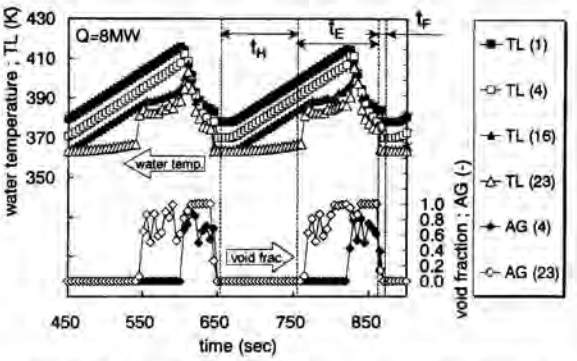

Figure 3: Calculated Water Temperature and Void Fraction when Q=8MW

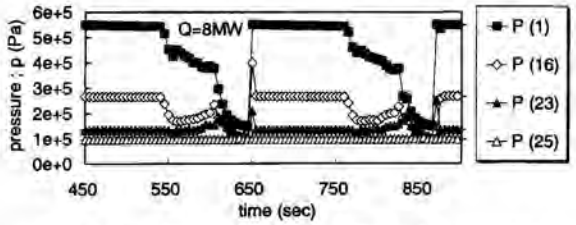

Figure 4: Calculated Pressure vs. Time when Q=8MW

A time series of the void distribution is shown in Fig. 6, and the flow pattern is illustrated in Fig. 7. Boiling starts at the top end of the heated zone at t=1180s; this is related to the "preplay" observed in real geysers, which consists of small bubbles that are visible at the surface. The preplays are often

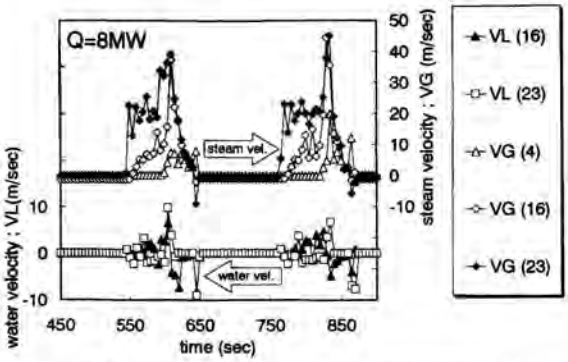

Figure 5: Calculated Water and Steam Velocities when Q=8MW

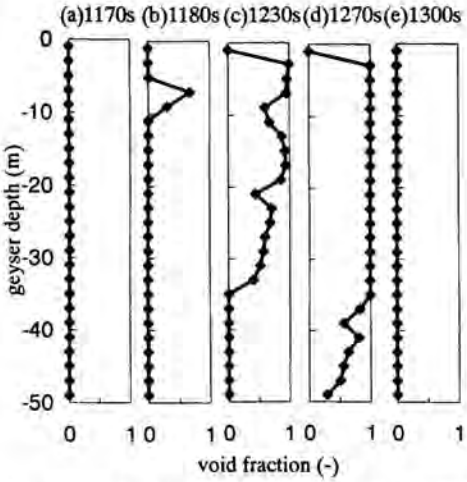

Figure 6: Calculated Void Distribution when Q=8MW

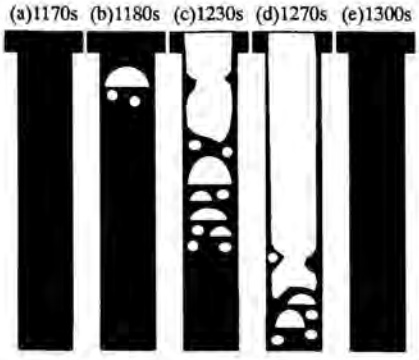

Figure 7: Flow Pattern of Geyser Cycle when Q=8MW
(Analysis was conducted in 1D model)

used to predict when the next eruption will occur. The boiling region extends downward with time, extending throughout most of the column. After the eruption, the column is refilled with water. The varied and unsteady void distribution shown in Fig.6(c) is one of the major causes of the large fluctuations in steam and water eruptions. Figure 8 shows the distribution of water and saturation temperatures. After the onset of boiling, saturation temperature T_S decreases with the pressure head (t=1230s). This causes the liquid temperature T_L to be higher than the boiling point in the lower part of the column, enhancing evaporation. The water temperature near the bottom of the column T_L is higher than the pool temperature T_P after the eruption, which may initiate boiling near the bottom of the column in certain conditions. The erupted mass in the case was 5.3tons, or 56% of the volume of water in the column. The period of fountain-type geysers is usually irregular, due to uncertainty in the erupted rate.

Cyclic geysering behavior did not form when Q=20MW because the high heat flux evaporated the unsteady downward flow of the pool water, preventing it from completely refilling the water column.

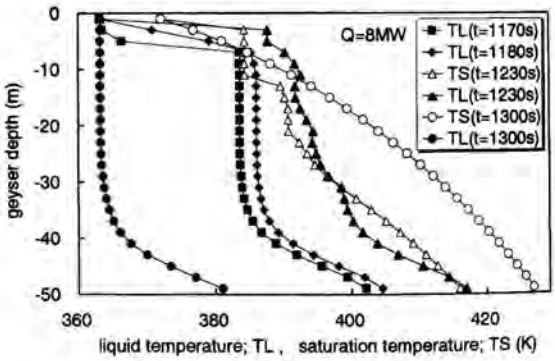

Figure 8: Temperature cycle when Q=8MW

LOW HEAT INPUT GEYSERS

The numerical results for Q=1MW are shown in Figs. 9-11. Figure 9 shows the time histories of the temperature and void fraction; the pressure time histories are shown in Fig. 10. A small-scale eruption between cyclic violent eruptions occurred at t=2700s. The vertical distributions of the temperature and void fraction are shown in Fig. 11. The water temperature in the non-heated zone increases before the onset of eruption, as shown in Fig.11(a), due to the rise of small bubbles at the top end of the heated zone. The eruption at t=2700s occurs only in the upper half of the column in the case. The water in the lower half does not self-evaporate because of a downward flow of colder water instead of steam upflow and a temporary increase in the outflow of steam over the pool. A violent eruption that ejects most of the water starts at t=3300s, after the water at the

bottom of the column begins to boil. It is possible that the small-scale eruptions would occur several times between violent eruptions if more cells were used in the column. In real geysers, several eruptions at relatively short intervals are separated from the next series of eruptions by a relatively long quiet period. This is consistent with the present analysis. The period, t_B, between the end of refill phase and the onset of the first small-scale eruption is illustrated in Fig. 9.

The time history of the liquid temperature when Q=0.1MW is shown in Fig. 12. The Q=0.1MW results are similar to those observed when Q=1MW.

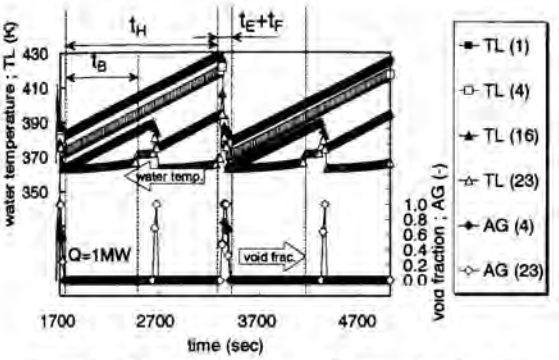

Figure 9: Calculated Temperature Change when Q=1MW

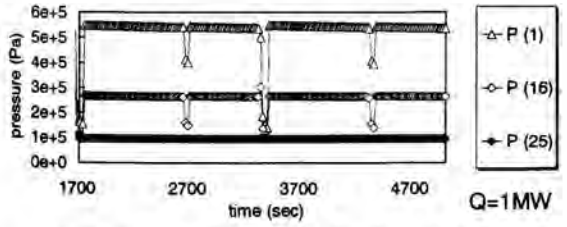

Figure 10: Calculated Pressure Change when Q=1MW

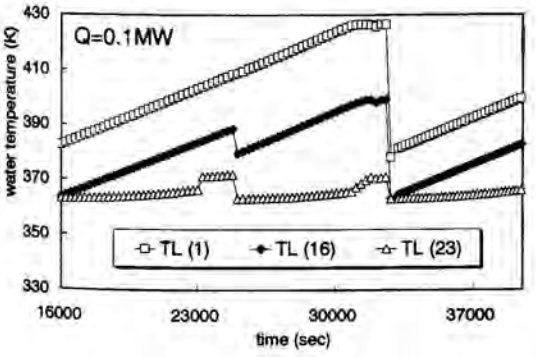

Figure 12: Calculated temperature when Q=0.1MW

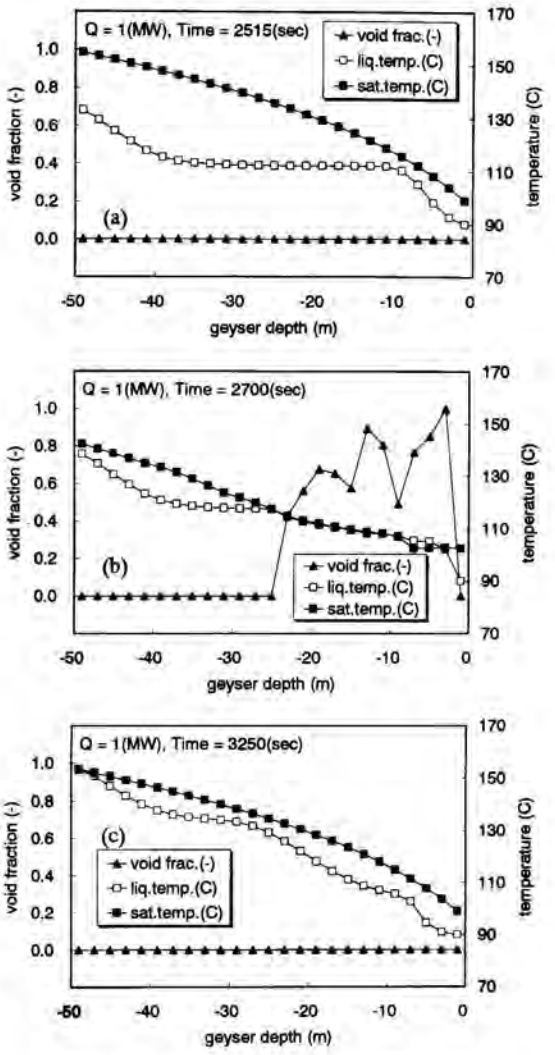

Figure 11: Calculated Temperature Distribution when Q=1MW

GEYSER PERIOD

A simple model to predict when the next eruption will occur is proposed here. For the low heat input condition (Q=0.1 or 1 MW), the period between the end of refill phase and the onset of the first small-scale eruption t_B is given by

$$t_B = \frac{\rho_L \frac{\pi D_C^2}{4} \bar{L}_H c_p \{T_S(Z_H) - T_P\}}{Q} \qquad (7)$$

where c_p denotes the specific heat, $T_S(Z)$ the saturation temperature at vertical level Z, respectively. For ordinary heat input (Q=8MW), t_B calculated from Eq.(7) corresponds to the period between end of refill phase and the onset of violent eruptions t_H. When the heat flux is low, a violent eruption occurs after the water at the bottom of the column starts boiling. The water temperature at the bottom of the column at the end of the violent eruption is higher than the pool temperature T_P. This is because (1) not all of the water is erupted, (2) certain heat is added during the refill phase, and (3) the water temperature is higher than the saturation temperature in the non-equilibrium condition. Therefore, a heat input ratio K_H was introduced as follows:

$$\frac{1}{K_H} = \frac{\rho_L \frac{\pi D_C^2}{4} L_H c_p \{T_S(0) - T_P\}}{Q \cdot t_{H,CAL}} \qquad (8)$$

where $t_{H,CAL}$ is the calculated period of t_H for the low heat flux condition. If K_H=1.0, violent eruptions occur when the water at the bottom of column heated to saturation temperature.

Calculated periods of pre-heating, eruption, and refill phases, and the values predicted by Eqs. (7) and (8), are summarized in Table 3. The pre-heating phase period predicted using Eq. (7) for Q=8MW is in good agreement with the present analysis. The sum of the eruption and refill periods does not change much in the cases considered here. The onset of the first small-scale eruption or bubbling t_B is predicted well by Eq.(7) when Q=1 and 0.1 MW. The heat input ratio K_H is about 0.7 in the present analysis.

Table 3: Calculated and Predicted Periods and Durations

Q	present analysis	Eqs. (7,8)
8 MW	t_H=t_B=95(s) t_E=110(s) t_F=10(s)	t_H=t_B=89(s)
1 MW	t_B=740(s) $t_{H,CAL}$=1585(s) t_E+t_F=60(s)	t_B=714(s) K_H=0.7
0.1 MW	t_B=7520(s) $t_{H,CAL}$=17020(s) t_E+t_F=60(s)	t_B=7140(s) K_H=0.75

CONCLUSIONS

Numerical analysis of a geyser was performed to investigate the detailed flow mechanisms. The model was based on transient one-dimensional non-equilibrium two-fluid flow. A model of a fountain-type geyser was used, consisting of a single column with a large pool over the vent.

The calculated distributions and time histories of the void fraction and water temperature illustrated the detailed mechanisms of cyclic geyser behavior. This consisted of a pre-heating phase, an eruption phase, and a refill phase. Since the size of geyser was larger than the one of previous experiments, the refill period was relatively short. Small-scale preplays, such as bubbling, splashing, and surging before a violent eruption, were observed when a low heat flux was supplied. A simple model to predict when the next eruption will occur was proposed. Further studies must be performed to investigate the effects of node division, the geothermal conditions, the temperature of the pool, and the underground water inflow into the bottom of the column.

REFERENCES

[1] Tom, L. McKnight, Physical Geography, Prentice-Hall, Inc., 1984, pp.549-554.

[2] Ed. David, E. Clark, National Parks of the West, Lane Publishing Co., 1984, pp.195-205.

[3] Griffith, P., ASME Paper, No.62-HT-39, 1962, p.1.

[4] Nakanishi, S., et al., H., Trans. Jpn. Soc. Mech. Eng. (2), vol.44, no.388, 1978, pp. 4252-4262. (in Japanese).

[5] Lin, T.F., et. al., Experimental Investigation of Geyser Boiling in an Annular Two-Phase Closed Thermosyphon, Int. J. of Multiphase Flow, 22-1, 1996, Page 115.

[6] Janssens-Maenhout, G., et. al., Geysering with Two-dimensional Effects, Proc. 4th Int. Conf. on Multiphase Flows (ICMF-2001), 2001, pp.Paper No. DP3.

[7] Thurgood, M.J., et al., COBRA/TRAC, NUREG/CR-3046, PNL-4385, Vol.1, R4, 1983.

[8] Ninokata, H. et al., Proc. 4th Int. Seminar on Subchannel Analysis (ISSCA-4), NASCA, 1997, pp.231-265.

[9] Wallis, G.B., Trans. ASME J. Basic Engng., 1970, p. 59.

thickness downstream from the spacer did not recover to the thickness upstream to the spacer. A numerical study of high pressure annular flow around an obstacle was presented in [4] for various flow conditions. Vapour and droplets flows were modelled as two-dimensional, while one-dimensional liquid film flow on the wall was considered. The influence of the obstacle on the liquid film flow was demonstrated. In paper [3] both experimental and numerical results shows that the liquid film thickness decrease occurs along the whole gap between the obstacle and the wall, with the film recovery downstream of the obstacle. A different liquid film dynamics around obstacle is shown in [4]. These results show rapid liquid film decrease immediately at the wall-obstacle gap entrance and film thickness recovery already within the gap. These differences in results on liquid film dynamics around the spacers and the limitations of the previous numerical approaches, such as the application of the one-dimensional film model in [4], posed a need for further investigations of the numerical possibilities for liquid film flow predictions around an obstacle.

In this paper the numerical possibilities of liquid film hydro-dynamics prediction for flow around an obstacle is investigated. A two-dimensional simulation of air and water film flow around a rectangular obstacle is simulated. Predicted are air and liquid film velocity fields and mean liquid film thickness for different gas and liquid phase flow rates. These parametric analyses show the influence of phases velocities on the mean liquid film thickness dynamic change. Obtained results are in accordance with the measured liquid film flow characteristics.

NOMENCLATURE

C_D drag coefficient
$C_{\varepsilon 1}, C_{\varepsilon 2}, c_\mu$ experimental coefficients in k-e model (Table 1)
D diameter (m)
F force per unit volume (N/m^3)
g gravity (m/s^2)
k turbulent kinetic energy (m^2/s^2)
$\vec{n}$ unit vector (m)
p pressure (Pa)
t time (s)
u,v velocity (m/s)
x coordinate (m)

Greek letters:

α volume fraction
Γ effective dynamic viscosity (kg/ms)
ε turbulent dissipation rate (m^2/s^3)
η kinematic viscosity (m^2/s)
ρ density (kg/m^3)
σ surface tension (N/m^2)
$\sigma_k, \sigma_\varepsilon$ experimental coefficients in k-e model (Table 1)

Subscripts:

p particle
w wall
1 liquid film
2 gas phase

MODELLING APPROACH

Separated water and air two-phase flow is modelled by the "two fluid" model. Mass and momentum fluid flow conservation equations are written for each phase. Interface transfer processes are modelled by "closure laws" [5].

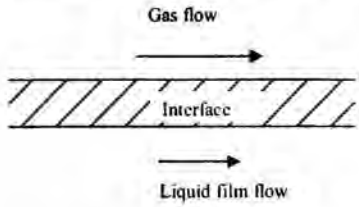

Fig. 1 A finite thickness of the modelled liquid film surface

Modelling Assumptions and Features

a) Two-dimensional separated air and water film two-phase flow is modelled. Liquid film flows on the wall. Both air and liquid film streams are observed to be continuous with phase volume fractions equal to 1.0. The air-water interface area (liquid film surface) has a finite thickness observed as a dispersed two-phase flow. Starting from the continuous liquid film area, the water volume fraction changes from 1 to 0 within the interface area, perpendicularly to the main flow direction, Fig. 1. The thickness of the interface is determined with the ability of the applied numerical method to track front propagation. Here applied third order numerical method is able to track interface within two to four control volumes.

b) At present, the water flow in form of droplets entrained within the air stream is omitted. The intention is to investigate the pure liquid film hydro-dynamics. The applied two-fluid model approach enables easy inclusion of the droplets flow in future work.

c) The flow is adiabatic under atmospheric conditions. Hence, the energy conservation equations are omitted.

d) The two-phase flow is observed as semi-compressible, that is the acoustic flow effects are neglected, while the influence of the pressure change on the vapour and liquid thermo-physical properties is taken into account. This assumption is valid since the two-phase velocity is not higher than 20 m/s – 30 m/s.

e) Turbulence is modelled with the k-ε model in both phases.
f) The surface tension is taken into account at the liquid film surface as the continuous body force determined by the liquid volume spatial distribution.

Governing Equations

Conservation equations take the following form in the indicial notation.

Continuity equation

$$\frac{\partial \alpha_k \rho_k}{\partial t} + \frac{\partial \left(\alpha_k \rho_k u_{k,i} \right)}{\partial x_i} = 0 \tag{1}$$

Momentum conservation

$$\frac{\partial \left(\alpha_k \rho_k u_{k,i} \right)}{\partial t} + \frac{\partial \left(\alpha_k \rho_k u_{k,i} u_{k,j} \right)}{\partial x_j} = -\alpha_k \frac{\partial p}{\partial x_i} + \frac{\partial}{\partial x_j} \left[\alpha_k (\rho_k \eta_k \frac{\partial u_{k,i}}{\partial x_j} - \rho_k \overline{u'_{k,i} u'_{k,j}}) \right] + \alpha_k \rho_k g_i + (-1)^{k+1} F_{21,i} + F_{\sigma,i} \tag{2}$$

Parameters α_k, $u_{k,i}$ and p are phase volume fraction, time averaged instantaneous velocity and pressure, respectively. As the consequence of the instantaneous equations time averaging the following turbulent (Reynolds) stress tensor term appears

$$\overline{u'_{k,i} u'_{k,j}} \tag{3}$$

In Eqs. (1,2) index k is 1 for water and 2 for steam. The source terms for mass and momentum conservations are written on the r.h.s. of Eqs. (1)-(2). The force of vapour and liquid interfacial drag per unit volume in i Cartesian direction is denoted with $F_{21,i}$. Term $F_{\sigma,i}$ represents surface tension force.

Volume fraction balance equation is added

$$\alpha_1 + \alpha_2 = 1 \tag{4}$$

Turbulence modelling

The Boussinesq's eddy viscosity concept is applied, which is generalized in the following form for momentum turbulent transport

$$-\overline{u'_{k,i} u'_{k,j}} = \eta_{k,t} \left(\frac{\partial u_{k,i}}{\partial x_j} + \frac{\partial u_{k,j}}{\partial x_i} \right) - \frac{2}{3} k_k \delta_{ij} \tag{5}$$

The Kolmogorov-Prandtl relation is applied for the eddy viscosity prediction

$$\eta_{k,t} = c_\mu \frac{k_k^2}{\varepsilon_k} \tag{6}$$

Turbulent kinetic energy and dissipation are predicted by the two-equation k-ε model, which has the following form in Cartesian coordinate system

Turbulence Kinetic Energy Equation

$$\frac{\partial \left(\alpha_k \rho_k k_k \right)}{\partial t} + \frac{\partial \left(\alpha_k \rho_k u_{k,i} k_k \right)}{\partial x_i} = \frac{\partial}{\partial x_i} \left(\alpha_k \Gamma_{k,k} \frac{\partial k_k}{\partial x_i} \right) + \alpha_k (P_k - \rho_k \varepsilon_k) \tag{7}$$

Turbulence Dissipation Rate Equation

$$\frac{\partial \left(\alpha_k \rho_k \varepsilon_k \right)}{\partial t} + \frac{\partial \left(\alpha_k \rho_k u_{k,i} \varepsilon_k \right)}{\partial x_i} = \frac{\partial}{\partial x_i} \left(\alpha_k \Gamma_{k,\varepsilon} \frac{\partial \varepsilon_k}{\partial x_i} \right) + \alpha_k C_{\varepsilon 1} P \frac{\varepsilon}{k} - \alpha_k C_{\varepsilon 2} \rho \frac{\varepsilon^2}{k} \tag{8}$$

where P_k is the turbulent kinetic energy production for the phase k

$$P_k = \rho_k \eta_{k,t} \left[\left(\frac{\partial u_{k,i}}{\partial x_j} \right) + \left(\frac{\partial u_{k,j}}{\partial x_i} \right) \right] \left(\frac{\partial u_{k,i}}{\partial x_j} \right) \tag{9}$$

and diffusion coefficients are given by

$$\Gamma_{k,k} = \rho_k \left(\eta_k + \frac{\eta_{k,t}}{\sigma_k} \right) \tag{10}$$

and

$$\Gamma_{k,\varepsilon} = \rho_k \left(\eta_k + \frac{\eta_{k,t}}{\sigma_\varepsilon} \right) \tag{11}$$

Empirical constants are presented in the following Table.

Table 1 Empirical constants for the standard k-ε model

C_μ	$C_{\varepsilon 1}$	$C_{\varepsilon 2}$	σ_k	σ_ε
0.09	1.44	1.92	1.0	1.3

Boundary turbulent flow parameters are predicted with the "wall functions" at the flow channel wall and spacer's surface, as presented in Section 3.

Closure laws

The interfacial drag force is calculated as (Ishii, 1987)

$$F_{21,i} = \frac{3}{4}\alpha_2 \rho_1 \frac{C_D}{D_p}\sqrt{\sum_{i=1}^{3}(u_{2,i}-u_{1,i})^2}\,(u_{2,i}-u_{1,i}), \qquad (12)$$

where C_D is the interfacial drag coefficient, and D_p is the diameter of the dispersed particle. For dispersed flow patterns, C_D is proportional to the square of the vapour velocity [5]

$$C_D = 0.15 D_p \left(\frac{g\Delta\rho}{\sigma}\right)^{1/2}(1-\alpha_2)^2_2 \qquad (13)$$

The surface tension force is calculated as

$$F_{\sigma,i} = \sigma(\delta_{ji} - n_j \cdot n_i)|\nabla\alpha| \qquad (14)$$

where

$$\vec{n} = \frac{\nabla\alpha}{|\nabla\alpha|} \qquad (15)$$

NUMERICAL EXPERIMENTS BOUNDARY CONDITIONS

The flow channel geometry and applied numerical mesh are shown in Fig. 2. The obstacle is positioned in the narrow channel, 1 mm from the wall. The obstacle length is 30 mm and width is 0.5 mm. These dimensions correspond to the geometry of one flow channel in the 3x3 rod bundle experimental test section [3]. A chosen channel length is sufficient to comprise the relaxation length downstream the spacer. Dimensions of the control volume are 2x0.05 mm and the flow domain is discretized with 50x40 control volumes in x and y direction respectively. Further refinement of the computational mesh has shown no practical change in predicted velocity fields and film thickness. Axis of symmetry is assumed at the channel upper boundary with the so called "adiabatic" conditions for all flow parameters. Zero change of the flow parameters is taken at the channel exit. Uniform inlet air and liquid film velocity profiles are assumed. No velocity slip conditions are applied at the channel walls and at the obstacle surface. "Wall functions"

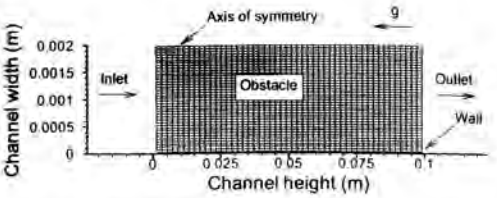

Fig. 2 Geometry of the flow channel and numerical mesh

are used for the prediction of turbulent kinetic energy and dissipation rate at the channel wall and obstacle surface.

NUMERICAL METHOD OF SOLUTION

The control volume based finite difference method is applied for the numerical solution of momentum conservation equations and a newly developed third order accurate numerical scheme for the solution of the liquid phase volume fraction conservation (propagation) equation [6]. A pressure-correction equation is derived according to the SIMPLE numerical method [7] from the momentum and mass balance equations. Two-dimensional flow field is discretized with rectangular control volumes. Two grids are formed, the basic one for the solution of scalar parameter equations (void fraction conservation equation and pressure correction equation) and a staggered grid for the solution of the momentum equations (prediction of velocity fields). A discretization of the momentum partial differential equations is carried out by their integration over control volumes of basic and staggered grids. The convection terms in momentum equations are approximated with upwind finite differences, while diffusion and source terms are approximated with central differences. Fully implicit time integration is applied. The resulting set of discretized momentum equations is solved iteratively by the Alternating Direction Implicit (ADI) method. For the calculation of a steady-state condition, the transient calculation procedure is performed with constant boundary conditions.

A third order accurate numerical method is applied to the solution of gas-liquid interface tracking in two-phase flow. The method is based on the transformation of the liquid volume fraction conservation equation into the form with the substantial derivative and the approximation of the substantial derivative with the finite difference along the fluid particle characteristic path. The fluid particle characteristic path in the temporal-spatial system is tracked from the solution of the momentum conservation equation. The initial value of the scalar parameter on the characteristic path is predicted by the application of the Lagrange's interpolation polynomial of the third degree in one or two-dimensional space. This method effectively suppresses numerical diffusion and enables the interface tracking in two-phase flow by the application of the standard two-fluid model of two-phase flow.

RESULTS AND DISCUSSIONS

Figures 3 and 4 show liquid film thickness change for three different inlet air velocities 12, 18 and 25 m/s, where the middle velocity value corresponds to the experimental conditions of the air-water flow within 3x3 rod bundle [3]. Inlet uniform water velocity is 0.5 m/s and inlet thickness is 0.2 mm, the same values as in the rod bundle experiment [3]. Liquid film surface is represented with the void value of 0.5. A wavy liquid film surface is predicted for air inlet velocity of 12 m/s. For this flow condition, the liquid film surface constantly changes and a typical shape is shown. For inlet air velocity of 18 m/s a decrease of liquid film thickness is shown in the gap between the wall and the obstacle with film thickness recovery downstream from the obstacle. This film thickness change is in accordance with the measured liquid film behaviour presented in [3]. Measured and predicted film thickness upstream from the obstacle is 0.2 mm, while it is reduced to 0.1 mm within the gap. The reduction of the film thickness is caused by the acceleration of the air stream within the gap, increase of the air flow shear on the liquid film surface, and consequent film velocity increase. Calculated film thickness downstream from the obstacle is the same as the upstream value, while measured downstream

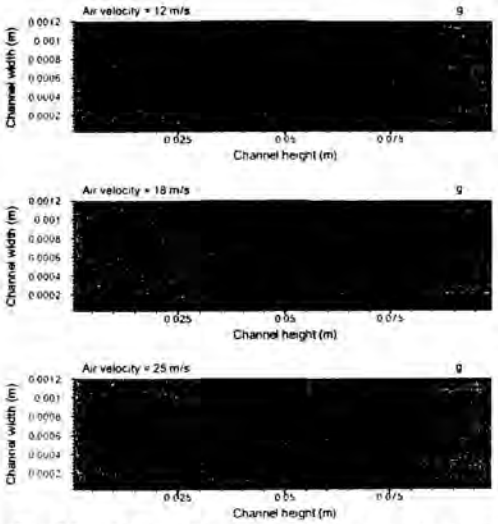

Fig. 3 Liquid film thickness change around the spacer

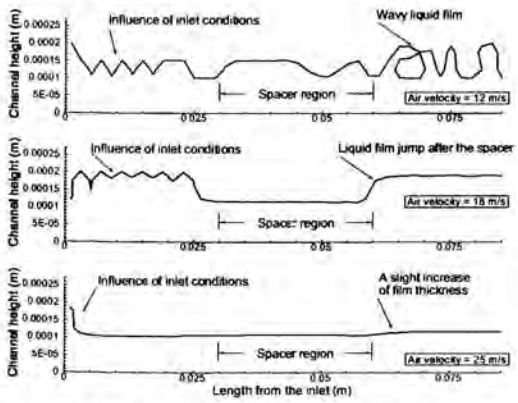

Fig. 4 Liquid film profile around the spacer

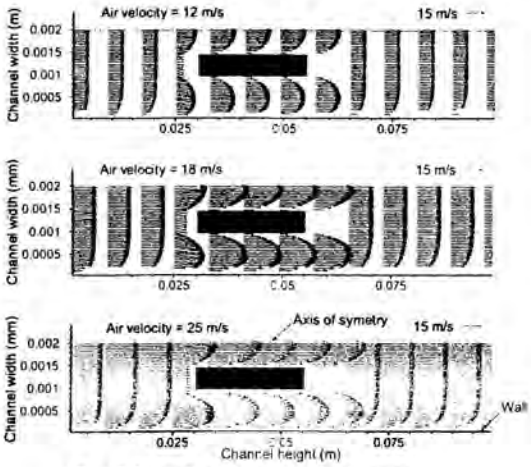

Fig. 5 Air velocity field around spacer

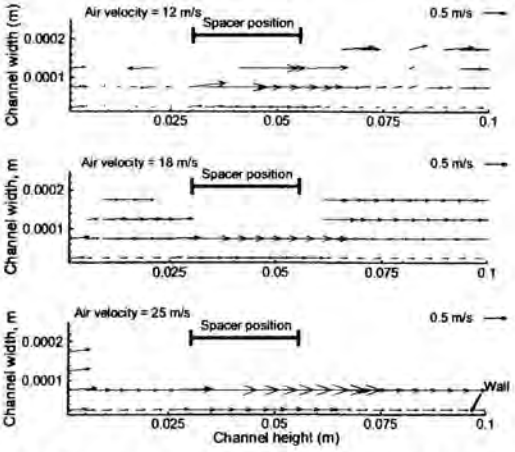

Fig. 6 Liquid film velocity profiles around the spacer

value is approximately 0.02 mm higher then upstream from the obstacle. This is attributed to the deposition of the water droplets which leave the obstacle area. This effect is not included into the present numerical calculation. For the highest inlet air velocity of 25 m/s the influence of the air – liquid film shear stress is high and the liquid film is nearly flat with only slight increase of film thickness downstream from the obstacle. Presented results, except in the case of the lowest inlet velocity of 12 m/s, show no liquid film waves propagation. Therefore, they present averaged film thickness values. Experimental evidence in [3] shows very intensive film surface waves propagation, with 3 to 4 times higher maximum than minimum film thickness. The wavy film in case of 12 m/s inlet air velocity is caused by the low interfacial shear. Further reduction of the air flow will lead to the reverse film flow (the condition of flooding).

Figure 5 shows air velocity fields around obstacle for presented three inlet air velocity values. Air flow acceleration around the obstacle is clearly shown. Also, it is shown that the position of the air velocity vectors close to the wall change according to the change of the liquid film thickness.

Figure 6 shows liquid film velocity field. In case of low air inlet velocity (12 m/s) the velocity field is highly perturbed, due to the low interfacial shear and the influence of gravity in the direction opposite to the flow and interfacial shear direction. For 18 and 25 m/s of inlet air velocity, the correspondence between liquid film velocity and film thickness is clearly shown. A decrease of film thickness leads to an increase of film velocity and vice versa. Also, the shown width of the water velocity field corresponds to the predicted film thickness.

Additionally performed parametric analyses have shown that the variation of the liquid inlet velocity (two times lower or higher values) have practically no influence on the liquid film thickness change along the channel. Otherwise, the main influence on the film behaviour is caused by the air stream.

CONCLUSION

Two-dimensional numerical investigation of the air and liquid film flow around the obstacle is presented. Numerical results shows the same hydro-dynamic liquid film behaviour as it was observed in the experiment of air-water flow within 3x3 nuclear fuel rod bundle [3]. The following conclusion are drawn based on the obtained numerical results under atmospheric flow conditions:

a) The gas phase velocity has strong influence on the liquid film behaviour, while the influence of the liquid film flow rate is negligible.

b) Wavy and unstable liquid film flow takes place for low mean air velocity, with the possibility of flooding occurrence. For analysed atmospheric flow conditions these conditions correspond to the 12 m/s velocity.

c) Dynamic change of the liquid film thickness is achieved for the moderate air velocities. It is characterised with the liquid film thickness decrease in the gap between the wall and obstacle and subsequent film thickness recovery downstream from the obstacle. For analysed atmospheric flow conditions, these moderate flow conditions are approximately 18 m/s. Approximately the same air velocity is applied in the 3x3 rod bundle experiment, and the same liquid film dynamic behaviour is obtained experimentally and numerically.

d) For high air velocities, the mean liquid film thickness is nearly flat and the presence of the obstacle has little influence on the liquid film dynamic behaviour.

Further investigation of the two-phase flow around obstacle will include coupled liquid film and entrained droplets flow, as well as the influence of the obstacle with the fin on the liquid film and two-phase flow behaviour.

REFERENCES

1. Stosic, Z., 1999, *Study on Thermal Performance and Margins of BWR Fuel Elements*, 7th Int. Conf. On Nuclear Engineering, April 19-23, Tokyo, Japan.
2. Stosic, Z., 1995, *The Rod Bundle Spacer Grid Effects on Post-Dryout Heat Transfer Augmentation Analysed by the model HECHAN 2.1*, 4th, ASME/JSME Thermal Engineering Joint Conference, March 19-24, Maui, Hawaii, USA.
3. Noriyasu, K., Kumagai, K., Tsuji, Y., Kunugi, T., Serizawa, A., 2001, *Multi-dimensional Characteristics of Surface Waves on the Liquid Film Flow in a 3x3 Rod Bundle*, 4th International Conference on Multiphase Flow, May 27-June 1, New Orleans, Louisiana, USA.
4. Antal, S. P., Nagrath, S., Podowski, M. Z., 2001, *Multidimensional Simulations of Two-Phase Flows in Large Volumes with Injection Spargers*, 4th International Conference on Multiphase Flow, May 27-June 1, New Orleans, Louisiana, USA.
5. Stosic, Z. and Stevanovic, V., 2001, *A Numerical Approach to the Simulation of One-Phase and Two-Phase Reactor Coolant Flow around Nuclear Fuel Spacers*, 9th International Conference on Nuclear Engineering - ICONE 9, April 8-12, Nice, France.
6. V. Stevanovic, High-Order Accurate Scheme for the Numerical Solution of Scalar Parameter Transport Equation Applied to Enthalpy Transport and Interface Tracking, 4th International Conference on Multiphase Flow, New Orleans, Louisiana, USA, May 27-June 1, 2001.
7. Patankar, S., 1980, *Numerical Heat Transfer and Fluid Flow*, Hemisphere Publ. Co.
8. Stosic, Z. and Stevanovic, V., 2001, *Prediction of Thermal and Hydraulic Relaxation Length Behind Obstacle in Two-Phase Turbulent Coolant Flow*, 39th European Two-Phase Flow Group Meeting, June 17-20, Aveiro, Portugal.

HEFAT2002
1st International Conference on Heat Transfer Fluid Mechanics, and Thermodynamics
8-10 April 2002, Kruger Park, South Africa
TS1

PROPAGATION PHENOMENA DURING ASYMMETRICAL COLLISION OF THERMAL WAVES IN A VERY THIN FILM

Shuichi TORII
Department of Mechanical Engineering,
Kagoshima University,
1-21-40 Korimoto, Kagoshima 890-0065, JAPAN
E-mail: torii@mech.kagoshima-u.ac.jp

Wen-Jei YANG
Department of Mechanical Engineering
and Applied Mechanics,
University of Michigan,
Ann Arbor, Michigan 48109, USA
E-mail: wjyang@engin.umich.edu

ABSTRACT

A numerical study is performed to investigate wave nature of thermal propagation in a very thin film subjected to an asymmetrical temperature change, i.e., heating or cooling, on both sides. The non-Fourier, hyperbolic heat conduction equation is solved using a numerical technique based on MacCormak's predictor-corrector scheme. Consideration is given to the time history of heat transfer behavior before and after asymmetrical collision of wave fronts from two sides of a film. It is disclosed that in transient heat conduction, a heat pulse is transported as a wave in the film, and that non-Fourier heat conduction is extremely significant with certain range of film thickness and time. That is, sudden heating on both sides of the extremely thin film causes temperature overshoot within a very short period of time, while sudden cooling on both sides yields temperature undershoot. These thermal wave behavior is in accord with the existing theoretical results obtained by means of the method of separation of variables.

NOMENCLATURE

C	speed of thermal wave (m/s)
c_p	specific heat (J/kgK)
k	thermal conductivity (W/Km)
$Q(\eta, \xi)$	dimensionless heat flux
$q(\xi,\tau)$	heat flux (W/m^2)
$T(\xi,\tau)$	temperature (K)
T_0	reference temperature (K)
t	time (sec)
x	space variable
x_0	film thickness (m)

Greek Letters

α	thermal diffusivity (m^2/s)
η	dimensionless space variable
$\theta(\eta, \xi)$	dimensionless temperature
ξ	dimensionless time variable
ρ	density (kg/m^3)
τ	relaxation time, a/C^2 (sec)

Subscript

n	time level

INTRODUCTION

The heat conduction in materials in dimension such that Fourier's law is accurate and appropriate, is usually treated as a diffusion process. In other words, Fourier's law predicts that conduction is a diffusion phenomenon in which temperature disturbances propagate at an infinite velocity and at time t=0, the heat flux at the wall is infinite while the temperature change is nonzero everywhere except at infinity. Despite such an unacceptable notation pertinent to physical reality, Fourier's law gives quite reliable results in most practical heat transfer applications. However, the classical Fourier heat conduction equation breaks down at temperatures near absolute zero or at moderate temperatures when the elapsed time during a transient is extremely small. This is because the wave nature of thermal propagation is dominant, that is, a thermal disturbance travels in the medium with a finite speed of propagation (Baumeister and Hamill, 1969; Chan et al., 1971; Kazimi and Erdman, 1975; Maurer and Thompson, 1973). Several issues of basic scientific interest arise in cases such as laser penetration and welding, explosive bonding, electrical discharge machining, and heating and cooling of micro-electronic elements involving a duration time of nanosecond or even picosecond in which energy is absorbed within a distance of microns from the surface. For example, the issue of energy transfer into a lattice and resulting temperature in the lattices during such a short period of time and over such a tiny region is of fundamental

importance but remains a matter of controversy (Bloembergen et al., 1982).

The above phenomena are physically anomalous and can be remedied through the introduction of a hyperbolic equation based on a relaxation model for heat conduction which accounts for a finite thermal propagation speed. Recently, considerable interest has been generated toward the hyperbolic heat conduction (HHC) equation and its potential applications in engineering and technology. A comprehensive survey of the relevant literature is available in reference (Ozisik and Tzou, 1994). Some dealt with wave characteristics and finite propagation speed in transient heat transfer conduction (Kazimi and Erdman, 1975; Glass et al., 1985a; Wiggert, 1977; Yuen and Lee, 1989; Kao, 1977). Several analytical and numerical solutions of the HHC equation have been presented in the literature. In studying the propagation of temperature pulse in a semi-infinite medium, Baumeister and Hamill (1969) used Laplace transforms to solve the HHC equation. The same method was employed by Maurer and Thompson (1973). They reported the importance of the wave effect in response to a high heat flux irradiation. Carey and Tsai (1982) analyzed a propagating heat wave reflected at a boundary, in which the numerical methods based on a variational formulation of the problem and the Galerkin finite-element method are employed. Vick and Ozisik (1983) and Ozisik and Vick (1984) predict the growth and decay of a thermal pulse in one-dimensional solid. In particular, Ozisik and Vick (1984) used integral transforms to study the effect of pulses. Glass et al. (1985b) employed a numerical technique based on MacCormack's predictor-corrector scheme to solve the HHC equation. By using the same method, Glass et al. (1986, 1990) analyzed numerically hyperbolic heat conduction in a semi-infinite slab with temperature-dependent thermal conductivity and investigated the effects of Stefan number, melt temperature, and variable thermal conductivity. As the other method, Frankel et al. (1985) developed a general three-dimensional constant property heat flux formulation based on the hyperbolic heat conduction approximation. They reported that the flux-formulation is more convenient to solve problems involving flux-specified boundary conditions. Tan and Yang (1997a) investigated heat transfer resulting from symmetrical collision of thermal waves induced by a step change in the wall temperature of the thin film by means of the method of separation of variables. They obtained theoretical results for the time history of propagation process, magnitude and shape of thermal waves and the range of film thickness and duration time. By using the same method, Tan and Yang (1997b) predicted wave nature of heat propagation in a very thin film subjected to an asymmetrical temperature change on both sides. It was found that (i) when a thin film is heated on both side walls, temperature overshoot occurs within a very shot period of time, and (ii) in contrast, when it is cooled, temperature undershoot occurs. Furthermore, Tan and Yang (1997c) treated heat propagation in a very film subjected to an exponentially decaying temperature change on both sides. They reported that both temperature overshoot and temperature undershoot occur in the films within a very short period of time.

This paper treats the wave behavior during transient heat conduction in a very thin film (solid plate) subjected to an asymmetrical temperature change on both side surfaces. Analytical solutions are obtained by means of a numerical technique based on MacCormak's predictor-corrector scheme to solve the non-Fourier, hyperbolic heat conduction equation. Numerical results are compared with theoretical solutions (Tan and Yang 1997b).

FORMULATION AND NUMERICAL METHOD

Consider a very thin film with thickness of x_0 maintained at a uniform, initial temperature T_0. The walls at x=0 and x_0 are suddenly heated or cooled to a temperature T_{w1} and T_{w2}, respectively. In the present study, there is no heat generation in a film. Nonequilibrium convection and radiation are assumed negligible. Under the conditions and assumption, the modified Fourier equation (Ozisik and Tzou, 1994) and the energy equation can be represented in the one-dimensional flow of heat, as

$$\tau\frac{\partial q}{\partial t} + q + k\frac{\partial T}{\partial x} = 0 \qquad (1)$$

$$\rho c_p\frac{\partial T}{\partial t} + \frac{\partial q}{\partial x} = 0 \qquad (2)$$

respectively. Note that the relaxation time τ defined as $\tau=\alpha/C^2$ is assumed constant, where C is the speed of "second sound" (thermal shock wave). For convenience in analysis and computation, the initial and boundary conditions to be imposed here are given for heating and cooling cases, as

Heating:

$T = T_0, \frac{\partial T}{\partial x} = 0$ at t=0, $0<x<x_0$,

$T = T_{w1}\ (= 1.5T_0)$ at t>0, x=0,

$T = T_{w2}\ (= 2.0T_0)$ at t>0, $x=x_0$

Cooling:

$T = T_0, \frac{\partial T}{\partial x} = 0$ at t=0, $0<x<x_0$,

$T = T_{w1}\ (= -1.5T_0)$ at t>0, x=0,

$T = T_{w2}\ (= -2.0T_0)$ at t>0, $x=x_0$

The following dimensionless quantities, i.e., dimensionless temperature, dimensionless heat flux, and dimensionless time and space variables are introduced

$$\theta_{(\xi,\eta)} = \frac{T}{T_0} \qquad (3a)$$

$$Q_{(\xi,\eta)} = \frac{\alpha q}{T_0 k C} \qquad (3b)$$

$$\xi = \frac{C^2 t}{2\alpha} \qquad (3c)$$

$$\eta = \frac{Cx}{2\alpha} \qquad (3d)$$

Equations (1) and (2) can be expressed in terms of the above dimensionless variables as

$$\frac{\partial Q}{\partial \xi} + 2Q + \frac{\partial \theta}{\partial \eta} = 0 \qquad (4)$$

$$\frac{\partial Q}{\partial \eta} + \frac{\partial \theta}{\partial \xi} = 0 \qquad (5)$$

Initial and boundary conditions are represented for wall-heating and -cooling, respectively, as

heating:

$\theta = 1,\ Q = 0$ at $\xi=0,\ 0<\eta<\frac{Cx_0}{2\alpha}$

$\theta = 1.5,\ \frac{\partial Q}{\partial \eta} = 0$ at $\xi>0,\ \eta=0,$

$\theta = 2.0,\ \frac{\partial Q}{\partial \eta} = 0$ at $\xi>0,\ \eta=\frac{Cx_0}{2\alpha}$

cooling:

$\theta = 1,\ Q = 0$ at $\xi=0,\ 0<\eta<\frac{Cx_0}{2\alpha}$

$\theta = -1.5,\ \frac{\partial Q}{\partial \eta} = 0$ at $\xi>0,\ \eta=0,$

$\theta = -2.0,\ \frac{\partial Q}{\partial \eta} = 0$ at $\xi>0,\ \eta=\frac{Cx_0}{2\alpha}$

Note that the boundary condition of Q at $\xi > 0$ are derived from Eqs. (4) and (5).

In general, many investigators combine the energy and flux equations (i.e. Eqs. (4) and (5)) into a single second-order partial differential equation to solve the HHC problem. As for this solution method, Glass et al. (1985a and b) reported that MacCormack's method (Anderson et al., 1983), which is a second-order accurate explicit scheme, can handle these moving discontinuities quite well and is valid for the HHC problems. Since the hyperbolic problems considered here have step discontinuities at the thermal wave front, MacCormack's prediction-correction scheme can be used in the present study. When the HHC problem is numerically solved through the scheme employed here, it is convenient to solve Eqs. (4) and (5) rather than to combine these two equations into a single second-order partial differential equation before solving (Glass et al., 1985b). When MacCormack's method is applied to Eqs. (4) and (5), the following finite difference formulation results:

Predictor:

$$\overline{\theta_i^{n+1}} = \theta_i^n - \frac{\Delta\xi}{\Delta\eta}\left(Q_{i+1}^n - Q_i^n\right) \qquad (6)$$

$$\overline{Q_i^{n+1}} = Q_i^n - \frac{\Delta\xi}{\Delta\eta}\left(\theta_{i+1}^n - \theta_i^n\right) - 2\Delta\xi Q_i^n \qquad (7)$$

Corrector:

$$\theta_i^{n+1} = \frac{1}{2}\left\{\theta_i^n + \overline{\theta_i^{n+1}} - \frac{\Delta\xi}{\Delta\eta}\left(\overline{Q_i^{n+1}} - \overline{Q_{i-1}^{n+1}}\right)\right\}, \qquad (8)$$

$$Q_i^{n+1} = \frac{1}{2}\left\{Q_i^n + \overline{Q_i^{n+1}} - \frac{\Delta\xi}{\Delta\eta}\left(\overline{\theta_i^{n+1}} - \overline{\theta_{i-1}^{n+1}}\right) - 2\Delta\xi\,\overline{Q_i^{n+1}}\right\}, \qquad (9)$$

where the subscript i denotes the grid points in the space domain, superscript n denotes the time level, and $\Delta\eta$ and $\Delta\xi$ are the space and time steps, respectively. The circumflex terms, i.e., Q_i^{n+1}, $\overline{\theta^{n+1}}$, etc. are a temporary predicted value at the time level n+1.

Computations are processed in the following order:

1. Specify the values of Q and θ at n=0, i.e., the initial values.
2. Solve Eqs. (6) and (7) for θ and Q to obtain temporary predicted value at the time level n+1.
3. Calculate new values of θ and Q at the time step n+1 using Eqs. (8) and (9).
4. Repeat steps 2-3 until n reaches a desired time level from the onset of calculation.

Throughout numerical calculations, the number of grids is properly selected between 1,000 and 5,000 to obtain a grid-independent solution, resulting in no appreciable difference between the numerical results with different grid spacing. In solving the governing equations employed here, i.e., the HHC problem including the nonlinear nature, the stability is affected by the ratio of $\Delta\xi$ to $\Delta\eta$, $\Delta\xi/\Delta\eta$, which is called the Courant number (Glass et al. 1986). For example, as the Courant number becomes smaller, the effect of odd derivative truncation-error terms becomes larger, and oscillations occur in the vicinity of discontinuities in the solution. Thus, $\Delta\xi/\Delta\eta$ is fixed at 0.98 in the present study. The ranges of the parameters are nondimensional plate thickness $Cx_0/2\alpha$=0.5, 1.0 and 5. Numerical computations were performed on a personal computer (32 bit).

NUMERICAL RESULTS AND DISCUSSION

Figures 1 through 6, illustrate the timewise variation of the temperature distribution, θ, in films having $Cx_0/2\alpha$ of 0.5, 1.0, and 5, respectively. Figures 1, 3 and 5 correspond to numerical predictions resulting from heating a film at both side surfaces, while Figs. 2, 4 and 6 correspond to the results cooled from both sides. In particular, Figs. 1 and 2 depict, in detail, the propagation process of thermal waves in a film with the value of $Cx_0/2\alpha$ of 0.5. It is observed in Figs. 1 and 2 that (i) sharp wavefronts exist in the thermal wave propagation, which is the same as the other wave phenomena, (ii) after the wall temperatures on two sides are suddenly raised or decreased, a set of wavefronts appears and advances towards the center in the physical domain which separates the heat- or cool-affected zone from the thermally undisturbed zone, as seen in Fig. 1(a), (iii) at ξ=0.5, thermal wavefronts meet and collide with each other at the center of the film, (iv) after first collision, the center temperature in a film, for the case of heating, causes a significant amplification resulting a much higher temperature in this region, while the corresponding temperature, for the case of cooling, causes a substantial attenuation resulting a much lower temperature in the same region, (v) after that, reverse thermal wavefronts take place and travel towards both side walls of the film, as shown in Figs. 1(b) and 2(b), (vi) when thermal wavefronts reach at both side walls at ξ=1.0, the film temperatures at both sides of strongly heated walls exceed the imposed wall temperature, called temperature overshoot, while the film temperatures at both cooled-walls are lower than the imposed one, called temperature undershoot, and (vii) after thermal wavefronts are reflected from both side walls of the film, the similar pattern is continued as seen in Figs. 1(c) and 2(c) through 1(e) and 2(e). By several times of collision, reflection and continuous attenuation of the thermal waves, the wavefronts become weak. These thermal wave behavior was also predicted by Tan and Yang (1997b), who obtained the theoretical results by solving the hyperbolic heat conduction

equation by means of the method of separation of variables. Similarly, one observes in other figures that an asymmetrical temperature change on both sides of a film gives rise to the propagation of two severe thermal wavefronts in the film at finite velocity. Each of these wavefronts decays with time and simultaneously dissipates heat along its path by diffusion.

The present numerical solution predicts the existence of thermal waves, particularly in a very thin film and presents the propagation process of thermal waves, the magnitude and shape of thermal waves, and the regular decaying process of thermal wave in films with different values of $Cx_0/2\alpha$. Such behavior is characteristic of a thermal system with a relaxation or nonlinear diffusion theory. It is found from Figs. 1 through 6 that as time progresses, the peak of the wave decays and disappears within $\xi=10$ for any films with different thickness. One observes that after wavefronts arrive at the center of the film with $Cx_0/2\alpha=5$, they gradually disappear in the absence of reverse temperature waves and temperature overshoot or temperature undershoot, as seen in Figs. 5 and 6. It behaves like diffusion domination. A very interesting phenomenon of temperature overshoot or temperature undershoot occurs in the very thin film, i.e., in the film of smaller values of $Cx_0/2\alpha$, over a very short period of time, which is induced by the collision of the wave fronts. Such wave behaviour can not predicted by the classical heat conduction theory, i.e., Fourier's law. This is because it allows for the immediate diffusion of heat as soon as the energy is released in the absence of a relaxation time, that is, heat propagates at an infinite speed. Thus, the presence of the thermal relaxation time yields non-Fourier effect and this trend becomes more significant when the relaxation time is longer. For example, larger reverse waves can be seen in a film with $Cx_0/2\alpha=0.5$, with the temperature greatly exceeding the imposed wall temperatures of the film, as shown in Figs. 1 and 2.

It is found from these results that the thermal relaxation time τ plays a primary role in distinguishing a domain to be wave dominating or diffusion dominating. Several investigators have estimated the magnitude of thermal relaxation time τ to range from 10^{-10} second for gases at standard conditions to 10^{-14} second for metals (Maurer, 1969) with that for liquids (Nettleton, 1960) and insulators (Chester, 1963), falling within this range. If τ is known, one can obtain the range of film thickness within which heat propagates as a wave. The criterion for thermal wave dominating in the present study is $Cx_0/\alpha(=X_0/\sqrt{\alpha\tau})<10$, as seen in Figs. 1 through 3. For example, the value of silicon corresponds to the thickness of the film in the order of about 0.01 micron using 10^{-14} s and 93.4×10^{-6} m^2/s as the relaxation time and thermal difffusivity (Kreith and Bohn, 1986), respectively.

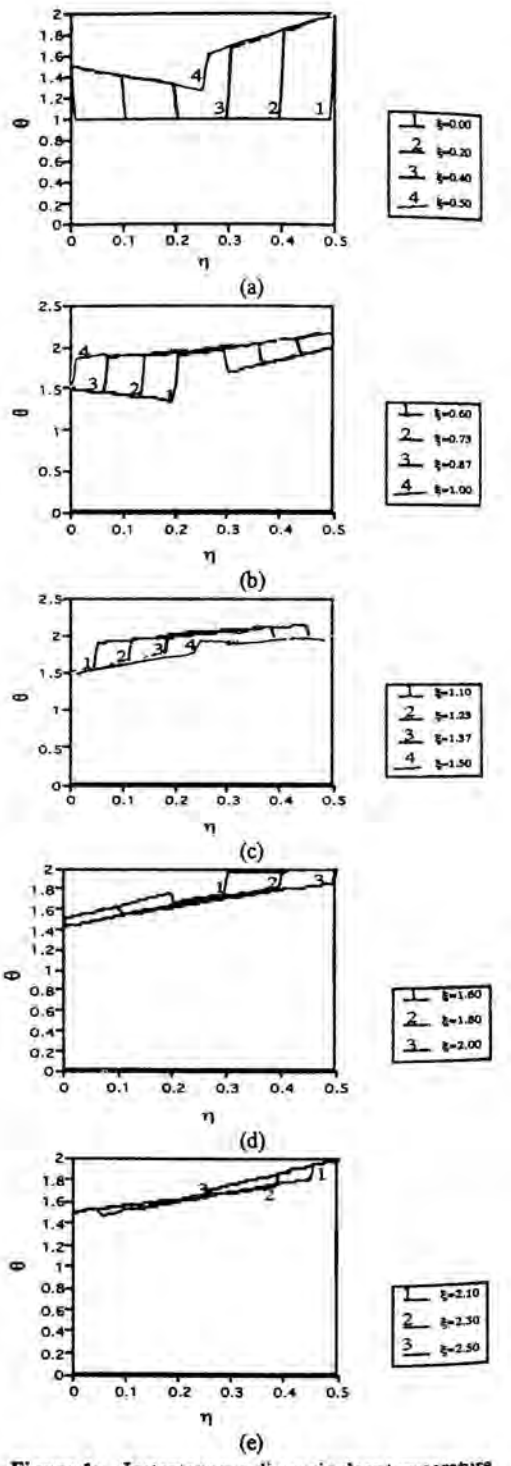

Figure 1: Instantaneous dimensionless temperature distribution in the film at $Cx_0/\alpha=1$ with an asymmetrical temperature change

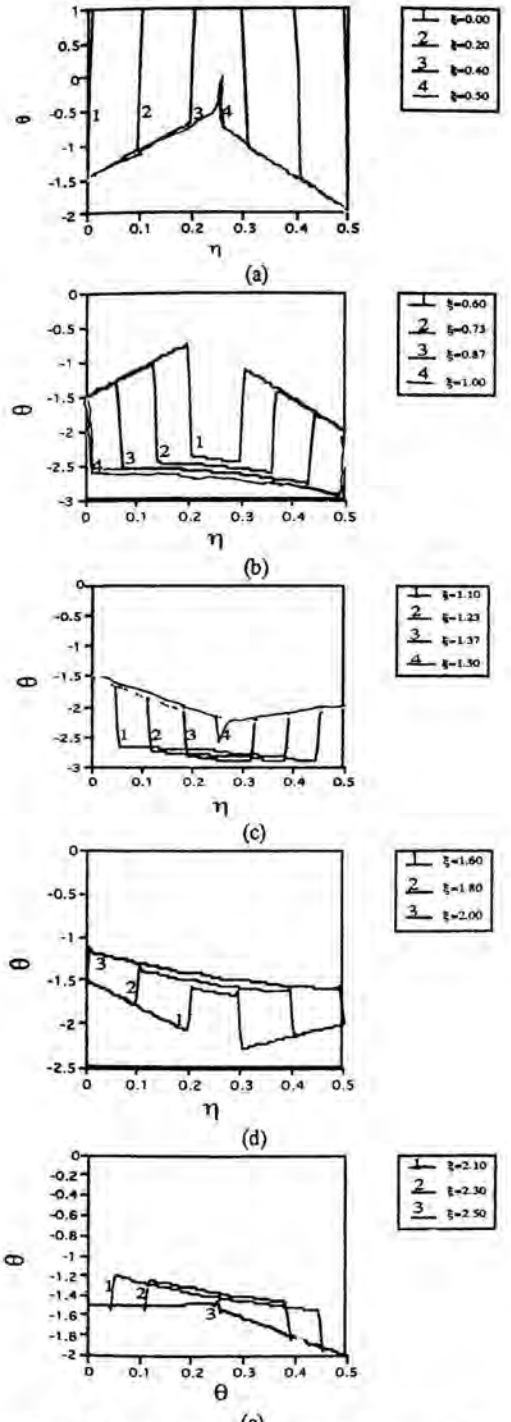

Figure 2: Instantaneous dimensionless temperature distribution in the film at $Cx_0/\alpha=1$ with an asymmetrical temperature change

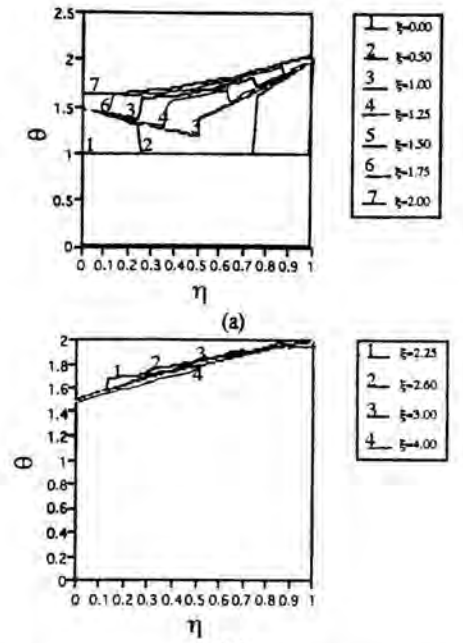

Figure 3: Instantaneous dimensionless temperature distribution in the film at $Cx_0/\alpha=2$ with an asymmetrical temperature change

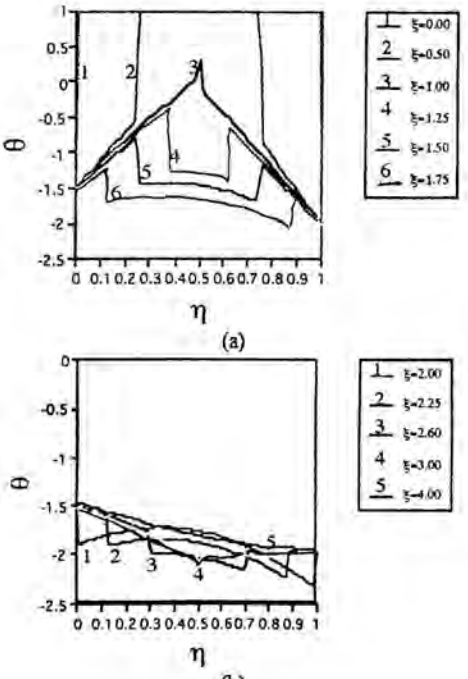

Figure 4: Instantaneous dimensionless temperature distribution in the film at $Cx_0/\alpha=2$ with an asymmetrical temperature change

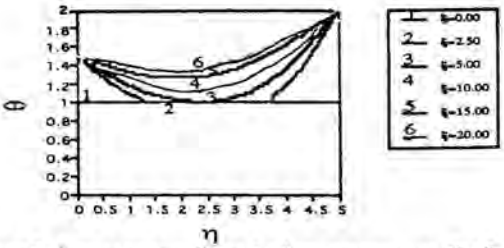

Figure 5: Instantaneous dimensionless temperature distribution in the film at $Cx_0/\alpha=10$ with an asymmetrical temperature change

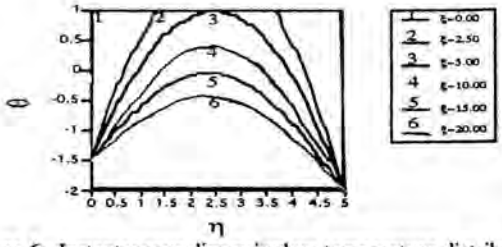

Figure 6: Instantaneous dimensionless temperature distribution in the film at $Cx_0/\alpha=10$ with an asymmetrical temperature change

SUMMARY

Heat waves have been theoretically studied in a very thin film subjected to a sudden asymmetric temperature change at two side walls. It is revealed that only when C is of the same order as or larger than one half the film thickness, thermal waves can appear. The smaller the value of $x_0/2\tau C$, the more pronounced the temperature waves. The criterion for the occurrence of thermal shock waves in a thin film is the film thickness in the order of 0.01 micron for metals. If a film is strongly heated or cooled, temperature overshoot or temperature undershoot may take place in the films of smaller values of $x_0/2\tau C$ within a very short period of time, respectively.

REFERENCES

Anderson, D. A. Tannehill, J. C. and Pletcher, R. H., 1983, Computational Fluid Mechanics and Heat Transfer, Hemispherer, New York.

Baumeister, K. J. and Hamill, T. D., 1969, "Hyperbolic Heat Conduction Equation - A Solution for the Semi-Infinite Body Problem," J. Heat Transfer, Vol. 91, pp. 543-548.

Bloembergen, N. Kurz, H. Kiu, J. M. and Yen, R., 1982, "Fundamentals of Energy Transfer during Picosecond Irradiation of Silicon, in Laser and Electron-Beam Interactions with Solids," Elsevier Science Publishing Co., Inc., Neq York, pp. 3-20.

Carey, G. F. and Tsai, M., 1982, "Hyperbolic Heat Transfer with Reflection", Numerical Heat Transfer, Vol. 5, pp. 309-327.

Chan, S. H. Low, J. D. and Mueller, W. K., 1971, "Hyperbolic Heat Conduction in Catalytic Supported Crystallites," AIChE Journal, Vol. 17, pp. 1499- 1507.

Chester, M., 1963, "Second Sound in Solids," Physical Review, Vol. 131, pp. 2013-2015.

Frankel, J. I., Vick, B. and Ozisik, M. N., 1985, "Flux Formulation of Hyperbolic Heat Conduction," J. Applied Physics, Vol. 58, pp. 3340-3345.

Glass, D. E. Ozisik, M. N. and Vick. B., 1985a, "Hyperbolic Heat Conduction with Surface Radiation," Int. J. Heat and Mass Transfer, Vol. 28, pp. 1823-1830.

Glass, D. E. Ozisik, M. N. McRae, D. S. and Vick, B., 1985b, "On the Numerical Solution of Hyperbolic Heat Conduction," Numerical Heat Transfer, Vol. 8, pp. 497-504.

Glass, D. E. Ozisik, M. N. McRae, D. S. and Vick, B., 1986, "Hyperbolic Heat Conduction with Temperature-Dependent Thermal Conductivity," J. Applied Physics, Vol. 59, pp. 1861-1865.

Glass, D. E. Ozisik, M. N. Kim, W. S., 1990, "On the Numerical Solution of Hyperbolic Heat Conduction," Numerical Heat Transfer, Vol. 18, pp. 503-516.

Kao, T. T., 1977, "Non-Fourier Heat Conduction in Thin Surface Layers," J. Heat Transfer, Vol. 99, pp. 343-345.

Kazimi, M. S. and Erdman, C. A., 1975, "On the Interface Temperature of Two Suddenly Contacting Materials," J. Heat Transfer, Vol. 97, pp. 615-617.

Keith, F. and Bohn, M. S., 1986, Principles of Heat Transfer, Fourth Edition, Harper & Row, New York.

Maurer, M. J., 1969, "Relaxation Model for Heat Conduction in Metals," J. Applied Physics, Vol. 40, pp. 5123-5130.

Maurer, M. J. and Thompson, H. A., 1973, "Non-Fourier Effects at High Heat Flux," J. Heat Transfer, Vol. 95, pp. 284-286.

Nettleton, R. E., 1960, "Relaxation Theory of Thermal Conduction in Liquids," Physics of Fluids, Vol. 3, pp. 316-225.

Ozisik, M. N. and Tzou, D. Y., 1994, "On the Wave Theory in Heat Conduction," J. Heat Transfer, Vol. 116, pp. 526-535.

Ozisik, M. N. and Vick, B., 1984, "Propagation and Reflection of Thermal Waves in a Finite Medium," International J. Heat Mass Transfer, Vol. 27, pp. 1845-1854.

Tan, Z. M. and Yang, W.-J., 1997a, "Non-Fourier Heat Conduction in a Thin Film Subjected to a Sudden Temperature Change on Two Sides," J. Non-Equilibrium Thermodynamics, Vol. 22.

Tan, Z. M. and Yang, W.-J., 1997b, "Heat Transfer during Asymmetrical Collision of Thermal Waves in a Thin Film," Int. J. Heat Mass Transfer, Vol. 40, No. 17, pp. 3999-4006.

Tan, Z. M. and Yang, W.-J., 1997c, "Propagation of Thermal Waves in Transient Heat Conduction in a Thin Film," J. Non-Equilibrium Thermodynamics, Vol. 32, pp. 345-365.

Yuen, W. W. and Lee, S. C., 1989, "Non-Fourier Heat Conduction in a Semi-Infinite Solid Subjected to Oscillatory Surface Thermal Disturbances," J. Heat Transfer, Vol. 111, pp. 178-181.

Vick, B. and Ozisik, M. N., 1983, "Growth and Decay of a Thermal Pulse Predicted by the Hyperbolic Heat Conduction Equation," J. Heat Transfer, Vol. 105, pp. 902-907.

Wiggert, D. C., 1977, "Analysis of Early-Time Transient Heat Conduction by Method of Characteristics," J. Heat Transfer, Vol. 99, pp. 35-40.

HEFAT2002
1st International Conference on Heat Transfer, Fluid Mechanics and Thermodynamics
8-10 April 2002, Kruger National Park, South Africa
WG1

A COLLOCATED GALERKIN METHOD FOR INCOMPRESSIBLE FLOWS

Gang Wang
ANSYS, Inc.
275 Technology Drive
Canonsburg, PA 15317-9565

ABSTRACT

The finite-element program, ANSYS/FLOTRAN, has been enhanced at Release 6.0 with an original collocated Galerkin finite-element method. Similar to the collocated finite volume method, the collocated Galerkin method introduces a second set of velocities, namely the element-based nodal velocities. Those new velocities are made to satisfy the conservation of mass, whereas the conventional nodal velocities are made to satisfy the conservation of momentum. This new scheme will be validated in three model problems: shear-driven flow in a square cavity, flow through a circular duct with a constriction, and shear-driven flow in a triangular cavity.

INTRODUCTION

The finite element method (FEM) has become one of the most popular approaches for fluid flows and heat transfers due to its ease of handling complex geometrical configurations (Zienkiewicz and Taylor, 1989). One popular approach is the equal-order finite element method (Taylor and Hood, 1973; Schneider et al., 1978). There were a number of improvements over the original equal-order methods using the SIMPLE-type solution procedures (Schnipke and Rice, 1985; du Toit, 1998; Wang, 2001). Although the finite element method is shown to preserve the global energy balance for heat conduction problems (Comini and Giudice, 1991), such a conservation property is generally not warranted for convection-dominated flows. The present paper aimed to make a contribution in this subject by the development of a consistent equal-order Galerkin method.

One popular method that preserves the conservation property is the finite volume method (FVM) (Harlow and Welch, 1965; Patankar and Spalding, 1972). The finite volume method adopts a staggered arrangement between the pressure and the velocity, and it was initially limited to regular-shaped solution domains. Another method is to locate all of them at the center of the control volume (Rhie and Chow, 1983) where a staggered arrangement is implicitly incorporated for the velocity and the pressure. In their collocated scheme, the cell-centered velocity components satisfy the momentum equations and the cell-faced velocity components satisfy the mass conservation equations. Comparison of the staggered and the collocated grids was given in Peric et al. (1988).

Winslow (1967) and Williamson (1969) were among the first to combine the concepts of the finite volume method and the finite element method. Since then, there has been a large amount of research in that direction, resulting in the developments of the control-volume finite element method (CVFEM) (Baliga and Patanka, 1980; Prakash and Patankar, 1985; Schneider and Raw, 1987; Saabas and Baliga, 1994). The control-volume finite element method is a sub-domain collocation method, and can be viewed as a special class of the weighted residual formulation (Zienkiewicz and Taylor, 1989). In this method, the weighting function is set to unity within a control volume containing a given node and zero elsewhere (Baliga and Patanka, 1980). This method enjoys the advantage of providing geometrical flexibility as well as satisfying the conservation requirements.

The main contribution of the present work is to incorporate the collocated concept of finite volume schemes into the Galerkin finite element methods. Similar to the collocated finite volume method, the present work introduces a second set of velocities, namely the element-based nodal velocity. The pressure equation is formulated in such a way that the updated element-based velocity satisfies the mass conservation equations exactly in the weak form. The nodal velocity, on the other hand, is made to satisfy the momentum equations. The present collocated Galerkin method preserves the conservation property locally in the Galerkin sense, and it also satisfies the global conservation requirement up to the convergence of the governing equations. In this paper, the author will describe in detail the mathematical formulation, the collocated concept, segregated solution algorithm, and computational results for a number of benchmark problems.

NUMERICAL METHODOLOGY

Mathematical Formulation

The partial differential equations governing two-dimensional transient motion of an incompressible fluid are the Navier-Stokes

equations. To calculate the flow fields, the Navier-Stokes are integrated with a weighted residual method.

$$\int_\Omega \nabla W^p \cdot (\rho \vec{v}) d\Omega = \int_\Gamma W^p \rho \vec{v} \cdot \hat{n} d\Gamma \tag{1}$$

$$\int_\Omega \{\vec{W}^v \cdot \rho(\frac{\partial \vec{v}}{\partial t} + \vec{v} \cdot \nabla \vec{v}) + \mu \nabla \vec{W}^v : \nabla \vec{v}\} d\Omega = -\int_\Omega \vec{W}^v \cdot \nabla p d\Omega + \int_\Omega \vec{W}^v \cdot \vec{F} d\Omega + \int_\Gamma \vec{W}^v \cdot (\mu \hat{n} \cdot \nabla \vec{v}) d\Gamma \tag{2}$$

where $\vec{v}, p, \vec{F}$ and μ are the velocity, pressure, body force and dynamic viscosity, respectively. Here, Ω is the finite element domain, and Γ is the domain boundary with $\hat{n}$ as its unit normal vector. Further, W^p and $\vec{W}^v$ are the weighting functions corresponding to the pressure and velocity degrees of freedom, respectively. Since equal-order interpolation functions are used for the pressure and velocity degrees of freedom, the superscripts will be dropped in the later discussion for clarity.

For brevity, we shall restrict our attention to two-dimensional problems in Cartesian coordinate systems. The extensions to three-dimensional problems and other coordinate systems have been implemented in the commercial software, ANSYS/FLOTRAN at the release 6.0. In the present work, element-based nodal velocities $\tilde{v}^e$ are first introduced to eliminate the inconsistency between the pressure and the momentum equations inherent in previous equal-order methods. The continuity and momentum equations are then recast in the following form:

$$\int_\Omega \nabla W \cdot (\rho \tilde{v}^e) d\Omega = \int_\Gamma W \rho \tilde{v} \cdot \hat{n} d\Gamma \tag{3}$$

$$\int_\Omega \{W \rho \tilde{v}^e \cdot \nabla \vec{v} + \mu \nabla W \cdot \nabla \vec{v}\} d\Omega = -\int_\Omega W \nabla p d\Omega + \int_\Omega W \vec{F} d\Omega + \int_\Gamma W \mu \hat{n} \cdot \nabla \vec{v} d\Gamma \tag{4}$$

It shall be noted that the element-based nodal velocities have replaced the conventional nodal velocities in the following two distinct places. One is to satisfy the continuity equation, and the other is to serve as the gross fluid motion for the advective transport in the momentum equations. The concepts used here are quite similar to those in the collocated finite volume method where the cell-faced velocities serve essentially the same purposes.

Segregated Solution Algorithm

In this paper, the pressure and the velocity fields are solved in a sequential manner. At a global iteration, the momentum equations are first solved with guessed values of other degrees of freedom from the previous iteration. A pressure Poisson equation is then derived and solved. Finally, the new pressure field is used to obtain the divergence-free velocity fields. Bilinear shape functions are used to approximate all terms except the advection term where a perturbation term is added for stability using the streamline upwind petrov-Galerkin (SUPG) method (Brooks and Hughes, 1982). For the momentum equations, the discretization process first derives the element matrices due to convection, diffusion and source terms, and then put together all these contributions into a global matrix equation. Finally, the momentum equations are partially discretized in the following form:

$$a_{ii}^u u_i = -\sum_j^{j \neq i} a_{ij}^u u_j + f_i^u - \sum_e \int_{\Omega^e} W_i^e \left[\frac{\partial p}{\partial x}\right]^e d\Omega \tag{5}$$

$$a_{ii}^v v_i = -\sum_j^{j \neq i} a_{ij}^v v_j + f_i^v - \sum_e \int_{\Omega^e} W_i^e \left[\frac{\partial p}{\partial y}\right]^e d\Omega \tag{6}$$

where a_{ij} is the element of the coefficient matrix and f_i is the source term. Here, the subscript i represents a given node where the equations are discretized, the subscript j represents its neighboring nodes, and the superscript e represents its neighboring elements. In the above two equations, the pressure gradient terms are kept separate for the derivation of the pressure equation.

The velocity-pressure coupling equations are used to relate the velocity to the pressure, and they are obtained from a rearrangement of the partially discretized momentum equations:

$$u_i = \hat{u}_i - \frac{1}{a_{ii}^u} \sum_e \int_{\Omega^e} W_i^e \left[\frac{\partial p}{\partial x}\right]^e d\Omega \tag{7}$$

$$v_i = \hat{v}_i - \frac{1}{a_{ii}^v} \sum_e \int_{\Omega^e} W_i^e \left[\frac{\partial p}{\partial y}\right]^e d\Omega \tag{8}$$

where the expressions for $\hat{u}$ and $\hat{v}$ are given in the reference (Schnipke and Rice, 1985).

The element-based nodal velocities can be derived in a similar fashion except with local information within the corresponding element, e:

$$u_i^e = \hat{u}_i - G_x^e(p, a_{ii}^u)_i \tag{9}$$

$$v_i^e = \hat{v}_i - G_y^e(p, a_{ii}^v)_i \tag{10}$$

In this article, the element-based pressure gradient terms, $G_x^e(p, a_{ii}^u)_i$ and $G_y^e(p, a_{ii}^v)_i$, are weighted by the inverse of a_{ii}^u and a_{ii}^v, respectively. They are calculated by first integrating the pressure gradient within the element e, and then extrapolating these values over all elements containing the node i.

$$G_x^e(p, a_{ii}^u)_i = \frac{\sum_e \int_{\Omega^e} W_i^e d\Omega}{a_{ii}^u \int_{\Omega^e} W_i^e d\Omega} \int_{\Omega^e} W_i^e \left[\frac{\partial p}{\partial x}\right]^e d\Omega \tag{11}$$

$$G_y^e(p, a_{ii}^v)_i = \frac{\sum_e \int_{\Omega^e} W_i^e d\Omega}{a_{ii}^v \int_{\Omega^e} W_i^e d\Omega} \int_{\Omega^e} W_i^e \left[\frac{\partial p}{\partial y}\right]^e d\Omega \tag{12}$$

This way, the element-based nodal velocities will only depends on the local variations of the pressure gradient with the corresponding element, maintaining a tight coupling between the velocity and the pressure.

The formulation of the pressure equation is the most important ingredient of all segregate solution algorithms. The early equal-order implementation of the finite element method (Taylor and Hood, 1973) suffers from a spurious pressure mode referred to as checkerboard oscillations. Although the pressure oscillations can be prevented by unequal-order interpolation functions for the velocity and the pressure (Donea and Giuliani, 1981), unequal-order methods are derived in a way that the pressure field is interpolated from a function of one-order less accurate than those for the velocity field. Therefore, an equal-order implementation is desired for its accuracy.

When the pressure equation is derived from a continuous approach, the resulting equal-order method can successfully overcome the spurious checkerboard pressure distributions (Schneider et al., 1978; Schnipke and Rice, 1985). The derivation is based on an *ad hoc* assumption that the pressure gradient is constant over a given element in the velocity-pressure coupling equations. After taking the pressure gradient terms out of the integrals in equations (7) and (8), the two equations are substituted into the continuity equation to obtain a continuous equation for the pressure. The resulting pressure equation

can subsequently be discretized with the Galerkin methods using weighting functions of the same order with the velocities. One drawback of such continuous equal-order methods is that the discretization of the pressure in the pressure equation is not consistent with that in the momentum equations. As a result, the updated velocity field will not be able to satisfy both the continuity and the momentum equations at the same time. On the other hand, when the pressure equation is derived through substituting the discretized pressure gradient terms into the discretized continuity equation, the inconsistency can be removed between the pressure equation and the pressure gradient terms in the momentum equation. Unfortunately, this approach also gives rise to spurious checkerboard oscillations in the pressure field (Zienkiewicz et al., 1994; Comini et al., 1997).

In this article, the above dilemma will be resolved in a novel manner. The inconsistency between the two is removed through the introduction of element-based nodal velocities. These new velocities are made satisfy the continuity equation, whereas the conventional velocities satisfy the momentum equations. Consequently, a consistent formulation of the pressure equation is derived from the equations involving the element-based nodal velocities. Rather than using conventional velocity-pressure coupling equations, the present formulation substitutes the element-based nodal velocity-pressure coupling equations into the element-based continuity equation, and obtains the following equation.

$$\sum_e \int_{\Omega^e} \left[\frac{\partial W^e}{\partial x} \rho G_x^e(p, a_{ii}^u) + \frac{\partial W^e}{\partial y} \rho G_y^e(p, a_{ii}^v) \right] d\Omega = \sum_e \int_{\Omega^e} \frac{\partial W^e}{\partial x} \rho \tilde{u} + \frac{\partial W^e}{\partial y} \rho \tilde{v} d\Omega - \int_\Gamma W^\Gamma (\rho u)^\Gamma d\Gamma_x - \int_\Gamma W^\Gamma (\rho v)^\Gamma d\Gamma_y \quad (13)$$

The key step in the consistent discretization of the pressure equation is to obtain a continuous expression for the weighted pressure gradient operator within each element. To this end, the values are first evaluated at each vertex through numerical integration of equations (11) and (12). Here, the integration is performed using the four-point Gaussian quadrature for quadrilateral elements and the pyramid functions for triangular elements. The weighted pressure gradient operator is then expressed in terms of the shape functions in the normalized coordinates:

$$G_x^e(p, a_{ii}^u) = \sum_{i=1}^n N_i^e G_x^e(p, a_{ii}^u)_i = \sum_{i=1}^n \sum_{j=1}^n N_i^e g_x^e(a_{ii}^u)_{ij} p_j \quad (14)$$

$$G_y^e(p, a_{ii}^v) = \sum_{i=1}^n N_i^e G_y^e(p, a_{ii}^v)_i = \sum_{i=1}^n \sum_{j=1}^n N_i^e g_y^e(a_{ii}^v)_{ij} p_j \quad (15)$$

where $g_x^e(a_{ii}^u)_{ij}$ and $g_y^e(a_{ii}^v)_{ij}$ are the pressure gradient coefficients evaluated at the node i and contributed from node j. Here, the number of local nodes, n is equal to four for quadrilateral element and three for triangular elements.

The next step is to substitute the expressions for the weighted pressure gradient operator into equation (13), and integrate the equations over each element. The linear system for the pressure equations is then obtained by summing contributions to the coefficients and the source over all elements. It is important to keep the numerical integration of equation (13) consistent between the pressure coefficient in the left hand side and the first source term in the right hand side. In this paper, the two terms are integrated using the four-point Gaussian quadrature for quadrilateral elements and the pyramid functions for triangular elements. When a direct solver is used for Equation (13), the updated element-based nodal velocities will satisfy the discretized continuity equation exactly as shown below.

$$\sum_e \int_{\Omega^e} \left[\frac{\partial W^e}{\partial x} \rho u^e + \frac{\partial W^e}{\partial y} \rho v^e \right] d\Omega = \sum_e \int_{\Omega^e} \left[\frac{\partial W^e}{\partial x} \rho \left(\hat{u} - G_x^e(p, a_{ii}^u) \right) + \frac{\partial W^e}{\partial y} \rho \left(\hat{v} - G_y^e(p, a_{ii}^v) \right) \right] d\Omega = \int_\Gamma W^\Gamma (\rho u)^\Gamma d\Gamma_x + \int_\Gamma W^\Gamma (\rho v)^\Gamma d\Gamma_y \quad (16)$$

When an iterative solver is used, the error for the continuity equation is up to the convergence of the pressure equation. Further, if the solver fails to converge, element-based nodal velocities will not be able to conserve the mass. Therefore, it is crucial to select a robust iterative solver for the pressure equation in the collocated Galerkin method. In this work, the preconditioned BiCGStab(l) algorithm is used for the pressure equation (Werner, 2000). On the other hand, the conventional nodal velocities do not satisfy the continuity equation precisely, even when an exact solver is used for the pressure equation. The corresponding error of mass imbalance is of the same order in the spatial discretization.

NUMERICAL RESULTS

The accuracy of the collocated Galerkin method is evaluated for two different kinds of flow situations. One involves recirculating flows in an enclosed cavity driven by a moving wall at the top, and the other involves flow separation and reattachment due to an obstruction in a circular duct. The present method is also evaluated for a shear-driven flow in a triangular cavity with a free mesh.

Shear Driven Flow in a Square Cavity

The laminar flow in a square cavity has been favored by a number of researchers due to the simplicity of the geometry coupled with some interesting flow features (Ghia et al., 1982; Vanka, 1986). In this paper, the Reynolds number, based on the shear velocity at the top and the length of the cavity, is set to 100. The computational domain is mapped with non-uniform quadrilateral elements. Three meshes, employing 32x32, 64x64 and 128x128 elements respectively, are investigated here. In each case, the grid points are clustered near the walls in order to resolve the gradients that occur in the region of singularities at the top corners. It is found that the refinement near the corners plays an important role on the accuracy of the solution especially on the coarsest grid. Figure 1 shows the distribution of x-velocity along the vertical centerline of the cavity, and it is seen that even the coarsest grid of 32x32 elements gives good accuracy. The results of the two finer girds are indistinguishable. Figure 2 shows the variation of y-velocity along the horizontal centerline. The coarsest grid under-predicts the peaks of the y-velocity component, but grid independent solutions are achieved on the other two finer grids. The calculated results of x- and y-velocity components also agree well with previously reported results (Ghia et al., 1982; Vanka, 1986).

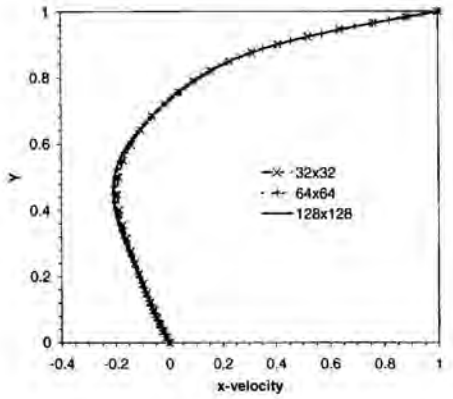

Figure 1: X-velocity profile along the vertical centerline.

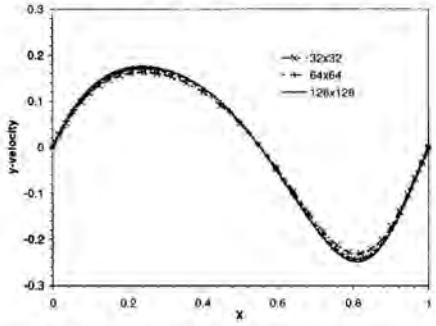

Figure 2: Y-velocity profile along the horizontal centerline.

Flow in a Circular Duct with a Constriction

In this example, laminar flow through a circular duct with an axisymmetric duct is considered. The computational geometry is chosen according to Ray and Date (2000), and the shape of the constriction is given as

$$\frac{r}{r_0} = 1 - \frac{\delta}{2r_0}\left[1 + \cos\left(\frac{\pi x}{X_0}\right)\right] \qquad (17)$$

where r_0 is the radius of the unconstricted duct and it is set to unity. Here, the amplitude δ is set to 2/3 and X_0 is set to 4.0. A fully developed velocity profile is specified at the inlet (x = -8.0) with a mean velocity (U_m) of unity, and the pressure is set to zero at the outlet (x = 50.0).

Figure 3 shows variations of the streamwise velocity in the radial direction at the line $x = X_0$ for a Reynolds number of 100. Here, the Reynolds number is defined as $\mathrm{Re} = 2U_m r_0 / \nu$. Three computational grids are used here, consisting of 46x10, 92x20 and 184x40 quadrilateral elements respectively. Figure 3 shows that the coarsest grid gives a good solution away from the center ($r = 0$), and it only under-predicts the peaks of the streamwise velocity by about 3% at the center. Although the results are almost indistinguishable on the two finer grids, calculations are performed on the finest grid at other Reynolds numbers to ensure accuracy.

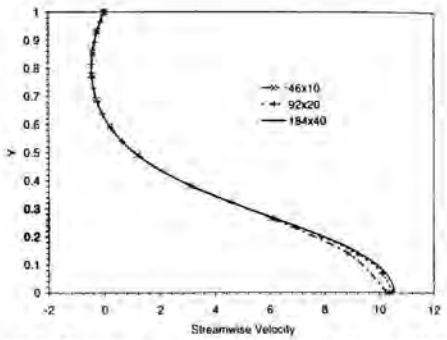

Figure 3: Streamwise velocity profile in the radial direction at the line x = X_0.

Tables 1 and 2 show the calculated separation and reattachment lengths for five different Reynolds number from 20 to 100. The results are compared with previous experimental data (Young and Tsai, 1973) and recent numerical results (Ray and Date, 2000). For the separation length, the present method agrees well with both the experimental and the other numerical data. For the reattachment length, on the other hand, the present method gives a better agreement with the experimental data than the other numerical results at the four higher Reynolds numbers. The largest difference from the experimental value is observed to occur at the Reynolds number of 20, and both the present method and the finite difference method by Ray and Date under-predict the reattachment length over 30%. At the three higher Reynolds numbers of 60, 80 and 100, the present solution agrees quite well with the experimental data, and the deviation from the experiment is less than 3%.

Table 1: Comparison of separation length.

Re	Experiment	Ray and Date	Present Method
20	0.49	0.496	0.508
40	**0.37**	0.358	0.360
60	**0.34**	0.307	0.316
80	**0.30**	0.288	0.292
100	0.29	0.276	0.275

Table 2: Comparison of reattachment length.

Re	Experiment	Ray and Date	Present Method
20	1.46	0.947	0.940
40	1.87	1.626	1.739
60	**2.54**	2.291	2.517
80	3.29	2.933	3.277
100	4.15	3.553	4.025

Shear Driven Flow in a Triangular Cavity

This example investigates the interesting features of laminar flow in a triangular cavity. This problem has been theoretically analyzed both in the inviscid regime (Batchelor, 1956) and in the Stokes regime (Moffat, 1963). The key feature of this flow is the appearance of an

infinite number of eddies toward the stationary corner. Sufficiently close to this corner, the flow is independent of the disturbances in the farther regions, and both the intensities and the locations of eddies will depend only on the geometric configurations (Moffat, 1963). Jyotsna and Vanka (1995) recently confirmed this interesting feature using a control-volume based finite-element method.

In this paper, the computational geometry and the coordinate system are selected to be the same with that used by Jyotsna and Vanka (1995). For this geometry, the height of the triangle is twice the length of the top wall. Two Reynolds numbers of 50 and 800 are considered here, and the results are compared with both the analytical and the numerical solutions. Here, the Reynolds number is defined with respect to the height of the cavity and the shear velocity of the top wall. The computational domain is mapped with unstructured triangular elements, and calculations are performed on three different grids consisting of 3594, 14538 and 58612 elements respectively. Figure 4 shows the variation of the x-velocity along the vertical centerline for the Reynolds number of 50. The results of the two finer girds are seen to be nearly the same, and even the coarsest grid of 3594 elements is able to provide a reasonable x-velocity distribution.

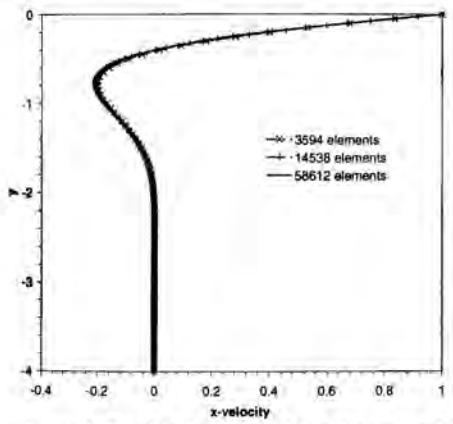

Figure 4: X-velocity profile along the vertical centerline.

Tables 3 and 4 compare the y-locations of the eddy centers with the numerical prediction of Jyotsna and Vanka (1995) for two Reynolds numbers of 50 and 800 respectively. Calculations are performed on the finest grid of 58612 elements to ensure accuracy. Rather than the graphical method used by Jyotsna and Vanka (1995), the present method determines the y-locations of the eddy centers by an interpolation procedure based on the x-velocity profile along the centerline. According to Jyotsna and Vanka (1995), centers of the lower three eddies lie along the centerline of the cavity. Therefore, the x-velocity shall vanish at the centers for those eddies, and the points where the curve intersects the y-axis coincide with the centers of those eddies. Therefore, an interpolation procedure is performed between two adjacent points where the x-velocity changes sign. For the topmost eddy, the eddy center moves to the right of the centerline due to inertial effects, and there will be some errors for the present interpolation procedure. However, the present interpolation procedure is still able to give a good approximation for the topmost eddy center since the distance between this center and the centerline is relatively small for the Reynolds numbers of 50 and 800. As seen in Tables 3 and 4 the present predictions of the y-locations of the eddy centers agree quite well with those of Jyotsna and Vanka (1995). Also listed in the two tables is the ratio of distances (Y_{i+1}/Y_i) from the lower corner between two adjacent eddies, where Y_i is the distance of the ith eddy center and the lower corner ($Y_i = y_i + H$). At Re = 50, the inertial effects are relatively less important, all eddy centers follow a geometric sequence, $Y_4/Y_3 = Y_3/Y_2 = Y_2/Y_1 = 2$, as determined by Moffat (1963). At Re = 800, the ratio between the two topmost eddy centers deviates from this ratio since the inertial effects are more important near the top wall at this Reynolds number. The other two ratios, on the other hand, follow this sequence, $Y_3/Y_2 = Y_2/Y_1 = 2$. This is consistent with Moffat's observation that the flow field near the stationary corner is independent of any disturbances far away from it.

Table 3: Location of the eddy center at Re = 50.

	Jyotsna and Vanka		Present Method	
	y_i	Y_{i+1}/Y_i	y_i	Y_{i+1}/Y_i
$i=1$	-3.550	N/A	-3.550	N/A
$i=2$	-3.092	2.018	-3.096	2.009
$i=3$	-2.182	2.002	-2.182	2.011
$i=4$	-0.395	1.983	-0.399	1.981

Table 4: Location of the eddy center at Re = 800.

	Jyotsna and Vanka		Present Method	
	y_i	Y_{i+1}/Y_i	y_i	Y_{i+1}/Y_i
$i=1$	-3.427	N/A	-3.426	N/A
$i=2$	-2.852	2.003	-2.846	2.010
$i=3$	-1.695	2.008	-1.685	2.006
$i=4$	-0.545	1.500	-0.576	1.479

SUMMARY AND CONCLUSION

ANSYS/FLOTRAN at release 6.0 has been enhanced with an original collocated Galerkin finite-element method. In this method, element-based nodal velocities are introduced to satisfy the conservation of mass exactly in the weak form, and the conventional nodal velocities are made to satisfy the conservation of momentum. The pressure and velocity fields are solved in a sequential manner, and an equal-order interpolation function is used for both the pressure and the velocity degrees of freedom. The pressure equation is derived in a novel way such that the discretization of the pressure in the pressure equation is consistent with that in the momentum equation. As a result, the updated element-based nodal velocities satisfy the mass conservation to the convergence of the governing equations. Computational predictions by this new scheme have shown good agreement with experimental, analytical and other numerical results in the three model problems.

ACKNOWLEDGEMENT

The author would like to thank his colleagues at the Multiphysics group for many helpful discussions throughout this development. Many thanks are owed to Mr. Wolfgang Werner and Prof. Artur Walter for providing the preconditioned BiCGStab(*l*) algorithm.

REFERENCE

Baliga BR and Patankar SV. "A New Finite Element Formulation for Convection Diffusion Problems." Numerical Heat Transfer, vol. 3, pp. 393-409, 1980.

Batchelor GK. "On Steady Laminar Flow with Closed Streamlines at Large Reynolds number." *Journal of Fluid Mechanics*, vol. 1, pp. 177-190, 1956.

Brooks AN and Hughes JTR. "Streamline UpWind / Petrov-Galerkin Formulations for Convective Dominated Flows with Particular Emphasis of the Incompressible Navier-Stokes Equations." *Computer Methods for Applied Mechanics and Engineering*, vol. 32, pp. 199-219, 1982.

Comini G and Guidice SD. "A Physical Interpretation of Conventional Finite Element Formulations of Conduction-Type Problems." *International Journal for Numerical Methods in Engineering*, vol. 32, pp. 559-569, 1991.

Comini G, Minkowycz WJ and Shyy W. "General Algorithms for the Finite Element Solution of Incompressible Flow Problems Using Primitive Variables." In Advances in Numerical Heat Transfer, Volume 1. (Edited by Minkowycz W.J. and Sparrow E.M.) Taylor & Francis, 1997.

Du Toit CG. "Finite Element Solution of the Navier-Stokes Equations for Incompressible Flow Using a Segregated Algorithm." *Computer Methods in Applied Mechanics and Engineering*, vol. 151, pp. 131-141, 1998.

Ghia U, Ghia KN and Shin CT. "High-Re Solutions for Incompressible Flow Using the Navier-Stokes Equations and a Multigrid Method." *Journal of Computational Physics*, vol. 48, pp. 387-411, 1982.

Harlow FH and Welch JE. "Numerical Calculation of Time-Dependent Viscous Incompressible Flow of a Fluid with Free Surface." *Physics of Fluids*, vol. 8, pp. 2182-2189, 1965.

Jyotsna R and Vanka SP. "Multigrid Calculation of Steady, Viscous Flow in a Triangular Cavity." *Journal of Computational Physics*, vol. 122, pp. 107-117, 1995.

Moffat HK. "Viscous and Resistive Eddies Near a Sharp Corner." *Journal of Fluid Mechanics*, vol. 18, pp. 1-18, 1963.

Patankar SV and Spalding DB. "A calculation procedure for heat, mass and momentum transfer in three-dimensional parabolic flows." *International Journal of Heat and Mass Transfer*, vol. 15, pp. 1787-1806, 1972.

Peric M, Kessler R and Scheuerer G. "Comparison of Finite Volume Numerical Methods with Staggered and Collocated Grids." *Computers and Fluids*, vol. 16, pp. 389-403, 1988.

Prakash C and Patankar SV. "A Control-Volume-Based Finite-Element Method for Solving the Navier-Stokes Equations Using Equal-Order velocity-Pressure Interpolation,." *Numerical Heat Transfer*, vol. 8, pp. 259-280, 1985.

Ray S and Date AW. "A Calculation Procedure for Solution of Incompressible Navier-Stokes Equations on Curvilinear Non-Staggered Grids." *Numerical Heat Transfer, Part B*, vol. 38, pp. 93-131, 2000.

Rhie CM and Chow WL. "Numerical Study of the Turbulent Flow Past an Airfoil with Trailing Edge Separation." *AIAA Journal*, vol. 21, pp. 1525-1532, 1983.

Saabas HJ and Baliga BR. "Co-Located Equal-Order Control-Volume Finite-Element Method for Multidimensional, Incompressible, Fluid Flow – Part 1, Formulation." *Numerical Heat Transfer, Part B*, vol. 26, pp. 381-407, 1994.

Schneider GE and Raw MJ. "Control Volume Finite-Element Method for Heat Transfer and Fluid Flow Using Colocated Variables - 1, Computational Procedure." *Numerical Heat Transfer*, vol. 11, pp. 363-390, 1987.

Schneider GE, Raithby GD and Yovanovich MM. "Finite Element Solution Procedure for Solving the Incompressible Navier-Stokes Equations Using Equal-order Variable Interpolation." *Nemerical Heat Transfer*, vol. 1, pp. 415-451, 1978.

Schnipke RJ and Rice JG. "Application of a new finite element method to convection heat transfer." Fourth International Conference on Numerical Methods in Thermal Problems, Swansea, U.K., July 1985.

Taylor C and Hood P. "A Numerical Solution of the Navier-Stokes Equations Using the Finite Element Techniques." *Computers and Fluids*, vol. 1, pp. 73-100, 1973.

Vanka SP. "Block-Implicit Multigrid Solution of Navier-Stokes Equations in Primitive Variables." *Journal of Computational Physics*, vol. 65, pp. 138-158, 1986.

Wang G. "A Fast and Robust Variant of the SIMPLE Algorithm for Finite-Element Simulations of Incompressible Flows." the First MIT Conference on Computational Fluid and Solid Mechanics, Cambridge, MA. June 12-15, 2001.

Werner W. Iterative solution for sparse linear systems from CFD problems. (in German) M.S. Thesis, University of Applied Sciences, Stuttgart, 2000.

Williamson D. "Numerical Integration of Fluid Flow Over Triangular Grids." *Monthly Weather Review*, vol. 97, pp. 885-895, 1969.

Winslow AM. "Numerical Solution of the Quasilinear Poisson Equation in a Nonuniform Mesh." *Journal of Computational Physics*, vol. 2, pp. 149-172, 1967.

Young DF and Tsai FY. "Flow Characteristics in Models of Arterial Stenoses – I. Steady Flow." *Journal of Biomechanics*, vol. 6, pp. 395-410, 1973.

Zienkiewicz OC and Taylor RL. The Finite Element Method, 4th Edition, vol. 1, McGraw-Hill, London, 1989

HEFAT2002
1st International Conference on Heat Transfer, Fluid Dynamics and Thermodynamics
8-10 April 2002, Kruger National Park, South Africa
HF1

EXPERIMENTAL STUDY OF AERODYNAMIC CHARACTERISTICS ABOUT A FIXED-WING MICRO AERIAL VEHICLE

Fei-Bin Hsiao*, Ming-Hao Yang and Cheng-Chiang Hsu
Institute of Aeronautics and Astronautics, National Cheng Kung University, Tainan, Taiwan
Chao-Yih Chen and Pei-Fang Liang
Center for Aerospace Science and Technology, Industrial Technology Research Institute, Hsinchu, Taiwan
***Tel: (+886)6-2757575 ext 63667, Fax: (+886)6-2389940**
***E-mail: fbhsiao@mail.ncku.edu.tw**

ABSTRACT

The aerodynamic characteristics of a fixed-wing micro aerial vehicle (MAV), named Creator, are studied by wind tunnel measurements and water tunnel flow visualization. The Creator is a box-type, biplane MAV with the lower wing to produce the main lift and the upper wing to act as a horizontal stabilizer. Both wings have the airfoil section of SD7062(B). The design flight speed is less than 12 m/sec, which is much lower than the low Reynolds number (Re) range based on the wing chord. The experimental results indicate that the aspect ratio (AR) of the main wing has a very strong influence on the flow behaviors above the wing surface, and seriously affect the aerodynamic properties of the entire vehicle. In addition, due to the low Reynolds number effect, a very pronounced circulating bubble will be formed on the top of the wing surface at the low angle of attack range, which will in turn trigger severe flow separation at higher angles of attack to deteriorate the vehicle's aerodynamics. In order to provide enough aerodynamic properties for MAV Creator's design phases, this paper is therefore in particular to emphasize on the aerodynamic characteristic study of wings at low Reynolds number and low aspect ratio.

KEYWORDS

Micro Aerial Vehicle, Low Reynolds Number Aerodynamics, Flow Visualization, Wind Tunnel Test

INTRODUCTION

The wide and ample applications of unmanned aerial vehicles (UAV) have been quickly adopted for usage in many areas, in particular, in military and civil aspects. This is simply due to the nature of unmanned on board the plane and less lethal to the human beings involved while operations. It is therefore getting more important of research and development in unmanned vehicle study today. For the past few years, there is another need of applications from various situations that the usage of hand-held sized, light weight, but still maneuverable unmanned vehicle has arouse to capture the focal attractions in special missions. The potential missions for requiring the so-called Micro Aerial Vehicle (MAV) may include the execution of remote data/image acquisition, approaching to hazardous, chemical-contaminated, restricted areas, some unknown dangerous sites, or for surveillance and reconnaissance, etc. To achieve such limited, unique missions, and perhaps easy to be carried along and stored in the pocket of a person, a miniaturized UAV or called MAV is hence proposed and have immediately become a focal research topic in academia and military agencies for the past few years [1, 2, 3]. The Remotely Piloted and Micro Satellite Research Laboratory (RMRL) in the Institute of Aeronautics and Astronautics (IAA) in National Cheng Kung University (NCKU) has devoted to the academic research and development of unmanned vehicles for many years [4, 5]. The recent mission concerning the MAV project in RMRL is particularly emphasized on the development of a micro vehicle which has the capability of transporting a small CCD camera onboard the vehicle, real-time image data transmission, and low cost in production.

Because the micro aerial vehicle is a new flying vehicle and still under investigations in many sectors and agencies, there is a worldwide MAV design and flight competition, which is held annually and sponsored by ISSMO [1], to

promote the public interest and attract research activities. The typical papers can be referred to the reference [6, 7, 8], which in general is contributed from the industries and the university student projects. Due to the small size in wing span and usually low flight speed, the aerodynamic properties of MAV will commonly become big challenges in providing enough aerodynamic forces and moments for balancing its weight and flying stability [9]. The low Reynolds number and low aspect ratio wing are the key issues in question and needs further thorough investigations, which, in fact, easily induces poor aerodynamic efficiency. Meanwhile, it is still lack of understanding in improving the MAV's aerodynamic performance in the current literature, and needs urgent investigations into acquiring the new information as much as possible. Physically, the low aspect ratio wing will induce and trigger more 3-D flow phenomena after the leading edge of the wing, which will cause some difficulties in predicting the aerodynamic properties [10, 11]. In addition, as the MAV usually flies in the low Reynolds number range, i.e. $Re<10^6$, the following characteristics of the wing need very special care in study: (1) laminar separation bubble including laminar separation location and reattachment, (2) transition, and (3) turbulent separation and reattachment. The occurrence of flow separation will increase the drag force, decrease the stall angle of wing and induce the poor performance of the vehicle.

In the present study in this paper, an MAV named Creator is designed and investigated concerning its aerodynamic properties through the wind tunnel and water tunnel testing. The cruise speed of Creator is 11.5 m/sec and the wingspan is 30cm having the airfoil section of SD7062(B). Figure 1 shows the configuration of the Creator, which is indeed a box-typed, bi-plane vehicle. For the wind tunnel and water tunnel tests, several wing models are used at various aspect ratios with the same airfoil section. The flow structures over the wing will be especially investigated through visualization technique in a water tunnel.

EXPERIMENTAL SETUP OF WATER AND WIND TUNNEL TESTS

Apparatus for Water Tunnel Tests

Flow visualization is carried out in a water tunnel, which is a closed type tunnel. A water pump manually controls the water flow velocity in the test section. The dye-injection technique and watercolor spot technique are employed to visualize the flow structures around the wing models. The setup of the water tunnel and its accessories is shown in Figure 2. A digital camera made by Ricoh, RDC-2, is used to record pictures of the flow patterns. In this water tunnel experiments, the aspect ratios of the wing models include 0.2, 0.5 and 1, all having the same airfoil section of SD7062(B). Before proceeds the flow visualization, the flow velocity is calibrated by counting the vortex frequency shed from a small circular cylinder located in the test section of the water tunnel. An assumption is made that the water flow velocity is proportional to the cylinder diameter, based on the constant Strouhal number approximation in the Reynolds number range operated in the current study. In the flow visualization, the water is fixed at 11.6 cm/sec and the chord length of the model is fixed at 18 cm as well. Therefore, the corresponding Reynolds number based on the wing chord is 1.89×10^4.

Apparatus for Wind Tunnel Tests

The wind tunnel experiments are conducted in the subsonic wind tunnel, which is an open suction type and the geometric contraction ratio of the nozzle is 9:1. The wing model used in the experiments is also SD7062(B) airfoil and the aspect ratios of the wing include 1.66 and 3.33. The flow velocity ranges between 0~21 m/sec, which is adjusted by an electric motor manually controlled by a frequency inverter, and is measured by the pitot-static tube with a pressure transducer. The force/moment sensor used to measure the lift and drag forces of the wing is made by Chung-Shan Institute Science and Technology, which is a three-component strain-gage balance of bending beam type. The measurement data acquisition systems are Wavebook/512 Analog/Digital (A/D) conversion and Personal Computer (PC). The sampling rate of the A/D converter is set at 300 Hz per sample. Figure 3 displays all the experimental devices as related to the wind tunnel measurements. The experimental procedures are described as follows:

(1) Measure the lift and drag forces of the supporting device;
(2) Fix the wing model on the supporting device and then take the balance data from the A/D converter;
(3) Change the wing velocity by frequency converter for conducting the model of 60 cm in wingspan and AR=3.33, and another model of 30 cm in wingspan and AR=1.67;
(4) Record all aerodynamic data for further analysis.

It should be noted that, in order to avoid the measurements of the lift and drag forces from over the force limits of the balance, the maximum wind speed for the AR=3.33 wing model is limited. Table 1 shows the model and flow conditions for the wind tunnel measurements.

EXPERIMENT RESULTS AND DISCUSSION

As mentioned previously, the micro aerial vehicle (MAV) is usually small in size and lower cruise speed in comparison with the normal airplanes [12]. Therefore, the aerodynamic characteristics of the MAV should be as small as a human palm and usually flies in the range of low Reynolds number, for which the Reynolds number is commonly less than 10^5 as shown in Table 1. This paper hence makes emphasis on the study of the flow behaviors

for low aspect ration wing at low Reynolds number. The nature of the flow behaviors is investigated in a water tunnel, and the lift and drag forces are measured in a wind tunnel. In addition, the results from the wind tunnel experiments will be further explained through the flow visualization in the water tunnel testing.

Flow Visualization of Wing Models

In the flow visualization, three aspect ratios of the wing models are investigated at the water flow velocity of 11.6 cm/sec with the Reynolds number of 1.89×10^4. Figure 4 depicts a typical flow pattern, tagged by the dye traces ejected from the leading edge of the wing, showing the flow separation phenomena at low angle of attack case. The dye stream clearly exhibits the flow with laminar separation and reattachment when it passes over the wing model. Due to flow diffusion, the dye is getting smeared out as approaching the trailing edge of the model. Therefore, the dye injection technique is replaced by using the watercolor spot to directly applying on the top surface of the models. As the water passes by to scrape the surface, the watercolor spots hence will be slowly diffusing its color to form a sort of dye traces above the model surface. Figure 5 is obtained using this technique, which also shows the flow pattern results for the aspect ratios of 0.2, 0.5 and 1, respectively. Figures 5-(a)~(c) clearly reveal the flow being reserved in the middle section of the model, in which the reversed-pressure gradient shall take place in the flow field. In particular, a separation bubble significantly persists in the middle for AR=0.2, showing a very strong three-dimensional (3-D) effect is created from both ends of the model, from which the tip vortices are formed. The middle bubble zone gets bigger and wider when the aspect ratio of the model is higher. Note that the existence of the negative pressure gradient to form the flow separation in flow field matches very well with the result in Figure 4, where the separation bubble does exist on the airfoil. In addition, the 3-D effect is further investigated through injecting the dyes near the leading edge of the wing for detailed visualization. The results for the 3-D effect at different aspect ratios are shown in Figure 6. The difference between Figures 6-(b) and (c) are originated from the results at different angles of attack. Through Figure 6-(b) and (c), the 3-D effects are strongly prevailing at high angle of attack, which is also gradually decreased by increasing the aspect ratio of the wing.

Therefore, the leading edge vortex is clearly influenced by the increasing strength of the vortices from both sides of the wing. The strength of the side edge vortices gets stronger when decreasing the aspect ratio and increasing the angle of attack. Then, the leading edge vortex is moving toward the middle portion of the wing due to the generation of stronger strength over the wing.

Aerodynamic Investigations of Wing Models

The main wing used for the Creator MAV is also investigated in the wind tunnel. Here, two different wing models are tested. In the wind tunnel testing, a force balance is employed to measure the lift and drag forces with variations of Reynolds number and angle of attack (AOA) as well. The operating conditions for the wind tunnel testing are shown in Table 1. The force data are then used to calculate the lift and drag coefficients through the conventional non-dimensional normalization. The results of lift and drag coefficients with Reynolds number and AOA are respectively shown in Figure 7 till 13. In Figure 7 for AR=1.67 at lower Reynolds number below 50000 when the angle of attack is over the stall angle, the lift coefficient variation with angle of attack is very small. One thing very interesting is that the result of the lift coefficient is very much unlike the traditional one, where the value of lift changes very rapidly in the small angle of attack range. This could be due to a strong 3-D effect from the both sides of the wing to induce a sudden jump of lift when the AOA is increased. In addition, the lift coefficient increases a little bit after the stall angle. Except for the result of lift in Figure 7, the rest of the lift coefficients exhibit a very normal behavior in variation with AOA for various Reynolds numbers tested. All lift curves behave linearly at the lower AOA range, where the flow is only partially separated from the wing surface, and then starts to be separated from the surface and then attached subsequently when the bobble takes place somewhere over the wingspan, or the flow simply continues to be detached when the AOA is over the stall angle. Results also indicate that the maximum lift coefficient occurs when the AOA is at the stall angle, and the maximum lift increases a little bit with the increase of AOA. In addition, the stall angle ranges between 2 – 12 degrees and is strongly influenced by the Reynolds number, as shown in Figure 14. The stall angle is very small at small Reynolds number but almost linearly increased with the Reynolds number and then becomes a plateau value around the Reynolds number being 1×10^5, as shown in Figure 14. Furthermore, the stall angle for AR=1.66 at the same Reynolds number is larger or equal than the one of AR= 3.33. Shown in Figure 15 is the result of the maximum lift coefficient, in which the maximum lift coefficient is increased with the increase of the aspect ration, and increased with the Reynolds number as well until the value reaches a saturation when Reynolds number is about 1×10^5.

CONCLUDING REMARKS

In this paper, the flow behaviors and aerodynamic characteristics of wing models used for a micro aerial vehicle (MAV) are respectively studied in a wind tunnel and a water tunnel. The lift and drag coefficients are obtained through wind tunnel measurements, while the flow structures and separation behaviors of the wing

models are visualized in use of a water tunnel, which also help to explain the measurement data. In wind tunnel measurements, the untraditional behavior of lift curve variation with angle of attack for low aspect ratio and low Reynolds number seems to originate from the 3-D effect, such as when the aspect ratio is equal to 1.67 and the Reynolds number below 50000. When the Reynolds number is higher than 50000, the lift curve behavior becomes normal and like any other results in a traditional wing. Therefore, the results show that when the flow speed and aspect ratio is low, the flow field is strongly affected by the 3-D rotational flow, which comes from the tip vortices to enhance the leading edge vortex and to translate energy and help to stabilize the separation bubble to fix and prevent it from extending to the tailing edge. This phenomenon can be seen in water tunnel visualization, when the aspect ratio is small and the separation bubble is clipped by the leading edge vortex. For the SD7062(B) airfoil is concerned, the separation behavior belongs to the long separation bubble, and the stall will occur when the bubble is extended to the trailing edge of the airfoil. In this way, the stall angle for the low aspect ratio is larger and, in this experiment, the stall angles at the aspect ratio of 1.66 and 3.33 indeed shows not too much difference with the Reynolds number operated.

In MAV design process, if the flight Reynolds number is in the region of 50000, the designer has to be careful about the aerodynamic performance of the wing used. Because the stall angle is very small, in order to avoid the wing stall rapidly, the best choice for the designer is to choose a wing with a lower aspect ratio. In this way, nonetheless, the drag force is increased and the engine power accordingly has to be large enough. However, the increase of the engine size will prevent the payload from loading the vehicle. Therefore, some flow control method may be needed in the design phase of MAV. In addition, the study on low Reynolds number at low aspect ratio wing has to be studied in further detail to improve the aerodynamic performance of MAV.

ACKNOWLEDGEMENTS

This work is supported in part by a research grand funded by the Center for Aerospace Science and Technology, Industrial Technology Research Institute, and the National Science Council, Taiwan, under Contract No. NSC 89-2218-E-006-107.

REFERENCES

1. The International Society of Structure and Multidisciplinary Optimization (ISSMO), http://www.aero.ufl.edu/~issmo/
2. DARPA, Defense Advanced Research Project Agency, http://www.darpa.mil/
3. University of Florida, http://www.aero.ufl.edu/~domenico/mav/index.html
4. Hsiao, F.B. and Lee, M.T., "The Development of Unmanned Aerial Vehicle in RMRL/NCKU," 4th Pacific International Conference on Aerospace Science and Technology, Kaohsiung, Taiwan, May 21-23, 2001.
5. Guan, W.L., Hsiao, F.B., Ho, C.S., and Huang, J.M., "Development of Low-Cost Differential Global Positioning System for Remotely Piloted Vehicles," AIAA Journal of Aircraft, Vol. 36, No. 4, pp. 617-625, July-August, 1999.
6. Masoud, R.R., "Multidisciplinary Design, Construction, and Flight Testing of a Remotely Piloted Micro Reconnaissance Airplane (Final Report)," ISSMO Report, 1998.
7. Moeis, S.J., "Design and Flight Test Result for Micro-sized Fixed Wing and VTOL Aircraft," MLB Co. Report, 1999.
8. Gabrial, T. and Muller, T.J., "Micro Aerial Vehicle Development: Design, Components, Fabrication, and Flight Testing," ISSMO Report, 2000.
9. Grasmeyer, J.M. and Keennon, M.T., "Development of the Black Widow Micro Aerial Vehicle," AIAA Paper no. 2001-0127, Reno, NV, January 2001.
10. Hsiao, F.B., Liu, C.F. and Tang, Z., "Experimental Studies of Airfoil Performance and Flow Structures on a Low Reynolds Number Airfoil", AIAA Journal, Vol. 27, No. 2, Feb. 1989, pp. 129-137.
11. Hsiao, F.B. and Hsu, C.C., "Numerical Prediction of Aerodynamic Performance for Low Reynolds Number Airfoils," Journal of Aircraft, Vol. 26, No. 7, July 1989, pp. 689-692.
12. Tennekes, H., "The Simple Science of Flight, From Insects to Jumble Jets," 2nd Ed., MIT Cambridge, MA, 1996.

Span=30 AR=1.67		Span=60 AR=3.33	
Re(1.0e+5)	V	Re(1.0e+5)	V
0.313	2.53	0.323	2.66
0.419	3.4	0.415	3.44
0.483	3.92	0.495	3.95
0.572	4.64	0.586	4.74
0.657	5.33	0.658	5.48
0.728	5.91	0.732	6.05
0.819	6.65	0.807	6.77
0.904	7.33	0.921	7.19
0.981	7.96	1	8.17
1.06	8.66	1.06	8.76
1.15	9.35	1.15	9.36
1.24	10.06	1.27	10.04
1.3	10.55		
1.42	11.5		
1.49	12.11		
1.54	12.49		
1.63	13.2		

Creator Flight Condtion

Table 1 Wind tunnel measurement experiment

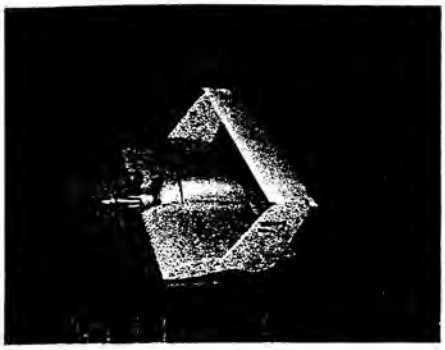

Figure 1: Designed MAV named Creator

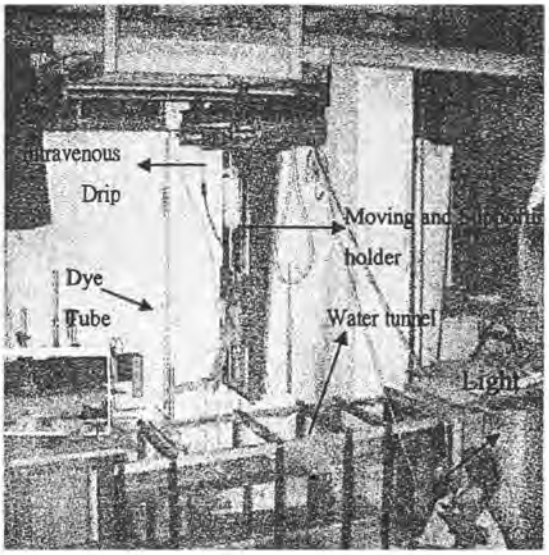

Figure 2: Equipment and accessories for water tunnel

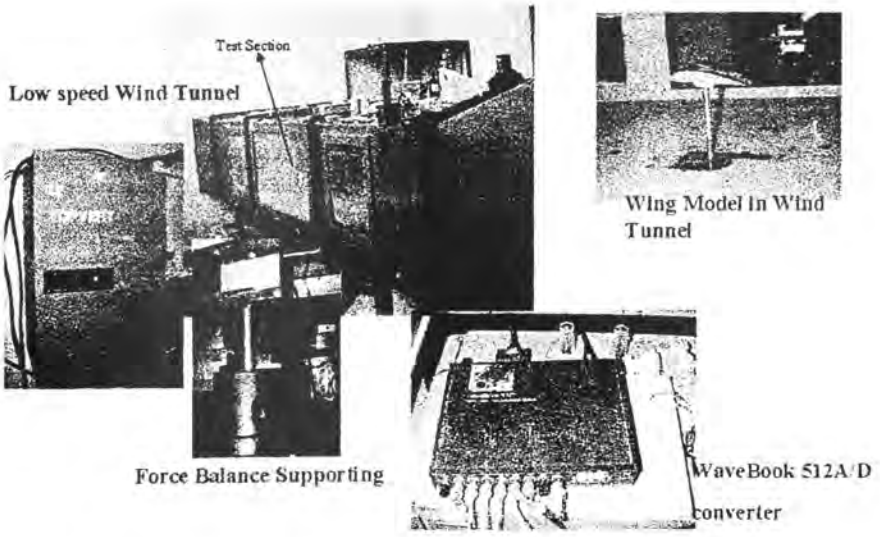

Figure 3: Equipment and accessories for wind tunnel

Figure4: Flow separation behaviors at $Re=1.89\times10^4$

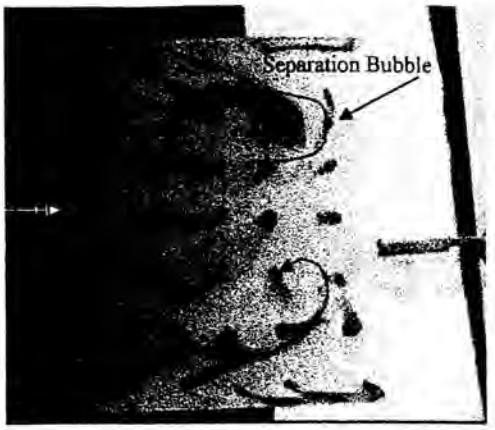

(c)

Figure 5: Flow pattern on wing surface for (a) AR=0.2 (b) AR=0.5 (c) AR=1

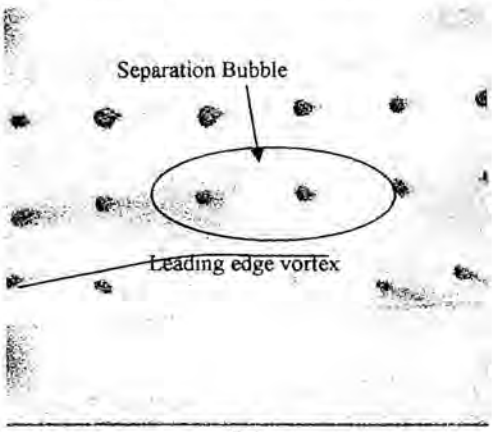

(a)

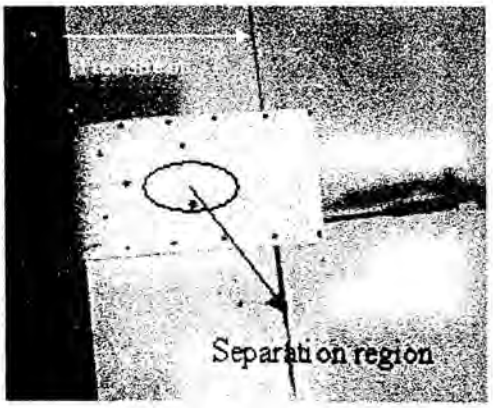

(b)

(a)

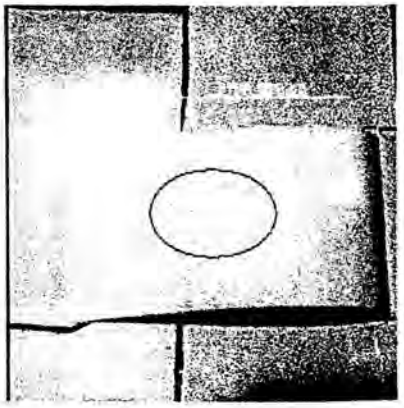

(b)

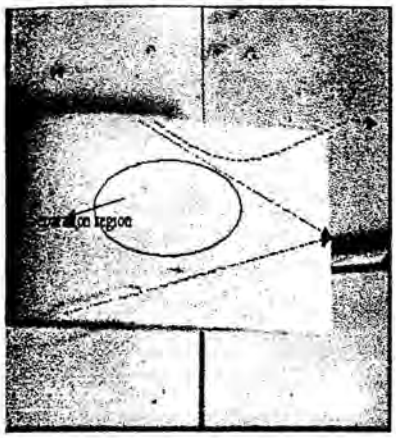

(c)

(d)

Figure 6: 3-D effect for (a) AR=0.2 (b) AR=0.5 at low AOA; (c) AR=0.5 at light AOA; (d) AR=1

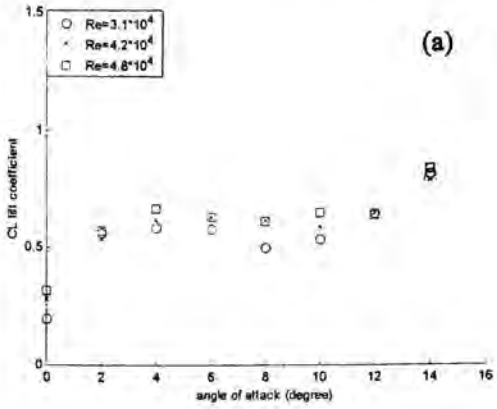

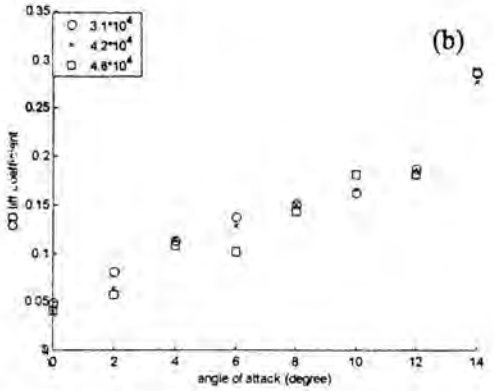

Figure 7: Variations of lift and drag coefficient with angle of attack at Re=3.12~4.8 × 10^4 for AR=1.67

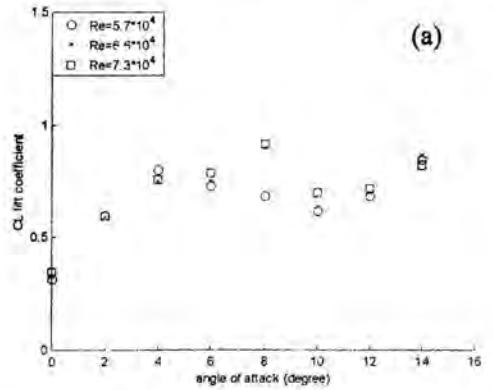

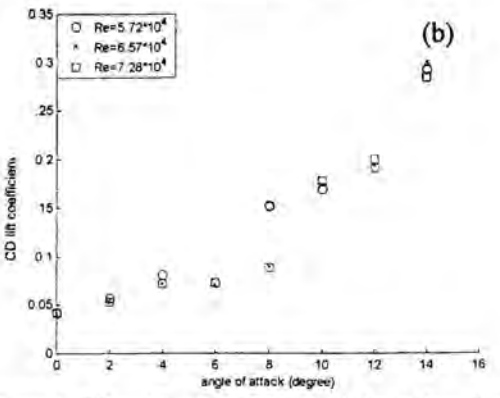

Figure 8: Lift and Drag coefficient variation with angle of attack at Re=6.7~7.3 × 10^4 for AR=1.67

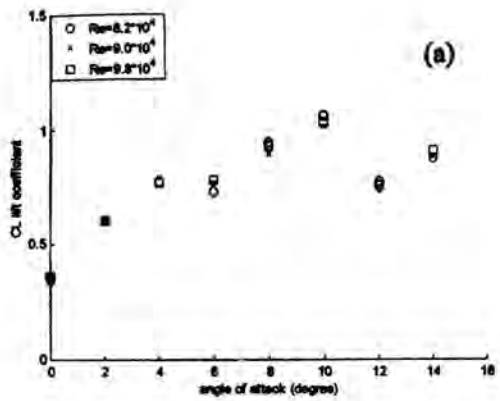

Figure 9-a Lift coefficient variation with angle of attack at Re=8.2~9.8× 10^4 for AR=1.67

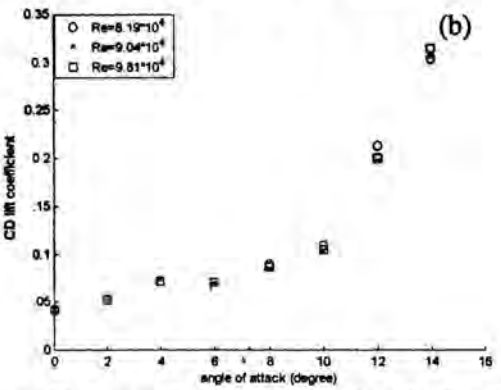

Figure 9-b Drag coefficient variation with angle of attack at Re=8.2~9.8× 10^4 (AR=1.67)

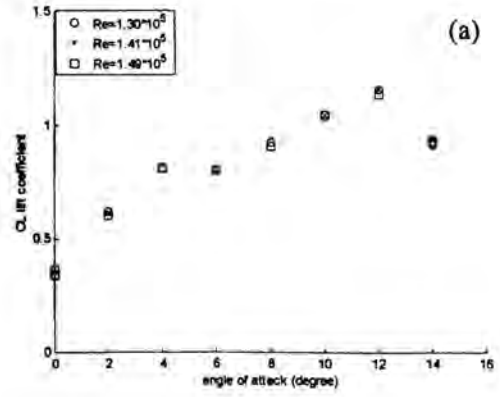

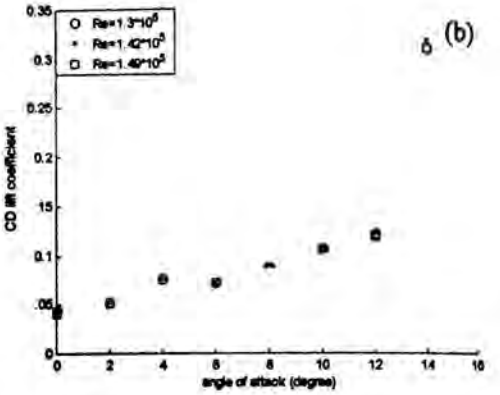

Figure 10 Lift and drag coefficient variation with angle of attack at Re=1.3~1.5× 10^5 (AR=1.67)

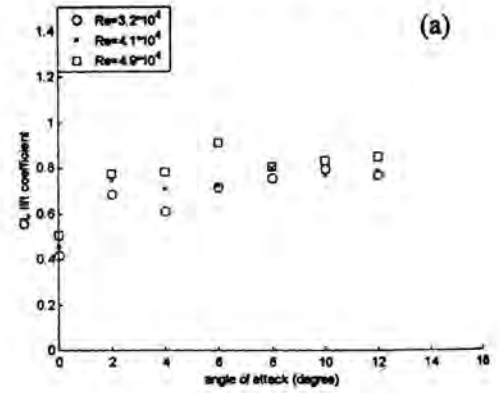

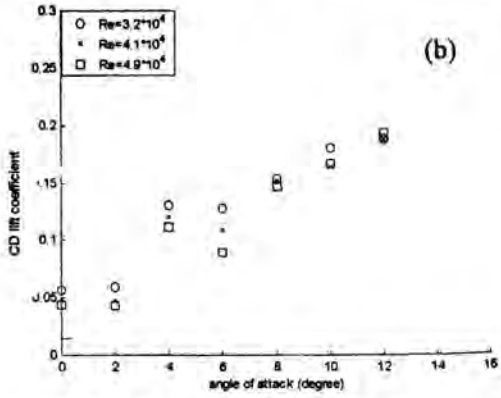

Figure 11 Lift and drag coefficient variation with angle of attack at Re=3.2~4.9× 10^4 (AR=3.33)

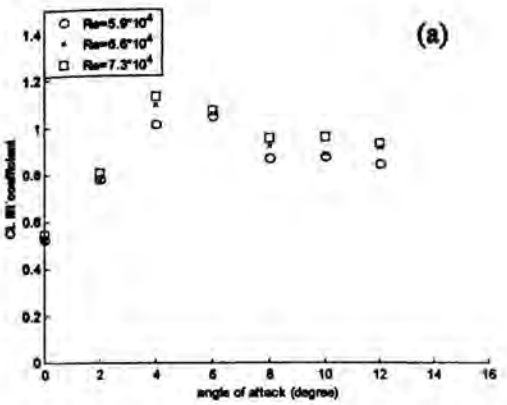

Figure 12-a Lift coefficient variation with angle of attack at Re=5.9~7.3 × 10^4 (AR=3.33)

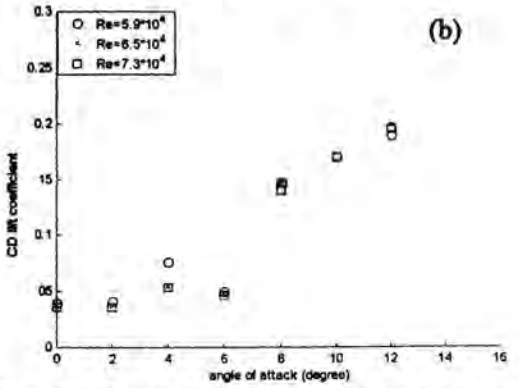

Figure 12-b Drag coefficient variation with angle of attack at Re=5.9~7.3 × 10^4 (AR=3.33)

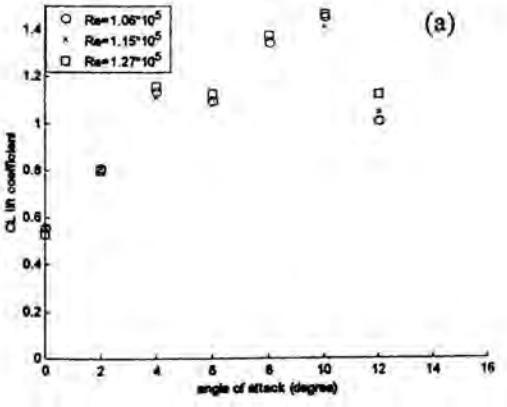

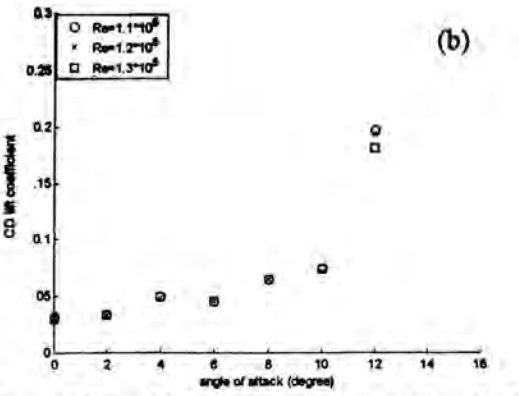

Figure 13 Lift and drag coefficient variation with angle of attack at Re=1.1~1.3 × 10^5 (AR=3.33)

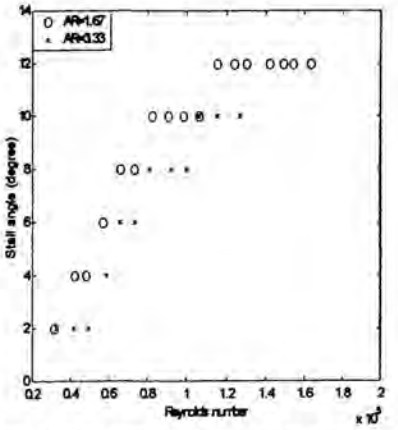

Figure 14 Stall angle variations with Reynolds number

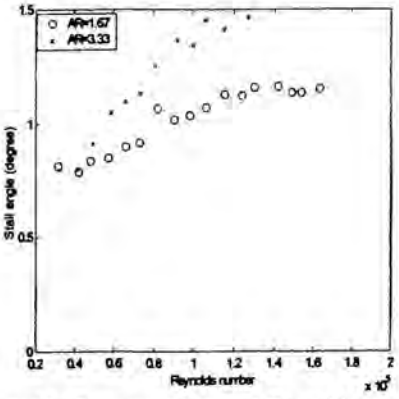

Figure 15 $C_{L_{MAX}}$ variations with Reynolds number

HEFAT2002
1st International Conference on Heat Transfer, Fluid Mechanics, and Thermodynamics
8-10 April 2002, Kruger Park, South Africa
KM1

INFLUENCE OF ASPECT RATIO ON THE DYNAMIC CHARACTER OF END-WALL FLOW

Mohammad Javed Khan
mjkhan@tusk.edu
Associate Professor, Aerospace Science Engineering Department
Tuskegee University, AL 36088
Anwar Ahmed
aahmed@eng.auburn.edu
Associate Professor, Aerospace Engineering Department
Auburn University, AL 36849

ABSTRACT

Flow in the end-wall junction of a NACA 0015-based wing mounted on a flat surface was experimentally investigated for the influence of aspect ratio and tip-geometry. A total of eleven aspect ratios from 1 to 10.6 were tested in a water tunnel through a Reynolds number range of 2300-4800 so as to capture the characteristics in all the three main regimes for such a flow. The transition from a static vortex system to a dynamic system was observed to be occurring at lower Reynolds number with increasing aspect ratio. The flow became insensitive to aspect ratios of 3.6 and higher. Sensitivity of the primary separation point to aspect ratio was also observed. Wing tip geometry did not influence the flow character.

INTRODUCTION

Flow in the end-wall region of 'wing-body' configurations has been the subject of extensive investigations. This geometry is observable in many forms e.g. submarine hull-appendage, blade-hub, wing-pylon and of course as wing-fuselage configurations etc. Flow in the end wall region of a surface mounted obstacle is dominated by a complex three-dimensional flow with a system of vortices imbedded in it. This three-dimensionality is imparted to the flow when a nominally two-dimensional boundary layer approaches a surface mounted obstacle. A pressure-gradient imposed on the boundary layer due to streamlines curvature around the obstacle introduces a cross-flow in the lower region of the boundary layer and the boundary layer becomes three-dimensional in character. This phenomenon has been termed as 'secondary flow of the first kind'[1]. Secondary flow of the 'second kind' is also present in such geometries in case of turbulent flows. However, such secondary flow manifests itself in the corner region and is therefore observable downstream of the leading edge[2,3]. Additionally the three-dimensional boundary layer separates upstream of the obstacle due to the adverse pressure imposed by the obstacle. The separated boundary layer rolls up into a system of vortices and wraps around the obstacle in the classical 'horse-shoe' pattern. Figure 1 is a simple schematic of the phenomena.

Characteristics of flow in the end-wall region are primarily dependent on Reynolds number[4,5] and is characterized primarily by three regimes[5], which are: a steady system of vortices, an oscillating system and shedding system transitioning from one to the other with increasing Reynolds number. The number of vortices in the steady regime depends on the Reynolds number varying from one at very low Reynolds numbers (eg starting flow) to a maximum of three. In the other two regimes, which are: oscillatory about a mean, and shedding, the number of vortices oscillates between three and four.

Flow in the end-wall however is dependent upon certain geometric factors as well e.g. sweep[6] and aspect ratio etc. The influence of aspect ratio for a cylinder mounted on a flat plate has been investigated by Kawamura et. al[7]. (Fig. 2). They reported the presence of von Karman vortex shedding for aspect ratios larger than 4. The configuration also exhibited an oblique up-wash towards the free end of cylinder. Flow separation at the front edge of the free-end along with a blow-down forming a pair of trailing vortices were observed by them in addition to the juncture vortex. Okamoto and Sunabashiri[8] reported an augmentation of the down-wash from the free end of the cylinder due to the influence of the juncture vortex system for

cylinders with aspect ratios of 2 and lesser. They further observed that as the aspect ratio was increased, the size of the juncture vortex and influence of down-wash reduced. Thomas[9] captured an interesting phenomenon during water-tunnel flow visualization studies of the juncture region for the cylinder mounted on a flat plate, reporting a three-way splitting of the shed vortex for cylinders with aspect ratios less than 4. Though, he did not comment on the mechanism causing it, it is the opinion of the present authors that this was due to axial straining of the vortex because of the up-wash towards the free end of the cylinder due to its low aspect ratio. This phenomenon, as a consequence of span-wise flow, has also been reported for swept wing configurations by Khan[10]. Earlier studies[4, 9] have indicated that boundary layer characteristics do not have a primary impact on the dynamic aspects of the flow.

The present investigation is part of a comprehensive study of end-wall flows. It reports the results of an experimental study and attempts to explain the influence of aspect ratio, and tip geometry on end-wall flow as a consequence of the varying characteristics of the wake flow.

NOMENCLATURE

ν	kinematic viscosity
b	span or length
t_{max}	maximum thickness or diameter
f	frequency of oscillation/shedding
V_∞	free stream velocity
St	Strouhal Number ($t_{max}*f/V_\infty$)
Re	Reynolds Number ($V_\infty* t_{max}/\nu$)
AR	Aspect Ratio (b/t_{max})

EXPERIMENTAL SETUP

The investigation was carried out in the end-wall region of a wing, based on a NACA 0015 airfoil section with a maximum thickness of 0.0422m, mounted vertically on flat plexi-glass surface. Not only that a stream-lined geometry rather than a cylinder is prevalent in configurations of practical interest, but it also allows minimizing the influences of von Karman shedding on the dynamics of end-wall flow. The plexi-glass plate simulating the body was 0.508m wide and 1.20m in length, with elliptic leading and trailing edges. The boundary layer was tripped at the leading edge of the plate. The plexi-glass horizontal flat plate was mounted between two vertical plates (with elliptic leading edges) (Fig. 3) in the test section of a 0.6m x 0.9m water tunnel. The model resulted in a blockage of approximately 7%. Minimal influence of the end-plates was therefore expected on the end-wall flow. The vortex system was visualized using laser-induced fluorescence of Sodium Fluorescin with a 4-watt Ar-ion laser, light-sheet optics as well as hydrogen bubbles using a rake of three horizontal platinum wires (0.127mm dia) placed 2 mm apart. Tests were conducted for a Reynolds number (based on maximum thickness) range of 2300-4800. The boundary layer had the characteristics of a transitional boundary layer. Aspect ratios (maximum thickness / span) of 1.0, 1.6, 2.1, 2.5, 3.0, 3.6, 4.5, 5.6, 6.5, 7.6 and 10.5 were investigated. The flow-visualization was captured at 60 frames/sec using a NEC TI-23A CCD camera. Frequency estimates were made by averaging the measurements of a large number of cycles of the video data utilizing the frame advance/slow motion capabilities of a Toshiba SV-F990 VCR

RESULTS & DISCUSSION

Three distinct flow regimes were observed for flow in the end wall region. These regions were a static vortex system, an oscillatory vortex system and a shedding vortex system essentially duplicating what had been reported earlier by Khan et. al[5]. Flow visualization results in the plane of symmetry for the dynamic regimes are shown in Figure 4 with the direction of flow being from the left to right. The oscillatory regime (Mode II) shown in Fig. 4a, captures the upstream movement of the oldest vortex as it is being engulfed by the next older vortex. Mode III (the shedding mode) is shown in Fig. 4b in which the shed vortex convecting towards the wing in visible. Quantitative influences of aspect ratio would now be presented.

Influence on Dynamic Characteristics

It was observed that the Reynolds number at which transition was initiated from a static system to an oscillatory system of vortices was influenced by aspect ratio (Fig. 5). Vortex system for the low aspect ratio configurations maintained a static mode for higher Reynolds numbers. This points to the stabilizing influence of the pair of trailing vortices from the free end of the cylinder (Fig. 2b) since the influence of these vortices were observed[8] to increase with decrease in aspect ratio. Critical aspect ratio for this characteristic was observed to be a value of 2.5 beyond which transition was insensitive to aspect ratio. It also shows that von Karman shedding is not the primary cause for transition

from a static system to a dynamic system but rather instabilities in the shear layer amplifying with increasing Re to levels causing a global instability of the vortex system. This is a useful observation if the configuration is to be considered for applications where enhanced mixing (e.g. heat transfer) is needed.

The dynamic response for aspect ratios 1.0, 1.6, 2.1, 3.0 is shown in Figure 6. For these aspect ratios the slopes of the response curve (Strouhal number vs Reynolds number) is fairly constant. However, a change in the slope is observed (Fig. 7) for an aspect ratio of 3.6. Slopes of response curves of higher aspect ratios are shown in Figure 8. The variation of slopes with aspect ratio for the best curve fits through each response curve is shown in Figure 9 in which a distinct transition is visible for an aspect ratio of 3.6. With increasing aspect ratio however the impact is observed to reduce and asymptote towards a constant value. This change in response is attributed to the influence of von Karman shedding which becomes dominant at an aspect ratio of 3.6 but starts to lose it influence for higher aspect ratios. The presence of von Karman shedding has been reported[7] for aspect ratios of 4 and higher. Flow in the end wall region becomes insensitive to the influence of von Karman shedding for aspect ratios of 6 and higher.

Since free-end flow influences the end-wall flow, especially for low aspect ratios, the effect of wing tip shape was also investigated. Characteristics of low aspect ratio configurations with flat-end tip configurations are shown in Figure 10. No major impact was observed suggesting the dependence to be on the adverse pressure relaxation due to the up-wash induced by reduction in aspect ratio and the tip-trailing vortices rather than the local effect of the wing tip shape on these parameters.

Influence on Separation

The influence of aspect ratio on the primary separation point upstream of the wing on the plate surface is shown in Figure 11. The movement of the separation point towards the wing with decreasing aspect ratio is the consequence of a relaxation in the adverse pressure gradient due to the up-wash and flow over the free end. This characteristic is similar to the separation point for the juncture vortex system for swept wings configurations reported by Ahmed and Khan[6] for which a relaxation in the pressure gradient is due to the wing sweep. The separation characteristics for increasing Reynolds number again are quite typical where an increased momentum of the back flow causes separation of the boundary layer further upstream.

CONCLUSIONS

End-wall flow characteristics were experimentally studied for the effect of aspect ratio. The following observations were made:

(a) The system of vortices in the end-wall region exhibited the characteristic Reynolds number-dependent regimes ie a static system, an oscillating system and a shedding system.

(b) Reynolds number for a system of vortices in the end-wall region to transition from a static system to a dynamic system is aspect ratio dependent. Increase in aspect ratio resulted in the transition at a lower Reynolds number. The critical aspect ratio beyond which the flow was insensitive to this parameter was 2.5.

(c) The transition is conjectured to be due to the shear layer instabilities rather than the von Karman shedding.

(d) The Strouhal number response with Reynolds number for aspect ratios below 3.6 and higher than 6 showed relative insensitivity to aspect ratio. A transition in the slope of the Strouhal number vs Reynolds number curve was observe for an aspect ratio of 3.6.

(e) Flow in the end-wall region was relatively insensitive to wing tip shape.

(f) Primary separation point was observed to be dependent on aspect ratio and moved closer to the wing leading in the plane of symmetry with reducing aspect ratio.

ACKNOWLEDGEMENT

The authors would like to acknowledge the assistance of Mr. Marcus D. Wernig with the experimental work.

REFERENCES

[1]Prandtl, L., Essentials of Fluid Dynamics,Blackie & Sons Ltd., Glasgow, Britain, 1952

[2]Shabaka, I. M. M. and Bradshaw, P., 'Turbulent Flow Measurements in an Idealized Wing/Body Junction,' *AIAA Journal*, Vol. 19, No. 2, Feb. 1981, pp . 131-132
[3]Kornilov,V. I. And Kharitonov, A. M., 'Investigation of the Structure of Turbulent Glows in Streamwise Assymetric Corner Configurations,' *Experiments in Fluids*, Vol. 2, 1984, pp. 205-212
[4]Baker C. J., 'The Turbulent Horseshoe Vortex,' *Journal of Wind Engineering and Industrial Aerodynamics*, No. 6, 1980, pp. 9-23
[5]Khan, M. J., Ahmed, A., Trosper, R. J., 'Dynamics of the Juncture Vortex,' Vol. 33, No. 7, *AIAA Journal*, Jul. 1995, pp. 1273-1278
[6]Ahmed, A. and Khan, M. J., 'Effect of Sweep on Wing-body Juncture Flow,' AIAA Paper# 95-0868, Presented at the 33rd Aeropsace Sciences Meeting & Exhibit, Jan. 9-12,1995, Reno, NV
[7]Kawamura, T., Hiwada, M., Hibino, T., Mabuchi, I. and Kumada, M., 'Flow Around a Finite Cylinder on a Flat Plate,' Bulletin of JSME, Vol. 27, No 232, Oct. 1984, pp. 2142-2151.
[8]Okamoto, S. and Sunabashiri, Y., 'Vortex Shedding From a Circular Cylinder of Finite Length Placed on a Ground Plane,' ASME Journal of Fluids Engineering, Vol. 114, December,1992, pp512-521.
[9]Thomas, A. S. W., 'The Unsteady Characteristics of Horseshoe Vortex System,' *Physics of Fluids*, Vol. 30, No. 2, Feb. 1987, pp. 283-283
[10]Khan, M. J., 'Experimental Investigation of the Influence of Wing Sweep on Juncture Flow,' PhD Dissertation, Aerospace Engineering Department, Texas A&M University, May 1994

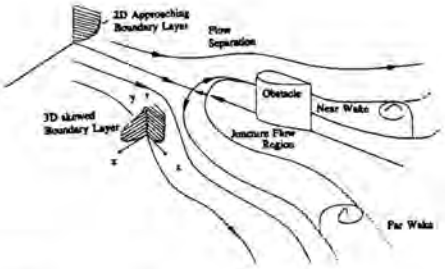

Fig. 1: Simple Schematic of Juncture Flow

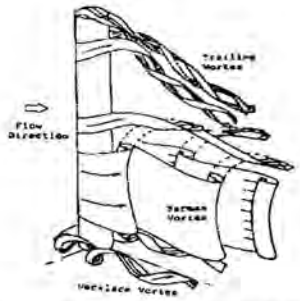

Fig. 2a: Wake of Large AR Cylinder (Ref. 7)

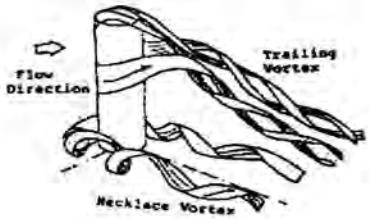

Fig. 2b: Wake of Short AR Cylinder (Ref. 7)

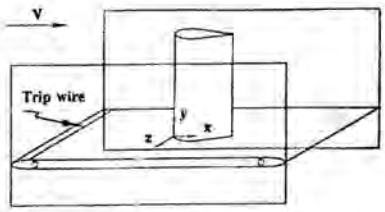

Fig. 3: Schematic of Experimental Setup

Fig. 4a: Flow Visualization (Mode II)

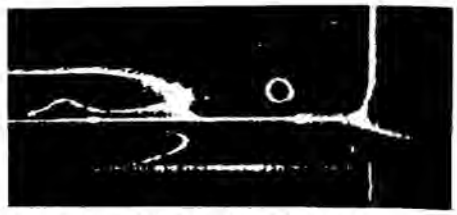

Fig. 4b: Flow Visualization (Mode III)

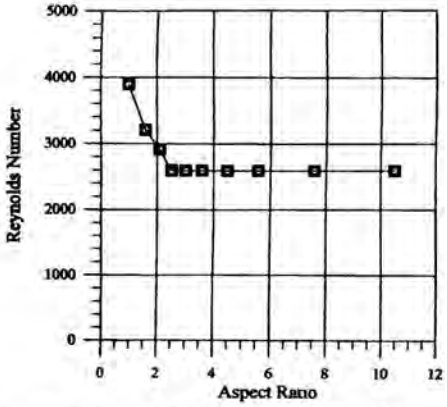

Fig. 5: Influence of Aspect Ratio on Transition Reynolds Number

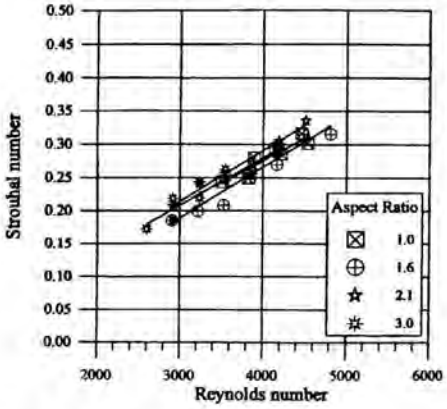

Fig. 6: Low Aspect Ratio Response

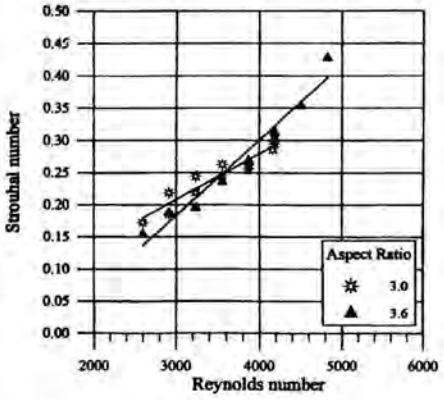

Fig. 7: Critical Aspect Ratio Response

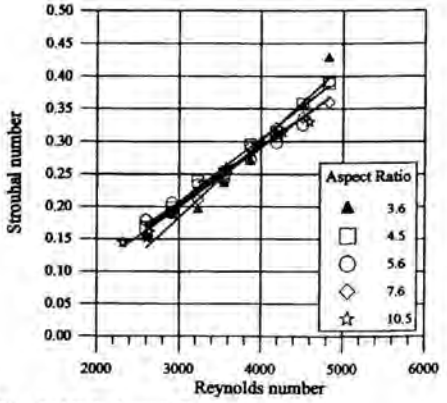

Fig. 8: High Aspect Ratio Response

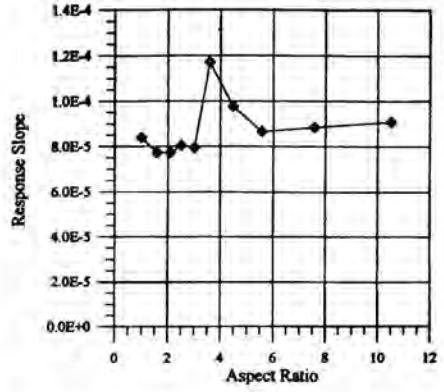

Fig. 9: Response Curve Slopes

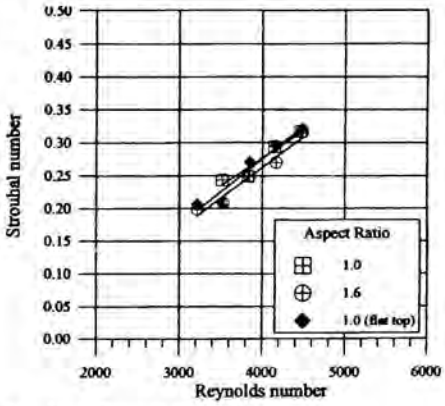

Fig. 10: Influence of Wing Tip

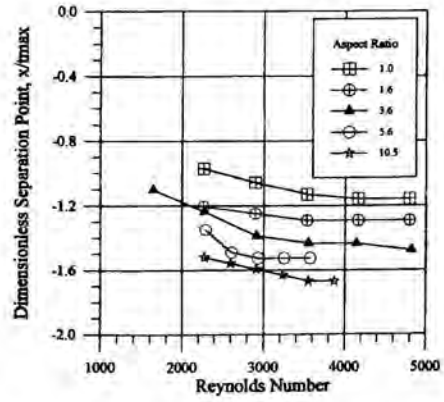

Fig. 11: Influence on Separation point

HEFAT2002
1ST International Conference on Heat Transfer, Fluid Mechanics, and Thermodynamics
8-10 April 2002, Kruger Park, South Africa
GA2

CONTROLLING AND MAXIMISING SOLAR CHIMNEY POWER OUTPUT

Anthony J. Gannon and Theodor W. von Backström
Department of Mechanical Engineering, University of Stellenbosch
Private Bag X1, Matieland 7602, South Africa

ABSTRACT

To determine the performance of a solar chimney power plant the solar collector must be correctly modeled. This requires the development of a transient model to account for the thermal storage effects of the ground beneath the collector. The model couples the temperature rise of the air as it moves through the collector to a transient model of the ground resulting in a simple and stable method for predicting the collector air temperature rise. The method is used to simulate a small experimental plant using the measured turbine pressure drop and mass flow rate and the results are compared with the measured data. Using the simulation the effect of increasing the turbine pressure drop is investigated. It is found that the potential power output is significantly higher than that obtained in the experimental plant. The simulation is then applied to a full-scale plant to determine the maximum power output and the corresponding turbine pressure drop and mass flow rate to achieve this. Two methods of power limitation by increasing and decreasing the turbine pressure drop are also investigated.

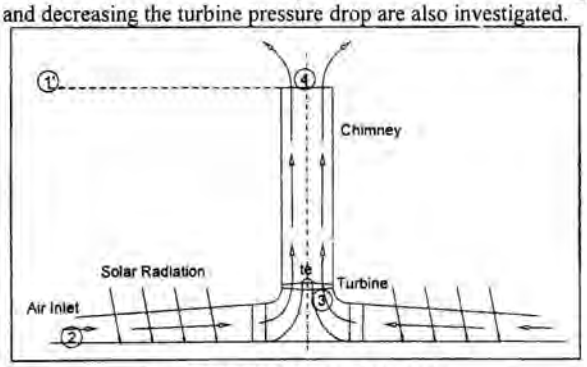

Figure 1. Solar Chimney Schematic.

INTRODUCTION

In brief the solar chimney is a simple renewable energy source consisting of three main components, a solar collector, chimney and turbine. Air under the collector is heated by the greenhouse effect. This less dense air rises up the chimney at the collector centre driving an electricity generating turbine. Various theoretical analyses and feasibility studies have been performed to determine the performance of the solar chimney, Haaf et al, (1983), Schlaich, (1995), Trieb et al, (1997). Gannon and Von Backström (2000) present a thermodynamic cycle analysis of the plant that requires the collector air temperature rise, ΔT_{23} to determine the power output. Of the total incoming solar radiation only part is absorbed by the collector air. Part is lost back to the environment while part is absorbed by the soil under the collector. Later in the day as the incoming solar radiation decreases this heat is released back into the collector. Quantifying this transient effect is important in predicting the plant power output for given environmental conditions.

NOMENCLATURE

Bi(r)	Biot number (radiation)	c	Specific heat
c_p	Specific heat (gas)	e	Emissivity
F_o	Fourier number	G	Solar radiation
h	Heat transfer coeff.	H	Heat flow into air
k	Conductivity	K	Extinction coefficient
L	Thickness	m	Mass flow
n	Refractive index	r	Radius
T	Temperature	t	time
Q	Heat flow in collector	x	Soil control volume
α	thermal diffusivity	Δ	Increment
ϕ	Latitude	ϕ_d	Solar declination
θ	Radiation angle	ρ	Density
τ	Absorbtivity	ω_h	Hour angle
σ	Stefan-Boltzmann const.		

Indices

1	Incident	2	transmitted
a	Absorbtive	abs	Absorbed
atm	Atmospheric	col	Collector
cov	Cover	cov in	Absorbed Solar rad.
cond	Conduction	conv	Convection
cov out	Absorbed Diffuse rad.	diff	Diffuse
gla	Glass	gla in	Inlet transmissivity
gli	Glass inner	o	Outer, surface
i	Inner	m	Soil index
P	time index	r	Reflective
soil	Subsurface soil	sol	Solar
surf	Surface	trans	Transmitted
//	parallel	$\perp$	perpendicular

SOLAR COLLECTOR ANALYSIS

The simplest analysis of the collector is to assume that all incoming solar radiation is used to heat the collector air.

$$G = \dot{m} c_p \Delta T \qquad (1)$$

This gives insight into the coupling between mass-flow and temperature rise. If G remains constant then a decreasing mass flow will result in a lower temperature rise and vice versa. In a real collector very high temperatures are not obtained due to heat loss. A control volume approach is used to simulate the collector (Figure 2). It is simplest to separate each control volume into three parts, the collector air, the cover material and ground. The collector air and cover material can be modeled using steady state assumptions as their heat storage capacities are very small. In the ground, generally soil, transient effects are significant as heat is absorbed and conducted more slowly. An overview of each component including the assumptions used is presented. This is followed by the governing equations used.

Collector Air: Figure 2 shows the radial control volume used along with the heat flow in the collector air. 4 basic assumptions are made. 1) no evaporation takes place, 2) conditions are steady state, and 3) the vertical temperature gradient is zero. 4) Air heating only occurs through convection at the lower and upper surfaces.

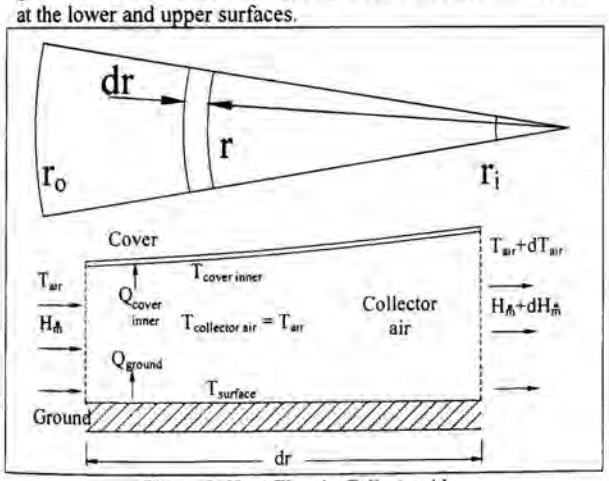

Figure 2. Heat Flow in Collector Air.

Governing equations: The convective heat gain in the collector air is dependent on the temperature gradients and heat transfer coefficients, h, at the soil and inner glass surface. It is represented by the following ordinary differential equation.

$$\frac{dT_{col}}{dr} = \frac{2\pi r}{\dot{m} c_p}\left(h_{surf}\left(T_{surf} - T_{col}\right) - h_{gli}\left(T_{col} - T_{gli}\right)\right) \qquad (2)$$

Cover Material: Figure 3 shows the heat flow in the cover material with convection occurring at the top and bottom surfaces. Part of the incoming radiation is reflected and lost, part is absorbed and the rest transmitted through the material. Diffuse radiation released by the ground is assumed to be absorbed by the cover. It is also assumed that no internal reflection occurs in the cover.

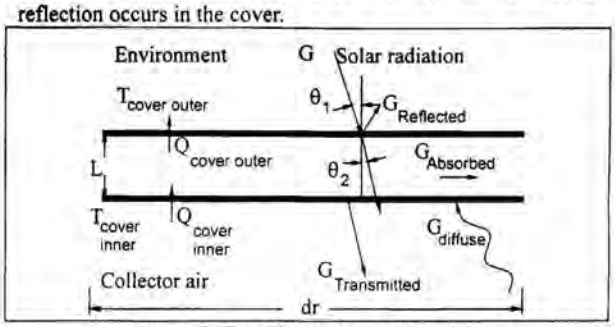

Figure 3. Heat Flow in Cover Material.

Governing equations: At the upper surface heat is conducted from the lower surface and a certain amount of solar radiation absorbed. Heat is lost to the atmosphere by convection and emitted radiation.

$$\underbrace{h_{glo}\left(T_{glo} - T_{atm}\right)}_{\text{convection}} + G_{loss} = \underbrace{\frac{k_{gla}}{L_{gla}}\left(T_{gli} - T_{glo}\right)}_{\text{conduction}} + G_{abs} \qquad (3)$$

where

$$G_{abs} = \underbrace{G\left(1 - \tau_{cov\,in}\right)}_{\text{absorbed solar radiation}} \qquad G_{loss} = \underbrace{\sigma\left(T_{glo}^4 - T_{atm}^4\right)}_{\text{emitted radiation}}$$

At the lower surface heat is transferred by convection and diffuse radiation from the ground. This heat is conducted to the outer surface.

$$\underbrace{h_{glo}\left(T_{glo} - T_{atm}\right)}_{\text{convection}} = \underbrace{\frac{k_{gla}}{L_{gla}}\left(T_{gli} - T_{glo}\right)}_{\text{conduction}} + G_{diff} \qquad (4)$$

where $G_{diff} = \underbrace{\left(1 - \tau_{cov\,out}\right)\varepsilon_{soil}\sigma\left(T_{surf}^4 - T_{gli}^4\right)}_{\text{diffuse radiation}}$

Ground: Figure 4 shows the heat flow into the ground by conduction and into the air by convection. Part of the radiation transmitted through the cover is reflected and assumed lost back to the environment. As mentioned above the collector absorbs the diffuse long wave radiation emitted from the ground.

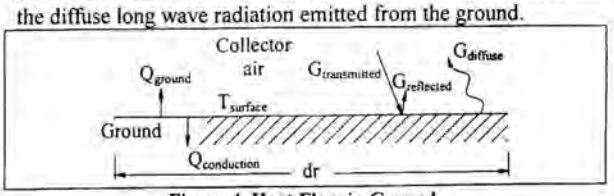

Figure 4. Heat Flow in Ground.

Governing equations: A discrete approach is most suitable in analyzing the collector soil. The equation describing the

lower soil layers is the transient one dimensional conduction equation (Incropera and De Witt 1990).

$$\frac{\partial^2 T}{\partial x^2} = \frac{1}{\alpha}\frac{\partial T}{\partial t} \quad \left(\alpha = \frac{k_{soil}}{\rho_{soil} c_{soil}}\right) \qquad (5)$$

The surface soil layer is heated by the transmitted solar radiation. Heat is lost through conduction to the lower soil layers and by convection and radiation to the collector.

$$\frac{\partial^2 T}{\partial x^2} + \frac{e_{soil} G_{trans}}{k_{soil}} - \frac{G_{diff}}{k_{soil}} - \frac{h_{surf}}{k_{soil}}\left(T_{surf} - T_{col}\right) = \frac{1}{\alpha}\frac{\partial T}{\partial t} \qquad (6)$$

with

$$G_{trans} = \left(1 - \tau_{gla\,in}\right) G$$

The above equations are discretised using an implicit scheme as this is unconditionally stable. The grid and nomenclature used is shown in Figure 5

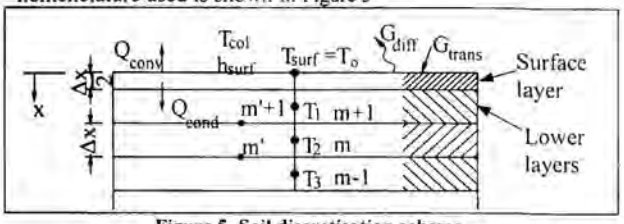

Figure 5. Soil discretisation scheme.

Discretisation of Eq. (5) gives,

$$\left(1 + 2F_o\right)T_m^{P+1} - F_o\left(T_{m-1}^{P+1} + T_{m+1}^{P+1}\right) = T_m^P \quad \left(F_o = \frac{\alpha \Delta t}{(\Delta x)^2}\right) \qquad (7)$$

Discretisation of Eq. (6) gives,

$$\left(1 + 2F_o + 2F_o B_i + 2F_o B_{ir}\right)T_o^{P+1} - 2F_o T_1^{P+1} = T_o^P + 2F_o B_i T_{col} + 2F_o B_{ir} T_{gli} + 2F_o \frac{\Delta x}{k_{soil}} G_{trans} \qquad (8)$$

The finite difference forms of the Biot (B_i) and Fourier (F_o) numbers and linearised radiative heat transfer coefficient, h_r^P are ,

$$B_i = \frac{h_{surf}\Delta x}{k_{soil}} \qquad F_o = \frac{\alpha \Delta t}{(\Delta x)^2}$$

$$B_{ir} = \frac{h_r \Delta x}{k_{soil}} \qquad h_r^P = e_{soil}\sigma\left(T_o^P + T_{gli}\right)\left(\left(T_o^P\right)^2 + \left(T_{gli}\right)^2\right) \qquad (9)$$

Additional equations: The inlet transmittance, $\tau_{cov\,in}$, of the cover material is dependent on the solar radiation incidence angle, θ_1. $\tau_{cov\,in}$ is a product of the reflective transmittance, τ_r, and absorbtive transmittance, τ_a (Duffie & Beckman, 1991).

$$\tau_{gla\,in} = \tau_a \tau_r$$

$$\tau_a = \exp\left(-\frac{KL_{cov}}{\cos\theta_2}\right) \qquad \tau_r = \frac{1}{2}\left(\frac{1 - r_{//}}{1 + r_{//}} + \frac{1 - r_{\perp}}{1 + r_{\perp}}\right) \qquad (10)$$

$$r_{//} = \frac{\tan^2\left(\theta_2 - \theta_1\right)}{\tan^2\left(\theta_2 + \theta_1\right)} \qquad r_{\perp} = \frac{\sin^2\left(\theta_2 - \theta_1\right)}{\sin^2\left(\theta_2 + \theta_1\right)}$$

The law of refraction, Sears *et al* (1987), gives θ_1 and θ_2,

$$\frac{n_{cov}}{n_{atm}} = \frac{\sin\theta_1}{\sin\theta_2} \qquad (11)$$

The angle of incident solar radiation, θ_1, is dependent on, the solar declination, ϕ_d, the angle of sun north or south of equator. The latitude, ϕ, and the time of day defined by the hour angle ω_h (Preston-Whyte & Tyson (1989)).

$$\cos\theta_1 = \sin\phi\cos\phi_d + \cos\phi\cos\phi_d\cos\omega_h$$

$$\phi_d = 23.45\left(\frac{2\pi\left(284 + Date_{sol}\right)}{365}\right) \qquad (12)$$

$$\omega_h = 15^\circ\left(12 - Time_{sol}\right)$$

In general the conductivity of the collector soil changes with depth. For a specific soil layer this must be calculated using the harmonic mean of the conductivities at the top and bottom of the specific layer (Patankar, 1980).

$$c_m = \frac{2c_{m'}c_{m'+1}}{c_{m'} + c_{m'+1}} \qquad (13)$$

Solution method: A personal computer using the program MATLAB was used to solve the above equations. The solution marches inwards from the collector inlet using the Runge-Kutta method to solve Eqn (2). At each radial station the glass inner and outer and soil surface temperatures are calculated using an iterative Newton scheme. The new soil temperature distribution is calculated using the previous time step's values and the tri-diagonal matrix algorithm. Due to the implicit transient scheme convergence is achieved using time steps of 20 min.

VERIFICATION OF SOLAR COLLECTOR MODEL

The collector of the small experimental plant in Manzanares, Spain is simulated using the above model. Using the published mass flow and collector temperature rise the heat addition to the collector air can be calculated and compared to the simulated results, Eq (14).

$$Q_{col} = \dot{m} c_p \Delta T_{col} \qquad (14)$$

Values for the material constants, soil properties and environmental data can be found in Haaf et al, (1983). A conservative value of heat transfer coefficient, h = 5 W/m^2.K (Incropera and De Witt, 1990) is used. Figure 6 compares the simulated and measured values of heat gained in the collector air. Comparing the experimental measurements with the simulated results shows the simulation to be pessimistic at midday while optimistic in the morning and afternoon. At very low mass flow rates the prediction tends to be inaccurate but this accounts for only a small fraction of plant output power. Overall the agreement was thought reasonable and the model used to simulate different solar chimney plants.

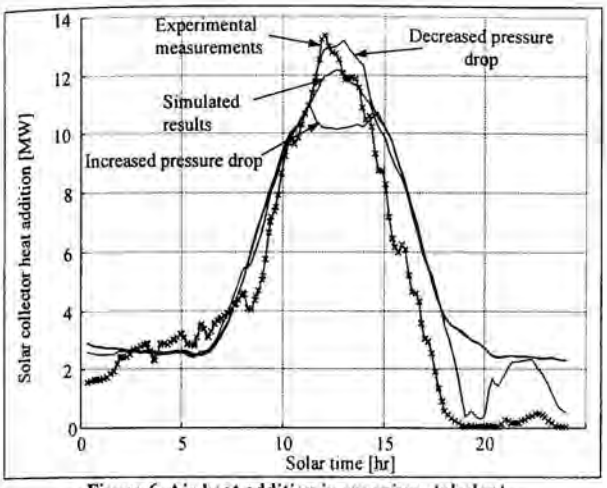

Figure 6. Air heat addition in experimental plant.

Once the collector temperature rise is determined and the chimney height and diameter known, the power output of the plant can be calculated (Gannon and Von Backström, 2000). Figure 7 is taken directly from that paper and compares the measured and simulated plant power output. Using the published turbine design efficiency of 83% results in optimistic power predictions. Using the measured turbine pressure drop, volume flow rate and power output the operational efficiency can be calculated. Using this resulted in a reasonable prediction of the plant power output.

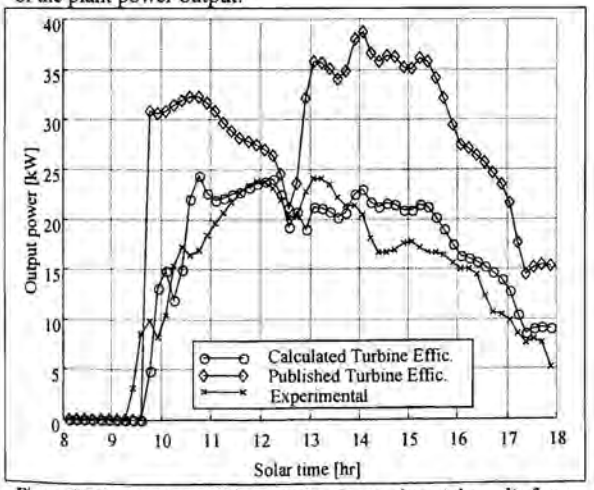

Figure 7. Comparison of simulated and experimental results from Manzanares, Spain.

EXPERIMENTAL PLANT SIMULATION

It is now assumed that the present simulation can with reasonable accuracy predict the power output of the solar chimney. The effect of increasing the turbine pressure drop to obtain the maximum power output is investigated. A turbine efficiency of 80% is assumed and the sizes and environmental data of the Manzanares plant used in the simulation. Figure 8 compares the measured output power with the simulated theoretical maximum. The two experimental plots are taken from Haaf (1984). It can be seen that the turbine must be correctly designed to be able to handle the correct pressure drop to ensure maximum power output.

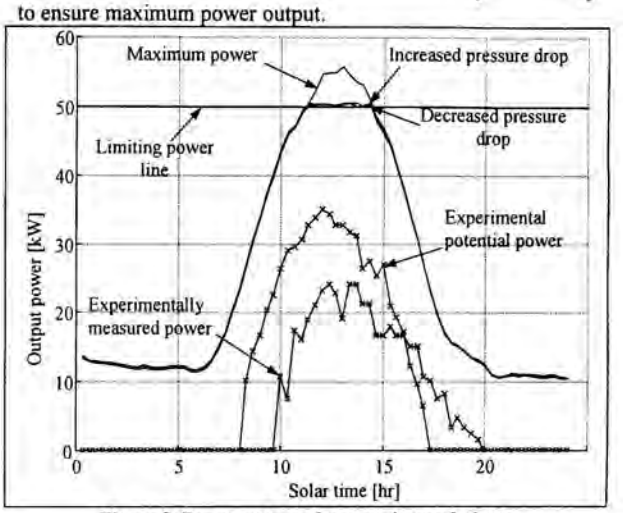

Figure 8. Power outputs for experimental plant.

Three different operational modes are simulated

- pressure is adjusted for max power over the entire day
- power limitation by decreasing the turbine pressure drop
- power limitation by increasing the turbine pressure drop.

The power output may be limited due to the generator capacity. It would be expensive to buy a generator just to handle peak load. Figure 9 compares the experimentally measured turbine pressure drop to the three simulated pressure drops.

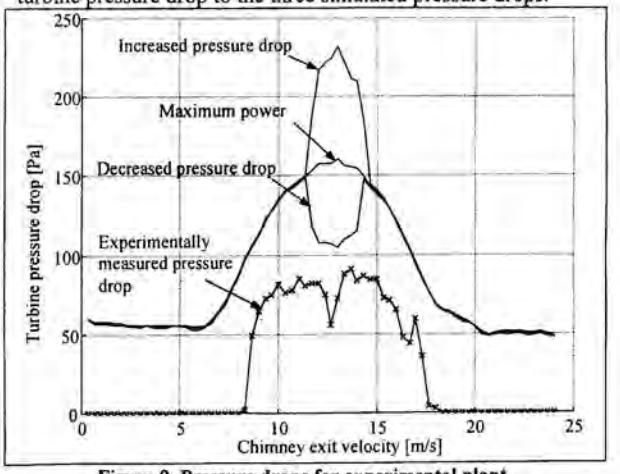

Figure 9. Pressure drops for experimental plant.

It is possible to limit the power due to the coupling between mass flow and pressure drop. Decreasing the pressure drop increases the mass flow and exit kinetic energy loss. Increasing the turbine pressure drop lowers the mass flow rate and hence

the exit kinetic energy but recall (Eq (1)) that the collector temperature rise will then increase. This results in an increased heat loss, part to the atmosphere and part to the soil but also recall that the later is re-released in the afternoon and evening. In all the simulations the assumption is made that a suitable turbine is available to operate at the desired pressure drop.

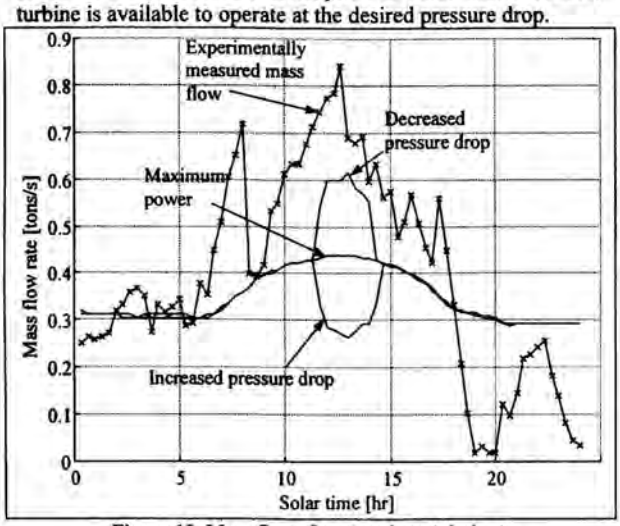

Figure 10. Mass flows for experimental plant.

Figure 10 shows the mass flows corresponding to the pressure drops in Figure 9. This demonstrates the coupling between the mass flow and pressure drop. The extra power generated is gained only by increasing the pressure drop. There is no significant change to the heat absorbed by the collector air (Figure 6). The effect of operating at a lower mass flow rate during the day results in higher temperatures under the collector. This results in more energy being stored in the ground and is beneficial to the nighttime operation. This is released fairly constantly through the night and may results in the plant being able to run at approximately 20% of the daytime output.

FULL SCALE PLANT SIMULATION

Using the same environmental data as above a full-scale plant is simulated. The chimney is 1500m high and 160m in diameter (Gannon and Von Backström, 2000)). Two collectors of 4 km and 6 km are simulated to cover the proposed range of diameters. Simulation of a large plant shows more clearly the effect of the two different control methods (Figure 11). Table 1 compares the total daily energy output of the 3 simulations.

Table 1. Total power outputs over 24 hrs.

	Max power	Inc. pres.	Dec. pres.
Full-scale 6km	3064 [MWh]	2802 [MWh]	2718 [MWh]
Manzanares	605.8 [kWh]	598.1 [kWh]	592.4 [kWh]

As more heat is stored in the ground when limiting power by increasing the pressure drop the design power in maintained for slightly longer. The off peak power is also slightly increased. The turbine pressure drop in the 4km diameter collector is always adjusted for maximum power as the limiting power is never obtained.

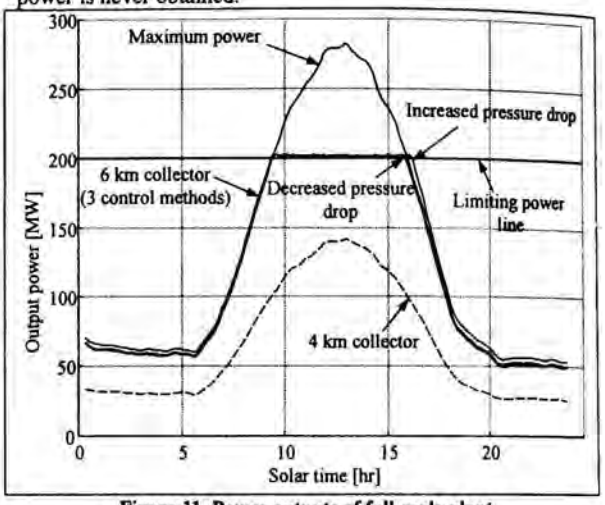

Figure 11. Power outputs of full-scale plant.

Figure 12 shows that using the pressure drop to limit the power requires a large increase in this value. The benefits are small with only a 3.1% increase in the total power output compared to decreasing the pressure. Figure 13 shows however that decreasing the pressure drop will significantly increase the mass flow that may lead to problems with high velocities in parts of the plant. The inclusion of a thermal storage system using water would absorb more heat in the middle of the day thus reducing maximum power and making plant control simpler. Increasing the turbine pressure drop in this case may make a thermal storage system more effective. This aspect needs to be investigated but would require modification of the collector model.

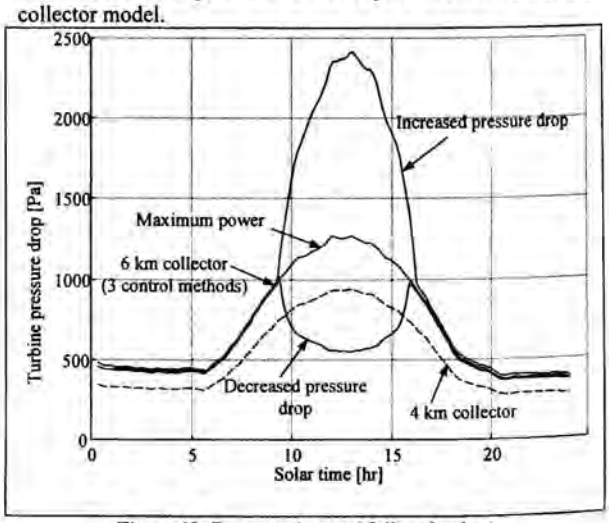

Figure 12. Pressure drops of full-scale plant.

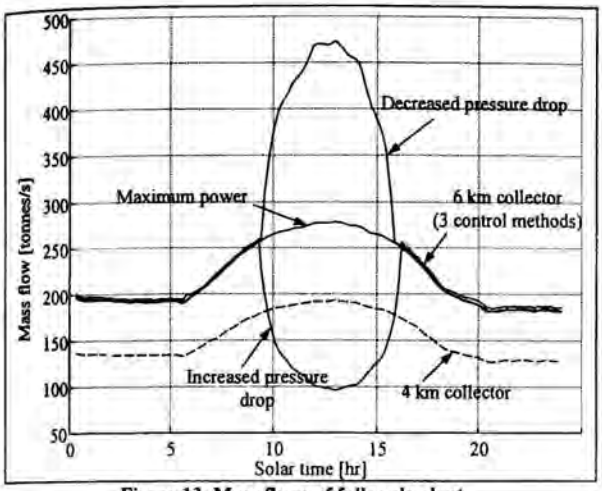

Figure 13. Mass flows of full-scale plant.

Turbine requirements: Using Figure 12 and Figure 13 the operating range for a solar chimney turbine can be defined. For the 6km diameter collector and for powers below the limiting value of 200 MW the mass flow is in the range 190-260 [tonnes/s] and the pressure drop 450-1000 Pa. The manufacture of a turbine for the maximum power case would require this range to be extended slightly. For the decreased pressure drop high throughflow velocities will be experienced but this would not change the turbine design significantly. The design of a turbine to control the plant by increasing the pressure drop may not be feasible. It would be difficult to design a turbine to operate at a high pressure drop at midday and then operate efficiently at lower power settings.

Other control methods: Increasing and decreasing the turbine pressure drop is not the only method of controlling the plant power. Another method suggested here is to introduce cool bleed air through the collector roof just before the turbine. This would lower the mass flow through the majority of the collector improving the thermal storage of the collector and not require high pressure drops from the turbine.

CONCLUSION

Using simple heat transfer and numerical techniques a transient solar collector model has been developed for the solar chimney. The model has been verified by comparing the simulated heat gain with measured heat gain in a small experimental plant.

The required pressure drop to obtain the maximum power for the small-scale and full-scale plant was calculated. It has been demonstrated that to achieve the maximum output power from the solar chimney it is important to run the turbine at the correct pressure drop. Two methods of controlling the plant output power by either decreasing or increasing the turbine pressure drop were investigated. Increasing the turbine pressure drop resulted in a slight improvement in the total daily energy output. The simulated data of the full-scale plant is required to design a suitable turbine for the plant

ACKNOWLEDGMENTS

The authors wish to thank Francois Lombaard and Meiring Beyers for their advice in the practical implementation of the collector model.

REFERENCES

Duffy, J.A., Beckman, W.A., (1991), *Solar Energy Thermal Processes*, John Wiley and Sons.

Haaf, W.,Friedrich, K., Mayr, G., Schlaich, J., (Oct 1983), "Solar Chimneys: Part I: Principle and Construction of the Pilot Plant in Manzanares," International Journal of Solar Energy, vol. 2, no. 1, pp 3-20.

Haaf, W., (Jan 1984), "Solar Chimneys: Part II: Preliminary Test Results from the Manzanares Pilot Plant," International Journal of Solar Energy, vol. 2, no. 2, pp 141-161.

Gannon, AJ, and Von Backström, TW, (August 2000), "Solar Chimney Cycle Analysis with System Loss and Solar Collector Performance," ASME Journal of Solar Energy Engineering, Vol 122, pp. 133-137.

Incropera, F.P., De Witt, D.P., (1990), "Introduction to Heat Transfer," John Wiley & Sons, Singapore.

Patankar, S.V., (1980), "Numerical Heat Transfer and Fluid Flow," Hemisphere Publishing Corporation, New York.

Preston-Whyte, R.A., Tyson, P.D., (1989), "The Atmosphere and Weather of Southern Africa," Oxford University Press, Cape Town, South Africa.

Schlaich, J., (1995), The Solar Chimney: Electricity from the Sun, C. Maurer, Geislingen, Germany.

Sears, F.W., Zemansky, M.W., Young, H.D., (1987), "University Physics 7th Edition," Addison-Wesley Publishing Company, USA.

Trieb, F., Langniß, O., Klaiß, H., (1997), "Solar Electricity Generation-a Comparative View of Technologies, Costs and Environmental Impact," Solar Energy, Vol 59, nos 1-3, pp 89–99.

HEFAT 2002
1st International Conference on Heat Transfer, Fluid Mechanics, and Thermodynamics
8-10 April 2002, Kruger Park, South Africa
MS4

SMALL HYBRID SOLAR POWER SYSTEM: FIRST FIELD TEST RESULTS

Samuel Martin, Malick Kane and Daniel Favrat

Laboratory for Industrial Energy Systems
Swiss Federal Institute of Technology of Lausanne
CH-1015 Lausanne, Switzerland
E-mail: daniel.favrat@epfl.ch

ABSTRACT

This paper presents field tests of an original concept of a small hybrid solar power plant integrating three technologies: hermetic volumetric scroll expander-generators installed in two superposed Organic Rankine Cycles (ORC), a (bio-)Diesel engine with heat recovery exchangers and a solar field made of two rows of sun following flat plate concentrators with vacuumed isolated collector tubes.

The basic idea of the concept is to exploit the synergy between equipment, use cheap and maintenance free expander-generators, guaranty power availability at all time and improve the efficiency of the engine when it has to operate alone at night time by converting the waste heat with the solar ORC. This type of hybrid power plant is intended for rural electrification purposes in developing countries or cogeneration in applications like heated swimming pools in other countries.

Pressurized hot water is used at this time as a thermal fluid in the collectors with HCFC123 in the topping cycle and HFC134a in the bottoming cycle.

The field tests have been performed during the summer 2001 in Lausanne (Switzerland) and the plant proved operationally reliable. However performance results (with exergetic efficiencies up to 45%) did not meet the expectations but measures to improve the concept have been identified.

INTRODUCTION

In most developing countries, electricity grids are available mainly, and often only, in urbanized areas. At the beginning of this XXIst century, numerous rural areas throughout the world still do not have access to a reliable source of electricity, fact which impairs their development. Even if development involves a complex problematic which cannot be solved only by access to electricity, its availability together with a rational use of it can have very positive effects. On the other hand, poor areas are most of the time isolated and decentralized electricity production seems to be the most rational solution, especially in large countries, like South-Africa for example. Moreover, this production mode avoids grid losses and transportation costs, and is suitable for waste heat utilization (co-generation).

Different concepts of small decentralized power plants currently exist, but for sustainability reasons solar energy is often considered especially in countries with a significant average solar radiation. However, the drawbacks of solutions relying only on solar supply are well-known and include, among others, the low density of incident energy requiring large collector areas and therefore high investment costs. Another problem is the production dependence on the meteorological conditions with the associated reduced power availability unless bulky and expensive storage systems are introduced. When using photovoltaics the latter drawback is often avoided by adding a fossil fuel engine, generally Diesel, resulting in two technologies in parallel with only a weak exploitation of the synergies between these equipments. However, technological developments integrating solar thermal power plant technologies with similar technologies fired by easily storable fuels open new and more interesting perspectives. The general idea in so-called Integrated Solar Fossil Cycle Systems (ISFCS) is to provide heat both from solar collectors and from a cogeneration power plant or engine, reducing then the above mentioned drawbacks and offering a way to

gradually substitute fossil fuel by solar (Favrat, 1995; Allani et al., 1996). The most often mentioned ISFCS concepts deal with high power production (up to several hundreds of MWe) and are reviewed in (Buck et al., 1998 or Kane et al. 2000). Earlier work is also reported in (Koai, Lior and Yeh, 1984).

However to meet the needs of rural areas in emerging countries , mini- ISFCS are required and one such concept has been designed at the Laboratory for Industrial Energy Systems (LENI) in the frame of a project called Solar Power System (SPS).

SPS Concept

The prototype designed in Lausanne is composed by two rows of linear solar concentrators, two superposed ORC both equipped with hermetic volumetric scroll expander-generators and a Diesel cogeneration engine (15 kWe) with heat recovery on its exhaust gases as well as on its cooling water circuit. Therefore, heat sources at different temperature levels are available. One, at approximately 150°C, is pressurized hot water heated first by the solar collectors and then further heated by the exhaust gases of the engine. A second one is the engine cooling water at about 80°C (at present with a potential to go up to 95°C). In the single solar mode, the second source as well as the heat from the exhaust gases are no more available and the pressurized hot water is heated by the sun only .

At present the solar collectors are designed to heat water up to 170°C, but higher temperatures using thermal oil instead of water are envisaged in order to increase the efficiency of the ORC. Pressurized water flows in vacuum insolated tubes which are at the focusing line of the concentrators. These are made of series of thin plate mirrors (CEP) of different width and fixed at calculated angle on linear supports in order to concentrate the solar radiation on the insulated tubes. These can be assimilated to Fresnel mirrors. The two rows of collector are oriented North-South with a tracking system from East to West. As mentioned above pressurized water has first been chosen for simplicity reasons. When total reliability of the concept will be proven, switch to thermal oil (allowing much higher temperatures at moderate pressure and avoiding freezing problems) is planned.

One option taken from the start has been to rely on fully hermetic cycles with hermetic expander-generators to avoid any shaft seals which could induce undesired leakage and long term maintenance problems. Furthermore cost reasons with the interest of using cheap large production components oriented the choice of turbine towards hermetic scroll compressors modified into expanders . This latter option had been proven to work successfully in previous studies (Zanelli, Favrat 1994, Favrat, 1995; Kane et al., 1999,2000). However those volumetric expanders have a range of efficient expansion ratios which is limited which constrains the cycle design. Accounting for those constraints and to maximize the efficiency of the plant and allow future extension to higher driving temperatures, it has been decided to implement two superposed ORC each with its own working fluid. In the present setup the High Temperature (HT) cycle uses HCFC123 and the Low Temperature (LT) cycle HFC134a. After having been pumped by a variable speed membrane piston pump into a plate evaporator, the topping cycle fluid is heated, evaporated and superheated (with pressurized water heat) before being expanded[1] in the HT scroll. Discharged vapor is then cooled, condensed and sub-cooled in a condenser-evaporator plate heat exchanger. Heat recovery is transferred to the bottoming cycle fluid for heating, evaporation and superheating. In hybrid mode, heat is also supplied to the HFC134a by the engine cooling water. Therefore, an additional plate heat exchanger, called preheater, is placed in series upstream of the evaporator of the bottoming cycle. The same type of pump and expander technologies are used for the bottoming cycle. The fluid is condensed in a plate condenser with cold water (°7C). Accounting for the heat recovered from the engine cooling network, the LT expander is oversized compared to the topping cycle one (8kWe versus 5kWe). The variable speed control of the pumps facilitate operation at part load.

To lubricate the bearings of the expanders and to avoid additional oil pumps, oil circulates with refrigerant from turbine outlet to the condenser, pump and evaporator at the outlet of which a separator is placed. The latter recovers oil to be injected within the hollow expander shaft, using the pressure ratio available. The efficiency of the separator doesn't need to be very high, as some amount of oil is desirable at the expander inlet to seal the inner gaps during expansion.

[1] During warm-up, vapor is by-passed

Pressure and temperature sensors are installed before and after each components of the plant and the values can be directly checked on a computer, with a special designed LabView Vi, allowing post-processing calculation of all the operation parameters. Figure 1 shows a schematic view of the plant (screen shot).

The cogeneration group showed in Figure 2 is composed of a Diesel engine, a shell-in-tube high temperature heat recovery exchanger for exhaust gases (leaving the engine at temperatures up to 650°C), and a preheater plate exchanger for the cooling water network. Regarding this cooling network, temperature at the engine outlet is kept constant at 82.5°C with a thermostatic valve regulating the water flow rate. The Diesel engine is a Lombardini LW 903 designed for industrial purposes. Its 3 cylinders in lines have a total capacity of 913 cm^3 and the engine is coupled with a three-phase asynchronous generator.

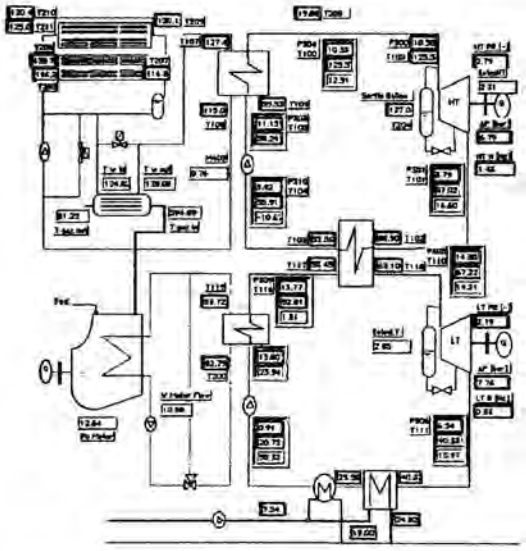

Figure 1. Schematic representation of the SPS power plant and typical parameters values (LabView screen shot).

Experimental results

ORC, solar concentrators and engine have been tested separately or only partially integrated during the year 2000 and detailed results are presented in (Larrain et al., 2000; Kane et al., 2001) and (Thély, 2000). During the summer 2001, the aim has then been to proceed with the integration on the field of the three technologies. The experimental analysis included the study of the cycles with a variable temperature heat source and in the various modes allowed by the integration of the engine.

In 2000, heat was supplied to the cycles by an oil heater at a constant (adjustable) temperature. This is no more possible with solar concentrators, available heat at evaporator being given by the direct solar radiation (varying along the day) and the concentrator efficiency (sensitive to solar radiation). To facilitate the startup of the cycles, the first approach tested was to allow time for the preheating of the heat source, typically up to 150 to 160°C[2]. However for such temperatures, the required heat supply to heat, evaporate and superheat the HCFC123 is about 55 to 65 kWth (based on last year measurements). Such values turned out to be hard to achieve in the field because of a mismatch between the design nominal values of the power plant and of the solar field[3]. In such a starting mode the power demand being higher[4] than the supply, the water inlet temperature decreases with time, before reaching an equilibrium.

[2] With a direct solar radiation of 800 W/m^2, the average rising temperature rate in closed loop from 25°C is about 2°C/min.

[3] This is due to a reduction in budget which did not allow the construction of the complete solar field as initially planned (100 m^2 instead of 160 m^2)

[4] Although the speed of rotation of the volumetric scroll expanders could potentially be varied within a range from 50 to 110%, the choice was made here, for simplicity reasons to operate them at constant speed (direct connection to the grid).

Figure 2. The cogeneration unit

This transition period duration as well as the equilibrium temperature depend on the direct solar radiation and the working mode (solar or hybrid); For the different tests cited in this paper the allowed stabilization temperature is in the range of 115 to 135°C.

Typical working days

The direct solar radiation varied along the summer and the best values were measured during the month of June with more than 850 W/m^2. The output electrical power of the engine is around 12 kWe[5] and approximately 11 kWt, respectively 20 kWt are recovered from the exhaust gases, respectively from the engine cooling network. The main values obtained for two typical days are presented in the table 1 below[6].

	26.06.2001	*26.09.2001*
Direct Solar Radiation (Average) [w/m^2]	740	597
Direct Solar Radiation (Peak) [w/m^2]	783	654
Working Mode	Solar	Hybrid
Working time [hours]	7.9	3.9
Total Electricity production [kWh]	33.3	67.5
Turbines Electricity production [kWh]	33.3	19.3
Diesel Consumption (l)	0	18.8
ORC Efficiency (Average) [%]	10.2	7.93
ORC Efficiency (Best) [%]	16	8.5
ORC Exergetic Efficiency (Average) [%]	44.0	43.1
ORC Exergetic Efficiency (Best) [%]	61.0	47.02
Plant Global Efficiency (Average) [%]	4.9	15.59
Plant Global Efficiency (Best) [%]	7.3	16.29
Fossil Efficiency (Average) [%]	-	35.3
Fossil Global Efficiency (Best) [%]	-	36.7

Table1. Main values of the ORC cycles for 2 typical days

The cycles efficiencies are quite low, with averages of 10% in solar mode and around 8% in hybrid mode. First of all, it is important to notice that ORC are working at low temperature (heat source at about 130°C) and at that temperature the maximum theoretical efficiency (Carnot) is 25%. Moreover, the lowest efficiency value for the hybrid working mode is easily explained by the fact that a large part of heat power given to the cycles is supplied at low temperature (80°C) and only for the bottom cycle. In these conditions, the exergy efficiency is much more representative and reaches about 44%.

Important sources of losses are most of the heat exchangers and in particular the condenser-evaporator linking the two cycles. In fact, as it can be noticed in figure 3 and 4, the temperature difference between condensation and evaporation stage in this exchanger is about 20°C which is much too high. This can partly be explained by the large amount of oil mixed with the evaporating working fluid (134a), whose boiling temperature strongly increases in the dryout region of the evaporator (non linearity not represented in Figure 4).

One solution would be to introduce a falling film shell in tube evaporator instead of the plate evaporator with an

[5] This value could be easily increased by a better ventilation of the engine.

[6] All the efficiency given are calculated in subtracting pump powers to electricity production. The exact expressions are given at the end of the present paper

accurate and fine control of the liquid pump, the topping fluid 123 condensing inside the tubes.

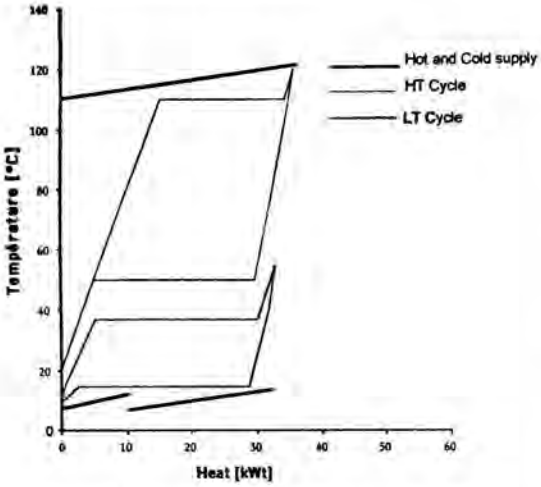

Figure 3. Heat-Temperature diagram of the ORC in hybrid mode

It can also be pointed out that the ORC are over-dimensioned for the existing heat supply. Indeed, as shown in figure 5, both expanders are used at very part load, especially the LT one, in solar mode. The latter turbine was in fact designed to work with heat recovered from the engine cooling network. A compromise has to be found and alternatives include either a variable speed LT expander or the introduction of two LT expanders in parallel to better adjust the load.

A last remark regarding the cogeneration group and its role on the power plant, is that the preheater works in parallel-flow mode (as it can be noticed on Figure 4). This was done to facilitate the regulation of the temperatures of the cooling network at the engine outlet. The valve keeps a constant water temperature (82.5°C) whereas the heat exchanger being oversized results in a very small pinch (about 1°C). In counter-flow mode, the pinch would move at the ORC working fluid inlet, with potentially too high temperature variations, not ideal for the engine.

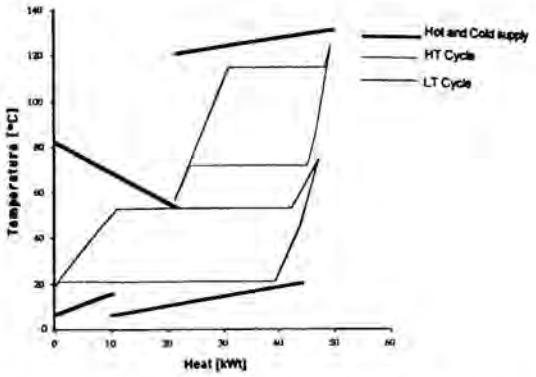

Figure 4. Heat-Temperature diagram of the ORC in solar mode

Another problem appeared during the test period and concerns the condenser. Indeed, probably due to variable cold water flow rate, the condensation pressure of LT cycle could not be maintained at 5 bars as it was first planned and realized during the laboratory test. This is also an important point to notice in order to improve the efficiency concept.

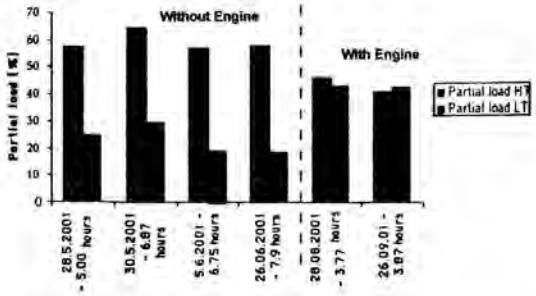

Figure 5: Part load average of the two turbines for 6 typical days

As it has been said, exergetic efficiency of the cycles is fair for this size of plant and with a significant potential for improvement. Figure 6 shows that in hybrid mode, this efficiency increases with the solar share.(ratio of the part of solar versus engine heat recovered).

This latter figure also illustrates the heat exergy limit (about 37 kWth and 115°C evaporator temperature) at which one of the turbine has to be disconnected. For lower values, the plant can still be maintained in

operation but with the HT cycle only (and at very part load). The LT expander is then bypassed and the bottoming cycle plays only a heat transfer role to the condenser.

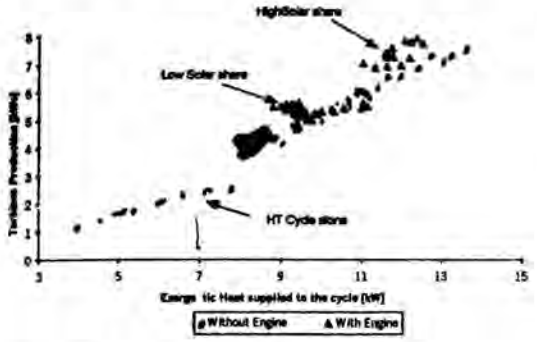

Figure 6: Turbines electricity production vs heat exergy provided to the cycles

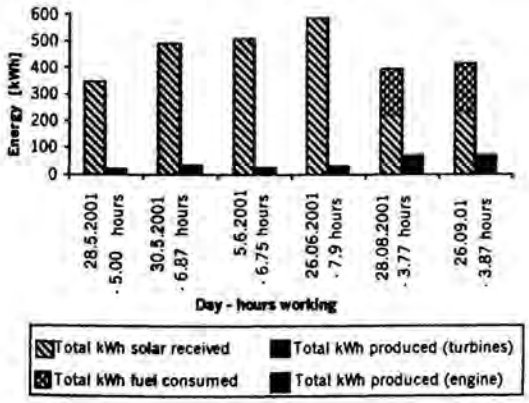

Figure 7: Total energy received and produced for 6 typical days

The latter figure summarizes the balances of energy in both working mode.

Conclusion

A new concept of mini hybrid solar power plant designed at LENI was field tested in Lausanne (Switzerland) during the summer 2001. The plant integrating three technologies (Linear Fresnel concentrators, Organic Rankine cycles and a Diesel engine) operated in a satisfactory way in various modes (from pure solar to hybrid with engine at full load). The hermetic scroll expander-generators equipped with a special in-shaft oil injection system performed adequately and reliably in spite of the strong variations of thermodynamic conditions. Fluctuations of solar radiation can be coped with the adaptation of the mass flow rates of the ORC working fluids and a reasonable range of vapor superheating can be maintained. Of course, the variation of solar radiation makes the cycles work at part load, which is detrimental for the efficiency.

Low ORC and global efficiencies (exergetic efficiencies below 45%) have been obtained and can mainly be explained by the mismatched nominal design between the ORC expanders and the solar field. This resulted in too low heat supply inducing too low evaporation temperatures of the topping cycle. Another reason is the low efficiency of the condenser-evaporator heat exchanger. A new design of the evaporator-condenser is being studied and new laboratory tests with a higher heat rate thermal oil source are being planned for the winter 2001-2002. . Other improvement possibilities include better and less expensive pumps, variable speed expanders, direct evaporation in the collectors, higher temperatures of the topping cycle, etc.

The concept of ORC with hermetic scroll expander-generators can be applied to a whole range of heat recovery applications. Two single cycles are presently being installed to increase the efficiency of biogas engines in a green waste fermentation plant in Geneva, converting only the engine cooling energy in a first approach.

The field experience gained is being used to improve the automatic control of such plants which is currently underway. Tests replacing Diesel fossil fuel by biodiesel can also be imagined, resulting in a fully renewable hybrid power plant.

Acknowledgments

The authors would like to acknowledge the financial support provided by the Swiss Federal Office of Energy and the contribution of the Swiss company COGENER which is responsible for the equipment of the solar field .

Equations

Different efficiencies given in table 1 are calculated with

the following expressions:

$$\varepsilon_{ORC} = \frac{\dot{E}_{elecORC} - \dot{E}_{ORCpump}}{\dot{M}_{pw} \cdot (h_{inpw} - h_{outpw}) + \dot{M}_{cw} \cdot (h_{incw} - h_{outcw})}$$

$$\eta_{ORC} = \frac{\dot{E}_{elecORC} - \dot{E}_{ORCpump}}{\dot{M}_{pw} \cdot (k_{inpw} - k_{outpw}) + \dot{M}_{cw} \cdot (k_{incw} - k_{outcw})}$$

$$\varepsilon_{plant} = \frac{\dot{E}_{elecORC} - \dot{E}_{ORCpump} + \dot{E}_{elecengine}}{\dot{Q}_{directsolar} + \dot{M}_{fuel} \cdot LHV}$$

$$\varepsilon_{fossil} = \frac{\dot{E}_{elecORC} - \dot{E}_{ORCpump} + \dot{E}_{elecengine}}{\dot{M}_{fuel} \cdot LHV}$$

With:

ε_{ORC}: ORC efficiency [%]
η_{ORC}: ORC Exergetic Efficiency [%]
ε_{plant}: Plant Global Efficiency [%]
ε_{fossil}: Fossil Global Efficiency [%]

Symbols:

$\dot{E}$: Power [W]
$\dot{M}$: Mass flow rate [kg/s]
h : Specific enthalpy [J/kg]
$k = h - T_a \cdot s$: Massflow specific exergy[J/kg]
s : Specific entropy [J/kg°K]
T_a : Atmospheric temperature [°K]
$\dot{Q}$: Heating power [W]
LHV : Low Heating Value [J/kg]

Subscripts

pw: Pressurized water
cw: Engine cooling water
in: Heat exchanger inlet
out: Heat exchanger outlet
directsolar: Direct solar radiation
elecORC: Cumulated for both expanders
pumpORC: Cumulated for both pumps
elecengine: Engine electricity

REFERENCES

- Allani Y., Favrat D., von Spakovsky M., *CO_2 mitigation through the use of hybrid solar-combined cycles*, Third International Conference on Carbon Dioxide Removal Technologies (ICCDR-3), MIT, Cambridge, USA, 1996.
- Buck R., Goebel O., Koehne R., Tamme R., Trieb F., *Advanced solar/fossil combined power plants*, Proceedings of the International Energy and Environment Conference , pp. 423-434, Changai, 1998.
- Favrat D., *Concept de centrale électrothermosolaire alpine*, CISBAT'95, EPFL, 1995.
- Kane M, Favrat D et al. *Thermoeconomic analysis of advanced solar-fossil combined cycle power plants.* Int. Journal of Applied Thermodynamics, vol.3, No 4, pp191-198, 2000
- Kane M., Brand F., Favrat D., *SPS: Projet d'une minicentrale pilote électro-thermosolaire de 10 kWe*, Final Report to Swiss Federal Office of Energy, 1999.
- Kane M, Larrain D, Favrat D, Allani Y. Small Hybrid Solar Power System, ECOS01, Istanbul, Jul 2001.
- Kane M, Martin S.,Favrat D., SPS Solar Power Systems: Minicentrale hybride électrothermosolaire Final Report to Swiss Federal Office of Energy, 2001
- Koai K., Lior N., Yeh H., *Performance analysis of a Solar-Powered/Fuel-Assisted Rankine Cycle with a Novel 30HP Turbine*, Solar Energy,32,6,pp 753-764, 1984.
- Larrain D., Kane M., Favrat D., *SPS: Projet pilote d'une mini-centrale électro-thermo-solaire*, Final Report to Swiss Federal Office of Energy, 2000.
- Thély J.-S., *SPS: Rapport final 2000. Amélioration de la première ligne et construction de la deuxième*, Final report to Swiss Federal Office of Energy, 2000.
- Zanelli R., Favrat D., *Experimental Investigation of a Hermetic Scroll Expander-generator*, 12th International Compressor Engineering Conference, Purdue, July 1994.

HEFAT2002
1st International Conference on Heat Transfer, Fluid Mechanics, and Thermodynamics
April 8-10, 2002, Kruger Park, South Africa
TG1

PRELIMINARY CFD ANALYSIS OF A SOLAR CHIMNEY

GD Thiart
Associate Professor
Department of Mechanical Engineering,
Stellenbosch University,
Private Bag X1, Matieland, 7602,
South Africa
E-mail: thiart@ing.sun.ac.za

ABSTRACT

Results from a numerical study regarding the characteristics of the flow field in and around a typical solar chimney are presented. A commercial CFD software package was used for the computations. Compressibility was modelled by means of a buoyancy term in the momentum equation, and turbulence by means of the k–ε turbulence model. The computations were carried out on two grids: a relatively coarse grid and a relatively fine grid. The flow fields computed on the two grids are similar, although the predicted mass flow rates differ by more than 30%. A probable reason for this large discrepancy is that of inadequate modelling of wall boundary conditions. Nevertheless, an important conclusion that can be inferred from the results is that the height above the ground up to which air is drawn into the collector is almost independent of the mass flow rate.

INTRODUCTION

The aim of this study was to determine the characteristics of the flow field in and around a solar chimney of the type proposed by Schlaich [1]. Specifically of interest was the height above the ground up to which air is drawn into the collector, as the presence of temperature inversions near the ground may adversely affect the operation of the system.

All the results presented in this paper were computed with a commercial CFD software package. This software was evaluated and was found to be suitable for the analysis, as long as the general flow is modelled as incompressible.

Only a brief overview of the geometry, governing equations and boundary conditions of the flow situation is presented in this paper. The main focus is on the numerical modelling and the results.

NOMENCLATURE

Symbols

c_p	specific heat at constant pressure
D	chimney diameter
$\vec{e}_z$	unit vector in the vertical direction
g	acceleration of gravity constant
h	collector height
H	chimney height
k	thermal conductivity, turbulence kinetic energy
K	kinematic momentum
p, p^*	static pressure, reduced static pressure
r,z	radial, vertical co-ordinates
R	radius
T, T^*	temperature, reduced temperature
v,w	radial, vertical velocity components
Z	height
β	volume expansion coefficient
ε	decay rate of turbulence kinetic energy
λ	lapse rate
μ	dynamic viscosity
ψ	stream function (volume flow rate)
ρ	density

Subscripts

i	inner, inlet
o	outer
w	wall
∞	ambient (at ground level)
0	reference value (at ground level)

GEOMETRICAL MODEL

The geometrical model used for the flow analysis is depicted in Figure 1. Note that the illustration is not to scale; if it was then it would have been difficult to distinguish the main features. Note also that, although the position of the turbine is indicated, the effect of a turbine on the flow field was not included in the analysis. The shape of the section between the collector and the turbine is elliptical (both the "top" surface and the "bottom" surface).

The principle of operation of the solar chimney is basically as follows: during the day the air between the ground surface and the collector surface is heated by the sun, caus-

ing the air to have a lower density than the ambient air; the heated air then rises up in the chimney, driving the turbine; air is drawn in through the inlet at the outer perimeter of the collector surface to replenish the air that escapes through the chimney.

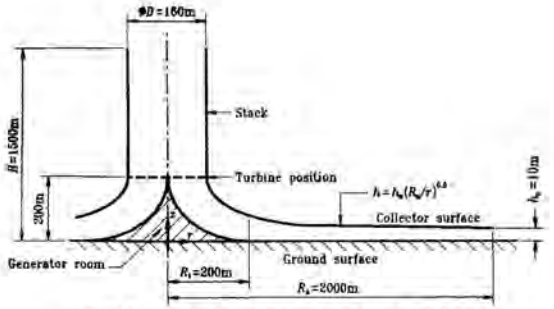

Figure 1. Geometrical model of the solar chimney

GOVERNING EQUATIONS

The governing equations for the flow situation under consideration are the laws for the conservation of mass, momentum and energy for axially symmetric turbulent compressible flow. The relevant equations are presented in most handbooks on CFD, for example those by Ferzigier & Perić [2] & Malalasekera [3], and will therefore not be repeated here.

For the results presented in this paper, the flow was deemed to be incompressible, with variations in density accounted for by means of a volume expansion term in the momentum equation, i.e. a "momentum source term" of magnitude $g(\rho - \rho_\infty)\vec{e}_z$ (for details about the principle of this technique, see for example Rohsenow & Choi [4]). Turbulence was modelled by means of the well-known k–ε turbulence model (also described in the cited references).

Note that the governing equations can be written in terms of the "reduced" pressure and temperature (p^* and T^* respectively), i.e. the "real" pressure and temperature (p and T respectively) minus their hydrostatic distributions (p_∞ and T_∞ respectively):

$$p^* = p - p_\infty = p - [p_0 - \rho g(z - z_0)] \qquad (1)$$

$$T^* = T - T_\infty = T - [T_0 - \lambda(z - z_0)] \qquad (2)$$

The only substantial difference between the transformed equations and the original equations, is that an extra "energy source term" of magnitude $\rho w(c_p\lambda - g)$ appears in the energy equation. This term is zero if the atmosphere is in neutral equilibrium, i.e. if the lapse rate λ is equal to its adiabatic value g/c_p. The results presented in this paper were computed with this adiabatic value of the lapse rate.

BOUNDARY CONDITIONS

The boundary conditions used for the CFD analysis are shown in Figure 2. The meanings of these boundary conditions are as follows:

Adiabatic wall: A one-sided no-slip adiabatic boundary. Wall functions are used at the "outside" of the boundary.

Baffle: A two-sided no-slip adiabatic boundary of zero thickness. Wall functions are used at both the "inside" and the "outside" of the boundary.

Pressure: If the flow is into the computational domain, then $p^* = T^* = 0$, $k = k_i$ and $\varepsilon = \varepsilon_i$. If the flow is out of the computational domain, zero gradients (of p^*, T^*, k and ε) perpendicular to the boundary are enforced.

Wall: A one-sided no-slip constant-temperature boundary, with $T^* = T_w^*$. Wall functions are used at the "outside" of the boundary.

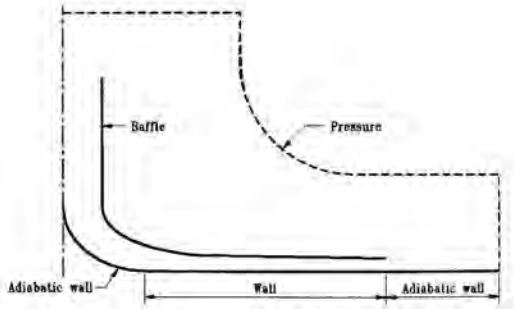

Figure 2. Boundary conditions for the solar chimney analysis

SOLUTIONS

The actual values of flow properties and boundary conditions used in the analysis are given in Table 1. The computations were done using the Ultimate Quick differencing scheme of Leonard [5].

ρ	1.0344 kg/m^3
c_p	1005.7 J/kg·K
k	0.02624 W/m·K
μ	1.8525×10^{-5} kg/m·K
g	9.8 m/s^2
β	0.0034123 /K
T_w^*	25 K
k_i	0.001 m^2/s^2
ε_i	0.00001 m^2/s^3

Table 1. Values of flow parameters

Two solutions were obtained: the first one on a relatively coarse grid (90 × 53 grid points), and the second one on a relatively fine grid (135 × 79 grid points). In both cases a boundary-fitted grid was generated by means of the automatic grid generator developed by Thiart [6].

During both computations the wall temperature of the ground surface under the collector had to be increased gradually to its value specified in Table 1 in order to prevent the solution from diverging. For the coarse grid, this "start-up" phase lasted for 20000 iterations, whereafter the computation was continued for another 30000 iterations. For the fine grid, the two phases lasted for 25000 and 50000 iterations respectively.

In addition, heavy underrelaxation had to be applied to all variables except for the static pressure, as indicated in Table 2. During the final phase of each of the computations, the underrelaxation factors were reduced even further (the values in brackets) in order to drive the solutions to convergence. Note that the underrelaxation factors for pressure were always an order of magnitude larger than those for the other variables, which is necessary to ensure that conservation of mass is enforced more aggressively than conservation of momentum, energy, etc.

Variable	Coarse grid	Fine grid
v	0.05 [0.02]	0.02 [0.005]
w	0.05 [0.02]	0.02 [0.005]
p	0.8 [0.8]	0.4 [0.2]
T	0.05 [0.02]	0.02 [0.005]
k	0.05 [0.02]	0.02 [0.005]
ε	0.05 [0.02]	0.02 [0.005]

Table 2. Underrelaxation factors

Coarse grid solution

The coarse grid is illustrated in Figure 3; the lines are those connecting the cell vertices.

The streamlines of the flow field solution is shown in Figure 4. These streamlines are actually the contour lines of the stream function, which is essentially the accumalative mass flow rate measured from the ground surface. The predicted mass flow rate through the installation is approximately 22600 kg/s, which means that the average velocity through the chimney is about 1.1 m/s. The corresponding Reynolds number based on the diameter of the chimney is approximately 9.7×10^6.

Fine grid solution

The fine grid is illustrated in Figure 5; here also the lines are those connecting the cell vertices.

The contour lines of stream function is shown in Figure 6. The predicted flow rate through the installation is approximately 16000 kg/s, which means that the average velocity through the chimney is about 0.77 m/s. The corresponding Reynolds number based on the diameter of the chimney is approximately 6.9×10^6.

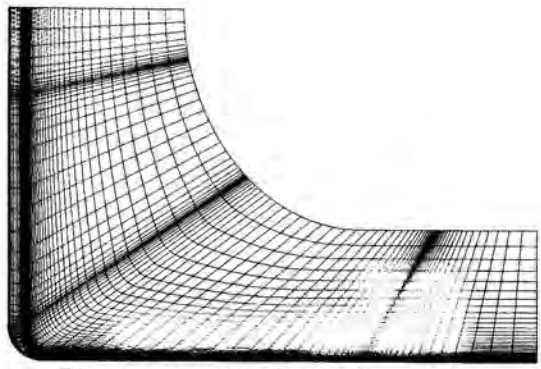

Figure 3. Coarse grid for the solar chimney analysis

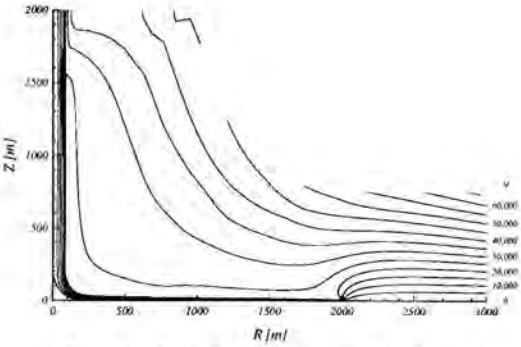

Figure 4. Streamlines of the coarse grid solution

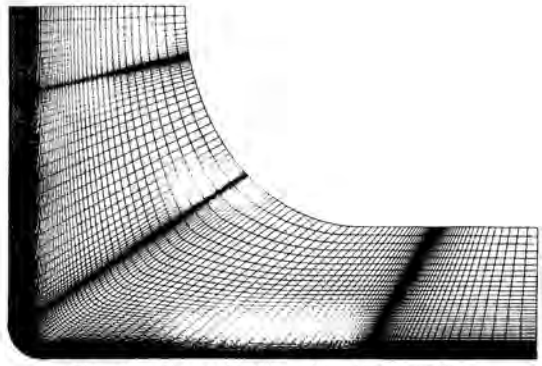

Figure 5. Fine grid for the solar chimney analysis

DISCUSSION

The large difference between the predicted mass flow rates for the two solutions is cause for concern: a few percent difference would have been acceptable, but the differ-

HEFAT 2002
1 ST International Conference on Heat Transfer, Fluid Mechanics and Thermodynamics
8 – 10 April 2002, Kruger Park, South Africa
VT1

CALCULATION OF PRESSURE AND DENSITY IN SOLAR POWER PLANT CHIMNEYS

TW von Backström and AJ Gannon
Department of Mechanical Engineering, University of Stellenbosch
Private Bag X1, Matieland 7602, Stellenbosch, South Africa

ABSTRACT

The paper develops accurate calculation methods for the pressure drop in very tall chimneys, as in solar chimney power plants. The methods allow for density and flow area change with height, for wall friction and internal bracing drag. The paper shows that the use of static temperature in the adiabatic temperature lapse rate equation is incorrect when there is flow in the chimney. It presents equations for the vertical pressure and density distributions in terms of Mach number. One of these is a generalisation of the adiabatic pressure lapse ratio equation to include non-zero, small Mach numbers. The other is analogous to the hydrostatic relationship between pressure, and density times depth, but extends it to small Mach numbers. Its integration leads to an equation for the average density in the chimney for the non-zero small Mach number case. A very accurate value of the average density is exactly what the commonly used incompressible flow approach requires to calculate the hydrostatic pressure difference in a chimney when there is flow. The approach satisfies all the conservation equations, and is simple enough to use in spreadsheets or for checking the accuracy of incompressible flow approximations.

INTRODUCTION

Typical analyses of flow through solar power plant tall chimneys (Fig 1) make the assumption of incompressible flow [1,2,3,4,5,6] thereby introducing inaccuracies of unknown magnitude [7].

The chimney of a typical 200 MW solar chimney power plant could be 1500 m tall and 160 m in diameter [3,5,6,7]. The thickness of the reinforced concrete walls could range from 0.99 to 0.25 m [8] for a 1000 m tall chimney and from 2.19 to 0.25 m for a 1500 m tall chimney.

Since the wall thickness is small compared to the diameter, the construction requires stiffening to avoid wind-induced ovaling and subsequent failure. Sclaich [1] proposed "spokes" (radial rods, or bars, tensioned by their own weight), between compression rings at the chimney walls and central hubs. The drag of these bracing rods adds to the wall friction pressure drop. In addition, the density gradient in a tall chimney induces an acceleration pressure drop [7].

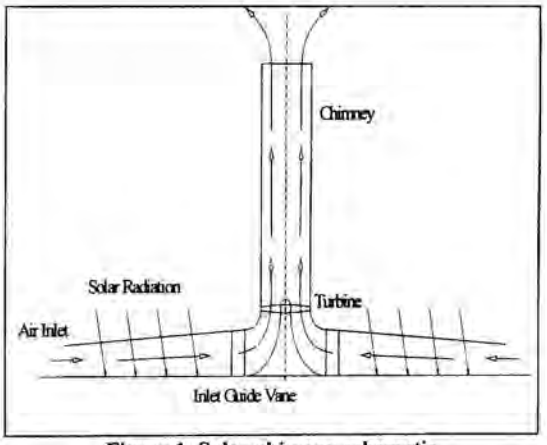

Figure 1. Solar chimney schematic

The primary objective of this study is to develop a practical but accurate method of calculating the pressure drop in tall chimneys with wall friction, internal drag and area change with height. A secondary objective is to investigate the accuracy of incompressible flow solutions.

NOMENCLATURE

A	flow area	[m^2]
c	constant	-
C_p	specific heat	[J/kgK]
D	chimney inside diameter	[m]

F_D	drag force	**[N]**
f	friction coefficient	-
g	gravitational acceleration	[m/s^2]
K	pressure drop coefficient	-
L	sum of loss terms	-
M	Mach number	-
$\dot{m}$	mass flow	**[kg/s]**
P	stagnation pressure	**[Pa]**
p	static pressure	**[Pa]**
Q	heat	[W]
R	gas constant	[J/kgK]
Re	Reynolds number	-
T	stagnation temperature	[K]
t	static temperature	[K]
V	velocity	[m/s]
W	work	[W]
z	height	**[m]**
	Greek	
γ	Specific heat ratio	
μ	dynamic viscosity	[Ns/m^2]
ρ	density	[kg/m^3]
	Prefix	
Δ	change over chimney height	
δ	change over interval	
	Subscript	
D	drag	
I	integration interval number	
1	inlet (or coefficient number)	
2	exit (or coefficient number)	

GOVERNING EQUATIONS

The vertical momentum equation for a control volume of differential height dz (Fig 2) has been derived [7] and can be written in terms of Mach number as in eq. (2).

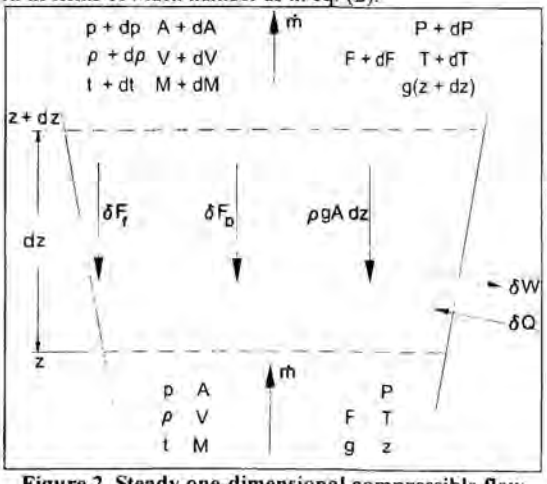

Figure 2. Steady one-dimensional compressible flow

Assume constant values of the gas constant and specific heat ratios. The adiabatic stagnation temperature lapse rate equation, derived from energy conservation, is the core equation in the analysis:

$$T = T_i - \frac{g\,z}{c_p} \tag{1}$$

Combine the friction and drag terms in the vertical momentum equation derived in [7], assuming that the loss coefficient, K applies over a certain finite length, δz:

$$\frac{f\,dz}{D}\frac{\gamma M^2}{2} + \frac{\delta F_D}{pA} = \frac{f\,dz}{D}\frac{\gamma M^2}{2} + \frac{\frac{K}{\delta z}\frac{1}{2}\rho V^2 A\,dz}{pA} = \left(\frac{f}{D} + \frac{K}{\delta z}\right)\frac{\gamma M^2}{2}dz = L\frac{\gamma M^2}{2}dz \tag{2}$$

Write the vertical momentum equation from [7] as:

$$\frac{dM}{M} = \frac{1+\frac{\gamma-1}{2}M^2}{1-M^2}\left(-\frac{dA}{A} + L\frac{\gamma M^2}{2}dz + \frac{g\,dz}{R\,t} + \frac{1+\gamma M^2}{2}\frac{dT}{T}\right) \tag{3}$$

Simplify eq. (1) by writing the static temperature term, gdz/Rt in terms of stagnation temperature and substituting $g\,dz/(c_pT) = -dT/T$, from eq. (1):

$$\frac{gdz}{Rt} + \frac{1+\gamma M^2}{2}\frac{dT}{T} = \frac{gdz}{c_pT}\frac{\gamma}{\gamma-1}\left(1+\frac{\gamma-1}{2}M^2\right) + \frac{1+\gamma M^2}{2}\frac{dT}{T} = -\frac{1}{2}\frac{\gamma+1}{\gamma-1}\frac{dT}{T} \tag{4}$$

This eliminates Mach number from the temperature variation terms. Substitute eq. (4) into eq. (3) :

$$\frac{dM}{M} = \frac{1+\frac{\gamma-1}{2}M^2}{1-M^2}\left(-\frac{dA}{A} - \frac{1}{2}\frac{\gamma+1}{\gamma-1}\frac{dT}{T} + L\frac{\gamma M^2}{2}dz\right) \tag{5}$$

Eq.(5) has no general analytical solution. However, when the flow area and stagnation temperature are constant, the variables do separate, and the classical solution for (horizontal) adiabatic compressible frictional flow through constant area ducts follows. When there are no friction or drag losses, and the area is constant, the classical solution for frictionless constant area flow with heat transfer follows. Note that there is no heat transfer through the chimney walls, but that, according to eq. (1), the stagnation enthalpy decreases with height as the potential energy increases.

The adiabatic stagnation temperature drop expressed as a fraction of the inlet temperature in a 1500 m vertical chimney is $dT/T \approx 15/300 = 0.05$ and the coefficient, $\frac{1}{2}(\gamma+1)/(\gamma-1)$ is equal to 3, so the stagnation temperature term is ≈ 0.15. The friction loss coefficient $f\,dz/D \approx 0.01*1500/160 \approx 0.1$. In the absence of internal obstructions the friction-and-drag-term is then $0.1*1.4*0.05^2/2 \approx 0.00018$ for a Mach number of 0.05. That is almost three orders of magnitude less than the stagnation temperature term. A reasonable approach will then be to calculate the friction part of the L-term with the known Mach

number at the beginning of the integration interval. This assumption agrees with the incompressible flow approach where everything is referred to the upstream position.

Across a short internal obstruction, however, where the stagnation temperature does not change much, the K $M^2 \gamma/2$ loss term may not be negligible. For a typical K= 0.1, and M=0.05 this term is 0.00018, about equal to the temperature term for a 1 m interval. If the flow area is also constant over the interval length, a normal Fanno-line type solution is possible. But to keep the calculation method consistent it would be better to keep to the method proposed above where the Mach number is assumed to be fixed at the value just upstream of the interval. The Mach number change induced by the the $K(M^2 \gamma/2)$ loss term above would be about 0.02 %. Using the upstream in stead of the correctly averaged Mach number in the term would cause a negligible error of about 0.01 %. compared to the uncertainty in the value of an experimentally determined value of K.

Once the Mach number distribution has been found at the end of each interval, the pressure at each level can be found from the mass conservation equation below [9]:

$$p = \frac{m}{A\,M\left(1+\frac{\gamma-1}{2}M^2\right)^{\frac{1}{2}}\left(\frac{\gamma}{R\,T}\right)^{\frac{1}{2}}} \qquad (6)$$

Values of other variables follow from standard gas dynamics.

SOLVING FOR MACH NUMBER

Write eq. (5), in terms of left (LHS) and right hand sides (RHS):

$$\begin{aligned} LHS &= \frac{1-M^2}{1+\frac{\gamma-1}{2}M^2}\frac{dM}{M} \\ &= \left(-\frac{dA}{A}-\frac{1}{2}\frac{\gamma+1}{\gamma-1}\frac{dT}{T}+L\frac{\gamma M^2}{2}dz\right) = RHS \end{aligned} \qquad (7)$$

$$\begin{aligned} \int RHS &= -\int\frac{dA}{A}-\frac{1}{2}\left(\frac{\gamma+1}{\gamma-1}\right)\int\frac{dT}{T}+\int L\frac{\gamma M^2}{2}dz \\ &= -\ln A-\ln T^{\frac{1}{2}\left(\frac{\gamma+1}{\gamma-1}\right)}+\ln\left[\exp\left(L\frac{\gamma M_1^2}{2}z\right)\right]+cons \end{aligned} \qquad (8)$$

Integrate the LHS with the assumption that γ is constant throughout the chimney

$$\begin{aligned} \int LHS &= \int\frac{1-M^2}{1+\frac{\gamma-1}{2}M^2}\frac{dM}{M} \\ &= \ln\frac{M}{\left(\frac{2}{\gamma-1}+M^2\right)^{\frac{1}{2}\left(\frac{\gamma+1}{\gamma-1}\right)}}+cons \end{aligned} \qquad (9)$$

Apply the integration limits to thje LHS and RHS across an incremental height between an initial position 1 and any general position. Note that one of the integration intervals should coincide with each length δz_i over which the loss coefficient L in eq. (8) has a fixed value

$$\begin{aligned} &\frac{M}{\left(\frac{2}{\gamma-1}+M^2\right)^{\frac{1}{2}\left(\frac{\gamma+1}{\gamma-1}\right)}} \\ &= \frac{M_1}{\left(\frac{2}{\gamma-1}+M_1^2\right)^{\frac{1}{2}\left(\frac{\gamma+1}{\gamma-1}\right)}}\left(\frac{A_1}{A}\right)\left(\frac{T_1}{T}\right)^{\frac{1}{2}\left(\frac{\gamma+1}{\gamma-1}\right)}\exp\left(L\frac{\gamma M_1^2}{2}\delta z\right) \end{aligned} \qquad (10)$$

Assuming that A and L are known at each chimney height, the RHS of eq. (10) can be calculated, once the stagnation temperature has been calculated from the lapse rate. The value of M in the LHS must then be found iteratively.

An approximate explicit equation for M follows below. First multiply the denominators on both sides of eq. (10) by $((\gamma-1)/2)$ to the power $\frac{1}{2}(\gamma+1)/(\gamma-1)$:

$$\begin{aligned} &\frac{M}{\left(1+\frac{\gamma-1}{2}M^2\right)^{\frac{1}{2}\left(\frac{\gamma+1}{\gamma-1}\right)}} = \\ &\frac{M_1}{\left(1+\frac{\gamma-1}{2}M_1^2\right)^{\frac{1}{2}\left(\frac{\gamma+1}{\gamma-1}\right)}}\left(\frac{A_1}{A}\right)\left(\frac{T_1}{T}\right)^{\frac{1}{2}\left(\frac{\gamma+1}{\gamma-1}\right)}\exp\left(L\frac{\gamma M_1^2}{2}\delta z\right) \end{aligned} \qquad (11)$$

Since $M_1^2 << 1$, approximate the denominators by two-term binomial expansions:

$$\begin{aligned} \frac{M}{M_1} &\approx \frac{1+\frac{\gamma+1}{4}M^2}{1+\frac{\gamma+1}{4}M_1^2}\left(\frac{A_1}{A}\right)\left(\frac{T_1}{T}\right)^{\frac{1}{2}\left(\frac{\gamma+1}{\gamma-1}\right)}\exp\left(L\frac{\gamma M_1^2}{2}\delta z\right) \\ M &= \left(1+\frac{\gamma+1}{4}M^2\right)C_{12} \end{aligned} \qquad (12)$$

Here C_{12} is:

$$C_{12} = \frac{M_1}{1+\frac{\gamma+1}{4}M_1^2}\left(\frac{A_1}{A}\right)\left(\frac{T_1}{T}\right)^{\frac{1}{2}\left(\frac{\gamma+1}{\gamma-1}\right)}\exp\left(L\frac{\gamma M_1^2}{2}\delta z\right) \qquad (13)$$

The quadratic equation, (12) has the following analytical solution:

$$M = \left(1-\sqrt{1-4\frac{\gamma+1}{4}C_{12}^2}\right)\frac{1}{2\left(\frac{\gamma+1}{4}\right)C_{12}} \qquad (14)$$

For a simpler, but approximate, solution note that for $M_1^2 << 1$, $(\gamma+1)\,C_{12}^2$ is much less than 1, so that by the binomial theorem:

$$M \approx \left(1-\left(1-\frac{\gamma+1}{2}C_{12}^2\right)\right)\frac{1}{\left(\frac{\gamma+1}{2}\right)C_{12}} \qquad (15)$$
$$= C_{12}$$

where C_{12} is given by eq. (13). That M is approximately equal to C_{12} when $M^2 << 1$, is also evident from eq. (12).

SIMPLIFIED TEST CASE

As a simplified standard test case consider a 1500 m tall, 160 m inner diameter chimney with inlet stagnation temperature, T_1=323.15 K, inlet stagnation pressure, P_1 = 90 kPa, and a mass flow of 250000 kg/s. The inlet Mach number is then M_1 = 0.0355907 and the inlet static pressure is, $p_1 = P_1/(1+M_1^2(\gamma-1)/2)^{(\gamma-1)/\gamma}$ = 89920.2 Pa. Also assume that the the gas constant R = 287.08 J/kgK and the specific heat ratio, γ =1.400, giving c_p = 1004.78 J/kgK and an adiabatic temperature lapse rate constant, g/c_p = 9.800/1004.78 = 0.00975338 K/m. Since an accuracy of about 1 Pa is required, it is clear from Table 1 that the approximate solution is not acceptable, but the analytical solution of the quadratic equation is.

Table 1 Comparison of calculation schemes for exit Mach numbers and static pressures for ideal standard chimney

Approximate scheme		Quadratic scheme		Iterative scheme	
C_{12}	p_2 (Pa)	M_2	p_2 (Pa)	M_2	p_2 (Pa)
0.040867	76515.01	0.0409077	76438.23	0.0409077	76438.22

ACCURACY CHECK

To investigate the accuracy of the procedure, check how well values obtained from it satisfy the conservation equations.

Mass conservation

The inlet mass flow is 250000kg/s. The exit stagnation temperature, from eq. (1), is 308.52 K. The exit static temperature is:

$$t_2 = T_2/(1+\frac{\gamma-1}{2}M_2^2)$$
$$= 308.520/\left(1+0.2*0.0409077^2\right) \qquad (16)$$
$$= 308.417\ \text{K}$$

The exit velocity is:

$$V_2 = M_2(\gamma R t_2)^{\frac{1}{2}}$$
$$= 0.0409077\left(1.4\times 287.080\times 308.417\right)^{\frac{1}{2}} \qquad (17)$$
$$= 14.4026\ \text{m/s}$$

The exit mass flow is:

$$\dot{m}_2 = \rho_2 V_2 A_2 = \frac{p_2}{R t_2} V_2 A_2$$
$$= \frac{76438.2}{287.080\times 308.417}14.4026\times 20106.2 \qquad (18)$$
$$= 250\,000\ \text{kg/s}$$

Energy conservation

Consider frictionless flow through a 1500 m tall chimney. The inlet energy per unit mass flow is:

$$c_p t_1 + \frac{V_1^2}{2} + g z_1$$
$$= 1004.78\times 323.068 + \frac{12.8248^2}{2} + 9.8\times 0 \qquad (19)$$
$$= 324\,695\ \text{J/kg}$$

The exit energy per unit mass flow is:

$$c_p t_2 + \frac{V_2^2}{2} + g z_2$$
$$= 1004.78\times 308.417 + \frac{14.40256^2}{2} + 9.8\times 1500 \qquad (20)$$
$$= 324\,695\ \text{J/kg}$$

Momentum equation

The incompressible control volume momentum equation for flow through a constant area vertical chimney of height, Δz is:

$$p_1 A - p_2 A - \rho_{ave} g \Delta z A = \dot{m}(V_2 - V_1)$$
$$p_1 - p_2 = \rho_{ave} g \Delta z + \frac{\dot{m}}{A}\left(\frac{\dot{m}}{\rho_2 A} - \frac{\dot{m}}{\rho_1 A}\right) \qquad (21)$$
$$= \rho_{ave} g \Delta z + \left(\frac{\dot{m}}{A}\right)^2\left(\frac{1}{\rho_2} - \frac{1}{\rho_1}\right)$$
$$= \Delta p_h + \Delta p_a$$

The pressure drop consists of a hydrostatic (weight) component and an acceleration component. The average density in the hydrostatic component needs to be known very accurately (to about 5 significant figures) to satisfy the momentum equation to within 1 Pa. An analytical solution for average density follows later.

The average density may however be calculated by numerical integration of the density at each chimney height. Accurate equations for the average density follow later. By meanwhile taking ten steps over the chimney height the average density for the conditions under consideration is: ρ_{ave} = 0.915871 kg/m^3. The hydrostatic pressure drop is then 13463.3 Pa.

To calculate the acceleration term in the momentum equation, find: ρ_1 = 89920.2/(287.08*323.068) = 0.969528 kg/m^3 and ρ_2 = 76438.2/(287.08*308.417) = 0.863316 kg/m^3.

$$\Delta p_a = \left(\frac{\dot{m}}{A}\right)^2\left(\frac{1}{\rho_2} - \frac{1}{\rho_1}\right)$$
$$= \left(\frac{250000}{20106.2}\right)^2\left(\frac{1}{0.863316} - \frac{1}{0.969528}\right) \qquad (22)$$
$$= 19.6\ \text{Pa}$$

The exit pressure is then:

$p_2 = p_1 - \Delta p_h - \Delta p_a$ = 89920.2 – 13463.3 – 19.6 = 76437.3 Pa. The difference between it and the value of p_2 = 76438.2 kPa from eq. (6) is 1 Pa. A more accurate check follows later, after formulating an analytical equation for average density.

THE EFFECT OF MACH NUMBER ON PRESSURE LAPSE RATIO

By applying logarithmic differentiation to eq.(6), Von Backström and Gannon [7] derived the following equation for pressure variation in terms of Mach number and stagnation temperature variation:

$$\frac{dp}{p} = \frac{1+(\gamma-1)M^2}{1+\frac{(\gamma-1)}{2}M^2}\frac{dM}{M} + \frac{1}{2}\frac{dT}{T} \qquad (23)$$

Substitute eq. (5) for dM/M:

$$\begin{aligned}\frac{dp}{p} &= -\frac{1+(\gamma-1)M^2}{1-M^2}\left(-\frac{dA}{A} - \frac{1}{2}\frac{\gamma+1}{\gamma-1}\frac{dT}{T} + L\frac{\gamma M^2}{2}\delta z\right) + \frac{1}{2}\frac{dT}{T} \\ &= -\left(1+\gamma\frac{M^2}{1-M^2}\right)\left(-\frac{dA}{A} - \frac{1}{2}\frac{\gamma+1}{\gamma-1}\frac{dT}{T} + L\frac{\gamma M^2}{2}\delta z\right) + \frac{1}{2}\frac{dT}{T} \\ &= \frac{\gamma}{\gamma-1}\left(1+\frac{\gamma+1}{2}\frac{M^2}{1-M^2}\right)\frac{dT}{T} + \left(1+\gamma\frac{M^2}{1-M^2}\right)\left(\frac{dA}{A} - L\frac{\gamma M^2}{2}\delta z\right)\end{aligned} \qquad (24)$$

The Mach number distribution is required for an accurate solution, but since $M^2 << 1$ and it changes little through the chimney, we investigate the effect of using $M = M_1$ constant throughout the chimney. Integrate over δz between z_1 and z:

$$\begin{aligned}\ln\frac{p}{p_1} &= \ln\left(\frac{T}{T_1}\right)^{\frac{\gamma}{\gamma-1}\left(1+\frac{\gamma+1}{2}\frac{M^2}{1-M^2}\right)} + \ln\left(\frac{A}{A_1}\right)^{\left(1+\gamma\frac{M^2}{1-M^2}\right)} \\ &\quad -\left(1+\gamma\frac{M^2}{1-M^2}\right)\left(L\frac{\gamma M^2}{2}(z-z_1)\right)\end{aligned} \qquad (25)$$

And:

$$\frac{p}{p_1} = \left(\frac{T}{T_1}\right)^{\frac{\gamma}{\gamma-1}\left(1+\frac{\gamma+1}{2}\frac{M^2}{1-M^2}\right)}\left(\frac{A}{A_1}\right)^{\left(1+\gamma\frac{M^2}{1-M^2}\right)} e^{-\left(1+\gamma\frac{M^2}{1-M^2}\right)\left(L\frac{\gamma M^2}{2}\delta z\right)} \qquad (26)$$

Eq. (26) shows that the pressure lapse ratio is a function of not only the stagnation temperature lapse rate, but also of the chimney area ratio and chimney friction and other losses, and that the effects of these parameters are modified by the Mach number.

To check the accuracy, at least for constant area frictionless flow, substitute the previously used data in eq. (26)

$$\begin{aligned}\frac{p}{p_1} &= \left(\frac{T}{T_1}\right)^{\frac{\gamma}{\gamma-1}\left(1+\frac{\gamma+1}{2}\frac{M^2}{1-M^2}\right)} \\ &= 89920.2\left(\frac{308.520}{323.150}\right)^{3.5\left(1+1.2\frac{0.0355907^2}{1-0.0355907^2}\right)} \\ &= 76441.1\text{Pa}\end{aligned} \qquad (27)$$

This differs by 2.9 Pa from the correct answer of 76438.2 Pa. A more accurate approach would be to use the average value of M, where:

$M_{ave} = (M_1 + M_2)/2 = (0.0355907 + 0.0409077)/2 = 0.0382492$. Then p =76438.2 Pa. This answer is correct to 0.0 Pa.

To investigate the use of the no-flow lapse ratio equation, put M = 0, in eq. (27). Then the exit pressure due to hydrostatic effects alone is: p = 76460.0 Pa. Now subtract the acceleration pressure drop of 19.6 Pa from the exit pressure to find p_2 = 76440.4 Pa. The error of 2.4 Pa is small, but optimistic (pressure too high). Note that the temperature ratio must be based on stagnation temperatures, as seen from the energy equation, (1).

THE EFFECT OF MACH NUMBER ON DENSITY

Differentiate the equation of state logarithmically:

$$\frac{d\rho}{\rho} = \frac{dp}{p} - \frac{dt}{t} \qquad (28)$$

Differentiate logarithmically the equation for T in terms of t and M:

$$\frac{dt}{t} = \frac{dT}{T} - \frac{(\gamma-1)M^2}{\left(1+\frac{\gamma-1}{2}M^2\right)}\frac{dM}{M} \qquad (29)$$

Substitute eq. (5):

$$\frac{dt}{t} = \frac{dT}{T} - \frac{(\gamma-1)M^2}{1-M^2}\left(-\frac{dA}{A} - \frac{1}{2}\frac{\gamma+1}{\gamma-1}\frac{dT}{T} + L\frac{\gamma M^2}{2}\delta z\right) \qquad (30)$$

Substitute eqs. (24) and (30) in (28):

$$\begin{aligned}\frac{d\rho}{\rho} &= -\frac{1+(\gamma-1)M^2}{1-M^2}\left(-\frac{dA}{A} - \frac{1}{2}\frac{\gamma+1}{\gamma-1}\frac{dT}{T} + L\frac{\gamma M^2}{2}\delta z\right) + \frac{1}{2}\frac{dT}{T} \\ &\quad -\frac{dT}{T} + \frac{(\gamma-1)M^2}{1-M^2}\left(-\frac{dA}{A} - \frac{1}{2}\frac{\gamma+1}{\gamma-1}\frac{dT}{T} + L\frac{\gamma M^2}{2}\delta z\right) \\ &= \frac{1}{1-M^2}\left(\frac{dA}{A} - L\frac{\gamma M^2}{2}\delta z\right) + \frac{1}{1-M^2}\left(\frac{1}{\gamma-1} + M^2\right)\frac{dT}{T}\end{aligned} \qquad (31)$$

Since $M^2 << 1$ and does not change much, assume the terms containing Mach number are constant, and integrate for the density lapse ratio between z_1 and z:

$$\begin{aligned}\ln\left(\frac{\rho}{\rho_1}\right) &= \ln\left(\frac{T}{T_1}\right)^{\left(\frac{1}{\gamma-1}\right)\frac{1+(\gamma-1)M^2}{1-M^2}} + \ln\left(\frac{A}{A_1}\right)^{\frac{1}{1-M^2}} \\ &\quad -\frac{1}{1-M^2}\left(L\frac{\gamma M^2}{2}\delta z\right)\end{aligned} \qquad (32)$$

Simplify:

$$\frac{\rho}{\rho_1} = \left(\frac{T}{T_1}\right)^{\left(\frac{1}{\gamma-1}\right)\frac{1+(\gamma-1)M^2}{1-M^2}}\left(\frac{A}{A_1}\right)^{\frac{1}{1-M^2}} e^{-\left(\frac{L}{2}\right)\frac{\gamma M^2}{(1-M^2)}\delta z} \qquad (33)$$

Numerical integration of eq. (33) is possible if A and L are expressed as functions of z. For constant area, frictionless flow, under the assumption of constant Mach number terms, the average density may be found by substituting eq. (1) into eq. (33) and integrating analytically:

$$\frac{\rho_{ave}}{\rho_1} = \frac{1}{\left(\frac{\gamma}{\gamma-1}\right)\frac{1}{1-M^2}} \frac{c_p T_1}{g(z-z_1)} \left(1-\left(1-\frac{g\delta z}{c_p T_1}\right)^{\left(\frac{\gamma}{\gamma-1}\right)\frac{1}{1-M^2}}\right)$$

$$= \frac{1}{\left(\frac{\gamma}{\gamma-1}\right)\frac{1}{1-M^2}} \frac{1}{\left(1-\frac{T}{T_1}\right)} \left(1-\left(\frac{T}{T_1}\right)^{\left(\frac{\gamma}{\gamma-1}\right)\frac{1}{1-M^2}}\right) \qquad (34)$$

Substitution of $M = M_1 = 0.0355907$ and the rest of the values used previously in the example under consideration, gives $\rho_{ave} = 0.915804$ kg/m^2 and $\Delta p_h = 13462.3$ Pa.The exit pressure is then:$p_2 = p_1 - \Delta p_h - \Delta p_a = 89920.2 - 13462.3 - 19.6 = 76438.3$ Pa. The difference between it and the value of $p_2 = 76438.2$ kPa from eq. (6) is 0.1 Pa. Substitution of $M = M_{ave} = 0.0382492$ and the rest of the values used previously gives $\rho_{ave} = 0.915804$ kg/m^2 and $\Delta p_h = 13462.1$ Pa. Using M_{ave} is not worthwhile since the agreement with the value of $p_2 = 76438.2$ Pa found when using eq. (6) does not improve, but deteriorates by an additional 0.2 Pa.

No-flow average density

When M = 0 and T = t, eq. (34) simplifies to:

$$\frac{\rho_{ave,M=0}}{\rho_1} = \frac{1}{\left(\frac{\gamma}{\gamma-1}\right)} \frac{c_p t_1}{g\delta z} \left(1-\left(1-\frac{g\delta z}{c_p t_1}\right)^{\left(\frac{\gamma}{\gamma-1}\right)}\right) \qquad (35)$$

$$\rho_{ave,M=0} = \frac{p_1}{g\delta z}\left(1-\left(\frac{p}{p_1}\right)\right) = \frac{p_1 - p}{g\delta z} \qquad (36)$$

This is in fact the well-known hydrostatic equation: $\Delta p = -\rho_{ave}\, g\, \Delta z$. Eq. (34) gives the equivalent equation for a vertically accelerating compressible fluid

CONCLUSION

The paper develops methods for finding all the thermodynamic properties for compressible frictional flow through a tall vertical chimney. The chimney flow area may change with height and it may have internal bracing, causing pressure drops. The method finds the stagnation temperature distribution directly from the altitude, by applying the energy equation. It then finds the Mach number distribution from the vertical distributions of stagnation temperature, friction factor, bracing drag loss coefficient and flow area. The static pressure at each altitude follows from the continuity equation.

The paper points out that the generally used adiabatic temperature lapse rate equation in principle applies to the stagnation temperature, and applying it to the static temperature is valid only when the Mach number is equal to zero.

It presents two equations for the vertical pressure and density distributions in terms of Mach number. One of these is a generalisation of the adiabatic pressure lapse ratio equation to include non-zero, but small Mach numbers. The other is analogous to the hydrostatic relationship between pressure and density but extends it to small Mach numbers. Its integration leads to an equation for the average density in the chimney for the non-zero small Mach number case. A very accurate value of the average density is exactly what the commonly used incompressible flow approach to the problem requires, to represent the hydrostatic pressure drop in the chimney accurately.

Methods of solving the equations for low Mach numbers are presented. They are simple enough to use in spreadsheet solutions or for checking the accuracy of incompressible flow approximations. The methods satisfy the energy, mass conservation and momentum equations exactly, in contrast to the incompressible approach, that only satisfies some of them

REFERENCES

1. Haaf W, Friedrich K, Mayr G and Schlaich J, Solar chimneys Part 1: Principle and construction of the pilot plant in Manzanares, International Journal of Solar Energy, Vol. 2 pp 3-20, 1983.
2. Mullett LB, The solar chimney - overall efficiency, design and performance, International Journal of Ambient Energy, Vol 8 No 1, pp 35-40, Jan 1987.
3. Schlaich J, The solar chimney, electricity from the sun, Axel Menges, Stuttgart, 1995
4. Kröger, D.G. and Blaine, D. Analysis of the driving potential of a solar chimney power plant, S.A. Inst. of Mech. Eng. R + D Journal, Vol. 15, pp. 85 – 94, 1999.
5. Von Backström, T.W., The solar chimney air standard cycle. SAIMechE R&D Journal, Vol 16, No 1, pp 16-24, 2000.
6. Gannon, AJ. and Von Backström, T.W. Solar chimney analysis with system loss and solar collector performance. ASME Journal of Solar Energy Engineering, Vol 122, pp 133-137, August 2000.
7. Von Backström, TW and Gannon, AJ., Compressible flow through solar power plant chimneys. ASME Journal of Solar Energy Engineering, Vol 122, pp 138-145, August 2000.
8. Schlaich, J. Tension structures for solar electricity generation. Engineering Structures, Vol. 21 pp. 658-668.
9. Zucrow, MJ and Hoffman JD, *Gas Dynamics*. Wiley, New York, 1976.

HEFAT2002
1st International Conference on Heat Transfer, Fluid Mechanics, and Thermodynamics
8-10 April 2002, Kruger Park, South Africa
BM2

HEAT TRANSFER CHARACTERISTICS OF A BIFACIAL SOLAR COLLECTOR WITH COMPLEX GEOMETRY

N. Groenhout, M. Behnia and G.L. Morrison
School of Mechanical and Manufacturing Engineering
The University of New South Wales
SYDNEY 2052 AUSTRALIA
Ph: + 61 2 9385 5127 Fax: +61 2 9663 1222 Email: nathang@unsw.edu.au

ABSTRACT

A study of the heat transfer in a novel solar collector is presented. The design incorporates a number of features that provide improved performance over conventional flat plate collectors. The complex design of the collector means that standard experimental and empirical heat transfer correlations do not adequately describe the collector performance. The aim of this study is to develop experimentally validated numerical models to create a design optimisation tool for advanced solar collectors.

The numerical model created, using a commercial CFD code on PC, can be used to model a large range of parameters and environmental conditions without the need for extensive and costly experimentation. The results show that whilst the accuracy of the model is related to its complexity, good agreement with experimental data can be achieved through simplification of the model. This study shows that the use of PC based commercial CFD software is a valid and useful tool for the solution of heat transfer phenomena within systems with complex geometry.

INTRODUCTION

In this study a novel design for a flat plate solar collector has been proposed that incorporates a number of features offering improved performance over traditional designs [1]. These features include a double-sided flat plate absorber and stationary reflectors with compound curve surfaces as shown in figure 1. Heat transfer in solar collectors such as the one proposed here occurs through a complex combination of conduction, convection and radiation. The modelling and analysis of heat transfer within air-filled cavities with complex geometries presents a number of difficulties that require innovative and novel approaches to achieve sensible results. In this instance, the complexities of the design means that standard heat transfer correlations cannot adequately describe or predict the heat transfer phenomena occurring in the collector and a numerical approach is therefore required. This numerical approach must then be validated with experimental results. Eventually the validated model may be used as a design optimisation tool, improving performance and reducing the design cycle and hence the cost of developing new products.

The study is part of a multifaceted project investigating heat transfer and fluid flow as well as expanding the use of existing software modelling tools for the solution of complex heat transfer and fluid flow problems.

NOMENCLATURE

A	= Exposed surface area of individual heater, m^2
A_t	= Combined total exposed surface area of the heater plate, m^2
g	= Acceleration due to gravity (taken to be 9.797 m/s2 in Sydney, Australia)
L	= Characteristic length, m
$\bar{P}$	= Time weighted average power of individual heater, W
Ra	= Rayleigh Number
$\bar{T}_{amb}$	= Time weighted average ambient temperature, °C
$\bar{T}_{ave}$	= Time weighted average of combined heaters, °C
$\bar{U}_o$	= Overall heat transfer coefficient, W/m^2 K

Greek Letters

α	= Thermal diffusivity, m^2/s
β	= Temperature co-efficient of expansion, 1/K
ΔT	= $(\bar{T}_{ave} - \bar{T}_{amb})$, °C
ν	= Kinematic viscosity, m^2/s

DESCRIPTION OF EXPERIMENTAL SET-UP

A number of experiments have carried out on an indoor experimental rig to assess the heat loss characteristics of the collector. The experimental set-up is shown in figure 2, whilst figure 3 shows a photograph of the experimental rig.

The experimental rig is a full-scale timber and glass model, located in a small temperature controlled room. The dimensions of the collector are approximately 2 m (W) x 2 m (L) x 0.45 m (H). The absorber plate is simulated by three 1kW heater plates connected to variable power supplies. Thermocouples are used to measure surface temperatures at a number of locations on the heaters and throughout the collector. This data along with

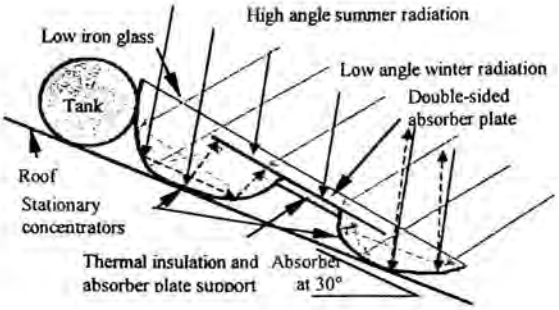

Figure 1: Cross-section of the proposed collector design showing the compound curve reflectors

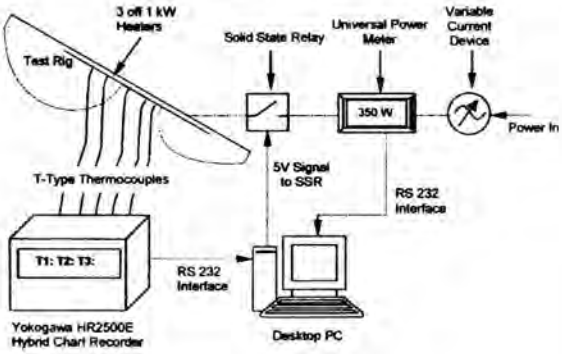

Figure 2: Schematic diagram showing the experimental configuration

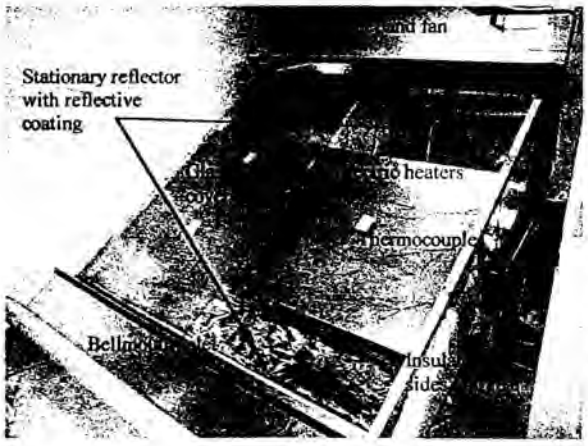

Figure 3: Photograph showing the various features of the experimental rig

ambient temperature and power consumption are recorded on a PC for later analysis. To enable a consistent measurement of the heat transfer coefficient of the glass cover, and to allow simulation of wind across the top cover, a ducted airflow has been installed over the inclined glass surface. A more comprehensive description of the experimental set-up and procedure is provided in [2].

EXPERIMENTAL RESULTS

Experiments were performed to determine the overall heat loss characteristics of the proposed design. These have been carried out over temperatures ranging from 30°C to 100°C. At steady state, the heat lost by the system is equal to the heat input to the collector and hence the sum of the convective, conductive and radiative losses through the glass cover and the insulated walls is equal to the power input to the heaters. The average overall heat transfer coefficient, $\overline{U}_o$, is then given by Eq. (1).

$$\overline{U}_o = \frac{\sum_{i=1}^{3} \overline{U}_i A_i}{A_i} \quad \text{where } \overline{U}_i = \frac{P}{A\Delta T} \tag{1}$$

The overall measured heat transfer coefficients obtained from the experiments were plotted as a function of the temperature difference between the average plate temperature and the ambient temperature, and the equation for the line of best fit was obtained. Figure 4 shows the variation of the overall heat transfer coefficient as a function of ΔT. The dimensional equation describing this data is given by Eq. (2):

$$\overline{U}_o = -1.96\times10^{-4}(\overline{T}_{pa} - \overline{T}_{am})^2 + 0.0406(\overline{T}_{pa} - \overline{T}_{am}) + 2.00 \tag{2}$$

The overall heat transfer coefficient varies between 2.37 and 4.03 W/m^2 K. Flat plate collectors of the type used in most domestic applications typically have overall heat transfer coefficients in the range 5.5 W/m^2 K for the best selective surfaces to 10-11 W/m^2 K for plain black absorber surfaces. This significant reduction in heat loss, particularly at lower temperatures is attributable to a number of factors including the coupling between the radiation and convection within the collector.

The experimental rig was subsequently modified to include a convection suppression barrier from the top edge of the heater plate to the bottom of the large cavity (approximately 300 mm). The purpose of this barrier is to investigate the effect that natural convection on the underside of the absorber plate contributes to the overall heat loss of the collector. The experiments were run over the same temperature range as the original experiments and the results for overall heat transfer coefficient were again plotted against temperature difference. Table 1 summarises these results, whilst figure 4 shows the plotted data. This data is described by Eq. (3):

$$\overline{U}_o = -2.11\times10^{-4}(\overline{T}_{pa} - \overline{T}_{am})^2 + 0.0405(\overline{T}_{pa} - \overline{T}_{am}) + 1.83 \tag{3}$$

It can be seen from both figure 4 and table 1 that the effect of the convective suppression is reasonably significant in that it reduces the overall heat transfer coefficient by more than six percent over the range of temperatures tested. In addition, the results indicate that its effect is independent of temperature.

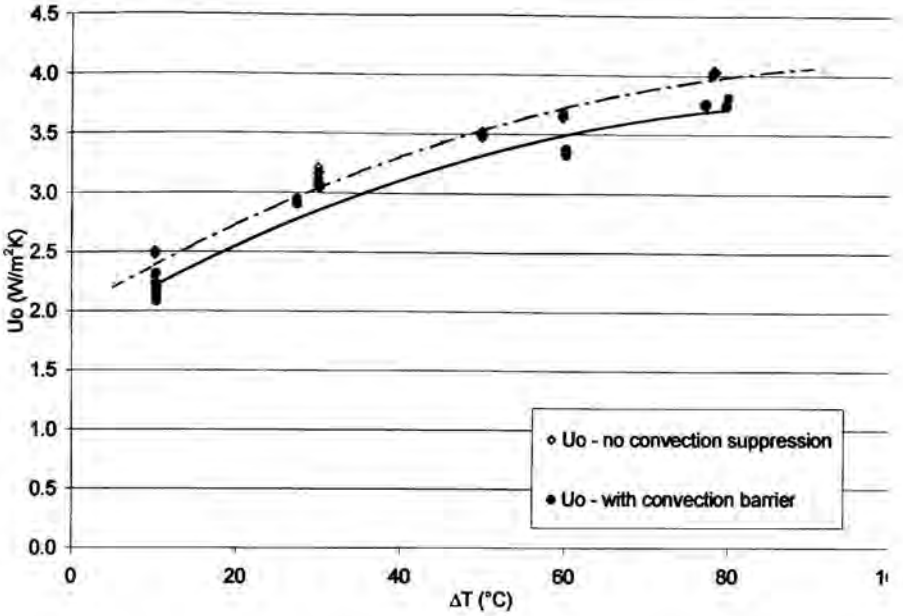

Figure 4: Plot of U_o vs ΔT from experimental data with and without convection suppression

Table 1: Comparison between overall heat transfer for configurations with and without convection suppression

	Overall Heat Loss Coefficient, U_O (W/m^2K)			
Absorber Temperature (°C)	30	50	80	100
No Suppression	2.34	3.11	3.65	4.03
~300 mm long Barrier	2.19	2.92	3.36	3.77
% Decrease in U_O	6.80	6.54	8.72	6.96

NUMERICAL MODELLING

Model formulation

The computational fluid dynamics (CFD) modelling approach has been utilised for two important reasons. Firstly, the complex geometry of the collector means that existing experimental and empirical heat transfer correlations cannot adequately describe the natural convection within the collector. Secondly, experimental techniques are expensive, time consuming and have limited scope for parametric analysis when compared with computational techniques. Numerical modelling allows results to be obtained for a large range of variables, which traditionally required a range of experiments to be performed often on more than one experimental rig. Once the model is validated it may be used to investigate changes in boundary conditions, the collector geometry and the environment.

The collector has been modelled using a commercial CFD package, FLUENT, running on a PC. The model formulation has been described previously in [3]. The purpose of the modelling is to study both the heat loss characteristics of the collector and the flow patterns of the air within the collector to investigate methods of reducing natural convection.

The modelling is being undertaken in two phases. Initially a 2-D model of the collector was created, taking a vertical slice through the centre of the collector. This approach assumes that the ends are sufficiently distant from the plane of interest to avoid edge effects in the solution. Fluent assumes a unit width of one metre for 2-D models. The second phase involves extending the models into 3-D.

The Rayleigh Number, which is a measure of the strength of the natural convective forces in the cavities, is in the range of $8.8 \times 10^8 - 4.6 \times 10^9$ and is calculated using Eq.(4).

$$Ra = \frac{g\beta(T_w - T_\infty)L}{\alpha\nu} \qquad (4)$$

These values suggest the natural convection plays a dominant role in the heat loss and that the flow inside the collector cavity is turbulent [4]. Furthermore, for solar collectors the energy flux is generally significantly less than in conventional heat transfer equipment making radiation a significant factor in the heat transfer of the system [5]. The model is therefore complicated requiring both turbulence and radiation terms to be included. The addition of these parameters

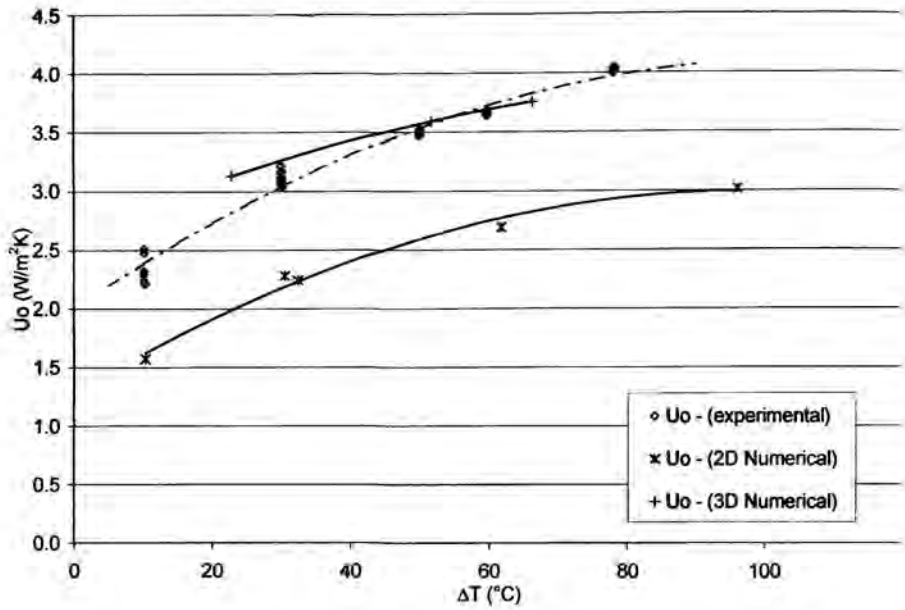

Figure 5: Plot of U_o vs ΔT comparing experimental results with 2-D and 3-D numerical data

greatly increases computational time and memory requirements.

Boundary conditions for the model have been taken from the experimental data. The walls of the collector are assumed to be insulated and to have very low heat loss, whilst the glass has a heat loss coefficient an order of magnitude higher.

The absorber plate was modelled initially as a single isothermal surface with the plate temperature varied between 50°C and 80°C. This was then modified to more accurately represent the experimental set-up, which consists of three heaters side by side. A heat flux, q'' W/m^2, boundary condition based on experimental results was then incorporated into the model. The ambient air temperature was constant for all cases and equal to the experimental ambient temperature.

NUMERICAL RESULTS

Results from a number of 2-D cases were obtained and compared. These cases included configurations with no convection suppression and with a 100 mm and 200 mm, thin convection suppression barrier. For the cases with no convection suppression, the absorber plate was given a constant heat flux as determined from experimental conditions. The other two cases used an isothermal temperature condition The results for the 2-D case with no convection suppression are plotted on the same curve as the experimental data as shown in figure 5. This graph shows that the 2-D model under predicts the overall heat loss by approximately 30 % over the range of temperatures modelled, however, the overall fit of the data is similar.

The flow patterns observed in 2-D model show a strong convective plume in the upper cavity of the collector with thermally stratified flow in the lower one as shown in figure 6. The presence of Rayleigh-Benard type cells between the top of the absorber plate and the underside of the glass cover indicates that the two regions do not interact with each other, and as a consequence the lower cavity plays a less significant role in the heat loss. In the upper cavity the large convective cell draws heat away from the underside of the absorber plate up to the glass cover, where it is transferred to the environment.

When a barrier was added to the 2-D model the heat loss dropped as expected. Again, however, the model under predicted the experimental results. Table 2 shows a comparison of the three models for a plate temperature of approximately 50°C.

Table 2: Effect of the inclusion of convection suppression in the upper cavity of the collector

Case	Absorber Heat Flux (W/m2)	Overall Heat Transfer Coefficient Uo (W/m2 K)	Decrease in Uo
No Convection Suppression	78.83	2.52	
~ 100 mm Tefzel Barrier	74.26	2.48	1.59%
~ 200 mm Tefzel Barrier	71.09	2.37	5.95%

The model was then extended into 3-D and the preliminary results show a strong axial flow present in the larger cavity. The 2-D model assumes the cavity has no end effects, however, the dimensions of the collector are such that the aspect ratio

L/D of the large cavity is approximately 4.5. As a consequence, the cooler sidewalls draw the warm air away from the centre of the collector in a manner that cannot be predicted in the 2-D modelling and these models under predict the amount of heat being lost through the sidewalls. It also showed that the structure of the strong convective plume in the upper cavity changes along the length of the cavity.

The amount of time required to solve a full model of the collector is computationally very expensive and it was therefore considered necessary to modify the model to include only the larger cavity. A number of preliminary cases have been run for this reduced model and the results are shown in figure 6. Figure 7 shows the complex flow structure present in the large cavity. There is better agreement between the 3-D model and the experimental data. The reduced geometry model generally over predicts the overall heat loss compared to the experimental results since the regions with lower than average heat loss in the collector have not been included.

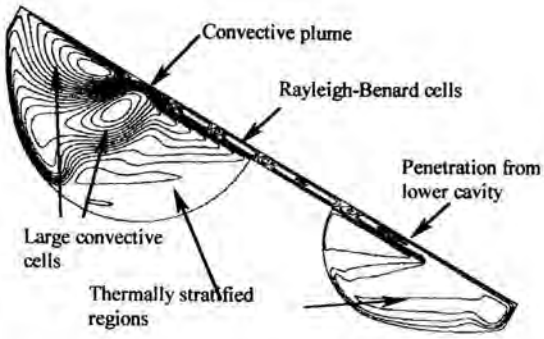

Figure 6: Plot of streamline contours from 2-D model showing the complex flow structure present in the collector

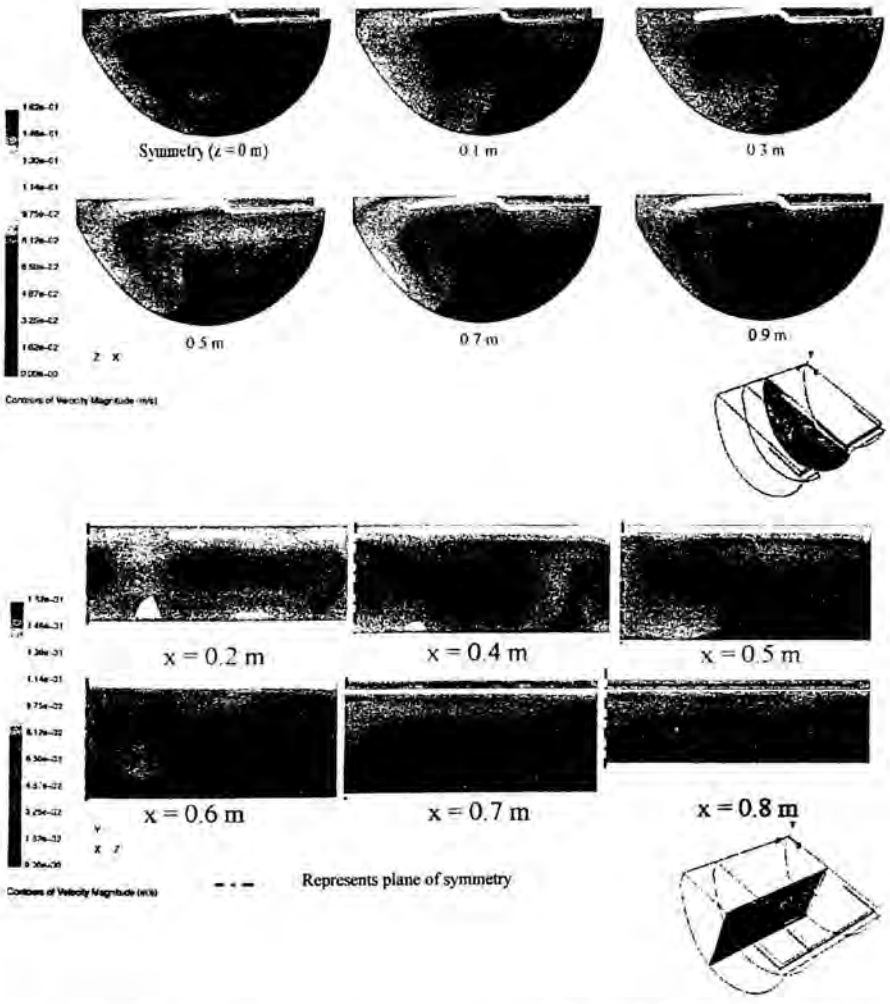

Figure 7: Plot of velocity contours in two planes from 3-D model showing the complex flow structure present in the large cavity

CONCLUDING REMARKS

An approach for determining the heat transfer characteristics of complex geometry problems using experimentally validated numerical models has been presented. In this instance the geometry consists of compound curve reflectors forming large air filled cavities. An experimental rig has been used to develop boundary conditions for a numerical model. The numerical model uses commercial CFD software, running on a desktop PC, to solve complicated heat transfer phenomena involving natural convection, turbulence and radiation. Results have been obtained for both 2-D and 3-D cases and the model has been simplified to reduce computational requirements. The numerical results have been compared with the experimentally determined data. The results of the study to date show that the accuracy of the simulations is directly related to the level of complexity in the model, though good agreement with experimental results is achievable even with simplified models of complex systems.

The speed of analysis using numerical techniques is restricted by computational resources, however, the level of analysis and the amount of information and detail available to the researcher is far greater than that obtained from a single set of experiments. The use of computational tools allows the researcher to investigate a large range of parameters without the need for continual changes to experimental apparatus. The study shows that experimentally validated numerical models are valid tools for the solution of complex heat transfer problems.

REFERENCES

[1] Groenhout, N.K., Morrison G.L., and Behnia, M. (2000). *Design of Advanced Solar Water Heaters,* Proc. ANZSES Solar 2000 Conf, Brisbane Nov 29 – Dec 3, 2000, pp. 295-303

[2] Groenhout, N.K., Behnia, M., and Morrison, G.L. (2001), *Investigation of heat loss from advanced solar water heaters*, Proc. 5th World Conf Expt Heat Transfer, Fluid Mechanics & Thermodynamics, Thessaloniki, Greece, Sept. 2001, pp 765-770

[3] Groenhout, N.K., Behnia, M. and Morrison, G.L. (2001). *Numerical Modelling of Natural Convection and Radiation Heat Transfer in Advanced Solar Water Heaters*, Proc. 1st Asian-Pacific Cong. Comp. Mech., Sydney, Nov 20-23, 2001, pp 1705-1710

[4] Bejan, A. (1995), *Convective Heat Transfer*, Wiley

[5] Duffie, J.A. & Beckman, W.A. (1991), *Solar Engineering of Thermal Processes*, Wiley

HEFAT2002
1st International Conference on Heat Transfer, Fluid Mechanics, and Thermodynamics
8-10 April 2002, Kruger National Park, South Africa
BA3

CONDENSATION OF STEAM ON PIN-FIN TUBES

A Briggs
Department of Engineering
Queen Mary, University of London
Mile End Road
London E1 4NS
United Kingdom
Email: A.Briggs@qmw.ac.uk

ABSTRACT

Experimental data are reported for condensation of near quiescent steam on four three-dimensional pin-fin tubes. Enhancements of up to 350% in heat transfer were found when compared to a plain tube at the same vapour-side temperature difference, greater than previously found for simple two-dimensional integral-fin tubes with the same tube diameter in earlier investigations. The heat-transfer enhancement on the best performing tubes was almost double the increase in surface area due to the addition of the pin-fins. It is thought that a reduction in condensate retention, or flooding, is a strong contributing factor.

INTRODUCTION

There is developing interest in the use of integral-fin tubes in shell-side condensers to enhance the vapour-side, heat-transfer coefficient. The mechanism of heat-transfer enhancement on simple rectangular and trapezoidal cross-section integral-fin tubes is relatively well understood (see for instance, Marto [1], Briggs and Rose [2]). Surface tension induced pressure gradients drain condensate from the tips and flanks of the fins, thinning the film and enhancing the heat transfer, while at the bottom of the tube condensate is retained in the inter-fin spaces leading to a decrease in the available area for heat transfer. For low surface tension fluids such as refrigerants the first of these effects dominates leading to enhancements in heat transfer above the increase in surface area due to the fins. For high surface tension water, however, the two effects appear to be of similar magnitude and the enhancement in heat transfer is comparable to increases in surface area.

In recent years advanced manufacturing techniques have meant that tubes with complex, three-dimensional fin profiles can be produced. Briggs et al. [3] presented data for condensation of R-113 on ten commercially available tubes with complex three-dimensional fin profiles as well as seven tubes with two-dimensional trapezoidal cross-section fins. Their results showed that the best of the three-dimensional tubes gave similar heat transfer performance to the best of the simpler two-dimensional tubes. Sukhatme et al. [4] condensed R-11 on tubes with simple three-dimensional fins, made by machining longitudinal grooves of various depths into trapezoidal cross-section fins. They found that the heat transfer increased by up to 25% (at the same vapour-side temperature difference) compared to the original tube. They suggested that a reduction in condensate retention between the fins of the grooved tubes may have been a contributing factor in the increase in heat transfer.

There is some evidence, then, that complex, three-dimensional fin profiles can produce worthwhile enhancement over those obtained from simpler two-dimensional integral-fin tubes. In the present work, which reports on the start of a systematic investigation into condensation on tubes with three-dimensional fin profiles, data are presented for condensation of near quiescent steam on four pin-fin tubes.

NOMENCLATURE

A	Constant in Eq. (2) ($W/m^2 K^n$)
A_{root}	Tube surface area between pins (m^2)
A_{pin}	Surface area of pins (m^2)
A_{plain}	Surface area of plain tube with diameter equal to pin root diameter (m^2)
c_{pc}	Specific isobaric heat capacity of coolant at temperature T_c (J/kgK)
d_i	Inside diameter of tube (m)
h	Pin height (m)
k_c	Thermal conductivity of coolant at temperature T_c (W/m K)
Nu_c	Coolant Nusselt number, $\alpha_c d_i / k_c$
n	Constant in Eq. (2)

Pr_c	Coolant Prandtle number, $\mu_c c_{pc}/k_c$
q	Heat flux, based on area of plain tube with diameter equal to pin-root diameter (W/m^2)
q_i	Heat flux, based on inside tube surface area (W/m^2)
Re_c	Coolant Reynolds number, $\rho_c u_c d_i/\mu_c$
s_c	Circumferential pin spacing (m)
s_l	Longitudinal pin spacing (m)
T_c	Mean coolant temperature (K)
T_v	Vapour temperature (K)
T_{wi}	Mean inside wall temperature (K)
T_{wo}	Mean outside wall temperature (K)
t_c	Circumferential pin thickness (m)
t_l	Longitudinal fin thickness (m)
U_o	Overall heat-transfer coefficient, $q/(T_v - T_c)$ (W/m^2 K)
u_c	Mean coolant velocity (m/s)

Greek Letters

α_c	Coolant-side heat-transfer coefficient, $q_i/(T_{wi} - T_c)$ (W/m^2K)
ΔT	Vapour-side temperature difference, $T_v - T_{wo}$ (K)
$\varepsilon_{\Delta T}$	Heat-transfer enhancement ratio, ratio of heat fluxes for pin-fin and plain tube at same vapour-side temperature difference
ε_{area}	Area enhancement ratio, ratio of total surface areas of pin-fin tube and plain tube
$\varepsilon_{area\text{-}corr}$	Area enhancement ratio corrected for fin efficiency (see Eq. (4))
η	Fin efficiency
μ_c	Viscosity of coolant at temperature T_c (kg/m s)
μ_w	Viscosity of coolant at temperature T_{wi} (kg/m s)
ρ_c	Density of coolant at temperature T_c (kg/m^3)

EXPERIMENTAL APPARATUS

Steam was used as the condensing fluid and all tests were done at a little above atmospheric pressure with downward flowing vapour at a constant, low, approach velocity of approximately 0.75 m/s. The stainless-steel test apparatus, shown schematically in Fig. 1, consisted of a closed loop, with vapour generated in an electrically-heated boiler (maximum power 12 kW). The saturated vapour was directed vertically downward through a calming section, before flowing over the horizontal, water-cooled, test condenser tube. Excess vapour passed to an auxiliary condenser from which the condensate returned to the boiler by gravity.

Four pin-fin tubes made from copper were tested (see Fig. 2). The pins were made by machining circumferential and longitudinal rectangular grooves into thick walled copper tube. All the tubes had an inside diameter of 9.6 mm, a condensing length of 100 mm and a diameter at the pin root of 12.7 mm. Tubes 1 and 2 had square pins with 0.5 mm sides, 1 mm spacing in both directions and heights of 0.9 and 1.6 mm respectively. Tubes 3 and 4 had rectangular pins with circumferential thickness of 0.75 mm, longitudinal thickness of 0.5 mm, 0.5 mm spacing in both directions and heights of 0.9 and 1.6 mm respectively (see Table 1 for more details). A plain tube with an outside diameter of 12.7 mm was also tested for comparison.

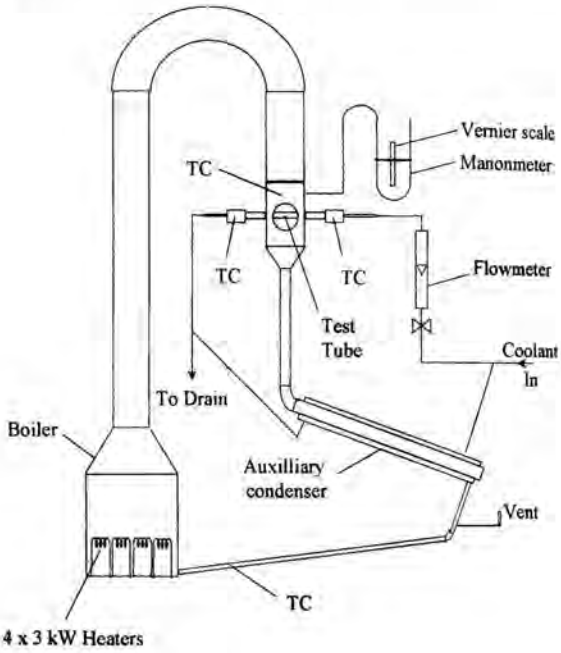

Figure 1: Experimental Apparatus

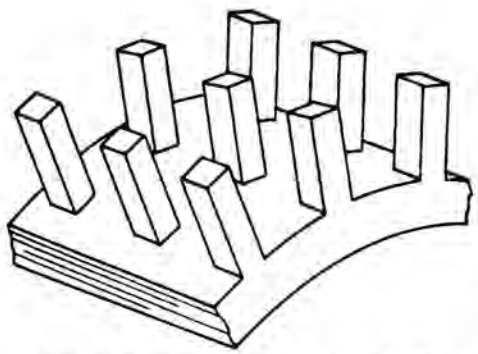

Figure 2: Schematic of Section of Pin-Fin Tube

	Tube 1	Tube 2	Tube 3	Tube 4
t_c(root)*	0.36	0.35	0.66	0.66
t_c(tip)*	0.55	0.69	0.82	0.94
t_c(mean)*	0.45	0.52	0.74	0.80
t_1	0.45	0.45	0.50	0.50
s_c	0.97	0.98	0.45	0.45
s_1	1.07	1.05	0.50	0.50
h	0.90	1.60	0.90	1.60

Table 1: Dimensions (in mm) of Pin-Fin Tubes

(* Note that, as the pins were formed by machining rectangular grooves into the tubes, all the pins had slightly smaller circumferential thickness at the root than at the tip)

The cooling water temperature rise, from which the heat-transfer rate to the test tube was calculated, was measured using a 10-junction thermopile. Care was taken to ensure adequate mixing and isothermal immersion of the leads in the vicinity of the junctions. A small predetermined correction for the dissipative temperature rise of the cooling water in the tube and mixing boxes was incorporated in the calculation of the heat-transfer rate. The estimated accuracy of the measurement of the coolant temperature rise (using the ten-junction thermopile) was better than 0.01 K (All thermocouples were calibrated in a high precision constant temperature bath against a platinum resistance thermometer, accurate to 0.005 K.) The range of coolant temperature rise was 1.3 to 4.5 K. The coolant flow rate was measured using a variable aperture, float type flow meter with an accuracy better than 2%. The vapour velocity at approach to the test section was found from the measured power input to the boiler, with a small, predetermined correction for the heat loss from the well-insulated apparatus (see Lee and Rose [5]).

The vapour-side, heat-transfer coefficient was found by subtracting the coolant and wall resistances from the measured overall thermal resistance. The tube-wall resistance was calculated assuming uniform radial conduction (inside surface to fin root diameter) and the coolant-side resistance was found from the following correlation

$$Nu_c = 0.030\, Re_c^{0.8}\, Pr_c^{1/3} \left(\frac{\mu_c}{\mu_w}\right)^{0.14} + 23.2 \qquad (1)$$

Equation (1) is based on directly-measured tube wall and coolant temperatures from an instrumented plain tube with identical inside geometry as the test tubes and over the range of coolant flow rates used for the present tests (see Briggs et al., [6]). The constant 23.2 was included to give a better fit at low coolant flow rates (see uncertainty analysis below).

UNCERTAINTY ANALYSIS

An uncertainty analysis was carried out on the results using the method of Kline and McClintock [7]. This method uses the estimated uncertainties in the experimental data (e.g. in coolant mass flow rate, coolant temperature rise etc) to calculate the propagation of these uncertainties in the reported results (e.g. heat flux, vapour-side temperature difference etc). Using this method and the uncertainties in the measured parameters given above the calculated uncertainty in the heat flux was never greater than 3%, the main contribution to this value being the uncertainty in the coolant mass flow rate.

The main uncertainty in the calculated vapour-side temperature difference arose from the use of Eq. (1) to calculate the coolant-side thermal resistance. For the enhanced tubes, and particularly at low coolant flow rates, the coolant-side resistance dominates leading to uncertainties in the vapour-side temperature difference for these tubes of up to 2 K at the lowest vapour-side temperature difference. At a vapour-side temperature difference of 20 K where the enhancement ratios were calculated (see later) this was reduced to 1 K or 5%. For the plain tube, where coolant and vapour-side resistances are comparable in magnitude, the uncertainty in the vapour-side temperature difference was never greater than 0.9 K, or about 3%.

EXPERIMENTAL RESULTS

Figures 3 and 4 show the results for the four pin-fin tubes plotted as heat flux, based on the area of a plain tube with diameter equal to the pin root diameter of the pin-fin tubes, against vapour-side temperature difference. All tests were repeated on different days and the data show good repeatability. Also shown are the data of Briggs et al. [6] for a plain tube identical to the one tested in the present investigation and two integral-fin tubes, with fin thickness and spacing equal to the longitudinal thickness and spacing of Tubes 1 and 2 of the present investigation. The plain tube data are in very good agreement with the earlier work and with the theory of Nusselt [8] for condensation of stationary vapour on horizontal plain tubes.

It can be seen that the pin-fin tubes give up to 50% higher heat flux than the equivalent integral-fin tubes (i.e. with the same fin thickness, spacing and height) at the same vapour-side temperature difference and over 3 times the heat flux of the plain tube. Increasing fin height from 0.9 mm to 1.6 mm increased the heat transfer although the effect was smaller for Tubes 1 and 2 than for Tubes 3 and 4.

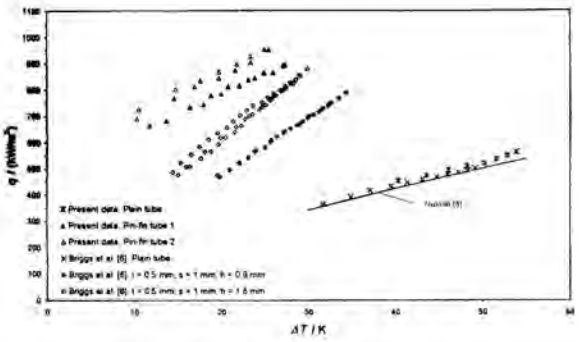

Figure 3: Results for Tubes 1 and 2

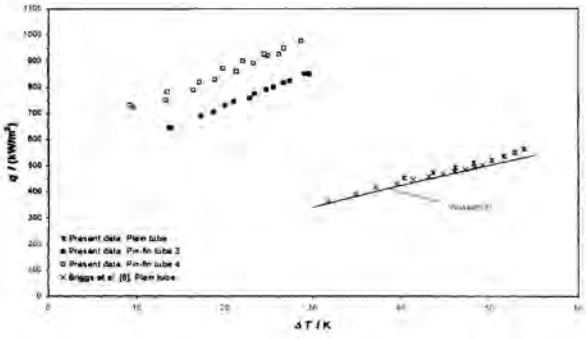

Figure 4: Results for Tubes 3 and 4

Table 2 lists heat-transfer enhancement ratios for the pin-fin tubes at a vapour-side temperature difference of 20 K. These were calculated by fitting equations of the form

$$q = A\Delta T^n \tag{2}$$

to the data for the plain and pin-fin tubes and using these equations to calculate the heat flux at ΔT = 20 K. The enhancement ration is then found from

$$\varepsilon_{\Delta T} = \frac{q_{\text{pin-fin}}(\Delta T = 20\text{K})}{q_{\text{plain}}(\Delta T = 20\text{K})} \tag{3}$$

Although the plain tube data did not extend as low as ΔT = 20 K, the origin will always be a point on the curves described by Eq. (2) hence it was thought reasonable to extrapolate the plain tube data back to this point. Similar results were obtained when using the Nusselt [8] expression for the plain tube.

Also listed in Table 2 is the area ratio, $\varepsilon_{\text{area}}$, of the pin-fin tubes, defined as the total area of the pin-fin tube divided by the area of a plain tube with pin-root diameter, and the area ratio corrected for fin efficiency, calculated from

$$\varepsilon_{\text{area-corr}} = \frac{A_{\text{root}} + \eta A_{\text{pin}}}{A_{\text{plain}}} \tag{4}$$

The fin efficiency in Eq. (4) was calculated assuming simple one-dimensional conduction in the pin (slender-fin theory) and using a mean surface heat-transfer coefficient based on the total surface area of the pin-fin tube.

	Tube 1	Tube 2	Tube 3	Tube 4
$\varepsilon_{\Delta T}$(20 K)	2.97	3.26	2.75	3.24
$\varepsilon_{\text{area}}$	1.85	2.63	3.08	4.87
$\varepsilon_{\text{area corr}}$	1.72	2.22	2.92	4.35
η	0.86	0.76	0.93	0.87

Table 2: Enhancement and Area Ratios of Pin-Fin Tubes

The best performing tube, Tube 2, had an enhancement ratio of 3.26. To the best of the authors knowledge the highest enhancement ratio reported in the open literature for condensation of steam on a simple two-dimensional integral-fin tube with the same diameter as those of the present study (12.7 mm) was 2.95 reported by Briggs et al. [9]. This tube had fin height and thickness of 1.6 mm and 0.5 mm respectively, the same as Tube 2, but a fin spacing of 1.5 mm, compared to 0.5 mm for Tube 2. For condensation of steam on integral-fin tubes, a fin spacing of 1.5 mm has been found to be the optimum value in most cases. Smaller spacing results in excessive condensate retention or flooding between the fins, reducing the area available for heat transfer. An integral-fin tube with a fin spacing of 0.5 mm would be completely flooded, leaving only the fin tips available for heat transfer. In the present tests it was difficult to accurately judge the extent of flooding on the pin-fin tubes due to the test section design. However, it was quite clear that Tube 2 (or any of the pin-fin tubes tested here) was not completely flooded and this could be a major contributor to the higher enhancement ratios. Tests are currently underway to accurately measure the extent of flooding on the pin-fin tubes.

Figure 5 shows the enhancement ratios for the four pin-fin tubes plotted against area ratios (uncorrected and corrected for fin efficiency). As can be seen there is little correlation between the increase in heat-transfer area and the actual heat-transfer enhancement, the best performing tube, Tube 2, having the second lowest area enhancement. It is also interesting to note that Tube 2 had the lowest fin efficiency of the four tubes tested, illustrating that low fin efficiency is not necessarily an indication of low performance (see Heggs, [10]).

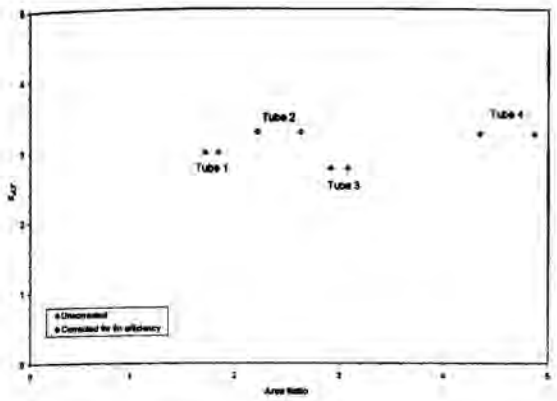

Figure 5: Variation of Heat-Transfer Enhancement Ratio with Area Ratios

Finally, in Fig. 6, the overall heat-transfer coefficient for Tubes 1 and 2 and the plain tube are plotted against coolant velocity. It can be seen that overall coefficients for the pin-fin tubes are approximately double those for the plain tube over the range of coolant flow rates tested. This is despite the fact that for condensation of steam the dominant thermal resistance is on the coolant side.

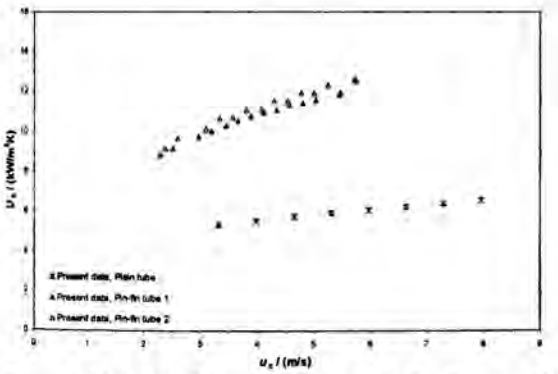

Figure 6: Variation of Overall Heat-Transfer Coefficient with Coolant Velocity

CONCLUSIONS

Experimental data are presented for condensation of steam at atmospheric pressure on four pin-fin tubes and a plain tube. The highest heat-transfer enhancement ratio of 3.26 was found for Tube 2, and is larger than the highest value found in the literature for a simple two-dimensional integral-fin tube of the same diameter. For this tube, the heat-transfer enhancement was approximately 25% greater than the increase in surface area due to the addition of the pin-fins.

Further tests are underway to find the optimum values of pin-fin spacings, thicknesses and height for condensation of steam and other fluids and to provide data to aid the development of correlations for calculating heat transfer to three-dimensional fin profiles.

REFERENCES

[1] Marto, P. J., (1988), An Evaluation of Film Condensation on Horizontal Integral Fin Tubes, ASME Journal of Heat Transfer, Vol. 110, 1287-1305.

[2] Briggs, A. and Rose, J. W., (1999), An Evaluation of Models for Condensation Heat Transfer on Low-Finned Tubes, Journal of Enhanced Heat Transfer, Vol. 6, 51 - 60.

[3] Briggs, A., Yang, X. X. and Rose, J. W., 1995, "An Evaluation of Various Enhanced Tubes for Shell-Side Condensation of Refrigerant", Heat Transfer in Condensation, Procedures Eurotherm Seminar No 47, Paris, Elsevier Pub. Co., pp. 62-70.

[4] Sukhatme, S. P., Jagadish, B. S. and Prabhakaran, P., 1990, "Film Condensation of R-11 Vapor on Single Horizontal Enhanced Condenser Tubes", ASME Journal of Heat Transfer, Vol. 112, pp. 229-234.

[5] Lee, W. C. and Rose, J. W., 1984, "Forced-Convection Film Condensation on a Horizontal Tube With and Without Non-Condensing Gases", International Journal Heat Mass Transfer, Vol. 27, pp. 519-528.

[6] Briggs, A., Huang, X. S. and Rose, J. W., 1995, "An Experimental Investigation of Condensation on Integral-Fin Tubes: Effect of Fin Thickness, Height and Thermal Conductivity", Procedures ASME National Heat Transfer Conference, Portland, HTD-Vol. 308, pp. 21-29.

[7] Kline, S. J. and McClintock, F. A., 1953, Describing Uncertainties in Single-Sample Experiments, Mechanical Engineer, 3-8.

[8] Nusselt, W., 1916, "Die Oblerflachenkondensation des Wasserdampfes", Z. Vereines Deutsch. Ing., Vol. 60, pp. 541-546, 569-575.

[9] Briggs, A., Wen, X. L. and Rose, J. W, (1992), Accurate Heat-Transfer Measurements for Condensation on Horizontal Integral-Fin Tubes, ASME, Journal of Heat Transfer, Vol. 114, 719-726.

[10] Heggs. P. J., 1999, "Fin Effectiveness is a better Performance Indicator than Fin Efficiency", Proceedings 6th UK National Conference on Heat Transfer, pp. 3-12.

HEFAT2002
1st International Conference on Heat Transfer, Fluid Mechanics, and Thermodynamics
8-10 April 2002, Kruger Park, South Africa
CC1

COMBINED FREE AND FORCED CONVECTION FILM CONDENSATION ON A FINITE-SIZE HORIZONTAL WAVY PLATE

C. K. Chen* and C. C. Wang**
* Professor; ** Graduate student
Department of Mechanical Engineering,
National Cheng Kung University, Tainan, 701,
Taiwan,
E-mail:ckchen@mail.ncku.edu.tw

ABSTRACT

Mixed-convection film condensation with downward flowing vapors onto a finite-size horizontal wavy plate is studied by a simple mathematical model and the spline alternating-direction implicit method. Effects of the wavy geometry, the interfacial vapor shear and the pressure gradient on the local condensate film thickness and the heat transfer characteristics have been studied independently. Results show that the pressure gradient tends to increase the heat transfer rate and to decrease the influence of the wavy amplitude. The appropriate wave number which can enhance the maximum condensation heat transfer rate is found in the neighborhood of 1 under all circumstances.

NOMENCLATURE

C_p	specific heat of the fluid at constant pressure
F	dimensionless parameter
g	acceleration of gravity
h_{fg}	latent heat of condensate
h'_{fg}	modified latent heat of condensate
Ja	Jacob number
k	thermal conductivity of condensate
L	plate half length
$\dot{m}$	condensate mass flow rate
n	wavy number
Nu_x,Nu_m	local and mean Nusselt number
p	pressure
P	dimensionless pressure gradient parameter
Pr	Prandtl number
Ra	Rayleigh number
Re	generalized Reynolds number
S(x)	surface geometry function
u_e	tangential vapor velocity at the edge of the boundary layer
U_∞	free stream vapor velocity
T	temperature
u,v	velocity components
x,y	horizontal and vertical coordinate axes

Greek symbols

α	amplitude of wavy surface
δ	condensate film thickness
μ	dynamic viscosity
ρ, ρ_v	density of condensate and vapor
τ_i	interface vapor shear

Superscripts

-	dimensionless variables
'	derivative with respect to x, i.e. d/dx

INTRODUCTION

The problem of laminar film condensation of pure vapor on surfaces of various forms has been studied since Nusselt (1916) obtained simple and explicit solutions for varied parameters. Following this, geometries such as plates and tubes have been studied under various conditions by many investigators. The free convection film condensation on the horizontal flat plate has been studied by Leppert and Nimmo (1967) and Shigechi et al. (1990). Moreover, Shigechi proposed the following equation

$$Nu_m = 0.82(Ra/Ja)^{0.2} \quad (1)$$

In Shigechi's study, the inclined angle of the vapor-liquid interface was used as the necessary boundary condition at the plate edge. The inclined angle, however, was continuously adjusted to minimize the thickness of the condensate film. In previous studies, the film condensation thickness at the plate edge (a necessary boundary condition) is either arbitrarily assumed or established by means of "trial and error". Afterward, Yang and Chen (1992) and Chiou and Chang

(1994) considered laminar film condensation in the same situation and used the concept of the minimum mechanical energy to resolve the steady flow rate at the plate edge.

The prediction of heat transfer from irregular surface is a topic of fundamental importance. Irregularities frequently occur in the process of manufacture. Moreover, surfaces are sometimes intentionally roughened to enhance heat transfer since the presence of rough surfaces disturbs the flow and alters the heat transfer rate. Some problems with irregular surfaces have been studied by Webb et. al (1985) and Honda et. al (1999). Another method to enhance heat transfer rate is about the velocity of the oncoming vapor. When the vapor surrounding a horizontal plate is moving at a high velocity, the problem becomes a type of forced convection film condensation and the analysis must consider the interfacial vapor shear force and the pressure gradient force. For forced convection condensation on a horizontal cylinder, Shekriladze and Gomelauri (1966) assumed that the shear stress at the liquid vapor interface was equal to the loss of momentum flux of condensing vapor. So they might eliminate the momentum equation in the vapor phase and get good agreement with experimental data for low vapor velocities. Afterward, based upon Shekriladze and Gomelauri's model, studies of the forced-convection film condensation have been focused mainly on a horizontal circular tube (Mosaad, 1999) or horizontal elliptic tubes (Memory et. al, 1997).

The above literature survey shows that the free- and forced- convection film condensation on a horizontal plate with roughened surface has not been studied so far. The objective of this study is to analyze the mixed-convection film condensation on a finite-size horizontal wavy plate, which is based on Nusselt's assumptions, together with adopting the vapor shear model of Shekriladze and Gomelauri. Moreover, the film thickness at the plate edge will be determined by the concept of minimum mechanical energy.

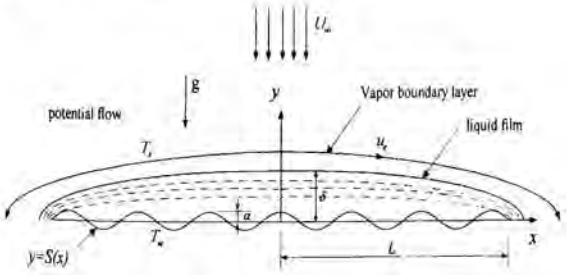

Fig. 1 Physic model and coordinate system.

MATHEMATICAL FORMULATION

The physical model and the coordinate system used are shown in Fig. 1. A wavy horizontal plate is immersed in a downward flowing pure vapor that is at its saturation temperature T_s and moves at uniform velocity U_∞. The wavy surface is described by

$$S(x) = \alpha \cos(n\pi x / L) \tag{2}$$

where α is the amplitude of the wavy surface and n is the total wave number of half wavy plate. This horizontal wavy plate is cooled internally thus the wall temperature T_w is uniform and lower than the vapor saturation temperature T_s. A continuous condensate film will occur on the wall and run outward from the plate center to the plate edge under the combined effect of gravity, pressure gradient force, and interfacial vapor shear force.

It is expected that the thickness of condensate film and the vapor boundary layer are much smaller than the plate length, thus, the following simplifying assumptions have been made: (1) The wall temperature is constant. (2) All physical properties are constant. (3) Surface tension effect is negligible. (4) Inertia terms in the momentum equation and convection terms in the energy equation are insignificant. (5) The vapor is saturated and dry. (6) Vapor flow outside the vapor boundary layer is potential. Based on these assumptions, the mass equation, x and y momentum equations, and the energy equation for the liquid laminar flow are described by the following equations:

$$\dot{m} = \int_{S(x)}^{\delta(x)} \rho u dy \tag{3}$$

$$0 = -\frac{\partial p}{\partial x} + \mu \frac{\partial^2 u}{\partial y^2} \tag{4}$$

$$0 = -\frac{\partial p}{\partial y} - \rho g \tag{5}$$

$$h_{fg}' \dot{m}' = k \left.\frac{\partial T}{\partial y}\right|_{y=S(x)} \tag{6}$$

with the boundary and interface conditions

(a) at the wavy-wall, i.e. $y = S(x)$

$$u = 0, \quad T = T_w \tag{7}$$

(b) at the interface, i.e. $y = \delta(x)$

$$\mu \frac{\partial u}{\partial y} = \tau_\delta, \quad T = T_s, \quad p = p_s(x) \tag{8}$$

where $h_{fg}' = h_{fg} + 3Cp\Delta T/8$ is the modified latent heat of condensate proposed by Rohsenow (1956) to account for the effects of heat convection in the film. And the symbol τ_δ denotes the interfacial shear stress at $y = \delta(x)$.

In Eq. (5), the pressure p in the liquid film includes the static pressure and the hydraulic pressure, i.e.

$$p = p_s(x) + \rho g(\delta - y) \tag{9}$$

Furthermore, $p_s(x)$ is the pressure at the interface (i.e. $y = \delta$) and can be gotten from the Bernoulli equation. Substituting Eq. (9) into Eq. (4), one may rewrite the momentum equation

$$\mu \frac{\partial^2 u}{\partial y^2} = \rho g \delta' - \rho_v u_e u_e' \tag{10}$$

Where u_e is the vapor velocity at the edge of the boundary layer. On the other hand, the interfacial shear stress τ_δ in Eq. (8) is first approximated by the asymptotic expression assuming an infinite condensation rate, similar to that used by Shekriladze and Gomelauri's (1966)

$$\tau_\delta = \dot{m}'(u_e - u_\delta) \approx \dot{m}' u_e \tag{11}$$

Here, it is assumed that the film velocity at the interface is negligible as compared with u_e.

By solving u in Eq. (10) and using the boundary conditions (7), (8) and (11), the following equation can be obtained

$$u = \frac{1}{\mu}\left(\rho g\delta' - \rho_v u_e u_e'\right)\left(\frac{y^2+S^2}{2} - y\delta + \delta S\right) + \frac{\dot{m}'}{\mu}u_e(y-S) \tag{12}$$

Since the condensate film thickness compared with the plate length is quite small, a linear temperature profile through the condensate film may be assumed, and thus,

$$k\left.\frac{\partial T}{\partial y}\right|_{y=S} \approx k\frac{T_s - T_w}{\delta - S} = k\frac{\Delta T}{\delta - S} \tag{13}$$

Substituting Eqs. (3), (12) and (13) into Eq. (6) yields

$$(\delta - S)\frac{d}{dx}\left\{\left(\frac{\rho^2 g h_{fg}'}{\mu k\Delta T}\delta' - \frac{\mu h_{fg}'}{k\Delta T}\frac{\rho}{\rho_v}u_e u_e'\right)\frac{(S-\delta)^3}{3} + \frac{\rho u_e}{\mu}\frac{\delta - S}{2}\right\} = 1 \tag{14}$$

with the relevant boundary conditions

$$d\delta/dx = 0 \qquad \text{at} \quad x = 0 \tag{15}$$

$$\delta = \delta_{min} \qquad \text{at} \quad x = L \tag{16}$$

where δ_{min} is still unknown, thus, the steady-state laminar film condensation boundary layer is established with a minimum depth at the edge of the plate.

Obviously, the film thickness at the plate edge can't go to zero and is established by the application of minimum mechanical energy principle (Bakhmeteff 1945), i.e.

$$\left[\frac{\partial}{\partial\delta}\int_S^\delta\left(\frac{u^2}{2} + gy + \frac{p}{\rho}\right)\rho u dy\right]_{\dot{m}_c} = 0 \tag{17}$$

Substitution of Eqs. (9) and (12) into (3), we can obtain the following equation.

$$\delta' = \frac{-6\mu u_e\dot{m}_c + \rho(\delta - S)\left(3\frac{k\Delta T}{h_{fg}'}u_e + 2\rho_v u_e u_e'(\delta - S)^2\right)}{2g\rho^2(\delta - S)^3} \tag{18}$$

Similarly, we substitute Eq. (18) into Eq. (12). After integration Eq. (17), the relation between the critical flowing mass and the minimum film thickness at the plate edge can be obtained as

$$3456\dot{m}_c^3 + 180\dot{m}_c^2\frac{k\Delta T}{\mu h_{fg}'}\rho u_e(\delta - S) - \left(2240\dot{m}_c g\rho^2 + \left(\frac{k\Delta T}{\mu h_{fg}'}\rho u_e\right)^3\right)(\delta - S)^3 = 0 \tag{19}$$

The next step in the analysis is to transform these equations into a dimensionless form. Therefore, the dimensionless variables are defined as

$$\bar{x} = \frac{x}{L},\quad \bar{\delta} = \frac{\delta}{L}\sqrt{\mathrm{Re}},\quad \bar{\alpha} = \frac{\alpha}{L}\sqrt{\mathrm{Re}},\quad \bar{S}(\bar{x}) = \frac{S(x)}{L}\sqrt{\mathrm{Re}}$$

$$\bar{u}_e = \frac{u_e}{U_\infty},\quad Ja = \frac{C_p\Delta T}{h_{fg}'},\quad Ra = \frac{\rho^2 g\,\mathrm{Pr}\,L^3}{\mu},\quad \mathrm{Re} = \frac{\rho U_\infty L}{\mu}$$

$$\mathrm{Pr} = \frac{\mu C_p}{k},\quad F = \frac{Ra}{Ja\,\mathrm{Re}^{5/2}},\quad P = \frac{\mathrm{Pr}}{Ja}\frac{\rho_v}{\rho} \tag{20}$$

Substituting Eq. (20) into Eqs. (2), (14)-(16) and (19) gives the following dimensionless equations

$$\bar{S}(\bar{x}) = \bar{\alpha}\cos(n\pi\bar{x}) \tag{21}$$

$$\left(\bar{\delta} - \bar{S}\right)\frac{d}{d\bar{x}}\left\{\left(F\bar{\delta}' - P\bar{u}_e\bar{u}_e'\right)\frac{\left(\bar{S} - \bar{\delta}\right)^3}{3} + \bar{u}_e\frac{\bar{\delta} - \bar{S}}{2}\right\} = 1 \tag{22}$$

with the boundary conditions

(a) at the center of the plate, i.e. $\bar{x} = 0$

$$d\bar{\delta}/d\bar{x} = 0 \tag{23}$$

(b) at the edge of the plate, i.e. $\bar{x} = 1$

$$3456\bar{m}^3 + 180\bar{m}^2\bar{u}_e - \left(2240\frac{\mathrm{Pr}}{Ja}F\bar{m}\left(\bar{\delta} - \bar{S}\right) + \bar{u}_c^3\right) = 0 \tag{24}$$

where

$$\bar{m} = \frac{\mathrm{Pr}}{Ja\sqrt{\mathrm{Re}}}\frac{\dot{m}}{\mu}\frac{1}{\bar{\delta} - \bar{S}} = \frac{\bar{u}_c}{2} + \frac{1}{3}\left(P\bar{u}_c\bar{u}_c' - F\bar{\delta}'\right)\left(\bar{\delta} - \bar{S}\right)^2 \tag{25}$$

and P is the effect of pressure gradient due to the potential flow. F means the ratio of free-convection to forced-convection.

To solve the dimensionless governing differential Eq. (22) with the appropriate boundary conditions in Eqs. (23)-(25), we need to know the tangential vapor velocity, i.e. $\bar{u}_e$, at the edge of the boundary layer. In this study, the inviscid flow can be obtained from the streamline equation as following

$$\frac{\partial^2\psi}{\partial\bar{x}^2} + \frac{\partial^2\psi}{\partial\bar{y}^2} = 0 \tag{26}$$

The resulting streamlines are plotted in Fig. 2. Next, the tangential vapor velocity at the edge of the boundary layer can be obtained by

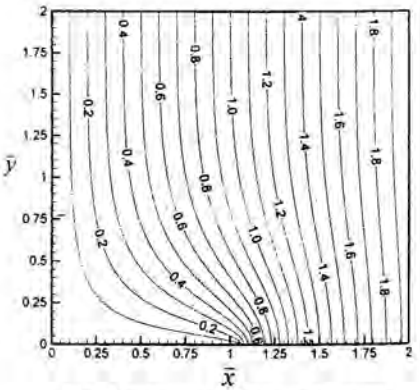

Fig. 2 streamline of flow in the plate

$$\bar{u}_c = (\partial\varphi / \partial\bar{y})\big|_{y=0} \quad (27)$$

Once the governing differential equation of condensate film thickness is obtained, two important quantities can be calculated as follows:

The local Nusselt number is defined as

$$Nu_x = \frac{h_x x}{k} = \frac{-(\partial T\ \partial n)x}{T_w - T_\infty} \quad (28)$$

where $\partial/\partial n$ represents differentiation along the normal to the surface. Therefore, the axial distribution of $\mathrm{Re}^{-1/2} Nu_x$ is given by

$$\mathrm{Re}^{-1/2} Nu_x = (\bar{\delta} - \bar{S})^{-1} \quad (29)$$

The mean Nusselt number is defined as

$$Nu_m = \frac{h_m L}{k}\frac{\sigma(x)}{x} \quad (30)$$

where

$$h_m = \frac{-k}{\sigma(T_w - T_\infty)}\int_0^\sigma \frac{\partial T}{\partial n}\, d\sigma \quad (31)$$

$$\sigma = \int_0^x \left(1 + S'^2\right)^{1/2} dx \quad (32)$$

Thus, we can calculate the value of $\mathrm{Re}^{1/2} Nu_m$ from

$$\mathrm{Re}^{1/2} Nu_m = \frac{1}{\bar{x}}\int_0^{\bar{x}} \frac{1}{\bar{\delta} - \bar{S}}\, d\bar{x} \quad (33)$$

NUMERICAL PROCEDURE

Eq. (22) has been solved numerically using the cubic spline approximation (Rubin and Graves, 1975; Chen and Wang, 2000) since this method can evaluate the spatial derivative terms directly without any finite difference discretization and the requirement of a uniform mesh is not necessary. As shown in Table 1a, the test of grid independence, which shows that the difference between results for grids of 300 and 500 is less than 0.1% in both condensate film thickness and mean Nusselt number. Therefore, the nonuniform grid of 300 with smaller spacing mesh near the plate edge is employed in this study. To verify the accuracy of the present method, the compared with Shigechi (1990) have also been shown in Table 1b and found to agree favorably.

RESULTS AND DISCUSSION

Numerical results have been obtained for the surface described by $\bar{S}(\bar{x}) = \bar{\alpha}\cos(n\pi\bar{x})$ for dimensionless wavy amplitudes (i.e. $\bar{\alpha}$) of 0, 0.05 and 0.1. The influence of governing physical parameters such as F, Pr/Ja and wave number (i.e. n) are explored for a wide range. The dimensionless pressure gradient parameters P=0, 0.5, 1 and 3 are taken throughout this study since P is usually less than 1.0 for steam and less than 3.0 for refrigerant.

Figures 3 and 4 show the variation of the film thickness and the local Nusselt number along the wavy plate. As shown

Table 1. (a) Comparison of δ and $\mathrm{Re}^{-1/2} Nu_m$ for defferent grid sizes; (b) Comparison mean Nusselt number for natural film condensation ($F \to \infty$) on horizontal flat plates

(a) For different grid sizes: F=20, P=1, α=0.05, n=5.5

Grid sizes	δ		$\mathrm{Re}^{-1/2} Nu_m$	
	x=0	x=1	x=0	x=4
100	0.696986	0.003280	1.545628	1.738114
300	0.684907	0.003291	1.575033	1.789175
500	0.684962	0.003324	1.574898	1.787904

(b) Natural film condensation on horizontal flat plates

Ra/Ja	Present method			Shigechi(1990)
	Pr/Ja=1	Pr/Ja=10	Pr/Ja=100	
10^2	1.86924	2.03384	2.05738	2.0597
10^4	4.69501	5.10805	5.16716	5.1739
10^6	11.79302	12.83157	12.98005	12.996
10^8	29.62201	32.23073	32.60368	32.644

in Fig. 3, the dimensionless film thickness at the middle plate ($\bar{x} = 0$) increases with the dimensionless wavy amplitude $\bar{\alpha}$. Next, the dimensionless film thickness of the wavy plate tends to decrease rapidly near the plate edge ($\bar{x} = 1$) as the fluid moves downstream, which is different from the behavior of

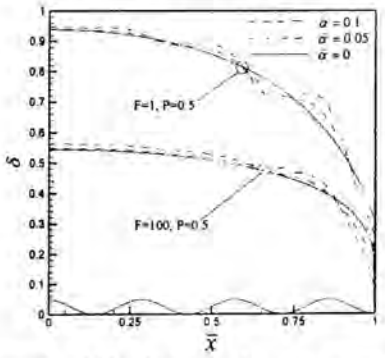

Fig. 3 Normalized film thickness along wavy plate for P=0.5, n=7, Pr/Ja=50.

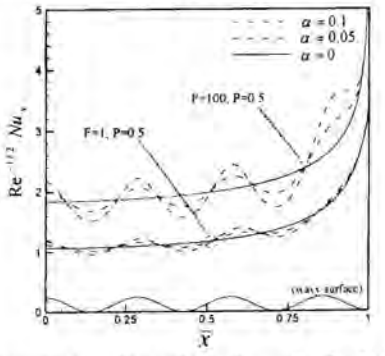

Fig. 4 Distribution of local Nusselt number for P=0.5, n=7. Pr/Ja=50.

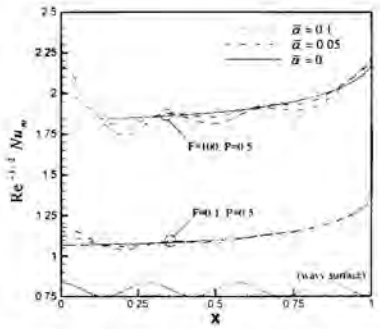

Fig. 5 Distribution of mean Nusselt number for P=0.5, n=7, Pr/Ja=50.

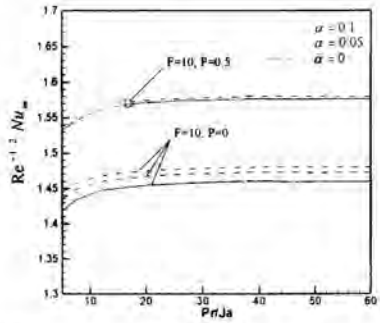

Fig. 6 A comparison of the mean Nussetl number for flat plate and wavy plate (F=10, n=7).

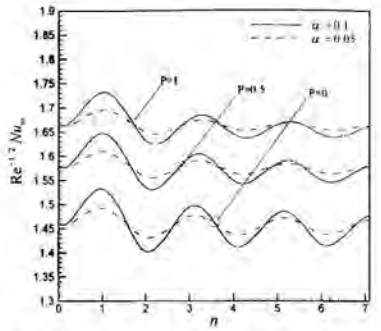

Fig. 7 Dependence of mean Nusselt number on wave number for F=10 and Pr/Ja=100.

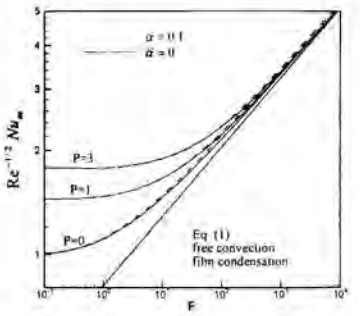

Fig. 8 Dependence of mean Nusselt number on F for mixed convection condensation (n=7, Pr/Ja=100).

the flat plate. It is also found that the amplitude of the dimensionless film thickness tends to increase as the axial coordinate $\bar{x}$ and the wavy amplitude $\bar{\alpha}$ increase. Therefore, the distribution of the dimensionless film thickness of the flat plate is more uniform than that of the wavy surface. This outcome is due to that the condensed liquid will be accumulated between the trough and the crest in wavy plate cases.

Figure 4 shows that the local Nusselt number has the same frequency as that of the wavy surface. The crests and troughs of $Re^{-1/2} Nu_x$ occur near the crests and troughs of the wavy surface and are shifted downstream for smaller F. This is because, in the film condensate, the forced convection dominates over the natural convection for smaller F. Thus, as F decreases, the characteristic of the local Nusselt number will be changed by both influence of the interfacial vapor shear force and the pressure gradient. Furthermore, the Nusselt number is seen to increase with the axial coordinate $\bar{x}$ because of the condensate flow rate increases from zero at the plate center to the maximum value at the edge of the plate.

As shown in Eq. (31), the mean Nusselt number can be obtained by averaging the heat transfer flux over the surface from the center of plate to $\sigma(x)$. Figure 5 shows the variation of $Re^{-1/2} Nu_m$ with $\bar{x}$. As the axial coordinate increases or the dimensionless wavy amplitude decreases, the amplitude of the mean Nusselt number will decrease. Therefore, we can observe that the variation of the mean Nusselt number only occurs near the plate center when larger wavy amplitudes are used. Also, a lower F results in a lower $Re^{-1/2} Nu_m$ for all wavy surfaces.

Figure 6 shows the variation of the mean Nusselt number with Pr/Ja. The parameter Pr/Ja is only found in Eq. (24) that can determine the film thickness $\bar{\delta}_{min}$ at the plate edge. In cases of the flat surface and the wavy surface, both mean Nusselt numbers increase with parameter Pr/Ja and approach constant values. Moreover, the mean Nusselt number of wavy surface is higher than that of the flat plate, especially if the dimensionless pressure gradient parameter is small.

Figure 7 shows the dependence of the mean Nusselt number on the wave number and the wavy amplitude. It is found that, for increasing the wave number the mean Nusselt numbers of the wavy surface show the sinusoidal curves, whose amplitudes decrease with the pressure gradient and increase with the wave amplitude. Peaks of the mean Nusselt number curres will occur under the wave number approaches to be odd (i.e. 1,3,5...), and the quantity of shift is more obvious for larger pressure gradients or wave numbers. As the wave number is quite large (i.e. the case of a rough surface),

the mean Nusselt number tends to be a constant value, which equals that of the flat plate (i.e. n=0). This outcome is due to that although the wavy surface has a larger heat transfer area, the thermal resistance will also increase for the condensate accumulates between the trough and crest. The high thermal resistance will also decrease the mean Nusselt number, thus, the optimum wave number is found near n=1 under all circumstances. The results reflect that the case of n=1 means smaller thermal resistance and the better angle to accelerate the flow outward from the plate edge.

Figure 8 shows the dependence of the mean Nusselt number on F for combined forced and natural convection condensation. It is seen that as F is greater than 100, all solutions in Eq. (22) tend to blend with the free convection (quiescent vapor) film condensation solution. For the other extreme, when F decreases to be zero (e.g. vapor velocity increases), the mean heat transfer coefficient will change from the free-convection region into the forced convection region through a transition zone. In this region, it is now well recognized that the effects of the vapor shear force and the pressure gradient force are more important than that of gravity in a condensation process. Figure 9 also shows that, as F decreases, the mean Nusselt number will early tend to be that of the forced convection under larger pressure gradients. Also, increasing the pressure gradient makes the mean heat transfer coefficient increase for the flat plate or wavy plate. These increases are more significant in the forced convection region than in the free convection region. Besides, the influence of the dimensionless wavy amplitude is obvious in the region of free convection (F>>1) and under the lower pressure gradient.

CONCLUSIONS

Numerical result shows that the harmonic curves for the dimensionless film thickness, and the local and mean Nusselt numbers have the same frequency as the frequency of the wavy surface. The mean Nusselt number increases leisurely with Pr/Ja and tends to a constant value. For larger pressure gradient will increases the total heat transfer but decreases the influences of wavy amplitude. Furthermore, the optimum wave number will change due to the high-pressure gradient.

It is found that the mean Nusselt number of wavy surface is higher than plate surface as wave number closes to odd value. While the enhancement of heat transfer is manifest for larger wavy amplitude and smaller pressure gradient, especially for free convection (i.e. F>>1). As wave number goes to infinity, the mean Nusselt number tends to a constant value, which equal the case of plate surface. As wave number approach 1 (i.e. $n \to 1$), which has smallest thermal resistance and the best angle to accelerate the flow outward at the plate edge, and the best heat transform ratio will be given. These facts may be helpful in choosing a proper irregular plate for a given practical application.

ACKNOWLEDGMENT

This research work was supported by the National Science Council of Taiwan, Republic of China, under Grant No. NSC90-2212-E-006-002.

REFERENCES

Bakhmeteff, B. A, 1945, Hydraulics of Open Channels, McGraw-Hill, New York, pp. 39-41.

Chen, C. K. and Wang, C. C., 2000, "Transient Analysis of Forced Convection Along a Wavy Surface in Micropolar Fluids," *J. of Thermophysics and Heat Transfer*, Vol. 14, pp. 340-347.

Chiou, J. S. and Chang, T. B., 1994, "Laminar Film Condensation on a Horizontal Disk," *Warme-und Stoffubertragung*, Vol. 29, pp. 141-144.

Honda, H., Takamatsu, H. and Takata, N., 1999, "Experimental Measurements for Condensation of Downward-Flowing R123/R134a in a Staggered Bundle of Horizontal Low-Finned Tubes with Four Fin Geometries," *Int. J. of Refrigeration*, Vol. 22, 615-624.

Leppert, G. and Nimmo, B., 1968, "Laminar Film Condensation on Surfaces Normal to Body of Inertial Forces," *ASME J. Heat Trans.* Vol. 80, pp. 178-179.

Memory, S. B., Adams, V. H. and Marto, P. J., 1997, "Free and Forced Convection Laminar Film Condensation on Horizontal Elliptical Tubes," *Int. J. Heat Mass Transfer*, Vol. 40, No. 14, pp. 3395-3406.

Mosaad, M., 1999, "Combined Free and Forced Convection Laminar Film Condensation on an Inclined Circular Tube with Isothermal Surface," *Int. J. Heat and Mass Transfer*, Vol. 42, pp. 4017-4025.

Nusselt, W., 1916, "Oberflachen Condensation Des Wasserdampfes," *Zeitschrift des Vereines Deutscher Ininuere* Vol. 60, pp. 541-569.

Rohsenow, W. M., 1956, "Heat Transfer and Temperature Distribution in Laminar Film Condensation on a Horizontal Tube," *Int. J. Heat Mass Transfer*, Vol. 27, pp. 39-47.

Rubin, S. G. and Graves, R. A., 1975, "Viscous Flow Solution with a Cubic Spline Approximation," *Computers and Fluids*, Vol. 1, No. 5, pp. 1-36.

Shekriladze, I. G. and Gomelauri, V. I., 1966, "The Theoretical Study of Laminar Film Condensation of a Flowing Vapor," *Int. J. Heat Mass Transfer*, Vol. 9, pp. 581-591.

Shigechi, T., Kawa, N., Tokita, Y. and Yamada, T. 1990, "Film Condensation Heat Transfer on a Finite-Size Horizontal Plate Facing Upward," *Trans. JSME series B*, Vol. 56, pp. 205-210.

Webb, R. L, Rudy, T. M. and Kedzierski, M. A., 1985, " Prediction of the Condensation Coefficient on Horizontal Integral-Fin Tubes," *ASME J. Heat Transfer*, Vol. 107, 369-376.

Yang, S. A. and Chen, C. K, 1992, "Laminar Film Condensation on a Finite-Size Horizontal Plate with Suction at The Wall," *Appl. Math. Modeling*, Vol. 16, pp. 325-329.

HEFAT2002
1st International Conference on Heat Transfer, Fluid Mechanics, and Thermodynamics
8-10 April 2002, Kruger Park, South Africa
DA3

NATURAL CONVECTION HEAT TRANSFER UNDERNEATH A DOWNWARD FACING HOT FIN ARRAY

A. Dayan, R. Kushnir, G. Mittelman and A. Ullmann
Department of Fluid Mechanics and Heat transfer,
Tel Aviv University,
Ramat Aviv, 69978 Tel Aviv,
Israel
E-mail:dayan@eng.tau.ac.il

ABSTRACT

A combined theoretical and experimental study was conducted to investigate the problem of natural convection underneath a horizontal rectangular hot fin array. A useful semi-empirical correlation for the heat transfer coefficient is offered. Owing to the lack of published data on the subject, it was necessary to conduct extensive experimental testing to support the analytical efforts. To enable a thorough verification of the correlation a numerical model was developed as well. The correlation clearly reveals the dependence of the Nusselt number on the Rayleigh number, the Prandtl number and the fin's height to spacing ratio. The model can be easily used to calculate the dimensions of a fin array for optimal cooling. Recently, there exists a growing industrial interest in this passive-cooling device, specifically in the telecommunication industry.

INTRODUCTION

An investigation of the problem of free convection underneath a hot and isothermal horizontal fin array is presented. A downward facing fin array is not the preferred orientation for effective cooling by means of natural convection. Thus, this problem has been largely neglected in the past. However, the development of modern telecommunication equipment changed this fact and the interest in this subject is on the rise. Architectural design requirements give preference specifically to such hidden cooling devices (such as below the bottom of a telecommunication box). The current research effort was undertaken to provide analytical tools for calculating the cooling capabilities of downward facing rectangular fin arrays. The results can be easily used to size the dimensions of arrays that yield optimal cooling.

An extensive literature survey did not unveil any work on the subject of free convection underneath a horizontal fin array. As opposed to that, considerable literature exists on the problem of free convection underneath hot isothermal flat strips. The latter, however, exhibits many heat and mass transfer characteristics that apply to cooling surface regardless if finned or not. It has been demonstrated that buoyancy forces induce a flow from the center of the hot surface toward the edges (Aihara et al. [1], Fujii and Imura [2]). Furthermore, in a practical sense, the flow near the surface exhibits some boundary layer characteristics. The ambient airflow rises from below upward and towards the surface center. At a certain distance δ from the surface the airflow reverses its lateral movement direction and flows towards the surface edges, as indicated in Fig. 1. The points of flow reversal form a virtual surface that represents a boundary where the flow lacks any lateral velocity component. The flow confined between this boundary and the hot surface moves towards the surface edges. As mentioned, this flow exhibits boundary layer characteristics. While picking up heat, it accelerates as it moves toward the surface

edges. The boundary layer is thickest at the surface center and thinnest at the edges.

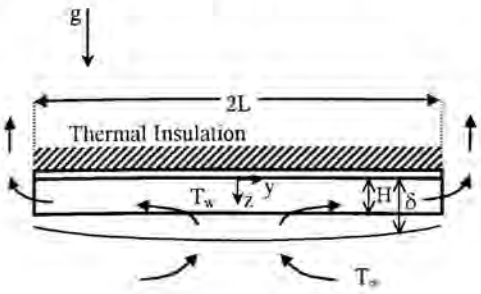

Figure 1: A Schematic Representation of The Free Convection Underneath a Hot Fin Array

Practically all the heat transfer correlations for natural convection underneath hot flat strips for laminar flow (see Bejan [3]) have the form of

$$Nu=C' Ra^{1/5} \qquad (1)$$

Where Nu is the averaged Nusselt number, Ra the Rayleigh number, and C' is a coefficient that depends on the surface geometry and Prandtl number. The relevance of these correlations, for the present study, stems from the fact that they represent a limiting case for arrays with largely spaced fins. In this respect, Aihara et al. [1] investigated experimentally a two-dimensional airflow underneath a rectangular plate. In their work, velocity and temperature profiles were measured by tracers' photography and with thermocouples, respectively. Their investigation indicated that it is reasonable to define a boundary layer zone with characteristic temperature and velocity profiles for integral method analyses. They demonstrated that such profiles approximate fairly well the measured data along most of the plate length. This was an important conclusion since most subsequent analyses incorporated the integral solution method.

Before conducting the fin array investigation, we studied the horizontal strip case in depth. The integral method enabled development of a closed form solution [4]. Among other merits, that study also revealed the reason for the discrepancy that exists amongst published heat transfer correlations. The solution that was obtained for Pr=0.7 is

$$Nu=C\,Ra^{1/5}=[1+0.24\exp(-0.0025L^*)]\,0.46\,Ra^{1/5} \qquad (2)$$

The dimensionless length L^* is based on a group of properties that reflect the boundary layer thickness which tends to increase with α and ν, and decreases with g. This correlation in effect sheds new light on the importance of the strip length on the free convection heat transport characteristics. The coefficient C of this solution appears in the correlation that was developed in the current work for fin arrays.

Similar to the flow near a flat surface, a "boundary layer" type flow is expected to develop also underneath a finned surface. In house measurements indeed confirmed that fact. The current work is focused on arrays that are reasonably long as compared to their channel hydraulic diameters ($L/D_h>8$). Such surfaces contain enough fins to make them better heat radiators. The length condition implies that the boundary layer thickness extend beyond the fin height. For portable communication, the small wall to ambient temperature differences combined with small equipment dimensions entail small Rayleigh numbers. Consequently, the natural convection is expected to be governed primarily by buoyancy and frictional forces, and to a lesser degree by inertia forces.

NOMENCLATURE

a	half the space between fins (mm)
C'	coefficient of Eq. 1
C	coefficient of Eq. 2
D_h	hydraulic diameter (cm)
H	fin height (cm)
g	gravitational acceleration (m/s^2)
h	averaged heat transfer coefficient ($W/m^2\,°C$)
k	thermal conductivity ($W/m\,°C$)
L	array half lengh (cm)
L^*	dimensionless length, $L/(\alpha\nu/g)^{1/3}$
Nu	averaged Nusselt number, hL/k
Pr	Prandtl number, ν/α
Ra	Rayleigh number, $g\beta L^3\theta_w/\alpha\nu$
T	temperature (°C)
y,z	horizontal and vertical coordinate axes (cm)

Greek Letters

α	thermal diffusivity (m^2/s)
β	thermal expansion coefficient (1/K)
δ	boundary layer thickness (cm)
ν	kinematic viscosity (m^2/s)
θ	temperature difference ($T-T_\infty$) (°C)

subscripts

w	wall conditions
∞	ambient conditions

ANALYSES AND RESULTS

As mentioned, the research work was initiated by a development of a closed form solution for the limiting case of a flat strip. The solution of the continuity, momentum and energy equations was obtained by the integral method. In parallel, we constructed a test facility to obtain supporting experimental data. Furthermore, to extend the experimental results scope, a numerical model was developed and verified. The limiting case solution, the experimental results and the numerical model were used to develop semi-empirically a correlation for the heat transfer coefficient of free convection underneath a horizontal hot rectangular fin array.

The test apparatus consisted of insulated horizontal aluminum fin arrays that were electrically heated on their upper surface, as shown in Fig. 2. The insulation, made of Calcium Silikat was 3 cm thick sideways and 9 cm upwards. Copper/Constantan thermocouples were used for temperature measurements at various points of the fin array. All temperature measurements indicated that the exposed fin-array surface was fairly isothermal (owing to the small Biot number). To calculate the convective heat transfer rate, radiative heat fluxes and heat losses through the insulation were calculated and deducted from the input power. The test apparatus reliability was demonstrated through the successful reproduction of published experimental data for flat strips [1].

Figure 2: Experimental Apparatus.

The numerical solution was obtained with the Icepak CFD code. In principle, the code solves the governing set of elliptic partial differential equations for conservation of mass, momentum and energy. Buoyancy forces are based on the Boussinesq approximation. The fluid properties are assumed constant and are evaluated at the average temperature between the hot surface and the ambient fluid. The solution is for conditions of steady state laminar free convection. Illustration of the boundaries used for the numerical model is presented in Fig. 3. The fin array is located at the upper surface of the rectangular control volume. Its upper surface is isothermal and its thermal conductivity is prescribed. The size of the control volume was extended horizontally and vertically up to the point that it ceased to influence the calculated flow and temperature fields within the surface boundary layer. In particular, this applies to the dimensions "A" and "B" shown in the figure. Clearly, the ambient circulatory flow is seen as streamlines entering and leaving the control volume enclosure. At these free boundaries, viscosity effects are neglected, and the pressure is assumed to be equal to the ambient pressure. Likewise, the flow entering the control volume is assumed to be at the ambient temperature.

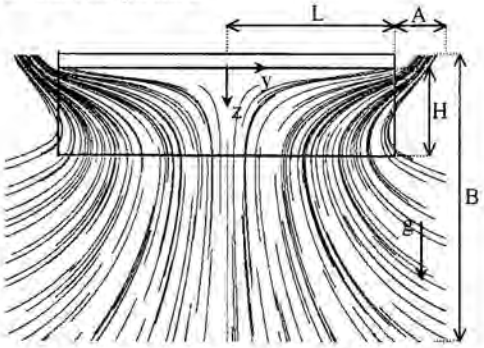

Figure 3: Numerically Calculated Streamlines of Free Convection Underneath a Hot Fin Array (at The Mid-Plane of a Channel in Between Two Adjacent Fins).

To solve the problem, the code divides the flow domain into sub-control volumes. The numerical scheme integrates the governing equations over each sub-control volume to construct a set of algebraic equations, after linearization of the results. The set is then solved iteratively by the Gauss-Seidel linear equation solver for algebraic multi-grid systems (AMG) until convergence is achieved. For convergence determination, the dimensionless residual term of each equation was calculated continuously. Convergence was achieved when the residuals terms of the continuity and momentum equations were smaller than 10^{-3}, and smaller than 10^{-7} for the energy equation. The computation results provided numerical velocity and temperature

profiles. The numerical computation was verified by the successful prediction of the experimental results as well as the limiting case of the horizontal strip (Aihara et at. [1] test results).

A semi-empirical correlation was developed by equating buoyancy force terms to drag forces across the thermal and kinematics boundary layers for a simple box type model [5]. Three correlation coefficients were left for model calibration. This was accomplished by matching the results to, both, the limiting case solution and the experimental data. The result for the averaged heat transfer coefficient of a horizontal fin array is

$$Nu = \frac{C\,Ra^{1/5}}{1.137(1+0.375\frac{H}{a})^{3/5} - 0.48\frac{H}{L}C\,Ra^{1/5}} \qquad (3)$$

For H/a>1, and where C is the coefficient of Eq. (2), "a" is half the space between fins, H the fin height, and L the fin array length. Testing predictions of Eq. (3) against experimental data and numerical results, as seen in Fig. 4, revealed an exceptional match. Four arrays of substantially different fin heights and lengths are shown in the figures. For all the four arrays, as expected, the heat transfer coefficient increases with temperature. It is seen that the fin array length tends to adversely affect the heat transfer coefficient, owing to the enhanced influence of the drag force that limits the circulatory flow rate. As to the fin heights, inspection of the figures indicates that the heat transfer coefficient tends to slightly increase with fin heights.

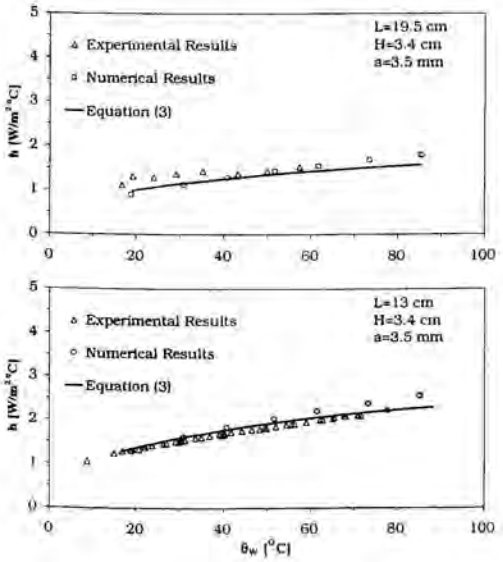

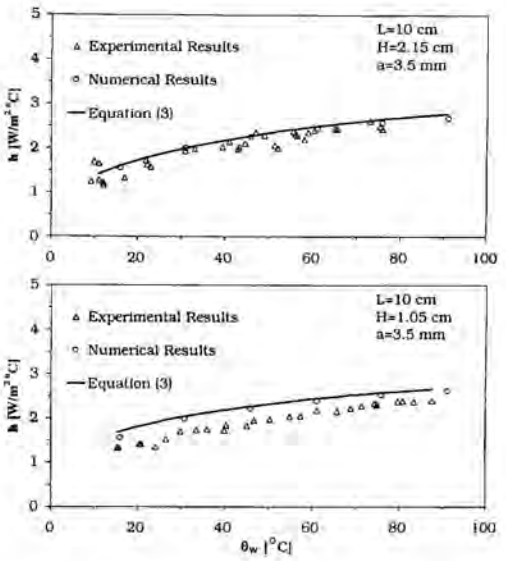

Figure 4: The Dependence of the Heat Transfer Coefficient on Temperature.

CONCLUSION

A simple and useful free convection heat transfer correlation was developed for a downward facing fin array. The correlation is in excellent agreement with a wide range of experimental data and numerical results. Furthermore, it reveals the relative importance of the governing dimensionless physical parameters. Both the correlation and the numerical model can be used to calculate the dimensions of a fin array that would provide maximum cooling for a given base area.

REFERENCES

[1] Aihara T., Yamada Y. and Endo S., 1972, "Free Convection Along the Downward Facing Surface of a Heated Horizontal Plate", Int. J. of Heat and Mass Transfer, vol. 15, pp. 2535-49.

[2] Fujii T. and Imura H., 1972, "Natural Convection Heat Transfer from a Plate with Arbitrary Inclination", Int. J. of Heat and Mass Transfer, vol. 15, pp. 755-767.

[3] Bejan, A., 1993, *Heat Transfer*, John Wiley & Sons.

[4] Dayan A., Kushnir R. and Ullmann A., "Laminar Free Convection underneath a Hot Horizontal Infinite Flat Strip", Submitted to the Int. J. of Heat and Mass Transfer, November 2000.

[5] Mittelman, G. "Experimental study of free convection from a hot finned surface facing down" M.Sc. Thesis, Tel-Aviv Uni., 2001.

HEFAT2002
1st International Conference on Heat transfer, Fluid Mechanics, and Thermodynamics
8-10 April 2002, Kruger Park, South Africa
DG1

PROBLEMS OF EFFECTIVE HEAT TRANSFER ENHANCEMENT IN THE CHANNELS

G.A. Dreitser
Department of Aviation and Space Thermal Technics,
Moscow Aviation Institute,
4, Volokolamskoe shosse, Moscow, 125993, Russia
E-mail: heat204@mai.ru

ABSTRACT

Analysis is made of the modern trends in heat transfer enhancement in tubes and another channels with reference to different-purpose compact heat exchangers. Requirements are formulated for high-effective heating surfaces and, bearing this in mind, different methods of heat transfer enhancement are analyzed. It is shown that the methods of artificial flow turbulization which are based an a detailed analysis of the flow structure can give the most advantageous results.

At the Moscow Aviation Institute the high-effective method was developed to enhance heat transfer in tubular heat exchangers, and comprehensive studies were made of the effectiveness of this method when applied to gas and liquid flow in tubes, circular channels and in tube bundles over a wide range of performance parameters as well as to boiling and condensation of heat carriers.

The present paper deals with the results of new experimental investigations or heat transfer enhancement using the method proposed. The results on introducing this method in different-purpose heat transfer apparatuses are presented, too.

The experimental data presented in previous publications of the author and in this paper were confirmed by test in commercial heat exchangers. Introduction of the developed heat transfer enhancement method allowed both a 1.5...2.5 fold reduction of heating surface at present heat power and pumping power of heat carrier and improvement of the performance parameters of heat exchangers due to reduced fouling.

INTRODUCTION

Heat exchangers are widely used in power engineering, chemical industry, petroleum refineries, and food industry; in heat engines, cars, tractors, boats, and ships; in aviation and space vehicles; in refrigerating and cryogenic engineering; in space conditioning, heating, and hot water supply systems; and in many other fields of technology.

The problem of decreasing a mass and size of heat exchangers is urgent. Enhancement of convective heat transfer processes is a promising means for solving this problem. It should be noted that use of heat transfer enhancement enables solving some other, no less important problem, such as lowering maximum temperatures of heat exchanger working surfaces, improving the operational reliability, and reducing the fouling and other contamination.

At present, different methods of convective heat transfer enhancement in heat transfer channels have been proposed and studied [1]. These include flow turbulators on a surface, a rough surface, a developed surface due to finning, flow swirling by spiral fins, worm devices, swirlers mounted at the channel entrance, gas bubble mixing in the liquid flow, mixing of particles or liquid drops in the gas flow, rotation of a heat transfer surface, surface vibration, heat carrier pulsation, action of an electrostatic field on the flow, flow suction from the boundary layer. Use of jet cooling systems is a means for heat transfer enhancement in single-phase heat carrier flow.

Along with turbulators, twisting and finning, low heat conducting and porous coatings called nonisothermal fins are also utilized for boiling heat transfer enhancement. Turbulators or fins that break up a condensate film, nonwetted coatings, liquid stimulators to produce drop condensation, flow swirling, and rotation of a heat transfer surface are proposed as the ways to enhance condensation heat transfer from heat carriers.

The number of publications on heat transfer enhancement progressively increases. These publications are mentioned in [2-4]. However, the results of these investigations are often

contradictory, and the enhancement methods proposed are not always adaptable to production and/or efficient. In a number of cases, the choice is not supported and is accidental in nature. This situation hampers a substantiated choice of efficient methods of heat transfer enhancement as well as the evaluation of different methods. This is attributed to weak use of heat transfer enhancement methods, which undoubtedly causes large economic losses and retards the reduction of metal consumption for heat exchangers.

NOMENCLATURE

C water hardness, mg.eq/l;
D, D_{out} inner and outer diameter respectively, m;
d annular diaphragm diameter, m;
d_o screw core diameter, m;
d_{an} annular groove diameter, m;
G mass flow rate, kg/s;
K heat transfer coefficient, W/m^2 K;
Nu Nusselt number, dimensionless;
$\left(\frac{Nu}{Nu_{sm}}\right)_{Re}$ ratio of heat transfer coefficients for the same Re number;
p pressure, Pa;
R_{foul} thermal resistance of a fouling layer, m^{2}K/W;
Re Reynolds number, dimensionless;
S spiral inserts pitch, m ;
t turbulizer pitch, distance between the grooves, m;
T temperature, K;
ΔT temperature drop, K;
V heat exchanger volume, m^3;

Greek letter

α heat transfer coefficient, W/ m^2 K;
ξ hydraulic resistance coefficient, dimensionless;
$\left(\frac{\xi}{\xi_{sm}}\right)_{Re}$ ratio of hydraulic resistance coefficients for the same Re number;
τ time, hr;

Subscripts:

foul fouling;
Re at the same Re number;
s saturated
sm smooth;
w wall;
0, ∞ initial and final moment of process;

EXPERIMENTAL RESULTS

Turbular Heat Exchangers with One-Phase Heat Carriers

At the Moscow Aviation Institute the high-effective method was developed to enhance heat transfer in tubular heat exchangers, and comprehensive studies were made of the efficiency of this method when applied to gas and liquid flow in tubes, circular channels, and in tube bundles over a wide range of performance parameters.

The essence of the method proposed is as follows. Equidistant annular grooves are rolled on an outer surface of a heat transfer tube. In this case, the annular smooth-wall diaphragms are formed over on an inner tube surface. Annular grooves and diaphragms swirl the flow in a wall layer and provide heat transfer enhancement outside and inside the tubes (Fig.1).

The outer diameter of the tubes does not increase, which permits their use in compact bundles and does not require change in the existing way of assembling heat exchangers.

The technology worked out at the Institute VNIMetMash

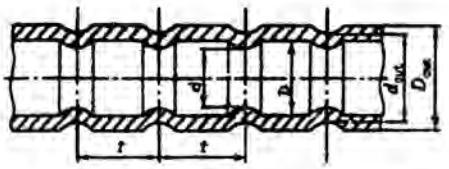

Figure 1: A tube with annular turbulators

for manufacturing knurled tubes is not complicated and makes use of standard equipment. The knurling cost is not more than several percent of that of the tubes. Knurling can be done at a rate of one to two meters per minute using a facility installed on a lathe. A special facility provides knurling at a rate of 9 m/min.

The tubes with annular turbulators can be installed in heat exchangers using gases and liquids with boiling and condensation of heat carriers; that is, they possess the versatility required for practical applications. Moreover, as shown below, these tubes are less susceptible to fouling. Thus, tubes with annular turbulators satisfy virtually all of the requirements necessary for their widespread practical application.

Use of the developed method for heat transfer enhancement permitted both the 1.5÷2.5 –fold reduction of a heating surface, at present heat power and pumping power of heat carriers as well as the improvement of the performance parameters of heat exchangers due to reducing fouling.

For laminar flow in a tube with diaphragms, the space near the wall between the diaphragms is filled with a stagnant liquid that reduces heat transfer; the higher the height of a diaphragm, the more the heat transfer reduction. However, the diaphragm itself reduces the critical Reynolds numbers because the separated flow zones formed by the diaphragms disturb the stability of viscous flow, which extends the range (Re=2000÷5000) over which the most effective relationships are obtained between the growth of heat transfer and pressure drop coefficients (Nu/Nu_{sm}=2.83, with ξ/ξ_{sm}=2.85). The interaction mechanism was evolved between specially

designed turbulators and the flow at a transition to weakly developed turbulent flow. On the basis of this mechanism, it is established that reasonable augmentation can be achieved under these conditions with sufficiently high diaphragms (d/D=0.92) and an optimum pitch of t/D=1 (Fig.1).

In the developed turbulent flow zone, the best results are obtained with low diaphragms (d/D=0.94) and small pitches (t/D=0.25...0.5). At higher heights of diaphragms (when d/D becomes smaller), the ratio Nu/Nu_{sm}, at first, sharply rises and then levels off, reaching a value of 3 to 3.1 with gas flow and 2.3 with liquid flow. As the height of a diaphragm increases, the pressure drop rises first gradually. In the range of low diaphragms (d/D=0.96÷0.993), values of d/D and t/D exist, over which the growth of heat transfer is equal to or leads to an increase in pressure drop, that is, $Nu/Nu_{sm} \geq \xi/\xi_{sm}$. The ratio d/D, which $Nu/Nu_{sm}=\xi/\xi_{sm}$, becomes smaller as Re increases and t/D becomes greater. With smaller d/D, we have $Nu/Nu_{sm}<\xi/\xi_{sm}$. When t/D=0.25, the ratio $Nu/Nu_{sm}=\xi/\xi_{sm}$ increases with Re and attains a value of 2 when $Re=4\times10^5$. When t/D=1, the ratio $Nu/Nu_{sm}=\xi/\xi_{sm}$ falls as Re increases and attains 1.78 when $Re=2\times10^4$.

It was shown [3,4], that if in a tubular heat exchanger the heat transfer coefficient inside tubes is significantly smaller than that in the intertube space, then the volume ratio of compared heat exchangers (in one of them, facilities to enhance heat transfer are located inside tubes and in another, tubes are smooth) in the turbulent flow is

$$\frac{V}{V_{sm}} = \frac{(\xi\ \xi_{sm})^{0.4}_{Re\,0}}{(\alpha\ \alpha_{sm})^{1.4}_{Re}} \qquad (1)$$

In this case, to calculate the Reynolds number for a turbulator-equipped tube, the mean velocity is determined from the smooth tube cross-section, and the smooth tube diameter is taken as a determining size, i.e., comparison is made under the same mass flow rates of heat carriers in the compared tubes.

Continuous flow swirling can be arranged by twisted strips or screw inserts located along the entire tube (Fig.3). Unlike local flow swirling, these are simple in manufacturing and offer a larger increase of mean heat transfer since the flow swirling degree along the channel is not diminished. However, the hydraulic resistance in this case also increases because of additional friction pressure losses on the surface of a strip or a screw.

Shchukin [5] obtained the appropriate relations that allow numerous experimental data of various researchers to be generalized. But their application for analyzing the flow swirling efficiency is difficult, as according to these data the flow velocity in insert-provided tubes taken with regard to the insert blocking diameter of the insert-containing tube serves as a determining size spiral screw.

Having used these results, Dreitser [6] obtained the formulas for $(\xi/\xi_{sm})_{Re}$ and $(\alpha/\alpha_{sm})_{Re}$ convenient for practical calculations.

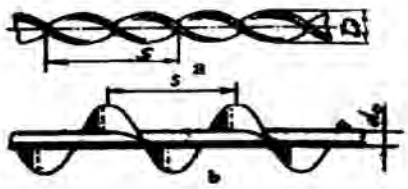

Figure 2: Spiral inserts: a, twisted tape; b, spiral screw.

The hydraulic resistance coefficient, ξ, of the strip insert-equipped tube is determined in terms of the flow velocity w in the insert-free tube. The tube diameter D serves as a determining size and the local hydraulic resistances in the flow at the entrance and exit of the turbulator-provided tube are allowed for.

Then for screw-shaped inserts an increase of heat transfer and hydraulic resistance coefficients can be easily determined as against the tube having no inserts at given geometry of inserts and constant flow rates of heat carrier and, hence, the efficiency of heat transfer enhancement can be found. Use of these relations allows one to immediately answer the question of interest to practical workers: how will the location of helical inserts inside tubes enhance hydraulic resistance and heat flux under the same flow rate and other conditions being equal.

At $Re_D=10^4$ when the strip twisting pitch S/D varies between 4 and 12, the heat transfer increase $\alpha/\alpha_{sm}=2.34\div1.8$ is accompanied by the hydraulic resistance growth $\xi/\xi_{sm}=4.05\div2.5$. This enables decreasing the heat exchanger volume $V/V_{sm}=0.53\div0.64$, i.e., the heat exchanger volume can be decreased by a factor of 1.8 to 1.51.

As the Reynolds number grows, the efficiency of heat transfer enhancement by means of strip inserts substantially degrades: at $Re = 10^5$ we have $\alpha/\alpha_{sm} = 1.88\div1.49$, $\xi/\xi_{sm} = 5.55\div1.65$, which yields $V/V_{sm} = 0.822\div0.70$, i.e., the heat exchanger volume can be decreased by a factor of 1.21 to 1.43.

It should be noted that at no values of the Reynolds number and strip twisting pitches we could not obtain $\alpha/\alpha_{sm}>\xi/\xi_{sm}$, i.e., we could not achieve an advancing increase in the heat transfer coefficient as against the hydraulic resistance growth.

Fig. 3 plots α/α_{sm}, ξ/ξ_{sm} and V/V_{sm} as a function of Reynolds number for different values of a twisting pitch S/D.

Use of strip inserts is seen to be most effective at $Re_D=10^4\div2\cdot10^4$ and at small twisting pitches $S/D\cong4\div6$.

Compare the obtained data on the efficiency of heat transfer enhancement by a twisted strip with the results for annular smooth-wall diaphragms. Having utilized such turbulators, we could strive for a larger increase of heat transfer coefficient in tubes as against that of hydraulic resistance. Fig. 3 plots the appropriate data for an annular-diaphragmed tube with a relative diameter d/D=0.94 and a diaphragm pitch t/D=0.25.

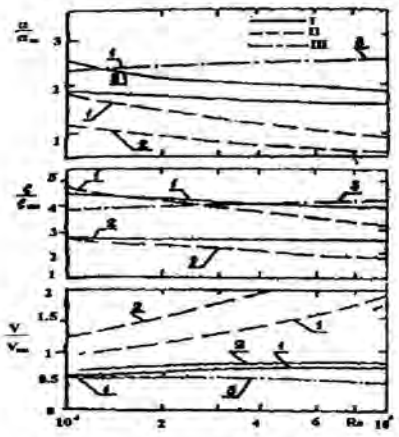

Figure 3: Influence of the Reynolds number on heat transfer enhancement α/α_{sm}, on the hydraulic resistance coefficient ratio ξ/ξ_{sm} and on the heat exchanger volume ratio V/V_{sm}: I, twisted tape; II, spiral screw; III, circular diaphragms; 1,S/D=4; 2, S/D=10; 3, circular diaphragms with d/D=0.94 and t/D=0.25.

As seen from this figure, use of an annular turbulator allows one to gain a stable 2.3÷2.43-fold increase of heat transfer over the range $Re=10^4\div10^5$ typical of heat exchangers when hydraulic resistance grows 3.8÷4.15 times, yielding $V/V_{sm}=0.52\div0.5$, or to decrease the heat exchanger volume 1.95÷2 times (in such tubes an advancing growth of heat transfer is larger d/D=0.97÷0.98 with $V/V_{sm}=0.5\div0.6$). Thus, the efficiency of heat transfer enhancement by strip inserts is somewhat lower at $Re=10^4$ and is substantially lower at $Re=10^5$ as against the one initiated by annular turbulators.

As seen from Fig. 3, the efficiency of screw inserts is much worse than that of strip ones. Even at minimum values of $d_0/D=0.33$ and for S/D=4÷12, we have $\alpha/\alpha_{sm}=1.75\div1.16$ and $\xi/\xi_{sm}=4.74\div2.64$ at $Re_D=10^4$ and $\alpha/\alpha_{sm}=0.88\div0.58$ and $\xi/\xi_{sm}=3.4\div1.38$ at $Re_D=10^5$. In this case, at $Re_D=10^4$ we obtain $V/V_{sm}=0.84\div1.19$, and at $Re_D=10^5$ we have $V/V_{sm}=1.9\div2.67$. Thus, a moderate improvement of efficiency ($V/V_{sm}<1$) can be attained only at $S/D\cong4$ and $Re_D\cong10^4$.

As the Reynolds numbers and the twisting pitches grow, we have $V/V_{sm}>1$, i.e., the application of screw inserts yields an adverse result since it does not improve but degrades heat exchanger parameters. Screw inserts with large relative screw core diameters d_0/D are still less effective.

High efficiency of annular smooth-wall turbulators used to enhance heat transfer inside tubes with liquid and gas flow in them as well as ease of their manufacture and good operating characteristics allows this heat transfer enhancement method to be recommended for heat transfer improvement inside tubes.

Turbular Evaporative Heat Exchangers

As seen from foregoing section, tubes with annular turbulators are very effective for single-phase heat carriers, especially for heat transfer enhancement inside a tube. There, when a choice is being made of a method for heat transfer enhancement in heat exchangers with boiling of heat carriers, obviously preference should be given to these tubes. Tubes having annular turbulators are particularly effective for this-type heat exchangers with single-phase heat carrier flow inside tubes.

Analysis was made by the example of a tubular evaporative heat exchanger of air cooling system meant for a conditioning system of aircrafts. Cooled air flowed inside the tubes, and boiling water filled the intertube space of the heat exchanger. Nucleate boiling occurred, a distance between the tubes was assigned and chosen such as not to hinder a vapor bubble rise to a liquid surface. A tubular smooth-wall heat exchanger and several variants of tubular heat exchangers with annular turbulators (Fig. 1) were calculated at the same value of heat power, heat carrier flow rate, air hydraulic resistance, inlet and outlet temperatures of heat carriers, and heat carrier pressures.

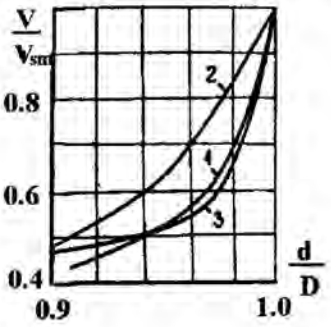

Figure 4: V/V_{sm} for evaporates with different d/D and t/D. 1-3 t/D = 0.25; 1; 05 respectively

Fig. 4 plots the volume ratio of the compared heat exchangers V/V_{sm} vs. the diaphragm-to-inner tube diameter ratio d/D at t/D=0.25÷1.

Thus, use of heat transfer enhancement permits an evaporative heat exchanger volume to be decreased more than 2 times at the same values of heat power, cooled air flow rate, and hydraulic resistance of a heat exchanger. The largest efficiency is seen for tubes with d/D=0.9÷0.92 and t/D=0.25÷0.5.

Turbular Condensers

Kalinin and Dreitser [3,4] investigated heat transfer enhancement involving vapour condensation on the outer surface of tubes with annular grooves. For horizontal tubes heat transfer enhancement was attained equal to $\alpha/\alpha_{sm}=2\div2.65$.

If account is taken of the fact that heat transfer inside these tubes with cooling water flow in them also substantially increases up to 2.3 times, then the high efficiency of tubes with annular turbulators is true for condensers.

Analysis was made by the example of a tubular condenser of an industrial heat power plant. Calculations were performed for tubes with D_{out}/D=20/18 mm under saturated water vapour condensation at pressures p_s=0.1; 1; 2 bars (T_s=45.83; 94.63; 120.23°C). Cooling water flowed inside the tubes horizontally located in a bundle, and condensation of saturated water vapour occurred outside the tubes. A tubular smooth-wall heat exchanger and several variants of tubular heat exchangers with annular turbulators (Fig.1) were calculated at the same values of heat power, heat carrier flow rate, cooling water hydraulic resistance, and temperatures and pressures of heat carriers. Design was based on the methods [1] of calculating a tubular heat exchanger for a specified hydraulic resistance. Calculations were preformed at d_{out}/D_{out} = 0.85÷0.95; t/D_{out} = 0.37; in this case, d/D = 0.86÷0.97; t/D = 0.41. In this range of the parameters of turbulators outside the tubes, α/α_{sm}=2.11÷3.16; inside the tubes, $(Nu/Nu_{sm})_{Re}$ = 1.8÷2.3. However, for the same hydraulic resistance inside the tubes with turbulators, it is necessary somewhat to decrease a water velocity and to increase the number of tubes; in this case, a real value of α/α_{sm} decreases. The calculation results for V/V_{sm} are plotted in Fig. 6. The quantity V/V_{sm}=0.50÷0.65; in this case, V/V_{sm} decreases with increasing T_s and depends weakly on d/D.

Thus, use of tubes with annular turbulators to enhance heat transfer outside and inside the tubes allows the condenser volume to be decreased up to 2 times at the same values of heat power, cooling water flow rate, and hydraulic resistance of a heat exchanger. The largest efficiency is seen for tubes with d/D = 0.86÷0.9 and t/D = 0.4 (d_{out}/D_{out} = 0.85÷0.89; t/D_{out} = 0.35÷0.4).

It should be noted that the efficiency of the investigated tubes with annular turbulators used in condensers is much higher than that of helical tubes that enhance the heat transfer coefficient by 25%.

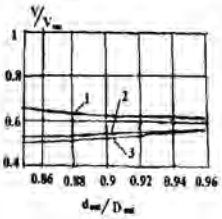

Figure 5: V/V_{sm} for condensators with different T_s and d/D
1-3 T_s=120.23; 99.63; 45.85°C respectively.

Also, use of different fins welded to the outer surface of a tube is less effective because in this case heat transfer inside the tubes is not enhanced.

Heat Exchangers Operating under Fouling Conditions

In many fields of engineering, the fouling control on a heat transfer surface is a serious problem. Use of water containing temporary-hardness salts as a cooling medium yields their deposition on heat transfer surfaces, as a cold water temperature grows. Therefore, in designing high-efficiency refrigerators and water-cooled condensers, it is necessary, along with heat transfer enhancement, to prevent or decrease a rate of the fouling growth on a heat transfer surface.

The existing methods of controlling salt deposition mainly amount to preliminary water treatment mostly by chemical reagents. These methods are inapplicable for those productions that require a great amount of water for cooling. Open-cycle cooling is made. Of late, great interest has been paid to the problem how to reduce salt deposits on the heat transfer surface from flow swirling.

Tubes with annular turbulators turned out to be very effective in service when water had elevated bicarbonate hardness (up to C=20 mg-equiv./l). This was proved in special experiments, in which water with elevated hardness flowed over the outside and inside surfaces of tubes with turbulators of different parameters. A water velocity was varied from 0.1 to 1.5 m/s, a temperature was in the range 50÷90°C, and experiments lasted for about 360 h. As a result, the thermal resistance of a scale layer R_{foul} outside and inside the tubes was obtained as a function of the parameters of the turbulators, water velocity, and time.

Fig. 6 shows the increase of fouling thermal resistance R_{foul} inside smooth tubes versus time.

Turbulators reduce salt deposition on both surfaces of the tubes by a factor of 3÷5. The time dependence of R_{foul} is asymptotic; after 100÷150 h, the value of R_{foul} becomes constant.

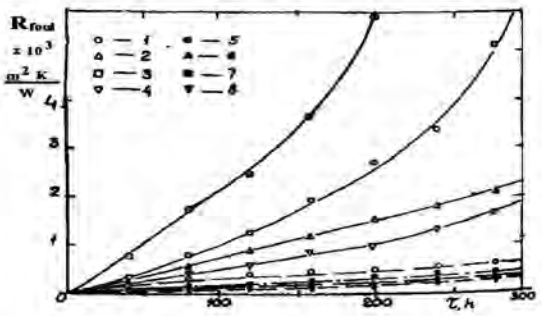

Figure 6: Time variations of the fouling thermal resistance inside the smooth tubes (1-4). annular diaphragm-equipped tubes with d/D=0.91 and t/D=0.5 (5-8).
1, 5 – Re=3200;C=20 mg eq./l;
2, 6 – Re=16000;C=20 mg eq./l;
3, 7 – Re=3200;C=10 mg eq./1;

4, 8 – Re=16000;C=10 mg eq./l;

Less scale is formed on the tubes with turbulators when the height of a diaphragm increases, the depth of grooves grows or their pitch decreases. Typically, after water of elevated hardness flowed in a tube with diaphragms for 100 h, the heat transfer coefficient fell by a factor not more than 10%, and the pressure drop did not change at all. During this time, if the tube had smooth walls, the heat transfer coefficient fell by 30% and the pressure drop rose by 25%. The effectiveness of tubes with turbulators was increased in the presence of scale. When there was no scale (at $\tau=0$), the ratio of heat transfer coefficients $k_f/k_{fs}=2.5\div3$; then at $\tau/\tau_*=1$ we have $k_f/k_{fsm}=3.5\div5$. A generalization of the experimental data has led us to the following dependences for the thermal resistance of a scale layer [R_{foul},(m^2K)/W] that were reported by Kalinin and Dreitser [3,4]. Under the fouling conditions the turbulator parameters are as follows: d/D=0.9÷0.92; t/D=0.25÷0.5.

CONCLUSIONS

1. Tubes with annular turbulators can substantially augment heat transfer involving gas and liquid flow in the tubes under the conditions of surface and film boiling inside the tubes as well as condensation on the outside surface of horizontal and vertical tubes.

2. Tests of commercial heat exchangers with the tubes have supported that equipment is highly effective and can reduce a heat transfer surface 1.5-2.5 times, as compared to a similar apparatus with smooth-wall tubes.

3. Much less scale is formed inside and outside the tubes with turbulators as against that on smooth-wall tubes; moreover, the scale grows asymptotically in time. Therefore, heat exchangers having no special facilities to clean their surface can be used.

ACKNOWLEDGEMENTS

The support of the Russian Research Foundation under its Project No.00-15-96654 (The Program of Support of Leading Scientific Schools of Russia) and the Russian Ministry of Education (Program "Thermal Energetics and Electrical Technics") is gratefully acknowledged.

REFERENCES

[1] Dreitser G.A., 1986, Compact Heat Exchangers, MAI Publishers, Moscow.

[2] Dreitser G.A., Dubrovsky E.V., Dzybenko B.V., Iyevlev V.M., Kalinin E.K., Shimonis V.M., Shlenchiauskas A.A., Vilemas J.V., Voronin G.I., Zukauskas A.A., and Yarkho S.A., 1990, Enhancement of Heat Transfer, Heat Transfer Soviet Reviews, Vol.2, Hemisphere Publishing, New York.

[3] Kalinin E.K., and Dreitser G.A., 1998, 1, Heat Transfer Enhancement in Heat Exchangers. Advances in Heat Transfer, Vol. 31, pp.159-332, Academic Press, New York.

[4] Kalinin E.K., Dreitser G.A., Kopp I.Z., and Myakotchin A.S., 1998,2, Effective Heat Transfer Surfaces, Energoatoizdat, Moscow.

[5] Shchukin V.K., 1970, 1980, Heat Transfer and Hydrodynamics of Internal Flows in Mass Force Fields, Mashinostroyeniye, Moscow, 1st ed., 2nd ed.

[6] Dreitser G.A., 1997, Modern Problems in Creating Compact Turbular Heat Exchangers. Compact Heat Exchangers for the Process Industries, Snowbird USA, Ed. by N.K. Shan, Begell House Inc., New York, Wellington (UK), pp.121-140.

HEFAT2002
1ST International Conference on Heat Transfer, Fluid Mechanics, and Thermodynamics
8-10 April 2002, Kruger Park, South Africa
GE1

MIXED CONVECTION HEAT TRANSFER IN A CORRUGATED HORIZONTAL CHANNEL

Emmanuel K. Glakpe* and Shawn C. McLeod**
*Professor; **M. Eng. Graduate
Department of Mechanical Engineering
Howard University
Washington, DC 20059, USA
E-mail: glakpe@cldc.howard.edu

ABSTRACT

The problem of mixed convective fluid flow and heat transfer in a horizontal corrugated channel is addressed in the paper. Results of the numerical analyses are applicable to the design of solar collectors. The results can also be used in the design of novel compact heat exchangers. Starting with the three dimensional governing equations for fluid flow and heat transfer for a Newtonian fluid with appropriate boundary conditions, the problem is solved numerically in a transformed geometric domain due the presence of the corrugated surface. A heat flux condition is imposed on the corrugated surface and due to the nature of the application, the other sides of the duct are assumed to be perfectly insulated. The finite volume method is extensively used to obtain discretized equations that are solved using standard methods of solution. From the results of the numerical calculations, the solar collector heat exchanger with a corrugated surface produces heat transfer coefficients that are higher than those obtained from a flat plate surface and will therefore yield a more compact design. Representative heat transfer coefficients in the form of Nusselt numbers are presented for both surfaces as functions of the various dimensionless parameters.

NOMENCLATURE

A	amplitude of corrugation
AR	aspect ratio
C_p	specific heat at constant pressure
D	diffusion coefficient
D_h	hydraulic diameter of duct
e_x, e_y, e_z	unit vectors in the x, y, z directions of the physical domain
e_ξ,e_η,e_ζ	unit vectors in the ξ, η, and ζ directions of the transformed domain
F	mass flow rate at a control volume face
F_x, F_y, F_z	body forces in the x, y, and z directions of the physical domain
g	acceleration due to gravity
Gr	Grashof number
H	height of the duct
J	total flux across a control volume face
k	thermal conductivity
L	length of duct in the x-direction
l	height of corrugation
n′	number of corrugation cycles
Nu	Local Nusselt number $=\frac{hD_h}{k}=\frac{\dot{q}_w D_h}{k(T_w-T_K)}=\frac{1}{\theta_w-\theta_K}$
Nu_p	Average Nusselt number for a plane $=\frac{1}{\xi}\int_0^\xi Nu d\xi$
Nu_z	Average Nusselt number along the Z-axis $=\frac{1}{\zeta}\int_0^\zeta Nu_p d\zeta$
P, P′	pressure, reduced pressure
Pr	Prandtl number
$\dot{q}$	uniform heat flux
Ra	Rayleigh number for uniform heat flux
Re	Reynolds number in terms of the inlet velocity and hydraulic diameter
S	source term
T	temperature
u ,U_x	x-component of velocity in physical domain, dimensional/dimensionless
U_η	η-component of velocity in the transformed domain
U_ζ	ζ-component of velocity in the transformed domain
U_o	reference velocity, α′/D_h
v, w	dimensional velocity components in the y and z directions
X, Y, Z	dimensionless coordinates in the physical domain
w	length of duct in z-direction
U ,V	dimensionless velocity components in the x and y-directions
W	dimensionless velocity component in the z-direction

Greek Symbols

α	a geometric coefficient, $(1+\beta^2)$

α'	thermal diffusivity $[(k / \rho_o C_p)]$
A	a diffusion term, $[-\delta(\partial\Phi/\partial\xi)]$
β'	coefficient of thermal expansion,
β	a geometric coefficient, $[(1-\eta)(\partial l /\partial\xi)]$
δ	dimensionless gap between corrugated and upper wall
τ	time
ϕ	inclination angle
ξ, η, ζ	coordinates in the transformed domain
Π	a diffusion term, $[-\delta(\partial\Phi/\partial\zeta)]$
Ω	a diffusion term, $[(-\alpha/\delta)(\partial\Phi/\partial\eta)]$
Λ	a pseudo-diffusion term, $[\beta(\partial\Phi/\partial\xi)]$
Ψ	a pseudo-diffusion term, $[\beta(\partial\Phi/\partial\eta)]$
μ	dynamic viscosity
ν	kinematic viscosity
ρ	density
θ	dimensionless temperature
θ_κ	dimensionless bulk fluid temperature
θ_w	dimensionless wall temperature

INTRODUCTION

Considerable research involving the phenomena of convection inside ducts has been performed over the past several decades [1-9]. Initial research efforts focused on forced convection in rectangular and circular ducts with the assumptions of fully developed flows. A testament to the importance and value of this research is the extensive compilation of data documented in Shah and London [6]. The overwhelming number of investigations that were undertaken had industrial applications; these included the design of heat exchanger, electronic packages, solar energy collectors and turbomachinery.

In the more recent decades, there has been a renewed interest in the study of flows confined in ducts. Investigators are presently concerned with the phenomena of mixed convection in simple geometries in addition to emerging complex configurations that have the potential to produce desirable flow properties in engineering applications. Additionally, researchers are attempting to solve more challenging problems by deviating from the popular assumption of fully developed flow at the entrance of the duct and to consider hydrodynamic and thermal entry length problems. More efficient numerical schemes and better data acquisition systems are being developed to help predict and measure accurately the velocity and temperature fields associated with mixed convection in various types of ducts. Motivated by the needs of industry and the rapidly advancing computer technologies, researches have sought to shrink heat exchanger sizes while maximizing heat transfer, control the process of chemical vapor deposition and safeguard important electronic equipment through better product design via research and development

This paper presents numerical solutions to the steady, laminar, three-dimensional mixed convection problem in a duct with three flat surfaces and a surface that is corrugated. A schematic view of the duct is shown in Fig. 1. A heat flux condition is imposed on the corrugated surface whereas the other surfaces are treated as perfectly insulated. Results are presented for the flow of water (Pr=6.5) entering the duct with uniform velocity and temperature. The geometric and flow parameters that affect the heat transfer and fluid flow in such a geometry include the duct aspect ratio, a height ratio, the

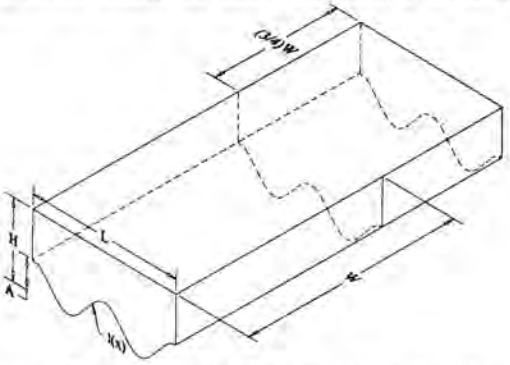

Figure 1: Physical Geometry of Corrugated Duct

number of corrugation cycles per unit of duct, the angle of inclination of the duct to the horizontal axis, the Reynolds number, the modified Rayleigh number and the Prandtl number. In the present investigation, results are presented for a horizontal duct with aspect ratio of 2, two corrugation cycles, and an amplitude that is 40% of the total duct height, A/H= 0.40. The duct has a total length composed of heated and unheated sections. The unheated section has a length equal to 75% of the unheated section.

Due to the irregular nature of the geometry, a convenient natural coordinate system may not be used to describe the equations that govern the fluid flow and heat transfer. Therefore, a non-orthogonal algebraic coordinate transformation similar to that of Faghri et al [10] is employed, in which the transformed governing equations are solved in a rectangular domain system. The control volume approach of Patankar [11] is used to integrate the transformed equations over control volumes whereas finite-difference representations are employed appropriately to facilitate solution by an efficient numerical scheme. In the present work, the discretized equations of motion and energy are solved within the framework of the SIMPLEST scheme proposed by Domanus et al [12] for orthogonal systems. The approach not only ensures global conservation of mass, momentum and energy but it also facilitates physical interpretation of the terms generated in the coordinate transformation.

PROBLEM STATEMENT

A schematic view of the corrugated duct is shown in Fig. 1. Fluid entering from the left side with uniform velocity and temperature is heated by the bottom corrugated surface with a constant heat flux. The other three surfaces are maintained at perfectly insulated conditions. The duct fluid is water with a Prandtl number of 6.5. By introducing the following dimensionless variables:

$$X = \frac{x}{D_h}, \quad Y = \frac{y}{D_h}, \quad Z = \frac{z}{D_h \, Re \, Pr}$$

$$U = \frac{u}{U_o}, \quad V = \frac{v}{U_o}, \quad W = \frac{w}{w_{in}}, \quad P = \frac{P - p_\infty}{\rho_o U_o^2 PR}, \quad \tau = \frac{tU_o}{D_h},$$

$$\theta = \frac{T - T_{in}}{T_w - T_{in}}, \; \theta = \frac{T - T_{in}}{\dot{q}_w D_h / k}, \text{ (uniform heat flux)}$$

$$Re = \frac{\rho_o w_{in} D_h}{\mu}, \quad Pr = \frac{\nu}{\alpha'}, \quad U_o = \frac{\alpha'}{D_h}, \quad D_h = \frac{2LH}{LH}, \quad \alpha' = \frac{k}{\rho_o c_p}$$

(where $\dot{q}_w$ = the heat transfer rate at the wall per unit area; T_{in} = dimensional temperature at duct entrance; T_w = dimensional wall temperature; and D_h = hydraulic diameter), the resulting non-dimensional equations, with the asterisks omitted for convenience, are given by:

Continuity Equation

$$\frac{\partial \rho}{\partial \tau} + \frac{\partial (\rho U)}{\partial X} + \frac{\partial (\rho V)}{\partial Y} + \frac{\partial (\rho W)}{\partial Z} = 0$$

X -Momentum

$$\frac{1}{Pr}\frac{\partial U}{\partial \tau} + \frac{1}{Pr}\left[U\frac{\partial U}{\partial X} + V\frac{\partial U}{\partial Y} + W\frac{\partial U}{\partial Z}\right] = -\frac{\partial P}{\partial X} + Ra * \theta * \sin\varphi + \left[\frac{\partial^2 U}{\partial X^2} + \frac{\partial^2 U}{\partial Y^2} + \frac{1}{(Re\,Pr)^2}\frac{\partial^2 U}{\partial Z^2}\right]$$

Y - Momentum

$$\frac{1}{Pr}\frac{\partial V}{\partial \tau} + \frac{1}{Pr}\left[U\frac{\partial V}{\partial X} + V\frac{\partial V}{\partial Y} + W\frac{\partial V}{\partial Z}\right] = -\frac{\partial P}{\partial Y} + Ra * \theta * \cos\varphi + \left[\frac{\partial^2 V}{\partial X^2} + \frac{\partial^2 V}{\partial Y^2} + \frac{1}{(Re\,Pr)^2}\frac{\partial^2 V}{\partial Z^2}\right]$$

Z - Momentum

$$\frac{1}{Pr}\frac{\partial Z}{\partial \tau} + \frac{1}{Pr}\left[U\frac{\partial W}{\partial X} + V\frac{\partial W}{\partial Y} + W\frac{\partial W}{\partial Z}\right] = -\frac{1}{(Re\,Pr)^2}\frac{\partial P}{\partial Z} + \left[\frac{\partial^2 W}{\partial X^2} + \frac{\partial^2 W}{\partial Y^2} + \frac{1}{(Re\,Pr)^2}\frac{\partial^2 W}{\partial Z^2}\right]$$

Energy

$$\frac{\partial \theta}{\partial \tau} + U\frac{\partial \theta}{\partial X} + V\frac{\partial \theta}{\partial Y} + W\frac{\partial \theta}{\partial Z} = \frac{\partial^2 \theta}{\partial X^2} + \frac{\partial^2 \theta}{\partial Y^2} + \frac{\partial^2 \theta}{\partial Z^2}$$

The fluid properties are assumed to be constant except the density in the body force terms which are expressed in terms of the Boussinesq approximation. The governing equations are parabolic in time and elliptic in the spatial coordinates and therefore require the specification of boundary and initial conditions for solutions to be obtained. The no-slip boundary condition is applied to all solid surfaces of the enclosure. In addition to the Rayleigh and Prandtl numbers, the fluid flow and heat transfer characteristics in the cavity depend on dimensionless geometric parameters A/H and L/H.

SOLUTION METHOD

Due to the irregular nature of the geometric configuration, that eliminates representation for numerical analysis by a convenient natural coordinate system, a non-orthogonal algebraic transformation is proposed. Specifically, the X, Y, and Z coordinates are transformed to ξ, η, and ζ coordinates with the following algebraic equations:

$$\xi = X \; ; \quad \eta = \frac{Y - l(X)}{H - l(X)} \; ; \quad \zeta = Z$$

In the equation for η, the function $l(X)$ is the dimensionless height of the corrugated surface; the sinusoidal expression for $l(X)$ is:

$$l(X) = \frac{l(x)}{D_h} = \frac{1}{4}\frac{A}{H}\left(1 + \frac{H}{L}\right)\left[1 + \cos\left(\frac{4\pi n' X}{1 + \frac{L}{H}}\right)\right]$$

The solution domain created by the transformation is defined by: $0 \le \eta \le 1$; $0 \le \xi \le L/D_h$; and $\zeta > 0$. It should be noted that the geometric transformation equations are applicable to a general class of three-dimensional convection problems in which the one surface is "irregular" relative to the other surfaces. An analytical or discrete specification of the function l(X)is the only input required in order to use the solution method described in this paper.

Transformation of Governing Equations

The dimensionless momentum equations, can be combined into a vector equation by multiplying the X and Y-Momentum equations with unit vectors e_X and e_Y, respectively, and adding the results to the product of the Z-Momentum equation with the unit vector in the Z direction e_Z. The result of this operation can be written in a compact form as:

$$[X \text{ - momentum}]\, e_X + [Y \text{ - momentum}]\, e_Y + [Z \text{ - momentum}]\, e_Z = 0$$

Substituting for e_X, e_Y, *and* e_Z yields an equation in terms of e_η, e_ξ, and e_ζ. Since the latter unit vectors are independent, their resulting coefficients in this equation are set equal to zero to produce the transformed momentum equations in the η, ξ, and ζ coordinate directions. Results of the lengthy algebraic and differential operations can be found in McLeod [13]. For simplicity, the original equations for the X and Z-momentum are retained with U and W as the primary dependent variable instead of U_ξ and U_ζ. The forms of the continuity and energy equations are maintained to retain their simplicity; however, during the discretization process, appropriate relationships between physical and transformed coordinate systems are employed. The mathematical operations result in a a general integral form of the governing equations when integrated over the appropriate control volume. This equation is written in generic form (with variable Φ) as:

$$\int_v \frac{\partial \Phi}{\partial \tau} dV = \int_{s1}\left[U_x \Phi\delta + \Gamma(E + \Psi)\right] d\eta d\zeta - \int_{s2}\left[U_x \Phi\delta + \Gamma(E + \Psi)\right] d\eta d\zeta +$$

$$\int_{s3}\left[U_\eta \Phi + \Gamma(\Lambda + \Omega)\right] d\xi d\zeta - \int_{s4}\left[U_\eta \Phi + \Gamma(\Lambda + \Omega)\right] d\xi d\zeta +$$

$$\int_{s5}\left[U_\zeta \Phi\delta + \left(\frac{\Gamma}{(Re\,Pr)^2}\right)\Pi\right] d\xi d\eta - \int_{s6}\left[U_\zeta \Phi\delta + \left(\frac{\Gamma}{(Re\,Pr)^2}\right)\Pi\right] d\xi d\eta + (Pr)(b)$$

In this equation, "Γ" is the diffusion coefficient. For the momentum equations, it takes on the value associated with the dimensionless number, Pr. In the energy and continuity equations, Γ takes on the values, 1 and 0, respectively. The last term in the above equation, b, is the source term.

RESULTS AND DISCUSSION

In solving for the flow and temperature variables, the integral forms of the transformed governing equations are

converted to finite difference equations as follows. The integral operations indicated in the equations above are performed for each location of the variable Φ over the control volume that encloses this location. The grid layout used is a "staggered" grid system, in which the velocity components are stored midway between the algebraically generated grid points, while other dependent variables are stored at the grid points themselves. The integrations are performed after making assumptions about the manner in which each variable is distributed between grid nodes. The convective terms are represented by upwind differences while the diffusive and other terms are approximated by central differences. Details of the numerical solution procedure are documented in the thesis work of McLeod [13].

Numerical results for the steady flow of fluid flow and heat transfer in the corrugated duct have been obtained for Reynolds number values of 300 and 425, and for Rayleigh numbers between 6800 and $1.8x10^5$ while holding the Prandtl number and the corrugation amplitude aspect ratio at 6.5 and 2.0 respectively. Grid independence was established at a distribution of 41x31x70. Two tests were performed to establish the validity of results from the numerical code. The first test closely reproduced the results of the forced convection experiment performed by Goldstein and Kreid 14], in which the centerline velocities for the laminar flow of water in a square duct were measured using a laser-doppler technique. Specifically, for Re=286, the code predicted a maximum centerline velocity of 2.037, which is about 2.78 % less than the value measured in the experiment, Fig. 2. The code also predicted qualitatively the secondary flow in a rectangular duct as determined by the numerical and experimental results of Incropera et al. [3]. For a lower wall uniform heat flux boundary condition, an aspect ratio of AR=2, and a Grashof number of Gr= $2.5x10^6$, the code accurately predicted at a specific cross section, the number of vortices present, the direction of their rotation, and the character of the isotherms.

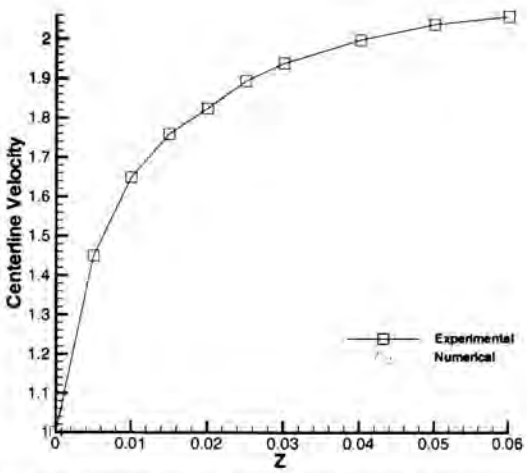

Figure 2: Comparison of Centerline Velocities with Goldstein and Kreid [14] for Isothermal Flow in a Square Duct

Fluid Flow and Temperature Profile

For a geometric aspect ratio of 2 and a Reynolds number of 300, results for the mixed convection flow in a corrugated duct show very little variance in the flow variables for Rayleigh numbers greater than $8.6x10^4$. The dominance of the Reynolds number on the flow is more pronounced at a value of 425 in which invariance in the data was observed at Rayleigh numbers greater than 6800. Results for a Reynolds number of 300 show that on either side of the line of symmetry for the physical geometry, there exist three vortices, Fig. 3. There is a large vortex at the center crest, a smaller vortex at the crest near the sidewall and a very small region of circulation near the upper corner. From the perspective of the left side of the duct, the vortices rotate in a counterclockwise, clockwise, and counterclockwise direction, respectively. These conditions exist throughout the duct for all Z-planes that were studied and at all Rayleigh numbers.

Considering the first plane of study, Z-step of 6 (a Z-step of 6 is equivalent to a dimensionless value of 6xΔz where Δz is a function of the Reynolds number), the temperature contour, Fig. 3, depicts a large region of cool fluid, which is bounded on the left by warmer fluid that has been lifted along the sidewall. On the right hand side, the larger vortex lifts warmer fluid until it extends to the upper wall; yet, it also forms an elliptical region of warm fluid that sits just above and to the right of the center crest. At a higher Rayleigh number, Ra=$8.6x10^4$, a

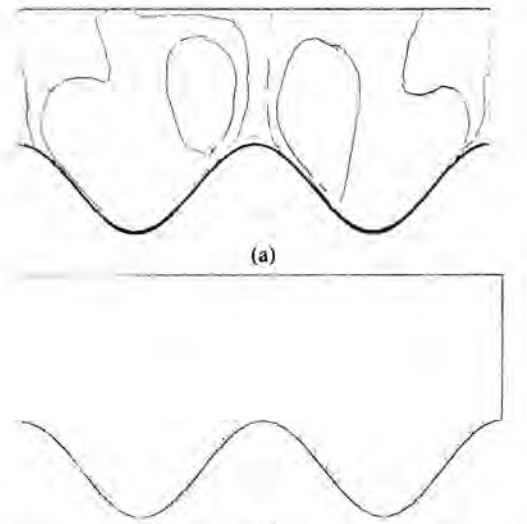

Figure 3: Temperature Contour (a) and Vector Plot (b) for Z-Step 6, Re=300,Ra=6800

different picture results. Figure 4 shows that the large vortex at the center extends its influence into the trough of the corrugation and the temperature contour dips into the trough. Secondly, the smaller vortex at the sidewall has generated an area of warm fluid that sits just above the outside crest. An apparent peak at the line of symmetry also suggests enhanced mixing.

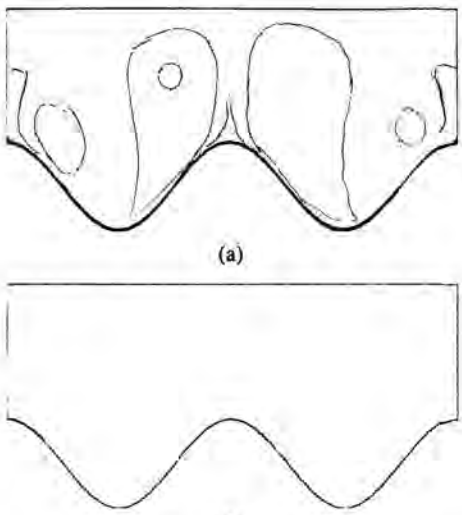

(a)

(b)

Figure 4: Temperature Contour (a) and Vector Plot (b) for Z-Step of 6, Re = 300, Ra = 86,000

At Z-step of 11 for Ra=6800, there still exists a region of warm fluid that sits above the center crest; yet, this region is reduced in size and is at a higher temperature than in the previous step. The more apparent trait is the formation of a "finger" of warm fluid that develops from the line of symmetry and the left boundary to dip into the colder interior region. Contrasting this picture with it's counterpart at the higher Rayleigh number, $Ra=8.6x10^4$, one sees that the larger body of warm fluid that rested at the crest and extended into the trough in the previous step still remains. Yet, the magnitude of the temperature of these bodies has increased; the decline in the peak size at the line of symmetry and the shrinkage of the fluid body that rests along the crest at the left wall denotes a warming of the core fluid within the duct, which is contrary to the existence of a "finger".

At Z-step of 16, the flow characterized by Ra=6800 has developed one of the traits that was seen in the earlier steps of the flow having a Rayleigh number of $8.6x10^4$; there now exists a warm fluid body that rests at the center crest and impinges into the trough. There is a spike at the line of symmetry whose contour runs along the bottom surface and develops into a jutting "finger" due to the presence of the smaller vortex at the sidewall. For the higher Rayleigh number, there is a decrease in the influence of the vortex at the center crest, as seen by the absence of an interior ring inside the temperature contour. As with the lower Rayleigh number, there is a "finger" jutting from the sidewall; yet it is far more intrusive. But, unlike the peak, there exists a column whose contour line runs along the bottom boundary. The formation of this column suggests a greater permeation of heat within the duct.

The two cases, Ra=6800 and $Ra=8.6x10^4$ appear to be at an almost equivalent state at Z-step of 26, the temperature contours and velocity vector plots have only a very slight difference. Each case shows that a large portion of the fluid has the same temperature, but for Ra=6800 the size of this body of fluid is smaller. The case where $Ra= 8.6x10^4$ also shows the formation of an impinging finger from the sidewall.

There are some similarities and differences in the results obtained for the two Reynolds numbers. The results for Re=425 at Z-step of 6, are similar to those at Z-step of 16 for Re=300 and $Ra=8.6x10^4$. For Re=425, a column at the line of symmetry is present and there is an impinging "finger" at the sidewall although it is smaller than its counterpart. Also, an elliptic and warmer body of fluid rests above the center crest. Even though the temperature of these formations are different than their counterparts in the case of Re=300, their presence suggests that the flow development at these cross sections are similar; the increase in the Reynolds number has shortened the length it takes for this particular pattern to develop. This phenomenon continues through Z-step of 11, and is similar with the results for Re=300 and Ra=86,000. At the Z-step of 16, the vortex at the center has created a warmer body of fluid that reaches far above the crest and into the trough of the bottom plate. The vortex at the sidewall has generated a warm fluid body that sits beside the crest at the sidewall. The ensuing Z-step values, 26 and 39, depict the occurrence of a more uniform fluid temperature as denoted by the loss of the interior contour of the fluid body resting at the center crest, and the development of a large contour which occupies the majority of the duct.

Heat Transfer Results

To investigate the effect of mixed convection and the bottom plate corrugation on heat transfer within the duct, Nusselt numbers were generated for three cases: mixed convection with a corrugated bottom plate, mixed convection with a flat bottom plate, and forced convection with a corrugated bottom plate. Results were generated for an aspect ratio, AR=2, a Rayleigh number of $Ra=8.6 \times 10^4$ and a Reynolds number of 300. The average Nusselt number for each Z-plane, Nu_p, was generated by numerically integrating the curve created by plotting the local Nusselt numbers and subsequently dividing the resulting area by the width of the computational domain.

The results presented in Figs. 5 and 6 show that the corrugated geometry greatly enhances the heat transfer beyond that which occurred in the duct with the flat bottom plate. The average Nusselt number in the plane was found to exceed its counterpart by a factor ranging from 2.5 at the duct entrance to 21 at the duct exit. Along the length of the duct, the magnitude of Nu_z was 3 to 13 times greater than the values calculated for the duct without corrugation. In comparison with the pure forced convection results, mixed convection only slightly affected the average Nusselt number in the Z-plane; the difference between the forced convection and mixed convection values is negligible except for a 2.5% decrease at the end of the duct. For the average Nusselt number along the length of the duct, a decrease of approximately 0.3% occurred.

SUMMARY

Numerical solutions for three-dimensional mixed convective fluid flow and heat transfer in a horizontal duct with a corrugated bottom surface have been obtained. Solutions were

also generated for the limiting case of forced convection in the duct and for mixed convection in a duct with a bottom flat

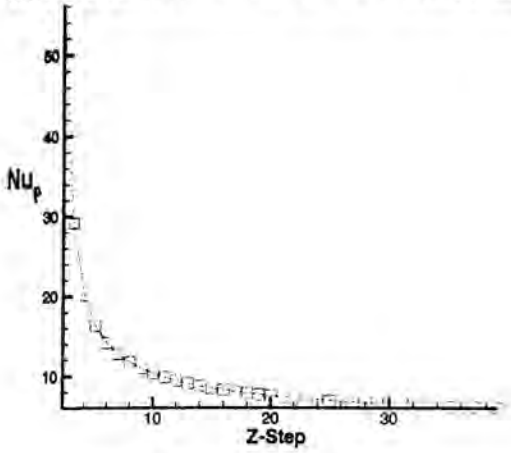

Figure 5: Average Nusselt Number for Z-Planes at Re=300, Ra=86,000; Rectangular Duct; AR=2

plate. The solutions were obtained for Reynolds numbers of 300 and 425, a Rayleigh number in the range of 6800 and

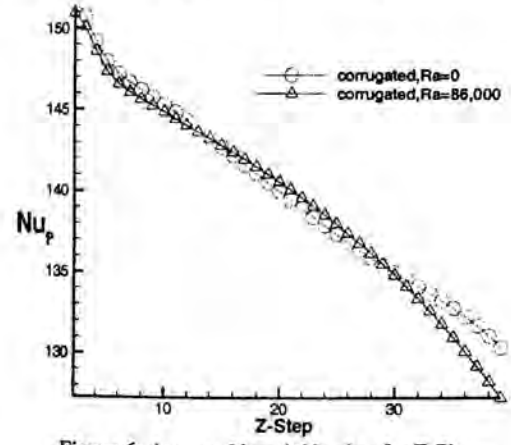

Figure 6: Average Nusselt Number for Z-Planes

1.8×10^5, a Prandtl number of 6.5 and a geometric aspect ratio of 2. Velocity vector plots throughout the regime of study showed that the duct is filled by six vortices, three on each side of the line of symmetry. The two larger vortices are buoyancy driven, while the third results from a corner effect. The larger vortices are situated at the crests of the corrugated plate.

As expected, the comparison of mixed convection in the corrugated geometry to mixed convection in a simple rectangular duct of the same aspect ratio highlighted the substantial effect that the corrugation has on lowering the average wall temperature and increasing the Nusselt number. The Nusselt numbers in the Z-planes were increased by a factor as high as 21 while the largest increase for the Nusselt number at each Z-step was about 13 times the value in the rectangular duct. The results presented in this paper are for a horizontal duct; it is the intent of the authors to extend the work in order to obtain and publish results for inclination angles greater than zero degrees.

REFERENCES

[1] Abou-Ellail, M. M., and Morcos S. M., 1983, "Bouyancy Effects in the Entrance Region of Horizontal Rectangular Channels," ASME Journal of Heat Transfer, **105**, pp. 924 –928.

[2] Morcos, S. M., Hilal, M. M., Kamel, M. M., and Soliman, M. S., 1986, "Experimental Investigation of Mixed Laminar Convection in the Entrance Region of Inclined Rectangular Channels," ASME Journal of Heat Transfer, **108**,pp. 574-579.

[3] Incropera, F. P., Knox, A. L., and Maughan, J. R., 1987, " Mixed-Convective Flow and Heat Transfer in the Entry Region of a Horizontal Rectangular Duct,"ASME Journal of Heat Transfer, **109**, pp.434-439.

[4] Mahaney, H. V., Incropera, F.P. and Ramadhyani, S., 1988, "Effects of Wall Heat Flux Distribution on Laminar Mixed Convection in the Entrance Region of a Horizontal Rectangular Duct," Numerical Heat Transfer, **13**, pp.427-450.

[5] Narusawa, U., 1992, "Numerical Analysis of Mixed Convection at the Entrance Region of a Rectangular Duct heated from Below," Int. Journal of Heat and Mass Transfer, **36**, No. 9, pp. 2375-2384.

[6] Shah, R. K., and London, A. L., *Laminar Flow Forced Convection in Ducts*, 1978, Academic Press, New York.

[7] Haung, C. C., and Lin, T. F., 1993, " Numerical Simulation of Transitional Aiding Mixed Convection Air Flow in a Bottom Heated Inclined Rectangular Duct," Int. Journal of Heat and Mass Transfer, **39**, No.8, pp. 1697-1710.

[8] Lin, W. L., Ker, Y. T., and Lin, T. F., 1996, "Experimental Observation and Conjugate Heat Transfer Analysis of Vortex Flow Development in Mixed Convection of Air in a Horizontal Rectangular Duct," Int. Journal of Heat and Mass Transfer, **39**, No 17, pp. 3667-3686.

[9] Elliott, L., Ingham, D. B., and Wood, J. D., 1998, "A Two-Dimensional Model of the Three Dimensional Mixed-Convection Flow of Newtonian and Non-Newtonian Fluids in a Rectangular Duct," Int. Journal of Heat and Mass Transfer, **41**, No 1, pp. 33-44.

[10] Faghri, E., Sparrow, M., and Prata, A.T., 1984, "Finite-Difference Solutions of Convection-Diffusion Problems in Irregular Domains, Using A Non-Orthogonal Coordinate Transformation," Numerical Heat Transfer, Vol. 7, pp.183-209.

[11] Patankar, S. V.,1980, *Numerical Heat Transfer and Fluid Flow*, Hemisphere Publishing Corporation., Washington, D.C.

[12] Domanus, H. M., Schmitt, R. C., Shah, V. L., 1983, "A New Implicit Numerical Solution Scheme in the COMMIX-1A Computer Program," Argonne National Laboratory, Report No. ANL-83-64

[13] McLeod, S. C., 2001, "Numerical Analysis of Mixed Convection Fluid Flow and Heat Transfer in a Horizontal Corrugated Duct," M.S. Thesis, Department of Mechanical Engineering, Howard University, Washington, DC.

[14] Goldstein, R. J., and Kreid, D. K., 1967, "Measurement of Laminar Flow Development in a Square Duct Using a Laser-Doppler Flowmeter," ASME Journal of Applied Mechanics, **34**, pp. 813-817.

HEFAT2002
1st International Conference on Heat Transfer, Fluid Mechanics, and Thermodynamics
8-10 April 2002, Kruger Park, South Africa
KJ3

MICROSCOPIC PHENOMENA AND MACROSCOPIC EVALUATION OF HEAT TRANSFER FROM PLATE FINS/CIRCULAR TUBE ASSEMBLY USING NAPHTHALENE SUBLIMATION TECHNIQUE

Jin-Yoon Kim* and Tae-Ho Song**
*M. Eng. Student; **Professor
Department of Mechanical Engineering,
Korea Advanced Institute of Science and Technology,
Kusong-dong 373-1, Yusong-gu, Taejon,
South Korea,
E-mail: thsong@kaist.ac.kr

ABSTRACT

Flow and heat transfer in a plate fins/circular tube assembly is examined using naphthalene sublimation technique to scrutinize the microscopic flow and heat transfer phenomena and also to evaluate the overall performance to find out the optimal tube location. The examined parameters are the gap(δ) to tube diameter(D) ratio δ/D, the Reynolds number Re_D and the tube location l/D. Single tube is simulated by Plexiglas disk between two parallel naphthalene molds.

A preliminary flow visualization shows the existence of large recirculating twin vortices behind the tube from $Re_D \cong 200$. It also reveals the occurrence of weak oscillatory trailing streakline behind the tube at higher Reynolds number. The sublimation tests are considered to accompany large recirculating twin vortices and a weak downstream oscillatory streakline. The local mass transfer coefficient on the plate is calculated from measurement of the sublimated naphthalene depth. It is large at the leading edge of the plate and also in front of the tube. It is relatively small behind the tube and it approaches the fully developed asymptotic value far downstream. The overall effect of the existence of the tube is to promote the total heat/mass transfer rate.

The high mass transfer coefficient in front of the tube is considered to be due to the so-called horseshoe vortex. A high local mass transfer coefficient contour occurs around the frontal area of the tube in the shape of a horseshoe. When the Reynolds number is even higher, a smaller subsidiary horseshoe vortex is attached to the upstream of the main one, resulting in an additional increase in the mass transfer rate.

The positive effect of the horseshoe vortices is prominent when the tube is placed in the downstream region where the mass transfer coefficient is close to the fully developed value. Consequently, it is better to place the tube in the downstream position. Proper positioning of the tube is estimated to increase the total heat/mass transfer rate up to 25%.

INTRODUCTION

Plate fins/circular tube assembly is used in a wide variety of thermal engineering applications, for example, in air conditioning units, process gas heaters and coolers, compressor inter- and after-coolers, etc. Because of its wide use and simple geometry, many researcher groups have examined the performance.

Saboya and Sparrow [1,2] use the naphthalene mass transfer method to measure the local coefficients for one-row and two-row plate-fin and tube heat exchangers for δ/D=0.193. They report that the transfer rate is high on the forward part of the fins due to developing boundary layers as well as in front of the tube due to a vortex system there. However, no extensive search for optimal tube location is made. Jang et al. [3] compare the staggered arrangement of tubes with aligned one using experimental and numerical methods. Their study shows that the staggered arrangement gives greater heat transfer rate at the expense of increased pressure drop. Tsai and Sheu [4] study the complicated vortex systems in a two-row fin tube heat exchanger by using a three-dimensional numerical code. They give a highly detailed view of the physical processes. Onishi et al. [5,6] compute numerically a three-dimensional steady flow and conjugate heat transfer for one-row and two-row plate-fin tube heat exchangers. They report the effect of fin spacing, fin thickness, fin length, tube spacing and tube arrangement and the heat transfer performance though not completely extensive. Romero-Mendez et al. [7] study the effect of fin spacing over the overall heat transfer rate using flow visualization and numerical analysis, and report that the heat transfer can be increased by the increase of fin spacing at a fixed fluid velocity.

Until now, however, only minor attention is paid on the optimal configuration of the fin/tube assembly. To find out the optimal tube location, for instance, is as much important as to examine the microscopic thermophysical processes. In the present research, flow and heat transfer in a plate fins/circular tube assembly is examined using the naphthalene sublimation

technique. It is intended to scrutinize the microscopic flow and heat transfer phenomena and also to evaluate the overall performance to find out the optimal tube location.

NOMENCLATURE

D	disk diameter
D_N	diffusion coefficient of naphthalene vapor in air
h_m	mass transfer coefficient
k	thermal conductivity
L	length of test section
l	x-coordinates of disk center location
$\dot{m}''$	sublimation mass flux
$\dot{M}$	total mass flow rate of sublimated naphthalene
$\dot{Q}$	volume flow rate of air
Re_D	the Reynolds number ($\equiv UD/\nu$)
Sh_D	the Sherwood number ($\equiv h_m D/D_N$)
U	bulk velocity of air
W	span of test section
x	coordinates along the airflow
y	coordinates transverse to the airflow
z	vertical coordinates

Greek symbols

δ	gap size between two plates
τ	naphthalene sublimation depth
ν	kinematic viscosity of air
ρ_s	density of solid naphthalene
ρ_{sat}	saturation density of naphthalene vapor
ρ_{bulk}	bulk density of naphthalene vapor

PRELIMINARY FLOW VISUALIZATION

To find the overall flow field around the circular tube between two parallel plates, flow visualization is made using water. The plates are simulated by two glass plates. One glass plate is clear for observation and the other is backed with black paper to contrast with the white milk injected in front of the tube. The milk line reveals the streaklines. Two gap(δ) to tube diameter(D) ratios are arbitrarily tried, i.e., 0.06 and 0.11.

When the Reynolds number based on D is less than about 200, no appreciable wake behind the tube is observed for both of the δ/D ratios (see Fig. 1(a).) As the Reynolds number is increased, a pair of twin vortices appears behind the tube (see Fig. 1(b).)

When it is further increased (see Fig. 1(c)), the size of the twin vortices increases up to the tube diameter and the trailing streakline begins to oscillate. The Reynolds number at which this oscillation begins depends heavily on δ/D, i.e., it is about 1,000 when δ/D=0.06 and 600 when δ/D=0.11. Note that Romero-Mendez et al. [7] report further evolution of twin vortices into oscillatory alternating vortices when Re_D=420 and δ/D=0.265. It is obvious that the parallel plates suppress

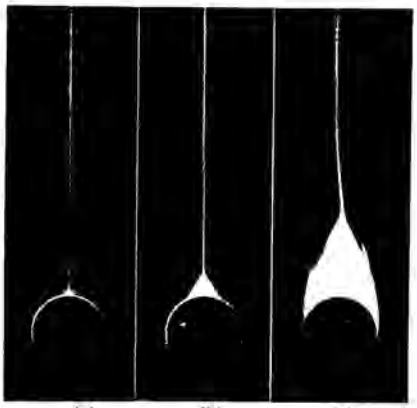

Figure 1: Evolution of flow field behind the tube with increasing Reynolds number for δ/D =0.06, (a) Re_D=114, (b) Re_D=425, (c) Re_D=1,270.

instability of the flow so that the evolution is suspended to greater Re_D when δ/D becomes smaller.

It is of interest that, for typical configurations in practical fin/tube assemblies, the flow field is neither turbulent nor Hele-Shaw. Mostly, it is almost steady accompanied by large twin vortices behind the tube. This flow pattern is also well described by Tsai and Sheu [4] for $Re_D \leq 1000$ and δ/D=0.19. Note that the microscopic flow field ahead of the tube is not well visualized. Naphthalene sublimation experiment to be explained next will further reveal other aspects.

EXPERIMENTAL METHOD USING NAPHTHALENE SUBLIMATION TECHNIQUE

Test section

Fig. 2 is a schematic of the test section. The naphthalene plate is 130×130×10(t) mm^3, and made of stainless steel. The surface is polished and naphthalene is molded into a cavity. The molded naphthalene size is 100(W)×120(L)×2(t) mm^3. The circular Plexiglas disk to simulate the tube is 20mm in diameter. It thus corresponds to a heat transfer problem where the fin efficiency is 100% while the heat transfer from the tube is not very important. The gap size(δ) is controlled by the thickness of the spacer made of Teflon and placed between the plates. The examined gap sizes are 4mm and 6mm. Actually, the flow at the inlet of test section is forward-facing step flow. But comparing the results of numerical simulations of two inlet conditions, forward-facing step flow and uniform flow, difference between the two cases disappears in the region behind 5mm from the entrance where the naphthalene layer starts. Therefore, the inlet flow can be treated as uniform flow. And there is no effect of the spacer on the flow but nearby the spacer in the size of the gap (the numerical results are not shown here due to space limitation.) In the experiments, the test section is completely

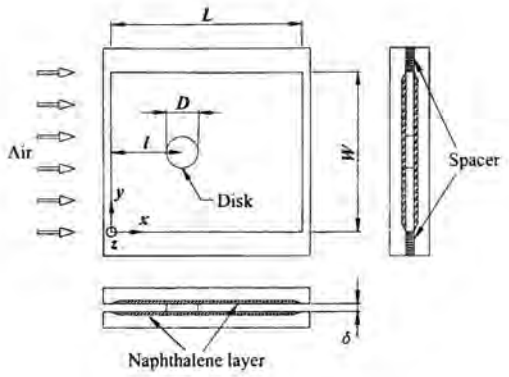

Figure 2: Schematic of the test section.

sealed and immersed in water bath. The water in the bath is vigorously agitated and it is connected to a constant temperature water circulator to maintain uniform temperature.

Apparatus

Fig. 3 shows a schematic diagram of the experimental apparatus. This apparatus consists of two parts, one is for measurement and control of the volume flow rate of air and the other is for control of the water temperature. Dry air is supplied from an air bomb through pressure regulators. Room air is not used to avoid hydration effect. The volume flow rate of air is measured with micro-manometer (max. 200Pa) by measuring the pressure drop across a laminar-flow meter. This flow meter is made using 12 tubes of 4mm inner diameter and 500mm long. Airflow inside the tubes is perfectly laminar so that the theoretical Hagen-Poiseuille flow rate is almost identical with actual calibration using a bubble meter.

The vapor pressure of naphthalene is very sensitive to temperature. Pure naphthalene shows sublimation vapor pressure as [8],

$$T \log P = 0.5a_0 + \sum_{i=1}^{3} a_i E_i(x), \qquad (1)$$

where

$$a_0 = 301.6247; a_1 = 791.4937; a_2 = -8.2536;$$
$$a_3 = 0.4043,$$
$$x = (2T - 574)/114, \qquad (2)$$
$$E_1(x) = x; E_2(x) = 2x^2 - 1; E_3(x) = 4x^3 - 3x,$$

P in Pa; and T in K.

At room temperature, it varies about 10% per °C. Therefore the test section temperature is accurately maintained within 30±0.1°C by using the aforementioned water bath and circulator.

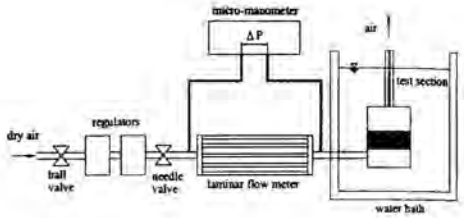

Figure 3: Schematic diagram of the experimental apparatus.

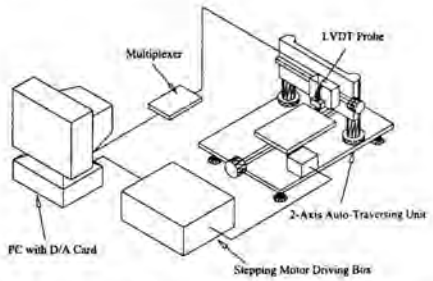

Figure 4: Schematic diagram of the sublimated depth measurement system.

The schematic diagram of the sublimated naphthalene depth measurement system is shown in Fig. 4. It consists of a 2-axis auto-traverse system, a depth gauge (LVDT) along with a data acquisition card and a personal computer for data storage and reduction. The 2-axis auto-traverse system has step motors with a resolution of 1.8° per step (0.02 mm in linear direction). The depth gauge has range of ±0.508mm and linearity error of 0.170%. The total resolution of the LVDT and the analog-to-digital card is 0.25μm and the sublimation depth uncertainty of the entire measurement system is 2um.

Procedure

Reagent grade (99% pure) naphthalene crystals are melted in a clean Pyrex glass beaker on a hot plate. The test section and the cover mold are cleaned with ethyl alcohol and pre-heated to prevent rapid solidification and subsequent clogging while pouring the molten naphthalene. The pouring speed and the naphthalene temperature are carefully controlled also. The cast plates are then separated from the cover mold by gentle hammering from side to apply shear stress.

Before blowing air over the naphthalene plates, they are scanned by the depth measurement system. The scanning area is $100(x)\times60(y)$ mm^2 and scanned points are 1mm apart in both of the longitudinal and transverse directions. The total scanning time is about 1 hour.

Then the plates are assembled and the whole assembly is immersed in the water bath, and the air flows over the naphthalene plates. The total blowing time is varied from 90 minutes to 150 minutes depending on the rate of volume flow and the sublimation depth. Long blowing time gives greater sublimation depth. It thus improves the relative accuracy of the sublimation depth measurement. However, excessively long time changes δ significantly. In this experiment, the maximum distortion of geometry ($d\delta/\delta$) is 0.038.

The local naphthalene sublimation depth is calculated from the local change of two surface elevation of before and after blowing. Difference in the mounting forces on the depth measuring system before and after blowing causes different overall warping of the plate. Thus, a reference surface is generated to compensate the warping. It is formed by measuring the elevation of 8 points on the plate and smoothly connecting them.

Data processing

The local mass flux $\dot{m}''$ at each location is calculated from the following expression,

$$\dot{m}''(x,y) = \rho_s \frac{\tau(x,y)}{\Delta t}, \qquad (3)$$

where ρ_s is the density of solid naphthalene, τ is the local sublimation depth, and Δt is the blowing time. The thermophysical properties of naphthalene, as well as the saturation vapor pressure, are obtained from Goldstein and Cho [8]. The local mass transfer coefficient h_m can then be calculated as follows,

$$h_m(x,y) = \frac{\dot{m}''(x,y)}{\rho_{sat} - \rho_{bulk}(x)}, \qquad (4)$$

where ρ_{sat} is the saturation vapor density of naphthalene and represents the density of naphthalene vapor at the wall , and ρ_{bulk} is the bulk density of naphthalene vapor in the local airflow passing through the cross section $x = \text{const}$. The saturation vapor density can be evaluated from the saturation vapor pressure and the perfect gas law, and the bulk density can be evaluated as

$$\rho_{bulk}(x) = \rho_{bulk}(0) + \frac{\dot{M}(x)}{\dot{Q}}, \qquad (5)$$

where $\dot{Q}$ is the volume flow rate passing through the test section and $\dot{M}$ is the rate of mass transfer from both of plates between 0 to x in x-direction, and 0 to W (span) in y-direction. Since $\rho_{bulk}(0) = 0$ and $\dot{M}$ at x is given by (note that we have two naphthalene surfaces, up and down),

$$\dot{M}(x) = 2\int_0^x \int_0^W \dot{m}''(x,y)\,dy\,dx, \qquad (6)$$

the local mass transfer coefficient h_m is finally expressed as

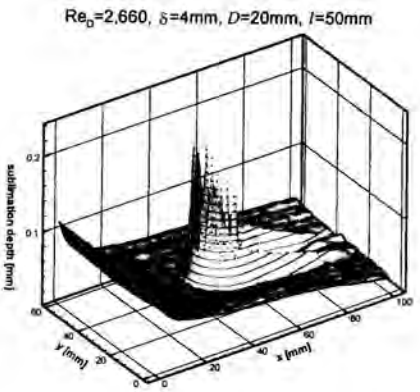

Figure 5: A typical 3-D plot of the sublimation depth.

$$h_m(x,y) = \frac{\dot{m}''(x,y)}{\rho_{sat} - \frac{2}{\dot{Q}}\int_0^x \int_0^W \dot{m}''(x,y)\,dy\,dx} \qquad (7)$$

The local Sherwood number $\mathrm{Sh_D}$ based on tube diameter D is then calculated by

$$\mathrm{Sh_D} = \frac{h_m D}{D_N}, \qquad (8)$$

when D_N is the binary diffusion coefficient for naphthalene vapor in air. In this study, both local and span-averaged results are compared. Span-averaging is performed as a simple arithmetic mean of the central 31 data points at 1mm interval in y-direction.

Comprising all sources of error, the net uncertainty in $\mathrm{Sh_D}$ is found to be 9.9% (details not shown due to space limitation.)

RESULTS AND DISCUSSION

The following parameters are taken in the experiments. The span to diameter ratio W/D is fixed to 5.0 and the length to span ratio L/W is fixed to 1.2. For the varied parameters, δ/D is taken as 0.2 and 0.3, $\mathrm{Re_D}$ is taken as 950 and 2,660 for δ/D =0.2 and 1,770 for δ/D =0.3, and finally l/D is extensively varied as 0.75, 1.0, 1.5, 2.5 and 3.5. These are taken to be as much realistic as possible, and they give a reasonable air-side effectiveness of around 0.2 to 0.6.

First of all, a qualitative evaluation of the microscopic phenomena is provided. Fig. 5 shows a 3-dimensional plot of sublimation depth with $\mathrm{Re_D}$=2,660 (corresponding to U=2.1m/s), l/D=2.5 and δ/D=0.2. It is obtained after 90min of air blowing. It is large at the leading edge of the plate and also in front of the tube. It is relatively small behind the tube and it decreases asymptotically to the fully developed value far downstream.

The high mass transfer rate at the leading edge is due to the thin boundary layer beginning to develop. It is almost identical with the case of a flat plate in infinite stream. The mass transfer rate decreases rapidly along the downstream. The local Sherwood number approaches asymptotically to the fully developed value (7.54 times $D/2\delta$) in the far downstream. The entrance or developing length is greater for greater air velocity and gap size. Greater entrance length means thinner boundary layer on the fin resulting in the increase in the total heat transfer rate, as also has been depicted by Romero-Mendez et al. [7].

When the boundary layer is developed fully in the gap, the mass transfer coefficient becomes a constant while the bulk flow is being saturated with naphthalene vapor. Consequently, the mass transfer rate in the downstream is further reduced, approaching zero eventually.

Flow around the tube is typified by the existence of trailing twin vortices and a leading horseshoe vortex. The former is very detrimental to mass transfer. Air velocity is very low in the recirculating twin vortices and it is almost saturated with naphthalene vapor. The mass transfer rate thus becomes very small, and for this reason, Onishi et al. [5] assert that the recirculating twin vortices region behind the tube may well be eliminated for more efficient heat transfer.

Saboya and Sparrow [1] clearly shows that a horseshoe vortex exists ahead of the tube and it is larger for larger Reynolds number. In their experiments, Re_D is from 496 to 2,950 based on the tube diameter. The experimental results of this research confirm their finding: there exists a horseshoe vortex in front of the tube rotating in a clockwise direction above the bottom side plate in the x-z plane. It wraps around the tube and extends its trail along the side of the tube. The upper plate has a mirror-image horseshoe vortex rotating in the opposite direction. Its existence is clearly marked by a deep U-shaped groove around the tube, shown in Fig. 5 as the high wall ahead and beside the tube. Though not shown here due to limited space, the mass transfer coefficient along the frontal line of the groove is very small since the flow is separated there.

When Re_D is as large as 2,660 for δ/D=0.2, another small horseshoe vortex appears ahead of the main horseshoe vortex, in contrast to the only appreciable main one for Re_D=950. Though the overall size is small, it leaves a smaller groove ahead of the main groove. Saboya and Sparrow's experiments [1] also shows a clear evidence of the subsidiary horseshoe vortex for Re_D=2,950. Fig. 6 gives an illustration of the two pairs of horseshoe vortices for better understanding.

The span-averaged local Sh_D with various location of the tube is shown in Fig. 7. The Sherwood number is greatest at the leading edge of the plate and then in front of the tube as shown previously. The effect of the location of the tube is clearly shown in this figure. As the tube is placed in the downstream region, the positive effect of the horseshoe vortex on mass transfer rate is prominent and the negative effect of the recirculating twin vortices behind of the tube is diminished.

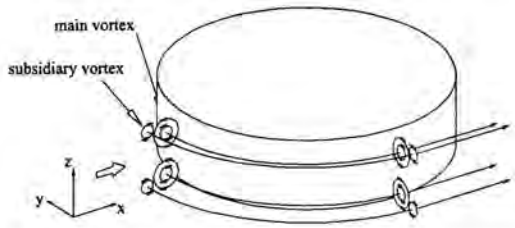

Figure 6: Illustration of the main and the subsidiary horseshoe vortices around the tube.

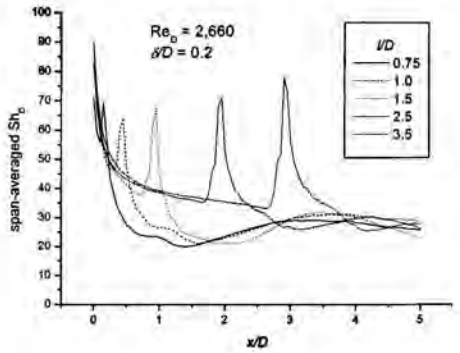

(a)

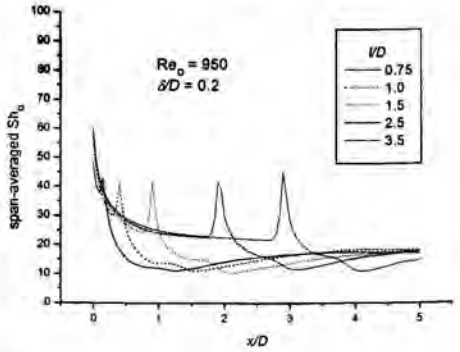

(b)

Figure 7: Span-averaged Sh_D along the longitudinal direction with various tube positioning.

Therefore, it is better to place the tube in downstream position for enhanced heat transfer. Another evaluation of this judgment comes from the fact that magnitude of the local mass transfer coefficient around the horseshoe vortex is almost independent

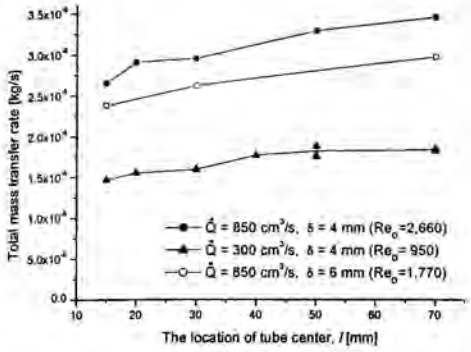

Figure 8: Effect of the location of tube center (D=20mm) on total mass transfer rate with various Re_D and gap size.

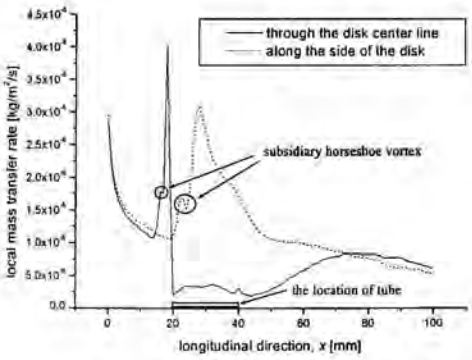

Figure 9: Local mass transfer rate along the center line, when $\dot{Q}$=850cm³/s, δ=4mm (Re_D=2,660).

of the tube location. When the tube is located close to the leading edge the mass transfer coefficient in front of the tube is not increased appreciably since it is already very high there. To the contrary, placing the tube in the downstream region greatly increases the total mass transfer rate. Fig. 8 concisely shows the effect of the positioning of the tube. Proper positioning of the tube in the view point of heat/mass transfer is estimated to increase the total mass transfer rate by about 25%, compared with the case of l/D =0.75 for any δ/D and Re_D. With respect to Re_D, 180% increase of Re_D causes 85% increase in the total mass transfer rate (compare the two cases of δ=4mm with $\dot{Q}$ =850cm³/s and $\dot{Q}$ =300cm³/s in Fig. 8.) If the total mass transfer rate is proportional to Re_D, then the proper positioning is equivalent to about 50% increase of Re_D. As can be seen from Fig. 8 also, the total mass transfer rate is decreased by 10% by 50% increase of the gap size at a fixed airflow rate of 850cm³/s (compare the two cases of $\dot{Q}$ =850cm³/s with δ=4mm and 6mm.) It shouldn't be confused, however, that increase of airflow rate proportional to the gap size (thus maintaining the same air velocity) increases the total mass transfer rate also [7].

Fig. 9 shows the existence of the subsidiary horseshoe vortex through the secondary peaks of the curves. Though the results is not shown here, the size of the horseshoe vortex is increased with the gap size at the same airflow rate. However at the same time, the strength of vortex is reduced, so the total mass transfer rate is decreased.

CONCLUSION

To investigate the microscopic flow and heat transfer phenomena and also to evaluate the overall performance to find out the optimal tube location, the local mass transfer coefficient on the plate is calculated from the measurement of sublimated naphthalene depth. The examined parameters are the gap to tube diameter ratio δ/D, the Reynolds number Re_D and the tube location l/D.

The local mass transfer rate is large at the leading edge of the plate and also in front of the tube in all examined cases. The horseshoe vortex formed in front of tube gives significant increase in the total heat/mass transfer rate.

The subsidiary horseshoe vortex is formed when Re_D is increased to as high as about 2,660 for δ/D=0.2.

Mass transfer is very inactive in the recirculating twin vortex and in the far downstream.

The tube is better placed at downstream to increase the total heat/mass transfer rate at any δ/D and Re_D. Proper positioning of the tube is estimated to increase the total mass transfer rate up to 25%. Further researches on the pressure drop and multiple tube interaction are recommended.

REFERENCES

[1] Saboya, F. E. M. and Sparrow, E. M., 1974, "Local and Average Transfer Coefficients for One-Row Plate Fin and Tube Heat Exchanger Configurations," *ASME J. Heat Transfer*, Vol. 96, pp. 265-272.

[2] Saboya, F. E. M. and Sparrow, E. M., 1976, "Transfer Characteristics of Two-Row Plate Fin and Tube Heat Exchanger Configurations," *Int. J. Heat Mass Transfer*, Vol. 19, pp. 41-49.

[3] Jang, J. Y., Wu, M. C. and Chang, W. J., 1996, "Numerical and Experimental Studies of Three-Dimensional Plate-Fin and Tube Heat Exchangers," *Int. J. Heat Mass Transfer*, Vol. 39, No. 14, pp. 3057-3066.

[4] Tsai, S. F. and Sheu, Tony W. H., 1998, "Some Physical Insights into a Two-Row Finned-Tube Heat Transfer," *Computers & Fluids*, Vol. 27, No. 1, pp. 29-46.

[5] Onishi, H., Inaoka, K., Matsubara, K. and Suzuki, K., 1998, "Heat Transfer Performance of a Plate-Finned Tube Heat Exchanger (A Three-Dimensional Steady Numerical

Analysis for a Single Row Tube)," *Proc. 11th Int'l Heat Transfer conference, Kyongju*, Vol. 6, pp. 227-232.

[6] Onishi, H., Inaoka, K., Matsubara, K. and Suzuki, K., 1999, "Numerical Analysis of Flow and Conjugate Heat Transfer of a Two-Row Plate-Finned Tube Heat Exchanger," *Proc. 2nd Int'l Conference on Compact Heat Exchangers and Enhancement Technology for the Process Industries, Banff*, pp. 175-182.

[7] Romero-Mendez, R., Sen, M., Yang, K. T. and McClain, R., 2000, "Effect of Fin Spacing on Convection in a Plate Fin and Tube Heat Exchanger," *Int. J. Heat Mass Transfer*, Vol. 43, pp. 39-51.

[8] Goldstein, R. J. and Cho, H. H., 1995, "A Review of Mass Transfer Measurements Using Naphthalene Sublimation," *Experimental Thermal and Fluid Science*, Vol. 10, pp. 416-434.

HEFAT2002
1st International Conference on Heat Transfer, Fluid Mechanics, and Thermodynamics
8-10 April 2002, Kruger Park, South Africa
LY2

EXPERIMENTAL STUDY OF HEAT TRANSFER OF CORRUGATED CHANNELS

Y.S. Lee*, Y.M. Sun*, and C.C. Su**
*M. Eng. Student; **Professor
Department of Mechanical Engineering,
Nation Taiwan University,
Taipei, Taiwan 106,
Republic of China
Email: f6522106@ms.cc.ntu.edu.tw

ABSTRACT

This experimental study investigated the heat transfer characteristics of the corrugated channel appeared in plate heat exchangers (PHEs). A flow channel with wavy surfaces was constructed within which air was passed through. The temperature of the wall was maintained constant. Starting from the entrance, the air temperatures within two wavelengths were measured at about 300 locations. The Reynolds number of air was varied from 300 to 9000. Results show that both the average and local Nusselt numbers increase with the Reynolds number. However, the local Nusselt number decreases with the distance from the entrance and is greater at sections near the crest. In addition, both the average and local Nusselt numbers are apparently greater in the entrance region.

INTRODUCTION

Plate heat exchangers (PHEs) are widely used in small refrigeration systems. The major characteristics of PHEs are the corrugated flow channels with large surface area for great heat transfer.

Many researches had been performed on available PHEs. Overall Nusselt number (Nu) and friction factor (f) of PHEs in different ranges of Reynolds number (Re) can be obtained from literatures. For example, Wang and Zhao [1] investigated the performance of PHE with condensing water and air as the working fluid. Similar work in a large Reynolds number was done by Bogaert and Bölcs [2] and Yan and Lin [3]. Furthermore, the effects of the corrugated angles of the plates within the PHEs were investigated. Heggs *et al.* [4] used an electrochemical mass transfer technique to calculate values of the local transfer coefficients. Muley and Manglik [5] studied the PHEs with three different chevron plate arrangements. Some correlations were presented by Muley *et al.* [6]. On the other hand, researches with modeling and numerical methods of PHEs had also been performed. For example, performance evaluation of PHE in geothermal district heating systems was made by Karlsson [7]. Georgiadis and Macchietto [8] presented a dynamic modeling and simulation of PHEs with milk as the working medium.

As for corrugated channels with different shapes, some researches had also been conducted with theoretical derivations, numerical approaches, or experiments. For example, Yalamanchili *et al.* [9] modeled the flow of dilute polymer solutions through corrugated channels. Ros *et al.* [10] used transient techniques for the heat transfer coefficient measurement in a corrugated PHE channel. Manglik and Ding [11] investigated the heat transfer of laminar flow in double-sine ducts with mathematical analysis. Bontozoglou and Papapolymerou [12] studied the laminar gas-liquid flow through a channel with corrugated bottom. Sawyers *et al.* [13] used analytical and numerical techniques to investigate the laminar heat transfer in three-dimensional corrugated channels. Mehrabian and Poulter [14] used CFD modeling to investigate the microscopic flow and thermal characteristics within some individual channels. Gradeck and Lebouché [15] explored two-phase gas-liquid flow in horizontal corrugated channels. Fabbri [16] uses a finite element model to determine the velocity and temperature distributions in corrugated channels. Mehrabian *et al.* [17] investigated the local pressure and temperature in the corrugated channel.

Unfortunately, the above-mentioned works do not reveal detailed heat transfer characteristics of the flow in corrugated channels. Even though the local details of the flow were presented in [17], the local temperature distributions and Nusselt number had not been probed experimentally. In addition, the characteristics of heat transfer in the flow direction had not been obtained. To this end, this experimental study is intended to investigate the local temperature distribution and

Nusselt number for the flow within the corrugated channel. Average Nusselt number is also obtained from the integral of local ones.

NOMENCLATURE

A	surface area
c_p	specific heat
D_h	hydraulic diameter
k	thermal conductivity
L	wave length
H	height of the channel
h_x	local heat transfer coefficient
$\dot{m}$	mass flow rate
Nu_{a-b}	average Nusselt number from sections a to b
Nu_x	local Nusselt number
Q	rate of heat transfer
R	radius of curvature
Re	Reynolds number
S	length of straight section of the wavy channel
T	temperature
T_i	inlet temperature of the flow
T_b	average bulk temperature
T_W	wall temperature
$\overline{T}$	average temperature
u	average velocity
$\dot{V}$	volumetric flow rate
W	width of the channel
x, y	coordinate
β	corrugated angle
ρ	density of air
μ	viscosity of air

EXPERIMENTS

The experimental apparatus was composed of an air loop, a water loop, and a measurement system, as shown in Fig. 1. The air loop consisted the test section with the corrugated channel, a fan with the maximum power of 5HP, two flow meters for air, and some valves to adjust the flow rates. Two hollow cases, made of stainless steel 304 with wavy surfaces, were clipped between two horizontal, metal plates to construct the required flow channel, within which air was passed through. A flow straightener made of hundreds of straws was placed before the test section. The water loop included a water barrel, a 2HP-pump, a flow meter for water, a temperature controller, and a 3kW-heater within the water barrel. All components of the water system were heat-insulated. Hot water was forced into the hollow stainless steel cases through 6 entrances and 5 exits provided on the cases. The wall temperature of the hollow cases was thus kept nearly constant.

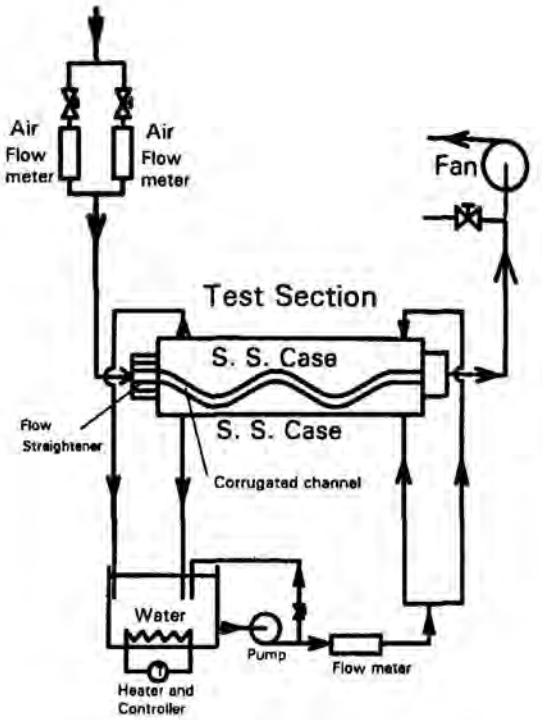

Fig. 1 Schematic of the test system

Fig. 2 shows the schematic of the corrugated channel, while Table 1 lists the details. Note the x direction does not follow the wavy channel, while the y coordinate starts from the lower wall for each section. The aspect ratio of the channel was designed as 6 to simulate the channel within the PHEs. In addition, end effects may thus be avoided with this aspect ratio. The temperature distributions in the horizontal, middle plane of the channel were monitored with T-type thermocouples. 2400 holes of grid were drilled on the upper metal plate to insert thermocouples into the flow channel. The thermocouple was wrapped in the straight copper tube of 3 mm outer diameter. In this experiment, the temperatures at about 300 points were monitored. The measuring points consisted a matrix in x, y directions, as shown. In the y direction there were 8 points, each of which is 5 mm apart. Starting from the entrance, the temperatures of 42 rows were monitored in the x direction, as shown in Fig. 2. The distance between two rows was 20mm. To minimize flow disturbances induced by the thermocouples, only three points separate at least 10mm one another were inserted in a row each time. Therefore, three times of measurements were required for each Reynolds number. The holes not in use were stuffed with plastic sticks to prevent from leakage of air.

The flow rates of air were adjusted to study the effects of the Reynolds number from 300 to 9000 to cover the regimes of laminar and turbulent flows. Room air was drawn through the

channel by the fan. The wall temperature of the wavy surfaces was maintained at 60 and 45°C with hot water to simulate the condensing temperature in refrigeration systems. The volumetric flow rates of hot water were set at 450 L/min, which was high enough to keep the wall temperature constant. The top and bottom of the channel were heat-insulated.

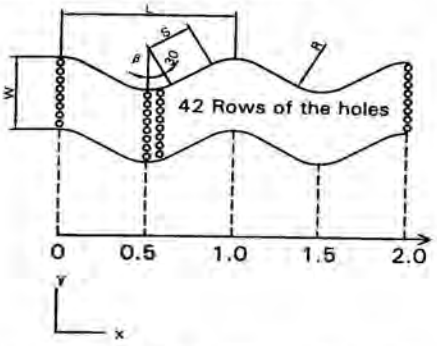

Fig. 2 Schematic of the corrugated channel

Plate material	Stainless steel 304
Number of waves	2
Wave length, L	447.84mm
Thickness of the plate	2 mm
Corrugation angle, β	30°
Radius of curvature, R	120mm
Straight length, S	120mm
Width of the channel, W	40mm
Height of the channel, H	240mm
Hydraulic diameter, D_h	68.571mm
Corrugation ratio, R/L	0.268 (120mm/447.84mm)
Straight ratio, S/L	1 (120mm/120mm)
Width ratio, W/L	1/3 (40mm/120mm)
Aspect ratio, W/H	6 (240mm/40mm)
Area of the cross section of the channel	0.0096 m^2 (0.24m* 0.04m)
Surface area of the corrugated plate	0.48 m^2

Table 1 Details of the wavy channel

DATA REDUCTIONS

To present the experimental results in a traditional form, the measured data were reduced as follows.

Reynolds number (Re)

The Reynolds number is defined as

$$\mathrm{Re} \equiv \frac{\rho u D_h}{\mu} = \frac{\rho D_h}{\mu}\left(\frac{\dot{V}}{WH}\right) \tag{1}$$

where ρ is the density, u is the average velocity, μ is the viscosity of the air, $\dot{V}$ is the volumetric flow rate, W is the width, H is the height of the channel, and D_h is the hydraulic diameter of the channel.

Nusselt number (Nu_x and Nu_{x-b})

To obtain Nu_x, a differential control volume is chosen, as shown in Fig. 3.

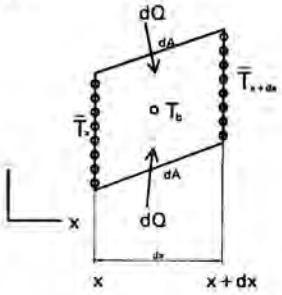

Fig. 3 Schematic of the control volume

The heat transferred from the wall to the flow, dQ, is evaluated as

$$dQ = \dot{m} c_p \left(\bar{T}_{x+dx} - \bar{T}_x\right) \tag{2}$$

where $\dot{m}$ is the mass flow rate, c_p is the specific heat of air, and $\bar{T}_x$ and $\bar{T}_{x+dx}$ are the average temperatures at sections x and x+dx :

$$\bar{T}_x = \frac{\sum_{n=1}^{8} T_x}{8} \quad \text{and} \quad \bar{T}_{x+dx} = \frac{\sum_{n=1}^{8} T_{x+dx}}{8} \tag{3}$$

The heat, dQ, may also be expressed as

$$dQ = h_x \left(T_w - T_b\right) dA \tag{4}$$

where h_x is the local heat transfer coefficient, T_w is the temperature of the wall, dA is the surface area of the wall, and T_b is the bulk temperature of the fluid defined as

$$T_b = \frac{\bar{T}_x + \bar{T}_{x+dx}}{2} \tag{5}$$

Combining Eqns. (2) and (4), the local heat transfer coefficient can be expressed as

$$h_x = \frac{\dot{m} c_p \left(\bar{T}_{x+dx} - \bar{T}_x\right)}{\left(T_w - T_b\right) dA} \tag{6}$$

The local Nesselt number is defined as

$$Nu_x \equiv \frac{h_x D_h}{k} = \frac{\dot{m} c_p \left(\bar{T}_{x+dx} - \bar{T}_x\right) WH}{k(W+H)(T_w - T_b)dA} \tag{7}$$

while the average Nesselt number is evaluated as

$$Nu_{a-b} = \frac{\int_a^b Nu_x dA}{\int_a^b dA} \tag{8}$$

where a and b indicate the locations of the cross sections at x/L.

The experimental error in Nu was about 7 %, while that in Re was about 5 %. The errors were mainly induced by the uncertainly of the location measurement, which was taken 3 %.

RESULTS AND DISCUSSIONS

Temperature distributions

The average temperatures ($\bar{T}$) measured along the channel for a given flow condition are shown in Fig. 4. It can be seen that $\bar{T}$ increases with the distance from the entrance (x/L). The increase is rapid in the entrance region, as expected for the great temperature difference between the wall and the fluid. In addition, high heat transfer coefficient also plays an important role in this aspect, which would be discussed later. After the entrance region, the rate of increase reduces, as shown in Fig. 4.

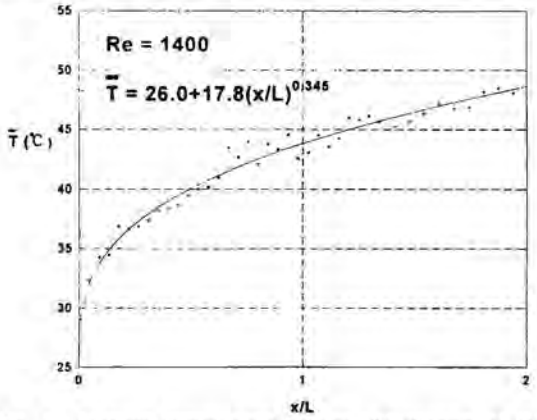

Fig. 4 Average temperatures along the channel at Re = 1400

Note the curve shown in this figure was obtained by curve fitting of $\bar{T}$ with the least RMS. The empirical equation for the curve is

$$\bar{T} = 26.0 + 17.8\left(\frac{x}{L}\right)^{0.345} \quad \text{for Re} = 1400 \tag{9}$$

Local heat transfer and Nusselt number can thus be evaluated with Eqns. (7) and (9).

Fig. 5 shows the local temperature distribution in five crest areas. It can be seen that the thermal boundary layers on both sides grow rapidly along the channel. Experimental errors might be the main reason for the temperature variations for each cross section. At the same cross section near a crest, however, the increasing rate of local temperatures decreases with Re, as shown in Fig. 6.

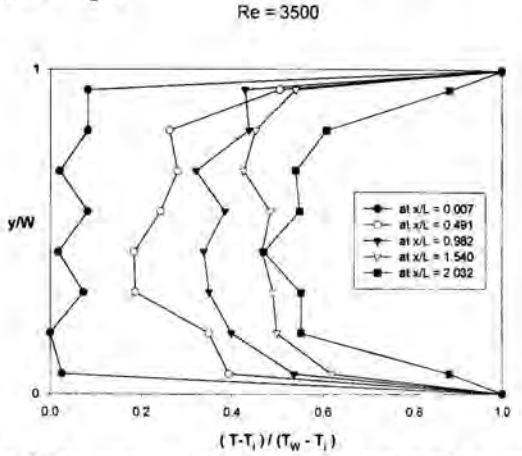

Fig. 5 Temperature distributions near the area of the crest

Local Nusselt number

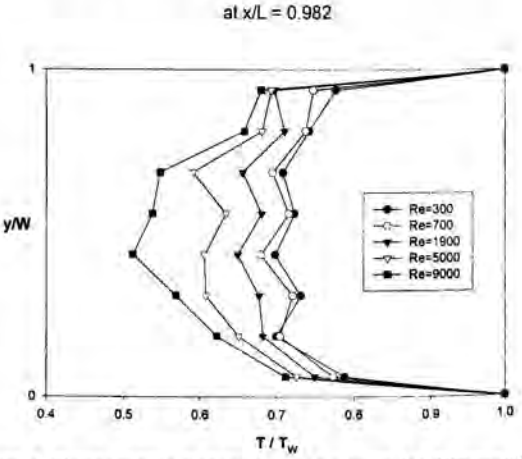

Fig. 6 Temperature distributions at a crest for different Re

For the flow within the wavy channel, Nu_x decreases with x/L but increases with Re, as shown in Fig. 7. Basically, the local heat transfer coefficient can be expressed as

$$h_x \propto \left(\frac{\partial T}{\partial y}\right)_{wall}$$

Since the temperature gradient in the y direction decreases with x/L, as shown in Fig. 5, h_x decreases with x/L, and Nu_x follows. On the contrary, this temperature gradient increases with Re at the same cross section. Therefore, both h_x and Nu_x increases with Re. In addition, Nu_x in the entrance region is much higher than that in other regions.

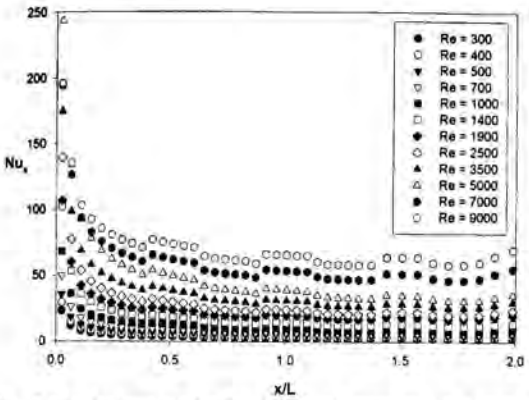

Fig. 7 Variations of the local Nusselt number in along the channel

After the entrance region, Nu_x decreases slowly with x/L, as shown in Fig. 7. However, increases in Nu_x can be observed at regions around the crest areas of the channel, as shown in Fig. 8.The mixing of the fluid in these areas induced by the change of the flow direction may explain this phenomenon. More researches may be necessary to explore the details.

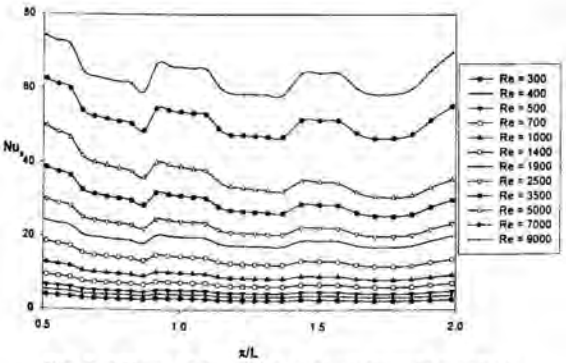

Fig. 8 Effects of the crest on local Nusselt number

Average Nusselt number

The relation between Nu and Re is shown in Fig. 9. Since both the entrance region and the area around the crest have high heat transfer rate, the former is defined as the region from x/L = 0 to 0.25 to separate the entrance and crest effects. The range of Re is from 300 to 9000.

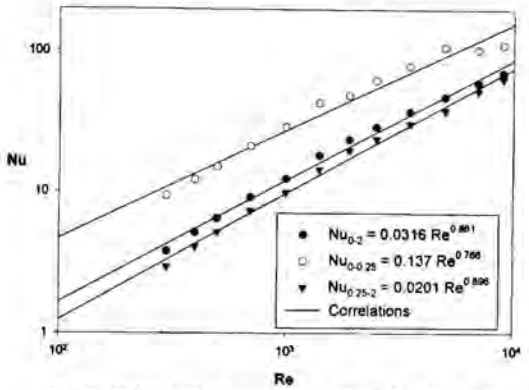

Fig. 9 Relation between the average Nu and Re

For the complete channel, the empirical relation between Nu and Re is

$$Nu_{0-2} = 0.0316\,\mathrm{Re}^{0.861} \tag{10}$$

where the subscript 0-2 means the evaluation is conducted from x/L = 0 to 2.The error is about ± 11 % for this empirical equation.

As for the entrance region, the relation changes as

$$Nu_{0-0.25} = 0.137\,\mathrm{Re}^{0.766} \tag{11}$$

The error is about ± 20 %. This value is not uncommon in the studies on entrance flows.

Finally, the relation for the regions excluding the entrance one is

$$Nu_{0.25-2} = 0.0201\,\mathrm{Re}^{0.896} \tag{12}$$

The error is about ± 12 %.

Of course, if the entrance region is defined other than from x/L = 0 to 0.25, both Eqns. (11) and (12) may vary a little. As disturbance is expected to be induced by the crests of the flow channel, the flow within the laminar regime may not be so "laminar" as that in straight channels. No distinct difference in heat transfer characteristics is observed for the flows covering laminar and turbulent regimes.

In this work, the effect of the crest can be seen from Fig. 8, as there is a jump in Nu_x around each crest. More studies are currently conducted to explore the details.

Effect of wall temperature

Although theoretically the wall temperature will not affect the relation between Nu and Re, a check has been made by

running the experiment with different wall temperatures. Results obtained are plotted in Fig. 10. It can be seen that the values of Nu in different wall temperatures are within about ± 10 % errors.

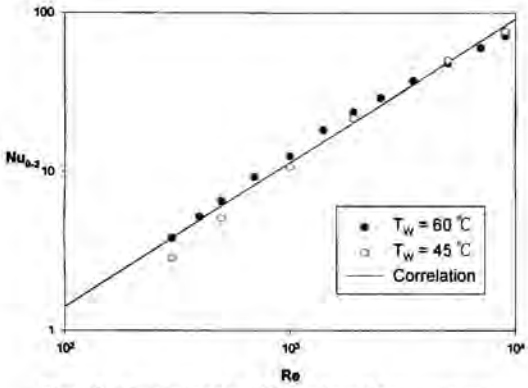

Fig. 10 Check for the effect of wall temperatures

CONCLUSIONS

From this experimental study, some details of heat transfer within corrugated channel were revealed. Local temperature distributions in both x and y directions were measured for different Reynolds numbers. Results indicate that both the local and average Nusselt numbers increase with the Reynolds number. However, the local Nusselt number decreases with the distance from the entrance. In addition to the high heat transfer in the entrance region, the crest of the wavy channel shows some enhancement effects on heat transfer. Some correlations between the average Nusselt number and the Reynolds number for different regions of the channel have been obtained in this work.

REFERENCES

[1] Wang, Z. Z. and Zhao, Z. N., 1993, "Analysis of performances of steam condensation heat transfer and pressure drop in plate condensers," Heat Transfer Engineering, 14(4), pp. 32-41.

[2] Bogaert, R. and Bölcs, A., 1995, "Global Performance of a Prototype Brazed Plate Exchanger in a Large Reynolds Number Range," Experimental Heat Transfer, 8, pp. 293-311.

[3] Yan, Y. Y. and Lin T. F., February 1999, "Evaporation Heat Transfer and Pressure Drop of Refrigerant R-134a in a Plate Heat Exchanger," Transactions of the ASME, Vol. 121, pp. 118-127.

[4] Heggs, P. J., Sandham, P., Hallam, R. A., and Walton, C., October 1997, "Local Transfer Coefficients in Corrugated Plate Heat Exchanger Channels," Trans IchemE, Vol 75, Part A, pp.641-645.

[5] Muley, A. and Manglik, R. M., February 1999, "Experimental Study of Turbulent Flow Heat Transfer and Pressure Drop in a Plate Heat Exchanger With Chevron Plates," Journal of Heat Transfer, Transactions of the ASME, Vol. 121, pp. 110-117.

[6] Muley, A., Manglik, R. M., and Metwally, H. M., November 1999, "Enhanced Heat Transfer Characteristics of Viscous Liquid Flows in a Chevron Plate Heat Exchanger," Journal of Heat Transfer, Transactions of the ASME, Vol. 121, pp. 1011-1017.

[7] Karlsson, T., 1996, "Numerical evaluation of plate heat exchanger performance in geothermal district heating systems," Pro Instn Mech Engrs, Vol. 210, pp. 139-147.

[8] Georgiadis, M. C. and Macchietto, S., 2000, "Dynamic modelling and simulation of plate heat exchangers under milk fouling," Chemical Engineering Science, 55, pp. 1605-1619.

[9] Yalamanchili, R. C., Sirivat, A., and Rajagopal, K. R., 1995, "An experimental investigation of the flow of dilute polymer solutions through corrugated channels," J. Non-Newtonian Fluid Mech., 58, pp. 243-277.

[10] Ros, S., Jallut, C., Grillot. J. M., and Amblard, M., 1995, "A transient-state technique for the heat transfer coefficient measurement in a corrugated plate heat exchanger channel based on frequency response and residence time distribution," Int. J. Heat Mass Transfer, Vol. 38, No. 7, pp. 1317-1325.

[11] Manglik, R. M. and Ding, J., 1997, "Laminar flow heat transfer to viscous power-law fluids in double-sine ducts," Int. J. Heat Mass Transfer, Vol. 40, No. 6, pp. 1379-1390.

[12] Bontozoglou, V. and Papapolymerou, G., 1998, "Wall-Triggered Interfacial Resonance in Laminar Gas-Liquid Flow," Int. J. Multiphase Flow, Vol. 24, No. 1, pp. 131-143.

[13] Sawyers, D. R., Sen, M., and Chang, H. C., 1998, "Heat transfer enhancement in three-dimensional corrugated channel flow," International Journal of Heat and Mass Transfer, 41, pp. 3559-3573.

[14] Mehrabian, M. A. and Poulter, R., 2000, "Hydrodynamic and Thermal Characteristics of Corrugated Channels: Computational approach," Applied Mathematical Modelling, 24, pp. 343-364.

[15] Gradeck, M. and Lebouché, M., 2000, "Two-phase gas-liquid flow in horizontal corrugated channels," International Journal of Multiphase Flow, 26, pp. 435-443.

[16] Fabbri, G., 2000, "Heat transfer optimization in corrugated wall channels," International Journal of Heat and Mass Transfer, 43, pp. 4299-4310.

[17] Mehrabian, M. A., Poulter, R., and Quarini, G. L., 2000, "Hydrodynamic and Thermal Characteristics of Corrugated Channels: Experimental Approach," Experimental Heat Transfer, 13, pp. 223-234.

[18] Béreiziat, D. and Devienne, R., 1999, "Experimental characterization of Newtonian and non-Newtonian fluid flows in corrugated channels," International Journal of Engineering Science, 37, pp. 1461-1479.

HEFAT2002
1st International Conference on Heat Transfer, Fluid Mechanics, and Thermodynamics
8-10 April 2002, Kruger Park, South Africa
MI2

PRESSURE MEASUREMENTS ON FIN AND TUBE SURFACES DURING FLOW OF AIR OVER A TUBE FITTED WITH INCLINED FINS

*I. Carvajal-Mariscal,
F. Sanchez-Silva, G. P. Polupan
National Polytechnic Institute
SEPI-ESIME-IPN-COFAA, Edif. 5 – 3er piso
UPALM, 07738 Mexico D.F.
*e-mail: icarvaja@maya.esimez.ipn.mx

Vladimir A. Pronin
Moscow Power Engineering Institute
Faculty of Heat Engineering
Krasnokazarmennaya, 14
111250 Moscow, Russia

ABSTRACT

A flow dynamic physical model for a flow over a finned pipe with inclined fins is presented. The local aerodynamics characteristics were studied when the pipe is exposed to a transversal airflow, the pipe was provided with 45° inclined fins respect to the axial axis. In order to determine the aerodynamic characteristics of the pipe, the static pressure distribution on the internal and external inclined fin surfaces, and on the own pipe external surface was studied.

The flow visualization and the static pressure distribution on the external pipe wall and on the inclined fin surface as well, permitted to identify the characteristic regions where the vortex took place, where the boundary layer is in contact with the surface and the point where it detaches the wall as well. The analysis indicates the presence of volumetric streams (secondary flows) in the internal side channel formed by two inclined fins. On the external fin's face, the flow has a similar tendency as in the case of the cylinder but with a later detachment of the boundary layer in the fin's tip.

INTRODUCTION

Most of the fin's geometry modifications to increase the heat transfer, are based on the interruption or brake of the laminar boundary layer (drilled holes, picks and roughness), or in the channel curvature between the fins to organize the flow contact and the boundary layer detachment, that is, the macrovortex formation. In general, in both cases, a small increment in heat transfer intensity is compensated with an increment of the aerodynamic resistance of the heating surface, so that, finally we obtain a minimum or even a null increment of the total thermal efficiency.

It is obvious that the development of effective methods to increase heat transfer must be based on the detailed study of the fluid dynamics in the channels, formed by the fins and the space between the pipes in a bank of pipes. This experimental investigation should provide a vision of the flow dynamics and the way to increase the heat transfer process without increasing dramatically the aerodynamic resistance.

Some of the fundamental studies, in this area, were developed by Pismennyi [1, 2] both theoretical and experimentally. He has studied the flow behavior and convection coefficient distribution on the surface of conventional straight fins in a bank of finned tubes.

After the above mentioned research, several fin modifications appeared, all of them were developed to reduce the material quantity employed in the finned pipes, other to increase the heat transfer in the lateral and rear regions, others to increase the heating surface compactness and some to diminish the aerodynamic resistance produced by the finned surface. Each one of these modifications has its own particularity regarding heat transfer and fluid dynamics between a couple of fins, so that, it is very important to know the thermal and aerodynamic characteristics of these fined pipes in order to be used in the industrial application. As was mentioned here above, the study of these characteristics must have a local character.

Pronin and Carvajal-Mariscal [3] shown experimentally that by inclining the squared cross section radial fins an angle γ respect to the pipe axis, it is possible to increase the compactness β (that is the relationship between the surface A and its volume V) of a bank of finned pipes when they have a dense disposal (figure 1). At the same time, the increase of the inclined fin height H increases even more the compactness of the pipes bank as shown in line 2, figure 1, comparing with the case when the space between the pipes ($S_1 \times S_2$) is reduced in a squared shifted matrix very dense, line 1 in figure 1.

To determine the thermal and aerodynamic characteristics of this kind of finned pipes, it is necessary to undertake a detailed local study of these kind of devices. In this work, a

fluid dynamics physical model for a finned pipe provided with inclined fins respect to the axial axis (see figure 2) is presented. Some information presented in this paper was taken from the reference [4].

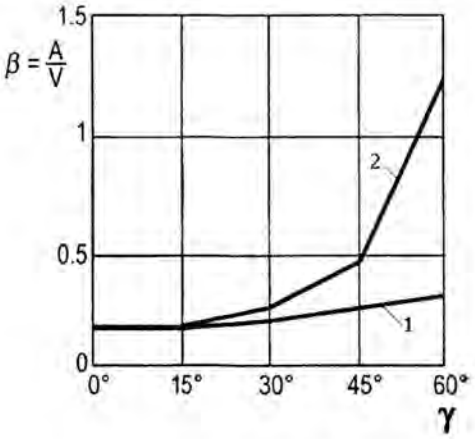

Figure 1: Effect of inclination angle γ, on compactness β, of a bundle of finned pipes with dense disposal [5].
1 – H = *cons.*, $(S_n \times S_p)$ = *var.*; 2 – H = *var.*, $(S_n \times S_p)$ = *cons.*

NOMENCLATURE

A	surface of the bank of tubes (m^2)
C_p	pressure coefficient
d	finned tube diameter (m)
H	height of the fin (m)
$P\varphi$	local pressure on the surfaces (Pa)
P_0	pressure in front of the finned tube (Pa)
Re_d	Reynolds number based on the finned tube diameter
$S_p \times S_n$	transverse and longitudinal tube pitch (m)
u	flow velocity based on the frontal area (m/s)
V	volume of the bank of tubes (m^3)

Greek Letters

β	compactness (m^2/m^3)
γ	inclination angle of fin (°)
δ	fin thickness (m)
ν	cinematic viscosity (m^2/s)
ρ	density (kg/m^3)
φ	revolution angle of the finned tube (°)

AERODYNAMIC CHARACTERISTICS DETERMINATION

To determine the aerodynamic characteristics, a set up was built. It consisted of a 42 mm diameter tube with inclined fins. The base of the set up was a steel tube (38 mm of diameter) in which five plastic fins inclined $\gamma = 45°$ and six metal rings 42×38 mm, 16 mm of height (distance between two fins) were installed.

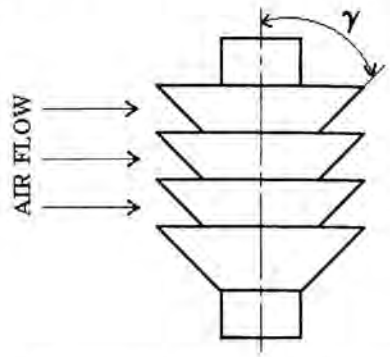

Figure 2: Tube with inclined fins. γ - angle of inclination.

In this way, six channels between the fins and the experimental channel wall were formed. The fin's characteristics are: height H = 20 mm, thickness δ = 2 mm.

In the central fin of the pipe, 16 pressure taps of 0.3 mm diameter were drilled and distributed all along the two faces of the inclined fin (figure 3). On both fin faces were distributed 8 pressure taps with a separation of 2 mm between them, starting in the fin's tip. The pressure transmission lines go through a channel, axially inside the tube to a potentiometer. To measure the local static pressure distribution along the fin surface, the finned tube was twisted around its own axis and for the local static pressure distribution on the cylindrical surface between two fins, three more pressure taps of the same diameter were drilled on this tube surface (figure 3). These pressure taps were distributed starting at 4.5 mm from the base of the fin and separated 3.5 mm.

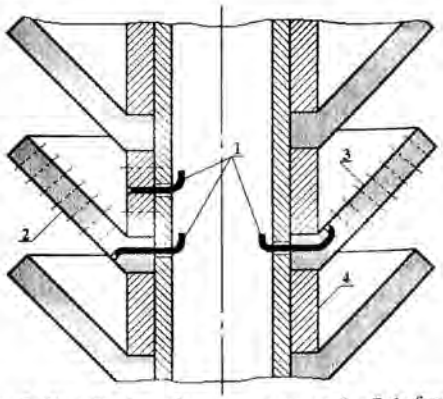

Figure 3: Distribution of pressure taps on the fin's faces and on the cylindrical surface. 1 – pressure transmission lines; 2 – external fin's face; 3 – internal fin's face; 4 – ring for the fin separation.

The model was exposed to a transversal airflow in a wind tunnel, which was formed by a 120x106 mm cross section channel and 950 mm length. The inlet of the channel is formed by rounded tips and it has a chamber for the velocity profile homogenisation before the finned tube. A centrifugal compressor provided air at a rate of 0.5 kg/s and 700 mm water column of gage pressure.

The airflow rate was measured using a subsonic nozzle connected to a U manometer. A manometer, with 19 inclined 2 mm diameter tubes, was used to measure the static pressure; this device was built and calibrated in our laboratory. The measurement error using the manometer above described was estimated to be around 3%.

The velocity range of the experiments was Re_d = (6 - 56)x10^3, because is the range more representative for heat exchangers with extended surfaces used in industry [5].

EXPERIMENTAL RESULTS

It is well known that the local static pressure distribution characterises the external flow respect the boundary layer. So, if we know the local static pressure distribution in both faces of the fin and in the cylindrical region between two fins, it is possible to understand the flow characteristics. It is also possible to identify the regions of contact and flow detachment, the region where the vortices are formed and also the flow direction in different points of the fin-tube system.

The pressure coefficient C_p was computed using the equation suggested in [6]:

$$C_p = 1 - \frac{P_0 - P_\varphi}{\frac{1}{2}\cdot\rho\cdot u^2} \qquad (1)$$

In the plots, φ represents the revolution angle of the finned tube. The geometrical symmetry of the system permits to analyse only half of the circumference.

Figures 4 and 5 show the distribution of the pressure coefficient in the middle and the periphery of the cylindrical zone for two air flow velocities. In the frontal region, the pressure decreases and after φ > 90° it increases again. Figure 4 shows the typical C_p behaviour, in the frontal part (0° ≤ φ ≤ 90°) the flow accelerates and in the rear region, there are counter current flows due to the boundary layer separation.

The flow direction, on the cylinder in the frontal region of the tube (0° ≤ φ ≤ 90°), is inverted in the rear region (90° ≤ φ ≤ 180°). This fact is shown in figure 4, where the flow direction is indicated with arrows. We can conclude that this phenomenon is associated to the vortex formation in this area.

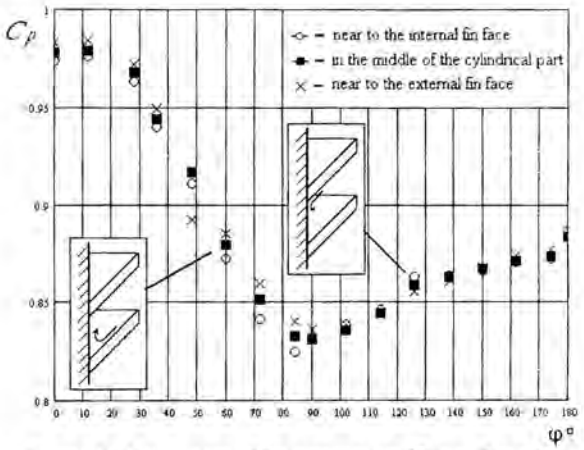

Figure 4: Distribution of the pressure coefficient C_p on the cylindrical surface for Re_d = 56 000.

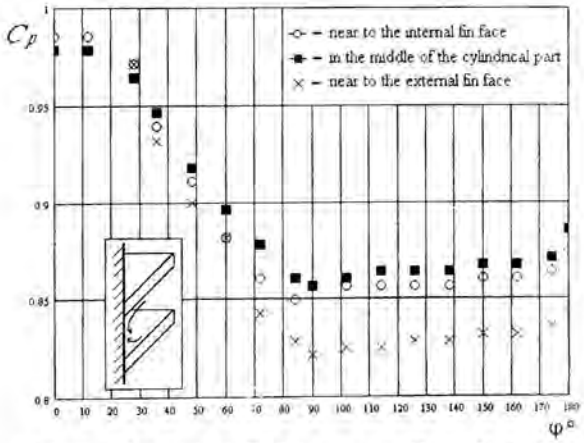

Figure 5: Distribution of the pressure coefficient C_p on the cylindrical surface for Re_d = 9 000

For Reynolds around Re_d < 20 000, this phenomenon disappears. On the other hand, it is possible to observe an abrupt pressure reduction on the rear region (90° ≤ φ ≤ 180°). This means that the current extends toward the neighborhood of the external surface of the fin as shown in figure 5.

Figure 6 shows the pressure coefficient distribution in the tip and in the root of the external fin face for Re_d = 56 000. There is a similar behaviour of the stream in this face and the one for the cylinder.

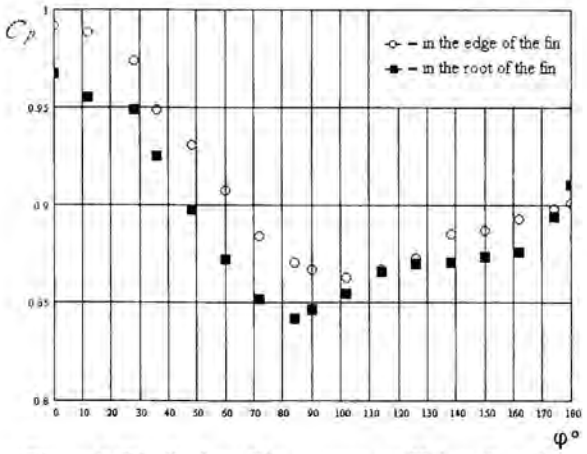

Figure 6: Distribution of the pressure coefficient C_P on the external fin's face for $Re_d = 56\,000$.

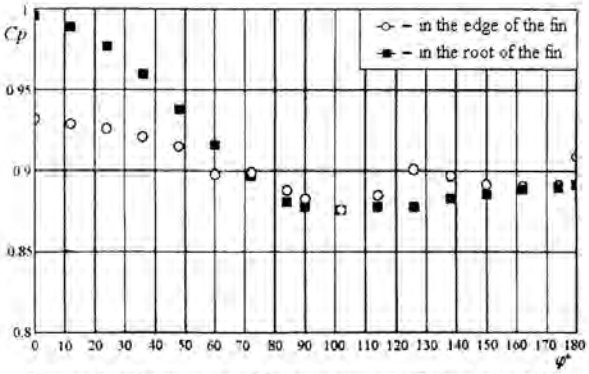

Figure 7: Distribution of the pressure coefficient C_P on the internal fin's face for $Re_d = 56\,000$.

It is also possible to remark that the flow detachment in the fin's tip occurs with certain delay ($\varphi \approx 100°$) respect to the one observed in the fin's root and occurs practically in the same point as in the cylinder case ($\varphi \approx 85°$).

The pressure coefficients distributions in the tip and the root of the internal face of the fin are shown in figures 7 and 8 for two air velocities. there are some vortices in this area that make difficult the flow dynamics.

In figure 7 some results for $Re_d = 56\,000$ are presented, we can distinguish that in the frontal part ($0° \leq \varphi \leq 90°$) of the fin, the pressure coefficient values in the root of the fin are lower than in the tip, indicating that the flow accelerates, getting the static pressure its minimum value in the position $\varphi \approx 90°$, when the flow detaches from the surface. Behind this point, the local static pressure has a small increment indicating that there are countercurrent flows.

In the fin's tip the pressure coefficient distribution is very different, presenting a maximum ($\varphi \approx 125°$) and a minimum ($\varphi \approx 100°$) points (figure 7). This behaviour indicates the presence of some vortices in this area, which detaches and attaches to the internal face of the fin.

For $Re_d < 9{,}000$ the pressure coefficient distribution, in the root of the internal fin surface, is different from the ones for higher Reynolds numbers, as shown in figure 8. In this place the static pressure decreases from the frontal critical point until the point where $\varphi \approx 110°$, after this point it is stable again, showing that in this region there is probably a stagnant point produced by the low velocity of the flow.

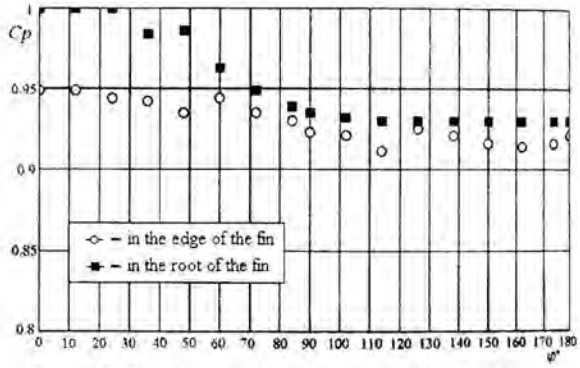

Figure 8: Distribution of the pressure coefficient C_P on the internal fin's face for $Re_d = 8\,000$.

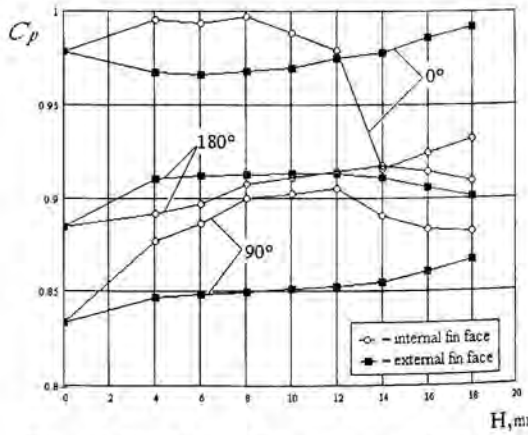

Figure 9: Distribution of the pressure coefficient C_P for the height of the internal fin's face for $Re_d = 56\,000$ at different revolution angles of the finned tube $\varphi° = 0°, 90°, 180°$.

On the contrary, on the fin's tip, there is a similar tendency to the one presented for $Re_d = 56{,}000$ shown in figure 7, where there are several detachments and reattachments of the flow with the fin surface.

In order to better understand the flow dynamics on the channel formed by two inclined fins, figure 9 shows the point where the distribution of pressure coefficient for the height of the inclined fin is expected to give more information about vortex formation.

In the frontal region of the fin ($\varphi = 0°$), there is a maximum and a minimum, due to the flow reattachment and flow detachment from the fin surface (figure 9). In this way, we can consider that vortices are formed not exactly at the tip of the fin but at a certain defined distance (in our case at 6 mm from the tip). The vortex touches the surface at approximately 6 mm from the root. We can conclude that at the middle of the fin there is a recirculation zone.

In the point $\varphi = 90°$ of the fin's lateral part, we can observe that the vortices formed in the frontal region of the channel, from external face to internal face, makes contact with the centre of the fin (figure 9). At low velocities the contact occurs near the tip of the fin.

In the point $\varphi = 180°$, in the rear region of the tube, the flow coming from the channel formed by two fins creates a recirculation zone as big as ¾ of the fin length (figure 9).

Analysing all the flow dynamics in the channel formed by all the inclined fins, it is possible to show that the frontal part of the flow, in the internal fin face, is an independent area where the vortices are formed. On the contrary, in the rear part of the channel the flow has a structure which is formed as a result of the created eddies in the internal face of the frontal part and the detachment of the boundary layer in the cylindrical part, and in the external face of the inclined fin as well.

FLUID DYNAMICS MODEL

The fluid dynamics model allow to determine the flow pattern and the stream distribution in the channel formed by a pair of inclined fins. With the model, it is also possible to explain the reasons why the aerodynamic resistance increases and also to identify the typical regions where the vortices are formed, the point where the boundary layer is in contact or detaches from the wall.

Taking into consideration the local static pressure distribution obtained experimentally at the height of the fin at different rotation angles of the tube, and according to the analysis below exposed, it is possible to propose a model for the flow dynamics in the channel formed by the set of inclined fins (figure 10).

This model differs from the one obtained for the conventional straight fins presented by Pismennyi [1, 2] where the vortices originated in the frontal side of the tube have a different behavior in its rear region. In the case of the straight fins, there is not a recirculation zone that covers ¾ of the fin height when $\varphi = 180°$.

This model of the flow dynamics allows us to determine the characteristics and structure of the flow in different regions of the channel.

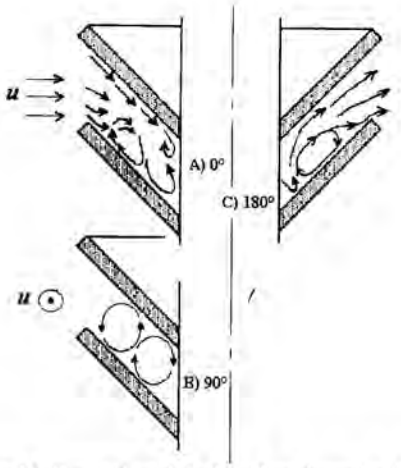

Figure 10: Physical model of the flow dynamics in the channel formed by the set of inclined fins for different revolution angles $\varphi°$ of the finned tube.

Also we can analyze the reasons of the increment of the aerodynamic resistance, besides, we can distinguish the regions where the eddies are formed and determine their magnitude as well.

FLOW VISUALIZATION

To visualize the flow a finned pipe provided with inclined fins was used. The technical characteristics of the fins are: fins height $H = 16$ mm, thickness $\delta = 1.6$ mm, distance between fins 8.5 mm, pipe diameter $d = 15$ mm and the inclination angle was $\gamma = 45°$. The pipe was machined from a solid aluminium cylindrical bar with inclined non helical fins so that it allowed to visualize the flow under the same geometrical conditions of the previous set up. The pipe was exposed to a transversal air flow in a low velocity wind tunnel.

The hot wire technique was used for the flow visualization, the wire was installed 5 cm away from the axial axis of the pipe. The images here presented were obtained for the air velocity of 5 m/s.

In the channel formed by two inclined fins, the air flow suffers an acceleration, producing a low pressure zone. The smoke wake went across only one channel, so that turbulence formations were avoided and we were able to see the flow dynamics without any perturbations.

In figure 11 it is possible to observe that a part of the flow goes around the pipe while the complementary part flows upwards in the back region of the pipe. A recirculation zone is formed in the rear region of the finned pipe and is due to the flow acceleration and its slip on the surface of the superior fin. This situation produces a macrovortex because part of the flow comes back.

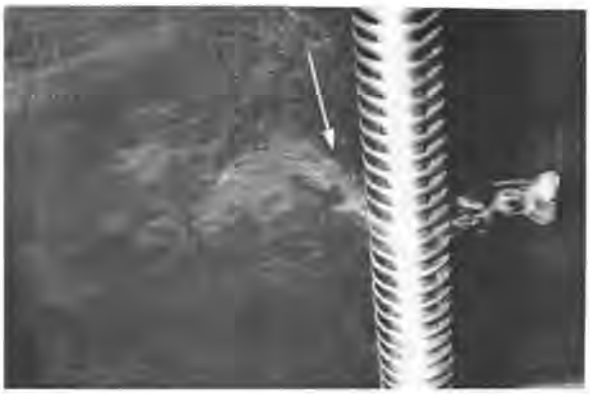

Figure 11: Flow visualization in the back region of the pipe with inclined fins.

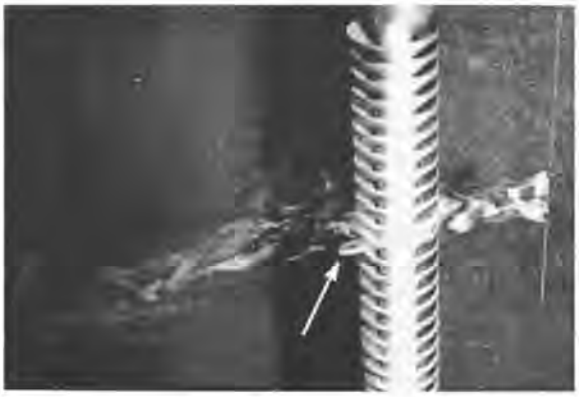

Figure 12: Flow visualization in the lateral region of the pipe with inclined fins.

In figure 12 we can observe how the detached boundary layer, from the cylindrical and conical part of the inclined fin, joins the flow coming from the internal channel formed by two inclined fins in the pipe backwards. In this region the flow is highly turbulent and has the tendency to go up forming a typical dynamic wake.

The smoke wake behind the pipe is turbulent, apparently without a pattern. This is due to the complicated flow structure at the exit of the channel and its joint point with the part detaching from the sides of the pipe.

The images here presented support, in some way, the analysis previously discussed.

In the case of heat exchanger applications, the inclined fins would be helical, therefore we suppose there will be some variations in the flow dynamics behavior, for instance in the drag coefficient.

We also consider that in the frontal part of the tube, the physical model could be conserved as shown in this paper, but in the rear region an asymmetry will present, part of the flow will touch the internal face of the helical fin and will try to climb to the upper fin. Meanwhile on the other face there will be countercurrent flows mixing with the flow coming from the lower fin. This situation of high turbulence probably will produce a stagnant zone.

ACKNOWLEDGMENTS

The authors thank the economical support provided by CONACyT of Mexico to undertake the present project.

CONCLUSIONS

The pressure coefficient distribution on the inclined fin surface and the pipe as well, and also the visualization of flow and physical model show us that its aerodynamic characteristics are very similar to the ones for the pipes with conventional straight fins.

On the other hand, with the pipes with inclined fins it is possible to obtain a compactness up to 50 % in the case of an inclination angle of $\gamma = 45°$, so that, it is possible to reduce the row number of pipes and in this way we can increase the flow velocity and of course the heat transfer could be increased substantially. So we can conclude that the use of extended surfaces composed of inclined fins are more efficient, since the thermal point of view compared against the finned pipes provided with conventional straight fins.

REFERENCES

[1] Pismennyi, E.N., 1984, "Investigation of Flow Dynamics in Surface of Fin of Cross-finned Pipe" (Russian), J. of Engineering & Physics, Vol. 47, № 1, pp. 28-34.

[2] Pismennyi, E.N., 1994, "Physical Model of Flow Dynamic and Heat Transfer of Convectional Cross-fined Heat Transfer Surfaces" (Russian), Proc. I Russian National Conference of Heat Transfer, Vol. 8, pp. 132-136.

[3] Pronin, V. A. and Carvajal-Mariscal, I., 1996, "Increase of Compactness and Energy Effectiveness of Convectional Cross-fined Heat Transfer Surfaces" (Russian), Proc. III Minsk International Forum for Heat Transfer, Vol. 10, pp. 150-154.

[4] Carvajal-Mariscal I., 1999, "Experimental Investigation of the Local Heat Transfer and Aerodynamics of Banks of Tubes with Inclined Fins", Ph.D. dissertation, Faculty of Heat Engineering, Moscow Power Engineering Institute, Moscow, Russia.

[5] Zukauskas A. A., 1982, "Convection heat transfer in heat exchanger" (Russian), "NAUKA", Moscow pp. 269-291.

[6] White F. M., 1988, "Fluid Mechanics" (Spanish), McGRAW-HILL/INTERAMERICANA de Mexico, pp. 299.

HEFAT2002
1st International Conference on Heat Transfer, Fluid Mechanics, and Thermodynamics
8-10 April 2002, Kruger Park, South Africa
MR1

POOL BOILING FROM SMOOTH AND ENHANCED TUBULAR HEAT TRANSFER SURFACES

Rudi Kulenovic, Rainer Mertz and Manfred Groll

Institute for Nuclear Technology and Energy Systems (IKE), University of Stuttgart
Pfaffenwaldring 31, D-70550 Stuttgart, Germany

ABSTRACT

The paper deals with pool boiling from tubular heat transfer surfaces using propane as working fluid. Experiments at heat fluxes below 125 kW/m^2 are carried out at different saturation temperatures (243 K to 293 K). The heat transfer surfaces are smooth tubes as reference and tubes with structured surfaces (re-entrant cavities) made from cooper and carbon steel. On the one hand the experimental work comprises the determination of the heat transfer coefficient (thermocouple measurements). On the other hand flow visualization experiments are carried out using a high speed video system and digital image processing for data evaluation. The parameters of interest are the bubble characteristics, e.g. the bubble departure diameter, the frequency of bubble generation and the bubble motion velocity map.

These parameters are employed in numerical models and in empirical correlations to predict the heat transfer performance of the heat transfer surfaces.

The background of the work is the demonstration of the heat transfer improvement of enhanced structured tubes compared to standard smooth or low-finned tubes which shall be used in future industrial compact heat exchangers. Thus, the major objectives of current and past R&D projects (sponsored by the European Commission) are/were to find out optimum surfaces in dependence of the thermal operating conditions, the used working fluid, the applied heat flux range, etc..

The paper describes the experimental set-up, the employed measurement techniques and the digital image processing methods (e.g. image filtering, frequency analysis, bubble detection and tracking). The results of the experimental investigations are shown as heat transfer coefficient vs. heat flux. The visualization results are both qualitatively and quantitatively presented and the quantitative results of the digital evaluation of the high speed video data, e.g. the bubble departure diameters and the bubble generation frequencies, are discussed.

INTRODUCTION

As substitute for conventional shell-and-tube heat exchangers with smooth tube bundles, compact heat exchangers are used for various industrial applications, especially in the process and petrochemical industries. Compact heat exchangers have smaller volumes with reduced material and energy consumption during their manufacturing and their use and they operate with very small temperature differences, improving the exergetic efficiency and allowing the use of low quality heat sources.

For compact heat exchangers novel enhanced heat transfer surfaces are required, e.g. structured tubes with sub-surface channels and cavities. Due to the dimensions of these structures which are in the sub-millimeter range, boiling phenomena different from those on smooth or low-finned tubes become dominant. Various authors have presented results of experimental investigations with such kind of surfaces, e.g. Chien and Webb [1,2], Gorenflo [3], Mohrlok et al. [4], Wang et al. [5], but there is still a significant lack of information about boiling on enhanced heat exchanger tubes.

For this reason the European Commission has funded a R&D project with the aim to develop and investigate structured heat exchanger tubes for compact heat exchangers for the process industry. In the frame of the project experiments were carried out at IKE with one smooth reference tube and four structured tubes provided by Wieland Werke AG, Germany (Mertz et al. [6]). Because there is a strong interest of the industry in hydrocarbons as substitutes for the banned FHC's, propane is used as working fluid and for further experiments it is planned to use butane. The experiments are carried out in the pool boiling mode at saturation temperatures in the range from 243 K to 293 K and with employed heat fluxes between 2 kW/m^2 and 125 kW/m^2. The main task of IKE is to identify the best variant of the investigated structured tubes, which will then be employed in experiments with larger tube bundles in a test facility of a project partner.

A high speed video system is used to visualize the boiling phenomena on the enhanced tubes and to provide information about important boiling parameters. The visualization of the bubble generation and two-phase flow from the tubular heat exchanger surfaces is carried out by a Kodak high speed video system. A software for digital image processing, designed at IKE, is used for the evaluation of the videos to provide boiling

parameters like bubble departure diameter and bubble generation frequency.

EXPERIMENTAL SET-UP

Test Rig

Due to the use of hydrocarbons as working fluid the pool boiling test rig was designed for pressures up to 16 bar and, for safety reasons, explosion-proof. Two separate stainless steel vessels, connected by flexible pipes, are used as test vessel and fluid tank, respectively (Fig. 1). The fluid tank is used to store the working fluid during the time period when no experiments are carried out. This design allows to open the test vessel, e.g. for changing of the test specimen, without contaminating the laboratory with working fluid.

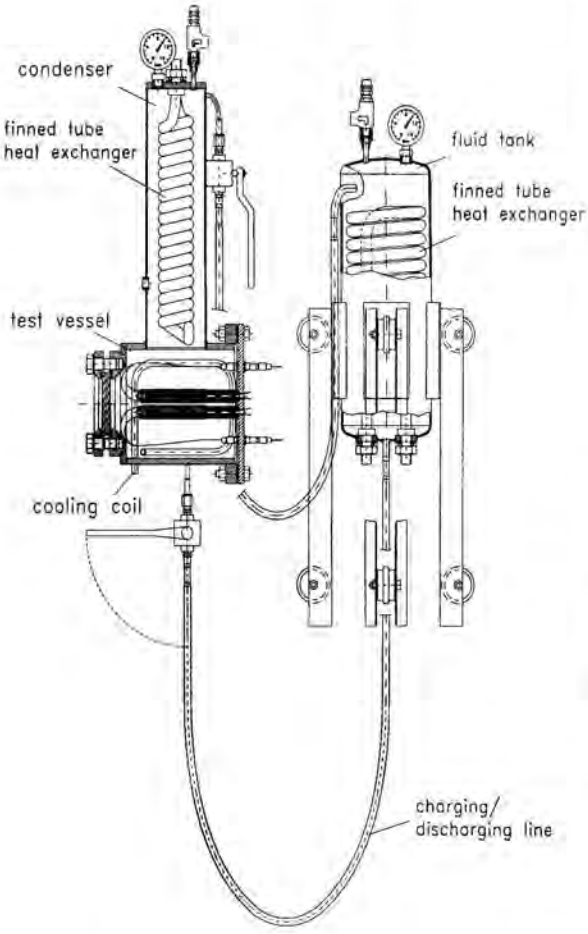

Figure 1 View of test rig

For thermal control a reflux condenser is employed on the top of the test vessel connected to external cooling systems. A removable flange is used as mounting support for the test section.

A Hewlett-Packard data acquisition system (HP-3852A) is used to measure the temperatures (calibrated temperature accuracy ±0.2 K between 233 K to 313 K) in the test rig, two temperatures in the fluid and one in the vapour, and 4 temperatures of the test section, the pressure in the vessel and the electric power input for heating. The absolute pressure inside the test vessel can be measured with an accuracy of ±0.1 bar, the electric power input with ±1 W.

For the visualization of the evaporation phenomena and the two-phase flow from the test surface three sight glasses are available in the test vessel.

Test Section

One aim of the test rig design was to change the test sections (Fig. 2) very fast, i.e. to be able to test many different surfaces in a relatively short time. Therefore, the test sections are assembled completely outside of the test vessel. The test section consists of an inner copper tube and an outer tube with the evaporation test surface. The inner tube is shrunk into the outer tube to minimize the thermal resistance between these tubes. Four thermocouples (type K, NiCr-Ni) are guided in four grooves (in 90° steps circumferentially and at different lengths) which are milled into the outer surface of the inner tube.

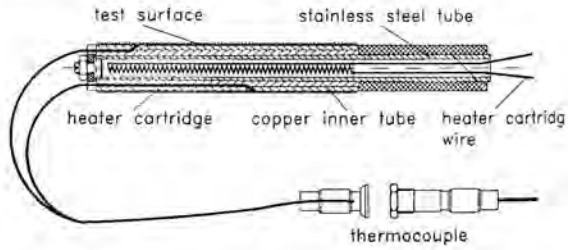

Figure 2 View of test section

A stainless steel tube, which is welded on the removeable flange of the test vessel is used as mounting support for the test section. The stainless steel tube is closed to the inside of the vessel, so it can be provided with an electric heater cartridge (heating power ~1000 W) from the outside without any contact between the heater cartridge and the flammable working fluid.

Visualization system and digital image processing

The boiling phenomena close to the tube surface are recorded with the high speed video system Kodak HS 4540 (8-bit grey-level, maximum 256×256 pixel resolution, maximum frame rate 40500 frms/s with reduced resolution 64×64 pixels) using a magnification optic. The recording frame rate and the observation area in the experiments are in general 1125 frms/s resp. 3×3 mm^2. The two-phase flow is illuminated in backlight with a strong cold-light source. The visualization data are stored on video tapes and from this representative sequences are digitized for further quantitative evaluation by digital image processing. The software library IKE_DBV is applied which calculates the boiling parameters like bubble departure diameter, bubble generation frequency and bubble flow velocity [7]. The determination of the bubble departure diameter is carried out by a 2D- gradient Laplacian filter which outlines the bubble con-

tours in a defined sub-region of the observation area. To distinguish between sharp and unsharp bubble contours a thresholding calculation step is applied to the Laplacian-filtered images and finally, after labelling of the sharp bubbles, their areas, gravity centers and maximum/minimum diameters are calculated. In case of the bubble generation frequency the passing through of the bubble gravity centers in a small region of interest (ROI) close to active nucleation sites is analysed by 1D-Fourier transform. In Fig. 3 a typical "digital" signal and the correspondent power frequency spectrum obtained from an enhanced surface are depicted. t_a and t_g are the pore activation and bubble generation time interval, f_a and f_g are the corresponding frequencies.

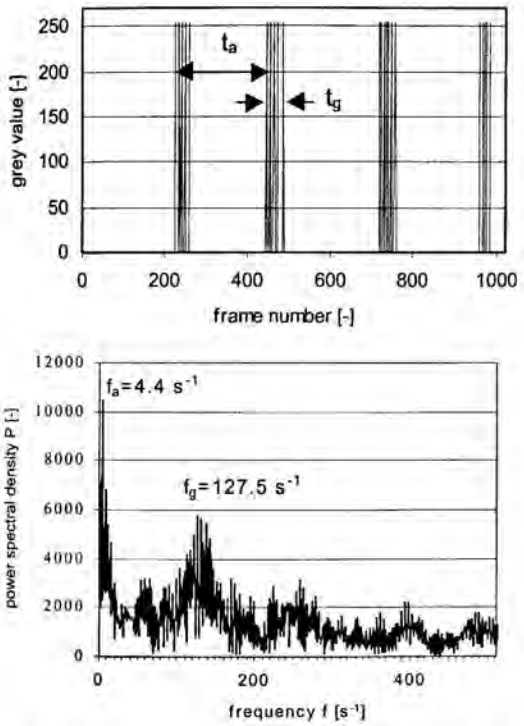

Figure 3 Time-dependent signal of gravity center in ROI and calculated power spectrum at one pore of enhanced surface

By means of a modified 2D-cross-correlation function (minimum-quadratic differences [8]) the upward movement of the bubbles is tracked and the velocity vectors are quantified.

In case of bubble departure diameter and bubble generation frequency a statistical post-processing of the data is done from series of evaluated video sequences with 1024 images which are obtained under same experimental conditions.

Experimental Parameters

The pool boiling experiments are carried out with one reference smooth tube (surface roughness r_a=1.09 µm) and four tubes with structured surfaces (type 1 to type 4), all made of carbon steel St35.8. The tubes have an outer diameter of 19 mm and a length of 115 mm (heated length 100 mm). Figure 4 shows the sub-surface structure of an enhanced tube. The tubes were provided by Wieland-Werke AG, Ulm. Propane N35 (N35, ≥ 99.95%) under saturation condition (saturation temperatures 243 K≤T_s≤ 293 K, resp. normalised pressure 0.04≤p,≤0.2) is used as working fluid. Employed heat fluxes are from about 2 kW/m^2 to 125 kW/m^2.

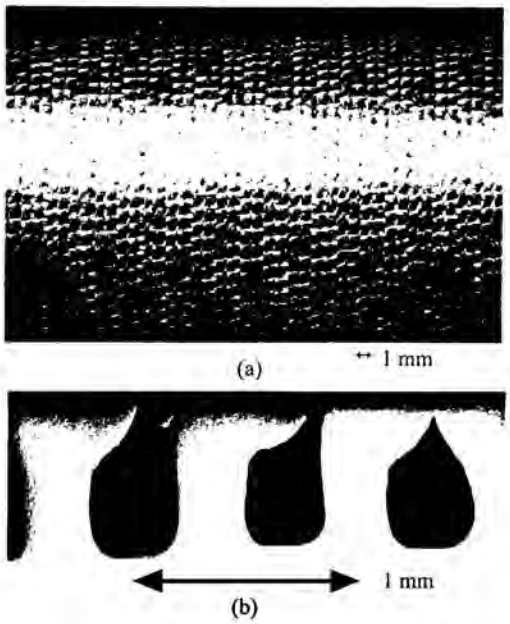

Figure 4 Enhanced surface type 4 (a), longitudinal cross-section (b)

EXPERIMENTAL RESULTS

Heat Transfer Coefficients

The comparisons between the smooth reference tube and the enhanced surfaces show in general significant improvements of the heat transfer coefficients of the enhanced surfaces (Figs. 5 and 6). The measurement accuracies, indicated in the figures by bars, are in general between 4% for q=125 kW/m^2, T_s=243 K and 40% for q=2 kW/m^2, T_s=293 K. The heat transfer coefficients of the smooth reference tube (Fig. 5) range from 0.6 kW/m^{2}K (q=2 kW/m^2 at T_s=243 K) up to 18 kW/m^{2}K (q=125 kW/m^2 at T_s=293 K). The heat transfer coefficients of the enhanced tube type 4 (Fig. 6) are in the range from 1.3 kW/m^{2}K up to 28 kW/m^{2}K for q=2 kW/m^2, T_s=243 K and q=125 kW/m^2, T_s=293 K. In contrast to the smooth reference tube the enhanced surfaces show a decreasing slope of the heat transfer coefficient curves with increasing heat fluxes which even becomes negative for high heat fluxes (q>70 kW/m^2) and high saturation temperatures (T_s≥273 K). There, the heat transfer coefficient reaches a maximum of 28 kW/m^{2}K for T_s=283 K and of 25 kW/m^{2}K for T_s=293 K at heat fluxes of about q=60 kW/m^2 and q=70 kW/m^2, respectively. This behaviour is due to a partial resp. total blockage of the internal heat transfer area by vapour, which, at the upper part of the tube, cannot leave the sub-surface channels and cavities

fast enough through the small pores to the surrounding fluid. It is assumed that enough liquid can enter the sub-surface channels at the bottom part of the tube. The same phenomenon was found in experiments with working fluid propane N25 [6].

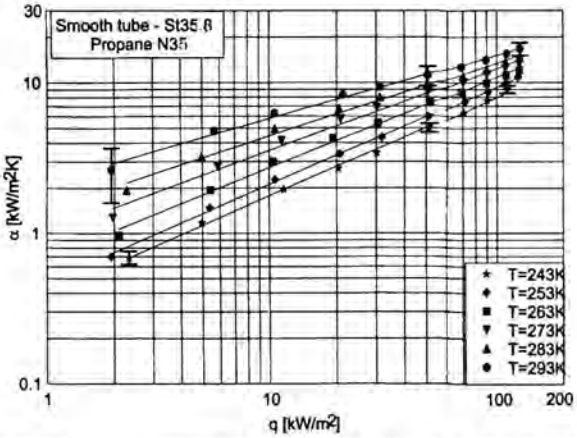

Figure 5 Smooth reference tube - St35.8, working fluid propane N35

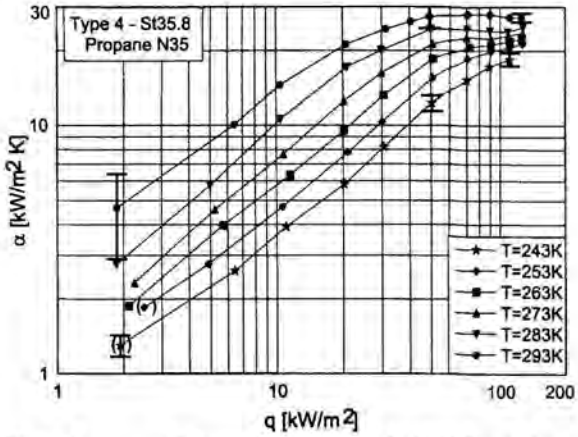

Figure 6 Enhanced surface type 4 - St35.8,working fluid propane N35

Summarizing the experimental results, the quality of the enhanced surfaces is expressed in terms of improvement factors F_i which are defined as heat transfer coefficient ratio of enhanced to smooth tube (Fig. 7). For type 4 the improvement factor can reach a maximum of 2.7 (at q=20 to 40 kW/m^2, T_s=283 K and 293 K).

Visualization

Figure 8 shows the visualized two phase flow for a smooth and a structured tube (type 4) operating under the same experimental conditions (working fluid propane, heat flux q=1.1 kW/m^2, saturation temperature T_s=283 K). It can be clearly seen that the boiling behaviour differs significantly. Whereas the smooth reference tube generates continuously very small bubbles

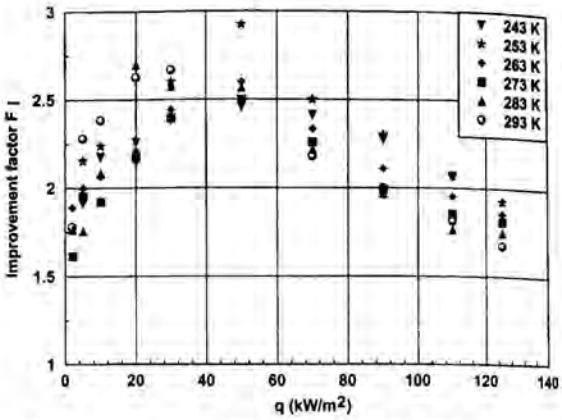

Figure 7 Improvement factors for tube type 4

nearly over the whole tube surface, the bubbles of the structured tube are much larger, and they are released periodically only from few active pores on the top side of the surface. With increasing heat flux first more pores of the structured tube become active and finally, nucleation sites on the smooth surface areas between the pores are activated.

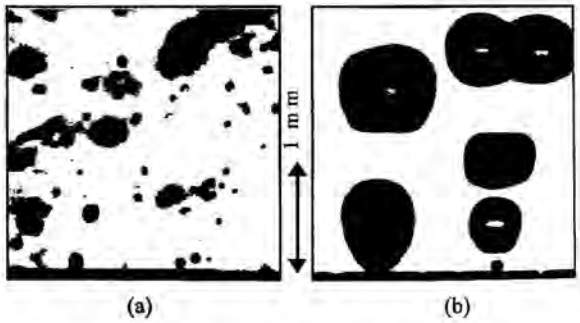

Figure 8 Bubble vizualization at smooth tube (a) and structured tube type 4 (b)

The quantitative evaluation of the digitized image data provides information about the bubble departure diameter, the bubble frequency and the bubble rising velocity [9]. These parameters are important with regard to the generation of a correlation for the heat transfer coefficient or a numerical boiling model.

Because of the more complex image contents of the visualized boiling phenomena of the smooth tube compared to a structured tube (much smaller bubbles, much higher bubble density) presently only preliminary results about the bubble departure diameter and the bubble generation frequency for the smooth tube are presented. The diameter distribution ranges from 0.1 mm to 0.4 mm, and the observed bubble generation frequencies are between 25 s^{-1} and 60 s^{-1}, according to the individual active nucleation sites (working fluid propane, q=1.1 kW/m^2, T_s=283 K).

For the structured tube (type 4) a statistical evaluation of 40 video sequences (1024 images/sequence, 1 to 4 active pores)

yields three main bubble departure diameters between 0.7 mm and 1.2 mm due to the different opening widths of the pores (Fig. 9, working fluid propane, q=2 kW/m², T_s=283 K).

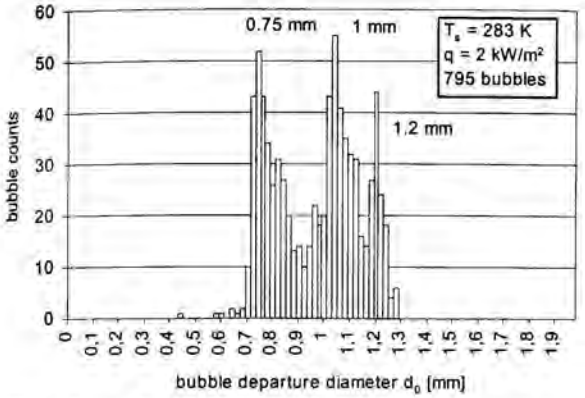

Figure 9 Bubble departure diameter d_0 for enhanced tube type 4

The bubble generation frequencies are depicted in Fig. 10 (evaluation of 10 video sequences, 1024 images/sequence, at two representative active pores). In contrast to the smooth tube several main frequency maxima can be observed in the frequency domain. The low frequency part f_a=5 to 10 s^{-1} corresponds to the periodical activation of the pore, whereas the high frequency part f_g=85 to 200 s^{-1} characterizes the bubble generation frequency during the active state of the individual pores.

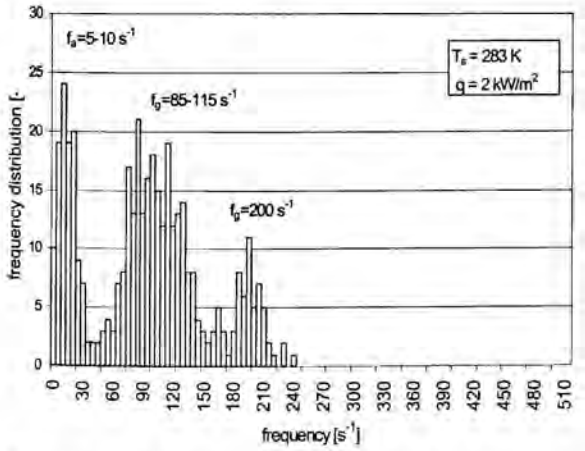

Figure 10 Bubble generation frequencies f_a and f_g for enhanced tube type 4

The flow velocity vector map of 8 bubbles generated at 2 adjacent active pores (x=42.25 mm and 42.8 mm) are shown in Fig. 11 (working fluid propane, q=2 kW/m², T_s=283 K). The individual bubble detachment time t_d is listed in the diagram table. The bubble flow path shows a staggering upward movement. The maximum bubble flow velocity rises to 218 mm/s for the larger bubble at nucleation site 2. Due to the different bubble diameters (nucleation site 1: d_0=0.7 mm; nucleation site 2: d_0=1.2 mm) the upward acceleration of the bubbles is finished at different vertical positions y (nucleation site 1: y=1 mm; nucleation site 2: y=2 mm) after about the same time interval of 0.014 s.

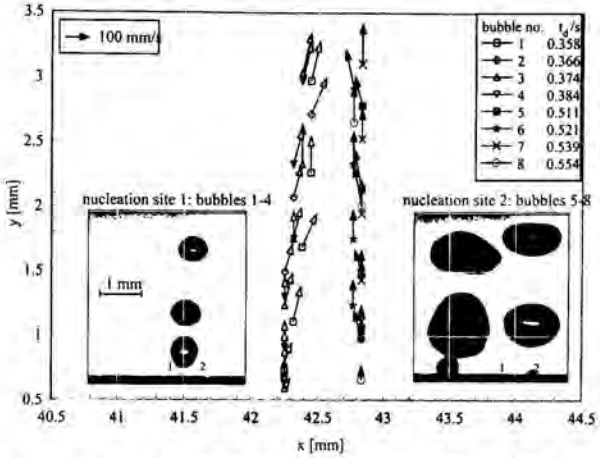

Figure 11 Bubble upward flow path for enhanced tube type 4 after bubble detachment

SUMMARY AND CONCLUSIONS

Enhanced heat transfer tubes with structured surfaces were investigated with the main objective to identify optimum novel enhanced surfaces of evaporator tubes for commercial shell-and-tube heat exchangers for the process industry. Pool boiling experiments were carried out with single tubes, one smooth reference tube and 4 enhanced tubes with re-entrant cavities. The best tested tube (type 4) has an improvement of the heat transfer coefficient of nearly 3 compared with the smooth reference tube.

A high speed video system was used to visualize the heat transfer phenomena and the two-phase flow from the surface. The video data are evaluated with the digital image processing software IKE_DBV, providing boiling parameters like the bubble departure diameter and the bubble generation frequency.

The bubble departure diameters for the smooth reference tube range from 0.1 to 0.4 mm, and the bubble generation frequencies are between 25 to 60 s^{-1}. For the enhanced tube the equivalent bubble departure diameters and bubble generation frequencies are larger (0.7 to 1.2 mm, 85 to 200 s^{-1}) and the maximum upward bubble flow velocity is about 220 mm/s.

ACKNOWLEDGEMENT

This research has been supported by the European Commission, Brussels, in the frame of the Non-nuclear Energy Programme (Contract no. JOE3CT970061).

REFERENCES

[1] L.-H. Chien, R.L. Webb, Measurement of bubble dynamics on an enhanced boiling surface. Experimental Thermal and Fluid Science, Vol. 16, pp. 177-186, 1998.

[2] L.-H. Chien, R.L. Webb, Visualization of pool boiling on enhanced surfaces, Experimental Thermal and Fluid Sciences, Vol. 16, pp. 332-341, 1998.

[3] D. Gorenflo, A. Luke, E. Danger, Interactions between heat transfer and bubble formation in nucleate boiling. Proc. 11th Int. Heat Transfer Conf., vol. 1, pp. 149-174, Kyongju, Korea, 1998.

[4] K. Mohrlok, K. Spindler, E. Hahne, Pool boiling heat transfer of R134a-oil mixture on a smooth tube and an enhanced tube. Proc. 3rd European Thermal Sciences Conf., vol. 2, pp. 785-790, Heidelberg, Germany, 2000.

[5] C.-C. Wang, W.-Y. Shieh, Y.-J. Chang, C.-Y. Yan, Nucleate boiling performance of R-22, R-123, R-134a, R-410A, and R407C on smooth and enhanced tubes, ASHRAE Trans. Symp., SF-98-15-4, vol. 104, part 1, pp. 1314-1321, 1998.

[6] R. Mertz, R. Kulenovic, M. Groll, T. Lang,, B. Thonon, High performance boiling tubes. European Seminar on Heat Equipment for the Process and Refrigeration Industries. Grenoble, France, 2000.

[7] R. Kulenovic, R. Mertz, M. Groll, High speed flow visualization of pool boiling from enhanced evaporator tubes. Proc. 3rd European Thermal Sciences Conf., vol. 2, pp. 755-760, Heidelberg, Germany, 2000.

[8] L. Gui, W. Merzkirch, A method of tracking ensembles of particle images. Experiments in Fluids, vol. 21, pp. 465-468, 1996.

[9] R. Kulenovic, R. Mertz, P. Schäfer, M. Groll, Quantitative microscale high speed visualization of pool boiling phenomena from enhanced evaporator tubes. Engineering Foundation Conference: Heat Transfer and Transport Phenomena in Microsystems. Banff, Canada, 2000.

HEFAT2002
1st International Conference on Heat Transfer, Fluid Mechanics and Thermodynamics
8-10 April 2002, Kruger Park, South Africa
RJ1

FALLING FILM TRANSITIONS BETWEEN DROPLETS, COLUMN AND SHEET FLOW MODES ON A VERTICAL ARRAY OF HORIZONTAL 19 FPI AND 40 FPI LOW FINNED TUBES

J.-F. Roques* and J. R. Thome**
*PhD. Student; **Professor
Laboratory of Heat and Mass Transfer,
Department of Mechanical Engineering,
Swiss Federal Institute of Technology Lausanne (EPFL),
CH 1015 Lausanne,
Switzerland
E-mail: john.thome@epfl.ch

ABSTRACT

Intertube flow modes for falling film condensers and evaporators with plain and enhanced horizontal tube bundles are thought to be key to their tube row effects. Three principal types of flow modes are typically observed (droplet mode, column mode and sheet mode) together with intermediate modes (coexistence of droplet-column modes and of column-sheet modes). All act as falling jets from the upper tube onto the tube directly below. In a previous study by Roques, Dupont and Thome [1], the transitions between these intertube flow modes were observed and measured for rows of plain tubes, Thermoexcel-C enhanced condensing tubes, Turbo-Bii enhanced boiling tubes and 26 fpi (1024 fpm) low finned tubes for water, glycol and a 50%-50% water-glycol mixture. Significant differences were observed in the transition thresholds for these tube surface geometries. In the present study, this investigation has been extended to 19 fpi and 40 fpi (748 and 1575 fpm) low finned Wieland tubes. A comparison between plain, 19 fpi, 26 fpi and 40 fpi tubes shows similar transition thresholds between the high fin density (40 fpi) tube and plain tube and secondly higher transition thresholds for the 19 fpi and 26 fpi tubes.

INTRODUCTION

The tube row effect in falling film condensation on a vertical row of horizontal plain tubes was first modelled by Jakob [2] applying the Nusselt [3] theory for a vertical plate to a row of tubes, assuming that the condensate flowed from one tube to the next as a continuous sheet of liquid, such that the performance on the Nth tube is:

$$\frac{\alpha(N)}{\alpha(N=1)} = N^{3/4} - (N-1)^{3/4} \qquad (1)$$

where $\alpha(N)$ is the local coefficient on tube N from the top and $\alpha(N=1)$ is the Nusselt solution for the top tube. Kern [4] modified this expression to reduce the tube row effect based on his experience with actual condensers to:

$$\frac{\alpha(N)}{\alpha(N=1)} = N^{5/6} - (N-1)^{5/6} \qquad (2)$$

Referring to Figure 1, Marto [5] compared these two expressions to the tube row effect measured experimentally for plain tubes in various independent studies. The Jakob equation for sheet flow underpredicts most of the data while the Kern equation is more representative of the mean trend in the data. The logical question thus arises as to why there is such a large scatter in the condensation tube row data. Rather than experimental error, the most likely answer is that this scatter is caused by the different intertube film flow modes from tube to tube. For instance, sheet mode should have the most severe tube row effect since the entire length of the tube is inundated. The tube row effect for the

column flow mode should be less since lower tubes are only partially inundated by condensate from above. Similarly, the droplet mode should have an even weaker tube row effect since the flow is also intermittent.

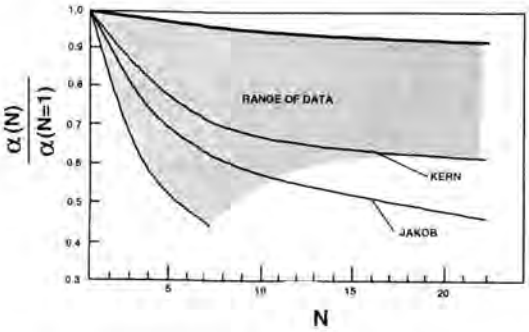

Fig. 1 Comparison by Marto [5] of Jakob and Kern tube row expressions to experimental data.

For low fin tubes, condensation heat transfer data typically show much less tube row degradation than plain tubes, e.g. many tests show less than 10% fall off in heat transfer on the first 4 tube rows. For condensation on enhanced condensing tubes, the degradation is typically reported to be more severe than for low finned tubes; this may or may not be true depending on how the comparison is made. Since their heat transfer coefficients are much larger, they produce much more condensate and hence more inundation occurs if the condensing temperature difference is held constant. Apparently no generalized flow mode map is currently available for predicting flow mode transitions for either plain or enhanced types of tubes under condensing or evaporating conditions. Honda et al. [6], however, have presented several transition expressions for individual fluids condensing on low finned tubes.

Falling film transitions for liquid under adiabatic conditions has been studied extensively by Hu and Jacobi [7] for a variety of fluids, tube diameters, tube pitches and flow rates and with/without cocurrent gas flow. Based on their observations, they proposed a flow mode transition map with coordinates of film Reynolds number (Re) versus the Galileo number (Ga). The map delineates the transitions between the three dominant modes (sheet, column and droplet) with two mixed mode zones (column-sheet and droplet-column) in which both modes are present. The modified Gallileo number of the liquid, which is the ratio between the gravity and the viscous force based on the capillary length scale, is defined as:

$$Ga = \frac{\rho\sigma^3}{\mu^4 g} \tag{3}$$

and the liquid film Reynolds number is defined as:

$$\mathrm{Re} = \frac{2\Gamma}{\mu} \tag{4}$$

where Γ is the total flow rate on both sides of the tube [kg/m s], ρ is the density of the liquid, μ is liquid dynamic viscosity, σ is the surface tension and g is the acceleration due to gravity. Their transition map is applicable to plain tubes for cocurrent air velocities less than 15 m/s.

An investigation on falling film flow mode transitions of adiabatic and non-phase change films was presented for plain tubes by Mitrovic [8]. Hu and Jacobi [9] obtained subcooled heat transfer data, and fit them with a distinct correlation for each flow mode. Hu and Jacobi [10] have recently reported additional data on tube spacing effects on column and droplet departure wavelengths.

In the present study, our tests on enhanced tubes has been extended to two additional low finned tubes, which are widely used in shell-and-tube condensers in the refrigeration and petrochemical industries.

DESCRIPTION OF THE TEST FACILITY

The test facility used for these adiabatic falling film tests is shown in Fig. 2 and is comprised of three main parts:

- *Fluid circuit*: The fluid in the tank is circulated by a small centrifugal pump through a filter and then one of two rotameters to measure the flow rate. The fluid then goes on to the top of the tranquilization chamber.

- *Flow tranquilization chamber*. This is a rectangular box (300x260x10mm inside dimensions: *Height* x *Width* x *Depth*) whose function is to provide a uniform flow onto the top tube and hence onto the second tube. The fluid leaves at the bottom of the chamber through 1-mm diameter holes spaced 2mm apart. The length of this distribution system (and the resulting film visualized) is 200mm.

Test section. It is comprised of three tubes on which the fluid flows. They are held at one end and the distance between them is fixed with tube spacers. Care is taken to obtain a very precise alignment of the horizontal tubes in a vertical array.

The temperature in the bath is maintained constant with an external regulated cooling-heating unit.

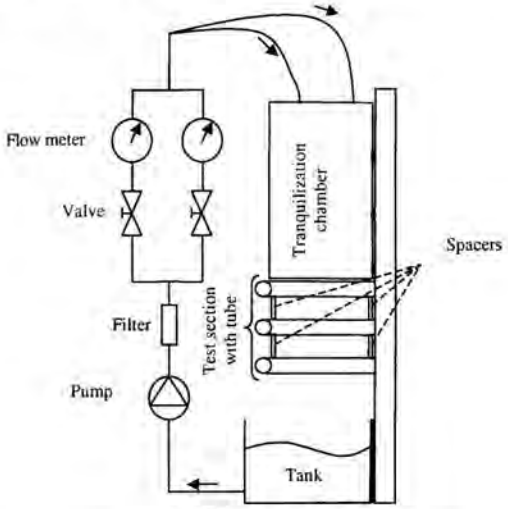

Fig. 2 Diagram of test facility.

DESCRIPTION OF TUBES AND TEST CONDITIONS

Two low finned tubes has been tested in this study: Wieland Gewa-K19 (19 fpi) and Wieland Gewa-K40 (40 fpi). Precedent transition results with a Wolverine Turbo-Chil (26fpi) tube are used for comparison. All those three tubes are ¾ inch diameter. Fig. 3 depicts close-up photographs of these tubes. The 19, 26 and 40 fpi tubes have fin heights of 1.42, 1.52 and 0.83 mm, respectively.

Fig. 3 Photographs of the low finned tube of this study: Wieland 19 fpi (left), Wolverine 26 fpi (middle) and Wieland 40 fpi (right).

For this study, the test conditions are identical as the ones in Roques, Dupont and Thome [1]. Intertube spacings tested are again 3.2, 4.8, 6.4, 9.5, 19.4 and 24.9 mm and the test fluids are water, glycol and a water-glycol mixture. These three fluids cover a range of modified Ga number from 84.10^3 to 49.10^9 while the modified Ga numbers of the refrigerant R113, R123 and R134a are respectively $3.3.10^9$,12.10^9 and 41.10^9. The results are presented using two dimensionless groups.

DEFINITION OF INTERTUBE FLOW MODE

The three principals flow modes mentioned before are depicted in Figure 4. Two intermediate transition modes have been observed. They are all defined as follows:

Droplet mode. The flow is in droplet mode when only droplets are falling between the tubes.

Droplet-Column mode. This is an intermediate mode with both droplets and columns occurring side by side from the upper tube to the lower tube.

Column mode. A column jet is a continuous fluid link between tubes. This mode is when there are only liquid columns observed between the tubes.

Column-Sheet mode. This is an intermediate mode with both columns and short liquid sheets occurring simultaneously side-by-side along the tubes. The merging of two neighboring columns forms a small sheet.

Sheet mode. This mode occurs when the fluid flows uniformly between the tubes as a continuous liquid film. The surface of the sheet is often disturbed by ripples and waves.

The thresholds between these modes is detected visually during the experiments. When it is necessary, a high speed camera is used to have a slow motion video sequence and detect accurately the transition of a droplet site to a column site.

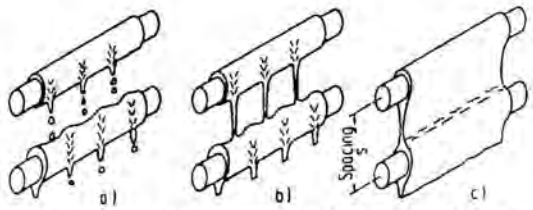

Fig 4 Schematic of the three main flow modes: a) droplet mode, b) column mode and c) sheet mode from Mitrovic [8].

FLOW MODE TRANSITIONS

The fluid is characterized by the modified Gallileo number (Ga). The mass flow rate is included in the film Reynolds number (Re). Neglecting the effect of tube spacing, the Reynolds number at transition can be correlated as a function of the Galileo number as:

$$\mathrm{Re} = a\,\mathrm{Ga}^{b} \qquad (5)$$

where a transition is the change from one flow mode to another one. As there are five modes, there are four transitions (or eight if one takes into account the hysterisis effect for increasing or decreasing flow conditions). Since we observed only a small degree of hysteresis, the observations of these two cases are put together to find the transitions.

The results are presented in the four following figures, each figure for one transition. The new results for this study are for the two Wieland tubes: 19 and 40 fpi but the results for a Wolverine 26 fpi tube and a plain tube obtained previously have been added for comparison purposes. It is so possible to see the fins density influence on the flow mode transitions. To keep the graph simple only the trend line calculated from the measurements with a mean square method are presented. Insets have been included in the graphs to give a better view at low Ga.

Figure 5 shows a composite diagram of transition between droplet mode and droplet-column mode observed for the plain tube and the three finned tubes. The transitions for the 26 fpi, the 40 fpi and the plain tube are similar while the one for the 19 fpi tube is above. That means that the first column needs a higher flow rate to become stable on this type of tube.

Figure 6 shows a composite diagram of the transition between droplet-column mode and column mode observed for the same tubes. The transition occurs at the same Re number for the 19 fpi and 26 fpi tubes and these two curves are above the 40 fpi and plain tube ones. As the column mode is reached when the flow presents only stable columns, the bottom attachment points of the columns to the tube is important. With this in mind, one explanation of the trend could be:

At high fins density (40 fpi) the columns cannot "feel" the fins on the bottom tube because the fins are too close each other. The transition is then similar to that on the plain tube.

At lower fin density, the columns start to "feel" the fins and they need more liquid to be stable. If the space between fins is sufficient at 26 fpi so that each column is well attached on one fin below. Increasing the space between fins (going to 19 fpi tube) does not change anything for the columns. There is only more space around the attachment point. That could explain why the transition is similar for 19 and 26 fpi tubes.

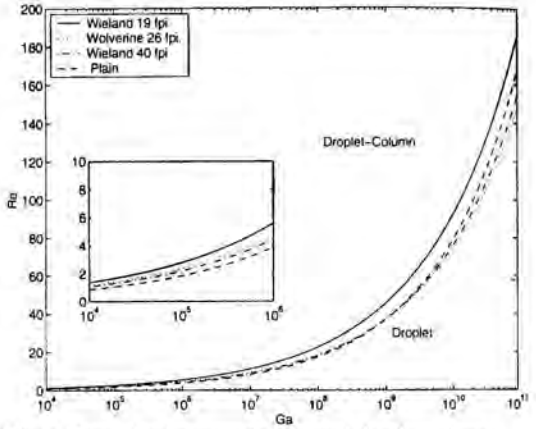

Fig 5 Transition between droplet and droplet-column mode for the plain and the three finned tubes

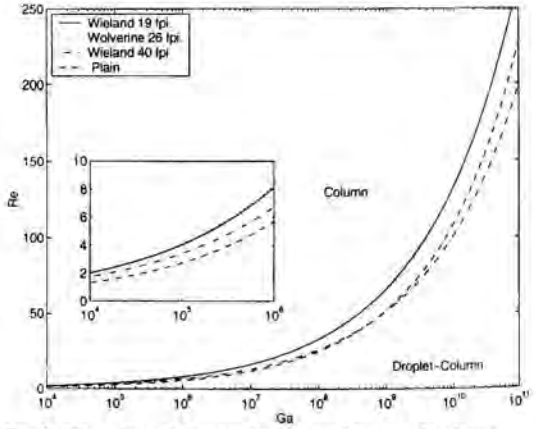

Fig 6 Transition between droplet-column and column mode for the plain and the three finned tubes

Figure 7 shows a composite diagram of the transition between column mode and column-sheet mode observed for the same tubes. Like on the last figure, the Re transition numbers are similar for the 40 fpi tube and the plain tube. The effect of relatively high fins density is negligible for this mode at high Ga number.

When the space between fins increases (19 and 26 fpi) they become destabilizing for the "small sheets" and the column-sheet mode is reached at higher flow rate. The highest destabilizing effect is for the 26 fpi tube, not the 19 fpi tube as might be expected.

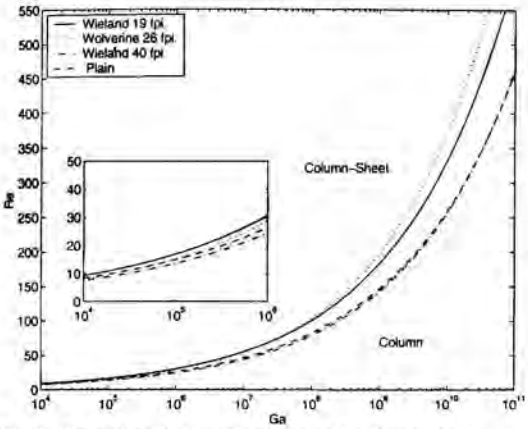

Fig 7 Transition between column and column-sheet mode for the plain and the three finned tubes

Figure 8 shows a composite diagram of the transition between column-sheet mode and sheet mode observed for the same tubes. The plain tube presents the lowest transition Re number and the effect of the fins is to delay the formation of large sheets. The trend between the number of fins and the column-sheet mode to/from sheet mode transition is not yet well explained because one has: the curve of the highest fins density (40 fpi) tube just above the plain tube ones. Then is the curve of the lowest fins density (19 fpi) tube. Finally the curve of the middle fins density (26 fpi) tube is at the top. Based on these measurements, there is no direct link between fins density and these transition thresholds. The fins also appear to have a "corrugating" effect to the sheet since the surface tension tends to make the sheet thicker at each fin and thinner between fins.

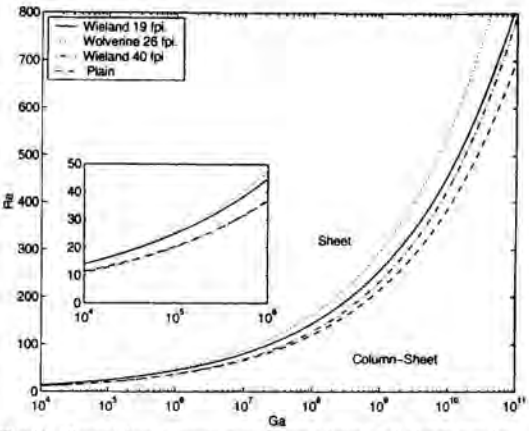

Fig 8 Transition between column-sheet and sheet mode for the plain and the three finned tubes

The numerical values of the coefficients a and b of the relation (5) for each tube and transition are presented in Table 1 (see annex). They have been used to draw the curves in the Figures 5 to 8. The log mean deviation corresponds to a mean of $Re_{meas}/Re_{pred.}$ For more details, see Roques, Dupont and Thome [1]. In this publication, a comparison between the measurements with the 26 fpi tube and the relations from Honda [6] is made. The result is a log mean deviation of 1.35 for the two first transitions and 1.14 for the two last ones.

Some trends are evident in Table 1. For instance, the value of b for the first transition remains nearly fixed with values of b from 0.3 to 0.3278 while a increases from 0.0417, 0.0622, 0.0743 and 0.0827 as the fin density descreases (assuming the plain tube can be thought of as having a very high fin density). Hence, the 40 fpi fin density tends to be closest to plain tube threshold value of a, and the effect on the transition threshold becomes more evident as the fin pitch increases.

CONCLUSION

In this study, observations of the flow modes between tubes oriented one above each other in a vertical array were made. Based on these observations, relations to predict the flow mode transitions between droplet, column and sheet modes are presented. These relations concern two new types of tubes: a Wieland Gewa-K40 (40 fpi) and Wieland Gewa-K19 (19 fpi). Comparisons between these two tubes, a Wolverine low fin tube (26 fpi) and a plain tube are made to see the effect of fins and fins density on the transitions. The main results are: the high fin density

(40fpi) does not affect the transition so much compared to the plain tube transitions while the lower fins density (29 and 26 fpi) tends to increase the transition Re numbers.

ACKNOWLEDGEMENTS

This research was sponsored by the EPFL/LTCM Falling Film Research Club together with a financial contribution by the EPFL. Club members are: Dunham-Bush Inc., Sulzer Friotherm SA, UOP Inc., Wieland-Werke AG and Wolverine Tube Inc. The 19 fpi and 40 fpi low finned tube samples were provided by Wieland Werke AG.

NOMENCLATURE

a	multiplicative factor in relations
b	power of Ga number
g	acceleration due to gravity (9.81 m/s^2)
Ga	modified Gallileo number
N	tube number
Re	film Reynolds number

Greek Letters

$\alpha(N)$	heat transfer coefficient on tube N (W/m^2K)
Γ	liquid flow rate per unit length on both sides (kg/m s)
μ	dynamic viscosity ($N\ s/m^2$)
ρ	density (kg/m^3)
σ	surface tension (N/m)

REFERENCES

[1] Roques, J.F., Dupont, V. and Thome, J.R. (2000). Falling Film Transition on Plain and Enhanced Tubes, *J. Heat Transfer*, in press.

[2] Jakob, M. (1936). *Mech. Engng.*, Vol. 58, 163.

[3] Nusselt, W. (1916). Die oberflächenkondensation des wasserdampfes, *Zeitschr. Ver. Deutch. Ing.*, Vol. 60, 541-569.

[4] Kern, D.Q. (1958). Mathematical development of loading in horizontal condensers, *AIChE J.*, Vol. 4(2), 157-160.

[5] Marto, P.J. (1986). Recent progress in enhancing film condensation heat transfer on horizontal tubes, *Heat Transfer Engng.*, Vol. 7, 53-63.

[6] Honda, H., Nozu, S. and Takeda, Y. (1987). Flow characteristics of condensation on a vertical column of horizontal tubes, *Proc. 1987 ASME-JSME Thermal Engineering Joint Conference*, Honolulu, Vol. 1, 517-524.

[7] Hu, X. and Jacobi, A.M. (1996a). The intertube falling film Part 1 – Flow chararcteristics, mode transitions and hysteresis, *J. Heat Transfer*, Vol. 118, 616-625.

[8] Mitrovic, J. (1986). Influence of tube spacing and flow rate on heat transfer from a horizontal tube to a falling liquid film, *Proc. 8th International Heat Transfer Conf.*, San Francisco, Vol. 4, 1949-1956.

[9] Hu, X. and Jacobi, A.M. (1996b). The intertube falling film Part 2 – Mode effects on sensible heat transfer to a falling liquid film, *J. Heat Transfer*, Vol. 118, 626-633.

[10] Hu, X. and Jacobi, A.M. (1998). Departure-site spacing for liquid droplets and jets falling between horizontal circular tubes, *Experimental Thermal and Fluid Science*, Vol. 16, 322-331.

ANNEX

Tube	Transition	a	b	Log deviation between measured and prediction
Plain	Droplet to/from Droplet-Column	0.0417	0.3278	1.3256
	Droplet-Column to/from Column	0.0683	0.3204	1.2014
	Column to/from Column-Sheet	0.8553	0.2483	1.3183
	Column-Sheet to/from Sheet	1.068	0.2563	1.2238
Wieland K19	Droplet to/from Droplet-Column	0.0827	0.3048	1.2177
	Droplet-Column to/from Column	0.1217	0.3041	1.1948
	Column to/from Column-Sheet	0.8573	0.2589	1.1246
	Column-Sheet to/from Sheet	1.3557	0.2532	1.2702
Wolverine 26 fpi	Droplet to/from Droplet-Column	0.0743	0.3	1.1386
	Droplet-Column to/from Column	0.1263	0.3025	1.2425
	Column to/from Column-Sheet	0.6172	0.2783	1.0804
	Column-Sheet to/from Sheet	1.2015	0.2661	1.1159
Wieland K40	Droplet to/from Droplet-Column	0.0622	0.3087	1.2949
	Droplet-Column to/from Column	0.1148	0.2947	1.1269
	Column to/from Column-Sheet	0.7198	0.2553	1.3587
	Column-Sheet to/from Sheet	0.9414	0.2662	1.1223

Table 1. Coefficients for transition relations.

HEFAT2002
1st International Conference on Heat Transfer, Fluid Mechanics, and Thermodynamics
8-10 April 2002, Kruger Park, South Africa
RP2

A CRITICAL REVIEW OF EXTENDED SURFACE HEAT TRANSFER

Dr. P. Razelos
Professor Emeritus CUNY, N.Y USA
Associate Editor HTE Life Member ASME

ABSTRACT

This paper is devoted to the re-examination of extended surface's basic treatment, which appear in the heat transfer textbooks. It is shown that unlikely, of what is suggested in the textbooks, the emphasis on the efficiency should be instead shifted to the effectiveness. Graphs are provided that permit to obtain directly the heat dissipation of a given fin without any reference to the efficiency, which is now the usual approach, and a total effectiveness is proposed to replace the total efficiency. It is further shown that the effectiveness approach helps to verify some of the simplifying assumptions, and that extended surfaces must be thermally and geometrically thin in order to fulfill their function. The results of a brief excursion to the optimum fin problem will help the students to become involved in a preliminary fin design, a subject that is conspicuously absent from the textbooks. Three postulates help to extend certain results of the unidirectional analysis of the constant thickness fins to other shapes and the two-dimensional problems.

NOMENCLATURE

B_i	Biot number	hw/k or $2hw/k$
B_r	surface Biot Number	hr_b/k
C_h	ratio of heat transfer coefficients Eq. (22)	
C_S	ratio of surfaces in spines S/S_c	
C_V	ratio of volumes V/V_c	
D	function defined by Eqs. (19,11,12, and 14)	
h	heat transfer coefficient	W/m^2-K
I_n	first kind modified Bessel function of order n	
K_n	second kind modified Bessel function of order n	
k	thermal conductivity	W/m –K
LAI	Length -of Arc Idealization	
O(n)	Order of magnitude n	
q	heat dissipation	W/m or W
Q	dimensionless heat dissipation	Eqs.(5,11,12,14)
r	radial distance	m
S	surface	m^2
T	temperature	K
ΔT	T_b-T_a	K
u	dimensionless parameter	$(L/w)B_i^{1/2}$
U	dimensionless volume	Eqs.(25,26,27)
V	volume of the fin	m^3/m or m^3
v	dimensionless parameter	$r_bB_i^{1/2}$
x,y,z	Cartesian coordinates	m

Greek symbols

β	ratio of	r_e/r_b
β-1	reduced fin height	L/r_b
ε	fin effectiveness	Eqs.(2,4)
η	fin efficiency	Eqs.(1a, 3a)

Subscripts

b	base of the fin
c	constant thickness
e	tip of the fin
f	fin
l	longitudinal fin
r	radial fin
s	spine
t	total

INTRODUCTION

Extended surfaces have been used widely for enhancing the heat transfer from a surface (primary) to the surrounding medium. They are referred in the literature as fins, a concise generic name, which also going to be used here. Because of their wide applicability, fins have attracted the attention of numerous investigators, and a vast literature is devoted to their analysis.

In this paper we do not attempt to review the entire literature, instead we re-examine the basic treatment of fins that the students are exposed to through their textbooks and handbooks for more than five decades. It is then logical, from the many forms or fin types of fins, to consider here only three basic ones: longitudinal (straight), circular pin (spines), and annular (radial, circular) fins. The variation of the fin thickness along the

fin's height from its base to its tip is called the profile. The coordinates and terminology of these three types of fins are shown schematically in Fig.1.

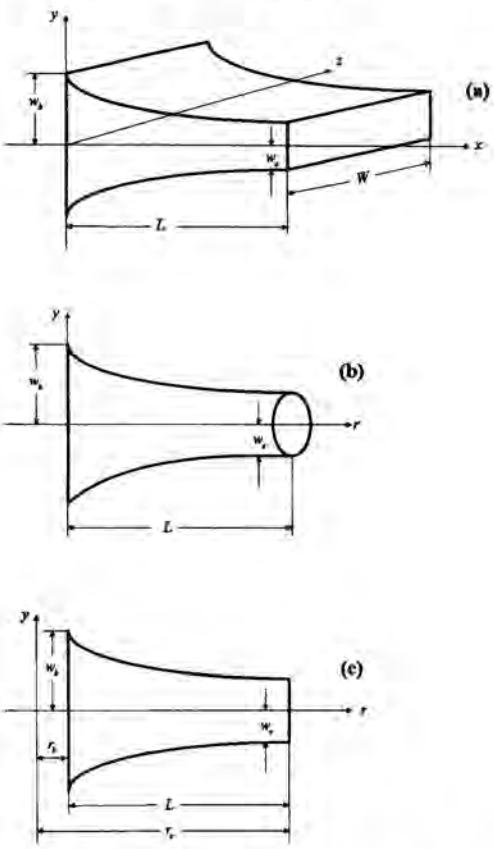

Figure 1. Schematic fin diagrams (a-longitudinal, b-pin fins, c-radial fins).

The decision to re-examine this rather elementary fin treatment originates in two basic observations: firstly in our firm belief that a thorough basic understanding of this simple problem will help in the endeavor to solve the more complicated cases, and secondly in the inadequate treatment shown in the textbooks and in several research papers. For example, by perusing the pertinent heat transfer literature, we observe that in fin analysis the similarity analysis is missing, and most important the authors tend to ignore the basic function of the fin. The consequences of the above observations are the erroneous conclusions of misleading statements by several authors. Worth noting is also the absence of any fin design, including optimization, in almost all the textbooks. Hence, our work is focused on the educational aspects of this subject instead of on the research-oriented approach. In addition, the goal of this work is to present a simple method that will permit the students to evaluate the performance of an extended surface, and above all to perform at least a rudimentary design analysis. In order to accomplish this goal, we have included graphs and correlations of the results.

To introduce the readers in this subject, it is helpful to present first a brief historical background introduction here.

BRIEF HISTORICAL BACKROUND

The first mathematical treatment of fins started some eighty years ago with the appearance of the pioneer work by Harper and Brown [1]. They investigated the heat transfer in air-cooled engines, equipped with rectangular or wedge-like type fins. Jakob [2] in discussing their work states, "In addition to their tremendous mathematical accomplishments, they introduced a new practical term, η_f the effectiveness of the surface, defined the as the "ratio of the of heat dissipated by the fin to that, which would have been dissipated under same conditions if the entire surface of the fin was held at the base temperature." This is equivalent to the assumption that the fin is made of a material with an infinite thermal conductivity. From this definition it follows, that the value of the effectiveness is always between zero and one. Therefore, we have the following expressions:

$$\eta_f = \frac{q_f}{\Delta T \int_{S_f} h dS_f} = \bar{h} S_f \Delta T \qquad (1a)$$

$$q_f = \eta_f \bar{h} S_f \Delta T \qquad (1b)$$

The symbol $\bar{h}$ represents the space average heat transfer coefficient. Hence if the effectiveness, which was renamed later by Gardner [3] **efficiency**, of **a given fin** is known, the heat dissipation q_f can be readily obtained. In a comprehensive paper Gardner [3] employed a rigorous mathematical analysis and determined the efficiency of eleven profiles of longitudinal, radial, and pin fins. In order to obtain his solution, he had to assume zero tip surfaces, with the exception of the constant thickness straight and hyperbolic profile annular fins. Gardner's treatment is based on the following simplified assumptions, known as the Gardner-Murray [4] simplified assumptions, which we have modified here:

1. Steady-state one-dimensional condition.
2. The fin material is homogeneous and isotropic
3. There are no heat sources or sinks in the fin

4. The mode of heat transfer is by convection
5. The thermal conductivity of the fin material is constant.
6. The heat transfer coefficient is constant.
7. The temperature of the surrounding fluid is uniform.
8. The temperature at the base of the fin is uniform.
9. The fin thickness is so small in comparison to fin's height that the temperature gradient normal to the surface is negligible. (This assumption will be also modified later)
10. The tip of the fin is insulated.
11. The square of the slope of the lateral surface is small compared to unity. (LAI)
12. In longitudinal fins the width is much larger than either the height or the base thickness, and the two end sides along the width are considered adiabatic.
13. The temperature along the width of the fin is constant.

Assumption 11 is referred in the literature as the "Length of arc idealization", LAI. Gardner [3] mentions that his solutions are based on assumption 11, though the added assumption 12 and 13 were also required of for his analysis. Gardner [3] also introduced another parameter ε_f, which he calls *effectiveness*. It is defined "*the ratio of the heat transferred by the fin to that, which would have been transferred from the primary surface, that covered by the fin's base surface, under the same thermal conditions, in the absence of the fin.*" Although different names are used for efficiency and effectiveness, Gardner's definitions of η_f and ε_f are almost universally accepted in the heat transfer literature. Assuming the temperature at the base of the primary surface equal to T_b, the effectiveness can be expressed in terms of the efficiency

$$\varepsilon_f = \frac{q_f}{q_b} = \frac{S_f}{S_b}\eta_f \qquad (2)$$

Gardner [3] points out: "In most practical cases, the addition of the extended surface to the metal wall would cause a temperature depression of the base temperature." "The effectiveness is a misleading indication of the value of the extended surface." Eq.(1) has been further modified to include the portion of the primary surface corresponding to each fin, (unfinned surface), to obtain an overall or total efficiency. Under the assumption that the heat transfer coefficient in the entire surface is the same, the overall or total efficiency is equal to

$$\eta_t = \frac{q_f + q_u}{hS_t\Delta T} = \frac{(\eta_f hS_f + hS_u)\Delta T}{hS_t\Delta T} = 1 - \frac{S_f}{S_t}(1-\eta_f) \qquad (3a)$$

The total heat transfer is then equal to

$$q_t = \eta_t hS_t(T_b - T_a) \qquad (3b)$$

According to equation (3a) η_t increases, hence q_t with η_f increasing. However, this is a contradiction since with increasing η_f the heat transfer from the fin decreases. In order to eliminate this paradox, we introduce the total effectiveness as follows:

$$\varepsilon_t = 1 + (\varepsilon_f - 1)\frac{S_b}{S_t} \qquad (4)$$

We shall see that Gardner's [3] comments about the efficiency and effectiveness had a profound effect on fin analysis. Fin efficiency became the only parameter that indicates the value of an extended surface, and his mathematical expressions together with his efficiency graphs, appear virtually in all textbooks and handbooks. Even today, many authors treat fin efficiency with the same meaning as the *efficiency of a thermal engine or a thermodynamic cycle*. Since the efficiencies η_f and η_t appear like proportionality factors in the Eqs. (1b) and (3b) and are used to determine the heat dissipation, many authors are tempted to use fins with the highest possible values of efficiency. Indeed, the literature reveals that this attitude of "*Higher efficiency means better fin performance*" is not a mere temptation but the general practice. In virtually all the handbooks and textbooks it is suggested to use fins that have large (close to one) values of η_f, and many fin experiments have been designed on large efficiency values. Following are some typical examples from the heat transfer literature, which by all means are not exhaustive, that clearly indicate this attitude Trumpler, discussing Gardner's [3] work states, "In most commercial installations, fin efficiency is greater than 90 percent." This statement is also cited by Kraus [5]. In the handbook of Heat Transfer edited by Rohsenow et al. [6] state, "In a good fin design, the efficiency is usually greater than 80 percent." Huang and Shah [7] assert: "In practice the fins in compact heat exchangers have efficiencies greater than 96 percent." In the handbooks by Fraas and Ozisik [8] and the one by Kakac et. al. [9] it stated, "Fin efficiencies typically will be of the order of 90 percent, for shell and tube heat exchangers." In his excellent analytical solution, Rong-Hua Yeh [10] points out "It is interesting to observe that the optimum efficiency of a pin fin is higher than that of an optimum longitudinal fin." However, there is no explanation what this superiority of the pin fin exactly means. White [11] recommends, "For longitudinal constant thickness fins, the parameter u (this important parameter is defined in the next section), should be

limited to the **O**(1.5), otherwise the fins will become inefficient. In examples cited in the textbooks by Bayazitoglou and Ozisik [12], Holman [13] Incropera and Dewitt [14], Kreith and Bohn [15], Leinhard [16] Mills [17] Thomas [18] and White [11], the parameters are chosen so that the resulting efficiencies are between 89 and 99.5 percent. Bejan [19] classifies long fins with small efficiencies as "*poor*" and gives an example where $\eta_f = 0.85$. In the experimental work of Kraus and Peters [20] it is stated, "In all cases, the small particle system exhibits a general trend of higher values of fin efficiency, hence better heat transfer characteristics." Mote *et. al.* [21] assert that "The fin's efficiency under present circumstances was always slightly, 2%, less than unity." Samie and Sparrow [22] designed their experiments so that "η_f varied between 93 and 98 percent." Mutlu and Al-Shemmeri [23] report "efficiencies larger than 0.95." while Karagiozis *et. al.* [24] refer to efficiencies near unity. However, there is an apparent contradiction for using Eq.,(1b), because as η_f increases q_f decreases and eventually when η_f is equal to one that is materialized when $S_f = 0$, and in this case **q_f is zero**. Kraus [5] using Gardner's [3] arguments, states: "The use of the effectiveness is somewhat limited and the employment of fin efficiency as design parameter has prevailed." However, from the definition of the efficiency, Eq.(1a), we can see that it is impossible for η_f to be considered as a design parameter. Leinhard [16] realized the above limitation of the efficiency, and asserts, "*The efficiency cannot be used to determine a priori the heat transfer from the fin but only after the fin has been designed.*" In addition the following statements that are widely accepted by the heat transfer community, result from the above efficiency discussion: i) Fins should be very efficient i.e., the efficiency should be close to one. ii) Fins should always be made from high thermal conductivity materials. iii) In a primary surface that separates two streams it is more efficient to place the fins in the stream with the lower heat transfer coefficient. From these statements, the first is incorrect while the two others must be carefully examined, because the thermal parameters k and h alone cannot determine where the fins should be placed. Finally, the key question regarding Eq.(1) is: "*Since this expression indicates that, in order to obtain the efficiency we must first calculate the heat dissipation from the fin, then why do we need to go back to the efficiency to calculate the heat dissipation?*" It will be shown shortly that instead of the efficiency graphs, we can create similar heat dissipation graphs; hence the efficiency can be eliminated.

FIN PERFOMANCE

We start this section by introducing three postulates, which will be helpful in the subsequent fin analysis.

1. *The one-dimensional analysis always over-estimates the heat transfer from the fin in comparison to the two-dimensional treatment.*
2. *The heat transfer for constant thickness fins is always larger in comparison to any other fin, with the same base thickness and height, and its borders lie within the boundaries of the constant thickness fin. (Fins with tip thickness smaller than the base).*
3. *For any fin with a heat transfer coefficient, which increases monotonically from the base to the tip, the heat dissipation is over- estimated, when evaluated assuming constant heat transfer coefficient equal to its average value. (Case of most convecting fins).*

The proof of the above postulates is rather simple, although beyond the scope of this work. However, some results obtained here will confirm the first two postulates. For example, from the Gardner's [3] efficiency graphs for straight fins, the second postulate is readily verified. We consider now the fins treated by Gardner [3] since his results are included in the textbooks. Clearly, all the assumptions 1-13, simplify the analysis, and their validity has been the subject of many researchers. To illustrate the usefulness of the missing similarity analysis, we consider the constant thickness fin of base thickness $2w$, height L, and width W that satisfy all simplified assumptions with exception of the 10th. Razelos and Georgiou [25] employ the following non-dimensional heat dissipation formula:

$$Q_i = \frac{q_f}{2k\Delta T} = \sqrt{B_i}\,\frac{\tanh(u)+\sqrt{B_i}}{1+\sqrt{B_i}\,\tanh(u)} = \sqrt{B_i}\,D(u,\sqrt{B_i}) \quad (5)$$

Notice, that $B_i = hw/k = (w/k)/(1/h)$ is the well-known Biot number, which represents the ratio of the wall to the ambient fluid thermal resistances, and $u^2 = hL/(kw/L)$, which is known in the literature as the convection conduction coefficient. Taking the derivative of Eq.(5) with respect to u we get

$$\frac{dQ_i}{du} = \frac{\sqrt{B_i}(1+\sqrt{B_i})(1-\sqrt{B_i})}{\cosh^2(u)\left(1+\sqrt{B_i}\,\tanh(u)\right)^2} \quad (6)$$

The second derivative is obviously negative. Because the value of $B_i = 1$, actually $\sqrt{B_i} = 1$, maximizes the heat dissipation, $Q_i = 1$, Schneider [25] and others named this value of B_i *optimum*, although the word *optimum* is meaningless here. Schneider [26] pointed out that in order for the fin to have a cooling effect the value of the

Biot number, (he calls this Nusselt number), must satisfy the inequality $B_i \le 1$. Notice that the correct inequality is $\sqrt{B_i} < 1$. Although this inequality sets a boundary on the value of B_i, it is a rather vague criterion that does not prescribe how much smaller than one the value of B_i should be. To obtain this information we resort to the effectiveness. The dimensionless heat dissipation from the fin's base area $Q_b = q_b / 2k\Delta T$ is determined from Eq.(4) by setting $u=0$, hence $Q_b = \sqrt{B_i}$. The effectiveness then is

$$\varepsilon_f = \left(\frac{1}{\sqrt{B_i}}\right)\frac{\tanh(u)+\sqrt{B_i}}{1+\sqrt{B_i}\tanh(u)} \qquad (7)$$

The above equation is indeed very useful. For example, the maximum value of the second fraction is one. This value can be achieved in two ways: the first one is to set the value $\sqrt{B_i} = 1$ for any value of u, and the second, for any value of B_i when u tends to infinity, (actually $u=3$ suffices). In the first case we get $\varepsilon_f = 1$, which indicates that the finned and the unfinned surface dissipate the same amount of heat, which confirms the previously obtained constrain of $\sqrt{B_i} < 1$. This means that the fin should be thermally thin. In the second case we obtain the following result:

$$\varepsilon_f < \frac{1}{\sqrt{B_i}} \qquad (8)$$

The two first postulates extend the validity of the above inequality to the two-dimensional fin analysis, and to fins of all other shapes. It should be recognized that the above inequality provides only qualitative results and does not again indicate how smaller the value of $\sqrt{B_i}$ or B_i should be. The decision for a suitable value of the Biot number will be determined from space availability, economic and other considerations. The authors in [25] suggest that due to the many simplifying assumptions, especially the constant heat transfer coefficient, that over-estimates the heat dissipation, one should consider the values of $\sqrt{B_i}$ to be of the order of $\mathbf{O}(0.1)$. Benjan [19] using the definition of effectiveness concludes that for longitudinal and pin fins $\varepsilon_f \gg 1$. Therefore, fins operating with such effectiveness must also have $B_i \ll 1$. Bejan [19] arrives in the interesting conclusion: "The criterion for the validity of the unidirectional heat conduction has a new meaning, which is the restriction of the values of the effectiveness." However, perhaps from an oversight, he states "If ε_f is marginal larger than one, this does not mean that the fin is not effective, it means that the unidirectional treatment is invalid and the two-dimensional analysis should be applied." This statement obviously contradicts the first postulate.

One should carefully consider inequality (8), and not to expect that a decreasing B_i will automatically increase heat dissipation. We have not yet said anything about the appropriate value of u, which will be discussed later. Having established, at least for the moment, that the assumptions 10 and 11 seem to be reasonable, we obtain the following simple expressions:

$$Q_t / \sqrt{B_i} = \tanh(u) = D(u) \qquad (9)$$

$$\varepsilon_f = \frac{\tanh(u)}{\sqrt{B_i}} \qquad (10)$$

$$\eta_f = \frac{D(u)}{u} \quad \textit{for longitudinal fins and spines} \qquad (10a)$$

$$\eta_f = \frac{2 \times D(u,\beta)}{\nu(\beta^2 - 1)} \quad \textit{for annular fins} \qquad (10b)$$

The expressions of the function $D(u)$, and $D(u,\beta)$, for the Gardner's [3] results, are shown in Table 1. Comparing the expressions for η_f presented here with those shown in the textbooks, we see that similarity analysis considerably simplifies the efficiency equations. For radial fins the efficiency is given as a function of u and β. However, it will be shown later that u is not the proper dimensionless parameter and leads to some contradictions. Note that without the assumptions of insulated tip and or LAI, η_f is a function of two variables, while for radial fins of three variables. Therefore, their graphical representation would have been cumbersome. For pin fins Razelos [27] defines the dimensionless heat dissipation as

$$Q_s = \frac{hq_f}{2^{1/2}\pi k^2 \Delta T} = B_i^{3/2} D(u) \qquad (11)$$

For radial fins we define the dimensionless heat dissipation similar to the one for straight fins as follows:

$$Q_r = \frac{q_f / 2\pi r_o}{2k\Delta T} = \frac{q_r}{2k\Delta T} = \sqrt{B_i} D(u,\beta) \qquad (12)$$

We shall see later that the above expression is also not the appropriate one to use. Here we are using it only in order to keep the parameters consistent with those used

by Gardner [3]. The variation of the function D versus u or u and β are shown in the Figs 2-5. Consequently, for a given fin, one can obtain the heat dissipation directly, without any reference to η_f. One other important information that we can obtain from the shape of the aforementioned figures is the suitable value of the parameter u, already mentioned by Leinhard [16]. A close inspection of these graphs shown in Figs. 2-5, under consideration of the principle of diminishing returns, reveals that for longitudinal fins the value of u must be at of the **O**(1.5), for longitudinal and radial fins, and for spines of **O**(2). Taking into consideration the previous results regarding the effectiveness, which dictates that $\sqrt{B_i}$ must of **O**(0.1), we obtain an order of magnitude for the ratio L/w, which is **O**(15). Therefore, in practice there are not, or there should not be, any thick fins. It is noteworthy that Figs. 2 and 3 confirm the second postulate. We can also observe from these two figures that, for a given base thickness, the heat dissipation increases as u (L) increases. However, the results plotted in graphs Fig.5 and 6 show an inconsistency, since for increasing u the heat dissipation, with fixed w and β, goes through a maximum, and then decreases as u continues to increase. In addition, a closer inspection of these two figures reveal that the second postulate is not confirmed. This is an example of not using the correct non-dimensional variables. To explain this discrepancy let us examine the parameter u,

$$u = L\sqrt{h/wk} = (\beta - 1)\sqrt{hr_b^2/wk} = (\beta - 1)v \qquad (13)$$

Therefore using u as a parameter the ratio β, which is a given parameter, it appears also in the abscissa. Razelos and Imre [28] analyzed the circular fins using the independent dimensionless variables β and v. Note that $v^2 = hr_b^2/kw = B_r^2/B_i$, where $B_r = hr_b/k$ (the latter is known as the surface Biot number). Substituting in Eq.(12) the parameter $\sqrt{B_i} = B_r/v$ we obtain the following dimensionless heat dissipation:

$$Q_r = \frac{q_f}{4\pi hr_b^2 \Delta T} = \frac{D(v,\beta)}{v} \qquad (14)$$

Here the functions $D(u,v)=vQ_r$ are shown also shown in Table 1, and they are plotted, in Fig 6 and 7 versus β-*1* with different values of v, for the constant thickness and hyperbolic profile-fins. Also, for the record, Fig.8 the efficiency of the constant thickness fin is plotted. Now, the comparison of the results shown in Figs. 6 and 7 does confirm the second postulate. We must emphasize here that the Figs. 2-7 should be used strictly to determine the performance of a **given fin**, in exactly the same way that it was done up to now with the efficiency. We feel that it will be educationally more advantageous to the students to use these graphs that visualize what happens to the heat dissipation by changing some parameters, instead of obtaining it from the efficiency. In the next section, in which we will discuss the optimization of fins, we shall present a method that permits the students to become familiar with preliminary fin design. This method, which considerably simplifies the design process, allows the designers to determine the influence of the thermal parameters h and k upon the fin's optimum dimensions. We conclude this section with the derivation of an interesting relationship that will enable anyone to evaluate the fin's performance only from its geometry. Considering Eq.(3) and taking into account that the efficiency is always less than one, we obtain the inequality

$$\varepsilon_f < \frac{S_f}{S_b} \qquad (15)$$

For the fins considered here we obtain the following expression:

$$\varepsilon_f < \frac{L}{w} \quad \textit{for longitudinal fins} \qquad (16)$$

$$\varepsilon_f < \frac{2L}{w} \quad \textit{for pin fins} \qquad (17)$$

$$\varepsilon_f < \frac{L(\beta+1)}{2w} \quad \textit{for radial fins} \qquad (18)$$

Therefore, one can now estimate the limits of the fin's effectiveness, without embarking into any mathematical analysis. Note that the above expressions and those obtained earlier show that the fins should be always thermally and geometrically thin. It is therefore surprising that many authors who analyze fins use values of the Biot number as large as 10, and values of L/w between 0.1 and 1.

ASSESSMENT OF THE SIMPLIFYING ASSUMPTION

In this section we discuss briefly the validity of the simplifying assumptions. We start with the two assumptions 1 and 11 that both depend on the Biot number.

a) One-dimensional conduction.

Irey [29], and Lau and Tan [30] investigated the criterion for the validity of the one-dimensional conduction for the three types fins considered here. Irey [29] examined the cylindrical spine using B_i and L/w

with values ranging, between 0.04 and 10,and, between 0.01 and 100 respectively, while Lau and Tan [30] examined the straight and annular types, using the same values $0.01 \le L/w \le 500$, and $0.01 \le B_i \le 0.1$. In both papers the conclusions are confusing, due to the incorrect dimensionless parameter L/w and B_i and the wide range of their values. However, their graphs that are confined in the range of L/w and B_i encountered in practical applications, reveal that the error by using the unidirectional conduction, is less than 1 percent. Both graphs confirm the first postulate. Since, we have already established that for fins, which act as good heat transfer-enhancing devices, the Biot number must be $B_i \ll 1$, the one-dimensional conduction is valid. Despite all the previous results, several authors have attempted to solve the two-dimensional fin problem either analytically or numerically, and compare their results with those obtained with the one-dimensional approach. However, they never accounted for, the very reasons for using fins. With all due respect to the authors I am compelled to cite some examples. Aziz and Nguyen [31] employed the finite element method to obtain he two-dimensional effects in a triangular convecting fin. They use the same parameters and same range of values as in [30]. We believe that their results are not correct. Even in the practical region of $5 \le L/w \le 15$, and $B_i = 0.01$ the errors are not only very large, but their results indicate that the heat dissipation obtained using the two-dimensional method can be larger than the one determined by the one-dimensional conduction, which contradicts postulate one. Thomas [18] states "For values of B_i much greater than 0.1 multidimensionality must be accounted for in the fin analysis." This statement contradicts the first postulate and the two-dimensional approach is not going to be of any help. Aparecido and Cotta [32] present "an improved one-dimensional fin solutions," which is also cited by Huang and Shah [7]. They use the dimensionless parameters $1 \le L/w \le 5$ and values of B_i 0.01, 0.1, 1, and 10. They also considered a tip Biot number $B_i^* = h_e w/k \ne B_i$. They justify their analysis with the erroneous statement "Application of one-dimensional classical approach is severely restricted to situations with Biot numbers much larger than unity." Apparently the authors were not even aware of Schneider's mild restriction that $B_i < 1$. Their solution is an infinite series where the eigen values determined from the roots of a transcendental equation. It has been shown in [25] that for the three types of fins, due to the nature of the roots of the transcendental functions, the solution is represented adequately by the first term of the series hence the two-dimensional solution is no more complicated than the one-dimensional one. For example, in this case of a constant thickness longitudinal fin, the two-dimensional solution is reduced to

$$Q_{l2-d} = \frac{q_f}{2k\Delta T} = 2\sqrt{B_i}\left[\frac{C_h\sqrt{B_i} + \alpha_o \tanh(\alpha_o u)}{\alpha_o(1 + B_i + \alpha_o^2)}\right] \qquad (19)$$

where in the above equations we use the symbols $C_h = h_e/h_-$ and $\alpha_o = 1 - B_i/6$.

b) The length of arc idealization

This problem has been examined by Razelos and Georgiou [34] for the fins considered here. We assume a general fin profile of the form

$$f(x) = \frac{y}{w} = \lambda + (1-\lambda)\xi^n \qquad (20)$$

where in Eq.(23) $\xi = 1 - x/L$, and $\lambda = w_e/w$. In this case the lateral surface without the LAI becomes

$$\frac{dS}{d\xi} = \left(1 + \frac{B_i}{u^2}(1-\lambda)^2 n^2 \xi^{2(n-1)}\right)^{1/2} \qquad (21)$$

Evidently, the maximum error is introduced in when $\xi=1$ and $\lambda=0$. There is no error for $n=0$, the constant thickness fin. Note that from the eleven profiles considered by Gardner [3], nine of them have $\lambda=0$. The error in the heat dissipation that is introduced by taking $dS/d\xi$ in Eq.(21) equal to one, has been evaluated in [34] and it has been found that for the values of B_i and u that are dictated by the effectiveness it was less than 1%. We have obtained similar results for spines and radial fins.

c) Variable thermal heat transfer coefficient (assumptions 5 and 6)

In this case new parameters will enter in the differential equations and the solution can be obtained either analytically or numerically. One simple case is the one where the heat transfer coefficient at the top and the bottom of the fin are different. Look [35] addressed this problem by the two-dimensional equations but he did not obtain any results. His argument for choosing the two-dimensional was "the one-dimensional solution couldn't handle this problem is unfounded." However, this problem admits a simple unidirectional solution provided the criterion of validity is retained. Consider a constant thickness rectangular fin of thickness b and height L. The heat transfer coefficients at the top and bottom of the fin are h_+ and h_- respectively. In this case the x-axis is located at the bottom of fin and the y-axis along the thickness. We define an equivalent fin thickness w_e as follows:

$$w_{eq} = \frac{b}{(1+C_h)} \quad where \; C_h = h_-/h_+ \qquad (22)$$

Introducing the usual dimensionless parameters are $B_{ieq}=h_* w_{eq}/k$, $u_{eq}=(L/w_{eq})\sqrt{B_{ie}q}$, $\xi=x/L$ we obtain the solution of the fin problem that was previously discussed. Note that in this case the adiabatic surface is $y=w_e$. For $h_*=h_-$, $w_{eq}=b/2$ the case that we analysed. For $h_-=0$, $w_{eq}=b$, a case that we know since the surface y=0 is now adiabatic.

d) Variable base temperature. (Assumption 8)

Look [36] has also considered this problem but instead of focusing on the temperature variation, he considered different coefficients on all three surfaces of the fin. His solution contains the roots of some non-existing transcendental functions. We consider the base temperature of a longitudinal fin to be

$$T_b = f(y/w) = f(\xi) \tag{23}$$

Carslaw and Jaeger [33] solved this problem assuming a constant heat transfer coefficient and an insulated tip. They have shown that the heat flow of the fin is determined from the following expression:

$$q_f \approx \sum_{m=0}^{\infty} \int_{-1}^{1} f(\xi)\cos(\lambda_m \xi)\, d\xi \tag{24}$$

We feel that the temperature variation at the base of the fin across its thickness is not important. However, in longitudinal fins the variation of the base temperature, along the z-axis might be important. Razelos [37] examined this problem and he has shown that, under the simplifying assumption 13, the heat transfer from the fin can be obtained simply by using the space average base temperature.

OPTIMIZATION

Fletcher [38] considers the subject of optimization to be a fascinating blend of heuristics and rigor of theory and experiment. Considering only an isolated fin, by optimization we mean, *"Given the volume or the desired heat dissipation of the fin, determine its dimensions that will maximize the heat dissipation or will minimize its volume."* However, the problem is not completely specified and an additional information is needed, which separates the problem in two distinct cases: in the first one the *profile* of the fin is prescribed, while in the second case we are searching to determine the *profile*. A third type, which we are not going to examine here, is an extension of the above two problems, where the optimization considers the entire fin assembly. The results of the first two types will introduce the students to preliminary fin design.

I.) **Problem one (Given fin profile).**

In line with our principle of using always the similarity analysis, we define a dimensionless volume U for each type of fin listed below

$$U_l = \frac{h^2 V}{2k^2 C_V} = uB_i^{3/2} \quad \textit{for longitudinal fins} \tag{25}$$

$$U_s = \frac{2^{1/2} h^3 V}{\pi k^3 C_V} = uB_i^{5/2} \quad \textit{for pin fins} \tag{26}$$

$$U_r = \frac{kV}{4\pi h r_b^4} = \frac{(\beta-1)(\beta+1)}{3v^2} \quad \textit{const. thickness radial fin} \tag{27}$$

The symbol C_V represents the ratio V/V_e. For longitudinal fins and spines the stationary values of Q and U must satisfy the relation [27], [42]

$$\left(\frac{\partial Q}{\partial B_i}\right)\left(\frac{\partial U}{\partial u}\right) - \left(\frac{\partial Q}{\partial B_i}\right)\left(\frac{\partial U}{\partial u}\right) = 0 \tag{28}$$

Note that we refer always to the optimum parameters B_i and u. Introducing the corresponding expressions of Q and U into Eq.(28) and carrying out the algebra we obtain the transcendental equations

$$3u\frac{dD(u)}{du} - D(u) = 0 \quad \textit{for longitudinal fins} \tag{29}$$

$$5u\frac{dD(u)}{du} - 3D(u) = 0 \quad \textit{for pin fins} \tag{30}$$

The solution of the above equations determine the optimum values of u and D hence the parameters B_i and L/w. The important result here is that the solutions are independent of the values of U or Q. They depend *only* on the fin profile. Razelos [39] introduced the following optimum dimensionless quantities, that serve to determine directly the optimum dimensions of the fin, for a given q_f or V, and clearly show how they are influenced by the thermal parameters h, k and the given q_f or V:

i) Given heat dissipation.

$$w^* = \frac{hkw_{opt}}{\left(q_f/\Delta T\right)^2} = \frac{0.25}{D^2} \tag{31a}$$

$$L^* = \frac{hL_{opt}}{\left(q_f/\Delta T\right)} = \frac{0.5u}{D} \tag{31b}$$

$$V^* = 2w^* L^* = \frac{h^2 k V_{opt}}{\left(q_f / \Delta T\right)^3} = \frac{0.25 C_v u}{D^3} \qquad (31c)$$

ii) Given fin volume.

$$w_V^* \left(\frac{k}{hV^2}\right)^{1/3} \times w_{opt} = \frac{w^*}{(V^*)^{2/3}} \qquad (32a)$$

$$L_V^* = \left(\frac{h}{kV}\right)^{1/3} \times L_{opt} = \frac{L^*}{(V^*)^{1/3}} \qquad (32b)$$

$$Q^* = \frac{q_f}{\Delta T (h^2 k V)^{1/3}} = \frac{1}{(V^*)^{1/3}} \qquad (32c)$$

It should be reminded that in the above equations the symbols u and D refer always to their optimum values, (the subscript opt is omitted). Therefore, the optimum dimensions of any fin are determined from the above stated quantities, which depend solely on the fin's profile hence we can call them *profile coefficients*. The interesting observation here is that the influence of the thermal parameters upon the optimum dimensions is quite different when the optimization is based on a given q_f or V. Notice that the coefficients for given volume can be obtained from those for given q_f. Therefore, suffices to give only their values for given q_f, which are shown in for all Gardner's fins in Table 2. From this tabulated results we see that the optimum efficiencies of straight fins are $0.5 \le \eta_f \le 0.6257$, that may prompt someone to declare these fins quite inefficient. In radial fins the optimum dimensions, the fin's reduced height β-1, and the parameter ν depend on both the profile and on the values of Q or U, (q_f or V), whichever is specified. The results: plots of β and ν versus Q, are exhibited in [28] and in the paper by Aziz [40]. In practical applications there are no zero tip surface or even nearly zero, and the most common profile is the trapezoidal, which is described the ratio $\lambda = w_b / w_e$. This practical reality was recognized first by Chung et. al. [41] who determined the optimum dimensions of longitudinal fins with trapezoidal profile. Razelos and Satyaprakash [42] and Das and Razelos [43] also considered trapezoidal profiles for straight fins and spines. To facilitate the calculations in [42,43] correlations of the profile coefficients have been obtained in terms of the parameter λ. For the longitudinal fins the author proposes the following expression valid for $0\lambda \le \lambda \le 0.5$ when q_f is specified:

$$w^* = 1/(2.41704 + 0.90496 \times \lambda - 0.18124 \times \lambda^2) \quad (33a)$$

$$L^* = 1/(1.87783 + 0.21467\lambda - 0.39364\lambda^2 + 0.32341\lambda^2) \quad (33b)$$

$$V^* = 0.34607 + 0.16199 \times \lambda + 0.00216 \times \lambda^2 \quad (33c)$$

In [43] the authors give the following correlations for the optimum values of u and D;

$$u_{opt} = 1.4183 - 1.28137\lambda + 1.39199\lambda^2 - 0.65847 \times \lambda^3 \quad (34a)$$

$$D_{opt} = 0.54413 + 0.07513 \times \lambda + 0.12241 \times \lambda^2 \quad (34b)$$

Radial trapezoidal profile fins are considered in [28]. Razelos used the results obtained in [27] with values of λ=1 and 0.001, and obtained the following correlations:

i) For constant thickness annular fins

$$\beta - 1 = [(0.39554 + 1.07298Q)^{1/2} - 0.62892]/0.53649 \quad (35a)$$

$$w^* = 1/[3.15343 + 1.66650(\beta - 1) + 0.18469(\beta - 1)^2] \quad (35b)$$

$$V^* = 1/[1.97522 + 0.91766(\beta - 1) + 0.10042(\beta - 1)^2]) \quad (35c)$$

ii) For triangular profile annular fins

$$\beta - 1 = [(0.33589 + 1.021326Q)^{1/2} - 0.57956]/0.51066 \quad (36a)$$

$$w^* = 1/[2.41100 + 1.21249(\beta - 1) + 0.14477(\beta - 1)^2] \quad (36b)$$

$$V^* = 1/[2.85386 + 1.65653(\beta - 1) + 0.22798(\beta - 1)^2] \quad (36c)$$

The quantities w^*, V^* are similar to the ones with longitudinal fins, with the exception q_f is now heat dissipation per unit length of the base perimeter $2\pi r_b$. The optimum dimensions of circular fins with variable profiles, have also been recently obtained by Zubair et. al. [44], Laor and Kalman [45], Ulmann and Kalman [46], and Unal [47].

II.) **The quest for the optimum profile.**

Schmidt [48] has shown heuristically that in order to maximize q_f in a longitudinal fin of volume V, the temperature distribution should be linear along the height of the fin. This linear temperature variation results in a parabolic profile. Later Focke [49] with the same intuitive argument obtained the same results for the pin fins. More than three decades later Duffin [50] gave a rigorous proof of the Schmidt problem assuming the heat dissipation given. We wish to emphasize here that all the above results were obtained under the Gardner-Murray

assumptions. Jany and Bejan [51] extended the Schmidt problem by altering the 5th assumption, considering k to be a function of the temperature. They proved that in this case the requirement is not the slope dT/dx to be constant but the product $k(T)dT/dx$ instead. In this case the profiles are not parabolic. Razelos and Imre [52] extended also Schmidt's problem. They changed 6th assumption, simply assuming $h=h(x)$. They examined all three types of fins. They have shown that the temperature variation must be linear for straight and annular fins but not for spines. The optimum dimensions of the Schmidt-Duffin longitudinal and pin fins are obtained as before from their parabolic profiles. Here we give the profile and the correlations for the optimum dimensions of annular fins from [52] that we have not seen in the literature.

$$\frac{y}{w}=\frac{(\beta-\xi)^2(\beta+2\xi)}{\xi(\beta-1)^2(\beta+2)} \quad \xi=r/r_o \quad profile \qquad (37a)$$

$$\beta-1=0.5\times[(9+24\times Q_r)^{1/2}-3] \qquad (37b)$$

$$w^*=\frac{hkw_{opt}}{(q_r/\Delta T)^2}=\frac{1.5}{\beta+2} \qquad (37c)$$

$$V^*=\frac{kh^2V_{opt}}{(q_r/\Delta T)^3}=\frac{0.75\times(\beta^2-1)}{(\beta+2)^2} \qquad (37d)$$

Maday [53], Gucery and Maday [54] and Snider and Kraus [55] challenged, unsuccessfully, the above optimum profiles for the three types of fins, by considering the Schmidt-Duffin problem without the LAI assumption. In the first two papers the authors have obtained a wavy optimum profile by over-specifying the boundary conditions. In the third paper the authors have based their analysis on "an apparent contradiction," which resulted in from the performance comparison between a triangular and a parabolic profile fins. However, it was pointed out in by Razelos [56] that their apparent contradiction was incorrect. This incorrect contradiction was later acknowledged by Graff and Snider in [57]. We should emphasize here that these problems are rather of academic interest and the resulting profiles, two parabolic and one hyperbolic, are impractical. They are given here for the benefit of the students, who can compare these results with those obtained using other more practical profiles.

Finally, we should add here the following remark with regard to the optimization of a given profile fin: as we depart from the constant thickness fin, to the triangular, parabolic etc., the fin is reshaped so that its height and thickness increase. This observation is verified from the results shown in Table 2, which also show that for given the heat dissipation, the volume of the fin or spine decreases. For given volume the heat dissipation increases. Evidently, these results make these profiles advantageous. However, since in these profiles the base thickness increases, the effectiveness decreases. Therefore, these fins are less effective and the number of fins that we can put on a given available area of the primary surface decreases. Hence, these advantages and disadvantages of the various profiles should be carefully examined.

CONCLUDING REMARKS

In the present work we have re-examined the basic treatment of fins that appears in the textbooks. We propose a new method for evaluating the fin's performance, which can determine directly the heat dissipation of a given fin, without any reference to the efficiency. The later gives a misleading impression since an increase of η_f results in a decrease of the heat dissipation.

For this reason we have introduced heat dissipation graphs that will replace those showing the efficiency. Attention has been drawn to the fact that emphasis must be given rather to effectiveness instead to efficiency, the former been instrumental to fin design, while the later cannot be used for this purpose. We have also introduced a total effectiveness to be used instead of the total efficiency. Furthermore, effectiveness is used to verify the validity of some of the simplifying assumptions and the conclusion that effective fins must be thermally and geometrically thin. The discussion and results presented here on the optimum fin problem will help the students to become involved with the design of extended surfaces

REFERENCES

[1] Harper, D., R., and Brown, W., B., 1922, "Mathematical Equations for Heat Conduction in the Fins in Air Cooled Engines," NACA Report, 158.

[2] Jakob, M., 1956, *Heat Transfer*, Vol I, John Wiley and Sons, New York.

[3] Gardner, K., A., 1945, "Efficiency of Extended Surfaces," Trans.of ASME Vol. 67, pp. 621-631.

[4] Murray, W., M., 1938, Heat Dissipation through an Annular Disk or Fin of Uniform Thickness, Jr. of-Applied Mechanics, Vol 5, A78.

[5] Kraus, A., D., 1988, "Analysis of Extended Surface," ASME Jr Heat Transfer, 110, pp. 1071-1081.

[6] Rohsenow, W., M., et. al., 1995, *"Handbook of Heat Transfer,"* Vol.2 Mac McGraw-Hill, New York.

[7] Huang, L., J., and Shah, R., K., 1992, "Assessment of Calculations Methods for Efficiency of Straight Fins of Rectangular Profile," Int. Jr. of Heat and Fluid Flow, Vo.13, no. 3, pp. 282-293.

[8] Fraas, A. T. and Ozisik, M. N., 1965, *Heat Exchanger Design*, John Wiley and Sons, New York.

[9] Kakaç, A., et. al., 1981, *Heat Exchanger Thermal-Hydraulic Fundamentals and Design*. Hemisphere Publishing Corp. New York.

[10] Yeh, R. H, 1996, "Optimum Dimensions of Longitudinal Rectangular Fins and Cylindrical Pin Fins with Variable Heat Transfer Coefficients." Canadian Jr. of Chem. Engr., Vol. 74, pp.144-151.

[11] White, F. M., 1984, *Heat Trnsfer*.1984, Addison-Wesley, New York..

[12] Bayazitoglou, Y. and Ozisik, M. N., 1988, *Elements of Heat Transfer*, McGraw-Hill, New York.

[13] Holman, J., P., 1990, *Heat Transfer*, McGraw-Hill, New York.

[14] Incropera, F. N. and Dewitt, D. P., 1990, *Fundamentals of Heat and Mass Transfer*, John Wiley and Sons, New York.

[15] Kreith, F., and Bohn, M., S., 1986, "*Principles of Heat Transfer,*" Harper and Row Publishers, New York.

[16] Leinhard, J., H., 1981, "*A heat Transfer Textbook,*" Prentice Hall, Inc. New Jersey.

[17] Mills, A. M., 1992, "*Heat Transfer,*" R. D. Irwin, Inc. Boston MA.

[18] Tomas, C. L., 1992, "*Heat Transfer,*" Prentice Hall, New Jersey.

[19] Bejan, A., 1993, "*Heat Transfer,*" John Wiley and Sons, New York.

[20] Krause, W. B. and Peters, A. B., 1983, "Heat Transfer from Horizontal Serrated Finned Tubes in an Air-Fluidized Bed of Uniformly Sized Particles," ASME Heat Transfer, Vol. 105, p.319.

[21] Mote, R. et. al., 1991, "The performance of a Coiled Finned-Tube Heat Exchanger in a Hot Water Store: The Effect of the Exchanger's Orientation," Appl. Energy, Vol. 38, no.1, pp.1-19.

[22] Samie, F. and Sparrow, E. M., 1986, "Heat Transfer from a Yawed Finned Tube," ASME Vol. 108. pp. 479-482.

[23] Mutlu, I. and Al-Shemmeri, T. T., 1993, "Steady-State and Transient Performance Longitudinal fin array," Int. Comm. Heat Transfer, Vol.20, pp.133-143.

[24] Karagiozis, A. et. al., 1994, "Natural Convection Heat Transfer from Arrays of Isothermal Triangular fins," ASME Jr Heat Transfer, Vol.116, pp. 105-11.

[25] Razelos, P. and Georgiou, E., 1992, "Two-Dimensional Effects and Design Criteria for Convective Extended Surfaces," Heat Transfer. Eng., Vol.13, pp.38-48.

[26] Schneider, P. J., 1955, "Conduction heat Transfer." Addison-Wesley, New York.

[27] Razelos, P., 1983, "The Optimum Dimensions of Convective Pin Fins," ASME, Heat Transfer, Vol. 105,412-413.

[28] Razelos, P. and Imre, R., 1983, "Minimum Mass of Circular Fins." ASME, Heat Transfer, Vol. 102, pp.420-425.

[29] Irey, R. K., 1968, "Errors in One-Dimensional Fin Solution." ASME Jr Heat Transfer, Vol. 80, pp. 175-176.

[30] Lau, W. and Tan, C. W., 1973, "Errors in One-Dimensional Heat Transfer Analysis in Straight and Annular Fins," ASME, Heat Transfer, Vol. 95, pp. 549-551.

[31] Aziz, A. and Nguyen, H., 1992, "Two-Dimensional Effects in a Triangular Convecting Fins, Jr. Thermophysics, Vol. 6, no. 1, pp. 165-167.

[32] Aparecido, J. B. and Cotta, R. M., 1990, "Improved One-Dimensional Fin Solution," Heat Transfer Engr., Vol. 11, no. 1, pp.49-59.

[33] Carslaw, H.S. and Jaeger J.C., 1959, "*Conduction of Heat in Solids,*" Oxford University Press, Oxford.

[34] Razelos, P. and Georgiou, E., 1994, "Errors Due to the Length of Arc Idealization in Convective Extended Surfaces," Heat Transfer. Eng. Vol.15, pp.1924.

[35] Look, Jr., D. C., 1988, "Two-Dimensional Fin Performance: B_i (top surface) $\geq B_i$ (bottom surface), ASME Heat Transfer, Vol. 110, pp. 780-782.

[36] Look, Jr., D. C., 1989, "Two-Dimensional Fin with Non-Constant root Temperature," Int. Jr. Heat and Mass Transfer, Vol.32, pp. 977-980.

[37] Razelos, P., 1982, "*Heat Transfer Notes*", The College of Staten Island, C.U.N.Y, Staten Island N.Y.

[38] Fletcher, R., 2000, "*Practical Methods of Optimization,*" John Wiley and Sons, New York.

[39] Razelos, P., 1979, "The Optimization of Longitudinal Convective Fins with Internal Heat Generation," Nucl. Eng. and Design, Vol. 54, no. 2, pp.289-299.

[40] Aziz, A., 1992, "Optimum Dimensions of Extended Surfaces Operating in a Convective Environment," Appl. Mech. Rev. Vol.45, no. 5, pp.155-173.

[41] Chung, B., T., F., and Abdallai, M., H., 1989, Optimization of Convective Longitudinal Fins of Trapezoidal Profile." Chem. Comm. Vol. 80,pp. 211-223.

[42] Razelos, P. and Satyapraksh, B. R., 1993, "Analysis and Optimization of Trapezoidal Profile Fins," ASME, Jr Heat Transfer, Vol.115, pp. 461-463.

[43] Satyaprakash Das and Razelos, P., 1997, "Optimization of Convective Circular Pin Fins," Int. Comm. Heat and Mass Transfer, Vol. 24, no.4, pp. 533-541.

[44] Zubair, S., M., et. al. 1996, "The Optimal Dimensions of Circular Fins with Variable profile and Temperature-Dependent Thermal Conductivity," Int. Jr. Heat and Mass Transfer, Vol.39, no.16,.pp.3431-3439.

[45] Laor, K., and Kalman, H., 1996, Performance and Optimum Dimensions of Different Cooling Fins with Temperature Dependent Heat Transfer Coefficient," Int. Jr. Heat and Mass Transfer, Vol.15, pp. 1003-2003.

[46] Ulmann, A., and Kalman, H., 1989, "Efficiency an Optimized Dimensions of Annular Fins of Different cross-sections, Int. Jr. Heat and mass Transfer Vol. 32 pp. 1105-1110.

[47] Unal, H., C., 1985, "Determination of the Temperature Distribution in an Extended Surface with a Non-Uniform Heat Transfer Coefficient," Int. Jr. Jeat and Mass Transfer, Vol. 28, 2279-2284.

[48] Schmidt, E., 1926, "Die Warmeubertragung durch Rippen," Z. Ver. Dt. Ing. Vol.70, pp. 885-889.

[49] Focke, R., 1946, "Die Nadel als Kuhilement," Forchung auf dem Gebitete, Ing. Vol.13, no,3 p.38.

[50] Duffin, R. J., 1959, "A variation Problem Related to Cooling Fins," Jr. Math. Mech. Vol.8, pp. 47-46.

[51] Jany, P. and Bejan, A., 1988, "Ernest Schmidt's Approach to Fin Optimization: An Extension to Fins with Variable Thermal Conductivity and the design of Ducts in Fluid Flow," Int. Jr. of Heat and fluid Flow, Vol.31, no.8, pp.1635-643.

[52] Razelos, P. and Imre, K., 1983 "Minimum Mass Convective Fins with Variable Heat Transfer Coefficients," Jr. Franklin Inst. Vol.315, no. 4, pp. 269-282.

[53] Maday, J., C., 1974, "The Minimum Weight One-Dimensional Straight Fin," ASME, Jr. of Engr. For Industry, Vol.92, pp. 461-463.

[54] Guceri, S., and Maday, J., C., 2975, "The Least Weight Circular Cooling Fins" , Jr. of Engr. For Industry, Vol.93, pp. 1190-1193.

[55] Snider, A., D., and Kraus, D., 1987, "The Quest for the Optimum Longitudinal Fin Profile," Heat Transfer Engineering, Vol. 8, pp. 19-25.

[56] Razelos, P., 1995, " The Quest for the Optimum Longitudinal Fin Profile," Heat Transfer Engineering, vol. 16, pp. 19-29.

[57] Graff, S., and Snider, A., D., 1996, "Mathematical Analysis of the Length-of-Arc Assumption," Heat Transfer Engineering, vol. 17, pp. 67-71.Put references here.

Table 1 Function D for Gardner's Fins

I. Straight Fins, profile $y/w=(1-\xi)^n$ $\xi=x/L$ $B_i=hw/k$	n
$\tanh(u)$	0
$I_{2/3}(4u/3)/I_{-1/3}(4u/3)$	½
$I_1(2u)/I_0(2u)$	1
$I_2(4u)/I_1(4u)$	3/2
$2u/(1+\sqrt{1+4u^2})$	2
II. Spines, profile $y/w=(1-\xi)^n$ $\xi=x/L$ L $B_i=2hw/k$	
$\tanh(u)$	0
$I_1(4u/3)/I_0(4u/3)$	½
$I_2(2u)/I_1(2u)$	1
$(2u/3)/(1+\sqrt{1+4u^2/9})$	2
III. Radial Fins profile $y/w=\xi^n$ $\xi=r_o/r$ $B_i=hw/k$	
$\dfrac{G_1\times K_1(u/(\beta-1))-I_1(u/(\beta-1))}{G_1\times K_0(u/\beta-1))+I_0(u/(\beta-1))}$	0 $u,.\beta$
$\dfrac{G_2\times I_{-2/3}(2u/3(\beta-1))-I_{2/3}(2u/3(\beta-1))}{I_{-1/3}(2u/3(\beta-1))-G_2\times I_{1/3}(2u/3(\beta-1))}$	1 $u,.\beta$
$\dfrac{G_3\times K_1(v)-I_1(v)}{G_3\times K_0(v)+I_0(v)}$	0 v,β
$\dfrac{G_4\times I_{-2/3}(2v/3)-I_{2/3}(2v/3)}{I_{-1/3}(2v/3)-G_4\times I_{1/3}(2v/3)}$	1 v,β
$G_1=\dfrac{I_1(u\beta/(\beta-1))}{K_1(u\beta/(\beta-1))}$, $G_2=\dfrac{I_{2/3}(2u\beta/3(\beta-1))}{I_{-2/3}(2u\beta/3(\beta-1))}$	
$G_3=\dfrac{I_1(v\beta)}{K_1(v\beta)}$, $G_4=\dfrac{I_{2/3}(2v\beta/3)}{I_{-2/3}(2v\beta/3)}$	

Table. 2 Optimum values of D, u, w^*, L^*, V^*, and η, for Gardner's fins

Longitudinal Fins wit profile $y/w=(1-x/L)^n$					
n	0	1/2	1	3/2	2
C_V	1	2/3	½	2/5	1/3
D	0.8894	0.8323	0.7773	0.7333	0.7071
u	1.4192	1.3540	1.3094	1.3218	1.4142
w^*	0.3160	0.3609	0.4138	0.4649	0.5000
L^*	0.7978	0.8139	0.8423	0.9013	1.0000
V^*	0.5043	0,3906	0.3485	0.3352	0.3333
η	0.6267	0.6147	0.5936	0.5548	0.5000

Pin Fins with profile $y/w=(1-x/L)^n$				
n	0	½	1	2
C_V	1	½	1/3	1/5
C_s	1	2/3	1/2	1/3
D	0.7256	0.6123	0.5526	0.5000
u	0.9193	1.1749	1.4322	2.0000
W^*	0.4582	0.5131	0.5494	0.5873
L^*	0.4400	0.5951	0.7505	1.0838
V^*	0.2903	0.2462	0.2373	0.2349
η	0.7893	0.7817	0.7717	0.7500

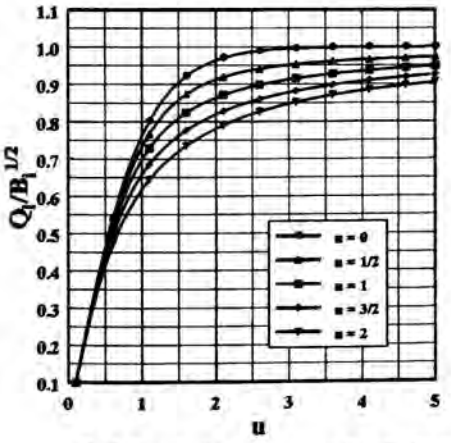

Fig.2 Heat dissipation versus u for straght fins

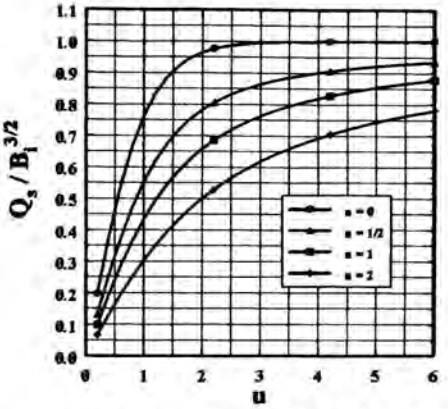

Fig.3 Heat dissipaton of spines versu u

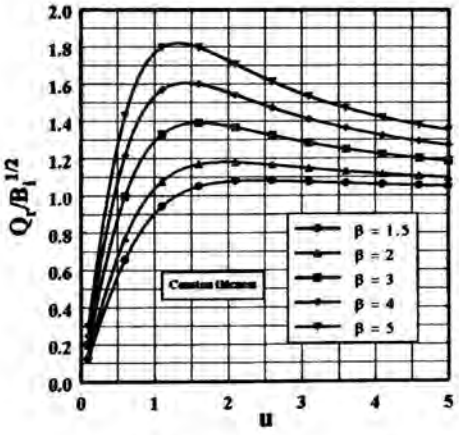

Fig.4 Heat dissipation for radial fins versus u

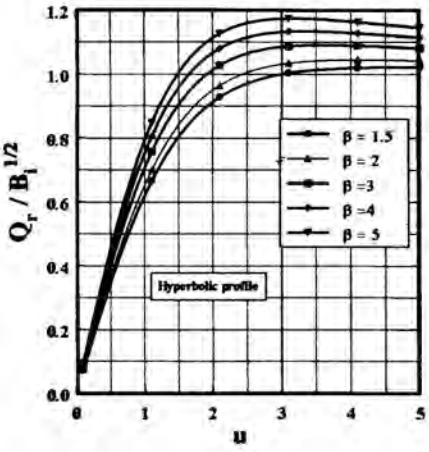

Fig.5 Heat dissipation of radial fins versus u

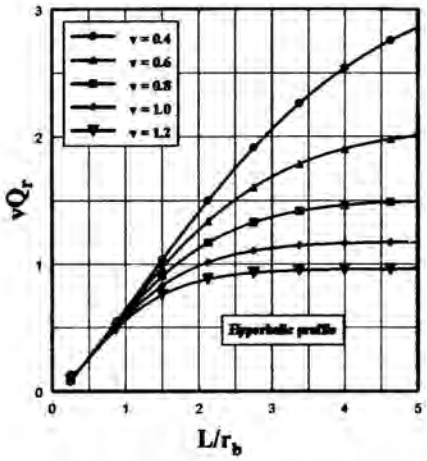

Fig.7 Heat dissipation in radial fins versus reduced lenght

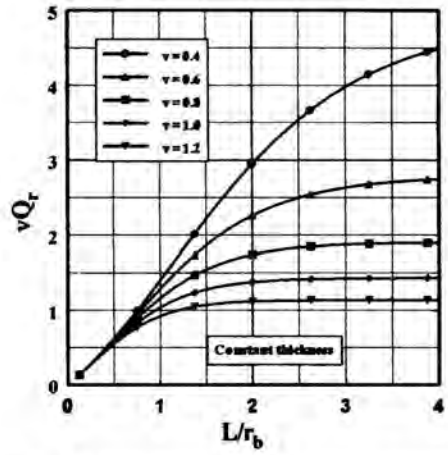

Fig.6 Heat dissipation in radial fins versus reduced height

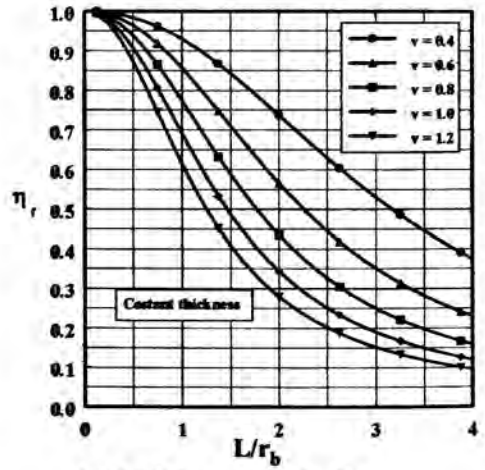

Fig.8 Efficiency of annular fin

HEFAT2002
1st International Conference on Heat Transfer, Fluid Mechanics, and Thermodynamics
8-10 April 2002, Kruger Park, South Africa
YT1

THE EXPERIMENTAL RESEARCH ON STRUCTURE OPTIMIZATION OF THE TWISTED STRIPS WITH HOLES FOR ENHANCING HEAT TRANSFER AND SELF-CLEANING THE FOULING OF HEAT EXCHANGERS

T.L Yu*, D.Q Peng*, T.X Yu*, SH.Q Jiang**, G.Y Liu**, Y.P Liu**, X.M Yu***
*M. Eng. lecturer; **Associate Professor; ***Professor
Zhuzhou Institute of Technology,
Zhuzhou, Hunan Province, 412008,
China,
Email: shuaike_zz@hotmail.com tianlan_yu@263.net

ABSTRACT

The fouling makes water coolers efficiency is reduced by average 50% in China. The structural principle of self-cleaning fouling and enhancing heat transfer with the twisted tapes is that the tape inserted in each heat transfer pipe can self-rotate stably, scrape and hit the pipe inner wall at random just by the action of the flowing fluid, thus the dual purposes mentioned above are achieved. This paper researches the structure optimization of the twisted tapes with holes. The experimental results show that when Re is less than 25,000, the enhancement ranges from 2% to 18% and then it goes down as Re increases; when the hole ratio y is less than 18%, there is a monotonously upward trend for the resistance coefficient λ. But when y exceeds 18%, λ will be reduced monotonously. For those tapes, whose the hole ratio y is 45.7%, the comprehensive performance is the best.

FOREWORD

The literature [1] specially about the fouling says that the fouling makes water coolers efficiency is reduced by average 50% in China. The fouling has such a serious influence on the heat exchangers efficiency that the equipment, operation and clean costs increase greatly and the product equality decreases notably. According to the literature [2], the economic loss reaches $8—10 billion every year caused by the fouling of heat exchangers just in USA.

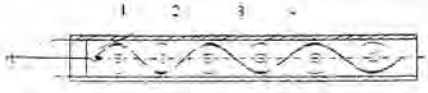

1. axle 2 bearing 3.heat transfer pipe 4.twisted strips
Fig 1:continuous self-clean principle

The structural principle of the on-line self-cleaning technology with the self-rotation twisted tapes is showed as Fig.1. The twisted tape, inserted in each heat transfer pipe, can self-rotate continuously and stably driven by the flowing fluid. Meanwhile it scrapes and hits the pipe inner wall continuously; thus the dual aims are achieved of preventing fouling and enhancing heat transfer.

This paper researches the structural optimization of the new self-cleaning twisted tape, which can be widely used.

THE STRUCTURAL OPTIMIZATION PRINCIPLES OF THE TWISTED TAPE

The literature [3] emphasizes that the fouling on the heat transfer surfaces can make any efforts to enhance heat transfer in vain. So far as the measure to save energy is concerned, the main focus is to prevent and clean off the fouling. Therefore, the first optimization principle is to keep the heat transfer surfaces clean. According to the basic principle, the research lays the emphasis on the structural optimization of the twisted tape with holes. The cleaning performance of the tape with holes is better than that without holes because the tape with holes is more flexible than that without holes.

The secondary principle is to enhance heat transfer and reduce the flowing resistance. When Re is low, the former is more important. However when the flowing velocity is high, the latter is more important. The holes, distributed well along the centerline of the twisted tape, provide certain space of straight flow for the flowing fluid. Thus, the spirally flowing speed of the fluid near the inner wall will be reduced. So, it helps reduce the flowing resistance, but it is

disadvantageous to enhance heat transfer. On the other hand, the separation of the throttle boundary layer near the holes and the agitation of the holes bridges strengthen the flowing turbulence of the fluid. Especially, that the boundary layer is disturbed enhances the convection heat transfer inside pipes, but it increases the flowing resistance. Which is the controlling factor between the positive and negative factors? This is a very complicated problem. For this reason, the experiments of heat transfer and resistance characteristics were conducted to optimize the structure of the twisted tapes with holes.

THE SYSTEM AND METHOD OF THE OPTIMIZATION EXPERIMENTS

The experiments system is showed as Fig.2. Cooling water flows through the brass heat transfer pipe (Φ20mm×1mm). The flowing velocity is measured with the rotation flowmeter. The steam flows in the casing pipe, which is generated by the steamer (40KW). The temperature of water and steam is measured with the precision thermometer, whose minimum graduation is 0.1℃. The flowing resistance is measured with the differential manometer (D022P3MB3). The common structural parameters of the experimental twisted tapes are that the length is 2000mm and the spiral pitch (H) is 188mm. At the low Re, the main purpose is to enhance heat transfer so the twisted tapes with little holes are selected. At the high flowing velocity, the main purpose is to avoid the large flowing resistance, so the twisted tapes with big holes are selected. All the holes are distributed well along the central line. The structure parameters of all the tapes are showed as table 1. In this table, the hole ratio y is all the holes area A_1 to the whole tape area A, that is to say $y=(A_1/A)\times 100\%$. Furthermore, when there is no tape in the pipe, it is assumed that there is a fictitious tape whose y is 100%. After the flowing velocity of cooling water exceeds 0.8m/s, all the twisted tapes with various holes begin to self-rotate.

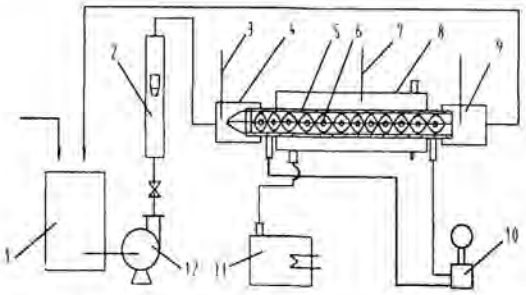

1.cistern 2.rotation flowmeter 3. thermometer
4.inlet end 5.heat transfer pipe 6.twisted strip
7.thermometer 8.shell 9.outlet end
10.differential manometer 11. steamer 12. pump

Fig.2: the optimization experiments system

Table 1: the structure parameters of the twisted tapes

twisted tapes	dimensions of the hole	y (%)
1#	no holes	0
2#	d=8mm, l=H/2	4.33
3#	d=8mm, l=H/4	8.66
4#	d=8mm, l=H/8	17.3
5#	The former 2 adjacent holes become a hole every 4 adjacent holes on the basis of the tape no.4.	26.8
6#	The former 3 adjacent holes become a hole every 4 adjacent holes on the basis of the tape no.4.	36.3
7#	The former 4 adjacent holes become a hole every 8 adjacent holes on the basis of the tape no.4	45.7

THE RESULTS AND ANALYSES OF THE EXPERIMENTS

Experiments of the Flowing Resistance Characteristics

The cooling water flows spirally led by the twister tape. The complicated flow is compound motion composed of forced vortexes and axial flow. Meanwhile the complicated second vortex flow will be induced. The existence of the twisted tapes reduces the flowing space of fluid and increases the flowing velocity. Furthermore, the flowing resistance will be increased by many factors such as the forced vortexes, the second vortex flow, the boundary layer being disturbed by the twisted tape, the throttle agitation caused by the holes, the central area of turbulent flow being agitated by the holes bridges. On the other hand, the holes help reduce the flowing resistance because they provide certain space of straight flow for the fluid. Therefore, the final effect of the tapes on the flowing resistance characteristics mainly depends on which the controlling factors are. The resistance experiment results are plotted in Fig 3 and Fig 4. The flowing resistance with the little holes tapes is larger than that without any holes, and the flowing resistance will be increased as the ratio y

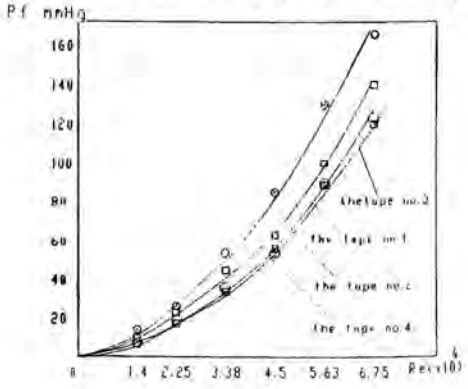

Fig.3: the Re-P_f curve

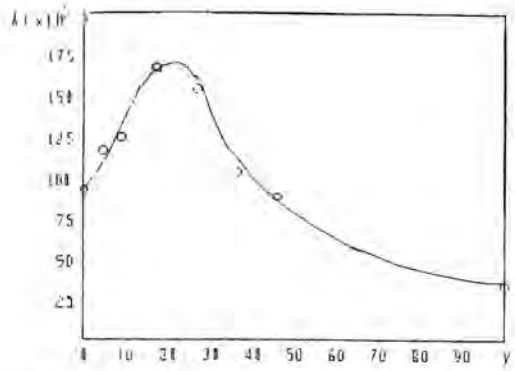

Fig.4: the y-□urve at the flowing velocity 1.5m/s

rises It can be inferred that firstly the inner vortexes resistance increase, caused by the holes bridges agitation, are the main factor which leads to the flowing resistance increase, when the ratio y is little; secondly when the y reaches a certain magnitude(18%), the resistance will be the maximum; and then when the y rises continuously, the increase in the straight flow area becomes the main factor and meanwhile the resistance begins to reduce; finally when the y reaches about 40%, the coefficient λ of friction resistance of the tapes with holes is nearly equal to that of those without holes.

The Experiment and Analyses of Heat Transfer Enhancement

The principles of heat transfer enhancement of the self-rotating twisted tapes is that firstly the tapes motion makes the fluid rotate near the pipe inner wall and the fluid flow becomes more turbulent there, secondly the boundary layer is disturbed directly by the rotating and scraping of the tapes. Furthermore, because of the holes, that the central area of turbulent flow is agitated enhances the heat and mass transfer notably in the pipe central area. As the ratio y increases, such agitation is strengthened firstly, and then weakened. So, for the heat transfer enhancement, there is also correspondingly firstly an upward, and then a downward trend. The experimental results of heat transfer enhancement are plotted as Fig.5. The experiment indicates that heat transfer can be enhanced markedly whether the twisted tape has holes or not and the coefficient K of heat transfer rises as the flowing velocity increases for the same kind tape.

When the flowing velocity exceeds certain magnitude, there is a downward trend for the heat transfer coefficient K. The reason may be that the condensing liquid film becomes thicker as the flowing velocity increases. The increase in K caused by the increase in the velocity can not counteract the decrease in K caused by the increase in the film thickness, so the coefficients K will be reduced inevitably.

To compare the different structures of the tapes ratio y

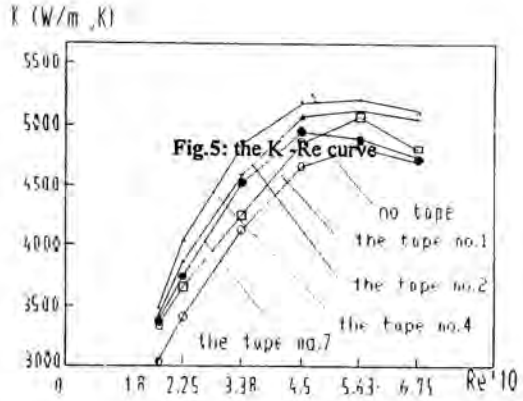

Fig.5: the K -Re curve

Fig.5: the Re-K curve

holes, when the ratio y is within certain extent, as the ratio y increases, the K will be increased because the fluid turbulence is strengthened by the agitation of the holes bridges. After the ratio y exceeds the extent, there will be a monotonously downward trend for the coefficient K as the ratio increases monotonously because the action of the hole bridges agitation is weakened. The experimental data of the ratio K'/K are showed as table 2 when the flowing velocity is 1.5m/s. K' is the overall heat transfer coefficient with the twisted tapes and K is the overall heat transfer coefficient without any tape.

Table 2: the K increase (K'/K)

twisted strips No.	1	2	3	4	5	6	7
K'/K	1.05	1.114	1.132	1.173	1.157	1.146	1.113

By comparison at the different flow velocity, it is evident that the effect of heat transfer enhancement is different for the twisted tapes of various holes structure. At the low velocity, the enhancement is great, while at the high velocity the enhancement is little. The main reason is that the twisted tapes motion can improve the fluid turbulence at low flowing velocity, and then enhance heat transfer effectively, but the turbulence has been developed nearly completely at high velocity, so the enhancement of convection heat transfer is not so great. The ranges of heat transfer enhance-

Table 3: the ranges of K'/K at different flowing velocity

Flowing velocity (m/s)	0.8	1.0	1.5	2.0	2.5	3.0
K'/K	1.097 □ 1.15	1.07 □ 1.185	1.05 □ 1.173	1.04 □ 1.113	1.02 □ 1.08	1.014 □ 1.06

ment are showed as table 3 by using the tapes at different flowing velocity.

The Comprehensive Performances of the Twisted Tapes with Holes

The flowing resistance rises markedly while the twisted tapes enhance heat transfer, and the flowing resistance

$$\xi = \frac{K'/K}{\lambda'/\lambda}$$

coefficient□ises rapidly as the heat transfer coefficient K increases. Therefore, to optimize the hole ratio y of the twisted tape, the parameter □ of comprehensive performances, which includes enhancing heat transfer and reducing the flowing resistance, must be given the first consider. It is showed as Table 4 as following at the flowing velocity of 1.5m/s. It is quite evident that the hole structure of the twisted tape no.7 is better than any other.

Table 4 : the □f the twisted tapes of the different ratio y

the No. of the twisted tapes	1	2	3	4	5	6	7
□	0.38	0.32	0.30	0.24	0.26	0.37	0.49

CONCLUSION

(1) When the ratio y is less than 18%, the coefficient λ of friction resistance will goes up monotonously as y increases. However, when y is more than 18%, the coefficient λ will go down monotonously as y increases. So, the twisted tapes of great y are selected on the conditions of high flowing velocity.

(2) For the hole ratio y effect on heat transfer enhancement, the K firstly increases and then decreases as the y increases. It varies with the hole structure and flowing velocity. The enhancement ranges from 2% to 18%. So, the twisted tapes with holes are relatively suitable on the conditions of the intermediate and little Re.

(3) By optimizing the parameter□f comprehensive performance, it is indicated that the ratio y of the twisted tape no.7 is the optimum, i.e. y=0.49 .

(4) Because the flowing resistance of the self-cleaning twisted tape is relatively great, the self-cleaning twisted tapes are suitable on the conditions of the intermediate and low flowing velocity. (For instance, the flowing velocity less than 2.0 m/s is appropriate for the heat transfer pipe Φ20mm×1mm.)

(5) For the twisted tape, whose y is larger than 0.49, the physical structure actually becomes gradually twin spiral tapes [5]. So, the research on such tapes is actually on the heat transfer enhancement of the helical line, which has been researched a lot currently. For the plastic helical line, there are many new problems such as the cleaning rigidity.

REFERENCES

[1] D.Y Yu, 1988, "The Research and Industrial Development of Heat Exchangers in China", The Report Specially on the Fouling from Petroleum Machinery Institute in Lanzhou, pp.3

[2] Garret-Price, B.A., etc., "The Cost of Heat Exchangers, Characteristics, Cost, Prevention, Control and Removal", Noyes Publications, Park Ridge, NJ. 1985

[3] 1987, "The Corpus of the Practical technologies of saving energy" (Chinese translated from Japanese), Chemical Industry Publishing House, pp87

[4] Z.H Lin, 1987, "Heat Transfer Enhancement and Engineering Application", Mechanical Industry Publishing House, Beijing.

[5] SU1788424-A

NONMENCLATURE

A the whole tape area (m^2)
A_1 all the holes area of a tape (m^2)
d the diameter of a hole (mm)
H the spiral pitch (mm)
l the distance between two adjacent holes (mm)
K the overall heat transfer coefficient of the twisted tape without any tape ($w/m^2.k$)
K' the overall heat transfer coefficient of the twisted tape with tapes ($w/m^2.k$)
P_f the flowing resistance (mmHg)
Re the Reynolds number
y the hole ratio of A_1 to A
□ the flowing resistance coefficient of the twisted tape without any tape
□ the flowing resistance coefficient of the twisted tape with tapes

HEFAT 2002
1st International Conference on Heat Transfer, Fluid Mechanics, and Thermodynamics
8-10 April 2002, Kruger Park, South Africa
ZV1

COMPOUND HEAT TRANSFER AUGMENTATION BY A COMBINATION OF SPIRALLY CORRUGATED TUBES WITH A TWISTED TAPE

V. D. Zimparov and V. M. Petkov
Department of Mechanical Engineering
Gabrovo Technical University
4, Hadji Dimitar, St.
5300 Gabrovo
Bulgaria
E-mail: vdzim@tugab.bg

ABSTRACT

Heat transfer and isothermal friction pressure drop results have been obtained experimentally for two single start spirally corrugated tubes combined with five twisted tape inserts with different relative pitch in the range of Reynolds number $4\times10^3 - 6\times10^4$. The characteristic parameters of the tubes are: height to diameter ratio $e/D_i = 0.0224$ and 0.0451 and relative pitch $H/D_i = 7.7, 6.25, 3.95, 2.95, 2.4$. Extended performance evaluation criteria equations for enhanced heat transfer surfaces have been used to assess the multiplicative effect. Thermodynamic optimum can be defined by minimizing the entropy generation number compared with the relative increase of heat transfer rate or relative reduction of heat transfer area.

INTRODUCTION

Many different methods have been considered for increasing the rate of heat transfer in forced convection while reducing the size of the heat exchanger and effecting energy savings [1]. Surface methods include any techniques which directly involve the heat exchanger surface. They are used on the side of the surface that comes into contact with a fluid of low heat transfer coefficient in order to reduce the thickness of the boundary layer and to introduce better fluid mixing. The primary mechanisms for thinning the boundary layer are increased stream velocity and turbulent mixing. Secondary recirculation flows can further enhance convective heat transfer. Flows from the core to the wall reduce the thickness of the boundary layer and the secondary flows from the wall to the core promote mixing. Flow separation and reattachment within the flow channel also contribute to heat transfer enhancement.

Some of the existing methods for enhancing heat transfer in a single-phase, fully developed turbulent flow in a round tube are one of the two types: a) methods in which the inner surface of the tube is roughened, e.g., with repeated or helical ribbing, by sanding or with internal fins, and b) methods in which a heat transfer promoter, e.g., a twisted tape, disk or streamlined shape, is inserted into the tube.

It is well known that two or more of the existing techniques can be utilized simultaneously to produce an enhancement larger than that produced by only one technique. The combination of different techniques acting simultaneously is known as compound augmentation. Interactions between different augmentation methods contribute to greater values of the heat transfer coefficients compared to the sum of the corresponding values for the individual techniques used alone. Preliminary studies in compound passive augmentation techniques are encouraging. Earlier investigations are: rough tube wall with twisted tape inserts Bergles et al. [2] and grooved rough tube with twisted tape Usui et al.[3].

The latest publications of Zimparov [4, 5] have revealed that a combination of a corrugated tube with a twisted tape would be superior to either combination of passive surface techniques.

NOMENCLATURE

e	ridge height (m)
h	heat transfer coefficient (W/m^{2}K)
N_t	number of tubes
P	pumping power (W)
p	pitch of ridging (m)
U	overall heat transfer coefficient (W/m^{2}K)
W	mass flow rate in heat exchanger (kg/s)

Greek symbols

β	helix angle of rib (deg)
ϑ	temperature difference between wall and fluid, $T_w - T$ (K)

Dimensionless groups

A_*	dimensionless heat transfer surface, A_R / A_S

$B = \frac{4St_S}{D_S} L_S$

D_* dimensionless tube diameter, D_R / D_S

f Fanning friction factor, $2\tau_w / (\rho u_m^2)$

L_* dimensionless tube length, L_R / L_S

N_S augmentation entropy generation number

N_* ratio of number of tubes, $N_{t,R} / N_{t,S}$

Pr Prandtl number, $\mu c_p / k_f$

P_* dimensionless pumping power, P_R / P_S

Q_* dimensionless heat transfer rate, $\dot{Q}_R / \dot{Q}_S$

Re Reynolds number, $\rho u_m D / \mu$

St Stanton number, $h_i / (\rho u_m c_p)$

ΔT_i^* dimensionless inlet temperature difference between hot and cold streams, $\Delta T_{i,R} / \Delta T_{i,S}$

$u_{m,*}$ dimensionless flow velocity, $u_{m,R} / u_{m,S}$

W_* dimensionless mass flow rate, W_R / W_S

β_* $\beta / 90$

ε_* ratio of heat exchanger effectiveness, $\varepsilon_R / \varepsilon_S$

ϕ_0 irreversibility distribution ratio

Subscripts

i inside, or value at $x = 0$

m mean value

R rough tube

S smooth tube

o outside, or value at $x = L$

EXPERIMENTAL PROGRAM

In the present experimental program two single start spirally corrugated tubes of varying geometries combined with five twisted tapes with different pitches have been studied. The smooth tube had an inside diameter of 16.0 mm with wall thickness of 1.0 mm before rolling operation. A smooth tube was used for standardizing the experimental set-up and for comparing the enhancement in heat transfer and fluid friction. The characteristic parameters – pitch of corrugation p, height of corrugation e, spiral angle β and dimensionless parameters e/D_i, p/e, β_*, are presented in Table 1 and Fig.1.

Table 1 Geometrical parameters of the tubes

	D_i	e	p	β	e/D_i	p/e	β_*
	mm	mm	mm	deg	-	-	-
3010	13.90	0.312	5.76	82.4	0.0224	18.5	0.916
3050	13.15	0.593	5.06	83.0	0.0451	8.5	0.922

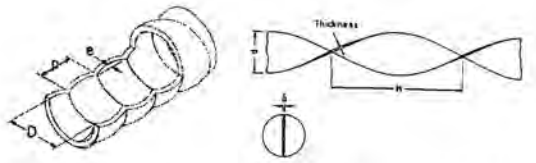

Figure 1: Characteristic parameters of the corrugated tube and the twisted tape

The twisted tape comprised a heat treated brass tape, 0.8 mm thick and 12.5 mm wide. With the length of the tape in 180° twist defined as H, five different tapes were used: $H/D_i = 7.7$ (tubes 3011 and 3051); 6.25 (tubes 3012 and 3052); 3.95 (tubes 3013 and 3053); 2.95 (tubes 3014 and 3054); and 2.4 (tubes 3015 and 3055).

Full details of the experimental set-up consisting of two heat transfer tubes 1200 mm long in a conventional recirculating system can be found in Zimparov et al. [6]. The pressure difference across the heat transfer section was measured and friction factors were calculated. The heating section was heated by condensing steam generated into a boiler. The flow rate of the test fluid, the tube wall temperatures, inlet and outlet water temperatures and the temperature of the saturated steam were measured. The bulk temperature of the water ranged from 54 to 92°C and the corresponding variation of the Prandtl number was 2.9-1.9.

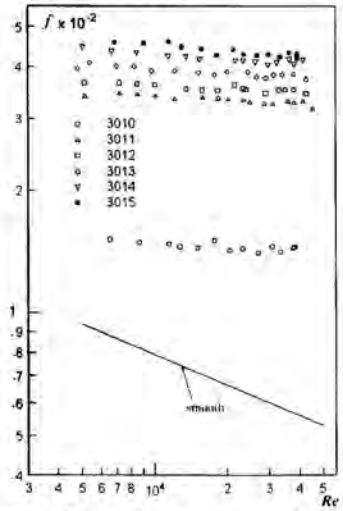

Figure 2: Friction factor vs Reynolds number

RESULTS AND DISCUSSION

The isothermal pressure drop studies were conducted at different temperatures of the water in the range from 50 to 90°C in all tubes over a range of Reynolds number $4 \times 10^3 < Re < 6 \times 10^4$. As expected, the turbulent flow friction factors f_R were significantly higher than those in the smooth

tube f_s under the same operating conditions Figs.2-3. A characteristic feature of the flow is that even at high flow rates, the friction factor continues to decrease with the increase of Re although not so rapidly as in the smooth tube. The isothermal friction factors for straight flow and swirl flow in the corrugated tubes increase when the relative pitch H/D_i decreases.

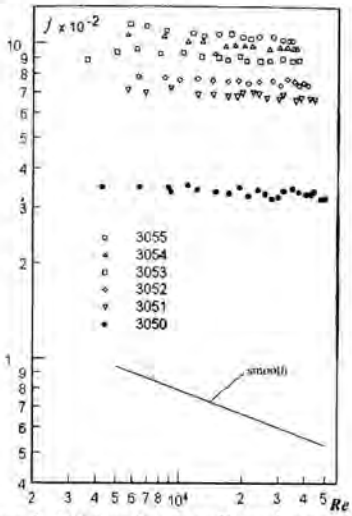

Figure 3: Friction factor vs Reynolds number

The values for e/D_i in the range of Re studied are as follows: for tubes №3010–3015- $f_R/f_S = 1.6-2.8$ (3010); 3.6-6.3 (3011); 3.9 – 6.8 (3012); 4.3-7.4 (3013); 4.7 - 7.8 (3014); 4.9-8.2 (3015) and for tubes №3050-3055- $f_R/f_S = 3.5-6.5$ (3050); 7.2-13.1 (3051); 8.0 - 14.8 (3052); 9.5-17.1 (3053); 11.0-18.1 (3054); 11.5 - 19.5 (3055).

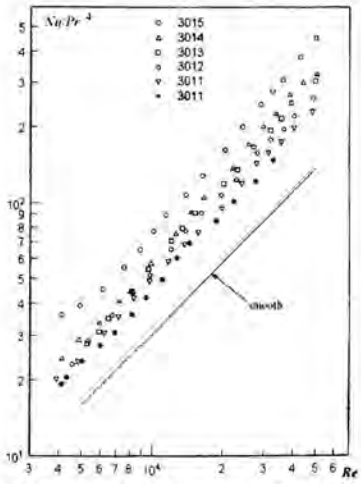

Figure 4: Heat transfer coefficient vs Reynolds number

Heat transfer studies in single-start spirally corrugated tubes were carried out to obtain values for the water side heat transfer coefficients h_i and the steam condensing coefficients h_o. Since the metal wall temperatures were measured, the individual film coefficients were determined. Figs. 4-5 show the heat transfer data in the form $Nu_i Pr^{-0.4}$ as a function of the Reynolds number Re, a counterpart of the friction factor data shown on Figs. 2-3.

As can be seen the water side heat transfer coefficients are particularly high when the height to diameter ratio e/D_i increases and the relative pitch H/D_i decreases.

The values for Nu_R/Nu_S in the range of Re studied are as follows: for tubes №3010 – 3015 - $Nu_R/Nu_S = 1.45-1.63$ (3010), .56-1.80 (3011), 1.68 – 2.06 (3012), 1.66-2.35 (3013); 1.79 – 2.54 (3014); 2.40-3.17 (3015) and for tubes №3050-3055 - $Nu_R/Nu_S = 2.50-2.95$ (3050); 3.10-4.20 (3051); 3.30 –4.60 (3052); 3.80-5.60 (3053); 4.00-6.50 (3054); 4.20-7.50 (3055).

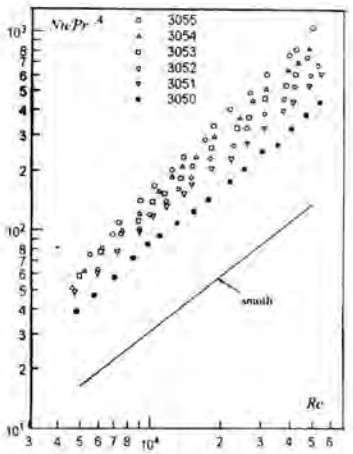

Figure 5: Heat transfer coefficient vs Reynolds number

PERFORMANCE EVALUATION

On the basis of the first law analysis several authors, e.g. Bergles et al. [7] and Webb [8] have proposed performance evaluation criteria (PEC) which define the performance benefits of an exchanger having enhanced surfaces, relative to a standard exchanger with smooth surfaces subject to various design constraints. On the other hand it is well established that the minimization of the entropy generation in any process leads to the conservation of useful energy. A solid thermodynamic basis to evaluate the merit of augmentation techniques by second law analysis has been proposed by Bejan [9, 10] developing the entropy generation minimization (EGM) method also known as "thermodynamic optimization". Extended PEC equations including the fluid temperature variation along the heat transfer passage for heat transfer from ducts with constant wall

temperature have been developed by Zimparov [11]. These PEC equations have been used to assess the multiplicative effect of a corrugated tube combined with a twisted tape. The equations originate from various design constraints and generalize the performance evaluation criteria (PEC) for enhanced heat transfer techniques obtained by means of first law analysis.

The equations are developed for tubes with different diameters and heat transfer and friction factors based on the presentation format of performance data for enhanced tubes Marner et al. [12]. The relative equations for single-phase flow inside enhanced tubes are:

$$A_* = N_* L_* D_* \tag{1}$$

$$P_* = W_* \Delta p_* = f_R / f_S D_* L_* N_* u_{m,*}^3 = \frac{W_*^3 L_*}{N_*^2 D_*^5} f_R / f_S \tag{2}$$

$$Q_* = W_* \varepsilon_* \Delta T_i^* \tag{3}$$

$$W_* = u_{m,*} D_*^2 N_* = \frac{Re_R}{Re_S} D_* N_* \tag{4}$$

$$\Delta p_* = f_R / f_S \frac{L_*}{D_*} u_{m,*}^2 = f_R / f_S \frac{L_*}{D_*^3} \frac{Re_R^2}{Re_S^2} \tag{5}$$

$$\frac{(UA)_{i,R}}{(UA)_{i,S}} = \frac{1 + R_S}{\frac{St_S}{St_R}\left(f_R / f_S P_*^{-1} A_*^{-2}\right)^{1/3} + R_R A_*^{-1}} \tag{6}$$

where R_S and R_R are the different thermal resistances on both sides of the tube wall.

The effect of the thermal resistance external to the surface is also taken into consideration by including external heat transfer coefficient $h_{o,S}$. The analysis includes the possibility that the augmented exchanger may have an enhanced outer tube surface $E_{ii} = h_{o,R} / h_{o,S}$. The fouling resistances on both sides of the tube wall are neglected.

The heat transfer efficiency of the investigated tubes has been evaluated for the following cases:

Fixed geometry criteria (FG)

These criteria involve a one-for-one replacement of smooth tubes by augmented ones of the same basic geometry, e.g., tube envelope diameter, tube length and number of tubes for in-tube flow. The *FG*-1 cases [7, 8] seek increased heat duty or overall conductance *UA* for constant exchanger flow rate. The pumping power of the enhanced tube exchanger will increase due to the increased fluid friction characteristics of the augmented surface. For these cases the constraints $\Delta T_i^* = 1$, $W_* = 1$, $N_* = 1$ and $L_* = 1$ require $P_* > 1$.

When the objective is increased heat duty $Q_* > 1$, this corresponds to the case *FG*-1a, [7, 8]. In this case, the heat duty of the unit with spirally corrugated tubes combined with a twisted tape increases significantly, approaching the values of the order of 1.76 (for tube 3015), and 2.17 (for tube 3055), whereas the unit with spirally corrugated tubes alone attains values of $Q_* = 1.42 - 1.79$.

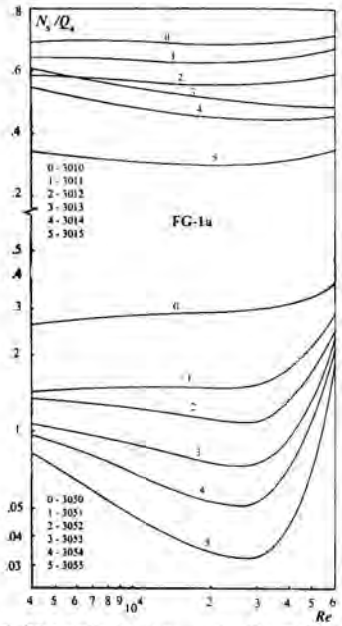

Figure 6: The ratio N_S / Q_* vs the Reynolds number

The augmentation entropy generation number N_S, given by Zimparov [11] is

$$N_S = \frac{1}{1+\phi_o}\left\{Q_* \exp\left[B\left(1 - \frac{St_R}{St_S} D_*^{-0.8}\right)\right]\left[\frac{T_{i,S}}{T_{o,S}} + Q_*\left(1 - \frac{T_{i,S}}{T_{o,S}}\right)\right]^{-1} + \phi_o \frac{f_R / f_S}{D_*^{4.75}}\right\} = f\left(Re_R\right). \tag{7}$$

All the tubes reduce the entropy generation evaluated through the number N_S. The minimum values of N_S for the corrugated tubes applied alone are 0.9 (for tube 3010) and 0.44 (for tube 3050). When the compound enhancement technique of this kind is applied this minimum values of N_S approach 0.52 (for tube 3015) and 0.07 (for tube 3055) The *FG*-2 [7, 8] criteria have the same objectives as *FG*-1, but require that the augmented tube unit should operate at the same pumping power as the reference smooth tube unit. The pumping power is maintained constant by reducing the tube-side velocity and thus the exchanger flow rate. The constraints are: $N_* = 1$, $L_* = 1$ and $P_* = 1$ requiring $W_* < 1$ and $Re_R < Re_S$. In the case *FG*-2a the goal is increased heat transfer rate $Q_* > 1$. For this case, the corrugated tubes alone 3010 and 3050 have the greatest values of $Q_* = 1.12 - 1.18$, whereas all the combinations of corrugated tubes and twisted tape inserts have the values of Q_* lower than those.

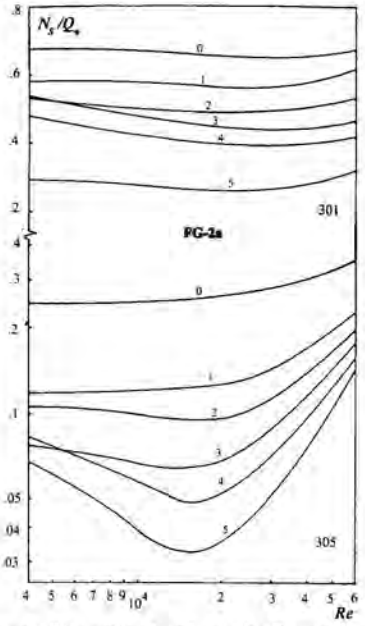

Figure 7: The ratio N_S/Q_* vs the Reynolds number

The augmentation entropy generation number N_S [11] is

$$N_S = \frac{1}{1+\phi_o}\left\{Q_* \exp\left[B\left(1-\frac{St_R}{St_S}D_*^{-1.145}\left(f_R/f_S\right)^{0.073}\right)\right]\right.$$

$$\left.\times\left[\frac{T_{i,S}}{T_{o,S}}+Q_*\left(f_R/f_S\right)^{0.364}D_*^{-1.727}\left(1-\frac{T_{i,S}}{T_{o,S}}\right)\right]^{-1}+\phi_o\right\}=f\left(Re_R\right) \quad (8)$$

Despite of the fact that the goal imposed by the first law, $Q_* > 1$ has not been always achieved, the entropy generation number is substantially diminished. The values of the N_S reach 0.74-0.26 for corrugated tube alone and attains 0.29-0.03 for the compound enhancement technique.

Variable geometry criteria (VG)

In most cases a heat exchanger is designed for a required thermal duty with a specified flow rate. Since the tube-side velocity must be reduced to accommodate the higher friction characteristics of the augmented surface, it is necessary to increase the flow area to maintain $W_* = 1$ and permit the exchanger flow frontal area to vary in order to meet the pumping power constraint: $N_* > 1$; $L_* < 1$; $Re_R < Re_S$. In the case VG-1 [7,8] the objective is to reduce surface area $A_* < 1$ with $W_* = 1$ for $Q_* = P_* = 1$. In this case the reduction of heat transfer area is 30-50% when the corrugated tubes are used alone and 37-53% when they are combined with a twisted tape.

The entropy generation number is calculated from [11].

$$N_S = \frac{1}{1+\phi_o}\left\{\left(\frac{f_R}{f_S}A_*\right)^{-0.364}D_*^{2.091}\right. \quad (9)$$

$$\left.\times\exp\left[B\left(1-\frac{St_R}{St_S}\left(f_R/f_S\right)^{-0.291}A_*^{0.709}D_*^{-0.127}\right)\right]+\phi_o\right\}=f\left(Re_R\right)$$

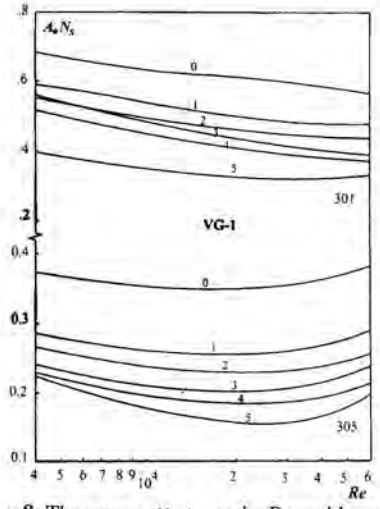

Figure 8: The group $N_S A_*$ vs the Reynolds number

The reduction of the entropy generation is also significant, $N_S = 0.80$-0.49 for the corrugated tubes alone and $N_S = 0.50$-0.31 for the compound enhancement technique.

The cases *VG*-2 [7, 8] aim at increased thermal performance ($U_R A_R / U_S A_S$ or $Q_* > 1$) for $A_* = 1$ and $P_* = 1$. They are similar to the cases *FG*-2. When the objective is $Q_* > 1$, case *VG*-2a [7, 8], an additional constraint is $\Delta T_i^* = 1$. The last case considered is *VG*-2a where the objective is increased heat rate $Q_* > 1$ for $W_* = 1$ and $A_* = P_* = 1$. When the unit is furnished with corrugated tubes alone $Q_* = 1.28-1.42$. When a combination with a twisted tape is used the values of Q_* reach 1.40-1.60. The values of N_S are calculated following [11].

$$N_S = \frac{1}{1+\phi_o}\left\{Q_*\left(\frac{f_R}{f_S}\right)^{-0.364}D_*^{2.091}\right.$$

$$\times\exp\left[B\left(1-\frac{St_R}{St_S}\left(f_R/f_S\right)^{-0.291}D_*^{-0.127}\right)\right]$$

$$\left.\times\left[\frac{T_{i,S}}{T_{o,S}}+Q_*\left(1-\frac{T_{i,S}}{T_{o,S}}\right)\right]^{-1}+\phi_o\right\}=f\left(Re_R\right), \quad (10)$$

and the values are as follows: 0.78-0.48 for corrugated tubes alone and 0.46-0.22 for a compound enhancement technique.

The results discussed imply that the evaluation and comparison of the heat transfer augmentation techniques should be made on the basis of both first and second law analysis. Thus it is possible to determine the thermodynamic optimum in a heat exchanger by minimizing the augmentation entropy generation number compared with the relative increase of heat transfer rate $Q_* > 1$, or relative reduction of heat transfer area $A_* < 1$ or pumping power $P_* < 1$. Consequently, a ratio N_S / Q_* and a group $N_S A_* = f(Re_R)$ might be defined to connect the two objectives pursued by the first and second law analysis and as a basis for thermodynamic optimization.

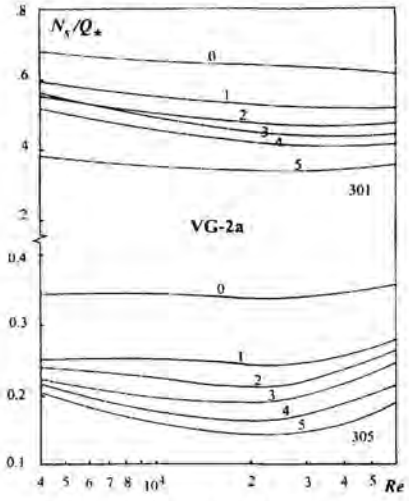

Figure 9: The ratio N_S / Q_* vs the Reynolds number

Figures 6, 7 and 9 show $N_S / Q_* = f(Re_R)$ for the cases FG-1a, FG-2a, VG-2a and Fig. 8 shows $N_S A_* = f(Re_R)$ for the case VG-1. For all the cases considered the best performance have one and the same tube – 3055 being far superior to others. Therefore, the analysis using new performance evaluation criteria shows that an optimum rib height-to-diameter ratio (e/D_i) and relative pitch H/D_i can be obtained for this kind of compound heat transfer enhancement.

CONCLUSIONS

The use of corrugated tube in conjunction with twisted tape is proposed as method of enhancing heat transfer in single-phase turbulent flow. It has been shown experimentally that the heat transfer is enhanced very considerably when the roughness of the corrugated tube has a certain value ($e/D_i = 0.0451$) and the relative pitch H/D_i decreases.

Extended performance evaluation criteria have been used to assess the benefits of replacing the smooth tubes with spirally corrugated tubes combined with twisted tape inserts.An additional increase of the heat transfer rate or reduction of heat transfer area up to 15% and more can be achieved by an appropriate combination of corrugated tube with twisted tape. The reduction of the entropy generation is also significant. The results discussed imply that the evaluation and comparison of the heat transfer augmentation techniques should be made on the basis of both first and second law analysis.

It is expected that further research will reveal that the method will also produce higher heat transfer efficiencies in condensing systems and single–phase heat transfer as well.

REFERENCES

[1] Webb, R. L., 1994, "Principals of Enhanced Heat Transfer", John Wiley & Sons.

[2] Bergles, A. E., Lee, R. A. and Mikic, B. B., 1969, "Heat transfer in rough tubes with tape-generated swirl flow", ASME Journal of Heat Transfer vol. 91, pp. 443-445.

[3] Usui, H., Sano, Y., Iwashita, K. and Isozaki A., 1986, "Enhancement of heat transfer by a combination of internally grooved rough tube and a twisted tape", Int. Chem. Eng., vol. 26 (1), pp. 97-104.

[4] Zimparov V. D., 2000, "Enhancement of heat transfer by a combination of single start corrugated tube with at twisted tape", Proceedings of the ASME-ZSITS Interna- tional Thermal Science Seminar, June 11-14, 2000, Bled, Slovenia (eds. A. E. Bergles and Iz. Golobic), pp.395-401.

[5] Zimparov, V. D., 2001, "Enhancement of heat transfer by a combination of three-start spirally corrugated tubes with a twisted tape", Int. J. Heat Mass Transfer, vol.44, pp. 551-574.

[6] Zimparov, V. D., Vulchanov, N. L. and Delov, L. B., 1991, "Heat transfer and friction characteristics of spirally corrugated tubes for power plant condensers –1. Experimental investigation and performance evaluation", Int. J. Heat Mass Transfer, vol. 34 (9), pp. 2187-2197.

[7] Bergles, A. E., Bunn R. L. and Junkhan, G. H., 1974, "Extended performance evaluation criteria for enhanced heat transfer surfaces", Letters of Heat and Mass Transfer, vol. 1, pp. 113-120.

[8] Webb, R. L., 1981, "Performance evaluation criteria for use of enhanced heat transfer surfaces in heat exchanger design", Int. J. Heat Mass Transfer, vol. 24, pp. 715-726.

[9] Bejan, A., 1982, "Entropy Generation Through Heat and Fluid Flow", Wiley, New York.

[10] Bejan, A., 1996, "Entropy Generation Minimization", CRC Press, Boca Raton.

[11] Zimparov, V. D., 2000, "Extended performance evaluation criteria for heat transfer surfaces: Heat transfer through ducts with constant wall temperature", Int. J. Heat Mass Transfer, vol. 43 (17), pp. 3137-3155.

[12] Marner, W. J, Bergles, A. E. and Chenoweth, J. M., 1983, "On the presentation of performance data for enhanced tubes used in shell-and-tube heat exchangers", ASME Journal of Heat Transfer, vol. 105, pp. 358-365.

HEFAT2002
1st International Conference on Heat Transfer, Fluid Mechanics, and Thermodynamics
8-10 April 2002, Kruger Park, South Africa
AC1

EMISSION TESTS AT FULL LOAD CONDITIONS IN WANKEL ENGINE

Arapatsakos I. Charalampos* and Sparis D. Panagiotis
*Democritus University of Thrace,Department of Agricultural Development, 68200 Orestiada
Greece
E-mail:xarapat@agro.duth.gr

ABSTRACT

It is generally accepted that the process of catalyst deactivation originates from the entrance sections of the converter and gradually progresses towards the exit. The purpose of this paper is to investigate the possibility of a catalyst operating life extension via a mounting inversion, when the catalyst is close to its limits in the normal position. The experimental results indicate that under full load conditions at 1000, 2000 and 3000 rpm improvement of catalyst efficiency can be accomplished reaching approximately 30% for CO and HC. This mounting inversion can be easily accomplished by an appropriate symmetric design of the monolith casing and mounting flanges, so that smooth gas flow conditions can be attained in both flow directions.

Keyword: catalyst inversion, gas emission

INTRODUCTION

The catalytic efficiency of a three-way converter (TWC) gradually deteriorates due to thermal, chemical and mechanical effects. If we exclude the case of an abrupt destruction due to extreme mechanical or thermal stresses or lead poisoning, it is generally accepted that, under normal operating conditions, the deterioration of catalyst efficiency due to chemical deactivation originates from the entrance sections of the converter and gradually progresses towards the exit. This phenomenon affects also the temperature of catalyst light off that is around 250°C for a new catalyst and tends to increase as the converter ages [1,2,3].

Some of the chemical effects that cause catalyst efficiency reduction are reversible, as HC and CO storage due to temporary λ sensor malfunction or engine misfire [4], whereas other processes as lead, sulfur, zinc poisoning are permanent. Thermal effects as Pt/Ph, Pd/Rh sintering are also permanent. Higher temperatures are normally measured near the exit of the converter, whereas the chemical deactivation of the catalyst surface is greater at the inlet section and gradually progresses to the interior as the catalyst ages [2,5,6]. Therefore, it is quite natural to investigate the possibility of a catalyst operating life extension via a mounting inversion, when the catalyst is close to its limits in the normal position. In this way the later sections of the catalyst that are normally more chemically active will form the new inlet section and could cause catalyst regeneration. This simple procedure is physically possible because the catalytic performance is strongly affected by the temperature of the exhaust gases. Therefore, as the converter ages and the chemically active region retreats to the exit sections, the temperature of the exhaust gases that reach this region becomes progressively lower due to the heat convection losses in the previous inactive region. This effect reduces the overall efficiency; the heat production and the gas temperature rise even further. On the other hand the proposed mounting inversion places the more active sections at the catalyst inlet where the exhaust gases are hotter, thus increasing the rate of catalysis, the heat production and the overall temperature level. The mounting inversion can be easily accomplished if a symmetric design of the monolith casing and mounting flanges is adopted, so that smooth gas flow conditions can be attained in both flow directions, a feature that is essential for high catalytic efficiency.

EXPERIMENT FACILITY

The tests were carried out on a MAZDA RX-7 2000 cm^3. This is a 4-cylinder engine with a multipoint injection. The experimental procedure included tests with normal and inverse catalyst mounting with constant engine speed under full load conditions. The catalyst which was used had exceeded exhaust limits (>150.000km).The test duration was 2500s. The engine speed was 3000 rpm. During the test the CO, HC emissions

were monitored and the catalyst inlet Ti and outlet To temperatures. For this purpose the HP 3497 Data Acquisition Unit was used interfaced to an IBM-486.
For the exhaust gas high temperature measurements K type thermocouples with a range 0-1100 °C were installed. Their response time was 0.2 s and their accuracy +/- 3 °C for 0-400 °C and +/- 0.75 % for 400- 1100 °C. The positions of the thermocouples are shown on picture 1.

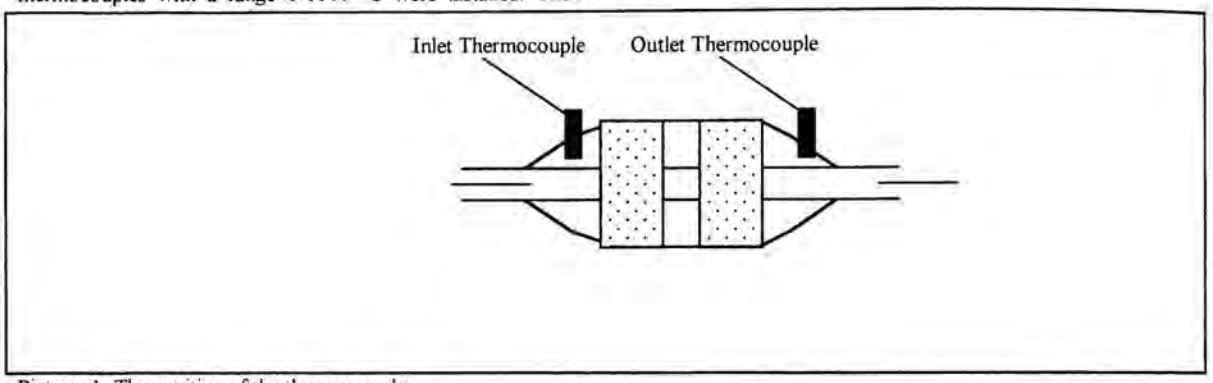

Picture. 1. The position of the thermocouples

For the CO, HC measurements the HORIBA MEXA-574E with an accuracy of 0 - 10% vol. for CO and 0 - 10000 ppm for HC NMOG. This unit uses for calibration a special gas mixture (n-hexane). With respect to the catalyst inverse mounting a suitable adapter was machined, however, the monolith operated in its original stainless steel casing. We will return to this point in a later section.

RESULTS AND DISCUSSION

The results obtained for the CO emissions and normal and inverse converter mounting are illustrated in Fig. 1.

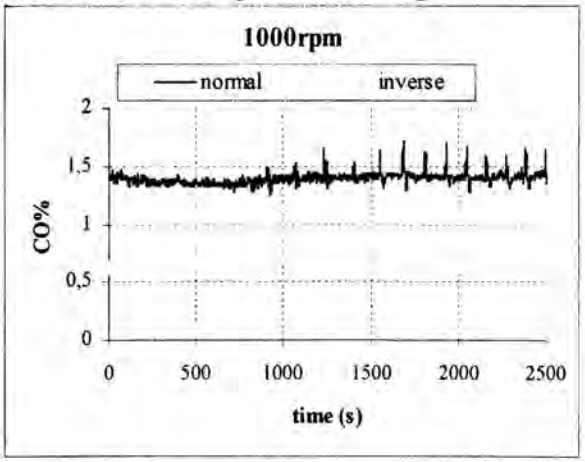

Figure 1. CO emissions for normal and inverse converter mounting at 1000rpm under full load conditions.

Figure 1 shows the CO in the case of normal and inverse converter. In case of the inverse converter mounting the CO emissions decreases.

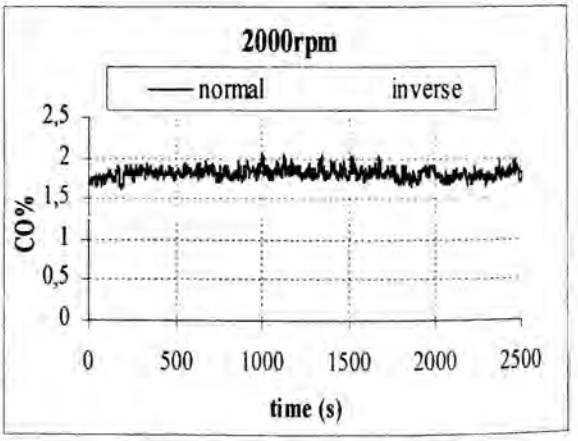

Figure 2. CO emissions for normal and inverse converter mounting at 2000rpm under full load conditions.

As in the case of figure 1, figure 2 shows the decrease of the CO emissions in the case of inverse converter mounting.

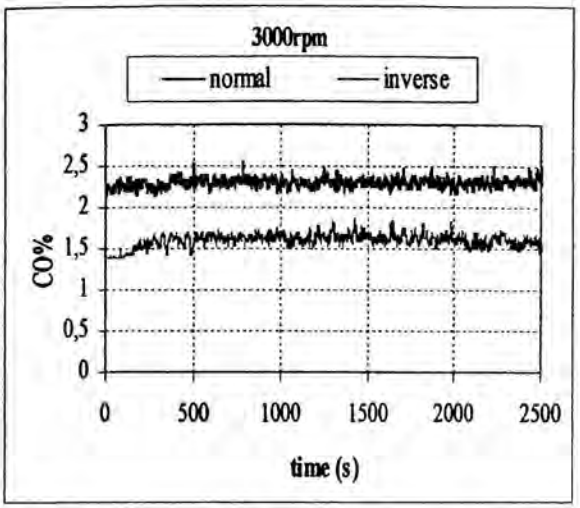

Figure 3. CO emissions for normal and inverse converter mounting at 3000rpm under full load conditions.

Figures 1, 2 and 3 shows that in 1000, 2000, 3000 rpm, in the case of inverse converter mounting the CO emissions decreases which indicates that the converter has a better function.

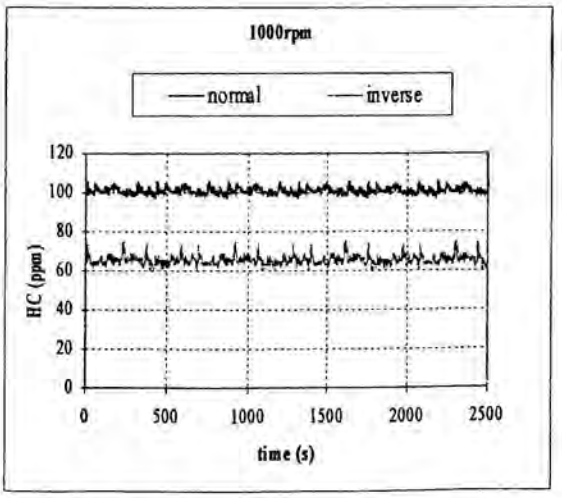

Figure 4. HC emissions for normal and inverse converter mounting at 1000rpm under full load conditions.

Also in the case of HC emissions the inverse converter produces lower emissions.

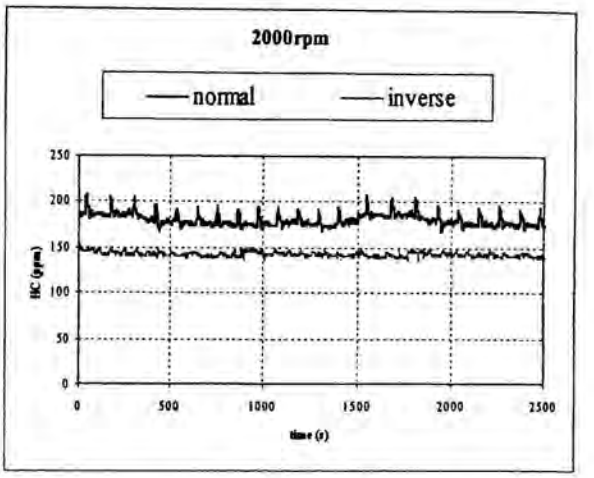

Figure 5. HC emissions for normal and inverse converter mounting at 2000rpm under full load conditions.

In figure 5 the corresponding HC emissions measurements are presented in the case of 2000 rpm. Figures 2, 5 indicate that the CO and the HC emissions decrease in the case of inverse converter.

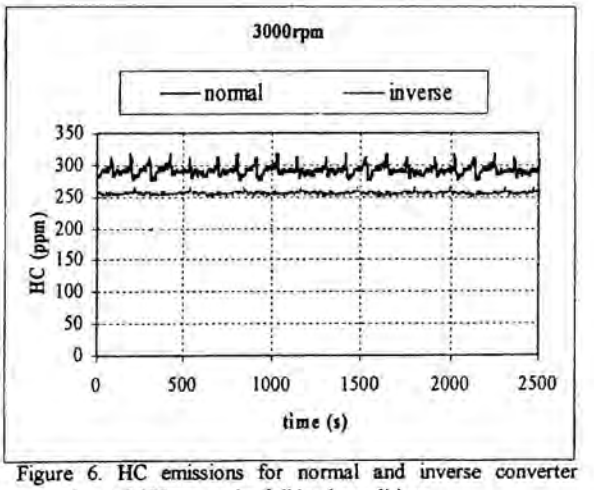

Figure 6. HC emissions for normal and inverse converter mounting at 3000rpm under full load conditions.

In all cases of different rpm (1000, 2000, 3000 rpm) decrease of emissions is observed. This means that the converter operates better.

During the experiments the temperature difference is also measured. It was observed that in the case of the inverse converter mounting the temperature difference in the catalyst (Tin-Tout) was smaller. This shows that the efficiency of the catalyst increases in the case of inverse mounting.

CONCLUSIONS

The present paper is an investigation of a possible catalyst life extension via inverse mounting. The tests were carried out using a converter with asymmetric design at the inlet and outlet sections. The experimental results indicate that during tests at full load at 1000, 2000 and 3000 rpm conditions there is a noticeable catalytic efficiency improvement for CO, HC.

It should be clear that the proper answers to these questions must be given through a series of future engine tests.

ACKNOWLEDGEMENTS

This work was conducted in Democritus University of Thrace – Greece from the authors

REFERENCES

[1]. Funabiki, M., Yamada, T., "A Study of Three-Way Conversion Catalyst Thermal Deactivation and Improvement", SAE Paper 881684, pp. 3.1185- 3.1143, 1985.

[2]. Pelters, S., Schwartzenthal, D., Maus, W., Swars, H., Bruck, R.,"Alternative Technologies for Studying Catalyst Behaviour to Meet OBD II Requirements", SAE Paper 932854, 1993.

[3]. Church, L.M., Thoss, E.J., Fizz, L.D., "Operating Temperature Effects on Catalyst Performance and Durability", SAE Paper 910845, pp. 1-9, 1991.

[4]. Sparis, P.D., Botsaris, P.N., Karkanis, A., "An Investigation of Three - Way Catalyst Rich Mixture Poisoning", ISATA Paper 95ATS860, 1995.

[5]. Burkholder, S., P., Cooper, B., J., "Effect of Aging and Testing Conditions on Catalyst Performance", SAE Paper 911734, pp. 254-259, 1991.

[6] Wendland, D.W., Matthes, W.R., "Visualisation of Automotive Catalytic Converter Internal Flows", SAE Paper 861554, pp. 6.729-6.742, 1986.

HEFAT 2002
1st International Conference on Heat Transfer, Fluid Mechanics, and Thermodynamics
8-10 April 2002, Kruger Park, South Africa
MB1

NEAR-STIRLING ENGINE REGENERATOR ANALYSES

B Muissa Mangaya * and Costa J Rallis **
Postdoctoral Researcher, **Emeritus Professor and Honorary Professorial Research Fellow
School of Mechanical, Aeronautical and Industrial Engineering, University of the Witwatersrand
Private Bag 3, Wits 2050, Johannesburg, South Africa

ABSTRACT

Stirling type engines use a regenerator to recycle energy which would otherwise be rejected to the surroundings. This is achieved by transferring energy stored at the end of one cycle to the next cycle.

An understanding of the behaviour of such devices has provided a major challenge over a long period of time. Comprehensive methods for analysing the performance of these devices in Stirling engines have been proposed by Organ [1, 2, 3] and by Finkelstein and Organ [4]. This paper attempts to throw some lights on the characteristics of these devices in Near-Stirling cycle engines.

The Near-Stirling regenerator behaviour is described by mass, momentum and energy (fluid and matrix) conservation equations. In its simplest description, parabolic equations are obtained. They are solved numerically using the Crank-Nicholson or Lax-Wendroff scheme with the boundary and initial conditions obtained from the cycle analyses.

A detailed analysis of the regenerator is important because the increase in fuel energy conversion efficiency is critically dependent on its correct operation. Although adequate for preliminary design purposes first- or second-order models do not predict accurately what is happening in the regenerator.

INTRODUCTION

The Near-Stirling cycle (figure 1) consists of [5, 6, 7, 8, 9, 10]:

- near-isothermal compression (1_C-2_C),
- constant volume regeneration (in the compressor: 2_C-3_C; in the expander: 2_E-3_E) and constant volume combustion (in the compressor: 3_C-4_C; in the expander: 3_E-4_E),
- near-isothermal combustion (4_E-5_E),
- near-isentropic expansion (5_E-6_E), and
- constant volume heat rejection to the regenerator (6_E-1_E).

An approximation to this cycle can be achieved by using a reciprocating compressor (1_C-2_C-3_C-4_C-5_C-1_C) and expander (1_E-2_E-3_E-4_E-5_E-6_E-7_E-1_E) connected to each other by a regenerator - usually a tube filled with a wire matrix. Intake (5_C-1_C) and compression (1_C-2_C) take place in the compressor. Combustion (3_E-5_E), isentropic expansion (5_E-6_E) and exhaust (6_E-1_E) occur in the expander. Just before the compressor piston reaches its top dead centre the delivery/transfer valve is opened. The working fluid is transferred from the compressor, via the regenerator to the expander - at essentially constant volume - and is heated up during this process. Fuel is then injected into the expander combustion chamber and burned at nearly constant volume. This is followed by near-isothermal combustion and then by near-isentropic expansion until the start of blowdown and exhaust. During the latter processes, energy is stored in the regenerator matrix before exiting to atmosphere.

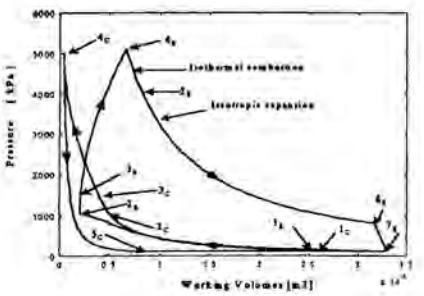

Figure 1: Calculated *p-V* diagrams for the compressor and expander [9]

The transfer process timing is optimized for minimal compression work and maximal energy conversion efficiency. This process is divided into two parts. No combustion takes place during the first part. The combustion starts in the expansion space during the second part of the transfer process. This leads to a transfer of mass from the compressor and the expander spaces into the regenerator. Since the achievement of a constant volume combustion process is a primary goal, transfer takes place from one reciprocating cylinder to another

one. In such a case the total volume, defined by the compression space, regenerator and expansion space remain essentially constant. Near-isothermal combustion can be achieved by the porous medium combustion technique [11]

Thermodynamic states prevailing during regeneration are known by cycle analyses of the Near-Stirling engine operation. For analysis purposes, the engine is divided into three control volumes - compressor, regenerator and expander. The latter two are always connected but all three are only interconnected during the transfer process. Analysis of the cycle is based on the application of the unsteady flow open system energy equation. Neglecting kinetic and potential terms, this is given by

$$\dot{Q} = \dot{W} + (\dot{m}h)_{out} - (\dot{m}h)_{in} + \frac{d}{d\tau}(mu) \qquad (1)$$

The proximate goal of these analyses is the determination of pressure-volume diagrams for the compression and expansion spaces (figure 1). The equation of state:

$$\frac{dp}{p} + \frac{dV}{V} = \frac{dm}{m} + \frac{dT}{T} \qquad (2)$$

is used together with equation (1).

NOMENCLATURE

A : area (m^2), coefficient
B : coefficient
Bi : Biot number ($Bi = h_c R / k$)
c : specific heat capacity, velocity of sound (kJ/kg K, m/s)
C : Courant number, coefficient
c_p : specific heat capacity at constant pressure (kJ/kg K)
c_v : specific heat capacity at constant volume (kJ/kg K)
D : equivalent diameter (m), coefficient
f : function of space and time
F, G, H : functions of space and time
Fo : Fourier number ($Fo = \alpha t / R^2$)
h : specific enthalpy (kJ/kg)
i : position reference
k : thermal conductivity (W/m K)
l : connecting rod length (m)
L_r : length of the regenerator (m)
m : mass (kg)
$\dot{m}$: mass flow rate (kg/s)
n : time reference
p : pressure, total pressure (Pa)
r : crank radius
r_c : volume compression ratio
r_e : volume expansion ratio
R : radius, gas constant (m, kJ/kg K)
Re : Reynolds number ($Re = \rho v d / \mu$)
s : specific entropy (kJ/kg)
t : characteristic time (s), time reference
T : temperature (K)
u : specific internal energy, velocity (kJ/kg, m/s)
U : total internal energy, fluid velocity (kJ, m/s)
v : specific volume, velocity (m^3/kg , m/s)
V : total volume (m^3)
$\dot{W}$: rate of work, power (kW)
x, y, z : spatial coordinates

Greek letters
α : thermal diffusivity ($\alpha = k / \rho c$)
γ : specific heat capacity ratio c_p / c_v
ρ : density (kg/m^3)
τ : time (s)
ω : angular velocity (rad/s)
ξ : friction coefficient

Subscript
c : convection
C: compressor
E : expander
m : matrix
p : constant pressure
s : constant entropy
v : constant volume
w : wall

Frictionless and constant section regenerator, with identical wall and fluid temperatures

Once the thermodynamic states in the compressor and in the expander have been solved, the gas dynamic model can be used to study the regenerator heat transfer and flow processes.

The following equations (mass, momentum and energy conservation) can be written [12]:

$$\frac{\partial \rho}{\partial t} + \frac{\partial (\rho U)}{\partial x} = -\rho U \frac{dA}{dx} \qquad (3)$$

$$\frac{\partial}{\partial t}(\rho U) + \frac{\partial}{\partial x}\left(\rho U^2 + p\right) = -\rho \frac{U^2}{A}\frac{dA}{dx} - \rho \frac{2\xi U|U|}{D} \qquad (4)$$

$$\frac{\partial}{\partial t}(\rho u) + \frac{\partial}{\partial x}\left[pU + \rho U u\right] = -\frac{4h_c\left[T - T_w\right]}{D\rho} - \frac{1}{A}\frac{dA}{dx}\left[\frac{1}{2}\rho U^3 + \frac{\gamma}{\gamma - 1}Up\right] \qquad (5)$$

For a frictionless regenerator, $\partial p/\partial x \approx 0$, $d\lambda/dx = 0$, $T \approx T_w$ equations (3), (4) and (5) become :

$$\frac{\partial \rho}{\partial t} + \frac{\partial (\rho U)}{\partial x} = 0 \qquad (6)$$

$$\frac{\partial U}{\partial t} + U\frac{\partial U}{\partial x} = 0 \qquad (7)$$

$$\frac{\partial (\rho u)}{\partial t} + \frac{\partial}{\partial x}[pU + \rho U u] = 0 \qquad (8a)$$

where $u = c_v T$ and $p = RT/v = \rho RT$.

Equations (8a) can also be written as

$$\frac{\partial}{\partial t}(\rho T) + \frac{\partial}{\partial x}(\rho \gamma U T) = 0 \qquad (8b)$$

Equations (6), (7) and (8b) are solved by the Lax-Wendroff scheme. The vector form of these equations is :

$$\frac{\partial F}{\partial t} + \frac{\partial G}{\partial x} = 0 \qquad (9)$$

The Lax-Wendroff one-step scheme is written as [12, 13, 14]

$$F_j^{n+1} = F_j^n - \frac{1}{2}\frac{\Delta t}{\Delta x}\left(G_{j+1}^n - G_{j-1}^n\right) + \frac{1}{4}\left(\frac{\Delta t}{\Delta x}\right)^2 \left(G'^n_{j+1} + G'^n_j\right)\left(G_{j+1}^n - G_j^n\right)$$

$$- \left(G'^n_j + G'^n_{j-1}\right)\left(G_j^n - G_{j-1}^n\right) \qquad (10)$$

where $G' = \partial G/\partial F$; n stands for the time increment and j for the position increment.

The scheme is based upon a Taylor series expansion with respect to time. It uses central differences for the spatial derivative and forward difference for the time derivative. For stability in the integration process, the time step and mesh size must satisfy the requirement that :

$$C = (|U| + c)\frac{\Delta t}{\Delta x} < 1 \qquad (11)$$

where

C , the Courant number
U , the velocity

$$c = \sqrt{\gamma RT} = \left(\frac{\partial p}{\partial \rho}\right)_s$$

Other schemes such as that of MacCormack or Stetter [13, 14] can also be used to find pressure, velocity, density and temperature distributions.

Fluid velocity at the entrance of the regenerator, for the compressor leading the expander by 40° of crankangle, is given by:

$$U(1,t) = -r_c \omega \sin\left[\left(\frac{\pi}{180}320\right) + (\omega t \Delta t)\right] + 0.5\frac{r_c}{l_c}\sin\left[2\left(\frac{\pi}{180}320\right) + (\omega t \Delta t)\right] \qquad (12)$$

At the exit of the regenerator, the fluid velocity is given by:

$$U(N_{j+1},t) = r_e \omega \sin\left[\left(\frac{\pi}{180}360\right) + (\omega t \Delta t)\right] + 0.5\frac{r_e}{l_e}\sin\left[2\left(\frac{\pi}{180}360\right) + (\omega t \Delta t)\right] \qquad (13)$$

In equation (12) and (13), the ratio $\pi/180$ stands for the conversion of degree to radian , while 320 and 360 stand for the phase difference between the compressor and the expander pistons.

Using equation (7) and the Lax-Wendroff scheme, the fluid velocity is given by :

$$U(i,t) = U(i,t-1) - 0.5\frac{\Delta t}{\Delta x}\left[\frac{U^2}{2}(i+1,t-1) - \frac{U^2}{2}(i-1,t-1)\right]$$

$$+ 0.25\left(\frac{\Delta t}{\Delta x}\right)^2\left[\left\{\left(U(i+1,i-1) - U(i,t-1)\right)\left(\frac{U^2}{2}(i+1,t-1)\right.\right.\right.$$

$$\left.\left.\left. - \frac{U^2}{2}(i,t-1)\right)\right\} - \left\{\left(U(i,t-1) - U(i-1,t-1)\right)\left(\frac{U^2}{2}(i,t-1)\right.\right.\right.$$

$$\left.\left.\left. - \frac{U^2}{2}(i-1,t-1)\right)\right\}\right] \qquad (14)$$

where i refers to the position and t to the time.

The pressure distribution is calculated using the equation of state

$$p = \rho RT \qquad (15)$$

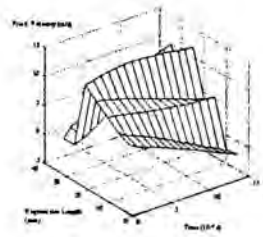

Figure 2 : Velocity distribution inside the regenerator (Lax-Wendroff scheme)

In figure 2, the fluid velocities at the regenerator ends (0 and 40 mm) correspond respectively to those at the compressor and the expander. From the compressor and moving into the regenerator, the fluid velocity increases linearly before decreasing at the regenerator exit to the expander value.

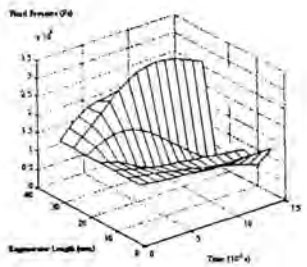

Figure 3: Pressure distribution inside the regenerator (Lax-Wendroff scheme)

In figure 3, the fluid pressures at the regenerator ends (0 and 40 mm) correspond respectively to those at the compressor and at the expander. As time increases, the fluid is more and more compressed inside the regenerator. The pressure in the compressor (0 mm) is almost constant and corresponds to the delivery pressure.

Frictionless and constant section regenerator, with identical matrix and fluid temperature distribution

Equations (6) and (7) still apply. Energy conservation for the fluid is given by:

$$\rho c_p \frac{\partial\left(\frac{T}{\gamma}\right)}{\partial t} + \rho c_p \frac{\partial}{\partial x}(UT) = -\frac{4h_c}{D\rho}(T - T_m) + k\frac{\partial^2 T}{\partial x^2} \qquad (16)$$

and energy conservation for the matrix is given by:

$$\rho_m c_m \frac{\partial T_m}{\partial t} = \frac{4h_c}{D\rho}(T - T_m) + k_m \frac{\partial^2 T_m}{\partial x^2} \qquad (17)$$

Assuming the same temperature distribution for the fluid and for the matrix, and adding (16) to (17) gives:

$$\frac{\partial T}{\partial t} + U\frac{\gamma}{\left(1 + \frac{\gamma\rho_m c_m}{\rho c_p}\right)}\frac{\partial T}{\partial x} - \frac{(k + k_m)}{\left(\frac{\rho c_p}{\gamma} + \rho_m c_m\right)}\frac{\partial^2 T}{\partial x^2} = 0 \qquad (18)$$

Equations (16), (17) and (18), in their general form can be written as [13]:

$$A\frac{\partial^2 f}{\partial x^2} + B\frac{\partial^2 f}{\partial x \partial t} + C\frac{\partial^2 f}{\partial t^2} + D\left(x, t, f, \frac{\partial f}{\partial x}, \frac{\partial f}{\partial t}\right) = 0 \qquad (19)$$

They are classed as parabolic ($B = C = 0$) and can be solved with appropriate assumptions.

The simplest scheme that can be used to solve equation (16), (17) and (18) is the explicit scheme [13, 15]:

$$\frac{f_i^{n+1} - f_i^n}{\Delta t} + A\frac{f_{i+1}^n - 2f_i^n + f_{i-1}^n}{\Delta x^2} + D\frac{f_{i+1}^n - f_{i-1}^n}{2\Delta x} = 0 \qquad (20)$$

where $x = i\Delta x$ and $t = n\Delta t$; $B = C = 0$.

For stability, time and space sizes are limited. In this scheme, a forward difference replaces the time derivative and a central difference replaces the space derivative. Both space and time are divided into discrete uniform intervals.

The Crank-Nicholson scheme can also be used to solve equations (16), (17) and (18). It is written as follows [13, 15]:

$$\frac{f_i^{n+1}-f_i^n}{\Delta t}=-D\frac{f_{i+1}^{n+1}-f_{i-1}^{n+1}}{2\Delta x}-D\frac{f_{i+1}^n-f_{i-1}^n}{2\Delta x}+A\frac{f_{i+1}^{n+1}-2f_i^{n+1}+f_{i-1}^{n+1}}{(\Delta x)^2}$$

$$+A\frac{f_{i+1}^n-2f_i^n+f_{i-1}^n}{(\Delta x)^2} \qquad (21)$$

The solution of equation (18) obtained using the Crank-Nicholson scheme (21) is obtained by Gaussian elimination or by an iterative method [15]. This is depicted by figure 4.

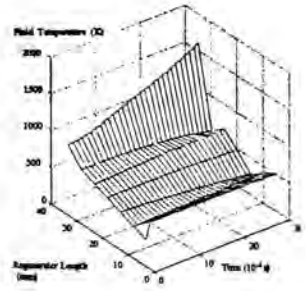

Figure 4: Temperature distribution inside the regenerator (Crank-Nicholson scheme)

In figure 4, it is observed that the fluid temperature varies slightly for the first 30 mm and then abruptly in order to reach the expander value. Only a small fraction of the regenerator is submitted to a large temperature gradient. The same phenomenon appears in the case of unsteady conduction and the term of skin depth has been introduced to characterize the part of the material affected by the thermal wave. The variation with time is not as accentuated as it is in the case of the fluid velocity and pressure.

Equations (3), (4) and (5) show that a source term can exist. In this case, the equations have the following vector form:

$$\frac{\partial F}{\partial t}+\frac{\partial G}{\partial x}=H \qquad (22)$$

The solution is given by the following Lax-Wendroff scheme [13]:

$$F_j^{n+1}=F_j^n-\frac{1}{2}\frac{\Delta t}{\Delta x}\left(G_{j+1}^n-G_{j-1}^n\right)+\Delta t H_j^n+\frac{1}{4}\left(\frac{\Delta t}{\Delta x}\right)^2\left[\left(G_{j+1}^n-G_j^n\right)\left(G_{j+1}^n-G_j^n\right)-\left(G_j^n-G_{j-1}^n\right)\left(G_j^n-G_{j-1}^n\right)\right] \qquad (23)$$

If the assumption of the same temperature distribution for the matrix and the fluid does not hold, the matrix temperature can be expressed as a function of the fluid temperature :

$$T_m=\frac{D\rho^2}{4h_c}c_p\frac{\partial\left(\frac{T}{\gamma}\right)}{\partial t}+\frac{D\rho^2}{4h_c}c_p\frac{\partial}{\partial x}(UT)-\frac{D\rho k}{4h_c}\frac{\partial^2 T}{\partial x^2}+T \qquad (24)$$

Equation (24) can be introduced into equation (17) and be solved numerically to get the fluid temperature.

CONCLUSIONS

- The aim of the analysis here is to present a third-order model for the design of the Near-Stirling regenerator. Since the fuel energy conversion efficiency increase depends mainly on its correct operation, it is then adequate to analyze it in more details. The general conservation equations are such a way of getting more insight in the operation of the regenerator.
- At low Reynolds numbers or high values of convective heat transfer coefficient, the heat exchange process reduces to pure unsteady conduction. A temperature front moves like a shock wave through the regenerator. The matrix temperature is identical to the fluid temperature. Analytical solutions exist [16] and are known as lumped parameter model (Bi < 0.1), semi-infinite solid (Bi >0.1; Fo < 0.05), complete series (Bi > 0.1; 0.05 < Fo < 0.2) and long - time approximate (Bi > 0.1 ; Fo > 0.2).
- As shown by different workers [17, 18, 19], the temperature distribution for both the matrix and the fluid can be time invariant and dependent only on the axial distance. In this case, the temperature difference between the fluid and the matrix is also time invariant along the regenerator.
- Although not dealing directly with regenerators, the work of Durst F and Weclas M [11] is also relevant. To solve the unsteady combustion in a porous medium, they define a short time-scale of heat transfer between the gas mixture and the porous medium. They also use parameters such as the Peclet number the Nusselt number, the Prandtl number, the Reynolds number and the porosity of the medium.

number, the Reynolds number and the porosity of the medium.

Kuwahara *et al.* carried out research on flow in porous media. Depending on the Reynolds number, the Peclet number and the direction of the flow, different flow patterns were obtained. Interesting cases with flow recirculation occurring inside the porous medium, resulting in thermal dispersion were pointed out [20].

ACKNOWLEDGMENTS

The authors would like to thank S Ramage and R Gunter of the Mechanical Engineering Computer Network, Wits University, Johannesburg.

REFERENCES

[1] Organ A J (1994). Solution of the Classic Thermal Regenerator Problem. *Proc. Instn Mech. Engrs, Part C, Journal of Mechanical Engineering Science*, 208 (C3), 187-197.

[2] Organ A J (1997). *The Regenerator and the Stirling Engine*, Mechanical Engineering Publications, London.

[3] Organ A J (2000). Regenerator Thermal Design in a Nutshell. *Journal of Mechanical Engineering Science*, Vol. 11, issue 11.

[4] Finkelstein T and Organ A J (2001). *Air Engines*, Instn Mech. Engrs Publications, UK.

[5] Rallis C J (1997). Near-Stirling Regenerative Engine Cycle. *Proceedings of the 8th International Stirling Engine Conference*, Ancona, Italy, pp. 189-198.

[6] Rallis C J and Muissa Mangaya B (1997). Lumped Parameter Computer Simulation of a Reciprocating Regenerative Internal Combustion Engine Operating on a Near-Stirling Cycle. *ibid.*, pp. 199-209.

[7] Rallis C J and Muissa Mangaya B (1999). Single Compression and Expansion of a Gas Contained in a Piston/Cylinder Arrangement in which Part of the Gas is Compressed Adiabatically and Part Isothermally. *Proceedings of the 9th International Stirling Engine Conference*, Pilanesburg, Republic of South Africa, pp. 165-175.

[8] Muissa Mangaya B and Rallis C J (1999). Modified Petter Engine Operating on a Near-Stirling Cycle. *ibid.*, pp. 207-215.

[9] Muissa Mangaya B and Rallis C J (2000). Preliminary Tests of a Near-Stirling Cycle Internal Combustion Engine. *Journal of Energy in Southern Africa*, Cape Town, Vol. 11, No 4, pp. 279-287.

[10] Muissa Mangaya B (2000). *The Design, Construction and Testing of a Modified Two-Cylinder Petter Engine Operating on a Near-Stirling Cycle*, PhD Thesis, School of Mechanical Engineering, University of the Witwatersrand, Johannesburg.

[11] Durst and Weclas M (2001). A New Type of Internal Combustion Engine Based on the Porous-Medium Combustion Technique. *Proc. Instn Mech. Engrs, Part D, Journal of Automobile Engineering*, Vol. 215, pp. 63-81.

[12] Heywood J B (1988). *Internal Combustion Engine Fundamentals*, McGraw-Hill Book Company, New York.

[13] Peyret R and Taylor T D (1983). *Computational Methods for Fluid Flow*, Springer-Verlag, New York.

[14] Bose T K (1988). *Computational Fluid Dynamics*, John Wiley & Sons, New York.

[15] Gerald C F and Wheatley P O (1994). *Applied Numerical Analysis*, fifth edition, Addison Wesley Publishing Company, New York.

[16] Mills A F (1992). *Heat Transfer*, Richard D Irwin Inc, Boston.

[17] Lazarides Y G, Rallis C J and Kilgour D B (1984). Analysis and Design of Regenerators for Stirling Cycles Machines. *Proceedings of the 19th IECEC*, San Francisco, California, pp. 2061-2066.

[18] Hausen H (1950). *Heat Exchange in Counter, Parallel and Cross Flow*, Springer, Berlin.

[19] Kays W M and London A L (1964). *Compact Heat Exchangers*, McGraw-Hill, New York.

[20] Kuwahara F, Nakayama A and Koyama H (1996). A Numerical Study of Thermal Dispersion in Porous Media. *Journal of Heat Transfer*, Vol. 118, pp. 756-761.

HEFAT 2002
1st International Conference on Heat Transfer, Fluid Mechanics, and Thermodynamics
8-10 April 2002, Kruger Park, South Africa
MB2

COMPRESSION AND EXPANSION OF A GAS IN A RECIPROCATING COMPRESSOR WITH ADIABATIC AND ISOTHERMAL SUB-SPACES

B Muissa Mangaya * and Costa J Rallis **
* Postdoctoral Research Fellow, Technikon Witwatersrand, P O Box 17011, Doornfontein 2028
** Emeritus Professor and Honorary Professorial Research Fellow
School of Mechanical, Aeronautical and Industrial Engineering, University of the Witwatersrand
Private Bag 3, Wits 2050, Johannesburg, South Africa

ABSTRACT

One of the major problems encountered in Stirling type engines is the achievement of isothermal compression. Closed cycle machines are restricted to the use of non-intrusive methods for transferring heat to the surroundings. Open cycle machines can use a number of ways to solve this problem. These include:

- the injection of volatile liquids into the compression space (open cycle machines),
- multi-stage compression with cooling between stages followed by aftercooling (closed and open cycle machines),
- use of a wire matrix mesh placed on the top of the compressor piston which is cooled at the end of each cycle by mixing with the cool clearance space air (reported in this paper) and,
- the use of a multiplicity of fins forming an integral part of the piston crown, the crank side of which is cooled continually by an oil spray (to be reported in a subsequent paper).

In order to establish the efficacy of the last two methods a research program was undertaken. This made use of the compression cylinder of a modified 2-cylinder Petter engine.

For both of the last two methods reported the compression space was made up of two subspaces – the usual adiabatic region and an isothermal space. Although the importance of the heat transfer to and from the matrix was established, the isothermalizer was not cooled sufficiently during the expansion of the clearance volume.

INTRODUCTION

In a previous publication [1], it was established that when dealing with two sub-spaces in a piston/cylinder arrangement, part of the gas in the adiabatic sub-space followed the path given by:

$$p\left(\frac{V_a^2}{T_a}\right)^{\frac{\gamma}{\gamma+1}} = \text{constant} \qquad (1)$$

In the isothermal sub-space, the variation of the mean temperature was given by the following expression:

$$\frac{dT_R}{\gamma T_a + T_R} = \frac{dm_a}{m_{tot} - m_a - m_m \frac{c_{v,m}}{c_v}} \qquad (2)$$

$$\dot{Q}_i + (\dot{m}h)_{in} = \frac{d}{d\tau}(mu)_{is} \qquad (3)$$

where

$$\dot{Q}_i = \frac{d}{d\tau}\left(m_m c_{v,m} T_R\right) \qquad (4)$$

$$(\dot{m}h)_{in} = c_p T_a \frac{dm_a}{d\tau} \qquad (5)$$

Equation (2) was derived by considering energy conservation in the isothermal sub-space:

Equations (1) and (2) were established for a single compression/expansion of the working fluid. To operate a compressor near-isothermally continuously, the mean temperature of the isothermal sub-space should be reset at its initial value, at each new cycle, by removing the heat given by equation (4).

APPARATUS

The engine used for the tests reported here was a 2-cylinder, water-cooled Petter compression engine modified to operate on our Near-Stirling cycle [1,2,3,4,5].

For the purpose of these tests the fuel system was disconnected and the cylinder head assembly containing the rotary valve removed and replaced by a flat plate cylinder head over the delivery reed valve assembly. This was connected to a

receiver, which could be pumped up to a predetermined value, and the pressure controlled by a throttle valve leak to atmosphere. The compressor cylinder pressure was measured with a Kistler piezoelectric transducer the output of which was fed to a Gould memory oscilloscope. A shaft encoder provided trigger pulses at ten-degree intervals. It also provided a top dead center marker.

The engine was set up on a transmission dynamometer test bed fitted with a variable speed motor/generator, and connected to the mains electrical power supply. This motor was used to drive the engine at different speeds. For the tests reported herein the motor torque was unfortunately not measured because of the failure of the strain gauge bridge. Rotational speed was measured with a hand-held tachometer. Although other readings were taken they are not relevant to the present set, and are thus not reported here.

NOMENCLATURE

c : specific heat capacity, velocity of sound (kJ/kg K, m/s)
c_p : specific heat capacity at constant pressure (kJ/kg K)
c_v : specific heat capacity at constant volume (kJ/kg K)
h : specific enthalpy (kJ/kg)
m : mass (kg)
$\dot{m}$: mass flow rate (kg/s)
p : pressure, total pressure (Pa)
$\dot{Q}$: heat transfer rate (kW)
T : temperature (K)
v : specific volume, velocity (m^3/kg , m/s)
V : total volume, cylinder volume (m^3)

Greek letters
γ : specific heat capacity ratio c_p / c_v
τ : time (s)
θ : crankangle (radians)

Subscript
a: dry air, initial value
ai: air in isothermal space
i : initial value, state of a substance entering a control volume
is : isothermal
m : matrix
out : state of a substance exiting a control volume
p : constant pressure
R : regenerator space
tot : total
v : constant volume

EXPERIMENTAL PROCEDURE

Two sets of motoring tests were carried out. One with a wire mesh isothermalizer fitted to the top of the compressor piston and the other with this replaced by a flat solid aluminium disc. For all the tests reported here the fuel system of the engine was disconnected and the cylinder barrels of the compressor and expander cylinder water-cooled. In all cases the engine was run at a steady speed for a while before taking test readings.

EXPERIMENTAL RESULTS

With a wire matrix isothermalizer

The following tests were carried out:

- compressor delivering to atmosphere, 357 rpm
- compressor delivering into a receiver (300 kPa), 425 rpm
- compressor delivering into a receiver (500 kPa), 520 rpm
- compressor delivering into a receiver (750 kPa), 413 rpm

In all cases, the delivery valve opened 60 degrees before the compressor piston reached its top dead center and, a pressure rise was recorded and identified as due to the spring loading of the delivery valve. Also, the maximum pressure occurred at the opening of the delivery valve.

Typical plots obtained are shown in figures 1 and 2. From figure 1 it is evident that although the compressor was delivering to the atmosphere the delivery valve only opened at a cylinder pressure of approximately 325 kPa. This was attributed to the spring loading of the delivery valve.

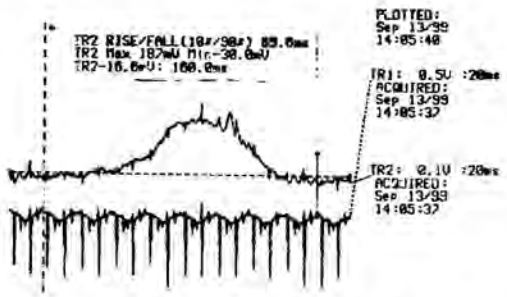

Figure 1: Compressor delivering to atmosphere, 357 rpm

All the oscilloscope plots obtained were analysed using a Matlab Code specially for that purpose.

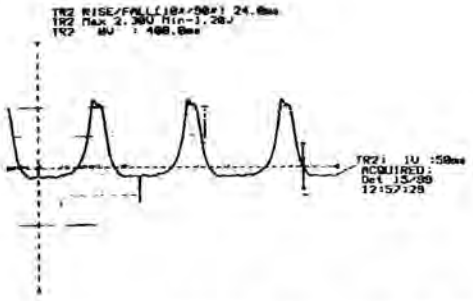

Figure 2: Compressor delivering into a receiver (700 kPa), 418 rpm

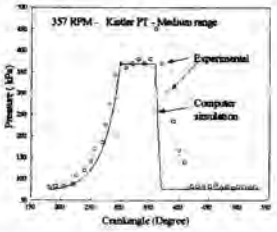

Figure 3: Pressure versus crankangle for the compressor delivering to atmosphere

Figure 3 shows a plot of the cylinder pressure versus crankangle for the compressor delivering to atmosphere. Evidently the compression process followed the lumped parameter simulation [6] fairly closely. However modeling the expansion process of the air remaining in the clearance space was totally inadequate. These results suggest that due to the presence of the regenerator matrix on the piston crown, heat transfer from the matrix to the expanding gas cannot be ignored. The gas temperature trend observed in the compressor during the expansion process appeared to remain close to the matrix mesh temperature. Introducing heat transfer into the lumped parameter model showed good agreement between experimental and simulated expansion curves as illustrates in figure 4.

Variations of the polytropic index 'n', in the path equation pV^n=constant, occurred during both the compression process and the expansion of the clearance volume air. Figure 5 shows a typical plot of $\ln(p/p_o)$ versus $\ln(V/V_o)$. The slopes of the various processes yield values of the index 'n'. From this figure it is evident that partial isothermalization occurred during the compression process since n (=1.18) is less than γ(=1.4). That is, heat is transferred *from* the working fluid *to* the matrix.

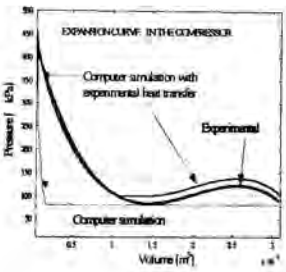

Figure 4: Experimental and simulation expansion curves for the compressor delivering to receiver (500 kPa), 520 rpm

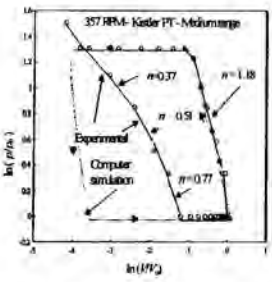

Figure 5: $\ln(V/V_o)$ versus $\ln(p/p_o)$ for the compressor delivering to atmosphere

Similarly heat was transferred *from* the regenerator matrix *to* the working fluid during expansion of the clearance volume air, the temperature of which tended to remain close to the temperature of the matrix mesh.

An analysis of the compressor when delivering into a receiver was carried out in the same way as the foregoing.

Without a wire matrix isothermalizer

In order to quantify the effect of the compressor isothermalizer on performance, tests were conducted without this device. It was replaced with a 5.8 mm thick aluminium plate. As can be seen in figure 6 the compression processes were significantly different. More work was needed to drive the compressor without the isothermalizer. However the volumetric efficiency was increased.

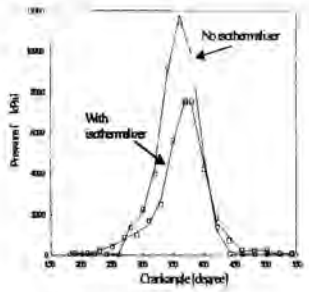

Figure 6: Experimental $p\theta$ diagram for compression process with and without isothermalizer

CONCLUSIONS

The lumped parameter model developed for the Near-Stirling engine proved an appropriate analysis and design tool. Only one domain was poorly described – the expansion process of the clearance gas in the compressor. This because no account was taken of heat transfer to and from the isothermalizer. The correlation between the lumped parameter model and experiment became very much better when provision was made for heat transfer to and from the wire matrix isothermalizer [6].

The use of a multiplicity of fins forming an integral part of the compressor piston crown, the crank side of which is continuously cooled by a lubricating oil spray, would appear to be indicated. Clearly the lubricating oil would have to be cooled by an external heat exchanger. Results using this concept will be reported in a subsequent paper.

ACKNOWLEDGMENTS

The authors would like to thank Mr Cooper and the technicians of the Mechanical Engineering North-West Laboratory, Wits University Johannesburg, for their willing assistance at all times.

REFERENCES

1. RALLIS C J. Near-Stirling regenerative engine cycle. *Proceedings of the 8th International Stirling Engine Conference, Ancona, Italy,* 1997, *pp 189-198*
2. MUISSA MANGAYA B and RALLIS C J. Preliminary tests of a Near-Stirling cycle internal combustion engine, *Journal of energy in Southern Africa*, Vol. 11, No 4, Novembre 2000, pp 279-287
3. RALLIS C J and MUISSA MANGAYA B. Lumped parameter computer simulation of a reciprocating regenerative internal combustion engine operating on a Near-Stirling cycle. *Proceedings of the 8th International Stirling Engine Conference,* 1997, pp 199-209
4. RALLIS C J and MUISSA MANGAYA B. Single Compression and Expansion of a Gas Contained in a Piston/Cylinder Arrangement in which Part of the Gas is Compressed Adiabatically and Part Isothermally. *Proceedings of the 9th International Stirling Engine Conference,* Pilanesburg, Republic of South Africa, 1999, pp 165-175.
5. MUISSA MANGAYA B and RALLIS C J. Modified Petter engine operating on a Near-Stirling cycle, *ibid.* , pp 207-215
6. MUISSA MANGAYA B. *The design, construction and testing of a modified two-cylinder Petter engine operating on a Near-Stirling cycle.* PhD Thesis. School of Mechanical Engineering, University of the Witwatersrand, Johannesburg, 2000.

HEFAT2002
1st International Conference on Heat Transfer, Fluid Mechanics, and Thermodynamics
8-10 April 2002, Kruger Park, South Africa
MM1

PREDICTING THE EFFECTS OF INJECTION PRESSURE ON DUAL FUEL COMBUSTION UNDER DIESEL CONDITIONS

M. Mbarawa
Department of Mechanical Engineering, Technikon Pretoria,
Private Bag X680, Pretoria 0001
South Africa
E-mail:mmbarawa@techpta.ac.za

ABSTRACT

The effects of diesel fuel pilot injection pressure on the dual-fuel (DF) combustion of natural gas (NG)-air mixtures under natural aspirated direct injection diesel engine conditions were studied experimentally in a constant volume combustion vessel (CVCV) and computationally using a three-dimensional (3D) combustion model. Experimental tests were conducted on the DF combustion of pre-mixed NG-air mixtures with diesel fuel pilot injection pressures of 30 MPa and 20 MPa respectively. The 3D model, incorporating complex interaction between the fuels during combustion, was used to predict the influences of diesel pilot injection pressures on the DF combustion of NG-air mixtures. The predictions of the effects of injection pressures were carried out by varying the nozzle hole diameter to maintain a constant mass of diesel fuel for the different injection velocities at different injection pressures. Four injection pressures were investigated; these being 20 MPa, 30 MPa, 60 MPa and 120 MPa. For these studies, the dimensions of the CVCV were taken as those of the experimental ones but the pre-ignition conditions of the NG-air mixture charge were simulated at the higher values more typical of natural aspirated direct injection diesel engine at Top Dead Center (P_o = 3MPa, T_o = 800 K). Predicted combustion pressure values compared well with experimental values although some incongruity between calculated and measured pressure results after the peak pressure was noticed. The reasons for this discrepancy are discussed in the paper. It is shown that the improvement of the NG-air mixtures combustion at any stage can be achieved by using higher injection pressures.

INTRODUCTION

In recent times, the importance of environment and energy are emphasized and among various energy sources, the fuels for automotive use are attracting attention as they are closely related to our daily life. The fossil fuels which are widely used nowadays have some serious problem. One of these is the limit in reserves, another that they cannot be recycled and yet another that they produce many kinds of pollutant emissions. As a consequence much research on the use of alternative to fossil fuel has been carried out. Of these NG has the outstanding advantage of being one of the most environmentally benign fuels, with most potential ozone reduction.

DF engines use a low cetane number primary fuel such as NG ignited by a pilot diesel spray so that alternative fuel is operationally viable. While they have existed for a considerable period of time in stationary installations, they are now being considered for road transport to help reduce both local and global emissions levels.

The combustion process in DF engines involve the ignition of a small quantity of pilot diesel fuel injected into a homogeneously premixed NG-air mixture. The introduction of a NG fuel with air in the cylinder modifies greatly the mixture formation and combustion process of the pilot diesel fuel spray which is usually retained to provide a deliberate source of ignition. The ignition and combustion of the small quantity of pilot diesel fuel contributes directly to the combustion of some of the entrained gaseous charge in its immediate vicinity and indirectly to the rest of the charge. The flame subsequently consumes the gas with the spray in the direct manner or establishes a progressive flame front which moves away from the ignition sources. However, the turbulent flame which moves away from the pilot ignition sources will not proceed throughout the charge when the concentration of the gaseous fuel is beyond a limiting concentration that would vary with the fuel being employed and local operating conditions. From this point of view, this type of the combustion has complex features of both diesel and Otto-cycle combustion. From diesel combustion, the combustion process is governed by spray characteristics such as the spray tip penetration, injection pressure, quantity of the pilot fuel employed etc. Higher injection pressure give more energy to the fuel and produce a finer, faster spray and faster tip penetration. Increased fuel

injection pressure in direct injection diesel engine has been found to be effective in improving the fuel/air mixing and reducing particulate emissions [11]. Although many studies have been reported on the effects of the injection pressure on the performance and emissions of direct injection diesel engines [7,10,11,13], information is lacking in the literature about the effects of pilot injection pressures on DF engines. Provision of such information would be beneficial, since the results thus obtained can be extremely useful in improving the performance and emissions of DF engines at the light load operations which is a crucial problem in these types of engines. This motivated the present study on the effects of pilot diesel fuel injection pressure on the combustion of NG-air mixtures.

The objective of this work was to develop a better understanding of the effects of pilot diesel fuel injection pressures on the combustion of NG-air mixtures. In this study only two sets of pilot diesel injection pressures were calibrated and verified due to the capability of the diesel fuel injection pump. However, high pilot diesel fuel injection pressures (60 & 120 MPa) which are found in real modern diesel engines were analyzed through numerical simulation.

NOMENCLATURE

a_i	Finite-difference coefficients	
A_A	Pre-exponential factor	$m^3.kg^{-1}.s^{-1}$
A_{eff}	Effective area	m^2
C_d	Discharge coefficient	
C_R	Reaction spread factor	
D	Diffusion flow rate	$kg.s^{-1}$
E_A	Activation energy	$kJ.mol^{-1}$
F	Convection flow rate	$kg.s^{-1}$
m	Mass	kg
P	Pressure	kPa
R_m	Fuel reaction rate in multi-fuel	$kg.m^{-3}.s^{-1}$
R_s	Fuel reaction rate in single fuel	$kg.m^{-3}.s^{-1}$
R_u	Universal gas constant	$kJ.kmole^{-1}\ K^{-1}$
S_c	Linearised source term	
S_ϕ	Source term in the model	
T	Temperature	°C
t	Time	ms
X	Mass fraction	
U_r, U_θ, U_z	Velocity	$m.s^{-1}$

Greeks letters

ϕ	Dependent variable	
Γ_ϕ	Eddy diffusivity	$kg.m^{-1}.s^{-1}$
ρ	Density	$kg.m^{-3}$

Subscripts

c	point indicator
E,W,N,S,T,B	face indicators
f	fuel
f	fuel
g	gaseous charge
m	mixture
O_2	oxygen
0	stagnation value
s	single fuel
r, θ, z	cylindrical co-ordinates

EXPERIMENT FACILITY

A schematic diagram of the experimental equipment is shown in Fig. 1. A CVCV was designed specifically for study of combustion process of NG-air mixtures. The CVCV consists of an outer casing, combustion chamber, heating element, insulation materials, injector and different fittings. The combustion chamber consists of an inner cylinder (chamber) and chamber head. An annealed copper ring was placed between the chamber and inner cylinder to prevent gas leakage. The inner cylinder has dimensions of 108 mm and 30 mm. The chamber head was machined to accept a water-cooled transducer and a water-cooled injector nozzle, which was located at the center of the CVCV. The injector was inserted to a depth of 8mm below the chamber head. A water-cooled piezoelectric pressure transducer and a thermocouple probe were placed at 10 and 17 mm respectively from the canter. In addition, different fittings for air, NG filling and for the discharge of exhaust gases were placed in the head of the CVCV. The CVCV was electrically heated and was pressurized so that quiescent pre-ignition conditions of NG-air mixtures

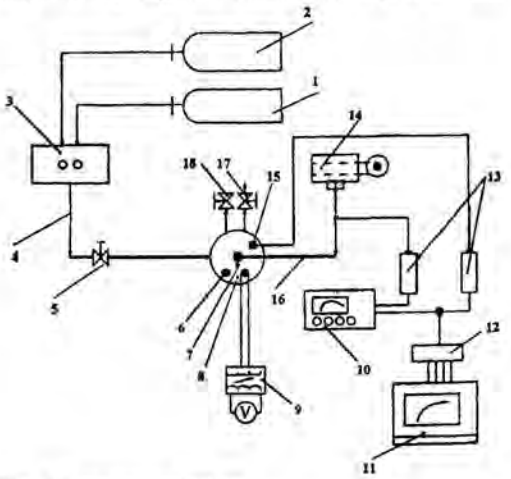

Fig. 1 Experimental set-up

1.compressed air, 2. compressed NG, 3. control panel, 4. air/NG line, 5. inlet valve, 6. thermocouple, 7. water cooled injector, 8. CVCV, 9. heater power supply control, 10. oscilloscope, 11. PC, 12. data acquisition, 13. charge amplifier, 14. fuel pump, 15. pressure transducer, 16. fuel line, 17. outlet valve, 18. safety valve

can be obtained. The heating element has a power of 1.5 kW at 240 V. To ensure that a minimum heat loss occurs, the inner chamber and outer casing were wrapped with econtronic ceramic fibre blanks, which can withstand continuous heat at temperature of up to 1640 °C.

In diesel engines the diesel fuel injection pumps driven continuously by cams, provide a regular, pulsed high pressure fuel output. For a CVCV a similar profile is required during injection, but it must consist of a single shot only. Thus a special diesel fuel injection device was developed using a multi-cylinder diesel engine injection pump (Caterpillar) driven by an electric motor. The pencil type injector with four holes was mounted centrally and vertically, spray from each orifice being oriented 15° below the horizontal. In the current experiments injection pressures of 20 MPa and 30MPa were used. Details of the experimental set-up and the procedures are described in Mbarawa [4].

BRIEF DESCRIPTION OF THE 3-D MODEL

A simplified 3D, numerical model [1] was developed for simulation of the DF combustion in the cylindrical CVCV. The model incorporates the main processes taking place in the chamber, i.e., fuel spray development, spray impingement on the wall, droplet evaporation, heat transfer and combustion which includes the complex interaction between the fuels. The NG may be incorporated into the system either pre-mixed with air or injected in a separate spray near the diesel spray. In this study, only the DF combustion with pre-mixed NG is reported. The diesel fuel is simulated in a similar, although simplified manner, to that of a normal diesel engine.

In the formulation, a cylindrical co-ordinate (r, θ, z) system was employed in which velocity components are denoted by (U_r, U_θ, U_z). The turbulence model is described by means of the κ-ε eddy diffusivity model of Launder and Spalding [3]. The governing equation consists of equations for continuity, momentum and energy in cylindrical co-ordinate expressed in general form as follows:

$$\frac{\partial(\rho_g\phi)}{\partial t}+\frac{1}{r}\frac{\partial(\rho_g r U_r\phi)}{\partial r}+\frac{1}{r}\frac{\partial(\rho_g U_\theta\phi)}{\partial\theta}+\frac{\partial(\rho_g U_z\phi)}{\partial z}$$
$$-\frac{1}{r}\frac{\partial}{\partial r}\left(r\Gamma_\phi\frac{\partial\phi}{\partial r}\right)-\frac{1}{r}\frac{\partial}{\partial\theta}\left(\frac{\Gamma_\phi}{r}\frac{\partial\phi}{\partial\theta}\right)-\frac{\partial}{\partial z}\left(\Gamma_\phi\frac{\partial\phi}{\partial z}\right)=S_\phi \qquad (1)$$

where,

- (ϕ) represents the dependent variables which denote either the mass fractions of the chemical species, the specific enthalpy or the momentum due to diesel evaporation
- Γ_ϕ is the effective diffusity;
- S_ϕ is the source term;
- ρ is the density

In reality, diesel fuel consists of many different components. However, because the diesel fuel in this dual-fuelling application supplies only a small proportion of the overall energy, it is, for simplification, considered here only as a single substance $C_{12}H_{26}$. This provides an approximate, average value of its properties. In this model, 16 chemical species are considered. They are diesel vapor ($C_{12}H_{26}$), the NG fuel components (CH_4, C_2H_6, C_3H_8), 11 dissociated species of air, NG and combustion products, H, O, N, OH, CO, NO, O_2, H_2O, CO_2, H_2, and N_2.

SOLUTION OF THE PARTIAL DIFFERENTIAL EQUATION

In the current model, equation [1] is discretised by using a finite volume method as suggested by Patankar [9]. The equation for ϕ can then be expressed as follows:

$$a_c\phi_c = a_W\phi_W + a_E\phi_E + a_N\phi_N + a_S\phi_S + a_T\phi_T + a_B\phi_B + s_c \qquad (2)$$

where, $a_i (i = E,W,N,S,T,B)$ are finite difference coefficients around the point. The convection-diffusion flux is evaluated using the power-law scheme.

$$a_i = D_i\left[0,\left(1-0.1\left|\frac{F_i}{D_i}\right|\right)^5\right]+[0,-F_i] \qquad (3)$$

where, F and D are the convection flow rate and the diffusion flow rate respectively.

COMPUTATIONAL METHOD

A finite-difference equation for each cell derived from equation (2) is solved implicitly in terms of time and space. All unknown variables at the next time step in every grid point are obtained by a Gauss–Seidel iteration [9]. The source terms required in the model are obtained from the sub-models of the pilot diesel injection, DF combustion of NG-air mixture and heat transfer.

The injector with its four equally spaced-holes is centered in the combustion chamber enabling the computation to be confined to one quarter of the chamber. For this, the computational domain consists of a single sector with 40 radial grid points, 44 in the azimuthal direction and 24 in the axial direction. Before the computational calculations were performed, a convergence grid study was undertaken, details of which are provided in Mbarawa [4].

DIESEL INJECTION AND ITS TRAJECTORY

The approach, developed by Hiroyasu and Nishida [2], was used for the fuel flow rate and spray penetration. The spray was assumed to be conical, divided arbitrarily into many 3D parcels. The spray cone was segmented at every calculation time step in the spray growth direction (L), into 3 layers in the radial (M) direction and 8 divisions in the circumferential (N) direction. The radial layer division in the N direction was staggered. The evaporation process was modeled from a quasi-steady analysis of a single droplet based on its heat and mass transfer. After the impingement on the wall the spray parcels were assumed to penetrate radially from the impingement point along the wall. The droplets in each spray parcel were assumed to be spherical with identical size, velocity and properties.

MIXED BURNING OF DISTILLATE AND NATURAL GAS

Chemical reaction schemes are available for simple hydrocarbons but these are not readily applicable to 3D modeling of either diesel or DF combustion. The basic model used is that given by Westbrook and Dryer [12]. That is, a simple global model [equation (4)] of the fuel-burning rate has been adopted.

$$R_{si} = -A_A \rho_g^{a+b} X_f^a X_{O_2}^b \exp\left(\frac{-E_A}{R_u T_g}\right) \quad (4)$$

Values for the various constants (A_A, a, b, and E_A) appropriate to the present study are given in Table 1.

The single fuel reaction rate of equation (4) considers only one fuel and the oxygen mass fractions. In the case of DF combustion, several fuel species react simultaneously modifying the diesel fuel combustion which is providing the ignition. All these fuel species are involved in the oxygen reaction and will interact to stimulate the chain reactions of others. Hence, a "reaction spread factor" C_R, [1] was introduced to evaluate the effect of the individual fuel reaction rates on the multi-fuel combustion. It applies to each fuel component i, i varying from 1 to n, where n is the number of individual fuels. To understand this, assume that the reaction rate of each fuel parcel, which consists of one of the n different fuels in the mixture, is R_{mi} when burning in the presence of all the other fuels. If it is defined such that the total reaction rate of the mixture R_m can be obtained by summing the individual values, then:

$$R_m = \sum_{i=1}^{n} R_{mi} \quad (5)$$

The value of R_{mi} will not be identical to the reaction rate R_{si} determined from equation (4), for the same fuel reacting alone at its appropriate mass fraction. To accommodate this difference, the presence of the other burning species is approximated by introducing the "reaction spread factor" which assumes that the principal modifying effect of the other fuels stems from their mass fractions. When applied to the global multi-fuel reaction, it gives:

$$R_m = R_{si} C_{R,i}^{a_i - 1}, \text{ where } C_{R,i} = \frac{\sum_{j=1}^{n} R_{sj}}{R_{si}} \quad (6)$$

Consider the burning of diesel fuel in a NG-air mixture. If the NG proportions approach zero, all the fuel species other than those of the diesel fuel become negligible. The reaction spread factor for the diesel fuel becomes unity (equation 6) and its reaction rate calculated by this method is identical to that of the diesel fuel from equation (4). The same argument applies to any of the other fuel species. However, when more than one fuel is in significant quantities, the reaction spread factor is not unity and the overall reaction rate from equation (6) is modified from that of equation (4).

Once an overall reaction rate has been determined, the procedure within the computational domain is relatively straightforward. That is, the temperature and hence the equilibrium combustion products can be calculated using well-known methods such as that of Olikara and Borman [8]. Subsequently, the heat release rate follows from the enthalpy difference of the products and reactants depending on their composition in each cell.

Table 1 Data for combustion calculations: constants for single-fuel reaction rates

Fuel Type	A_A ($m^3.kg^{-1}.s^{-1}$)	a	b	E, $kJ.mol^{-1}$
Diesel ($C_{12}H_{26}$)	6.96×10^6	1.25	1.50	100,000
Methane (CH_4)	1.87×10^8	0.70	1.30	202,000
Ethane (C_2H_6)	8.11×10^8	1.10	1.65	125,000
Propane (C_3H_8)	6.16×10^8	1.10	1.65	125,00

NG FUEL INTRODUCTION

During the pre-mixed DF combustion studies, the mass of NG can be determined simply from the ideal gas equation of state using the partial pressure of each constituent at the beginning of the test. This is because the pressure is low.

ACCURACY OF THE SIMULATION

Fig. 2 compares the calculated pressure traces for the injection pressure, over the full time period with experimental values. It can be seen that combustion is sensitive to the pilot distillate injection pressure. As injection pressure increases from 20 MPa to 30 MPa, the combustion pressure also increases. The pressure rise is due to the improved injection which increases the activity of the partial oxidation reactions and the overall temperature, thereby providing a greater ignition center and a larger combustion region. Consequently, the burning of the NG fuel takes place rapidly. The decay following the combustion peak is predominantly due to the heat transfer only in the numerics while in the experiments the time constant of the pressure transducer provides an additional

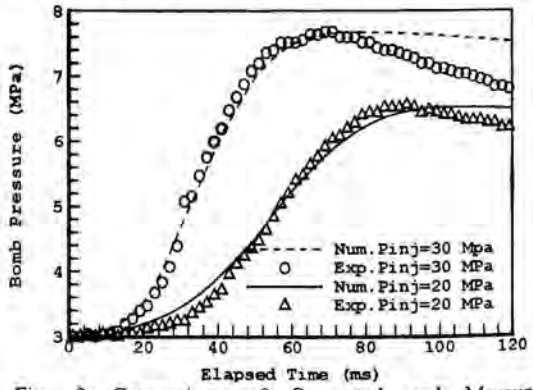

Fig. 2 Comparison of Computed and Measured Combustion Vessel Pressure for different Injection Pressures, P_g= 0.08 MPa, P_o= 3Mpa, T_o= 623 K

effect. The numerical heat transfer model may require some improvement but the good agreement to the point of maximum pressure indicates that it is adequate. Some pressure leakage from the CVCV may have occurred in the experiments but tests for this indicate that it is minimal.

RESULTS AND DISCUSSION

A detailed analysis has been carried out to investigate both the spatial and temporal variation of the DF combustion of NG-air mixtures with different diesel injection pressures.

For this study, the dimensions of the combustion chamber for the numerical analysis were taken as being identical to those of the experimental CVCV but the other parameters, such as air charge temperature, pressure and diesel injection pressure were simulated using higher values similar to those which apply in real natural aspirated diesel engines (i.e 3 MPa, 800K). The partial pressure of NG was taken as 0.2 MPa, thus giving a NG/air equivalence ratio ϕ_{NG} of 0.72. In general, it takes long computing time to generate the results. Therefore, the results reported here were for only part of the combustion period (40 ms). The predicted values are pressure, temperature, mass of diesel vapor, mass of unburnt methane and mass of unburnt ethane. All these data vary with time.

Four different injection pressures were examined, the nozzle diameter being varied to maintain a constant mass of fuel injected for the different injection velocity. Four different configurations of injector nozzles investigated in this study are shown in Table 2.

Table 2 Calculation conditions for the study of Injection Pressure on the DF Combustion of NG-air mixture

	K1	K2	K3	K4
Diesel Injection Pressure (MPa)	120	60	30	20
Diesel Injected Mass (mg)	26.7	26.7	26.7	26.7
Nozzle hole dia. (mm)	0.123	0.148	0.178	0.2

Fig. 3 shows pressure traces for different diesel fuel injection pressures. In all four cases during the early stages of combustion, the burning of the NG is restricted to a small region near the injector. This is due to the high combustion temperature resulting from the initial, rapid combustion which tends to vaporize the fuel spray so quickly that the diesel fuel is unable to penetrate deeply into the combustion chamber. As the combustion continues, a slowly propagating flame front moves across the chamber. When the pilot-diesel injection pressure is increased from 20 MPa to 120 MPa, the combustion pressure rise rate becomes higher as does the corresponding mass averaged gas temperature (Fig. 4).

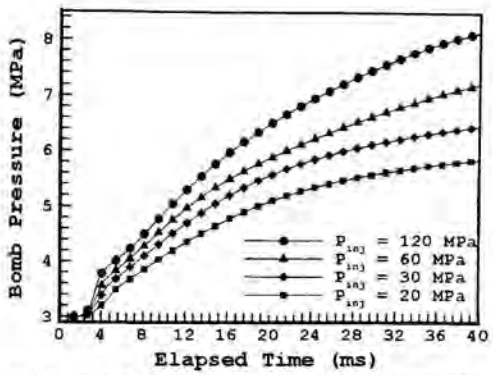

Fig. 3 Effects of Injection Pressure on the Combustion Pressure. P_g =0.2MPa

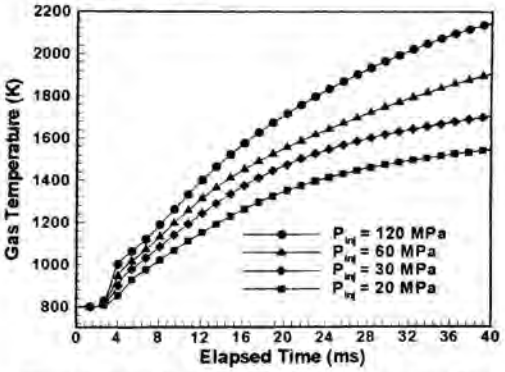

Fig. 4 Effects of Injection on Gas Temperature, P_g = 0.2 MPa

Fig. 5 compares mass of distillate vapor at different injection pressures. The mass of distillate vapor for all injection pressures peaks at approximately the same time and accounts for nearly all diesel fuel injected. This implies that the rate of vaporization is much the same for all cases. The consumption of diesel vapor in combustion reactions is higher at 120 MPa than at lower injection pressures, due to the improvement in the diesel vapor/air mixing.

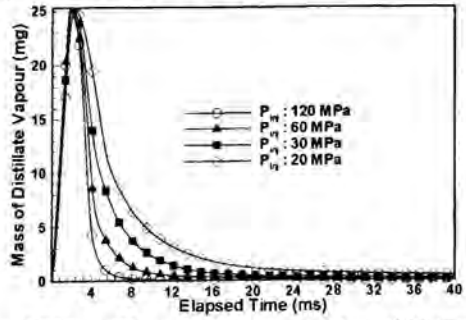

Fig. 5 Effects of Injection Pressure on Mass of Distillate Vapor

The methane starts to burn between 1 and 2 ms after the diesel fuel injection is nearly completed. Following this, the flames from the various ignition centers originating from the pilot diesel fuel propagate throughout the chamber. As the pilot fuel pressure increases, the burning rate of the methane rises faster. As shown Figure 6, at 40 ms, about 26mg of methane (case K1) has burnt compared with the case K4, where only about 14 mg of methane has burnt. The main reason for this is that, as the pilot injection pressure increases, the outlet velocity and spray penetration increase. This produces an increased quantity of well-mixed combustible gases of the two fuels before ignition. As a result, the pilot fuel will burn faster which will increase the activity of the partial oxidation reactions by increasing the overall temperature, thereby providing a greater multiplicity centers and a larger combustion zone. A similar effect occurs with the ethane in the NG although its burning commences almost simultaneously with the diesel and it is consumed at a much faster rate than the methane as shown in Fig. 7.

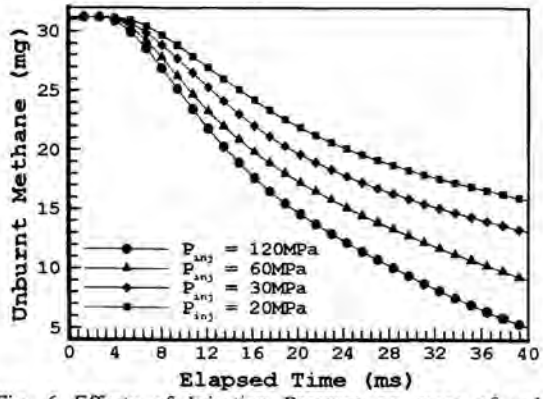

Fig. 6 Effects of Injection Pressure on mass of unburnt methane, P_g = 0.2 MPa

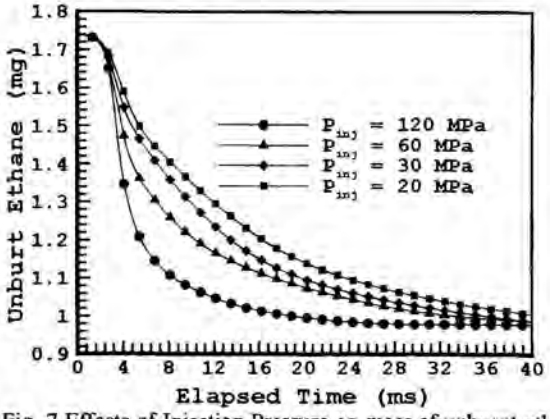

Fig. 7 Effects of Injection Pressure on mass of unburnt ethane, P_g = 0.2 MPa

LOCAL VARIATIONS WITHIN THE COMBUSTION CHAMBER

In addition to the global effect, it is informative to examine the local variations. Since the main aim of this study was to examine the effects of the injection pressure on the DF combustion of NG-air mixture, it is necessary to select a fixed time to examine these effects for all cases, rather that to select different times to examine progression of the combustion of one case only. Hence, the present study the gas temperatures are plotted at 16 ms after injection to examine the combustion and flame propagation throughout the NG-air mixtures. The contour plots are drawn along the pilot distillate spray axis in the r-θ section (top) and the r-z section (bottom). From these contour (see Fig. 8) it is clearly shown that the spray enveloped has barely reached the chamber walls for 20 MPa, whereas for the 120 MPa the envelope fills a large part of the chamber quadrant. Also, it can been seen that the flame propagates into the inner region of the diesel spray plume while simultaneously progressing outwards across the combustion chamber.

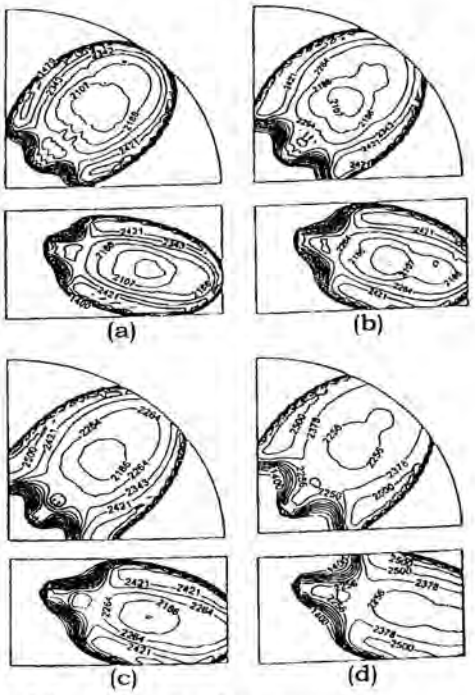

Fig. 8 Spatial variation of gas temperature.
(a) 20 MPa, (b) 30 MPa, (c). 60 MPa, (d) 120MPa

Fig. 9 a (top views) and 9 b (side views) show the % of the area covered by the flame at 16 ms for each injection pressure. As the pilot injection pressure increases, the faster the flame

propagation throughout the chamber. The rate of change is most noticeable from 20 MPa to 60 MPa.

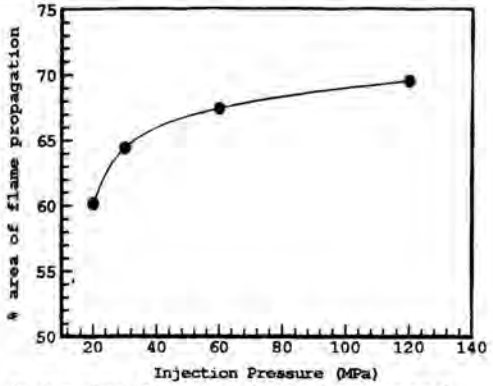

Fig. 9a (top view) Effects of Injection Pressures on the Flame Propagation

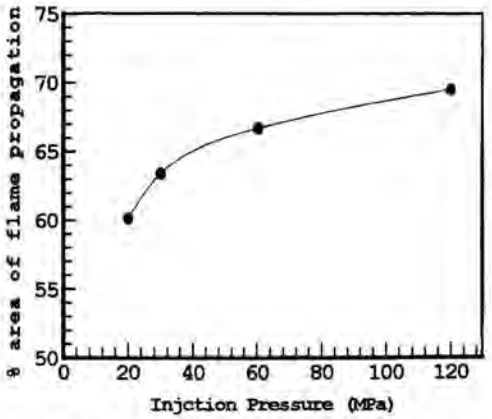

Fig. 9b (bottom view) Effects of Injection Pressure on the Flame Propagation

CONCLUSIONS

The present work has highlighted the importance of the effects of the injection pressures on the DF combustion of NG-air mixtures. The study provides some suggestion for the improvement of DF combustion of NG-air mixtures.

The CVCV has provided useful data for validation of the model. However, it was difficult to obtain normal diesel engine pre-ignition conditions, such as higher pressure and temperature, swirling and turbulence. Hence, further verification of these effects is required to be carried out in a real diesel engine, where its combustion process is quite different from the quiescent nature of the combustion of CVCV. The 3D model has been used to examine the effects of injection pressures of the pilot spray fuel on the DF combustion of NG-air mixtures and the important conclusions of the study can be summarized as follows:

- The results show good agreement between measured and predicted cylinder pressure. However, at the tail of the burning period, the experimental results fall more rapidly than do those of the simulation.
- When the injection pressure increases from 20 MPa to 60 MPa (a factor of 3), the combustion pressure increases by 30 % at 40 ms. Higher fuel injection pressures, give faster burning of the gaseous fuels.
- The results show that the high injection pressure has the beneficial effect of increasing the performance of the combustion of NG-air mixtures.

ACKNOWLEDGMENTS

The author would like to thank Prof. Brain Milton and Dr. Robert Casey of University of the New South Wales for providing significant valuable suggestions in this study.

REFERENCES

1. Choi, I.S and Milton, B.E., "Dual -Fuel Combustion with Injected Natural Gas and Distillate", Int. Symposium on Advanced Computational Heat Transfer, Cesme, Turkey, 1997.
2. Hiroyasu, H. and Nishida, K., "Fuel spray trajectory and dispersion in a DI diesel combustion chamber". SAE Paper 890462.
3. Launder, B. E. and Spalding, D. B., "The Numerical Computation of Turbulent Flows", Computer Methods in Applied Mechanics and Engineering, Vol. 3, pp 269-289, 1974.
4. Mbarawa, M., "Problems Related to the Combustion of Gaseous Fuels (Natural Gas) in Diesel Engines", PhD Thesis, University of New South Wales, 1998.
5. Mbarawa, M., Casey, R. T. and Milton, B. E., " Experiments and Numerical simulation of the dual-fuel combustion process for a constant volume combustion vessel", 4th Asian-Pacific International Symposium and Energy Utilisation, p 421-434, 1997.
6. Mbarawa, M., Milton, B.E. and Casey, R. T., "Simulated ignition of Natural Gas at Compression Ignition Conditions", Proceeding Symposium on Energy Engineering in the 21th Century (SEE). Hong Kong Italy, pp 1524 - 1531, 2000.
7. Oblaender, K., Kollmann, K., Kraemer, M., and Kutschera, L., "The Influence of High Pressure Injection on Performance and Exhaust Emissions of a High Speed Direct Injection Diesel Engine", SAE Paper 890438, 1989.
8. Olikara, C. and Borman, G. L., (975), "A Computer Program for Calculating Properties for Equilibrium Combustion Products with Some Applications to IC Engines", SAE Paper 750468.

9. Patankar, S. V., "Numerical Heat Transfer and Fluid Flow", Hemisphere Publishing Corporation, 1980.
10. Pierpont, D. A., and Reitz, R. D., "Effects of Injection Pressure and Nozzle Geometry on D I. Diesel Emissions and Performance", SAE Paper 950604.
11. Su, T. F., Chang, C. T., Reitz, R. D., Farrell, P. V., Pierpont, A. D and Tow, T. C., "Effects of Injection and Nozzle Geometry on Spray and D. I. Emissions"' SAE Paper No. 952360 (1995).
12. Westbrook, C. K. and Dryer, F. L., "Simplified Reaction Mechanisms for the Oxidation of Hydrogen Fuels in Flames Combustion Science and Technology, Vol. 27, 31-43", 1981.
13. Xu, M., Nishida, K., and Hiroyasu, H., A practical calculation method for injection pressure and spray penetration in diesel engines. S.A.E. Paper 920624, (1992).

AUTHOR INDEX